

Zhenkun Wen
Tianrui Li *Editors*

Practical Applications of Intelligent Systems

Proceedings of the Eighth International
Conference on Intelligent Systems and
Knowledge Engineering, Shenzhen,
China, Nov 2013 (ISKE 2013)

Advances in Intelligent Systems and Computing

Volume 279

Series editor

Janusz Kacprzyk, Polish Academy of Sciences, Warsaw, Poland
e-mail: kacprzyk@ibspan.waw.pl

For further volumes:
<http://www.springer.com/series/11156>

About this Series

The series “Advances in Intelligent Systems and Computing” contains publications on theory, applications, and design methods of Intelligent Systems and Intelligent Computing. Virtually all disciplines such as engineering, natural sciences, computer and information science, ICT, economics, business, e-commerce, environment, healthcare, life science are covered. The list of topics spans all the areas of modern intelligent systems and computing.

The publications within “Advances in Intelligent Systems and Computing” are primarily textbooks and proceedings of important conferences, symposia and congresses. They cover significant recent developments in the field, both of a foundational and applicable character. An important characteristic feature of the series is the short publication time and world-wide distribution. This permits a rapid and broad dissemination of research results.

Advisory Board

Chairman

Nikhil R. Pal, Indian Statistical Institute, Kolkata, India
e-mail: nikhil@isical.ac.in

Members

Rafael Bello, Universidad Central “Marta Abreu” de Las Villas, Santa Clara, Cuba
e-mail: rbellop@uclv.edu.cu

Emilio S. Corchado, University of Salamanca, Salamanca, Spain
e-mail: escorchado@usal.es

Hani Hagrass, University of Essex, Colchester, UK
e-mail: hani@essex.ac.uk

László T. Kóczy, Széchenyi István University, Győr, Hungary
e-mail: koczy@sze.hu

Vladik Kreinovich, University of Texas at El Paso, El Paso, USA
e-mail: vladik@utep.edu

Chin-Teng Lin, National Chiao Tung University, Hsinchu, Taiwan
e-mail: ctlin@mail.nctu.edu.tw

Jie Lu, University of Technology, Sydney, Australia
e-mail: Jie.Lu@uts.edu.au

Patricia Melin, Tijuana Institute of Technology, Tijuana, Mexico
e-mail: epmelin@hafsamx.org

Nadia Nedjah, State University of Rio de Janeiro, Rio de Janeiro, Brazil
e-mail: nadia@eng.uerj.br

Ngoc Thanh Nguyen, Wroclaw University of Technology, Wroclaw, Poland
e-mail: Ngoc-Thanh.Nguyen@pwr.edu.pl

Jun Wang, The Chinese University of Hong Kong, Shatin, Hong Kong
e-mail: jwang@mae.cuhk.edu.hk

Zhenkun Wen · Tianrui Li
Editors

Practical Applications of Intelligent Systems

Proceedings of the Eighth International
Conference on Intelligent Systems
and Knowledge Engineering, Shenzhen,
China, Nov 2013 (ISKE 2013)

 Springer

Editors

Zhenkun Wen
College of Computer and Software
Engineering
Shenzhen University
Shenzhen
China

Tianrui Li
School of Information Science
and Technology
Southwest Jiaotong University
Chengdu
China

ISSN 2194-5357

ISSN 2194-5365 (electronic)

ISBN 978-3-642-54926-7

ISBN 978-3-642-54927-4 (eBook)

DOI 10.1007/978-3-642-54927-4

Springer Heidelberg New York Dordrecht London

Library of Congress Control Number: 2014939406

© Springer-Verlag Berlin Heidelberg 2014

This work is subject to copyright. All rights are reserved by the Publisher, whether the whole or part of the material is concerned, specifically the rights of translation, reprinting, reuse of illustrations, recitation, broadcasting, reproduction on microfilms or in any other physical way, and transmission or information storage and retrieval, electronic adaptation, computer software, or by similar or dissimilar methodology now known or hereafter developed. Exempted from this legal reservation are brief excerpts in connection with reviews or scholarly analysis or material supplied specifically for the purpose of being entered and executed on a computer system, for exclusive use by the purchaser of the work. Duplication of this publication or parts thereof is permitted only under the provisions of the Copyright Law of the Publisher's location, in its current version, and permission for use must always be obtained from Springer. Permissions for use may be obtained through RightsLink at the Copyright Clearance Center. Violations are liable to prosecution under the respective Copyright Law. The use of general descriptive names, registered names, trademarks, service marks, etc. in this publication does not imply, even in the absence of a specific statement, that such names are exempt from the relevant protective laws and regulations and therefore free for general use.

While the advice and information in this book are believed to be true and accurate at the date of publication, neither the authors nor the editors nor the publisher can accept any legal responsibility for any errors or omissions that may be made. The publisher makes no warranty, express or implied, with respect to the material contained herein.

Printed on acid-free paper

Springer is part of Springer Science+Business Media (www.springer.com)

Preface

This book is a part of the Proceedings of the Eighth International Conference on Intelligent Systems and Knowledge Engineering (ISKE 2013) held in Shenzhen, China, during November 20–23, 2013. ISKE is a prestigious annual conference on ISKE with the past events held in Shanghai (2006, 2011), Chengdu (2007), Xiamen (2008), Hasselt, Belgium (2009), Hangzhou (2010), and Beijing (2012). Over the past few years, ISKE has matured into a well-established series of international conferences on Intelligent Systems and Knowledge Engineering and related fields over the world.

ISKE 2013 received 609 submissions in total from about 1,434 authors from 18 countries (United States of America, Singapore, Russian Federation, Saudi Arabia, Spain, Sudan, Sweden, Tunisia, United Kingdom, Portugal, Norway, Korea, Japan, Germany, Finland, France, China, Argentina, Australia, and Belgium). Based on rigorous reviews by the Program Committee members and reviewers, among 263 papers contributed to ISKE 2013; high-quality papers were selected for publication in the proceedings with an acceptance rate of 43 %. The papers were organized into 22 cohesive sections covering all major topics of intelligent and cognitive science and applications. In addition to the contributed papers, the technical program included four plenary speeches by Ronald R. Yager (Iona College, USA), Yu Zheng (Microsoft Research Asia), and Hamido Fujita (Iwate Prefectural University, Japan).

As organizers of this conference, we are grateful to Shenzhen University, Science in China Press, Chinese Academy of Sciences for their sponsorship, grateful to IEEE Computational Intelligence Society, Chinese Association for Artificial Intelligence, State Key Laboratory on Complex Electronic System Simulation, Science and Technology on Integrated Information System Laboratory, Southwest Jiaotong University, University of Technology, Sydney for their technical co-sponsorship. We would also like to thank the members of the Advisory Committee for their guidance, the members of the International Program Committee and additional reviewers for reviewing the papers, and members of the Publications Committee for checking the accepted papers in a short period of time. Particularly, we are grateful to the publisher, Springer, for publishing the proceedings in the prestigious series of *Advances in Intelligent Systems and Computing*. Meanwhile, we wish to express our heartfelt appreciation to the plenary speakers, special session organizers, session chairs, and student helpers.

In addition, there are still many colleagues, associates, and friends who helped us in immeasurable ways. We are also grateful to them all. Last but not the least, we are thankful to all the authors and participants for their great contributions that made ISKE 2013 successful.

November 2013

Zhenkun Wen
Tianrui Li

Contents

| | |
|---|----|
| Knowledge-Based Expressive Technologies Within Cloud Computing Environments | 1 |
| Sergey V. Kovalchuk, Pavel A. Smirnov, Konstantin V. Knyazkov, Alexander S. Zagarskikh and Alexander V. Boukhanovsky | |
| Video Texture Smoothing Based on Relative Total Variation and Optical Flow Matching | 13 |
| Huisi Wu, Songtao Tu, Lei Wang and Zhenkun Wen | |
| Gas Recognition Under Sensor Drift by Using Deep Learning | 23 |
| Xiaonan Hu, Qihe Liu, Hongbin Cai and Fan Li | |
| Wheel Slip Ratio Adaptive Control for Distributed Drive Electric Vehicles | 35 |
| Yongqiang Deng, Liang Shao, Chi Jin and Lu Xiong | |
| Active Disturbance Rejection Control for Tension Regulation of Stainless Steel Strip Processing Line | 47 |
| Wei Zhang, Yin Cai, Bo Deng and Xiaolan Yao | |
| An Improved Coupled Metric Learning Method for Degraded Face Recognition | 59 |
| Guofeng Zou, Shuming Jiang, Yuanyuan Zhang, Guixia Fu and Kejun Wang | |
| A New Phase Estimator of Single Sinusoid by Restricted Phase Unwrapping | 71 |
| Fang Wang, Yong Chen and Zhiqing Ye | |
| An Improved Concurrent Multipath Transfer Mechanism in Wireless Potential Failure Network | 83 |
| Wenfeng Du, Liqian Lai and Shubing He | |

| | |
|--|-----|
| Model-Based Testing of Web Service with EFSM | 91 |
| Fuzhen Sun, Lejian Liao and Longbo Zhang | |
| Data Fault Detection Using Multi-label Classification in Sensor Network | 101 |
| Zhenhai Zhang, Shining Li and Zhigang Li | |
| A Cloud Evolution Based Handoff Decision Scheme with ABC Supported | 113 |
| Cheng-Bo Zhang, Xing-Wei Wang and Min Huang | |
| Ultra-Wideband Pulse Generator for Heart-Rate Monitor | 123 |
| Xiaoyan Liu, Zheng Fang and Jianguang Zhou | |
| Pseudorange Differential GPS-Based Relative Navigation for UAV Formation Flight | 133 |
| Hongyu Yang, Yandong Wang, Haifeng Fu and Jian Liu | |
| Image Fire Detection System Based on Feature Regression Analysis and Support Vector Machine | 145 |
| Yang Jia and Huiqin Wang | |
| Spur Bevel Gearbox Fault Diagnosis Using Wavelet Packet Transform for Feature Extraction | 155 |
| Wentao Huang, Peilu Niu and Xiaojun Lu | |
| Steering Nonholonomic Systems with Cosine Switch Control | 167 |
| Yifang Liu, Liang Li and Yuegang Tan | |
| Predicting and Verifying Forces by Using Different Cutters and Spaces | 177 |
| Zhaoqian Wang, W. S. Wang, Jiye Wang and Chunguang Liu | |
| The Segmentation and Adherence Separation Algorithm of Cotton Fiber | 187 |
| Li Yao, Dong Wang and Shanshan Jia | |
| Assessment Metrics for Unsupervised Non-intrusive Load Disaggregation Learning Algorithms | 197 |
| Lingling Zhang, Yangguang Liu, Genlang Chen, Xiaoqi He and Xinyou Guo | |

| | |
|--|-----|
| Optimal Sensor Placement of Long-Span Cable-Stayed Bridges Based on Particle Swarm Optimization Algorithm | 207 |
| Xun Zhang, Ping Wang, Jian-Chun Xing and Qi-Liang Yang | |
| A Method for the Shortest Distance Routing Considering Turn Penalties. | 219 |
| Lihua Zhang and Tao Wang | |
| Space Robot Teleoperation Based on Active Vision. | 229 |
| Cheng Huang, Huaping Liu, Fuchun Sun and Yuming Sheng | |
| Listed Company Reorganization Risk Evaluation Based on Neural Network Model | 241 |
| Wang Zuogong and Li Huiyang | |
| Fuzzy Prediction of Molten Iron Silicon Content in BF Based on Hierarchical System | 251 |
| Qihui Li | |
| An Evaluation of Integration Technologies to Expose Agent Actions as Web Services | 259 |
| Juan Pablo Paz Grau, Andrés Castillo Sanz and Rubén González Crespo | |
| Research on Evolution Mechanism of Runway Incursion Risks Based on System Dynamics. | 271 |
| Zhao Xianli and Luo Fan | |
| Simulation of Nonpoint Source Pollution Based on LUCC for Er-hai Lake’s Watershed in Dali of China | 281 |
| Quan-li Xu, Kun Yang and Jun-hua Yi | |
| Photograph’s Exposure Control by Fuzzy Logic | 293 |
| J. Martínez, Matilde Santos and Victoria López | |
| The Elastic Cloud Platform for the Large-Scale Domain Name System | 305 |
| Yunchun Li and Cheng Lv | |
| Applied Polyphase Filter Orthogonal Transformation Technology in Broadband Signal Receiving | 317 |
| Xiang Jian-hong and Dnong Chun-lei | |

| | |
|--|------------|
| Collaborative Recommendation System for Environmental Activities Management Mobile Application. | 327 |
| Inmaculada Pardines, Victoria López, Antonio Sanmartín, Mar Octavio de Toledo and Carlos Fernández | |
| Study of Algorithms for Interaction Between Flowing Water and Complex Terrain in Virtual Environment | 337 |
| Yue Yu and Yuhui Wang | |
| An Automatic Generating Method of 3D Personalized Clothing Prototype | 351 |
| Xiaping Shi and Bingbing Zhang | |
| Study of Migration Topology in Parallel Evolution Algorithm for Flight Assignment | 361 |
| Jiaxing Lei, Xuejun Zhang and Xiangmin Guan | |
| Improving the GPS Location Quality Using a Multi-agent Architecture Based on Social Collaboration | 371 |
| Jordán Pascual Espada, Vicente García-Díaz, Rubén González Crespo, B. Cristina Pelayo G-Bustelo and Juan Manuel Cueva Lovelle | |
| Simulation and Implementation of a Neural Network in a Multiagent System | 381 |
| D. Oviedo, M. C. Romero-Ternero, M. D. Hernández, A. Carrasco, F. Sivianes and J. I. Escudero | |
| Soft Computing Applied to the Supply Chain Management: A Method for Daily Sales Classification and Forecasting. | 391 |
| Fernando Turrado García, Luis Javier García Villalba and Victoria López | |
| The Self-Organizing City: An Agent-Based Approach to the Algorithmic Simulation of City-Growth Processes. | 397 |
| Adolfo Nadal and Juan Pavón | |
| Modeling and Robust Control of Splicing System | 409 |
| Yinghui Fan, Chaowen Li and Xingwei Zhang | |
| Single Observer Passive Location Using Phase Difference Rate | 421 |
| Taoyun Zhou, Yun Cheng and Tiebin Wu | |

Excluded Middle Forest Versus Vantage Point Tree: An Analytical and Empirical Comparison 431
 Qiaozhi Li, He Zhang, Fuli Lei, Gang Liu, Minhua Lu and Rui Mao

Research and Simulation of Trajectory Tracking Control Algorithm for Multiwheel Independent Drive Skid Steering Unmanned Ground Vehicle 439
 Yunan Zhang, Yongbao Yan, Nanming Yan and Peng Tian

A Fast Association Rule Mining Algorithm for Corpus. 449
 Shankai Yan and Pingjian Zhang

Research and Development of Ultrasonic Power with Frequency Auto-tracing System and Power Auto-controlling System 461
 Xinxing Tang and Dongquan Zhang

Simulation of STATCOM Effect on the Dynamic Response Performance of HVDC 473
 Wang Weiru and Shi Xincong

Research of Interface Composition Design Optimization Based on Visual Balance 483
 Lei Zhou, Cheng-Qi Xue and Kiyoshi Tomimatsu

3D Registration Based on the Front and Back Segments of Human Body for Reconstruction 495
 Wan Yan, Long Wenzheng and Tang Hongtai

Emotional Element Extraction Based on CRFs. 507
 Yashen Wang, Quanchao Liu and Heyan Huang

Study on Multi-class Text Classification Based on Improved SVM. 519
 Qiong Li and Li Chen

Online Evaluation System of Image Segmentation 527
 Khai Nguyen, Bo Peng, Tianrui Li and Qin Chen

Modeling of 3D Personalized Digital Apparel Whole-Human Body Based on Mannequin Components. 537
 Xiaping Shi and Senpeng He

The Fuzzy Controller Design for MEMS Gyro Stable Platform 549
 Jinlong Dong and Bo Mo

Tree Network Under Space L and Space P Model 557
Xi Chen, Jianghai Qian and Dingding Han

Ontology-Based Component Description and Intelligent Retrieval . . . 567
Li Liu and Youqun Shi

**A New Dynamic Credit Scoring Model Based
on the Objective Cluster Analysis** 579
Gao Wei, Cao Yun-Zhong and Cheng Ming-shu

**Application of the Fully Data-Driven Combination Model
for Water Demand Forecasting in the Mountainous Tourist Area . . .** 591
Li Jie, Li Qiang, Huang Yi, Ling Liang, Fang Cheng
and Jiang Zhenzhen

**Cascaded H-Bridge MV Grid and Power Balance Control
for PV Systems** 603
Bin Zhang, Zhiyun Bao, Donglai Zhang, Tiejai Li and Zicai Wang

**Research of Automatic Scoring System of Ship Power
Automation System** 615
Wei Nie, Ying Wu and Dabin Hu

**Investigating Individual Driver Performance:
Applying DEA on Simulator Data** 623
Seddigheh Babae, Yongjun Shen, Elke Hermans,
Geert Wets and Tom Brijs

**Military Information System Access Control Architecture
Based on SDO-ARBAC Model** 637
Lin Sun, Yan Jin, Hao Liu and Fangsheng Li

**Reliability Analysis of Driver Behaviour Under Effect
of Head-up Display System: A Probabilistic Risk
Assessment in Traffic Operation** 647
Rongjie Lin, Hongfei Mu, Hongwei Guo and Wuhong Wang

**Personalized Recommendation Based on Weighted
Sequence Similarity** 657
Wei Song and Kai Yang

Design and Analysis of DVMCK Transmission System 667
Yang Liu, Yanli Shang, Xiaoyu Yin and Guoxin Zheng

Research of Turbofan Engine Performance Assessment Method Based on Analytic Network Process Theory 677
 Shuming Li, Niansu Yang and Yanxiao Huang

A Cellular Automata Model on Bus Signal Priority Strategies Considering Resource Constraints 689
 Liying Wei, Lili Zhang and Zhilong Wang

A Fast Gradual Shot Boundary Detection Method Based on SURF 699
 Zhonglan Wu and Pin Xu

The Optimal Inventory Model of Two Warehouses: Time-Varying Demand Considering Credit Period 707
 Yuntao Hu

Sampled-Data Synchronization for Chaotic Neural Networks with Mixed Delays 721
 Rui-Xing Nie, Zhi-Yi Sun, Jian-An Wang and Yao Lu

The Design and Optimization of Inherent Frequency of Combined Triaxial High-g Accelerometer 735
 Xu He, Zhenhai Zhang, Kejie Li, Ran Lin, Zhiqing Li, Liang Zhang and Shuai Hou

Design and Simulation of Variable Pitch Control System Based on Fuzzy Model Reference Adaptive 745
 Hongche Guo, Manjia Hu, Tao Li and Gangqiang Li

Modeling Prices in Electricity Spanish Markets Under Uncertainty 755
 G. Miñana, H. Marrao, R. Caro, J. Gil, V. Lopez and B. González

Research on Key Technologies for Jail Incident Prevention and Response System 765
 Guofeng Su, Jianguo Chen, Fengzhi Liu and Quanyi huan

Design of Improved Fuzzy PID Controller Based on the Temperature Control System of Large Inertia and Time Delay 775
 Longkui Wang, HongXin Li and Yaru Wang

Research on Predictive Control of Evaporator Superheat System with Time-Delay Based on DMC Intelligent Optimization 785
Jun Xie, Songli Wang, Yuwei Wang and Jianzhong He

Fault Diagnosis Based on Principal Component Analysis and Support Vector Machine for Rolling Element Bearings 795
Zhikai Zhou, Dongfeng Liu and Xinfu Shi

The Study on Risk Rating Model of Commercial Bank Credit Based on SVM 805
Menggang Li, Zuoquan Zhang and Rongquan Bai

Development of a BCI Simulated Application System Based on DirectX 813
Banghua Yang, Qian Wang, Zhijun Han, Hong Wang and Liangfei He

A Research on Hybrid Simulated Annealing Algorithm for Cargo Loading Problem 823
Shaoyong Yu, Junrong Yan and Shunzhi Zhu

A Hub-Network Layout Problem Balancing the Budget and Passenger Transport Cost 831
Chunping Hu, Tiantian Gan, Zheng Zhang and Kun Qian

Synchronization Control in Vertical Ship Lift Based on Relative Coupling Strategy 839
Yang Gang and Zhang Jiabing

Study on Security Domain-Oriented Military Information Systems Access Control Model 849
Yan Jin, Hao Liu, Lin Sun and Jing Song

Optimizing Control of Multiobjective Based on Improved PSO Algorithm for Excavator 857
Bo Bi and Lei Li

Parallel Genetic Algorithm Applied to Spacecraft Reentry Trajectory 867
Wenya Zhou, Hongtu Ma, Zhigang Wu and Kuilong Yin

Predicting the Heating Value of Rice Husk with Neural Network 877
Wan Yu and Congping Chen

Research on UAV Collision Avoidance Strategy Considering Threat Levels 887
 Bin Fang and Tefang Chen

The Identification of Convex Function on Riemannian Manifold 899
 Xiaosong Cui, Xin Wen, Yunxia Zhang, Li Zou and Yang Xu

A Method for Dehazed Image Quality Assessment 909
 Zhongyi Hu and Qiu Liu

Tactics Decision-Making Based on Granular Computing in Cooperative Team Air Combat 915
 Dongqi Meng, Yufei Wang, Ying Chen and Lin Zhong

Graph Cuts-Based Feature Extraction of Plant Leaf 927
 Feng-hua Lv and Hang-jun Wang

Research on Integration of 3D Digital Definition for Marine Diesel Engine Parts 937
 Zhang Hui, Yang Ge and Zhang Sheng-wen

The Temperature Control of Laser Thermal Desorption System Based on Parameters Self-Tuning Fuzzy PID Algorithm 947
 Buyun Wang, Linna Ma, Xiaoyan Liu and Jianguang Zhou

Stock Market Forecast Based on RBF Neural Network 955
 Teng Ji, Wengang Che and Nana Zong

Research on the Fluid Capacitance Detector Using the Technology of Capacitance Detecting 963
 Zheng Fang, Jianguang Zhou, Xiaoyan Liu and Sijia Liang

Research on the Safety of Yangtze River LNG Transport and Storage System 973
 Shouhui He, Hanhua Zhu, Haofei Huang, Xiaowei Xu and Suping Zhao

Research on Reversal Lane Application Method of Urban Road Network Based on the Bi-level Programming 983
 Qihong Yu and Rui Tian

Multi-robot Formation Discrete Kinematics Model and Formation Control 993
 Jin Wu, Guoliang Zhang, Jing Zeng and Jun Xu

New Scheduling Algorithm in Hadoop Based on Resource Aware . . . 1011
 Peng Xu, Hong Wang and Ming Tian

Developing a New Counting Approach for the Corrugated Boards and Its Industrial Application by Using Image Processing Algorithm 1021
 Ufuk Cebeci, Fatih Aslan, Metin Çelik and Halil Aydın

Complex Systems Modelling for Virtual Agriculture. 1041
 Lei Zhang and Liqi Han

Analysis on the Concepts of Knowledge and Knowledge Engineering: Based on the Perspective of “Information Complex Holographic Person”. 1051
 Zhang Tianbo

High Precision Brushless DC Motor Position Feedback Technology for Three-Axis Turntable 1059
 Guanda Liu, Bo Mo, Haiwen Zhu and Jin Lin

Punctuation Prediction for Chinese Spoken Sentence Based on Model Combination 1069
 Xiao Chen, Dengfeng Ke and Bo Xu

Research on Book Purchases Evaluation System Based on EFGA Neural Networks 1079
 Hongxia Liu and Yuhua Liu

Study on Scene-Driven Emergency Drill Method 1089
 Xin Li, Guofeng Su, Shaobo Zhong, Fushen Zhang, Chao Huang, Hongyong Yuan, Quanyi Huang and Jianguo Chen

The Research of Component-Based Software Development Application on Data Management in Smart Education 1099
 Lijuan Liu, Youqun Shi and Ran Tao

Driving Intention Inference Based on Dynamic Bayesian Networks 1109
 Fang Li, Wuhong Wang, Guangdong Feng and Weiwei Guo

A Review on Hybrid Vehicle Powertrain Matching and Integrated Control Based on ECVT. 1121
 Guogeng Zhang

The Time Series Pattern of Traffic Flow on an Accident Section. . . . 1129
Feng Peng, Jifu Guo and Qi Xu

**The Hinterland Spatial Structure Evolvement of Competitive
Port Based on ArcGIS.** 1143
Jiafang Zhuang and Siqin Yu

**Research and Implementation of a General Model
for Agent Electronic Commerce Website** 1155
Xiaoling Xia and Niu Zhang

Singular Optimal Control for Uncertain Systems 1167
Shuhu Sun and Yuanguo Zhu

Knowledge-Based Expressive Technologies Within Cloud Computing Environments

Sergey V. Kovalchuk, Pavel A. Smirnov, Konstantin V. Knyazkov, Alexander S. Zagarskikh and Alexander V. Boukhanovsky

Abstract Presented paper describes the development of comprehensive approach for knowledge processing within e-Science tasks. Considering the task solving within a simulation-driven approach a set of knowledge-based procedures for task definition and composite application processing can be identified. These procedures could be supported by the use of domain-specific knowledge being formalized and used for automation purpose. Within this work the developed conceptual and technological knowledge-based toolbox for complex multidisciplinary task solving support is proposed. Using CLAVIRE cloud computing environment as a core platform a set of interconnected expressive technologies was developed.

Keywords Domain-specific language · Composite application · Complex system simulation · Cloud computing

1 Introduction

Today a lot of complex e-Science [1] tasks are solved using computer simulation which usually requires significant computational resources usage. Moreover the solutions, developed for such tasks are often characterized by structural complexity which causes a lot of different resources (informational, software or hardware) to be integrated within a single solution. The complexity of the solutions grows as the multidisciplinary tasks are considered. Today's common approach for building composite solutions is based on Service-Oriented Architecture [2] which forms the basis from interconnection of services and hiding their

S. V. Kovalchuk (✉) · P. A. Smirnov · K. V. Knyazkov · A. S. Zagarskikh
A. V. Boukhanovsky
Saint-Petersburg National University of IT, Mechanics and Optics, Saint-Petersburg Russia
e-mail: kovalchuk@mail.ifmo.ru

complexity behind their interfaces. Interconnection of the services within complex tasks is usually implemented in a form of workflow (WF) structures [3] which exploits graph-based structures to describe interconnection of used services. On the other hand, today the Cloud Computing [4] concept is developed as a business framework for providing on-demand services supporting resources' consolidation, abstraction, access automation and utility within a market environment. To support the consolidation and abstraction description of available resources should be provided; automatic services composition requires the tool for composite application management; utility and market properties should be supported with semantic domain-specific description. Thus cloud computing platforms should provide the domain-specific user-oriented tools for expression of descriptive artifacts.

Finally, today Problem Solving Environment (PSE) [5] brings a set of domain-specific tools together to solve the proposed domain problems. Still this approach requires a set of knowledge from different domains being available for the user of a PSE. Intelligent PSE (iPSE) [6] tries to extend the PSE concept with knowledge-based using formalized knowledge within these domains.

In the presented work the conceptual and technological solution for comprehensive knowledge-based support of human-computer interaction within the process complex e-Science task solving is described. The key goal of the work is to organize different knowledge-based technologies within a continuous solution which support the integration process within cloud computing environment and enable automatic solving of technological issues.

2 Knowledge-Based e-Science Technologies

The process of solving e-Science tasks is strongly related to the knowledge processing. This point of view (see Fig. 1) can discover a set of features:

1. Today the development of global networking technologies within the Internet makes the international scientific *society* an important source of knowledge. This trend causes to appear a concept of Science 2.0 [7] which gives the important role to the global collaboration of scientists. As a result all the knowledge which is used to define the e-Science tasks can be considered as the knowledge of society. Moreover all the results obtained during the task solving process also could belong to the society and extend its knowledge.
2. The implicit set of knowledge can be *obtained* for the further utilization using different approaches. The most important of them are: explicit knowledge formalization performed by or within collaboration with experts and automatic analysis of tests, data and experiments published by the society.
3. *Formalized knowledge* within e-Science tasks can be divided into three main groups: (a) domain-specific knowledge, which describes the specificity of the task within the particular problem domain(s); (b) IT-related knowledge which

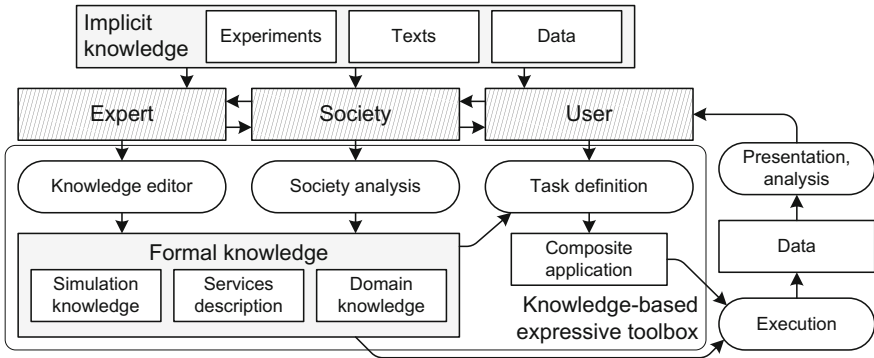


Fig. 1 Knowledge-based view to e-science tasks

is used for the automation services searching, tuning and calling; (c) system-level knowledge which supports the organization of simulation and data analysis. Today the idea of system-level science [8] appears which is focused more on comprehensive exploration of the system rather than on running particular procedures. Thus all these knowledge should be interconnected and coordinated around the process of simulation-based exploration of particular system.

4. The formalized knowledge can be used to *automatic support* of different procedures during the problem solving process. This knowledge allows designing human–computer interaction process in a way most suitable for the user, allowing to obtain all the necessary information to build, execute the composite application and analyze its results. Considering a WF-based technology there should be (a) a set of tools for building and monitoring the WF using domain-specific concepts; (b) a set of technologies which simplify the interpretation and execution of the WF by the use of knowledge on service usage.
5. As a result there should be a set of technological tools (domain-specific languages (DSL), editors, knowledge bases) which allows different users of the system (end-users, experts, developers, IT specialists etc.) to *express their knowledge* in a form which (a) can be easily used by the user; (b) will be understandable to any other user with the same knowledge background; (c) can be interpreted automatically by the software which performs computing.

The proposed knowledge-based expressive toolbox can be defined as a set of technologies which supports the process of composite application building, execution and results’ analysis. The knowledge base which incorporates the knowledge of different kind is a core of this technological toolbox. The toolbox includes the following classes of technology available for the users of different classes: (a) knowledge bases as a core integration technology; (b) a set of DSLs; (c) graphical user interfaces; (d) performance models describing the execution of services.

3 Expressive Technologies

Presented approach is developed as an extension to the iPSE [6] concept which provides knowledge-based support of the problem solving process. Considering main operation which requires knowledge expression and interpretation the following procedures and modules can be defined within the computational environment built within a framework of this concept (Fig. 2a). Each of these procedures can be associated with a specific descriptive language (with textual or graphical notation) which can provide (a) support of the expression process by the use of knowledge-based tools; (b) interpretability for the purpose of underlying simulation automation. These languages (Fig. 2b) can be interconnected within a continuous stack with relation (a) to the domain-specific entities within knowledge base; (b) objects on different abstraction levels of the complex e-Science solutions. The expressive technology for each level includes a pair of tools: (a) for expression of knowledge on corresponding level; (b) for interpretation of these expressions.

1. Services (including computing services, data services, interfaces to the specific devices, observation sources etc.), available within computational environment might be described with a set of knowledge which defines the interface of service, its domain-specific interpretation and usage of support procedures. This description can be implemented using declarative DSLs. As the main WF representation is usually implemented using abstract service description, the mapping of abstract workflow (AWF) onto particular services should be done during the WF interpretation. Also the description of the services might support the execution monitoring. Still the most significant meaning of this part of expressive toolbox is providing domain-specific information on the user level. The descriptive language on this level should include structures for service and data structures semantic description.
2. Composition of the services is usually implemented in a form of AWFs, where particular services call is specified by the description of service's type and input/output flows. The interpretation of the WF includes mapping to the particular services, calling of these services and execution monitoring. The WF development requires set of new technologies to be developed. E.g. WF management systems (WFMS) provide different tools for service discovery and usage. Also the language for composition of abstract services should be developed.
3. The process of system's exploration is usually focused on the properties of specific domain objects which can be explored through the simulated model. The description of such object can be translated into AWF form. Nevertheless the semantic structure of simulated object can be considered as a separate entity which can be defined by the domain expert and used for further model-based exploration and hiding the complexity of the underlying WF. Thus, this structure (predefined simulation WF and its semantic interpretation) could be considered as a part of domain-specific knowledge. This level presents interconnection between domain-specific and IT knowledge.

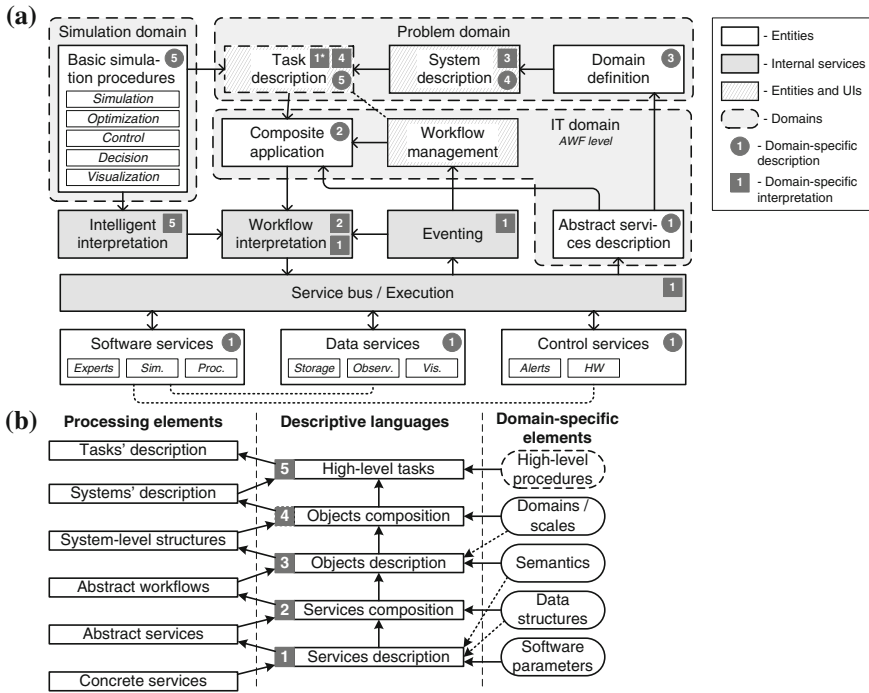


Fig. 2 Computational environment **a** high-level architecture; **b** descriptive languages

4. The description of domain-specific object is a core entity for the simulation-based system exploration. The composition of such object can be interpreted (a) as a semantic description of the system which is explored within the current task; (b) as a basic structure for complex simulation WF composition which can be further translated through the levels 3 to 1. Moreover the semantic description of the system can be used in conjunction with the spatial/temporal basis of the simulation. This type of integration allows switching from the procedural point of view (where procedures are equivalent to the service calls) to the simulation-based point of view with automatic construction of the procedural WFs.
5. High-level tasks description define additional techniques which can be applied to the system's structure, described earlier. Processing of the system's structure can be performed for the different purposes: visualization, parameters optimization, decision support etc. The simplest way of this technique implementation is development of heuristics or rule-based extension to the basic knowledge base.

4 Implementation Details

The proposed architecture was implemented on the basis of CLAVIRE cloud computing platform [9], which allows building composite applications using domain specific software available within the distributed environment. The platform implements the iPSE concept, thus, the knowledge based solution for composite application development and execution can be integrated into existing solution.

4.1 Basic Knowledge Structure

The core conceptual and technological solution for continuous integration is hierarchy of concepts within simulation process:

1. *Simulated object*, which represents the main entity being explored. The object can be considered as a composite entity, or system of objects.
2. *Simulated model*, which describes a set of static and dynamic characteristics of the object and can be used to explore it.
3. *Method* can be defined as an imperative description of the model usage process. Methods are implemented in different simulation software.
4. *Software packages* are used as algorithmic implementations of the defined methods. Usually this software is developed by the domain specialists.
5. *Service* within a distributed computational environment (in case we are using SOA) can be considered as the software deployed on computational resource.

This hierarchy is developed to integrate the domain-specific concepts (1–3) and technological concepts (4–5). It is the core concept for development of knowledge-based solutions, which support high-level task definition, which in turn can be automatically translated using interconnection between concepts of the hierarchy.

To implement the proposed conceptual hierarchy the knowledge base in a form of ontological structure was developed within a framework of Virtual Simulation Objects (VSO) technology [10]. This ontological structure implements domain-specific concept of the hierarchy (1–3) and their interconnection. The technological concepts (4–5) were described as links to corresponding knowledge expressed using a set of DSLs (see Sect. 4.2). The objects can be interconnected with a help of VSO technology to form the system’s semantic description. The VSO technology presents instrumental environment with graphical interface (see Sect. 4.3) for building a system’s description using the library of objects. Thus, the VSO presents an expressive technology for objects description; composition and high-level task definition (see Fig. 2b). The expressive technology includes: (a) descriptive languages with graphical notation for objects description and composition; (b) tools to design a composite solution for complex system’s simulation; (c) interpretation engine for translation the descriptions into the AWF form.

4.2 Domain-Specific Languages

Domain-specific languages [11] present a powerful technology for building expressive tools within different problem domains. CLAVIRE environment uses a couple of related DSLs [9]:

EasyPackage—a language for services description based on Ruby language. It is used to define the knowledge on software services: input and output parameters, used data and files structures etc. A specific part of knowledge, expressed using this language is parametric performance models, used to estimate and to optimize performance characteristics of the services within cloud computing environment [12]. Also the language provides the user with ability to describe semantic meaning of defined entities within the problem domain. Considering the conceptual hierarchy presented in Sect. 4.1 this language describe the knowledge of level 4. The knowledge on last level (5) of this hierarchy is described by the means of ResourceBase system within CLAVIRE environment which includes the description of particular services (using JSON format) linked with the software description in the EasyPackage language and used within the knowledge base.

EasyFlow—a language for composite application description in a form of AWF. The WF is a central object within the CLAVIRE environment which defines the structure of composite application. It is developed using ANTLR framework and uses the software description presented using EasyPackage language to define software calls. So, the language presents expressive tool for composite application description. The interpretation of the AWF described by the language includes searching for appropriate services, processing of the incoming and outgoing data, tuning services' execution parameters. These procedures also can be performed using the knowledge presented using EasyPackage language.

4.3 User Interfaces

A knowledge-based approach can be used to develop user interfaces (UI) which support human–computer interaction with required level of abstraction. Several classes of UI were developed using CLAVIRE environment:

UI 1 The high-level interfaces can be developed using VSO technology. Knowledge on the simulation of particular objects can be used to develop domain-specific graphical language to define simulated objects and systems. Figure 3a presents the UI of VSO-based workspace which can be used to define simulated system as a composition of objects available within a library. The designed description can be translated into a WF and executed as a regular composite application.

UI 2 The domain-specific support of composite application development can be performed using the interfaces which provide the user with qualitative comparison of available solutions. Figure 3b shows a tree-based UI which uses the concepts of levels (2–4) within conceptual hierarchy to compare different solutions for

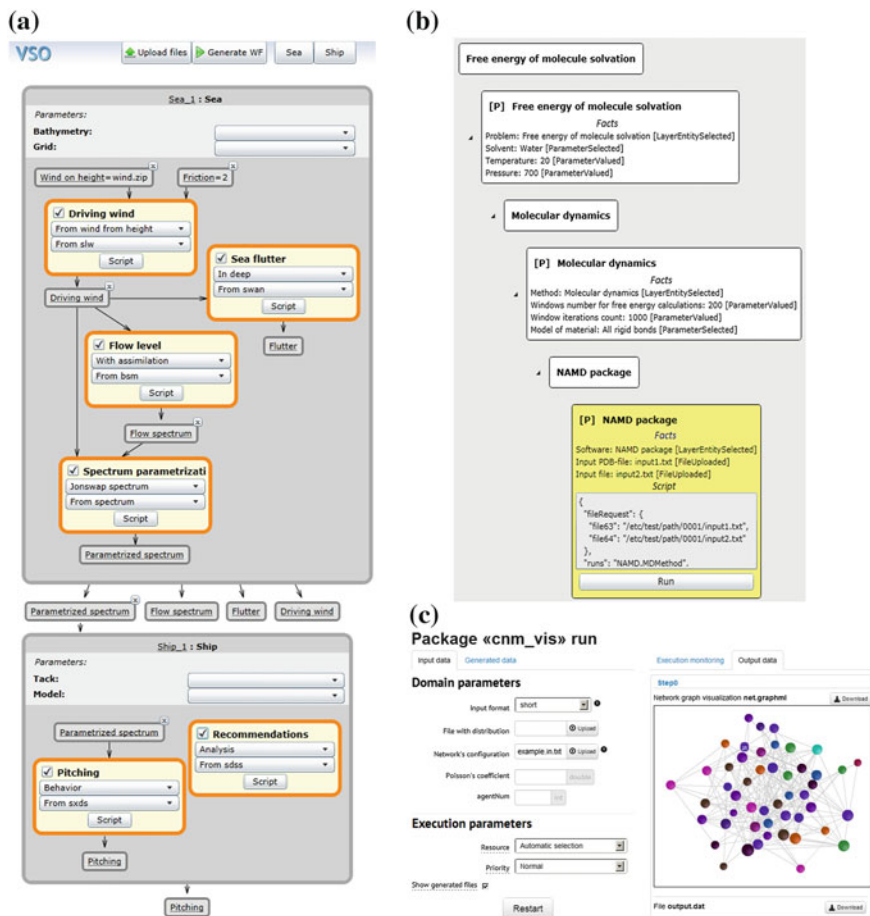


Fig. 3 Knowledge-based user interfaces

particular domain tasks [13]. The user can define the parameters of the task and the system will compare available solutions using a set of qualitative criteria.

UI 3 WFMS usually provide the user with an interface for graphical (typically in a form of graph) or textual description of WF. Most WFMSes have interfaces common to Integrated Development Environments (IDEs) including the capability to manage project files, run the WF, monitor the execution process, view the results, etc. CLAVIRE environment also uses graphical UI based on EasyFlow language (both with textual and graphical notation) to define the AWF structure.

UI 4 Problem-oriented interfaces (Fig. 3c) allow the user to input all the required parameters for running particular task within cloud computing environment. The system performs automatic input checking; fulfill all the necessary procedures to translate input data into required format. Also the results of the

execution can be obtained and viewed using the same interface. This UI is generated automatically using the EasyPackage description.

UI 5 The lowest level of the UI is provided by a command-line interface and API library to access the computational environment. This type of interface is rarely used (mainly for the purpose of software integration).

4.4 Touch Table Application: An Example

Among the other tasks, which require simulation, decision support system can be mentioned as a complex example which involves different type of users interacting with the system and with each other. An application for collaborative decision support for the task of surge floods prevention in St. Petersburg [14] was developed using touch table hardware for collaboration (Fig. 4a). While the main interface of this application presents geographic information system based on the map of sea near the St. Petersburg city (Fig. 4b) the decision making process can be supported by the mean of additional expressive technologies mentioned earlier: (a) WFMS (UI 3) is used to run simulation and decision making WFs, which provide the analysis of the forecast of sea level and possible plans to prevent the flood; (b) problem-oriented interfaces (UI 4) is used for more detailed simulation using the available software; (c) high-level knowledge-based interfaces (UI 1–2) are used to build, extend and analyze different scenarios of the situation development during the collaborative decision making; (d) finally the API (UI 5) is used to integrate the parts of the solution (touch table, decision makers UIs) with CLAVIRE environment. The DSLs are used within the application to express the knowledge of experts (in form of predefined simulation WFs) and description of available cloud services, while ontological structure can be used to support semantic integration of different parts within the solution.

5 Discussion and Conclusion

Solving contemporary e-Science tasks requires involvement of knowledge from different domains: a set of problem domains should be extended with IT domain (as the underlying software often is characterized by a complex usage), simulation domain (as a lot of techniques for complex system simulation require specific knowledge). All these knowledge needs to be formalized and dynamically integrated because the parts of knowledge might be updated separately. Today the ontology is often used as an integration technology (see, e.g. [15]). On the other hand, DSLs [11] present powerful technology for declarative and imperative knowledge expression using graphical or textual notation. As a result, the combination of these technologies can be used as a core technological solution for comprehensive knowledge-based support of human–computer interaction.

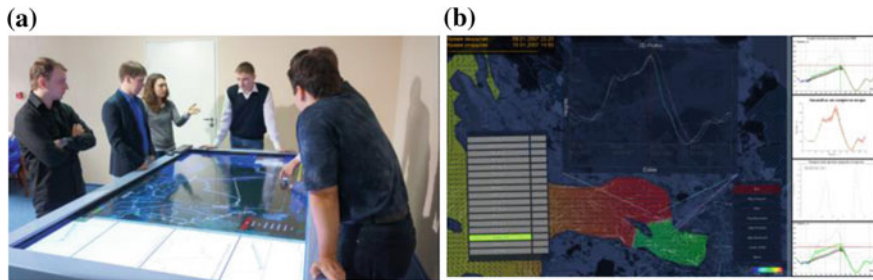


Fig. 4 Touch table application **a** collaborative decision making; **b** main user interface

Presented work is devoted to development of the expressive toolbox which will support the processes of expression and interpretation in the most convenient and easiest way for the user. The continuous integration of different technologies using core ontological structure allows automatic interpretation and translation of the information provided by the user on different levels of abstraction. The developed expressive toolbox was implemented using CLAVIRE cloud computing environment.

Acknowledgements This work is supported by the projects “Technology of system-level design and development of inter-disciplinary applications within cloud computing environment” (agreement 14.B37.21.1.870), “Virtual testbed for complex system supercomputing simulation” (agreement 14.B37.21.0596) granted from the Ministry of Education and Science of the Russian Federation and project “Urgent Distributed Computing for Time-Critical Emergency Decision Support” performed under Decree 220 of Government of the Russian Federation.

References

1. Hey T, Tansley S, Tolle K (2009) The fourth paradigm : data-intensive scientific, discovery. Microsoft, Redmond, p 252
2. Lublinsky B (2007) Defining SOA as an architectural style. <http://www.ibm.com/developerworks/architecture/library/ar-soastyle/>
3. Gil Y et al (2007) Examining the challenges of scientific workflows. IEEE Comput 40(12):24–32
4. Foster I et al (2008) Cloud computing and grid computing 360 degree compared. eprint arXiv:0901.0131
5. Rice JR, Boisvert RF (1996) From scientific software libraries to problem-solving environments. IEEE Comput Sci Eng 3(3):44–53
6. Boukhanovsky AV, Kovalchuk SV, Maryin SV (2009) Intelligent software platform for complex system computer simulation: conception, architecture and implementation. Izvestiya VUZov Priborostroenie 10:5–24 (in Russian)
7. Shneiderman B (2008) Science 2.0. Science 319:1349–1350
8. Foster I, Kesselman C (2006) Scaling system-level science: scientific exploration and IT implications. IEEE Comput 39(11):31–39
9. Knyazkov KV et al (2012) CLAVIRE: e-science infrastructure for data-driven computing. J Comput Sci 3(6):504–510

10. Kovalchuk SV et al (2012) Virtual simulation objects concept as a framework for system-level simulation. In: IEEE 8th international conference on e-science, pp 1–8
11. van Deursen A, Klint P, Visser J (2000) Domain-specific languages: an annotated bibliography. *ACM SIGPLAN Notices* 35(6):26–36
12. Kovalchuk SV et al (2013) Deadline-driven resource management within urgent computing cyberinfrastructure. *Procedia Computer Science* 18:2203–2212
13. Kovalchuk S, Larchenko A, Boukhanovsky A (2011) Knowledge-based resource management for distributed problem solving. In: Proceedings of the sixth international conference on intelligent systems and knowledge engineering. Shanghai, China, pp 121–128
14. Ivanov SV et al (2012) Simulation-based collaborative decision support for surge floods prevention in St. Petersburg. *J Comput Sci* 3(6):450–455
15. Walter T, Ebert J (2009) Combining DSLs and ontologies using metamodel integration. In: Proceedings of the IFIP TC 2 working conference on domain-specific languages, pp 148–169

Video Texture Smoothing Based on Relative Total Variation and Optical Flow Matching

Huisi Wu, Songtao Tu, Lei Wang and Zhenkun Wen

Abstract Images and videos usually express perceptual information with meaningful structures. By removing fine details and reserving important structures, video texture smoothing can better display the useful structural information, and thus is significant in the video understandings for both human and computers. Compared with the image texture smoothing, video texture smoothing is much more challenging. This paper proposes a novel video texture smoothing method through combining existing Relative Total Variation (RTV) and optical flow matching. By considering both special relationship and color/gradient similarity between adjacent frames, we build an optimization framework with two novel regularization terms and solve the smoothed video texture via iterations. Convincing experiment results demonstrate the effectiveness of our method.

Keywords Texture · Structure · Smoothness · Relative total variation · Optical flow · Probability model

1 Introduction

Video contents usually contain more or less natural or artificial textures, such as the grasses on the grounds or repeated patterns on the buildings. Such textural contents make the video more attractive. However, humans normally perceive video content by capturing the meaningful large scale structures. Thus, video texture smoothing becomes extremely important in computer vision and video pattern recognition, especially for video abstraction and object tracking.

H. Wu · S. Tu · L. Wang · Z. Wen (✉)
College of Computer Science and Software Engineering, Shenzhen University,
Shenzhen, China
e-mail: wenzk@szu.edu.cn

To smooth the fine texture from image, most existing methods define the texture region based on total variation of the gradient fields [1, 2], and use an optimization algorithm to filter out fine details. Recently, Xu et al. [3] proposed a method for texture smoothing based on Relative Total Variation (RTV), where better smoothed effects can be obtained. Compared with the studies carried out on the image texture smoothing, video smoothing is more challenging and none of the existing methods can obtain favorable results. For video smoothing, not only the main structures should be persevered in each frame image, but also the correspondences between frames should be considered to solve stable-smoothed video results.

In this paper, we propose a novel video smoothing method based on RTV and optical flow matching. Since RTV is a well-validated method in the separation of texture and structure, it provides better effects compared with other methods. As an important method in the analysis of visual motion, optical flow method provides dense correspondences for large scale structures between two frames. By estimating the displacement for each pixel via optical flow, we formulate an inter-frame constraint to optimize video smoothing. Compared to existing methods, which only consider the video smoothing frame by frame, our method achieves a more stable smoothing effect by preserving the video continuity. Specifically, we applied optical flow to describe a constraint between two adjacent frames in both original and smoothed video. Based the combination of RTV and optical flow, we propose a graph model to express the spatial and temporal relation between the adjacent frames. The probability model is analyzed to form an object function. Finally, we obtain the smoothed video by solving the object function. Experimental results show that our method outperforms the existing RTV in terms of main structures preserving and texture details smoothing.

2 Related Work

Since texture smoothing can extract salient structures from textures, it has been a hot research topic in computer vision and pattern recognition. Rudin et al. [4] first proposed TV-L2 model, which can be easily expressed through fidelity data term and regularization term. Aujol et al. [5] had studied four kinds of TV models and come to the conclusion that TV-L2 had best effects in dealing images without knowledge of its texture model in advance, but it had some demerits in distinguishing the strong structural textures and edges. Farbman et al. [6] and Xu et al. [7], respectively, proposed WLS and L0 gradient minimization. Different from the regularization term and optimized procedure in TV-L2 model, their models have some disadvantages in dealing texture of different scales, and they still rely on gradient. Kass and Solomon [8] pointed out that local histogram-based filtering can well resist image details and maintain the structure edges at the time. But this method is not designed to process texture, and the direct usage of this method will not get desirable effects. Xu et al. [3] proposed the Relative Total Variation (RTV)

method, which is based on the TV-L2 model, and this method can better remove image texture, while maintaining the structural edge. However, we cannot directly use RTV to smooth video textures because RTV can only smooth single image and does not consider the inter-frame relationship if it is used to smooth video.

Optical flow is state-of-the-art technique in calculating the pixel-wise correspondences between two images, especially for the neighboring frames in a video. The computation of optical flow field was first discussed by Horn and Schunck [9] in 1981. Based on the optical flow constraint equation, they supposed that the speed field is smooth, and then they get a dense optical flow field. Nagel [10] comes up with the idea that second derivative can be used to deal with the optical flow field. With the application of an oriented smooth constraint to deal with the occlusion problem, the computation of the reciprocal value of second derivative can be easily impacted by the noise. Ghosal and Vanek [11] proposed that smooth constraints of different natures in speed fields can be used to compute the optical flow field. Lucase and Kanade [12] researched and developed many new concepts for dealing with shortcomings of previous models.

In this paper, we present a simple and yet effective model based on Relative Total Variation and optical flow matching to realize video texture smoothing. By adding spatial constraint to RTV based on optical flow, we can obtain a better result than only smoothing video frame by frame using RTV. The combination between RTV and optical flow turns out a nonlinear optimization problem. So we also propose an optimization solution to obtain the video smoothing results.

3 Approach

3.1 Model

For the video to be smoothed, obviously, there are spatial and temporal relations between the original image and the smoothed one, which is shown in Fig. 1.

Suppose p_t is the pixel in the original image while s_t in the smoothed one, respectively. Both of them are in the same frame. The same position pixels in adjacent frame connect with each other through optical flow, for example, the connection between p_{t-1} and p_t as well as s_{t-1} and s_t . The original image and the smoothed one in the same frame connect with each other through Relative Total Variation [6], for example, the connection between s_t and p_t . From Fig. 1, it can be assumed that:

$$P(p_t|p_{t-1}) = \exp\left(-\|p_t - p_{t-1}\|^2\right) \quad (1)$$

$$P(s_t|s_{t-1}) = \exp\left(-\|s_t - s_{t-1}\|^2\right) \quad (2)$$

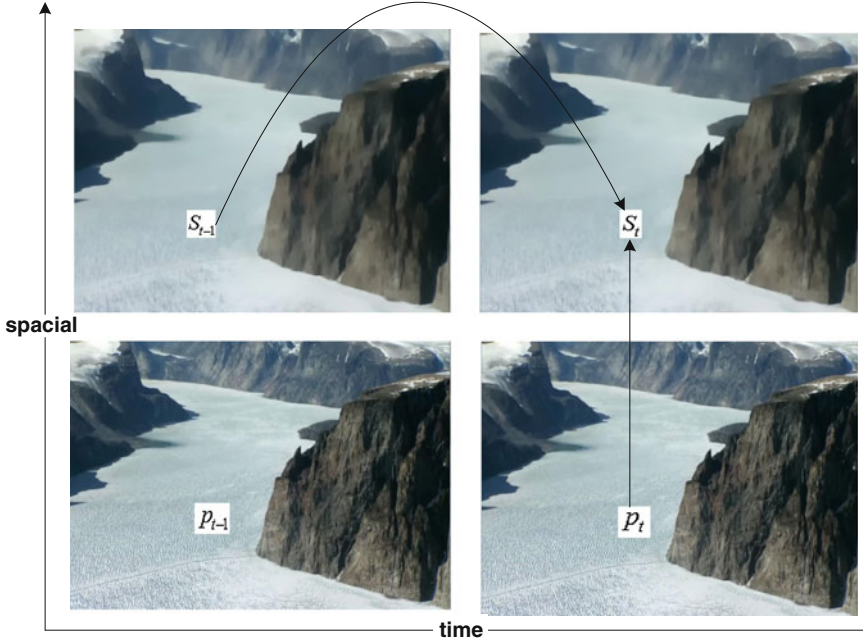


Fig. 1 From *left to right* display constrain relation between previous frame and the current frame, from *bottom to top* display constrain relation between original images and smoothed

$$P(p_t|s_t) = \exp(-u(s_t, p_t)) \quad (3)$$

Assume:

$$A = \|p_t - p_{t-1}\|^2; B = \|s_t - s_{t-1}\|^2; C = u(s_t, p_t)$$

It can be concluded:

$$\begin{aligned} P(p_t, s_t, p_{t-1}, s_{t-1}) &= P(p_{t-1})P(s_{t-1})P(s_t|s_{t-1})P(p_t|p_{t-1}, s_t) \\ &= P(p_t|p_{t-1})P(s_t|s_{t-1})P(p_{t-1})P(s_{t-1})P(p_t|s_t) \end{aligned} \quad (4)$$

From Bayes function:

$$P(p_t|s_t, p_{t-1}, s_{t-1}) = P(p_t, s_t, p_{t-1}, s_{t-1})/P(p_{t-1}, s_t, s_{t-1}) \quad (5)$$

From (4) and (5):

$$P(p_t|s_t, p_{t-1}, s_{t-1}) \propto P(p_t|p_{t-1})P(s_t|s_{t-1})P(p_t|s_t) \quad (6)$$

$$\log P(p_t | s_t, p_{t-1}, s_{t-1}) = -(A + B + C) \quad (7)$$

To maximize the probability, we should minimize the value of $A + B + C$. And we can obtain $(\Delta x, \Delta y)$ according the constraint conditions of optical flow

$$p_t(x, y) = p_{t-1}(x - \Delta x, y - \Delta y) \quad (8)$$

If t denotes any time, $p_t(x, y)$ can be effectively estimated by $p_{t-1}(x - \Delta x, y - \Delta y)$. Thus we assumes:

$$p_t(x, y) - p_{t-1}(x - \Delta x, y - \Delta y) \propto N(0, \sigma^2) \quad (9)$$

Similarly, $s_t(x, y) - s_{t-1}(x - \Delta x, y - \Delta y)$ is also Gaussian distribution. As the original image and the smoothed one take Relative Total Variation as constraint condition [6], it can be said:

$$D = \sum_p (P_p - S_p)^2 + \lambda \cdot \left(\frac{D_x(p)}{\Phi_x(p) + \varepsilon} + \frac{D_y(p)}{\Phi_y(p) + \varepsilon} \right) \quad (10)$$

From (9) and (10), the objective function is finally expressed as:

$$\begin{aligned} \arg \min_s \sum_p & (p_t(x_p, y_p) - p_{t-1}(x_p - \Delta x, y_p - \Delta y))^2 + (P_p - s_p)^2 \\ & + (s_t(x_p, y_p) - s_{t-1}(x_p - \Delta x, y_p - \Delta y)) + \lambda \cdot \left(\frac{D_x(p)}{\Phi_x(p) + \varepsilon} + \frac{D_y(p)}{\Phi_y(p) + \varepsilon} \right) \end{aligned} \quad (11)$$

3.2 Numerical Solution

It is not easy to solve the target equation (11) as it is nonlinear. It contains three constraints: Item A, Item B, and Item C. Its solution thus cannot be obtained trivially. Therefore, we proposed a segmenting method to optimize the equation. Firstly, we use Item A and Item B to optimize it. Secondly, Item C will be applied to deal with the result got from last step. Finally, the whole target equation will get optimized. The Fig. 2 showed the flow chart. This method is clear in structure and simple in processing. Besides, after the process of optical flow matching, it will be very close to the result we want. Hence, the number of iterations will be reduced when we utilize Item C.

The steps involved are as follows:

- (a) In Item A, $p_t(x, y)$ and $p_{t-1}(x, y)$ refer to the original image pixels, t means time. Δx and Δy can be accessed through $p_t(x, y)$ and $p_{t-1}(x, y)$ by optical flow matching. Item A can be viewed as a constant.

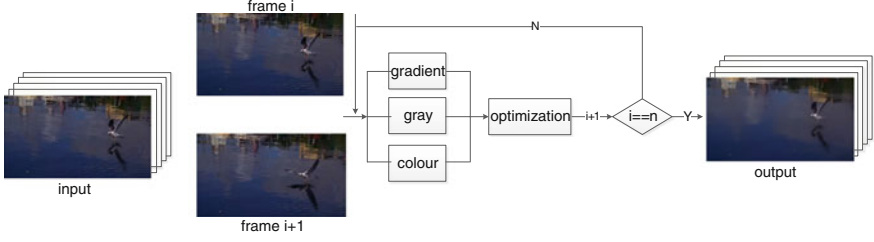


Fig. 2 The framework of our system

- (b) Take Item C as the initial condition, through optimization, we get S_{t-1} .
- (c) Optimize Item B through optical flow matching. The gray level of certain image point $w = (x, y)^T$ on time t is $I(x, y, t)$. After a timeslot of Δt , the correspond value for gray level is : $I(x + \Delta x, y + \Delta y, t + \Delta t)$. *Because the video image is continuous, the image changes slowly with x, y, t . With the Taylor series expansion and ignorance of the second-order infinitesimal items, we get*

$$\frac{\partial I}{\partial x} dx + \frac{\partial I}{\partial y} dy + \frac{\partial I}{\partial t} dt = 0 \quad (12)$$

It can be supposed that $u = \frac{dx}{dt}$, $v = \frac{dy}{dt}$, $I_x = \frac{\partial I}{\partial x}$, $I_y = \frac{\partial I}{\partial y}$, $I_t = \frac{\partial I}{\partial t}$ then function (12) can be rewritten as $I_x u + I_y v + I_t = 0$, $v_w = (u, v)$ is the optical flow for point w . Besides the gray value constancy assumption, we also consider color and gradient constancy assumption. After the above optimization, we get $S_t(x, y)$.

- (d) Utilize Item C to constrain the equation to get the optimized solution. Taking the result got from step c as input, we apply the numerical solution in [3] to optimize the equation and get the final result.

4 Results

We collected a video datasets to evaluate our method, which contains 20 videos with different kinds of textures. Typical video smoothing results are as shown in Figs. 3 and 4. From the results shown in Fig. 3, we can clearly see that our method not only preserves the salient structures for each frame in the video, but also maintains the video consistency when smoothing a sequence of images, including color consistency and lighting consistency for the corresponding pixels along the time dimension.

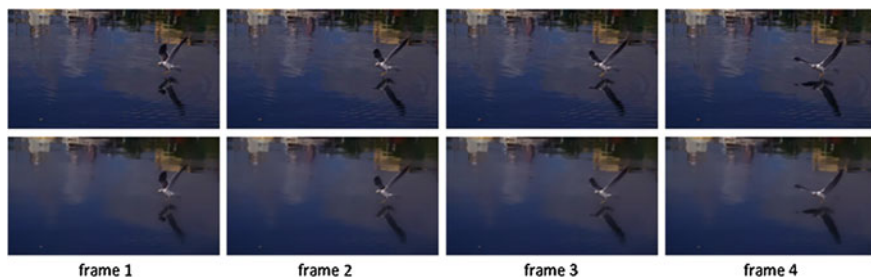


Fig. 3 Video smoothing results using our method. The *top row* is the original video from frame 1–4, and the smoothed results are shown in the *bottom row*

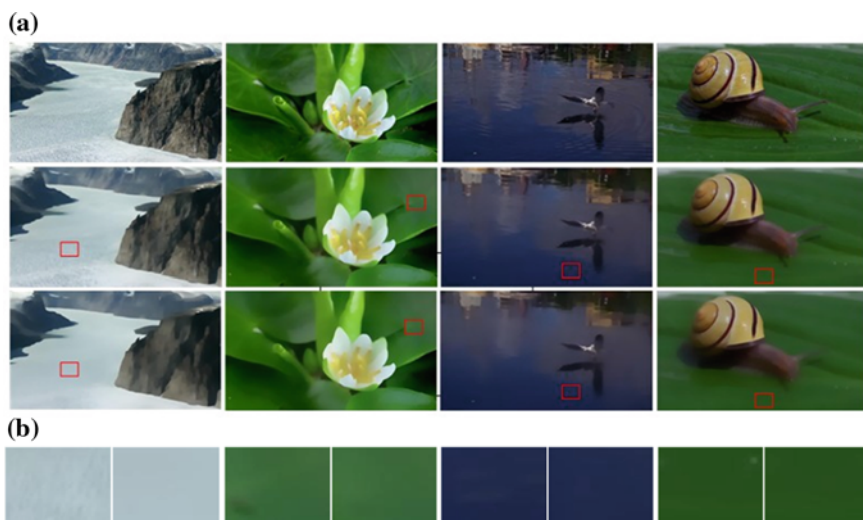
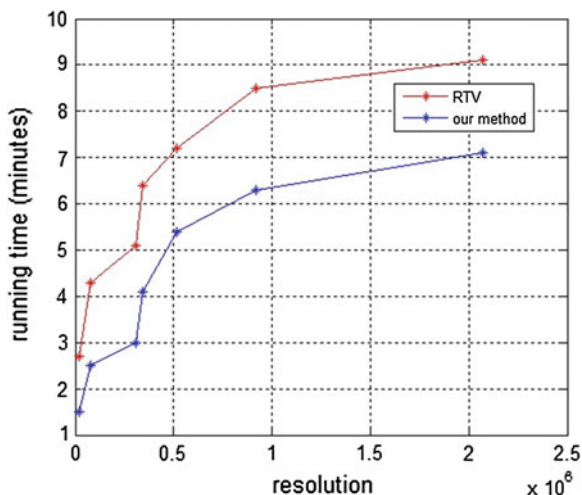


Fig. 4 Comparison between our method and the RTV. The original frames are shown in the *upper row* of (a). Corresponding results of RTV and our method are as shown in the *middle row* and the *bottom row*, respectively. Detail comparisons with blow-up resolutions are shown in (b)

In addition, we also implemented the existing RTV method for video smoothing and compared it with our proposed method. Figure 4 shows the videos smoothed using RTV and our method, respectively. For detail comparison, we selected one frame with dense textures to compare our method with RTV. As shown in Fig. 4a, the images in the top row are selected from the original videos. The middle row and the bottom row which are in Fig. 4a are the smoothed results with RTV and our method, respectively. From the visual comparisons, we can see that our smoothed results obviously are much better than the RTV results, especially for the regions marked with red boxes. From the blow-up results shown in Fig. 4b, we can even clearly observe that our method outperforms the existing RTV method, in

Fig. 5 Average running time comparison between RTV and our method for video with different resolutions



terms of salient structure preserving and fine detail smoothing, which points out that the combination of RTV and optical flow matching is effective in video smoothing.

On the other hand, we also performed a running-time statistics to compare our method and the RTV. In our experiments, we applied RTV and our method to 20 videos, which are about 10 s (250 frames). Each of them is up-sampled or down-sampled to be different resolutions, and we collected the average running time of RTV and our method applied on them. Figure 5 plots the average running time comparison between RTV and our method. The blue line in Fig. 5 indicates the average running time of RTV on the datasets, while the red line in Fig. 5 is ours. From the results shown in Fig. 5, we can see that our method generally faster than the RTV method, because the optical flow provides accurate correspondences and makes the optimization quickly converged. With the additional constraint of optical flow, our method turns out efficient by reducing iteration times.

5 Conclusion

In this paper, we present a novel model to handle the video texture smoothing based on RTV and optical flow matching. We contribute mainly in the following two aspects. Firstly, we set up a new probability model combined RTV with optical flow. Based on this probability model, we can easily realize the inner structure of the problem to be solved, and therefore bring up the objective function to be optimized. Secondly, we come up with an optimizing scheme to transform the original nonlinear problem to a set of subproblems that are much easier and faster to be solved. Experiments show that our method outperforms the existing

RTV method, in terms of both spatial–temporal consistency and efficiency. In the future, we plan to implement our method in GPU to achieve a real-time performance.

Acknowledgments The authors would like to thank our anonymous reviewers for their valuable comments. This work was supported in part by grants from National Natural Science Foundation of China (No. 61303101, 61170326, 61170077), the Natural Science Foundation of Guangdong Province, China (No. S2012040008028, S2013010012555), the Shenzhen Research Foundation for Basic Research, China (No. JCYJ20120613170718514, JCYJ20130326112201234, JC201005250052A, JC20130325014346, JCYJ20130329102051856, ZD201010250104A), the Shenzhen Peacock Plan (No. KQCX20130621101205783), the Start-up Research Foundation of Shenzhen University (No. 2012-801, 2013-000009), and Shenzhen Nanshan District entrepreneurship research (308298210022).

References

1. Meyer Y (2001) Oscillating patterns in image processing and nonlinear evolution equations: the fifteenth Dean Jacqueline B. Lewis memorial lectures, vol 22. American Mathematical Society
2. Yin W, Goldfarb D, Osher S (2005) Image cartoontexture decomposition and feature selection using the total variation regularized l1 functional. In: VLISM, pp 73–84
3. Xu L, Yan Q, Xia Y, Jia J (2012) ACM transactions on graphics (TOG)
4. Rudin L, Osher S, Fatemi E (1992) Nonlinear total variation based noise removal algorithms. *Phys D* 60(1–4):259–268
5. Aujol J-F, Gilboa G, Chan TF, Osher S (2006) Structure-texture image decomposition— modeling, algorithms, and parameter selection. *Int J Comput Vis* 67(1):111–136
6. Farbman Z, Fattal R, Lischinski D, Szeliski R (2008) Edge-preserving decompositions for multi-scale tone and detail manipulation. *ACM Trans Graph* 27:3
7. Xu L, Lu C, Xu Y, Jia J (2011) Image smoothing via L0 gradient minimization. *ACM Trans Graph* 30:6
8. Kass M, Solomon J (2010) Smoothed local histogram filters. *ACM Trans Graph* 29:4
9. Horn BKP, Schunck BG (1981) Determining optical flow. *J Artif Intell* 17:1852203
10. Nagel HH (1983) Displacement vectors derived from second-order intensity variations in image sequences. *J Comput Vis, Graph Image Process* 21(1):852117
11. Ghosal S, Vanek P (1996) A fast scalable algorithm for discontinuous optical flow estimation. *J IEEE Trans Pattern Anal Mach Intell* 18(2):1812194
12. Lucas B, Kanade T (1981) An iterative image registration technique with an application to stereo vision. In: *Proceedings of DARPA Image Understanding Workshop*, p 1212130

Gas Recognition Under Sensor Drift by Using Deep Learning

Xiaonan Hu, Qihe Liu, Hongbin Cai and Fan Li

Abstract Machine olfaction is an intelligent system that combines cross-sensitivity chemical sensor array and an effective pattern recognition algorithm for the detection, identification, or quantification of various odors. Data collected by the sensor array are multivariate time-series signals with complex structure, and these signals become more difficult to analyze due to sensor drift. In this work, we focus on improving the classification performance under sensor drift by using the deep learning method, which is popular among these years. Compared with other methods, our method can effectively tackle sensor drift by automatically extracting features, thus not only removing the complexity of designing the hand-made features, but also making it pervasive for a variety of application in machine olfaction. Our experimental results show that the deep learning method can learn the features that are more robust to drift than the original input and achieves high classification accuracy.

Keywords Sensor drift · Deep learning · Machine olfaction

X. Hu · Q. Liu (✉) · H. Cai · F. Li

Digital Media Technology Key Laboratory of Sichuan Province,
The School of Computer Science and Engineering,
University of Electronic Science and Technology of China, Chengdu 611731, China
e-mail: qiheliu@uestc.edu.cn

X. Hu

e-mail: hxn1025@foxmail.com

H. Cai

e-mail: caihb@uestc.edu.cn

F. Li

e-mail: lifan@uestc.edu.cn

1 Introduction

The principle of Machine olfaction is: (i) sensor array produces electrical signal response by absorbing the odor molecules; (ii) various methods are used to process these signals; (iii) pattern recognition system analyzes the input data and make decisions, accomplishing scheduled tasks, for instance, gas recognition and concentration measurement [1, 2]. In practical applications, sensor signals tend to show a significant variation due to changes in the experimental operating environment, aging of the sensor materials, and poisoning effects [3]. Sensor drift will change the cluster distribution in the data space and degrade the classification accuracy gradually [3, 4].

In the field of signal processing, the most effective methods for drift compensation are periodic recalibrations [4], whose main idea is using a reference gas to correct drift direction for individual sensor or for the entire array [5–7]. However, these techniques are all based on the assumption that the drift model is linear, which has not been confirmed yet, and they mostly need a reference gas that is chemically stable and highly correlated with the target gas in terms of sensor behavior, which is undoubtedly harsh in practical applications [4, 7].

Recently, machine learning methods are also applied to cope with drift [3, 8, 9]. In Vergara et al. [3], authors used ensemble learning methods to adapt a classifier to drift. This ensemble method is expensive in practice because it requires a large number of labeled data to dynamically train the classifiers. Semi-supervised methods used unlabeled data to improve performance of classification [8]. Compared with the ensemble methods, the semi-supervised methods are cheap because they only use unlabeled data to tackle drift. However, the above methods are not pervasive in real world applications because they need kinds of hand-designed features. In Långkvist and Loutfi [9], the authors proposed the e-nose data classification using deep learning, but they did not consider constructing suitable network structure to handle drift.

Keeping the research line based on machine learning methods, we present a new method to handle gas recognition under sensor drift using deep learning. The main idea of our method is automatically extracting unsupervised features by using deep learning and then training a gas classifier based on these features. Motivated by the characteristics of gas signal response, we designed two network structures, Deep Belief Networks (DBNs) based on Restricted Boltzmann Machines (RBM) and stacked Auto-Encoders (sAE) stacked by Auto-Encoders, to extract abstract features. Secondly, the softmax classifiers are constructed by using these features. Finally, we simulate both the network structures and experimental results show that they outperform support vector machine (SVM).

Compared with other methods, the advantages of our method are in the following three aspects. First, our method is pervasive. Since this method does not

use hand-extracted features, it can be applied to process signals sampled by any sensor and identify any type of gas. Second, our method is cheap. The method does not need reference gas to correct the drift direction of original data and only uses unlabeled data to learn features. Finally, our method is efficient for complex data. The feature extraction step in deep learning always implies a nonlinear process of dimensionality reduction, which not only increases efficiency but also improves the ability of expression for complex data. Based on these advantages, our method can effectively cope with gas recognition and sensor drift.

Our main contributions are: (i) to the best of our knowledge, we first used deep learning to handle sensor drift; (ii) we designed DBNs and sAE to tackle sensor drift and gas recognition, and empirical results prove that our method can effectively process sensor drift.

The rest of this paper is organized as follows: We first introduce deep learning and propose our method in [Sect. 2](#). Then we simulate the proposed method and in detail describe our experimental results in [Sect. 3](#). Finally, conclusions are given in [Sect. 4](#).

2 Methods

In this section, we demonstrate two types of deep networks, namely DBNs and sAE, and how we use them for gas recognition.

An auto-encoder can be seen as a neural network with three layers, as shown in [Fig. 1](#), including one input layer, one hidden layer, and one output layer. The aim of this kind of network is not classification or regression, but reconstructing the input in the output layer to obtain the activations of the hidden layer, which are thought to be the better representation than the original input. Except the input layer, activation of each unit is calculated as:

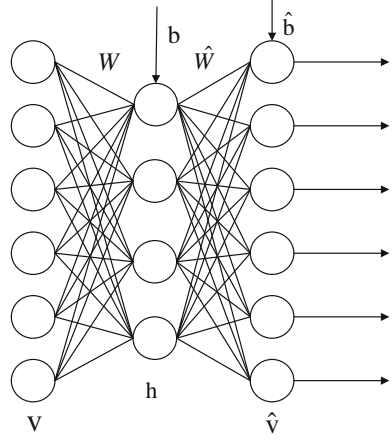
$$\alpha = \sigma(Wv + b) \quad (1)$$

where $\sigma(x) = \frac{1}{1+e^{-x}}$ is the logistic function, the cost function to be minimized is:

$$J = \frac{1}{2N} \sum_i \left(v^{(i)} - \hat{v}^{(i)} \right)^2 + \frac{\lambda}{2} \sum_i \sum_j W_{ij}^2 + \beta \sum_j \left[\rho \log \frac{\rho}{p_j} + (1 - \rho) \log \frac{1 - \rho}{1 - p_j} \right] \quad (2)$$

The first term is the reconstruction error term indicating the difference between the input and the output, the second is the weight decay term aiming at decreasing

Fig. 1 An auto-encoder with one hidden layer



the magnitude of the weights in case of overfitting, and the others are the sparse penalty terms whose purpose is enforcing the average activation of all the hidden units to be close to a small number ρ . The parameters λ and β control the relative importance of the three terms.

A stacked auto-encoder is a neural network consisting of multiple layers of auto-encoders in which the outputs of each layer is wired to the inputs of the successive layer. There are usually too many parameters for such a deep network to be trained effectively and therefore it is easy to converge to some bad local optima. Greedy layer-wise training has proved to be an algorithm effective to solve the above problem [10, 11]. The main idea was to train the parameters of each layer individually, then unroll all the layers into the architectures shown in Fig. 2 and fine-tune all parameters at the same time.

Since our task is to classify gasses but not simply generate features, we use the architectures with a softmax layer on the last layer of the encoder part, see Fig. 2b. The probability that the predicted class y belongs to class j given input vector x and weight matrix θ is given by:

$$P(y_i = j|x_i; \theta) = \frac{\exp \theta_j^T x_i}{\sum_{l=1}^k \exp \theta_l^T x_i} \quad (3)$$

We can minimize the cost function to train the weight matrix θ :

$$J(\theta) = -\frac{1}{m} \left[\sum_{i=1}^m \sum_{j=1}^k 1\{y_i = j\} \log P(y_i = j) \right] + \frac{\lambda}{2} \sum_{i=1}^m \sum_{j=1}^n \theta_{ij}^2 \quad (4)$$

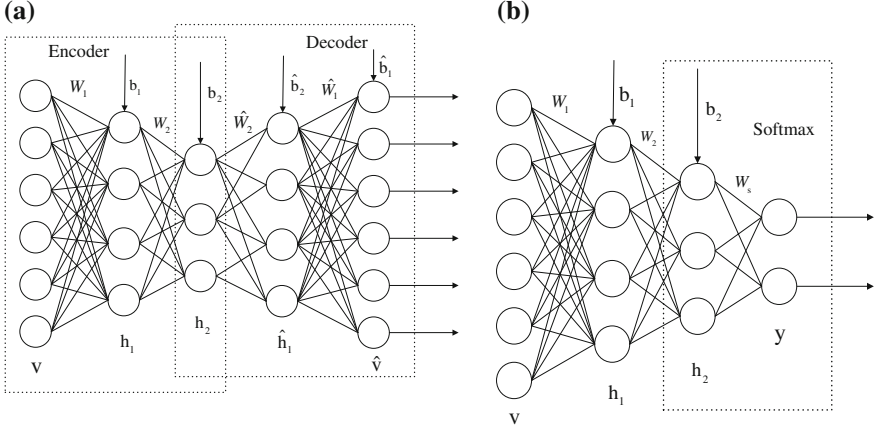


Fig. 2 Stacked auto-encoder with two hidden layers **a** Unsupervised and **b** supervised fine-tuning for different purposes

where $1\{\cdot\}$ is the indicator function, whose value is 1 if the statement is true and otherwise 0.

For gas data, the input vector of a single example is given by $v = (s_1, s_2, \dots, s_n)$, where s_i is the i th feature (or raw signal). So the entire input matrix is $V = (v_1^T, v_2^T, \dots, v_m^T)$. We scale each element of this matrix to $[0,1]$ by using the following normalization method:

$$V'_{i,j} = \frac{V_{i,j} - \min_i}{\max_i - \min_i} * [U - L] + L \tag{5}$$

where L and U denote the desired bound, namely 0 and 1, \min (\max) is a vector containing the minimum (maximum) of each row.

Assuming that we use an sAE with n hidden layers, now we present a detailed description of our method, see Algorithm 1. We use conjugate gradient [12] to train each layer or the entire network.

Algorithm 1 A gas recognition algorithm by sAE

Input: Train data $V = (v_1^T, v_2^T, \dots, v_m^T)$, corresponding labels $Y = (y_1, y_2 \dots y_m)$, and a new input v_p

Output: y_p : the label of v_p

Method: sAE

```

1: Normalize  $V$  by equation (5)
   // Pre-training
2:  $I = V'$ 
3: for (  $i = 1$  to  $n$ ) do
4:   Randomly initialize  $W, b, \widehat{W}, \widehat{b}$ 
5:   Train layer  $i$  (an auto-encoder) on data  $I$ 
6:    $W_i = W, b_i = b$ 
7:    $I = \sigma(WI + b)$ 
8: end for
9: Randomly initialize  $\theta$ 
10: Train softmax classifier on data  $I$  and labels  $Y$ 
11:  $W_s = \theta$ 
   // Fine-tuning
12:  $I = V'$ 
13: Train the entire network on data  $I$  and labels  $Y$ 
   // The predict steps
14: Normalize  $I = v_p'$ 
15: for (  $i = 1$  to  $n$ ) do
16:    $I = \sigma(W_i I + b_i)$ 
17: end for
18: Compute probability vector  $P$  on data  $I$  and parameter  $\theta$ 
19:  $y_p = \max(P)$ 
20: Return  $y_p$ 

```

A Restricted Boltzmann Machine consists of the following elements: Visible units v with bias vector c , hidden units h with bias vector b , and a weight matrix W connecting the hidden and visible units. Although its aim is the same as AE, an RBM can reconstruct the input by the transposition of W because it is a generative model, so that there is no actual output layer and the corresponding weights, see Fig. 3a.

The parameters W , b , and c are trained using contrastive divergence [13]. DBNs is formed by stacking several RBMs, see in Fig. 3b. For our experiment, we use DBNs with a softmax layer to classify gas data. The steps are very similar to sAE, except that we train an RBM instead of an auto-encoder in each layer.

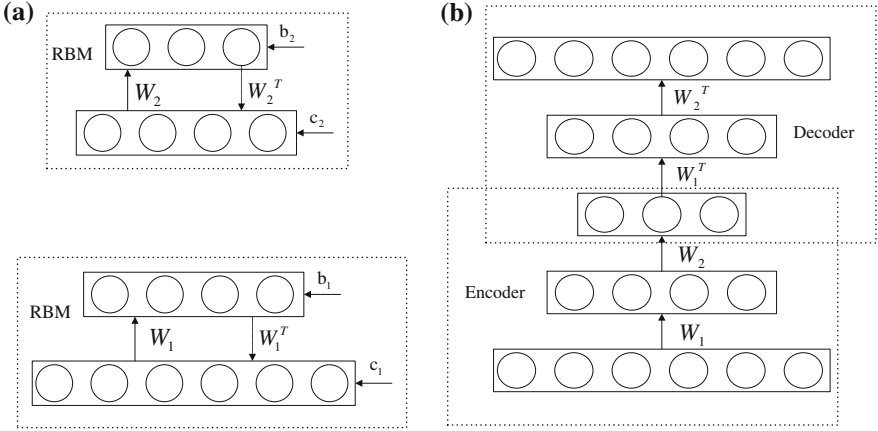


Fig. 3 Graphic depiction of **a** RBM and **b** unrolling two RBMs to form DBNs

3 Experiment

The experimental dataset comes from the UCI machine learning repository [14]. The collection period lasted for 36 months, which made sure that sensor drift happened over a long time. Authors divided the dataset into 10 batches, and each of them contained data of one or several successive months. More details refer to [3].

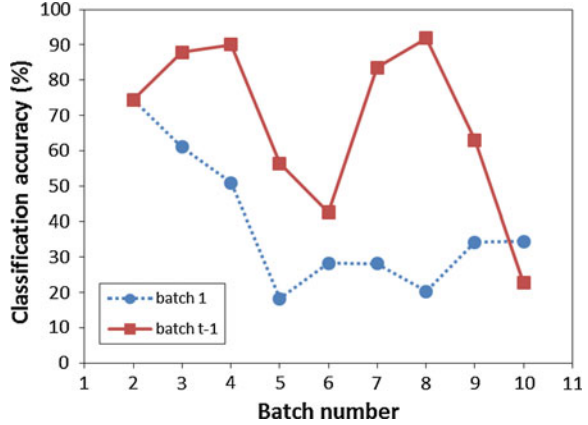
In our experiments, we consider two settings: (i) we trained a classifier on batch 1 and tested it on the reminder batches; (ii) we trained a classifier on batch $t-1$ and tested it on batch t . For reference, we use SVM [15] as a baseline method, we deploy LibSVM [16] to classify our data under the two settings, and the results are shown in Fig. 4.

Under setting 1, after trained on batch 1, the classifier is not adjusted and tested on the successive batches. Usually, we intuitively believe the more faraway from batch 1 a batch is, the larger sensor drift is. Therefore, performance of classifiers will degrade when the batch ID increases. In fact, as the dotted line in Fig. 4 indicates, there is an overall degradation of performance over time due to sensor drift. The merit of this setting is that we only provide labeled data on the initial time (batch 1).

Under setting 2, as opposed to setting 1, the training batches are dynamically changed according to the test batches. Since batch $t-1$ is close to batch t , we think sensor drift quantity is small between the two batches, and the classifiers should obtain good performance. Figure 4 proves our view, and performance of setting 2 is better than that of setting 1 except batch 10. The drawback of this setting is that we must provide new labeled data after time interval, so it is more expensive and laborious than setting 1.

In what follows, we used DBNs and sAE to extract features from data, respectively, and then applied a softmax layer to construct classifiers. We took

Fig. 4 Performance of SVM under two different settings



some efforts to achieve a better comparison and reference. On the one hand, we fixed the number of iterations and initialized a set of default parameters. For instance, in sAE we set 600 iterations for both pre-training and fine-tuning, and the default parameters are $\lambda = 3e - 3$, $\beta = 3e - 4$ and $\rho = 0.1$. On the other hand, we chose some fixed values for the random initialization in the pre-training step so that the networks were trained with the same initialization sequence every time.

The size of input layer and output layer is 128 and 6 due to the dataset. For simplicity, we describe the architecture of a deep network as $(h_1 - h_2 - \dots - h_n)$, where h_i denotes the number of units in hidden layer i . First, we used a sAE(40-40) and a DBNs(40-40) to run our experiments. The classification accuracy details on every batch are shown in Fig. 5.

We clearly see that the deep networks performed better than SVM under setting 1, which indicates that, by using deep learning, we can automatically extract new features from batch 1. The new features are robust to sensor drift. As opposed to setting 1, under setting 2, sAE and DBNs did not improve performance. We analyzed and found that different features caused this result. SVM used the same hand-features on different batches. However, deep networks learn to automatically extract features from these batches, and these features are unreliable because of sensor drift. Naturally, classifiers trained on the unreliable features did not improve performance. On the contrary, under setting 1, data from batch 1 had almost no drift because it was the first collection. Therefore, features extracted from batch1 are reliable. It is necessary to further research how to extract features from drifted data.

Next we attempted to improve the performance further by changing the parameters and the architecture of deep networks. We recorded the minimum and maximum of classification accuracy on every batch and listed them in Table 1. Notice that these results were under either setting 1 or setting 2, and we did not describe the parameters and network architecture corresponding to every single value for the sake of brevity.

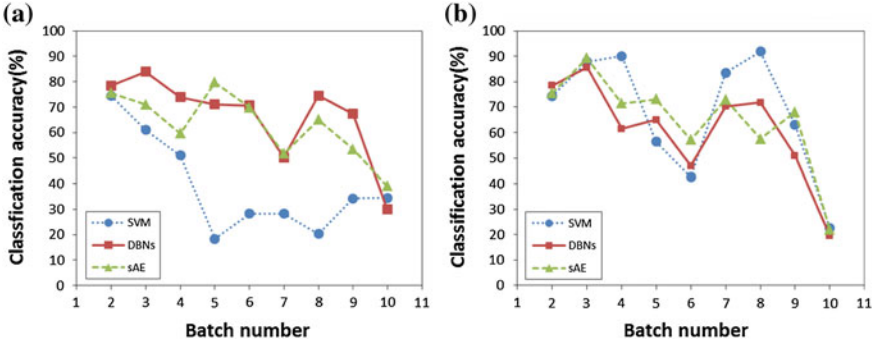


Fig. 5 Performances of SVM, sAE and DBNs under **a** setting 1 and **b** setting 2

Table 1 Min and max classification accuracy (%) on every batch

| ID | 2 | 3 | 4 | 5 | 6 | 7 | 8 | 9 | 10 |
|-----|-------|-------|-------|-------|-------|-------|-------|-------|-------|
| Min | 69.21 | 64.31 | 60.25 | 62.94 | 44.70 | 45.89 | 43.20 | 30.85 | 15.22 |
| Max | 80.68 | 92.75 | 86.34 | 87.82 | 78.65 | 82.93 | 94.22 | 72.13 | 48.05 |

In terms of the maxima, we see the improvement of performance on these batches. However, we found that the minima would reach a very low level. All this indicates that most of the batches were sensitive to the adjustment of parameters and network architecture, and we could not find a set of parameters or a kind of network to achieve good results on all the batches simultaneously. Moreover, there is no effective method for parameter selection in deep learning presently, so it is not practical to optimize especially parameter and network structures for data in different periods of time. Therefore, it is not meaningful to seek high accuracy on individual batch, and we only consider the average accuracy on the entire dataset under setting 1.

As shown in Table 2, we modified the default parameters for the previously used sAE(40-40) in the way of changing one parameter, while fixing the other two parameters. And we adjusted the network architecture for both sAE and DBNs, and the results are shown in Table 3.

Although there was a large fluctuation of classification accuracy on individual batch, the average performance was maintained at a certain level (around 65 %) throughout our experiments and much more superior to that of SVM (39 %), which suggests that the deep learning method is very appropriate and robust to mitigate the sensor drift.

Table 2 Performance (%) of sAE by different parameters

| $\rho = 0.05$ | $\rho = 0.1$ | $\beta = 3e - 3$ | $\beta = 3e - 5$ | $\lambda = 3e - 4$ | $\lambda = 3e - 5$ |
|---------------|--------------|------------------|------------------|--------------------|--------------------|
| 63.01 | 65.28 | 64.94 | 63.94 | 63.01 | 63.60 |

Table 3 Performance (%) of different network structure

| DBNs(40) | sAE(80) | DBNs(40-40) | sAE(40-40) | DBNs(80-40-40) | sAE(80-40-40) |
|----------|---------|-------------|------------|----------------|---------------|
| 67.49 | 63.20 | 66.65 | 62.75 | 67.17 | 65.71 |

4 Conclusions

In this work, we first applied deep learning to handle gas sensor drift. The main idea of our method is automatically extracting unsupervised features by using deep learning and then training a gas classifier based on these features. Since automatically extracted abstract features can cope with very complex data and non-linear transformation, our method is not only robust to gas sensor drift, but also pervasive. In addition, this method is cheap because it does not need many labeled data and reference gas, but only need suitable labeled data and unlabeled data. Concretely speaking, we designed two network structures, DBNs and sAE to extract abstract features, and then the softmax classifier are constructed by using these features. Finally, we simulate the both network structures and experimental results show that they outperform SVM. This turns out that deep learning is a simple and effective solution to sensor drift and gas recognition.

In the future work, we will investigate how to dynamically optimize parameters of deep networks according to the training data. It is also necessary to research how to use deep learning to extract features on data with drift.

Acknowledgment We would like to thank Alexander Vergara, San Diego and Ramon Huerta for providing public gas sensor drift data. This work is supported by the Opening Project of State key Laboratory of Electronic Thin Films and Integrated Device No. KFJJ201113, Project on the Integration of Industry, Education and Research of Guangdong Province No. 2012A090300001 and Chinese Central High Education Fund No. ZYGX2012J086.

References

1. Gardner JW, Bartlett PN (1999) Electronic noses: principles and applications. Oxford University Press, Oxford
2. Pearce TC, Schiffman SS, Nagle HT et al (2003) Handbook of machine olfaction: electronic nose technology. Wiley, Weinheim
3. Vergara A, Vembu S, Ayhan T et al (2012) Chemical gas sensor drift compensation using classifier ensembles. Sens Actuators, B 166:320–329

4. Gutierrez-Osuna R (2002) Pattern analysis for machine olfaction: a review. *Sens J IEEE* 2(3):189–202
5. Gutierrez-Osuna R (2000) Drift reduction for metal-oxide sensor arrays using canonical correlation regression and partial least squares. In: *Proceedings of the 7th international symposium on olfaction and electronic nose*
6. Artursson T, Eklöv T, Lundström I et al (2000) Drift correction for gas sensors using multivariate methods. *J Chemom* 14(5–6):711–723
7. Haugen JE, Tomic O, Kvaal K (2000) A calibration method for handling the temporal drift of solid state gas-sensors. *Anal Chim Acta* 407(1):23–39
8. De Vito S, Fattoruso G, Pardo M et al (2012) Semi-Supervised Learning Techniques in Artificial Olfaction: A Novel Approach to Classification Problems and Drift Counteraction. *IEEE Sens J* 12(11):3215–3223
9. Långkvist M, Loutfi A (2011) Unsupervised feature learning for electronic nose data applied to bacteria identification in blood. *NIPS 2011* In: *Workshop on deep learning and unsupervised feature learning*
10. Hinton GE, Osindero S, Teh YW (2006) A fast learning algorithm for deep belief nets. *Neural Comput* 18(7):1527–1554
11. Erhan D, Manzagol PA, Bengio Y et al (2009) The difficulty of training deep architectures and the effect of unsupervised pre-training. In: *International Conference on artificial intelligence and statistics*. pp 153–160
12. Ngiam J, Coates A, Lahiri A et al (2011) On optimization methods for deep learning. In: *Proceedings of the 28th International conference on machine learning* pp 265–272
13. Hinton GE (2002) Training products of experts by minimizing contrastive divergence. *Neural Comput* 14(8):1771–1800
14. Data available at <http://archive.ics.uci.edu/ml/datasets/Gas+Sensor+Array+Drift+Dataset>
15. Cortes C, Vapnik V (1995) Support-vector networks. *Mach Learn* 20(3):273–297
16. Chang CC, Lin CJ (2011) LIBSVM: a library for support vector machines. *ACM Trans Intell Syst Technol* 2(3):27

Wheel Slip Ratio Adaptive Control for Distributed Drive Electric Vehicles

Yongqiang Deng, Liang Shao, Chi Jin and Lu Xiong

Abstract This article conducts a research on wheel slip ratio control for distributed drive electric vehicles. In consideration of wheel rotation dynamics and its strong nonlinear properties, a proportional–integral controller is designed in this paper aimed at regulating the wheel slip ratio to a constant value regardless of the road adhesion conditions. At the same time, an online road coefficient estimator is proposed to provide optimal slip ratio for the designed wheel slip ratio controller. The global asymptotic stability of the system is proved by the Lyapunov stability theory. In addition, a distributed drive electric vehicle model is established for performance assessment due to its precise and fast-response torque control. Simulation results show that the proposed controller adaptively regulates the wheel slip ratio to the optimal value of current road with fast convergence speed and high accuracy. Generally, the proposed adaptive controller greatly improves the driving performance of the electric vehicle.

Keywords Adaptive control · Road adhesion estimation · Wheel slip ratio · Electric vehicle

Y. Deng · C. Jin · L. Xiong (✉)

School of Automotive Studies and Clean Energy Automotive Engineering Centre,
Tongji University, Shanghai 201804, China
e-mail: xionglu.gm@gmail.com

Y. Deng
e-mail: 543956156@qq.com

C. Jin
e-mail: jinchitru@163.com

L. Shao
Sino-German College for Graduate Study and Clean Energy Automotive Engineering
Centre, Tongji University, Shanghai 201804, China
e-mail: shaoliangtjauto@gmail.com

1 Introduction

As global energy crisis and environmental pollution is worsening, electric vehicles (EV) become vigorous. Distributed drive EV has been an issue in research now because electric wheels have properties of fast torque control and quick response [1]. It makes possible for electric wheel to regulate slip ratio to the optimum value under different road adhesion conditions which contributes to the driving efficiency.

In terms of wheel rotate dynamics, the object of wheel slip ratio control is a nonlinear system with uncertainty of road adhesion coefficient. Anti-slip regulation system is a mature technique in traditional vehicle wheel dynamics control which is trying to keep the wheel from drifting by limiting the wheel slip ratio in a region [2, 3]. The common controller attached in traditional vehicles uses wheel rotation speed and acceleration as logic thresholds [2]. A sacrifice of driving efficiency is premised on this method and it behaves differently under different adhesion conditions. Recently, some approaches based on fuzzy method [4–6], PID control [2, 7], and sliding mode control [8, 9] are used in this field. When it comes to wheel slip ratio adaptive control, an online road estimator for the identification of optimal wheel slip ratio cannot be ignored which remains to be a difficult problem. Methods to estimate the road coefficient today [10–12] have several problems such as lack of accuracy, long time computation, and unsatisfied real-time performance. As shown in Fig. 1, this article proposes a brand new wheel slip ratio adaptive controller for distributed drive EV. Presented with theoretical strict proof and simulation results, this approach can significantly improve the driving performance of distributed drive EV.

2 Wheel Slip Ratio Control

2.1 Description of Wheel Rotating Dynamic

Electric wheel torque control works independently for distributed drive electric vehicle. A single wheel model is established to design the slip ratio controller.

As shown in Fig. 2, the single wheel model can be described as:

$$I_{\omega}\dot{\omega} = T_m - F_x r. \quad (1)$$

Definition of wheel slip ratio (accelerating):

$$\lambda = (\omega r - v)/\omega r > 0. \quad (2)$$

Wheel slip ratio dynamic can be described as:

Fig. 1 Wheel slip ratio adaptive controller

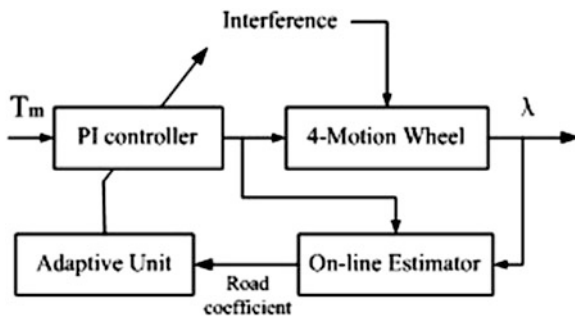
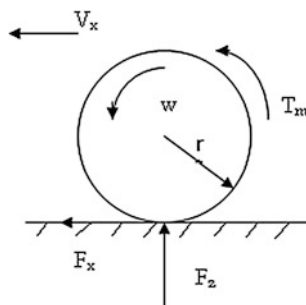


Fig. 2 Single wheel model



$$\dot{\lambda} = \frac{r}{vI_{\omega}} \left[-r\mu(\lambda)F_z(1 - \lambda)^2 + T_m(1 - \lambda)^2 \right] - \frac{\dot{v}}{\omega r}. \tag{3}$$

2.2 Proof of Proportional–Integral Control

Consider the first-order nonlinear system:

$$\dot{x} = f(x) + u \tag{4}$$

where $x \in R$, u is control input and f is an unknown zero-axial function. f is Lipchitz with Lipchitz constant L_f .

To stabilize the system, an input of $u = -k_1x - k_2 \int_0^t xdt$ is introduced into it which can make the system asymptotically stable.

Proof In order to use Lyapunov stability theory to analyze the system, an extended order method is applied:

$$\dot{x}_1 = g(x_1) + u = f(x_1) + b + u; \quad \dot{x}_2 = x_1. \quad (5)$$

Proportional–integral control input of $u = -(Lx_1 + kx_2)$ leads to:

$$\dot{x}_1 - f(x_1) + Lx_1 + k \int x_1 dt = b. \quad (6)$$

Consequently, this system is equivalent to a spring-damper system which can reach an equilibrium point. To prove that, we usually set the equilibrium point to the origin:

$$\begin{cases} \dot{\bar{x}}_1 = \dot{x}_1 \\ \dot{\bar{x}}_2 = \dot{x}_2 = x_1 = \bar{x}_1 \end{cases}. \quad (7)$$

Constructing a Lyapunov function as:

$$V(\bar{x}) = \bar{x}_1^2/2 + k\bar{x}_2^2/2 \geq 0. \quad (8)$$

We can see that:

$$\dot{V}(\bar{x}) = \bar{x}_1 \cdot \dot{\bar{x}}_1 + k\bar{x}_2 \cdot \dot{\bar{x}}_2 = -(L\bar{x} - f(\bar{x}_1)) \cdot \bar{x}_1 \leq 0 \quad (9)$$

1. $V(\bar{x}) \geq 0$, with equality if and only if $x = 0$, positive definite;
2. $\dot{V}(\bar{x}) \leq 0$, with equality if and only if $x = 0$, negative definite;
3. For $\bar{x} \in R$, when $\|\bar{x}\| \rightarrow \infty$, $V(\bar{x}) \rightarrow \infty$.

It is concluded that this first-order system is globally asymptotically stable in the sense of Lyapunov.

2.3 Wheel Slip Ratio PI Controller

The tracking error is defined as $e = \lambda - \lambda_{\text{ref}}$, and its dynamics:

$$\dot{e} = \frac{r}{vI_\omega} \left[-r\mu(e)F_z - r\mu(\lambda_{\text{ref}})F_z + T_m - \frac{v\dot{I}_\omega}{\omega r^2} \right]. \quad (10)$$

Obviously, when $e = 0$, $\phi(e) = 0$.

The proportional–integral control method is applied to this physical system, from which we can obtain the output controlling electric wheel torque:

Table 1 Parameters of designed PI controller

| k_1 | k_2 |
|-------|-------|
| 1.5 | 12 |

$$T_m = \frac{v\dot{v}I_\omega}{\omega r^2} - rF_z \left(k_1 e + k_2 \int e dt \right). \quad (11)$$

Theoretically, the system is Lyapunov stable and the wheel slip ratio can be regulated to the preset value regardless of the road uncertainties.

2.4 Simulation Verification

2.4.1 Simulation Configuration

To verify the PI controller's viability and effectiveness, a distributed drive EV model is established with an inner Magic Formula tire-road model. A series simulation tests were conducted on different road coefficients. Through repeated simulation experiments, tuning parameters of PI controller are shown in Table 1.

Simulation settings:

The distributed drive EV starts with a velocity of 2 m/s; three different road adhesion coefficients (0.2, 0.5, and 0.8); optimal wheel slip ratio is set to 0.2.

2.4.2 Simulation Results

As it is shown in Fig. 3, the proposed wheel slip PI controller for distributed drive EV can regulate the wheel slip to the preset value with fast and accurate convergence. Therefore, the reliable guarantee is provided for wheel slip ratio adaptive control due to its independent properties.

3 Design of Road Estimator

3.1 Problem Formulation

The wheel slip ratio dynamic control can be modeled as:

$$\dot{\omega} = [g(t, \omega, \theta) + T_m]/I_\omega \quad (12)$$

where $g(t, \omega, \theta)$ is specified as $-F_z r \mu(\theta, \omega)$ which stands for the wheel longitudinal force.

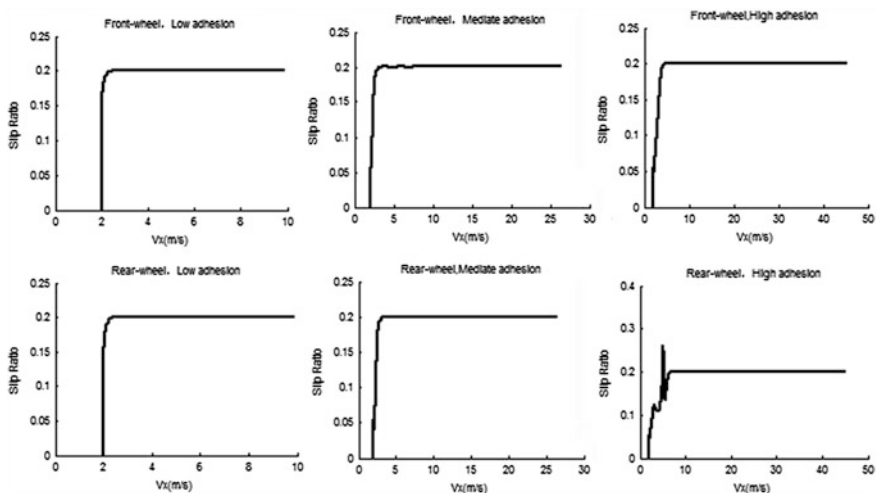


Fig. 3 Slip control results under different adhesion road

Table 2 Parameters of improved Burckhardt model

| c_1 | c_2 | c_3 | c_4 |
|-------|-------|-------|-------|
| 18 | 8 | 0.11 | 0.25 |

The fitting parameters of tire-road model are shown in Table 2 where road coefficient u can be evaluated by θ as:

$$\mu(\theta, \lambda) = \theta - \theta e^{-\frac{c_1}{\theta}(\lambda + c_2 \lambda^2)} - c_3 \lambda \operatorname{sgn}(\lambda) + c_4 \lambda^2. \quad (13)$$

3.2 Parameter Estimation

Thus, a full estimator of road coefficient is introduced:

$$\begin{aligned} \dot{y} &= -K_i \left(\frac{1}{I_w} T_m + \hat{\phi} \right) - \frac{1}{I_w} \cdot f(t, \omega, \hat{\phi}, \hat{\theta}) \cdot \left(-F_z r \frac{\partial \mu(\hat{\theta}, \omega)}{\partial \omega} \right) \\ \hat{\phi} &= y + K_i \omega - \frac{1}{I_w} F_z r \cdot \mu(\hat{\theta}, \omega) \\ \hat{\theta} &= f(t, \omega, \hat{\phi}, \hat{\theta}) = \gamma [\theta * (t, w, \hat{\phi}) - \hat{\theta}]. \end{aligned} \quad (14)$$

Table 3 Estimator parameters

| K_i | γ |
|-------|----------|
| 100 | 10 |

The estimator generally consists of two parts: an estimator for ϕ and an update law for θ .

Where K_i and γ are positive gain coefficients, $\theta^*(t, w, \hat{\phi})$ denotes the solution of the inversion problem found from $\hat{\phi} = \mu(\theta^*, \omega) \cdot F_z r / I_\omega$.

3.3 Simulation Verification

3.3.1 Simulation Configuration

A distributed driving electric vehicle model is established and the slip ratio control system is turned off in order to see if the road estimator works correctly in different conditions. The tuning parameters for estimator are shown in Table 3.

Simulation settings: Initial speed 5 m/s; different throttle accelerating (0.25, 0.5, 0.8); constant road adhesion coefficient (0.2, 0.5, 0.8).

3.3.2 Simulation Results

As shown in Fig. 4, the designed road coefficient estimator gains a fast convergence to the real value under different circumstances. Furthermore, it obtains accurate estimated results of the real road conditions. The throttle is varying in order to get the proper wheel slip ratio on different road condition. Thus, a good wheel slip ratio controller is necessary to keep the property of designed estimator.

4 Wheel Slip Ratio Adaptive Control

4.1 Adaptive Controller Modeling

From the referred tire-road model, we can get the optimal slip ratios on different road conditions, as shown in Fig. 5.

We assume that the designed estimator obtains the adhesion coefficient and outputs a real-time optimal slip ratio to the designed PI slip controller. Thus, we can get an adaptive controller for slip ratio and it is applied to the distributed driving electric vehicle. The simulation model is shown in Fig. 6. Here we list the tuned parameters of the slip ratio adaptive controller, shown in Table 4.

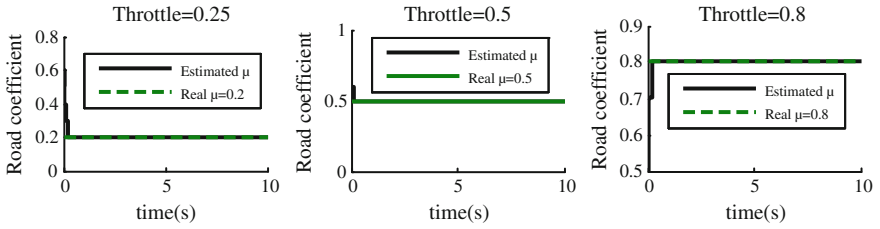


Fig. 4 Different adhesion road estimation results

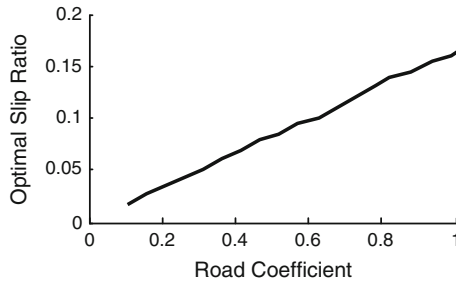


Fig. 5 Optimal slip ratio

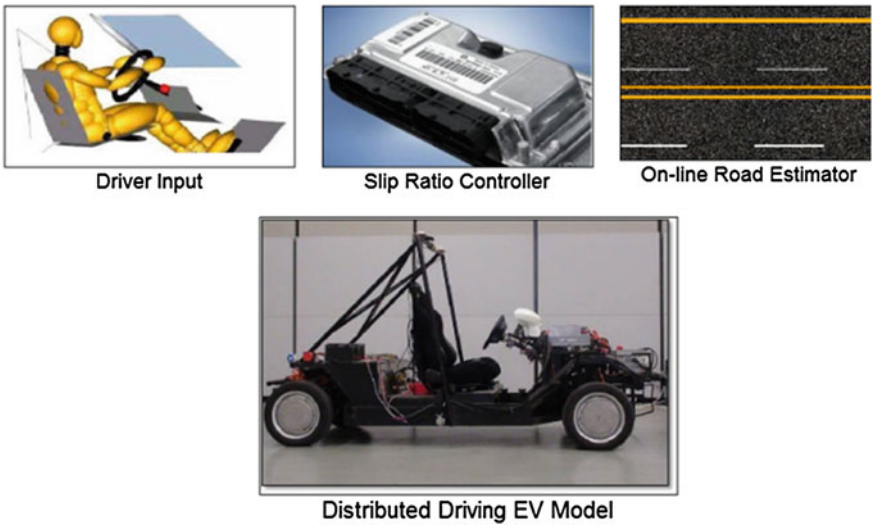


Fig. 6 Simulation model

Table 4 Parameters of slip ratio adaptive controller

| k_1 | k_2 | K_i | γ |
|-------|-------|-------|----------|
| 1.5 | 12 | 100 | 10 |

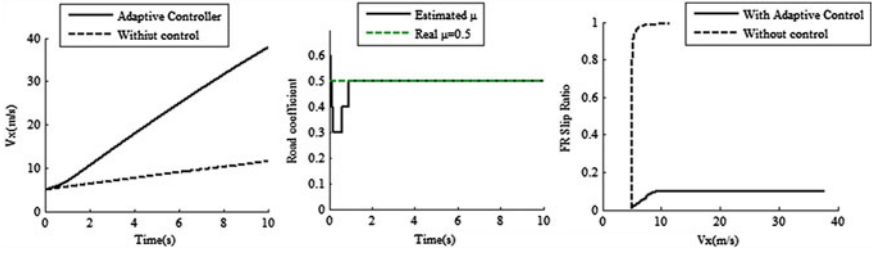


Fig. 7 Performance of adaptive slip ratio controller on constant adhesion road

4.2 Simulation Verification

In order to check out the performance of the designed wheel slip ratio adaptive controller, we conduct a constant road test and changing road test.

4.2.1 Constant Road Simulation

- Simulation settings:
Initial speed 5 m/s; full throttle; constant road adhesion coefficient $u = 0.5$.
- Simulation results:

As shown in Fig. 7, the designed road adhesion coefficient estimator converges to the true value within 1 s which sets up an accurate and stable property. Distributed driving EV with wheel slip ratio adaptive controller accelerates quicker than the one without control. As a result, the adaptive controller dramatically improves the driving efficiency of the vehicle.

4.2.2 Changing Road Simulation

- Simulation settings:
Full throttle accelerating; changing road adhesion coefficient (Fig. 8).
- Simulation results:

As shown in Fig. 9, simulation results show that the designed wheel slip ratio adaptive controller has a sensitive perception of road changes which owes to the uniform asymptotic stability of the designed estimator. When road changes, the wheel slip ratio will adaptively converge to the optimal value which greatly improves the driving performance of distributed driving electric vehicles.

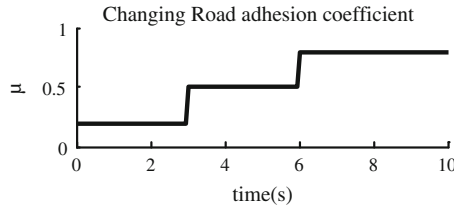


Fig. 8 Changing road adhesion coefficient

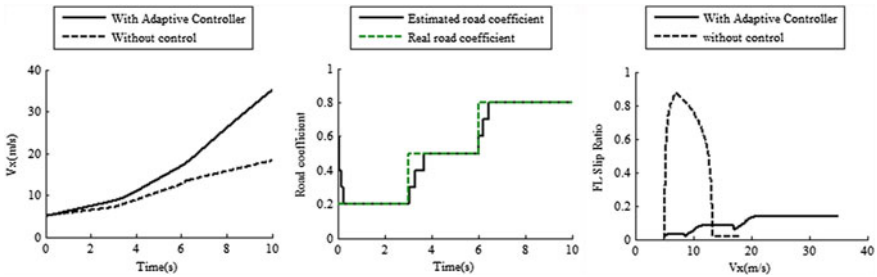


Fig. 9 Performance of adaptive slip ratio controller on changing adhesion road

5 Conclusions

This article proposes a self-tuning adaptive control method for electric wheel slip ratio. Compared to the thresholds or fuzzy logic controllers done before, the new adaptive controller claims a more stable property. The stability of the controller is guaranteed by Lyapunov stability theory which is essential for adaptive control of a real physical system.

The proposed wheel slip ratio adaptive controller for distributed drive EV consists of PI controller and online road estimator. Both of them are verified under different conditions, respectively. Furthermore, constant and changing road adhesion coefficients are simulated with the proposed adaptive controller based on a distributed drive EV model. The simulation results show that wheel slip ratio can be regulated to the optimum point of the real road quickly, accurately, and adaptively. It contributes to an excellent drive performance in the view of driving efficiency.

For the further work, tire-road demarcating experiments are necessary for the proposed controller and it remains to be verified on our distributed drive electric vehicle in practice

Acknowledgements This work was supported by National Basic Research Program of China (No. 2011CB711200).

References

1. Yu Z, Feng Y, Xiong L (2013) Review on vehicle dynamics control of distributed drive electric vehicle. *J Mech Eng* 49(8):105–107
2. Guangqiang W, Zhang C et al (2000) A research on the control method of vehicle anti-slip regulation. *Automot Eng* 22:324–327
3. Wang W, Ding N et al (1999) A research on the control algorithm and its HIL simulation of automotive asr systems. *Autom Eng* 31:1043–1045
4. Li Gang, Zong Chang-fu et al (2012) Acceleration slip regulation control of 4WID electric vehicles based on fuzzy road identification. *J S China Univ Technol* 40:99–103
5. Zhang X, Luo Yet al (2007) A research on optimal slip ratio identification-based traction control system implemented on EV. *Veh Power Technol* 3:15–17
6. Zhao Z, Jun G, Zhuoping Y (2011) Study of acceleration slip regulation strategy for four wheel drive hybrid electric car. *J Mech Eng* 47:91–95
7. Jiang Z, Chen X, Li D (2012) Acceleration slip regulation of four-wheel drive electric vehicle based on road automatic identification. *J Chongqing Univ Techn* 26:18–21
8. Zou G, Luo Y et al (2008) Slip ratio control for independent AWD electric vehicles based on fuzzy DSMC. *J Tsinghua Univ* 48:860–863
9. Jalili-Kharaajoo M, Besharati F (2003). Sliding mode traction control of an electric vehicle with four separate wheel drives. In: *Proceedings of emerging technologies and factory automation*, vol 2, pp 291–296
10. Zhao L, Liu Z, Chen H (2009) The estimation of vehicle speed and tire-road adhesion coefficient using moving horizon strategy. *Automot Eng* 31:520–525
11. Gu Q, Cheng X (2011) Study on optimal slip ratio identification and traction control for electric vehicle. In: *Proceedings of international conference on mechatronic science*, pp 738–742
12. Wang W-Y, Li I-H et al (2009) Dynamic slip-ratio estimation and control of antilock braking systems using an observer based direct adaptive fuzzy neural controller. *Indus Electr* 56:1746–1756

Active Disturbance Rejection Control for Tension Regulation of Stainless Steel Strip Processing Line

Wei Zhang, Yin Cai, Bo Deng and Xiaolan Yao

Abstract To describe sagging dynamics of processing stainless steel strip, the concept “equivalent elastic modulus” is introduced in this paper. Based on which, a tension dynamic model of steel strip is then built. Considering the nonlinear nature and the rapid change in operating conditions of the stainless steel strip processing line, and industrial controller cannot resist disturbance effectively, a tension control method based on active disturbance rejection control (ADRC) strategy is presented. Meanwhile, the parameter tuning method for this ADRC is also proposed. Simulation results show the effectiveness of the proposed strategy.

Keywords Web winding system · Stainless steel strip processing line · Sagging · Tension control · Active disturbance rejection control · Nonlinear

1 Introduction

Stainless steel strip processing line is a typical winding system. It usually includes unwinder, rewinder, bridle, looper, processing segment, skin pass mill, etc. The main control objective of processing line is to keep strip tension stable during the production process, especially in the processing segment. However, the tension problem is crucial because of its nonlinear dynamics and coupled relationship with velocity.

In the past few decades, various advanced control strategies and methods have been proposed and applied to solve tension control problem of winding system,

W. Zhang (✉) · X. Yao

School of Automation, Beijing Institute of Technology, Beijing, China
e-mail: zwbxj4889475@163.com

Y. Cai · B. Deng

Metals, ABB (China), Beijing, China

such as fuzzy logic [1], optimal control [2], neural network [3], robust control approaches [4], etc. But most of them are difficult to implement in the real world. In addition, due to large density of stainless steel and far distance between two transporting rolls in stainless steel strip processing line, the impact of strip sagging on tension dynamic cannot be ignored. While the impact has not been considered in the foregone papers, these methods cannot be directly applied to the stainless steel strip processing line. In this area, PI control is the only strategy that has been applied in industry applications. But PI control cannot meet all the requirements of the control objects and specifications: (1) PI control cannot solve the conflict between rise time and overshoot; (2) PI controller cannot reject tension disturbance quickly and effectively. Therefore, to further improve the quality and efficiency in industry, researchers and engineers alike to explore better methods for tension control.

The emergence of active disturbance rejection control (ADRC) brings a new way to solve the tension control problem [5, 6]. The proposed control strategy actively estimates and rejects the effects of both dynamic changes in the system and external disturbances, which is more suitable for tension regulation theoretically. Wankun and Zhiqiang [7] applied ADRC to the tension control of looper firstly. Based on it, this paper applies ADRC to stainless steel strip processing line. Considering the characteristics of the processing line, the paper first uses research method of cable dynamics [8] to describe strip sagging dynamics and put forward the concept of “equivalent elastic modulus” in modeling tension dynamics of stainless steel strip processing line. Then design ADRC to this tension dynamic and give the tuning method of ADRC. In order to validate the efficiency of the proposed strategy, we apply ADRC to industrial simulation model of pickling section of stainless steel strip processing line, and compare with the industrial PI controller in tracking and disturbance rejection performance.

2 Tension Dynamics Model

Figure 1 is an n -span stainless steel strip processing line, which consists of the unwinder/rewinder and $(N - 1)$ intermediate-driven rollers. Each roller is associated with r_i , v_i , t_{qi} , and each strip span is associated with F_i . r , v , t_q , F denote the radius of roll, roll surface velocity, motor torque, and strip tension, respectively.

2.1 Equivalent Elastic Modulus

To discuss sagging dynamics of processing stainless steel strip, consider a steel strip span between two successive rollers in processing line as shown in Fig. 2. For the sake of simplicity, the following three assumptions are made on system as follows.

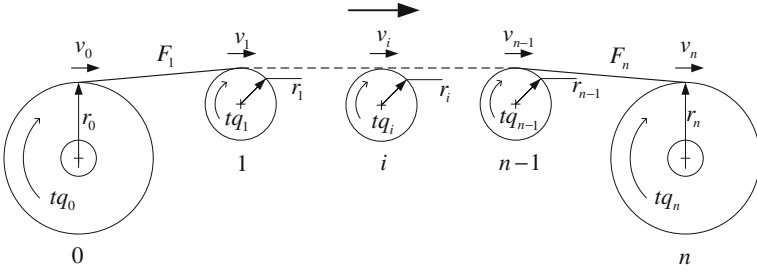
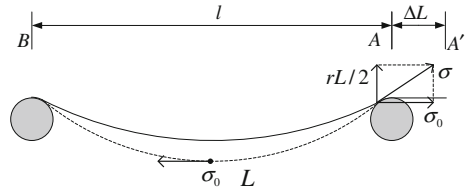


Fig. 1 Schematic of an n -span stainless steel strip processing line

Fig. 2 Sagging steel strip model



Assumption 1 When the curvature of steel strip is moderate, the shape of sagging strip can be treated as a second-order parabolic.

Assumption 2 There is no slippage between roller and steel strip.

Under Assumption 1, the length of sagging strip can be expressed as

$$L = l + \frac{\gamma^2 l^3}{24\sigma_0^2} \tag{1}$$

where L and l are the length of sagging and without sagging strip, respectively. $\gamma = g\rho \approx 9.8\rho$ is bulk density of strip. g and ρ are acceleration of gravity and the density of strip, respectively. σ_0 is the normal stress in the center of the sagging strip.

Definition 1 When sagging dynamics of strip between two consecutive rolls changed, define the concept “equivalent elastic modulus” as:

$$E_s = d\sigma / (\Delta L / L) \tag{2}$$

where $d\sigma$ is the incremental of the normal stress in the center of the sagging strip. As shown in Fig. 2, ΔL is elongation of strip. L is the length of strip in original sagging state.

Theorem 1 *The impact of strip sagging on strip tension dynamic can be taken as the change of equivalent elastic modulus of strip.*

Proof Suppose the end point of strip moves from A to A' when the normal stress in the center of the sagging strip increases to $\sigma_0 + d\sigma$, while the total elongation of strip is as follows:

$$\Delta L = \Delta L_e + \Delta L_c \quad (3)$$

where ΔL , ΔL_e , and ΔL_c are total elongation of strip, elongation caused by elastic deformation, and elongation caused by the change of sagging state, respectively.

Based on Hooke's law, we have

$$\Delta L_e = \frac{L}{E_0} d\sigma \quad (4)$$

where E_0 is elastic modulus of strip.

From Eq. (1), we have

$$\Delta L_c = L_c(\sigma_0) - L_c(\sigma_0 + d\sigma) \quad (5)$$

Since magnitude of σ_0 is generally as big as 10^7 and $d\sigma$ can be ignored compared to σ_0 , using (1) and (5), the following expression of ΔL_c can be obtained:

$$\Delta L_c = \frac{\gamma^2 l^3}{24} \left(\frac{2\sigma_0 d\sigma + (d\sigma)^2}{(\sigma_0 + d\sigma)^2 \sigma_0^2} \right) \approx L \frac{\gamma^2 l^2}{12\sigma_0^3} d\sigma \quad (6)$$

Substituting (3), (4), (6) to (2), and we can get:

$$E_s = \frac{1}{1 + \frac{\gamma^2 l^2}{12\sigma_0^3} E_0} E_0 = f_s E_0 \quad (7)$$

where f_s is stiffness coefficient of sagging strip.

Thus, the effect of strip sagging on tension dynamic can be equivalent to the change of equivalent elastic modulus. The theorem is proved.

2.2 Mathematical Model of Strip Tension Dynamics

Based on reference [7], the equations of strip tension behavior between two consecutive rollers and the equations describing the velocity of roll are presented as

$$\frac{dF_{T_i}}{dt} = \frac{E_{S_i}S}{L_i} \left[(v_i - v_{i-1}) + d_p \left(\frac{dv_i}{dt} - \frac{dv_{i-1}}{dt} \right) \right] + \frac{1}{L_i} (F_{T_{i-1}}v_{i-1} - F_{T_i}v_i) \quad (8)$$

$$\frac{dv_i}{dt} = \frac{r_i}{J_i} [r_i(F_{T_{i+1}} - F_{T_i}) + T_{q_i} - T_{q_{loss_i}}] \quad (9)$$

where E_{S_i} and S are equivalent elasticity modulus and the cross-section area of the strip, respectively. L_i is the length of the strip span between two adjunct rollers. d_p is damping coefficient. J_i is the inertia. T_{q_i} is the input motor torques. $T_{q_{loss_i}}$ is loss torque main of which is friction loss and bending loss.

There is product of the tension and speed in Eq. (9), which shows the tension dynamics are highly nonlinear and sensitive to velocity variations.

3 ADRC Design

In industrial site, strip tension is commonly adjusted by regulating the speed of the adjacent rollers. The reference [7] designed ADRC for both speed loop and tension loop of winding system, respectively. From velocity dynamic expression (10), it is known that the velocity dynamic has a good linearity, so it is relatively easy to control. Practices in industrial site also show that it has met the requirements of the rapidity and control accuracy that applying PI to speed regulation. Therefore, this paper will focus on the ADRC design for tension regulation.

To design the ADRC, linearize the nonlinear tension dynamic (9) at stable operating point $(\bar{F}_{T_i}, \bar{v}_i)$

$$\dot{\bar{F}}_{T_i} = f_i(t) + b_i u \quad (10)$$

where $u = v_i$ is the control signal, and $b_i = (E_{S_i}S - \bar{F}_{T_i})/L_i$ is the coefficient of the control input. $f_i(t) = d + \hat{f}_i(t)$ denotes the total uncertainty including external disturbance d and unknown internal dynamic \hat{f}_i :

$$d = -\frac{E_{S_i}S - \bar{F}_{T_i}}{L_i} v_{i-1} - \frac{d_p E_{S_i}S}{L_i} \dot{v}_{i-1} + \frac{\bar{v}_i}{L_i} F_{T_{i-1}} + \frac{d_p E_{S_i}S r_i}{L_i J_i} (r_i F_{T_{i+1}} + T_{q_i} - T_{q_{loss_i}}) \quad (11)$$

$$\hat{f}_i(t) = -(d_p E_{S_i}S r_i^2 + J_i \bar{v}_i) F_{T_i} / (L_i J_i) \quad (12)$$

Due to parameter E_{S_i} is time-varying in the process, the value of b_i cannot be determined. Introduce the adjustable parameter b_0 that is the estimated value of b_i . Taking $\tilde{f}_i(t) = f_i(t) + (b_i - b_0)u$ as the total disturbance, the Eq. (11) can be rewritten as:

$$\dot{F}_{Ti} = \bar{f}_i(t) + b_0 u \quad (13)$$

Equation (13) shows the internal dynamic of strip tension system is first-order and coupled with velocity. So the first-order ADRC is adopted.

3.1 Expand State Observer Design

The key to the control design is to compensate for $\bar{f}_i(t)$, and the job will be much simpler if its value can be determined at any given time. To this end, an extended state observer (ESO) is designed to achieve the online estimation of $\bar{f}_i(t)$.

Writing the plant in (14) in a state space form:

$$\begin{cases} \dot{x}_1 = x_2 + b_0 u \\ \dot{x}_2 = h \\ y = x_1 \end{cases} \quad (14)$$

Let $x_1 = F_{Ti}$, $x_2 = \bar{f}_i(t)$, where x_2 is the augmented state variable, and $h = \dot{\bar{f}}_i(t)$ as unknown disturbance.

Now $\bar{f}_i(t)$ can be estimated using a state observer based on the state space model (15). A state observer, referred to as linear extended state observer (LESO), can be constructed as to estimate both $x_1 = F_{Ti}$ and $x_2 = \bar{f}_i(t)$:

$$\begin{cases} \dot{z}_1 = z_2 + b_0 u + l_1(y - z_1) \\ \dot{z}_2 = l_2(y - z_1) \end{cases} \quad (15)$$

where $L = [l_1 \quad l_2]^T$ is observer gain vector. With a functioning LESO, Z_1 and Z_2 are closely track x_1 and x_2 , respectively.

3.2 State Error Feedback Law Design

If the total disturbance \bar{f}_i can be estimated, the control law is

$$u = (-z_2 + u_0)/b_0 \quad (16)$$

Then the system is reduced to a simple first-order integral plant:

$$\dot{F}_{Ti} = \bar{f}_i(t) - z_2 + u_0 \approx u_0 \quad (17)$$

The control design is now standardized to that of a simply integral plant. For this first-order integral plant, the control problem is become much easier, where

can be easily controlled using a proportional term. Because the tensions of stainless steel strip processing line are measured by load cells, we can take the output as a feedback signal directly:

$$u_0 = k_p(F_{Ti_ref} - F_{Ti}) \quad (18)$$

where F_{Ti_ref} is tension reference, and k_p is proportional gain.

3.3 ADRC Parameters Regulation

b_0 is the approximate value of b_i , so the smaller the error of estimate is, the better the control effect of ADRC is. From linearized dynamic model (11), the expression of b_i is

$$b_i = (E_{Si}S - \bar{F}_{Ti})/L_i \quad (19)$$

If tension can be controlled, the tension expected value should be the reference tension when system is stable. Therefore, let strip tension at stable operating point is the reference tension, that is $\bar{F}_{Ti} = F_{Ti_ref}$. Then b_0 is obtained as follows:

$$b_0 = (E_{Si}S - F_{Ti_ref})/L_i \quad (20)$$

The key element of ADRC is LESO, so the key to make the ADRC work well is LESO tuning. According to literature [9], by setting characteristic polynomial of observer:

$$s^2 + l_1s + l_2 = s^2 + 2\zeta\omega_o + \omega_o^2 \quad (21)$$

The observer gains are $l_1 = 2\zeta\omega_o$, $l_2 = \omega_o^2$. ω_o and ζ are realized the rough and fine adjustment of observer, respectively.

With a functioning LESO, which results in $z_2 \rightarrow \bar{f}_i$. The closed-loop transfer function is $G_c(s) = k_p/(s + k_p)$. According to the definition of system regulation time, k_p can be tuned according to the desired regulation time, $k_p \approx 3/t_s$.

In sum, the tuning rules of first-order ADRC is below:

1. The value of b_0 is determined by Eq. (21);
2. In the premise of ensuring the stability of system, tune ω_o and ζ to make LESO estimate output and total disturbance as accurately and quickly as possible;
3. k_p is determined by the desired regulation time and generally not more than $\omega_o/3$.

The values of ω_o , ζ , and k_p are through repeated adjustment to get.

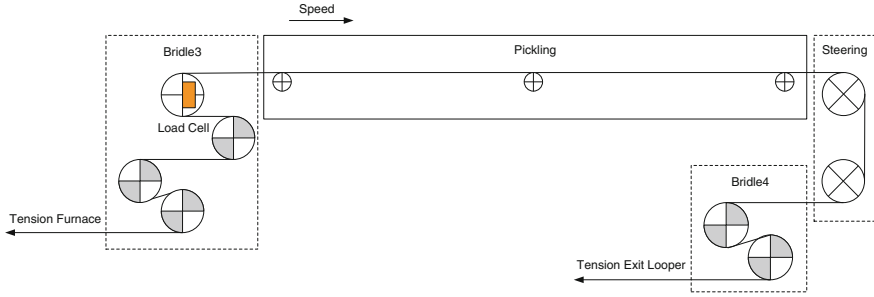


Fig. 3 Structure of pickling section

Table 1 Parameters of stainless steel strip

| | Cross-section area | Elastic modulus | Density | Span |
|-------|------------------------|-----------------|------------------------|------|
| Value | 1.6E-03 m ² | 2.06E + 11 Pa | 8710 Kg/m ³ | 3 m |

4 Simulation Results

As a real industrial example of stainless steel strip processing line will be studied in ADRC in this chapter. In this processing line, the number of rolls contacted with the surface of the strip is over 130. All driven rolls have been done friction loss test respectively, which as the basis of friction load compensation in controlling. In this simulation example, all mechanical and electrical parameters of the module are completely from the production line and the module was validated same with the site. For the sake of simplicity, this simulation example selected pickling section between third bridle and fourth bridle. Structure of pickling section is shown in Fig. 3. The third bridle is speed master of the whole pickling section; tension is adjusted by changing the speed of the fourth bridle. The parameters of stainless steel strip are shown in Table 1.

The reference tension in pickling section is 62,000 N. Following the parameters tuning procedure described in the third part, the parameters of ADRC are shown in Table 2.

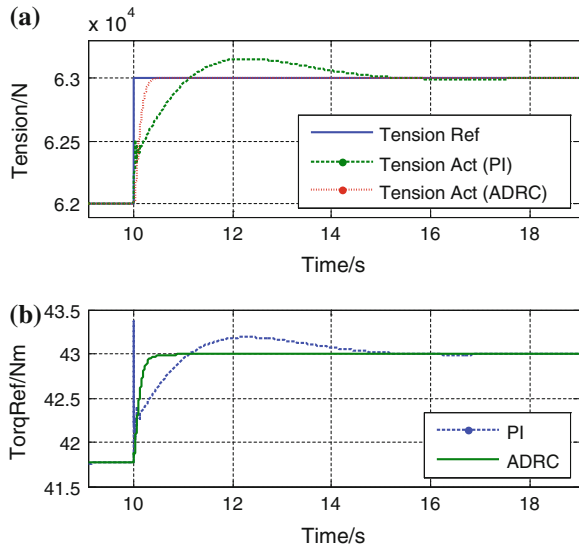
4.1 Tracking Performance

If the thickness and width of strip changed during the manufacturing process, the reference tension must make the corresponding adjustment. When the tension reference changed from 62,000 to 63,000 N, the simulation results are shown in Fig. 4. From Fig. 4a, the rise time of ADRC and PI are 0.34 and 1 s, respectively.

Table 2 Parameters of ADRC and PI controller

| | Values of the gains used in the simulation |
|------|---|
| PI | $k_p = 1.0 \times 10^{-6}$ $k_i = 1.0 \times 10^{-6}$ |
| ADRC | $\omega_0 = 90$ $\zeta = 0.01$ $k_p = 10$ $b_0 = 1.2 \times 10^8$ |

Fig. 4 Step response of ADRC and PI controller. **a** Tension of stainless steel strip. **b** Torque reference of driven roller



And there is no tension overshoot under the control of ADRC. Their impacts on transmission of fourth bridle are shown in Fig. 4b. Compared with PI, ADRC has no impact on transmission. So ADRC is superior to PI in tracking performance.

4.2 Disturbance Rejection Performance

Pickling section tension disturbance are usually come from acceleration and deceleration of processing line and the exit looper after fourth bridle. When the processing line decelerates, the original velocity–tension balance has been broken, so the tension must be disturbed. A typical speed disturbance is depicted in Fig. 5a. The simulation results shown in Fig. 5b indicate that ADRC is much better than PI.

When tension reference of the adjacent exit looper changed from 28,000 to 36,000 N, looper tension tends to generate large fluctuations shown in Fig. 6a, which directly causes velocity fluctuations of the fourth bridle and thus affects pickling section tension. From the simulation results shown in Fig. 6b, it can be seen that ADRC has a much better disturbance rejection performance.

Fig. 5 Speed disturbance and simulation results. **a** Velocity disturbance. **b** Tension of stainless steel strip

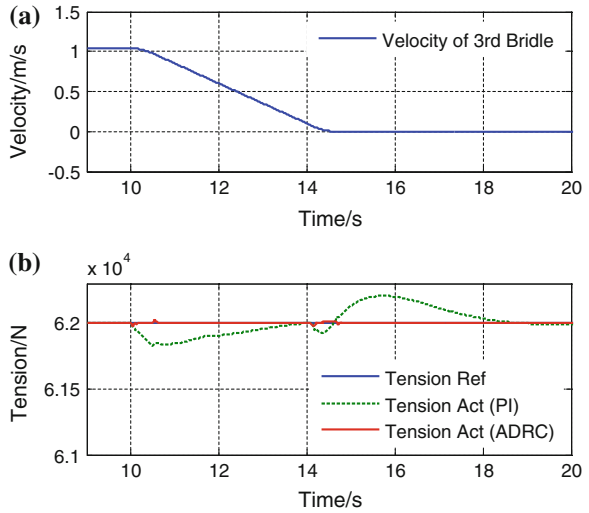
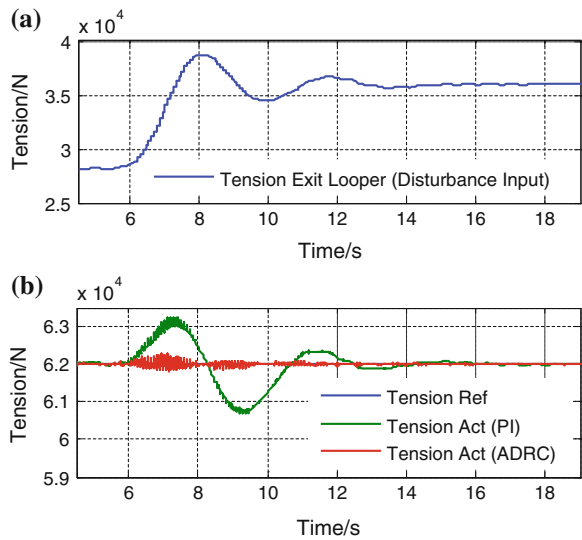


Fig. 6 Looper tension disturbance and simulation results. **a** Tension disturbance. **b** Tension of stainless steel strip



5 Conclusion

This paper established dynamic tension model to describe sagging dynamics of strip, then designed first-order ADRC for tension loop, and gave parameters tuning procedure. Take pickling section of stainless steel strip processing line as an example, we compared the control effect of ADRC and traditional industry

controller in tracking performance and disturbance inhibition performance. Tracking experiments show that ADRC solved the conflict between rise time and overshoot. And the disturbance rejection experiments show that ADRC does a much better job at rejecting the disturbances. Thus, to the time-varying and coupling nonlinear system, the ADRC has much better performance than the conventional industry controller.

References

1. Okada K, Sakamoto T (1998) An adaptive fuzzy control for web tension control system. *IEEE transaction on industry applications*, vol 3. IEEE, Aachen, pp 1762–1767
2. Angermann A, Aicher M, Schroder D (2000) Time-optimal tension control for processing plants with continuous moving webs. In: *Proceedings of 35th annual meeting-IEEE industry applications society*, vol 5. IEEE, Rome, pp 3505–3511
3. Chunxiang W, Yongzhang W, Ruqing Y, Hua L (2004) Research on precision tension control system based on neural network. *IEEE Trans Ind Electron* 51(2):381–386
4. Gassmann V, Knittel D (2011) Robust PI-LPV tension control with elasticity observer for roll-to-roll system. In: *Preprints of the 18th IFAC world congress*, vol 18. IFAC, Milano, pp 8639–8644
5. Jingqing H (2009) *Active disturbance rejection control technique*. National Defense Industry Press, Beijing
6. Yi H, Wenchao X (2012) Active disturbance rejection control: thought, application and theoretical analysis. *Syst Sci Math Sci* 32(10):1287–1307
7. Wankun Z, Zhiqiang G (2007) An active disturbance rejection approach to tension and velocity regulations in web processing lines. In: *Proceedings of the 16th IEEE international conference on control applications*. IEEE, Singapore, pp 842–848
8. Freire AMS, Negrao JHO, Lopes AV (2006) Geometrical nonlinearities on the static analysis of highly flexible steel cable-stayed bridges. *Comput Struct* 84(31–32):2128–2140
9. Zhiqiang G (2003) Scaling and bandwidth-parameterization based controller tuning. In: *Proceedings of the 2003 American control conference*, vol 6. IEEE, New York, pp 4989–4996

An Improved Coupled Metric Learning Method for Degraded Face Recognition

Guofeng Zou, Shuming Jiang, Yuanyuan Zhang, Guixia Fu
and Kejun Wang

Abstract In this paper, to solve the matching problem of elements in different sets, we proposed an improved metric method based on coupled metric learning. First, we improved the supervised locality preserving projection algorithm, and then the within-class and between-class information of this algorithm are added to the coupled metric learning, so an improved coupled metric learning method is proposed. This method can effectively extract the nonlinear feature information, and the operation is simple. The experiments based on two face databases show that, our proposed method can get higher recognition rate in low-resolution face recognition, and it can reduce the computing time; it is an effective metric method.

Keywords Metric learning · Coupled metric · Degraded face recognition

1 Introduction

Distance metric is an important basis for similarity measure between samples, and it is one of the core issues in pattern recognition. The essence of distance metric learning is to obtain another representation method with better class separability by linear or nonlinear transformation. In recent years, some researches about distance metric have been done by researchers [1–7]. They learn a distance metric by introducing sample similarity constraint or category information, the distance metric is used to improve the data clustering or classification. These researches can be concluded to two categories: linear distance metric learning and nonlinear

G. Zou (✉) · S. Jiang · Y. Zhang
Shandong University of Technology, Zibo, China
e-mail: zgf841122@163.com

G. Fu · K. Wang
College of Automation, Harbin Engineering University, Harbin, China

distance metric learning. The linear distance metric learning is equivalent to learning a linear transformation in sample space, including a variety of common linear dimensionality reduction method, such as PCA, LDA, and ICA. The nonlinear distance metric learning is equivalent to learning a nonlinear transformation in sample space, such as locally linear embedding [8], isometric mapping [9], Laplace mapping [10], in addition, there is a more flexible distance metric learning algorithm, which is based on kernel matrix [7].

These traditional distance metric learning methods are defined on the set of single attribute, which are incapable for the metric of elements in different set with different attribute. Aiming at the shortage of traditional distance metric, the coupled metric learning [11–13] is proposed. The goal is to find a coupled distance function to meet the specific requirement. First, the data in different set is projected to same coupled space, and then the elements with a correlation should be as close as possible in the new space after projection, and then further metric learning is performed in this common coupled space. Therefore, this new distance metric should have broader application scope and better recognition effect.

In this paper, we improved the supervised locality preserving projection algorithm and added supervised locality preserving information to coupled metric learning. Then the supervised locality preserving projection kernel coupled metric learning (SLPP–KCML) is proposed. This method can solve the matching problem of different faces and extract the nonlinear feature, the operation is simple and the training speed is fast. The experiments based on two face databases show that, a higher recognition rate can be achieved in the proposed algorithm.

2 Related Works

The traditional distance metric algorithm is to learn a distance function $d(x_i, x_j)$:

$$d(x_i, x_j) = \|x_i - x_j\|_A = \sqrt{(x_i - x_j)^T A (x_i - x_j)} \quad (1)$$

The distance metric aims to find a distance metric matrix A , it is required that A is a real symmetric and positive semidefinite matrix, namely $A = P^T P$, where P is a transformation matrix.

$$d_A(x_i, x_j) = d_P(x_i, x_j) = \sqrt{(Px_i - Px_j)^T (Px_i - Px_j)} \quad (2)$$

Obviously, the distance metric learning is realized by learning a transformation matrix P . So the process of distance metric learning is equivalent to the process of obtaining another representation form through some transformation of samples.

If $X \subset R^{D_x}$, $Y \subset R^{D_y}$ represent two different collections respectively, the data $x \in X$ and data $y \in Y$. The elements of collections X and Y are mapped from

original space to a common coupled space \mathbb{R}^{D_c} by using the mapping functions f_x and f_y . Then the distance metric is performed in the coupled space.

$$d^c(x, y) = d_A(f_x(x), f_y(y)) = \sqrt{(f_x(x) - f_y(y))^T A (f_x(x) - f_y(y))} \quad (3)$$

where A is a real symmetric and positive semidefinite matrix. Letting $A = W_a W_a^T$, we can get:

$$d^c(x, y) = \sqrt{(f_x(x) - f_y(y))^T W_a W_a^T (f_x(x) - f_y(y))} = \|W_a^T (f_x(x) - f_y(y))\| \quad (4)$$

The goal of coupled metric learning can be achieved by minimizing the distance function, the objective function is as follows:

$$\min J = \min \sum_{(i,j) \in C} \|W_a^T (f_x(x_i) - f_y(y_j))\|^2 \quad (5)$$

where C is a correlation matrix of elements in collection X and Y .

3 SLPP-KCML

The coupled distance metric learning must be used under the constraints of supervised information. We improved the SLPP algorithm [14] and proposed the supervised locality preserving projection coupled metric learning (SLPP-CML) based on improved SLPP, The SLPP-CML includes the following steps:

- Step 1: Building the neighborhood relation in same collection. We use the k nearest neighbor method. First, building within-class adjacency graph in same collection: if the data point $x_i(y_i)$, is one of the k within-class nearest neighbors of data point $x_i(y_j)$, we connect these two data points; then, building between-class adjacency graph in the same collection: if the data point $x_i(y_i)$ is one of the k between-class nearest neighbors of data point $x_i(y_j)$, these two data points are connected.
- Step 2: Building the connected relation between two collections. If the data points x_i and y_j in two different collections belong to the same class, then these two points are connected, otherwise not connected.
- Step 3: Constructing the relation matrix in same collection. According to the neighborhood relation collections, the relation matrixes (similarity matrixes) of within-class and between-class are constructed in same collection, respectively.

Within-class similarity matrix is W corresponding to within-class adjacency graph and the within-class similarity value is W_{ij} . The definition is as follows:

$$W_{ij} = \begin{cases} \exp(-\|x_i - x_j\|^2/t) & \text{if } x_i \text{ connected } x_j \\ 0 & \text{otherwise} \end{cases} \quad (6)$$

Between-class similarity matrix is B corresponding to between-class adjacency graph and the between-class similarity value is B_{ij} . It can be defined as follows:

$$B_{ij} = \begin{cases} \exp(-\|x_i - x_j\|^2/t) & \text{if } x_i \text{ connected } x_j \\ 0 & \text{otherwise} \end{cases} \quad (7)$$

where parameter t is the average distance between all sample points.

Step 4: Constructing relation matrix S between two collections as follows:

$$S_{ij} = \begin{cases} 1 & \text{if } x_i \text{ connected } y_j \\ 0 & \text{otherwise} \end{cases} \quad (8)$$

Step 5: Calculating the final similarity matrix C between two collections. As shown in Fig. 1, the similarity relations between element $x_1 \in X$ and elements of collection Y include the following several situations.

- (a) The similarity between x_1 and y_1 . These two data points in different collections belong to the same class and they are connected to each other, so the similarity of which is $C_{11} = S_{11} = 1$.
- (b) The similarity between x_1 and y_5 . These two data points belong to different class, but the relationship between y_5 and y_3 is the between-class neighborhood relation in the same collection, and the similarity B_{35} is the maximum similarity value, so similarity between x_1 and y_5 is $C_{15} = B_{35}$.
- (c) The similarity between x_1 and y_6 . The y_6 does not have between-class neighborhood relation with any element in collection Y of class 1. But there is a between-class neighborhood relation of same collection between y_5 and y_3 , and within-class neighborhood relation between y_5 and y_6 . So the similarity between x_1 and y_6 is defined as the product of similarity B_{35} and similarity W_{56} , which is the maximum similarity between y_6 and y_3 , that is $C_{16} = B_{35} W_{56}$.
- (d) The similarity between x_1 and y_9 . These two data points belong to different class, there are not any between-class neighborhood relations between the elements of class 1 and class 3 in collection Y , namely $C_{19} = 0$.

Step 6: Constructing the optimal objective function:

$$J = \sum_{(i,j) \in C} \|W_a^T(f_x(x_i) - f_y(y_j))\|^2 = \sum_i \sum_j \|W_a^T(f_x(x_i) - f_y(y_j))\|^2 \cdot C_{ij} \quad (9)$$

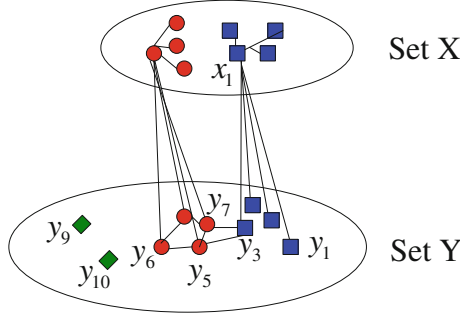


Fig. 1 The relationship between elements. \square represents class 1, \circ represents class 2, \diamond represents class 3

where the functions f_x and f_y are considered to be linear, that is $f_x(x) = W_x^T x$, $f_y(y) = W_y^T y$. The optimal objective function can be rewritten as follows:

$$\begin{aligned} J &= \sum_i \sum_j \left\| W_a^T (f_x(x_i) - f_y(y_j)) \right\|^2 \cdot C_{ij} \\ &= \sum_i \sum_j \left\| W_a^T W_x^T x_i - W_a^T W_y^T y_j \right\|^2 \cdot C_{ij} \end{aligned} \quad (10)$$

Letting $P_x = W_x W_a$, $P_y = W_y W_a$, we can get:

$$J = \sum_i \sum_j \left\| W_a^T W_x^T x_i - W_a^T W_y^T y_j \right\|^2 \cdot C_{ij} = \sum_i \sum_j \left\| P_x^T x_i - P_y^T y_j \right\|^2 \cdot C_{ij} \quad (11)$$

Therefore, our method aims to learn two linear transformations P_x and P_y . Equation (12) is an alternate matrix expression of Eq. (11):

$$\begin{aligned} J &= \text{Tr} \left[P_x^T X F_1(C) X^T P_x + P_y^T Y F_2(C) Y^T P_y - P_x^T X C Y^T P_y - P_y^T Y C^T X^T P_x \right] \\ &= \text{Tr} \left(\begin{bmatrix} P_x \\ P_y \end{bmatrix}^T \begin{bmatrix} X \\ Y \end{bmatrix} \begin{bmatrix} F_1(C) & -C \\ -C^T & F_2(C) \end{bmatrix} \begin{bmatrix} X \\ Y \end{bmatrix} \begin{bmatrix} P_x \\ P_y \end{bmatrix} \right) \end{aligned} \quad (12)$$

where $\text{Tr}(X)$ represent computing the trace of matrix X , $F_1(C)$ and $F_2(C)$ are diagonal matrixes, their diagonal elements are the row or column sums of similarity matrix C , respectively.

Assuming that $P = \begin{bmatrix} P_x \\ P_y \end{bmatrix}$, $Z = \begin{bmatrix} X & \\ & Y \end{bmatrix}$, $\Gamma = \begin{bmatrix} F_1(C) & -C \\ -C^T & F_2(C) \end{bmatrix}$, Eq. (12)

can be rewritten as follows:

$$J(P) = \text{Tr}[P^T Z \Gamma Z^T P] \quad (13)$$

The solution to make Eq. (13) minimized is obtained by generalized eigen-decomposition of $(Z \Gamma Z^T)p = \lambda(ZZ^T)p$ and taking the eigenvectors p_2, p_3, \dots, p_{m+1} corresponding to the second to $(m+1)$ th smallest eigenvalues $\lambda_2, \lambda_3, \dots, \lambda_{m+1}$, and $P = [p_2, p_3, \dots, p_{m+1}]$, its dimension is $(D_x + D_y) \times m \cdot D_x$ and D_y are the dimensions of samples in collection X and Y , so the transformation matrix P_x corresponds to the 1st to D_x th rows of P and P_y corresponds to the $(D_x + 1)$ th to D_y th rows.

Step 7: Bringing the matrix P_x and P_y to the Eq. (11), the distance metric of the elements belonging to different collections can be realized

Assuming that the mapping functions f_x and f_y are nonlinear functions, namely $f_x = \phi_x(x)$, $f_y = \phi_y(y)$, using the nonlinear mapping $\phi: R^n \rightarrow F$, $x \rightarrow \phi_x(x)$, $y \rightarrow \phi_y(y)$, The sample data can be mapped to the high dimensional Hilbert space. The criterion can be defined by:

$$J = \sum_{(i,j) \in C} \|W_a^T \phi_x(x_i) - W_a^T \phi_y(y_j)\|^2 \quad (14)$$

An alternate matrix expression is as follow:

$$\begin{aligned} J &= \text{Tr}(W_a^T \Phi_x(x) G_x \Phi_x(x)^T W_a + W_a^T \Phi_y(y) G_y \Phi_y(y)^T W_a \\ &\quad - W_a^T \Phi_x(x) C \Phi_y(y)^T W_a - W_a^T \Phi_y(y) C^T \Phi_x(x)^T W_a) \\ &= \text{Tr} \left(\begin{bmatrix} W_a \\ W_a \end{bmatrix}^T \begin{bmatrix} \Phi_x(x) \\ \Phi_y(y) \end{bmatrix} \begin{bmatrix} G_x & -C \\ -C^T & G_y \end{bmatrix} \begin{bmatrix} \Phi_x(x) \\ \Phi_y(y) \end{bmatrix}^T \begin{bmatrix} W_a \\ W_a \end{bmatrix} \right) \end{aligned} \quad (15)$$

where Tr represent computing the trace of matrix, G_x and G_y are diagonal matrixes, their diagonal elements are the row or column sums of similarity matrix C , respectively. Letting $W_a = \Phi_x(x)A_x$, $W_a = \Phi_y(y)A_y$, we can get:

$$J = \text{Tr} \left(\begin{bmatrix} \Phi_x(x)A_x \\ \Phi_y(y)A_y \end{bmatrix}^T \begin{bmatrix} \Phi_x(x) \\ \Phi_y(y) \end{bmatrix} \begin{bmatrix} G_x & -C \\ -C^T & G_y \end{bmatrix} \begin{bmatrix} \Phi_x(x) \\ \Phi_y(y) \end{bmatrix}^T \begin{bmatrix} \Phi_x(x)A_x \\ \Phi_y(y)A_y \end{bmatrix} \right) \quad (16)$$

The kernel function $K_{i,j}^x = (\phi(x_i) \cdot \phi(x_j))$, $K_{i,j}^y = (\phi(y_i) \cdot \phi(y_j))$, the kernel matrixes K^x and K^y are real symmetric matrixes. Equation (17) is an alternative expression of Eq. (16):

$$J(A_x, A_y) = Tr \left(\begin{bmatrix} A_x \\ A_y \end{bmatrix}^T \begin{bmatrix} K^x & \\ & K^y \end{bmatrix} \begin{bmatrix} G_x & -C \\ -C^T & G_y \end{bmatrix} \begin{bmatrix} K^x & \\ & K^y \end{bmatrix}^T \begin{bmatrix} A_x \\ A_y \end{bmatrix} \right) \quad (17)$$

Obviously, the coupled metrics learning in kernel space is a process of calculating the transformation matrix A_x and A_y .

Assuming that $A = \begin{bmatrix} A_x \\ A_y \end{bmatrix}$, $K = \begin{bmatrix} K^x & \\ & K^y \end{bmatrix}$, $\Gamma = \begin{bmatrix} G_x & -C \\ -C^T & G_y \end{bmatrix}$, the generalized characteristic equation is $Ea = \lambda Fa$, and $E = K\Gamma K^T$, a is the eigenvector corresponding to eigenvalue λ . The eigenvectors corresponding to the minimum to the D_c th smallest eigenvalues construct the feature matrix A , the size of matrix A is $(N_x + N_y) \times D_c$, where N_x and N_y are the number of training samples of collection X and Y . Finally, we can get the feature matrix A_x corresponding to X and the feature matrix A_y corresponding to Y .

4 Experiment and Analysis

The proposed coupled metric learning approach is tested on Yale face database and CAS-PEAL-R1 face database. The Yale face database contains 165 pictures of 15 people with the size of 100×100 and 256 gray levels. We used six images per person for training, and the other images were used as test sample, a total of 75.

The face images per person in CAS-PEAL-R-accessory data set include six different appendages; there are three images with different glasses and 3 images with different hats. We selected 300 images corresponding to 50 people, the odd-numbered images were training samples and other images were test samples.

4.1 Experiment 1: The Low-Resolution Face Recognition Based on SLPP-CML

Traditional measure method can not calculate the distance between two images with different resolution. So the general handling method is interpolation operation for the low-resolution image, but it is easy to introduce false information. With the increase of false information, the distortion degree increases, as shown in Fig. 2. Aiming at the problem of recognition rate declining because of image distortion, the researchers realized the low-resolution image compensation by restoration preprocessing, but the image restoration algorithm is often more complex, and the quality of restoration has great impact on final recognition results. The proposed coupled metric learning method can directly realize the feature extraction and measurement of two different resolution images, which do not need to do image

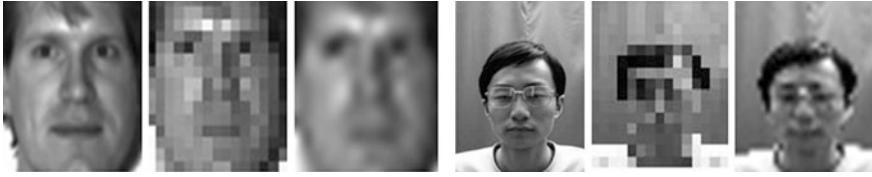


Fig. 2 The normal face image, low-resolution image, and the result after restoration

restoration. This method not only saves computing time, but also avoids the negative impact of image restoration on recognition performance.

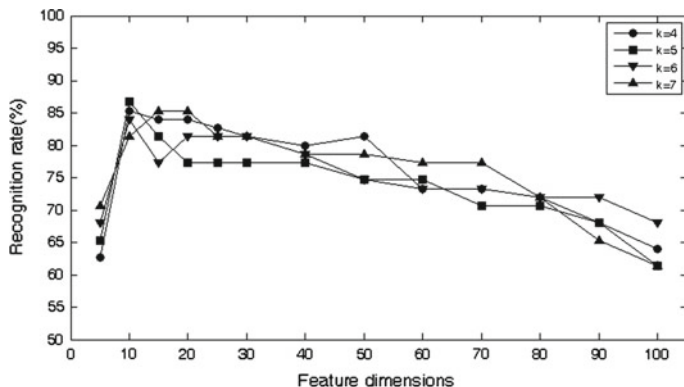
In the experiment, the normal face is clear image with the size of 64×64 pixel, the low-resolution face image can be obtained through blurring and sampling, which is corresponded to normal resolution face image. The size of low-resolution face image is 16×16 . The training set is consisted of normal training face image and corresponding low-resolution face image. The test set is the low-resolution face image generated by the normal test face image.

The SLPP–CML algorithm has two influence factors: (1) the neighbor number k of supervised locality preserving projection; (2) the reserved dimensions D_c of the feature. Therefore, the recognition results based on different parameters should be discussed and analyzed, as shown in Fig. 3.

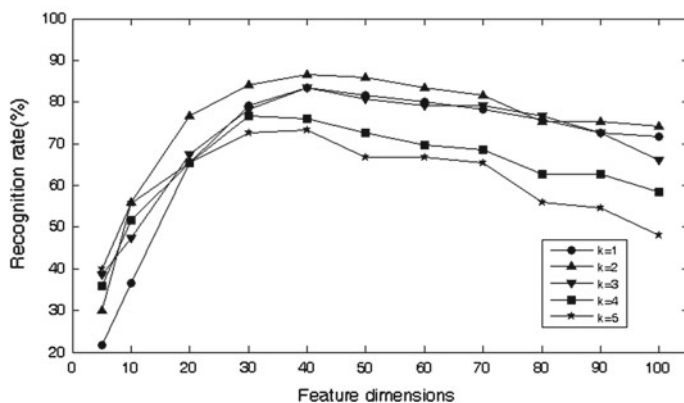
The curve has a general change law, with the increase of feature dimensions, the recognition rate kept a decreasing trend after increasing, and the best recognition results can be achieved only in the optimal feature dimensions. In Yale face database, the recognition rate kept a higher trend when feature dimensions remain 10–20. The optimal recognition rate is 86.67 % when feature dimension is 10 and neighbor number is 5. In CAS-PEAL-R1 face database, the recognition rate can reach the maximum value 86.67 %, when feature dimension is 40 and neighbor number is 2.

Obviously, the neighbor number has some influence on recognition rate, but does not change the overall trend of the curve. The training sample number is 6 in Yale face database, and the recognition effect is optimal when the neighbor number is 5; In CAS-PEAL-R1 face database, the training sample number is 3, the neighbor number $k = 2$ we can obtain optimal recognition rate. In addition, in order to illustrate the effectiveness of the proposed method. Based on the face after restoration, we used the principal component analysis for feature extraction and recognition. And then the comparative experiments were carried out with Ref. [11, 13], respectively. The experiment results are shown in Table 1.

The experiment data illustrated that the recognition results of feature extraction after restoration is not satisfactory. The method in Ref. [11] cannot overcome the influences of within-class multiple modes, so the identification effect is not good. The method in Ref. [13] is conducive to resolving within-class multiple modes; the recognition effects have been greatly improved, but it does not fully consider the between-class relationships of training samples. The proposed SLPP–CML takes



The experiment result in Yale face database



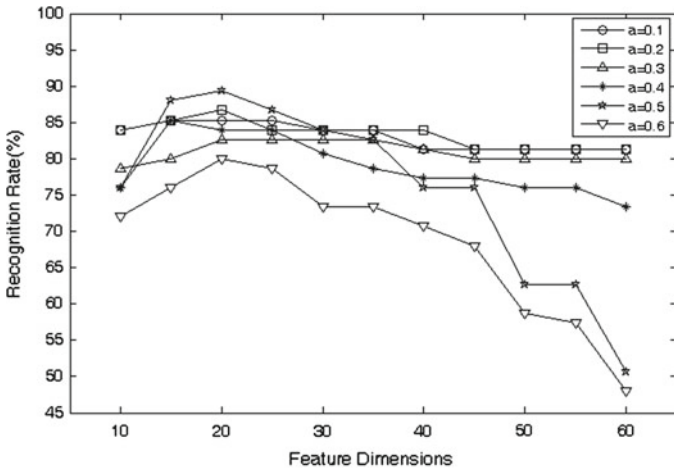
The experiment result in CAS-PEAL-R1 face database

Fig. 3 The recognition rate under different dimensions and different nearest neighbor numbers

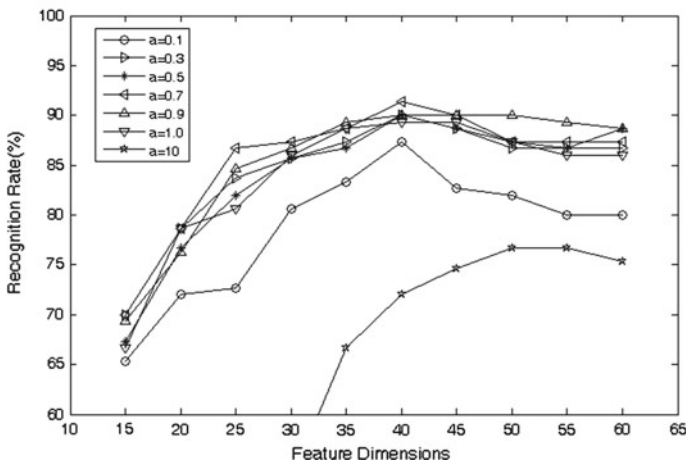
Table 1 Experimental comparison of our proposed method with other methods

| Method | Yale face database | CAS-PEAL-R1 face database |
|------------------------------|--------------------|---------------------------|
| Image restoration [15] + PCA | 61.33 | 55.33 |
| CML [11] | 77.33 | 74.67 |
| CLPM [13] | 82.67 | 80.67 |
| Our method | 86.67 | 86.67 |

advantage of the supervisory of category information, while the within-class and between-class relationship information of training samples have been considered into the metric learning, so we can get better recognition results.



The experiment result in Yale face database



The experiment result in CAS-PEAL-R1 face database

Fig. 4 The recognition rate under different dimensions and different adjustable factors

4.2 Experiment 2: The Low-Resolution Face Recognition Based on SLPP-KCML

The SLPP-KCML algorithm is a nonlinear coupled metric learning algorithm, there are three factors which affect the algorithm: (1) the neighbor number k of supervised locality preserving projection; (2) the reserved dimensions D_c of the feature; and (3) the kernel function. The nearest neighbor number is the same as that of SLPP-CML. The kernel function, we choose the Gauss function, the value of adjustable factor affects the function performance. So in this paper, the

experiments were carried out according to the different adjustable factors and the change of feature dimensions on recognition rate, the results are shown in Fig. 4.

The curve indicated that, In Yale face database, the optimal recognition rate is 89.33 % when the value of α is 0.5 and the feature dimension is 20, compared with the SLPP-CML, the recognition rate increased by 2.66 %. In CAS-PEAL-R1 face database, when $\alpha = 0.7$ and $D_c = 40$, recognition rate is 91.33 %, compared with the SLPP-CML algorithm, the recognition rate increased by 4.66 %.

5 Conclusions

Aiming at the problem that the traditional metric method can not calculate the distance of the elements in different data sets, we proposed the kernel coupled metric learning method based on SLPP. The elements of different sets are mapped to the same space combined with the within-class and between-class information, and then the metric matrix learning is performed. This algorithm can effectively extract the face nonlinear features. Low-resolution face recognition experiments show that the proposed method can obtain a higher recognition rate, and has a high computational efficiency.

References

1. Davis JV, Kulis B, Jain P (2007) Information-theoretic metric learning. In: The 24th international conference on machine learning, pp 209–216
2. Xiang S, Nie F, Zhang C (2008) Learning a Mahalanobis distance metric for data clustering and classification. *Pattern Recogn* 41(12):3600–3612
3. Kulis B, Jain P, Grauman K (2009) Fast similarity search for learned metrics. *IEEE Trans Pattern Anal Mach Intell* 31(12):2143–2157
4. Weinberger KQ, Saul LK (2009) Distance metric learning for large margin nearest neighbor classification. *J Mach Learn Res* 10:207–244
5. Wang L, Liu T, Jia H (2011) Chunk incremental distance metric learning algorithm based on manifold regularization. *Acta Electron Sinica* 39(5):1131–1135
6. Hu Z, Lu L, Xu C (2011) Sparse distance metric learning with L1-norm constraint for one-class samples in high-dimensional space and its application. *Math Pract Theory* 41(6):116–124
7. Mahdiah SB, Saeed BS (2010) Kernel-based metric learning for semi-supervised clustering. *Neurocomputing* 73:1352–1361
8. Roweis ST, Saul LK (2000) Nonlinear dimensionality reduction by locally linear embedding. *Science* 290:2323–2326
9. Tenenbaum J, Silva V, Langford J (2000) A global geometric framework for nonlinear dimensionality reduction. *Science* 290:2319–2323
10. Belkin M, Niyogi P (2002) Laplacian Eigenmaps and spectral techniques for embedding and clustering. *Adv Neural Inf Process Syst* 14:585–591
11. Li B, Chang H (2009) Coupled metric learning for face recognition with degraded images. In: *ACML2009*, pp 220–233

12. Ben X, Meng W, Yan R (2012) An improved biometrics technique based on metric learning approach. *Neurocomputing* 79(11):44–51
13. Li B, Chang H, Shan S (2010) Low-resolution face recognition via coupled locality preserving mappings. *IEEE Signal Process Lett* 17(1):20–23
14. Shen Z, Pan Y (2008) A supervised locality preserving projection algorithm for dimensionality reduction. *Pattern Recog Artif Intell* 21(2):233–239
15. Wang Y, Sun Z, Cai Z (2008) Super-resolution image restoration based on maximum likelihood estimation. *Chin J Sci Instrum* 29(5):949–953

A New Phase Estimator of Single Sinusoid by Restricted Phase Unwrapping

Fang Wang, Yong Chen and Zhiqing Ye

Abstract In order to estimate the original phase of a sinusoid corrupted by additive noise accurately, this paper proposes a novel phase estimator which based on restricted phase unwrapping and Tretter's phase estimation algorithm. Using appropriate linear combinations for observed phase, restricted phase unwrapping is easily performed on the basis of the principle of minimum phase error. A formula for evaluating the error probability of restricted phase unwrapping is presented. Simulation results show that the SNR threshold of restricted phase unwrapping method is much lower than that of traditional unwrapping methods, and the estimator derived attains the Cramer–Rao lower bound (CRB) at high SNR, which has better performance than the segmented DFT estimator developed in [10, 13] and the all-phase FFT estimator in [14].

Keywords Phase estimation · Restricted phase unwrapping · Linear combination · Cramer–Rao lower bound

1 Introduction

Estimation of the frequency and phase of a single noisy sinusoid is a classic subject in signal processing with application domains including radar, communication, etc. Converting the additive noise into an equivalent additive phase noise, Tretter presented a method of least squares linear regression on the instantaneous signal phase for estimating the frequency and phase [1]. In theory, the variances of the estimates are identical to the Cramer–Rao lower bound (CRB) [2]. But actually, the range of observed signal phase is far greater than 2π , that is to say, there

F. Wang (✉) · Y. Chen · Z. Ye
College of Physics and Communication Electronics, Jiangxi Normal University, Nanchang, China
e-mail: juniorfang@hotmail.com

exists the problem of ambiguity in phase measurement. Therefore, a variety of methods have been proposed for overcoming the cumbersome ambiguity in phase estimation by many scholars, which can be divided into two kinds.

One alternative method is called phase unwrapping. The difference of the argument is calculated by adjacent signal samples in traditional unwrapping. If the difference is greater than π or less than $-\pi$, it is considered as phase ambiguity, then all the subsequent arguments should be increased or decreased by 2π [3]. This method is easy to implement, but the error propagation always exists at low SNR. An improved unwrapping algorithm was researched for achieving better performance at low SNR by restricting the samples of each period [4]. In addition, the least squares phase unwrapping algorithm based on the nearest lattice point problem in algorithmic number theory was proposed, but the computational complexity attains $O(N^3 \log N)$ [5]. A regression unwrapping algorithm was presented via the result of iterative frequency estimation. Although the computational complexity is relatively low, the error propagation also occurs at low SNR [6].

Another approach is to avoid processing the phase ambiguity. The frequency estimation is carried on by the instantaneous phase difference of signal samples. With the phase ambiguity avoided, the initial phase information is also lost [7]. Similarly, the difference of the argument of the sample autocorrelation function is used for estimating the frequency, while the computing complexity and the SNR threshold are both high [8]. Besides, in [9] the coarse frequency estimation based on FFT is utilized for frequency shift. With the phase limited to a certain range, the unwound sequence can be selected according to the principle of minimum phase variance.

Apart from Tretter's phase estimation method, there are several phase estimation techniques for sinusoidal signal. The difference of phase of two-segmented DFT spectrum in [10] is used to estimate the phase, and the root-mean-square error (RMSE) of phase estimation is about 2 times of CRB. Since the variance of phase estimation in [10] depended on the frequency of the signal, a modified algorithm based on [10] was presented, in which the variance of phase estimation has better stability during the whole dynamic range of frequency [11]. In [12] and [13], a multi-segmented DFT phase averaging algorithm with optimal weighting coefficients was proposed, the phase estimation variance obtained is slightly lower than that of [10]. Using all-phase FFT for phase estimation in [14] and [15], the phase estimation accuracy can be enhanced double compared with the result of [10]. Additionally, a method based on Gauss–Newton iterative algorithm was proposed, which was able to estimate the amplitude, phase, and frequency of a time-varying sinusoid accurately at high SNR [16]. In this paper, we present a novel estimator based on Tretter's phase estimation algorithm, which using the technique of restricted phase unwrapping. Simulation results show that the SNR threshold of restricted phase unwrapping method is much lower than that of traditional unwrapping methods, and the estimator derived achieves the CRB at high SNR, which has better performance than the segmented DFT estimator developed in [10, 13] and the all-phase FFT estimator in [14].

2 Tretter's Phase Estimation Algorithm

The observed sequence is assumed to have the form

$$r(n) = A \exp[j(\omega_0 n T + \theta)] + z(n), \text{ for } n = n_0, n_0 + 1, \dots, n_0 + N - 1 \quad (1)$$

where $z(n)$ is a white Gaussian complex noise sequence; $\text{var } z(n) = E\{|z(n)|^2\} = \sigma_z^2$; A , ω_0 , θ are unknown constants; and T is the sampling period. The SNR is defined as $\text{SNR}_r = A^2/\sigma_z^2$. The additive noise $z(n)$ can be converted into an equivalent additive phase noise $v_Q(n)$

$$r(n) \approx A \exp[j(\omega_0 n T + \theta + v_Q(n))]. \quad (2)$$

Using the method of least squares linear regression for the observed phase $\phi(n) = \omega_0 n T + \theta + v_Q(n)$, the parameters ω_0 and θ can be estimated as

$$\begin{bmatrix} \bar{\omega}_0 \\ \bar{\theta} \end{bmatrix} = \frac{12}{N^2(N^2 - 1)T^2} \begin{bmatrix} N & -(P + Nn_0)T \\ -(P + Nn_0)T & (Q + Nn_0^2 + 2Pn_0)T^2 \end{bmatrix} \begin{bmatrix} \sum_{k=n_0}^{n_0+N-1} kT\phi(k) \\ \sum_{k=n_0}^{n_0+N-1} \phi(k) \end{bmatrix} \quad (3)$$

where $P = \sum_{n=0}^{N-1} n$, $Q = \sum_{n=0}^{N-1} n^2$. These estimators have been proved to be unbiased by [1], and the variances of the frequency and phase are exactly the same as the CRB on condition that the observed phase should be unwrapped correctly [2]. But the problem is that current phase unwrapping algorithms all need higher SNR threshold, so it's essential to study the issue of phase unwrapping at low SNR.

3 Phase Estimation by Using Restricted Phase Unwrapping

The traditional process of phase wrapping and unwrapping are separately described as below

$$\phi_w(n) = w[\phi(n)] = \phi(n) - 2\pi \cdot k_n \quad (4)$$

$$\phi_{un}(n) = w^{-1}[\phi_w(n)] = \phi_w(n) + 2\pi \cdot k'_n \quad (5)$$

where $\phi_w(n)$ is the ambiguous phase observed, $\phi(n)$ is the original phase, $\phi_{un}(n)$ is the unwrapped phase, k_n is the ambiguity number of whole cycle, $w[\cdot]$ represents the process of phase wrapping by using proper k_n to make $\phi(n) - 2\pi \cdot k_n \in [-\pi, \pi)$.

π]; and $w^{-1}[\cdot]$ represents the process of phase unwrapping which means that we should choose a certain k'_n from the integer set \mathbb{Z} to make $k'_n = k_n$.

We define a set of observed phase as $\{\phi_w(n_1), \phi_w(n_2), \dots, \phi_w(n_m)\}$, and the linear combination phase $\Phi_w(n) = \sum_{i=1}^m l_i \cdot \phi_w(n_i)$, where l_i is constant. The corresponding original phase is defined as $\{\phi(n_1), \phi(n_2), \dots, \phi(n_m)\}$, which has the same linear combination form $\Phi(n) = \sum_{i=1}^m l_i \cdot \phi(n_i)$. we find that $\Phi_w(n) = \Phi(n) - 2\pi K$, where $K = \sum_{i=1}^m l_i \cdot k_{n_i}$.

It can be inferred that there still has the issue of phase unwrapping between $\Phi_w(n)$ and $\Phi(n)$. But it is to be noted that K may be restricted in the subset \mathbb{Z}_0 of the integer set \mathbb{Z} by choosing appropriate l_i and n_i . Apparently, we can have better unwrapping performance for Φ_w with fewer elements in \mathbb{Z}_0 . For the sake of distinction, we call this method as restricted phase wrapping and unwrapping which are denoted as $w_r[\cdot]$ and $w_r^{-1}[\cdot]$ respectively. Thus, we can describe the process as below

$$\Phi_w(n) = w_r[\Phi(n)] = \Phi(n) - 2\pi K \quad (6)$$

$$\Phi_{un}(n) = w_r^{-1}[\Phi_w(n)] = \Phi_w(n) + 2\pi K' \quad (7)$$

In order to realize the initial phase estimation by using restricted phase unwrapping, we let $P + Nn_0 = 0$, i.e. $n_0 = -(N-1)/2$, then (3) can be simplified as

$$\bar{\theta} = \frac{1}{N} \left\{ \phi(0) + \sum_{n=1}^{(N-1)/2} [\phi(n) + \phi(-n)] \right\}. \quad (8)$$

It is evident that the linear combination of original phase is included in (8), then let $\Phi(n) = \phi(n) + \phi(-n)$ and $\Phi_w(n) = \phi_w(n) + \phi_w(-n)$, where $\phi_w(n) = \phi(n) - 2\pi \cdot k_+$, $\phi_w(-n) = \phi(-n) - 2\pi \cdot k_-$. Substituting these into (6), we can derive $K = k_+ + k_-$, and the set \mathbb{Z}_0 that K belonged to is just what we focus on in this paper. The relationship between $\phi_w(n)$ and $\phi(-n)$ can be derived as below

$$\phi(-n) = -\phi_w(n) + 2\theta + v_Q(n) + v_Q(-n) - k_+ \cdot 2\pi \quad (9)$$

Since $\theta \in [-\pi, \pi]$, $\phi_w(n) \in [-\pi, \pi]$, and $v_Q(n)$, $v_Q(-n)$ is very small, there are only three situations: $k_- = -k_+$, $k_- = -k_+ + 1$ or $k_- = -k_+ - 1$, which can make $\phi(-n)$ wrapped to $[-\pi, \pi]$. It appears that when the linear combination coefficients $l_1 = 1$, $l_2 = 1$ and observation time $n_1 = n$, $n_2 = -n$, K can be restricted in the subset $\mathbb{Z}_0 = \{-1, 0, 1\}$ which is much smaller than the integer set \mathbb{Z} . According to the principle of least phase error between the unwrapping phase $\Phi_{un}(n)$ and $E[\Phi(n)] = 2\theta$, K' can be expressed as

$$K' = \arg \min_{K' \in \mathbb{Z}_0} |\Phi_w(n) + 2\pi K' - 2\theta| \quad (10)$$

But actually, the initial phase θ is unknown, K' cannot be directly calculated by (10). One attempt is to substitute $\phi_w(0)$ for θ , but it is infeasible at low SNR. Therefore, we should explain our coarse phase estimation method as below.

First, the former $N-1$ points are selected to make the length even with $T_p = (N-1)T$, and then the sequence is divided into two parts. Not considering the noise, the two subsequences are separately expressed as

$$r_1(n) = r_2(n) \exp(-j\omega_0 T_p/2), \quad n = 0, 1, \dots, (N-3)/2 \quad (11)$$

$$r_2(n) = A \exp[j(\omega_0 n T + \theta)], \quad n = 0, 1, \dots, (N-3)/2 \quad (12)$$

Performing FFT for $r_1(n)$ and $r_2(n)$, the discrete spectra are separately derived as

$$R_1(k) = R_2(k) \exp(-j\omega_0 T_p/2), \quad k = 0, 1, \dots, (N-3)/2 \quad (13)$$

$$R_2(k) = A_k \exp(j\varphi_k), \quad k = 0, 1, \dots, (N-3)/2 \quad (14)$$

where the amplitude A_k and argument φ_k of $R_2(k)$ are as below

$$A_k = \frac{A \sin[\pi(k - \omega_0 T_p/4\pi)]}{\sin[2\pi(k - \omega_0 T_p/4\pi)/(N-1)]} \quad (15)$$

$$\varphi_k = \theta + (1 - 2/N)(\omega_0 T_p/4\pi - k)\pi \quad (16)$$

From (15), the discrete frequency corresponding to the maximum amplitude is given by $k_0 = [\omega_0 T_p/4\pi]$, where $[x]$ denotes the nearest integer to x , φ_1 and φ_2 denote the argument corresponding to the maximum amplitude of $R_1(k)$ and $R_2(k)$, respectively, then the phase difference can be described as:

$$\Delta\varphi = \varphi_2 - \varphi_1 = \omega_0 T_p/2 - 2k_0\pi \quad (17)$$

Substituting (17) into (16), we obtain the coarse value of initial phase

$$\bar{\theta}_c = \frac{N-2}{2N}\varphi_1 + \frac{N+2}{2N}\varphi_2 \quad (18)$$

When $N \gg 1$, the coarse value is approximately expressed as $\bar{\theta}_c = 0.5\varphi_1 + 0.5\varphi_2$. Substituting this into (10), K' becomes

$$K' = \arg \min_{K' \in \mathbb{Z}_0} |\Phi_w(n) + 2\pi K' - \varphi_1 - \varphi_2| \quad (19)$$

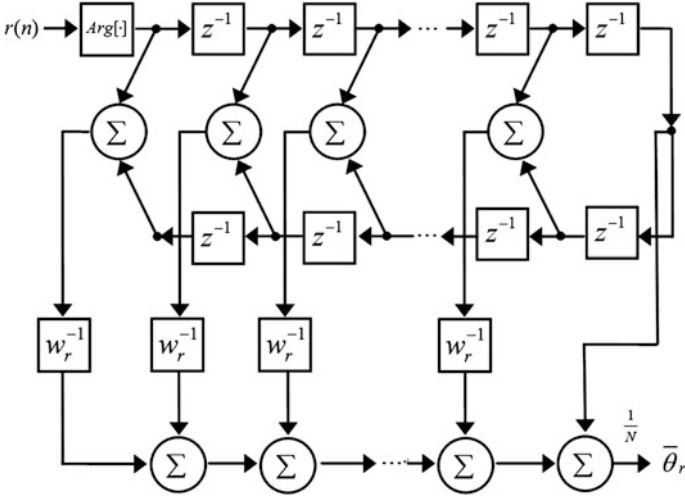


Fig. 1 Phase estimation system based on the restricted phase unwrapping

Substituting (19) into (7), we can get the restricted unwrapping phase $\Phi_{un}(n)$, then the final phase estimation is obtained

$$\bar{\theta}_r = \frac{1}{N} \left\{ \phi(0) + \sum_{n=1}^{(N-1)/2} \Phi_{un}(n) \right\} \quad (20)$$

Our phase estimation system based on the restricted phase unwrapping is shown in Fig. 1, where $\text{Arg}[\cdot]$ denotes the process of computing observed phase $\phi_w(n)$, z^{-1} and w_r^{-1} means time-delay and restricted phase unwrapping respectively.

4 The Statistical Performance Analysis of Phase Estimation

It is supposed that the process of restricted phase unwrapping given by (19) is correct, that is to say $K' = K$, $\Phi_{un}(n) = \Phi(n)$, then the phase is estimated as:

$$\bar{\theta}_r = \theta + \frac{1}{N} \sum_{n=-(N-1)/2}^{(N-1)/2} v_Q(n) \quad (21)$$

Here, $v_Q(n)$ is the imaginary part of the noise with $\text{var}[v_Q(n)] = 1/(2 \cdot \text{SNR}_r)$. It can be easily proved that $E(\bar{\theta}_r) = \theta$, $\text{var}(\bar{\theta}_r) = 1/(2N \cdot \text{SNR}_r)$, so the phase estimation $\bar{\theta}_r$ is unbiased, and the variance of $\bar{\theta}_r$ is the same as the CRB [2].

Substituting (6) into (19), it results in wrong restricted phase unwrapping provided that $|\Phi(n) - 2\bar{\theta}_c| > \pi$, i.e., $K' \neq K$. For $N \gg 1$, $\bar{\theta}_c \approx \theta$, the condition above can be simplified as $|\Phi(n) - 2\theta| > \pi$, and the corresponding error probability of restricted phase unwrapping P_e is

$$P_e = 2 \cdot P[\sqrt{\text{SNR}_r}(v_Q(n) + v_Q(-n)) > \pi\sqrt{\text{SNR}_r}] \quad (22)$$

Since $n \neq 0$, $v_Q(n)$ and $v_Q(-n)$ are normally distributed and uncorrelated with each other, and $\text{var}[\sqrt{\text{SNR}_r}(v_Q(n) + v_Q(-n))] = 1$, then

$$P_e = \text{erfc}(\pi\sqrt{\text{SNR}_r}/2) \quad (23)$$

Since $v_Q(n)$ and $v_Q(-n)$ are normally distributed and uncorrelated with each other, $P(\pi < \Phi(n) - 2\theta \leq 3\pi) = P(-\pi > \Phi(n) - 2\theta \geq -3\pi)$, $P(\Phi(n) - 2\theta > 3\pi) = P(\Phi(n) - 2\theta < -3\pi)$, then the error of $\Phi_{un}(n)$ will be offset. That is to say, when $N \gg 1$, $\bar{\theta}_r$ can also be estimated by (21) even though $\Phi_{un}(n)$ is different with the original phase $\Phi(n)$, finally the variance of $\bar{\theta}_r$ still achieves the CRB. But as a matter of fact, the data length N is finite, so the numbers of four types above are not exactly the same. For example, the number of $K' = K - 1$ is probably different from that of $K' = K + 1$, then the actual variance of phase estimation is slightly higher than the CRB.

5 Computer Simulations

First, computer simulations have been carried out to compare the theoretical result given by (23) with traditional phase unwrapping and restricted phase unwrapping which are shown in Table 1. The simulations of phase unwrapping error probability were run with $N = 1,023$, SNR varied between -1 and 7 dB, and 1,000 trials were run for each SNR value. As it is shown in Table 1, the SNR threshold of traditional phase unwrapping is about 6 dB, and the error probability is increased seriously as the SNR reduces. In addition, the actual error probability of restricted phase unwrapping basically agrees with the theoretical result, and the SNR threshold is about 3 dB or less than that. When $\text{SNR} = 0$ dB, the corresponding error probability can reach level of 10^{-3} .

Second, simulation results of the proposed phase estimator have also been listed in Table 2. The mean and RMSE of phase estimation were simulated under the condition of $\text{SNR} = 5$ dB, $N = 1,023$, and 1,000 trials were run for each phase. It is clear that the RMSE is close to the CRB, and the result remains almost the same for each phase. For $N = 1,023$, the RMSE of phase estimation with SNR varied between 0 and 20 dB is shown in Fig. 2. It appears that when $\text{SNR} \geq 5$ dB, the RMSE attains the CRB, while it is higher than the CRB with low SNR. For $\text{SNR} = 5$ dB, the RMSE of phase estimation with N varied between 10^3 and 10^5 is

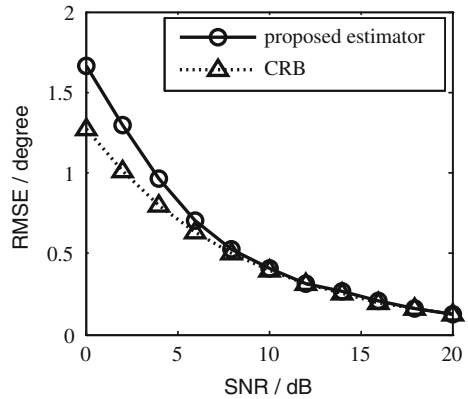
Table 1 Comparison of error probability of phase unwrapping ($N = 1023$)

| SNR/dB | Traditional phase unwrapping | Restricted phase unwrapping | Theoretical result |
|--------|------------------------------|-----------------------------|--------------------|
| -1 | 0.92794 | 0.00524 | 0.00511 |
| 0 | 0.87013 | 0.00166 | 0.00168 |
| 1 | 0.73564 | 0.00045 | 0.00042 |
| 2 | 0.49960 | 0.00006 | 0.00008 |
| 3 | 0.21837 | 0.00002 | 0.00001 |
| 4 | 0.06677 | 0 | 0 |
| 5 | 0.01328 | 0 | 0 |
| 6 | 0.00093 | 0 | 0 |
| 7 | 0 | 0 | 0 |

Table 2 Performance of the proposed phase estimator ($\text{CRB} = 0.7123^\circ$)

| $\theta / ^\circ$ | 0 | 30 | 60 | 90 | 120 | 150 | 180 |
|------------------------------------|--------|---------|---------|---------|----------|----------|----------|
| $E(\bar{\theta}_r) / ^\circ$ | 0.0307 | 30.0419 | 60.0288 | 90.0575 | 120.0117 | 149.9316 | 179.8400 |
| $\sigma_{\bar{\theta}_r} / ^\circ$ | 0.8652 | 0.8199 | 0.7957 | 0.8155 | 0.8255 | 0.7969 | 0.8471 |

Fig. 2 RMSE in phase versus SNR when $N = 1023$



depicted in Fig. 3. The RMSE gradually approaches the CRB as N increases. Therefore, the simulation results above agree with the theoretical analysis in Sect. 4.

Finally, we have compared the performance of four phase estimators: the proposed estimator based on restricted phase unwrapping (denoted as estimator 1); the estimators based on the difference of phase of two-segmented and four-segmented DFT spectrum in [10, 13] (denoted as estimator 2, 3, respectively); the all-phase FFT estimator in [14] (denoted as estimator 4). The data length of estimator

Fig. 3 RMSE in phase versus N when SNR = 5 dB

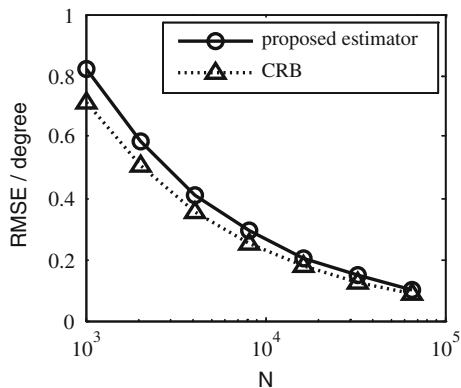


Table 3 Comparison of RMSE in degrees among four phase estimators

| | | $\delta = 0$ | $\delta = 0.1$ | $\delta = 0.2$ | $\delta = 0.3$ | $\delta = 0.4$ | $\delta = 0.5$ |
|-------------------------------|-------------|--------------|----------------|----------------|----------------|----------------|----------------|
| SNR = 5 dB (CRB = 0.7123) | Estimator 1 | 0.8057 | 0.8055 | 0.8335 | 0.8290 | 0.8067 | 0.8185 |
| | Estimator 2 | 1.5920 | 1.6185 | 1.7018 | 1.8546 | 2.1035 | 2.5007 |
| | Estimator 3 | 1.4591 | 1.4834 | 1.5597 | 1.6998 | 1.9279 | 2.2919 |
| | Estimator 4 | 0.8221 | 0.8497 | 0.9394 | 1.1157 | 1.4353 | 2.0285 |
| SNR = 10 dB (CRB = 0.4006) | Estimator 1 | 0.4246 | 0.4177 | 0.4196 | 0.4132 | 0.4096 | 0.4046 |
| | Estimator 2 | 0.8952 | 0.9101 | 0.9570 | 1.0429 | 1.1829 | 1.4062 |
| | Estimator 3 | 0.8205 | 0.8342 | 0.8771 | 0.9559 | 1.0841 | 1.2888 |
| | Estimator 4 | 0.4623 | 0.4778 | 0.5283 | 0.6274 | 0.8071 | 1.1407 |
| SNR = 15 dB (CRB = 0.2253) | Estimator 1 | 0.2257 | 0.2272 | 0.2300 | 0.2359 | 0.2345 | 0.2340 |
| | Estimator 2 | 0.5034 | 0.5118 | 0.5382 | 0.5865 | 0.6652 | 0.7908 |
| | Estimator 3 | 0.4614 | 0.4691 | 0.4932 | 0.5375 | 0.6097 | 0.7248 |
| | Estimator 4 | 0.2600 | 0.2687 | 0.2971 | 0.3528 | 0.4539 | 0.6415 |

1 and 4 should be odd and thus $N = 1023$ is selected, while it should be even for estimator 2 and 3 and thus $N = 1024$ is selected. The RMSE simulation results of four estimators above are shown in Table 3 with following conditions: the signal should be a complex sinusoid sequence in AWGN; the window function is rectangular; 1,000 trials were run for each SNR and relative frequency deviation δ , where $|\delta| \leq 0.5$ and δ is defined in [10]. From Table 3, we can see that the RMSE of estimator 1 has no significant change as δ increases, while other estimators change a lot, and the RMSE of estimator 1 is much lower than the other three for each SNR and δ .

6 Conclusions

This paper proposes a novel phase estimator based on restricted phase unwrapping and Tretter's phase estimation algorithm, which is able to estimate the original phase of a sinusoidal signal under noisy circumstances precisely. This new estimator has the advantages of low SNR threshold and RMSE. When $\text{SNR} = 0$ dB, the error probability of restricted phase unwrapping can reach level of 10^{-3} , while it is high in traditional methods because of the error propagation. When $\text{SNR} \geq 5$ dB, the RMSE of the proposed estimator is close to the CRB, with the performance of phase estimation better than the segmented DFT estimator developed in [10, 13] and the all-phase FFT estimator in [14].

Acknowledgements This material is based upon project supported by the National Natural Science Foundation of China grant No. 11164008, and the Key Laboratory of Photoelectronics and Telecommunication of Jiangxi Province grant Nos. 2013001 and 2011013.

References

1. Tretter SA (1985) Estimating the frequency of a noisy sinusoid by linear regression. *IEEE Trans Inf Theory* 31(6):832–835
2. Rife DC, Boorstyn RR (1974) Single-tone parameter estimation from discrete-time observations. *IEEE Trans Inf Theory* 20(5):591–598
3. Qi G (2004) A new frequency estimator of single sinusoid based on Fitz's algorithm. In: 7th IEEE international conference on signal processing. IEEE Press, Beijing, pp 1790–1793
4. Huang X, Deng Z (2009) An improved phase unwrapping algorithm and its application to instantaneous frequency estimation. *Acta Electronica Sinica* 37(10):2266–2272 (in Chinese)
5. McWilliam RG, Quinn BG, Clarkson IL et al (2010) Frequency estimation by phase unwrapping. *IEEE Trans Signal Process* 58(6):2953–2963
6. Fu H, Kam PY (2012) Sample-autocorrelation-function-based frequency estimation of a single sinusoid in AWGN. In: 75th IEEE vehicular technology conference. IEEE Press, Yokohama, pp 1–5
7. Kay S (1989) A fast and accurate single frequency estimator. *IEEE Trans Acoust Speech Signal Process* 37(12):1987–1990
8. Mengali U, Morelli M (1997) Data-aided frequency estimation for burst digital transmission. *IEEE Trans Commun* 45(1):23–25
9. Li X, Xu L, Zhou X (2009) High accuracy complex sinusoid frequency estimator in low SNR environment. *J Xidian Univ* 36(6):1010–1014 (in Chinese)
10. Qi G, Jia X (2001) High-accuracy frequency and phase estimation of single-tone based on phase of DFT. *Acta Electronica Sinica* 29(9):1164–1167 (in Chinese)
11. Zhan Y, Zhang B, Pan X (2012) Simulation and modification of carrier estimation algorithm based on difference of FFT's phase. *J Syst Simul* 24(11):2414–2417 (in Chinese)
12. Zhu L, Ding H, Ding K (2004) Phase regression approach for estimating the parameters of a noisy multifrequency signal. *IEE Proc-Vis Image Signal Process* 151(5):411–420
13. Li J, Wang Y (2009) DFT phase estimation algorithm and noise sensitive frequency region. *J Electron Inf Technol* 31(9):2099–2103 (in Chinese)
14. Huang X, Wang Z (2011) Anti-noise performance of all-phase FFT phase measuring method. *J Data Acquisition Process* 26(3):286–291 (in Chinese)

15. Zhang T, Ren Z, Chen G et al (2011) Improved spectrum analysis algorithm for all-phase time-shift phase difference. *Syst Eng Electron* 33(7):1468–1472 (in Chinese)
16. Dash PK, Hasan S (2011) A fast recursive algorithm for the estimation of frequency, amplitude, and phase of noisy sinusoid. *IEEE Trans Industr Electron* 58(10):4847–4856

An Improved Concurrent Multipath Transfer Mechanism in Wireless Potential Failure Network

Wenfeng Du, Liqian Lai and Shubing He

Abstract To avoid unnecessary performance degradation caused by accidental packet loss in unreliable wireless network, a simple congestion distinguishing mechanism is introduced to the CMT. This mechanism can distinguish an accidental packet loss from a real congestion with a special system state and can improve the performance of CMT in wireless potential failure network.

Keywords CMT · Congestion distinguishing · QoS

1 Introduction

The Stream Control Transport Protocol (SCTP) defined in RFC 4960 [1] is originally designed for signaling transport in telephony networks and can provide attractive features such as multihoming and multistreaming. Multihoming binds multiple IP addresses to a single association between two SCTP endpoints. Multistreaming means that multiple streams could be concluded in only one SCTP association and each stream is logical, unidirectional data flow.

Concurrent Multipath Transfer (CMT) [2], which utilizes the multihoming feature of SCTP protocol and distributes data across multiple end-to-end paths, is the concurrent transfer of data from a multihomed source to a multihomed destination via a SCTP association.

With the default congestion control algorithm, a time out event or fast retransmit event reduces the throughput by decreasing the size of congestion window, *cwnd*, or the slow start threshold, *ssthresh*.

W. Du (✉) · L. Lai · S. He

Department of Network Engineering, College of Computer Science and Software Engineering, Shenzhen University, Shenzhen 518060, People's Republic of China
e-mail: duwf@szu.edu.cn

However, the nature of wireless radios makes wireless networks have much more packet losses than wired networks, especially when the environment of transmission is terrible. Since the packet loss is quite different in wired and wireless scenes, an accidental packet loss cannot always indicate congestion in transmission. How to improve the transmission performance of CMT in wireless potential failure network has become an important research issue.

To avoid unnecessary congestion avoidance process incurred by accidental packet loss, an improved congestion distinguishing mechanism has been introduced to CMT in wireless potential failure network, CMT-PF, in which a possible loss state has been introduced to avoid performance degrade when an accidental packet loss happen.

2 Related Work

Since SCTP is originally designed for the wired network environment, it does not consider the various situations happen in the wireless network. In wired network environment, packet loss is a rare event and is considered to be a signal of congestion. However, many reasons could frequently cause accidental packet loss in the wireless network environment: (1) mobility, (2) link-layer contention, and (3) transmission errors [3].

Currently, the SCTP sender does not identify whether the network is congested or just considers it as an accidental packet loss. According to the default congestion control algorithm in CMT, the *ssthresh* is set to $1/2 cwnd$ or $2MTU$ and the *cwnd* is set 1 MTU when a time out happens or it is set to the changed *ssthresh* value when a fast retransmission happens. And then, the SCTP returns to the stage of slow start again. It can be found the performance of CMT, it is deteriorated frequently in wireless scenario especially in packet loss prone case.

Currently, some research works have been presented to improve the performance of CMT transmission, such as retransmission policies [2], Potentially Failed (PF) destination state [4, 5], loss differentiation algorithm [6], dynamic CMT enable algorithm [7], meanwhile, some research focus on improving TCP transmission in wireless network [3, 8, 9]. To detect the route restoration and address the issue of Multiconnection's fairness in TCP, this paper [10] proposes a SCTP-Fixed RTO mechanism from the TCP-Fixed RTO. It counts the number of successive retransmission timeout events. When the number exceeds a certain threshold, it adjusts the RTO value.

However, there is little work to discuss how to avoid unnecessary performance reduction in wireless potential failure network for CMT in case of accidental packet loss.

3 Congestion Distinguishing Mechanism

With the principle of CMT, the receiver sends a Gap ACK to the sender and informs a data chunk is like being potentially lost when it receives an out-of-order data chunk. Gap ACK do not cause any change of *cwnd* and *ssthresh*. The sender increases by a counter of potential missing reports for the data chunk. A fast retransmission is enabled when the counter reaches the forth stroke and the data sender retransmit the possible lost data chunk.

To distinguish an accidental packet loss from a real congestion, a Possible Congestion state has been introduced in the proposed congestion distinguish mechanism to represents the state of CMT association recently experiences a fast retransmission. The sender counts recent fast retransmission and switch to different working state. (1) If there is no fast retransmission happens, the sender holds the Normal state; In this case, *ssthresh* and *cwnd* grow as normal. (2) If the counter number is more than zero and does not exceed PMR threshold, the sender enters the Possible Congestion state, in which the sender does not change its configuration on *cwnd* and *ssthresh*. (3) Otherwise, the sender is in the Congestion state, in which *ssthresh* and *cwnd* decrease as the original congestion control algorithm mentioned.

To distinguish these three different working states, three additional variables are introduced for each destination.

Congestion_state represents the working state of a CMT sender.

times_uninterrupted_ack keep the number of uninterrupted heartbeat ACK of each destination when it leaves Possible Congestion state and enters Normal state.

times_uninterrupted_ack[i] represents the number of received uninterrupted heartbeat ACK of the *i*th Possible Congestion state. It can be found this variable is updated as follows.

$$times_uninterrupted_ack[1] = 1 \quad (1)$$

$$times_uninterrupted_ack[2] = 2 \quad (2)$$

.....

if $loss[i] \geq loss[i]-1$

$$times_uninterrupted_ack[i] = times_uninterrupted_ack[i - 1] + 1 \quad (3)$$

else

$$times_uninterrupted_ack[i] = times_uninterrupted_ack[i - 1] - 1 \quad (4)$$

times_current_loss keeps the number of recent fast retransmission or timeouts event.

The detail of state transition of a CMT sender is shown in Fig. 1.

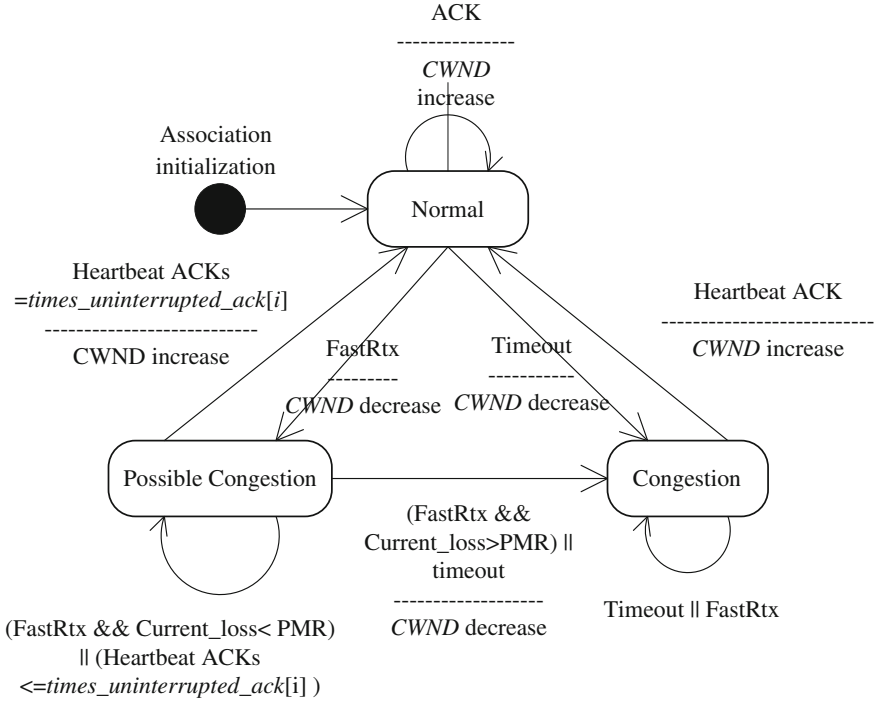


Fig. 1 The working state of a CMT sender

The sender enters Normal state after its association initialization and begins data transmission. However, the sender enters Possible Congestion state when a fast retransmission event happens, instead of Congestion state. In Possible Congestion state, the sender can only send and receive heartbeat chunks. The *times_uninterrupted_ack* increases by 1, when receive a heartbeat ACK chunk. When the received heartbeat ACK chunk reach a special threshold, the sender leaves Possible Congestion state and enter Normal state.

In case of Possible Congestion, the special *times_current_loss* increases by 1 when a fast retransmit event happens. If *times_current_loss* > PMR, the sender enters into Congestion state. The sender directly enters Congestion state when a time out event happens.

4 Simulation

To evaluate the performance of CMT association with the proposed congestion distinguish mechanism, a series of simulations results have been presented with ns2 [11]. A random loss error model is applied to simulate the wireless potential failure network.

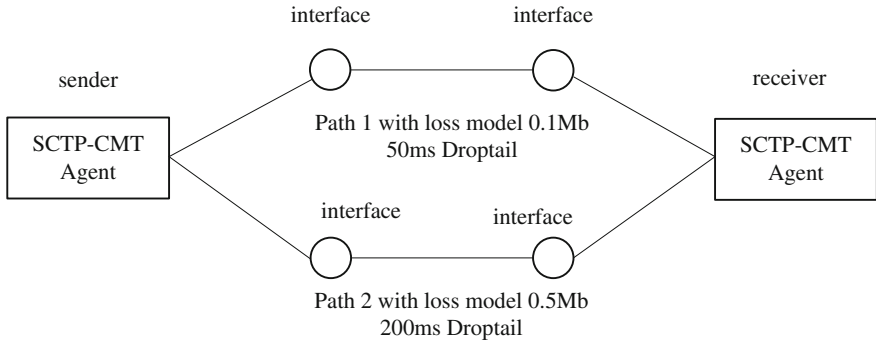
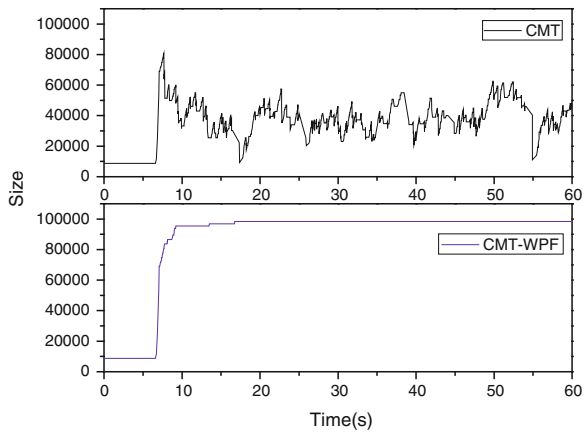


Fig. 2 The simulation topology

Fig. 3 The realtime *cwnd*

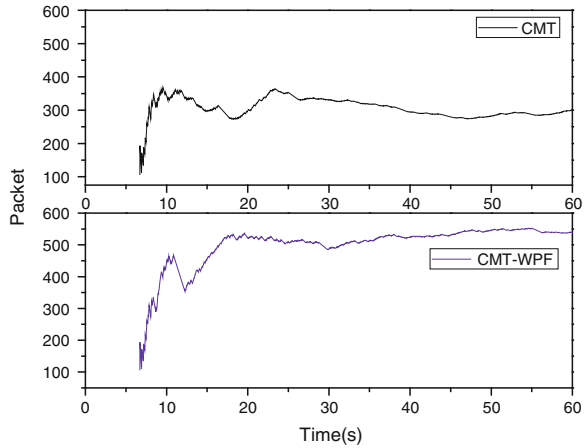


To achieve a random chunk lost list, the second random seed in ns2 is applied to generate a lost event list. The loss rate is set as 0.01. The topology of our simulation is shown in Fig. 2.

The whole simulation process last 60 s. A FTP application starts establishing an association to transport data at 0.1 s. With the generated lost event list, the initiation control chunk INIT is lost at 0.15 s. The HEARTBEAT chunk is lost at 3.3 s. The data chunk transmission began at 6.4 s indeed.

Figures 3 and 4 present some simulation result of the standard CMT and CMT-WPF mechanism on different performance metrics. Since the proposed CMT-WPF mechanism can prevent spurious triggering of congestion control mechanism, the CMT with congestion distinguishing mechanism can achieve better performance than the standard CMT association in all metrics.

Fig. 4 The realtime throughput



5 Conclusion

To avoid performance degrade in wireless potential failure environment, a congestion distinguishing mechanism for the CMT has been proposed in this paper. A Possible Congestion state is introduced to distinguish the real congestion from accidental packet loss due to link-layer contention or transmission errors and avoid unnecessary *cwnd* and *ssthresh* reduction. A series of simulations in ns-2 is performed and the results show the proposed mechanism performs better than the standard one in wireless potential failure network.

References

1. Stewart R (2007) RFC 4960, Stream control transmission protocol (SCTP) Sept 2007. Available at <http://www.ietf.org/rfc/rfc4960.txt>
2. Iyengar J et al (2006) Concurrent multipath transfer using SCTP multihoming over Independent end-to-end paths. *IEEE/ACM Trans Netw* 14(5):951–964
3. Fu Z, Luo H, Zerfos P, Lu S, Zhang L, Gerla M (2005) The impact of multihop wireless channel on TCP performance. *IEEE Trans. Mob Comput* 4(2):209–221
4. Natarajan P, Iyengar J, Amer P, Stewart R (2006) Concurrent multipath transfer using transport layer multihoming: performance under network failures. In: *IEEE MAILCOM*, Washington, Oct 2006
5. Natarajan P, Ekiz N, Amer P, Iyengar J, Stewart R (2008) Concurrent multipath transfer using SCTP multihoming: introducing the potentially-failed destination state. *Networking 2008 Ad Hoc and Sensor Networks, Wireless Networks, Next Generation Internet*. Springer Berlin, Heidelberg pp 727–734
6. Cen S, Cosman PC, Voelker GM (2003) End-to-end differentiation of congestion and wireless losses. *IEEE/ACM Trans Netw* 11(5):1063–6692
7. Kim T, Lee J, Eom YI (2010) Concurrent multipath transfer using SCTP multihoming over heterogeneous network paths. In: *International conference on control, automation and systems 2010 in KINTEX*. Gyeonggi-do, pp 27–30

8. Prasanthi S, Chung S-H, Kim W-S (2011) An enhanced tcp scheme for distinguishing non-congestion losses from packet reordering over wireless mesh networks. In: IEEE International conference on high performance computing and communications, pp 440–447
9. Balakrishnan H, Padmanabhan VN, Seshan S, Katz RH (1997) A comparison of mechanisms for improving TCP performance over wireless links. *IEEE/ACM Trans Netw* 5(6):756–769
10. Takemoto Y, Funasaka J, Teshima S, Ohta T, Kakuda Y (2009) SCTP performance improvement for reliable end-to-end communication in ad hoc networks. In: International symposium on autonomous decentralized systems. doi:10.1109/ISADS.2009.5207338
11. Network Simulator, NS-2 (2011) <http://www.isi.edu/nsnam/ns/>

Model-Based Testing of Web Service with EFSM

Fuzhen Sun, Lejian Liao and Longbo Zhang

Abstract Web services are becoming more and more widespread as an emerging technology; it is hard to test Web services because they are distributed applications with numerous aspects of runtime behavior that are different from typical applications. This paper presents a new approach to testing Web services based on Extended Finite State Machine (EFSM). Web Services Description Language (WSDL) file alone does not provide dynamic behavior information. This problem can be overcome by appending the formal model of EFSM to standard WSDL, we can generate a set of test cases which has a better test coverage than other methods. Moreover, a procedure for deriving an EFSM model from WSDL specification is provided to help a service provider augment, the EFSM model describing dynamic behaviors of the Web service. To show the efficacy of our approach, we applied our approach to Parlay-X Web services. In this way, we can test Web services with greater confidence in potential fault detection.

Keywords Web service · Model-based testing · Extended finite state machine (EFSM) · Fault detection

F. Sun · L. Liao

Beijing Engineering Research Centre of High Volume Language Information Processing and Cloud Computing Applications, Beijing Key Laboratory of Intelligent Information Technology, School of Computer Science, Beijing Institute of Technology, Beijing China

F. Sun · L. Zhang (✉)

School of Computer Science and Technology, Shandong University of Technology, Zibo China

e-mail: 10907023@bit.edu.cn

1 Introduction

Some testing techniques that are used to test software components are being extended to Web services [1–3]. A few papers have presented testing techniques for Web services, but the dynamic discovery and invocation capabilities of Web services bring up many testing issues. Existing Web service testing methods try to take advantage of syntactic aspects of Web service rather than semantic, dynamic, and behavioral information because standard Web Services Description Language (WSDL) is not capable of containing such information. Therefore, they focused on testing of single operations rather than testing sequences of operations. Furthermore, they heavily rely on the test engineers' experience.

Heckel and Mariani [4] generate test cases for Web services with individual rules by selecting “likely” inputs. Possible inputs are further restricted by the preconditions of the graph transformation (GT) rules [5]. This suggests the derivation of test cases using a domain-based strategy, known as partition testing [6]. The idea is to select test cases by dividing the input domain into subsets and choosing one or more elements from each domain [7]. The execution of an operation can alter parts of service's state that are used by other operations. GT rules specify state modifications at a conceptual level. By analyzing these rules, we can understand dependencies and conflicts between operations without inspecting their actual implementation. In this method, data flow testing technique is used to test the interaction among production rules if creation of nodes and edge is interpreted as “definition” and deletion as “use” [8]. Test cases are derived from default boundary values of XML schemas. Tests are created by replacing each value with each boundary value, in turn, for appropriate type. In the paper [9, 10, 12], the authors propose a method of extending WSDL to describe dependency information which is useful for Web service testing. They suggest several extensions such as input–output dependency, invocation sequences, hierarchical functional description, and concurrent sequence specification.

In this paper, we propose a new approach to test Web services. This idea stems from similarities between communication protocol testing and stateful Web services testing. Second, using the Extended Finite State Machine (EFSM)-based approach, we can generate a set of test cases with a very high test coverage which covers both control flow and data flow. Third, we applied our method to an industry-level example and showed the efficacy of our method in terms of test coverage and fault detection.

2 Test Cases Generation for Web Services Using EFSM

2.1 Modeling Web Service with EFSM

A WSDL specification does not provide sufficient information for Web service test derivation because it only provides the interface for the service. An EFSM starts from an initial state and moves from one state to another through interactions with

its environment. The EFSM model extends the FSM model with variables, statements, and conditions. An EFSM is a six-tuple $\langle S, s0, I, O, T, V \rangle$, where S is a nonempty set of states, $s0$ is the initial state, I is a nonempty set of input interactions, O is a nonempty set of output interactions, T is a nonempty set of transitions, and V is a set of variables. Each element of T is a five-tuple of the form: $\langle \text{source_state}, \text{dest_state}, \text{input}, \text{predicate}, \text{compute_block} \rangle$, where “source state” and “dest state” are states in S corresponding to the starting state and the target state of T , respectively; “input” is either an input interaction from I or empty; “predicates” is a predicate expressed in terms of variables in V , the parameters of the input interaction and some constants, and “compute-block” is a computation block consisting of assignment and output statements. We will only consider deterministic EFSMs that are completely specified. In addition, the initial state is always reachable from any state with a given valid context.

Figure 1 presents our procedure for deriving EFSM model from a WSDL specification. First of all, we have to decide whether the Web service to be modeled is stateful or not. A Stateful Web service in general can be modeled as an EFSM. Stateful Web service has several operations which change the service’s internal state that are used by other operations. In that case, the operations may response with different output messages according to the internal state of Web service server. If the Web service is stateless, then we have to use other Web service testing methods such as [4] and [11]. Otherwise, we continue with Steps 1 through 4.

Step (1) We analyze the WSDL specification and the web service specification in informal language and fill the WSDL analysis template. For example, Table 1 shows the WSDL analysis template filled out for a banking Web service. From WSDL description, we find out that the banking Web service provides four public operations, i.e., *openAccount*, *deposit*, *withdraw*, and *closeAccount*. The operation *openAccount* expects a single parameter *init* which means an initial deposit, and returns an account number identifier. The operation *closeAccount* expects a single parameter *Id*, which means account number, and returns the result of operation such as *ResultOK* and *Error*. The operations *deposit* and *withdraw* expect two parameters *id* (*identifier*) and *v* (*value*), and return results such as *ResultOK* and *Error*.

Step (2) To construct EFSM, it is necessary to classify variables in the precondition and postcondition of step 1 into control variables and data variables.

Figure 2 shows an initial version of EFSM for the banking Web service. The states are constructed by combining possible value range of control variables. The variable *accountId* and *value* have two possible values: ranges 0 and greater than 0. If the control variables have value 0, it means that it is not initialized yet. When the variable *accountId* is initialized by *openAccount* operation, the variable has a value greater than 0 until it is closed by *closeAccount* operation. After initialization, the variable *value* keep a balance greater than 0 according to the operation *withdraw* and *deposit*. Therefore, we make four different states with combinations of the two control variables. Then we associate transitions with the appropriate operations by examining the precondition and postcondition of an operation.

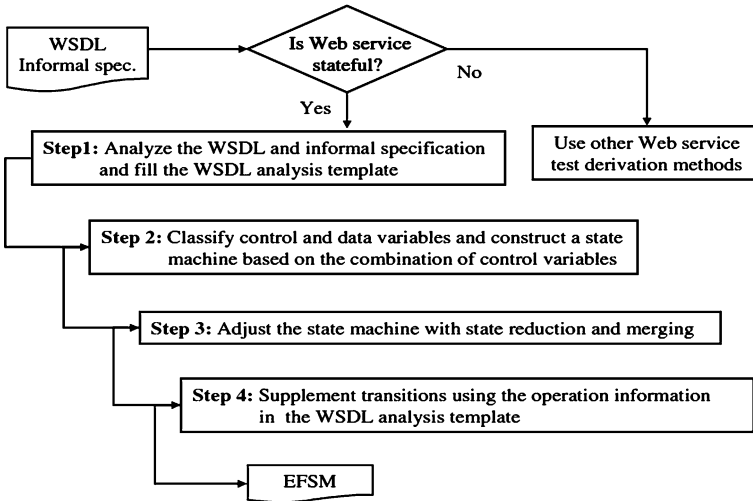


Fig. 1 Procedure for deriving an EFSM model from a WSDL description of a service

Table 1 Classification of variables for banking Web service

| Operation | Precondition | | Postcondition | |
|--|--------------------|---------------|--------------------|---------------|
| | Control variable | Data variable | Control variable | Data variable |
| Name: openAccount Parameter: init Return: identifier | – | init | accountId value | init |
| Name: deposit Parameter: id, v Return: res | accountId | v id | value | – |
| Name: withdraw Parameter: id, v Return: res | accountId value | v id | value | – |
| Name: closeAccount Parameter: id Return: res | accountId | id | accountId value | – |

Step (3) It is desirable to reduce states in the initial version of EFSM model because, first, often the number of states would be otherwise huge and, second, there is a possibility that unreachable states may exist. For example, the state with value >0 and $accountId = 0$ is an unreachable state. Unreachable states should be deleted for the state reduction. Some states could be merged into one state according to test engineer’s judgment. Figure 3 gives an enhanced EFSM obtained by removing an unreachable state and merging two states into a state named Active. For human readability, we assign a meaningful name to each state.

Fig. 2 EFSM construction with control variables

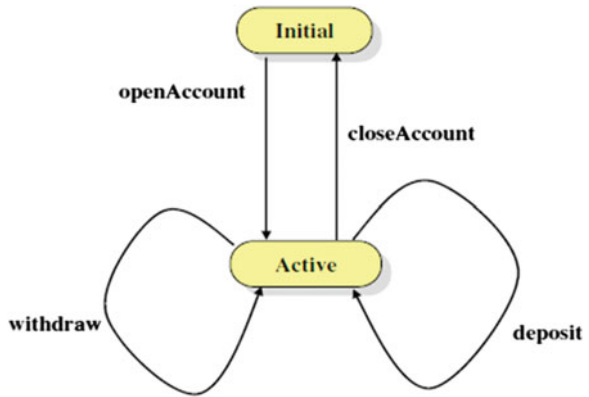
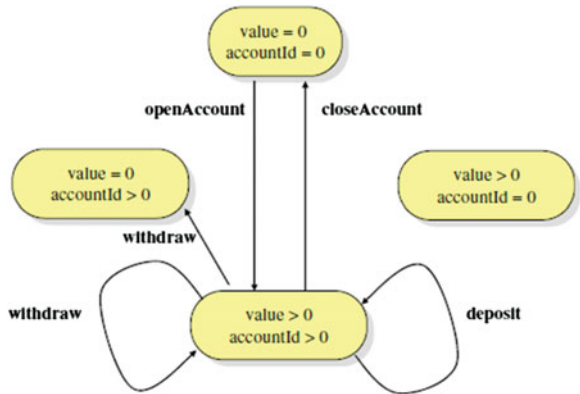


Fig. 3 Enhanced EFSM with state reduction and merging



Step (4) To make a concrete transition in EFSM, operation information in the WSDL is used. An operation has input and output message. Input message is transformed into input event and output message is transformed into output event in the transition. Precondition is transformed into guard condition in the transition. Postcondition is transformed into actions in the transition. Figure 4 shows our final EFSM model derived from the WSDL specification for the banking Web service.

2.2 Test Cases Generation Algorithm Using EFSM

We choose Bourhfir’s algorithm [13] as our test case generation method for Web services because the algorithm considers both control and data flow with better test coverage. The control flow criterion used is Unique Input Output (UIO) sequence [14] and the data flow criterion is “all-definition-uses” criterion [15] where all the paths in the specification containing a definition of a variable and its uses are

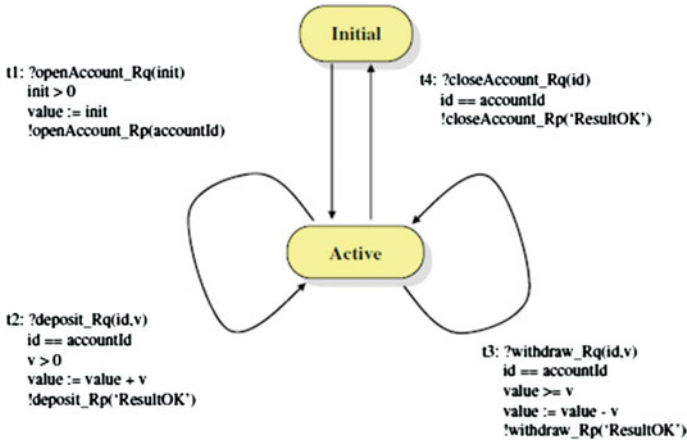


Fig. 4 Final EFSM for banking Web service

generated. Moreover, the algorithm uses a technique called cycle analysis to handle executability of test cases.

The detailed algorithm is described in Fig. 5. For each state *S* in the EFSM, the algorithm generates all its executable preambles (a preamble is a path such that its first transition’s initial state is the initial state of the system and its last transition’s tail state is *S*) and all its postambles (a postamble is a path such that its first transition’s start state is *S* and its last transition’s tail state is the initial state). To generate the “all-definition-uses” paths, the algorithm generates all paths between each definition of a variable and each of its uses and verifies if these paths are executable, i.e., if all the predicates in the paths are true. After handling executability problem, the algorithms remove the paths which are included in the already existing ones, complete the remaining paths (by adding postambles) and add paths to cover the transitions which are not covered by the generated test cases.

3 Case Study for Parlay-X Web Services

To show that our method can be effectively used for nontrivial real-world problems, we applied it to Parlay-X Web services [15]. A Parlay-X Web service, Third Party Call, is used to create and manage a call initiated by an application.

The overall scope of this Web service is to provide functions to application developers to create a call in a simple way. Using the Third Party Call Web service, application developers can invoke call handling functions without detailed telecommunication knowledge. The Third Party Call Web service provides four operations: *MakeCall*, *GetCallInformation*, *EndCall*, and *CancelCall*.

Algorithm. *Extended FSM Test Generation***Begin**

Generate the dataflow graph G from the EFSM specification
 Choose a value for each input parameter influencing the control flow
 Call *Executable-Du-Path-Generation(G)* procedure
 Remove the paths that are included in already existing ones
 Add a postamble to each du-path to form a complete path
 Make it executable for each complete path using cycle analysis
 Add paths to cover the uncovered transitions
 Generate its input/output sequence using symbolic evaluation

End.**Procedure** *Executable-Du-Path-Generation(flowgraph G)***Begin**

Generate the shortest executable preamble for each transition
For each transition T in G
 For each variable v which has an A-Use in T
 For each transition U which has a P-Use or a C-Use of v
 Find-All-Paths(T,U)
 EndFor
 EndFor
EndFor
End;

Fig. 5 Test case generation algorithm using EFSM

For comparison, we generated test cases for the Third Party Call Web service with three different methods, the method of Offtutt et al. [11] and finally our method. For the method of Heckel et al. [4], we defined a domain based on GT production rules. Eight production rules for the four operations were found. After that, we found attributes for each production rule. Test cases are generated by fixing a boundary value for at least one of them and randomly generating the other two values.

To generate test cases using our method, we followed the procedure described in Sect. 2.1. First, we analyzed the WSDL specification of Third Party Call and the informal specification of the Third Party Call Web service. For Step 2, three control variables were identified by analyzing the WSDL analysis template. Then we constructed an EFSM based on these three control variables and the four operations. The final EFSM shown in Fig. 6 have five states and fifteen transitions. Using the EFSM and the algorithm described in Sect. 3.2, 95 test cases were generated for Third Party Call.

Fig. 6 EFSM model for the third party call Web service

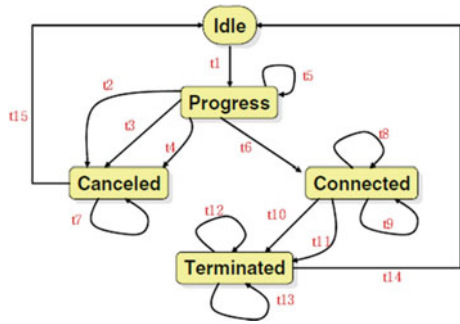


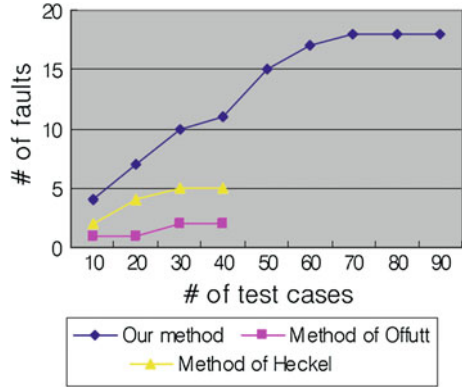
Table 2 Test cases and results

| | Method of Heckel et al. [4] | Method of Offutt et al. [11] | Our method |
|--------------------------------|-----------------------------|------------------------------|------------|
| Number of test cases generated | 36 | 40 | 95 |
| Number of faults found | 5 | 2 | 18 |
| Total execution time (s) | 90 | 80 | 859 |
| Average execution time (s) | 2.5 | 2 | 9 |

Test cases and results of different methods are summarized in Table 2. As we expected, our method located more faults than the other methods even though it spent more time for executing a test case. Our method spent more time than other method because test cases generated using our method consist of the complex sequences of operations but almost all test cases generated using other method is made of a single operation. To show the efficacy of our method, the number of test cases and the accumulated number of faults detected are analyzed in Fig. 7.

As shown in Fig. 7, our method detected many faults in the early phase of testing. Our methods detected many errors that occurred during executing complex sequences of operations. For example, the operation GetCallInformation worked well in the initial state and at the progress state, but the operation caused an error when it executed in the connected state. The method [4] located some faults related with boundary value and incorrect input values in the case of testing for single operations. However, the sequences of operations derived from the method [4] were not effective for locating faults. Even if the method [4] expected the data flow coverage criterion “all-definitions-uses” for generated test cases, the generated test cases using relations of conflicts and casual dependencies between productions rules did not find out any faults which were located by our method. During testing using this method [11], it was difficult to find faults because faults rarely occurred when we executed single operations with different boundary values. Only two faults related with message parameter value with maximum length were founded.

Fig. 7 Number of test cases and number of faults found



4 Conclusion

In summary, the main contributions of this paper are as follows: First, this paper introduces a new Web service testing method that augments WSDL specification with an EFSM formal model and applies a formal technique to Web service test generation. Second, using the EFSM-based approach, we can generate a set of test cases with a very high test coverage which covers both control flow and data flow. Third, we applied our method to an industry-level example and showed the efficacy of our method in terms of test coverage and fault detection.

One of drawbacks of our approach is the overhead to generate test cases based on an EFSM. Without any automatic tool for generating test cases using EFSM, it is a very tedious task to generate test cases manually. Currently, we focused on testing of a Web service with single EFSM derived from a WSDL specification. For future work, we plan to extend our method to treat more complex situations such as test cases generation for compositions of Web services.

Acknowledgment This work is funded by the Shandong Provincial Natural Science Foundation of China (Grant No.ZR2011FL013) and partially supported by the Natural Science Foundation of China (NSFC, Grant No.60873237), Natural Science Foundation of Beijing (Grant No.4092037).

References

1. Booth D, Haas H, McCabe F, Newcomer E, Champion M, Ferris C, Orchard D (2004) Web services architecture. W3C working group note, W3C, 1201 Massachusetts Avenue, Cambridge, USA
2. Shafique M, Labiche Y (2010) A systematic review of model based testing tool support. Carleton University, Technical report, May 2010
3. Bourhfir C, Aboulhamid E, Khendek F, Dssouli R (2012) Test cases selection from SDL specifications. *Comput Netw* 35(6):693–708

4. Heckel R, Mariani L (2005) Automatic conformance testing of web services, vol 3442. Springer LNCS, New York, pp 34–48
5. Baldan P, König B, Sturmer I (2011) Generating test cases for code generators by unfolding graph transformation systems. In: Proceedings of 9th International conference on graph transformation, Rome
6. Ammann P, Offutt J (2011) Introduction to software testing. Cambridge University Press, New York
7. Weyuker E, Jeng B (2006) Analyzing partition testing strategies. *IEEE Trans Softw Eng* 31:703–711
8. White L, Cohen EJ (1980) A domain strategy for computer program testing. *IEEE Trans Softw Eng* 6:247–257
9. Tsai WT, Paul R, Wang Y, Fan C, Wang D (2008) In: Extending WSDL to facilitate web services testing. HASE 2008
10. Bourhfir C, Dssouli R, Aboulhamid E, Rico N (1997) Automatic executable test case generation for EFSM specified protocols. *IWTCS'97*, pp 75–90
11. Offutt J, Xu W (2004) Generating test cases for web services using data perturbation. *ACM SIGSOFT Softw Eng Notes* 29:1–10
12. Li Y, Li M, Yu J (2009) “Web service testing, the methodology, and the implementation of the automation-testing tool”, *GCC2009*. LNCS 3032:940–947
13. Sabnani K, Dahbura A (1985) A new technique for generating protocol tests. *ACM Comput Commun* 15(4):39–48
14. Hausmann JH, Heckel R, Lohmann M (2006) Model-based discovery of web services. *ICWS'06*, pp 63–75
15. Parlay X (2012) Working group, Parlay-X White Paper. <http://www.parlay.org>

Data Fault Detection Using Multi-label Classification in Sensor Network

Zhenhai Zhang, Shining Li and Zhigang Li

Abstract Detection of data fault is a hit point in sensor network in recent years and multiple data faults may occur at the same time. However the existing detection methods can only detect one type of data fault at the same time. To solve this problem, the detection of data fault is model as multi-label classification task, where an instance may belong to more than one label. We firstly break down the sensor data into instances using sliding window and then employ feature extraction methods to extract data features from instances. After this we associate each instance with corresponding data fault labels. A comparative experimental evaluation of five multi-label classification algorithms is conducted on aforementioned multi-label dataset using a variety of evaluation measures. Experimental results and their analysis show preliminarily that: (1) LP outperforms other classification algorithms on all evaluation measures since it takes the correlation of multiple data fault labels into account in detection of data fault; (2) outlier is the easiest data fault to detect and high noise is the hardest data fault to detect.

Keywords Algorithms · Classification · Fault detection · Sensor network · Multi-label classification

Z. Zhang (✉) · S. Li · Z. Li
School of Computer Science, Northwestern Polytechnical University, Xi'an, China
e-mail: http326@163.com

S. Li
e-mail: lishining@nwpu.edu.cn

Z. Li
e-mail: lizhigang@nwpu.edu.cn

1 Introduction

Sensor network, a data-centric network, has received worldwide attention in recent years and has a lot of important applications such as military [1], agriculture [2], architecture [3], and so on. Sensor network is used to sense and collect information from physical world, which provides people with significant evidences when trying to make meaningful conclusions. Therefore, the data sensor network collected must be true and reliable, which is the key that whether sensor network has been applied successfully or not in practical deployments. If there are some faulty sensor readings in collected data, it is possible to make an improper decision or draw meaningless conclusions. Several practical deployments have observed faulty sensor readings caused by improper data calibration, or hardware failures, or low battery levels, or interference around environment, and so on [4, 5]. To ensure the data quality of the collected data, fault detection in sensor network have been an important research direction [6].

Noise is an important factor of affecting data quality. Eiman [7] proposed a Bayesian approach, combining prior knowledge of true sensor readings, the noise characteristics of the sensor and the observed noisy readings, to reduce the uncertainty due to noise and enhance the reliability of sensor readings. Spatial-temporal correlation is an important characteristic of sensor data, aiming at which several researchers have proposed some fault detection approaches [8, 9]. Tulone [10] presented an approach relies on autoregressive models of time series forecasting to predict the approximate values of sensors in sensor network, which could detect outlier fault but do nothing for noise fault. Jeffery [11] proposed a framework for fault detection based on spatial and temporal characteristics of sensor data. Zhang [12] transformed sensor data using Principal Component Analysis (PCA) and then within which sensor identification indices were calculated. If difference of sensor identification indices between the absence of the sensor and it included was greater than threshold value, there was a fault in the sensor. Kevin [13] systematically described common sensor data faults and defined a data fault to be data reported by a sensor inconsistent with the interest's true behavior. The paper described the fault from data-centric view called data fault and not only divided data fault into four types but also presented a detailed study of each data fault. The four types of data faults are described as follows:

1. Outlier

Outlier is defined as an isolated sample whose value is significantly greater than the expected. Outlier is one of the most seen data faults in sensor network, and occurs randomly and instantaneously. Outlier affects only one sample in sensor data.

2. Spike

Spike is defined as that the rates of change are significantly greater than the expected during a short period of time. The obvious difference between outlier and spike is that spike affects more than one sample while outlier affects only one sample.

3. Stuck-at

Stuck-at is defined as that there are no changes over a series of sample values; that is to say, the sample value is almost a constant. The characteristic of stuck-at is that variation of sample values stuck-at affects is zero or nearly zero, which is one of the most important differences between spike and stuck-at.

4. High Noise

High noise is considered as sample values that exhibits high amount of variation over a period of time. Although noise is common in sensor data, high noise may be a sign that there are faults in sensors. High noise may be caused by hardware fault or low battery level in sensors.

Based on Kevin's work, Abhishek [6] used rule-based methods, estimation methods, time-series analysis-based methods, and learning-based methods to detect three types of data faults. The experimental results showed that rule-based methods could detect data faults effectively but it was seriously dependent on the choose of parameters, and estimation methods could detect data faults but it could not discriminate which data fault was, and time-series analysis-based methods were good at detecting short duration faults, and learning-based methods could not only detect data faults effectively but also discriminate which data fault was.

However, the existing data fault detection methods can detect only one type of data fault at the same time. If multiple data faults occurs simultaneously, it cannot detect all of them at the same time. In practical applications, multiple faults may occur at the same time [13] and it is impossible to model each fault separately due to a lot of potential faults [14]. Hence, it is necessary to develop a fault detection method which can detect multiple faults at the same time. To achieve this, this paper models fault detection problem as a multi-label classification task.

The main contributions of this paper are as follows: (1) the sensor data is first resolved into instances using sliding window and then data features are extracted from instances and finally a multi-label dataset for data fault detection is created; (2) comparative experiments with five multi-label classifiers using several evaluation measures are performed on the aforementioned dataset.

The rest of the paper is organized as follows. [Section 2](#) provides background material about multi-label classification. [Section 3](#) presents dataset creation including data feature extraction and labeling in detail. [Section 4](#) reports experimental results and analysis. Conclusions are drawn in [Sect. 5](#).

2 Multi-label Classification

In this section, we introduce the formal notations of multi-label classification used throughout this paper.

An instance is associated with only one label in single-label classification. For example, a document can only be classified to economy or politics. However, an instance can be associated with multiple labels simultaneously in multi-label

classification. For example, a document may belong to economy and politics at the same time.

Definition 1 Let a vector of n attribute values $X = (x_1, x_2, \dots, x_n)$ represent an instance, $x_i \in R$ and $L = \{l_1, l_2, \dots, l_m\}$ be a finite set of labels. The label set with which an instance is associated is $Y = \{y_1, y_2, \dots, y_p\}$, $p \leq m$, and it is the subset of L , $Y \subseteq L$. Then the multi-label dataset containing t instances is denoted by

$$D = \{(X_i, Y_i) | 1 \leq i \leq t, X_i \in R^n, Y_i \subseteq L\} \quad (1)$$

3 Feature Extraction and Labeling

Sensors collect data periodically in sensor network and then transmit them to the data center, hence sensor data is the continuous data stream. It is necessary to resolve the continuous data stream into instances of finite length and assign labels to them before multi-label classification algorithms are used. We employ a sliding window to break down the continuous data stream into instances of finite length.

Definition 2 Let $T = (t_1, t_2, \dots, t_n)$ be the continuous data stream with length n collected periodically by sensors in sensor network. $W = (t_u, t_{u+1}, \dots, t_{u+l})$ represents the sliding window with length l , here $1 \leq u \leq n - l$. The number of samples over which the sliding window W slides forward or backward one step is called the step size of the sliding window, which is s .

When sliding window is adopted to resolve T , it is first placed on the first sample t_1 , and right now the first instance resolved by sliding window is $X_1 = (t_1, t_2, \dots, t_l)$. Second, sliding window slides forward one step and then the second instance resolved is $X_2 = (t_{s+1}, t_{s+2}, \dots, t_{s+l})$. And so on, it can obtain $\lfloor \frac{n-l}{s} \rfloor + 1$ instances.

3.1 Data Feature Extraction

Data features are used to describe characteristics or natures of the data. We adopt sliding window to break down the sensor data into instances which consist of original data values, nevertheless instances which consist of original values cannot describe characteristics of sensor data enough. As a result, they cannot be used straightforward in multi-label classification. Hence, it is necessary to extract appropriate data features from them, which helps to promote the performance of data fault detection of multi-label classification algorithms.

Standard deviation, variance, and mean are used to represent features of data in the statistics. For instance $X_i = (t_{i+1}, t_{i+2}, \dots, t_{i+l})$ we calculate standard deviation, variance, and mean of X_i as data features of X_i .

The rate of change is an important data feature for detecting data faults. The rate of change employed in this paper is defined as follows:

Definition 3 Let $X = (t_1, t_2, \dots, t_l)$ be an instance. $CR = \frac{|t_i - t_{i+1}|}{t_i}$ is called the rate of change between samples t_i and t_{i+1} , here $1 \leq t_i < l$.

For an instance $X = (t_1, t_2, \dots, t_l)$, we calculate the rate of change of each pair of samples, and then obtain a set of rates of change $C = \{CR_1, CR_2, \dots, CR_{l-1}\}$. Finally, we calculate maximal value, minimum value, standard deviation, variance, and mean of C as data features of the instance.

The goal of PCA is to find an array of orthogonal bases to maximize variance between variables. Data transformed by PCA can describe difference between instances better, which helps to detect data fault. Hence, we transform instances consisting of original data values using PCA, and take the transformed results as data features of instances.

The Fourier Transform can transform the signal from the time domain to the frequency domain. Usually, characteristics of the signal cannot be understood easily in time domain while they can be observed obviously in frequency domain. Therefore, for each instance we transform it from the time domain to the frequency domain using Discrete Fourier Transform, and take the transformed results as data features of the instance.

Although the Fourier Transform can transform the signal from the time domain to the frequency domain, it loses information of the time domain, which makes it suitable for depicting global characteristics of the signal. The Wavelet Transform can hold information of the time domain and the frequency domain simultaneously, which makes it suitable for depicting local characteristics of the signal. Hence, for each instance we transform it using Discrete Wavelet Transform, and take the transformed results as data features of the instance.

3.2 Data Fault Labels

In Sect. 1 we have presented four types of data fault in sensor network: (1) outlier fault; (2) spike fault; (3) stuck-at fault; (4) high noise fault. The four types of data fault are used as data fault labels. If an instance occurs at a data fault, it is associated with the corresponding data fault label, otherwise normal label. The information of data fault labels are described in Table 1.

According to Definition 1, the finite set of labels is $L = \{L - \text{Outlier}, L - \text{Spike}, L - \text{Stuck}, L - \text{Noise}, L - \text{Normal}\}$

Table 1 Information of data fault labels

| Label | Corresponding data fault |
|-----------|--------------------------|
| L-Outlier | Outlier fault |
| L-Spike | Spike fault |
| L-Stuck | Stuck-at fault |
| L-Noise | High noise fault |
| L-Normal | Normal, no fault |

4 Experiments

To evaluate the performance of data fault detection of multi-label classification algorithms in sensor network, we conducted experiments on Mulan. We compared the following multi-label classification algorithms: binary relevance (BR) [15], label powerset (LP) [15], multi-label k-nearest neighbor (MLkNN) [16], classifier chains for multi-label classification (CC) [17] and random k-labelsets for multi-label classification (RAkEL) [18], which have outstanding performance in other application domains. The number of neighbors in MLkNN was set to 10. LP, BR, and RAkEL were run using the decision tree algorithm C4.5 as the base classifier. Experiments were performed using 10-fold cross-validation for evaluation.

4.1 DataSet

The dataset used in experiments are collected by the temperature sensor in Networked Aquatic Microbial Observing System (NAMOS), which is available at http://robotics.usc.edu/~namos/data/jr_aug_06/. The sensor collected data every 10 s, and obtained 30,823 samples totally. To evaluate the performance of aforementioned five classifiers in data fault detection, we artificially injected four types of data faults presented in Sect. 1 into the dataset, since injecting data faults into the dataset can give us exact result that help us to better understand the performance of multi-label classification algorithms in data fault detection. The information of injecting faults are described as follows:

1. Outlier Faults

To inject outlier faults, we chose a sample i and replaced the reported value t_i with $\tilde{t}_i = t_i \times f$. f is chosen from $\{1.3, 1.5, 1.8\}$ randomly.

2. Spike Faults

To inject spike faults, we chose a set of successive samples W and replaced the reported values of W with the values generated from the aperiodic triangle signal.

3. Stuck-at Faults

To inject stuck-at faults, we chose a set of successive samples W and replaced each reported value t_i in W with $\tilde{t}_i = t \times f$. Here, t is the reported value of the first sample in W and f is chosen from $\{1.5, 1.8\}$ randomly.

Table 2 Statistics of dataset

| Instances | Features | Labels | Cardinality | Density |
|-----------|----------|--------|-------------|---------|
| 3010 | 1809 | 5 | 1.101 | 0.22 |

4. High Noise Faults

To inject high noise faults, we chose a set of successive samples W and added a random value from a normal distribution, $N(0, \beta^2)$, to each sample in W . β is chosen from $\{\delta, 1.5\delta\}$ randomly and δ is the standard deviation of samples in W .

According to Definition 3, we chose parameters $l = 720$ and $s = 10$ to resolve the sensor data using sliding window, which obtained 3,010 instances of length of 720. Then feature extraction methods discussed in Sect. 3 were employed to extract data features from 3,010 instances, which obtained 1,809 data features. The statistics of the generated multi-label data set are listed in Table 2.

4.2 Evaluation Measures

Let the predicting label set of a classifier predicting an unseen instance be Z , and the evaluation measures are defined as follows according to Definition 1.

Micro FMeasure is defined as

$$\text{Micro FMeasure} = \frac{2 \times tp}{2 \times tp + fp + fn} \quad (2)$$

Here tp , fp , and fn represent the number of true positives, false positives, and false negatives, respectively. The larger Micro FMeasure is, the better the prediction performance is.

Hamming Loss is defined as

$$\text{Hamming Loss} = \frac{1}{t} \sum_{i=1}^t \frac{|Y_i \Delta Z_i|}{m} \quad (3)$$

Here Δ stands for the symmetrical difference of two label sets. The smaller Hamming Loss is, the better the predicting performance is.

Average Precision is defined as

$$\text{Average Precision} = \frac{1}{t} \sum_{i=1}^t \frac{1}{|Y_i|} \sum_{\lambda \in Y_i} \frac{|\{\lambda' \in Y_i : r_i(\lambda') \leq r_i(\lambda)\}|}{r_i(\lambda)} \quad (4)$$

The larger Average Precision is, the better the prediction performance is. OneError is defined as

$$\text{OneError} = \frac{1}{t} \sum_{i=1}^t \delta(\arg \min_{\lambda \in L} r_i(\lambda)) \quad (5)$$

where

$$\delta(\lambda) = \begin{cases} 1 & \text{if } \lambda \notin Y_i \\ 0 & \text{otherwise} \end{cases} \quad (6)$$

The smaller OneError is, the better the predicting performance is. Coverage is defined as

$$\text{Coverage} = \frac{1}{t} \sum_{i=1}^t \max_{\lambda \in Y_i} r_i(\lambda) - 1 \quad (7)$$

The smaller Coverage is, the better the predicting performance is. Ranking Loss is defined as

$$\text{Ranking Loss} = \frac{1}{t} \sum_{i=1}^t \frac{1}{|Y_i| |\overline{Y}_i|} \left| \{(\lambda_a, \lambda_b) : r_i(\lambda_a) > r_i(\lambda_b), (\lambda_a, \lambda_b) \in Y_i \times \overline{Y}_i\} \right| \quad (8)$$

where \overline{Y}_i is the complementary set of Y_i with respect to L . The smaller Ranking Loss is, the better the predicting performance is.

Macro FMeasure is defined as

$$\text{Macro FMeasure} = \frac{1}{m} \frac{2 \times \sum_{j=1}^t |Y_j^i \cap Z_j^i|}{\sum_{i=1}^m \left(2 \times \sum_{j=1}^t |Y_j^i \cap Z_j^i| + \sum_{j=1}^t |\overline{Y}_j^i \cap Z_j^i| + \sum_{j=1}^t |Y_j^i \cap \overline{Z}_j^i| \right)} \quad (9)$$

The larger Macro FMeasure is, the better the prediction performance is.

4.3 Experimental Results and Analysis

The experimental results are reported in the form of average \pm standard deviation. The two-tailed paired t-tests at 0.05 significance level is employed to analyze the experimental results in order to examine whether the results have a statistical significant advantage. In the following tables, the results in bold represent the performance of the classifier is optimal in comparative classifiers. The sign \uparrow means that the larger value the better performance while the sign \downarrow is inverse.

Table 3 Performance of multi-label classification algorithms in data fault detection

| Name | Ranking loss (\downarrow) | Coverage (\downarrow) | OneError (\downarrow) | Average precision (\uparrow) | Hamming loss (\downarrow) | Micro FMeasure (\uparrow) |
|-------|---------------------------------------|---------------------------------------|---------------------------------------|---------------------------------------|---------------------------------------|---------------------------------------|
| BR | 0.0183 \pm 0.0060 | 0.1797 \pm 0.0313 | 0.0369 \pm 0.0086 | 0.9761 \pm 0.0059 | 0.0149 \pm 0.0023 | 0.9660 \pm 0.0052 |
| LP | 0.0084 \pm 0.0033 | 0.1365 \pm 0.0208 | 0.0169 \pm 0.0075 | 0.9894 \pm 0.0044 | 0.0077 \pm 0.0035 | 0.9825 \pm 0.0081 |
| MLkNN | 0.0365 \pm 0.0050 | 0.2475 \pm 0.0290 | 0.1199 \pm 0.0151 | 0.9360 \pm 0.0079 | 0.0580 \pm 0.0061 | 0.8658 \pm 0.0138 |
| CC | 0.0225 \pm 0.0100 | 0.1963 \pm 0.0481 | 0.0375 \pm 0.0107 | 0.9740 \pm 0.0082 | 0.0160 \pm 0.0031 | 0.9634 \pm 0.0069 |
| RAkEL | 0.0141 \pm 0.0028 | 0.1625 \pm 0.0240 | 0.0362 \pm 0.0064 | 0.9786 \pm 0.0032 | 0.0149 \pm 0.0023 | 0.9660 \pm 0.0052 |

Table 4 Micro FMeasure (\uparrow) of multi-label classification algorithms for per label

| Name | L-Outlier | L-Spike | L-Stuck | L-Noise |
|-------|---------------------------------------|---------------------------------------|---------------------------------------|---------------------------------------|
| BR | 0.9835 \pm 0.0986 | 0.9583 \pm 0.1042 | 0.9591 \pm 0.0971 | 0.8673 \pm 0.0845 |
| LP | 0.9810 \pm 0.0979 | 0.9746 \pm 0.1011 | 0.9628 \pm 0.0907 | 0.9671 \pm 0.0910 |
| MLkNN | 0.9331 \pm 0.0917 | 0.8527 \pm 0.1011 | 0.9307 \pm 0.1008 | 0.2697 \pm 0.0129 |
| CC | 0.9835 \pm 0.0986 | 0.9583 \pm 0.1042 | 0.9591 \pm 0.0971 | 0.8673 \pm 0.0845 |
| RAkEL | 0.9835 \pm 0.0986 | 0.9583 \pm 0.1042 | 0.9591 \pm 0.0971 | 0.8673 \pm 0.0845 |

The performance of five comparative multi-label classification algorithms using six different measures is shown in Table 3. It can be seen that LP dominates the other algorithms in all measures in data fault detection. The reason may be that LP takes correlations among multiple labels into account when LP is trained. Hence, we can infer that taking correlations among different data fault types helps to promote the performance of multi-label classification algorithms in data fault detection. We further analyze the results using the two-tailed paired t-tests at 0.05 significance level, and it shows that LP outperform than other classifiers significantly under all measures.

The predicting performance of multi-label classification algorithms using Macro FMeasure measure for each label is shown in Table 4. It can be seen that LP dominates the other algorithms for three of all data fault labels. We calculate the average of Macro FMeasure of all algorithms for each label and the results are that L-Outlier is 0.97292 and L-Spike is 0.94044 and L-Stuck is 0.95416 and L-Noise is 0.76774. From the average of Macro FMeasure, we can see that the label hardest to predict is L-Noise and the easiest label to predict is L-Outlier. This can be interpreted that outlier fault affects only one sample, which leads to distinguish it from others more easily. While high noise fault affects a set of samples and noise is common in sensor data, hence it is more difficult to distinguish them from other samples.

5 Conclusions and Future Work

This paper proposes to model the data fault detection using multi-label classification in sensor network, which could detect multiple types of data faults simultaneously. The task of transforming the sensor data into multi-label data set is investigated. An experimental evaluation of five multi-label classification algorithms was carried out using a variety of measures. Experimental results show that LP is the most effective of five comparative algorithms and five algorithms show good performance in data fault detection.

LP exhibits excellent performance compared with other classification algorithms, since it take correlations between labels into account. Therefore, future work will further exploit correlations among different types of data fault to enhance the detection of data fault.

Acknowledgment This research was supported by National Science and Technology Major Project of the Ministry of Science and Technology of China under Grants 2012ZX03005007.

References

1. Sang Hyuk L, Soobin L, Heecheol S, Hwang-Soo L (2009) Wireless sensor network design for tactical military applications: remote large-scale environments. In: Proceedings of 2009 IEEE military communications conference. Institute of Electrical and Electronics Engineers, New York, pp 1–7
2. Burrell J, Brooke T, Beckwith R (2004) Vineyard computing: sensor networks in agricultural production. *IEEE Pervasive Comput* 3(1):38–45
3. Mascarenas D, Flynn E, Farrar C, Park G, Todd M (2009) A mobile host approach for wireless powering and interrogation of structural health monitoring sensor networks. *IEEE Sens J* 9(12):1719–1726
4. Tolle G, Polastre J, Szewczyk R, Culler D, Turner N, Tu K et al (2005) A macroscope in the redwoods. In: Proceedings of the 3rd international conference on embedded networked sensor systems. ACM, New York, pp 51–63
5. Buonadonna P, Gay D, Hellerstein JM, Wei Hong H, Madden S (2005) TASK: sensor network in a box. In: Proceedings of 2nd European workshop on wireless sensor networks. Institute of Electrical and Electronics Engineers Computer Society, New York, pp 133–144
6. Sharma AB, Golubchik L, Govindan R (2010) Sensor faults: detection methods and prevalence in real-world datasets. *ACM Trans Sens Netw* 6(3):1–39
7. Elnahrawy E, Nath B (2003) Cleaning and querying noisy sensors. In: Proceedings of the 2nd ACM international workshop on wireless sensor networks and applications. Association for Computing Machinery, New York, pp 78–87
8. Shahid N, Naqvi IH, Bin Qaisar S (2012) Quarter-sphere SVM: attribute and spatio-temporal correlations based outlier and event detection in wireless sensor networks. In: Proceedings of 2012 IEEE wireless communications and networking conference. Institute of Electrical and Electronics Engineers, New York, pp 2048–2053
9. Shahid N, Naqvi IH (2011) Energy efficient outlier detection in WSNs based on temporal and attribute correlations. In: Proceedings of 2011 7th international conference on emerging technologies. IEEE Computer Society, New York, pp 1–6
10. Tulone D, Madden S (2006) PAQ: time series forecasting for approximate query answering in sensor networks. In: Proceedings of the wireless sensor networks, pp 21–37
11. Jeffery SR, Alonso G, Franklin MJ, Hong W, Widom J (2006) Declarative support for sensor data cleaning. In: Proceedings of 4th international conference on pervasive computing. Springer, New York, pp 83–100
12. Yu Z, Bingham C, Gallimore M, Zhijing Y, Stewart J (2012) Fault detection and diagnosis based on Y-indices and residual errors. In: Proceedings of 15th international conference on mechatronics. IEEE Computer Society, New York, pp 1–9 (in press)
13. Ni K, Ramanathan N, Chehade MNH, Balzano L, Nair S, Zahedi S et al (2009) Sensor network data fault types. *ACM Trans Sens Netw* 5(3):1–29
14. Dereszynski EW, Dietterich TG (2011) Spatiotemporal models for data-anomaly detection in dynamic environmental monitoring campaigns. *ACM Trans Sens Netw* 8(1):1–36
15. Tsoumakas G, Katakis I, Vlahavas I (2010) Mining multi-label data. In: Maimon O, Rokach L (ed) Data mining and knowledge discovery handbook. Springer, New York, pp 667–685
16. Zhang M-L, Zhou Z-H (2007) ML-KNN: a lazy learning approach to multi-label learning. *Pattern Recogn* 40(7):2038–2048
17. Read J, Pfahringer B, Holmes G, Frank E (2011) Classifier chains for multi-label classification. *Mach Learn* 85(3):333–359
18. Tsoumakas G, Katakis I, Vlahavas I (2011) Random k-labelsets for multilabel classification. *IEEE Trans Knowl Data Eng* 23(7):1079–1089

A Cloud Evolution Based Handoff Decision Scheme with ABC Supported

Cheng-Bo Zhang, Xing-Wei Wang and Min Huang

Abstract With wireless access technologies maturing, the wireless network environments have a characteristic of multiple networks overlapping, called heterogeneous wireless networks. As a key procedure of the always best connected (ABC) concept, handoff decision schemes need to consider with plenty of factors. Based on the game analysis and a cloud evolution algorithm, it is proposed that a cloud evolution-based handoff decision scheme with ABC supported to maximize user utility and network provider utility. Simulation results show that this scheme can search the optimal solution efficiently and has good performance.

Keywords Wireless networks · Always best connected (ABC) · Handoff decision · Cloud evolution algorithm · User utility · Network provider utility

1 Introduction

The access network technologies have been rapidly developed, and 2, 2.5, 3 and 4G networks appear. And they constitute heterogeneous access networks with plenty of networks overlapping at the same time. With the support of Software defined radio (SDR) and multimode intelligent terminals, it becomes the core issue for heterogeneous access networks that the Always Best Connected (ABC) concept [1] allows an application to connect with any network anywhere and anytime. And ABC supporting handoff technologies insures the application Quality of service (QoS) and the seamless roaming [2] for users among a multitude of access network technologies. But it is difficult for users to describe QoS requirements accurately, and QoS requirements have strong fuzziness [3]. In addition, handoff decision

C.-B. Zhang (✉) · X.-W. Wang · M. Huang
College of Information Science and Engineering, Northeastern University,
Shenyang 110819, Liaoning, China
e-mail: Anson771711@126.com

schemes need to ensure that terminals have reasonable dwell time for each decision, so as to prevent terminals from frequent handoffs. On this base, we think that handoff decision schemes should consider with the will of users and network providers besides many internal factors.

Some existing algorithms [4, 5] made handoff decisions to decrease the probabilities of handoff dropping, call blocking, and frequent handoffs. Some algorithms [6, 7] considered with some factors, such as Received signal strength (RSS), load balancing, bandwidths, delay, service types, service prices, terminal velocities, power, and user preferences to select the better wireless access technology. However, network environments and influence factors of ABC supporting handoff schemes are not considered comprehensively at the same time in these schemes. The most important thing is that they do not make users and access network providers achieve the win-win situation. So we propose a handoff decision scheme with ABC supported. This scheme should consider with application types, QoS requirements, service prices, access network provider preferences, mobile terminal conditions and access network conditions to find optimal handoff solutions, and ensure the rationality of handoff and the equilibrium of user utility and network provider utility. To improve the efficiency of decisions, we use the evolutionary algorithm based on cloud model [8], which converges more rapidly with retaining diversities.

2 Model Descriptions

According to the DiffServ (differentiated services) model, this scheme supports different types of applications, and $ATS = \{AT_1, \dots, AT_{|ATS|}\}$ is the set of applications. QS_i is the QoS requirements of AT_i type applications, where $QS_i = \{[B-W'_i, BW'_i], [DL_i^l, DL_i^h], [JT_i^l, JT_i^h], [ER_i^l, ER_i^h]\}$, $i = 1, \dots, |ATS|$. Since it is difficult to describe QoS requirements accurately, the form of interval is adopted to describe QoS.

Assume that the order number of an access network is $j \in [1, M]$, where M represents the total number of access networks. The access network model is defined as follows.

The access network provider and access network type are $NP_j \in NPS$ and $NT_j \in NTS$, where $NPS = \{NP_1, \dots, NP_{|NPS|}\}$ and $NTS = \{NT_1, \dots, NT_{|NTS|}\}$ are the corresponding sets. Similarly, $NAS_j \subseteq ATS$ and $SL_j \subseteq SL$ are the sets of application types and service levels supported by the access network, where SL is the set of all service levels. And there are some parameters of the access network described, such as the coverage CA_j , lowest signal strength LS_j , highest terminal velocity HV_j , work frequency FR_j , total bandwidth TB_j , available bandwidth AB_j , and overload threshold AB_j^{\min} . If $AB_j < AB_j^{\min}$, access network cannot accept any of the terminal requests.

Assume that the access network provides a k level service to an AT_i type application, and $k \in SL_j$. So that the QoS is $QS_{ji}^k = \left\{ \left[bw_{ji}^{kl}, bw_{ji}^{kh} \right], \left[dl_{ji}^{kl}, dl_{ji}^{kh} \right], \left[jt_{ji}^{kl}, jt_{ji}^{kh} \right], \left[er_{ji}^{kl}, er_{ji}^{kh} \right] \right\}$, where the parameter intervals are subsets of the ones of

AT_i type applications, such as $[bw_{ji}^{kl}, bw_{ji}^{kh}] \subseteq [BW_i^l, BW_i^h]$. And sc_{ji}^k and sp_{ji}^k are the service cost and service price of access network for k level services. For seeking the greater utilities of both sides, this handoff decision scheme can support the cooperation among terminals or access networks. If there is a cooperation, pr_{ji}^k should be cut or risen.

Assume that the order number of a terminal is $t \in [1, N]$, where N represents the total number of terminals. The terminal model is defined as follows.

$TAS_t \subseteq ATS$ is the set of application types with the terminal supported. And there are some parameters of the terminal described, such as the work frequency WF_t , lowest received signal strength RS_t , current velocity of the terminal CV_t , threshold of high velocity CV_h , remainder battery capacity RB_t , and threshold of low battery capacity RB_{th} . If $CV_t \geq CV_h$, the terminal is considered at high velocity conditions; if $RB_t \leq RB_{th}$, the terminal is considered at low capacity conditions.

$PP_t = \{PP_{t1}, PP_{t2}, \dots, PP_{tm}\} \subseteq NPS$ is the sequence of user preferences to access network providers, where PP_t is sorted by preference degrees from high to low. And WP_{ti} is the price that the user is willing to pay for AT_i type applications.

In summary, $HR_t = \{AT_i, PP_t, WP_{ti}\}$ is the handoff request of terminal t .

On the base of above-mentioned models, the QoS satisfaction model is defined as follows.

In this paper, the grey relational analysis method [9] is adopted to evaluate service levels. According to handoff request HR_t , access network j provides a k level service to terminal t with an AT_i type application running based on the access network conditions. So the weighted fuzzy satisfactions for bandwidth $[bw_{ji}^{kl}, bw_{ji}^{kh}]$ and delay $[dl_{ji}^{kl}, dl_{ji}^{kh}]$ are BS_{ji}^k and DS_{ji}^k , as Eqs. (1) and (2). And weighted fuzzy satisfactions for delay jitters and error rates are JS_{ji}^k and ES_{ji}^k , which are calculated like Eq. (2).

Assume that k^* is the ideal service level, and $BS_i^{k^*} = \max_j BS_{ji}^k$ is the bandwidth satisfaction. Similarly, $DS_i^{k^*}$, $JS_i^{k^*}$ and $ES_i^{k^*}$ can be obtained. The grey relational degrees of four parameters, GR_{ji}^{kB} , GR_{ji}^{kD} , GR_{ji}^{kJ} , and GR_{ji}^{kE} , are regarded as the evaluations of them. And the mean of them is the evaluation QE_{ji}^k of k level service. Where GR_{ji}^{kB} is obtained as Eq. (3), and then GR_{ji}^{kD} , GR_{ji}^{kJ} , and GR_{ji}^{kE} are calculated like Eq. (3). CB_{ji}^k and CD_{ji}^k are the conformity of bandwidth $[bw_{ji}^{kl}, bw_{ji}^{kh}]$ and delay $[dl_{ji}^{kl}, dl_{ji}^{kh}]$ to bandwidth request $[BW_i^l, BW_i^h]$ and delay request $[DL_i^l, DL_i^h]$. They can be calculated by Eqs. (4) and (5), where α is a constant. And conformity CJ_{ji}^k and CE_{ji}^k are calculated like Eq. (5).

$$BS_{ji}^k = \frac{\frac{1}{2}(bw_{ji}^{kl} + bw_{ji}^{kh}) - \min_j \frac{1}{2}(bw_{ji}^{kl} + bw_{ji}^{kh})}{\max_j \frac{1}{2}(bw_{ji}^{kl} + bw_{ji}^{kh}) - \min_j \frac{1}{2}(bw_{ji}^{kl} + bw_{ji}^{kh})} \quad (1)$$

$$DS_{ji}^k = \frac{\max_j \frac{1}{2} (dl_{ji}^{kl} + dl_{ji}^{kh}) - \frac{1}{2} (dl_{ji}^{kl} + dl_{ji}^{kh})}{\max_j \frac{1}{2} (dl_{ji}^{kl} + dl_{ji}^{kh}) - \min_j \frac{1}{2} (dl_{ji}^{kl} + dl_{ji}^{kh})} \quad (2)$$

$$GR_{ji}^{kB} = \frac{\min_i \min_j |BS_{ji}^k - BS_i^{k*}| + \frac{1}{2} \min_i \max_j |BS_{ji}^k - BS_i^{k*}|}{|BS_{ji}^k - BS_i^{k*}| + \frac{1}{2} \min_i \max_j |BS_{ji}^k - BS_i^{k*}|} \quad (3)$$

There are four coefficients ϖ_i^B , ϖ_i^D , ϖ_i^J , and ϖ_i^E representing the importance of bandwidth, delay, delay jitter, and error rate, respectively, and $\varpi_i^B + \varpi_i^D + \varpi_i^J + \varpi_i^E = 1$. They are assigned by access network providers according to application types. CQ_{ji}^k is the suitability of QS_{ji}^k to the QoS requirements of AT_i type applications, and $CQ_{ji}^k = \varpi_i^B \cdot CB_{ji}^k + \varpi_i^D \cdot CD_{ji}^k + \varpi_i^J \cdot CJ_{ji}^k + \varpi_i^E \cdot CE_{ji}^k$. In summary, $SQ_{ji}^k = QE_{ji}^k \cdot CQ_{ji}^k$ is the QoS satisfaction of a user for the k level service which is provided by access network j to AT_i type application.

$$CB_{ji}^k = \left(\frac{\frac{bw_{ji}^{kl} + bw_{ji}^{kh}}{2} - BW_i^l}{BW_i^h - BW_i^l} \right)^\alpha \quad (4)$$

$$CD_{ji}^k = \frac{1}{2} - \frac{1}{2} \sin \frac{\pi}{DL_i^h - DL_i^l} \left(\frac{dl_{ji}^{kh} + dl_{ji}^{kl}}{2} - \frac{DL_i^h + DL_i^l}{2} \right) \quad (5)$$

Apart from the QoS satisfaction model, there are other evaluating indicators defined as follows. SP_{tj} is the satisfaction of a user for the price of an access network. If $sp_{ji}^k \leq WP_{it}$, $SP_{tj} = 1$; otherwise, $SP_{tj} = 0$. SR_{tj} is the satisfaction of a user for an access network provider. If $NP_{tj} \in PP_t$, $SR_{tj} = 1/x^2$; otherwise, $SR_{tj} = 0$, where x is the order number of NP_{tj} in PP_t , and $1 \leq x \leq |PP_t|$. If the velocity of a terminal is high at current, an access network with larger coverage should be selected to decreasing the number of handoffs. Oppositely, if the battery capacity of a terminal is low at current, an access network with smaller coverage should be selected to decreasing the power of receiving and sending to extend terminal working time. SV_{tj} is the velocity satisfaction of access network j to terminal t . If $CV_t < CV_h$, $SV_{tj} = 1$; if $CV_h \leq CV_t \leq HV_j$, $SV_{tj} = 1/y^2$; otherwise, $SV_{tj} = 0$. Where y is the order number of access network type NT_j in NTS sorted by the coverage from high to low, and $1 \leq y \leq |NTS|$. SB_{tj} is the battery capacity suitability of access network j . If $RB_t \leq RB_{th}$, $SB_{tj} = 1/(|NTS| - y)^2$; otherwise, $SB_{tj} = 1$.

To make users and access network providers achieve the win-win situation, the game analysis is used in this paper. In the game analysis, a terminal and an access network play the game. And the payoff matrices of the terminal and access network are TG and NG , as Eqs. (6) and (7), where the rows of the matrices show willingness and unwillingness of a terminal in turn, and the columns of the matrices show willingness and unwillingness of an access network; the minus sign

shows the lost payoff; the penalty factor, $\tau > 1$, shows that it would have negative effect in future if one side refuses to accept the other. If $tg_{u^*v^*} \geq tg_{u^*v} \wedge ng_{u^*v^*} \geq ng_{u^*v}$, $\{u^*, v^*\}$ is a pair of policies which can achieve Nash equilibrium of the terminal payoff and access network payoff, where $u^*, v^*, u, v = 1, 2$.

$$TG = \begin{bmatrix} WP_{ii} - sp_{ji}^k & WP_{ii} - sp_{ji}^k \\ -\tau \cdot (WP_{ii} - sp_{ji}^k) & -(WP_{ii} - sp_{ji}^k) \end{bmatrix} \quad (6)$$

$$NG = \begin{bmatrix} sp_{ji}^k - sc_{ji}^k & -\tau \cdot (sp_{ji}^k - sc_{ji}^k) \\ sp_{ji}^k - sc_{ji}^k & -(sp_{ji}^k - sc_{ji}^k) \end{bmatrix} \quad (7)$$

In this paper, a coefficient matrix $\Lambda = [\lambda_1 \dots \lambda_5]$ expressing the relative importance of factors is utilized, and the factors include QoS requirements, service prices, access network providers, terminal velocities, and terminal battery capacities, where $\sum_{i=1}^5 \lambda_i = 1$. The value of λ_i is assigned by access network providers.

An evaluation matrix $G_{tj} = [SQ_{ji}^k SP_{tj} SR_{tj} SV_{tj} SB_{tj}]^T$ and a control coefficient Ω are introduced. And Ω expresses the influence on the utilities of both sides. If they achieve Nash equilibrium, $\Omega = 1$; otherwise, $0 < \Omega < 1$. If terminal t transfers to access network j , the terminal utility $uu_{tj} = \Omega \cdot A \cdot G_{tj} \cdot ((WP_{ii} - sp_{ji}^k)/WP_{ii})$, and the network provider utility $nu_{tj} = \Omega \cdot A \cdot G_{tj} \cdot ((sp_{ji}^k - sc_{ji}^k)/sp_{ji}^k)$; otherwise, both are 0.

3 Algorithm Design

3.1 Species and Initialization

Assume that S is the total number of individuals, and P is the number of populations. The m th population is PS_m , so that $S = \sum_{m=1}^P PS_m$. According to the sizes of populations, populations are divided into the building population, advantage populations, and disadvantage populations. The building population is the most representative one of a species, and its size is larger than all advantage populations. There are many advantage populations and disadvantage populations in a species, and the sizes of advantage ones are much larger than all disadvantage ones. The populations are sorted by the sizes from high to low, then $|PS_1| > \dots > |PS_p|$. Individual I_{mn} of population m is a decision solution. So that I_{mn} is N dimensional code, $I_{mn} = (x_{nm}^1, \dots, x_{nm}^N)$, where x_{nm}^t is the t th dimension of individual n in population m . Each dimension shows access network information j and service level information k , and $n \in [1, PS_m]$, $t \in [1, N]$, $j \in [1, M]$, $k \in SL$. The population initialization is a process of assigning an initial value to each individual, where j and k from each dimension of each individual are randomly assigned with the values of interval $[1, M]$ and interval $[1, |SL_j|]$, respectively.

3.2 Fitness Function and Forward Cloud Generator

If $\forall t((TAS_t \subseteq NAS_j) \wedge (WF_t \subseteq FR_j) \wedge (RS_t \leq LS_j) \wedge (CV_t \leq HV_j) \wedge ((AB_j - bw_{ji}^{kh}) \geq AB_j^{\min}))$, handoff solution I_{mn} is feasible, and the fitness function $FT_{UN}(I_{mn}) = \sum_{t=1}^N (1/uu_{tj} + 1/nu_{tj})$; otherwise, $FT_{UN}(I_{mn}) = +\infty$. Obviously, the smaller the value of $FT_{UN}(I_{mn})$ is, the better handoff solution is.

$Ar^{\text{Forward}}C(Ex, En, He)$ is the one dimensional forward cloud generator [10], which is a mapping from overall characteristics of qualitative concept to quantitative modality. The mapping is $\pi: C \rightarrow \Pi$ satisfying the following conditions: $\Theta = \{p_s | \text{Norm}(En, He)\}$; $X = \{x_s | \text{Norm}(Ex, p_s), p_s \in \Theta\}$; $\Pi = \{(x_s, y_s) | x_s \in X, y_s = e^{-(x_s - Ex)^2 / (2p_s^2)}, p_s \in \Theta\}$. Where $\text{Norm}(\mu, \delta)$ is a normal random variable, μ and δ are the expected value and standard deviation, and $s \in [1, S]$ is a cloud drop. In this paper, $Ar^{\text{Forward}}C(Ex_t, En_t, He_t), C(Ex'_t, En'_t, He'_t)$ is the evolving model of each dimension x_{mn}^t .

3.3 Evolving Control Strategies and Termination Condition

Evolving control strategies which adjust entropy En and hyper entropy He to control the evolving process includes the local search operation, local change operation, and mutation operation.

In this paper, the elite individual is the best individual of each generation with the minimum $FT_{UN}(I_{mn})$. If one individual is always the elite individual in consecutive generations, it is called as an intergenerational elitist. If a new intergenerational elitist appears, the current generation is called as a nontrivial generation. Otherwise, it is a trivial generation. And the number of generations between two nontrivial generations is called as the number of consecutive trivial generations.

If a new intergenerational elitist appears, this algorithm may find a new extreme neighborhood or approach for the previous extreme neighborhood. A local search operation is needed. This operation reduces En and he to decrease the evolutionary range and increase the stability, so as to increase the search accuracy and stability for more rapidly searching the optimal solution of this extreme neighborhood. In this paper, En and he are reduced to $1/K$ of the originals. And K called as the evolutionary coefficient is much bigger than 1.

If the number of consecutive trivial generations achieve threshold TH_{local} , this algorithm may fall into a local optimal neighborhood. It needs to jump out of this small range, and try to search a new optimal solution round this neighborhood. The local change operation raises En and he to increase the evolutionary range and decrease the stability. In this paper, En and He are raised to $L = \lceil \sqrt{K} \rceil$ of the originals, where L is the evolutionary mutation coefficient.

If the number of consecutive trivial generations achieve threshold $TH_{\text{global}} = TH_{\text{local}} + C_1$, this algorithm may fall into a local optimal solution and the local operation does not work, where C_1 is a constant. It needs to get itself off the

guarantee of local and search a new extreme in the global range. In this paper, the mean of some historical intergenerational elitist is regarded as the expectation Ex of forward cloud generator; entropy En and hyper entropy He are adjusted suitably; and the mutation operation is executed in all individuals of species.

If the number of consecutive trivial generations achieve threshold $TH_{end} = TH_{global} + C_2$, the intergenerational elitist does not change in C_1 local change operations and C_2 mutation operations, where C_2 is also a constant. So this algorithm has converged to the Pareto optimum solution, and the evolving process ends; otherwise, this algorithm does not terminate until it achieves the maximum of generation denoted by TH_{max} . Then, the elite individual is regarded as the optimal solution.

3.4 Algorithm Description

- Step 1: Initialize the size of species S , the number of populations P , the threshold of local search TH_{local} , the threshold of local change TH_{global} , the threshold of termination condition TH_{end} , and the maximum of generation TH_{max} .
- Step 2: According to Sect. 3.1, initialize the species. Then let the optimal fitness of species $FT_{UN}^* = +\infty$, the current optimal fitness $FT_{UN} = +\infty$, the number of consecutive trivial generations $ct = 0$, and the current number of generation $et = 0$.
- Step 3: Make the terminal and access network of each dimension to play the game, and determine the utilities of both sides based on cooperation conditions.
- Step 4: Calculate the fitness of each individual, assign the minimum of fitness to FT_{UN} , and $et = et + 1$. If $FT_{UN} \geq FT_{UN}^*$, $ct = ct + 1$; otherwise, $FT_{UN}^* = FT_{UN}$, and $ct = 0$.
- Step 5: If $et > TH_{max}$, go to Step 10.
- Step 6: If $FT_{UN}^* = +\infty$, initialize the species again, and go to Step 3.
- Step 7: If $ct > TH_{end}$, go to Step 10; if $ct > TH_{global}$, execute the mutation operation, and go to Step 9; if $ct > TH_{local}$, execute the local change operation; if $ct = 1$, execute the local search operation.
- Step 8: Select P individuals with the minima of fitness from the current individuals, and sort them by fitness from low to high. Regard them as the parent individual of each population, and put them into each population, respectively.
- Step 9: Utilize the forward cloud generator to generate P subpopulations, keep the size of each subpopulation, and go to Step 3.
- Step 10: If $FT_{UN}^* \neq +\infty$, regard the individual corresponding to FT_{UN}^* as the handoff decision solution, successfully finish. If there is more than one individual, randomly select one from them. Otherwise, there is no solution, failed.

Table 1 Simulation results 1

| User number | Summation utility | | | QoS satisfaction | | | Price satisfaction | | | Provider satisfaction | | |
|-------------|-------------------|-------|-------|------------------|-------|-------|--------------------|-------|-------|-----------------------|-------|-------|
| | 1 | 2 | 3 | 1 | 2 | 3 | 1 | 2 | 3 | 1 | 2 | 3 |
| 3 | 0.679 | 0.365 | 0.446 | 0.236 | 0.164 | 0.277 | 0.788 | 0.614 | 0.585 | 0.801 | 0.487 | 0.465 |
| 5 | 0.643 | 0.287 | 0.362 | 0.232 | 0.158 | 0.247 | 0.769 | 0.634 | 0.575 | 0.721 | 0.474 | 0.434 |
| 10 | 0.616 | 0.259 | 0.326 | 0.221 | 0.156 | 0.235 | 0.762 | 0.575 | 0.541 | 0.686 | 0.466 | 0.402 |
| 20 | 0.587 | 0.224 | 0.259 | 0.202 | 0.145 | 0.231 | 0.716 | 0.565 | 0.529 | 0.665 | 0.462 | 0.355 |
| 50 | 0.562 | 0.212 | 0.259 | 0.192 | 0.137 | 0.224 | 0.677 | 0.506 | 0.473 | 0.616 | 0.403 | 0.322 |

Table 2 Simulation results 2

| User number | Velocity satisfaction | | | Battery capacity satisfaction | | | Running time (ms) | | |
|-------------|-----------------------|-------|-------|-------------------------------|-------|-------|-------------------|--------|-------|
| | 1 | 2 | 3 | 1 | 2 | 3 | 1 | 2 | 3 |
| 3 | 0.987 | 0.712 | 0.624 | 0.857 | 0.484 | 0.424 | 0.170 | 0.138 | 0.004 |
| 5 | 0.963 | 0.708 | 0.657 | 0.853 | 0.508 | 0.478 | 0.204 | 0.392 | 0.021 |
| 10 | 0.909 | 0.686 | 0.591 | 0.806 | 0.489 | 0.429 | 0.408 | 1.592 | 0.025 |
| 20 | 0.884 | 0.582 | 0.547 | 0.728 | 0.426 | 0.396 | 0.893 | 6.091 | 0.037 |
| 50 | 0.875 | 0.565 | 0.493 | 0.677 | 0.376 | 0.357 | 1.942 | 39.223 | 0.086 |

4 Simulation Results and Discussions

With the help of NS2 (Network Simulator 2), this proposed scheme (Scheme 1) is compared with the greedy algorithm-based handoff decision scheme [11] (Scheme 2) and the QoS-based handoff decision scheme [12] (Scheme 3). We use three hexagonal honeycomb topologies, set two kinds of user cases, and implement 300 times of experiments for 3, 5, 10, 20, and 50 terminals. The means are regarded as results in Tables 1 and 2. All the summation utilities of three schemes fall with the numbers of terminals increasing, but the downward trend and the utility of Scheme 1 are slightly lower and higher. Because Scheme 1 aims to maximize the utilities of both sides, Scheme 2 looks for the load balancing of access networks, and Scheme 3 seeks the QoS satisfaction of users. So Scheme 3 has a higher performance of QoS satisfaction, but Scheme 1 is still better than Scheme 2. Because QoS is the main factor of Scheme 1, but it is not the only one. Scheme 1 has many more advantages than the other two in the other evaluating indicators. And Scheme 1 takes reasonable time to search optimal solutions.

5 Conclusions

With the continuous developments of wireless access technologies and mobile terminals, handoff decision schemes supporting the ABC concept have been the main motive force promoting the development of wireless network. We make a

close study of the factors influencing handoff decision schemes, and propose a handoff decision scheme with ABC supported with the help of the game analysis and the cloud evolution algorithm. This scheme takes into account of application types, QoS requirements, service prices, access network providers, terminal velocities, battery capacities and access network conditions, and realizes the maximization of user utility and network provider utility. The simulation results show that this proposed scheme has better performance compared with existing schemes.

Acknowledgments This work is supported by the National Science Foundation for Distinguished Young Scholars of China under Grant No. 61225012; the National Natural Science Foundation of China under Grant No. 61070162, No. 71071028, and No. 70931001; the Specialized Research Fund of the Doctoral Program of Higher Education for the Priority Development Areas under Grant No. 20120042130003; the Specialized Research Fund for the Doctoral Program of Higher Education under Grant No. 20100042110025 and No. 20110042110024; the Specialized Development Fund for the Internet of Things from the ministry of industry and information technology of the P.R. China; the Fundamental Research Funds for the Central Universities under Grant No. N110204003 and No. N120104001.

References

1. Gustafsson E, Jonsson A (2003) Always best connected. *IEEE Wirel Commun* 10(1):49–55
2. Cheng H, Wang XW, Yang SX et al (2010) QoS multicast tree construction in IP/DWDM optical internet by bio-inspired algorithms. *J Netw Comput Appl* 33(4):512–522
3. Wang XW, Qin PY, Huang M (2010) ABC supporting QoS unicast routing scheme based on the artificial fish swarm. *Chin J Comput* 33(4):718–725
4. Soungalo T, Li RF, Zeng FZ et al (2011) Vertical handoff analysis between WLAN and 3G networks under an adaptive QoS control. In: *Proceedings of the 2011 international conference on wireless networks*, pp 141–146
5. Ni L, Zhu YM, Li B et al (2011) Optimal mobility-aware handoff in mobile environments. In: *Proceedings of the 2011 IEEE international conference on parallel and distributed systems*, pp 534–540
6. He Q, Chen G, Zhang L et al (2010) A vertical handoff decision algorithm based on fuzzy control in WiMAX and TD-SCDMA heterogeneous wireless networks. In: *Proceedings of the 2010 international conference on wireless communications, networking and mobile computing*, pp 1–4
7. Nay P, Zhou C (2009) Vertical handoff decision algorithm for integrated UMTS and LEO satellite networks. In: *Proceedings of the 2009 WRI international conference on communications and mobile computing*, vol 2, pp 180–184
8. Zhang GW, He R, Liu Y et al (2008) An evolutionary algorithm based on cloud model. *Chin J Comput* 34(4):1082–1091
9. Li GL, Fu Q (2007) Grey relational analysis model based on weighted entropy and its application. In: *Proceedings of the 2007 international conference on wireless communications, networking, and mobile computing*, pp 5495–5498
10. Li DY, Liu CY, Du Y et al (2004) Artificial intelligence with uncertainty. *J Softw* 15(11):1853–1594

11. Hu YJ, Zhu JK (2003) A multiuser detector based on greedy algorithm for CDMA communication. *Comput Eng Appl* 39(17):17–19
12. Song QY, Jamalipour A (2005) A network selection mechanism for next generation networks. In: *Proceedings of the 2005 IEEE international conference on communications*, vol 2, pp 1418–1422

Ultra-Wideband Pulse Generator for Heart-Rate Monitor

Xiaoyan Liu, Zheng Fang and Jianguang Zhou

Abstract Ultra-wideband (UWB) heart-rate monitor designed in this text mainly consists of controller, pulse generator, pulse receiver, and displayer. Controller controls the pulse generating and receiving and heart-rate display. Based on the characteristics of avalanche of RF-BJT, we designed an UWB pulse generator in this paper. By simulating and debugging, we successfully obtained the bipolar UWB pulse, with the peak-to-valley voltage 6.7 V and peak-to-valley width 600 ps. The pulse generating circuit is suitable for the UWB heart-rate monitor, with its simple structure, low cost, and good performance.

Keywords Heart-rate monitor · UWB pulse generator · RF-BJT · Simulation · Circuit board

1 Introduction

With the improvement of the living standard, people have growing demands on medical care. Traditional heart-rate monitor may monitor one's heart-rate well, but most of the instrument structures are complex, contacting with human directly, and inconvenient to use. So we designed the potable ultra-wideband (UWB) heart-rate monitor. UWB heart-rate monitor based on UWB technology. The pulse generator of the monitor may emit UWB pulse to human body, and the receiver received the reflected signal from human body and then send the signal to the controller to deal with it, getting the heart-rate information at last. Besides, the controller determined when the pulse generator generating pulse and when the receiver receiving the reflected signal.

X. Liu (✉) · Z. Fang · J. Zhou

Department of Control Science and Engineering, Zhejiang University, Hangzhou China
e-mail: xiaoyanliuy@163.com

Ultra-wideband (UWB) is a wireless communication technology which is to transmit (telecommunications) or collect (radar) data using pulse signals of short duration and then would have a broad spectrum of frequencies [1]. In 2002, Federal Communications Commission (FCC) regulates that the frequency for the UWB technique is from 3.1 to 10.6 GHz in America. Now, UWB is defined as a signal that occupies a bandwidth larger than 500 MHz or a fractional bandwidth larger than 20 % [2]. Applying UWB technology in medical applications is an emerging research trend in recent years. First, attempt of using UWB radar in medical applications is in human body monitoring and imaging in 1993. On August 9, 1994, the first US Patent application was filed for medical UWB radar. One year later, MIT began an educational project for the ‘‘Radar Stethoscope.’’ In 1996, the biomedical use of UWB radars is better described with photo and sample tracings, and in the same year, the US Patent was awarded. Since then, UWB is often deemed as a possible alternative to remote sensing and imaging. By 1999, many works have begun for UWB medical applications in cardiology, obstetrics, breath pathways, and arteries [3, 4]. The UWB radar has very low average power level and is very power efficient. Thus, it is suitable to be a potentially cost effective way of heart-rate monitor.

2 Principle of UWB Heart-Rate Monitor

UWB heart-rate monitor system is mainly composed of pulse generator, pulse receiver, controlling, and processing part, as is shown in Fig. 1.

In the pulse generating part, signal source (in this article, positive 5 V square wave signal is adopted) produces pulse signals which would be modulated, and drive the pulse-forming circuit to form the UWB pulse. Then antenna sends the UWB pulse signal to human body. Normally, the waveform of the first derivative of the Gaussian function is adopted as the UWB radar pulse form. It can be expressed as the function (1)

$$S_1(t) = \pm \frac{4\sqrt{2}\pi}{\alpha^3} t e^{-\frac{2\pi t^2}{\alpha^2}} \quad (1)$$

In function (1), $\alpha^2 = 4\pi\sigma^2$ is the pulse shape parameter, and σ^2 is variance.

At the receiving end, reflected pulse signal is received by the antenna and then send to the sampling and amplifying circuit. The sampling and amplifying circuit samples amplify the signal, in accordance with the negative pulse which is transmitted by the time-delay circuit. Then matched filter extracts the available reflected signal and sends them to the AD converter and the microcontroller whose clock signal is generated by the signal source. Controller processed the received signal and gets the heart-rate information. Besides, the adjustable time-delay circuit is also manipulated by the microcontroller.

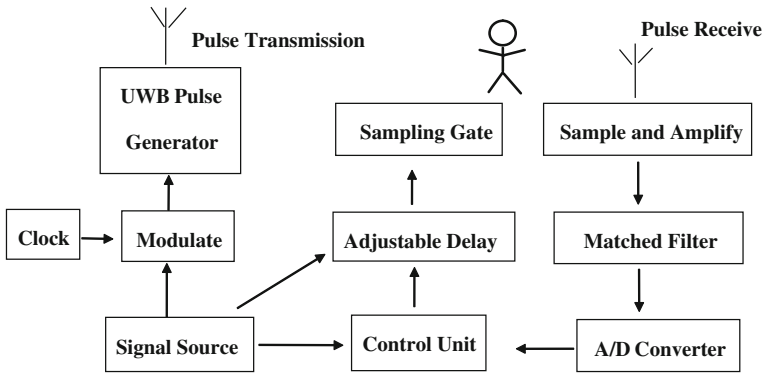


Fig. 1 Operating principle of UWB heart-rate monitor

Pulse generator plays an important role in the UWB heart-rate monitor system. The performance of the UWB pulse generator depends on the components in its circuit to a great extent. Now, devices with advantages of high frequency and high speed which can be used to produce picosecond pulse and nanosecond pulse are mainly these, step recovery diode (SRD), trapatt diode, tunnel diode (TD), and avalanche transistor. The power of SRD, trapatt diode, and TD is relatively lower, while the avalanche transistor may produce pulse with much higher power and the pulse duration is in nanoseconds and picoseconds [5, 6]. In consideration of these advantages of avalanche transistor, we applied it to form the UWB pulse generating circuit in this paper.

3 Generator of the Basic UWB Pulse

3.1 Principle of Avalanche Effect

Normally, the output characteristics of the triode transistor can be divided into four areas: saturation region, linear region, cutoff region, and avalanche region. When the voltage of collector increased, the field intensity of the space charge region would be enhanced, and the electron and hole in the space charge region would get more energy and collide with atom at the same time. The collision activates the electron in the covalent bond to form the electron–hole pairs when the electron and the hole are powerful enough. The new electron and hole would also play the role of originals, getting more energy and forming the new electron–hole pairs. This is called the multiplication effect of the charge carrier. When the voltage is high enough, the charge carrier will increase largely and quickly which is similar to the avalanche on the steep slopes, and make the countercurrent increase sharply. This is called the avalanche of triode transistor [7].

3.2 Principle of Pulse Generator

Figure 2 shows the circuit of the basic UWB pulse generator which is based on the avalanche of triode transistor. When there is no trigger impulse, the base electrode of the triode transistor is reverse-biased, and the HVDC VCC is added to the collector passing through resistor R_c and charge the capacitance C_2 at the same time. In this time, the triode transistor is in cutoff and critical avalanche condition.

Accompany with the input of the trigger pulse, the triode transistor avalanched and got break over quickly. Energy-storage capacitor C_2 discharged through triode transistor and load RL. So the voltage of C_2 dropped fastly. When the discharge current of C_2 cannot meet the needs of avalanche, the triode transistor would be saturated with the base trigger pulse still in rise condition. Once the trigger pulse is over, the base would be transferred to reverse bias again and the triode transistor would be in cutoff station [8]. At the same time, power source VCC charge the capacitor C_2 again, getting already for the next trigger.

3.3 Type of Components in the Circuit

Signal source: According to the needs of the circuit, we choose the square wave with impulse amplitude of +5 V, frequency of 10 MHz, and duty ratio of 50 % for the signal source.

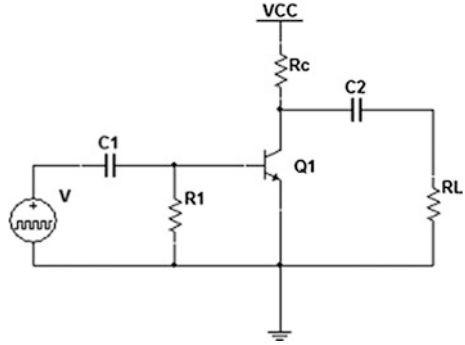
Triode transistor C_1 : In order to make sure that the triode transistor and the circuit will work well, the power loss of the triode transistor cannot exceed its maximum value. The power loss [9] of triode transistor can be expressed as the following expression.

$$P = \frac{1}{2} C_0 V_0^2 f \quad (2)$$

In expression (2), C_0 is storage capacitor, V_0 is output pulse amplitude, and f is operating frequency of the circuit. Besides, avalanche phenomenon of the triode transistor should be apparent, that is to say the triode transistor should be qualified with high, broad avalanche region, high characteristic frequency, and low saturation voltage drop. Considering comprehensively, we take use of RF-BJT MRF5812 in our experiments.

Capacitance C_2 : The output impulse width is determined by capacitance C_2 and load R_L . The value of C_2 should be moderate. If the value of C_2 was too high, the output impulse width would be broadened and the recovery time of circuit would be too long. On the contrary, if the value of C_2 is too low, the amplitude of the output impulse would be reduced and the distribution of capacitance C_2 would be destroyed. The charging process of C_2 should be finished before the arrival of

Fig. 2 Pulse generating circuit of basic UWB pulse



trigger pulse, and so the time constant of C_2 should be shorter than the cycle of trigger pulse. We choose the capacitance C_2 as several pF.

Bias voltage VCC: The value of bias voltage VCC should be large enough to make the triode transistor avalanche, while its highest value must be lower than BV_{CBO} .

Collector resistance R_C : To make sure the avalanche circuit recovered in quiescent stage, we should choose adequate collector resistance R_C to ensure that the charging time of C_2 should be shorter than the period of trigger pulse.

Resistance R_1 and capacity C_1 of the differentiating wave shaping circuit: The function of R_1 and C_1 is to accelerate the base impulse, steepen the rising edge of the trigger pulse, make the triode transistor avalanche more quickly, and protect the triode transistor from overlarge base sustained current.

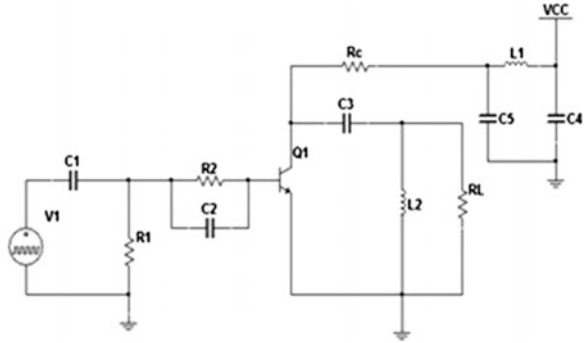
4 Generator of Bipolar UWB Pulse

4.1 Design of Bipolar UWB Pulse Generating Circuit

By estimating the value of the electronic devices and simulating the circuit in Fig. 2, we get the narrow impulse whose duration is between 120 and 500 ps. But the wave shape is not ideal, so we studied it further and got the circuit below, as is shown in Fig. 3.

Figure 3 shows the bipolar UWB pulse generating circuit which is based on the discharge of capacitance and inductance. The circuit in Fig. 3 added an accelerating circuit between the differentiating wave-shaping circuit C_1 , R_1 and the triode transistor Q_1 to the circuit in Fig. 1. Besides, we also added the capacitance C_4 , C_5 , and inductance L_1 to the basic circuit. Addition of the inductance L_1 makes sure that capacitance C_3 can be charged to 1.2 times of voltage VCC. Because of that when the voltage of capacitance C_3 is charged close to the power source VCC, inductance L_1 releases energy and then capacitance C_3 would be charged continuously.

Fig. 3 Bipolar UWB pulse generating circuit



Inductance L_1 also has the function of electrifying DC and blocking AC, so the harmonic AC noise in power source VCC can be filtered effectively. Capacitance C_4 and C_5 may copula the AC ripple of VCC to the ground, reducing the AC noise which would enter the intermediate frequency circuit. Inductance L_2 may discharge with capacitance C_3 by turns and form the bipolar narrow pulse on load R_L . Therefore, the charging circuit could be seen as cutting out in the charging process of capacitance C_3 , and the charging speed of capacitance C_3 is improved highly.

4.2 Simulation and Debugging of the Bipolar UWB Pulse Generating Circuit

The value of the components in Fig. 3 was chosen as: $C_1 = 150$ pF, $R_1 = 150$ Ω , $C_2 = 5$ μ F, $R_2 = 100$ Ω , $L_1 = 30$ μ H, $C_4 = 10$ μ F, $C_5 = 0.1$ μ F, $R_C = 800$ Ω , $L_2 = 6.8$ nH. The value of capacitance C_3 has great influence on the output impulse. We chose some typical values of capacitance C_3 to study its influence on the circuit, and determine the optimum value.

By simulating the circuit in Fig. 3, we get the following UWB pulse, as is shown in Fig. 4. In the debugging process, we changed the value of power source VCC, energy-storage capacitor C_3 , and load resistance R_L gradually, and got the different output UWB pulses. Increasing the value of power source VCC, amplitude of the output UWB pulse would be increased with it. While the value of the power source VCC is added too high, the output pulse would be distorted. So we chose the 24 V power source. The amplitude of the output UWB pulse can also be improved by increasing value of resistance R_L , but that may also bring about the increase of ultraharmonics. Consider comprehensively, we chose resistance R_L as 20 Ω .

In Fig. 3, small changes of capacitance C_3 may lead great variations to the output impulse. Maintaining the value of power source VCC and resistance R_L , we chose some typical values of capacitor C_3 to study its effect to the output UWB pulse.

Fig. 4 Bipolar UWB pulse

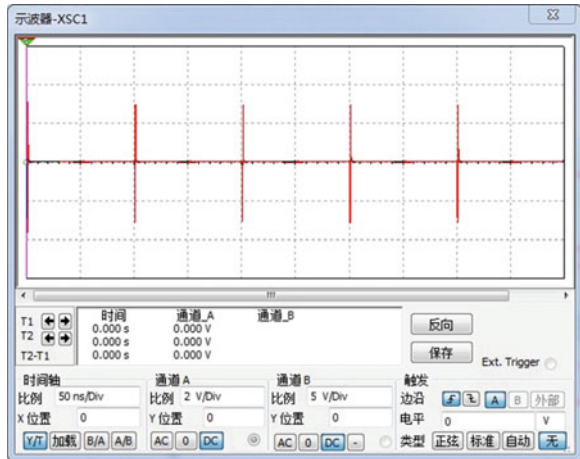


Table 1 Relationship of capacitor C_3 to output UWB pulse amplitude, bandwidth, duration, and mean power

| C_3 (pF) | Peak-to-valley amplitude (V) | Peak-to-valley width (ps) | Frequency range of 10 dB bandwidth (GHz) | Mean power (dB) |
|------------|------------------------------|---------------------------|--|-----------------|
| 1 | 2.413 | 220.2 | 0.115–2.351 | -38.6 |
| 2 | 3.950 | 293.5 | 0.116–2.133 | -32.5 |
| 3 | 5.110 | 293.6 | 0.135–1.781 | -28.9 |
| 4 | 6.020 | 348.7 | 0.129–1.620 | -26.4 |
| 5 | 6.792 | 367.1 | 0.120–1.556 | -24.5 |
| 6 | 7.419 | 460.1 | 0.115–1.385 | -22.9 |

We can see from Table 1 that capacitor C_3 has great influence on the UWB pulse generating circuit. Increasing the value of capacitor C_3 , the pulse amplitude and mean power would also increased, while pulse width would also added and the bandwidth decreased. When the value of C_3 is too small, the output UWB pulse would be distorted. On the contrary, when the value of C_3 was added up to 6 pF, positive part and negative part of the single UWB pulse was asymmetric. So by overall consideration, we choose the value of C_3 as 5 pF. And so we can see from the Fig. 5 that peak-to-valley amplitude of UWB pulse is about 6.79 V, and peak-to-valley width is about 367 ps. We may also see that the output waveform is similar to the first derivative of the Gaussian pulse form. Besides, we may also see from Fig. 5 that frequency range of 10 dB bandwidth is 120 MHz ~ 1.56 GHz.

From the experimental result, we may see that the output waveform of the bipolar UWB pulse has high bandwidth, high EFT and is suitable for short-distance transmission.

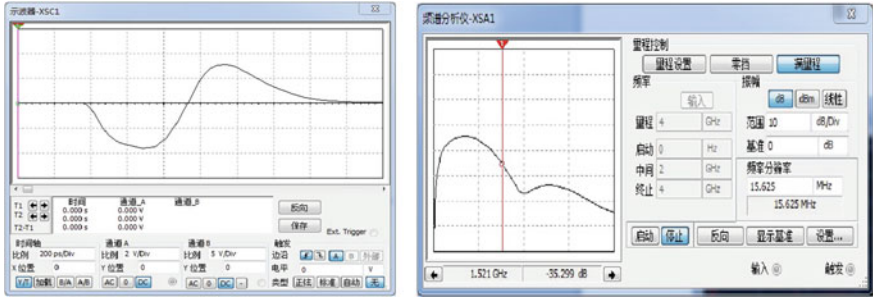
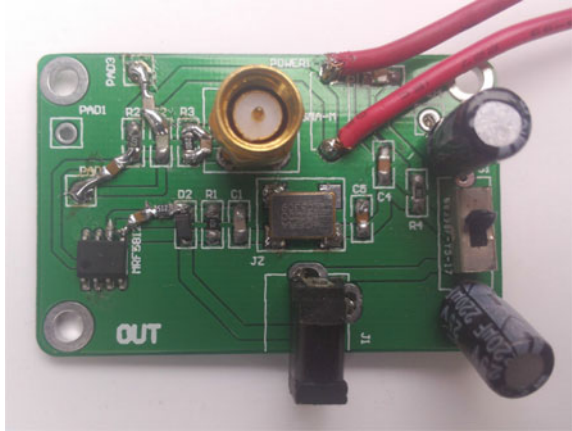


Fig. 5 Amplification map and power spectral density map of the output UWB pulse

Fig. 6 Photo of the actual circuit



4.3 Manufacturing of the Circuit Board and the Measuring Results

After the simulation of the bipolar UWB pulse, we designed and typeset the PCB board. We printed the pulse generating circuit on the glass-epoxy FR4 baseboard which was often used in high frequency circuit. In order to improve the performance of the circuit, all the packaging of the resistors and capacitors are adopted 0805 Surface Mount Device (SMD) and most of the other devices are also packaged in SMD. Considering the miniaturization and practicality request, the size of the circuit board produced only 4.8×3.2 cm. We applied the copper technology and connected all the GND together to decrease the signal disturb, as shown in Fig. 6.

In testing, we adopted the 24 V switching power supply as the board power supply and supplied the crystal oscillator with the filtered 5 V regulated power supply. We observe the output bipolar UWB pulse from the Agilent DSO6104A 1 GHz, as is shown in Fig. 7.

We may see from Fig. 7 that peak-to-valley amplitude of the bipolar UWB pulse is about 6.7 V, and peak-to-valley width is about 600 ps. Because of the

Fig. 7 Actual measurement of the bipolar UWB pulse



disturbance in the actual circuit, the amplitude of the actual UWB pulse is close to the simulation and the width of the actual UWB pulse is a little larger. In general, the two are well in agreement. And now, the bipolar UWB pulse generating circuit has been successfully used in a small size UWB transmitter, and the transmission pulse matched well with the UWB antenna, while the whole circuit works stably.

5 Conclusion

This paper designed a bipolar UWB pulse generator which is based on transistors RF-BJT MRF581. We generated the pulse by making use of the low voltage and avalanche characteristic of the RF-BJT and the function of magnetic storing and releasing of capacitances and inductances. Using the software multisim 11, we simulated and debugged the pulse generating circuit and get the ideal circuit for the heart-rate monitor. After that, we manufactured the circuit board of the bipolar UWB pulse generating circuit and test it. From the experimental results, we may see that the bipolar UWB pulse generating circuit in this paper can be used in medical applications well because of its good performance, simple construction, and low-budget produce.

References

1. Dhieb M, Lahiani M, Hariani HG (2010) Pulse generator monocycle Gaussian for UWB applications. *Wseas Trans Circ Syst* 9(12):756
2. Federal Communications Commission (2002) First report and order FCC 02-48
3. Allen B, Brown T, Schwieger K, Zimmermann E, Malik WQ, Edwards DJ et al (2005) Ultra wideband: applications, technology and future perspectives. In: *Proceeding of international workshop convergent technologies Oulu*

4. Xu Y, Lu YH, Zhang HX, Wang YQ (2007) An overview of ultra-wideband technique application for medical engineering. In: 2007 IEEE/ICME international conference on complex medical engineering (CME), Beijing
5. Fan XM, Lin JM, Zheng JYH, Qiu B (2006) Designation and generation of UWB pulse. *Modern Radar* 28(3):87–90
6. Yang F, Xue QZ, Chen H (2005) Designation of Gaussian pulse generator which based on RF-BJT. *J Commun* 26(10):69–77
7. Chang XF, Fu WX, Wang MG (2008) Designation of fuze testing system which based on lab Windows/CVI. *Electron Meas Technol* 31(8):89–92
8. Millman J, Taub H (1965) *Pulse, digital, and switching waveforms*. McGraw-Hill, New York
9. Yarovoy AG, Lighthart LP (2006) UWB radar for human being detection. *IEEEA&E Syst Mag* 3:10–14

Pseudorange Differential GPS-Based Relative Navigation for UAV Formation Flight

Hongyu Yang, Yandong Wang, Haifeng Fu and Jian Liu

Abstract In pseudorange differential GPS-based relative navigation, two linear models for UAV formation flight are designed, respectively, to simplify system equipment, reduce complexity of algorithm, and most of all weaken the effect of spatial-correlated errors such as satellite ephemeris error, ionosphere delay and troposphere delay. Above errors are analyzed and simulated to verify the feasibility of the method. Moreover, positioning deviation of lead plane is also under consideration in the system without base-station, demonstrating the effect of leader's deviation on position accuracy for the system. Both theoretical and practical results for the two models conclude that the system without base-station can reach a better precision and is more cost effective.

Keywords Formation flight · Pseudorange differential GPS · Relative navigation · Residual error · Base-station

1 Introduction

With the development of the control and navigation, formation flight has become a new warfare mode and received unprecedented attention throughout the world. Traditional Global Positioning System has a wide coverage area and high precision, but its weakness of susceptibility to interferences greatly affects position accuracy. In addition, relative navigation is a good remedy to weaken spatial-

H. Yang (✉) · Y. Wang
School of Automation Science and Electrical Engineering,
Beihang University, Beijing 100191, China
e-mail: hongyu.yang90@gmail.com

H. Fu · J. Liu
The No. 8 Research Institute of Air Force, PLA, Beijing 100076, China

correlated errors and the determination of relative position in aircrafts is of great importance to maintain formation flight. Considering the shortage mentioned above, relative navigation based on DGPS (differential GPS) has been put forward as an effective solution.

Present studies on DGPS relative navigation mostly focus on satellites formation flight and spacecraft autonomous rendezvous docking. D'Amico Simone puts forward some fundamental aspects about differential GPS in formation flight [1]. Afterward, methods such as double-differential carrier phase [2, 3], VISNAV (vision navigation) [4], INS/GPS/RF integrated navigation [5] are all applied to improve the precision of formation flight.

In recent research on DGPS relative navigation, single or more base-stations are generally contained in the UAV (Unmanned Aerial Vehicle) formation flight models. A correction is calculated by each base-station, and is then broadcasted to the users in order to figure out their absolute position. However, spatial-correlated errors still rise as distance between user and base-station increases notably, and the reliability is a significant issue to consider. Faced with above difficulties, model of DGPS relative navigation for formation flight without base-station is designed.

In the paper, two linear models of pseudorange DGPS relative navigation for UAV formation flight are established to weaken position errors (Sect. 2 is about system with single base-station and Sect. 3 is about system without base-station). A variety of position errors are considered in these sections as well. Performances of the two systems are simulated and compared in Sect. 4, and a conclusion is drawn that with the correction of leader plane, the new model can reach a better precision and is more available (Sect. 5).

2 Pseudorange DGPS Relative Navigation with Single Base-Station

2.1 System Model

In a UAV formation flight, pseudorange between base-station (b) and user (u) can be presented as [6]:

$$\rho_b^j = \sqrt{(x_b - x_s^j)^2 + (y_b - y_s^j)^2 + (z_b - z_s^j)^2} + c(\delta t_{b,r} - \delta t^{S_j}) + \varepsilon_b^j \quad (1)$$

$$\rho_u^j = \sqrt{(x_u - x_s^j)^2 + (y_u - y_s^j)^2 + (z_u - z_s^j)^2} + c(\delta t_{u,r} - \delta t^{S_j}) + \varepsilon_u^j \quad (2)$$

where (x_b, y_b, z_b) (x_u, y_u, z_u) and (x_s^j, y_s^j, z_s^j) each represents coordinates of base-station, user and the j .th GPS satellite in the ECEF (Earth-Centered, Earth-Fixed) coordinate system. ε^j includes $\varepsilon_{\text{eph}}^j$, $\varepsilon_{\text{ion}}^j$, $\varepsilon_{\text{trop}}^j$, $\varepsilon_{\text{multi}}^j$, $\varepsilon_{\text{rec}}^j$, which stands for ephemeris error, ionosphere delay, troposphere delay, multipath deviation, and receiver

observation noise, respectively. δt^{S_j} and δt_r are receiver clock errors of satellite and aircraft.

Pseudorange correction of base-station $\Delta \rho_b^j$ can be solved according to Eq. (3):

$$\Delta \rho_b^j = c(\delta t^{S_j} - \delta t_{b,r}) - \varepsilon_b^j \quad (3)$$

The result of Eq. (3) is sent in real time to every user afterward in order to correct their pseudorange data with measurement errors. Regardless of all position errors, revised pseudorange can be described as:

$$\rho_u^j + \Delta \rho_b^j = \sqrt{(x_u - x_s^j)^2 + (y_u - y_s^j)^2 + (z_u - z_s^j)^2} + c \cdot \delta t \quad (4)$$

There are four values unknown in Eq. (4), so by observing at least four satellites, the solution can be acquired.

2.2 Residual Position Errors

In the model above, residual errors are considered as observation noise, which will actually affect positioning precision to some extent. However, among those errors, satellite ephemeris error, troposphere delay and ionosphere delay all belong to spatial correlation errors, and can be weakened by differential calculation. These residual errors will be analyzed as follows.

Figure 1 shows the geometry relationship schematic of satellite ephemeris error. First, orbit error of the satellite is decomposed into two components $\vec{\zeta}$ and $\vec{\xi}$, among which $\vec{\xi}$ should be parallel to line SB, and $\vec{\zeta}$ be perpendicular to $\vec{\xi}$. Afterward, plane O is set to be perpendicular to $\vec{\zeta}$, and $\vec{\zeta}$ is composed into $\vec{\zeta}_1$ and $\vec{\zeta}_2$ as well, among which $\vec{\zeta}_1$ is on Plane SBU. Suppose η_1 and η_2 represent the distance error of SB and SU separately, so they can be expressed as [7]:

$$\eta_1 = |\vec{\xi}| \quad (5)$$

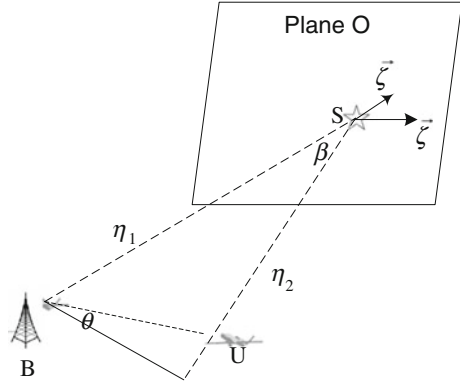
$$\eta_2 = |\vec{\xi}| \cdot \cos \beta - |\vec{\zeta}_1| \cdot \sin \beta \quad (6)$$

Furthermore, we can get Eqs. (7) and (8):

$$BS \cdot \sin \beta = BU \cdot \cos \theta \quad (7)$$

$$\beta \approx \arctan \frac{BU}{US} \quad (8)$$

Fig. 1 Ephemeris residual error



thus the residual error can be described as:

$$\eta_1 - \eta_2 = \left| \vec{\zeta} \right| (1 - \cos \beta) + \frac{BU}{BS} \cdot \left| \vec{\zeta}_1 \right| \cdot \cos \theta \tag{9}$$

Troposphere error can be evaluated by applying Hopfield model:

$$\Delta S = \Delta S_d + \Delta S_w = \frac{K_d}{\sin \sqrt{E^2 + 6.25}} + \frac{K_w}{\sin \sqrt{E^2 + 2.25}} \tag{10}$$

The geometry relationship schematic and derivation of troposphere residual error is complicated and can be obtained in [8].

Ionosphere error can also be obtained by an empirical model. Select Klobuchar model parameter:

$$I_Z(t) = \begin{cases} A_1 + A_2 \cdot \cos\left[\frac{2\pi(t-A_3)}{A_4}\right], & |t - A_3| < A_4/4 \\ A_1, & \text{others} \end{cases} \tag{11}$$

Theoretical deduce of ionosphere residual error is also given in detail in [9].

In the simulation, satellite orbit error is supposed to be 5 m, distance between satellite and airplane is approximately 20,000 km, satellite elevation angle is 70° and observation universal time is set at 14 o'clock. Then residual error curves are shown in Fig. 2.

$$m_P = \text{PDOP} \times m_C \tag{12}$$

Receiver three-dimensional position error can be calculated as follow:

PDOP represents the position dilution of precision, and can be replaced with 10 here. Then it can be observed from Fig. 2 that when the distance between base-station and user is 20 km, three-dimensional position residual of ephemeris error, troposphere delay and ionosphere delay turns to be 0.05, 0.09 and 0.15 m independently.

Fig. 2 Residual error (elevation 70°)

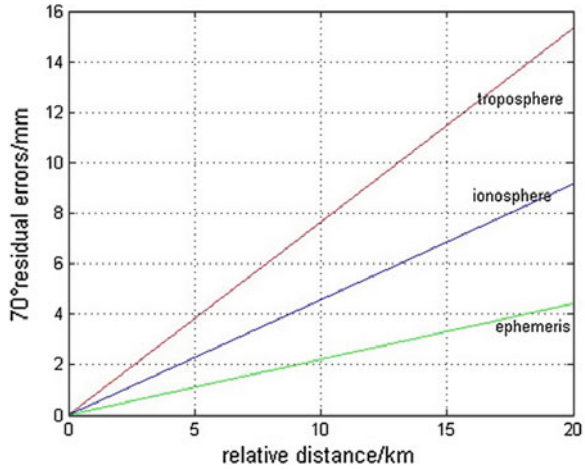


Table 1 Comparison Results

| | GPS point positioning/m | Pseudorange DGPS (Single base-station)/m |
|-------------------|-------------------------|--|
| Ephemeris error | 2.0 | 0.2 |
| Troposphere delay | 0.5 | 0.48 |
| Ionosphere delay | 6.0 | 0.75 |

Compared with some real-time experiments (relative distance is about 100 km), results are listed in Table 1.

Table 1 obviously reveals that pseudorange DGPS relative navigation has a higher positioning precision. However, with the increase of distance between base-station and user, these errors still remain in some degree. To solve this problem thoroughly, relative navigation without base-station is needed.

3 Pseudorange Differential GPS Relative Navigation Without Base-Station

3.1 System Model

In pseudorange differential GPS relative navigation technique with single base-station, spatial-correlated position errors decrease notably as shown in Table 1. However, as the relative distance rise to a certain amount, those errors turn to be unignorable. Furthermore, the construction and maintenance of base-stations increase the cost of the system by a large scale, and the reliability and inerrancy of base-station turns to be of great significance.

To handle with defects mentioned above, relative navigation without base-station is adopted in the study. Instead of applying ground position reference,

leader and follower plane are, respectively, treated as “base-station” and “user” in the model, and all the data are transmitted and processed in follower planes.

In Eqs. (13) and (14), difference between ρ_b^j , ρ_u^j can be obtained as follow:

$$\begin{aligned} \Delta\rho^j &= \rho_u^j - \rho_b^j = \sqrt{(x_u - x_s^j)^2 + (y_u - y_s^j)^2 + (z_u - z_s^j)^2} \\ &\quad - \sqrt{(x_b - x_s^j)^2 + (y_b - y_s^j)^2 + (z_b - z_s^j)^2} + c(\delta t_{u,r} - \delta t_{b,r}) + \varepsilon_u^j - \varepsilon_b^j \end{aligned} \quad (13)$$

V is selected as a base point near follower plane U, and coordinate of the point is assumed to be $(x_b + 500 y_b + 200 z_b)$, therefore the distance between point U and V can be expressed as:

$$\delta P = (x \ y \ z) = (x_u - x_v \ y_u - y_v \ z_u - z_v) \quad (14)$$

Expand Eq. (13) at $\delta P = (0 \ 0 \ 0)$, we get:

$$\begin{aligned} \Delta\rho^j &= \Delta\rho^j \Big|_{\delta P} + \frac{\partial\Delta\rho^j}{\partial x} \Big|_{\delta P} \cdot x + \frac{\partial\Delta\rho^j}{\partial y} \Big|_{\delta P} \cdot y + \frac{\partial\Delta\rho^j}{\partial z} \Big|_{\delta P} \cdot z \\ &= [(x_v - x_s^j)x + (y_v - y_s^j)y + (z_v - z_s^j)z] \frac{1}{\rho_{\delta P}^j} + \rho_{\delta P}^j - \rho_0^j + \delta d + v^j \end{aligned} \quad (15)$$

In Eq. (15), $\delta d = c(\delta t_{u,r} - \delta t_{b,r})$, v^j represents observation noise in the system,

$$\rho_0^j = \sqrt{(x_b - x_s^j)^2 + (y_b - y_s^j)^2 + (z_b - z_s^j)^2}, \quad \rho_{\delta P}^j = \sqrt{(x_v - x_s^j)^2 + (y_v - y_s^j)^2 + (z_v - z_s^j)^2}.$$

Differential three-dimensional position and clock correction value are selected as state variables:

$$x_{\Delta\rho} = [x \ y \ z \ \delta d]^T \quad (16)$$

Observation equation can be expressed as:

$$Z_{\Delta\rho} = H_{\Delta\rho} X_{\Delta\rho} + V_{\Delta\rho} \quad (17)$$

where

$$\begin{aligned} Z_{\Delta\rho} &= \begin{bmatrix} \Delta\rho_1 + \rho_0^1 - \rho_{\delta P}^1 \\ \Delta\rho_2 + \rho_0^2 - \rho_{\delta P}^2 \\ \dots \\ \Delta\rho_n + \rho_0^n - \rho_{\delta P}^n \end{bmatrix}, \quad H_{\Delta\rho} = \begin{bmatrix} H_1 \\ H_2 \\ \dots \\ H_n \end{bmatrix}, \\ H_j &= \left[\frac{(x_v - x_s^j)}{\rho_0^j}, \frac{(y_v - y_s^j)}{\rho_0^j}, \frac{(z_v - z_s^j)}{\rho_0^j}, 1 \right] \end{aligned}$$

When $n \geq 4$, relative position between leader and follower plane can be solved by least square method:

$$\hat{P}_{\Delta\rho}^e = (H_{\Delta\rho}^T H_{\Delta\rho})^{-1} H_{\Delta\rho}^T Z_{\Delta\rho} \quad (18)$$

Analysis of modeling error of linearization is given by [10], simulation result shows that observation error will be only several millimeters when distance between UV is less than one kilometer, which is negligible. So the method can be applied in close range formation flight.

3.2 Position Error of Leader Plane

As distance between airplanes in a close-range formation flight is usually only several hundred meters, those spatial-correlated errors mentioned in Sect. 2 can be neglected according to Fig. 2. However, there is another kind of position error that must be considered—position error of leader plane. As it is known that although leader plane is treated as “base-station”, its precise position cannot be acquired, so the positioning accuracy of leader plane itself also will affect the whole system. Theoretical derivation is given below. (x, y, z) represents the accurate position of a plane, regardless of any errors, expand Eqs. (1) and (2) at point $(x \ y \ z)$:

$$\begin{aligned} \rho_b^j &= \rho_b^j + \frac{\partial \rho_b^j}{\partial x_b} |_P \cdot \delta x_b + \frac{\partial \rho_b^j}{\partial y_b} |_P \cdot \delta y_b + \frac{\partial \rho_b^j}{\partial z_b} |_P \cdot \delta z_b \\ &= \rho_b^j + [(x_b - x_s^j) \cdot \delta x_b + (y_b - y_s^j) \cdot \delta y_b + (z_b - z_s^j) \cdot \delta z_b] \frac{1}{\rho_b^j} \end{aligned} \quad (19)$$

$$\begin{aligned} \rho_u^j &= \rho_u^j + \frac{\partial \rho_u^j}{\partial x_u} |_P \cdot \delta x_u + \frac{\partial \rho_u^j}{\partial y_u} |_P \cdot \delta y_u + \frac{\partial \rho_u^j}{\partial z_u} |_P \cdot \delta z_u \\ &= \rho_u^j + [(x_u - x_s^j) \cdot \delta x_u + (y_u - y_s^j) \cdot \delta y_u + (z_u - z_s^j) \cdot \delta z_u] \frac{1}{\rho_u^j} \end{aligned} \quad (20)$$

Subtracting the two equations, we get:

$$\begin{aligned} \Delta \rho^{ij} &= \rho_u^j - \rho_b^j = \rho_u^j - \rho_b^j - (l_u^j \ m_u^j \ n_u^j) \cdot \delta P_u \\ &\quad + (l_b^j \ m_b^j \ n_b^j) \cdot \delta P_b \end{aligned} \quad (21)$$

where $\delta P_i = (\delta x_i \ \delta y_i \ \delta z_i)^T$, $l_i^j = \frac{x_i^j - x_i}{\rho_i^j}$, $m_i^j = \frac{y_i^j - y_i}{\rho_i^j}$, $n_i^j = \frac{z_i^j - z_i}{\rho_i^j}$. Suppose n sat-

ellites can be observed, $L = \begin{pmatrix} \rho_u^1 - \rho_b^1 - \Delta \rho^{11} \\ \vdots \\ \rho_u^2 - \rho_b^2 - \Delta \rho^{12} \end{pmatrix}$, $A_i = \begin{pmatrix} l_i^1 & m_i^1 & n_i^1 \\ \vdots & \vdots & \vdots \\ l_i^n & m_i^n & n_i^n \end{pmatrix}$, Then

Table 2 Statistical properties of relative navigation errors with leader position error

| Leader deviation/m | | | Relative navigation/m | | |
|--------------------|----|----|-----------------------|---------|---------|
| X | Y | Z | X | Y | Z |
| 0 | 0 | 0 | -0.7706 | 0.8023 | 1.1023 |
| 5 | 0 | 0 | 4.0761 | 0.9569 | 1.0661 |
| 0 | 5 | 0 | -0.7856 | 5.9355 | 1.2121 |
| 0 | 0 | 5 | -0.8510 | 0.8090 | 6.2625 |
| 10 | 0 | 0 | 9.1585 | 0.9100 | 1.1390 |
| 0 | 10 | 0 | -0.7145 | 10.8577 | 1.3544 |
| 0 | 0 | 10 | -0.7701 | 1.2102 | 11.2887 |
| 15 | 0 | 0 | 14.2168 | 0.9839 | 1.1571 |
| 0 | 15 | 0 | -0.8485 | 15.9503 | 1.1545 |
| 0 | 0 | 15 | -0.9047 | 0.9122 | 16.2388 |

rewrite Eq. (21) as $L + A_b \cdot \delta P_b = A_u \cdot \delta P_u$, which can be solved by least squares method as Eq. (22).

$$\begin{aligned} \delta P_u &= (A_u^T P A_u)^{-1} A_u^T P (A_b \delta P_b + L) \\ &= (A_u^T P A_u)^{-1} A_u^T P L + (A_u^T P A_u)^{-1} A_u^T P (A_b - A_u) \delta P_b + \delta P_b \end{aligned} \quad (22)$$

P represents the weight of observation values. Equation (22) shows that position error of follower plane is increasing with leader one, and errors on each axis component of leader plane only affect the corresponding axis component of follower plane. Table 2 shows different leader error values and their simulation results.

From Table 2, it can be concluded that with the growth of positioning error of leader plane, positioning deviation of relative navigation increases accordingly. Also, the results are strongly directional. Adding a certain deviation in a certain direction will produce influence substantially the same degree. Simulation results prove the correctness of theoretical analysis.

4 Simulation Verification

Figure 3 shows a flow chart of DGPS relative navigation procedure.

This paper displays simulation results for a leader/follower pair of airplanes. Initial positions of ground base-station, leader plane and follower plane are, respectively, (30°, 110°, 0) (30°, 110°, 8000) and (29.9968°, 110.0028°, 8000), both of the planes fly straight toward north with a velocity of 200 m/s. Position error of leader plane is set as 5 m per axis, ephemeris error and satellite clock correction are constants of 3 and 1.5 m. Other errors all include both constant and random drift sections, which are handled as Gauss white noise. Table 3 shows the exact figures.

Fig. 3 Flow chart of DGPS navigation

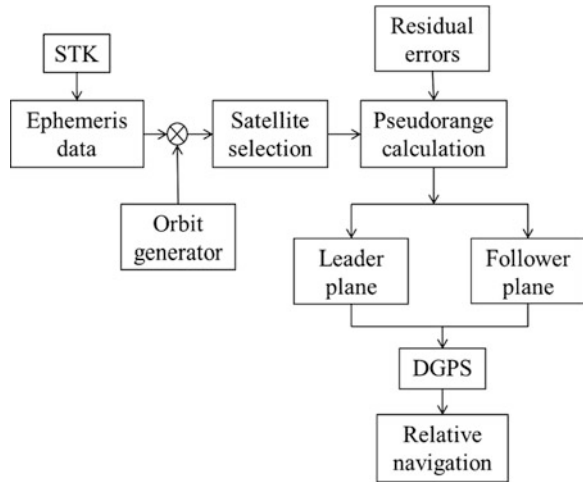


Table 3 Error parameter settings

| | Means | Square deviation/m ² |
|--------------------------------|-------|---------------------------------|
| Position error of leader plane | 5 | 0 |
| Clock correlation for receiver | 6 | 2 |
| Ionosphere delay | 3 | 3 |
| Troposphere delay | 3 | 3 |
| Multi-path effect | 2 | 2 |
| Receiver noise for receiver | 0 | 3 |

GPS satellite ephemeris is acquired by Satellite Tool Kit (STK), and the method of max V_e with constraints of two satellites is applied to select visible satellites as well.

Figure 4 demonstrates GPS point position error.

Next, in the simulation for pseudorange DGPS relative navigation with single base-station, it is considered that spatial-correlated errors change linearly according to Fig. 2 and Eq. (12). Simulation result is shown below in Fig. 5.

In the end, Simulation for relative navigation without base-station is conducted and results are shown in Fig. 6. In the simulation, spatial-correlated error parameters for DGPS relative navigation without base-station are set, respectively, as 5, 9 and 15 mm according to Fig. 2.

Figures 4, 5 and 6 shows the simulation results of above three situations. Statistical results are shown in Table 4. For relative navigation without base-station, means of each axis is acquired to summarize the characteristics, while for relative navigation with single base-station, due to the fact that position errors increase as the plane fly away from the base-station, several points of different relative distances are selected to describe the diverging curves.

Fig. 4 GPS point position error

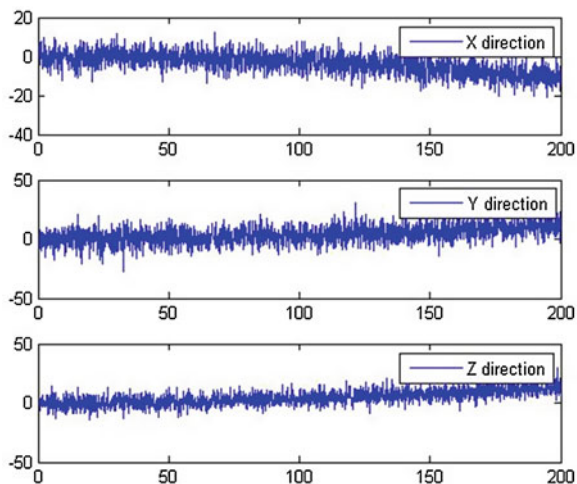
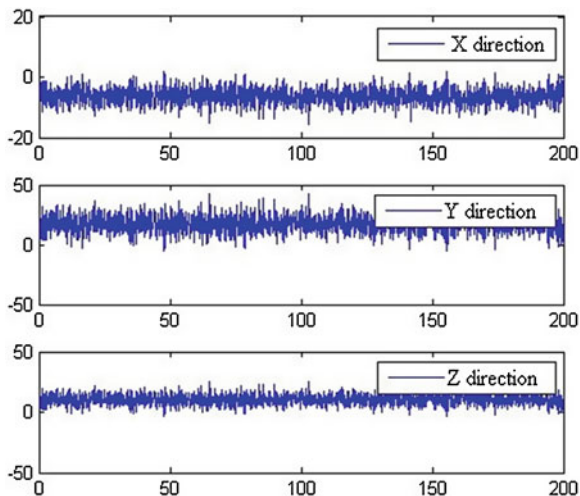


Fig. 5 GPS point position error



Statistical data in Table 4 indicates that when the distance between base-station and plane is approximately less than 20 km, position accuracy of single base-station can be better. However, with the further growth of relative distance, its performance begins to get worse.

In fact, if we can improve the positioning precision of leader plane, or get the error regularity beforehand, then relative positioning error can be impaired by a large amount. In this way, the performance of pseudorange differential DGPS relative navigation without base-station will be much better.

Fig. 6 Relative navigation error (No base-station)

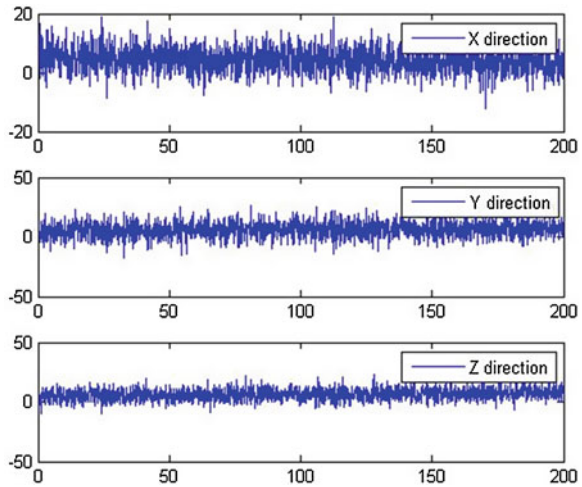


Table 4 Position errors

| | (km) | Axis X/m | Axis Y/m | Axis Z/m |
|---------------------|------|----------|----------|----------|
| Single base-station | 10 | 1.1511 | 3.7440 | 3.9491 |
| | 20 | -3.3878 | 4.7312 | 9.7242 |
| | 40 | -9.3130 | 14.5311 | 16.9692 |
| No base-station | | 4.1325 | 6.1381 | 6.3794 |

5 Conclusion

In the research on relative navigation, how to overcome the spatial correlation error is a significant issue. Linear model of both systems (pseudorange DGPS relative navigation with single base-station and without base-station) can be good solutions to this problem. However, comparison between the two methods proves that relative navigation without base-station is a better choice. Not only can the method simplify complexity of algorithm and reduce equipment spending, it also improves positioning accuracy better. Besides, in order to improve precision of the system further, it is necessary to improve the positioning accuracy of the lead plane or get its error regularity.

References

1. D'Amico S, Montenbruck O (2010) Differential GPS: an enabling technology for formation flying satellites: small satellite missions for earth observation. Springer, Berlin, pp 457–465
2. Li Y, Zhang S, Wu C (2012) Research on relative navigation for formation flying spacecrafts based on differential GNSS. In: Proceedings of China satellite navigation conference (CSNC). Springer, Berlin, pp 433–444
3. Li Y, Glennon E, Li R (2012) Development of a spaceborne GPS receiver for precise relative navigation of formation flying small satellites. In: Proceedings of China satellite navigation conference (CSNC). Springer, Berlin, pp 467–476
4. Wang X, Shao X, Gong D (2011) GPS/VISNAV integrated relative navigation and attitude determination system for ultra-close spacecraft formation flying. *J Syst Eng Electron* 22(2):283–291
5. Liu W, Wang Y, Chen P (2010) Research on relative navigation system for UAV formation flight. In: International symposium on inertial technology and navigation. Springer, Berlin, pp 481–489
6. Xiu-sen Wang, Hong-jin Zhou, Shang-yue Zhang (2012) Relative navigation between vessels based on GPS single difference. *J Chin Inert Technol* 20(4):464–467
7. Hai-song Jiao, Hong-fang Wang, Fei-juan Yao (2009) Effect and analyse of broadcast ephemeris errors on GPS survey precision. *GNSS World China* 1:24–28
8. Ji-chao M, Ye-shu Y (2010) Analysis of residual error in GPS pseudorange differential positioning error. In: Proceedings of 15th national youth communication conference. Beijing, pp 302–308
9. Hong-pin Z, Jin-song P, Wen-yao Z et al (2006) Brief review of the ionospheric delay models. *Prog Astron* 1:16–26
10. Tao Liu, Yong-chun Xie (2007) Study of relative navigation based on relative differential pseudo range of GPS. *Chin Space Sci Technol* 1:1–8

Image Fire Detection System Based on Feature Regression Analysis and Support Vector Machine

Yang Jia and Huiqin Wang

Abstract In order to improve the image fire detection rate in spacious buildings, regression analysis is used to find the inherent relationship between flame features. Then support vector machines (SVM) are used to finish recognition. First, suspected fire regions are detected depending on improved fire-colored pixel detection and hierarchical clustering method. Then, features are extracted and analyzed with regression method. Finally, features are applied to a two-class SVM classifier for fire region verification. The experimental results show that the new feature, area overlap, is efficient and the proposed algorithm has a lower positive false rate than the previous algorithm.

Keywords Image fire detection · Feature regression analysis · Support vector machines · Spacious buildings

1 Introduction

Spacious buildings, such as museums, stadiums, and airports, if they catch fire will cause huge loss of life and property. So there is an increasing need for improved early warning fire alarm systems. Image fire detector offers several advantages, because it can be built on the existing surveillance system and has a better response rate than temperature and smoke detector and is more cost-effective than other detectors. A number of methods have been proposed in the traditional image fire detection [1–7]. According to the methods used, they can be mainly classified

Y. Jia (✉) · H. Wang
Xi'an University of Architecture Technology, Xi'an, China
e-mail: yangjiaxuat@xuat.edu.cn

H. Wang
e-mail: whq463@263.net

as color segmentation, feature extraction, and recognition. All the methods focus on better detection rate. Actually, every stage needs to be considered and mutually coupled to improve the detection rate in a practical system. In this paper, series of methods are used to improve the fire detection effectiveness.

2 Candidate Region Detection

A flowchart of the fire detection algorithm using images is depicted in Fig. 1. The algorithm is composed of three phases: segmentation, feature extraction, and recognition. In the segmentation phase, the candidate fire pixels are segmented from a frame sequence. In the feature extraction phase, the features of fire are extracted and preprocessed for two-class SVM classifier. In the recognition phase, SVM is trained and utilized to distinguish between fire and non-fire. In the following sections, the proposed fire detection algorithm is presented in detail.

2.1 Fire-Colored Pixels Detection

Using YCbCr color space to separate luminance from chrominance is more effective than color spaces such as RGB, so YCbCr color space is used to construct a generic chrominance model for flame pixel classification. Rules used are as follows:

$$F_{\tau} = \begin{cases} 1, & \text{if } \begin{cases} Y(x, y) > Cb(x, y) \\ Y(x, y) > Y_{\text{mean}} \\ |Cb(x, y) - Cr(x, y)| > \tau \end{cases} \\ 0, & \text{else} \end{cases} \quad (1)$$

$$Y_{\text{mean}} = \frac{1}{k} \sum_{i=1}^k Y(x_i, y_i) \quad (2)$$

τ is a constant, values of τ can be selected with respect to required true positive and false positive rates. In this paper $\tau = 20$. The flame detection rate is higher than 95.65 %. Even in some extreme conditions, the flame can be segmented. Figure 2 illustrates the segmentation results. The tiny fire region could not be found using the present segmentation method.

Feature extraction and recognition are both based on the segmentation result. In order to improve the robustness of segmentation, a group of frames are computed to get a movement accumulation matrix. Finally, the matrix is binarized as the segmentation result [10].

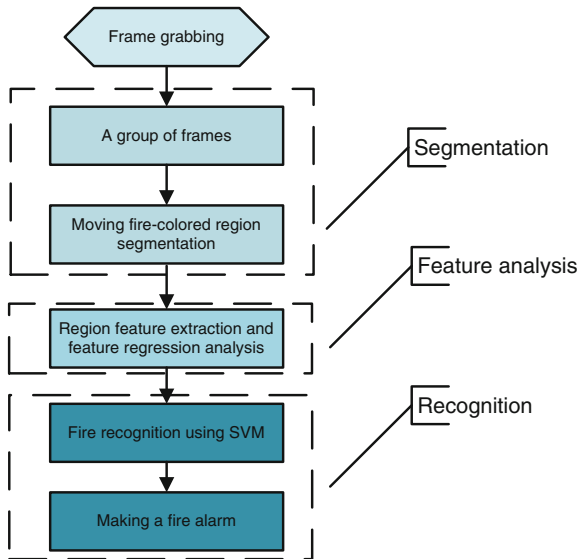


Fig. 1 Flowchart of the proposed image fire detection algorithm

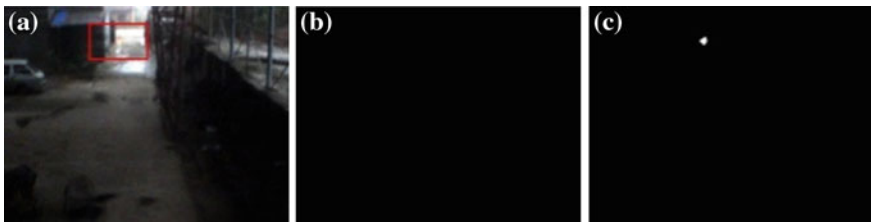


Fig. 2 Detection of fire-colored regions using the approximate method: **a** an original fire image, **b** the resulting image using the present segmentation method, **c** the resulting image using the proposed segmentation method in YCbCr color space

Because the initial segmentation result of flame is often not a complete connected domain, cluster is used to merge the discrete segmentation result [5]. Experiment results show that the method is good for feature extraction; however, if the number of discrete connected regions is too large or the area of the connected region is too large, time complexity becomes unbearable, video delay is increased seriously, so sampling the edge of connected areas to minimize time complexity is considered. Edge coordinates of the connected areas are treated as the total sample. Since each edge coordinate is independent, equiprobable, systematic sampling is used. If the sampling interval is N^2 , the statement execution time drops to $1/N^3$. The sampled data can also express the flame edge and the video delay is resolved.

After all of the distance between two classes are calculated, clustering is finished. If the number of pixels of a fire region is below 12 pixels after merging, it is declared as noise and removed.

3 Feature Analysis

To distinguish a fire-like color object moving similar to fire is difficult, although most of the background interference is removed using the algorithm above. Hence, more efficient features should be proposed to differentiate flame and non-flame regions. There are already some features used in fire detection, such as inter-frame correlation, area change rate [5], motion vector, average brightness, red and green component ratio. In this paper, a new feature, area overlap rate, is proposed and regress analysis is used to seek the internal relations between the dynamic features.

3.1 Dynamic Flame Features and Static Features

In this system, four dynamic features are used to describe fire. Area overlap rate is calculated to present the relative stability of flame. In two adjacent time frames, the rate is calculated as follows:

$$O_{xy} = \frac{S_x \cap S_y}{S_x \cup S_y} \quad O_{xy} = \frac{S_x \cap S_y}{S_x \cup S_y} \quad overlap_{xy} = \frac{S_x \cap S_y}{S_x \cup S_y} \quad (3)$$

S_x, S_y is the area of the same suspected region in two adjacent frames in a group. O_{xy} is the area overlap rate.

Because of image flame continuity in time domain, flame brightness changes within a range, the correlation coefficient is chosen as a description of the flame brightness changes. Because the area of wavering flame changes continually and it varies differently from non-fire areas, area change rate is chosen as a feature. As fire spreads, flame position moves constantly; although the whole of the flame is not a bouncing move, it keeps relative stability. The centroids of fire-like regions are used to express the continuous movement of flame.

Here, two static features are used. The average flame area brightness is higher than the background, so it can be used as a feature of flame. The ratio of RGB intensity values in the flame image is in a certain range; in this paper, green and red component area ratio is a flame feature.

In order to eliminate the influence of data scale, these six features are standardized to build the feature space.

3.2 Feature Regression Analysis

Area correlation coefficient describes the stability and variability of flame. It should be a number larger than zero and near one (if the value ranges between [0, 1]), which means in two consecutive frames most of the flame part occupies the same area. So it can be supposed that there was a positive correlation between area overlap rate and area correlation coefficient, and a negative correlation between area change rate and area correlation coefficient. In order to verify the validity of the hypothesis, regression analysis is used here.

Multivariable linear regression model can be described as follows:

$$Y = X\beta + \varepsilon \quad (4)$$

$$Y = (y_1, y_2, \dots, y_n)^T, \beta = (\beta_1, \beta_2, \dots, \beta_n)^T, \varepsilon = (\varepsilon_1, \varepsilon_2, \dots, \varepsilon_n)^T$$

Here, Y is area correlation coefficient vector. X is the independent variable, which can be a matrix consisting of several feature vectors, such as area overlap rate and area change rate. n is frame number and ε is random error; 298 frames from a video are tested in the experiment. Figure 3 is the regression result and it shows the residuals. The red bars are outliers which should be avoided, while they are the interference in the video, so the data are actually valid.

After regression, the significance of the regression equations should be verified. Table 1 shows the parameters of significance testing.

R2 statistic is coefficient of determination showing that the goodness of fit (a) and (c) are much better than (b). F statistic and p -value both show the significance and also show that (a) and (c) are better. p -value shows there are significant differences between the features. All of the data show that the models (a) and (c) are proper and the feature combinations are better than (b). So area correlation coefficient, area change rate, and area overlap rate should be chosen to describe flame.

4 Fire Alarm Using SVM

To classify the regions as fire regions or non-fire regions using several features seems difficult because the statistical analysis result shows that an obvious threshold discriminating the two regions could not be found; in other words, the feature value distribution is nonlinear. Therefore, a binary classification method in high-dimensional data space needs to be found. Two mutually parallel hyperplanes are established to separate the data locating on both sides of the hyperplanes and the optimal hyperplanes need to be found to maximize the distance of either class.

In order to get good generalization ability, a large set of 6,300 images cut from videos containing fire and interference at different resolutions are collected.

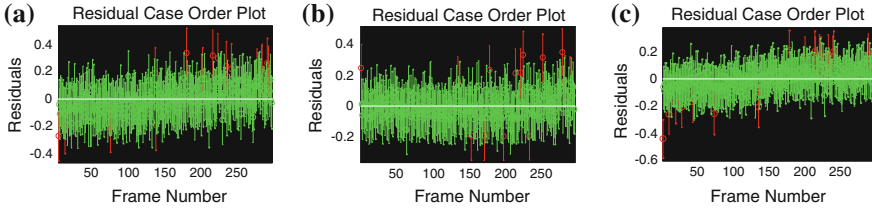


Fig. 3 The residual from regression of area correlation coefficient and other features **a** and area overlap rate; **b** and area change rate; **c** and area change rate, area overlap rate

Table 1 Parameters of significance testing

| | R^2 statistic | F statistic | p-value | Error variance |
|-----|-----------------|-------------|---------------------|----------------|
| (a) | 0.90 | 2707.50 | 0 | 0.0089 |
| (b) | 0.19 | 69.4 | 3×10^{-15} | 0.0065 |
| (c) | 0.93 | 1977.74 | 0 | 0.0063 |

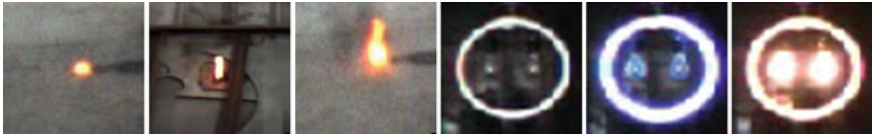


Fig. 4 Images of fire and interference clipped for SVM training

The flame and interference regions are clipped manually; several training images are shown in Fig. 4. As depicted in Fig. 4, only the regions including fire and interference are clipped to make sure that we can extract precise feature values of the regions without unknown data. The fire features are labeled 1 while the interference features are labeled 0, so the features are divided into two classes manually and correctly. A binary classification SVM can be trained after all the data are prepared.

First feature values are scaled into $[-1, +1]$. The main purpose is to prevent large numerical interval attributes from dominating small numerical control interval attribute excessively. In addition, scaling is used to avoid the numerical complexity of calculation. Then “grid-search” on the optimal parameter (c, γ) using cross-validation is proposed to solve the optimization problem. Because the number of training sets is much larger than the feature’s number, the experiment result shows that the recognition rate is much higher when using the RBF kernel [4]. Finally, the candidate flame regions are classified with the trained hyperplanes.

Table 2 Videos shot based on CNS

| Video sequence | Description | | | |
|---------------------------|-------------------|--------------------------------------|--------------------------------------|--------------|
| | Focal length (mm) | Distance between camera and fire (m) | Length of the square fire plate (cm) | Frame number |
| Movie 1 fire in warehouse | 4 | 5 | 2 | 300 |
| Movie 2 fire in warehouse | 6 | 5 | 4 | 300 |
| Movie 3 fire in warehouse | 8 | 50 | 40 | 300 |
| Movie 4 fire in warehouse | 12 | 25 | 9 | 300 |
| Movie 5 incandescent lamp | 4 | 10 | – | 300 |
| Movie 6 annular tube | 4 | 10 | – | 300 |

5 Experiment Result

All of the experiments are implemented on AMD 2.2 GHz PC with 640×480 image size, 15 Hz frame rate. The system is designed for real-time fire monitoring.

To validate the effectiveness of the proposed system, we conduct experiments with videos shot in spacious buildings, including indoor fire videos, annular lamp, light bulb, and the interference of combination of video with different focal length, fire plate, and distance between camera and fire. The test was performed using 21 videos. The mixture of petrol and diesel is kindled based on CNS. Part of the videos and parameters are stated in Table 2.

With the developed hierarchical cluster method ensuring the system real-time, the execution time drops to approximately 1/16 of Liang's method. The proposed method execution time ranges between 0.21 and 1.19 ms, while Liang's method costs 3.44 to 21.55 ms. Using the longest delay video with Liang's method to test the proposed method shows no signs of delay.

The dataset combines fire feature vectors and interference feature vectors. In order to test the classification accuracy, the fire part is clipped to make sure no interference data included in fire feature data. Then a training set, like a decision table is obtained. The data are permuted randomly and divided into two parts: training set and testing set. Training set is used to train the SVM and testing set is used to test the classification accuracy. Accuracy of SVM classification is displayed in Fig. 5.

The miscellaneous data training result shows that these features are enough to separate fire and interference. Tested with 21 videos, training set number is much larger than the feature number, so nonlinear RBF kernel is chosen, which has a

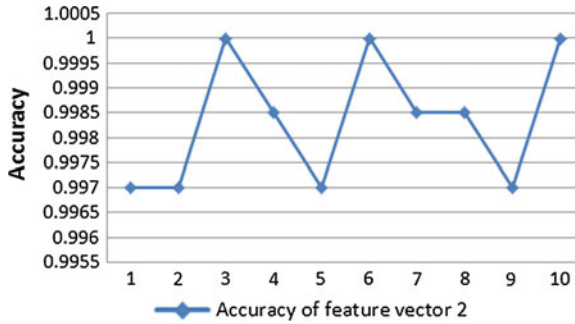


Fig. 5 Accuracy of SVM classification with feature vector

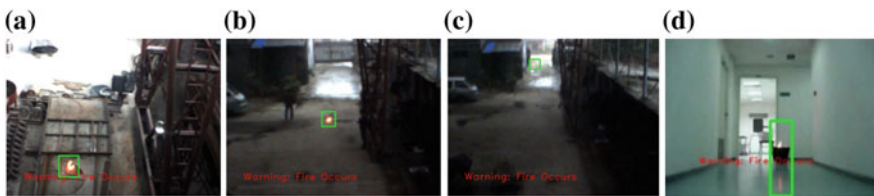


Fig. 6 Fire detection result: **a** In a warehouse, 5 m between camera and the fire; **b** In a warehouse, 25 m between camera and the fire; **c** In a warehouse, 50 m between camera and the fire; **d** <http://signal.ee.bilkent.edu.tr/VisiFire/Demo/SmokeClips/>, a video from the website

higher recognition rate than with polynomial kernel and sigmoid kernel. Some of the fire detection results are shown in Fig. 6.

6 Conclusion

Image fire detection approaches offer several advantages, while using cameras also poses challenges for the development of fire alarm systems. In this paper, in YCrCb color space, flame pixel movement accumulation matrix is obtained as the preliminary flame segmentation result. Then features are extracted and analyzed with regression and a method of selecting features is recommended. Features are used to train the SVM for classification. Because a group of images are used to segment the flame, the robustness of the algorithm is better. Features can be selected rationally, so that less features would work more efficiently. For future works, the system designed for real-time fire monitoring with DSP will be optimized.

Acknowledgments This research is supported by grants from Specialized Research Fund for the Doctoral Program of Higher Education of China (SRFDP) (20126120110008), Natural Science Basic Research Plan in Shaanxi Province of China (2012JQ8021), Industrialization Program

Funded by Shaanxi Provincial Education Department (2011JG12), and Scientific Research Program Funded by Shaanxi Provincial Education Department (11JK1048).

References

1. Michael Wirth RZ (2010) Flame region detection based on histogram backprojection. In: 2010 Canadian conference computer and robot vision
2. Phillips W, Shah M, Lobo NV (2000) Flame recognition in video. In: Proceedings of the fifth IEEE workshop on applications of computer vision, pp 224–229
3. Chen T-H, Wu P-H, Chiou Y-C (2004) An early fire-detection method based on image processing. In: 2004 international conference on image processing
4. Yang N-J, Wang H-Q, Ma Z-F (2010) Image fire detection algorithm based on support vector machine. *J Comput Appl* 30(4):1787–1791
5. Liang J-S, Wang H-Q, Hu Y, Zou T, Wu M (2012) Image fire detection based on fuzzy cluster. *Comput Eng* 38(04):196–198
6. Tung TX, Kim J-M (2011) An effective four-stage smoke-detection algorithm using video images for early fire-alarm systems. *Fire Saf J* 46:276–282
7. Ko BC, Cheong KH, Nam JY (2009) Fire detection based on vision sensor and support vector machines. *Fire Safety* 44(3):322–329

Spur Bevel Gearbox Fault Diagnosis Using Wavelet Packet Transform for Feature Extraction

Wentao Huang, Peilu Niu and Xiaojun Lu

Abstract Gear as an important transmission component in the production of modern industrial, used in all areas of production and life, its stable and reliable work has great social significance. In this paper, gear fault diagnosis based on wavelet packet for fault feature extraction has been proposed for gear fault detection and diagnosis. First, this paper analyzes the variations of gear fault vibration signal, using time-domain and frequency-domain sign attributes to characterize these gear vibration signal and then extract fault sign attributes by using wavelet packet. This paper introduces a kind of new method for wavelet de-noise, eliminating the problem of wavelet de-noise decompose level and de-noise threshold value selection, at the same time analysis a kind of wavelet packet transform method, eliminating the frequency and frequency band confusion, reducing the error in fault sign attribute extraction. At last, using fault simulation platform to simulate different conditions and different gear fault vibration signals. The results demonstrate that this method can accurately and reliably detect failure modes in a gearbox.

Keywords Fault diagnosis · Wavelet packet · Frequency aliasing

1 Introduction

Gearbox was an important component in industrial drives, its safe and reliable operation had great significance of industrial production. Used acceleration sensors can collect the vibration signal of the gearbox without disturb the gearbox normal working conditions, analysis the collected vibration acceleration signal to extracted the gearbox feature characteristics, so as to reflected the type of gearbox

W. Huang (✉) · P. Niu · X. Lu
School of Mechatronics Engineering, Harbin Institute of Technology, Harbin, China
e-mail: hwt@hit.edu.cn

failure and fault degree. So we can take appropriate measures to minimize economic losses and improve production efficiency. Thus, the effective fault diagnosis method for the gear failure mode classification had important significance.

The primary concepts of wavelet analysis are dilation and translation. In 1983, Morlet proposed the concept of wavelets in the analysis of seismic data. In 1997, Xiong, Ramchandran, Herley, and Orchard proposed variable wavelet packet transform (WPT) algorithms based on a tree structure [1]. In 1999, Newland introduced the WPT in the engineering field, with several calculation methods and examples of his application in vibratory signal analysis [2]. In 2002, Zheng et al. published a gear fault diagnosis method based on a continuous wavelet transform and proposed a new concept of time-averaged wavelet spectrum for reducing the enormous operand [3]. In 2010, Lei et al. introduced a multidimensional hybrid intelligent method for gear fault diagnosis; a Hilbert transform, WPT, and empirical mode decomposition were used for gear multidimensional fault diagnosis [4]. In 2010, Zhou et al. introduced a gearbox fault diagnosis based on a redundant second-generation WPT; a second-generation WPT has a redundancy feature that is able to maintain time-invariant properties to increase the effectiveness of the information [5].

Many gear faults are partial failures, reflected in the change of partial information in the spectrum; therefore, gear fault diagnosis should focus on the partial information of the signal. The WPT can describe partial signal characteristics; a low-band WPT has low time resolution and high frequency resolution, whereas a high-frequency-band WPT had high time resolution and low frequency resolution. By further decomposing high-frequency information, the WPT can be more flexible in dividing signals. WPT provides an efficient and a reliable tool for the separation of the characteristic frequencies of mechanical failure and fault feature extraction.

In this paper, the proposed WPT is used for feature extraction. WPT analysis has an acute partial locked ability to extract feature information from the vibration signals. Using a WPT for partial gear vibration signal spectrum analysis or time-domain frequency attributes can help to detect gear failure. The single-node reconstruction of the wavelet coefficients can lead to the generation of other frequency components. If the gear signal spectrum analysis and the time—and frequency-domain sign attributes are false, they can affect the accuracy of the gear fault diagnosis. In this paper, we introduce an improved WP algorithm to eliminate the excess frequency components to ensure the accuracy of the partial attribute.

2 Data Acquisition Experiment

2.1 Experimental Setup

The gear fault forms are varied; in the same types of gear fault, the different fault degrees causing the form of gear vibration signals are not the same. To study the form of gear fault vibration in further detail, more accurate detection of the gear

Table 1 Gear wheel and pinion details

| Parameters | Gear wheel | Pinion wheel |
|-----------------------------|--------------|--------------|
| No. of teeth | 27 | 18 |
| Module | M2 | M2 |
| Pitch angle | 56°19' | 33°41' |
| Normal pressure angle | 20° | 20° |
| Material | Forged steel | Forged steel |
| Backlash tolerance (inches) | 0.001–0.005 | 0.001–0.005 |
| Pitch diameter (inches) | 1.6875 | 1.125 |
| Pinion bearing | NSK 6202 (2) | NSK 6202 (1) |

fault is necessary. A mechanical failure simulator can be used to simulate different gear faults and provide analysis for the vibration signals of gear faults to obtain decision rules for the gear faults.

A variable speed DC motor (1 hp) with a speed of up to 6,000 rpm was used as the basic drive. A short shaft with a diameter of 0.75 inch was attached to the shaft of the motor through a flexible coupling; this scheme minimized the effects of misalignment and the transmission of vibrations from the motor.

The shaft was supported at its ends by two roller bearings. From this shaft, the motion was transmitted to the bevel gearbox via a belt drive. A torque attribute of 5 Nm was applied at the full load condition. Various defects were created in the pinion wheels, and the mating gear wheel was not disturbed. Gearbox vibration signals were obtained by mounting the accelerometer on the top of the gearbox.

2.2 Experimental Procedure

In this study, the gear pair details are listed in Table 1.

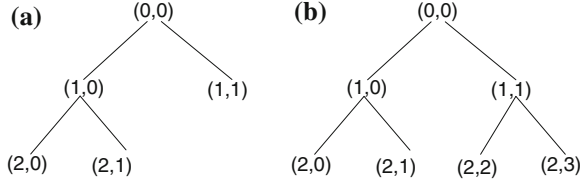
One wheel was new and assumed to be free from defects. In the other two pinion wheels, defects were created using an EDM to control the size of the defects. A piezoelectric acceleration sensor was mounted on the gearbox, and the electromagnetic spring loaded disc brake load was adjusted to 5 Nm. The DC motor speed adjusted the pinion shaft rotational speed to 11 Hz. The gearbox was initially run several times. The sampling frequency was 2,560 Hz, and the sample length was 2,048 for all data acquisition conditions. During the experiment, the normal pinion, tooth breakage pinion, and tooth surface wear pinion were used for data collection.

3 Wavelet Packet Transform Theory

3.1 Basic Concepts of WPT

For a discrete wavelet, the wavelet scale a and offset b must be discretized. To facilitate the calculation, a binary discrete of $a = 2^j, b = 2^j k$ was used, resulting in a binary discrete wavelet transform. The discrete wavelet transform at each level

Fig. 1 Structure of the wavelet tree. **a** Discrete Wavelet Transform, **b** Wavelet packet transform



as the decomposition of a low-frequency sub-band (and no longer the decomposition of the details of the high-frequency sub-band) is illustrated in Fig. 1a. When further analysis of the high-frequency part was required, the discrete wavelet could not meet the requirements. Therefore, Coifman and Wickerhauser proposed the concept of WPT. The high-frequency part of each level was decomposed to meet the demand, as shown in Fig. 1b.

$$I_j^k = [-(k+1)\pi 2^{-j}, -k\pi 2^{-j}] \cup [k\pi 2^{-j}, (k+1)\pi 2^{-j}] \quad (1)$$

In actual production applications, the meaningful signal frequencies were positive. Therefore, the actual signal of the i th wavelet packet at the level- j frequency band is the positive frequency portion, i.e.,

$$I_j^k = [k\pi 2^{-j}, (k+1)\pi 2^{-j}]. \quad (2)$$

Note that the frequency range of I_j^k was obtained under the assumption that the WPT filter was the ideal filter. However, this assumption was incorrect because the WPT filter did not have ideal cutoff characteristics. Therefore, in the single-node reconstruction algorithm, each sub-band contains some frequency components that do not belong to it, which generates frequency aliasing and causes artificial errors.

3.2 Frequency Aliasing

We next use an example to simulate the frequency aliasing. For the tooth breakage pinion, a sampling frequency of 2,560 Hz and a sample length of 2,048 were considered. The time- and frequency-domain waveforms of the tooth breakage are shown in Fig. 2. The signal was decomposed into three levels using a Db4 wavelet. The reconstructed signal spectrum waveform, whose node was reconstructed with a WPT, is presented in Fig. 3.

Based on WPT theory, the reconstructed signal of node (3, 0) only contains the information of (0, 160 Hz); node (3, 1) only contains the information of (160, 320 Hz); node (3, 2) only contains the information of (320, 480 Hz); and node (3, 3) only contains the information of (480, 640 Hz);

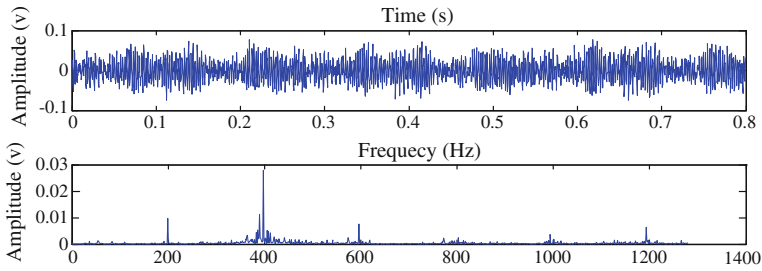


Fig. 2 Time- and frequency-domain waveforms of tooth breakage

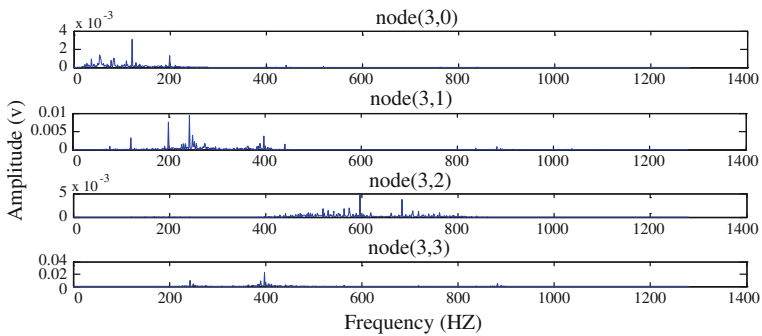


Fig. 3 Reconstructed signal spectrum waveform

Referring to Fig. 3, nodes (3, 0), (3, 1), (3, 2), and (3, 3) contain many other frequency components, resulting in a large amount of frequency aliasing. Node (3, 1) generated a pulse at 240 Hz, with a larger amplitude than that at 198 Hz. The initial signal did not generate a pulse frequency of 240 Hz, greatly affecting the accuracy of the gear fault diagnosis.

Based on WPT theory node (3, 2) only contains the information of (320, 480 Hz); node (3, 3) only contains the information of (480, 640 Hz); but referring to Fig. 3 node (3, 2) contains the information of (480, 640 Hz); and node (3, 3) contains the information of (320, 480 Hz), and nodes (3, 2) and (3, 3) had their frequency bands interleaved. The frequency band interleave becomes more complex as the level of decomposition increases. Analysis of the frequency aliasing indicates that the WPT frequency band interleave is regular; at each node, if the decomposition of the high frequency sub-band has a band interleave, the interleave of the low-level into the high-level will generate further interleave. According to the regular band interleave, reconstruction sorts the band interleave into the correct sequence to avoid a band interleave.

3.3 Eliminate Frequency Aliasing

WPT decomposition differs from discrete wavelet decomposition in that only the former decomposes the high-frequency portion of the signal. WPT filters do not have ideal characteristics; therefore, the detailed components of the level can generate frequency aliasing [6]. If the further decomposed detail parts are equivalent to the decomposed false signals, then reconstructing these parts also reconstructs false ingredients [7].

Frequency aliasing is inherent in WPT decomposition algorithms. To eliminate frequency aliasing, one must proceed with three basic operations of the algorithm. To improve the convolution of the wavelet packet filters, interval point sampling and interval dot zero insertion must be used to eliminate frequency aliasing.

Using a WPT for gearbox fault diagnosis generated the other frequency components due to frequency aliasing. In the spectral analysis, the node (3, 1) in Fig. 3 generated an additional pulse shock, causing the testing personnel to generate a judgment error. For gear sign attribute extraction, the extracted attributes also contained many false components, which influenced the accuracy of the gear fault diagnosis. Therefore, eliminate the single node reconstruct frequency aliasing was of great significance. Concrete steps to achieve the improved algorithm were as follows [8]:

- Each wavelet coefficient performs a Fourier transform after filter convolution.
- The superfluous portion of the spectrum is set to zero and then performs an inverse Fourier transform of the spectrum.
- The results of the inverse transformation replace the results of wavelet filter convolution. Wavelet packet decomposition and reconstruction continues.
- The interleaved band is adjusted to obtain the correct band of the spectrum signal.

Using the improved WPT algorithm in the above example, the reconstructed signal spectrum waveform is shown in Fig. 4.

Contrasting Fig. 3 with Fig. 4, one can observe that the improved WPT algorithm effectively eliminated the frequency aliasing. By adjusting the wavelet sub-band dislocation sequence, the sequence interleave problems were resolved.

The WPT algorithm achieved a reconstructed signal of each node that only contained the signal of the theoretical frequency domain without any additional frequency components. However, the nonideal cutoff characteristic of the wavelet filters caused a leakage of signal energy, therefore decreasing the amplitude of the reconstructed signal in each node.

The improved wavelet packet algorithm led each node to contain only the theoretical frequency information. The characteristics of the nonideal wavelet filter generated other frequency components. Applying this wavelet node information to the fault diagnosis could accurately express the respective frequency components, which can significantly increase the accuracy of fault diagnosis.

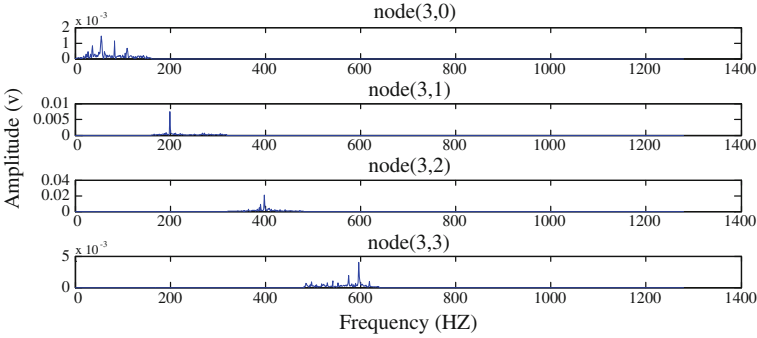


Fig. 4 Reconstructed signal spectrum waveforms using the improved algorithm

4 Fault Feature Extraction

Adjusting the rotational speed of the motor changed the pinion shaft speed to 11 Hz, resulting in a gear mesh frequency of 198 Hz. The gear vibration signal was extracted when the speed was stable. Figures 5, 6, and 7 present the time- and frequency-domain spectrum waveform of the normal pinion, tooth breakage pinion, and tooth wear pinion, respectively. These figures illustrate that the three pinion states are mainly distributed in the pinion mesh frequency at the second and third harmonics. The extracted signal features are $f = f_m = 198$ Hz, $f = 2 f_m = 396$ Hz, and $f = 3 f_m = 594$ Hz.

For the signal with a sampling frequency of 2,560 Hz, the WPT wavelet node (3, 0) contains a frequency component of (0, 160 Hz), node (3, 1) contains a frequency component of (160 Hz, 320 Hz), node (3, 2) contains a frequency component of (320 Hz, 480 Hz), and node (3, 3) contains a frequency component of (480 Hz, 640 Hz). We extracted features from the WPT decomposition and reconstruction nodes (3, 1), (3, 2), and (3, 3) for pinion fault diagnosis.

Using the WPT for single-node reconstruction, the single-node reconstruction time-domain waveform for the normal pinion, tooth breakage pinion, and tooth wear pinion are shown in Figs. 8, 9, and 10, respectively.

In this paper, we selected nondimensional time-domain parameters to characterize the gear state.

$$\text{Kurtosis : } x_q = \frac{1}{N} \sum_{i=0}^{N-1} x_i^4 / x_a^2 - 3 \tag{3}$$

$$\text{Waveform indicators : } K = x_{\text{rms}} / x' \tag{4}$$

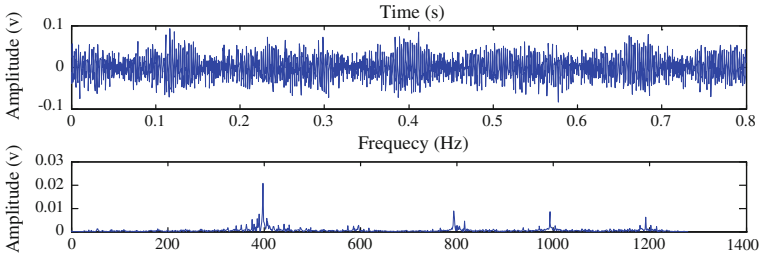


Fig. 5 Normal pinion time- and frequency-domain spectrum waveform

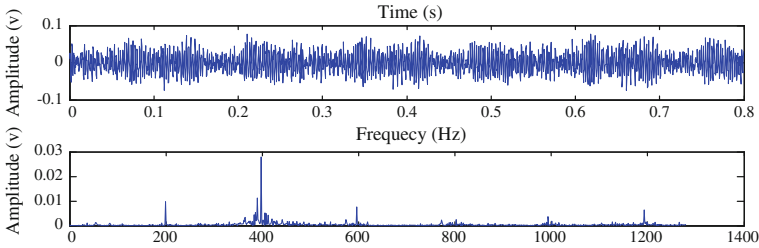


Fig. 6 Tooth breakage time- and frequency-domain spectrum waveform

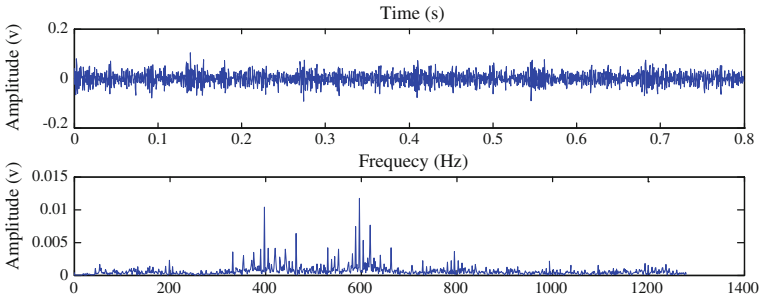


Fig. 7 Tooth wear pinion time- and frequency-domain spectrum waveform

$$\text{Peak indicators : } C = x_p / x_{\text{rms}} \quad (5)$$

$$\text{Pulse indicators : } I = x_p / x' \quad (6)$$

$$\text{Margin index : } L = x_p / x_r \quad (7)$$

Here, x_a is the mean square value, $x_a = \sum_{i=1}^N x_i^2 / N$; x' is the average amplitude, $x' = \sum_{i=1}^N x_i / N$; x_{rms} is the mean square amplitude; $x_{\text{rms}} = \sqrt{x_a}$; x_p is the peak value, $x_p = \max(x_i)$; and x_r is the amplitude of the square root, $x_r = (\sum_{i=1}^N \sqrt{|x_i|} / N)^2$.

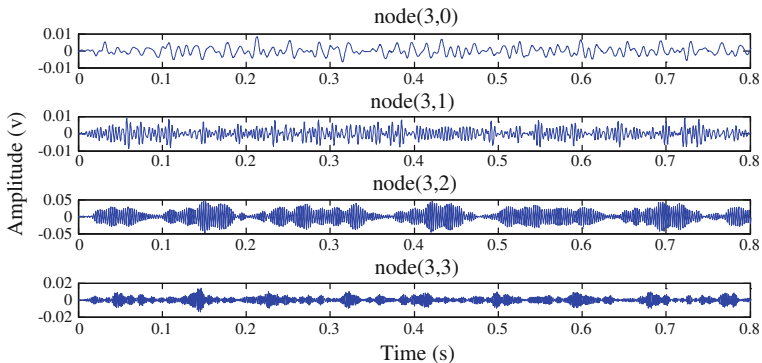


Fig. 8 Normal pinion single-node reconstruction time-domain waveform

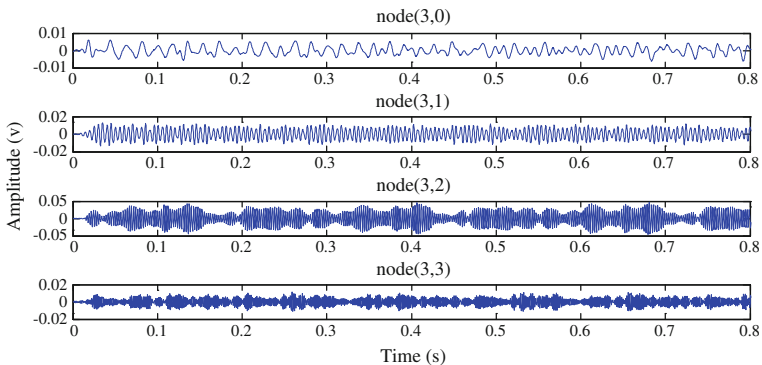


Fig. 9 Tooth breakage single-node reconstruction time-domain waveform

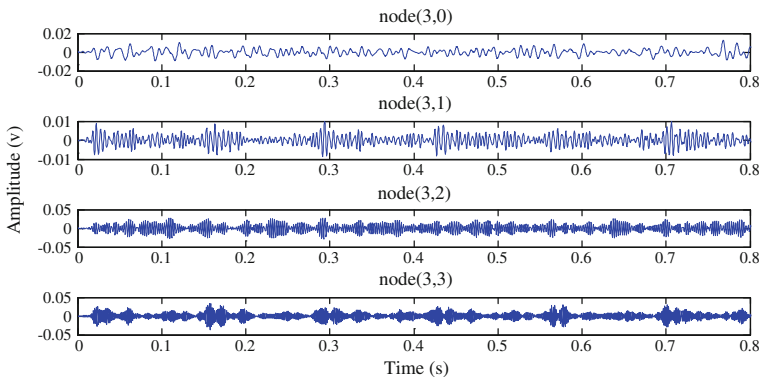


Fig. 10 Tooth wear single-node reconstruction time-domain waveform

In the selection time domain, we selected the sum of the node frequency-domain amplitude spectrum G to characterize the gear state.

$$G = \sum_{i=1}^N (|y_i| \times 2/N) \quad (8)$$

Here, y_i is the FFT of x_i .

The kurtosis indices of nodes (3, 1), (3, 2), and (3, 3) are defined as xq_1 , xq_2 , and xq_3 , respectively; other indicators are also defined with this method. We extracted 18 total attribute signs to characterize the state of the pinion, namely, [xq_1 , xq_2 , xq_3 , K_1 , K_2 , K_3 , C_1 , C_2 , C_3 , I_1 , I_2 , I_3 , L_1 , L_2 , L_3 , G_1 , G_2 , G_3]. Normal, tooth breakage and tooth wear were the three gear states; we sampled each state for 40 datasets, totaling 120 datasets as the raw data for fault diagnosis.

5 Discussion and Conclusion

In this paper, we did a full analysis and research on gear fault detection based on fault feature extraction using wavelet packet. First we analyzed gear dynamics, discussed the types of gear vibration signal. Based on the actual fault signal, we obtained different forms of gear fault vibration signal. According to the form of gear vibration signal chose appropriate characteristic parameters to describe the gear faults. Second, this paper introduces a kind of new method for wavelet de-noise, eliminating the problem of wavelet de-noise decompose level and de-noise threshold value selection, at the same time analysis a kind of wavelet packet transform method, eliminating the frequency and frequency band confusion, reducing the error in fault sign attribute extraction. Finally, through analyzing different gear fault vibration signal in different conditions; combined with theoretical analysis, extract symptom attributes by using signal wavelet packet analysis, so as to carry out the gear fault detection and diagnosis.

Acknowledgment This research is supported by the National Natural Science Foundation of China (51175102).

References

1. Xiong Z, Ramchandran K, Herley C, Orchard MT (1977) Flexible tree-structured signal expansions using time-varying wavelet packets. *IEEE Trans Signal Process* 45:333–345
2. Newland DE (1999) Ridge and phase identification in the frequency analysis of transient signals by harmonic Wavelets. *J Vibr Acoust Trans ASME* 121:149–155
3. Zheng H, Li Z, Chen X (2002) Gear fault diagnosis based on continuous wavelet transforms. *Mech Syst Signal Process* 16:447–457

4. Lei Y, Zuo MJ, He Z, Zi Y (2010) A multidimensional hybrid intelligent method for gear fault diagnosis. *Expert Syst Appl* 37:1419–1430
5. Zhou R, Bao W, Li N, Huang X, Yu D (2010) Mechanical equipment fault diagnosis based on redundant second generation wavelet packet transform. *Digit Signal Proc* 20:276–288
6. Pawlak Z (1982) Rough set. *Int J Comput Inform Sci* 11:341–356
7. Kryszkiewicz M (1998) Rough set to incomplete information systems. *Inf Sci* 112:39–49
8. Tay FEH, Shen LX (2003) Fault diagnosis based on rough set theory. *Eng Appl Artif Intell* 16:39–43

Steering Nonholonomic Systems with Cosine Switch Control

Yifang Liu, Liang Li and Yuegang Tan

Abstract In this paper, a cosine switch control method for nonholonomic chained form system is proposed. Inputs switch between two modes to steer the nonholonomic system from an initial configuration to an arbitrary final configuration. The motion trajectories of states are smooth and have low oscillation under the cosine switch control. It has proved that a mobile robot system can be converted into chained form system. Thus, a two-wheeled mobile robot model is discussed as an example to illustrate the application of this new control algorithm. Finally, simulations and experiments of mobile robot are implemented to verify the feasibility and effectiveness of the proposed method.

Keywords Nonholonomic motion planning · Chained form system · Mobile robot · Cosine switch control

1 Introduction

Nonholonomic motion planning is to design an appropriate bounded input to steer the system from an initial configuration to a desired final configuration over finite time. Nonholonomic system, unlike holonomic one, can't be expressed by a set of independent generalized coordinates. Therefore, the motion of nonholonomic system is not arbitrary, but one satisfied nonholonomic constrains is feasible.

In recent years, there are many works involved in nonholonomic motion planning. Among them, the study of chained form system has an important significance. Chained system is a class of standard controllable nonholonomic systems. In [1] a

Y. Liu (✉) · L. Li · Y. Tan
School of Mechanical and Electronic Engineering, Wuhan University of Technology,
Wuhan China
e-mail: liuyifang1990@126.com

set of sufficient conditions for converting a nonholonomic system to chained form were given. The basic character of chained form conversion was analyzed in [2]. The chained form conversion for a car with n trailers was discussed in [3]. A controllable n -joint manipulator was designed and controlled based on chained form conversion in [4].

Chained form system has simple structure and can be easily integrated. Most practical nonholonomic systems can be converted to chained systems through coordinate conversion and input feedback conversion. Therefore, many useful motion planning algorithms have been proposed based on chained form system. Murray and Sastry introduced a sinusoidal input control algorithm for chained form system [5]. The sinusoidal control algorithm is an open-loop control strategy based on optimal control theory. Each state moved to the final value step-by-step utilizing the periodicity of sinusoidal function. Tilbury used sinusoidal, piecewise constant and polynomial functions as inputs for the motion planning of chained form system, respectively in [6]. Yoshihiko Nakamura proposed an optimal three-point trailer system and applied open-loop control with time polynomial input and sinusoidal input to the new mechanism [7]. The polynomial input control for an underactuated manipulator was studied in [8]. Chelouah demonstrated the effectiveness of digital control method through two classical examples—the car with one trailer and the hopping robot [9]. A switch control method for chained form system based on bang-bang control was discussed in [10]. An algorithm was given to calculate the sequences of switching time.

In addition, the problem of nonholonomic motion planning with obstacle avoidance is more complex. Sekhavat combined geometric techniques of obstacle avoidance together with control techniques of nonholonomic motions in order to take into account constraints due both to the obstacles and to the kinematic limits of the system [11]. A curve fitting approach for nonholonomic motion planning was proposed in [12]. The path was required to pass a set of given points to avoid the collision with obstacles. Obstacle avoidance problem was considered as inequality constraints by Divelbiss in [13]. Exterior penalty functions were used to convert the inequality constraints into equality constraints. Then the motion planning problem can be solved by iterative path space algorithm. A constrained motion planning algorithm for mobile manipulators was introduced in [14].

Inspired by above studies, we propose a cosine switch control method for nonholonomic motion planning. This new algorithm combines the trigonometric functions with discrete control law. The problems of nonsmooth path at switching time for piecewise constant control and high oscillation for sinusoidal control can be solved effectively. We apply the cosine switch control to a two-wheeled mobile robot system based on chained form conversion. Simulation and experiment results prove the validity of this control algorithm.

2 Cosine Switch Control

Control inputs switch between two different modes to accomplish the cosine switch control. Using undetermined coefficients method, cosine functions with unknown coefficients are taken as control inputs. After integrating operation and obtaining the expression of terminal configuration, we can solve the undetermined coefficients by substituting boundary conditions. Cosine function is used to avoid the mutations of velocity and acceleration at switching time.

Consider a n dimensional chained form system with two inputs described as follows:

$$\dot{z}_1 = v_1, \dot{z}_2 = v_2, \dot{z}_3 = z_2 \cdot v_1, \dots, \dot{z}_n = z_{n-1} \cdot v_1 \quad (1)$$

For n dimensional chained form system, cosine switch control can steer it from a given initial configuration to a desired configuration through $2(n-2) + 1$ times of switch mostly. There are two cases to illustrate this control method.

2.1 Case One

When $z_1(0) \neq z_1(T)$, the total time T is divided into $2(n-2) + 1$ intervals equally. The length of each time interval is $\varepsilon = T/[2(n-2) + 1]$.

In odd time intervals, i.e., when $t \in [2i \cdot \varepsilon, (2i + 1) \cdot \varepsilon]$, ($i = 0, 1, 2, \dots, n-2$), the control inputs are represented by (2).

$$\begin{cases} v_1 = 0 \\ v_2 = c_{2i+1}(1 - \cos \omega t) \end{cases} \quad (2)$$

where c_{2i+1} are undetermined coefficients, ω is the angular frequency and $\omega = 2\pi/\varepsilon$. Using inputs (2) to steer system (1), we can get the configuration of system (1) at the end-point of odd time interval through integral operation.

$$\begin{cases} z_1(t_{2i+1}) = z_1(t_{2i}) \\ z_2(t_{2i+1}) = c_{2i+1} \cdot \varepsilon + z_2(t_{2i}) \\ z_3(t_{2i+1}) = z_3(t_{2i}) \\ \vdots \\ z_n(t_{2i+1}) = z_n(t_{2i}) \end{cases} \quad (3)$$

In even time intervals, i.e., when $t \in [(2j + 1) \cdot \varepsilon, (2j + 2) \cdot \varepsilon]$, ($j = 0, 1, 2, \dots, n-3$), the control inputs are represented by (4).

$$\begin{cases} v_1 = c_{2j+2}(1 - \cos \omega t) \\ v_2 = 0 \end{cases} \quad (4)$$

where c_{2j+2} are undetermined coefficients. Using inputs (4) to steer system (1), we can get the configuration of system (1) at the end-point of even time interval through integral operation.

$$\begin{cases} z_1(t_{2j+2}) = c_{2j+2} \cdot \varepsilon + z_1(t_{2j+1}) \\ z_2(t_{2j+2}) = z_2(t_{2j+1}) \\ z_3(t_{2j+2}) = c_{2j+2} \cdot z_2(t_{2j+1}) \cdot \varepsilon + z_3(t_{2j+1}) \\ \vdots \\ z_n(t_{2j+2}) = \sum_{k=1}^{n-2} \frac{(c_{2j+2} \cdot \varepsilon)^k \cdot z_{n-k}(t_{2j+1})}{k!} + z_n(t_{2j+1}) \end{cases} \quad (5)$$

The final configuration at T can be calculated by iterative operation via (3) and (5):

$$\begin{cases} z_1(T) = \sum_{j=0}^{n-3} c_{2j+2} \cdot \varepsilon + z_1(0) \\ z_2(T) = \sum_{i=0}^{n-2} c_{2i+1} \cdot \varepsilon + z_2(0) \\ z_3(T) = \sum_{i=0}^{n-3} \left(\sum_{j=i}^{n-3} c_{2j+2} \cdot \varepsilon \right) \cdot c_{2i+1} \cdot \varepsilon + \sum_{j=0}^{n-3} c_{2j+2} \cdot \varepsilon \cdot z_2(0) + z_3(0) \\ \vdots \\ z_n(T) = \sum_{i=0}^{n-3} \frac{\left(\sum_{j=i}^{n-3} c_{2j+2} \cdot \varepsilon \right)^{n-2}}{(n-2)!} \cdot c_{2i+1} \cdot \varepsilon + \sum_{k=1}^{n-2} \frac{\left(\sum_{j=0}^{n-3} c_{2j+2} \cdot \varepsilon \right)^k}{k!} \cdot z_{n-k}(0) + z_n(0) \end{cases} \quad (6)$$

Specify a set of coefficients c_{2j+2} , and they must be satisfied with (7).

$$\sum_{j=0}^{n-3} c_{2j+2} = \frac{z_1(T) - z_1(0)}{\varepsilon} \quad (7)$$

Then we can get the remaining coefficients c_{2i+1} by substituting initial state $z(0)$, final state $z(T)$ and total time T into (6).

2.2 Case Two

When $z_1(0) = z_1(T)$, c_{2j+2} are equal to zero. This problem can be solved by choosing an intermediate configuration different from initial and final configurations. Thus, the motion planning is divided into two parts, one from initial configuration to intermediate configuration and the other from intermediate configuration to final configuration.

We use control inputs $[c_0(1 - \cos \omega t), 0]^T$ to steer system to the intermediate configuration in advance. The motion planning from intermediate configuration to final configuration is similar to case one. Therefore, if control inputs switch between (2) and (4), it can steer a chained form system moving between two arbitrary configurations.

Remark 1 Cosine switch control algorithm is flexible by regulating the undetermined coefficients. A set of appropriate coefficients can help to reduce the overshoot. Total time T can also be divided into unequal intervals, and the equality intervals chosen here is for the convenience of computation.

Remark 2 Cosine function is used to ensure the continuity of velocity and acceleration curves. Displacement curves of states are smooth and differentiable. Thus, the system can move stable between two given configurations.

Remark 3 When $z_1(0) = z_1(T)$, there is no solution for (6). An intermediate configuration is chosen to overcome this problem.

3 An Example: Two-Wheeled Mobile Robot

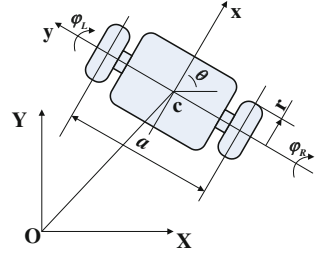
3.1 Two-Wheeled Mobile Robot

Mobile robot is an important canonical example of nonholonomic system. The nonholonomic constraints arise from constraining each wheel to roll without slipping during the movement. The structure of a two-wheeled mobile robot is shown in Fig. 1.

The configuration of a two-wheeled mobile robot is determined by three states: x , y indicate the barycenter position of car in a plane coordinate, θ indicates the angle between car body and x axis. The kinematic model of two-wheeled mobile robot can be described as follows [15]:

$$\begin{cases} \dot{x} = \cos \theta \cdot u_1 \\ \dot{y} = \sin \theta \cdot u_1 \\ \dot{\theta} = u_2 \end{cases} \quad (8)$$

Fig. 1 Mobile robot with two wheels



where u_1 stands for the forward velocity of car and u_2 stands for the steering velocity of car. u_1 and u_2 are determined by the following kinematic relationship:

$$\begin{bmatrix} u_1 \\ u_2 \end{bmatrix} = \begin{bmatrix} r/2 & r/2 \\ r/a & -r/a \end{bmatrix} \begin{bmatrix} \dot{\phi}_R \\ \dot{\phi}_L \end{bmatrix} \quad (9)$$

where r is the radius of each wheel and a is the distance between two wheels. The angular velocity of right wheel $\dot{\phi}_R$ and left wheel $\dot{\phi}_L$ are the two actual inputs of mobile robot. The steering velocity is caused by the differential of two wheels. The kinematic model of two-wheeled mobile robot can be converted to a two-input chained form system with three states by coordinate conversion and input feedback conversion as (10).

$$\begin{cases} z_1 = x \\ z_2 = \tan \theta \\ z_3 = y \end{cases} \quad \begin{cases} v_1 = \cos \theta \cdot u_1 \\ v_2 = \frac{1}{\cos^2 \theta} \cdot u_2 \end{cases} \quad (10)$$

When cosine switch control algorithm is applied to the two-wheeled mobile robot, the forward velocity and steering velocity effect alternately. Therefore, motion of the car is divided into three steps: rotary motion, linear motion, and rotary motion. This is due to the simply kinematic model and input conversion.

3.2 Simulations

Simulation 1 As the first task, the two-wheeled mobile robot is required to go from an initial configuration of $[x(0), y(0), \theta(0)]^T = [0, 1, 0]^T$ to a final configuration of $[x(T), y(T), \theta(T)]^T = [5, 0, \pi/4]^T$. The total time is 30 s.

The mobile robot system can convert to a three-dimensional chained system and $z_1(0) \neq z_1(T)$. According to case one, the mobile robot can move between initial and final configurations through $2(n-2) = 2$ times of input switch. Therefore, we divide T into three intervals. In time intervals of t_1 and t_3 , control

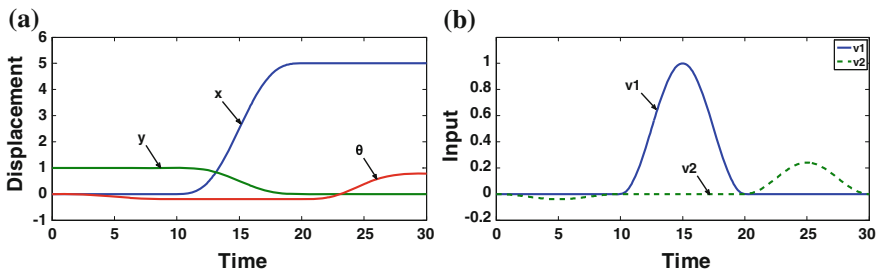


Fig. 2 Simulation 1 **a** Displacement versus time of simulation 1. **b** Input versus time of simulation 1

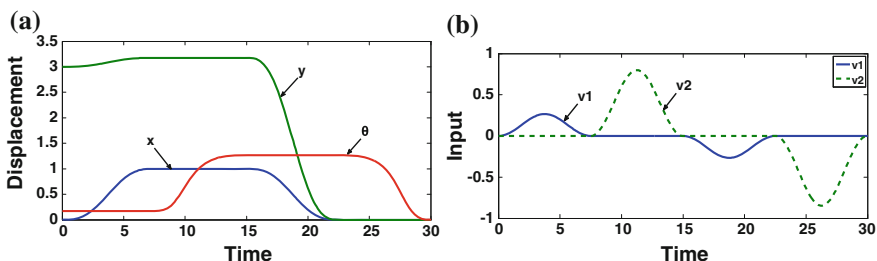


Fig. 3 Simulation 2. **a** Displacement versus time of simulation 2. **b** Input versus time of simulation 2

inputs are as (2). In time interval of t_2 , we use inputs (4) to steer the system. The expression of $z(T)$ for a three-dimensional system can be obtained by (6).

The value of c_2 is determined by $c_2 = [z_1(T) - z_1(0)]/\varepsilon$. Then substitute c_2 into (6) to solve the remaining coefficients. We can finally get the control inputs by substitute c_1, c_2 , and c_3 into inputs (2) and (4). The simulation results are as Fig. 2.

Simulation 2 The second task is a parallel parking for the two-wheeled mobile robot. The initial configuration is $[x(0), y(0), \theta(0)]^T = [0, 3, \pi/18]^T$ and the goal is $[x(T), y(T), \theta(T)]^T = [0, 0, 0]^T$. The total time is 30 s.

When $z_1(0) = z_1(T)$, according to case two, the mobile robot can move between initial and final configurations through $2(n - 2) + 1 = 3$ times of input switch. Therefore, total time T is divided into four intervals. We steer mobile robot in the first time interval t_0 with input $[c_0(1 - \cos \omega t), 0]^T$ in advance. Then $z(t_0)$ (the intermediate configuration) can be regarded as a new initial configuration, $z(T)$ is still the final configuration. The next calculation steps are similar to simulation 1. The simulation results are as Fig. 3.

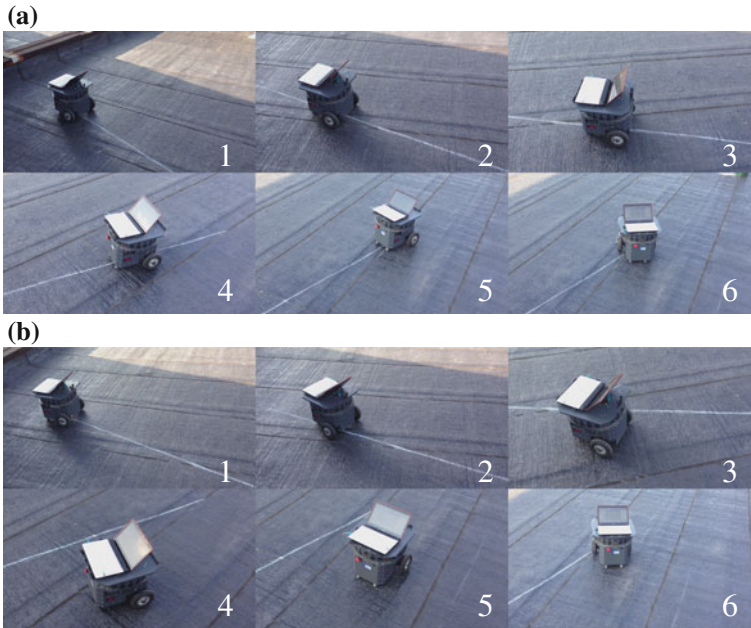


Fig. 4 Experiment 1 **a** Experiment 1 with cosine switch control. **b** Experiment 1 with polynomial control

4 Experiments

The cosine switch control is experimentally tested with prototype of the two-wheeled mobile robot. As a means of comparison, we have also used time polynomial input to steer the mobile robot under the same condition.

Experiments are carried out corresponding to simulation 1 and simulation 2. In the first experiment, a straight line connecting initial and goal positions is regarded as a reference line. In the second experiment, reference lines are two straight lines connecting initial position, intermediate position, and goal position successively. The experiment results are shown in Figs. 4 and 5.

Experimental results show that the mobile robot can move to the goal configuration under both cosine switch control and polynomial control. The speed variation of cosine switch control is more obvious than polynomial control. Since speed is a gradual change, the new method is still able to guarantee the stability of movement.

The trajectory of mobile robot has a significant overshoot in the first experiment with polynomial control. And cosine switch control is more efficient. This is because cosine switch control separates the effect of two inputs in chained form space. Therefore, a complex movement which is affected by two inputs is decomposed into two simple movements which are affected by only one input.

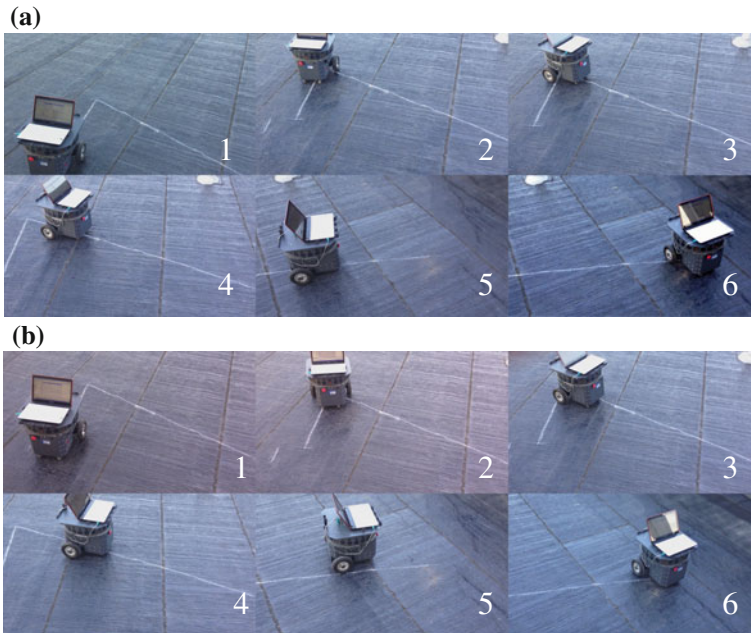


Fig. 5 Experiment 2 **a** Experiment 2 with cosine switch control. **b** Experiment 2 with polynomial control

Accordingly, the movement in state space is also simpler. It can be predicted that cosine switch control is more suitable for high coupling systems such as n trailer system and manipulator system mentioned in [3, 8].

5 Conclusions

In this paper, we propose a new cosine switch control algorithm based on non-holonomic chained form system. Two modes of control inputs effect alternately during the movement. Then the nonholonomic system can be controlled from an initial configuration to a final configuration by finite times of input switch. The algorithm is illustrated through two cases, initial and final values of the first state equality and inequality. The advantage of this new method is that the movement of system is rapid and smooth. By regulating coefficients, the overshoot of states can be reduced effectively. A two-wheeled mobile robot is taken as an example to carry out this new control method. The simulation and experiment results presented here to verify the practicality of this new method for steering nonholonomic chained form systems.

Acknowledgment This work is supported by Specialized Research Fund for the Doctoral Program of Higher Education (20100143110012).

References

1. Murray RM, Sastry SS (1991) Steering nonholonomic systems in chained form. In: Proceedings of the 30th conference on decision and control. doi:[10.1109/CDC.1991.261508](https://doi.org/10.1109/CDC.1991.261508)
2. Tan Y, Jiang Z, Zhou Z (2006) A nonholonomic motion planning and control based on chained form transformation. In: Proceedings of the 2006 IEEE/RSJ international conference on intelligent robots and systems. doi:[10.1109/IROS.2006.282337](https://doi.org/10.1109/IROS.2006.282337)
3. Sørtdalen OJ (1993) Conversion of the kinematics of a car with n trailers into a chained form. In: Proceedings of the 1993 IEEE international conference on robotics and automation. doi:[10.1109/ROBOT.1993.292011](https://doi.org/10.1109/ROBOT.1993.292011)
4. Nakamura Y, Chung W, Sørtdalen OJ (2001) Design and control of the nonholonomic manipulator. *IEEE Trans Robot Autom* 17:48–59. doi:[10.1109/70.917082](https://doi.org/10.1109/70.917082)
5. Murray RM, Sastry SS (1993) Nonholonomic motion planning: steering using sinusoids. *IEEE Trans Autom Control* 38:700–716. doi:[10.1109/9.277235](https://doi.org/10.1109/9.277235)
6. Tilbury D, Murray RM (1995) Trajectory generation for the n-trailer problem using Goursat normal form. *IEEE Trans Autom Control* 40:802–819. doi:[10.1109/9.384215](https://doi.org/10.1109/9.384215)
7. Nakamura Y, Tan Y, Chung W (2001) Design of steering mechanism and control of nonholonomic trailer systems. *IEEE Trans Robot Autom* 17:367–374. doi:[10.1109/70.938393](https://doi.org/10.1109/70.938393)
8. Tan Y, Li L, Liu M et al (2012) Design and path planning for controllable underactuated manipulator. *Int J Adv Comput Technol* 4:212–221. doi:[10.4156/ijact.vol4.issue2.26](https://doi.org/10.4156/ijact.vol4.issue2.26)
9. Chelouah A, Giamberardino PD, Monaco et al (1993) Digital control of nonholonomic systems: two case studies. In: Proceedings of the 32nd conference on decision and control. doi:[10.1109/CDC.1993.325680](https://doi.org/10.1109/CDC.1993.325680)
10. Li S, Ma G, Chen Q et al (2004) Nonholonomic motion planning: steering using bang-bang control. In: Proceeding of the 2004 American control conference, pp 4653–4656
11. Sekhavat S, Laumond J-P (1998) Topological property for collision-free nonholonomic motion planning: the case of sinusoidal inputs for chained form systems. *IEEE Trans Robot Autom* 14:671–680. doi:[10.1109/70.720344](https://doi.org/10.1109/70.720344)
12. Xu WL, Ma BL, Tso SK (1999) Curve fitting approach to motion planning of nonholonomic chained systems. In: Proceedings of the 1999 IEEE international conference on robotics and automation. doi:[10.1109/ROBOT.1999.770074](https://doi.org/10.1109/ROBOT.1999.770074)
13. Divelbiss AW, Wen JT (1997) A path space approach to nonholonomic motion planning in the presence of obstacles. *IEEE Trans Robot Autom* 13:443–451. doi:[10.1109/70.585905](https://doi.org/10.1109/70.585905)
14. Janiak M, Tchon K (2010) Towards constrained motion planning of mobile manipulators. In: Proceedings of the 2010 IEEE international conference on robotics and automation. doi:[10.1109/ROBOT.2010.5509827](https://doi.org/10.1109/ROBOT.2010.5509827)
15. Deng M, Inoue A, Sekiguchi K (2007) Parking control of a two wheeled mobile robot. In: Proceedings of the 2007 IEEE international conference on mechatronics and automation. doi:[10.1109/ICMA.2007.4303600](https://doi.org/10.1109/ICMA.2007.4303600)

Predicting and Verifying Forces by Using Different Cutters and Spaces

Zhaoqian Wang, W. S. Wang, Jiye Wang and Chunguang Liu

Abstract It is notoriously known there are lots of factors influence cutter efficiency and tool life for boring operations. The key problem is how much each influenced and where is the best balance point. This paper uses the orthogonal test method to simulate and verify the influence by the two most important cutting parameters, like cutting speed, cutting penetration (which is the same as cutting depth as in the mechanical machine). First, we used the optimized model and designed a new test mechanism. In the simulation part, we use Rock Failure Process Analysis simulates the rock fragments and the changes of stress field. With these new numerical algorithms, we can simulate the mass and cutting forces in the boring, and we finally find each balance point in the real boring in different cutting parameters. And we also updated a new liner cutting test experimental mechanism, which can simulate the real boring operations in the lab when we set different cutting parameters. We use the simulation and test method to verify our predicting result. We show that the best disc cutter shape is 10 mm flat cutter ring and the best cutting space in our project is 76 mm for 17 inch cutter ring in our cutting test. However, since we understand the complex of different factors we can bound the balance point to those values in certain boring condition.

Keywords Predicting model · Cutting parameters · Cutter forces · Tool lifetime

Z. Wang (✉) · W. S. Wang
School of Mechanical and Automation, Northeastern University, Shenyang, Liaoning, China
e-mail: wzqneu@gmail.com

J. Wang · C. Liu
State Key Lab of Tunnel Boring Machine, Northern Heavy Industries Group Co. Ltd,
Shenyang, Liaoning, China
e-mail: nhipmei@gmail.com

1 Introduction

As we all know, the motion of disc cutter is a composite motion in the real boring [1–3]. One is the straight penetration together with the cutter head in the boring axis, the second movement is the revolution motion around the main bearing, which is named cutting speed in this paper, the last but not the least one is the cutter ring self-rotation caused by the friction force between the cutter ring and the rock. This paper studied the boring effect and efficiency under different cutting factors especially on cutting speeds, penetration. We are trying to find the best penetration and cutting speed in our project. The result will greatly help in the tunnel boring operations and help the operators to decide how much penetration and cutting speed in the project. And from this we can calculate the thrust of the hydraulic cylinder and the cutter head speed. This will greatly reduce the project time and improve the boring efficiency.

2 Model Theories

Cutting forces is one of the impotent physics parameters in cutting process. In the real boring, there are two main forces on disc cutters, one is the thrust from the hydraulic cylinder and main drive, the other one is the forces between the cutter and rock [4]. We can divide this force into three parts, which we have optimized from the Colorado School of Mine predicting model [1]. The value of the force directly determines the power consumption and fatigue of the cutter in the boring process. The force value greatly affect the friction heat between cutter tool and rock, and this heat will further affect the cutter tool weariness, broken, fatigue, and etc. [5]. Mastering the cutting force variation can greatly help to analyze the cutting process, the selection of cutter tool structural parameters, and operating parameters, which will have important guiding significance in actually tunnel boring. The sum normal force is:

$$F_v = \left(\sqrt{Dh} \cdot h \tan \frac{\theta}{2} + \frac{Dr}{2} \sin \phi + \sqrt{Dh} \cdot w \right) (\sigma_c + \alpha \cdot \sigma_3^n) + \frac{h_z R \sin \phi}{\cos \theta} P \sin (\theta + \beta) \quad (1)$$

The rolling force is decided by the multiplication between normal force and constant C, C is cutter constant.

$$F_r = F_v C = F_v \frac{(1 - \cos \phi)^2}{\phi - \sin \phi \cos \phi} \quad (2)$$

There are no side forces in the lining cutting test in theory, but there are side forces in the actual cutting test. There are three reasons; the first one is the different sizes of Rock shear body on the both side of disc cutter; the second reason is the strength improvement under compression strength; the last but not least one is the rock boring is not in the same time.

$$\vec{F}_s = (h_{z1}P_1 + h_{z2}P_2) \frac{R \sin \phi}{2 \cos \theta} \cos(\theta + \beta) \quad (3)$$

3 Design of Simulate and Test Parameters

The best cutting of TBM is consuming smallest power to get biggest cutting length, and remove more mass with smallest forces [6, 7]. This paper studied the value of forces and the fragmentation of rock under different factors using orthogonal test method. We paid mostly attention on the operation parameters, such as cutting speed and penetration. Table I shows the effect factors and parameters in the simulation and test. Because our predicting model is based on the CSM force predicting model [1, 8–12], so we chose the same test parameters and rock samples as in the liner cutting test with the Colorado school of mine in our test and simulation, so that we can easily extend our predicting to more range by comparing our predict result from our mathematical model with the CSM liner cutting test data and. As we all know, the Colorado school of mine's rock sample is Colorado Red Granite. The uniaxial compressive strength 158 MPa; The punch shear strength is 22.8 MPa; The brazilian tensile strength is 6.78 Mpa; The Young's modulus of elasticity 41.0; The poisson's ratio is 0.234; The p-wave velocity is 4557 m/s and s-wave velocity is 2886 m/s. We use the 17 inch constant cross-section disc cutter, the width of test disc cutter is 13 mm.

This disc cutting test were performed on the two disc cutting boring machine in the state key lab of tunnel boring machine of 'Northern Heavy Industries Group Co. Ltd' (the test platform structure is shown in Fig. 1). The disc cutter rings used in the test and simulation all are made by Tiangong Company with a 432 mm (17 inch) diameter, made by standard hardened steel. This kind of disc cutter is common used in all the field of rock boring area. The rock samples are nominally 1500 mm × 800 mm × 500 mm. The rock samples were put in the rock holder tightly. We put concrete flow under and around the rock sample in order to avoid unexpectedly rock break. The rock holder is made up by a moveable table of Y axis, two cylinders for modulation of X axis, one shift sensor of X axis and one forces sensor of X axis. The physical properties of the samples are listed in Table 1. The cutting forces were measured by two three orientation force sensors named YBY-500, which are assembly between each disc cutter holder and the vertical telescopic cylinders. The maximum range is 500 KN. The total force from the vertical telescopic cylinders is 1000 KN, which is shared by two disc cutters

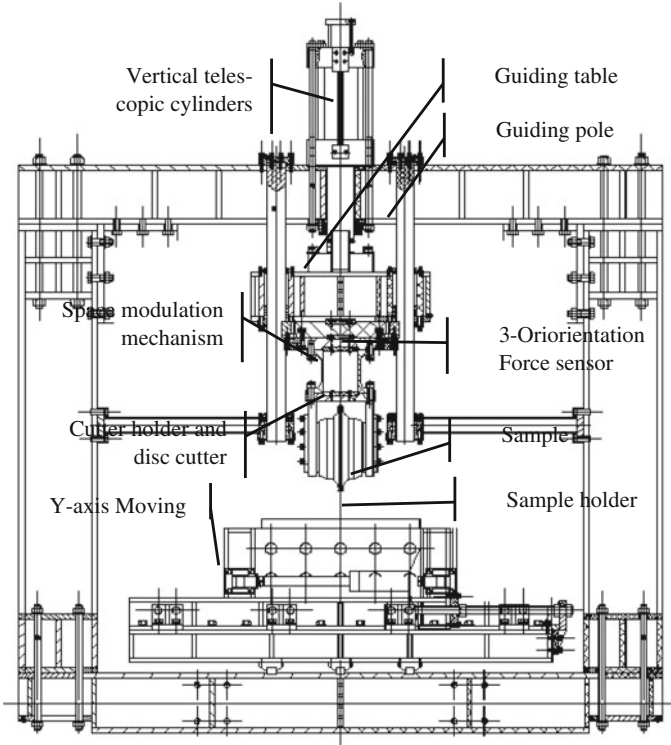


Fig. 1 Disc cutter boring machine in NHI. This linear cutting machine is different with the CSM linear cutting machine, we added two Space modulation mechanism. The range ability of vertical cylinder is 1000 KN; the longitudinal cylinder is 200 KN, and the side cylinder is 100 KN

Table 1 Penetration and spaces in simulation and test

| Factors | Levels | | | |
|-----------------|--------|-----|-------|-------|
| | 1 | 2 | 3 | 4 |
| Cutter Shape | 60° | 90° | 10 mm | 20 mm |
| Cutter Space/mm | 56 | 64 | 76 | 89 |

placed in different spaces. The penetration both in the test and simulation is 3.8 mm. We test different spaces in the other paper and find the different effect.

4 Cutter Ring Shape Influence

Cutter ring is the most easy to fail and replace in the whole cutter tool. There are two different kinds of cutter ring shape mostly used. One is V edge, the other one is flat edge [13]. Different kinds of cutter ring shape have different effect on the

rock boring efficiency and thrust [14, 15]. This paper designed four kinds of cutter ring shapes to study the different shapes in the boring. One is 60° V edge, one is 90° V edge, and one is 10 mm width flat edge, the last one is 20 mm width flat edge.

The stress concentration and deformation are mostly distributed under the inferior of the V shape cutter ring in the Fig. 2a. There is no lateral acoustic emission in this cutting condition, and the rock boring effect is not so entirely satisfied. On the other side, there is more lateral acoustic emission and more effect in boring in 90° V shape cutter ring in Fig 2b than the 60° V shape cutter ring. There is no big difference of the formation and development of lateral acoustic emission between the flat widths 10 mm (Fig. 2c) and 20 mm (Fig. 2d). The rock is hardly boring in Fig. 2d, and the crushed powder nuclear area is hardly deformed under the cutter ring, which is not used in the formation and the development of the acoustic emission. The boring area is very small and there is no radicalized acoustic emission in Fig. 2c, and all the acoustic emission is distributed on the surface. The boring effect of the V shape is much better and the boring area is much bigger than the flat shape. The cutting edge is little changed after longtime use from the view of the cutter tool wear. But there is great change of the cutting edge after longtime use, which will great affect the forces of the disc cutter and the stationary working state of the cutter head.

The mass of bored rock is increased with the increment of the cutter angle, which have great influence on the cutting efficiency. On the other side, the temperature of the cutter ring is also steep rise with the difference of the cutter angle, which will increase the wear of the cutter ring. The cutter forces are also different with different angle, as shown in Fig. 3. The value of the forces greatly increased with the increscent of the cutter width. The reasons are the contact area increase, the boring angle increase, and boring mass increase, which increase the reaction force of the totally cutter. The influence on the normal force is much larger than the influence of the rolling force with the change of cutter shape from the contrast of the forces in Fig. 4.

5 Influence of Cutter Space

The boring and transfixion of the crack is different with different spaces from the data in the simulation and test. As shown in Fig. 5, when the spaces are 25 and 38 mm, the space is too small. There are many tiny rock blocks between two cutter rings. But the total units are too small, and the unit boring power increase. The boring area is excessive coincidence between two cutter rings. The cracks are easily transfixion. And the rocks are excessive bored. The rock boring area is very similar between two disc cutters and one single cutter. In other words, two times power input only results in half boring, which reduced the mechanical efficiency and improve the cost of boring. As shown in Fig. 5, when the space is 89 mm, the space is too large. The rotation time is too short and the load working time is also

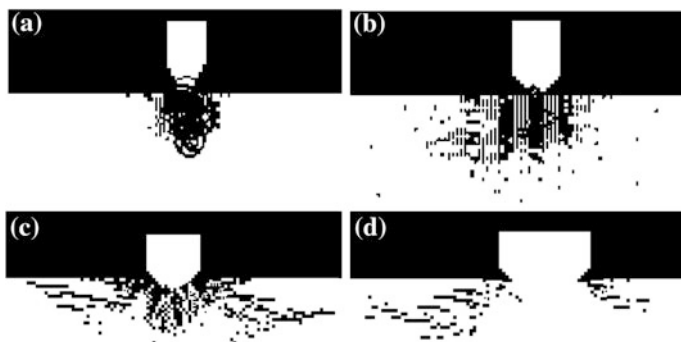


Fig. 2 Fail stress of different cutter's shape. **a** 60° V edge, **b** 90° V edge, **c** 10 mm width flat edge and **d** 20 mm width flat edge

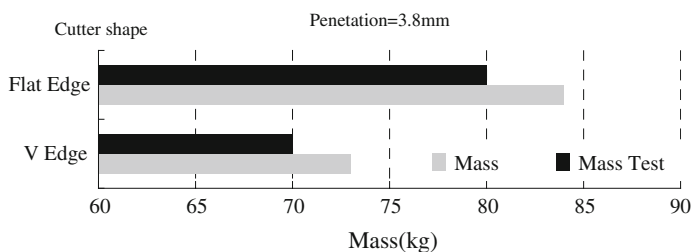


Fig. 3 Contrast of cutting mass with cutter shape's change

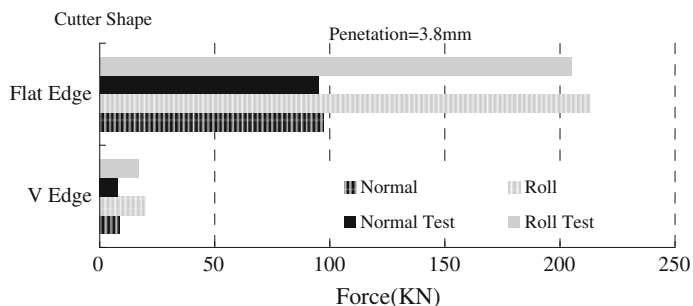


Fig. 4 Contrast of cutting force with cutter shape's change

very short. The boring range is too small. The length of the crack is not enough, which can't make adjacent cracks connected each other. The rocks between two cutters can't be bored, which will form the boring saddle. When the space is 64 mm, the cracks can be connected easily. There is big and suitable block between two cutters when space is 64 mm and 76 mm, as shown in Fig. 6, the masses are in large amount and cutting efficient is the most.

Fig. 5 Fracture mode under different spaces

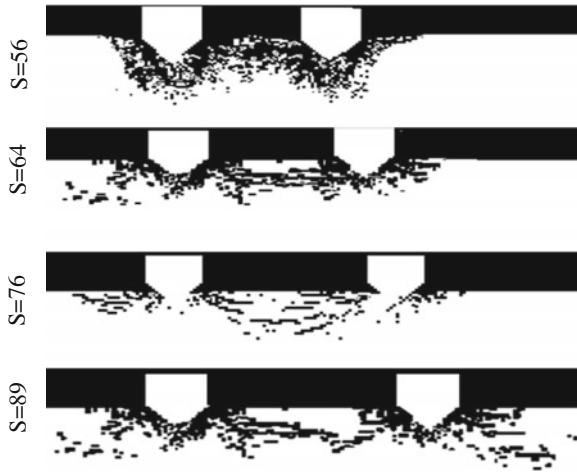
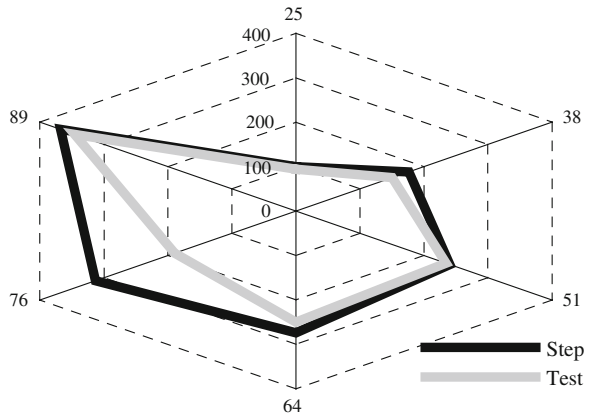


Fig. 6 Contrast of cutting mass with cutter space change



The cutting forces increases with the spaces increase. It will need more power. And on the other side, the boring units are also increased. This is clearly shown in Fig. 7, which is consistent with the CSM boring mechanism. The spaces also affect the forces of cutters as shown in Fig. 8. The forces will be increased with the increase of spaces in the same simulation conditions, such as the same rock parameters, the same penetrations, and the same cutter ring shape. The increase of spaces will make the boring area larger and will be easily developed into big block. On the other side, the block is tiny, and the total boring units is small. This will increase the power in every boring unit. The reasonable spaces are between 52 and 64 mm. When the space is in this range, the smallest boring power can bore most granite.

This paper also gives the simulation of boring when the space is 62 mm in three Dimensions. The boring stage is clearly divided into three stages, break zone independent into nuclear, break zone connection, and cracks extending. First stage,

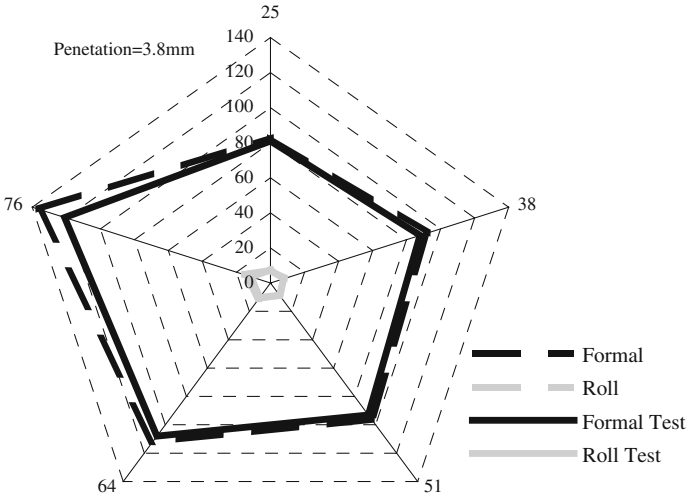


Fig. 7 Contrast of cutting forces with cutter shape's change

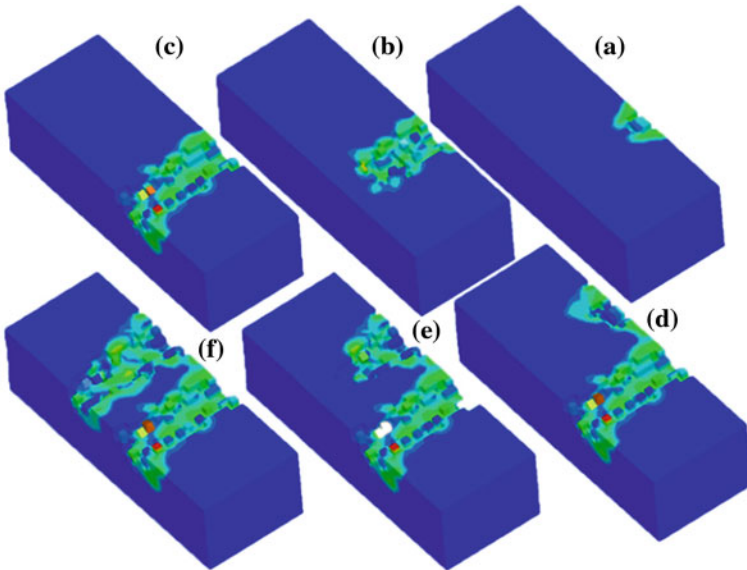


Fig. 8 Rock boring at space 62 mm. It describes the attrition crushing and shear crushing the boring process from (a) to (f); the attrition crushing occurred at the front part rock of the disc cutters; The side rock are failure for reaching the shear crushing limit

this stage is the same with one single cutter boring. There is independent break zone into nuclear. The tensile boring units are distributed around the boring zone, as shown in Fig. 8a–c. Second stage, nonlinear character is the most obvious characters after the second cutter added into cutting.

The failure stress is easily crossed, which will result in macroscopic failure. The total rock is bored from two adjacent cutters, as shown in Fig. 8d, e. The third stage, adjacent stress failure zone is formed after the boring area transfixion. The most failure is middle line boring failure under the combined action by vertical pressure and side pressure. There is also small radial stress on both sides. As shown in Fig. 8f.

6 Conclusions

This paper studied the influence in boring by orthogonal test method both in simulation and test under different disc cutter parameters, such as cutter shape and disc cutter space. All the research is based on the new optimized predicting model. It also gives different affect law, which gives a lot of theoretical basis and simulation experiment data on the future project. And we can find the best space is 76 mm in our new project. In this cutter layout, the cutting is the best and the rock between two disc cutters is more easily to boring and the flaw is more easily to be break through.

Acknowledgments This work was supported by grant No. 2010CB736000 from the national high technology research and development program of 973 Plan, the project name is Key research of tunnel boring machine and large grinding equipment. And thanks RFPA company support the software in simulation.

References

1. Gertsch R, Gertsch L, Rostami J (2007) Disc cutting tests in colorado red granite: implications for TBM performance prediction. *Int J Rock Mech Min Sci* 44:238–246
2. Rostami J, Ozdemir L (1993) A new model for performance prediction of hardrock TBMs. In: Bowerman LD, Monsees JE (eds) *Proceedings of rapid excavation and tunneling conference*. AIME, Boston, MA, pp 793–809
3. Rostami J, Ozdemir L, Nilson B (1996) Comparison between CSM and NTH hard rock TBM performance prediction models. ISDT, Las Vegas
4. Nilsen B, Ozdemir L (1993) Hard rock tunnel boring prediction and field performance. In: *Proceedings of rapid excavation and tunneling conference(RETTC)*, Boston, USA, pp 833–852
5. Okan Su, NuriAliAkcin (2011) Numerical simulation of rock cutting using the discrete element method. *Int J Rock Mech Min Sci* 48:434–442
6. Gong QM, Jiao YY, Zhao J (2006) Numerical modelling of the effects of joint spacing on rock fragmentation by TBM cutters. *Tunn Undergr Space Technol* 21:46–55
7. Liua HY, Koua SQ, Lindqvist P-A, Tang CA (2002) Numerical simulation of the rock fragmentation process induced by indenters. *Int J Rock Mech Min Sci* 39:491–505
8. Ozdemir L, Nilsen B (1993) Hard rock tunnel boring prediction and field performance. In: *Rapid excavation and tunneling conference (RETTC) proceedings*, Chap. 52, Boston, USA
9. Rostami J, Ozdemir L, Nilson B (1996) Comparison between CSM and NTH hard rock TBM performance prediction models. ISDT, Las Vegas

10. Lindqvist PA (1982) Rock fragmentation by indentation and disc cutting, Doctoral Thesis. University of Luleå, Sweden
11. Rostami J (1997) Development of a force estimation model for rock fragmentation with disc cutters through theoretical modeling and physical measurement of the crushed zone pressure, PhD thesis. Department of Mining Engineering, Colorado School of Mines
12. Alehossein H, Boland JN, et al (1995) Prediction of rock failure in rock indentation by a rock cutter. HDRK-CMTE report
13. TeAlehossein H, Hood M (1996) State-of-the-art review of rock models for disk roller-cutters. In: Aubertin M, Hassani F, Mitri H (eds) Second NARMS, rock mechanics tools and techniques. Balkema, Montreal, pp 693–700
14. Nilsen B, Ozdemir L (1993) Hard rock tunnel boring prediction and field performance. In: Proceedings of rapid excavation and tunneling conference (RETC), Boston, USA, pp 833–852
15. Rostami J, Ozdemir L (1993) A new model for performance prediction of hardrock TBMs. In: Bowerman LD, Monsees JE, (eds) Proceedings of rapid excavation and tunneling conference. AIME, Boston, MA, pp 793–809

The Segmentation and Adherence Separation Algorithm of Cotton Fiber

Li Yao, Dong Wang and Shanshan Jia

Abstract Accurate separation and extraction of natural cotton fiber's microscopic image are the required prerequisites for the feature analysis of cotton fiber. An edge detection algorithm based on level set combined with clustering idea is proposed as there were no significant differences between target area and background, and each cotton fiber has one lumen. Firstly, the small region is obtained by binarization algorithm, and the outer contour is got by level set algorithm based on it. Then combined the fiber's outer contour with OSTU, and the rough edge of the fiber is appeared after the burr and broken edge are eliminated. And the seed area of the fiber is emerged by using flooding algorithm and dilation algorithm. Finally, the adherence separation algorithm found on clustering idea is applied to gain the separated fibers. The experimental results show that this algorithm can not only ensure the integrity and the continuity of the fiber's edge, but also segment each fiber rapidly and reliably.

Keywords Level set · OSTU · K-means · Edge detection · Overlapped fiber

1 Introduction

Image segmentation is the required prerequisite for subsequent processing of image in image processing. The quality of image segmentation affects the precision of target identification in subsequent sections. Especially automatic processing and identifying of fiber's microscopic image by using computer technology, image segmentation is the basis of fiber quality's measuring.

Many different image segmentation algorithms have been raised base on the different between image and target in recent years. Now, the main stream of the image segmentation algorithm can be categorized as follows: threshold methods,

L. Yao · D. Wang (✉) · S. Jia

School of Computer Science and Technology, Donghua University, Shanghai China

e-mail: ideapanda@hotmail.com

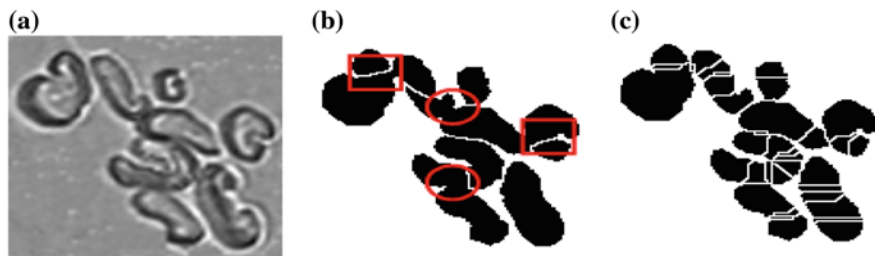


Fig. 1 Separation comparison of the concave points (b) and the watershed (c). a The fiber image, b The result of concave points algorithm, c The result of watershed algorithm

region growing method, edge detection, neural network approach, and method based on the fuzzy set theory, etc. But because of many fiber numbers, various shapes, extrusion in the image, result of the existing image segmentation algorithms are easily impacted. And then, the image is uneven light, in which case many algorithms will ignore weak edges. References [1–5] are proposing some methods, which are based on boundary tracing, morphology, and distance transformation, respectively. Some positive effect is obtained, but their research mainly focuses on some regular shape structures like cells. There is serious noise pollution in image, and it is easy to hit conditions, such as breakage, tortuosity, and distortion. So the existing image segmentation algorithms cannot be directly adapted to cotton fiber microscopic image. The edge detection results in Fig. 1 is the result of concave points algorithm and watershed algorithm.

The segmentation algorithm that can apply fiber image with poor quality and adhesions is the research aspect in this paper. An edge detection algorithm is proposed as there were no significant differences between target area and background, and cotton fibers are closely packed. Firstly, the small region is obtained by binarization algorithm, and the outer contour is got by level set algorithm based on it. Then combined the fiber's outer contour with OSTU, and the rough edge of the fiber is appeared after the burr and broken edge are eliminated. And the seed area of the fiber is emerged by using flooding algorithm and dilation algorithm. Finally, the adherence separation algorithm found on clustering idea is applied to gain the separated fibers. The experimental results show that this algorithm can not only ensure the integrity and the continuity of the fiber's edge, but also segment each fiber rapidly and reliably.

2 The Proposed Algorithm

2.1 The Segmentation Algorithm

The existing edge detection algorithm based on gradient cannot get the accurate edge of the cotton fiber's microscopic image, and tend to gain broken edge, which is mainly caused by the fabrication technique and illumination of the cotton fiber's

microscopic image. The level set algorithm adopts adaptive tracking topology changes, which guarantees the integrity of the fiber's profile, and it solves the problem very well.

There are a large number of cotton fibers in one image, so the paper uses the level set algorithm based on C-V model. This method, suitable for the target area of the cotton fiber, is uncertain, because it is not dependent on the gradient of the image, and the position of the initial curve has no limit. But it also has some defects, such as large calculated amount, low efficiency, and it aims to get the global value of the energy function, which cannot use narrow band. The paper proposes the method of divide and conquer based on the characteristic of the level set algorithm. It divides the image into many small images, which contain the target area, and then uses level set algorithm on the small image, which greatly speeds up the computational efficiency by narrowing the background area.

Detection of the local area of the target is the precondition of the proposed method. So this paper gets the target area by combing OSTU method with K-mean algorithm. OSTU method gets the auto threshold on the basis of statistical feature of the whole image, which is a global threshold algorithm. But it cannot achieve good result if the target area and background were different. K-mean algorithm stops until it gets the local optimum. This paper bonds OSTU method with K-mean algorithm, which not only satisfy the need of complex image's rough location, but also improve the efficiency of level set algorithm.

The rough outer contour can be gained after the level set algorithm, the accurate edge is achieved for the single fiber, but we can only get the outer contour for the adhered fiber. We can find that each fiber has an entocoele area, and regard the entocoele as the seed area. Then, separate the adhered fiber by using clustering method. This paper proposes a separation method to segment the adhered fiber based on this thought.

The experimental results of the proposed algorithm, which is applied to cotton fiber, show that the method not only has good anti-interference, but also accurately segments all fibers. The flow chart of this algorithm is shown in Fig. 2.

2.2 Contour Extraction based on Level Set

After the level set method was proposed by Sethian and Osher [6] in 1988, the effect of level set algorithm was widely recognized. In recent decades, level set method has been widely used for promotion, and it has found wide applications in image processing. Some progress has been made. The basic idea of this method is that we can see the curves in two spatial dimensions as zero level set of some function φ in three-dimensional space. Meanwhile the evolution of curves is also expanding to the higher dimensional space. The contour is represented by zero

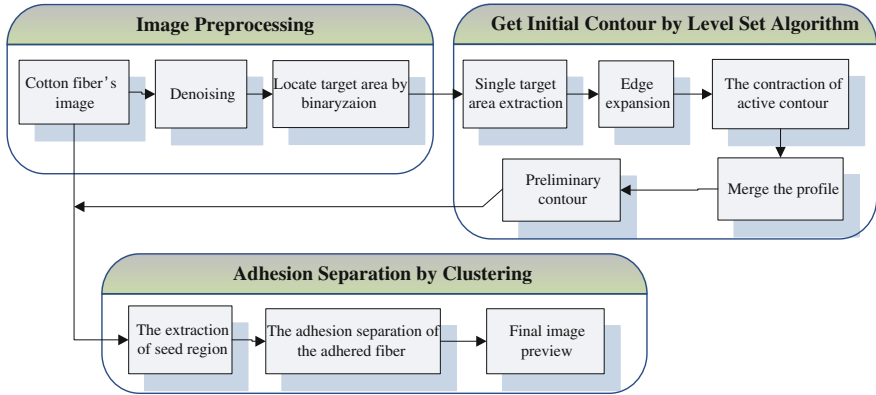


Fig. 2 The flow chart of segmentation algorithm

level set function and approached by evolution of the level set function. The fundamental of level set is as follows:

The signed distance function is defined as

$$\varphi(x, t) = 0 = \pm d \quad (1)$$

where d is the shortest distance between point x and initial curve $C(t = 0)$. d is positive when point x is inside the curve and vice versa.

If we have level set function $\varphi(x, y, t)$ and plane curve $C(x, y, t)$, then zero level set is defined as $C(x, y, t) = \{(x, y) \mid \varphi(x, y, t) = 0\}$. The Hamilton–Jacobi function, which represents the evolution of the level set function, is defined as

$$\begin{cases} \frac{\partial \phi}{\partial t} = F|\nabla \phi| \\ \phi(x, y, 0) = \phi_0(x, y) \end{cases} \quad (2)$$

where F is the diffusion speed of the points on curve. The direction often involves the gradient of the image and the curvatures of curve.

Level set method can efficiently resolve dynamic topological variation during the evolution of curve. We get the curve by finding the minimum of a function. The traditional level set method will be inefficient because the computational area is the entire image plane for optimal image. References [7, 8] put forward the narrowband algorithm, so the computational area becomes the area near the curve with corresponding computations. Reference [9] has put forward the famous C-V model, which is based on the simplified Mumford-Shah model and level set method. The model introduces information, which is based on area into the energy function, so the method is independent of gradient in an image and the demand for the initial curve location is not strict. But, it cannot be computing by the

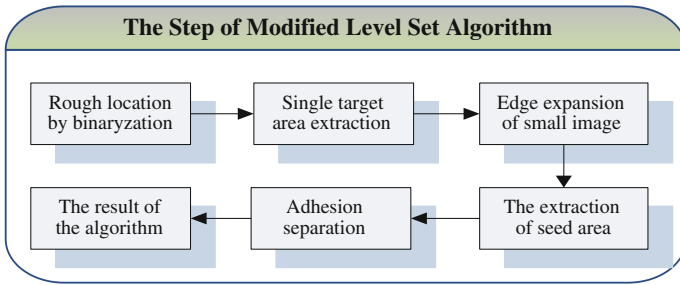


Fig. 3 The flow diagram of modified level set algorithm

narrowband algorithm in their evolution because the result it solved is the global solution of the energy function.

To overcome this weakness, this paper chooses a divide and conquer approach, and the main idea of this approach is equivalent to the following reasoning. We have an image with m by n pixels, if active contour shrink t times, the total calculation are $m \cdot n \cdot t$; but if we can divide original image into several small image based on targets, the total calculation can be reduced largely. So, this paper has taken the method that runs level set algorithm on subgraph of single target or target that was fused. In order to finish the segmentation, the method will combine the result of subgraph together. So it improves the effect of segmentation, and it gives the flow diagram of algorithm in Fig. 3.

2.3 Adherence Separation Algorithm Based on FCM

The level set algorithm cannot meet the requirement of separating each single fiber, although it can extract the complete fiber outer contour. The researchers introduce the other methods into the field of processing image in recent years, and many new adherence separation methods are proposed. The separation algorithm based on morphological operations was proposed in reference. The reference uses distance transformation after binary conversion, then applies the rapid reconstruction to rebuild the image after distance transformation, finally segments image by using watershed algorithm. It gets better separation results, but it still has the problem of excessive segmentation caused by the watershed algorithm. The reference separates the adhesive blood cells by adopting erosion. The research of adherence separation algorithm mainly focused on the regular object such as cell, and microscopic image of natural cotton fiber always presents a variety of forms, even overlaps, so the common used adherence separation algorithm can only extract the cotton fiber’s outer contour, and cannot get accurate separation for further, or simply cannot segment the cotton fiber. We can find that each cotton fiber contains an endocycle after careful observation of the fiber image, and the level set algorithm

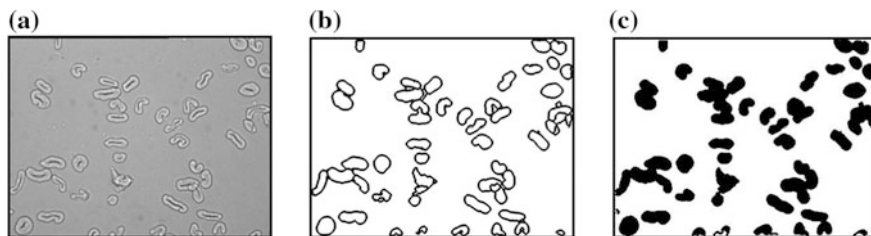


Fig. 4 Seed and alternative point. **a** original image, **b** image of seed, **c** image of alternative *black* points

can gain the accurate and continuous contour of the single fiber or the adhered fibers. According to the above characteristics, the adhesive fiber's separation algorithm based on the clustering is proposed in this paper. The basic idea of it is: regarding the cotton fiber's endocole as seed area, and dividing the fiber area which is obtained by the level set algorithm among the seed area on the basis of the Euclidean Distance, then we can get the accurate outer contour of each single fiber.

We can see that each fiber has only one seed region from Fig. 4b, c. The following problem is how we can distribute the fiber area, which is also named black candidate points that is calculated by the level set algorithm to the seed area. And the seed area remains the outer profile's shape of each fiber, so we segment the fiber area according to the shortest distance between each black candidate point and the outside edge of the current seed area, and it makes the seed area to grow unceasingly until it stops growing.

The black part is the point to be distributed, which is also named the black candidate point, as shown in Fig. 4c. There are a lot of methods that can be chosen to estimate the black candidate point shown in Fig. 4c belongs to what fiber by calculating the distance from each black candidate point to the outer edge of the seed area. But there is no doubt that it is too slow to determine the belonging of the black seed point by calculating the shortest distance between each black and the outer edge of the seed area. And we should calculate the shortest Euclidean Distance of each black candidate point and the outer edge of the seed area when assigned a black candidate point, because the seed area is increasing. In turn, we can regard the seed area is expanding outward if we calculate from the edge of the seed area, and it accords with the idea of the breadth-first algorithm, the schematic diagram is shown in Fig. 5.

The diagram of adhesion separation algorithm based on eight neighborhood breadth-first search shown in Fig. 5. The initial seed region is the area that is surrounded by red border and blue border and the point's value is zero, and then, we can determine the alternative black point belongs to which seed area by calculating the distance of the alternative point to the current edge. The algorithm expands the initial seed area by increasing new outer edge until there is no black alternative point to be calculated. Thus, we can get the single cotton fiber by proposed separation algorithm.

Fig. 5 Sketch of BFS algorithm



2.4 Algorithm Detailed Steps

Figure 6 depicts detailed steps of algorithm which is running on the fiber image:

- (1) Based on original image, we can get the binary images computed by OSTU and K-means. And then, we can combine the two binary images into one binary image. We can solve the low-fidelity problem from single binarization method by using two binarization methods, and it can also reduce noise. We have concluded by experiment that very small area is disturbance, so we can delete it. And then, we get the result shown in Fig. 6b.
- (2) The edge’s binary image gained by merging the binary image, respectively, got by the two binarization methods generally contains small holes, as shown in Fig. 6b. We can get the area of the signal fiber or the adhered fiber through the expansion operation and the filling algorithm, the result of which is shown in Fig. 6c, and it provides the basis for the level set algorithm that is used to the single fiber. Use the level set algorithm on small images shown in rectangle of the Fig. 6c, respectively, and combine the results; then the rough outer contour will emerge, as shown in Fig. 6d.
- (3) The next step is how to divide adhered fiber into single fiber. We find that each fiber has an entocoele when we observe fiber image carefully. We can assign the fiber area calculated by level set algorithm to those entocoeles, if we can get the entocoele, which is the adhesion separation. Merge the edge images respectively achieved by OSTU method and the level set algorithm, which not only solve the problem of fracture edge, but also retain the profile of single fiber. Then, the fiber’s accurate entocoele can be obtained by dilation and erosion, and the result is shown in Fig. 6f.
- (4) Consider the entocoele as the seed region, and use to allocate the target area to each seed region by using adhesion separation algorithm based on clustering thought, and then the final segmentation result emerged, as shown in Fig. 6h.

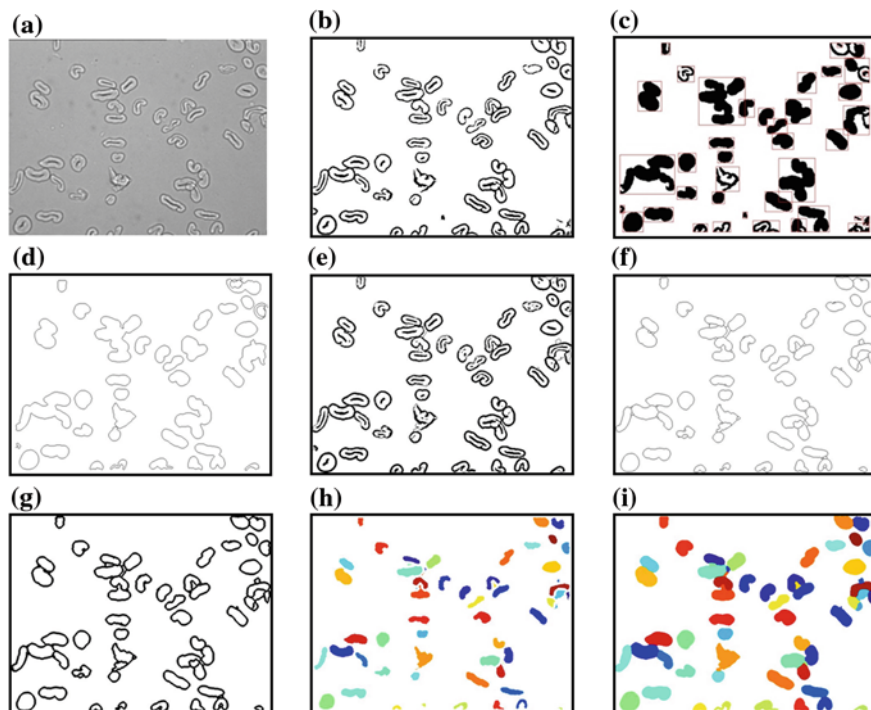


Fig. 6 The diagram of proposed algorithm. **a** Original image, **b** Binary image, **c** Blank image, **d** Result of level set algorithm, **e** Binary image of level set & Otsu method, **f** Image of shrink, **g** Image of dilate, **f** Image of seeds, **h** Result

3 Experimental Results and Discussion

The experiment uses the proposed algorithm and the fiber images provided by Shanghai's pledges inspect bureau to extract the fiber. We write experimental program under the VC++ 2010 environment, and it runs in the PC of a 1.5 GHz Intel core 2 DuoT5250, 2 GB RAM for testing. In the experimental results of nearly a thousand of images show that the proposed algorithm can not only very well solve the questions proposed in front of paper, but also accurately and quickly segment the fibers, and the recognition accuracy can reach 98.6 %.

Respectively, segment the common and serious adhered cotton fiber image use the proposed method in this paper.

Figure 7 is a gray-scale image of 279×316 pixel. It takes 11.08 s to be separated. As can be seen from the Figure, the three parts have been clearly separated, and the segmentation result meets our demand.

Figure 8 is a gray-scale image of 640×484 pixel. It takes 46.18 s to be separated. And we can see that the proposed algorithm can find the fiber's complete profile no matter the fiber is single or adhesive.

Fig. 7 Small image.
a Original image, **b** Result

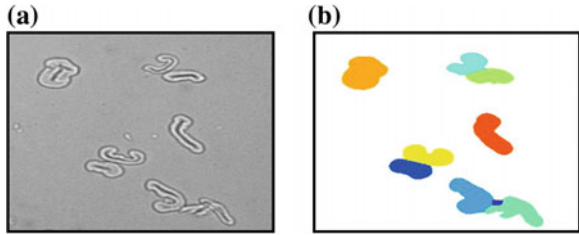


Fig. 8 Image of the more overlapped fiber. **a** Original image, **b** Result

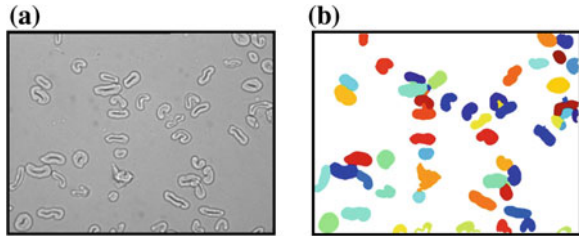


Fig. 9 Image of overlapped fiber. **a** Original image, **b** Result

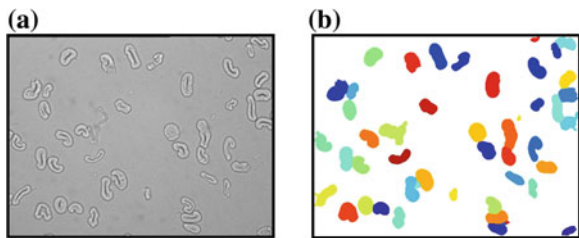


Figure 9 is also a gray-scale image of 640×484 pixel. It takes 40.56 s to be separated. As can be seen from the image, it segments precisely, and almost appears no error segmentation.

The experimental results show that the proposed method can not only resist noise very well, but also segment accurate and complete every fiber. Moreover, the method also solves problem that the common segmentation algorithm cannot be used to separate the adhered fiber.

4 Conclusion

The nature cotton fiber's microscopic image has the feature that the difference between the target area and background is little and each fiber has an entocoele, and according to this, this paper proposes a segmentation algorithm based on level set algorithm combined with clustering method. It sufficiently takes the advantage of the level set that it can get the weak edge when it is used to gain the fiber's outer

contour. In order to improve its efficiency, it proposes the divide and conquer method by combining the level set algorithm with the traditional binary method. It speeds up the segmentation efficiency on the condition of keeping the same segmentation accuracy. In addition, this paper puts forward the separation algorithm based on the clustering method, which according to the feature that each fiber has an entocoele. The proposed algorithm applies the BFS algorithm, which based on Euclidean distance to separate the adhered fiber on the foundation of the level set algorithm. This method can not only quickly and accurately obtain signal cotton fiber, but also guarantee the integrity of the profile, which makes fully preparations for the recognition.

The experimental results also show that the fiber will be divided into two parts, if the fiber's inner has connecting edge, which causes the inaccurate segmentation. And if several fibers are connected as a loop, its inner will be count as a fiber. But in view of the whole situation, this method makes great progress and makes the separation result better compared with the traditional segmentation algorithm.

References

1. Huang Y, Xu B (2002) Image analysis for cotton fibers, part1: longitudinal measurements. *Text Res J* 72(8):713–720
2. Xu XT, Yao L, Wan Y (2010) A new shaped fiber classification algorithm based on SVM [C] The 2nd international workshop on intelligent system and applications, 3–5, China, Wuhan
3. Lu JF, Yang JY, Tang ZM et al (2002) Design of a separating algorithm for overlapping vell images. *J Comput Res Dev* 37(2):228–232
4. Cong PS, Sun JZ (2006) Application of watershed algorithm for segmenting overlapping cells in microscopic image. *J Image Graph* 11(12):1781–1783, T0002
5. Ruberto CD, Dempstr A, Dhan S et al (2002) Analysis of infected blood cell images using morphological operators. *Image Vis Comput* 20(2):133–146
6. Osher S, Sethian JA (1988) Fronts propagating with curvature dependent speed: algorithms based on Hamilton-Jacobi formulation. *J Comput Phys* 79(1):12–49
7. Malladi R, Sethian J, Vemuri BC (2005) Shape modeling with front propagation: a level set approach. *IEEE Trans Pattern Anal Mach Intell* 17(2):158–174
8. Adalsteisson D, Sethian JA (1995) A fast level set method for propagating interfaces. *J Comput Phys* 118(2):269–277
9. Chan TF, Vese LA (2001) Active contours without edges. *IEEE Trans Image Process* 10(2):266–277

Assessment Metrics for Unsupervised Non-intrusive Load Disaggregation Learning Algorithms

Lingling Zhang, Yangguang Liu, Genlang Chen, Xiaoqi He and Xinyou Guo

Abstract Non-intrusive appliance load monitoring (NILM) is the process for disaggregating total electricity consumption into its contributing appliances. Unsupervised NILM algorithm is an attractive method as the need for data annotation can be eliminated. In order to evaluate the performance of unsupervised NILM learning algorithm, most of the research work evaluates the algorithm performance using accuracy type metrics. These assessment metrics can not only identify total disaggregation error, but also distinguish the disaggregation error of each other single appliance. In order to better quantify the nature of disaggregation algorithm, we propose two assessment metrics: the total disaggregation accuracy and the disaggregation accuracy for a single appliance. In this paper, we evaluate the performance of unsupervised disaggregation methods using these assessment metrics. The experiment results show that our assessment metrics can evaluate the unsupervised algorithms effectively.

Keywords NILM · Unsupervised disaggregation algorithms · Assessment metrics

1 Introduction

Energy and sustainability problems represent one of the greatest challenges facing society. Energy used in the residential sector is a significant contributor, but it is a very abstract concept to most consumers. Consumers are often mistaken about how

L. Zhang · Y. Liu (✉) · G. Chen · X. He · X. Guo
Ningbo Institute of Technology, Zhejiang University, Ningbo China
e-mail: ygliu@nit.zju.edu.cn

L. Zhang
Taiyuan University of Science and Technology, Taiyuan China

energy is used in the home, thus knowing about the power of each electric appliance would be most beneficial for conserving energy [1]. Non-intrusive appliance load monitoring [2] is concerned with how the total energy consumed in a household can be disaggregated into individual appliance. The motivations for such a process are twofold. First, informing a household's occupants of how much energy each appliance consume empowers them to take steps toward reducing their energy consumption. Second, if the NILM system is able to determine the current time of use of each appliance, a recommender system would be able to inform a household's occupants of the potential savings through deferring appliance use to a time of day when electricity is either cheaper or has a lower carbon footprint [3]. The aim is to calculate such information and provide it to the consumer through NILM.

Recently researchers have started to explore methods to achieve disaggregated energy sensing without a priori information. Hence, unsupervised learning approaches are needed for a wider applicability of NILM techniques. Shao et al. [4] describes motif mining approach for unsupervised load disaggregation. Power change has been considered in contrast to power consumption in order to recognize individual appliances. The approach is feasible for appliances that have repeatable and distinctive events. Kim et al. [5] presented a probabilistic model of appliance behavior using variants of factorial hidden Markov models. Kolter and Jaakkola [6] proposed an approximate inference algorithm, additive factorial approximate maximum a posteriori, with a convex formulation. However, they have a common problem; due to inconsistency in the assessment metrics it is not possible to draw meaningful comparisons between reported research works [7].

Most of the research works in NILM analyzes the performance of their algorithms using different metrics. Kim et al. adapted a metric from the information retrieval domain, F-measure. F-measure is widely used in this type of evaluation. Researchers also often use receiver operating curves [8] to compare the performance of different models. However, the metrics captures well the total disaggregation error, but does not directly identify error from single appliances. Parson et al. [9] used the average normalized error and root mean square error to evaluate the performance of each approach. In contrast to the previous metrics, the assessment metrics directly use disaggregation error of single appliance, but fail to evaluate the total disaggregation error, so combined with the two metrics is a good choice. In this paper, in order to better quantify the effectiveness of different disaggregation algorithms, we can analyze according to the following aspects: the total disaggregation accuracy of various disaggregation algorithms, the disaggregation accuracy of single appliance for a known database.

Apart from a common assessment metric there is also a lack of reference dataset on which the performance of algorithm can be compared. In order to draw meaning performance comparison of different NILM algorithms, the availability of common datasets is critical. There are currently four datasets that are briefly described as follows [10]. The first is Reference Energy Disaggregation Data Set (REDD) [11]. It is primarily released for the nonevent-based approach, and consists of whole-house and circuit/device level consumption data from six US houses collected.

The second is the Building-Level fully labeled Electricity Disaggregation dataset (BLUED) [12]. It is especially tailored for the evaluation of event-based NILM approaches. It consists of one week of whole-house current and voltage high frequency measurements from one US home. The third is UMASS Smart Home Date Set [13]. It provides power data for two submetered houses in the US. The last is Trace base [14] in which individual appliance consumption data was collected at 1 Hz frequently from 158 appliances instances in a total of 43 different appliance types. In this paper, we evaluate unsupervised disaggregation algorithms using low-frequency power measurements of REDD.

In this paper, we firstly define two types of accuracy, total accuracy, and single appliance disaggregating accuracy to distinguish single appliance error from total disaggregating error. Then we evaluate two unsupervised non-intrusive load disaggregation algorithms from two aspects: total disaggregation error, single appliance disaggregation error. And the experiment results running on six homes of power load data from real homes show the metrics can evaluate disaggregation algorithms effectively.

The remainder of the paper is organized as follows. In the next section, we provide a brief introduction to the NILM disaggregation algorithm and two unsupervised learning methods based on hidden Markov models. In Sect. 3, we describe algorithm performance from two aspects. Subsequently, we do six experiments for all households of REDD data set to evaluate each algorithm in Sect. 4. In Sect. 5, we summarize conclusions and discuss some future work.

2 Problem Descriptions

In this section, we provide an introduction to non-intrusive load monitoring. The problem can be formulated as follows: The power signals from the active appliances aggregate at the entry point of the meter of time t as y_t , where this can be mathematically defined as $y_t = y_t^{(1)} + y_t^{(2)} + \dots + y_t^{(n)}$, where $y_t^{(i)}$, $i = 1, 2, \dots, n$ is the power consumption of individual appliances contributing to the aggregated measurement and n is the total number of active appliances within the time period t . The task of the NILM is to perform decomposition of y_t into appliance specific power signals in order to achieve disaggregated energy sensing. Table 1 describes the notation used in this paper.

Recently, many researches make use of unsupervised learning algorithms and attempts to disaggregate the aggregated measurements directly without performing any sort of event detection. In the section, we introduce briefly two unsupervised disaggregation algorithms: additive factorial approximate maximum a posteriori (AFAMAP) and Exact maximum a posteriori (MAP) [6]. The two algorithm models are the variant of factorial hidden Markov models (FHMM) [15]. In a FHMM, if we consider $Y = (y_1, y_2, \dots, y_T)$ to be the observed sequence then

Table 1 Notations used in this paper

| Symbol | Description |
|--|--|
| N | The number of HMMs |
| M | The number of states |
| T | The number of time steps |
| $q_t^{(i)}$ | The state of device i in time t |
| $\mu_j^{(i)}$ | The mean of the i th HMM for state j |
| $\Sigma_1, \Sigma_2 \in \mathbb{R}^{n \times n}$ | The total observation variance and difference observation variance |
| $\phi^{(i)} \in [0, 1]^{m_i}$ | The initial state distribution for i th HMM |
| $P^{(i)} \in [0, 1]^{m_i \times m_i}$ | The transition matrix for i th HMM |
| $y_t^{(i)}$ | The given true output |
| $\hat{y}_t^{(i)}$ | Predicted individual HMM output |
| T_{error} | The total disaggregation error |
| $N_{\text{error}}(i)$ | The normal disaggregation error for i th device |
| $P_{\text{error}}(i)$ | The absolute percentage error for i th device |

$q = \{q^{(1)}, q^{(2)}, \dots, q^{(M)}\}$ represents the set of underlying state sequences, where $q^i = (q_1^{(i)} + y_2^{(i)} + \dots + y_T^{(i)})$ is the hidden state sequence of the chain i .

Firstly, consider optimization approaches to exact MAP inference and perform optimization over the variable $S = \{S(q_t^{(i)} \in \mathbb{R}^{m_i}, S(q_{t-1}^{(i)}, q_t^{(i)}) \in \mathbb{R}^{m_i \times m_i})\}$. In the exact MAP these variables case are indicators, so that $S(q_t^{(i)})_j = 1 \Leftrightarrow q_t^{(i)} = j$ and $S(q_{t-1}^{(i)}, q_t^{(i)})_{j,k} = 1 \Leftrightarrow q_{t-1}^{(i)} = j, q_t^{(i)} = k$. S must be obey the conditions

$$L = \begin{cases} \sum_j S(q_t^{(i)})_j & = 1 \\ \sum_k S(q_{t-1}^{(i)}, q_t^{(i)})_{j,k} & = S(q_{t-1}^{(i)})_j \\ \sum_k S(q_{t-1}^{(i)}, q_t^{(i)})_{k,j} & = S(q_{t-1}^{(i)})_j \\ S(q_t^{(i)})_j, S(q_{t-1}^{(i)}, q_t^{(i)})_{k,j} & > 0 \end{cases}$$

MAP inference can now be cast as optimizing the log-likelihood of the model. Due to the Gaussian likelihood term, these problems take the form of mixed-integer quadratic programs (MIQPS). For the additive FHMM, this leads to the optimization problem:

$$\min_{S \in L \cap \{0,1\}} \frac{1}{2} \sum_t \left\| y_t = \sum_{i,j} \mu_j^{(i)} S(q_t^{(i)})_j \right\|_{\Sigma_1^{-1}}^2 + \sum_{t,i,j,k} S(q_{t-1}^{(i)})_{j,k} (-\log P_{k,j}^{(i)})$$

We can obtain predicted individual HMM output $\hat{y}_t^{(i)} = \sum_j \mu_j^{(i)} S(q_t^{(i)})_j$.

Secondly, AFAMAP combines additive FHMM and difference FHMM. Naturally, as exact MAP involves non-convex integer constraints, and so some form the relaxation is necessary to obtain a tractable formulation. A typical method for converting binary integer problems into tractable optimization problems is to drop the constraint that S take on integer values. S obeys the one-at-a-time condition. That is, $O = \left\{ S : \sum_{i,j,k \neq j} S(q_{t-1}^{(i)}, q_t^{(i)})_{j,k} \leq 1 \right\}$, ($\Delta\mu_{j,k} = \Delta\mu_j - \Delta\mu_k$). For the difference FHMM and additive FHMM, this leads to the optimization problem:

$$\begin{aligned} \min_{S \in L \cap 0} ; & \frac{1}{2} \sum_t \left\| y_t = \sum_{i,j} \mu_j^{(i)} S(q_t^{(i)})_j \right\|_{\Sigma^{-1}}^2 \\ & + \frac{1}{2} \sum_t \left\| \Delta y_t - \Delta \mu_{k,j}^{(i)} \right\|_{\Sigma_2^{-1}}^2 S(q_{t-1}^{(i)}, q_t^{(i)})_{j,k} \\ & + \sum_{i,j,k} S(q_{t-1}^{(i)})_{j,k} \left(-\log P_{k,j}^{(i)} \right) \end{aligned}$$

We can obtain predicted individual HMM output $\hat{y}_t^{(i)} = \sum_j \mu_j^{(i)} S(q_t^{(i)})_j$.

3 Assessment Metrics

In the section, in order to evaluate disaggregation algorithm more fully and efficiently, we present and define two assessment metrics, total disaggregation error, disaggregation error of single appliance.

3.1 Total Disaggregation Error

To evaluate unsupervised disaggregation algorithm in global, we can use total disaggregation error, which directly measures how well the disaggregation algorithms recovered the total appliance outputs. For the whole family, the total disaggregation error is defined as

$$T_{\text{error}} = \sqrt{\frac{\sum_{t,i} (y_t^{(i)} - \hat{y}_t^{(i)})^2}{\sum_{t,i} (y_t^{(i)})^2}}$$

The numerator in the fraction is the square error sum, and denominator the square sum of the given observation. The less T_{error} is the better effect of the algorithm is. So we can evaluate various disaggregation algorithms by the value of T_{error} .

3.2 Accuracy of Single Appliance

However, the total disaggregation error only shows the disaggregation performance of whole household. The household occupants are more concerned about the power consumption of single appliance, so performance should be assessed according to how accurately a NILM can infer the energy consumption of each appliance. Next we consider appliance-based accuracy from two aspects in the meantime.

3.2.1 Proportion Error

In aggregate power, each electric appliance consumes different energy. So, we can evaluate the performance of each algorithm by computing the proportion of the power that the single appliance consumed in aggregate power.

The $\text{Tru}(i)$ presents the true proportion of the power that the i th appliance consumed. The $\text{Dis}(i)$ presents the proportion of the i th appliance after disaggregation. $P_{\text{error}}(i)$ is defined as

$$P_{\text{error}}(i) = |\text{Dis}(i) - \text{Tru}(i)|$$

where $\text{Tru}(i) = \sum_t (y_t^{(i)} / y_t) / T$ and $\text{Dis}(i) = \sum_t (\hat{y}_t^{(i)} / y_t) / T$. The smaller the value for $P_{\text{error}}(i)$, the nearer $\text{Dis}(i)$ approximates to $\text{Tru}(i)$. Otherwise, the more $\text{Dis}(i)$ deviates from $\text{Tru}(i)$. For example, if $P_{\text{error}}(i) = 0$, it means that $\text{Dis}(i)$ is equal to $\text{Tru}(i)$.

3.2.2 Normal Disaggregation Error

To evaluate disaggregation error for single appliance, we also can use the normal disaggregation error, which measures how well the algorithms disaggregated the individual appliance. Similar to the total disaggregation error, it is defined as

$$N_{\text{error}}(i) = \sqrt{\frac{\sum_t (y_t^{(i)} - \hat{y}_t^{(i)})^2}{\sum_t (y_t^{(i)})^2}}$$

Lower the value of $N_{\text{error}}(i)$ equates to better performance of disaggregation algorithms.

4 Experiment Results

In order to compare disaggregation algorithm, we use REDD data set described by Kolter and Johnson [11]. This data set is chosen as it is an open data set collected specifically for evaluating NILM methods. The data set comprises six houses, for which both household aggregate and circuit-level power demand data are collected. Even though each household has more than ten appliances, we choose six usual electric appliances of each home to test the performance of algorithms on all the six households from REDD data set. Because the other appliances were not active, that is, either they were never turned on, or consumed fewer power. To evaluate the performance of the method, we used the performance metrics described in Sect. 3.

Table 2 shows the disaggregation performance of two algorithms on the six households we consider. They describe the proportion of total energy disaggregated correctly, proportion error, and disaggregation error of single appliance using MAP and AFAMAP disaggregation algorithm. Table 2 describes the total disaggregation error of six households. As seen in the two tables, in each household, the proportion error of appliance using AFAMAP algorithm is much smaller than MAP algorithm. The disaggregate error of single appliance as well as total disaggregation error are much smaller than those of MAP. When the consumed power of device is low relatively, the proportion error of MAP algorithm is likely to be lower than that of AFAMAP algorithm. Specifically, we analysis the experiment results taking household 3 and household 6 as examples.

As seen in Fig. 1, the proportion error is absolute difference between predicted proportion and true proportion. Upper-left and lower-left corners of the figure represent the proportion error and disaggregation error of individual appliance in home 3, respectively. And the upper-right and lower-right are those of home 6. In home 3, the total disaggregation error using AFAMAP algorithm is lower than MAP algorithm. However, the proportion error and disaggregation error of the fourth appliance using AFAMAP algorithm are larger than using MAP. And proportion error of the other five appliance using AFAMAP algorithm is lower than using MAP. In general, the proportion error of six appliances using MAP algorithm is below 20 %, while using AFAMAP algorithm is below 18 %. In the home 6, the proportion error of the second appliance using AFAMAP algorithm is larger than using MAP, but disaggregation error is lower than using MAP. The proportion error and disaggregation error of appliance 1, 3, 4, 5, 6 are similar for the two algorithms. And for each home, the total disaggregation error is smaller than MAP algorithm as in the Table 3. That is to say, combining proportion error with normal disaggregation error is much more effective when we evaluate disaggregation algorithms.

Table 2 True Percent of single appliance, Proportion error and normal disaggregation error of single appliance in six homes

| Home and device | Tru% | MAP | AFAMAP | MAP | AFAMAP |
|-----------------|-------|----------------------|----------------------|----------------------|----------------------|
| | | $P_{\text{error}}\%$ | $P_{\text{error}}\%$ | $N_{\text{error}}\%$ | $N_{\text{error}}\%$ |
| Home 1 device 1 | 18.47 | 3.51 | 0.60 | 0.87 | 0.81 |
| Home 1 device 2 | 8.37 | 4.90 | 4.30 | 0.73 | 0.71 |
| Home 1 device 3 | 33.25 | 4.77 | 5.34 | 0.76 | 0.83 |
| Home 1 device 4 | 24.39 | 4.62 | 4.46 | 0.61 | 0.52 |
| Home 1 device 5 | 4.59 | 2.10 | 2.10 | 0.81 | 0.82 |
| Home 1 device 6 | 0.94 | 0.35 | 5.80 | 0.82 | 0.71 |
| Home 2 device 1 | 5.08 | 1.95 | 1.85 | 0.41 | 0.40 |
| Home 2 device 2 | 11.43 | 0.58 | 0.47 | 0.05 | 0.04 |
| Home 2 device 3 | 1.03 | 0.38 | 0.31 | 0.92 | 0.91 |
| Home 2 device 4 | 5.95 | 1.09 | 1.03 | 0.15 | 0.15 |
| Home 2 device 5 | 6.35 | 0.71 | 0.69 | 0.17 | 0.16 |
| Home 2 device 6 | 38.85 | 4.68 | 3.95 | 0.13 | 0.13 |
| Home 3 device 1 | 33.71 | 19.66 | 18.37 | 0.68 | 0.72 |
| Home 3 device 2 | 16.02 | 4.23 | 5.09 | 0.37 | 0.32 |
| Home 3 device 3 | 16.42 | 8.36 | 1.94 | 0.91 | 0.61 |
| Home 3 device 4 | 15.28 | 4.59 | 1.28 | 0.93 | 0.95 |
| Home 3 device 5 | 0.29 | 0.09 | 0.05 | 0.32 | 0.39 |
| Home 3 device 6 | 3.71 | 0.52 | 0.40 | 0.18 | 0.17 |
| Home 4 device 1 | 60.67 | 1.08 | 1.83 | 0.13 | 0.26 |
| Home 4 device 2 | 0.94 | 0.04 | 0.05 | 0.15 | 0.15 |
| Home 4 device 3 | 15.69 | 11.07 | 1.71 | 0.65 | 0.61 |
| Home 4 device 4 | 1.03 | 0.65 | 1.24 | 0.16 | 0.15 |
| Home 4 device 5 | 10.48 | 2.65 | 0.05 | 0.55 | 0.51 |
| Home 4 device 6 | 15.45 | 10.93 | 0.34 | 0.92 | 0.58 |
| Home 5 device 1 | 2.14 | 0.11 | 0.09 | 0.16 | 0.16 |
| Home 5 device 2 | 41.25 | 1.35 | 0.99 | 0.02 | 0.01 |
| Home 5 device 3 | 2.29 | 0.51 | 0.29 | 0.23 | 0.17 |
| Home 5 device 4 | 9.85 | 1.36 | 1.25 | 0.14 | 0.12 |
| Home 5 device 5 | 2.91 | 0.27 | 0.33 | 0.02 | 0.21 |
| Home 5 device 6 | 4.79 | 0.82 | 0.81 | 0.22 | 0.22 |
| Home 6 device 1 | 1.57 | 0.09 | 0.09 | 0.12 | 0.11 |
| Home 6 device 2 | 13.35 | 3.98 | 6.45 | 0.47 | 0.32 |
| Home 6 device 3 | 7.39 | 0.20 | 0.08 | 0.03 | 0.02 |
| Home 6 device 4 | 25.68 | 0.59 | 0.55 | 0.09 | 0.07 |
| Home 6 device 5 | 34.11 | 5.71 | 6.48 | 0.22 | 0.20 |
| Home 6 device 6 | 1.13 | 0.03 | 0.05 | 0.08 | 0.09 |

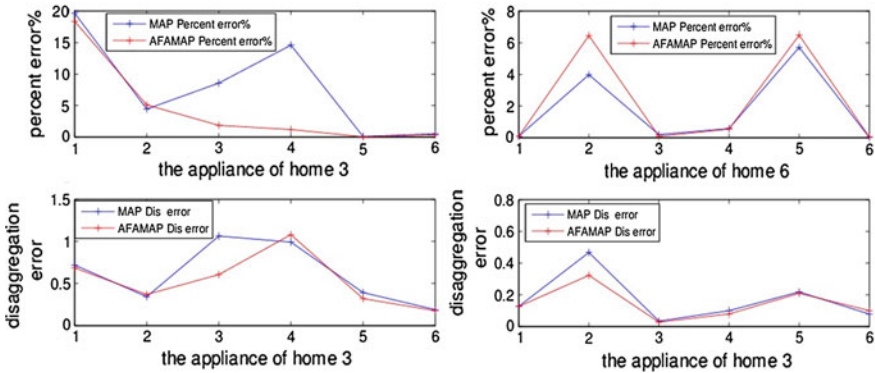


Fig. 1 Proportion error and normal disaggregation error of home 3(left) and home 6(right)

Table 3 The total disaggregation error of six homes

| T_{error} | Home 1 | Home 2 | Home 3 | Home 4 | Home 5 | Home 6 |
|-------------|--------|--------|--------|--------|--------|--------|
| MAP | 0.52 | 0.26 | 0.13 | 0.14 | 0.31 | 0.11 |
| AFAMAP | 0.14 | 0.25 | 0.05 | 0.04 | 0.09 | 0.08 |

5 Conclusions

In this paper, we describe assessment metrics of unsupervised disaggregation algorithms from two aspects: the total disaggregation accuracy and the disaggregation accuracy of single appliance. We evaluate two unsupervised disaggregation algorithms using the two assessment metrics. Through evaluation of two metrics using real data from six households, we have shown that the two metrics can evaluate unsupervised disaggregation algorithms fully.

Acknowledgements This work was supported by Scientific Research Fund of Zhejiang Provincial Education Department, China (Grant No. Y201327368).

References

1. Ritchie JB, McDougall GH, Claxton JD (1981) Complexities of household energy consumption and conservation. *J Consum Res* 8:233–242
2. Hart GW (1992) Nonintrusive appliance load monitoring. *Proc IEEE* 80(12):1870–1891
3. Parson O, Ghosh S, Weal M, Rogers A (2012) Non-intrusive load monitoring using prior models of general appliance types. In: *AAAI*, Apr 2012
4. Shao H, Marwah M, Ramakrishnan N (2013) A temporal motif mining approach to unsupervised energy disaggregation: applications to residential and commercial buildings. *Power (W)* 250(1700):2250

5. Kim H, Marwah M, Arlitt MF, Lyon G, Han J (2011) Unsupervised disaggregation of low frequency power measurements. In: Proceedings of the 11th SIAM international conference on data mining, pp 747–758
6. Kolter JZ, Jaakkola T (2012) Approximate inference in additive factorial HMMs with application to energy disaggregation. In: International conference on artificial intelligence and statistics
7. Zoha A, Gluhak A, Imran MA, Rajasegarar S (2012) Non-intrusive load monitoring approaches for disaggregated energy sensing: a survey. *Sensors* 12(12):16838–16866
8. Fawcett T (2006) An introduction to ROC analysis. *Pattern Recogn Lett* 27(8):861–874
9. Parson O, Ghosh S, Weal M, Rogers A (2011) Using hidden markov models for iterative non-intrusive appliance monitoring. In: *Neural Information Processing Systems, Workshop on Machine Learning for Sustainability*, 2011
10. Pereira L (2013) Towards automated non-intrusive load monitoring performance evaluation. In: *ICT4S 2013: Proceedings of the first international conference on information and communication technologies for sustainability*, ETH Zurich, 14–16 Feb 2013
11. Kolter JZ, Johnson MJ (2011) Redd: a public data set for energy disaggregation research. In: *Proceedings of the SustKDD workshop on data mining applications in sustainability*, Aug 2011, pp 1–6
12. Anderson K, Ocleanu A, Benitez D, Carlson D, Rowe A, Bergés M (2012) BLUEd: a fully labeled public dataset for event-based non-intrusive load monitoring research. In: *Proceedings of the 2nd KDD workshop on data mining applications in sustainability*, Beijing, China, Aug 2012, pp 12–16
13. Barker S, Mishra A, Irwin D, Cecchet E, Shenoy P, Albrecht J (2012) Smart*: an open data set and tools for enabling research in sustainable homes. In: *SustKDD*, Aug 2012
14. Reinhardt A, Baumann P, Burgstahler D, Hollick M, Chonov H, Werner M, Steinmetz R (2012). On the accuracy of appliance identification based on distributed load metering data. In: *IEEE international conference on Sustainable internet and ICT for sustainability (SustainIT)*, Oct 2012, pp 1–9
15. Ghahramani Z, Jordan MI (1997) Factorial hidden Markov models. *Mach learn* 29(2–3): 245–273

Optimal Sensor Placement of Long-Span Cable-Stayed Bridges Based on Particle Swarm Optimization Algorithm

Xun Zhang, Ping Wang, Jian-Chun Xing and Qi-Liang Yang

Abstract An optimization based on particle swarm optimization (PSO) algorithm was put forward for optimal sensor placement (OSP) in the structural health monitoring system (SHMs) of long-span cable-stayed bridges. The mathematical model was firstly presented and dual-structure coding was adopted to improve the individual encoding method in the PSO algorithm. Fitness function was established to solve the optimal problem based on the root-mean-square value of off-diagonal elements of modal assurance criterion matrix. Finally, one long-span cable-stayed bridge was taken as an example, and implemented the sensor placement based on PSO. The stimulation results show that the proposed PSO algorithm has better improvement in search ability and computation efficiency when compared with genetic algorithm (GA).

Keywords Optimal sensor placement · Particle swarm optimization · Cable-stayed bridge · Structural health monitoring

1 Introduction

In recent years, with the rapid development of bridge technology, the complex large-span bridges are emerging. There will be various damages because of the roles of external factors during these bridges' service period and will cause sudden destruction and huge economic losses if these damages are not processed timely. In order to monitor the health of the bridge, it is necessary to establish the structural health monitoring system (SHMs). Since sensor system is one of the

X. Zhang (✉) · P. Wang · J.-C. Xing · Q.-L. Yang
Intellectualization of National Defense Engineering,
PLA University of Science and Technology, Nanjing 210007, China
e-mail: xunzhang893@163.com

most important parts of the SHMs, optimal sensor placement (OSP) can not only reduce the cost, but also acquire the most reliable and comprehensive structural health information [1].

OSP can be regarded as an optimization problem that is the application of optimal theory in sensor placement. Using artificial intelligent algorithm to solve the issue becomes an investigation hotspot in recent years. Genetic algorithm (GA) as one of the intelligent algorithms occupies the property of global search, robustness, and high parallel efficiency. Many researchers studied this algorithm and applied it in the sensor placement of SHMs successfully, for example, Liu et al. [2] presented a decimal two-dimensional array coding approach instead of binary coding method to code the solutions. Ma et al. [3] proposed a kind of hybrid genetic algorithm to find the global optimum of the placement for sensors in SHMs for Nanjing Yangtze River Bridge (NYRB), and the algorithm is stable with rapid convergence. Dhuri and Seshu [4] presented multi-objective genetic algorithm to identify the optimal locations and sizing of piezoelectric sensors/actuators. These locations and sizing gave good controllability with minimal changes in system natural frequencies. Yi et al. [5] studied the dual-structure coding GA for selecting optimal sensor locations of Guangzhou New TV Tower. The optimal results demonstrated the algorithm can get better results with lower computational iterations.

Particle swarm optimization (PSO) algorithm, which is an evolution compute technique based on swarm intelligence, was firstly proposed by Kennedy and Eberhart [6] who were inspired by birds seeking food. This algorithm precludes the complex selection, crossover, and mutation operations of GA. It is easy in implementation and there are fewer parameters to adjust, and it has faster convergence rate. This algorithm has been successfully applied in some engineering field currently [7].

In view of the superior of PSO algorithm to solve optimal problems, this paper adopted dual-structure coding to improve the individual encoding method of PSO algorithm firstly, and then applied this improved algorithm to OSP in SHMs for an example of a long-span cable-stayed bridge. Comparing with other placement methods certified the superiority of the proposed algorithm. Finally, a few concluding remarks are given.

2 Mathematic Model

It is impossible to place sensors at every degree of freedom (DOF) of bridge because the high cost of sensors, data acquisition system, and data processing system. It is better to use few sensors to acquire the maximum structural health information, and make sure the sensor locations are the best. Assume the number of placement node is m , and compose a set N , where $N = \{n_1, n_2, \dots, n_m\}$, the DOF of node n_i is f_i ($i = 1, 2, \dots, m$), these nodes constitute a set X with $f_1 + f_2 + \dots + f_m$, now, we want to select x_1, x_2, \dots, x_s from the set X to place

sensors, so it can be presented as an optimal problem, which consist of objective function and constraint condition as follows [8]:

$$\begin{cases} \min & F(x) \\ \text{s.t.} & x = (x_1, x_2, \dots, x_s) \end{cases} \quad (1)$$

where $F(x)$ is the objective function with x_1, x_2, \dots, x_s . To solve the problem, the key point is how to determine variable x_j ($j = 1, 2, \dots, n$) and make objective function to be minimum, if $x_j = 1$, then a sensor is placed at the j th DOF, if $x_j = 0$, then no sensor is placed there. So if x_j is confirmed, the locations will be determined.

3 Particle Swarm Optimization

PSO algorithm is a randomly search algorithm that has been developed over the past decade. The new populations are generated through cooperation and competition among the particles and use fitness to evaluate the solution directly, thus to guide the optimization search. The algorithm uses a simple velocity-displacement model, which can not only avoid the complex genetic operation of the GA, but also get a higher efficiency of parallel search.

The position of each particle is used as the potential solution of n -dimensional space in standard PSO algorithm. It is assumed that each particle searches for the optimal value in the n -dimensional space, $X_i = (X_{i1}, X_{i2}, \dots, X_{in})$ represents the i th particle's position, where, $X_{id} \in [l_d, u_d]$, $d \in [1, n]$, l_d, u_d is the upper and lower limits of the d -dimensional position space. $V_i = (V_{i1}, V_{i2}, \dots, V_{in})$ is the velocity, which is used to control the particle flight direction and distance, and is limited by the maximum velocity of V_{\max} . P_i is the position of the best fitness achieved so far by the i th particle, and P_g is the global best fitness by the whole population. The particles update their own velocity and position based on the following two equations.

$$V_{id}^{t+1} = wV_{id}^t + c_1 \text{rand}() (P_{id} - X_{id}^t) + c_2 \text{rand}() (P_{gd} - X_{id}^t) \quad (2)$$

$$X_{id}^{t+1} = X_{id}^t + V_{id}^{t+1} \quad (3)$$

where w is the inertia weight, c_1, c_2 are the acceleration coefficients which usually take 2, rand is a rand number, generated uniformly in the range (0, 1), V_{id}^t and X_{id}^t are the velocity and position that the i th particle of t th iteration in the d -dimensional space. Shi and Eberhart [9] studied the w and pointed out that a large w facilitated global search while a small w facilitated local search. In order to balance the global and local search capabilities, a linear w adjustment strategy was proposed.

$$w(t) = w_{\max} - (w_{\max} - w_{\min}) \frac{t}{\text{iter}_{\max}} \quad (4)$$

where w_{\min} is the minimum value of the w , w_{\max} is the maximum value of the w , iter_{\max} is the maximum iteration, t is the current iteration.

3.1 Coding

Coding is the primary problem in application of PSO algorithm. It directly determines how to carry out the evolution of the population and the efficiency of evolutionary computation. Huang et al. [10] proposed an OSP method based on dual-structure coding GA and pointed out that this method can improve the search capability for constraint problems. In order to obtain better results, this paper also used dual-structure coding method to the particles' positions encoding of PSO algorithm. The specific method is as follows.

The extra code is generated randomly by the method of shuffling and put on the upper line firstly. Then the variable code is generated randomly (with the value of 0 or 1) and put on the lower line. Thus, an individual position is constituted with the extra code and the variable code. The particles' position that is obtained by the dual-structure method is shown as Table 1. The upper line is extra code line, $P(i)$ is the extra code of K_j , $P(i) = j$, the lower line is corresponding value to $P(i)$ of variable $K_{P(i)}$. When decoding, constraint conditions should be taken into consideration. It combines the extra codes of variables and penalty function to decode these variables. If a variable does not accord the constraint conditions, its corresponding value is supposed to be 0, or 1 otherwise until all variables are dealt with.

3.2 Fitness Function

Fitness function is the criterion that is used to judge the quality of individuals in evolutionary computation. PSO algorithm evaluates the solution through calculating and comparing the value of the fitness function in search space. So the fitness function is very important for PSO algorithm. Carne and Dohrmann [11] considered the modal assurance criterion (MAC) matrix was a good tool to evaluate the mode vector angle. Its matrix elements are expressed as:

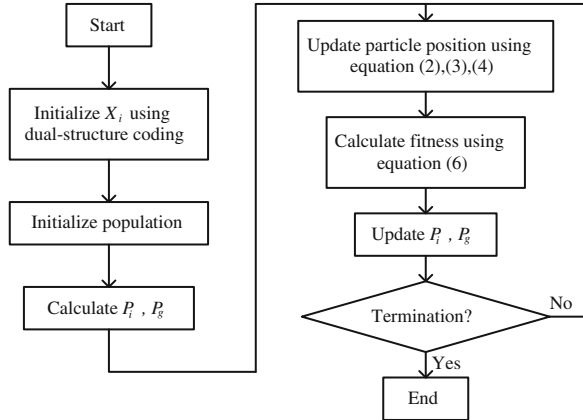
$$\text{MAC}_{ij} = \frac{(\phi_i^T \phi_j)^2}{(\phi_i^T \phi_i)(\phi_j^T \phi_j)} \quad (5)$$

where ϕ_i and ϕ_j represent the i th and j th column vectors of the matrix ϕ . In the MAC matrix defined by Eq. (5), the off-diagonal elements represent the intersection angle between the two different modal vectors and value is bound between 0 and 1. As the root-mean-square reflects the magnitude of a group of data and is a

Table 1 The new individual generated by dual-structure coding method

| | | | | | | |
|---------------|----------|----------|-----|----------|-----|----------|
| Extra code | $P(1)$ | $P(2)$ | ... | $P(i)$ | ... | $P(n)$ |
| Variable code | $K_p(1)$ | $K_p(2)$ | ... | $K_p(i)$ | ... | $K_p(n)$ |

Fig. 1 Flow chart of optimal sensor placement by using PSO algorithm



measurement of the size of this set of data. In order to measure the entire size of off-diagonal elements for MAC matrix, this paper selects the root-mean-square value of off-diagonal elements as the optimization objective function [12], that is:

$$f = \sqrt{\frac{1}{n} \sum_{i=1}^n X_i^2} \tag{6}$$

where X_i is the value of off-diagonal element of MAC matrix, and this fitness function reflects the change of off-diagonal elements of MAC matrix, the smaller the value of fitness function, the better.

3.3 Algorithm Design

From what has been discussed above, the sensor placement algorithm can be designed. Figure 1 is the program flow chart of the OSP based on PSO algorithm.

4 Case Study

This paper analyzes a 200 + 400 + 200 m three-span twin towers and double cable planes pre-stressed concrete cable-stayed bridge. There is isolation bearing connection between pier beams. Full-bridge length is 800 m and the main span is

Fig. 2 The finite element model of long-span cable-stayed bridge was established by ANSYS

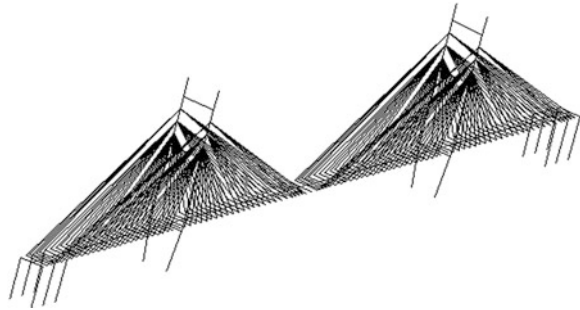


Table 2 First ten mode frequencies and descriptions of cable-stayed bridge by modal analysis

| | | | | | |
|----------------|---------|---------|---------|---------|---------|
| Mode order | 1 | 2 | 3 | 4 | 5 |
| Frequency (Hz) | 0.10463 | 0.27262 | 0.31498 | 0.39785 | 0.48316 |
| Mode order | 6 | 7 | 8 | 9 | 10 |
| Frequency (Hz) | 0.49986 | 0.65922 | 0.67557 | 0.74887 | 0.77755 |

400 m. The main structure are the main beam, main tower fishbone beams, the main pier, side piers, and cable-stayed, etc. The finite element modal analysis is carried out by ANSYS 10.0, and the fishbone model is adopted, finite element model shown in Fig. 2.

The frequencies and mode shapes of cable-stayed bridge can be obtained through modal analysis. Taking into account the lower modes with larger participation factors, only the first 10 mode shapes are extracted (shown in Table 2).

4.1 Algorithm Parameters Set

As parts of the bridge positions, such as the underwater and the pier are difficult to install sensors, this paper only selects deck part of the finite element model of 387 nodes, and places sensors in the DOFs of these nodes. The OSP program based on PSO algorithm is tested by MATLAB7.1 platform. The specific setting of the other parameters of the algorithm is shown in Table 3.

4.2 Number of Sensors

Theoretically, the more the number of sensors are, the more the modal information will be obtained. But excessive number of sensors will improve testing costs, thus increase the costs of the SHMs. It is necessary to select the appropriate number. In order to compare the results with different number of sensors, this paper takes $s = 10$, $s = 20$, $s = 30$ DOFs to place sensors. The procedures run on a host computer with Pentium dual-core processor, clock at 3.2 GHz and memory 2.0G.

Table 3 The parameters set in particle swarm optimization algorithm

| Parameter | Set | Parameter | Set |
|-----------------------------|---------|------------------------------|-----|
| Population size N | 80 | Maximum velocity v_{max} | 100 |
| Inertia weight range | 0.9–0.4 | Accelerate coefficient c_1 | 2 |
| Maximum iteration t_{max} | 500 | Accelerate coefficient c_2 | 2 |

It can obtain different evolutionary curves and MAC value, as shown from Figs. 3, 4, and 5.

As can be seen from the evolutionary curves, PSO algorithm can converge to an optimal value with three different numbers of sensors. It shows that the algorithm can search in the direction to minimize the objective function. When $s = 30$ the optimal value is the smallest. As can be seen from the MAC value, the off-diagonal elements of MAC matrix decrease gradually with the increase of the sensors, and when $s = 30$, the overall value of these off-diagonal elements preserve the lowest level, so it can get a better performance with respect to the two others. Therefore, considering the evolutionary curve and MAC value, the number of sensors is taken as 30 so as to obtain a better result.

4.3 Comparison of Placement Results

In order to illustrate the validity of the sensor placement based on PSO algorithm, using accumulative method [13] and Effective Independence (EI) method [14] to place sensors for the case of 30 ones. The MAC value obtained as shown in Fig. 6. The off-diagonal elements of these two methods are larger than PSO algorithm optimized ones, so this algorithm can be used in the OSP.

To illustrate the superiority of PSO algorithm, we can compare its optimal results with GA. For comparison, some of the major operations and parameters of GA set the same with PSO algorithm, mainly in the following aspects: (a) Use the same coding method; (b) Select the same fitness function; (c) Populations parameters set the same. Where the population size $N = 80$, maximum iteration $t_{max} = 500$. The differences are the genetic operators, where crossover probability $P_c = 0.8$, mutation probability $P_m = 0.001$. To ensure the reliability of the algorithms, these two methods calculated 10 times continuously on the same computer. Comparison of the average optimal fitness value curve of these two algorithms is shown in Fig. 7, and comparison of the optimal results can be seen in Table 4.

In Fig. 7, it can be seen that these two algorithms have roughly the same trend of convergence, and the PSO results are better than the GA, but the accuracy improvement is not great. In addition, analyzing the optimal results in Table 4 can come to the same conclusion. It indicates that these two algorithms get similar

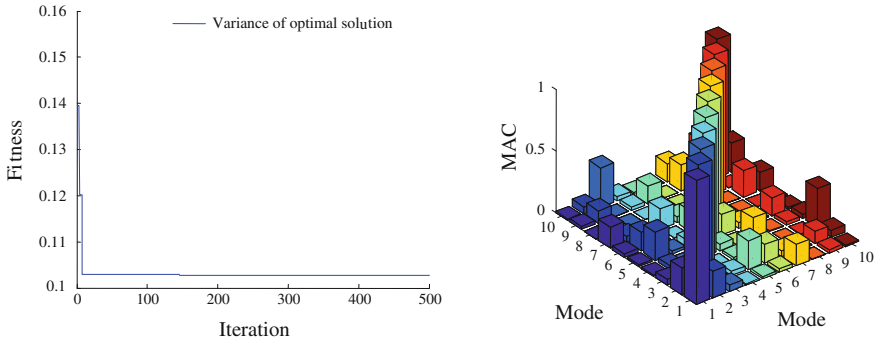


Fig. 3 The evolution curve (left) and MAC value (right) of 10 sensors from PSO algorithm

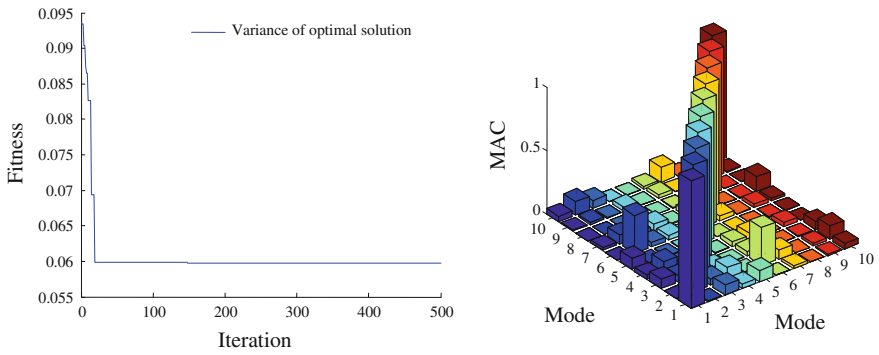


Fig. 4 The evolution curve (left) and MAC value (right) of 20 sensors from PSO algorithm

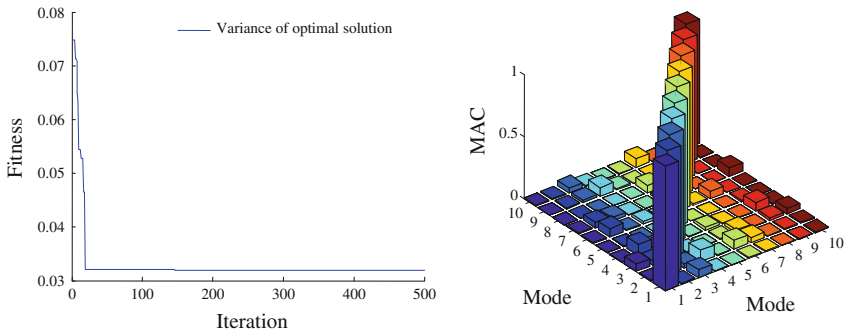


Fig. 5 The evolution curve (left) and MAC value (right) of 30 sensors from PSO algorithm

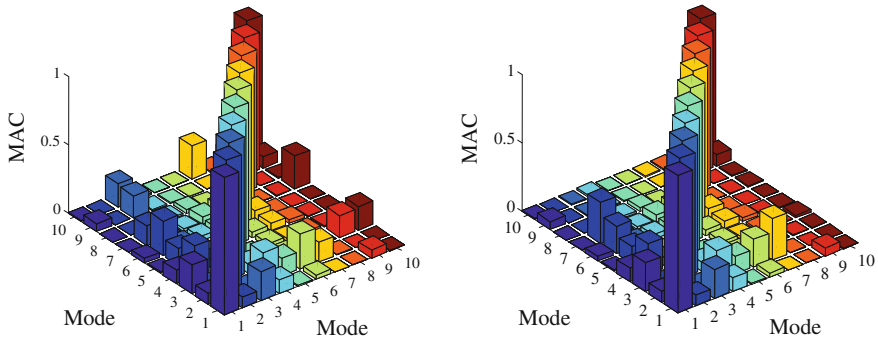


Fig. 6 The MAC value obtained by cumulative method (left) and EI method (right)

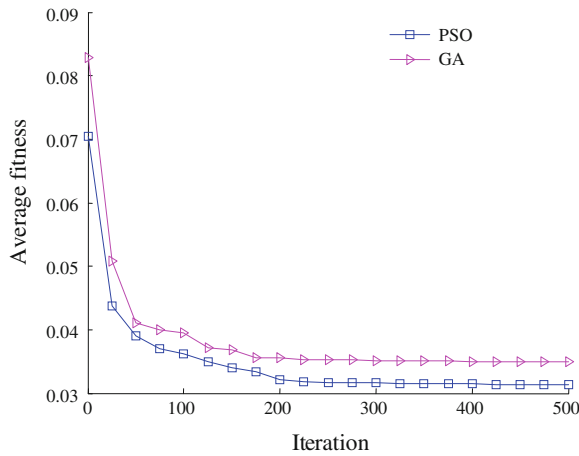


Fig. 7 Comparison of the average fitness value curve of GA and PSO algorithm

Table 4 Comparison of the optimal results of GA and PSO algorithm

| Algorithm | 1 | 2 | 3 | 4 | 5 | 6 | 7 | 8 | 9 | 10 | Average time (s) |
|-----------|-------|-------|-------|-------|-------|-------|-------|-------|-------|-------|------------------|
| GA | 0.034 | 0.042 | 0.039 | 0.033 | 0.039 | 0.032 | 0.040 | 0.032 | 0.033 | 0.035 | 18.26 |
| PSO | 0.029 | 0.035 | 0.026 | 0.033 | 0.029 | 0.039 | 0.029 | 0.035 | 0.026 | 0.033 | 9.850 |

results. But comparing the average time-consuming of each computation, PSO algorithm saves nearly half the time than GA, so it can greatly improve the computation efficiency of OSP based on PSO algorithm. The main reason for this result is that PSO algorithm avoids the complex genetic operators compared with GA. Thus, reducing the computation complexity of PSO algorithm significantly, and improving execution efficiency and saving computation time.

5 Conclusions and Future Work

For solving the OSP of long-span cable-stayed bridge, the PSO algorithm is studied to optimize the sensors placement. Following are the conclusions of OSP for a long-span cable-stayed bridge example.

PSO algorithm is simple, easy to understand, and the computation process is easy to program. The analysis of the stimulation example shows that this method can be applied in the long-span cable-stayed bridge OSP, and better results can be obtained. In initializing the population, we used dual-structure code to improve the encoding. In optimization process, linear decreasing inertia weight is adopted to balance the global and local search capacities of particles. So it can escape from the local optima, and also ensure the convergence of the algorithm at the same time. PSO algorithm abandons the complex genetic operations, so that it has higher computation efficiency and consumes less computation time than the GA for OSP problems. To determine the number of sensors, this paper just compares the sensor placement results of three cases to select the appropriate number and has not yet proposed system method. How to determine the number of sensors will be the next focus.

References

1. Shan DS, Wan ZH, Li Q (2011) Optimal sensors placement for long-span railway steel truss cable-stayed bridges. In: 2011 Third international conference on measuring technology and mechatronics automation, IEEE, vol 2, pp 795–798. doi:[10.1109/ICMTMA.2011.482](https://doi.org/10.1109/ICMTMA.2011.482)
2. Liu W, Gao W, Sun Y, Xu MJ (2008) Optimal sensor placement for spatial lattice structure based on genetic algorithms. *J Sound Vib* 317(1):175–189. doi:[10.1016/j.jsv.2008.03.026](https://doi.org/10.1016/j.jsv.2008.03.026)
3. Ma G, Huang FL, Wang XM (2008) Optimal placement of sensors in monitoring for bridge based on hybrid genetic algorithm. *J Vib Eng* 21(2):191–196. doi:[10.3969/j.issn.1004-4523.2008.02.016](https://doi.org/10.3969/j.issn.1004-4523.2008.02.016)
4. Dhuri KD, Seshu P (2009) Multi-objective optimization of piezo actuator placement and sizing using genetic algorithm. *J Sound Vib* 323(3):495–514. doi:[10.1016/j.jsv.2009.01.007](https://doi.org/10.1016/j.jsv.2009.01.007)
5. Yi TH, Li HN, Gu M (2011) Optimal sensor placement for structural health monitoring based on multiple optimization strategies. *Struct Des Tall Spec Build* 20(7):881–900. doi:[10.1002/tal.712](https://doi.org/10.1002/tal.712)
6. Kennedy J, Eberhart RC (1995) Particle swarm optimization. *IEEE international conference on neural networks*, IEEE, pp 1942–1948. doi:[10.1109/ICNN.1995.488968](https://doi.org/10.1109/ICNN.1995.488968)
7. Pan HX, Wei XY (2010) Optimal placement of sensor in gearbox fault diagnosis based on VPSO. 2010 Sixth international conference on natural computation, IEEE, pp 3383–3387. doi:[10.1109/ICNC.2010.5583680](https://doi.org/10.1109/ICNC.2010.5583680)
8. Wang H, Li AQ, Jiao CK, Spencer BF (2010) Damper placement for seismic control of super-long-span suspension bridges based on the first-order optimization method. *Sci China Technol Sci* 53(7):2008–2014. doi:[10.1007/s11431-010-4009-1](https://doi.org/10.1007/s11431-010-4009-1)
9. Shi YH, Eberhart RC (1999) Empirical study of particle swarm optimization. 1999 Congress on evolutionary computation, IEEE, p 3. doi:[10.1109/CEC.1999.785511](https://doi.org/10.1109/CEC.1999.785511)
10. Huang MS, Li J, Zhu H (2009) Optimal sensor layout for bridge health monitoring based on dual-structure coding genetic algorithm. 2009 International conference on computational intelligence and software engineering, IEEE, pp 1–4. doi:[10.1109/CISE.2009.5366481](https://doi.org/10.1109/CISE.2009.5366481)

11. Carne TG, Dohrmann CR (1995) A modal test design strategy for modal correlation. Proceeding—SPIE the International Society for Optical Engineering, pp 927–927
12. Liu Y, Bi D, Li ZX (2009) Optimal placement of accelerometers in long cable-stayed bridges based on genetic algorithm. *J Southeast Univ (Nat Sci Ed)* 39(4):825–829. doi:[10.3969/j.issn.1001-0505.2009.04.034](https://doi.org/10.3969/j.issn.1001-0505.2009.04.034)
13. Liu J, Huang WP (2003) Application of a cumulative method of sensor placement for offshore platforms. *J Ocean Univ Qingdao Chin Ed* 33(3):476–482. doi:[10.3969/j.issn.1672-5174.2003.03.019](https://doi.org/10.3969/j.issn.1672-5174.2003.03.019)
14. Kammer DC, Tinker ML (2004) Optimal placement of triaxial accelerometers for modal vibration tests. *Mech Syst Signal Proc* 18(1):29–41. doi:[10.1016/S0888-3270\(03\)00017-7](https://doi.org/10.1016/S0888-3270(03)00017-7)

A Method for the Shortest Distance Routing Considering Turn Penalties

Lihua Zhang and Tao Wang

Abstract A shortest distance route is crucial in emergent navigations including rescue and military applications. This paper proposes a method of the shortest distance routing considering turn penalties. First, unnavigable shallow areas are obtained based on tracing of the safety contours, and they are processed together with other fixed obstacle areas. Then paths bypassing two sides of obstacle areas are analyzed, a binary tree of route is created, navigable paths are tested, and a shortest route is acquired automatically. Finally, a penalty is considered for each turn, and different penalties of turn angles are further analyzed. Experimental results demonstrate that the proposed method can acquire a shortest distance route considering turn penalties.

Keywords Shortest distance · Route · Turn penalties · Obstacle

1 Introduction

The technology of Electronic Navigational Charts (ENC) has been used increasingly in marine navigation. In the ENC system, the most common application is to determine an optimal or a most economical route (path) from any start point to the destination point without crossing any landmass (also called obstacle or barrier area) including shoals [1, 2]. An optimal planned route is a foundation of safe navigation on the sea [2, 3]. The civilian routes are usually immutable [4], but it is necessary to search optimal routes for a prompt navigation in military, especially in the emergency. In recent years, many scholars have paid attentions to the study on the shortest distance routing between any two points in the chart using the computer's automatic solution. Zhang et al. build the mechanism of bypass the obstacle

L. Zhang (✉) · T. Wang
Department of Hydrography and Cartography, Dalian Naval Academy,
Dalian 116018, China
e-mail: zlhua@163.com

area automatically based on the predefined principles and propose the automatically creating algorithm for optimal routing on the platform of Electronic Chart Display and Information System [5, 6]. These methods have greatly improved in the quality and efficiency of the traditional routing. However, besides the index of the shortest distance in chart, these methods do not take into account the limiting conditions of maneuverability, such as the route's turning times and steering angle, etc. Although a method for automatic routing based on comprehensive evaluation on limiting conditions of maneuverability is proposed [7], a turn penalty is still not considered. The vessel has a certain turning radius and inertia, and will have a certain penalty (lose time and voyage) when turning. Therefore, it is significant to study the shortest routing considering turning penalties.

2 Acquisition of Obstacle Areas

2.1 Tracing of Safety Contours

In the process, safety contours, depending on the draft of the vessel, needs to be traced based on digital depth model. Nowadays there are two methods for contour plotting (i.e., triangulation and grid contouring). Because data used for navigation in a chart is an irregular distribution usually, this paper traces contour using triangulation contouring. Contouring from triangulated data uses a triangulation technique and interpolates values based on the source data, then traces all equal depth nodes orderly [5]. Figure 1 shows a part of TIN and contours in a sea area.

For the convenience of modeling, definitions are given as following: If the left of a contour is the shallow area and the right is the deep area along the tracing direction, the direction is defined as positive, or else negative. As Fig. 1 shows, the directions indicated by arrowheads are positive. Furthermore, contours are categorized into three classes: the class I is a closed curve, inside of which is at a lower elevation than that outside (i.e., a depression) (as c_1 shown in Fig. 1), the class II is closed curve whose inside is a highland (as c_2 shown in Fig. 1) and the class III is unclosed (as c_3 shown in Fig. 1) because of the limit of the local study area. The closed contours and the unclosed ones are distinguished depending on whether the start point and the end one are a superposition or not. However, both of the class I and the class II contours are closed. So they are further differentiated depending on whether nodes of a contour are a clockwise or anti-clockwise arrangement [5].

2.2 Safety Areas Derived from Contours

A safety contour is a boundary of a navigable area and a unnavigable one for a vessel. The inside of the class II is an island or a shallow ground, which is a shallow obstacle area for safe navigation. The class III contour is unclosed, and it needs to be

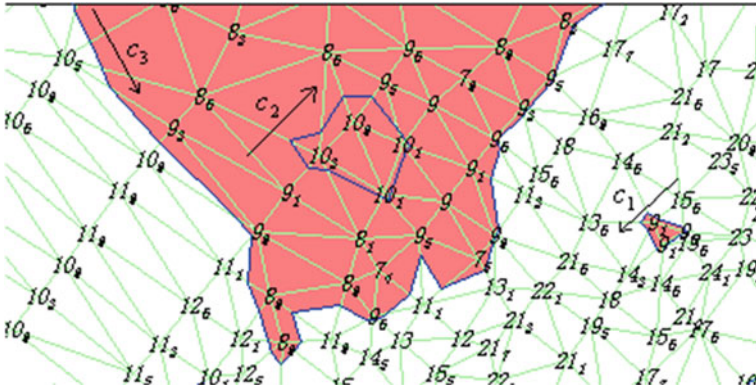


Fig. 1 TIN and contour

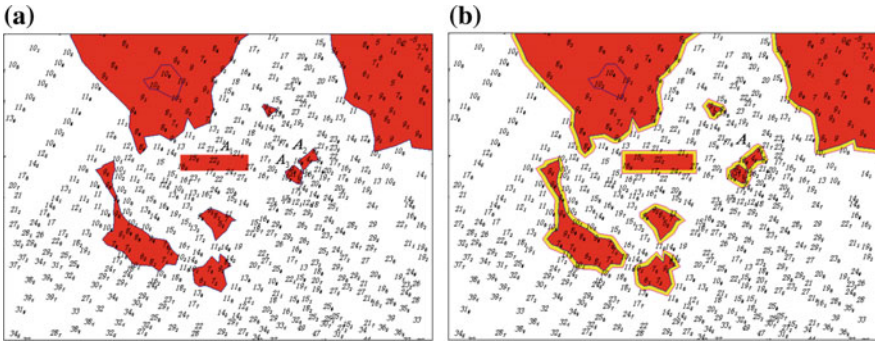


Fig. 2 Obstacle areas. Obstacle areas is represented by the red and avigable areas represented by the white. a Obstacle areas not including the extended areas. b Obstacle areas including the extended areas

closed with the boundary of the studied area along its positive direction. The inside of the closed polygon is also a shallow obstacle area. The class I contour located in inside of a greater shallow obstacle area. Although inner part of the contour is deeper than safety depth, yet the exterior obstacle of it cannot be traversed, the inside of the class I contour is also incorporated into shallow obstacle areas.

There are some influencing areas of fixed obstacles (i.e., shipwrecks and mines) except for shallow areas derived from safety contour. These influencing areas, not changing with a changing safety depth, are regarded as fixed obstacles areas, as a range represented using a rectangle (as A_1 shown in Fig. 2). To make the display neater, irregular boundary of source data is cut out, and a regular rectangle boundary is formed.

2.3 Extension of Obstacle Areas

Inaccuracy of obstacles' position and ships' positioning, a gyral buffer of ships' operation and influence of wind and flow might bring an uncertainty for safe navigation. In consideration of room for safety, initial obstacle areas are extended to a certain extent. A method of angular bisectrix is used to extend uncertain influence areas of obstacles in this paper, and the extended areas are delineated with the yellow, as shown in Fig. 2b.

2.4 Processing of Obstacle Areas

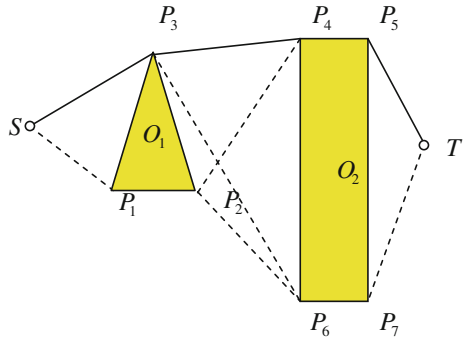
The areas might intersect each other (e.g., obstacle areas A_2 and A_3 shown in Fig. 2a) after some obstacle areas are extended. The intersected areas need to be merged further. An example for the merged area is A_4 as shown in Fig. 2b. The red areas represent obstacle scopes, the yellow area represents uncertain range for safe navigation, and the blank areas are navigable ones in the final result.

3 The Shortest Routing Considering Turning Penalties

3.1 Creation of a Route Binary Tree

As Fig. 3 shows, the test line ST is created from the start point S to the destination point T . If ST is not intersectant with any obstacle area, the line segment ST is the shortest route directly, otherwise a route binary tree needs to be created. First, the nearest obstacle area (O_1) to the current test point S needs to be searched, and each azimuth of the start point S to each vertex of the current obstacle polygon is computed, respectively. Two extremums of azimuths, respectively locating the left and right side of the nearest obstacle area are acquired, and two key points (P_1 and P_3) and corresponding paths are recorded, respectively. Second, two new test lines (P_1T , P_3T) are created from the two key points to the destination point. If the new test line (P_3T) is not intersectant with the current obstacle area (O_1), the point P_3 is recorded as a node of the route binary tree. If the new test line (P_1T) is intersectant with the current obstacle area (O_1), the point P_1 is only recorded as a transitional point, and tests are continued to be performed until P_2T is not intersectant with the current obstacle area (O_1) and the point P_2 is recorded as another node of the route binary tree. Then two nodes of the route binary tree (P_2 and P_3) are regarded as current test points, and the above operations are repeated until the test line from the node of the route binary tree to the destination point T is not intersectant with any obstacle area. Finally, navigable routes of the binary tree are analyzed and contrasted, and the shortest route is obtained, as $SP_3P_4P_5T$ shown in Fig. 3.

Fig. 3 Creation of route binary tree



3.2 Improvement of the Route Binary Tree

There maybe an excrescent point in the created route (e.g., the P_2 in the route $SP_1P_2P_6P_7T$, as Fig. 3 shows), so an additional test is necessary. If the test line linked by former point (P_1) and latter point (P_6) of the current point P_2 is not intersectant with any obstacle area, the current point is an excrescent point, and it should be deleted in the route.

On the other hand, the created path of the route binary tree is also possible to be intersectant with a new obstacle area (e.g., SP_3 is intersectant with O_3 , as shown in Fig. 5). If the binary tree motioned above is created, two paths SAP_3 and SBP_3 should be inserted to the original binary tree. Similarly, SA is still possible to be intersectant with a new obstacle area, the repeated test is necessary.

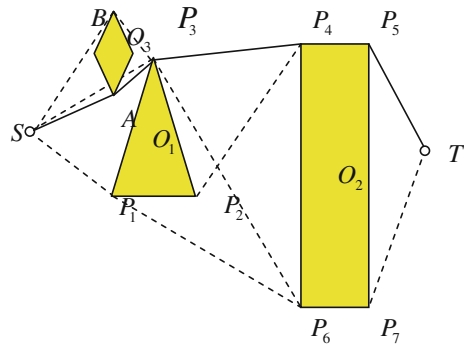
There maybe an excrescent point in the created route (e.g., the P_2 in the route $SP_1P_2P_6P_7T$, as shown in Fig. 3), so an additional test is necessary. If the test line linked by former point (P_1) and latter point (P_6) of the current point P_2 is not intersectant with any obstacle area, the current point is an excrescent point, and it should be deleted in the route.

On the other hand, the created path of the route binary tree is also possible to be intersectant with a new obstacle area (e.g., SP_3 is intersectant with O_3 , as shown in Fig. 4). If the binary tree motioned above is created, two paths SAP_3 and SBP_3 should be inserted to the original binary tree. Similarly, SA is still possible to be intersectant with a new obstacle area, the repeated test is necessary.

3.3 Turning Penalty

However, the maneuverability, besides the index of shortest distance in chart, is another important factor for the route evaluation [7]. The vessel has a certain turning radius and inertia, so a certain penalty should be considered for loss of voyage and time when turning [2]. Usually, the turning times should be as small as possible and the steering angle should be little during a voyage.

Fig. 4 Improvement of the route binary tree



To consider effect of the turning on the route, a certain penalty is added when turning one time. If the initial distance is s_0 , the distance considering a turning penalty is $s = s_0 + s_{TP}$. Given turning times are n , the distance considering the turning penalties is computed with the following expression:

$$s = s_0 + n \times s_{TP} \tag{1}$$

In fact, the steering angle should also be considered during a voyage. The course is altered from $\overrightarrow{P_{i-1}P_i}$ to $\overrightarrow{P_iP_{i+1}}$ during bypassing the point P_i along the route as Fig. 5 shows, and θ (difference of two courses) is the steering angle. As general, the larger the steering angle θ is, the maneuverability is more difficult to perform and the turning penalty should be increased correspondingly.

As Fig. 5 shows, the planned route is a direct line distance from A to B , namely is $AP_i + P_iB$. In fact, turning is a gradual progress, and an arc track will appear. At the same time, the arc track should be locating the side of safe areas, as in Fig. 6. Thus, the arc distance during turning can be represented $r \times 2\theta$ (r is a gyral radius, 1,244 m is used in this paper, unit of θ is radian), and the turning penalty can be computed with the following expression:

$$s_{TP} = r \times 2\theta - (AP_i + P_iB) \tag{2}$$

The expression is simplified as:

$$s_{TP} = 2r\theta - 4r \sin \frac{\theta}{2} \tag{3}$$

A regular arc during turning is an ideal case, an effective coefficient η is used in fact (for example $\eta = 0.6$), the expression can be as follows:

$$s_{TP} = 2\frac{1}{\eta}r\theta - 4r \sin \frac{\theta}{2} \tag{4}$$

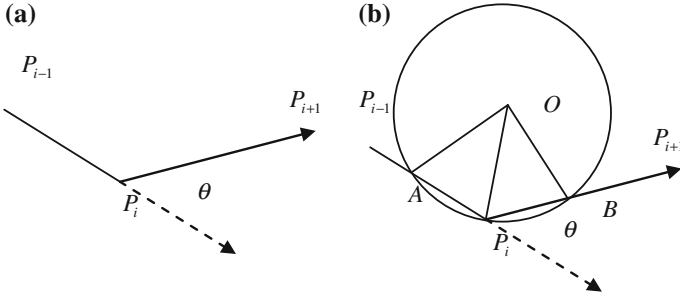


Fig. 5 Turning penalty. **a** The steering angle shown by difference of two courses. **b** An arc track during a gradual turning

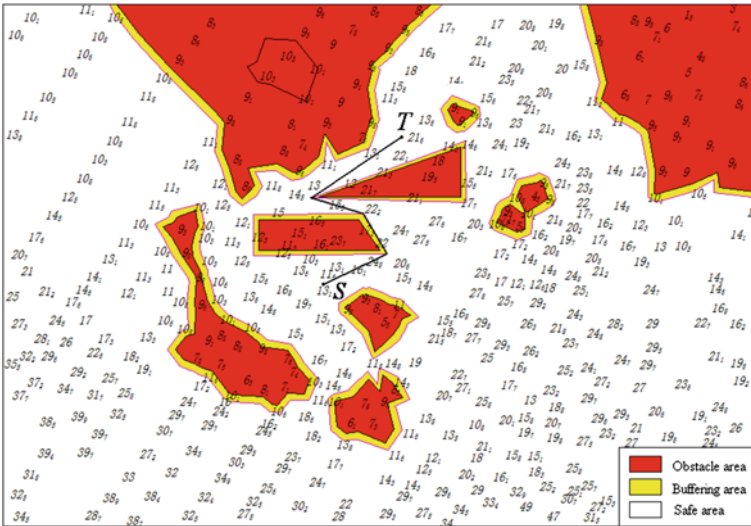


Fig. 6 The shortest routing not considering turning penalty

In addition, slowdown effect is also necessary to be considered during turning, a formula is cited directly [8].

$$\frac{V}{V_0} = -8.697 + 6.361 K' + 7.960 C_N - 5.295 K' C_N - 0.226 C_N \theta + 0.667 (K')^2 + 0.028 \theta^2 \tag{5}$$

V_0 is a normal velocity, V is a velocity considering slowdown effect, K' is an exponential coefficient (1.3966 is used in this paper), C_N is the normal force coefficient of the helm (1.2574 is used in this paper).

$$s_{TP} = \left(2 \frac{1}{\eta} r \theta - 4 r \sin \frac{\theta}{2} \right) \times \frac{V_0}{V} \tag{6}$$

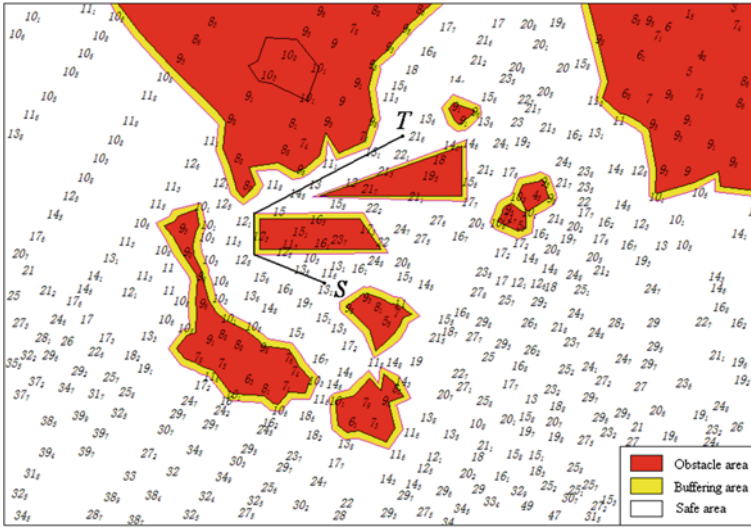


Fig. 7 The shortest routing considering turning penalty

4 Applications and Discussion

To demonstrate the proposed method that is available, this paper makes two experiments with the same data as shown in Figs. 6 and 7. A bold and black line from *S* to *T* (as shown in Figs. 6 and 7) is a route for vessels with safety depth of 10 m, which is the shortest route automatically created. Turning penalty is not considered in the shortest routing as Fig. 6 shown, while the shortest route considering turning penalty is changed obviously as shown in Fig. 7.

5 Conclusion

This method can acquire shallow areas by tracing safety contours and handling obstacle areas. Then the shortest route considering turning penalty is created automatically in ENC. Experimental results demonstrate that the shortest route is possible to change after turn penalty is considered. In future studies, dynamic changes of water levels, and other requirements should be considered.

Acknowledgments This study is supported by the National High Technology Research and Development Program of China (2012AA12A406) and the National Natural Science Foundation of China (41171349).

References

1. Chang KY, Jan GE, Parberry I (2003) A method for searching optimal routes with collision. Avoidance on raster charts. *J Navig* 56:371–384
2. Rafal S (2006) A new method of ship routing on raster grids, with turn penalties and collision avoidance. *J Navig* 59:371–384
3. Wang K (2004) A study for designing navigation route based on ECDIS. MS thesis, Dalian Naval Academy
4. Ye Q, Zhen ZW (2003) The improved shortcut algorithm and its application in selecting ship's optimum route. *Navig China* 55:15–17
5. Zhang LH, Zhu Q, Liu YC, Li SJ (2007) A method for automatic routing based on ENC. *J Dalian Marit Univ* 33:109–112
6. Zhang L, Zhang LH, Wang Z, Jia SD (2010) A method for shortest distance routing in a chart based on testing a spatial relation of a route segment and an obstacle area. In: Proceedings of the 2nd international conference on advanced computer control. Shenyang 142–147
7. Zhang L, Wang Z, Li SJ, Zhang LH (2010) A method for automatic routing based on comprehensive evaluation on limiting conditions of maneuverability. In: The 18th international conference on geoinformatics, Beijing
8. Li ZB, Zhang XK, Jia Y (2008) A study for slowdown effect during a ship altering its course. *Mar Technol* 3:1–4

Space Robot Teleoperation Based on Active Vision

Cheng Huang, Huaping Liu, Fuchun Sun and Yuming Sheng

Abstract In order to increase the robustness of space robot teleoperation system and good operational performance, the article design a set of haptic feedback system based on hand controller data glove and active vision system, which depend on the Pan-Tilt-Zoom (PTZ) camera and Kinect camera. It makes operators have the feeling of immersive. This system requires two operator cooperation, one processing Active Vision tracking and image processing, one controlling the movement of robot under the good perception environment. At the same time, Good interpersonal interface design to alleviate the pressure of the operator, in order to study the real space teleoperation scene, we use the software to set the delay system to make the operator to verify the performance of the system in the case of delay. The experiments show that no matter in the presence or absence of delay, the system completes the tasks at a high success rate.

Keywords Teleoperation · Active vision system · Time delay · Perception environment

This work is jointly supported by the National Natural Science Foundation of China (Grants No: 61075027, 91120011, 61210013), Tsinghua Self-innovation Project (Grant No: 20111081111) and Graduate student innovation fund project in Shanghai. Project approval no: JWCXSL1202.

C. Huang (✉) · Y. Sheng
School of Optical-Electrical Computer Engineering, University of Shanghai
for Science and Technology, Shanghai 200093, China
e-mail: hc1881758@163.com

C. Huang · H. Liu · F. Sun
State Key Laboratory of Intelligent Technology and Systems, Tsinghua National Laboratory
for Information Science and Technology, Beijing 100084, China

1 Introduction

With the rapid development of space technology and the establishment of space station and space shuttle, the demands for space robot teleoperation system are increasing as there's lots of space experiments and efforts. The main research of telerobot system is to ensure the robustness of the system (namely stability) and good operational performance (namely transparency). Transparency means the telerobot system can provide sound-surround ambiance, which includes sight and force sense with telepresence telerobot system, including visual presence and force Telepresent. The existence of delay during the transmission [1–4] is the major technical difficulties for the telerobot system, which made the operator unable to catch the operating ambient on time, and influences the operation. In order to improve the maneuverability, here we establish an Active Vision System which based on video camera with Pan-Tilt-Zoom (PTZ), which adjusts the visual perspective automatically to achieve the target tracking, and reconstruct the three-dimensional visual scene with Microsoft kinect camera. It makes operators have the feeling of immersive. It uses the technology of GPU [5] parallel with computing to accelerate the image information processing capabilities to reduce the time of information transmission. In this article, it uses software to set the delay system to simulate the real space teleoperation.

2 System Architecture

2.1 Ground-Based Monitoring Section

The main equipment is hand controller (data glove), four computers, three monitors, virtual reality equipment. The manipulator operating data and the entire system is controlled through a computer which connected with the hand controller. Take one computer as a display and control of the three-way image data. Virtual reality system is made of a computer, a monitor, and a virtual device. Statistics storage and dynamics simulation processed by the other two computers. The below is the framework of the program (Fig. 1).

2.2 Simulated Space in the Rail Section

Seven degrees of freedom in orbit manipulator is made of three PTZ cameras on kinect camera, one is for global scene acquisition, one is for robotic arm movement tracking, and one is for target supervision.

The three-way image acquisition card as a video capture interface plan and control the robotic arm movement, taking advantage of the orbit of the IPC. One

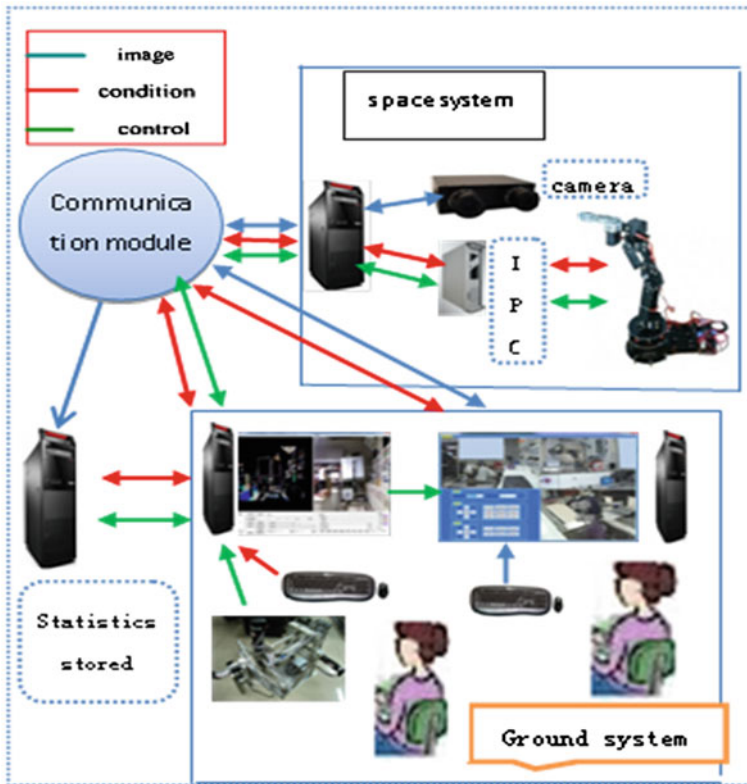


Fig. 1 Structure of control system for the space robot

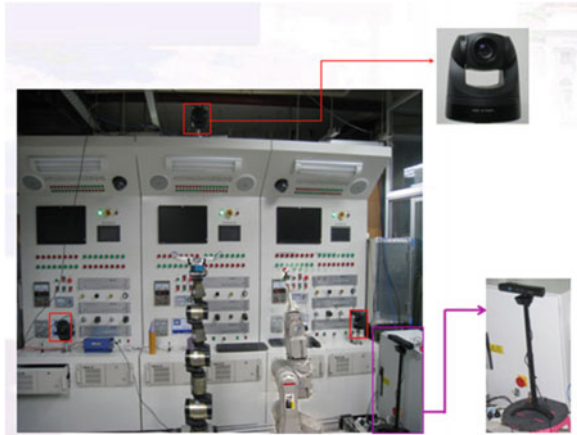
computer collect video signal got by the video capture board, and track and check to process data send by IPC. The below figure is the simulation scenario (Fig. 2).

3 Active Vision System

The vision system is the key technology for the Space teleoperation, and it made the robot arm system with high-level perception institutions, and provides information of the real image and special positions for the target object. Then the robot arm system react the surrounding environment in an intelligent and flexible way, and the reliability and safety be improved.

And at the same time, the visual system feedback the state and the environment of the manipulator to the operator, then the operator can make error diagnosis and take measurement. The active vision systems [6, 7] provide a sensitive perception system for the robot arm in remote control system, and the target information pass

Fig. 2 Space simulation scenarios



to the operator on the ground timely. It's easy for the operator to solve the problem in an effective way. He can take action before mechanical arm action, and feedback information in the course of action to suit the environment.

3.1 A Based on Active Vision Pan-Tilt-Zoom (PTZ) Camera

The robot arm system is a space station platform, it can change the angle of the camera, so it needs the camera with automatic adjust function to keep tracking. It is difficult to catch unless it's with a separated control system. But if so, it will be very complicated. We can solve this problem easily if we choose PTZ camera, as the PTZ camera can adjustment angle in the horizontal and vertical directions, so it suit for the system. The PTZ camera target tracking system shown in Fig. 3, we used two sets of wireless transceivers to achieve wireless transmission of the image and the control instruction.

3.2 Target Tracking Algorithm

In order to make the robot arm focus spatial capture job, it is very important to catch the target tracking. The basic idea is to use a series of targets which with reliable and characteristics descriptions, and then select the appropriate algorithm to detect these features in consecutive video frames, then get the movement locus of the target. Therefore, it is closely related between targets tracking algorithm with the selected characteristics. The key issue for the visual tracking is how to select effective features to achieve stable tracking. It has been studied extensively for various tracking algorithm, such as the particle filter tracking algorithm [8]

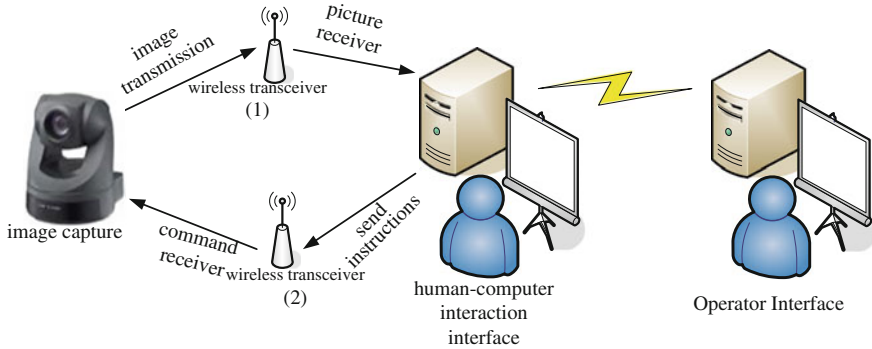


Fig. 3 Active visual tracking system diagram

based on the characteristics of color, Speed Up to Robust Features (SURF) tracking algorithm [9] based on local features, Principal Component Analysis (PCA) tracking algorithm [10, 11] based on the contour feature.

The target object can artificially increase the calibration points, suppress background noise with the bright colors characteristic, and guarantee high real-time in the ground simulation system. Finally, the particle filter tracking algorithm based on the characteristics of color is the main tracking algorithm.

In this article, we choose the Gaussian distribution function [12] as a density function (a priori probability density function), which is considering the target movement is a random process, and the process is similar to the Brownian motion of the particles, the state of motion in any time is independent of the previous states, and the path of movement is continuous, so this choice is reasonable. The experimental results show that, it can get better tracking results if takes the Gaussian distribution function as the important density function.

Color-based particle filter tracking algorithm [13] is divided into the following processes:

① Initialization process

Target region of interest in the image annotation manual observation produces the particle set, $\{\mathbf{x}_{t_0}^m\}$ as the Regional Center for the origin, and as $m = 1, \dots, M$, each particle represents a goal that may exist in the region.

② Particle propagation process

According to the dynamic model of target movement (Here, we illusion the target motion obeys normal distribution, and this is reasonable because of random motion), each particle follows the rules that transfer process from one sate to another independently, and get the new particle set of the next time. It means that the particle set of time in t $\{\mathbf{x}_t^m\}$, can get the particle set of time in $t + 1$ $\{\mathbf{x}_{t+1}^m\}$ by transfer state.

③ Observation process

Then turn to observe these new propagation particles, and calculate the similarity of their propagation state between the original sate, that is to calculate

the Bhattacharyya distance from the color histogram to the reference histogram of each new particle region (namely the weight of each particle). If the distance is very far, that means the particle set is closer to the reference model, and its weight is heavy, one the contrary, the weight is light.

④ The estimation procedure

Check the probability after calculating for those with heavy weight particles, which is more than $N \leq M$. And finally figure the expected value as below:

$$E(x_{t+1}) = \sum_{n=1}^N \omega_{t+1}^n x_{t+1}^n \quad (1)$$

The mark of ω_{t+1} represents for the weight (probability) of each particle region for each particle area obtained weights (probability). Take the expected value as the optimal estimation of the target state at time $t + 1$.

Experiments show that this algorithm reflects tracking the target with color characteristics in real-time, and the speed of video processing reach 14.58 FPS (frames per second). Figure 4 is a few frames of the video images captured from the tracking process, which be marked in the image. We can see that the color-based tracking is more effective, if there's a big difference between background and target.

3.3 Three-Dimensional Reconstruction for Kinect

The Light coding, the content of Kinect, technology, measures the space of code for needed ones under using lighting; it is also called structured light technique. But the light source is not a pair of two-dimensional periodic variation, but a "body code" with the 3D depth, and this is the main difference from the traditional method of structured light. This light source is called as laser speckle, it was formed by the laser irradiation on the rough objects or the random diffraction spots through the frosted glass. These speckle, with high randomness, changes different image according to the variation of the distance. That is to say the two speckle patterns in spatial arbitrary are different. As long as the space is with the structure light, the whole space is marked. We can know the exact position of the object only to find the speckle pattern on this object. Of course, we should record all speckle patterns in the whole space. And that needs to demarcate the light source. The calibration method is that, note the reference plane down in different positions. If the space activities if the range of 1–4 m from the Kinect, take a reference plane in each 10 cm, then we note 30 pcs speckle image.

Take a speckle image photo when needed measure, shooting a scene to be measured. Then we would make cross-correlation operation between this image and the saved 30 pcs reference images. In this way, we will get 30 pcs correlation

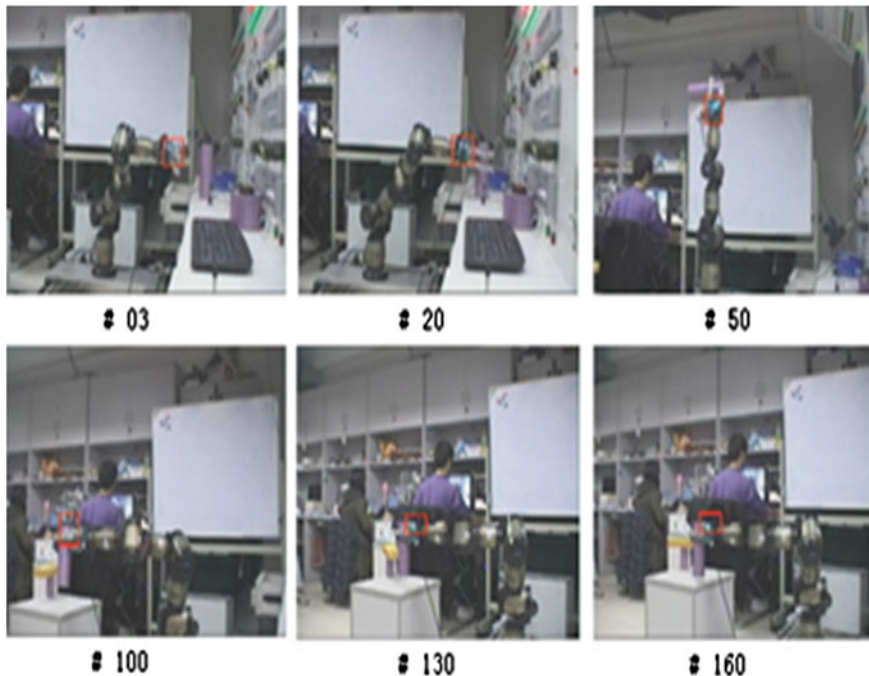


Fig. 4 Particle filter based on color tracking process

images, and find the locations of the object in the space. Also it shows the peak on these images. If we lay all data of the peak, and with some interpolation, we will get a 3D shape with whole scene. The Fig. 7 is the 3D reconstruction.

4 Design for Time Delay System

In order to research impact of network delay on teleoperation in the laboratory, we use software timer to simulate the delay. As each hardware sensor corresponds to a sensor object in the software system, data transmission and retransmission operation is based on each sensor object, therefore, each object should correspond to a timer.

Since the timer resend to the corresponding sensor if it meets overtime, and the timer be reset when the data be received. And the timer will not be reset if the date packet be received. Then the retransmission queue is sent to the sender as the timer expired after a period of time. After the sender receives the retransmission queue, he would check the corresponding bite bits, and send back. The one-way delay is around in 0–5 s. If simulation the communication delay and the universe communication delay, the delay date is showed by interface input or read from initialization file. Module controls the delay by compare the packet reception time

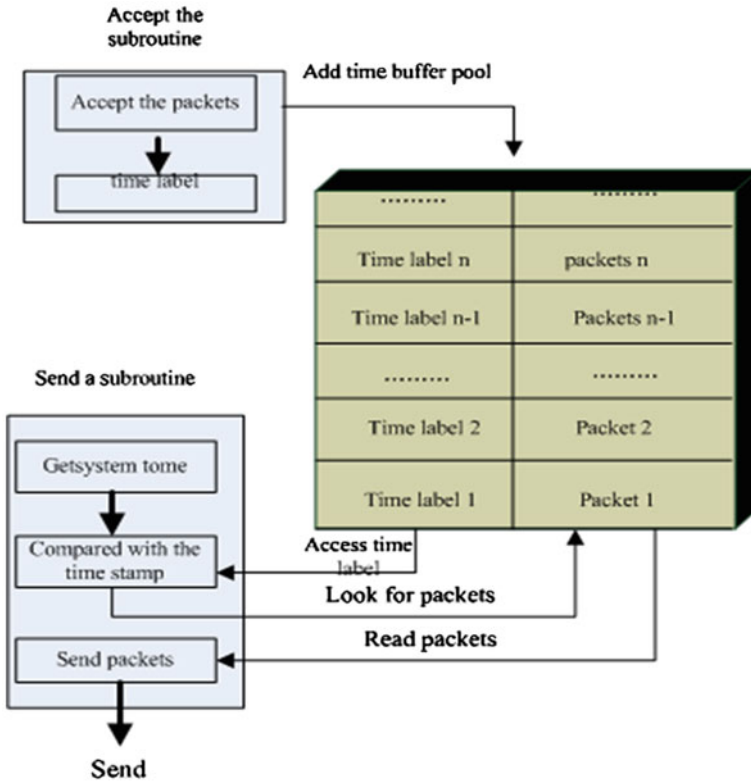


Fig. 5 Schematic diagram of the communication time delay mechanism

and transmission time. Figure 5 is a schematic diagram of the communication time delay mechanism.

5 Experimental Results and Analysis

As it is time-consuming for the image information processing, so here we use GPU to parallelize accelerated processing, for the detail parts, please check the paper wrote by Liu [5]. The whole ground control is mainly responsible for the content of the two parts. One is the human-computer interaction process of the operation control mechanical arm, and one is the tracking manipulator operation process by controlling the camera. So it needs two operators to cooperate and to finish the whole system. One person is responsible for tracking control; the other is responsible for human-computer interaction. The operation interface as below (Fig. 6):

Control the state of the camera can be controlled manually before the tracking (via *U, L, R, D, H* and other key artificial adjustment of the camera rotation), and search the interest targets in the searching range.



Fig. 6 Three image data display and control interface

Then choose tracking target through the observation window (Observer), and use the correlation algorithm which mentioned in this paper. In the process of tracking, he should adopt the heuristic judgment, and send commands to the camera by the computer, and keep the target always at the near of the center of the image coordinates. At the same time, the teleoperation controller sends control instructions to the mechanical arm system according to the images returned by camera, and finally catch the target (Fig. 7).

The control of mechanical arm mentioned in this paper mainly control by hand heterogeneous. It adopts the connection in series of a double parallel four-bar mechanism and a diamond connecting rod mechanism. The motor is almost on the base, reducing the moment of inertia of moving parts. The mechanism of the coupling movement light and it can achieve free translation in three different directions, and the influence between each other is almost neglected. Figure 8 shows the graph structure of a heterogeneous type master manipulator.

5.1 Experimental Verification

In the above-mentioned, we designed a seven degrees of freedom controller based on the vision system. Hand controller is the basic input device of robot teleoperation. On one hand, it can check the hand position information of the robot operator, as a control instruction to control the remote manipulator's position and movement. And on the other hand, it will feedback the interaction information of the mechanical hand and environment to the operator's hands, the operator can



Fig. 7 The manipulator control interface

Fig. 8 Structure of a heterogeneous type master manipulator

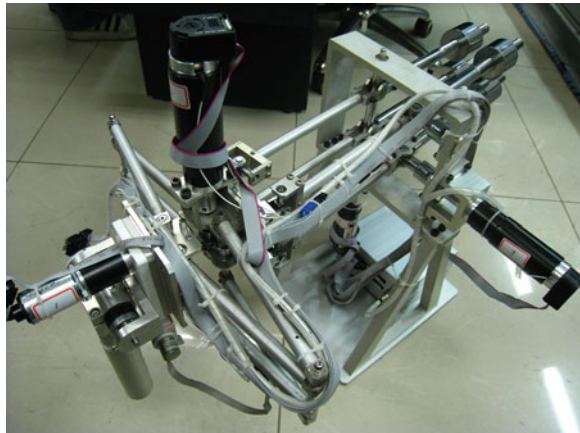




Fig. 9 Experimental process

understand and judge the environment and the robot according to the feedback, that the operator can control the feeling of robot with force telepresence, which helps the operator remote control robot to complete the work accurately.

The operator can judge the position between the end of arm and performed tasks with the active vision system and a three-dimensional Kinect view, to coordinate feedback information on data glove device. Then can get the vision and haptic information of space simulation scene. The operator has the feeling of immersive, the probability of success, and efficiency increasing.

5.2 The Experimental Results

We did two groups of experiments, one is with 5 s operation delay and one is without any delay based on the above-mentioned experiment system. Through the comparison of few experiments, we found that probability of success is almost same for within delay and without delay; the main difference is depending on the finishing time. The Completed tasks in the experiment: ① manipulator grasping the object, ② put the object into a large paper tube, ③ put the object to the drawer in safety, ④ close the drawer and return back. The experimental process is shown in Fig. 9.

6 Conclusion

In the paper, the active vision system and manipulator force feedback to the operator, provides visual and haptic information. That made the operator have a feeling of be personally on the scene with high transparency. At the same time, in order to simulate the delay of space robot teleoperation, we use software to set the delay system that made the operator experience real teleoperation scenarios. Through the experiment, the system can complete a certain complexity work.

References

1. Sheridan TB (1993) Space teleoperation through time delay: review and prognosis. In: IEEE Trans Robot Autom 9(5):592–606
2. Lee S (1993) Modeling, design, and evaluation of advanced teleoperator control systems with short time delay. IEEE Trans Robot Autom 9(5):607–623
3. Azorin JM, Reinoso O et al (2004) Generalized control method by state convergence for teleoperation systems with time delay. Automatica 40:1575–1582 (Elsevier)
4. Yoon WK, Goshozono T et al (2004) Model-based space robot teleoperation of ETS-VII manipulator. IEEE Trans Robot Autom 20(3):602–612
5. Liu YY, Liu HP et al (2011) GPU accelerate the online k-means clustering particle filter tracking algorithm. J Cent S Univ (JCR Sci Ed) 42 supplement 9:1–7
6. Jun M, Tsuyoshi K (2000) An active vision system for real time traffic sign recognition In: IEEE intelligent transportation systems conference proceedings Dearborn (MI), pp 52–57. Oct 1–3
7. Ma S (1996) A self-calibration technique for active vision systems. IEEE Trans Robot Autom 12(1):114–120
8. Pérez P, Hue C, Vermaak J et al (2002) Color based probabilistic tracking. In Proceedings of the 7th European conference on computer vision, vol 2002, no (1), Copenhagen. pp 661–675
9. Kim Z (2008) Real time object tracking based on dynamic feature grouping with background subtraction. In: IEEE conference on computer vision and pattern recognition, Anchorage. pp 1–8. <http://www.openni.org>
10. Blake A, Isard M et al (1994) Learning to track curves in motion. In: Proceedings of the IEEE conference on decision theory and control. pp 3788–3793
11. Black MJ, Jepson AD (1995) Eigen tracking: robust matching and tracking of articulated objects using a view-based representation. Technical report T95-00515, Xerox PARC
12. Doucet A, Godsill S et al (2000) On sequential Monte Carlo sampling method for Bayesian filtering. Stat Comput 10(3):197–208
13. Bradski GR (1998) Computer vision face tracking as a component of a perceptual user interface. In: Workshop on applications of computer vision. Princeton. pp 214–219

Listed Company Reorganization Risk Evaluation Based on Neural Network Model

Wang Zuogong and Li Huiyang

Abstract The reorganization of listed company is a complicated system engineer with great risk. While aiming at risk characteristics of listed company reorganization, this paper builds up evaluation index system of listed company reorganization risk, designs risk evaluation model based on variable structure neural network of re-linking random process, trains the model by using 10 cases of listed company reorganization and assess the reorganization risk of four listed company. The result shows that the average relative error of the model is 2.44 %, and the largest relative error is 2.96 %, which means that the model has a preferable prediction result.

Keywords Listed company · Reorganization · Neural network · Variable structure · Risk evaluation

1 Foreword

In addition to general requirements of unlisted company, the reorganization risk of listed company has its own characteristics. In particular, listed company is different with unlisted company in aspects such as applicable regulation, government supervision, information disclosure, and stock price volatility.

Research on risk evaluation of listed company reorganization is mainly focused on financial risk, financing risk, and integrated risk. Pan Jin proposed risk evaluation method [1] using three index, including risk factors, expected revenue, and risk rate. Tan considered that the financial risk of listed company reorganization is mainly manifested in target company valuation risk, financial risk, liquidity risk,

W. Zuogong · L. Huiyang (✉)
Institute of Economy, Henan University, Kaifeng, China
e-mail: 373674930@qq.com

and leverage risk [2]. Zhang considered that listed company financial risk could be divided into external risk and internal risk, which is important because of the imperfect environment for reorganization and financing, obstacle existed in the financial process and relatively great payment risk [3].

Traditional risk evaluation method is hardly to satisfy scientificness and accuracy of listed company reorganization risk evaluation at the same time. As a result, it has extremely important significance to find a new method that can be fit for freeway investment risk evaluation.

Neural network is defined as an engineering system that stimulates human brain structure and intelligent behavior based on the understanding of human brain operation mechanism and organization structure. The most common type of neural network is BP neural network. BP neural network is multilayer feed forward neural network based on error back propagation algorithm. BP neural network has several advantages like self-organized learning, fault tolerant, high nonlinear mapping, and generalization. Neural network has been widely used and has made great achievements in risk evaluation area. Lou [4] applies neural network to high-tech project risk evaluation; Cui [5] introduces artificial neural network modeling method and builds high-tech agriculture investment project risk evaluation model; Wang [6] summarized and analyzed the contradiction between traditional neural network operation speed and accuracy, improved the structure of traditional neural network evaluation model, built variable structure neural network evaluation model. While applying the model into freeway project investment risk evaluation, taking historical data and each project technology index as input value and each index that project evaluation depends on as output value, we can achieve a preferable evaluation result.

2 Modified BP Network Model and Algorithm

BP neural network, which belongs to learning algorithm with mentor (error back propagation algorithm), is made up with neuron and links between neuron. The BP network can be divided into input layer, hidden layer, which could contain several layers, and output layer. The structure and learning principle are shown in Fig. 1.

Based on the gaps of previous related research, the paper presents a quasi-three-BP (Back Propagation) neural Network in terms of structural optimization to improve accuracy. For a quasi-three-BP neural network, this paper presents random reconnection process from input layer neuron to hidden layer neuron and from hidden layer neuron to output layer neuron. Figure 2 shows the Quasi-BP neural network topology structure after the process of random reconnection when $C = 4$. Through the process of self-organized study, by using random reconnection study algorithm^[9], the operation precision of BP neural network is modified. The specific algorithm is shown below:

At the step N in the process of training study, for the weights of hidden layer and output layer, steps are as follows:

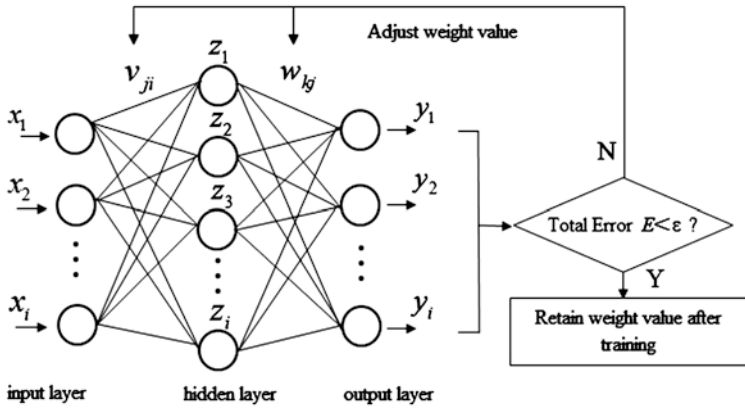


Fig. 1 The diagram of structure and learning method for BP network

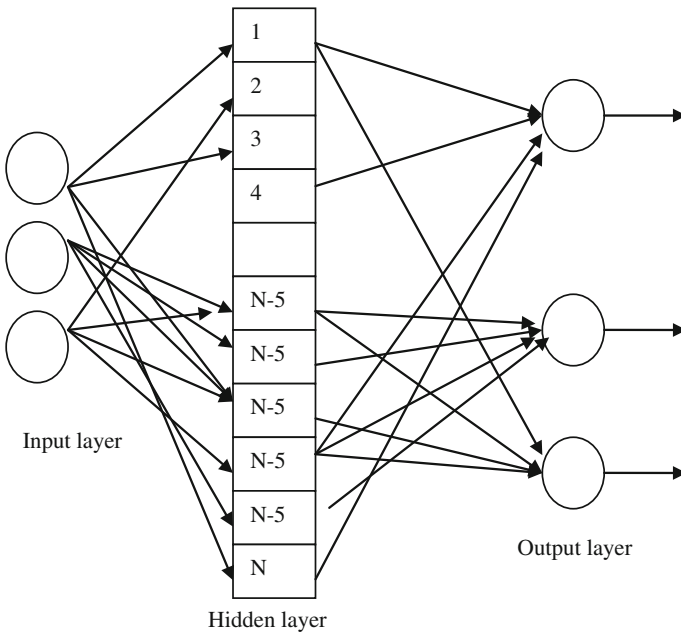


Fig. 2 The topology of quasi-BP neural network after re-linking randomly

- (1) Review the each neuron i of output layer one by one, and take the connecting hidden layer neuron $j \in [0, C]$;
- (2) Order $\xi_1 \in [0, 1]$ as a random number;
- (3) If $\xi_1 < \frac{\rho_1 E}{w_{ij}}$, disconnect the link and one end of hidden layer neuron;

- (4) Order that new hidden layer neuron g , $g \in \{1, 2, \dots, N\}$ is a random number while $g \neq j$, which means that new hidden layer neuron and former connecting C number hidden layer neurons are not overlapping at all;
- (5) Order $\zeta_2 \in [0, 1]$ as a random number;
- (6) If $\zeta_2 \in \frac{q_1 w_{ig}}{E}$, take hidden layer neuron as new connecting joint; otherwise turn to (4);
- (7) To each activated hidden layer neuron and its connection weights, according to the following way updating:

$$W_{kj}(n+1) = w_{kj}(n) + \eta \sum_{p=1}^P \delta_{kp} O_{jp}$$

$$d_{kp} = (d_k - O_{kp}) O_{kp} (1 - O_{kp})$$

- (8) When $E \leq \varepsilon$, the process of training study will be finished; otherwise, $n = n + 1$, turn to (1).

If weight value between hidden layer and input layer has similar algorithm, update as following:

$$v_{ji}(n+1) = v_{ji}(n) + \eta' \sum_{p=1}^P \delta_{kp} O_{jp}$$

$$d_{kp} = (d_k - O_{kp}) O_{kp} (1 - O_{kp})$$

Here, v_{ji} is original weight between input layer neuron and hidden layer neuron; w_{kj} is original weight between hidden layer neuron and output layer neuron, every v and w is larger than 1 and relatively small. C is the number of hidden layer neuron connecting with every input layer neuron or output layer neuron. N is taken as the neuron number of hidden layer in BP neural network, while E is taken as output error in BP neural network $p_1 = \frac{\min\{w\}}{E}$, $p_2 = \frac{\min\{v\}}{E}$, $q_1 = \frac{E}{\max\{w\}}$, $q_2 = \frac{E}{\max\{v\}}$, η and η' are the smaller number to make sure that learning algorithm cannot be shocked; P is shown as learning samples of neural network, O_{kp} is shown as the output of node k ($k = 1, 2, \dots, K$) in output layer, d_k is shown as the expectation value of output accordingly.

Variable structure BP neural network adjusts connection strength (V_{ji}) of input layer node and hidden layer node, connection strength (W_{kj}) of hidden layer node and output layer node and threshold through random reconnection learning algorithm, makes sure that error could satisfy requirements and the corresponding network parameter (weights and threshold) would be stored after training for several times. Here, the trained variable structure BP neural network can handle the input information from similar sample itself and output information which is with least error and have been nonlinear transformed.

3 Listed Company Reorganization Risk Evaluation Method

During the process of random disconnection and reconnection, due to self-learning, the connection number of hidden layer neuron is different. Neuron that plays an important role in risk evaluation always has more connection number, and its weight is an important parameter that can influence the evaluation. With more connection number, the neuron is more important in system evaluation. Variable structure BP neural network has advantages such as strong nonlinear mapping ability^[11], self-organized study, and no necessary to reveal equations that describes the relationship between inputs and outputs. Therefore, it has great adaptability to the risk evaluation project that has complicated factors and can solve contradictions between operation precision and efficiency.

Factors that can influence listed company reorganization risk are multiple and complex, and the risk evaluation is to figure out the final risk evaluation result by evaluating each factor in listed company reorganization. Therefore, different evaluation index has different weight. During the process of random disconnection and reconnection of variable structure BP neural network, different hidden layer neuron can correspond to different weight of different evaluation index in listed company reorganization risk evaluation model. Therefore, we can take factors of listed company reorganization risk evaluation as inputs, take final evaluation value as and output, and evaluate listed company reorganization risk by using BP neural network to describe the non-linear mapping relationship between the input and the output

3.1 Listed Company Reorganization Risk Evaluation Index System

Following the principles of considering suggestions of technical experts, investment experts, market experts, and venture capitalists, from the perspective of systemic risk and non-system analysis, this paper comprehensively analyzes risk factors of listed company reorganization and their characteristics and builds risk evaluation index system shown in Fig. 3:

1. Policy and regulation risk: The listed company reorganization is not only about cooperate law, contract law, and securities law, but also about series of rules such as merger regulation of listed company, information disclosure, and stock transaction in the secondary market. Policy and regulation risk mainly includes approval risk, violation risk, and policy change risk.
2. Business risk: business risk points to risk existed in acquired company during business development while mainly including industrial risk and production risk.

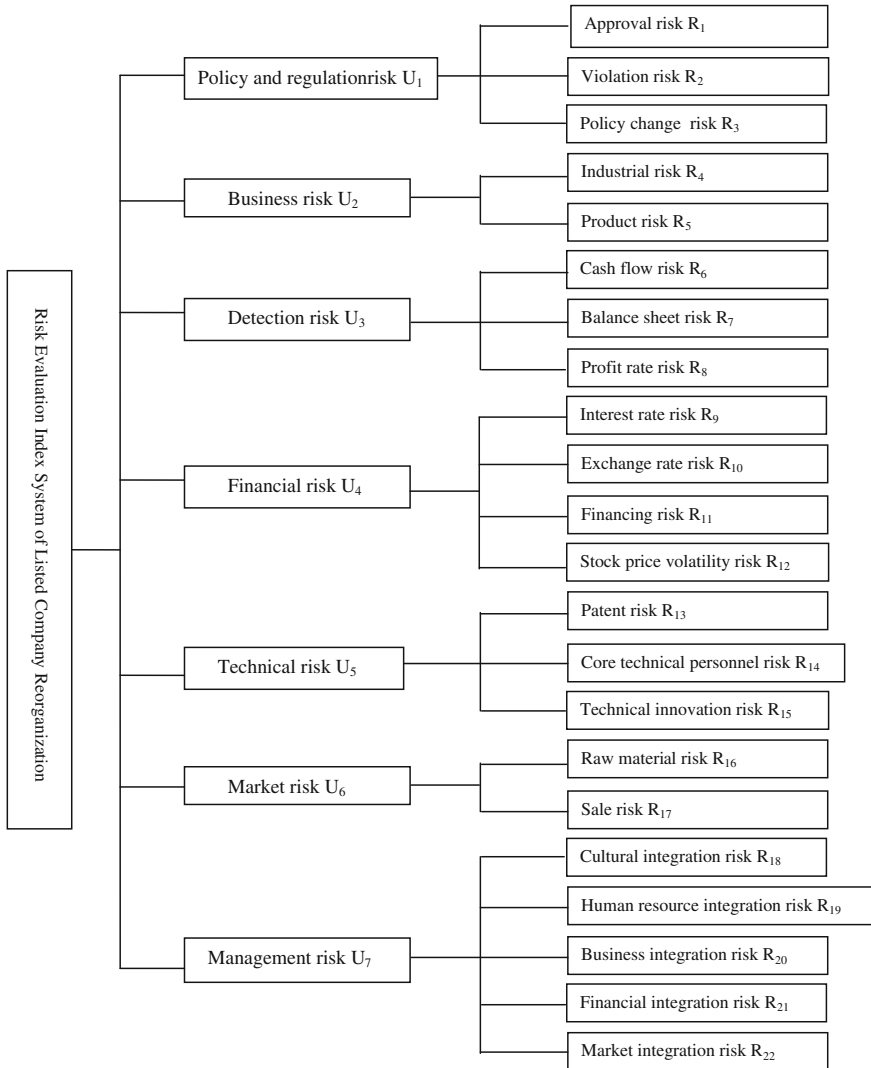


Fig. 3 Risk evaluation index system of listed company reorganization

3. Detection risk: detection risk points to risk existed in financial of acquired company while mainly including cash flow risk, balance sheet risk, and profit rate risk.
4. Financial risk: financial risk points to risk caused by the volatility of financial market while mainly including interest rate risk, exchange rate risk, financing risk, and stock price volatility risk.
5. Technical risk: technical risk points to risk existed in aspect of technology in acquired company while mainly including patent risk, core technical personnel risk, and technical innovation risk.

6. Market risk: market risk points to risk of raw material and production price volatility during managing in acquired company, while mainly including raw material price volatility risk, and sale risk.
7. Management risk: management risk points to risk existed between acquiring company and acquired company in reorganization process while mainly including culture integration, human resource integration, business integration, financial integration, and market integration.

3.2 Constructing a Variable Structure BP Neural Network

According to the index system of freeway investment project risk assessment, we decide the number of input layer neuron as $p = 21$. There is one neurons of output layer to evaluate conclusion; the number of hidden layer neuron are $C = \min(\frac{N}{K}, \frac{N}{p}) = \min(4, 84) = 4$. In the initial state, we can assume that the input layer neuron is connected with four hidden layer neurons successively; the output layer neuron is connected with four hidden layer neurons randomly. We can conduct Quasi-BP network with three layers by using random reconnection algorithm and error back propagation algorithm.

3.3 Comprehensive Evaluation

There are not only qualitative factors but also quantitative factors in the index system of listed company reorganization risk assessment. It is difficult to decide the weight even for quantitative factors. Thus, it is necessary to normalize each evaluation index and adopt expert scoring to the average risk index before applying the neural network model. The levels of expert scoring method and scores are as given in Table 1.

There is only one unit of comprehensive evaluation to output that uses evaluation results. If the score of the output is higher, the overall investment project risk is lower. On the contrary, if the score of the output is lower, the overall investment project risk is bigger.

When BP neural Network is applied to listed company reorganization risk assessment, it is necessary to collect a certain number of forensic testing results as training set to train the neural network. The choice of training set must be authoritative evaluation results with high reliability. After neural network is trained, the trained weight and threshold are stored and to forecast projects, which will be assessed. As long as experts give the values of the indexes, the neural network can figure out the average risk value of the project and the final evaluation result can be obtained from the output layer.

Table 1 Expert scoring corresponding to risk level

| Risk level | Lower | Low | Ordinary | High | Higher |
|----------------|-------|-----|----------|------|--------|
| Expert scoring | 1.0 | 0.7 | 0.5 | 0.3 | 0.0 |

4 Case Study

On the foundation of evaluation index system, evaluate the reorganization risk of four listed companies by using variable BP neural network model.

First, we employ experts to assess the investment risk of ten typical listed companies' reorganization cases. According to the designed index-evaluation system obtain the training set of the neural network, which are shown in Table 2. By using the BP neural network to train the risk of the ten listed company reorganization projects he results are obtained and are shown in Table 3.

As Table 3 shows, the average error of training sets of the ten freeway investment risk evaluation is 2.38 % and the maximum error of training testing is 5.19 %. Thus, the fitting of the neural network is good, and the error is near 5 %. Since the trained neural network have simulated and memorized function relation between input variables and output variables, the trained neural network can predict freeway investment risk.

Then we let experts take a risk evaluation to the freeway investment project and get the evaluation data, which is shown in Line A, B, C, D. Then we make predictions by using trained BP neural network, and the result is shown in Table 4.

From Table 4, it can be seen that the average relative error of prediction data set is 2.44 %, and the largest relative error of the prediction set is 2.96 % while the least relative error of the prediction set is 1.15 %, which means that the BP neural network model is trained well and with relatively accurate prediction result.

5 Conclusions

Factors that influence freeway investment project risk are multiple and complex, so it is with great reference significance for acquiring company, acquired company, and minority investors to find out an applicable listed company reorganization risk evaluation method. Based on traditional BP neural network, this paper presents variable structure BP neural network model. In this model, different hidden layer neuron connection numbers in the process of disconnection and reconnection represent different weight of factors in the listed company reorganization risk evaluation. In this paper, it takes factors of listed company reorganization risk evaluation as the input, takes the final evaluation value as the output, and then evaluates risks of four listed company reorganization projects. The result shows that the average relative error of prediction data set is 2.44 %, the largest relative error of the prediction set is 2.96 % while the least relative error of the

Table 2 The evaluation results of listed company reorganization risk

| No. | 1 | 2 | 3 | 4 | 5 | 6 | 7 | 8 | 9 | 10 | A | B | C | D |
|-----------------|-------|-------|-------|-------|-------|-------|-------|-------|-------|-------|-------|-------|-------|-------|
| R ₁ | 0.7 | 0.7 | 0.7 | 0.3 | 0.5 | 0.5 | 0.7 | 0.3 | 1.0 | 0.7 | 0.5 | 0.3 | 0.7 | 0.7 |
| R ₂ | 0.5 | 0.7 | 0.7 | 0.3 | 0.5 | 0.7 | 0.7 | 0.7 | 0.5 | 0.5 | 0.5 | 0.7 | 0.7 | 0.5 |
| R ₃ | 0.7 | 0.5 | 0.7 | 0.3 | 0.5 | 0.5 | 1.0 | 0.7 | 0.5 | 0.5 | 0.5 | 1.0 | 0.5 | 0.5 |
| R ₄ | 0.5 | 0.7 | 1.0 | 0.5 | 0.5 | 0.7 | 0.7 | 0.5 | 1.0 | 0.5 | 0.3 | 1.0 | 0.5 | 0.5 |
| R ₅ | 0.5 | 0.7 | 1.0 | 0.3 | 0.3 | 0.5 | 1.0 | 0.5 | 0.7 | 0.7 | 0.5 | 1.0 | 0.3 | 0.7 |
| R ₆ | 0.7 | 0.5 | 0.7 | 0.3 | 0.5 | 0.5 | 0.7 | 0.7 | 0.7 | 0.7 | 0.5 | 0.7 | 0.7 | 0.7 |
| R ₇ | 0.5 | 0.5 | 1.0 | 0.3 | 0.5 | 0.7 | 0.7 | 0.5 | 1.0 | 0.7 | 0.5 | 1.0 | 0.7 | 0.7 |
| R ₈ | 0.5 | 0.5 | 1.0 | 0.3 | 0.7 | 0.7 | 1.0 | 0.7 | 1.0 | 0.7 | 0.7 | 1.0 | 0.7 | 0.5 |
| R ₉ | 0.7 | 0.7 | 0.7 | 0.3 | 0.7 | 0.7 | 0.7 | 0.7 | 0.7 | 0.7 | 0.5 | 0.7 | 0.5 | 0.7 |
| R ₁₀ | 0.5 | 0.5 | 1.0 | 0.3 | 0.7 | 0.5 | 0.7 | 0.7 | 0.5 | 0.5 | 0.5 | 1.0 | 0.5 | 1.0 |
| R ₁₁ | 0.3 | 0.7 | 1.0 | 0.5 | 0.7 | 0.5 | 0.5 | 0.7 | 1.0 | 0.7 | 0.7 | 0.7 | 0.7 | 0.7 |
| R ₁₂ | 0.5 | 0.7 | 1.0 | 0.3 | 0.7 | 0.5 | 1.0 | 0.7 | 0.7 | 0.5 | 0.5 | 1.0 | 0.7 | 1.0 |
| R ₁₃ | 0.5 | 0.7 | 0.7 | 0.3 | 0.7 | 0.7 | 1.0 | 0.7 | 0.7 | 0.7 | 0.5 | 0.7 | 0.7 | 0.7 |
| R ₁₄ | 0.5 | 0.5 | 1.0 | 0.3 | 0.5 | 0.7 | 1.0 | 0.5 | 0.7 | 0.5 | 0.5 | 1.0 | 0.5 | 0.7 |
| R ₁₅ | 0.5 | 0.5 | 1.0 | 0.5 | 0.5 | 0.5 | 1.0 | 0.7 | 0.7 | 0.7 | 0.3 | 0.7 | 0.7 | 1.0 |
| R ₁₆ | 0.3 | 0.7 | 1.0 | 0.0 | 0.7 | 0.7 | 0.7 | 0.3 | 0.7 | 0.7 | 0.7 | 0.5 | 0.5 | 0.7 |
| R ₁₇ | 0.5 | 0.7 | 0.7 | 0.3 | 0.7 | 0.5 | 0.5 | 0.7 | 0.7 | 0.5 | 0.5 | 0.7 | 0.7 | 0.5 |
| R ₁₈ | 0.5 | 0.7 | 1.0 | 0.3 | 1.0 | 0.7 | 1.0 | 0.7 | 1.0 | 0.7 | 0.7 | 0.7 | 0.7 | 0.7 |
| R ₁₉ | 0.5 | 0.7 | 0.5 | 0.5 | 0.5 | 0.7 | 0.7 | 0.7 | 0.7 | 0.7 | 0.3 | 0.5 | 1.0 | 0.7 |
| R ₂₀ | 0.7 | 0.5 | 0.7 | 0.5 | 0.7 | 0.7 | 0.7 | 0.7 | 0.7 | 0.7 | 0.7 | 0.7 | 0.7 | 0.7 |
| R ₂₁ | 0.3 | 0.5 | 0.7 | 0.3 | 0.3 | 0.5 | 0.5 | 0.5 | 0.7 | 1.0 | 0.5 | 0.5 | 1.0 | 0.5 |
| R ₂₂ | 0.5 | 0.7 | 0.7 | 0.3 | 0.5 | 0.7 | 0.7 | 0.7 | 1.0 | 0.7 | 0.5 | 0.7 | 0.7 | 0.5 |
| Mark | 0.535 | 0.733 | 0.922 | 0.223 | 0.645 | 0.713 | 0.851 | 0.634 | 0.825 | 0.683 | 0.498 | 0.863 | 0.703 | 0.786 |

Table 3 The trained results of BP neural network for listed company reorganization risk evaluation

| No. | 1 | 2 | 3 | 4 | 5 | 6 | 7 | 8 | 9 | 10 |
|------------------|-------|-------|-------|-------|-------|-------|-------|-------|-------|-------|
| Evaluation value | 0.535 | 0.733 | 0.922 | 0.223 | 0.645 | 0.713 | 0.851 | 0.634 | 0.825 | 0.683 |
| Train result | 0.529 | 0.723 | 0.886 | 0.212 | 0.634 | 0.732 | 0.871 | 0.638 | 0.801 | 0.671 |
| Error (%) | 1.13 | 1.38 | 4.06 | 5.19 | 1.74 | 2.60 | 2.30 | 0.63 | 3.00 | 1.79 |

Table 4 Listed company reorganization risk evaluation value based on BP neural network

| No. | A | B | C | D |
|------------------|-------|-------|-------|-------|
| Evaluation value | 0.498 | 0.863 | 0.703 | 0.786 |
| Train result | 0.512 | 0.873 | 0.721 | 0.810 |
| Error (%) | 2.73 | 1.15 | 2.91 | 2.96 |

prediction set is 1.15 %, indicating that the result is quite accurate. Variable structure BP neural network has strong ability of self-organized study, and can solve the contradiction between operation precision and operation efficiency of traditional network algorithm well. This model has a great application prospect in the area of freeway investment and construction.

References

1. Jin P (2005) Empirical research of Chinese listed company reorganization risk. Shanghai Jiaotong University, Shanghai
2. Tan J (2009) Financial risk analyze of chinese listed company reorganization. J Nanjing Inst Ind Technol
3. Zhang Y (2010) Listed company reorganization financial risk evaluation and control research. J Harbin Eng Univ
4. Lou W (2005) Comprehensive evaluation model for the investing risk of using artificial neural networks in the Hi-tech projects. Res Manag 26(3):8–11
5. Cui W (2006) Risk evaluation model of high sci-tech agriculture projects based on ANN. J North Agric Technol Univ 34(7):160–164.v
6. Wang Z, Zheng J, Li H (2013) The risk evaluation model of mining project investment based on fuzzy comprehensive method. Appl Mech Mater

Fuzzy Prediction of Molten Iron Silicon Content in BF Based on Hierarchical System

Qihui Li

Abstract A hierarchical fuzzy system model is presented based on data driving, and then, the model is used to predict the molten iron silicon content in BF. As input variables this model uses the control parameters of a current BF such as moisture, pulverized coal injection, oxygen addition, coke ratio, etc. And variables employed to develop the model have been obtained from data collected online from Blast Furnace of Baotou Steel plant. This paper utilizes the fuzzy clustering algorithm combined nearest neighbor clustering and fuzzy c-means clustering to classify the input space. The simulation and error results show that the prediction based on hierarchical fuzzy model and data-driven method has good approximation and fit the output characteristics of the system. The most important point is that the number of fuzzy rules is greatly reduced.

Keywords Blast furnace · Hierarchical fuzzy system · Prediction · Silicon content

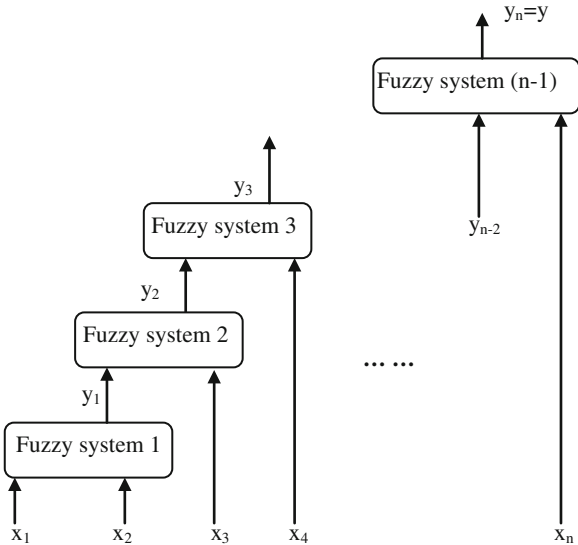
1 Introduction

In the Blast Furnace (BF) ironmaking production process, hot metal temperature is an important parameter to be controlled during the BF operation, and it should be kept around a set point to obtain a homogeneous pig iron quality and a stable BF performance [1]. Due to the fact that in the smelting, it is difficult to directly measure the BF temperature, the silicon content in the molten iron is usually used to reflect the BF temperature [2].

Q. Li (✉)

Mathematics Department of Jiaying University, 314001 Jiaying, China
e-mail: leeqihui@163.com

Fig. 1 An example of n -input hierarchical fuzzy system



As to the highly complex processes that take place inside a BF, then it should be mathematically modeled on fuzzy logic theory to achieve an approximate knowledge of their behavior. These applications of fuzzy prediction and control with standard fuzzy system to BF can be found in many literature studies. Although fuzzy prediction and control techniques have been successfully applied to BF ironmaking production process, the applications are usually limited to system with few variables. A fundamental limitation of standard fuzzy system is that as the number of variables increases, the number of rules increases exponentially.

The hierarchical fuzzy systems were proposed by Raju et al. in [3] as a way to deal with the rule-explosion for fuzzy control applications. Their hierarchical fuzzy system consists of a number of low-dimensional standard fuzzy systems connected in a hierarchical fashion. Figure 1 shows a typical example of hierarchical fuzzy systems.

It is well known that standard fuzzy systems, as well as hierarchical fuzzy systems are universal approximators [4]. The low-dimensional fuzzy systems are Takagi-Sugeno-Kang (TSK) fuzzy systems which were proposed in [5]. The control method based on the data-driven is a new control algorithm born in recent years [6]. This method only uses the saved large amount of input and output data to online learn and calculate the control variables which can match with current state, and can get all kinds of dynamic and static quality satisfying system requirements.

In Sect. 2, input and output variables employed to control the BF operation which could be controlled by plant operators are selected, and the hierarchical fuzzy systems are constructed. In Sect. 3, we use the hierarchical fuzzy systems constructed in Sect. 2 to control the BF Ironmaking Process. Section 4 concludes the paper.

Table 1 Input variables and delay time

| Variables | Delay times (h) |
|---|-----------------|
| Silicon content, % | 4 |
| Blast moisture, gm ⁻³ | 2 |
| Pulverized coal injection, kg t ⁻¹ HM | 2 |
| Ore to coke ratio, kg kg ⁻¹ | 8 |
| Coke charge, kg t ⁻¹ HM | 5 |
| Burden, kg t ⁻¹ HM | 5 |
| Blast rate, N m ³ h ⁻¹ | 2 |
| Oxygen injection, % in blast or N m ³ t ⁻¹ HM | 2 |

2 Variables Employed and Construction of Hierarchical Fuzzy Systems

2.1 Selecting Variables

Because not all monitored process variables have an influence on the silicon content in the molten iron, it is necessary to select which ones will be used as input data in the hierarchical fuzzy system. Input variables employed to control the BF operation which could be controlled by plant operators, having a precise set point assigned. Owing to their importance in BF control, the parameters used in the present work are selected in Table 1.

2.2 B Construction of Hierarchical Fuzzy Systems

The TSK fuzzy system is constructed from the following rules:

$$\text{If } x_1 \text{ is } A_1^l \text{ and } x_2 \text{ is } A_2^l \text{ and } \dots \text{ and } x_{n_i} \text{ is } A_{n_i}^l, \text{ Then } y_i = h_i^l(x_1, x_2 \dots x_{n_i}) \quad (1)$$

where A_j^l are fuzzy set, h_j^l are linear or nonlinear functions, and $l = 1, 2, \dots, M_i$. Given an input $x_i = (x_1, x_2 \dots x_{n_i})^T \in U^i \subset R^{n_i}$, the output $f_i(x_i) \in R$ of the TSK fuzzy system is computed as the weighted average of the h_i^l in (1), i.e.

$$f_i(x_i) = \frac{\sum_{l=1}^{M_i} h_i^l(x_1, x_2 \dots x_{n_i}) w_i^l}{\sum_{l=1}^{M_i} w_i^l} \quad (2)$$

where the weights w_i^l are computed as

$$w_i^l = \prod_{j=1}^{n_i} \mu_{A_j^l}(x_j) \quad (3)$$

Each low-dimensional TSK fuzzy system constitutes a level in the hierarchical fuzzy system, there are eight input variables. The hierarchical fuzzy system is to choose $n_1 = 2$ and $n_i = 1$ for $i = 2, 3, \dots, L$. All the TSK fuzzy systems in the hierarchy have two inputs, that is, 8-input hierarchical fuzzy system, which comprises seven two-input TSK fuzzy system is presented in this paper. This special hierarchical fuzzy system is illustrated in Fig. 1.

The first level is a TSK fuzzy system with two input variables (x_1, x_2) , that is, it is the $f_i(x_i)$ of (2) with $i = 1$.

The second level is a TSK fuzzy system with two input variables (x_3, y_1) which are constructed from the following rules:

$$\text{If } x_3 \text{ is } A_3^l \text{ and } y_1 \text{ is } C_1^l, \text{ Then } y_2 = h_2^l(x_3, y_1) \tag{4}$$

According to (2) and (3), this TSK fuzzy system is

$$f_2(x_3, x_4, y_1) = \frac{\sum_{l=1}^{M_i} h_i^l(x_3, y_1) \prod_{j=3}^3 \mu_{A_j^l}(x_j) \mu_1^l(y_1)}{\sum_{l=1}^{M_i} \prod_{j=3}^3 \mu_{A_j^l}(x_j) \mu_1^l(y_1)} \tag{5}$$

where $h_i^l(x_i, y_{i-2}) = a_0x_i + a_1y_{i-2} + a_2y_{i-2}^2 + \dots + a_{n-1}y_{i-2}^{n-1}$ ($i = 3, 4, \dots, 8$).

The construction continues until $i = L$ such that $\sum_{j=1}^L n_j = 8$, that is, until all the input variables are used in one of the level.

Theorem 1 [4] *For the hierarchical structure containing n system variables, if t is the number of variables contained in each of the hierarchical levels including the output variable of the preceding level. Suppose that m fuzzy sets are defined for each variable, then the total number of the rules K is*

$$K = \left[\frac{(n-t)}{(t-1)} + 1 \right] m^t = \frac{(n-1)}{(t-1)} m^t \tag{6}$$

The proof is omitted.

Theorem 2 [4] *Let the assumptions in Theorem 1 be true. If $n \geq 2$, then the total number of rules K of (6) is minimized where $t = 2$, that is, when TSK fuzzy systems in all the levels have two inputs as shown in Fig. 1.*

The proof of this theorem can be found in [7].

We see from (6) that the number of rules K in the whole hierarchical fuzzy system increases linearly with the number of input variables n . For the case in this paper $n = 8, t = 2$, and $m = 5$, we have $K = 7 \times 5^2 = 175$. If we use the standard fuzzy system, the number of rules is $K = 5^8 = 390625$. The reduction of rules is great.

Let the domains of x_i be $[\alpha_i, \beta_i]$ ($i = 1, 2 \dots 8$), and we design the domain of y_1 be $[0, 1]$. Define m fuzzy sets A_i^1, \dots, A_i^m in $[\alpha_i, \beta_i]$ with the following equal-spaced triangular membership functions:

$$\begin{aligned} \mu_{A_i^1}(x_i) &= \mu_{A_i^1}(x_i; e_i^1, e_i^1, e_i^2), \\ \mu_{A_i^j}(x_i) &= \mu_{A_i^j}(x_i; e_i^{j-1}, e_i^j, e_i^{j+1}), \text{ for } j = 2, 3 \dots m - 1, \text{ and} \\ \mu_{A_i^m}(x_i) &= \mu_{A_i^m}(x_i; e_i^{m-1}, e_i^m, e_i^m), \end{aligned} \tag{7}$$

where $i = 1, 2 \dots 8$, $e_i^j = \alpha_i + (j - 1)b_i$ with $b_i = (\beta_i - \alpha_i)/(m - 1)$, and the triangular membership functions are defined by

$$\mu_A(x; a, b, c) = \begin{cases} (x - a)/(b - a) & a \leq x \leq b \\ (c - x)/(c - b) & b \leq x \leq c \\ 0 & x < a \text{ or } x > c \end{cases} \tag{8}$$

And then define m fuzzy sets $B^1 \dots B^m$ in $[0, 1]$ with equal-spaced triangular membership functions as in (7). In this paper, we select $m = 5$.

3 Prediction of the Silicon Content Based on Hierarchical Fuzzy Model

A hierarchical fuzzy model was designed, using software tool to simulate the silicon content in the molten iron, then to study how the system will work and be implemented in a real BF.

In Baotou Steel plant of China, the operators use the moisture and the pulverized coal injection as input variables to control the BF and to obtain the desired hot metal properties, but sometimes these control actions are not taken in order to minimize the fuel and coke consumption [1]. Therefore, the objective of the present work is to determine which are the best input variables variations to reduce the fuel and coke consumption, yet obtain the desired hot metal properties. The effects produced for different moisture variations, keeping the rest of variables constant, were studied in a chosen and constant period of time. The method used was the introduction of different steps during the time period selected. First of all, a moisture value for a time period was introduced and answer from the model was obtained. After that, different moisture values steps were introduced in order to observe the silicon content behavior in each one. The same trials were carried out for both pulverized coal injection and the blast rate. It is well known that when the moisture is high the silicon content in hot metal decreases.

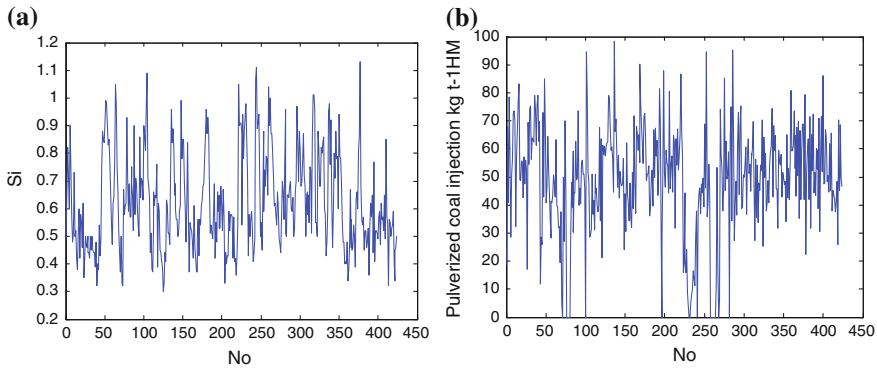


Fig. 2 a Silicon content and b Pulverized coal injection

As the input variables to the first level of the hierarchical fuzzy model are Blast moisture and Pulverized coal injection. The second-level input variable is Coke charge, and third-level input variable is Oxygen injection, the fourth-level input variable is silicon content, and so on (Fig. 2).

Through data processing and fuzzy clustering algorithm, the collected data are divided into five fuzzy states from low to high. Using the notation to express fuzzy classification is {NB, NS, ZE, PS, PB}, for every parameter of input and output variables, the data are collected from BF of Baotou steel using the nearest neighbor clustering to deal with the data roughly, and then finding out the data clustering center, and the data clustering membership matrix by using FCM.

Selecting 100 set of data of the Balst Furnace in Baotou to test the model, the simulation result is shown in Fig. 3.

The simulation result and the prediction error result show that the error between model output and actual data is small.

4 Conclusions

This paper utilizes hierarchical fuzzy system modeling method based on data-driven to prediction the molten iron silicon content in BF. Under the relatively stable conditions of the blast furnace, eight factors affecting silicon content are obtained. According to the ironmaking data collected online in Baotou Steel Blast Furnace, the nearest neighbor clustering algorithm and fuzzy C-means clustering algorithm are used to blur the parameters and identify the structure. The simulation and error results show that the prediction based on hierarchical fuzzy model and data-driven method has good approximation and fit the output characteristics

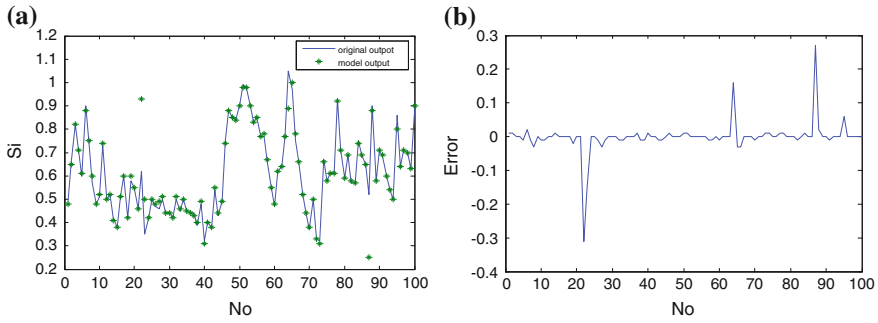


Fig. 3 **a** The prediction results and **b** The prediction error

of the system. Meanwhile the algorithm is simple and has high accuracy prediction. The most important point is that the number of fuzzy rules is greatly reduced.

References

1. Cui G, Liu M, Ma X (2012) Prediction of Si content in blast furnace based on fuzzy model. In: Proceeding of 24th Chinese control and decision conference (CCDC), 3175–3179
2. Li Q, Liu X (2007) Fuzzy prediction functional control of silicon content in hot metal. *J Zhejiang Univ (Nat Sci Ed)* 39(3):104–108
3. Raju GVS, Zhou J, Kisner RA (1991) Hierarchical fuzzy control. *Internat J Control* 54:1201–1216
4. Wang Li-Xin (1998) Universal approximation by hierarchical fuzzy systems. *Fuzzy Sets Syst* 93:223–230
5. Takagi T, Sugeno M (1985) Fuzzy identification of systems and its application to model and control. *IEEE Trans Systems Man Cybernet* 15:119–132
6. Rhodes C, Morari M, Tsimring LS (1997) Data-based control trajectory planning for nonlinear systems. *Phys Rev E* 6(3):2398–2406
7. Raju GVS, Zhou J (1993) Adaptive hierarchical fuzzy controller. *IEEE Trans Systems Man Cybernet* 23:973–980

An Evaluation of Integration Technologies to Expose Agent Actions as Web Services

Juan Pablo Paz Grau, Andrés Castillo Sanz
and Rubén González Crespo

Abstract Integration capabilities are a key feature of today's enterprise software systems; therefore, integration capabilities are necessary if Multi Agent Systems are to be successful on the enterprise current software landscape. This paper starts by presenting some remarks on exposing agent actions as web services, its pros and cons; then we present the results of exposing an agent action as a web service by exercising a contract net among agents and by invoking the contract net from a web service.

Keywords Multi agent systems · Agent-oriented software engineering · Agent modeling · Web services

1 Introduction

Integration technologies are currently the main enabler of enterprise information systems. When a new software component is to be deployed on an enterprise technology ecosystem, the first goal to achieve is the integration of this new subsystem with the pre-existing software components, permitting the new component to consume data and processes from its host environment and to provide interfaces for other components to take advantage of the data processing

J. P. P. Grau (✉) · A. C. Sanz · R. G. Crespo
Computer Science Department, College of Engineering and Architecture,
Universidad Pontificia de Salamanca, Madrid, Spain
e-mail: juan.paz@upsam.es

A. C. Sanz
e-mail: andres.castillo@upsam.es

R. G. Crespo
e-mail: ruben.gonzalez@upsam.es

capabilities of the deployed subsystem. The integration task should not only cover the existing components; the interfaces from the newly deployed component should also consider the interactions with already planned or yet to be implemented components.

The integration technology that has become the de facto standard to enable integration among software components and enterprises are web services. Web services have been chosen by the software engineering community as an integration enabler because of its simplicity and its reliance on existing technologies; that is, to implement a web services solution an enterprise does not need to deploy and configure a variety of complex execution platforms or to perform intricate configurations on their server software; instead, web services lie on top of the enterprise's web infrastructure.

From an operational perspective, web services can be classified as entity services, functional services, or process services [1]. Entity services represent domain entities, and therefore, their operations usually perform CRUD operations on the domain objects they represent. Functional services provide functionalities that other services can use for their own objectives, and therefore, they are usually autonomous or independent, that is, they do not depend on the state of the system or of the domain entities to perform their actions. Finally, process services may represent a series of related tasks in a workflow, and it is very usual for such services to be implemented as an orchestration or composition of other web services.

From this perspective, it is clear that agent actions can be exposed as functional or process web services, as agent actions can perform the kind of complex task that these kind of web services enact. Web services are simple, reactive artifacts that only respond to service invocation [2], and although it is possible to implement intelligent-like behaviors with web services through service orchestration or compositions, an external (e.g., BPM) engine should be configured and deployed to achieve this goal. A multi agent system can overtake this task on a more effective and native way, as agents can more easily discover one another and talk to each other autonomously.

Despite this possibility, multi agent systems (MAS) are currently closed systems that are hardly integrated with other enterprise components when they are deployed. MAS are seen as standalone platforms that perform their actions to achieve a predefined set of goals, but do not interact with other enterprise components, nor expose their capabilities to allow other enterprise components to take advantage of its capabilities. Multi agent systems are able to provide an infrastructure that eases the construction of complex or composite tasks that can be orchestrated, composed, or arranged in a variety of ways that can provide as outcome intelligent behaviors.

In this paper, we present some grounding on the current status of the issues around exposing agent actions as web services, and continue by describing the workings of a small multi agent system that exposes some of its behaviors as web services, thus facilitating it to be easily integrated onto an enterprise solution. Then, we exercise the multi agent system behaviors by means of invoking the

exposed behaviors through its web service interface with a stress test tool. Following, we show the interaction results. Finally, we present some conclusions derived from the topics exposed in the paper.

2 Remarks on Exposing Agent Actions as Web Services

The printing area is 122 × 193 mm. The text should be justified to occupy the full the idea of exposing agent actions as web services have been around for a while, but there has been a significant disinclination from the multi agent systems community to follow this path of integration of MAS with other software entities [3]. The first identified issue is how to translate the agent stateful communication model into the web services stateless communication model. This seems a very strong issue, but from a practical point of view, not all agent actions are subjected to be exposed as web services. Moreover, a multi agent system will only expose agent actions engineered specifically to overcome this difficulty. Therefore, their external interface would be composed of a set of functional or process web services; this last set of services could start processes that can involve many agents and agent interactions, returning the final status after the process has finished.

Another issue is the lack of substantial theoretical work to support exposing agent actions as web services to provide an external interface to the multi agent system allowing it to fully integrate onto the enterprise architecture. This paper aims at widening the foundations of agents and web services integration.

Although much attention has been focused on enabling agents to invoke web services, on the other side, little attention has been paid in enabling multi agent systems to integrate into an enterprise software architecture by exposing its behaviors as web services; from the reviewed tools, many of them addressed only certain aspects of the web services stack, and among the tools that implemented the whole communication stack, their key goal was allowing agents to invoke web services. From the tools and frameworks reviewed, only two of them enable full 2-way integration of agents with web services, WSIG [4] (Web Services Integration Gateway), which is an add-on for the JADE platform and Agent Web Gateway [5, 6], a set of converter tools that perform conversions between agent standards and web services standards; e.g., ACL/SOAP conversion for the messaging standard, DF/UDDI conversion for the service publishing standard, and DF service to WSDL service description conversion. On the other hand, WS2JADE [7] grants the ability to create agent services definition that could be published on the Directory Facilitator (DF) so that the agents could invoke web services as if they were invoking an agent action, which would be performed by means of a proxy agent.

We have implemented a reference multi agent system using the JADE Java Agent Development Framework [8]. This decision has marked our choice to use the WSIG to expose some agent actions as web services. We chose WSIG because it is already specifically designed for JADE, and because of the flexibility to use an ontology mapper class to perform mapping between the exposed interface and the

agent actions present in the MAS ontology. As an alternative, we have also created web service interfaces by means of the JAX-WS technology using the same interface exposed by the WSIG's ontology mapper, which will invoke an agent action by means of a proxy agent. This is the same approach as that of WSIG architecture, but using another web services technology and without the dynamic service discovery features of WSIG.

3 Reference Multi Agent System

We have chosen a relatively small multi agent system with the aim of avoiding confusion and loss of focus while working or explaining complex agent interactions. Instead, we present a MAS composed of very few agents that perform concrete operations. Despite being a small multi agent system, our MAS is currently deployed in a production environment, where it is integrated with the other components of the enterprise IT architecture.

The MAS is composed of five kinds of agents:

- *Report Executor*: The report executor agent is part of a report execution contract net. It receives requests from the report contractor to execute Jasper Reports® reports. If the report executor gets awarded the contract to execute the report, it arranges to find the desired report in a report database, then passes the required parameters and executes the report, exporting it to the requested format (e.g., PDF, HTML, or XLS). It hands the executed report on to the caller agent as Base 64 encoded data, or stores it in a file.
- *Report Contractor*: It is also part of the report execution contract net. The report contractor directly receives requests to execute reports, and then, it issues a bid on the report executor's contract net to execute the report. Once a report executor is awarded the report execution, it handles the request to the winning report executor, which is transferred also the responsibility to answer the request to the original requestor. If all report executors refuse to participate in the report execution bid, the report contractor continues the bidding process until the report execution is awarded.
- *Mailer Agent*: The mailer agent receives as input a set of user ids and an e-mail message, and attempts to retrieve the e-mail of the proposed users from the user database, and sends every one of them a copy of the e-mail message. Depending on the request, it sends plain or MIME mail messages.
- *Reminder Agent*: This agent composes the services provided by the mailer and report contractor agent, performing an orchestration of their tasks. The reminder agent receives a scheduled job, which it executes at the specified time interval. The jobs currently implemented following the pattern of retrieving a set of user ids from the user database, and then, executing a report passing as parameter each of the user ids. Then, the report executions and the user list are passed to the mailer agent, to send the personalized report execution for each user.

Some of the reminder jobs we have implemented are: sending student counseling appointment reminders to students, daily student counseling appointment schedules to psychologists, pending teacher's coaching dates to students, daily coaching schedule to teachers, survey reminders to alumni at certain dates after graduation, and others.

The reminder agent acts autonomously, enacting a process workflow. It is an example of how services can be actively composed to perform complex tasks, based on a proactive behavior.

- *WSIG Agent*: The WSIG (Web Services Integration Gateway) agent exposes some agent actions as web services. In the reference multi agent system that has been described, the report and mail agent actions from the reporter and mailer agents are exposed as Web Services, thus enabling other artifacts of the enterprise architecture to run reports or send emails.

The agent ontology includes concepts like Report, Mail, and Schedule, which are used by the agents defined in the ontology. There are two agent actions executed by the Reporter Agent (Execute Report and Execute Save Report), two agent actions executed by the Mailer Agent (Send MIME and Send Plain), and an agent action (Execute Schedule) executed by the Reminder Agent; nevertheless, the Reminder Agent uses the Report and Mail concepts as well to perform its operations. Even though a minimal ontology, we followed the ontology design guidelines presented in [9, 10].

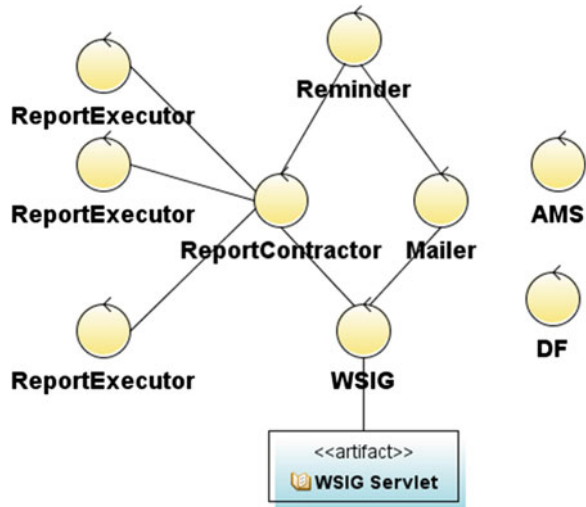
At the second stage of our experiments, the WSIG agent was replaced by a Proxy Agent that interfaces the Web Service invocation with JAX-WS with the agents that perform the requested operations. The system architecture remains the same as the situation with the WSIG, because after all, the Metro Web Services stack install a Servlet at our Tomcat 7.0 servlet container. The overall architecture for the reference multi agent system is shown in Fig. 1.

The DF and AMS agents are implemented by the JADE framework according to the FIPA specification; the WSIG servlet is the ultimate artifact that allows the publication of the exposed agent actions as web services, with its corresponding WSDL specification.

The reporter and mailer agents perform actions that are basic building blocks for other, existing, or future artifacts of the system. To bring on some examples, the report Web Service is the main component of the report launcher application, which centralizes the reports of all the system modules in a single control panel; it is also used by the financial software to generate bank payment orders at the online payments system; on the other hand, the mail Web Service is the main component of an application that allows university officials to create and operate mailing lists.

We emphasize in this paper the Reporter Contract Net because its performance is a key indicator of the multi agent system throughput. The Mailer Agent performance is not as important as mailing, although it indeed is a slow task and has no impact on the user experience. The Reminder agent is a scaled agent [11, 12] (that is, provides no observable primitives to the outside world) working on the

Fig. 1 The reference MAS system



backend of the system, so its performance is not observable directly; moreover, its performance is indirectly related to the performance of both the Mailer and Reporter agents; so any improvements on the performance of any of the two orchestrated agent actions will have a direct impact on the performance of the Reminder agent.

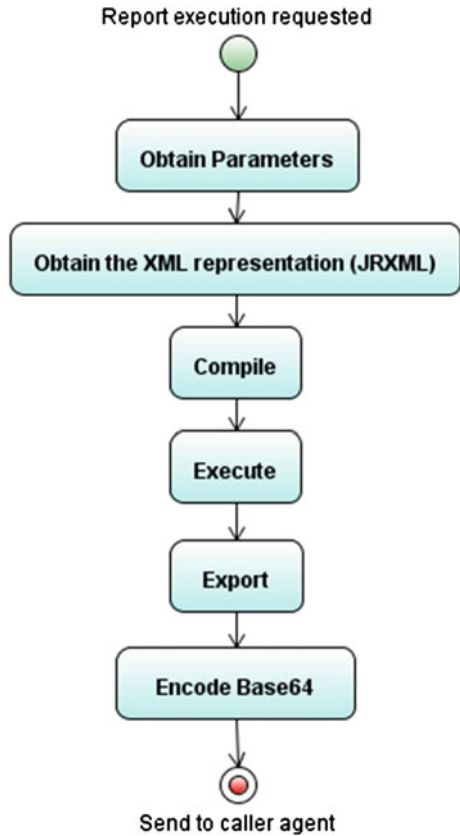
The report generation task is susceptible to generate bottlenecks because report execution is a very time- and resource-consuming task depending on the number of pages, the quantity and complexity of charts, and the selected export format. The execution time can grow significantly. Although for most cases reports are executed sparsely over time, there are some events that cause many university officials to run a large amount of reports at the same time, stressing the system. The report execution activity is depicted in Fig. 2.

The encoding Base 64 subtask includes gzip compressing the report output, and it is performed when the Reporter should return the report execution to a caller agent instead of writing the report to a file. This is needed as the content payload of the ACL message does not have support for the exchange of binary data between agents.

Our main interest is then to analyze how exposing the report execution contract net as a web service impacts on the global system, and to have insights into the process that would allow us to identify possible improvements to the contract net agents.

The following two sections of the paper describe how the stress test tool was set up to exercise the report execution contract net and the results we obtained from the stress tests performed over the system.

Fig. 2 Report execution task



4 Exposing the Report Execution Contract Net as a Web Service

To exercise the contract net and to be able to check the multi agent system in action, we performed some basic measurements of the execution of the system, exercising the MAS protocols by means of a stress test tool. The first step to achieve this was to record a session of the report launcher application with the packet sniffer Wire Shark [13], then we selected a set of 12 report request SOAP messages, choosing a heterogeneous set of reports, ranging from very simple, text only, one page reports, to complex, tens of pages, chart intensive reports. Then, we copied each report request and modified each SOAP message changing the report execution parameters. In this way, we could obtain a set of 24 report request SOAP messages to be chosen randomly by the stress test tool.

The report execution contract net protocol that will be enacted behind the report web service invocation is implemented as follows: the report contractor receives the report execution request and begins a contract net protocol with the report

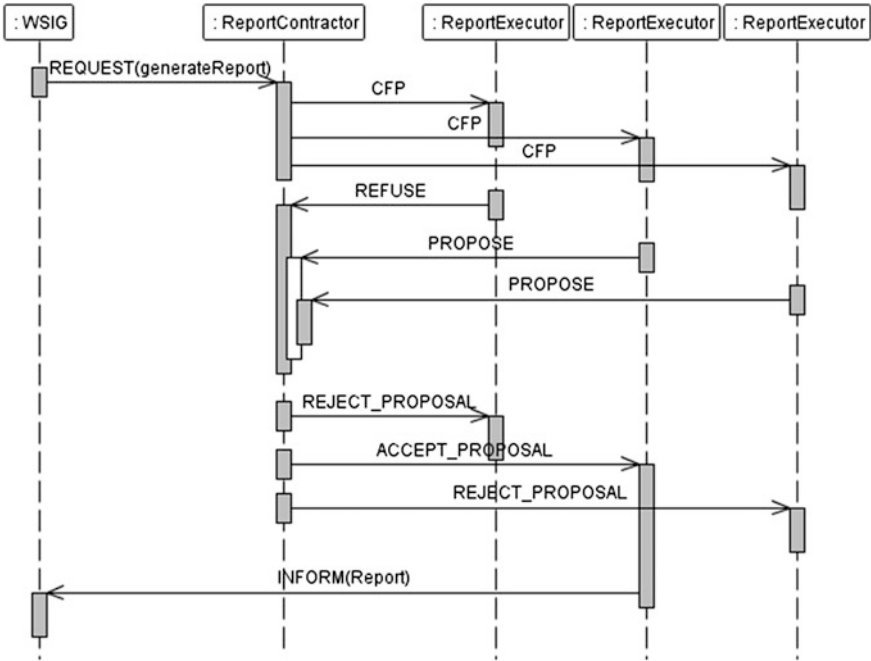


Fig. 3 The report contracting protocol

Table 1 JMeter parameters for layer two and three performance testing experiments

| Configuration element | Parameter | Value |
|-----------------------|--------------------------|-------|
| Thread group | Threads | 20 |
| | Up time | 300 s |
| | Loops | 50 |
| Constant timer | Time | 5 s |
| Uniform random timer | Max. time | 1 s |
| SOAP request | Use random SOAP messages | Yes |
| | Read SOAP response | Yes |

executors. The first executor to send a bid to the contractor gets awarded with the report execution. The report awarding protocol is shown in Fig. 3. We exercise the protocol varying the number of report executor agents.

The report execution contract net design favored stability over performance, that is, the invocation of a report should always give as a response the requested report; there should not be (and there were no) error messages as the invocation response, and the WS client should and did always get the requested report served, despite the running time of the report.

To exercise the multi agent system, we used the Apache JMeter stress test tool [14]. We developed a very conservative experiment setup as shown in Table 1 and the same test parameters were used for all the contract net exercising runs. As the

idea was not to stress the web service, but rather to emulate a group of users executing a set of reports, the execution times and the stress test configuration were very moderate. Although the tests took a very long time to complete, it emulated a fair execution scenario for the multi agent system report execution contract net.

Finally, the test environment was composed of a JADE platform containing all of the agents of the multi agent system and an Apache Tomcat Web Server 7.0 distribution. For the first execution scenario, the WSIG Servlet was deployed at the container; while for the second execution scenario we had to install the Metro web services layer to sit the JAX-WS web service implementation on top of it.

The test environment was run on an OracleTM VM Virtual BoxTM running Ubuntu Linux 12 with two cores of an Intel Core i3 processor and 1.95 GB of base memory.

5 MAS Execution Results

Once the JMeter test plan was defined and the test environment was ready, we proceeded to perform the experiments. In this section, we show and discuss the results obtained while exercising the subsystem of the Report Contractor and Report Executors shown in Fig. 2, while they enact the contract net protocol interaction protocol shown in Fig. 3.

We ran the performance experiment several times, varying the number of Report Executors from two agents to ten agents. The throughput of the reporting system, using the WSIG as the web services gateway, is shown in Fig. 4. As the figure shows, we obtained only a slight improvement on the reporting performance, although the improvement was very tiny.

We were curious about the small gain in throughput by adding more agents to the system, and by means of monitoring the contract net execution through the JADE's Sniffer Agent we found that when the system was serving simple reports, the gain in performance was noticeable, but when running complex reports with binary results of many megabytes, the WSIG response stalled and queued further report executions, responding after some time to the clients in "response bursts," thereby hurting the performance indicators of the queued responses. This phenomenon is depicted in Fig. 5, which shows the performance evolution over time while running the experiment, and the discontinuities in the graph are caused by the WSIG agent stalling at response time.

The graph corresponds to a test run of 200 samples of the Reporting System with four Report Executors.

In the next step, we kept the same JMeter configuration (as shown in Table 1), but used JAX-WS over the Metro Web Services stack as the web services gateway. Again, we varied the number of Report Executor agents from two agents to ten agents. The throughput of the stress test is shown in Fig. 6.

Fig. 4 Performance of the Report Contract Net exposing WS with WSIG

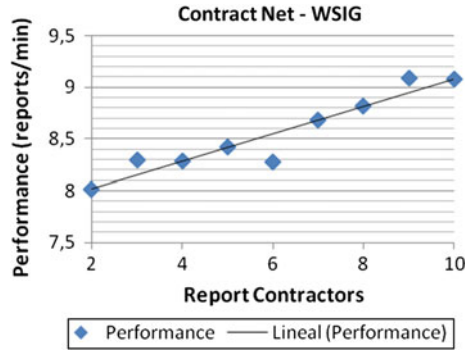


Fig. 5 The performance degradation problem identified in the WSIG response

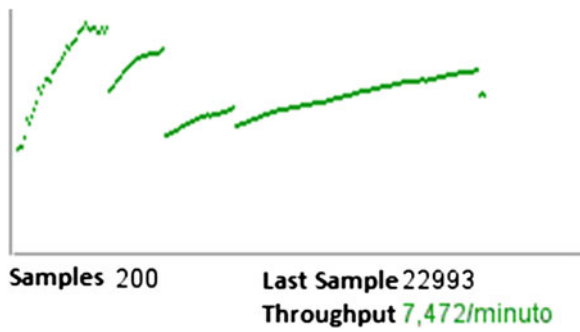
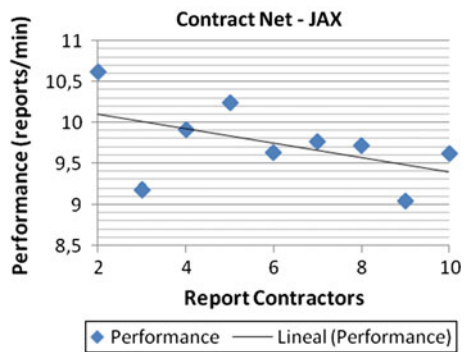


Fig. 6 Performance of the Report Contract Net exposing WS with JAX_WS



Surprisingly, the stress test results did not follow a linear pattern, but instead followed a disordered pattern, although we got better throughput with 2 and 5 agents (10.61 and 10.24, respectively) than the maximum throughput that we could get with the WSIG integration gateway. We also experienced the performance degradation phenomenon depicted in Fig. 5.

Although this was an unexpected result, we would not change the input reports to feed the report system only with text only or not with chart intensive report

requests, as these would suppose an unfair change in the test plan; instead we assumed it as an unexpected test result. We are currently analyzing the collected data to identify other stress points on the contract net to allow the system to escalate better when more report executor agents are added to the contract net.

6 Conclusions

We presented in this paper a reference MAS that uses a contract net and other agent compositions to perform its work; these behaviors can be also exposed as web services to allow other enterprise components to take advantage of the tasks implemented by the MAS. We put the MAS to work and execute the reports execution contract net, following the guidelines for stress tests in [15]. This protocol exercising permitted us to gain more insight into the inner workings of our implemented MAS, and it led to the identification of implementation issues that would otherwise have been difficult to identify.

As we plan to develop further MAS and to integrate them with different software architectures via exposing agent actions through Web Services, our next goal will be to develop a further stress plan method that allows us to have deeper insights into the inner workings and capabilities of our MAS system.

Finally, we expect that this paper could give an insight into multi agent systems integration technologies as a step to allow MAS to become more present in the current software landscape.

References

1. Hewitt E (2009) Java SOA cookbook. O'Reilly Books, ISBN: 978-0-596-52072-4
2. Payne TR (2008) Web services from an agent perspective. IEEE Intell Syst, ISSN, pp 1541–1672
3. Greenwood D, Lyell M, Mallya A, Siguri H (2007) The IEEE FIPA approach to integrating software agents and web services. In: Proceedings of the AAMAS'07
4. JADE Board (2008) JADE Web Services Integration Gateway (WSIG) Guide. TILab
5. Omair Shafiq M, Ali A, Suguri H, Ahmad HF (2006) AgentWeb gateway integration of FIPA multi agent system and W3C web service system. In: 3rd GGF semantic grid workshop, vol 13, p 16
6. Bolivar Baron H et al (2012) A multi-agent matchmaker based on hidden markov model for decentralized grid scheduling. IEEE Intell Netw Collab Syst (INCoS) pp 62–69
7. Nguyen XT (2005) Demonstration of WS2JADE. In: Proceedings of the fourth international joint conference on Autonomous agents and multiagent systems, ACM
8. JADE Java Agent Development Framework. <http://jade.tilab.com>
9. Isaza G, Castillo AG, López M, Castillo L (2009) Towards ontology-based intelligent model for intrusion detection and prevention. Computational intelligence in security for information systems advances in intelligent and soft computing, vol 63, pp 109–116. Springer

10. Isaza GA, Castillo AG, López M, Castillo LF, López M (2010) Proceedings of information security and assurance—4th International conference, ISA 2010, Miyazaki, Japan, 23–25 June 2010. Proceedings 01/2010, pp 51–63
11. Z. Houhamdi, “Multi-Agent systems Testing: A Survey”. International Journal of Advanced Computer Science and Applications Vol. 2, No. 6, ISSN 2156-5570 (2011)
12. Gutierrez C (2013) An analysis architecture for communications in multi-agent systems. Int J Interact Multimed Artif Intell 2(1):65–72. doi:10.9781/ijimai.2013.219
13. Sharpe R, Warnicke E WireShark User’s Guide. http://www.wireshark.org/docs/wsug_html_chunked/
14. The Apache Software Foundation. Apache JMeter User’s Manual. <http://jmeter.apache.org/usermanual/index.html>
15. Dikaiakos M, Samaras G (2001) Performance evaluation of mobile agents: issues and approaches. Performance engineering, state of the art and trends. Springer, London. ISBN 3-540-42145-9

Research on Evolution Mechanism of Runway Incursion Risks Based on System Dynamics

Xianli Zhao and Fan Luo

Abstract Based on system dynamics theory, the system boundary of runway incursion is confirmed. The causal loop diagram and system flow diagram of runway incursion risks evolution are built. The logical relationship and feedback mechanisms between the factors are analyzed. The process of runway incursion evolution is revealed and the trend of this evolution is forecasted. Based on the System Dynamics Software Vensim, the simulation results show that the risk value of runway incursion stabilizes after experiencing the peak value in a period of time. The finding is consistent with practical state of runway incursion in the civil aviation industry, which verifies the validity of the model.

Keywords Runway incursion · Evolution mechanism · System dynamics

1 Introduction

With the rapid development of China's civil aviation, the airline fleet and the scale of airport increased. The construction and management of runway is particularly important. Runway operations involved human factors and equipment factors. It is the multiple aspects of aviation ground accidents. According to the statistics, the United States has 3,156 runway incursion accidents from 1999 to 2007 in 450 airports with control towers [1]. From 2005 to 2011, China's civil aviation has 104 runway incursion events (not including D and E). The accident rate increased from 5.77 to 22.12 %, which shows significant growth trend. According to a study by the Canadian Department of transportation, an airport traffic flow increased by 20 % will make the possibility of runway incursions increase 140 % [2]. The world

X. Zhao (✉) · F. Luo
Management of School, Wuhan University of Technology,
Wuhan People's Republic of China
e-mail: zxli820@163.com

transportation passenger number is 2,439 million in 2010. The increased rate of passenger traffic is 7.3 % year-on-year. According to this development trend, the increase in traffic flow will inevitably bring about an increased risk of runway incursions.

At present, China's civil aviation in the vast majority of airports lack of effective means and measures to prevent runway incursions, the future increase in traffic flow will inevitably bring about increased risk of runway incursions. Runway incursion caused serious consequences, so the runway incursion is necessary for risk management, and provide theoretical basis for the prevention of runway accident from the aspect of risk control. Study on the airport runway incursion has important practical significance to reduce casualties and property losses, to ensure aviation safety.

2 Review of Literature

Domestic and foreign scholars in the area of runway incursion are concentrated on the study of influencing factors, risk assessment, and prediction, control model etc. In the aspect of influencing factors of runway incursion, Huo and Han [3] believed that the main factors affecting runway incursion in airfield management is in chaos, unauthorized personnel and vehicles to enter the runway, the combined military and civilian airport poor coordination, lack of personnel training, and no runway invasive consciousness. Luo et al. [4] used Gauss Bayesian network model analysis of runway incursions, including implicit human factors, equipment factors, airport and operation errors and other factors as well as low visibility, flight flow, field supervision, and lack of surface factors. Sun [5] analyzed factors of runway incursion from the air traffic control, flight operations, airport and ground navigation, and traffic flow to improve the capacity of program and for the airport design of four functional domains. In the aspect of runway incursion risk evaluation and prediction, Xu [6] proposed an improved correlation function calculation formula, and established a runway incursion risk extension assessment model. Gao [7] established runway incursion autoregressive moving average model on the forecast of the trend of runway incursions. In the aspect of runway incursion risk control model, Xu and Huang [8] proposed runway accident risk control based on risk defense, including technology research (starting from the angle of the influence factors of accident) and organizational support measures (starting from the angle of the airport security management global). For example, changing the surface distribution [9] and improving the air side traffic surveillance system [10, 11] and other means both can prevent the runway incursion events.

In summary, the current research methods of runway incursion risk evaluation focus on the extension evaluation model, Bayesian network model, fuzzy analytic hierarchy process, autoregressive moving average method, and so on. Few scholars use the evaluate dynamics. For the content of the study, most of the studies focus on risk assessment methods and models. Research on risk evolution mechanism

has not been involved in the intrusion on the runway. The risk of runway incursions is obviously nonlinear, open, dynamic characteristics. The system dynamics method is selected to study the evolution mechanism. The boundary of the system dynamics model is confirmed based on the analysis of factors which affects runway incursions. The logic relationship between each factors are analyzed. The system flow diagram of runway incursion is built. Based on the simulation, the risk rates of runway incursion between various elements are contrasted which provided a scientific basis for the prevention of runway incursion.

3 Runway Incursion Risks Evolution Model

3.1 System Boundaries

Usually, the general principles to determine the boundary of the model are to select the relevant state variables, and determine the state vectors that are classified, arranged to determine the variables to be studied are controlled by the state variables. Due to cognitive limitations, it is impossible to analyze an all-encompassing model. The boundary model in this paper shows below.

- (1) The research scope is runway incursion risks, regardless of the apron, taxiways, access road, and clearance risk;
- (2) Related factors of runway incursion only involved in the incident are taken into account, not considering the emergency management of unsafe accidents or incidents occurred;
- (3) Runway incursions are complex system, involving human, machine, environment and management. The environment factors are very uncontrollable. In order to ensure the relevance of the study, this model only considers the human factors, equipment factors, and management factors, without considering the influence of irresistible.

Boundary system dynamic model with endogenous, exogenous and do not consider the factors that three parts define the runway incursion risk, as shown in Table 1.

3.2 Circuit Diagram of Runway Incursion Risks

The risks of runway incursion is influenced by many factors, including primarily by control risk, the risk of plant unit operation, the risk of communications equipment, airfield lighting risk, risk of ground identification. There are correlating relationships between control risks and Flight Flow, training investment, job satisfaction and management capacity. The relationships between the risk of plant

Table 1 Variables in the model

| Endogenous variables | Exogenous variables | Irrespective factors |
|--------------------------|--------------------------|----------------------|
| Control risk | Working environment | Weather factors |
| Flight flow | Foreign flyer | Policy factors |
| Plant unit operation | Runway foreign matters | Social factors |
| Controller capacity | Military aircraft impact | Economic factors |
| Job satisfaction | Management system | |
| Communications equipment | Organizational climate | |
| Airfield lighting | | |
| Ground marks | | |
| Training investment | | |
| Management capabilities | | |

unit operation and investment in training, job satisfaction, management ability are existed. Circuit diagram of runway incursion risks is shown in Fig. 1.

3.3 System Flow Diagram of Runway Incursion Risks

The evolution process of runway incursion can be shown in Fig. 1, but more variables should be introduced to reflect the integrity of the system and evolution in order to analyze systematically. System flow diagram can be more detailed and incisive in the description of system running state. The logical relationship between the risk factors is depicted. The nature of variables is cleared so as to achieve the purpose of feedback and control the behavior of the system. Combining the system boundaries and the circuit diagram, the system flow diagram is built, which is shown in Fig. 2.

As is shown in Fig. 2, there are three main feedback loops.

- (1) The feedback loop of runway incursion risks as the center
 Runway incursion risks → + foreign Flyer → + the runway foreign object → + management capabilities → + management system → + organizational climate → + working environment → + job satisfaction → + controllers ability → - runway incursion risks
- (2) The feedback loop of control risks as the center
 Control risks → + flight flow → - management capabilities → + control risk increase → + + training inputs → + controllers ability → - control risks
- (3) The feedback loop of plant unit operating risks as the center
 Plant unit operating risks → + communications equipment risk → + equipment failure rate → - the error rate of control → - organizational climate → unit operation risk

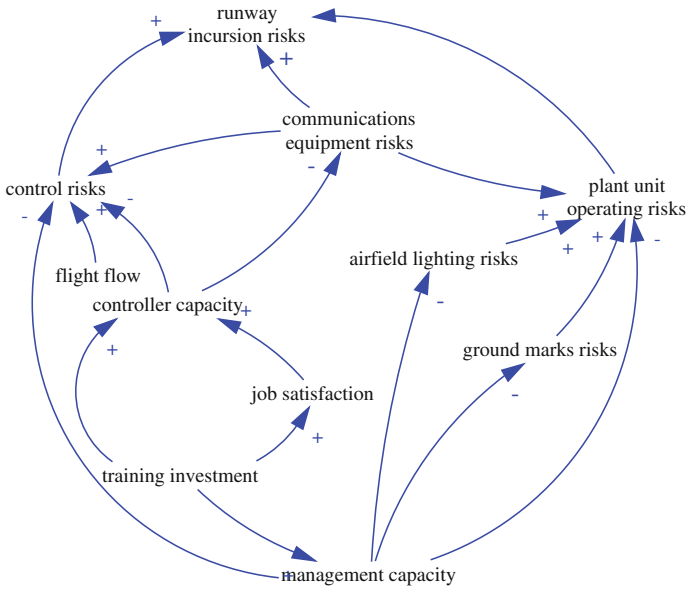


Fig. 1 Circuit diagram of runway incursion risks

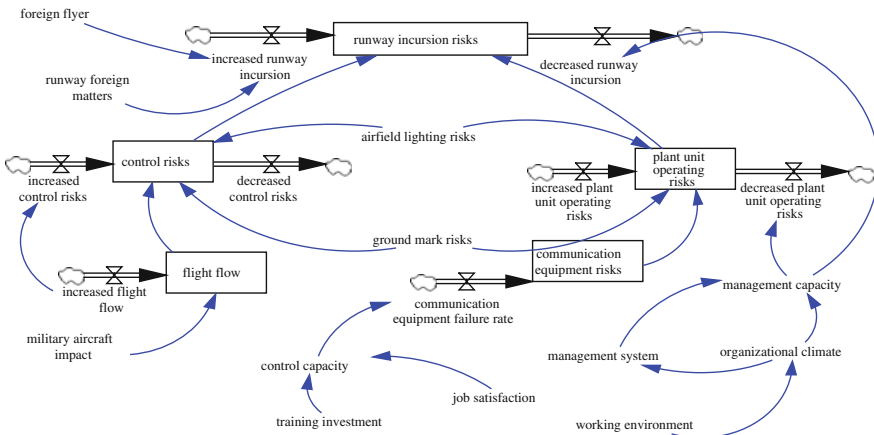


Fig. 2 System flow diagram of runway incursion risks

4 System Dynamics Simulation and Result Analysis

4.1 The Kinetic Equation

Based on the variables and the type of the system flow diagram, the key indicators are selected. The parameters are defined as shown in Table 2.

According to the circuit diagram and system flow diagram of runway incursion risks, the rate equations and auxiliary equations are established. The paper uses integral formula or differential formula to express level variables and rate variables. Literature summary and experts scoring are used to express soft variables. Comprehensive weight is used to express the dimensionless variables. The main equations in the paper are shown as below.

$$FFIR_t = (FTIR_t - FTIR_{t-1})/FTIR_{t-1} \quad (1)$$

In Eq. (1), FTIR_t stands for Flight Flow Increase Rate at time t. FTIR_{t-1} stands for Flight Flow Increase Rate at time t-1.

$$RV_t = RV_{t-1} + \left(\sum RV_{in} - \sum RV_{out} \right) \times DT \quad (2)$$

In Eq. (2), RV_t stands for Runway Incursion Risks Value at time t. RV_{t-1} stands for Runway Incursion Risks Value at time t-1. RV_{in} stands for the inflow rate variable in the period, and RV_{out} stands for the outflow rate variable in the period. DT stands for the simulation time step.

$$CEFR_t = (CEFR_t - CEFR_{t-1})/CEFR_{t-1} \quad (3)$$

In Eq. (3), CEFR_t stands for Communication Equipment Failure Rate at time t. CEFR_{t-1} stands for Communication Equipment Failure Rate at time t-1.

$$TIAV_t = \sum TIAV_t - \sum TIAV_{t-1} \quad (4)$$

In Eq. (4), TIAV_t stands for Training Inputs Added Value at time t. TIAV_{t-1} stands for Training Inputs Added Value at time t-1.

4.2 Equation Initial Values Setting

The paper uses expert scoring and empirical data to set the initial values. If the simulation results are not satisfactory, the initial values are reset to improve secondary analog. In the value of the variables, Flight Flow Increase Rate and Communication Equipment Failure Rate are percentage. Training Inputs Added Value is the absolute increasing value. Runway Incursion Risks Value and Job

Table 2 Parameters of key indicators

| Num | Variables | Properties | Units |
|-----|--------------------------------------|--------------------|------------------------|
| 1 | Flight flow increase rate | Rate variable | % |
| 2 | Runway incursion risks value | Level variable | Dimensionless |
| 3 | Communication equipment failure rate | Rate variable | % |
| 4 | Training inputs added value | Level variable | Ten thousand RMB/month |
| 5 | Job satisfaction | Auxiliary variable | Dimensionless |

Satisfaction are dimensionless numbers, which include 1, 2, 3, 4, 5 five levels. Set the time parameters of the system for 12 months. The time setting is : FINAL TIME:12,INITIAL TIME:1,TIME STEP:1,UNITS FOR TIME: MONTH. The initial values of the equations are set as follows: $FTIR_0 = 5.3\%$, $RV_0 = 2$, $CEFR_0 = 0.244\%$, $TIAV_0 = 5.5$ ten thousand RMB/month, $JS_0 = 3$.

4.3 Simulation Results and Analysis

Substituting the initial values and equations to system dynamics simulation software Vensim-PLE, the simulation results are shown in Fig. 3.

As can be seen from Fig. 3, the air traffic flow rises oscillatory in course of time. With the rapid development of the civil aviation industry in recent years, the number of aircraft increases, so f the air traffic flow presents upward trend overall. Communication equipment failure rate is upward slowly and stabilizes after a certain period of time. As the increasing of aircrafts, the carrying capacity of communications equipment enhances, so the failure rate exists. Training inputs added value stabilizes after a certain period of time. Training investment will increase the accident-prone period and will stabilize in the safety period. Job satisfaction fluctuates in the early time and stabilizes over time.

5 Conclusions

The above analysis show that the runway incursion risks value stabilizes after experiencing the peak value in a period of time. Analyzing the runway incursion risks as a complex system, this paper analysis the factors affecting the evolution based on System Dynamics. The simulation results are consistent with practical state of runway incursion in the civil aviation industry, which verifies the validity of the model. The application of system dynamics theory and simulation methods can be more intuitive display changes and evolution trend of the related factors in

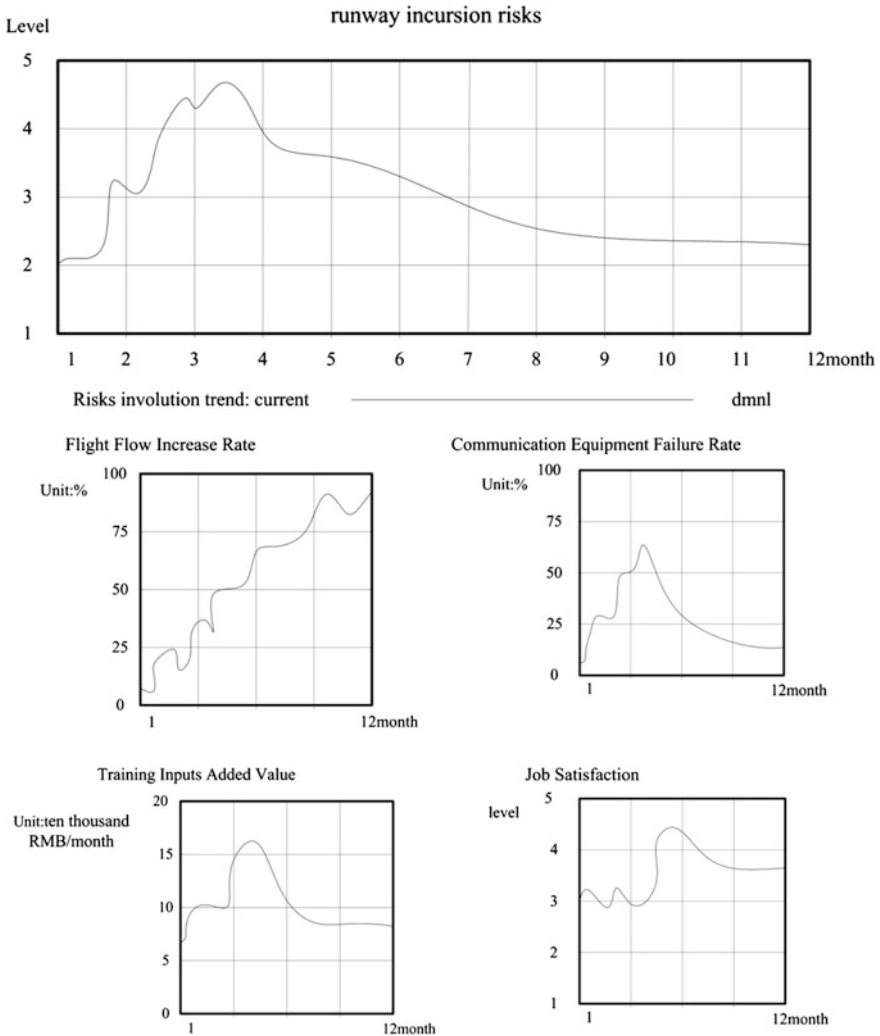


Fig. 3 Runway incursion risks value and related factors in the trends evolution

the system. It not only reveals the process of runway incursion evolution, but also predicts the trend of the evolution of runway incursion risks, which provide new idea on the prevention of runway incursions.

Acknowledgments The authors acknowledge the support from the National Nature Science Foundation of China “Research on the Evolution Mechanism and Early warning Simulation System of Safety Risks in the Flight Area of Airport” (No. 71271163).

References

1. Gao X (2009) Preventing runway incursion to avoid aircraft ground collision. *Safety Secur* 106(10):57–59
2. Transportation Canada (2001) National civil aviation safety committee sub-committee on runway incursions. Final report. Transportation Canada, Ottawa
3. Huo Z, Han S (2012) Threats and mistake analysis and control of runway incursion. *Safety Environ J* 12(4):192–196
4. Luo J, Lin X, Yan Y (2012) Research on runway incursion factors based on gaussian bayesian network model. *Safety Environ J* 12(3):196–199
5. Sun J, Huang S (2008) Analysis on runway incursion factors. *Sci Technol* 29:564–566
6. Xu G, Huang S (2010) Extension evaluation of runway incursion risks based on improved correlation functions. *Hum Ergon* 16(4):56–59
7. Gao Y, Li Y (2008) Analysis and forecast of runway incursions based on ARIMA model. *China Saf Sci J* 18(11):25–30
8. Xu G, Huang S (2010) Risk-based defense airport runway accident risk control. *Saf Sci Technol J* 6(3):106–109
9. Lockwood SM, Dorigin R et al (2002) Runway incursion studies in NASAs future flight central. The American Institute of Aeronautics and Astronautics, Los Angeles, pp 1–31
10. Sammuta Z, Manglon DZA (2006) Traffic movement monitoring computer for pre-emptive runway conflict detection. The American Institute of Aeronautics and Astronautics, Keystone, pp 21–241
11. Vernaleken C, Urvoyc K (2008) Simulator evaluation of a novel surface movement awareness and alerting system (SMAAS) for runway incursion avoidance. International Council of the Aeronautical Sciences, Anchorage, pp 14–191

Simulation of Nonpoint Source Pollution Based on LUCC for Er-hai Lake's Watershed in Dali of China

Quan-li Xu, Kun Yang and Jun-hua Yi

Abstract Many evidences have given that there is a chain process for water pollution formation in Er-hai Lake Watershed, which could be described like this: Human activities (more in agriculture) have changed LUCC, and LUCC leads nonpoint source pollution. As a result, in this paper, those have been discussed according to the driving mechanism of nonpoint source water pollution in Er-hai Lake, which include three explorations. The first is how to build a ABM-LUCC model by using Repast and GIS technology, and the second is the method and implementation for hydrological and water quality model by using SWAT model and GIS, as well as Remote sensing technology. And establishing a platform for comprehensively simulating the whole process of water pollution by integrating GIS, ABM-LUCC models, and hydrological model is the last work for this study.

Keywords Nonpoint source pollution · ABM · GIS · SWAT · Model integration

Q. Xu · K. Yang (✉)

Faculty of Tourism and Geographic Science, Yunnan Normal University, Kunming, China
e-mail: kmdcynu@163.com

Q. Xu

e-mail: go2happiness@163.com

Q. Xu

School of Remote Sensing Information Engineering, Wuhan University, Wuhan, China

J. Yi

Inspection Station of Surveying and Mapping Product in Yunnan Province, Kunming, China
e-mail: yih2ok@163.com

1 Introduction

Er-hai Lake lies on the state of Dali, which is so important to the local people that they consider her as the Mother Lake. Unfortunately, she is threatened by the more serious pollution of water. And from the water quality assessment of Er-hai Lake over the years, it is indicated that the major water pollution sources come from nonpoint source pollution. The arguments for water environmental protection of Er-hai Lake are focused on some issues such as what has formed the nonpoint source pollution of water? What has lead to the environmental change of Er-hai watershed? And the most important is how to get the efficient methods to simulate the temporal–spatial process for change on environment and nonpoint pollution? Those are the questions that we should give more attention to. Till the questions are clearly answered, the real reasons of producing for nonpoint source pollution maybe found and the reasonable suggestions for solving water pollution could be given for Er-hai Lake.

What has changed the hydrological cycle and increased the nonpoint pollution in the past several years in Er-hai Lake? The answer is the negative effect of the land use change and cover change of watershed, as we know, which is called LUCC. There is a consensus that LUCC effects greatly on water environment and it takes a major research field since the study of LUCC plan is developed in the 1990s of twentieth century. As declared by Veldkamp and Verburg, what is the biggest challenge for researchers in studying on LUCC is to explore the dynamic interaction and process between change of LUCC and response on water environments [1]. It is of no doubt that, as the carrier of water resources, the changes of environments of Er-hai Lake watershed will make effective changes to the cycle of hydrology as well as the space distribution and density of pollution loads. Thereby, we could conclude that a reasonable plan or structure for land use could improve the quality of water; otherwise, it may take a degradation of water quality. As a result, it could be declared that the driving force of nonpoint source pollution of Er-hai Lake is coming from the negative changes of LUCC such as the loss of soil and water, excessive fertilization, and so on.

However, what has been affecting the LUCC? It is another important question we should give an answer for water pollution. As we know, land is one of the important resources and material as concerned for human survival and development, as well as the foundation in the complex system of “Population—Resources—Environment—Development (PRED)” [2]. And many evidences have given that the change of LUCC is more due to the human activities in lake basin, [3] especially, those for agriculture production. Thereby, there is a chain rule for water pollution in Er-hai Lake watershed, which could be described like this: Human actions (more in agriculture) have changed the LUCC, and LUCC leads nonpoint source pollution. Finally, based on the approach of this chain, we could explore the effect between human activities and nonpoint water pollution by using the indicator of LUCC of Er-hai Lake watershed.

At last, the more important issues in the paper we should discuss is how to establish the models to simulate this chain that drives the producing of nonpoint

source pollution for Er-hai Lake. Obviously, the impact on LUCC from human activities is a complex system, whose modeling is not more better than using the theory of Complex Adaptive System (CAS) [4]. The emergence of complexity in science is questioning traditional methods and tools of modeling. Furthermore, as a popular method and a new approach to understand and learn complex systems, Agent-based modeling (ABM) is playing a very important role in the CAS world [5, 6]. ABM is used to simulate behaviors of agents in complex systems, as well as relations between the patterns in order to find the emergence of macro behavior [7]. As far as the modeling for space-time process of hydrologic and water quality as concerned, many distributed hydrological models are good for this work, such as SWAT, which is a power tool to simulate the space-time process of hydrology and the change of water quality [8].

As a result, in this paper, those have been discussed according to the driving mechanism of nonpoint source pollution in Er-hai Lake, which include three explorations. The first is how to build a ABM-LUCC model by using Repast and GIS technology, and the second is the method and implementation for hydrological and water quality model by using SWAT model and GIS, as well as Remote Sensing technology.

2 Methodology of Establishing for Simulating Model

2.1 Modeling for ABM-LUCC Model by Using GIS

The model of ABM-LUCC is based on multiagent systems, which are made-up of the environmental factors and many agents in those environments. The interactions between the agents as well as between agents and the environments influence the land using tendency in whole regional; in other words, the regional land use change is decided by agents through judging the comprehensive properties of the surrounding environment and the choice they want to make. Based on this approach, we established a model of land use change in Er-hai basin. The method for establishing ABM-LUCC model is shown as Fig. 1.

2.1.1 Agents Categories

The major purpose in this step is to define the varying agents those are incharge of simulating the human activities. This work includes finding the dynamic factors which could directly change the status of LUCC, and then making a classification for those factors, as well as giving some attributes for them. Through exploring the development of agriculture and economy in Er-hai watershed, there are two agents designed in this model, which are Farmer and Government. Government agents play a decisive role in land use. They often consider natural and cultural factors

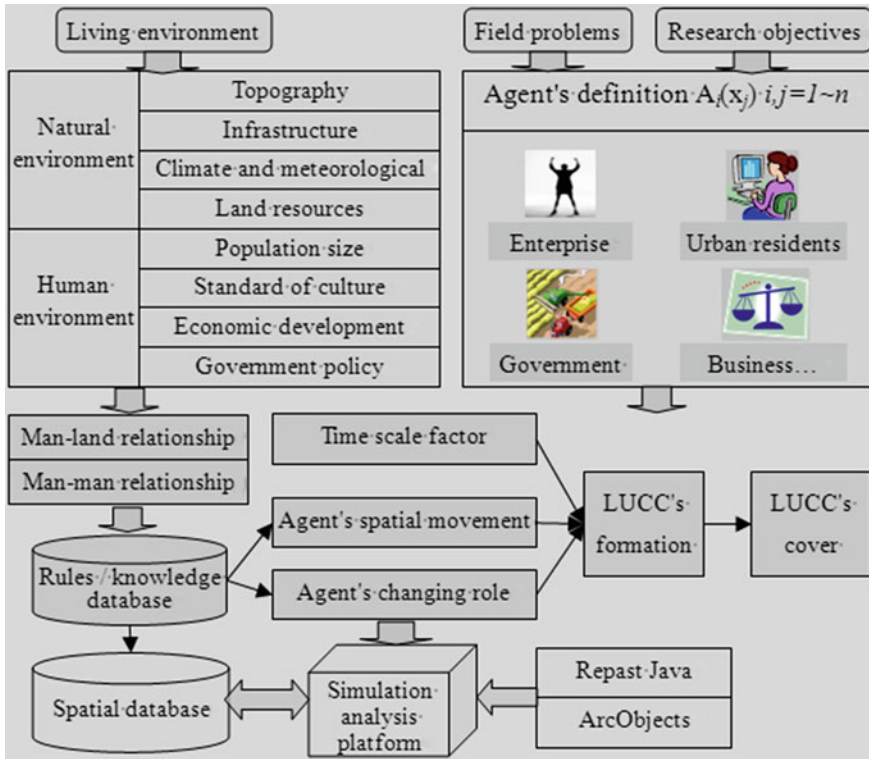


Fig. 1 The method of modeling for ABM-LUCC model by using GIS

and combine with government master plan so as to determine whether land use type is changed and how to converse them. Farmer agents are those people who have demanded for agricultural land, and they drive the change in agricultural land use by making their decisions based on their probable incoming in one year. In addition, all agents are attributed as some properties, such as age, sex, culture, and profession, etc., which would affect those agents' choices greatly during the process of their decisions.

2.1.2 Layers of Environmental Factors

These are two types of environment, which are natural environment and cultural environment. The former includes terrain, natural resources and infrastructures, etc. And those as the social and economic development, the model of cultivating are contained in the later. Each type may contain some layers that could impact the decision of different agents.

2.1.3 Agents' Behaviors and Status

Agents' behaviors and status are impacted by their attributes very much. What farmer agents do is to gain an individual development or to make some choices to find a job, and the later include two jobs which are cultivating and being migrant workers. And government agents may make policies for social development of economy, for planning of LUCC, or for residential expansion, etc.

2.1.4 Agents Decisions for Change of LUCC

In this step, the first work is to create the rules between agents and environment where they live through doing investigation in true world, as well as the interaction rules among agents themselves. Influenced by the rules, each agent's category does a special behavior and makes a different decision on LUCC. And then, a function for agent decision will be built, which translates the rules to an explicit and formal expression such as mathematic formula or spatial analysis model. Take farmer agents for instances, what they want to obtain mostly is maximize returns from the agricultural productions. Thereby, when the probable profits of maximization from some special land uses are coming to realize, they would tend to make a choice to keep those land uses, or they would like to change them to some other types of land use to get more benefits. We could give a formulation to express this rule [9].

$$\text{Maximize Profits (Bm)} = \text{Total Gains}(G) - \text{Total Costs}(C) \quad (1)$$

$$Bm = \text{Price in Marketplace}(P) \times \text{Output of Productions}(Q) \quad (2)$$

$$C = \text{Cost of Living}(Cl) + \text{Cost of Cultivating}(Cc) \quad (3)$$

However, the P , Q , and C are all deeply affected by natural and cultural environments, such as terrain, water resources, traffic condition, market place, population, and agents themselves. Taking those layers as weighting factors, we could improve the formulation (1) as follows:

$Bm = \text{Price}\{PIP = \text{Average of Price}(Pa) \times [1 + \text{Evaluation of Marketplace}(M) + \text{Evaluation of Population Density}(Pd) + \text{Evaluation of Individual}(I)]\} \times \text{Output}\{QIQ = \text{Average of}(Qa) \times [1 + \text{Evaluation of Traffic}(T) + \text{Evaluation of Water Resource}(W) + \text{Evaluation of Slope}(S) + \text{Evaluation of Aspect}(A)]\} - C$. Finally, this formula (2) could be simplified to formulas (4) and (5) as the last expression for farmer agents' decision.

$$Bm = Pa \times [1 + (M + Pd + I)] \times Qa \times [1 + (T)] - C \quad (4)$$

$$T = W + S + A \quad (5)$$

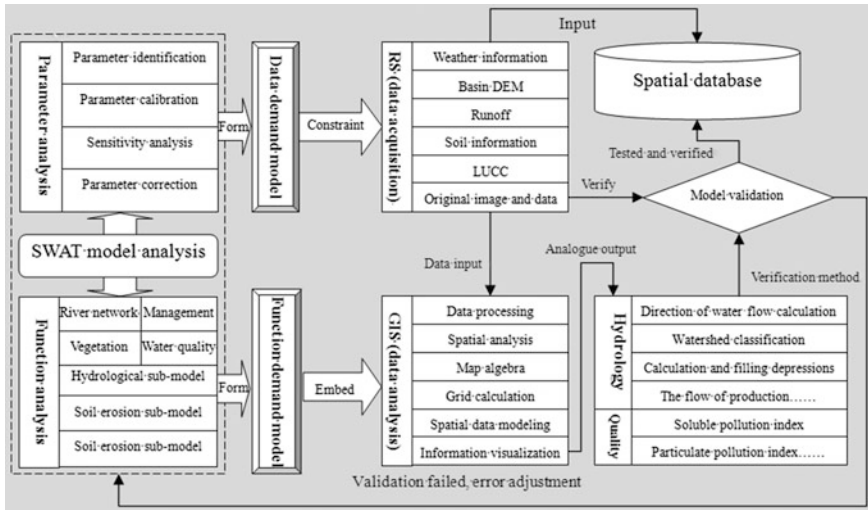


Fig. 2 The principle and method for SWAT-based hydrological modeling by using GIS and remote sensing

2.2 SWAT-Based Modeling for Hydrological Model by Integrating GIS

As we know, SWAT model has been providing many advantages in simulating nonpoint source water pollution, such as hydrological analysis based on DEM and LUCC, the spatial distribution of total N, total P, and COD, and so on. SWAT model could run now in ArcGIS as an embedding extension module, which will be beneficial to integrate hydrological model and GIS application. The principle and method of integrating SWAT-based hydrological model with GIS technology has been displaying in Fig. 2. As the picture shown, SWAT model is divided into two parts, one analysis is called data requirement that offers the services of parameters for model, another is called functional requirement which is responsible for special calculations in hydrological cycle and change of water quality. Remote sensing will be the major technology for getting and dealing parameters and ArcGIS will be the main software for analyzing the result of model output, such as visualization, report, statistics. and themes, etc.

Table 1 Data requirements for ABM-LUCC and SWAT model by Integrating ArcGIS

| Name | Application | Processing | Memo |
|---------------|--|--|---|
| DEM | Evaluation of Terrain for ABM-LUCC | Raster analysis for slope, aspect, and reclassify | 1:2,50,000 precision |
| | Hydrological analysis for SWAT | ArcHydro Tools in ArcGIS | |
| LUCC | Initialization for land use for ABM-LUCC | Extracting from TM and ETM of Watershed | Original image of 2009, and simulating to 2015 and 2020 |
| | Major impacting layer for N and P distribution | Coming from the result of simulating of ABM-LUCC | |
| Road | Evaluation of traffic for ABM-LUCC | Distance analysis | Raster |
| Water | Evaluation of agricultural irrigation for ABM-LUCC | Distance analysis | Raster |
| Marketplace | Evaluation of agricultural products' sale for ABM-LUCC | Interpolation and distance analysis | Raster |
| Economy | Evaluation of agricultural products' price for ABM-LUCC | Interpolation and distance analysis | Raster |
| Policy | As a weight parameter for ABM-LUCC | Convert text file to raster | Raster |
| Population | Evaluation of human resources for ABM-LUCC | Interpolation and density analysis | Raster |
| Soil type | Major impacting layer for transporting of pollution loads. Important parameter of SWAT model | Convert vector to raster | Raster |
| Hydrology | Important parameter of SWAT model | Containing rain down, runoff, and others in watershed | Text file |
| Water quality | Important parameter of SWAT model | Containing pollution load of N and P and others in watershed | Text file |

3 Experiments and Results

3.1 Designing and Processing for Experimental Data

As discussed in the context, it is clear for the data requirement of ABM-LUCC and SWAT model in Er-hai Lake watershed. The data list for designing and processing is shown in detail as the Table 1.

3.2 Result and Discussion

3.2.1 Results and Analysis of Simulation for ABM-LUCC Model

Through using the method of ABM-LUCC model designed on the above, we have gained two simulating results in future of 20 years by coding with JAVA in Repast-S. All are shown as Fig. 3.

The simulate results seem to tell us that the agricultural land areas would remain to be the major LUCC in watershed in future, and the increasing speed of residential areas for building should slowdown at the future two decades. The trends of residential land development are closing to the west bank of Er-hai Lake and the state city-Xia Guan. It seems to forecast that the high-economical development of city and natural environment of high quality would strongly attract the farmers and businessmen to settle and live.

3.2.2 Verification for ABM-LUCC Model

We have chosen the shaped index called Lee-Sallee (L-S) to validate this model. L-S is the ratio of two areas, one of which is the intersection of all land use between simulation and reality; another is the union of those. The formulation of L-S is shown as follow [10].

$$L = \frac{A_0 \cap A_1}{A_0 \cup A_1} \quad (6)$$

Here, A_0 is the total area of one of eight land use types for simulation, and A_1 is the total area for reality of LUCC. L (The value of L-S) is between 0 and 1, and it is closer to 1, the similarity of geographic shape is higher. Usually, if the value is between 0.3 and 0.7, the geospatial consistency is good. Through being programmed and computed with Matlab, the results of L-S index for Er-hai Lake watershed at the year of 2010 are shown as Table 2.

It could be declared from the results of L-S that all values of L-S for each land type are more than 0.3 besides wetland. The difference of wetland is due to the Dali state government sudden behavior on wetland development in recent years for the ecological restoration of watershed, which is difficult for this model to catch and simulate.

3.2.3 Results and Analysis of Simulation for Hydrology and Water Quality Model

The simulation for hydrology is divided into three steps that are hydrology analysis based on DEM, setting for parameters and calculation of space-time distribution for pollution loads such as N and P. What could be extracted from DEM are water

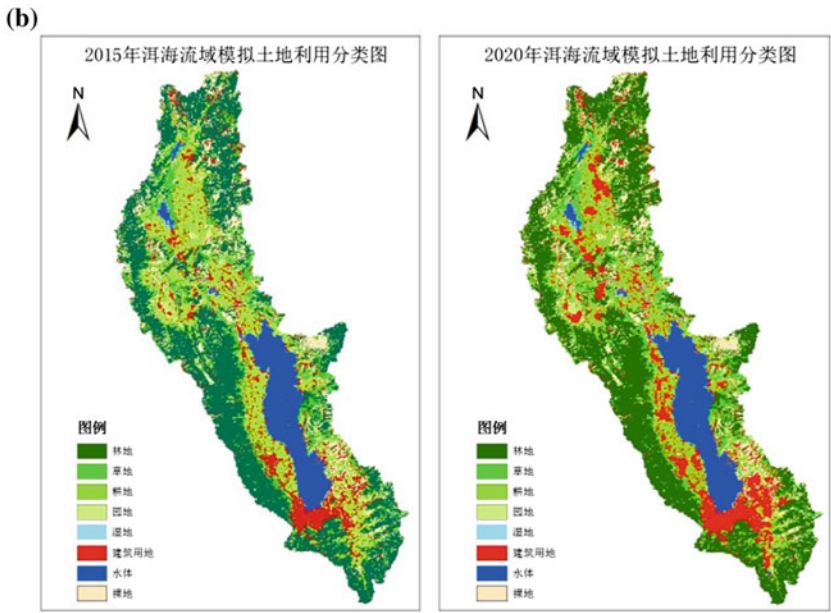
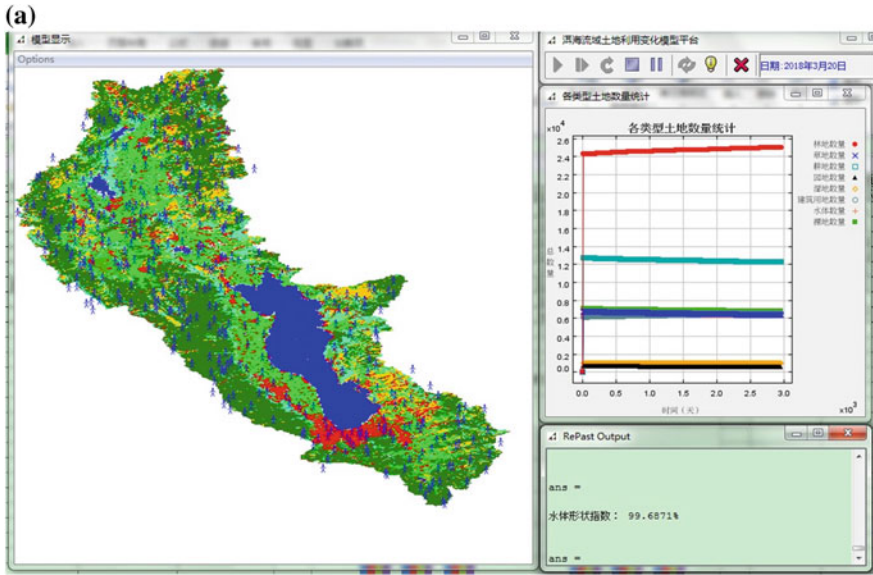


Fig. 3 The simulating interface and results with REPAST-S. a Integrating interface of simulation. b Simulating result of 2015. c Simulating result of 2020

flow, river network, subwatershed, and HRU (Hydrology Response Unit). And the HRU is the destination of hydrological analysis as well as the most important impact factor on calculation for water quality. The setting of parameters is also

Table 2 The values of L-S for simulation validation

| Forest land | Grass land | Farm land | Garden land | Wetland | Construct land | Water | Bare land | Total value |
|-------------|------------|-----------|-------------|---------|----------------|-------|-----------|-------------|
| 0.682 | 0.356 | 0.308 | 0.362 | 0.171 | 0.302 | 0.917 | 0.362 | 0.502 |

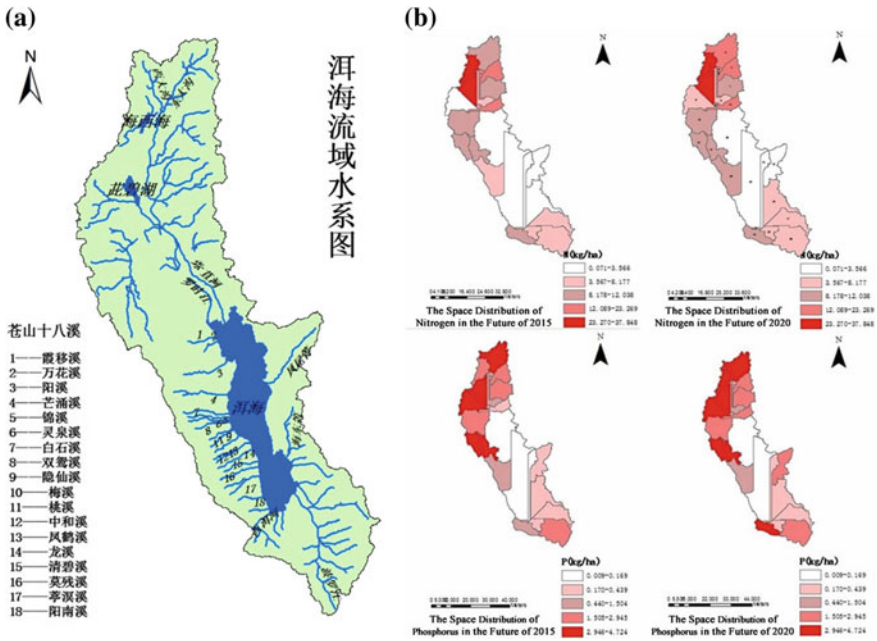


Fig. 4 The simulating results based on SWAT model by using simulating LUC from ABM-LUC model. **a** Er-hai basin and these water network. **b** The theme of *N* and *P* in 2015 and 2020

very important to simulation of SWAT because that could deeply affect the reasonability and validity of simulating process. The results for simulation in different step are shown as Fig. 4.

As depicted in results, in Er-hai Lake watershed, the more rapid development of economy and exploitation for agricultural land, the more loss for soil and water, as well as the more increase of soil erosion. Meanwhile, the high-level of nonpoint water pollution on *N* and *P* seems concentrate on the northern and western of lake, which is due to the major agriculture land use with high-fertilizing amount crops such as vegetable and garlic. And when it rains, a large number pollution loads such as *N* and *P* in the fertilizers and pesticides would be washed into the water from the soil along the runoff. Then, the loads of *N* and *P* in water become so much as the water quality is going to degradation, and finally, the nonpoint source pollution is forming in the watershed.

4 Conclusion

First, the dynamic driving mechanism of nonpoint water source in Er-hai Lake watershed was discussed in this text. And then, the methodology of how to establish the human activity-driven LUCC model based on agent-based modeling by integrating GIS is explored in detail. Meanwhile, by establishing the hydrological and water quality response model on LUCC result, we also give a method and integrating framework with GIS to simulate the hydrological process and space-time distribution of nonpoint water source pollution loads such as N and P based on SWAT model. And by simulating the LUCC-ABM model, we have forecasted the LUCC information in 2015 and 2020. Furthermore, based on the LUCC layers, the results of response on hydrology and water quality are also calculated by running the ArcSWAT model. And the explanations to all simulating results are also declared clearly.

However, the simulating models and their results are still primary because the cultural environment of Er-hai Lake is uncertain, and the precise of DEM in watershed is also short, let alone the lack of important information about climate, soil, and monitoring index of water quality. Therefore, how to improve the validity and stability of the simulating model will be the further study for this case.

Acknowledgments This paper has gained a financial support from two projects under grand No. 2012AA1214002 and 2012AA1214003 from Hi-Tech Research and Development Program of China (NO. 2012AA1214000), and from Yunnan Provincial Science and Technology Project under grand NO. 2011XX2005, and Yunnan Provincial Department of Education Research Fund under grand NO. 2011Y307.

References

1. Veldkamp A, Verburg PH (2004) Modeling land use change and environmental impact. *J Environ Manage* 72(1–2):1–3
2. Cai Yunlong (2001) Land use/land cover change: looking for a new integrated approach. *Geogr Res* 20(6):645–652
3. Wang X-L, Bao Y-H (1999) Land use change in research methodology. *Prog Geogr* 18(1):81–87
4. Deng H-Z, Tan Y-J, Chi Yan (2002) A study method for complex systems: policy of modeling in entirety based on multi-agent. *Syst Eng* 18(4):73–77
5. Batty M (2001) Agent-based pedestrian modeling. *Environ Plan B* 28(3):321–326
6. Allen PM (1997) Cities and regions as self-organizing systems: models of complexity. Gordon and Breach, Buffalo
7. Batty M (2005) Cities and complexity: understanding cities with cellular automata, agent-based models, and fractals. MIT Press, Cambridge
8. Arnold JG, Fohrer N (2005) SWAT2000: current capabilities and re-search opportunities in applied watershed modeling. *Hydrol Process* 19(3):563–572
9. Pan Li-hu, Huang He (2010) Application of artificial society model to study of land use change. *J Syst Simul* 22(8):1965–1969
10. Xu XB (2007) Simulation and optimizing for urban land use dynamic change based on GIS and CA. Lanzhou University, Lanzhou, pp 90–96

Photograph's Exposure Control by Fuzzy Logic

J. Martínez, Matilde Santos and Victoria López

Abstract This paper presents a fuzzy control system of the exposure value (EV) of a digital camera. The intelligent controller considers fuzzy input variables, applies fuzzy rules and provides fuzzy and crisp results for the focal length, EV, aperture, and speed of a digital camera in an automatic way. The control system calculates the most appropriate solution considering the distance to the subject and the lighting conditions. The results obtained resemble the behavior of an intermediate level photographer. The prototype controller was developed with Xfuzzy and Java.

Keywords Intelligent control · Fuzzy logic · Camera · Exposure value (EV) · Xfuzzy

1 Introduction

In last decades, automatic control systems built in digital cameras have developed considerably. Today it is almost impossible to make errors when exposing or focusing, and most of the pictures we take have high-technical quality because of the use of automatic shooting modes. Modern cameras include highly advanced technologies and control systems to ensure that exposure [1–7], white balance [1, 2, 8], focal length [9] or focusing [1, 2] are best suited for the conditions of the scene. Since the late 1980s, camera manufacturers have developed circuits for the exposure system based on fuzzy logic [2–4, 6], autofocus [2], automatic white balance [2, 8] or auto zoom [9]. Exposure control technologies are primarily based on the camera optics [10] to measure the luminance and contrast in different parts

J. Martínez (✉) · M. Santos · V. López
Computer Science Faculty, Complutense University of Madrid, Madrid, Spain
e-mail: jorge.martinez.ladron@googlemail.com

of the image. Automatic exposure systems (AE) apply fuzzy logic and light measuring to get the luminance of the image, make histograms and decide the best exposure. In our case this system works with a simple camera that uses incident light conditions given by the photographer and uses this subjective input to calculate the exposure value (EV).

This article is organized in five sections. [Section 2](#) describes the photograph's exposure process and shows the relationship between diaphragm aperture, speed, and sensitivity of the digital sensor. [Section 3](#) describes the fuzzy controller, its input and output variables, the representation of the data in fuzzy sets, the inference rules and their implementation in Xfuzzy. [Section 4](#) shows the results obtained with a subset of test cases, in order to see the behavior of the system in different scenarios. Finally, [Sect. 5](#) includes the conclusions of this work.

2 Photograph's Exposure Process

A photograph's exposure determines how light or dark an image will appear when it's been captured by a camera. The exposure control system of a camera is determined by the combination of three elements: aperture (f), shutter speed (s), and the sensitivity of the digital sensor (ISO). This is called the "exposure triangle".

The aperture controls the area over which light can enter your camera. Shutter speed controls the duration of the exposure. ISO speed controls the sensitivity of the camera's sensor to a given amount of light. Usually the digital cameras use an exposure meter to measure the light reflected of the scene and, once this value is calculated, the system recommends a combination of aperture (f) and shutter speed (s). This decision depends on the operating mode of the camera: automatic, aperture priority, speed priority, or predefined types of photography (portrait, landscape or sports). The combination of aperture and shutter speed determines the characteristics of an image. If you want to get a picture with high-contrast and minimal depth of field, you must choose a high-speed and wide open aperture, instead, if you want to get an image with low-contrast and maximal depth of field, you must choose a closed diaphragm and a slow shutter speed [11].

The objective of the control system proposed in this paper is to calculate the most suitable EV regarding the light conditions and the sensitivity of the sensor. There are many combinations of the above three settings to achieve the same exposure. The key, however, is to find the best combinations since each setting also influences other image properties. For example, aperture affects depth of field, shutter speed affects motion blur and ISO speed affects image noise. After calculating the EV, the system calculates the optimal combination of aperture and shutter speed for the type of picture given (Fig. 1). The relationship between the aperture and the shutter speed is inversely proportional. If one of this value increases, the other is reduced to maintain the same EV. In addition to the proportionality between these values, we must keep in mind that choosing a small or large aperture determines the depth of field, contrast, and motion blur. This defines

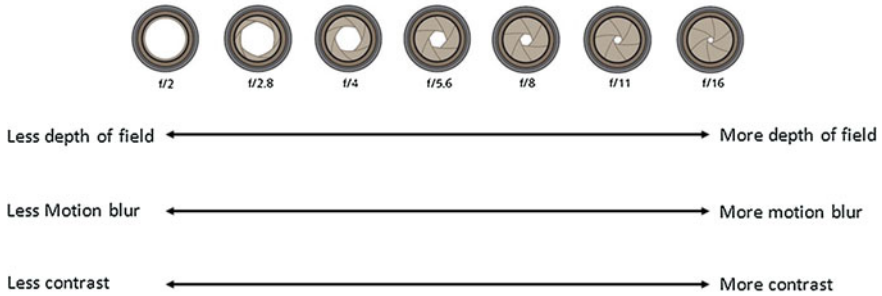


Fig. 1 Aperture versus shutter speed

the characteristics of the image and is given by one of the controller inputs: the type of photography. This system is designed for three modes: sports and action, portraits, and landscapes.

The EV determines the different combinations of aperture (f) and shutter speed (s) for a given value of sensitivity and lighting conditions. The EV is calculated as $\log_2(f/s)$ [11]. On the scale of EVs adopted internationally, EV value 1 corresponds to an aperture f of 1.4 and 1 s Table 1 (values of exposure VE) is adapted from [12], and shows the relationship between these values, the aperture (f) and shutter speed (s). For every unit increased in this scale, the EV is reduced by a half. For example, the exposure value VE 2 is a half of VE 1, VE 3 is a quarter of VE 1, VE 4 is one eighth of VE 1 and so on. EVs of Table 1 go from 1 to 20 because the range of the velocity reaches 1/200 s and f from 1 to 22.

As can be seen in Fig. 2, there are different combinations of aperture and shutter speeds with the same EV. For example, speed $f = 8$ and 1/15 s and speed $f = 1.4$ and 1/500 s are equivalent. Both combinations have VE 10 and let in the same light to the sensor. The images produced have the same exposure but its characteristics are completely different.

If we use $f = 8$ and 1/15 s it has greater depth of field and motion blur. When using $f = 1.4$ and 1/500 s, the depth of field is minimal, the picture is frozen and has no motion blur.

3 Fuzzy Controller Design

This prototype uses a fuzzy controller due to the lack of accuracy of the inputs of the system and mainly because these parameters are determined by the user in a subjective way. The goal of this control system is to calculate the EV, the aperture (f), the shutter speed (s), and the focal length. It uses as input values the bright-ness of the scene, the sensitivity of the sensor, the type of photography and the approximate distance to the subject (Fig. 3).

Table 1 Shutter speed (s), aperture (f) and EV

| s/f | 1.0 | 1.4 | 2.0 | 2.8 | 4.0 | 5.6 | 8.0 | 11 | 16 | 22 |
|-------|-----|-----|-----|-----|-----|-----|-----|----|----|----|
| 1 | 0 | 1 | 2 | 3 | 4 | 5 | 6 | 7 | 8 | 9 |
| 2 | 1 | 2 | 3 | 4 | 5 | 6 | 7 | 8 | 9 | 10 |
| 4 | 2 | 3 | 4 | 5 | 6 | 7 | 8 | 9 | 10 | 11 |
| 8 | 3 | 4 | 5 | 6 | 7 | 8 | 9 | 10 | 11 | 12 |
| 15 | 4 | 5 | 6 | 7 | 8 | 9 | 10 | 11 | 12 | 13 |
| 30 | 5 | 6 | 7 | 8 | 9 | 10 | 11 | 12 | 13 | 14 |
| 60 | 6 | 7 | 8 | 9 | 10 | 11 | 12 | 13 | 14 | 15 |
| 125 | 7 | 8 | 9 | 10 | 11 | 12 | 13 | 14 | 15 | 16 |
| 250 | 8 | 9 | 10 | 11 | 12 | 13 | 14 | 15 | 16 | 17 |
| 500 | 9 | 10 | 11 | 12 | 13 | 14 | 15 | 16 | 17 | 18 |
| 1,000 | 10 | 11 | 12 | 13 | 14 | 15 | 16 | 17 | 18 | 19 |
| 2,000 | 11 | 12 | 13 | 14 | 15 | 16 | 17 | 18 | 19 | 20 |

| | | | | | | | | | | | |
|---|-----|-----|-----|----|------|----|------|-----|------|------|------|
| 1 | 2 | 4 | 8 | 15 | 30 | 60 | 125 | 250 | 500 | 1000 | 2000 |
| | f22 | f16 | f11 | f8 | f5.6 | f4 | f2.8 | f2 | f1.4 | | |

Fig. 2 Combinations of aperture and shutter speed for a given EV

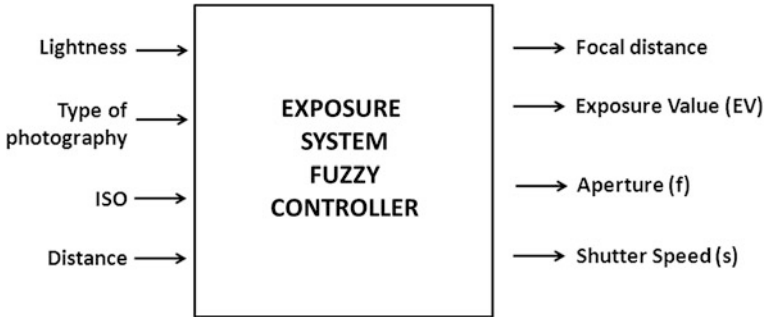


Fig. 3 Inputs and outputs of the fuzzy controller

The brightness of the scene is a fuzzy value defined for five different values (Table 2). The type of picture (Table 3) is not a fuzzy data, however, it may have different valid interpretations and so it is an approximate value. The distance to the subject is also a noncrisp value (Table 4). The sensitivity of the sensor can take the values 100, 200, 400, 800, and 1,600 ISO. The luminosity is a fuzzy data because the camera does not have any sensor to calculate it accurately. It considers five different brightness levels, from highest given by a bright sun with clear sky, to lower luminosity (Table 2). The picture type is defined by the set of values: sports, portrait, or land-scape (Table 3). The distance to the subject is also a fuzzy value described using linguistic terms such as very close, close, far, or very far (Table 4). This controller uses vague inputs to calculate the system's outputs.

3.1 Fuzzy Datasets

Fuzzy logic, unlike classical logic, represents imprecise values using membership functions that take values in a range between 0 and 1 [9]. In this work we use trapezoidal and singleton membership functions to represent the data.

The brightness levels are represented by fuzzy sets defined by trapezoidal membership functions with labels: very low, low, medium, high, or very high (Fig. 4a). The type of photography (Fig. 4b) and the sensitivity of the sensor (Fig. 4c) are represented by singletons. Finally, the distance is fuzzyfied with trapezoidal membership functions for the five fuzzy sets: very close, close, intermediate, far, and very far (Fig. 4d).

Table 2 Lighting





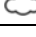
| | |
|---|----------------|
|  | Bright, sunny |
|  | Hazy sun |
|  | Partly cloudy |
|  | Mainly cloudy |
|  | Overcast, dull |

Table 3 Modes




| | |
|---|-----------|
|  | Sports |
|  | Portrait |
|  | Landscape |

Table 4 Distance

| | |
|------------|-------------------|
| Very close | Less than 1 m |
| Close | Between 1 and 2 m |
| Medium | Between 2 and 3 m |
| Far | Between 3 and 4 m |
| Very far | More than 4 m |

The outputs of the system are crisp values and are represented using singleton membership functions (Fig. 4e, f, g and h).

3.2 Fuzzy Inference Rules

The input values are converted to fuzzy values through a fuzzyfication process and then the system applies the inference rules of type IF—THEN [9] and eventually convert the fuzzy output values into crisp if necessary through a process of “de-fuzzyfication” [13]. We have used the Mamdani implication method because of its simplicity [14].

The controller uses three inference rules: one for calculating the focal length based on the approximate distance from the subject. For example, if the distance is small, the system recommends an open angle. As distance increases, the angle is closer. The other two are nested rules that calculate the exposure value (EV), the aperture (f) and shutter speed (s). These rules are based on relationships of shown in Tables 5, 6 and 7.

Inference rules are based on the information of the above tables. All of them are applied to select the combination of f and shutter speed that best suits the light conditions and the photography mode the user wants. For example, to determine the

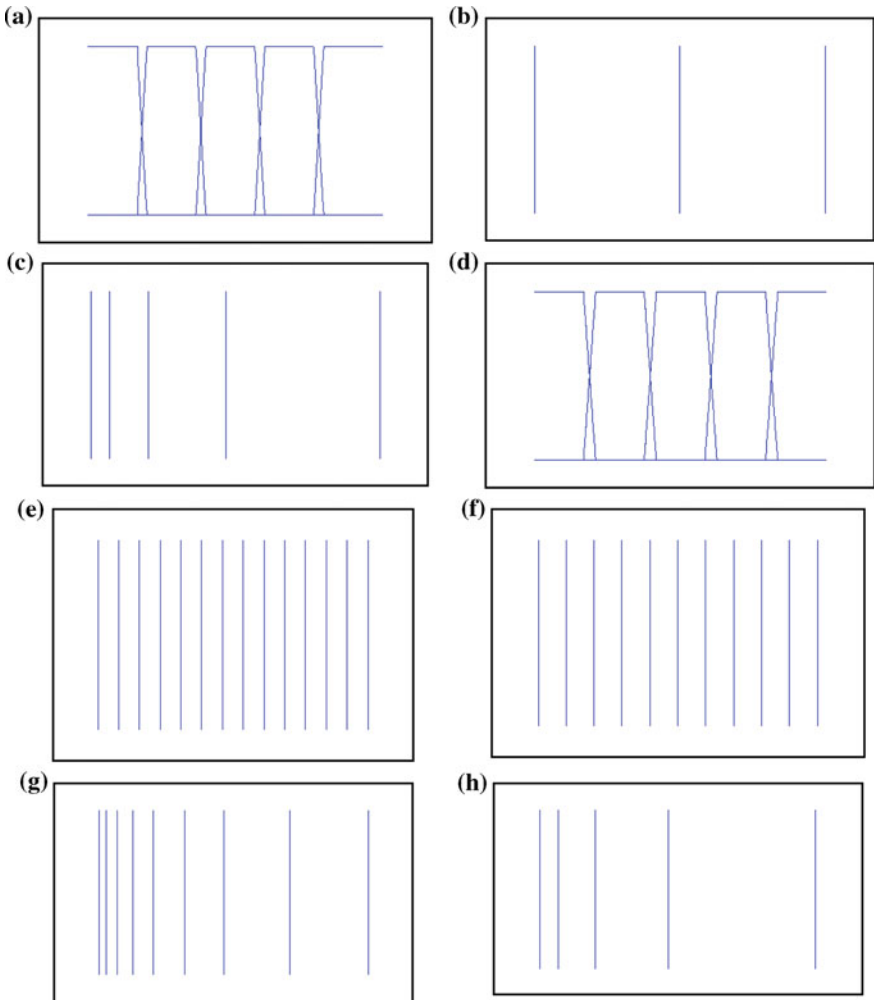


Fig. 4 Fuzzy sets of the control inputs and outputs. **a** Lightness. **b** Photography mode. **c** Sensitivity. **d** Distance. **e** Focal distance. **f** Exposure value (EV). **g** Aperture **(f)**. **h** Shutter speed

EV using rules that combine different levels of brightness for each sensitivity value. An example of the rules codified in Xfuzzy XFL3 language [15, 16] is shown.

```

if (ISO == iso100 & lightness == veryLow) - > VE = ve11;
if (ISO == iso100 & lightness == Low) - > VE = ve12;
if (ISO == iso100 & lightness == Medium) - > VE = ve13;
    
```

The relationship between aperture, speed, EV, and the photography mode is summarized in Tables 6 and 7. For example, the rules that relate the EV VE and the mode of the picture in XFL3 language are the following.

Table 5 Rules for EV as a function of lightness and sensitivity































| ISO |  |  |  |  |  |
|-------|---|---|---|---|--|
| 100 | 11 | 12 | 13 | 14 | 15 |
| 200 | 12 | 13 | 14 | 15 | 16 |
| 400 | 13 | 14 | 15 | 16 | 17 |
| 800 | 14 | 15 | 16 | 17 | 18 |
| 1,600 | 15 | 16 | 17 | 18 | 19 |

Table 6 Rules for EV as a function of aperture and speed

| f | 125 | 250 | 500 | 1,000 | 2,000 |
|--------|-----|-----|-----|-------|-------|
| f 4.0 | 11 | 12 | 13 | 14 | 15 |
| f 5.6 | 12 | 13 | 14 | 15 | 16 |
| f 8.0 | 13 | 14 | 15 | 16 | 17 |
| f 11.0 | 14 | 15 | 16 | 17 | 18 |
| f 16.0 | 15 | 16 | 17 | 18 | 19 |

Table 7 Relationship between aperture, speed and photography mode

| f | 125 | 250 | 500 | 1000 | 2000 |
|--------|---|---|---|---|--|
| f 4.0 |  |  |  |  |  |
| f 5.6 |  |  |  |  |  |
| f 8.0 |  |  |  |  |  |
| f 11.0 |  |  |  |  |  |
| f 16.0 |  |  |  |  |  |

```

if (VE == ve13 & photography == sports) -> s = v500, f = f4x0;
if (VE == ve13 & photography == portrait) -> s = v250,
f = f5x6;
if (VE == ve13 & photography == landscape) -> s = v125,
f = f8x0;
    
```

The fuzzy rules use the min function for the logical operator. We have tried different operators for the defuzzyfication of the outputs and eventually decide to use the max instead of the Centroid method. The controller calculates the VE from the relationship between brightness and ISO sensitivity from Table 5. Once we have the VE, we need to find the combination of aperture and shutter speed suitable for the type of photography the user wants. The system seeks the EV in Table 6 and chooses the combination of aperture diaphragm and speed using Table 7. For example, for light conditions “Partly cloudy”, 100 ISO, sport photography and a very far distance, the controller calculates VE 13, f 4.0 with s500 and 100 mm of focal length. First it obtains VE = 13 using Table 5. In Table 6

Table 8 Test cases and results

| Inputs | | | | Outputs | | | |
|-----------|-----------|-------|------------|---------|--------|-------|-------|
| Lightness | Type | ISO | Distance | EV | f | s | Focal |
| Very low | Portrait | 100 | Very far | EV 11 | f 4.0 | s125 | 100 |
| Very high | Sports | 800 | Far | EV 18 | f 16 | s1000 | 80 |
| Medium | Portrait | 100 | Very close | EV 13 | f 5.6 | s250 | 35 |
| Low | Sports | 400 | Far | EV 14 | f 5.6 | s500 | 80 |
| Very high | Portrait | 800 | Close | EV 18 | f 22.0 | s500 | 50 |
| Medium | Portrait | 100 | Medium | EV 13 | f 5.6 | s250 | 60 |
| Very low | Landscape | 1,600 | Far | EV 15 | f 11.0 | s250 | 80 |
| Very high | Sports | 400 | Very far | EV 17 | f 11.0 | s1000 | 100 |
| Low | Landscape | 100 | Close | EV 12 | f 8.0 | s60 | 50 |
| Medium | Portrait | 800 | Close | EV 16 | f 11.0 | s500 | 50 |
| High | Sports | 1,600 | Medium | EV 18 | f 16.0 | s1000 | 60 |
| Very low | Landscape | 200 | Very far | EV 12 | f 8.0 | s60 | 100 |
| Media | Portrait | 800 | Far | EV 16 | f 11.0 | s500 | 80 |
| High | Landscape | 200 | Very close | EV 15 | f 11.0 | s250 | 35 |
| Very low | Portrait | 400 | Close | EV 13 | f 5.6 | s250 | 50 |
| Low | Sports | 1,600 | Medium | EV 16 | f 8.0 | s1000 | 60 |
| Very low | Landscape | 100 | Close | EV 11 | f 5.6 | s60 | 50 |
| High | Portrait | 800 | Far | EV 17 | f 16.0 | s500 | 80 |

there are three exposure values VE 13, corresponding to the values f 4.0 with s500, f 5.6 with s250 and f 8.0 with s125. To choose one of these combinations it is necessary to use Table 7 depending on the mode of the photography. In this case the controller suggests f 4.0 with s500. This combination of large aperture and high-speed produces an image with minimal depth of field, suitable for sports. The distance is more than 4 m, so we recommend using a 100 mm lens.

4 Simulation results

In order to test the fuzzy controller a prototype has been carried out using Xfuzzy, a free software for designing fuzzy systems developed by the Institute of Micro-electronics of Seville (IMSE-CNM). The code has been developed in XFL3, a language for the definition of fuzzy logic-based systems. The Java prototype uses the Java code generated automatically by Xfuzzy [15–17].

The results obtained with a meaningful set of test cases are shown in Table 8, so we can see how the system behaves.

5 Conclusions and Future Work

In this paper we propose the use of fuzzy logic to design a controller for the EV of a digital camera because of the subjective nature of their input values.

The rules of the system are based on the relationships between the inputs and outputs and give the most suitable combination of setting parameters for each photo-graph, even though the controller uses fuzzy brightness levels and EVs that do not always match that of a meter. Moreover, this controller is limited by the range of speed and aperture values of Table 1. To use a higher speed range, all we have to do is to expand this table and its associated inference rules. If more knowledge was involved, we could change the tables that define the fuzzy rules to adjust the behavior of the controller. The results are satisfactory and resemble the behavior of a person having intermediate knowledge of photography.

References

1. Lee YM (1994) A fuzzy control processor for automatic focusing. *IEEE Trans Consum Electron* 40(2):138–144
2. Haruki T, Kikuchi K (1992) Video camera system using fuzzy logic. *IEEE Trans Consum Electron* 38(3):624, 634
3. Jiang T, Kuhnert K-D, Nguyen D, Kuhnert L (2011) Multiple templates auto exposure control based on luminance histogram for onboard camera. In: *Proceedings of IEEE International Conference on computer science and automation engineering (CSAE)*, vol 3, pp 237–241, 10–12 June 2011
4. Shimizu S et al (1992) A new algorithm for exposure control based on fuzzy logic for video cameras. *IEEE Trans Consum Electron* 38(3):617–623
5. Lee JS et al (2001) An advanced video camera system with robust AF, AE and AWB control. *IEEE Trans Consum Electron* 47(3):694–699
6. Murakami M, Honda N (1996) An exposure control system of video cameras based on fuzzy logic using color information. In: *Proceedings of 5th IEEE international conference on fuzzy Systems*, vol 3, issue 3, pp 2181–2187, 8–11 Sep 1996
7. Liang JY, Qin Y, Hong Z (2007) An auto-exposure algorithm for detecting high con-contrast lighting conditions. In: *Proceedings of ASICON*, pp 725–728
8. Liu Y-C, Chan W-H, Chen Y-Q (1995) Automatic white balance for digital still camera. *IEEE Trans Consum Electron* 41(3):460, 466
9. Elamvazuthi I, Vasant P, Webb J (2009) The application of Mandani fuzzy model for auto zoom function of a digital camera. *Appl Bioinf* 1(4):122–191
10. Kuno T, Sugiura H, Matoba N (1998) A new automatic exposure system for digital still cameras. *IEEE Trans Consum Electron* 44(1):192–199
11. Pradera A (1997) *El libro de la fotografía*. Alianza Editorial
12. Weston C (2009) *Domine la exposición digital*. Index Book
13. Jantzen J (1998) *Design of fuzzy controllers*. Technical University of Denmark, Department of Automation. Technical report no 98-E 864
14. Santos M (2011) Un enfoque aplicado del control inteligente. *RIAI* 8:283–296

15. Xfuzzy Team (2013) Herramientas de CAD para lógica difusa. CNM IMSE. http://www2.imse-cnm.csic.es/Xfuzzy/index_sp.html
16. Xfuzzy Team (2013) XFL3 El lenguaje de especificación de Xfuzzy 3. http://www2.imse-cnm.csic.es/Xfuzzy/Xfuzzy_3.3/xfl/index_sp.html
17. Xfuzzy Team (2013) Entorno de desarrollo Xfuzzy 3. CNM IMSE. http://www2.imse-cnm.csic.es/Xfuzzy/Xfuzzy_3.3/tools/xfuzzy_sp.html

The Elastic Cloud Platform for the Large-Scale Domain Name System

Yunchun Li and Cheng Lv

Abstract As the rapid popularity of IPv6, DNS need to adapt to the rapid growth of the name space and the explosive development of the clients. The DNS has high elasticity of QPS, which makes the contradictory between the resource utilization and the quality of service. To realize the flexible utilization of resources, it is necessary to build DNS elastic cloud support platform, which takes advantages of the elastic cloud platform. The platform realizes the elastic utilization of resources and guarantees the quality of service. Furthermore, the resource utilization increases and the waste of resource decrease. At the same time, the platform has good expansibility.

Keywords Domain name system · Cloud computing · Elastic scheduling · Load balancing

1 Introduction

As the IPv4 address resources drying up, IPv6 technology is gradually becoming the core of next generation Internet because of plenty of address space and other advantages [1]. DNS (domain name system) is the link of the two basic resources—the Internet domain name and the IP address. DNS play a key role in the process of the evolution from IPv4 to IPv6 [2]. DNS also must be adjusted

Y. Li · C. Lv (✉)

JSI, School of Computer Science and Engineering, Beihang University,
Beijing 100191, China
e-mail: charlie8844@126.com

Y. Li

e-mail: lych@buaa.edu.cn

accordingly to fit the namespace rapid growth and the explosive growth of the client [3].

Cloud computing is a new mode of information infrastructure. It is based on virtualization technology. It is characterized by service. Its business model is used on demand. Its core idea is management and scheduling resources, including computing, storage, and other resources over a network connection, to constitute a resource pool to provide services to the users or applications. Cloud computing is the result of the development of the traditional computer and network technology, such as grid computing, distributed computing, parallel computing, utility computing, network storage, virtualization, load balance [4].

Infrastructure as a Service (IaaS) is to provide users with server, storage, and network hardware as the service. In IaaS service, resources are shared and according to the user's request. But the actual need of resources is always changing, if the resource reserved is too much or too little, it can cause unreasonable distribution of resources. In addition, cloud computing platform needs to schedule for users of a resource required to service the requests according to the actual load of applications and services [5].

IaaS service infrastructure is generally using the virtualization technology to build the internal architecture of the cloud platform. Virtualization technology provides an effective solution for the resource management in the cloud computing model. Virtualization technology can be divided and it created different virtual machines, which are isolated, on one physical host. The management of cloud platform is realized by encapsulating applications and services in the virtual machines and scheduling the virtual machine and the physical resource according to the changing of the load [6].

Berkeley Internet Name Domain Service (BIND) is used by more than 90 % of the Domain Name. It is the most widely used DNS system on the Internet [7]. The BIND is developed by university of California, Berkeley. The BIND operation such as inquiry and authorization of the domain name is done through the management of the zone files. Its structure is shown below (Fig. 1).

BIND support master-slave server setup. The master servers get the data from the zone files, while the slave servers load the data from other servers through the network. This method is called zone transfer.

DNS system has many characteristics. DNS generally use UDP link, because its packages are small and relatively simple processed. The QPS (queries per second) of DNS have dramatic changes. These characteristics are particularly prominent in the large-scale system. The QPS lowest and highest may differ for several times a day. These features, especially the QPS severe changes, make the traditional load balancing methods inefficient. When the QPS is high, the servers are in a state of bad quality of service caused overload. While the QPS is low, caused a waste of resources and energy, and the resources utilization rate is low [8].

Therefore, this paper puts forward building a supporting platform for the elastic cloud framework to support DNS applications, which can automate flexible allocation of resources according to the load situation, realize the flexible utilization of resources, making it more rational. Its advantages include:

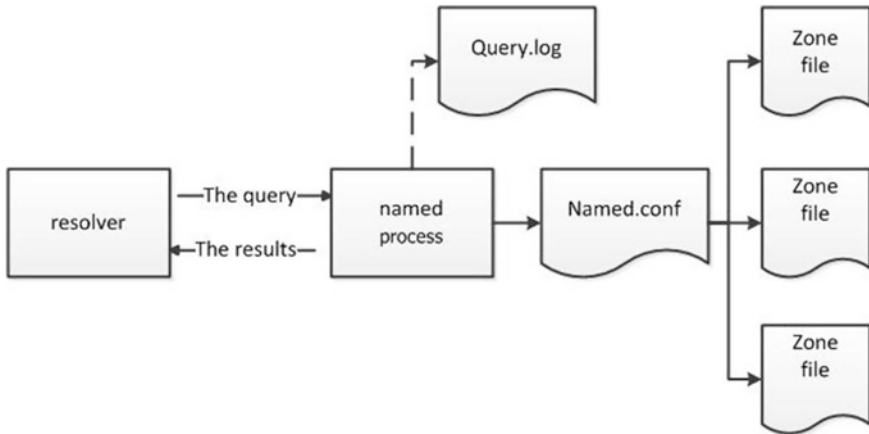


Fig. 1 The structure of BIND

1. Automatically allocate resources according to the load status, realizes the elastic stretch of utilization of resources.
2. Management method is simple and effective, with good scalability.
3. Reduces the waste of energy resources, improve resource utilization.

2 Load Balance of the Elastic Compute Cloud Platform

2.1 Load Balance Model Framework for Elastic Cloud

According to functions, cloud computing platform are often divided into the infrastructure layer, the platform layer, and the application layer. In addition, the traditional application layer, namely the DNS load balancing, the load balancing on platform layer is also considered (Fig. 2).

The virtual machine cluster includes many virtual machines. Virtual machine installs the application domain name system and the agent. The application receives and completes the name resolution request. The agent collects the virtual machine load data and the task execution information and regularly sends them to the load balancer. The management platform manages the life cycle of virtual machine. The image manager copies the virtual machine images from the virtual machine image library. The deployer builds and deploys the virtual machines. The virtual machine manager accepts instructions, according to the virtual machine platform feedback results and strategy implementation to create, open, close, migration, etc.

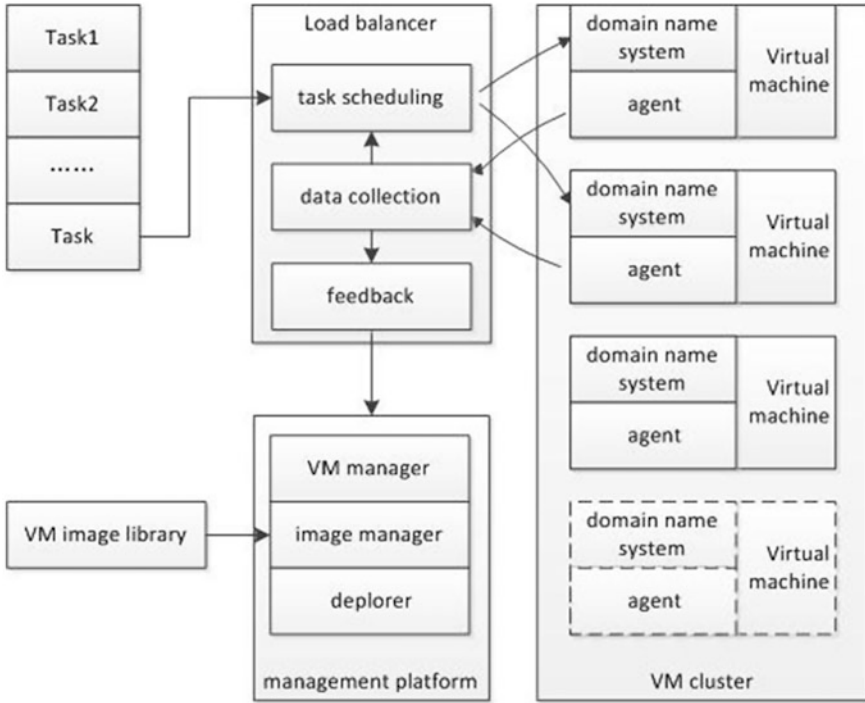


Fig. 2 The structure of the platform

2.2 Load Measurement

The agents sampling virtual machine loads condition regularly, and sent it to the load balance module. DNS is a network and I/O intensive applications. Its demand for resources has its own characteristics. Load balancing index mainly includes CPU utilization, memory utilization, network bandwidth, and so on.

Set the number of load indexes as p , m virtual machine is in the cluster, collecting time as n . l_{ij}^k is the i index of load for the virtual machine k in the time point j . L_k is the load data of virtual machine k . The load data collection of the whole virtual machine cluster is L . The applications in this platform are the DNS, so the task type is the same. W is the weight, w_i is the weights of i .

f^k is the load of the virtual machine k . Load is the main reference data of task scheduling algorithm. It describes the real-time load status of the virtual machine. The algorithm uses the load data closest time point n to analysis.

$$f^k = \sum_{i=1}^p w_i \times l_{in}^k \tag{1}$$

c_i^k is the ability on i for the virtual machine k . c^k is the ability of virtual machine k . The computing method of c^k is:

$$c^k = \sum_{i=1}^p w_i \times c_i^k \quad (2)$$

Δt is the sampling interval. Within the time period $1 \sim n$, the total resource of the virtual machine k consumes in i can be represented as:

$$R_i^k = \sum_{j=1}^n (l_{ij}^k \times c_i^k \times \Delta t) \quad (3)$$

The consumption on i for the whole virtual machine cluster is:

$$R_i = \sum_{k=1}^m R_i^k \quad (4)$$

S_i is the resource utilization on i , it can be expressed as follows:

$$S_i = \frac{R_i}{\sum_{k=1}^m c_i^k \times n \times \Delta t} = \frac{\sum_{k=1}^m \sum_{j=1}^n l_{ij}^k \times c_i^k}{\sum_{k=1}^m c_i^k \times n} \quad (5)$$

Define the resource utilization of the cluster S as:

$$S = \sum_{i=1}^p w_i \times S_i \quad (6)$$

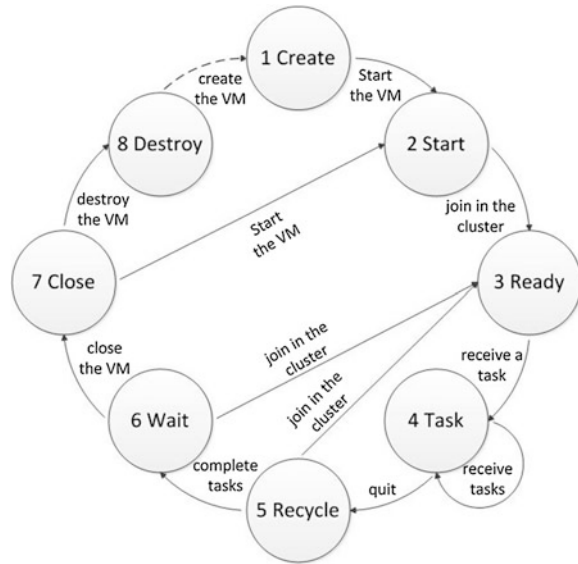
3 Task Scheduling and Elastically Stretchable

3.1 Elastic Cloud Model

According to the character of the domain name resolution process, the virtual machine state of life cycle is defined as the following.

Virtual machines are created by management platform through assembly deployment and started by management module. The open services virtual machines join into the cluster and become the ready state after configure and data synchronization. The virtual machine in ready state can receives a task. The ready

Fig. 3 Life cycle of the VMs



virtual machine joins in the scheduling sequence after the load balancer receives the messages. The virtual machine gets into the task state after it receives the tasks.

The virtual machines in the task status may quit from the cluster into the recycling status according to the instruction from the management module. The recycle state virtual machines send the messages to the load balancer and no longer accept new DNS requests. When the current requests processing are completed, the virtual machines get into the wait state. If the management module needs to increase the number of virtual machines in the cluster, the recycle and wait state of the virtual machine can be joined into the cluster. They send the message to the load balancer to make them back into the task cycle (Fig. 3).

3.2 Task Scheduling Method

The basic idea of the task scheduling algorithm is sorting the virtual machines according to the virtual machine cluster load condition, evaluation, and prediction and choosing the lightest load one to carry on the task.

The tasks scheduling system uses the Dynamic Weight Round-Robin Scheduling (DWRR) strategy. The service ability difference of the virtual machines and host machines is considered. Estimate all the virtual machines in the cluster server and obtain the corresponding weights. The weight and the estimated number of requests processed are proportional. The request is distributed according to the weight.

Algorithm principle is described as follows. The virtual machines in the cluster is a set of nodes $N = \{N_1, N_2, \dots, N_m\}$. $W(N_i)$ is the weight of the node N_i . $T(N_i)$ is the task of N_i . $\sum T(N_i)$ is the total task in a cycle. $\sum W(N_i)$ is the sum of the weights. Assignments should satisfy the relation $T(N_i)/\sum T(N_i) = W(N_i)/\sum W(N_i)$. Task assign is on the basis of the node weights representing the proportion of the total weight.

When the virtual machine is turned on, an initial weight is set according to the assigned resource configuration. With the nodes load changes, the load balancer adjusts the weights (overlay dynamic weight). Dynamic weights are calculated according to node runtime parameters. The intent of dynamic weight is to correctly reflect the status of the load node and to predict the load changes. In order to avoid dramatic changes in load balancing strategy caused by excessive jitter, the moving weighted average method is used to calculate predicted load of each node.

Dynamic weight value also reflects the overall load of the virtual machine cluster. If the weight of a node is increased, it explains that the node is in the light load state. Otherwise is overloaded state. When all the node weights were significantly lower than the initial weight, it indicates that the cluster state of overload, and new virtual machines should be added into the virtual machine cluster to process load. When the weight is higher than the initial value, it indicates that the load lighter, some virtual machines can be closed to improve resource utilization.

3.3 *Elastically Stretchable*

Elastically stretchable is an important feature of elastic cloud. Elastically stretchable primarily adjusts the number of virtual machines in the cluster dynamically based on the obtained resource utilization to determine. There are two ways—virtual machine recovery and virtual machine cluster expansion.

If resource utilization below a setted minimum threshold, indicating that the cluster resources are relatively filling. To reduce the energy consumption and to improve resource utilization, part of the virtual machine should be recycled. If the resource utilization is at or above the setted maximum threshold, the cluster is in a whole state of overload. In order to improve efficiency and service quality of the domain name resolution, the virtual machines cluster can be extended to increase service nodes to share the tasks. When the virtual machine cluster should be expanded, the virtual machines, which are in recycling, waiting, and closed state, have a smaller cost to rejoin in the virtual machine cluster. So in the expansion process, the cluster prefers to use these virtual machines. When there is no virtual machine in these states, the platform creates new virtual machines and adds them into the virtual machine cluster (Fig. 4).

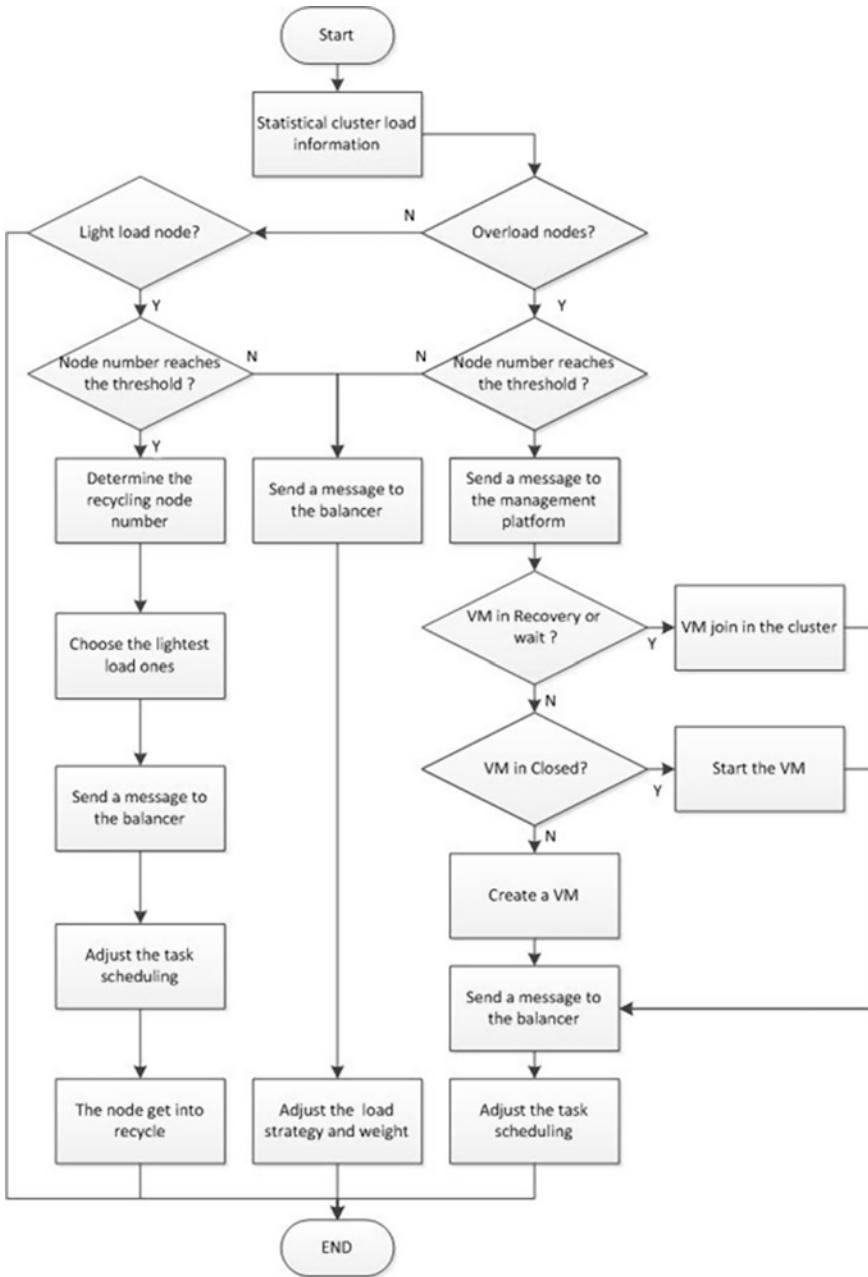


Fig. 4 Flow chart of the elastically stretchable

4 The DNS on Elastic Cloud

The application of the elastic cloud platform is domain name system. The load balancing of application layer uses the mode similar Linux Virtual Server (LVS). The actual virtual machine cluster outside works as a single server. The request is forwarded to the actual virtual machine by the load balancing module. The load balancer determines which virtual machine to process the request packets. Request packet destination IP address is rewritten actual appropriate server IP.

4.1 The Operation to Join the Cluster

Joining the virtual machine clusters is the operation after the deploying and the opening of a virtual machine. In the platform, to join the cluster, the virtual machines need to complete the following steps:

Step 1 Configuring BIND configuration files. The configurations include configuring the server as server mode and specify the master server. The configurations of the same group are generally same, so the configuration files can be generated by other ways and loaded from the network.

Step 2 Start the BIND (named process), and check if it is successful. If it is a successful start, go to the next step, or send the messages to the management platform after several (5) attempts.

Step 3 Load the zone data files from the network.

Step 4 Send the message to the load balancing module, that this virtual machine has been able to accept the task.

After these steps, the virtual machine enters the standby mode, and can actually respond to the requests.

4.2 Avoid Dramatic Changes

It will cause costs to create, start, and join into the cluster. These costs include: the virtual machine image network transmission time, the virtual machine startup time, and the configuration files and zone file network transmission time.

Because of the cost, the virtual machine requires some time to start and enter the task execution state. When requested quantity dramatically changes, the virtual machines may be on and off frequently. It leads to the actual reduced efficiency. To avoid this situation, two methods are used.

1. Make the load data smoothing. Weighted moving average is used to smooth the load data.
2. Predictive stretching Strategy. The QPS of DNS changes usually close to the same trend within a day. Therefore, the number of the virtual machines can be

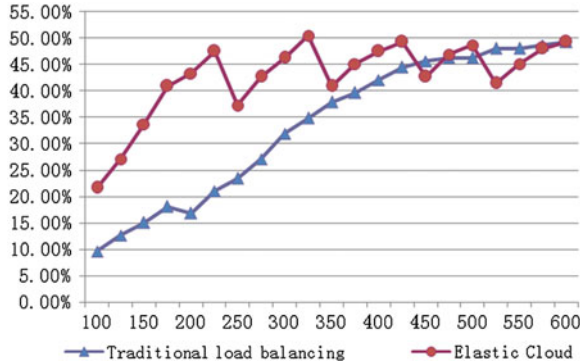


Fig. 5 Resource utilization in different QPS

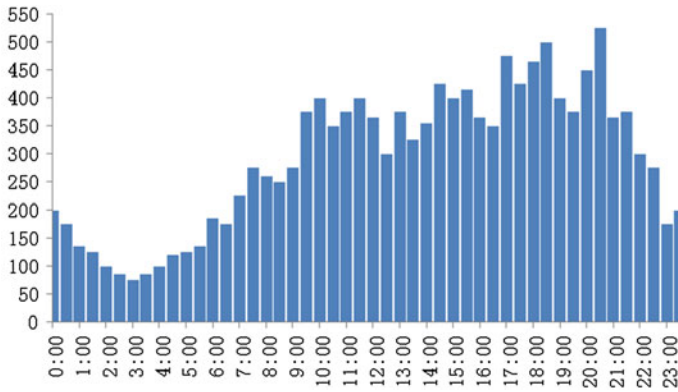


Fig. 6 QPS changing

notified preponsely. Quantity is based on the current number of virtual machines and the predicted proportion, rather than a fixed number. Increasing the proportion of the light load threshold in the request rising time and increasing the proportion of the over load threshold in the request declining time.

5 Experiment and Performance Evaluation

To verify the availability and effectiveness of the platform, build a cloud computing environment with several physical hosts. Experiments are mainly on the scheduling as the QPS changing. The resource utilization and the response time are the main investigation index.

First, we contrasted the resource utilization of the traditional load balancing and the elastic cloud way, in different QPS (Fig. 5).

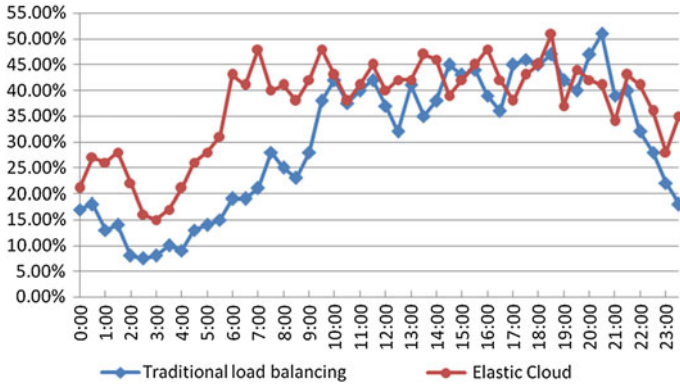


Fig. 7 Resource utilization

QPS changing simulated the real network environment in a day. The variation is as shown (Figs. 6 and 7).

Resource utilization in the 96 sampling are as shown.

From the experiments, we can see that the platform realizes the elastic utilization of resources, and ensure the quality of service. Furthermore, the resource utilization increases and the waste of resource decreases.

6 Summary

In this paper, we presented the method to build the the elastic cloud platform for the large-scale domain name system. The characteristics of the elastic cloud and the features of the DNS were fully considered and used. We also presented the measurements of the platform load. We realized the elastic utilization of resources through the elastic scheduling and the elastically stretchable. The experiments showed that the platform ensured the quality of service and the resource utilization increased.

The method should be improved in the case of the QPS dramatic changes, although weighted moving average and predictive stretching strategy were used. Meanwhile, the cost of load balancer is still need for further discussion when QPS is particularly high.

References

1. Zeadally S, Wasseem R, Raicu I (2004) Comparison of end-system IPv6 protocol stacks. *IEEE Proc Commun* 151(3):238–242
2. Ramasubramanian V, Sizer E (2004) The design and implementation of a next generation name service for the internet. In: *ACM SIGCOMM*

3. Cranor CD, Gansner E, Krishnamurthy B, Spatscheck O (2001) Characterizing large DNS traces using graphs. In: First ACM SIGCOMM workshop on internet measurement
4. Dillon T, Wu C, Chang E (2010) Cloud computing: issues and challenges. In: 24th IEEE international conference on advanced information networking and applications
5. Chen K, Zheng WM (2009) Cloud computing: system instances and current research. *J Softw* 20(5):1337–1348
6. Buyya R, Yeo CS, Venugopal S (2008) Market oriented cloud computing: vision, hype, and reality for delivering it services as computing utilities. In: Proceedings of the 10th IEEE international conference on high performance computing and communications, Dalian
7. Albitz P, Liu C (2002) DNS and BIND, 4th edn. O'Reilly
8. Jung J, Sit E, Balakrishnan H, Morris R (2001) DNS performance and effectiveness of caching. In: SIGCOMM internet measurement workshop

Applied Polyphase Filter Orthogonal Transformation Technology in Broadband Signal Receiving

Xiang Jian-hong and Dnong Chun-lei

Abstract In view of the present mature simulation orthogonal transformation mostly belongs to the narrow band signal processing. And the digital processing method of Hilbert orthogonal transformation is limited by the bandwidth and cannot be used in broadband signal receiving. In this paper, application of the polyphase filtering orthogonal transformation method realized intermediate frequency spectrum broadband signal receiving in the front-end processing. This method is good at solving the problem of digital frequency conversion of orthogonal transformation in broadband signals and is suitable for implementation on FPGA and the engineering real-time processing.

Keywords Polyphase filter · Digital orthogonal transformation · Broadband signal

1 Introduction

Signal orthogonal transformation (the radio frequency signal transformation for the baseband in phase and quadrature component) in the communication and radar system has an important role in signal processing. Along with the rapid development of the computer technology and the very large-scale integrated circuit

X. Jian-hong (✉) · D. Chun-lei
Information and Communication Engineering, Harbin Engineering University,
Harbin, China
e-mail: xiangjianhong@hrbeu.edu.cn

D. Chun-lei
e-mail: shawengui@163.com

X. Jian-hong
Chengdu Tian ao Industrial Co. Ltd, Chengdu, China

technology, and the operation speed of digital signal processing (DSP) increasing, and the emergence and wide application of high precision and wide dynamic range analog-to-digital converter (A/D), and field programmable logic device (FPGA) continuously introduce more powerful new device performance, it can be directly to intermediate frequency signal sampling, got the two orthogonal signals.

Traditionally, the technique of implemented signal orthogonal transformation is the simulation orthogonal decomposition. The main drawback of this method is which need to produce two orthogonal local vibration signals. When the local vibration signal cannot be orthogonal due to the error, it can produce false signals. The method of the digital orthogonal transformation mentioned in Ref. [1] is method and Hilbert transform method. The two methods can be summed up in a low-pass filter on the principle. The structure of low-pass filtering method is similar with the traditional simulation process; only put the frequency shift after A/D conversion, so the demand of the filter order is higher. Also filtering method and Hilbert transform is to filter one channel, the other channel is retained the original samples values. All above can cause I/Q amplitude inconsistencies and quadrature offset, which affect the reception.

Aiming at the shortcomings of the above methods, this paper introduces a method of using polyphase filter [2] to implement digital orthogonal transformation for intermediate frequency broadband signal. This method adopts dual filter, and due to the two channels used the same prototype filter, so the frequency response characteristics are similar, and they does not directly bring the I/Q two inconsistencies with respect to the ideal filter deviation. In addition, this method not only does not need to the local orthogonal vibration, but also the subsequent digital low-pass filter order number is low. This can greatly reduce the computational complexity and easy to real-time processing (Fig. 1).

2 The Method of Polyphase Filter Orthogonal Transformation

2.1 The Principle of Polyphase Filter Orthogonal Transformation

Set the input analog signal of intermediate frequency band-pass whose carrier frequency is f_0 to

$$\begin{aligned} x(t) &= A(t) \cos[2\pi f_0 t + \varphi(t)] \\ &= i(t) \cos 2\pi f_0 t - q(t) \sin 2\pi f_0 t \end{aligned} \quad (1)$$

When the sampling rate f_s is satisfied $f_s = \frac{4f_0}{(2m+1)}$ (m is an arbitrary positive integer), and $f_s > 2B$ (B is the bandwidth of the input signal) spectrum aliasing does not occur, the resulting sample sequence is

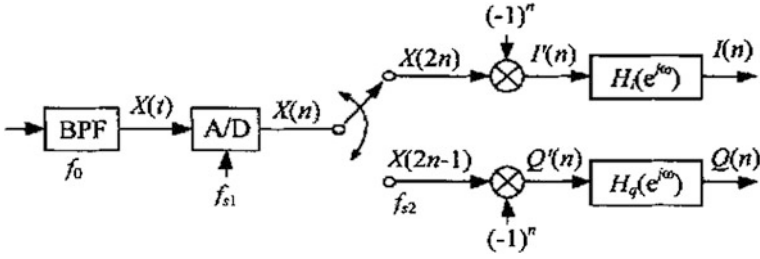


Fig. 1 Diagram of polyphase filter orthogonal transformation

$$\begin{aligned}
 X(n) &= I(n) \cos\left(2\pi f_0 \frac{n}{f_s}\right) - Q(n) \sin\left(2\pi f_0 \frac{n}{f_s}\right) \\
 &= I(n) \cos\left(\frac{2m+1}{2}\pi n\right) - Q(n) \sin\left(\frac{2m+1}{2}\pi n\right)
 \end{aligned}
 \tag{2}$$

Set $I'(n) = X(2n)$, Its sine value is zero.

$$\text{So } I'(n) = I(2n) \cos[(2m+1)\pi n] = I(2n)(-1)^n
 \tag{3}$$

Set $Q'(n) = X(2n+1)$, Its cosine value is zero.

$$\text{So } Q'(n) = Q(2n) \sin\left[\left(\frac{2m+1}{2}\right)\pi(2n-1)\right] = Q(2n+1)(-1)^n
 \tag{4}$$

Fourier transform of $I'(n), Q'(n)$, get:

$$I'(e^{j\omega}) = \frac{I\left(e^{\frac{j\omega}{2}}\right)}{2}
 \tag{5}$$

$$Q'(e^{j\omega}) = \frac{Q\left(e^{\frac{j\omega}{2}}\right)e^{\frac{j\omega}{2}}}{2}
 \tag{6}$$

Comparison expression (5), (6) found that they differ a delay factor $e^{-\frac{j\omega}{2}}$, because $I'(n), Q'(n)$, respectively, sampling from even items and odd items in the time domain, the sampling interval differ half the sampling point, and the reflection of the spectrum differ a delay factor. To correct the phenomenon of this “dislocation,” it should be calibrated using two delay filters, the requirements of the delay filters are:

$$\frac{H_Q(e^{j\omega})}{H_I(e^{j\omega})} = e^{-\frac{j\omega}{2}} |H_Q(e^{j\omega})| = |H_I(e^{j\omega})| = 1
 \tag{7}$$

To take into account the requirements of real-time processing, we use the structure of polyphase filter to achieve the above correction function.

2.2 The Structure of Polyphase Filter

The sub-filter's expression of polyphase filter is:

$$P_\rho(n) = h(nI + \rho) \quad (\rho = 0, 1, \dots, I - 1) \quad (8)$$

The Z transform of (8):

$$P_\rho(z) = \sum_{n=-\infty}^{+\infty} z^{-n} h(nI + \rho) \quad (\rho = 0, 1, \dots, I - 1) \quad (9)$$

Compared with the original filter $P_\rho(z) = \sum_{n=-\infty}^{+\infty} z^{-n} h(n)$ it can be found that the sub-filter is actually based on the original filter of the phase shift ρ then the transformation of decimation factor of I .

Because decimation Z transformation formula is $X_D(z) = \frac{1}{D} \sum_{i=0}^{D-1} z^{-i} X \left[e^{-j\frac{2\pi i}{D}} \cdot z^{\frac{i}{D}} \right]$ so

$$P_\rho(z) = \frac{1}{I} \sum_{i=0}^{I-1} e^{-j\frac{2\pi i \rho}{I}} z^{\frac{i}{I}} H \left(e^{-j\frac{2\pi i}{I}} \cdot z^{\frac{i}{I}} \right) \quad (10)$$

Replaced z with $e^{j\omega}$, it can get the frequency domain expression:

$$P_\rho(e^{j\omega}) = \frac{1}{I} \sum_{i=0}^{I-1} e^{-j\frac{2\pi i \rho}{I}} H \left(e^{-j\frac{2\pi i}{I}} e^{j\frac{i\omega}{I}} \right) \quad (11)$$

In order to suppress the image component, to improve the process accuracy, the request must satisfy the conditions of filters to $H(e^{j\omega}) = \begin{cases} 1, & |\omega| \leq \frac{\pi}{I} \\ 0, & \text{其他} \end{cases}$. According to this feature, it can be further simplified, obtain:

$$P_\rho(e^{j\omega}) = \frac{1}{I} e^{j\frac{\omega \rho}{I}} \cdot H(e^{j\frac{\omega}{I}}) = \frac{1}{I} e^{j\frac{\omega \rho}{I}} \quad (12)$$

Because $I = 4$, the value of ρ come from 0, 1, 2, 3, indicating the order of polyphase filter is a quarter of the original filter, Table 1 lists the corresponding parameters of impulse response polyphase filter. In practice, based on the obtained impulse response of filter and its branch polyphase filter, select the corresponding parameter correction function can be achieved, so the number-based orthogonal transform polyphase filter.

Table 1 The coefficients of polyphase filter

| Parameter | $h_0(n)$ | $h_1(n)$ | $h_2(n)$ | $h_3(n)$ |
|-----------|-----------------------------|-----------------------------|-----------------------------|-----------------------------|
| $h(0)$ | 4.5477904×10^{-4} | $-4.1116750 \times 10^{-3}$ | $-3.3321021 \times 10^{-3}$ | $-1.6398887 \times 10^{-3}$ |
| $h(1)$ | 1.9716606×10^{-3} | 5.7456471×10^{-3} | 6.8641502×10^{-3} | 3.3711092×10^{-3} |
| $h(2)$ | $-3.9650143 \times 10^{-3}$ | $-1.1231796 \times 10^{-2}$ | $-1.3124388 \times 10^{-2}$ | $-6.3408347 \times 10^{-3}$ |
| $h(3)$ | 7.3806625×10^{-3} | 2.0772609×10^{-2} | 2.4283706×10^{-2} | 1.1817166×10^{-2} |
| $h(4)$ | $-1.3982121 \times 10^{-2}$ | $-4.0451492 \times 10^{-2}$ | $-4.9369425 \times 10^{-2}$ | $-2.5669740 \times 10^{-2}$ |
| $h(5)$ | 3.3700226×10^{-2} | 0.1157211 | 0.1949037 | 0.2434685 |

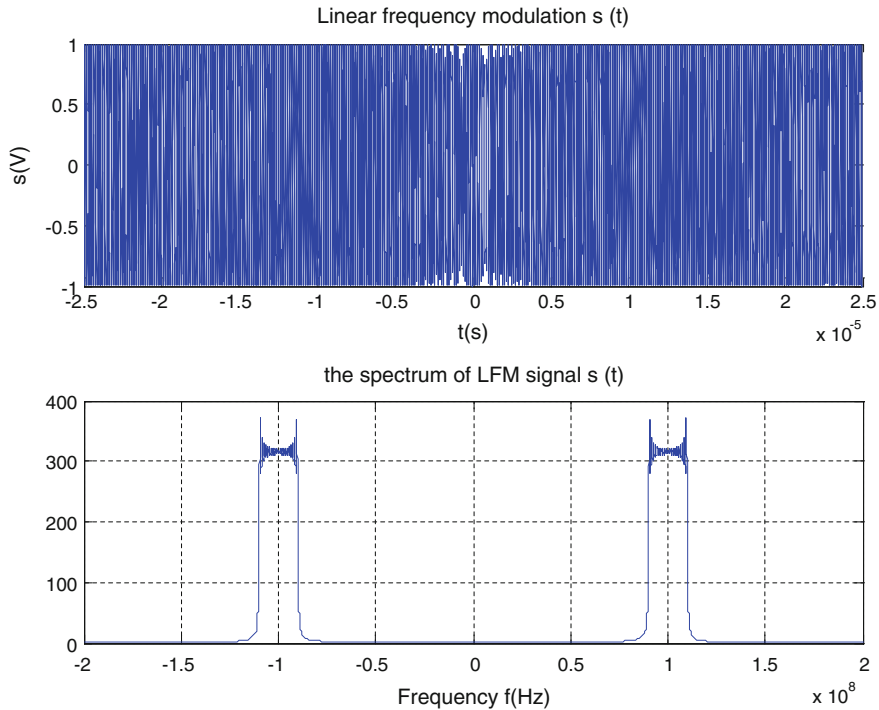


Fig. 2 Input signal and its spectrum

3 Simulation Comparison Verification

This paper uses the manner of comparison with the Hilbert orthogonal transform to carry on simulation.

In MATLAB simulation, the input signal is LFM signal where the carrier frequency $f_0 = 100$ MHz, the bandwidth $B = 10$ MHz, sampling frequency $f_s = 400$ MHz. We used the literature [3] constructs and methods. Hilbert transformer is used for bandwidth improvements. The polyphase filter used the filter coefficients of the $h_0(n)$, $h_2(n)$ in Table 1 (Fig. 2).

Respectively, after the Hilbert transform and polyphase filter orthogonal transform for the input signal it got the time-domain diagram of I/Q two signals.

From Fig. 3, it can be seen that two way signals exist inconsistent on the phase and amplitude after Hilbert orthogonal transformation, and can form false signal which cannot be subsequent processing; After polyphase filter orthogonal transformation and the phase and amplitude of two signals can ensure its consistency [4] in the allowed range, and this can also be verified which got from the signal spectrum diagram after transformation (Fig. 4).

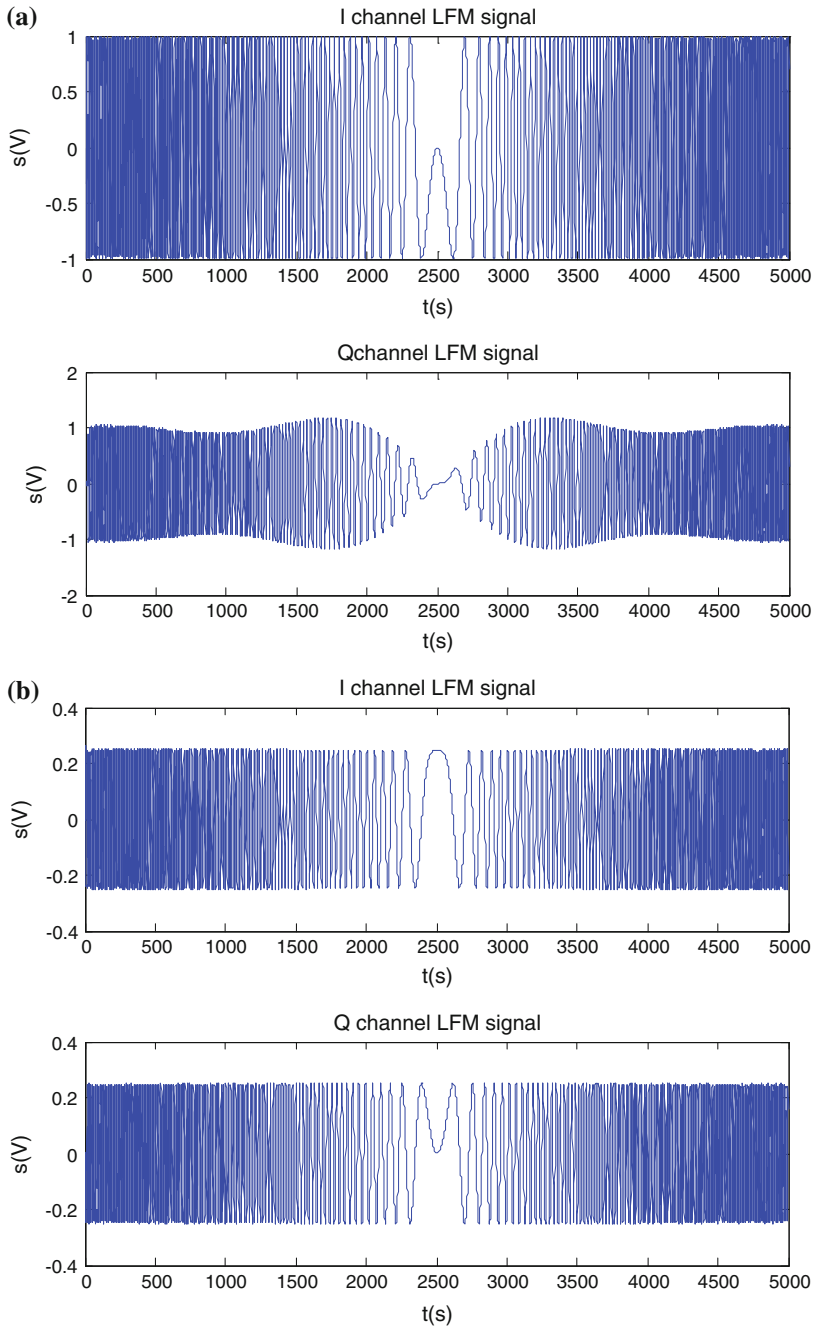
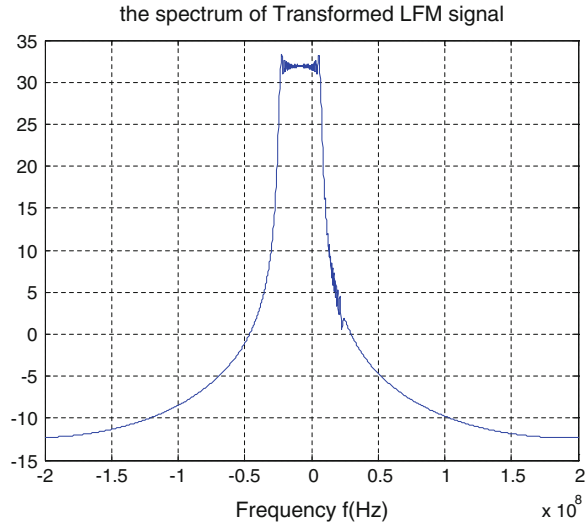


Fig. 3 The two-way signal after transform **a** Hilbert orthogonal transform. **b** Polyphase filter orthogonal transform

Fig. 4 Output spectrum of polyphase filter orthogonal transformation



The spectrum after decimation by 2-fold polyphase filtering the signal obtained after conversion has been broadening, but the bandwidth will not change [5], the results of simulation meet the requirements.

4 Performance Analysis

In the MATLAB simulation, comparing with the Hilbert orthogonal transformation, it is easy to find that polyphase filter transformation method has incomparable advantages in broadband signal receiving: increases the receiver adaptability of different signal. It is more suitable to be applied in front-end of software [6] broadband receiver.

Compared with the traditional method [7], on the one hand, it is directly on the intermediate frequency sampling, it is divided into orthogonal I/Q signals in digital signal, so it can overcome the phase and amplitude error between the two channels of which caused inconsistent and stability by the traditional method as I, Q channel simulator different parameters and other digital transformation method; On the other hand, the flow of data after A/D transformation passes the data selector and divided into odd and even data sequence to the rate of flow reduced by half, equal to A /D sampling frequency is reduced to 1/2, easy to back-end processing. And the back end of polyphase filter is fractional delay interpolation filter; the order can be done very low, so it can obtain good effect.

Moreover, the coefficients of polyphase filter regularly get from the same low-pass filter coefficients, and have similar frequency characteristics. It is in the digital domain signal processing, so even if the design of low-pass filtering characteristics is nonideal, it will not affect the quadrature of the two I/Q signals.

5 Conclusion

Polyphase filter orthogonal transform technique is applied to broadband access system. It has realized the application of DSP in frequency range. It is closer to the RF receiver. It can take advantage of the software radio technology, and easy to update algorithm. The function of below the intermediate frequency and medium frequency receiver can use software to realize, and improves the flexibility of the system while to reduce the production cost. At the same time, broadband receiver is developing direction of the future for a receiver: wider bandwidth, stronger signal received adaptability.

Acknowledgment This article has been supported by Fundamental Research Funds for the Central Universities (Grant No.HEUCF130805) and Science and Technology Foundation of State Key Laboratory (Grant No.9140C020201120C02002).

References

1. Xing-hua L, Tao SU (2008) Digital quadrature sampling techniques based on poly-phase filtering. *Mod Electron Tech* 3:28–30
2. Biao Y, Zong-ze X, Guo-liang Z (2003) Direct digital quadrature transformation Techniques based on poly-phase filtering. *J Shang Hai Univ (Natural Science)* 9(1):9–12
3. Xian-e N, Ai-guo X, He-ming Z, Chao Y (2011) Design of FIR Hilbert transformer based on matlab. *Mod Electron Tech* 34(7):113–116
4. Yong-liang W, Bing-kun G, Yun C (2008) Digital orthogonal transformation based on multiphase filtering. *J Yangtze Univ (Nat Sci Edit)* 5(4):184–187
5. Chun-yan J, Sheng-yuan Z, Xing C (2010) Digital orthogonal transformation technology based on ploy-phase filtering in software radio. *Electron Des Eng* 18(6):89–92
6. Xiao-hua Y, Yuan-cheng Y (2011) PCM/FM quadrature demodulation based on poly-phase filter. *Commun Technol* 44(11):1–3
7. Da-hai C, Hong W, You-xin L (2008) Efficient implemental structures for wideband digital down converter. *J Electron Meas Instrum* 22(5):43–46

Collaborative Recommendation System for Environmental Activities Management Mobile Application

Inmaculada Pardines, Victoria López, Antonio Sanmartín,
Mar Octavio de Toledo and Carlos Fernández

Abstract The use of a collaborative recommendation system applying fuzzy linguistic techniques is proposed in this paper. This system is included in a mobile application that manages information and the enrollment process in the activities of the Environmental Educational Program of the City of Madrid. This tool informs the user of all activities: workshops, routes, exhibitions, gardening, etc., that are made in the Environmental Education Centres of the City of Madrid. Because of the extra information that the user can receive is essential to have a system to provide the activities that may be most interesting for the user. These activities are selected based on the user's preferences profile and the register with the ratings of the activities previously performed by other users, especially, the evaluations of those with a similar profile.

Keywords Recommendation system · Collaborative filtering · Mobile application · Environmental activities · Fuzzy logic

1 Introduction

Mobile applications have made great progress in recent years, which has influenced the increased use of mobile phones to perform many of the tasks that the user carried out on his computer. Smartphones are being widely used for both commercial applications and for leisure time. Some companies see these devices as a mean to attract new customers, especially among young people.

Web applications offer great information to users making the process of finding information very difficult. Recommendation systems have proven to be an

I. Pardines (✉) · V. López · A. Sanmartín · M. O. de Toledo · C. Fernández
Departamento de Arquitectura de Computadores, Universidad Complutense de Madrid,
Prof. García Santesmases s/n, 28040 Madrid, Spain
e-mail: inmapl@ucm.es

effective solution to this problem. They are widely used especially in electronic commerce [1]. They are a complementary tool in an electronic store that shows the client, when he makes a purchase, a number of items related to what he has purchased, or it displays items that other users have bought after buying the same product as he is buying. These products may interest the customer but if he had to look inside the store, due to the large amount of existing products, he might not have found them.

In the literature, there are different models of recommendation systems that differ in the used information sources and in how the recommendations are obtained. It can be highlighted: collaborative-based systems [2], content-based systems [3], based on demographic information systems [4], knowledge-based systems [5], and utility-based systems [6].

Negative consequences of the information overload problem are increased in the case of mobile applications due to the problems inherent in this technology, such as greater difficulty in displaying contents in small screens or limitation in wireless networks due to user location. Therefore, there are previous works which have proposed recommendation systems for mobile applications [7, 8]. Some of them are developed for tourist applications and they exploit the importance of context-aware [8, 9].

Tourism has become the area which has taken most advantage of the mobile technology. It can be stood up tools with virtual tours for cities and museums [10, 11] or applications that recommend shops, restaurants, and places of interest in a city [12, 13]. Contextual information achieves special relevance: user's position, the daytime, and which is the group of friends with the user in a given time, can be the key to make a good recommendation.

The Hábitat Madrid mobile application presented in this article can be included in a context of overload information. This application reports all activities conducted by the Environmental Education Centres of the City of Madrid. The number of activities is varied; the amount of information available very large, which can make finding information becomes an arduous and unattractive task. To solve this problem, we propose the use of a recommender system that enables to personalize the information received by each user according to his preferences.

Therefore, in this paper, we propose a collaborative recommendation system integrated into a mobile application that manages the information and the registration process in the activities developed by the Environmental Education Centres of the City of Madrid. Recommendations are made based on a user's preferences profile, an analysis of the similarities with the other users of the system and a register which contains the ratings of the activities given by users who have participated in them.

The paper is organized as follows. [Section 2](#) provides a brief review of recommendation models and concepts of fuzzy logic techniques. [Section 3](#) describes the proposed recommender system. [Section 4](#) presents an example of the application performance. Finally, we show the main conclusions that can be drawn from this work.

2 Recommendation Systems and Fuzzy Logic

The recommendation system of the proposed mobile application is basically a collaborative system. Such systems collect user's evaluations with respect to an object within a given domain and generate recommendations based on the opinions of other users with a similar profile. Therefore, its implementation requires historical information about the assessment of objects that users have selected in the past.

A collaborative system must:

- Keep a history of the user ratings on all objects that have been selected.
- Measure the degree of similarity between the different users based on their preferences and object's evaluations.
- Generate recommendations best suited to a given user based on the information provided by other users of the system.

A collaborative system will be able to make a recommendation to a user on an object of the domain that has not yet evaluated for him. This recommendation is based on the assessments of other users similar to him. However, the weakness of this system is the poor quality of the recommendations, due to lack of information, the first time a user accesses the system. In the literature, there are different approaches to try to alleviate this problem [14]. A common solution is to use hybrid systems that combine the positive features of various models leaving aside negative characteristics. Other interesting approach is based on fuzzy logic recommendation [15].

Another problem in recommender systems is how to make assessments. There are domains in which the quality of the objects can be measured numerically, but in others it is more appropriate to make this assessment using words like fun, long, short, good, bad, ... instead of numeric values. Fuzzy linguistic techniques have proved adequate to model this kind of information [16]. Linguistic variables, introduced by Zadeh [17], are used to represent this information. A linguistic variable is characterized by a syntactic value (label) and a semantic (meaning). Zadeh in [17] formally define linguistic variable characterizing it by a tuple $(X, U, R(X: u))$, where X is the name of the variable; U is the universe of discourse; u is a generic name for the elements of U and $R(X: u)$ is a subset of U which represents a constraint on the values of u imposed by X .

3 Hábitat Madrid Recommendation System

Hábitat Madrid is a mobile application for Android systems [18, 19] which shows the user all the activities offered by the Environmental Education Centres of the City of Madrid. The number of activities proposed by these centres is so large that it is necessary for the use of a recommendation system to ensure that information

about these activities can be found on a mobile in a quick and easy way. Furthermore, the number of recommended activities must be small for an appropriate display of the provided information on the mobile device.

Therefore, we have decided to implement a recommendation system that sorts the activities depending on the user's preferences. The application, after pressing the *Recommendations* tab, shows a screen with the four activities which best suit the tastes and preferences of the user. However, the user will have the option of looking for more activities that may interest him simply by pressing the *Next* tab that will appear on the same screen. Thus, the application will show to the user the activities in fours in an order, previously calculated, adapted to the user preferences profile.

3.1 Overview of the Problem

Our recommendation system is basically characterized by a set of activities and a set of users. Its aim is to inform on the activities that may interest to a particular user. In general, can be described as follows:

Given the set of activities $A = \{a_1, \dots, a_m\}$, each activity $a_i \in A$ is defined by a title and a descriptor that summarizes what the activity is and to whom it is addressed.

In addition, the system will have a set of users $\{U = u_1, \dots, u_n\}$, each user $u_j \in U$ must fill in a profile with his preferences when he registers on the application. These preferences are selected from a number of keywords (routes, exhibitions, gardening, family activities ...) related to the type of activities that the user wants to perform.

The system also consists of a rating register with the assessments made by users of the activities in which they have participated. In each activity three characteristics are evaluated:

- *Environment and Resources*: bad, regular, and good
- *General*: bad, regular, and good
- *Staff*: bad, regular, and good

Environment and resources feature intended to assess both the place where the activity is performed as the means that are available to do it. In *General*, the user must evaluate the impression that has caused the whole activity to him. *Staff* feature qualifies the validity of monitors, for which the user can evaluate their communication skills, knowledge, attitude ... Every feature can be evaluated by choosing one of three options: bad, regular, and good.

Moreover, the system measures the degree of affinity between users from the existing preferences profiles. The recommendation system acts on information about the preferences introduced by different users and based on the assessments they make of the activities in which they have participated. Here is a formal description of the operation of the proposed recommendation system.

3.2 Mathematical Modeling

Given a user u , the system must go through three stages to generate a recommendation on activities that may be more interesting for this user. Following, a mathematical description of these steps is shown. This description can also be visualized by the flow diagram of Fig. 1.

- *Stage 1: Evaluation of activities.* The recommendation system calculates two ratings for all system activities, both assessments are performed in parallel.
 - *Rating 1:* It is calculated based on the value that other users have made on the activities in which they participated.
 $\forall a_i \in A, \forall u_j \in U$, calculate:
 1. $\text{sim}(u_j, u) = s_j$, $s_j \in [0, 1]$ is the degree of similarity of the user u_j with the user u
 2. $v(u_j, a_i) = \begin{cases} v_{ji} & \text{if } u_j \text{ carried out and assessed } a_i \\ \perp & \text{otherwise} \end{cases}$, v_{ji} is the assessment that the user u_j has made of activity a_i .
 3. $v(a_i, u) = \sum_{j=1}^{\text{nu}} v_{ij} = v_i$, nu is the number of users and v_i is the rating 1 of activity a_i
 - *Rating 2:* It is obtained from the user's preference profile of user u . Given a user u , $\forall a_i \in A$, calculate rating 2, v'_i as:

$$v'(a_i, u) = \frac{n_i}{N} = v'_i,$$

with

$$n_i = \sum_{k=1}^N x_k,$$

$$x_k \begin{cases} 1 & \text{if } p_k \in \text{Preferences profile of } u \text{ and descriptor of } a_i \text{ contains } k \\ 0 & \text{otherwise} \end{cases}$$

p_k is a keyword, n_i is the number of keywords of a_i that matches with the preferences that user u has marked on his preferences profile, and N is the total number of keywords that user u has selected as preferences.

- *Stage 2: Sorting.* Activities are arranged based on the assessment obtained in stage 1.
 - $\forall a_i \in A, u \in U$, calculate the total valuation v_i^* of activity a_i based on the two ratings of this activity calculated for user u in the previous stage.

$$v_i^* = v^*(a_i, u) = \alpha \cdot v(a_i, u) + (1 - \alpha) \cdot v'(a_i, u), \quad \alpha \in (0, 1)$$

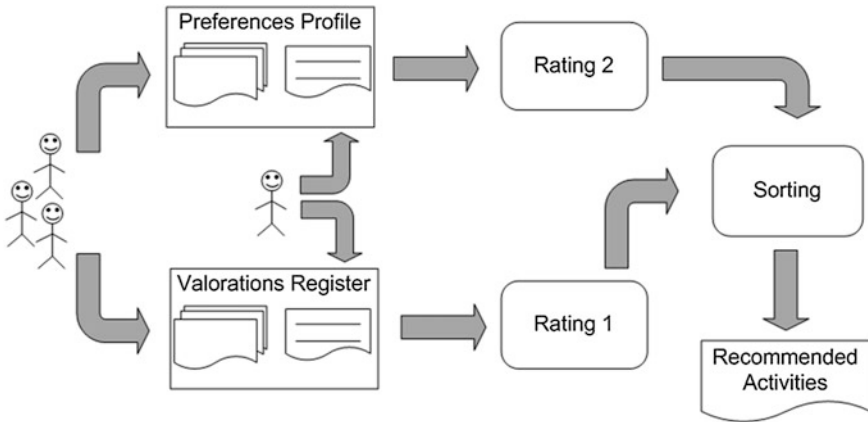


Fig. 1 Flowchart of the Hábitat Madrid recommendation system

- Sort the set of activities $A = \{a_1, \dots, a_m\}$ according to the valuation v_i^* calculated in step 2 (a).
- The w activities best rated are selected to be displayed on the first screen of the application.

4 An Example of How Operates the Hábitat Madrid Application

This section explains how the recommendation system of the Hábitat Madrid application works. An example with synthetic data on a true subset of the activities proposed by the Environmental Education Centres of the City of Madrid for the months of April, May, and June 2013 (see Table 2) is used.

Suppose a user u that enters the system for first time. He must select the *Settings* tab from the home screen of the application and then the *Preferences* option. In the new window will appear a series of keywords related to the topics of the proposed activities. The user will set the keywords referring to the type of activities that most interest him. In this way, the system will have information about the tastes and preferences of the user. In the example, the user has scored three keywords: routes, parks, and family activities, as shown in Fig. 2a.

Moreover, the system will have a database with information on the assessments that other users have made of the activities in which they have previously participated. It also has information on the degree of similarity s_j of each user u_j with the given user u .

Table 1 contains information on the history of ratings that the system users have made on the activities. If a user has not participated in an activity, he cannot

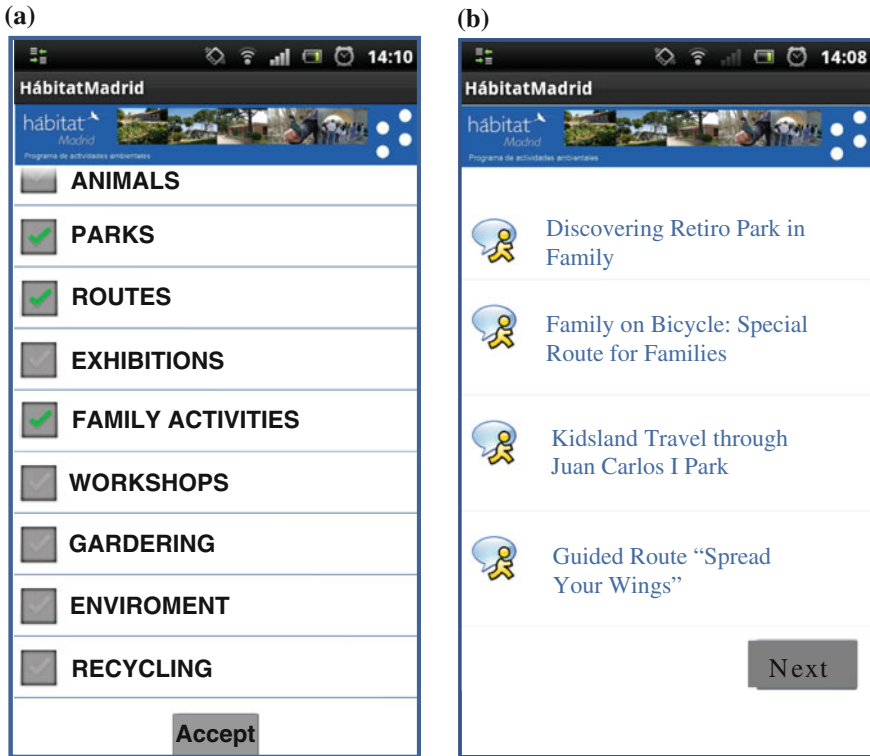


Fig. 2 Hábitat Madrid application screens. **a** User profile; **b** recommended activities

assess it, so its rating will be undefined (–). In each activity three characteristics are valued: Environment and Resources (E), General (GE), and Staff (S). The assigned rating can choose between three possibilities: Bad (B), Regular (R), and Good (G). In this table can also be observed, next to each user name, the degree of similarity of this user with user u .

In Table 2, the title of each activity is shown. The system searches for keywords related to each activity from its title and descriptor. After that, the keywords found are compared with the ones the user has set in his profile. The ratio n_i/N in Table 2 quantifies the adequacy of each activity from the point of view of the tastes and preferences of the user, by searching for keywords. These quantitative indices are combined into the algorithm to the quantification of the assessments of the activities that other users have made. These last estimations originally come from linguistic variables.

From the data of both tables, the system calculates the total rating of each activity (fourth column of Table 2). In this example, we have given equal weight to the user preferences than to the assessments that others have made on the activities, i.e., we have used a value of $\alpha = 0.5$ in Eq. 1 (Sect. 3). Finally, the

Table 1 Rating register of the activities

| | $u_1 (s_1 = 1)$ | | | $u_2 (s_2 = 0)$ | | | $u_3 (s_3 = 0.5)$ | | | $u_4 (s_4 = 0.75)$ | | |
|-------|-----------------|----|---|-----------------|----|---|-------------------|----|---|--------------------|----|---|
| | E | GE | S | E | GE | S | E | GE | S | E | GE | S |
| a_1 | G | R | G | R | R | R | - | - | - | G | G | G |
| a_2 | G | G | G | - | - | - | G | R | R | G | G | G |
| a_3 | - | - | - | G | G | G | G | G | G | R | R | G |
| a_4 | G | R | R | G | G | G | G | G | B | G | G | R |
| a_5 | G | G | G | R | R | R | G | G | G | - | - | - |
| a_6 | G | R | G | G | G | G | R | R | G | G | R | R |
| a_7 | G | R | R | R | R | G | G | G | G | R | B | R |

Table 2 Numerical value assigned to each activity for user

| | Title | n_i/N | v^* |
|-------|---|---------|-------|
| a_1 | Guided route “Spread Your Wings” | 0.67 | 1.13 |
| a_2 | Discovering retiro park in family | 1 | 1.54 |
| a_3 | Initiation ornithology workshop | 0 | 0.50 |
| a_4 | Family on bicycle: special route for families | 1 | 1.31 |
| a_5 | Ecological Kitchen garden course | 0 | 0.75 |
| a_6 | Kidsland travel through Juan Carlos I park | 0.67 | 1.17 |
| a_7 | “The Buen Retiro Trees” exhibition | 0.33 | 0.79 |

system sorts the activities according to their total valuation v^* , in the example, we would have: $a_2, a_4, a_6, a_1, a_7, a_5, a_3$. Therefore, the four best valued activities are displayed on the first screen of *Recommendations*.

To access the recommended activities, the user should select the *Recommendations* tab of the home screen. The four best rated activities will be shown, as we can see in Fig. 2b. The user can select any of the displayed activities to obtain more information or to enroll in it. If these activities havenot pleased him, he may seek others just pressing the *Next* icon of Fig. 2b. The application will display another screen with the next four highest rated activities.

5 Conclusions

In this paper, we describe a collaborative recommendation system integrated into a mobile application developed for the city of Madrid. The aim of this application is to inform users about the program activities proposed by the Environmental Education Centres of this City Hall. The amount of information provided is so abundant that it is essential to use a recommendation system.

The proposed recommendation system assesses the activities according to the preferences profile of each user and the ratings that other users (especially those similar to him) have made of each activity. The system will recommend to the user

about the four activities, which according to the applied model will be more attractive to him. However, it offers the possibility that if any of these four activities satisfied him, he can search information about other activities. All of them will be displayed, from high to low preference, depending on the assessments calculated by the proposed recommendation system.

As future work we are developing the inclusion of context-aware in the decision making of the recommender system. In this way, the system will recommend, in real time, the activities that best suit the user's preferences that take place at a center near the user's current location.

References

1. Palopoli L, Rosaci D, Sarné GML (2013) A Multi-tiered recommender system architecture for supporting E-commerce. *Intell Distrib Comput VI Stud Comput Intell* 446:71–81
2. Rostami B, Cremonesi P, Malucelli F (2013) A graph optimization approach to item-based collaborative filtering. *Recent Adv Comput Optim* 470:15–30
3. Martínez L, Pérez LG, Barranco M (2007) A multigranular linguistic content-based recommendation model. *Int J Intell Syst* 22:419–434
4. Pazzani MJ (1999) A framework for collaborative, content-based and demographic filtering. *Artif Intell Rev* 13(5–6):393–408
5. Burke RD (2000) Knowledge-based recommender systems. *Encycl Libr Inf Sci* 69(32)
6. Burke RD (2002) Hybrid recommender systems: survey and experiments. *User Model User-Adap Interact* 12(4):331–370
7. Ricci F, Nguyen QN (2007) Acquiring and revising preferences in a critique-based mobile recommender system. *Int J Intell Syst* 22(3):22–29
8. Setten M, Pokraev S, Koolwaaij J (2004) Context-aware recommendations in the mobile tourist application COMPASS. *Adap Hypermed Adap Web-Based Syst. Lect Notes Comput Sci* 3137:235–244
9. Adomavicius G, Tuzhilin A (2011) Context-aware recommender systems. In: *Recommender systems handbook*. Springer
10. Styliaras G, Koukopoulos D (2012) Educational scenarios with Smartphones in cultural heritage sites and environments. *J Educ Multimed Hypermed* 21(3):285–315
11. Kenteris M, Gavalas D, Economou D (2009) An innovative mobile electronic tourist guide application. *J Pers Ubiquit Comput Arch* 13(2):103–118
12. Cultura unam: <http://www.cultura.unam.mx/>
13. BCN cultural: <http://barcelonacultura.bcn.cat/es>
14. Bobadilla J, Ortega F, Hernando A, Bernal J (2012) A collaborative filtering approach to mitigate the new user cold start problem. *Knowl-Based Syst* 26:225–238
15. Yager RR (2003) Fuzzy logic methods in recommender systems. *Int J Fuzzy Sets Syst* 136(2):133–149
16. Delgado M, Herrera F, Herrera-Viedma E, Martín-Bautista MJ, Vila MA (2001) Combining linguistic information in a distributed intelligent agent model for information gathering on the internet. In: Wang PP (eds) *Computing with words*. Wiley, New York
17. Zadeh LA (1975) The concept of a linguistic variable and its application to approximate reasoning—I. *Inf Ser* 8:199–249
18. Seltzer L (2012) Android “Clear Leader” in Smartphone race Says report. *Byte*. <http://www.informationweek.com/byte/personal-tech/smart-phones/android-clear-leader-in-smartphone-race/240143823>
19. Gargenta M (2011) *Learning Android*, 1st edn. O'Reilly Media, Inc, Sebastopol

Study of Algorithms for Interaction Between Flowing Water and Complex Terrain in Virtual Environment

Yue Yu and Yuhui Wang

Abstract SPH scheme and GPU-accelerated method are combined to construct particle model of fluid for gaining realistic model of flowing water interacting to complex terrain in virtual environment. Furthermore, coordinate information of particles are accessed and isosurface model of fluid is constructed by combining metaballs model and marching cubes method for rendering of flowing water. Terrain model is constructed based on DEM data. Terrain data are extracted and displayed by boundary particles. Real-time rendering of flowing water interacting to complex terrain in virtual environment is implemented.

Keywords Fluid simulation · SPH · GPU accelerating · Metaballs · Marching cubes

1 Introduction

Simulation of fluid interacting to complex terrain is always a difficult issue in graphic simulation. For one thing complex terrain cannot be expressed by certain equations because of its irregularities and randomness, for another, the shape of fluid changes all time and its physical model is extremely complicated [1]. Many problems call for solution such as the realism of fluid and the expression of flying spray.

Modeling of fluid based on physical model has always been one of the main directions. Physic-based methods can be ranged into two principal types, Euler method and Lagrangian. In Euler method, changes of parameters such as velocity, pressure, and density of fluid with time are studied for every point of the fluid field

Y. Yu (✉) · Y. Wang

School of Mechanical Engineering and Automation, Beihang University, Beijing, China
e-mail: heryo_yo@me.buaa.edu.cn

by the study of movement of fluid in each point. And changes of parameters from one point to another are studied in fluid field. Euler method is one of the approaches based on grid. In Lagrangian, motion of the fluid is studied starting with motion of micro fluid. Changes of velocity, pressure, and density with time of certain micro fluid are studied and changes of parameters from one tiny to another are studied. Lagrangian is a method based on particles [2].

Many domestic and foreign scholars conducted a lot of research about fluid modeling based on physical model. Akinci and Ihmsen propose a momentum conserving two-way coupling method of SPH fluids and arbitrary rigid objects based on hydrodynamic forces. Their approach samples the surface of rigid bodies with boundary particles that interact with the fluid, preventing deficiency issues, and both spatial and temporal discontinuities. Their method adheres to the concept of SPH, is efficient to compute, and allows versatile fluid-rigid coupling [3]. Schechter and Bridson propose a new ghost fluid approach for free surface and solid boundary conditions in SPH liquid simulations. Their ghost treatment of solid and free surface boundaries, particle sampling algorithms, and new XSPH artificial viscosity allow significantly higher quality liquid simulations than basic SPH with only a moderate overhead [4]. Wangzhang, Zhang proposed a LBM-based efficiently modeling and rendering method for free surface fluid simulation. LBM model through the shallow water equations is used for fluid modeling and surface height field calculations. This method is more accurate in simulation of shallow water flow process [5]. Chen and Wang complete real-time simulation of the large-scale fluid scenes based on new sophistication to nonuniform sampling function. In order to make the calculation and simulation to achieve real-time fluid and fully utilize the high parallelism and programmability of GPU, they assigned all the adaptive SPH simulations and interactive computing boundaries to the GPU stream processor [6].

SPH algorithm is used to construct the fluid particle model for flowing water modeling in this paper, combined with GPU-accelerated computing. In the particle model building completion basis, we use the metaball method combined with the marching cubes algorithm to construct flowing water surface models. Finally, a terrain is constructed based on DEM data and extracted data tectonic boundary particles, and two-way coupled SPH method is used to complete the water interaction with the surrounding environment.

2 Construct the Fluid Particle Model Using SPH Algorithm Combined with GPU-Accelerated Computing

The basic idea of SPH-smoothed particle hydrodynamics method is to use interacted particles to describe continuous fluid or solid. Various physical quantities are hosted on each particle, including density, mass, speed, etc. By solving the kinetic equation of particle group and track the movement of each particle orbit, and seek

the mechanical behavior of the whole system, then form a complex fluid motion. SPH is an absolute Lagrangian method which can avoid the problem of material interface and grid in the Euler description; it is particularly suitable for solving dynamic large deformation problems such as high-speed collisions [7].

2.1 Mechanics of SPH Method

In SPH algorithm, each fluid particle follows the basic Newton's second law. Fluid mass is determined by the density of the fluid element, density is generally used instead of mass, so the force of the particles in the fluid by the movement is expressed by ρa . The force acting on a particle composed of three parts. It is given by formula (1).

$$F = F^{\text{External}} + F^{\text{Pressure}} + F^{\text{Viscosity}} \quad (1)$$

F^{External} is called external force, generally gravity, i.e., ρg . F^{Pressure} is the force caused by pressure differential of the fluid, the fluid flows as pressure difference exists. Its value is equal to the pressure field gradient, i.e., $-\nabla p$ its direction points from the high pressure area of the low pressure zone [8]. $F^{\text{Viscosity}}$ is determined by the particle velocity difference. In the flowing fluid, the fast-flowing portion gives the force which is similar to the shearing force is to the slow areas, value of the force is related to coefficient μ and the viscosity of the fluid on the speed difference, i.e., $\mu \nabla^2 u$.

The above values are substituted into the formula (1) and rewrite into the acceleration form. It is given by formula (2).

$$a = g - \frac{\nabla p}{\rho} + \frac{\mu \nabla^2 u}{\rho} \quad (2)$$

This formula is a simple form of Navier–Stokes equation which describes the viscous Newtonian fluid.

2.2 Smooth Kernel Function

The particle properties' effect becomes smaller as the distance increasing, this function whose attenuation with distance is called smooth kernel function, the maximum radius of influence is called the smooth kernel radius. For smooth kernel of each particle, only the particles in the smooth kernel have an effect on center particle's density, pressure, acceleration, and other attributes, otherwise particles outside the smooth kernel have no effect on the center particle [9]. By setting a

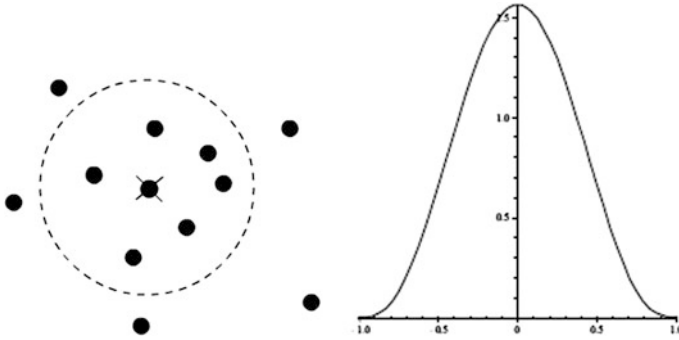


Fig. 1 Form of smooth kernel function

suitable smooth core radius, discrete particles are constructed as a whole through force and fluid mechanics model completes. Form of smooth kernel function is shown in Fig. 1.

There are n particles within the smooth core radius h of point r (here not necessarily particles) whose positions are $r_0, r_1, r_2, \dots, r_j$, accumulation of an attribute A is given by formula (3).

$$A_S(r) = \sum_j^n A_j \frac{m_j}{\rho_j} W(r - r_j, h) \tag{3}$$

A_j is some properties within smooth nuclear radius such as density, pressure, etc., m_j and ρ_j are mass and density of the particles around, r_j is the position of particle, h is the smooth nuclear radius. Function W is smooth kernel function, it has two important natures. First, it must be even function, i.e., $W(-r) = W(r)$; second, it must be a gauge function, i.e., $\int w(r)dr = 1$. According to the formula and the nature of smooth kernel functions we can get properties like particle density, pressure, viscosity, and then get the particle acceleration.

Fluid is in the process of constant flow, density of different parts is different, so the density of each particle needs to be calculated. Replace A with density ρ , use Poly6 function as smooth kernel function, then density of position r_i is got. It is given by formula (4).

$$\rho(r_i) = m \frac{315}{64\pi h^9} \sum_j \left(h^2 - |r_i - r_j|^2 \right)^2 \tag{4}$$

As calculating the acceleration generated by the pressure, force of particles from different areas of pressure varies, so the arithmetic mean of the pressure of two particles is generally used instead of the pressure of individual particles in calculating. As for the pressure p generated by individual particle, it can be calculated as independent variable in the continuous equation. Then pressure by gas

equation of state is got. This is a method of weakly compressible which can simulate incompressible flow [10]. Using Spiky function as smooth kernel function, we get acceleration generated by the pressure of position r_i . It is given by formula (5).

$$a_i^{\text{Pressure}} = -\frac{\nabla p(r_i)}{\rho_j} = -m \frac{45}{\pi h^6} \sum_j \left(\frac{p_i + p_j}{2\rho_i\rho_j} (h-r)^2 \frac{r_i - r_j}{r} \right) \quad (5)$$

$$\text{with } r = |r_i - r_j|$$

Acceleration generated by the pressure is generated by velocity difference between particles, i.e., relative velocity. It is given by formula (6).

$$a_i^{\text{Viscosity}} = \frac{F_i^{\text{Viscosity}}}{\rho_j} = m\mu \frac{45}{\pi h^6} \sum_j \frac{u_j - u_i}{2\rho_i\rho_j} (h - |r_i - r_j|) \quad (6)$$

Put function (5) and (6) into (2), we get the acceleration of particle. It is given by formula (7).

$$a(r_i) = g - m \frac{45}{\pi h^6} \sum_j \left(\frac{p_i + p_j}{2\rho_i\rho_j} (h-r)^2 \frac{r_i - r_j}{r} \right) + m\mu \frac{45}{\pi h^6} \sum_j \frac{u_j - u_i}{2\rho_i\rho_j} (h-r) \quad (7)$$

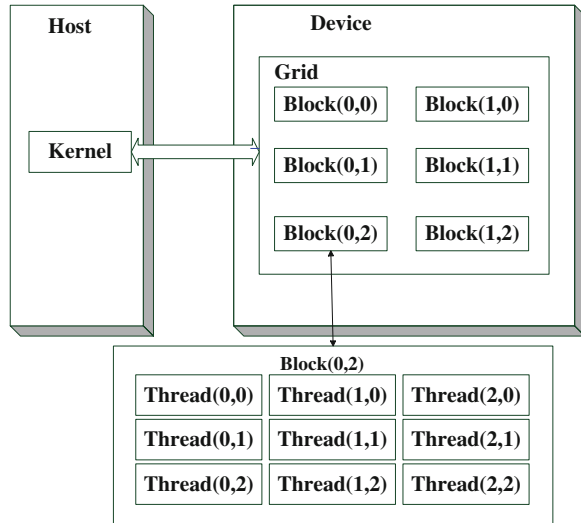
$$\text{with } r = |r_i - r_j|$$

After getting acceleration a_i by adding the respective force, we use Euler's method to update the speed and coordinates.

2.3 Accelerating by GPU Parallel Computing

In the calculation process of SPH, data to be calculated are large. CPU serial computing cannot meet the requirements for computing speed, so GPU parallel computing to accelerate is used. GPU and multi-core CPU are very different in the calculation architecture, GPU more focus on data parallel computing, which executes the same calculation in parallel on different data. In the calculation of large-scale data, GPU's CUDA architecture is used, by enabling a large number of blocks to implement parallel computing [11]. Each block also contains large number of threads, each thread or block has its own index, the internal organization of the set shown in Fig. 2. Through collaboration between the threads, large-scale data parallel computing can be fully guaranteed as each thread performs the same operations.

Fig. 2 Internal organization of CUDA architecture of GPU



In the simulation of SPH fluid, the new state value of a particle is calculated only by means of the state of all the particles of last moment, without affecting other particles' state of a new moment, which has a high parallelism. This makes it very suitable for SPH method implemented on the GPU. In SPH fluid simulation process, all arrays are mapped for the GPU cache. GPU cache is a memory of a video memory, simulator assigns multiple caches for all particle attributes, such as coordinates cache, speed cache, density cache, pressure cache, etc. These caches can be dynamically created and destroyed during the simulation [12]. GPU will initialize a large number of threads to run compute kernel based on the size of the computational domain (usually the output cache size). Computing cores will sample the data input buffer, does a series of numerical computation and output the result to the output cache. Since the calculation of all the particles can be carried out in parallel, so it can be executed to each GPU thread, taking full advantage of the GPU parallelism.

2.4 Algorithm Flow of SPH

- Step 1* Initialize particles, set initial position, initial velocity, and initial acceleration of each particle according to the design requirements of the scene to be simulated or actual condition
- Step 2* Calculate the density of each particle
- Step 3* Calculate the pressure of each particle
- Step 4* Calculate the acceleration of each particle
- Step 5* Adjust the acceleration according to boundary condition

- Step 6* Calculate velocity of each particle according to acceleration
- Step 7* Calculate position of each particle according to velocity
- Step 8* Draw particles
- Step 9* Go back to step 2.

3 Construct Fluid Isosurface by Metaball Combined with Marching Cubes

After fluid particle model is constructed by SPH algorithm, a realistic fluid model is need to build. Therefore, based on the particles' three-dimensional information of every time, we need to construct the function of the shape of the fluid and render the fluid surface. All points on this surface have the same function value, known as the isosurface. SPH algorithm is a Lagrangian method which emphasizes particles of fluid-structure. The metaball method determines the overall surface by precisely calculating each corner's function value in every voxel according to particles around. So it is very suitable to construct the function of isosurface based on particles model. After function is determined, we construct isosurface using marching cubes, which can guarantee a strong sense of reality of the overall model.

3.1 Metaball

Metaball is an important technology using implicit surfaces to model, mainly used to draw the object with irregular surface. It can control the surface shape via the potential function. The traditional three-dimensional scene modeling technique mostly constructs the polygon outline with massive pieces, realism of scene rendering enhances with an increase in the number of polygon. Unlike traditional modeling techniques, metaball technology simulates the shape of the surface through a specific potential function. The flexibility of potential function determines its superiority in the rendering of the irregular surface. In the drawing process, formula constructed by metaball can ensure the overall realism of the model, and show a good performance of the details of the fluid, such as the integration between water droplets and splashing effect [13].

The most common metaball Eq. (8) provides boundaries of movement of the surface of the object. Coordinate position (x, y, z) of surface of the object is determined by T_0 , q_i , and f_i in three-dimensional environment. T_0 is set threshold value in particular environment, which is the defined value of the function. q_i is the i -th object maximum density function. f_i is the i -th object metaball density function which is metaball potential function. It is given by formula (8).

$$f(x, y, z) = \sum_{i=0}^n q_i f_i - T_0 = 0 \quad (8)$$

There are many forms of potential functions f_i , the typical four kinds of equations are given by formula (9), (10), (11), (12), formula (11) is used in this paper:

$$f_i(x, y, z) = \exp(-ar^2) \quad (9)$$

$$f_i(x, y, z) = \begin{cases} 1 - 3\left(\frac{r}{R_i}\right)^2, & 0 \leq r \leq \frac{R_i}{3} \\ \frac{3}{2} \left[1 - \left(\frac{r}{R_i}\right)\right]^2, & 0 \leq r \leq R_i \end{cases} \quad (10)$$

$$f_i(x, y, z) = \begin{cases} \left[1 - \left(\frac{r}{R_i}\right)^2\right]^2, & 0 \leq r \leq R_i \\ 0, & r > R_i \end{cases} \quad (11)$$

$$f_i(x, y, z) = \begin{cases} -\frac{4}{9}\left(\frac{r}{R_i}\right)^6 + \frac{17}{9}\left(\frac{r}{R_i}\right)^2, & 0 \leq r \leq R_i \\ 0, & r > R_i \end{cases} \quad (12)$$

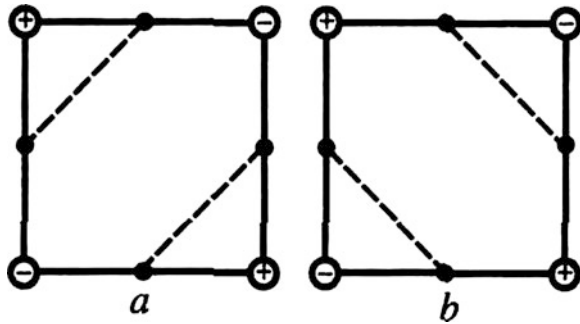
R is the distance from point (x, y, z) to the center point of metaball object. R_i is the maximum radius of i -th metaball object. Four different value of R according to the sparse level of particles in the overall are used in this paper.

3.2 Marching Cubes Method

Marching Cubes method is also known as MC method, which is the most representative method to construct isosurface in the three-dimensional regular data field. In MC method, original data are assumed discrete three-dimensional regular data field. In order to construct isosurface in this data field, set value of isosurface C_0 . MC method first locates the voxel position where isosurface pass through.

Each voxel in discrete three-dimensional regular data field has eight corners, get function value of each corner. If function value is greater than or equals to C_0 , the corner is set 1. If function value is smaller than C_0 , the corner is set 0. Then we get $2^8 = 256$ cases. By reversing the corner function value, topology relationships of eight corners do not change in many cases, and rotational symmetry exists, we can reduce the 256 different cases to 14 cases [14], these 14 cases can basically reflect all cases in a voxel.

Fig. 3 Two-dimensional representation of ambiguity of connection



3.3 Discriminate and Eliminate Ambiguity in Marching Cubes Using Asymptotic Methods

In MC methods, if the corner with value 1 and the one with value 0 are separately located at both ends of different diagonal on one plane of the voxel, there are two possible ways of connection, shown in Fig. 4, and thus there is ambiguity. It is shown in Fig. 3. Position of hyperbola of isosurface and the boundary is used to discriminate and eliminate ambiguity [15].

3.4 Algorithm Processes of Building Isosurface

- Step 1* Identify voxel containing the isosurface
- Step 2* Scan each voxel, calculate function value of every corner by metaballs and compare with the value C_0 of isosurface to get status table of every voxel.
- Step 3* Get the boundary plane which contains intersection with isosurface according to status table
- Step 4* Get intersections of boundary plane and isosurface through linear interpolation method
- Step 5* Get the normal of each corner in every voxel using the central differencing method then get the normal of each vertex of triangles.
- Step 6* Draw isosurface according to value and normal of vertexes of triangles.

4 Construct Terrain Model Based on DEM Data Resampling

Digital elevation model (DEM) is a method of digital representation of ground in surveying and mapping work. In the mathematical model, DEM elevation model is a finite discrete representation and a finite sequence of three-dimensional

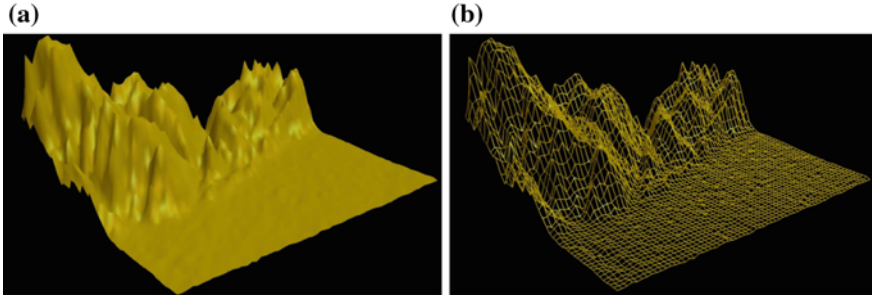


Fig. 4 Terrain constructed by DEM data: **a** surface rendering model, **b** grid model

vectors [16, 17]. Real terrain data are used here, so you can restore the true complexity of the terrain, it is suitable for the terrain rendering of this study.

The data actually collected into a $1025 * 1025$ array, in this paper, only need to be resampled to $65 * 65$ array to meet the requirement of boundary particles. After sampling, give every point a height value in this $65 * 65$ grid, and calculate the average normal vector of every vertex. Draw the terrain with the grid, as shown in Fig. 4.

5 Construct Model of Flowing Water

After building the terrain, vertexes of the terrain mesh model are sampled, get the position of every vertex. Place a fixed particle at each vertex. Particles model of the terrain is shown if Fig. 5.

In the specific calculation, these particles are as boundary particles to the calculation of fluid movement whose positions are fixed, but density, viscosity, and mass of these particles are different from fluid particles. A repulsive force will be given when the fluid particles are near, so these particles are the boundaries. Function of SPH need to be modified due terrain particles.

Function of fluid density is modified. It is given by formula (13).

$$\rho(r_i) = m \frac{315}{64\pi h^9} \sum_j \left(h^2 - |r_i - r_j|^2 \right)^2 + m_b \frac{315}{64\pi h^9} \sum_k \left(h^2 - |r_i - r_k|^2 \right)^2 \quad (13)$$

Acceleration generated by the pressure is modified. It is given by formula (14)

$$a_i^{\text{Pressure}} = -m \frac{45}{\pi h^6} \sum_j \left(\frac{p_i + p_j}{2\rho_i\rho_j} (h - r)^2 \frac{r_i - r_j}{r} \right) - m_b \frac{45}{\pi h^6} \sum_k \left(\frac{p_i + p_b}{2\rho_i\rho_b} (h - r)^2 \frac{r_i - r_k}{r} \right) \quad (14)$$

Fig. 5 Particles model of the terrain

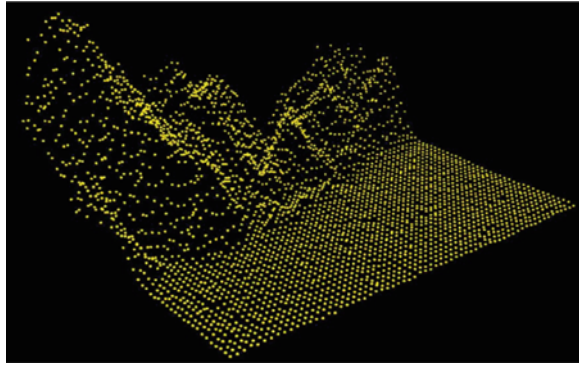


Table 1 Parameters of the experiment

| Parameter | Meaning of parameter | Value |
|-----------|------------------------------|---------|
| N_f | Number of fluid particles | 1920 |
| N_b | Number of boundary particles | 4,225 |
| N | Total number of particles | 6,145 |
| m_f | Mass of fluid particles | 0.001 |
| m_b | Mass of boundary particles | 0.003 |
| μ | Viscosity of fluid | 1 |
| h | Radius of smooth core | 1.1 |
| l | Edge length of voxel | 0.25 |
| N_v | Number of voxel | 696,320 |
| R_1 | Metaball radius 1 | 1.4 |
| R_2 | Metaball radius 2 | 1.0 |
| R_3 | Metaball radius 3 | 0.7 |
| R_4 | Metaball radius 4 | 0.5 |
| ρ | Density of fluid | 1,000 |
| ρ_b | Density of boundary | 1,500 |

Acceleration generated by the viscosity is modified. It is given by formula (15)

$$a_i^{\text{Viscosity}} = m\mu \frac{45}{\pi h^6} \sum_j \frac{u_j - u_i}{2\rho_i\rho_j} (h - |r_i - r_j|) + m_b\mu_b \frac{45}{\pi h^6} \sum_k \frac{-u_i}{2\rho_i\rho_b} (h - |r_i - r_k|) \tag{15}$$

Three functions above have some new parameter. m_b is mass of the boundary particle, μ_b is viscosity between boundary particles and fluid particles, ρ_b is density of boundary particles, P_b is pressure of boundary particles, and r_k is position of boundary particles (Table 1).

Simulation experiment of interaction of flowing water and complex terrain After particle model of fluid is calculated, construct the isosurface function using metaball, then render the isosurface with marching cubes. Here we simulate a model of interaction of flowing water and mountain.

Experimental results shown in Fig. 6.

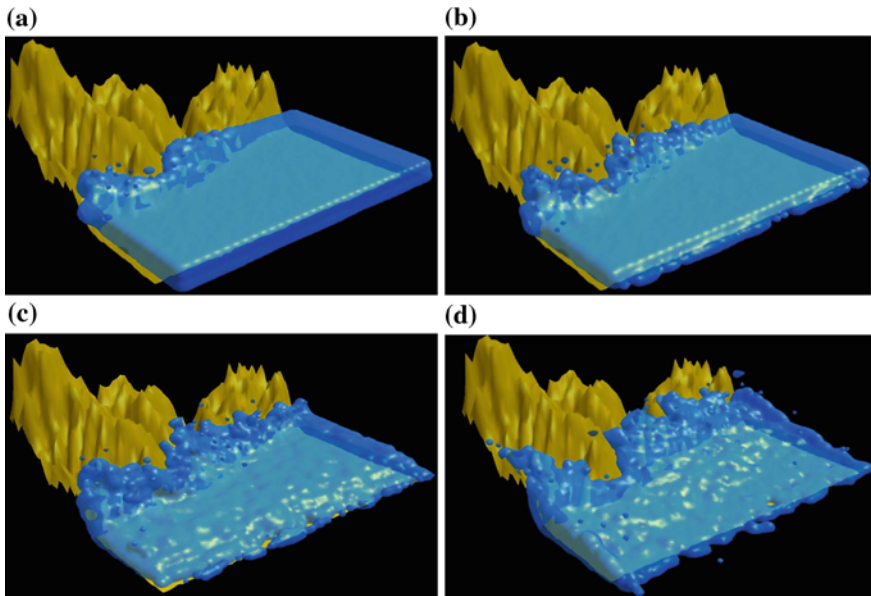


Fig. 6 Experimental results: **a** water just reach the boundary, **b** further interaction, **c** the effect of water splashed, **d** the effect of the water receded

6 Conclusion

Algorithm in this paper presented method of interaction of fluid in complex terrain and complete realistic rendering, at the same time, reflects physical characteristics of a fluid in the whole process of interaction in a good way and in good real time. Splashes and fusion caused by interaction of fluid in complex terrain meet the real scene rendering needs.

References

1. Liu Y, Liu X, Zhu H, Wu E (2005) Physically based fluid simulation in computer animation. *J Comput Aided Des Comput Graphics* 117(112):2581–2589
2. Carlson M, Mucha PJ, Horn RBV (2002) Melting and flowing. In: *Proceedings of the ACM SIGGRAPH, Symposium on computer animation*, pp 167–174, New York
3. Akinci N, Ihmsen M, Akinci G, Solenthalery B, Teschner M (2012) Versatile rigid-fluid coupling for incompressible SPH. *ACM Trans Graphics* 31(4), Article 62
4. Schechter H, Bridson R (2012) Ghost SPH for animating water. *ACM Trans Graphics* 31(4), Article 61
5. Wang C, Zhang Z, Zhang Q, Qian Y, Zhang J, Xu T (2011) Realistic rendering of free surface fluid based on lattice Boltzmann method. *J Comput Aided Des Comput Graphics* 23(1):104–110

6. Chen X, Wang Z, He J, Yan H, Peng Q (2010) An integrated algorithm of real time fluid simulation on GPU. *J Comput Aided Des Comput Graphics* 22(3):396–405
7. Muller M, Charypar D, Gross M (2003) Particle-based fluid simulation for interactive applications. In: *Proceedings of ACM SIGGRAPH/Euro graphics symposium on computer animation*, pp 154–159, San Diego
8. Li F, Wang J (2010) Numerical simulation of fluid based on SPH method. *Comput Technol Dev* 20(7):114–120
9. Chen J, Xu F, Huang Q (2008) Study on the smoothed particle hydrodynamics method. *J Mech Strength* 30(1):78–82
10. Amada T (2006) Real-time particle-based fluid simulation with rigid body interaction. *Game Gems 6*, Charles River Media, pp 189–206
11. Green S (2010) Particle simulation using CUDA. In *Nvidia CUDA sdk 4.0*. <http://developer.nvidia.com>
12. Harris MJ (2004) Fast fluid dynamics simulation on the GPU. In *GPU Gems*, pp 637–655
13. Fan Z, Tan J (2002) Imitation of wave based on metaball modeling. *J Hefei Univ Technol* 25(6):1125–1129
14. Sun W, Zhang C, Yang X (2007) Research review on marching cubes. *J Comput Aided Des Comput Graphics* 19(7):947–952
15. Nielson GM, Floey TA, Hamann B (1991) Visualizing and modeling scattered multivariate data. *IEEE Comput Graphics Appl* 11:47–55
16. O’Callaghan JF (1984) The extraction of drainage networks from digital elevation data. *Comput Vision Graphics Image Process* 28:323–344
17. Zhang J (2011) Water droplet simulation based on Gpu metaball. Wuhan

An Automatic Generating Method of 3D Personalized Clothing Prototype

Xiaping Shi and Bingbing Zhang

Abstract This paper utilizes an idea of relaxation to automatically generate three-dimensional (3D) clothing prototype according to the location of key positions on 3D personalized virtual mannequin created by the method of Electronic Made-to-Measure (eMTM). This approach is based on generating 3D personalized clothing body and a supplement to eMTM clothing part; it has advantages of low cost and good practicality compared with other clothing generation methods. Thus, it provides a new technical support for the wide use of eMTM.

Keywords Automatically generate · 3D prototype · Pieces · Relaxation · Location of key positions

1 Introduction

With the development of Internet and the e-commerce, many more people start to pursue personalized garment and join in Made-to-Measure (MTM). The way of customizing clothing traditionally applies a flexible ruler to measure customers by face-to-face, and then tailors based on the measured data make clothes. Although this way can get more accurate data, it also has shortcomings: first of all, it is time-consuming, second, it needs measuring face-to-face, and also it cannot be applied on the Internet. Therefore, eMTM has been developed and spread gradually. eMTM system is a completely customer-focused making clothing way, it has advantages in its efficiency and the individuality. Its 3D image will make the designing and showing of apparel more intuitive. eMTM system provides service for clothing design and manufacturing. Its efficiency makes eMTM become the

X. Shi (✉) · B. Zhang

School of Computer Science and Technology, Donghua University, Shanghai China
e-mail: xsp@dhu.edu.cn

best choice for apparel manufactures. eMTM will become the main way of modern clothing production.

Under such a background, this paper puts forward a new method to automatically generate 3D clothing prototype by 3D personalized virtual mannequin. This scheme not only provides full and accurate basis for apparel makers in personalized clothing production, but also fully implements individuation for customers.

2 Related Works

In the past years, many companies and universities at home and abroad have been studying virtual apparel fitting. For example, Fitiquette [1] generates online virtual images for users to provide fitting models in apparel electronic business platform. Users can make use of Fitiquette to create virtual 3D images for themselves and measure detailed dimensions of any parts of their body (e.g., arm length, waist girth, etc.), then according to the measurement results adjust the virtual images until the virtual images are corresponded with the users. Fitiquette can provide some advice for users on clothing, which has usually a different style and size for users to try on. Users can also rotate the virtual 3D clothing images to check the fitting effect from different angles. Fitiquette has many advantages, but its price is very high so that it cannot be widely spread. Me-Ality [2] builds up 3D simulation of human body for customers who only need to wear clothes and stand in a small space similar to the fitting room. 3D detection technology applied in this small space is high-cost. Eden [3] introduces a fitting technology of high simulation and can simulate clothing fold, material. In conclusion, these researches have some shortcomings, i.e., the cost is high and approaches cannot be spread easily.

Luo [4] puts forward a method to generate clothing prototype on a 3D human body obtained by 3D scanner, as shown in Fig. 1. This method cannot be effectively promoted on the Internet because it needs to use an expensive 3D scanner. Wang [5] presents a new approach to model a 3D garment intuitively around a 3D human model by 2D sketches input. He also researches different kinds of clothing [6]. Although his method can greatly improve the efficiency and the quality of pattern making in the garment industry, the human models have to be predefined. In 2001, the European textile and apparel organizations (EURATEX) presented applying 3D body scanner and establishing the electronic production of customized clothing combined with modern network and garment CAD technology, which is briefly called eMTM (Electronic Made-to-Measure) [7].

eMTM system exactly overcomes above shortcomings. Therefore, it is necessary to spread eMTM on the virtual human body generated. Based on Luo's method, this paper studies the process to generate clothing prototype on a 3D human body via 3D scanner, and then a constructed 3D clothing prototype is related with the features on a 3D human model which corresponds to a specific person. The approach of generating clothing prototype will be more suitable for

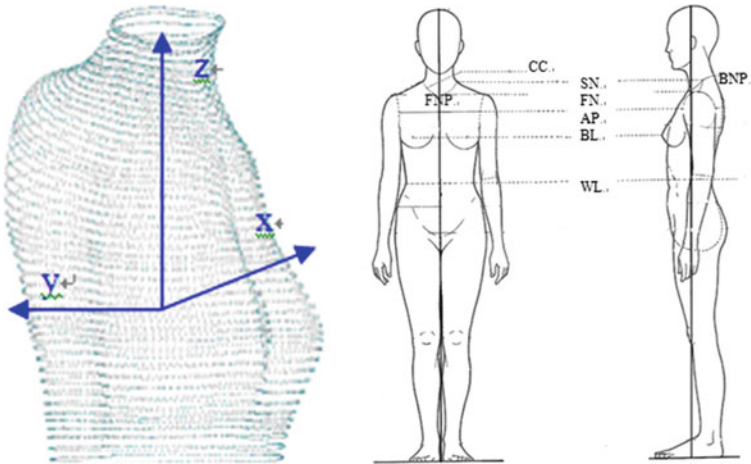


Fig. 1 The *left* means coordinate system and the *middle* and *right* show key-positions

various kinds of virtual human body which is applied in apparel engineering effectively and easily.

3 The Generation of 3D Personalized Clothing Prototype

Clothing prototype is a basic form of clothing added primary relaxation and based on net size of human body. Clothing prototype becomes a garment if clothing elements and style are added. Therefore, we take clothing prototype as research object which is the basis of clothing.

3.1 The Overview of the Method

The first step to make clothing prototype is to measure data from human body. So this method first locates critical parameters, that is, automatically generating the corresponding positions of clothing prototype based on a specific 3D human body and some gaps between the body and the clothing. The collar contour (CC) and Armhole-line (AH) which are the most important on the clothing prototype are implemented according to the features on the human body. It is vital to position the key points on the body and to deal with CC and AH. Other parts in prototype are body adding relaxations. The following aspect of paper will present these processes.



Fig. 2 Before and after dealing with problem in CC

3.2 Location of Key Positions

Through the analysis of human shape and the study of data distribution of 3D virtual human body, the key positions for 3D clothing prototype are bust-line (BL), waist-line (WL), front-neck-point (FNP), back-neck-point (BNP), side-neck (SN), armpit (AP). The coordinate system of the human body generated is shown as the left of Fig. 1. Some important key positions [8] are shown as the right of Fig. 2. How to get the key positions will be described in the following section.

The human body S is composed of many cross-sections $s_i (s_0 - s_{n-1})$ from the neck to hip, and every cross-section contains about 30 points $p_i (p_0 - p_{n-1})$. In every cross-section, $y_{\max}(s)$ and $y_{\min}(s)$ represent the maximum and the minimum on y-axis, respectively, and $x_{\max}(s)$, $x_{\min}(s)$ represent the maximum and the minimum on x-axis, respectively.

BL: BL is situated in the cross-section s_{BL} , which is the thickest cross-section in human body. s_{BL} can be described in the following expression.

$$s_{BL} = \left\{ \begin{array}{l} s_j | (y_{\max}(s_j) - y_{\min}(s_j)) > \forall (y_{\max}(s_i) - y_{\min}(s_i)), \\ i \neq j, s_0 \leq s_i, s_j < s_n \end{array} \right\} \quad (1)$$

WL: WL is located in the cross-section s_{WL} , which is the narrowest cross-section in the body. s_{WL} can be described in the following expression.

$$s_{WL} = \left\{ \begin{array}{l} s_j | (x_{\max}(s_j) - x_{\min}(s_j)) < \forall (x_{\max}(s_i) - x_{\min}(s_i)), \\ i \neq j, s_0 \leq s_i, s_j < s_n \end{array} \right\} \quad (2)$$

SN: SN lies in the cross-section s_{SN} , which is the narrowest cross-section in the neck. s_{SN} can be described in the following expression [9].

$$s_{SN} = \left\{ \begin{array}{l} s_j | \frac{x_{\max}(s_j) - x_{\min}(s_j)}{x_{\max}(s_{j+1}) - x_{\min}(s_{j+1})} < \forall \frac{x_{\max}(s_i) - x_{\min}(s_i)}{x_{\max}(s_{i+1}) - x_{\min}(s_{i+1})}, \\ i \neq j, 0 \leq i, j < n \end{array} \right\} \quad (3)$$

In s_{SN} , there are two important points, left-SNP (LSNP) and right-SNP (RSNP), LSNP is the right side point p_{LSNP} , and RSNP is the left side point p_{RSNP} .

$$\begin{aligned} p_{LSNP} &= \{p_j | p_j(x) = x_{\max}(s_{SN}), 0 \leq j < m\} \\ p_{RSNP} &= \{p_j | p_j(x) = x_{\min}(s_{SN}), 0 \leq j < m\} \end{aligned} \quad (4)$$

FN: FN is front neck situated in the cross-section s_{FN} , which is the most concave cross-section from neck and chest. In other words, $y_{\min}(s_{FN})$ is largest compared with other cross-sections. s_{FN} can be described in the following expression.

$$s_{FN} = \{s_j | y_{\min}(s_j) > \forall y_{\min}(s_i), i \neq j, s_{SN} \leq s_i, s_j \leq s_{\text{chest}}\} \quad (5)$$

FNP is front-neck-point on s_{FN} , marked in p_{FNP} . BNP is back-neck-point marked in p_{BNP} .

$$\begin{aligned} p_{FNP} &= \left\{ p_j | p_j(x) = \frac{x_{\max}(s_{FN}) + x_{\min}(s_{FN})}{2}, p_j(y) < 0, 0 \leq j < m \right\} \\ p_{BNP} &= \left\{ p_j | p_j(x) = \frac{x_{\max}(s_{SN}) + x_{\min}(s_{SN})}{2}, p_j(y) > 0, 0 \leq j < m \right\} \end{aligned} \quad (6)$$

AP: AP is in the cross-section s_{AP} , which is in the middle of s_{FN} and s_{BL} . s_{AP} can be described in the following expression.

$$s_{AP} = \left\{ s_j | s_j(z) = \frac{1}{2}(s_{FN}(z) + s_{BL}(z)), 0 \leq j < m \right\} \quad (7)$$

3.3 Determination of Collar Contour

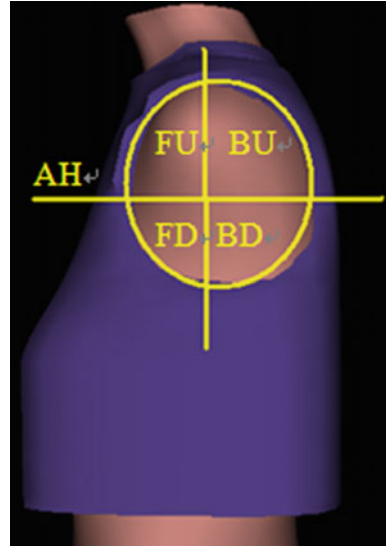
Every cross-section from SN to WL in the body can be divided into four parts to generate clothing prototype. They are from SN to FN, from FN to armpit, from armpit to chest, and from chest to waist.

In the part from SN to FN, it is the most important to confirm the collar contour (CC) on clothing prototype. Two-dimensional clothing prototype has two requirements to CC (1) smooth (2) perpendicular to the normal vector of LSNP, RSNP, FNP, and BNP. Based on both of these requirements, we can approximately regard CC as an ellipse. CC is divided into two semi-ellipses, CC_{front} and CC_{back} . CC_{back} is almost on the same cross-section with s_{SN} . CC_{front} can be expressed in the following expression.

$$CC_{\text{front}}(x, y, z) = \left\{ \frac{x^2}{a^2} + \frac{z^2}{b^2} = 1, (x, y, z) \in S, a = \frac{1}{2}w(s_{SN}), \right\} \quad (8)$$

$w(s_{SN})$ and $h(s_{SN})$ mean the width and height of s_{SN} .

Fig. 3 The composition of AH



For realizing the part of 3D clothing prototype, the points within the CC will be discarded on the basis of upper expression. There exists a problem. According to VRML file rules, if a cross-section does not have equal counts of points with its adjacent cross-sections, the boundary of CC will be not smooth in the clothing, as shown in Fig. 2.

To make clothing prototype integrated correctly, the adjacent cross-sections must have equivalent amount. A method is adopted for each cross-section that has less than m points, where m is the count of points in a normal cross-section. We calculate the number of lack points, and then insert these points into the cross-section averagely. The processing result can be seen in Fig. 2.

3.4 Determination of Armhole on Clothing Prototype

In parts from FN to AP and from AP to BL, there are two difficult points (1) how to determine armhole (AH) (2) how to deal with relaxation.

AH is a smooth curve across acromion and armpit. It is determined by clothing structure and shape of human body. Armhole structure consists of armhole depth, sleeve width, free-zone, and shoulder. According to above definition method of CC, we consider AH as four quarter-ellipse, AH_{FU} , AH_{BU} , AH_{FD} , and AH_{BD} , as shown in Fig. 3. The four parts can be expressed by the following formula.

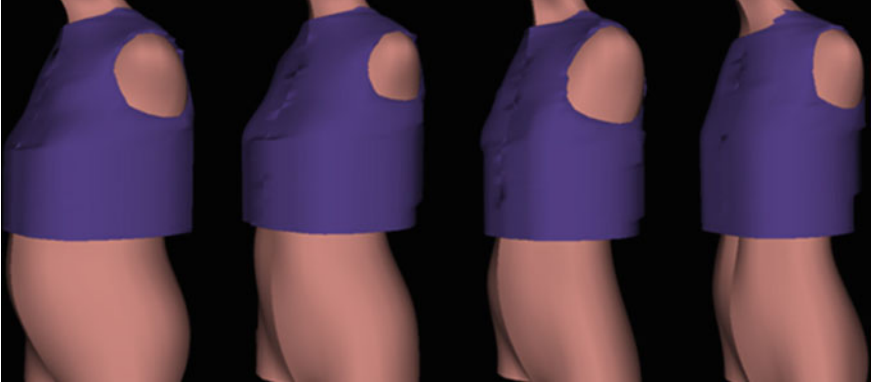


Fig. 4 The examples on different mannequins

$$\begin{aligned}
 \text{AH}_{\text{FU}}(x, y, z) &= \left\{ \frac{z^2}{a^2} + \frac{y^2}{b^2} = 1, (x, y, z) \in S, a = h(s_{\text{FN}}) - h(s_{\text{AP}}), b = th(s_{\text{FAP}}) \right\} \\
 \text{AH}_{\text{BU}}(x, y, z) &= \left\{ \frac{z^2}{a^2} + \frac{y^2}{b^2} = 1, (x, y, z) \in S, a = h(s_{\text{FN}}) - h(s_{\text{AP}}), b = th(s_{\text{BAP}}) \right\} \\
 \text{AH}_{\text{FD}}(x, y, z) &= \left\{ \frac{z^2}{a^2} + \frac{y^2}{b^2} = 1, (x, y, z) \in S, a = h(s_{\text{AP}}) - h(s_{\text{BL}}), b = th(s_{\text{FAP}}) \right\} \\
 \text{AH}_{\text{BD}}(x, y, z) &= \left\{ \frac{z^2}{a^2} + \frac{y^2}{b^2} = 1, (x, y, z) \in S, a = h(s_{\text{AP}}) - h(s_{\text{BL}}), b = th(s_{\text{BAP}}) \right\}
 \end{aligned} \tag{9}$$

$th(s_{\text{FAP}})$ means the thickness of front s_{AP} , $th(s_{\text{BAP}})$ means the thickness of back s_{AP} .

In order to make the size and style of armhole flexible [8], we set a free-zone in the bottom of front-axilla and back-axilla.

3.5 Determination of Relaxation

Relaxation is the gap between clothing and human body [8]. Setting relaxation has three effects: (1) to satisfy normal human physiological activities in dynamic (2) to be safe and comfortable in static [10].

Relaxation distribution ratio is based on the average value of clothing construction and human body moving parts, front-chest, underarm, back-chest. We define relaxation of each part as the following expressions [8].

$$f_{\text{cloth}}(x, y, z) = \left\{ \begin{array}{l} f_{\text{body}}(x, y, z) + R(\text{FC}), R(\text{FC}) = 30\% \times \frac{R(\text{chest})}{2} \\ f_{\text{body}}(x, y, z) + R(\text{UA}), R(\text{UA}) = 30\% \times \frac{R(\text{chest})}{2} \\ f_{\text{body}}(x, y, z) + R(\text{BC}), R(\text{BC}) = 40\% \times \frac{R(\text{chest})}{2} \\ f_{\text{body}}(x, y, z) \in S, \end{array} \right\} \quad (10)$$

$f_{\text{body}}(x, y, z)$ means 3D points of human body S . Relaxation $f_{\text{cloth}}(x, y, z)$ implies 3D points of clothing prototype. $R()$ indicates relaxation function of each part. $R(\text{chest})$ means chest relaxation. The fashion drawings in different human body can be seen in Fig. 4.

4 Conclusions

This paper presents a new approach to intuitively generate 3D clothing prototype on a 3D personalized virtual mannequin created by eMTM. The constructed clothing surfaces are related to the features on human models. Our approach consists of three parts: (1) positioning of key points on the human body; (2) construction of 3D personalized clothing prototype, and (3) the procession of relaxation. Compared with earlier approach, the method has the following advantages: (1) the personalized clothing prototype can be generated automatically; (2) because the 3D human body is created through the way of eMTM, which only need two photos input by a customer, therefore, the automatic generation of personalized clothing prototype is convenient and low cost; (3) it provides a new idea for online application and improves the applicability of eMTM. In summary, our technique can greatly improve the efficiency and the quality of pattern making in the garment industry.

References

1. Virtual fitting startup Fitiquette Myntra acquisitions by Indian electricity dealer. <http://www.36kr.com/p/202371.html>
2. Me-Ality launched the “3d body detection technology” digital guides to help you choose clothes. <http://www.chinasspp.com/News/detail/2012-10-15/12316.html>
3. 3D fitting revolution, Eden, (the garden of Eden) introduced the high simulation fitting technology, which can simulate clothing fold, material. <http://www.36kr.com/p/174394.html>
4. Luo L (2009) The research and implementation of three-dimensional individual garment prototype based on eMTM. Donghua University, Shanghai
5. Wang CCL, Wang Y, Yuen MMF (2002) Feature based 3D garment design through 2D sketches. *Comput Aided Des* 35:659–672
6. Lin J, Jin X, Wang CCL, Hui K-C (2005) Mesh Composition on models with arbitrary boundary topology. *IEEE Trans Visual Comput Graphics* 12(3):36–49

7. Kartsounis GA, Magnenat-Thalmann N (2000) The European Textile/Clothing Industry on the eve of the New Millennium. Brussels, Euratex
8. Zhong Z (2000) The human body with clothing. China Textile Press, Beijing
9. Luo L (2008) The key section positioning of virtual human based on eMTM. Chin Sshi-Tech Enterp 23:163
10. Hu J (2006) The research of 3D clothing style display based on planar graphs. Donghua University, Shanghai

Study of Migration Topology in Parallel Evolution Algorithm for Flight Assignment

Jiaxing Lei, Xuejun Zhang and Xiangmin Guan

Abstract Airspace congestion has become more and more serious in recent years due to the sharp increase of aircraft which has caused many unsafe factors and economic losses. Hence, how to assign flights to reduce congestion and delay has attracted much more attention. However, the flight assignment problem is very difficult to deal with it because in general has multiple objectives and involves in a large amount of flights. In this paper, we propose a new flight assignment method based on parallel evolution algorithm (PEA), which has great superiority for large-scale complicated problem. Besides, a left–right probability migration topology is presented to further improve the optimization capability. Experiments on real data of the national route of China show that our method outperforms the current three flight assignment approaches. Moreover, the congestion and delay are effectively alleviated.

Keywords Air traffic flow management · Flight assignment · Parallel evolution algorithm · Migration topology

1 Introduction

In the past few years, the global civil aviation transportation industry developed rapidly [1, 2]. More and more flights simultaneously present in the same airspace, but the airspace capacity keeps relatively steady, which has caused acute

J. Lei (✉) · X. Zhang · X. Guan
School of Electronic and Information Engineering, Beihang University,
Beijing 100191, People's Republic of China
e-mail: leijiaxing@ee.buaa.edu.cn

J. Lei · X. Zhang · X. Guan
National Key Laboratory of CNS/ATM, Beijing 100191, People's Republic of China

congestion and delay. Hence, the flight assignment problem with the aim to balance air traffic flow and reduce congestion has attracted much more attention.

However, with consideration of thousands of flights, it is a large-scale combinatorial optimization problem with tight coupling among variables and constraints. Besides, from a practical standpoint, the flight assignment problem often considers several objectives, which cause the problem difficult to deal with.

In the early time, the problem mainly considered to modify the flight plans for local regions, especially in the airports. The most typical approach was to convert the delay in the air into the delay on the ground by postponing departure time of flights. In 1987, Odoni first proposed effective algorithms to obtain optimal ground-holding strategies [3]. Terrab focused on ground-holding delay method in a single airport [4] and Varanas et al. proposed some heuristic algorithms to assign delays in multiple airports [5]. Delahaye and Odoni introduced stochastic optimization techniques and optimize the routes and time slots together [6]. Because of the strong complexity of the problem, the previous researches treated it as a mono-objective instance and partially solved it. In 2005, with consideration of reducing the congestion and delay, Delahaye et al. developed a multi-objective model, and adopted Multi-objective genetic algorithm (MOGA) to solve it [7]. They used the real data in France to test their method and obtained satisfied results. Recent years, Tian et al. used MOGA to deal with the same problem in China and they presented more objective functions including the congestion optimization in each sector and the overloaded time of sectors optimization [8]. Liu et al. used cooperative co-evolution to address route network flow assignment in a simplified network [9].

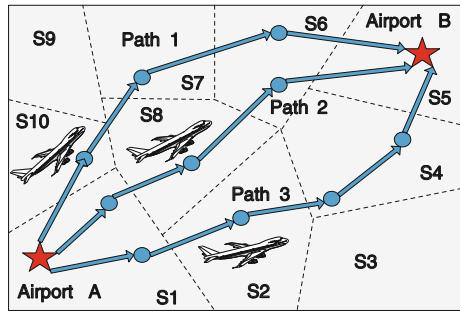
However, these methods are apt to fall into local optimum and cause slow convergence speed, especially in later period of the evolution, because the multi-objective optimization problem involves in thousands of flights and tight coupling exists among variables and constraints. In this paper, we propose a parallel evolution algorithm with a new migration topology. The parallel evolution algorithm adopts several populations to evolve simultaneously which can explore the searching space more fully. Besides, a left-right probability migration topology is presented to further improve the optimization capability via increasing communication among populations. The experiment on real data of the national route of China shows that the method can speed up the convergence and get better solution.

Our paper is organized as follows. The model is described in [Sect. 2](#). The framework of the parallel evolution algorithm is presented in [Sect. 3](#). [Section 4](#) summarizes our experimental results on real data of the national route of China. Finally, we conclude the work in [Sect. 5](#).

2 The Model

As an illustration, the explanation of the flight assignment problem is shown in [Fig. 1](#).

Fig. 1 The illustration of the flight assignment problem



The rectangular airspace is divided into several sectors with dotted lines as boundary. Supposed that there is a flight from airport A in the left bottom to airport B in the top right corner, and there are three feasible paths for the flight. For example, if the congestion in sector 6 is severe, the flight can choose path 3 to reduce congestion.

2.1 Decision Variables

For each flight, there is a pair of decision variable (δ_i, r_i) . And δ_i represents the delay slot and r_i is a feasible route. Hence, the slot set and path set can be described as follows:

$$\begin{aligned}
 A &= 0, 1, \dots, \delta_p - 1, \delta_p \\
 R &= r_0, r_1, r_2, \dots, r_{\max}
 \end{aligned}
 \tag{1}$$

where δ_p is the maximum delay time for a flight.

A flight plan can be described as follows:

$$L = (S_1, Tin_1, Tout_1), \dots, (S_k, Tin_k, Tout_k), \dots
 \tag{2}$$

where S_k is the k th sector the flight will pass, Tin_k is the time slot it enters into the sector, and $Tout_k$ is the time slot it leaves the sector.

2.2 Objective Functions

In real operation, safety and efficiency both need to be considered. Hence, in this paper, reducing congestion and delay are as the two objectives.

2.2.1 Congestion Objective

Workload in sector S_k at time t is related to the number of flights in the sector and passing the boundaries of the sector. It can be roughly expressed by [10]

$$W_{S_k}^t = W_{\text{mo}S_k}^t + W_{\text{co}S_k}^t \quad (3)$$

where $W_{\text{mo}S_k}^t$ is the monitoring workload which can be estimated by

$$W_{\text{mo}S_k}^t = \begin{cases} 1 + M_{S_k}^t - C_{mS_k}^t, & \text{if } M_{S_k}^t > C_{mS_k}^t \\ 0, & \text{else} \end{cases} \quad (4)$$

where $C_{mS_k}^t$ is the monitoring critical capacity of sector k at time t . $M_{S_k}^t$ is related to the number of aircraft in sector S_k at time t [7].

Similarly, $W_{\text{co}S_k}^t$ is the coordination workload and can be estimated by

$$W_{\text{co}S_k}^t = \begin{cases} 1 + C_{S_k}^t - C_{cS_k}^t, & \text{if } C_{S_k}^t > C_{cS_k}^t \\ 0, & \text{else} \end{cases} \quad (5)$$

where $C_{cS_k}^t$ is the critical coordination capacity of sector k at time t . $C_{S_k}^t$ is related to the number of aircraft passing the boundaries of sector S_k at time t .

Then, the first objective function can be defined as follow:

$$y_1 = \min \sum_{k=1}^{k=P} \left(\left(\sum_{t \in T} \widetilde{W}_{S_k}^t \right)^\phi \times \left(\max_{t \in T} \widetilde{W}_{S_k}^t \right)^\varphi \right) \quad (6)$$

where P is the number of sectors, T is the time period we considered, ϕ and φ are weight factors [5].

2.2.2 Delay Objective

Total delay consists of the delay on the ground and the delay in the air. The delay on the ground can be expressed as: $\delta_s(i) = t_n - t_k$, where t_k is the planned departure time slot and t_n is the actual departure time slot. The cost of air delay is three times of the ground delay, so the air delay can be presented as: $\delta_r(i) = 3 * (T_r - T_0)$, where T_r is the actual flying time and T_0 is the shortest flying time. Besides, with consideration of the equity between flights, the second objective function is defined by the mean of a quadratic summation of delays instead of a regular linear one [5]:

$$y_2 = \sum_{i=1}^N (\delta_s(i) + \delta_r(i))^2 \quad (7)$$

```

BEGIN
Initialize  $IM$  populations of size  $popsize$  each.  $g=0$ .  $archive[M]=NULL$ 
WHILE  $g < maxgen$ 
    FOR population  $j=0:(IM-1)$ 
        Divide the problem into  $n$  subcomponents
        FOR each subcomponent in the population
            Using DE to optimize
        END FOR
        Update  $archive[j]$ 
    END FOR
    IF (migration condition met)
        Exchange individuals among the populations selected
    END IF
     $g=g+1$ 
END WHILE
END

```

Fig. 2 Pseudocode of the algorithm

3 Optimization Method

As described previously, the flight assignment problem is a multi-objective large-scale problem with tight coupling among variables. The traditional multi-objective algorithms are difficult to solve it efficiently. Hence, we propose a new method based on parallel evolutionary algorithm (PEA), which has several populations evolve simultaneously. PEA can get satisfied results when dealing with this kind of problems for its distributed feature [11]. An archive for every population is introduced to store and update the nondominated solutions found so far. Besides, a left-right probability migration topology is designed to exchange individuals among subpopulations, which can speed up the evolution. The pseudocode of the algorithm is outlined in Fig. 2.

3.1 Coding

Each chromosome consists of the departure slot and route of all the flights. The departure slot and route of a flight can be chosen from two finite discrete sets. The structure of the chromosome is given in Fig. 3.

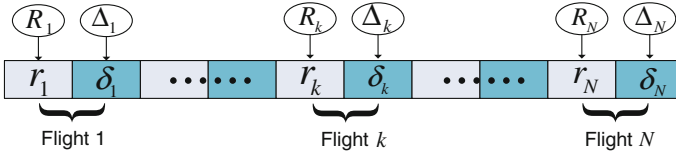


Fig. 3 The structure of the chromosome

3.2 Left-Right Probability Migration Topology

The exchange of individuals is called migration [12], and the migration topology determines the destination of the migrants which has an important influence on the quality of solutions. In this paper, a left-right probability migration topology is presented. All populations are in a special order, and the worst individual in a population is replaced by the best individual in the left or right population with equal probability.

The left-right probability topology $SL(n)$ for population n can be defined as follows:

$$SL(n) = \begin{cases} (n + N - 1)/N, & \text{if rand} < 0.5 \\ (n + N + 1)/N, & \text{if rand} \geq 0.5 \end{cases} \quad (8)$$

where $0 \leq n < N$, and rand is a random number between 0 and 1.

4 Experiment Results

In order to test and verify the effectiveness of the algorithm, the real data of the national route of China is used. There are 1,706 airway segments, 940 waypoints, and 150 airports. Besides, the data of 1,664 flights on January 1, 2009 was used. Other parameters in the experiments are set as follows: total population size popsize = 100, time period $T = 240$ min, maximum generation maxgen = 150, crossover probability $P_c = 0.9$, and mutation probability $P_m = 0.1$.

4.1 The Number of Populations

The number of populations IM in PEA has an important influence on the results. Hence, we first find the optimal number of populations.

It can be seen in Fig. 4(left) that the Pareto front under $IM = 5$ dominates Pareto fronts under other values of IM. Beside, three indicators are introduced to analyze the results with different number of populations. γ can measure the

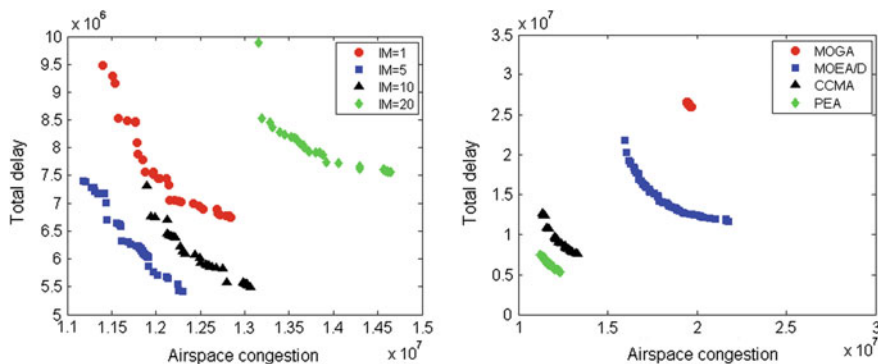


Fig. 4 The results under the different number of subpopulations (*left*) and the results of different algorithms (*right*)

Table 1 Comparison of different IM (Hypervolume, γ and Δ)

| IM | Hypervolume | γ | Δ |
|---------|---------------------|---------------------|---------------|
| IM = 1 | 8.8881e + 12 | 1.3669e + 06 | 0.9662 |
| IM = 5 | 1.4422e + 13 | 2.5595e + 05 | 0.9598 |
| IM = 10 | 1.1336e + 13 | 6.8483e + 05 | 1.2383 |
| IM = 20 | 2.8491e + 12 | 2.7682e + 06 | 1.1688 |

The value in bold is the best value.

convergence of the solutions to the Pareto front and Δ can measure the extent of spread achieved among the obtained solutions [13]. Moreover, another indicator hypervolume is also given which can evaluate the convergence and the extent of spread of the solutions simultaneously without the real Pareto front [14, 15]. It can be seen in Table 1 that the solution set under IM = 5 has the smallest value of γ and Δ , and the largest value of hypervolume (values in bold) which indicates that when IM = 5, our algorithm can get the best performance.

4.2 Comparison with Other Algorithms

Next, the experiment aims to evaluate the performance of the proposed PEA by comparing it with three existing algorithms, the MOGA, the MOEA/D [16], and the cooperative co-evolutionary multi-objective algorithm (CCMA) [17].

It can be seen in Fig. 4(right) that the Pareto front under PEA dominates Pareto fronts under other algorithms. And the best values (in bold) in Table 2 also shows PEA performs the best in every aspect.

Table 2 Comparison of different algorithms (Hypervolume, γ and Δ)

| Algorithm | Hypervolume | γ | Δ |
|-----------|---------------------|---------------------|---------------|
| MOGA | 1.3690e + 12 | 2.1414e + 07 | 1.0115 |
| MOEA/D | 7.2003e + 13 | 1.1160e + 07 | 1.0412 |
| CCMA | 1.9501e + 14 | 3.3108e + 06 | 1.0255 |
| PEA | 2.2314e + 14 | 3.9088e + 05 | 0.9413 |

The value in bold is the best value.

5 Conclusion

In this paper, we propose a new flight assignment method based on parallel evolution algorithm which has great superiority for large-scale complicated problem. Besides, a new migration topology called left–right migration topology is presented. Our migration topology can further improve the optimization capability. Experiments on real data of the national route of China show that our method outperforms the current three flight assignment approaches. Moreover, the congestion and delay are effectively reduced.

Acknowledgments This work is supported by the National High Technology Research and Development Program of China (Grant No. 2011AA110101), the National Natural Science Foundation of China (Grant No. 61201314), and the Specialized Research Fund for the Doctoral Program of Higher Education (Grant No. 20101102110005).

References

1. Zhang X, Guan X, Hwang I, Cai K (2012) A hybrid distributed-centralized conflict resolution approach for multi-aircraft based on cooperative co-evolutionary. *Sci Chin Inf Sci* 56:1–16
2. Su J, Zhang X, Guan X (2013) 4D-trajectory conflict resolution using cooperative coevolution. In: *Proceedings of the 2012 international conference on information technology and software engineering*. Springer, Berlin, pp 387–395
3. Odoni AR (1987) The flow management problem in air traffic control. *Flow control of congested networks*. Springer, Berlin, pp 269–288
4. Terrab M (1989) *ATC flow control through ground-holding*. MIT, Cambridge
5. Vranas PB, Bertsimas DJ, Odoni AR (1994) The multi-airport ground-holding problem in air traffic control. *Oper Res* 42(2):249–261
6. Delahaye D, Odoni AR (1997) Airspace congestion smoothing by stochastic optimization. *Evolutionary Programming VI*. Springer, Berlin, pp 163–176
7. Delahaye D, Sofiane O, Puechmorel S (2005) Airspace congestion smoothing by multi-objective genetic algorithm. In: *ACM symposium on applied computing*, pp 907–912
8. Tian W, Hu M (2010). Study of air traffic flow management optimization model and algorithm based on multi-objective programming. In: *ICCMS 2010–2010 international conference on computer modeling and simulation*. ICCMS, Sanya, China, pp 210–214
9. Liu H, Zhu Y, Cai K, Pan Q (2011) Route network flow assignment in the new generation of aviation by cooperative co-evolution, cybernetics and intelligent systems (CIS). In: *2011 IEEE 5th international conference on 17–19 Sept*, pp 175–180

10. Oussedik S, Delahaye D (1998) Reduction of air traffic congestion by genetic algorithms. In: Proceedings of the fifth international conference on parallel problem solving from nature. Springer, Berlin, pp 855–864
11. Tang J, Lim MH, Ong YS (2007) Diversity-adaptive parallel memetic algorithm for solving large scale combinatorial optimization problems. *Soft Comput* 11(9):873–888
12. Cantu-Paz E (2000) On the effects of migration on the fitness distribution of parallel evolutionary algorithms. In: Workshop on evolutionary computation and parallel processing at GECCO
13. Deb K, Pratap A, Agarwal S, Meyarivan T (2002) A fast and elitist multiobjective genetic algorithm: NSGA-II. *IEEE Trans Evol Comput* 6(2):182–197
14. Zitzler E, Thiele L, Laumanns M et al (2003) Performance assessment of multiobjective optimizers: an analysis and review. *IEEE Trans Evol Comput* 7(2):117–132
15. Fleischer M (2003) The measure of Pareto optima applications to multiobjective metaheuristics. *Evolutionary multi-criterion optimization*. Springer, Berlin, pp 519–533
16. Zhang Q, Li H (2007) MOEA/D: a multi-objective evolutionary algorithm based on decomposition. *IEEE Trans Evol Comput* 11(6):712–731
17. Yang Z, Tang K, Yao X (2008) Large scale evolutionary optimization using cooperative coevolution. *Inf Sci* 178(15):2985–2999

Improving the GPS Location Quality Using a Multi-agent Architecture Based on Social Collaboration

Jordán Pascual Espada, Vicente García-Díaz,
Rubén González Crespo, B. Cristina Pelayo G-Bustelo
and Juan Manuel Cueva Lovelle

Abstract Smartphones are very popular, every day these devices are used by millions of people for different purposes. One of the most popular smartphone services is the GPS geolocation, many different mobile applications use the location information in their business logic, such as: calculate routes, locate nearby places, locate people, etc. Obtaining a good quality GPS location can be a problem in some cities and places, since the coverage of GPS location is not always optimal, because of GPS signal is not always optimal. The quality of the GPS signal obtained at each moment may depend on many factors, mobile device technical characteristics, environmental factors, etc. This paper presents an approach to improve the quality of the GPS location applied multi-agent architecture where people's smartphones running intelligent agents can cooperate among them locally. The agents using a Wi-Fi Direct 2p2 communication to share the locations, then each agent analyzes the location parameters to calculate the location with higher quality level.

Keywords Multi-agent system · Ubiquitous computing · GPS · Navigation service

1 Introduction

Smartphones are evolving very fast. The latest versions of these devices include very sophisticated hardware and modern operating systems such as Android, iOS, or Windows Phone that essentially turn phones into computers. They are changing

J. P. Espada (✉) · V. García-Díaz · R. G. Crespo · B. C. Pelayo G-Bustelo
J. M. Cueva Lovelle
Department of Computer Science, University of Oviedo, c/Calvo Sotelo, s/n, 33007,
Asturias Oviedo Spain
e-mail: pascualjordan@uniovi.es

even the daily lives of millions of people. For instance, Marshall [1] shows how smartphones are being used to help people in poor countries with banking, education, and business since personal computers are less widespread among citizens. In addition, lots of research works show different use cases in which the use of smartphones proves to be positive in society: changes in the practice of medicine [2], enhance independent behavior in individuals who had memory and organizational problems [3], automatic observation in research studies [4], improvements in the way people learn [5], etc.

Unlike other types of computers, smartphones are light and people usually carry them. Thus, one of its strengths is the possibility of creating context-aware software in a range of domains like tourist-related applications [5], pervasive learning environments [6], or product comparison shopping [7]. The GPS location is one of the parameters more commonly used in context-aware applications. The functionality of these applications often depends on that the location obtained has a good level of accuracy, but this is not always possible [8]. Obtaining an accurate GPS location may depend on many different factors, the geographical position in which we are, the technical quality of the device and its components, the current GPS network status, the criteria and parameters used to apply for the GPS location, even, it also may depend on atmospheric factors. Therefore, it is not always easy to get a good quality GPS location, the approximate error of GPS is between 0 and 10 m, and the times of obtaining the first location can vary over a very wide range from a few seconds to minutes.

There are many research works that presents approaches to improve the quality of the GPS locations. Some of these approaches are based on different techniques, such as: using auxiliary hardware [9], using algorithms for processing the signal and detecting variations. [10] requesting information to the people [11], combining the GPS locations with other techniques such as artificial vision [12] or optical encoders [13] using particle filters [14], or using algorithms to predict or estimate the locations. [15].

In this paper, we propose a solution based on a multi-agent architecture, where each Smartphone that runs an autonomous intelligent agent is able to communicate and coordinate with other agents geographically very close about 5 m or less. Through a process of communication and negotiation agents share their GPS locations and analyze the metadata of the location (the GPS status, the accuracy level, the location timestamp, the number of satellites used to obtain the location, etc.) in order to decide which is the most accurate location, then all agents use the location with higher quality and therefore most accurate rate.

The remainder of this paper is structured as follows: in Sect. 2, we present a brief overview of the relevant state of the art; in Sect. 3, we describe our proposal in Sect. 4, conclusions and the future work to be done.

2 Related Work

One of the main features of mobile devices is the availability of environment sensors and the data they provide. Thus, a new range of applications have emerged with the smartphones. The GPS is one of the most used because it gives a wide range of applications beyond simply locating and guiding vehicles. The GPS enables new location-based applications such as local search, mobile social networks, and navigation, in addition to other uses like predicting interests of people [16]. Other works such as for instance Burigat and Chittaro [15] use de GPS data to explore and synchronize 3D visualization of the environment with the physical world in tourist applications.

However, systems equipped with GPS do not work properly always. Thus, the GPS needs different nontrivial amount of battery power [17] and provides results of different quality depending on external factors such as the number of satellites, the signal strength, antenna limitations, and atmospheric conditions at a given moment. For those reasons, there are different proposals to avoid the use of GPS. Thiagarajan et al. [18] propose an energy-efficient system for trajectory mapping using tracks obtained largely from cellular base station fingerprints but the accuracy is lower than using the GPS. Others authors such as Nishihara et al. [19] focus on methods to determine the minimum set of resources needed to meet a given level of performance to save energy. Zhuang et al. [20] create a framework based on some principles such as substitution, suppression, piggybacking, and adaptation of applications to reduce the power consumption of GPS usage.

In addition, other works focus on the improvement of the accuracy of the results obtained by the GPS devices and new receivers. Thus, in Kjærgaard et al. [21] authors explain indoor GPS reception characteristics by analyzing results from a measurement covering eight different buildings. The results generally are more promising than the suggested in the literature but there are some considerations to have into account like the position, the roof and wall materials, the number of walls or the number of closer buildings that can affect the results and therefore the power waste or the quality of the data obtained. There are works in which the GPS sensor is combined with other type the information to improve the accuracy of results like a postprocessing step combined with available data, GIS information, or through the use of historical records [25].

Multi-agent systems are also very much present in mobile devices, with a great number of examples covering uses different from the proposed in this paper. For instance, Bajo et al. [22] show a multiplatform agent-based tool for modeling the behavior of companies and providing a support for decision making. Yang and Hwang [23] present a recommender system for a mobile environment, under the assumption that users who visit the same attractions in a theme park are more likely to share similar tastes. The system is based on peer-to-peer communications for exchanging ratings through the smartphones. Other works like Zhou et al. [24] also focus on intelligent recommendations for enhancing mobile Web access

derived from frequent user access patterns. For that, a tree of patterns is created based on the sequential pattern mining results and finally, a set of rules create the specific recommendations for users.

3 Proposal

We propose the creation of a multi-agent architecture, which allows users to get their current GPS location with a higher accuracy degree. The proposed architecture is based on a network composed by intelligent agents that work autonomously on Smartphones users; these agents get the GPS location using the Smartphone hardware and then the agent share the GPS location information with the intelligent agents near to their position (Fig. 1). All available and geographically very close intelligent agents establish a process of cooperation and negotiation in order to analyze which of the GPS locations have a higher quality level. The agents use a reasoning system that compares the location information (the GPS status, the accuracy level, the location timestamp, the number of satellites used to obtain the location, etc.). This system is used to discuss which of the GPS locations have a higher level of quality and selected locations are shared between nearby intelligent agents. The GPS location may be used later by the user for any type of task or application.

The system architecture is formed by a network of intelligent agents that are running on users Smartphones background. The intelligent agent system is implemented as an Android Service. These intelligent agents are hybrids; they are deliberative reactive and manage a heterogeneous set of perceptions in order to get the most accurately GPS location at all times.

Intelligent agents perceive different information from the environment.

- *GPS Location Information* The GPS location coordinates (longitude and latitude) and other significant parameters that can be used to evaluate and compare the quality of GPS locations. This parameter group includes, among others: the GPS status, the application criteria for selecting a location provider, the accuracy level (coarse, fine, high, low, medium), the power requirement (high, low, medium), the location timestamp, the number of satellites used to obtain the location, and a flag indicating whether the satellite has sent a current or cached location.
- *Intelligent agents close geographically* The presence of other intelligent agents in geographically close environments. Detected intelligent agents will become part of a “localized cooperative environment.” In coordination, the agents share the GPS locations obtained. Then the agents that compose the “localized cooperative environment” initiate a negotiation process with the aim of resolving which of the GPS locations have a higher quality level.
- *Other smartphone sensors* Optionally, the agents can obtain other measures from the physical environment, such as the compass orientation; these measurements can be used in some circumstances to apply algorithms that try to

Fig. 1 Conceptual scheme, three intelligent agents geographically close obtains the GPS location and share it with nearby agents using a Wi-Fi Direct connection



improve the quality of the location. The initial version of the architecture is not going to use this type of information for possible optimization of the GPS location obtained.

By themselves the agents have a limited perspective about the location. Individually an agent may have obtained a GPS location (or not obtaining it for some reason), the location is accompanied by a few parameters that can be used to get an idea of the localization quality, but really the agent does not know if another nearby agent was able to get a GPS location with higher quality level. The location quality can be determined by the technical characteristics of the mobile device when requesting the location, network overhead, etc.

In the proposed architecture intelligent agents perceive all the information about the location and details of the location using the smartphone GPS chip (Fig. 2) (1a). The location information is stored in a repository to be analyzed and compared later (Fig. 2) (2a, 3a). The agent simultaneously receives the GPS location information obtained by other nearby agents belonging to the same “localized cooperative environment” (Fig. 2) (1b). These agents provide a Wi-Fi Direct P2P connection to exchange messages. The messages exchanged between the agents have Knowledge Query and Manipulation Language KQML syntax. Each agent is responsible for analyzing the location information that it has obtained and perceived through other agents (Fig. 2) (2b). The agent analyzes and compares in real-time all the parameters which determine the quality of the different locations it manages, assigning a quality coefficient ranging from 0 to 1 at each of the locations (both their own locations as those obtained by other agents). To assign the coefficient the agent applies a set of rules to the values of location parameters: the GPS status, the application criteria for selecting a location provider, the power requirement, the number of satellites used to obtain the location, etc. The GPS locations that have been considered by the agent as high quality are sent to the negotiator module. (Fig. 2) (4a). The negotiator analyzes the quality coefficients assigned to different agents in the environment and uses Wi-Fi Direct to communicate the best-rated locations to other agents (Fig. 2) (5a, 6a). Filtering

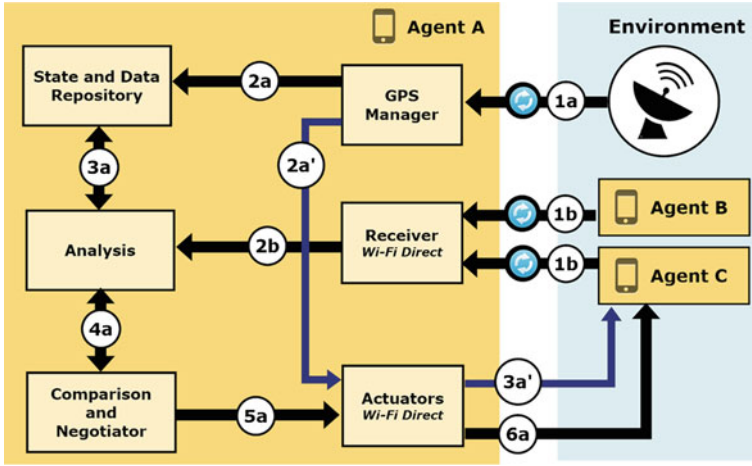


Fig. 2 Agent architecture. The figure shows the data flow

the pin of the Wi-Fi Direct communications using very low latencies we can ensure that the cooperating agents are actually very close geographically, the idea is that the agents cooperate with each other have to be less than five feet away. At any time the applications installed on the mobile device can request the current location, in each case the negotiator return the location with a higher quality factor.

The different types of messages that the intelligent agents uses to communicate will be defined using Knowledge Query and Manipulation Language KQML (Fig. 3). Messages are sent to:

- (1) Requesting participation of an agent in the “localized cooperative environment”.
- (2) Accept /Reject the participation of an agent in the “localized cooperative environment”.
- (3) Remove an agent of “localized cooperative environment”.
- (4) Submit an original location of an agent and the location Meta information that includes the configuration parameters used to obtain the location.
- (5) Send an analyzed GPS location which contains at least a quality coefficient. The locations may include several quality coefficient depending on how many agents have previously analyzed it. The quality coefficients assigned by different agents are an important factor for comparison and negotiation locations.

4 Conclusions and Future Work

In this research work, we propose an initial architecture of multi-agent system that aims to improve the quality of GPS location obtained by smartphones. With this approach a smartphone that this obtaining high quality locations may share them

```

1  (tell
2  □  :content {"agent":"agent-D0IC9BviRJS06bH",
3      "timestamp":"1374845548802",
4      "Latitude":"-5.845856",
5      "Longitude":"43.359135",
6      "Criteria-accuracy":"ACCURACY_FINE",
7      "Criteria-power":"POWER_MEDIUM",
8      "Satellites":"3",
9      "GpsStatus":"GPS_EVENT_STARTED",
10     "GpsSatellite-hasEphemeris":"false",
11     "GpsSatellite-usedInFix":"false",
12     "GPS_PROVIDER":"ACCESS_FINE_LOCATION",
13     □  "qualities": {
14         "value": "agent-6vts7ZIdXRCKwIV-0.67",
15         "value": "agent-D0IC9BviRJS06bH-0.83",
16         "value": "agent-hMSARKTnAVen2ET-0.41"}
17     }
18     :receiver agent-6vts7ZIdXRCKwIV
19     :languaje JSON
20     :ontology LOCATION-PARAMETERS)

```

Fig. 3 KQML message used to send a GPS location previously analyzed by several agents

with other devices. This approach aims to be a solution for those mobile devices that often get very low quality locations and also for those devices that technical reasons are slow to get the first location, even for devices that do not have GPS receiver.

The proposed approach can be very useful to save time, if an agent is about to request a GPS location but very close to other agent that has an optimal location, then it could use such information and save time and processing resources. This saves time and resources and it can also be significant for battery consumption, as this is a key aspect of modern smartphone. The GPS is one of the services that consumes more battery. The Wi-Fi Direct connection necessary to interconnect the agents also have a high battery consumption, but smaller than the GPS.

The GPS has an accuracy of about 10 m, the proposed approach provides the collaboration between geographically very close agents, who are less than 5 m. The Wi-Direct is effective detecting and communicating devices at rates up 50 m (although sometimes and depending on the technical characteristics of the device the distance can be much higher) order to narrow the distance between agents must apply strict filtering criteria in the scanning devices and the exchange of messages. The signal quality has to be very high and the response times have to be very low, to also ensure that the devices are really close, although these restrictions may prove to exclude even some devices if that they would be really within the appropriate distance range.

Currently, we have developed a first version of the proposal, following steps would improve the functionality of the same and undertake various studies on real

scenarios. These studies allow us to obtain qualitative measurements of quality improvement of the GPS location in different real scenarios, it will also be analyzed other important aspects such as the computational charge and the battery consumption [26].

References

1. Marshall J (2007) Smartphones are the PCs of developing world. *New Sci* 195:24–25
2. Burdette SD, Herchline TE, Oehler R (2008) Practicing medicine in a technological age: using smartphones in clinical practice. *Clin Infect Dis* 47:117–122
3. DePompei R, Gillette Y, Goetz E, Xenopoulos-Oddsson A, Bryen D, Dowds M (2008) Practical applications for use of PDAs and smartphones with children and adolescents who have traumatic brain injury. *NeuroRehabilitation* 23:487–499
4. Raento M, Oulasvirta A, Eagle N (2009) Smartphones: an emerging tool for social scientists. *Sociol Meth Res* 37:426–454
5. Setten M, Pokraev S, Koolwaaij J (2004) Context-aware recommendations in the mobile tourist application COMPASS. In: Bra PE, Nejd W (eds) *Adaptive hypermedia and adaptive web-based systems SE—27*. Springer, Berlin Heidelberg, pp 235–244
6. Syvanen A, Beale R, Sharples M, Ahonen M, Lonsdale P (2005) Supporting pervasive learning environments: adaptability and context awareness in mobile learning. *Proceedings of the 2005 IEEE International Workshop on Wireless and Mobile Technologies in Education (WMTE'05)*, pp 1–3
7. Mahmoud QH, Yu L (2006) Havana agents for comparison shopping and location-aware advertising in wireless mobile environments. *Electron Commer Res Appl* 5:220–228
8. He Y, Yu H, Fang H (2005) Study on improving GPS measurement Accuracy
9. Huang J-Y, Tsai C-H (2008) Improve GPS positioning accuracy with context awareness
10. Ya'acob N, Abdullah M, Ismail M (2007) Ionospheric modelling: improving the accuracy of differential GPS (dGPS) in equatorial regions
11. Bamis A, Savvides A (2011) Exploiting human state information to improve GPS sampling
12. Brilhault A, Kammoun S, Gutierrez O, Truillet P, Jouffrais C (2011) Fusion of artificial vision and GPS to Improve blind pedestrian positioning
13. Tian L, Zhou Y, Tang L (2000) Improving GPS positioning precision by using optical encoders
14. Wang E, Zhao W, Cai M (2013) Research on improving accuracy of GPS positioning based on particle filter
15. Zheng Z, Lu X, Chen Y (2008) Improved grey model and application in real-time GPS satellite clock bias prediction
16. Lane ND, Miluzzo E, Lu H, Peebles D, Choudhury T, Campbell AT (2010) A survey of mobile phone sensing
17. Analog Devices (2007) http://www.analog.com/static/imported-files/data_sheets/ADXL330.pdf
18. Thiagarajan A, Ravindranath L, Balakrishnan H, Madden S, Girod, L (2011) Accurate, low-energy trajectory mapping for mobile devices. In: *Proceedings of the 8th USENIX conference on networked systems design and implementation*, USENIX Association, Berkeley, CA, USA, p 20
19. Nishihara K, Ishizaka K, Sakai J (2010) Power saving in mobile devices using context-aware resource control
20. Zhuang Z, Kim K-H, Singh JP (2010) Improving energy efficiency of location sensing on smartphones. In: *Proceedings of the 8th international conference on mobile systems, applications, and services*, ACM, New York, USA, pp 315–330

21. Kjærgaard M, Blunck H, Godsk T, Toftkjær T, Christensen D, Grønbaek K (2010) Indoor positioning using GPS revisited. In: Floréen P, Krüger A, Spasojevic M (eds) *Pervasive computing SE—3*. Springer, Berlin Heidelberg, pp 38–56
22. Bajo J, Borrajo ML, De Paz JF, Corchado JM, Pellicer MA (2012) A multi-agent system for web-based risk management in small and medium business. *Expert Syst Appl* 39:6921–6931
23. Yang W-S, Hwang S-Y (2013) iTravel: a recommender system in mobile peer-to-peer environment. *J Syst Softw* 86:12–20
24. Zhou B, Hui SC, Chang K (2006) Enhancing mobile web access using intelligent recommendations. *IEEE Intell Syst* 21:28–34
25. Reddy S, Mun M, Burke J, Estrin D, Hansen M, Srivastava M (2010) Using mobile phones to determine transportation modes. *ACM Trans Sen Netw* 6(13):1–27
26. Oshin TO, Poslad S, Ma A (2012) Improving the energy-efficiency of GPS based location sensing smartphone applications. *Proceedings of the 2012 IEEE 11th International Conference on Trust, Security and Privacy in Computing and Communications (TrustCom)*, 1698–1705

Simulation and Implementation of a Neural Network in a Multiagent System

D. Oviedo, M. C. Romero-Ternerero, M. D. Hernández, A. Carrasco, F. Sivianes and J. I. Escudero

Abstract This paper presents the simulation and the implementation of a model of a neural network applied to a multiagent system by using the Neuroph framework. This tool enables several tests to be carried out and verify which structure is the best structure of our neural network for a specific application. In our case, we simulated the neural network for a sun-tracking control system in a solar farm. Initial implementation shows good results in performance, thereby providing an alternative to traditional solar-tracking systems.

Keywords Multiagent system · Neural network · Control systems · Position control · Solar-tracking · Solar energy · Renewable energy

1 Introduction

Multiagent technology has demonstrated its utility for the implementation of control systems, where it is necessary to control a distributed hardware platform [4, 9]. This requires agents to provide not only control capabilities, but also prediction and optimization capabilities.

The topic proposed in this paper refers to the simulations of a neural network model, whose design and implementation is described in detail in [6]. This model has been integrated in a multiagent system to support the prediction of the optimal movement patterns of solar panels for solar tracking.

Our neural network presents an adaptive two-dimensional auto-tracking control method suitable for a wide range of weather conditions. It utilizes real-time control

D. Oviedo · M. C. Romero-Ternerero (✉) · M. D. Hernández · A. Carrasco
F. Sivianes · J. I. Escudero
Departamento de Tecnología Electrónica, Universidad de Sevilla,
Avda. Reina Mercedes s/n, 41012, Seville Spain
e-mail: mcromerot@us.es

strategies and control parameter auto-optimization methods to realize flexible timing tracking and photoelectric tracking control.

This paper is organized as follows: [Sect. 2](#) presents the proposed neural network, while in [Sect. 3](#), the simulations, implementation, and integration of the neural network with the multiagent system are described. [Section 4](#) shows the tests performed and the results obtained. Finally, the concluding remarks are drawn in [Sect. 5](#).

2 Intelligence and Learning Model for Agents

The model developed is a neural network that can determine an appropriate movement pattern to maximize performance of a general control system at a particular time of day for a specific year, in the environment in which the solar panel is located. This network considers the previous position of the solar panel regarding previous instants, and therefore predicts the coordinates of the subsequent movement (which are close). Furthermore, training and output feedback is analyzed by comparing energy performance. The network adjusts to the movements or output patterns that are most suitable.

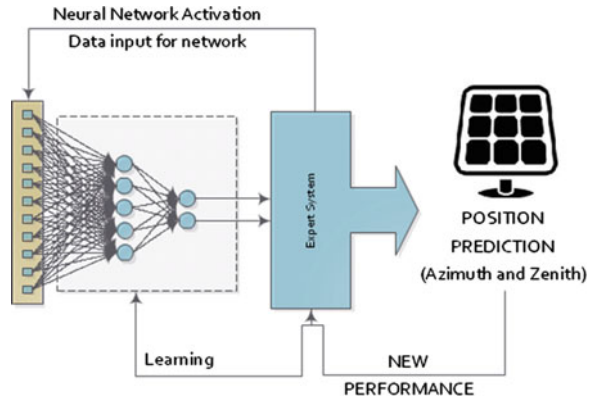
The neural network model described is integrated in the CARISMA system [5]. CARISMA presents a multiagent architecture to obtain an integrated system to supervise solar farm infrastructures. This system is able to monitor the environment by collecting data from distributed sensors. It provides both efficient maintenance and prevention of failures in solar farms in terms of acting over the environment or to initialize automatic recommendations to the telecontrol operators.

In order to provide the software agents with the ability to identify behavior patterns that optimize the performance of the solar panels controlled by the system, full integration into the system of our modeled neural network is required. To achieve this inference, the agents responsible for the overall control of the system implement a neural network that enables them to determine patterns of behavior that improve and optimize the overall system capacity to obtain solar energy. When the neural network finds patterns that improve behavior, the agent reports them to the expert system already implemented in CARISMA.

The expert system is then responsible for carrying out actions that introduce optimal states to the system and that serve as a learning element for the network through feedback.

Figure 1 shows the modeled neural network and how it interacts with the expert systems included in CARISMA.

Fig. 1 Architecture decision-making control to optimize energy efficiency



3 Simulations and Implementation Details

To integrate the neural network into the expert system, it is first necessary to validate the neural network model through simulations and then implement this model. The following sections describe the various stages and elements that are necessary to attain a correct final implementation of the system.

3.1 Simulation of Neural Network

The modeled networks should be validated using a set of simulations that helps to refine certain elements of the neural network. Therefore, simulation phases are performed prior to the final implementation of the network and its integration into the CARISMA system.

Regarding the type of neural network, we decided to use a fully connected multilayer back-propagation network often called a multilayer perceptron (MLP) [3], which allows time series predictions to be obtained. Feed-forward networks can be applied directly to problems of this form if the data provided are suitably pre-processed.

In the normalization of the input data to train the network, theoretical minimum and maximum data are used depending on the area where the tests are executed (Seville, Spain, in our case). For example, the temperature parameter remains within it has been found that under normal conditions, a range from 0 to 45 °C. For those cases where one of the input parameters lies outside the specified target range, the system does not use the neural network to calculate the new coordinates. In this case, the expert system is directly responsible for the decision.

Figure 2 shows the topology for the first network trained. This is a fully connected multilayer network with one input vector of 13 parameters and one output vector with 2 parameters corresponding to the subsequent azimuth and zenith coordinates for the solar panels. The input and output vectors are interconnected by a hidden layer which is composed of three artificial neurons.

The number of neurons in the hidden layer can be increased in accordance with the needs of network adjustment. The input values considered in the network are:

- Azimuth and Zenith solar-panel coordinates
- Solar time UTC
- Azimuth and Zenith sun coordinates
- Date
- Solar radiation (Kw/m^2)
- Temperature
- Humidity
- Wind speed
- Atmospheric Pressure
- Weather conditions (sunny, cloudy, rainy, etc.)
- Energy performance (kWh).

The simulation process is performed in order to determine various parameters of the network (maximum error, learning rate, momentum, impulse, etc.), to train the network through a training pattern preset based on theoretical maximum energy efficiency and to check its behavior in a variety of tests. The number of iterations required to train the network and to minimize the error are analyzed from the results of these simulations. The first results for our network, shown in Fig. 2, were inadequate, since the error was insufficiently low to consider the structure of this network as valid.

The number of hidden-layer neurons was therefore increased by following approximation rules [2]. First we tested the network with five neurons in the hidden layer and then with eight hidden neurons. Tests concluded that the latter type of network gives the best results for this problem, as shown in Fig. 3.

This network of eight neurons (and an additional “bias” neuron) in the hidden layer achieves better results in the tests performed, and shows minimal errors in most cases and a faster learning rate, as shown in Figs. 4 and 5. This neural network has been set with a maximum error of 0.01, a learning rate of 0.2, and a momentum of 0.5.

This network is selected and implemented in the CARISMA system, and other conditions of learning and operating over the time are included, as discussed in the following section.

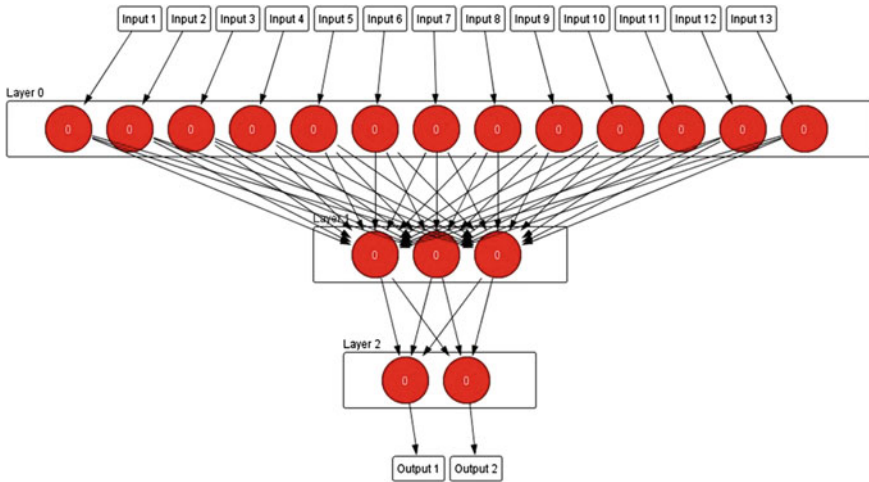


Fig. 2 First neural network simulation

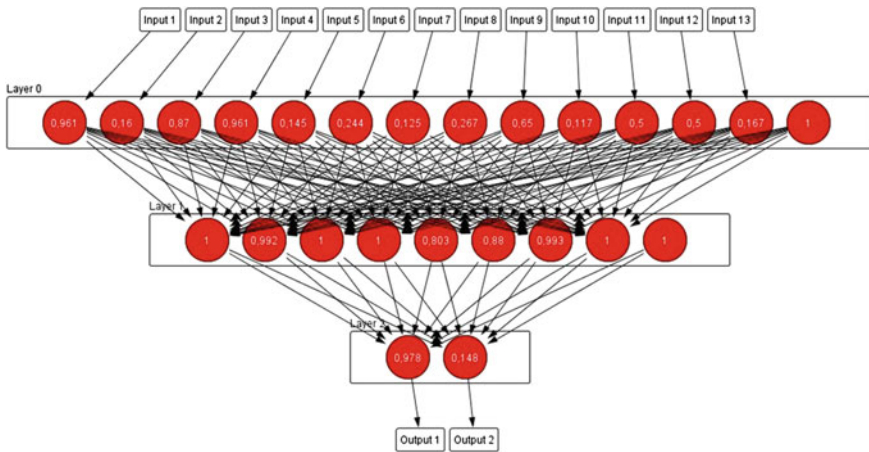


Fig. 3 Final topology of the neural network selected through simulation

3.2 Simulation of Neural Network

For the implementation of our neural network, the Neuroph framework [8] is used since it is the most suitable framework for integration into the CARISMA system. Neuroph offers a complete solution for creation, simulation, and implementation of neural networks in Java language. It provides a Java class library for integration into applications and a GUI tool “easyNeurons” for the creation and training of neural networks. Additionally, Neuroph is suitable for time-series prediction [7]. From the point of view of implementation, the expert system is responsible for

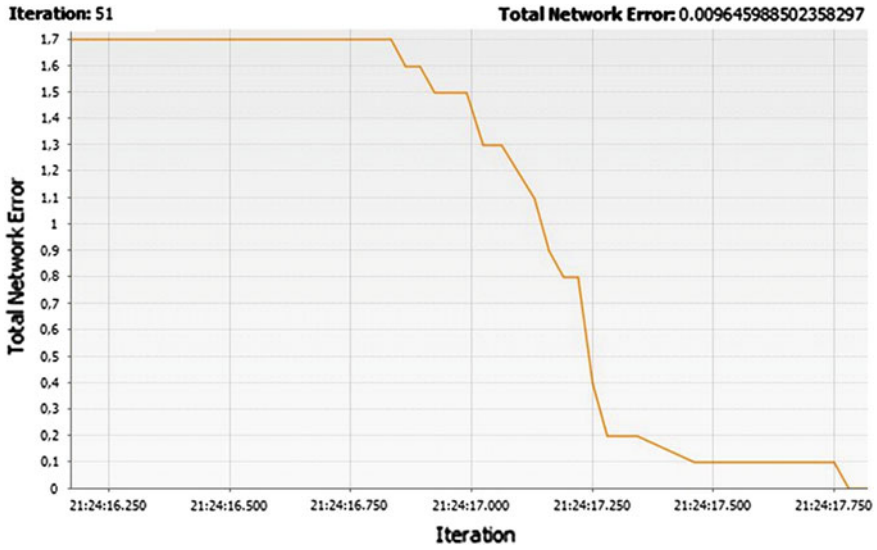


Fig. 4 Graphical comparison of the number of learning iterations and the total error on the neural network with eight neurons in the hidden layer (Minimum Test Time)

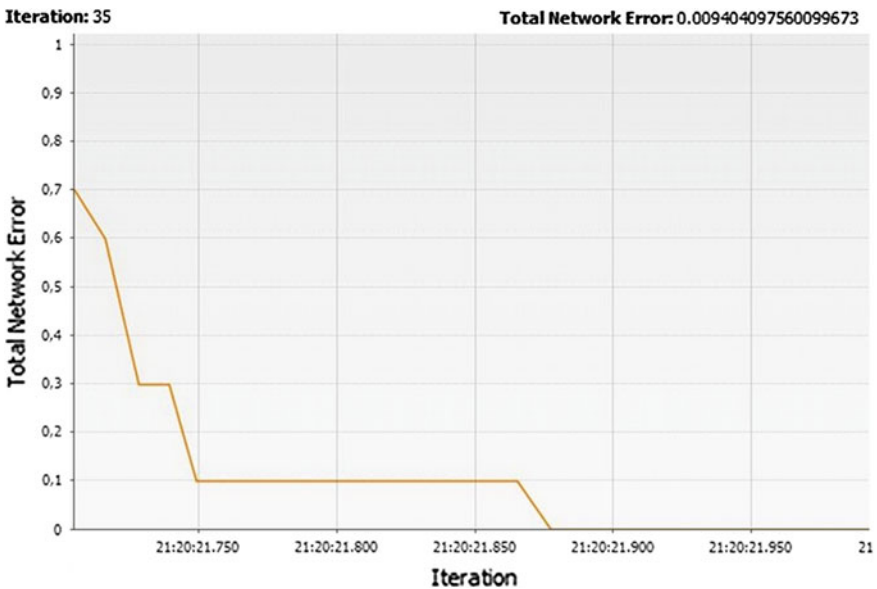


Fig. 5 Graphical comparison of the number of learning iterations and the total error on the neural network with eight neurons in the hidden layer (Maximum Test Time)

determining when the system makes use of a neural network in order to attain the subsequent movement for a given solar panel. Therefore, the expert system provides solar-panel environment data as the current position. Additionally, the expert system will be responsible for neural network learning, by comparing energy efficiency obtained from a particular movement. When output power from the system is less due to an executed movement, then the expert system reports the difference obtained to the neural network to adjust the weights. If output power is increased, then the expert system does not request new predictions from the neural network, and it sets suitable weights for future requests.

From the point of view of code, the creation of the network is encapsulated in the procedure “initializeNN()”. For network initialization, we have made use of a temporary directory, where at least the initial training file for the network must be defined. This training file is a plain text file with fields separated by a semicolon (;). It contains the input values of the network and the best theoretical output result to obtain the maximum energy solar performance. This file can be edited with new data obtained from the network. Its use is obviated if the training option is adopted, since the network is trained with each output movement, thereby resulting in increasing performance from previously obtained movements under the same conditions. The data supplied to the neural network must be normalized with values ranging from 0 to 1, as indicated above. This aspect is dynamically controlled.

In order to make the network available during the operation of CARISMA once the network is trained, the neural network is stored in the file “myMLPerceptron.nnet”, where it is encapsulated in a binary level. This network can be loaded and launched into the system from any agent. The procedure “execNN()” is called when the rules are triggered if the performance of the solar panels is inadequate. This procedure implements the following functionality:

- Launching the neural network for the current data.
- Comparing performance with the theoretical output, with a normal solar-tracking system, with fixed plates and a log of maximum energy efficiency for the same conditions.
- Training the network when a good result on the energy performance is obtained.
- Ensuring that the calculations do not run for nonlogical input values (for example, at night).
- Collecting times and system performance data.
- Storing returns and positions of the solar panels in a log file.

Finally, it has to be remembered that the network must be able to interact with the expert system integrated into the agent. Therefore, we implemented rules that are executed when the current energy efficiency (given by the current position of the solar panels) is less than the expected theoretical performance, which is reported by an alarm. In this case, the expert system updates the neural network using a process called “communicateNN()”.

4 Testing and Experimental Results

We used the PeMMAS system [1] for testing, and internal variables and scripts of the system for measurement control. With this tool, data on the use of system resources, flight times of global messages by type of agent, and processing times in behaviors can be obtained. It may also be used for other external measures of system agents. The information obtained by PeMMAS agents can be processed to generate various reports to provide the analysis of the multiagent system.

The set of tests are focused on analyzing the energy efficiency obtained in one day, based on a history of performance measures obtained on various days of the year. These measures have three variants: fixed-position solar panels, solar panels with classic solar tracking (based on the theoretical solar position), and maximum energy efficiency obtained at various times of the day. The neural network is trained with the data obtained for panels with a traditional solar-tracking system. From this training, the neural network is available in the CARISMA system and runs on each of the agents responsible for controlling a solar panel.

After various tests were performed, we obtained an average of the most significant measures for the set of all agents. From the results obtained, as shown in Table 1, we conclude that the integration of a Neural Network has enabled a slight increase in the production of energy by the system. This increase has been at an average of approximately 3 %, compared to that obtained with a traditional solar-tracking system. The subsequent movements predicted by the neural network are the same as those expected in over 10 % and close to those expected in more than 25 %. However, a large number of unsuitable movements are also obtained (approximately 15 %).

These results are derived from historical data training. If no such data were available, the neural network response would initially be significantly worse and it would take several cycles of testing under the same conditions to obtain responses with an increased energy efficiency. Similarly, when the network is trained in real time, then it provides better results since the weights of the neurons adapt more appropriately.

Regarding the battery of tests designed to test the impact of using neural networks on the consumption in terms of processor and disk in the system, the results are satisfactory but considerable quantities of memory are employed, in particular if the network is used simultaneously with other types of inference systems. As shown in Table 1, the execution of the neural network has no impact on the system, and CPU consumption is less than 0.5 % as a result of the limited and controlled use by the expert system. However, the neural network is higher in terms of RAM consumption, and reaches an average consumption of 3 mb.

Additionally, we have also analyzed the response times of expert systems integrated with a neural network in the agents of our system. As shown in Table 2, the response times (for inferences) in milliseconds obtained for each type of agent did not differ from those obtained for the operation of expert systems alone. These

Table 1 Average results obtained by the neural network in predicting movements of a solar panel for performance optimization

| <i>Global measures on the system</i> | | |
|--------------------------------------|---------|---|
| LIM_NUMBER_AGENTS | 27 | Number of agents in the system |
| LIM_CAPACITY_PROC | 16.78 % | % Average of CPU used |
| LIM_CAPACITY_STORAGE | 54.56 % | % Average of memory used in the system |
| <i>Neural network measures</i> | | |
| RN_TRAINING | 916.6 | ms |
| RN_RESPONSE SE | 1374.72 | ms |
| RN_CPU | 0.272 % | % Average of CPU used in the system |
| RN_MEM | 3079.4 | Amount (in KB) of memory used in the system |
| RN_QUALITY TRUE | 10.60 % | Expected resolution rate |
| RN_QUALITY FALSE | 15.3 % | Wrong resolution rate |
| RN_QUALITY_RESOLUTION | 5 % | Unexpected resolution rate |
| RN_ENERGY_EFFICIENCY_GLOBAL | 2.72 % | Global energy efficiency rate obtained |

Table 2 Average response times for the integrated expert system in a CARISMA agent when used in conjunction with a neural network

| Time for inferences in neural network | | |
|---------------------------------------|---------|----|
| TIME_INFERENCE_AT | 990.7 | ms |
| TIME_INFERENCE_AC | 940.7 | ms |
| TIME_INFERENCE_AO | 1070.02 | ms |
| TIME_INFERENCE_ADS | 683.5 | ms |

measures provided an average of one second per inference. Therefore, it can be concluded that the use of the neural network does not affect the use of other systems.

5 Conclusions

We have developed a complete multiagent system responsible for the supervision of an automated set of solar farms. The agents of this system have been equipped with artificial intelligence through the combination of expert systems and neural networks. Once the system has been verified through tests and simulations, the responses obtained from this system are suitable, and require very little human intervention.

The integration of the inference engine based on a neural network in an agent allows the system to optimize the energy efficiency obtained by adjusting the position of the solar panels to the variables of the particular environment and the position of the sun. This type of system enables the decision-making agents to adapt to their environment.

Future lines of work include the optimization of the neural network to improve the approaches on the movements of the solar panels, considering other environmental parameters. Therefore, one possible improvement would come from the implementation of a fully connected recurrent neural network, which, according to theoretical studies, would provide the best results.

Acknowledgements The work described in this paper has been funded by the Consejería de Innovación, Ciencia y Empresas (Junta de Andalucía) with reference number P08—TIC-03862 (CARISMA Project).

References

1. Carrasco A, Hernández MD, Sivianes F, Romero-Ternero MC, Oviedo D, Escudero JI (2014) PeMMAS: a tool that studying the performance of multi-agent systems developed in JADE, *IEEE Transactions on Human-Machine Systems* 44(2):180–189
2. Flórez RF, Fernández JMF (2008) *Las Redes Neuronales Artificiales: fundamentos teóricos y aplicaciones prácticas*. Netbiblo, Oleiros
3. Hertz J, Krogh A, Palmer RG (1991) *Introduction to the theory of neural computation*. Santa Fe Institute studies in the sciences of complexity: Lecture notes. Addison-Wesley, Massachusetts
4. Jennings NR, Bussmann S (2003) Agent-based control systems. *IEEE Control Syst Mag* 23:61–74
5. Oviedo D, Romero-Ternero MC, Hernández MD, Carrasco A, Sivianes F, Escudero JI (2010) Architecture for multiagent-based control systems, vol 79. Springer, Berlin, pp 97–104
6. Oviedo D, Romero-Ternero MC, Carrasco A, Sivianes F, Hernandez MD, Escudero JI (2013) Multiagent system powered by neural network for positioning control of solar panels: an optimization for sun tracking systems. In: 39th annual conference of the IEEE industrial electronics society (IECON 2013), Vienna, 10–13 Nov 2013
7. Paluch M, Jackowska-Strumillo J (2013) Prediction of closing prices on the stock exchange with the use of artificial neural networks. *Image Process Commun* 17(4):275–282
8. Sevarac Z, Goloskokovic I, Tait J, Carter-Greaves L, Morgan A (2013) *Neuroph*. <http://neuroph.sourceforge.net>
9. Wang Z, Yang R, Wang L (2010) Multiagent control system with intelligent optimization for smart and energy-efficient buildings. In: *IECON 2010—36th annual conference on IEEE industrial electronics society*, pp 1144, 1149, 7–10 Nov 2010

Soft Computing Applied to the Supply Chain Management: A Method for Daily Sales Classification and Forecasting

Fernando Turrado García, Luis Javier García Villalba
and Victoria López

Abstract The supply chain management is a vast field of study where intelligent techniques can be applied to obtain better results than other approaches. Resource planning, route optimizations, stock and ordering strategies amongst others are common problems in this field of study. In this paper we will focus on how to solve the problems related to making accurate daily sales forecasting in the retail sector. Solutions to this problem must deal with two inherent complexities: the huge amount of data involved in it and the selection of accurate forecasting models. Due to the first complexity, one of the main features of the solution has to be the independence of the system from user interaction.

Keywords Support vector machines · ARIMA · Time series analysis · Forecasting · Supply chain management

F. T. García · L. J. G. Villalba (✉)

Group of Analysis, Security and Systems (GASS), Department of Software Engineering and Artificial Intelligence (DISIA), School of Computer Science, Office 431, Universidad Complutense de Madrid (UCM), Calle Profesor José García Santesmases s/n, Ciudad Universitaria, 28040 Madrid Spain
e-mail: javiergv@fdi.ucm.es

F. T. García
e-mail: fturrado@fdi.ucm.es

V. López
Department of Computer Architecture, School of Computer Science, Universidad Complutense de Madrid (UCM), Calle Profesor José García Santesmases s/n, Ciudad Universitaria, 28040 Madrid Spain
e-mail: vlopez@fdi.ucm.es

1 Introduction

Analyzing customer behavior is a common practice in the retail sector. Modern companies are used to invest large amounts of resources in order to achieve higher levels of comprehension (or knowledge) about their customers and their purchasing habits. One of the main goals of these investments is to obtain the forecasts about future customer behavior or reactions to some events. For example, these forecasts allow those companies to make better advertising campaigns, marketing strategies. From another point of view, closer to the logistic processes present at those companies, the accurate sale forecasts allow an optimized strategy for stock handling and provisioning.

Let us introduce the problem to be studied using a simple case: consider a store that only sales one product or SKU (Stock Keeping Unit). This SKU is obtained from one provider that only allows and order on Mondays. Every Monday, the store manager has to place an order to the provider; but how many units are needed? Using a basic calculation, the total amount of the order is the difference between the sales forecasted for the entire week and the actual stock at the store.

In this approach, we have a time series formed by the daily sales of the SKU (Stock Keeping Unit) at that store. One expert can analyze the historical data and try to predict future sales using complex statistical models or use artificial intelligence techniques such as neural networks or support vector machines to achieve this goal.

But, how far is this case from a real world problem? In a real case, there are a lot of additional variables involved in the logistic process of merchandise replenishment. Some of them are transport delay time, stock limits (at the store or at the provider), pricing options that have special discounts on large orders, and so on and so forth.

However, the essence of the problem remains the same: the manager needs to know how much amount of merchandise has to place in an order to the provider for each SKU sold at his store. Now, instead of a small store consider the case of a hypermarket with more than 10,000 SKUs available to the customers. In this situation, the expert will have to analyze more than 10.000 time series (one for each SKU). But another level of generalization can be applied: this hypermarket belongs to large retailer that owns hundred of stores. At this level, the amount of time series to study is obtained by the multiplying the number of stores with the number of SKU per store. In large retailers this number is measured in millions.

So the problem is to build software solution capable of making accurate forecasts for all those time series. This paper will present a solution that combines advanced statistical models (ARIMA models, used for forecasting) with artificial intelligence techniques (Support Vector Machines, used for classification).

2 Overview of the Solution

The problem described above can be viewed as a combination of two different subproblems: a classification one and a model identification one.

The first subproblem is produced by the huge amount of data that has to be processed. To the large collection of time series there is another factor that increases the magnitude of the data involved: in order to detect annual behavior in those series two or more years of historical data has to be used for each one. So a minimum of 730 (2×365 days) values are stored; in a retailer that has 2 millions time series the amount of data involved raises to 1,460,000,000 values. This amount of data makes the manual treatment or analysis of that data set infeasible. The classification subproblem is to provide a fast and accurate classification method to reduce the data into the smaller one. The clusters have to be built with the following feature: all the time series that belong to it can be predicted using the same forecasting model.

The second subproblem is to identify or fit one forecasting model for each cluster defined in the solution of the prior problem. In this case, the complexity is produced by the diversity present in the nature of the time series; there are SKU's that have a rare sale pattern (as is in the case of high end electronic products); in the opposite side there are SKU's with a regular sale pattern (as is the case of diapers). In those time series, there are several effects like seasonality (for example, ice-creams), trends (women shoes are an example), cycles, promotions ... that make the model identification a hard task.

3 Time Series Classification

In our context, trying to solve the main problem not only the classification one, we will apply the following classification criterion: Two time series are similar if they can be forecasted (in an accurate way) using the same forecasting model.

But how different are the time series obtained from a given model? Let's study some time series generated using this formula over four different seeds:

$$X(t) = X(t - 4) \tag{1}$$

- Seed 1: 0,0,1,0. The time series obtained is 0,0,1,0,0,0,1,0,0,0,1,0,0,0,1,0, ...
- Seed 2: 0,0,9,0. The time series obtained is 0,0,9,0,0,0,9,0,0,0,9,0,0,0,9,0, ...
- Seed 3: 1,2,3,4. The time series obtained is 1,2,3,4,1,2,3,4,1,2,3,4,1,2,3,4, ...
- Seed 4: 1,0,0,0. The time series obtained is 1,0,0,0,1,0,0,0,1,0,0,0,1,0,0,0, ...

The above sample values show that direct value comparison is not enough to detect or identify the formula that produces them. Box & Jenkins [3], in their work in which ARIMA models are defined, used the values of two statistical functions to obtain the parameters of their model. Those functions were the autocorrelation (ACF) and the partial autocorrelation function (PACF).

The 16 first results of those functions applied to the above time series are:

- For the seeds 1,2 & 4:
 - ACF: 1, -0.3313514, -0.3113514, -0.3183784, 0.9219958, -0.3054054, -0.2854054, -0.2924324, 0.8439917, -0.2794595, -0.2594595, -0.2664865, 0.7659875, -0.2535135, -0.2335135, -0.2405405, and 0.6879834
 - PACF: -0.3313514, -0.4730871, -0.9075817, 0.3607015, -0.07368365, -0.01276824, 0.03457378, -0.0347388, -0.006880984, 0.001832035, 0.01738262, -0.03387359, -0.009749208, -0.001021495, 0.01596253, and -0.03782824
- For the seed 3:
 - ACF: 1, -0.1802563, -0.5755079, -0.2043384, 0.9197949, -0.1643384, -0.5275489, -0.1884204, 0.8395899, -0.1484204, -0.4795899, -0.1725024, 0.7593848, -0.1325024, -0.4316309, -0.1565844, and 0.6791798
 - PACF: -0.1802563, -0.6284190, -0.8310922, 0.5590696, -0.28098290, 0.06000333, 0.05766263, -0.0996166, 0.0429121, -0.001273668, -0.008467919, -0.03282086, 0.003629319, 0.001774411, -0.00339935, and -0.04603122

To do the calculations needed and obtain those values the open source statistical software R [2] was used.

It is clear that using the autocorrelation (Fig. 1) and partial autocorrelation (Fig. 2) values for time series classification is an interesting approach. An example of its use can be found at [1] where the authors applied this classification criterion (using support vector machines) to more than 14.000 time series. They obtained 12 clusters that represent more than 97 % of the original time series.

4 Forecasting Models Identification

Once the classification task is made, we need to find a forecasting model for each cluster. There are a lot of alternatives to study, from statistical models as the ARIMA ones or the exponential smoothing Holt-Winters to soft methods like neural networks or fuzzy systems (examples of these uses can be found at [6] or [7]).

There are several reasons to choose ARIMA models as the first choice: they are well known, proven statistical estimators that have been applied successfully before (as in [8]). Also they have support for trends, cycles, and seasonality in time series. And the last one, the ACF & PACF function had been calculated before so we can reuse computing effort that has been done previously.

But the ARIMA models have their own trade-offs. First of all, the time series must be stationary and there is no algorithmic way to check this requirement. Second issue, there is not a complete database containing the relations between the ARIMA models and the results of the ACF/PACF functions. Using R (with a simple script) someone can try to build that database but the autoregressive model

Fig. 1 ACF values

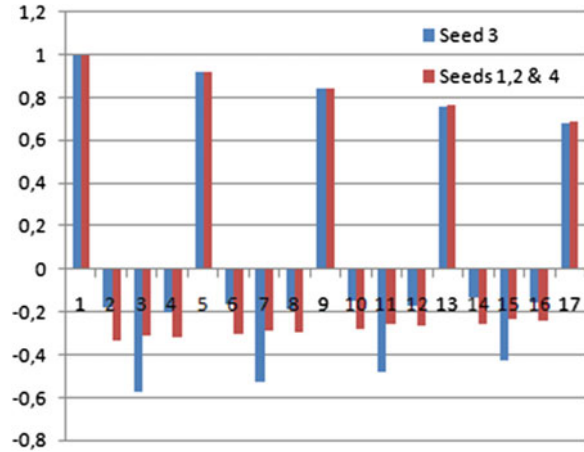
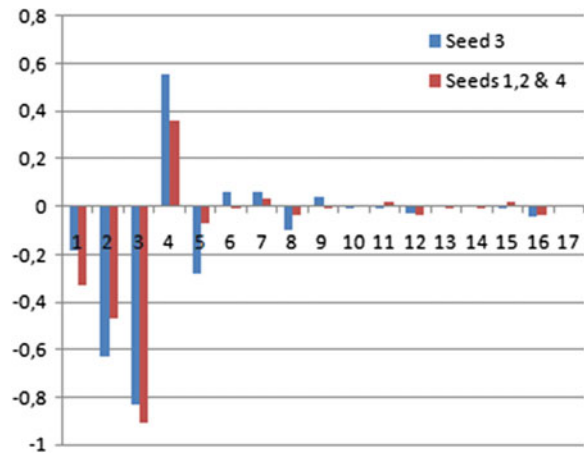


Fig. 2 PACF values



must be stationary. This is achieved by choosing these coefficients (autoregressive model in ARIMA) in a particular way. Some studies like [4] or [5] have been done regarding this matter; their conclusions try to get a work around to this issue but do not solve it as they do not provide a constructive method to obtain the parameters needed.

The last one and perhaps the most important is that not every time series can be forecasted with an ARIMA model. Only those that have significant ACF & PACF values can be estimated with one of these models. So, in order to give a complete solution, at least another model has to be applied to these time series. In [1] the 43.75 % of the time series fall in this category.

In a basic approach these time series can be forecasted with a simple statistical formula as the mean (over a period) or the last known value non zero.

5 Conclusions and Future Work

To classify time series using its ACF & PACF values allow their aggregation into clusters that share a common ARIMA model. As shown in [1], more than 14,000 time series were grouped into a small set of clusters (97 % in 12 categories).

However, additional work has to be done in automating the discovery of the forecasting models. The following aspects describe some potential enhancements that can be incorporated to the system:

- Build a database where ACF & PACF values of a time series can be related to forecasting models.
- Provide an efficient estimator to those cases where the ARIMA models do not apply.
- Evaluate other alternative forecasting models that can be trained or parameterized in an autonomous way.

References

1. F. Turrado García, L. J. García Villalba, J. Portela (2012). Intelligent system for time series classification using support vector machines applied to supply-chain. *Expert Systems with Applications*, 39(12), 10590–10599
2. R Development Core Team. R (2008). A language and environment for statistical computing. R Foundation for Statistical Computing, Vienna, Austria. url: <http://www.r-project.org>
3. Box G, Jenkins G (1970) Time series analysis: Forecasting and control. Holden-Day, San Francisco
4. Phillips PC, Perron P (1987) Testing for a unit root in time series regression. *Biometrika* 75(2):335–346
5. Said SE, Dickey DA (1984) Testing for unit roots in autoregressive-moving average models of unknown order. *Biometrika* 71(3):599–607
6. Zhang D-Y, Song H-W, Chen P (2008) Stock market forecasting model based on a hybrid ARMA and support vector machines. In: *Proceedings of the 15th international conference on management science and engineering*, pp 1312–1317
7. Kim K-J (2003) Financial time series forecasting using support vector machines. *Neurocomputing* 55(1–2):307–319
8. Shukla M, Jharkharia S (2011) ARIMA models to forecast demand in fresh supply chains. *International Journal of Operational Research* 11(1):1–18

The Self-Organizing City: An Agent-Based Approach to the Algorithmic Simulation of City-Growth Processes

Adolfo Nadal and Juan Pavón

Abstract This paper discusses the suitability of algorithmic-based modeling processes in the development of ad-hoc software for urban planning and urban design. Firstly, it involves the identification and discussion of former city computational models. Secondly, it shows the development of an application that deals with complex urban systems from an urban design point of view, by using an agent-based modeling approach.

Keywords Agent-based modeling · City growth simulation · Urban design · Self-organization · Complexity · Emergent behavior

1 Introduction

Computational techniques in the design of cities are being used more and more, fact that has also characterized the development of city and territorial planning through algorithms. From the development of Discourse in the sixties, the first computer language specifically designed for regional planning, a vast proliferation of computational models applied to urban building simulation have appeared, based on cellular automata, GIS informed models, and agent-based systems, among other techniques [1]. Nevertheless, there are almost no significant contributions from the point of view of the analysis and design of the city. Most of the software developed in this field belongs either to visual disciplines absorbed mainly by the videogame industry [2] or to non-informational 3D virtual model building [3]. Other approaches to informational city models, which work with user-accessible data bases, have a strong social imprint that partially neglects the

A. Nadal · J. Pavón (✉)

Facultad de Informática UCM, Ciudad Universitaria, s/n, 28040 Madrid Spain
e-mail: jpavon@fdi.ucm.es

morphological aspects of the study. For instance, Juval Portugali's examples [4] that study the social segregation in the Gaza Strip through mathematical models represented by Cellular Automata. Generally, computational simulations of urban models lack informational content specifically related to inherent characteristics of the city, such as the relationships between building density and functional complexity, their influence on racial or social distributions, the need for certain types of infrastructure and their quantification, or even an exhaustive study of the morphological body of the city itself, understood as a response to its internal, external, or environmental logics.

Cities cannot be described only as a series of volumes whose most representative rationale is their own spatial distribution and organization (cities have been largely described and studied as a “game of volumes under light”), but as a “game of volumes under information” [5]. This paradigm shift offers the possibility to study another model of cities and territories, one that is both informed and informative. Thus, designers will be able to simulate city growth and grasp the model's information through data visualization interfaces.

This work develops the concept of “self-organizing city”, an investigation on nonlinear phenomena in urban environments, with the aim of exploring and redefining the informative logics underlying the urban environment through a careful study of its multiple agencies. Agent-based modeling has been used as the appropriate tool to encapsulate the wide range of variables and issues involved in the complex urban systems: the relationship between private and public space, program and density, and infrastructures (telecommunication, transportation, waste management, and other information flows).

The paper follows by describing the issues that make the conception of the city as a complex adaptive system. Section 3 through 5 show an agent-based model for simulation of scenarios that display urban dynamics responding to user-controlled conditions and a series of internal logics that seek to optimize the urban configuration from functional, social, economic, and environmental points of view.

2 Interrelational Systems in Urban Spaces: The City as a Complex System

Complex theory states the existence of spontaneous anisotropic, nonhomogeneous states and the formation of complex structures that exhibit a wide range of feedback-based, dynamic relationships. Although initially applied to unstable chemical systems of reactions, those were an energetic input is required for some conditions to be maintained; this notion of “*far-from-equilibrium*” applies to situations where matter behaves in a different manner than in stable, “*close-to-equilibrium*” zones, where behaviors are highly predictable and linear (i.e., a certain consequence can be easily read in terms of some precisely definable causes). In “*far-from-equilibrium*” conditions, the sum of causes does not reflect back into a concrete, specific, predictable situation, but rather into another possible, yet unpredictable options.

This example shows that the relationship between the microscopic (agent) and the macroscopic (systemic) levels is no longer obvious and fluctuates depending on the varying relationships at both levels, producing bifurcation events and displaying a certain degree of self-organization as a result of its own internal properties. Cities can be described as well as a collection of strategies and structures interacting through a complex, dynamic network, which does not statically rely on the aggregation of the individual entities that constitute the network. These networks and their nodes are adaptive; in that the individual and collective behavior migrates and mutates to self-organize and respond to the change-initiating micro-event or collection of events [6]. The city, as much as it is an organization, can be treated as a complex adaptive system [7], exhibiting fundamental principles like *self-organization, complexity, emergence, coevolution, chaos, and self-similarity*.

Complex adaptive systems differ from organized or chaotic systems. Organized systems are characterized by rules, which control their agents' behavior. Chaotic systems, on the contrary, are fully unconstrained and suitable to statistical analysis, rather than design. In a complex adaptive system, the agents and the system coevolve while constraining each other by defining their action space and modes of behavior. The ability to simulate self-adaptive systems is central to the self-organization of the city.

The impact of this concept on the traditional model of the city has several consequences. Cities are not only exposed to their own structural logic, but to external limitations and influences, which vary their internal logics. The study of the urban structures requires a careful description of the multiple "infrastructures" [8] thereby implied and a critical analysis of their influence on the city as an open system.

Computer-generated models applied to complexity theory expand the scope of "infrastructure", a term that traditionally referred to transport, economic exchange, soil type, health care, and many other agents. The Central Place theory, for instance, characterizes cities as radial aggregations, in which density and distribution are a linear function of the distance to the center, independently from any other environmental conditions throughout time. Accordingly, the city becomes isotropic and homogeneous.

Classic models produce excessively diagrammatic cities whose relationships are closed, linear, and static. This limitation stems from their inability to deal with large information flows, becoming linear, closed, and static

3 Abstract Models of Urban Dynamics

In order to evaluate the appropriateness of agent-based systems for the modeling of behavioral simulations of urban dynamics, the project starts with an exploration of apparently disorganized systems, which stem from successive evolutive states of a certain algorithm. The algorithm evaluates the "fitness" or "suitability" of the system through a series of user-defined variables, adapting both these variables and

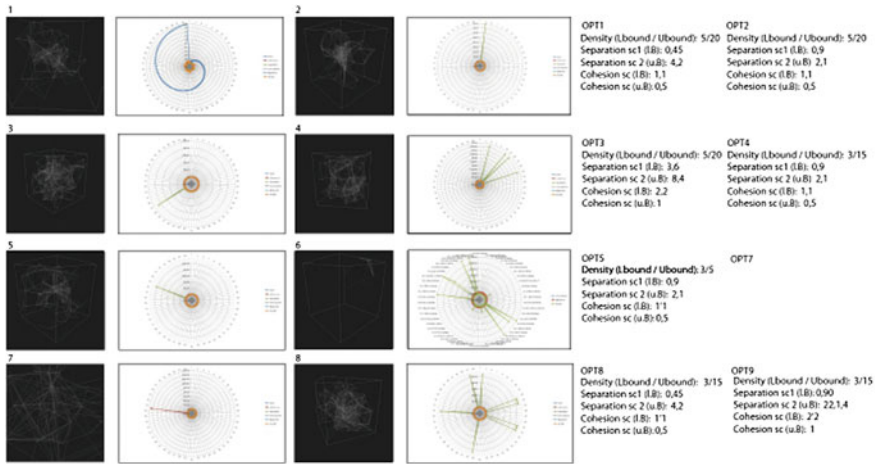


Fig. 1 Iterations of an algorithmic model that simulates a flock

its boundary conditions on a frame basis, which allows for the emergence of the temporal dimension. Global and local data are read, reinterpreted, and visualized separately. The initial static rule set that defines the algorithm resembles the generation of new knowledge through direct feedback. The behaviors of the agents involved in the system are tested through these feedback-based interactions by comparing them to themselves in different points in time, in an attempt to find an underlying logic that might prevail in the temporal evolution of the model.

Figure 1 shows several iterative options of a typical multi-agent algorithm used to simultaneously monitor self-adaptability. Although the algorithm is exactly the same, each iteration responds to a differentiated set of values or parameters: cohesion, separation, and alignment. These systems resemble urban environments and their behavior in several ways:

1. They develop in time, a particularly relevant dimension in the evolution of urban fabrics.
2. They implement systemic imperfections, noise, and uncertainty.
3. They adopt varying dynamics-evolution.
4. They are site-specific, displaying adaptation to shifting boundary conditions.

According to Christopher Alexander’s depiction of urban dynamics in [9], planning must first learn how “bottom-up” structures emerged in previous times in order to gain knowledge of complex urban dynamics. Simple structures give birth to higher-order structures via accumulation, combination, mutation, or metamorphosis through non-site-specific principles. Alexander offers a working methodology that can be applied to the study of today’s cities.

According to Alexander, the subsystems of cities already existed in the pre-modern era, and have increasingly evolved in complexity to their current structure, which, as homogeneous, monolithic, and continuous as it is, integrates and

articulates these logics. Algorithmic systems invoke a logic that is regulated at a systemic level, where internal coherence represents population density, traffic, and mobility, and validates the understanding of urban environment as dynamic systems.

The theory of Alexander is based on patterns. Patterns are independent organizations of parts that solve physical and conceptual problems, or design needs through different configurations. To a great extent, patterns are simply static behavioral rules. These rules apply to physical entities via relational concepts, hierarchical relationships that can be easily extended to infinity. It is then crucial to define the minimum elemental entities included in the definition of the model.

These relationships may be, nevertheless, considered static as much as Alexander's depiction does not include any mention to the evolutionary nature of pattern combination rules. Consequently, it is crucial to include the time factor in the study of the generative logics yielded by patterns. In implicit design models, *"the non-linear techniques used in simulation or iterative algorithmic design, generate form with a considerable level of abstraction from the parameters or rule sets comprising its inputs"* [10]. This logic is not univocal or unidirectional, but it can be reinterpreted back through the esthetics resulting from the design process. In other words, there is a place for a mutually beneficial logic for design and reality.

4 An Agent-Based Model of Urban Dynamics

As a consequence of the above, we can deal with cities as informational spaces. Specific and concrete models can characterize specific urban systems, as well as their representation and visualization. It is possible to build constructive and significant models through a careful agent selection process (elements, in Alexander's theory), a well-defined characterization, a limited, controlled scope, an interface to visualize and understand data, and an efficient method to obtain form.

The model proposed by the "Self-Organizing" city plays with the idea that certain urban agents can be described in terms of conflicting or colliding interests, their characteristics, and their morphological and spatial implications.

The model highlights its associative logics through: (i) the opposition of their characteristics (ii) the collision of agent's intents, and (iii) the synthesis of such logics in highly evolved geometrical and spatial entities.

Figure 2 shows the current model instantiation procedure. Starting with connective space agents, these deposit building seeds are responsible for the creation of building agents. Buildings build consistent network relationships and interact with one another and the connective agents already present in the model.

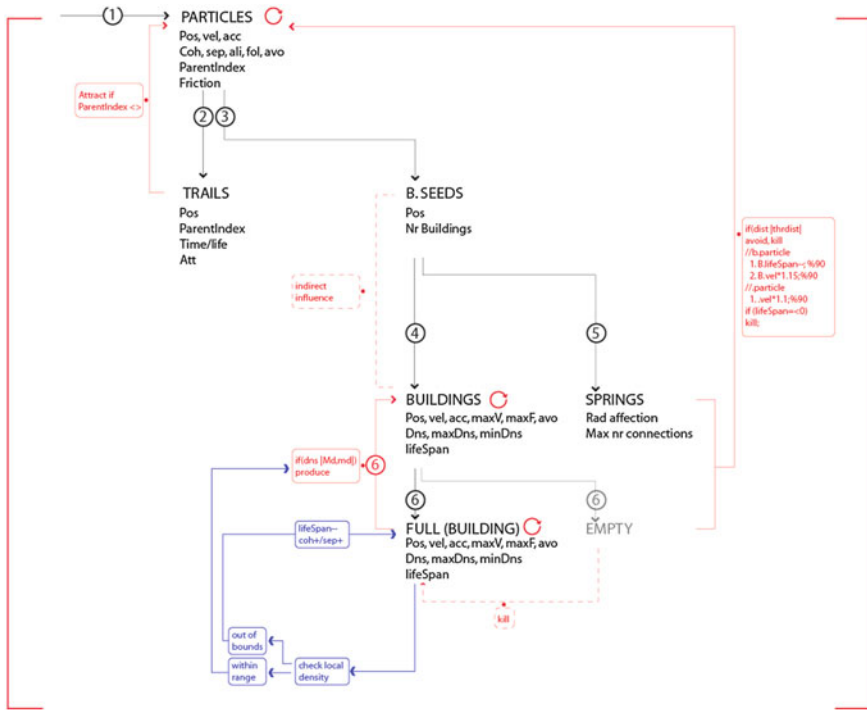


Fig. 2 First instance. Global internal systemic relationships. Agent states and fitness functions

4.1 Agents

The model considers three types of agents for the description of urban spaces: (i) buildings (ii) public space, and (iii) connective space. These agents are described in computational terms as “classes”, footprints for instances, which have differentiated behaviors and characteristics. All agents share a set of characteristics that define their velocity, acceleration, and position in the form of three-dimensional vectors. These shared properties allow monitoring their location and movement, as they interact with one another. The movements respond to reactions to the stimulus of other agents in their proximity, which triggers the aforementioned collision of interests.

4.2 The Model Space

The model space is the graphical interface in which agents carry out their activity and interactions.

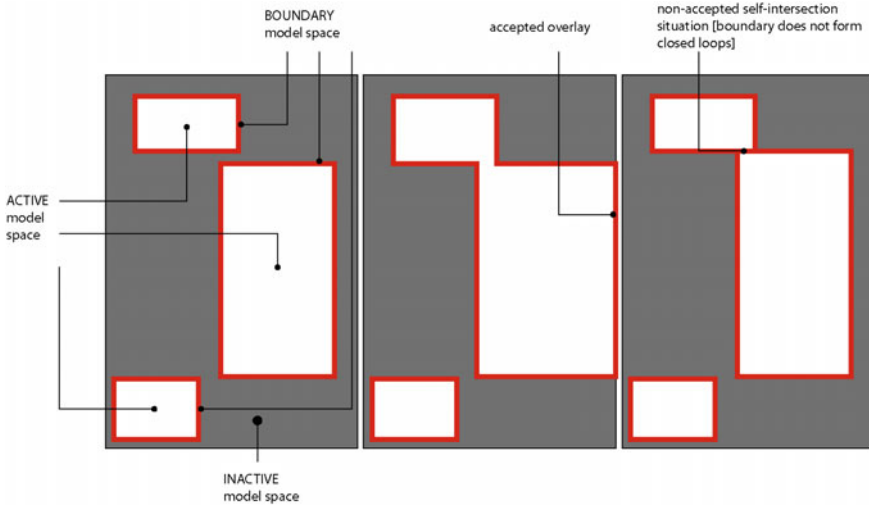


Fig. 3 Characterization of the model space

This space, depicted in Fig. 3, is homogeneous at this stage of the research, and has three possible states: (i) active (model space) (ii) inactive (model space), and (iii) boundary (model space).

The active model space hosts the building, public space, and connective agents, and does not interfere in how they react to one another. It is the area of the model that is subject to study. The inactive model space is basically empty space, and it is neither informed nor informative. Finally, the boundary model space represents the in-between areas and forms either single or multiple close loops that encloses the active model space.

The active model space can be associated with information, whether GIS-based, whether coming from a real-time interaction with the end-user. However, in this initial version of the system, the space is homogeneous, isotropic, and neutral.

4.2.1 Buildings

Buildings represent the built space in the urban fabric and define its final volume. They are conceived as abstract entities that host different functions, mainly residential and services. These functions have no affection on the final shape of the building agents, which are undifferentiated from a formal point of view. Program information is easily accessible through the option tools in the software environment.

Buildings are defined, beyond their common characteristics of position, velocity, and acceleration (which control how their position adapts to the surrounding conditions), by their:

- *Size* building footprint. This space cannot be occupied by any other agent.
- *Radius of action* influences distance of a building. The amount of nearby buildings is counted within this area, and is used as base for the calculation of aggregations or clusters. This radius is used for the detection of public or connective space agents. Within this radius, colliding agents will try to move away from one another.
- *Number of buildings* amount of building agents tolerated without rejection within the radius of action. Cluster formations benefit the survival of the system through the synergic action of building agents, which form resilient “*super entities*”.
- *Survival time (“life”)* measures a building’s adaptation to its environment. If a building is isolated then its life diminishes gradually. Clusters are rewarded while excessive scattering is penalized.
- *Stability* measures the amount of time (frames) that a building has been in a life-increasing situation (such as a cluster) or under a negative, life-depleting condition. The buildings that reach an optimal stability state mutate into static points of the simulation.
- *Local density* measures the amount of buildings within the area of affection.
- *Global density* measures the total amount of building agents by area of active model space.
- *Program* infers urban properties from local density and the degree of stability of building agents.

Furthermore, there are a series of interactions that emerge from the properties above:

- “building agent”—“building agent” relationships
 - Cohesion: agent’s tendency to stay in an aggregated formation through their movement toward the centroid of nearby agents of the same type.
 - Alignment: tendency to flow in the same direction as the surrounding agents.
 - Dispersion: tendency to maintain a certain minimum distance to avoid collisions.
 - Separation: individual locational divergence.
- “building agent”—“public space agent” relationships
 - Separation: public space is defined as the absence of built and connective spaces.
 - Public space formation: function of the local density.
- “building agent”—“connective space agent” relationships
 - Separation: connective space does not tolerate the presence of buildings and represents all kinds of spaces (streets, pedestrian zones, mixed areas, and of any other kind), which may allocate movement and transportation flows.
 - Building formation: buildings form around highly connected areas.

4.2.2 Connective Space

The connective space represents networks, which allocate physical communication and/or transportation of people and/or goods: highways, streets, mixed traffic, or pedestrian zones. It is represented as a series of constantly moving nodes whose trajectory leaves a long-lasting footprint thus creating a synergic effect that reinforces often-used paths as recognizable movement patterns. Zones between nodes and their footprints can be occupied by buildings and other agents.

These agents are characterized by:

- The *angle of vision* defines the cone of vision of an agent
- The *angle of turn* determined by the agent's velocity. It is smaller the higher the user's speed, and higher the lower the speed (this is, a car has a lower angle of turn than a person, since it occupies more physical space and runs much faster).
- The *attraction* the degree of correlation of other agents with regard to connective space.

4.2.3 Public Space

Public space is non-occupied active model space resulting from the application of building agents' hierarchical rules. This includes parks, green areas, gardens, urban squares, mixed-use areas, and any other form of non-built space suitable and designed to allocate human activities that imply free, unpredictable distributions and the gathering of people.

4.3 “Building Seeds” and Model Population

It is crucial to study agent generation processes within the model: first, connectivity agents are situated; second, they place “building seeds” in their immediate proximity; third, a number of buildings emerge from the seeds; finally, public space is generated as a consequence of the inner building relationships described earlier. These interactions are tested initially in an abstract, homogeneous, and undifferentiated space. Then, we study the consequences of unfolding a system in a variety of forms as its generation may influence the subsequent development of the system itself.

Figure 4 shows three different approaches toward the validation and population of the agent-based system: (a) A random distribution (b) A mesh condition (a grid-like distribution), and (c) A hierarchical distribution or pyramidal propagation.

The last one displays an interesting “cascading effect” that resembles the chain of effects present in many real-life events, where some agencies require the presence of others to exist.

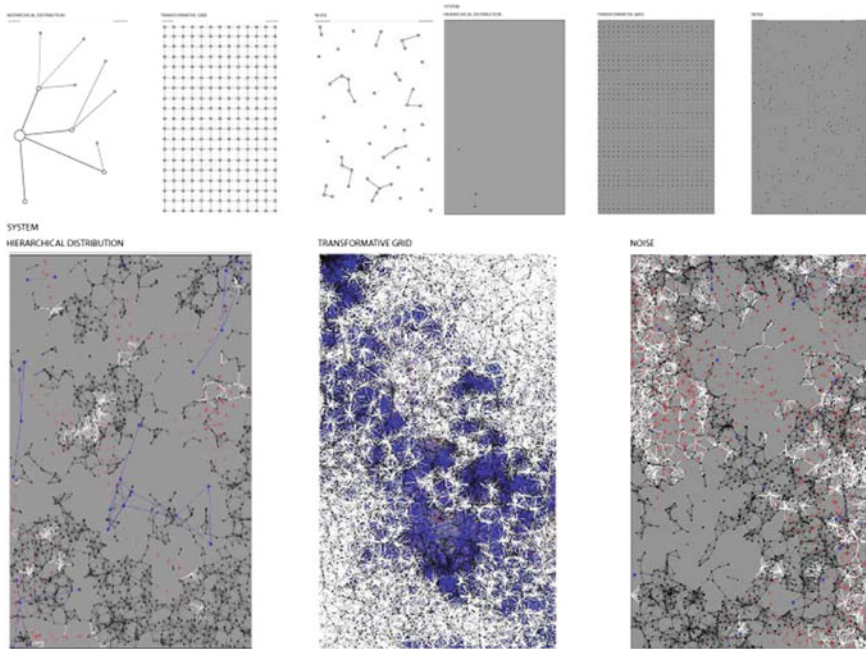


Fig. 4 Temporal role of initial system population distribution—multiagent system in a confined abstract space

In the proposed model, building and communication flows exert mutually excluding pressures in an attempt to reach an optimum state of connectivity, density, use, and programmatic diversity. Additionally, building objects tend to stabilize in time, which relates to their static nature in real life and implies the existence of imperfections and friction within the system. The continuous collision of interests causes the model to access successive far-from-equilibrium states, after which bifurcations may happen.

5 Conclusions and Further Work

Beyond traditional static urban-oriented tools, which focus primarily on design results (a sort of picture of a design proposal), agent-based modeling allows for a radical new interpretation of the design process emphasizing the process itself and showing the urban dynamics and their relationships through data and visualization. Instead of offering a single frame as a result of opaque calculations, “The Self-Organizing City” offers a valuable analysis and design tool that facilitates decision-making during the design process. Thus, the professional will be able to evaluate several design scenarios, while evaluating their appropriateness to certain ad-hoc conditions that will influence the project’s development.

Some aspects still need to be implemented, especially those related to the model's "fitness" criteria: the evaluation of sustainability indices, the quantification of urban density and population, and their relationship to urban program. A future version of the software will also include an improved GUI and more robust algorithms that will permit a more fluent user experience.

Acknowledgments This work has been supported by the project *SociAAL* (TIN2011-28335-C02-01), funded by the Spanish Ministry for Economy and Competitiveness.

References

1. Batty M (2007) *Cities and complexity: understanding cities with cellular automata, agent-based models, and fractals*. MIT Press, Cambridge
2. CityGen, RolePlaying City Map Generator. <http://citygen.crystalballsoft.com/>
3. Open City, Suicidator. 3D City Generator for Blender. <http://cgchan.com/suicidator/>
4. Portugali J (2000) *Self-organization and the city*. Springer, Berlin
5. Mitchell WJ (2000) *E-topia*. MIT Press, Cambridge
6. Nicolis G, Prigogine I (1977) *Self-organization in nonequilibrium systems: from dissipative structures to order through fluctuations*. Wiley, New York
7. Gupta A (2009) Insights from complexity theory: understanding organizations better. <http://tejas.iimb.ac.in/articles/12.php>
8. Easterling K (2007) *Enduring innocence: global architecture and its political masquerades*. MIT Press, Cambridge
9. Alexander C (1964) *Notes on the synthesis of form*. Harvard University Press, Cambridge
10. Snooks R (2007) *Observations on the algorithmic emergence of character, models*. 306090 Books, vol 11, Princeton Architectural Press, New York, p 96

Modeling and Robust Control of Splicing System

Yinghui Fan, Chaowen Li and Xingwei Zhang

Abstract Based on linear active disturbance rejection control (LADRC) method, the control algorithm is designed for web tension regulation of self-developed LJF650A zero-speed splicer. The switching repeatedly working conditions and varying web length make the tension control of zero-speed splicer more difficult than the general web tension control. The LADRC design can actively estimate and compensate both the internal uncertain dynamics and external disturbances in real time. In this study, a realistic nonlinear model of zero-speed splicer for printing machine is deduced, and a fourth order linear extended state observer (LESO) is designed based on the simplified model of the accumulator. Simulations are presented and discussed for the LADRC controller, resulting with a better performance compared with decentralized PI controller.

Keywords Tension control · LADRC · Zero-speed splicer · Modeling

1 Introduction

In web handling system, tension control is a very important problem. Excessive tension variations may cause web wrinkles and breakage, and it also does harm to register control. In the zero-speed splicer, tension control problem is particularly

Y. Fan · C. Li (✉) · X. Zhang

Department of Mechatronic Engineering, College of Engineering, Shantou University,
Shantou, China

e-mail: 11cwli@stu.edu.cn

Y. Fan

e-mail: yhfan@stu.edu.cn

X. Zhang

e-mail: xwzhang@stu.edu.cn

difficult and important, because the tension fluctuation is not only influenced by the time-varying unwind roll radius and inertia during the unwinding phase, but also influenced by the frequent acceleration and deceleration of the carriage during the splicing phase, accompanied by the change of the web length. Those factors have a severe negative effect on the exit tension, as we have observed in self-developed **LJF650A** zero-speed splicer. With the higher processing speed demand, this negative effect will be more intensive, and must be paid more attention.

Different works about web tension control have been done. For unwinding (winding) system, Koc et al. [1], designed a linear parameter varying (LPV) controller. Benlatreche et al. [2], designed a multivariable H_∞ controller, compared with decentralized PI control strategy and 2DOF control strategy. For accumulator, Pagilla et al. [3, 4], deduced a web tension model and obtained a simplified model with average tension. Kuhm et al. [5], designed a multi-model PI and a multi-model H_∞ controller. More works can be found in the reference of [1–5]. However, few works have been published for the web tension control of splicing system, which presents more severe nonlinearity and unmodeled uncertainty.

Han [6], firstly proposed the nonlinear ADRC control strategy independent on an accurate system model, which demonstrates its good robustness against the unknown external disturbance and internal uncertain dynamics, so it is fit for the case of complicated plant dynamics, such as the web tension control [7, 8]. Corresponding to the difficult parameter tuning, Gao [9], proposed a LADRC control strategy with an effective controller parameter tuning method [10].

This paper aims to design a LADRC tension controller for the self-developed **LJF650A** zero-speed splicer and is organized as follows. Section 2 gives the dynamics of the unwind roll and accumulator, and the simplified model for tension control are discussed. Section 3 designed velocity and tension LADRC controllers. Simulation results and conclusions are given in Sect. 4 and 5, respectively.

2 System Model

Figure 1 is the picture of self-developed LJF650 zero-speed splicer, and its schematic is shown in Fig. 2, consisting of an unwind roll driven by servo motor and a horizontal accumulator driven by air cylinder. For this splicer, the tension control is mainly achieved by the carriage motion control, i.e., air cylinder control, while the unwinding motor is to achieve the desired unwinding velocity control.

Unwind Roll In the process of unwinding, the unwind roll radius $R_w(t)$ and inertia $J_0(t)$ are time-varying. The velocity dynamics of the unwind roll should be written as



Fig. 1 LJF650 zero-speed splicer

$$\frac{d}{dt}(J_0 w_w) = (t_a - t_w)R_w(t) - K u_w(t) - b_{fw} w_w \quad (1)$$

where $u_w(t)$ is the input to the unwinding motor, and the motor model is considered as a proportional component K , b_{fw} is the friction coefficient of the unwind roll.

However, the splicing time usually only takes several seconds (less than 12 s in self-developed zero-speed splicer), $R_w(t)$ and $J_0(t)$ changes slowly compared with the web dynamics and accumulator dynamics. So the radius and inertia of the unwind roll can be considered as a constant during the splicing time, and (1) can be rewritten as

$$J_0 \dot{v}_w = (t_a(t) - t_w)R_w^2 - K R_w u_w(t) - b_{fw} v_w(t) \quad (2)$$

Accumulator. The accumulator typically consists of carriage, web spans, and rolls as shown in Fig. 2. The dynamics behavior of the horizontal carriage is given by

$$\frac{d^2 L_c(t)}{dt^2} = \frac{1}{M_c} u_c(t) - \frac{1}{M_c} F_d(t) - \frac{1}{M_i} \sum_{i=1}^{i=N} t_i(t) \quad (3)$$

where M_c is mass of the carriage, N and $L_c(t)$ are the number of rolls and the web length in accumulator, $u_c(t)$ is generated by air cylinder, and $F_d(t)$ is the whole resistance, including frictions in the air cylinder and the rod seals, and the friction in the carriage guide rail. By lots of experiments, $F_d(t)$ can be approximately given by

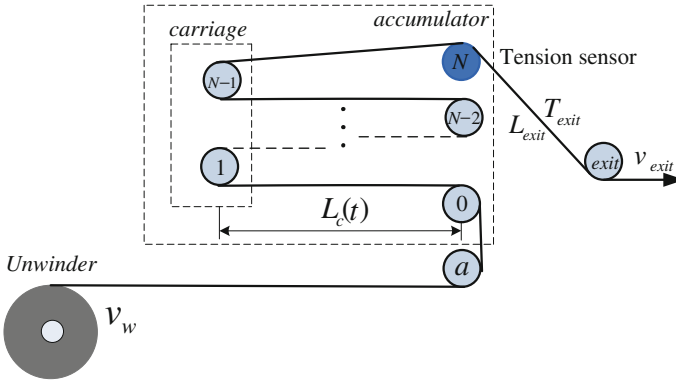


Fig. 2 Schematic diagram of the zero-speed splicer ($N = 20, R_{wmax} = 0.4, L_c \in [0.4, 2.7]$)

$$F_d = 3612v_c + 64.2(N) \tag{4}$$

Based on the principle of conservation of mass and Hooke law, the web tension dynamics of accumulator is generally given by [3]

$$\begin{aligned} \frac{dt_i(t)}{dt} &= \frac{AE}{L_c(t)}(v_i(t) - v_{i-1}(t)) + \frac{1}{L_c(t)}[t_{i-1}(t)v_{i-1}(t) - t_i(t)v_i(t)] + \frac{AE}{L_c(t)}\dot{L}_c(t) \\ &\quad - \frac{1}{L_c(t)}t_i(t)\dot{L}_c(t) \end{aligned} \tag{5}$$

where A is the cross-sectional area of web, E is young's modulus of web material. Assuming that the accumulator works under an idealized situation where the tension in each web span is same [4], an average tension can be defined as

$$t_c = \frac{1}{N} \sum_{i=1}^{i=N} t_i(t) \tag{6}$$

In general, for the value of AE is very big, the second term of (5) can be ignored, but the web length is varying with the movement of the carriage during the splicing phase, so the last two terms of (5) should be reserved because they reflect the particularity of the web tension dynamics in the accumulator. Taking the sum from $i = 0$ to $i = N$ of both sides of (5), the dynamic of free roll and tension in accumulator can be given by

$$\frac{dt_c(t)}{dt} = \frac{AE}{L_c(t)} \frac{1}{N} (v_N(t) - v_0(t)) + \frac{AE}{L_c(t)} \dot{L}_c(t) - \frac{1}{L_c(t)} t_c(t) \dot{L}_c(t) \tag{7}$$

$$J_r \frac{dv_i(t)}{dt} = R^2(t_{i+1}(t) - t_i(t)) - b_f v_i(t) \quad (8)$$

where R is the radius of roll, b_f is the friction coefficient on the roll shift. For the splicer, the goal of tension control is to maintain the exit tension at desired level, the dynamical behavior of exit tension t_{exit} can be written as follows [1]

$$\frac{dt_{\text{exit}}(t)}{dt} = \frac{AE}{L_{\text{exit}}} (v_{\text{exit}} - v_N(t)) + \frac{1}{L_{\text{exit}}} t_c(t) v_N(t) - \frac{1}{L_{\text{exit}}} t_{\text{exit}}(t) v_{\text{exit}} \quad (9)$$

where v_{exit} is the exit web velocity, which depends on process velocity, in general, it is considered as a constant. L_{exit} is the length of the exit web. In general, the roll dynamics in accumulator has less effect on the exit tension, so combining (3) (7), and (9), a simplified model of accumulator is given by

$$\begin{cases} \frac{d^2 L_c(t)}{dt^2} = \frac{1}{M_c} u_c(t) - \frac{1}{M_c} F_d(t) - \frac{N}{M_c} t_c(t) \\ \dot{t}_c(t) = \frac{AE}{L_c(t)N} (v_N - v_0(t)) + \frac{AE}{L_c(t)} \dot{L}_c(t) - \frac{1}{L_c(t)} t_c(t) \dot{L}_c(t) \\ \dot{t}_{\text{exit}}(t) = \frac{AE}{L_{\text{exit}}} (v_{\text{exit}} - v_N) + \frac{1}{L_{\text{exit}}} t_c(t) v_N - \frac{1}{L_{\text{exit}}} t_{\text{exit}}(t) v_{\text{exit}} \end{cases} \quad (10)$$

if we regard the $u_c(t)$ as the unique control signal of the accumulator, after differentiating t_{exit} (10) can be rewritten as

$$\frac{d^3 t_{\text{exit}}}{dt} = f_c(t) + b_{c0} u_c \quad (11)$$

where

$$\begin{aligned} f_c = & \frac{AE}{L_{\text{exit}}} v_{\text{exit}} \ddot{\bullet} - \frac{1}{L_{\text{exit}}} d^2(t_{\text{exit}} v_{\text{exit}}) / dt - \frac{2v_N}{L_{\text{exit}} L_c} \dot{L}_{\text{exit}} \dot{t}_c - \frac{(AE - t_c) v_N}{M_c L_{\text{exit}} L_c} (F_d + N t_c) \\ & + \frac{AE v_N}{L_{\text{exit}} L_c} \dot{v}_0 + \left(\frac{(AE - t_c) v_N}{M_c L_{\text{exit}} L_c} - b_{c0} \right) u_c \end{aligned}$$

then the accumulator can be regarded as a third-order linear system with one input $u_c(t)$ and one output t_{exit} . Similarly, the unwind roll can be regarded as a first-order linear system with one input $u_w(t)$ and one output v_w , and simplified as

$$\dot{v}_w = f_w(t) + b_{w0} u_w \quad (12)$$

where

$$f_w(t) = \frac{R^2}{J_0}(t_a(t) - t_w) - \frac{b_{fw}}{J_0}v_w - \left(b_{w0} + \frac{KR_w}{J_0}\right)u_w$$

the $f_w(t)$ and $f_c(t)$ represents the combined effects of internal neglected dynamics and external disturbance, and b_{w0} , b_{c0} become adjustable parameters, which are configured to obtain the linear model of the unwind roll and the accumulator.

3 Controller Design

In the zero-speed splicer system, we should control the exit tension and speed within the tolerance range during the normal unwinding phase and splicing phase. In LADRC, the disturbance is extended into a new state variable and estimated by the LESO, and the estimated value of the disturbance is used to compensate the actual disturbance in system, then a feedback controller is used to track the desired nominal value. From (11) and (12), the unwind roll is a first order system, and the accumulator can be regarded as a third order system, so a first order LADRC controller and a third order LADRC controller are needed for them, respectively. The diagram of the proposed controller is shown in Fig. 3, which mainly consists of two components: Linear Extended State Observer (LESO) and Feedback controller.

The basic idea of LESO is not only to track the system variables v_w and t_{exit} by z_{w1} and z_{c1} , and the differentiated signal of t_{exit} by z_{c2} , but also actively estimate the disturbances f_w and f_c by the extended state variables z_{w2} and z_{c4} , and use f_w and f_c in the control laws, $u_w = (-z_{w2} + u_{w0})/b_{w0}$ and $u_c = (-z_{c4} + u_{c0})/b_{c0}$, then the plant can be reduced to a unit-gain integrator control system. The forms of second order LESO for unwind roll and the fourth order LESO for the accumulator are as follows.

Unwind Roll LESO:

$$\begin{cases} e_w(t) = z_{w1}(t) - v_w(t) \\ \dot{z}_{w1} = z_{w2}(t) + \beta_{w1}e_w(t) + b_{w0}u_w \\ \dot{z}_{w2} = -\beta_{w2}e_w(t) \end{cases} \quad (13)$$

Accumulator LESO:

$$\begin{cases} e_c(t) = z_{c1}(t) - t_{\text{exit}}(t) \\ \dot{z}_{c1} = z_{c2}(t) + \beta_{c1}e_c(t) \\ \dot{z}_{c2} = z_{c3}(t) + \beta_{c2}e_c(t) \\ \dot{z}_{c3} = z_{c4}(t) + \beta_{c3}e_c(t) + b_{c0}u_c \\ \dot{z}_{c4} = -\beta_{c4}e_c(t) \end{cases} \quad (14)$$

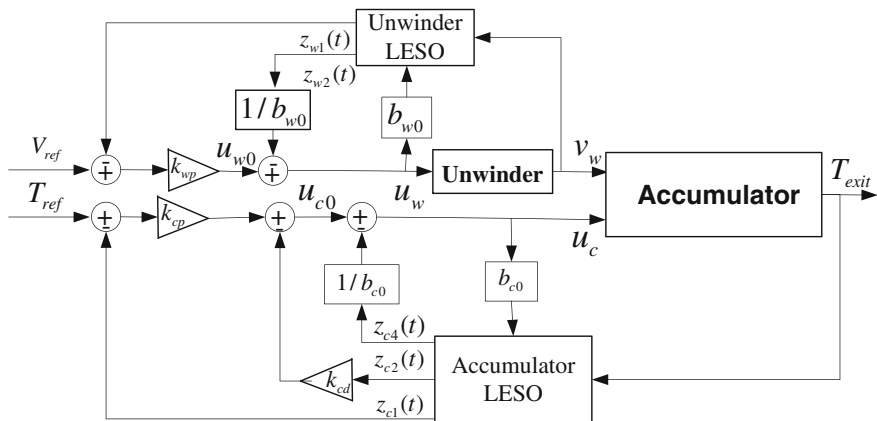


Fig. 3 Structure of the decentralized LADRC control scheme

As long as obtaining appropriate β_{w1} , β_{w2} and β_{c1} , β_{c2} , β_{c3} , β_{c4} the state variables and disturbance can be accurately estimated by the LESO outputs, and applied to the control laws:

$$u_w = \frac{-z_{w2} + u_{w0}}{b_{w0}} \text{ and } u_c = \frac{-z_{c4} + u_{c0}}{b_{c0}} \quad (15)$$

if ignoring the estimation error in z_{w2} and z_{c4} , then the plant can be regarded as a unit-gain integrator system approximately.

$$\dot{v}_w = f_w + \frac{-z_{w2} + u_{w0}}{b_{w0}} \bullet b_{w0} \approx u_{w0} \quad (16)$$

$$\frac{d^3 t_{20}}{dt} = f_c(t) + b_{c0} \bullet \frac{-z_{c4} + u_{c0}}{b_{c0}} \approx u_{c0} \quad (17)$$

as well known, they can be easily controlled with feedback controller.

$$u_{w0} = k_{wp}(V_{ref} - z_{w1}) \text{ and } u_{c0} = k_{cp}(T_{ref} - z_{c1}) - k_{cd}z_{c2} \quad (18)$$

where V_{ref} and T_{ref} are the set points of the unwinding velocity and exit tension.

4 Simulation Study

Through simulation with the realistic nonlinear model of the self-developed zero-speed splicer, the proposed control scheme is compared with decentralized PI controller. For the white cardboard paper used in the printing machine, the

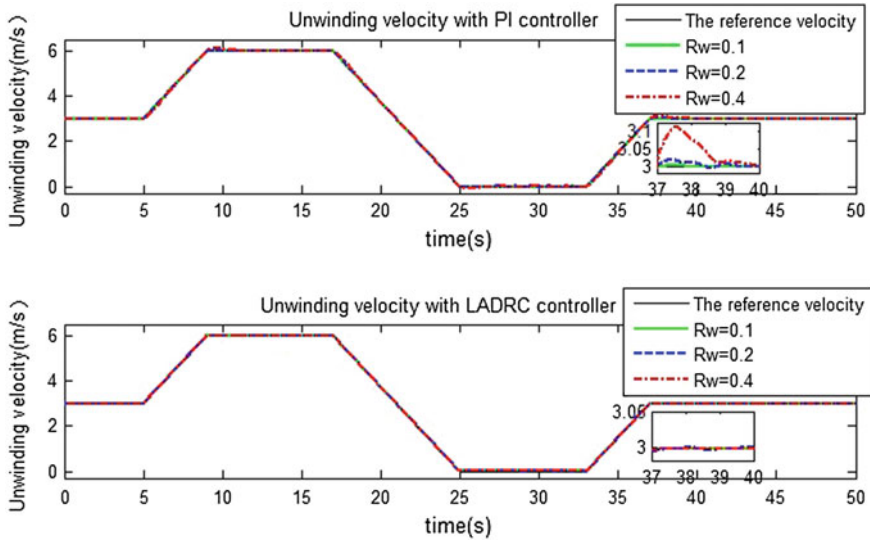


Fig. 4 The unwinding velocity during splicing phase when $R = 0.1, 0.2$ and 0.4 m

parameters of the self-developed splicer are: $K = 0.42$ Nm/V, $b_{fw} = 0.03$, $b_f = 0.02$, $M_c = 300$ Kg, $A = 0.000012$ m², $E = 5.69 \times 10^8$ Pa, $L_{exit} = 1.2$ m, $R = 0.075$ m, $L_a = 1.2$ m. The reference tension is 100 N, the desired exit velocity is 3 m/s, and the desired unwind velocity is depicted in Fig. 4.

The simulation includes Two Parts: (i) unwinding phase, from $t = 0$ to $t = 5$ s, the unwind roll releases web, and the accumulator is at its nominal web length; (ii) splicing phase, from $t = 5$ to $t = 21$ s, the accumulator stores the web with the carriage moving along the guide rail till web length reaches the maximum, and the unwinding velocity is increased to maintain nominal exit tension, from $t = 21$ to $t = 37$ s, the accumulator releases the web, and the unwinding velocity is decreased, Eventually carriage moves back to its initial position.

It is obvious that the numbers of LADRC controller parameters are more than PID controller. However, the LADRC controller parameters are related to the control loop bandwidth of the plant, w_c and the bandwidths of LESO, w_{w0} and w_{c0} . The relationship between them is given by [10]

$$\begin{cases} \beta_{w1} = 2w_{w0}, \beta_{w2} = w_{w0}^2 \\ k_{cp} = w_c^2, k_{cd} = 2w_c, \beta_{c1} = 4w_{c0}, \beta_{c2} = 6w_{c0}^2, \beta_{c3} = 4w_{c0}^3, \beta_{c4} = w_{c0}^4 \end{cases} \quad (19)$$

where w_{w0} is the bandwidth of unwind roll LESO, and w_{c0} is the accumulator LESO.

Generally, as long as the bandwidths b_{w0}, b_{c0} are chosen appropriately, and the controller parameters calculated based on (19), a good performance can be obtained, otherwise, the controller parameters should be adjusted separately one by

Table 1 Controller parameters

| Section | Unwind roll | Accumulator |
|------------------|---|--|
| LADRC controller | $\beta_{w1} = 705, \beta_{w2} = 78,$ $k_{wp} = 295,$ $b_{w0} = 0.3$ | $\beta_{c1} = 3,600, \beta_{c2} = 66,825, \beta_{c3} = 9,113,$ $\beta_{c4} = 36,085,500, k_{cp} = 55, k_{cd} = 62.2,$ $b_{c0} = 500$ |
| PI controller | $K_{p1} = 32.77,$ $T_{i1} = 0.060 \text{ s}$ | $K_{p2} = 0.44, T_{i2} = 0.066 \text{ s}$ |

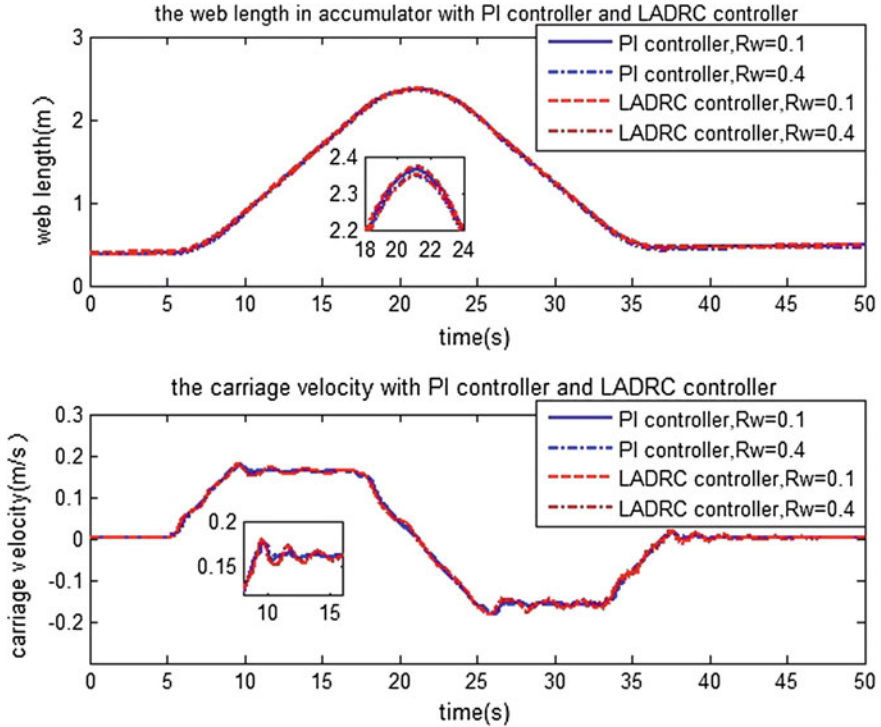


Fig. 5 The web length and carriage velocity during Splicing phase when $R = 0.1$ and 0.4 m

one. Under no vibration condition, β_{w2}, β_{c4} and b_{w0}, b_{c0} can be as big as possible. However, b_{w0}, b_{c0} cannot be too big, because it will lead to system responses slowly.

For splicing system, the principal concern is the maximum amplitude performance of exit tension variations in relation to the reference tension and the speed tracking performance. Meanwhile, it is necessary to verify the robustness to time-varying parameters $R_w(t)$. The decentralized PI and LADRC controller parameters with $R_w(t) = 0.2 \text{ m}$ are obtained, respectively, and their performance are compared with $R_w(t) = 0.1, 0.2, 0.4 \text{ m}$. All the adjusted controller parameters are shown in Table 1, and the simulation result is shown in Figs. 4, 5 and 6.

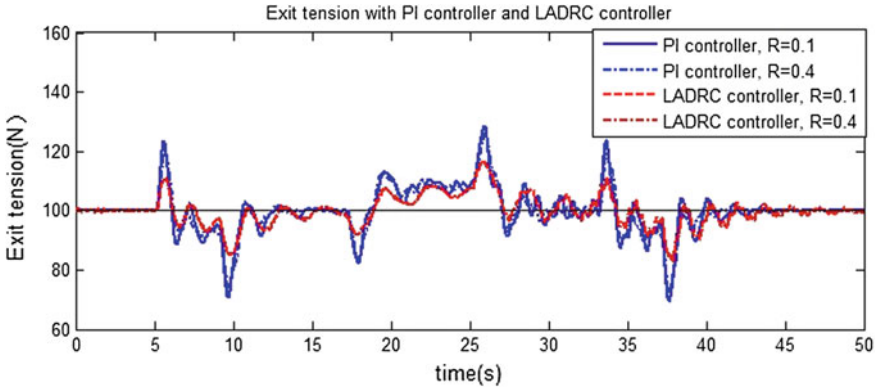


Fig. 6 The exit tension during splicing phase when $R = 0.1$ and 0.4 m

As shown in Fig. 4, under the existence of the tension fluctuation deduced by the accumulation, the unwind velocity overshoot of decentralized PI controller is much higher than that of LADRC controller during the unwinding process. However, as shown in Fig. 5, both methods achieved almost the same performance in the carriage velocity and the web length, the main reason is that the carriage, with large inertia, responds slowly to the exit tension fluctuations.

Figure 6 demonstrates that when the unwinding velocity has been well controlled, the time-varying R has a less impact on the exit tension. The LADRC controller can get lower amplitude of tension fluctuations than the PI controller; furthermore, the maximum amplitude of exit tension decreased from 30 % by PI controller to 16 % by LADRC controller during the splicing process.

Overall, the proposed controller obtains a better performance than the traditional PI controller. The proposed controller has demonstrated its superiority during the on-site testing of self-developed zero-speed splicer. Till now, with the splicing time kept within 12 s, we have achieved the tension fluctuations of the splicer within 5 % when the printing speed reaches 60 m/min and 15 % when 180 m/min.

5 Summary

This paper studies the tension control problem of a splicing system. And a new tension controller is designed based on the LADRC. With the realistic nonlinear model, the simulation study is done for both the proposed controller and the PI controller. As expected, the former obtains better stability and robustness than the latter. The on-site testing and operation of self-developed zero-speed splicer validates the feasibility of the proposed control scheme.

Acknowledgments This study is sponsored by Guangdong University E&T R&D center building fund: Soft-package printing machine center, and the Building Fund for the Academic Innovation Team of Shantou University (Grant No. ITC10003).

References

1. Koc H et al (2002) Modeling and robust control of winding systems for elastic webs. *IEEE Trans Control Syst Technol* 10(2):197–208
2. Benlatreche A, Knittel D, Ostertag E (2008) Robust decentralised control strategies for large-scale web handling systems. *Control Eng Pract* 16(6):736–750
3. Pagilla PR et al (2000) Robust observer-based control of an aluminum strip processing line. *IEEE Trans Ind Appl* 36(3):865–870
4. Pagilla PR, Singh I, Dwivedula RV (2003) A study on control of accumulators in web processing lines. In: *IEEE proceedings of the American control conference, 2003*, vol 5
5. Kuhm D, Knittel D (2012) New mathematical modelling and simulation of an industrial accumulator for elastic webs. *Appl Math Model* 36(9):4341–4355
6. Han J (1998) Auto-disturbance rejection control and its applications. *Control Decision* 13(1):19–23
7. Zhou W, Gao Z (2007) An active disturbance rejection approach to tension and velocity regulations in web processing lines. In: *IEEE international conference on control applications, 2007. IEEE CCA 2007*
8. Shanhui L, et al (2012) Tension controller design for unwinding tension system based on active disturbance rejection control. In: *IEEE international conference on mechatronics and automation (ICMA), 2012*
9. Gao Z (2006) Active disturbance rejection control: a paradigm shift in feedback control system design. In: *IEEE American control conference, 2006*
10. Gao Z (2006) Scaling and bandwidth-parameterization based controller tuning. In: *Proceedings of the American control conference, vol. 6*

Single Observer Passive Location Using Phase Difference Rate

Taoyun Zhou, Yun Cheng and Tiebin Wu

Abstract In single observer passive location system, traditional filtering algorithm for nonlinear system is Extended Kalman Filtering (EKF), which is usually affected by initial values and measurement noise of passive tracking. In order to overcome the disadvantages of EKF, we present an improved Modified Variance Extended Kalman Filter (MVEKF) method in single observer passive location system, using phase difference rate. Simulation results show that it can effectively restrict the measurement noise, being less affected by initial values. Furthermore, there is no need for searching observables modifiable function, so the proposed MVEKF is more accurate and useful than EKF in single observer passive location.

Keywords Single observer passive location · Phase difference rate · Modified variance extended Kalman filter (MVEKF)

1 Introduction

Passive positioning is a technology that the device itself does not transmit signals, but just passively rely on the information received from the emitter [1]. Traditional methods of single observer passive location, such as Doppler frequency positioning method and arrival time positioning method and so on, exist with disadvantages of low positioning accuracy and slow convergence speed and so on. Based on kinematics, phase difference rate positioning method can locate the

Y. Cheng (✉)

Department of Communication and Control Engineering, Hunan University of Humanities, Science and Technology, Hunan, China
e-mail: chy837002@gmail.com

T. Zhou · T. Wu

Hunan University of Humanities, Science and Technology, Hunan, China

target through extracting the relative motion information between the target and observation platform, which has higher positioning speed and positioning accuracy [2–4]. Russia, Israel, and other countries also have a strong technical strength in this area [5, 6]. In order to keep pace with the development of international rapid passive location technology, some departments in China have done some theoretical work [5, 7, 8], but the performance of the test prototype developed is not satisfactory. Here, we focus on the location algorithm of the single observer passive location system, in which the traditional nonlinear filtering method is Extended Kalman Filtering (EKF), which depends greatly on the estimation of the initial state and is always affected by measurement noise, resulting in instable results [9–11]. For these reasons, Song and Speyer proposed a Modified Gain Extended Kalman Filter (MGEKF) method [12, 13], whose positioning accuracy and convergence speed are better than those of EKF, but it needs to find the observables modifiable function. For the limitations of these two filtering methods, we present an improved Modified Variance Extended Kalman Filter (MVEKF) method in single observer passive location system.

The rest of this paper is organized as follows. Section 2 introduces the positioning principle based on phase difference rate. Section 3 describes the traditional EKF algorithm. The proposed MVEKF algorithm and simulation results are presented in Sect. 4. Finally, conclusions are given in Sect. 5.

2 Positioning Principle Based on Phase Difference Rate

Process of the positioning method using phase difference rate is: first obtain the information of phase difference and its rate through two mutually orthogonal phase interferometers, then compute the radial distance between the target and the observation platform so as to locate the target through passive location [3, 14].

Assuming that position of the observation platform is (x_o, y_o, z_o) , velocity is $(\dot{x}_o, \dot{y}_o, \dot{z}_o)$, and position of the target is (x_T, y_T, z_T) in the $O - XYZ$ coordinate system (Assume $z_T = 0$). Then, we can get the expression of the target as:

$$\begin{aligned} x_{Ti} &= x_{oi} + r_i \cos \varepsilon_i \sin \beta_i \\ &= x_{oi} + \dot{\beta}_i^{-1} (\dot{x}_{oi} \cos \beta_i - \dot{y}_{oi} \sin \beta_i) \sin \beta_i \\ &= x_{oi} + \dot{\varepsilon}_i^{-1} [-\dot{z}_{oi} \cos \varepsilon_i - (\dot{x}_{oi} \sin \beta_i + \dot{y}_{oi} \cos \beta_i) \sin \varepsilon_i] \cos \varepsilon_i \sin \beta_i \end{aligned} \quad (1)$$

$$\begin{aligned} y_{Ti} &= y_{oi} + r_i \cos \varepsilon_i \cos \beta_i \\ &= y_{oi} + \dot{\beta}_i^{-1} (\dot{x}_{oi} \cos \beta_i - \dot{y}_{oi} \sin \beta_i) \cos \beta_i \\ &= y_{oi} + \dot{\varepsilon}_i^{-1} [-\dot{z}_{oi} \cos \varepsilon_i - (\dot{x}_{oi} \sin \beta_i + \dot{y}_{oi} \cos \beta_i) \sin \varepsilon_i] \cos \varepsilon_i \cos \beta_i \end{aligned} \quad (2)$$

where, β_i and ε_i represent target azimuth and elevation respectively, $\dot{\beta}_i$ and $\dot{\varepsilon}_i$ represent the rate of β_i and ε_i , respectively, r_i is radial distance between the target and observation platform. What is more, they should satisfy the Eqs. (3)–(7):

$$\operatorname{tg} \beta_i = \frac{x_{Ti} - x_{oi}}{y_{Ti} - y_{oi}} = \frac{x_i}{y_i} \quad (3)$$

$$\operatorname{tg} \varepsilon_i = \frac{z_{oi} - z_{Ti}}{\sqrt{(x_{Ti} - x_{oi})^2 + (y_{Ti} - y_{oi})^2}} = \frac{z_i}{\sqrt{x_i^2 + y_i^2}} \quad (4)$$

$$\dot{\beta}_i = \frac{\dot{x}_i \cos \beta_i - \dot{y}_i \sin \beta_i}{r_i \cos \varepsilon_i} \quad (5)$$

$$r_i = \frac{\dot{x}_i \cos \beta_i - \dot{y}_i \sin \beta_i}{\beta_i \cos \dot{\varepsilon}_i} = \frac{\dot{z} \cos \dot{\varepsilon}_i - (\dot{x}_i \sin \beta_i + \dot{y}_i \cos \beta_i) \sin \varepsilon_i}{\varepsilon_i} \quad (6)$$

$$r_i = \frac{\dot{x}_i \cos \beta_i - \dot{y}_i \sin \beta_i}{\beta_i \cos \dot{\varepsilon}_i} = \frac{-\dot{z} \cos \dot{\varepsilon}_i - (\dot{x}_i \sin \beta_i + \dot{y}_i \cos \beta_i) \sin \varepsilon_i}{\varepsilon_i} \quad (7)$$

3 Traditional EKF Algorithm

In the passive location using phase difference rate, state equation of the system is linear in Cartesian coordinates. It can usually be written as:

$$X_i = \phi X_{i-1} + BU_{i-1} + W_{i-1} \quad (8)$$

where X_{i-1} is state variable of the system at $i - 1$ time, ϕ is transition matrix, U_{i-1} is control matrix, and W_{i-1} is state noise.

The observation equation can be written as:

$$Z_{mi} = G(X_i) + N_i \quad (9)$$

where N_i is the measurement noise, $G(\bullet)$ is the nonlinear function of the state variable. We need a linearization so as to make the use of Kalman filtering method. The EKF algorithm expands the state equation at the predicted value to Taylor series and takes its first term, so the measurement equation is approximately equal to the linear equation of the state variables. Then, the measurement matrix of the observation equation is also equal to the Jacobin matrix of the measurement equation at the predicting point, which is:

$$H_i^- = \left. \frac{\partial G(X)}{\partial X} \right|_{X=\hat{X}_{i/i-1}} \tag{10}$$

Then, we can use Kalman filter, which is simple and available. In EKF algorithm, the accuracy of the predicted value directly affects the accuracy and convergence speed, which will cause a bigger error. To solve this problem, we will propose an improved MVEKF in the next section.

4 Improved MVEKF Algorithm

4.1 Principle of MVEKF Filtering Algorithm

According to the linear Kalman filtering under the condition of Gaussian white noise [3], we can get:

$$E[\hat{Z}_i \tilde{X}_i^T] = 0 \tag{11}$$

where $\hat{Z}_i = H\hat{X}_i$ is observation information at i time, $\tilde{X}_i = X_i - \hat{X}_i$ is the state filtering error, for $E[\tilde{X}_i] = 0$, so:

$$E[(HX_i - H\hat{X}_i)(X_i - \hat{X}_i)^T] = HP_i = 0 \tag{12}$$

In EKF, due to the bias of the predicted value, there is a deviation of Jacobin matrix at the predicted point [13]. So:

$$H_i^- P_{i/i}^- \neq 0 \tag{13}$$

where $P_{i/i}^-$ is the covariance matrix of the state equation at the i measurement time of EKF.

The basic idea of MVEKF is recalculating the Jacobin matrix with state filtering values in EKF, where:

$$H_i^+ = \left. \frac{\partial G(X)}{\partial X} \right|_{X=\hat{X}_{i/i}} \tag{14}$$

Then, we use it as a measurement matrix to update the covariance matrix so as to obtain a more accurate modified covariance matrix. So:

$$P_{i/i}^+ H_i^+ \approx 0 \tag{15}$$

The computation of H_i^+ with $\hat{X}_{i/i}$, which implies the information of the measurement Z_{mi} at this time, can improve the performance of the nonlinear estimation.

4.2 Application of MVEKF in Single Observer Passive Location

For observation platform, initial velocity of the moving target is usually unknown, in order to obtain a more precise positioning with the target’s velocity and restrain the noise of the results, we use MVEKF to deal with these two issues. The basic idea of MVEKF is: first obtain an initial positioning of the target with the measured phase difference and its rate and velocity of the observation platform, without considering the velocity of the target, and then use the initial positioning results to obtain a rough velocity estimate of the target. With the two parameters we just get, we can make corrections on the positioning results, and so forth, after several measurements; we can get more accurate positioning results and estimate the velocity of the target. Here, we firstly need to build a mathematical modeling [2, 11].

Assuming that the target is moving uniformly and linearly, state variable is $X_i = (x_i, y_i, z_i, \dot{x}_i, \dot{y}_i, \dot{z}_i)^T$ and the observation variable is

$$Z(i) = [\phi_{xim}, \phi_{yim}, \dot{\phi}_{xim}, \dot{\phi}_{yim}]^T \tag{16}$$

State equation is:

$$X_T(i + 1) = \phi X_T(i) + BW(i) \tag{17}$$

where,

$$B = \begin{bmatrix} T & 0 \\ 1 & 0 \\ 0 & T \\ 0 & 1 \end{bmatrix}, \quad \phi = \begin{bmatrix} 1 & T & 0 & 0 \\ 0 & 1 & 0 & 0 \\ 0 & 0 & 1 & T \\ 0 & 0 & 0 & 1 \end{bmatrix}$$

$W(i) = [\Delta \dot{x}_i, \Delta \dot{y}_i]^T$ represents instantaneous velocity perturbation noise of the target, $\Delta \dot{x}_i$ and $\Delta \dot{y}_i$ are Gaussian white noise whose averaged value is zero, covariance matrix is written as Q_i .

Assuming that random errors are independent and obey zero-mean Gaussian distribution, estimation errors are independent and variance is time-invariant, $\Delta \dot{x}_i$ and $\Delta \dot{y}_i$ are of the same value. Then, the covariance matrix of the process noise and measurement noise are, respectively, written as:

$$Q_i = \begin{bmatrix} 0 & 0 & 0 & 0 \\ 0 & \delta_v^2 & 0 & 0 \\ 0 & 0 & \delta_v^2 & 0 \\ 0 & 0 & 0 & 0 \end{bmatrix}, R_i = E[N_i N_i^T] = \begin{bmatrix} \delta_\phi^2 & 0 & 0 & 0 \\ 0 & \delta_\phi^2 & 0 & 0 \\ 0 & 0 & \delta_\phi^2 & 0 \\ 0 & 0 & 0 & \delta_\phi^2 \end{bmatrix}$$

Observation equation can be written as:

$$Z_{mi} = G(X_i) + N_i \quad (18)$$

Jacobin matrix of observation equation is:

$$H_i^- = \begin{bmatrix} \frac{\partial \phi_{xi}}{\partial x_{Ti}} & 0 & \frac{\partial \phi_{xi}}{\partial y_{Ti}} & 0 \\ \frac{\partial \phi_{yi}}{\partial x_{Ti}} & 0 & \frac{\partial \phi_{yi}}{\partial y_{Ti}} & 0 \\ \frac{\partial \phi_{xi}}{\partial x_{Ti}} & \frac{\partial \phi_{xi}}{\partial x_{Ti}} & \frac{\partial \phi_{xi}}{\partial y_{Ti}} & \frac{\partial \phi_{xi}}{\partial y_{Ti}} \\ \frac{\partial \phi_{yi}}{\partial x_{Ti}} & \frac{\partial \phi_{yi}}{\partial x_{Ti}} & \frac{\partial \phi_{yi}}{\partial y_{Ti}} & \frac{\partial \phi_{yi}}{\partial y_{Ti}} \end{bmatrix}_{X=\hat{X}_{i/i-1}} \quad (19)$$

Thus, the MVKEF algorithm can be summarized as follows:

Step 1: Calculate the prediction equation:

$$\hat{X}_{i/i-1} = \phi \hat{X}_{i-1} \quad (20)$$

Step 2: Calculate the Jacobin matrix at the predicted point:

$$H_i^- = \left. \frac{\partial G(X)}{\partial X} \right|_{X=\hat{X}_{i/i-1}} \quad (21)$$

Step 3: Calculate the predicting covariance and Kalman gain:

$$P_{i/i-1} = \phi P_{i-1/i-1} \phi^T + B Q_i B^T \quad (22)$$

$$K_i' = P_{i/i-1} (H_i^-)^T [H_i^- P_{i/i-1} (H_i^-)^T + R_i]^{-1} \quad (23)$$

Step 4: Get the estimation of the filtering:

$$\hat{X}_{i/i} = \hat{X}_{i/i-1} + K_i' [Z_{mi} - G(\hat{X}_{i/i-1})] \quad (24)$$

Step 5: Recalculate the Jacobin matrix:

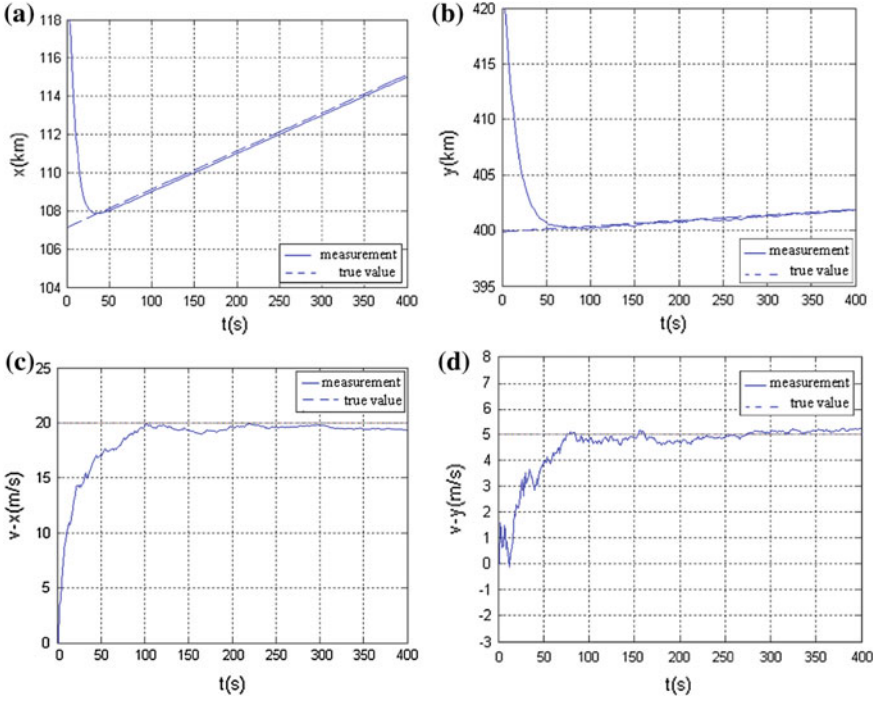


Fig. 1 $\delta_\phi = 0.008$ rad, $\delta_{\dot{\phi}} = 0.006$ rad/s. **a** Trajectory of X direction, **b** trajectory of Y direction, **c** velocity estimation of X direction, **d** velocity estimation of Y direction

$$H_i^+ = \left. \frac{\partial G(X)}{\partial X} \right|_{X=\hat{X}_{i/i}} \quad (25)$$

Step 6: Recalculate the predicting covariance and Kalman gain:

$$K_i = P_{i/i-1} (H_i^+)^T [H_i^+ P_{i/i-1} (H_i^+)^T + R_i]^{-1} \quad (26)$$

$$P_i = [I - K_i H_i^+] P_{i/i-1} [I - K_i H_i^+]^T + K_i R_i K_i^T \quad (27)$$

Based on the equations above, it can restrain the measurement noise and improve the accuracy of positioning.

4.3 Simulation Results and Analysis

From reference [14], we can learn that the radial distance between the target and observation platform is not less than 400 km in order to ensure flight safety during the high-altitude airborne positioning. In addition, there are no specific requirements,

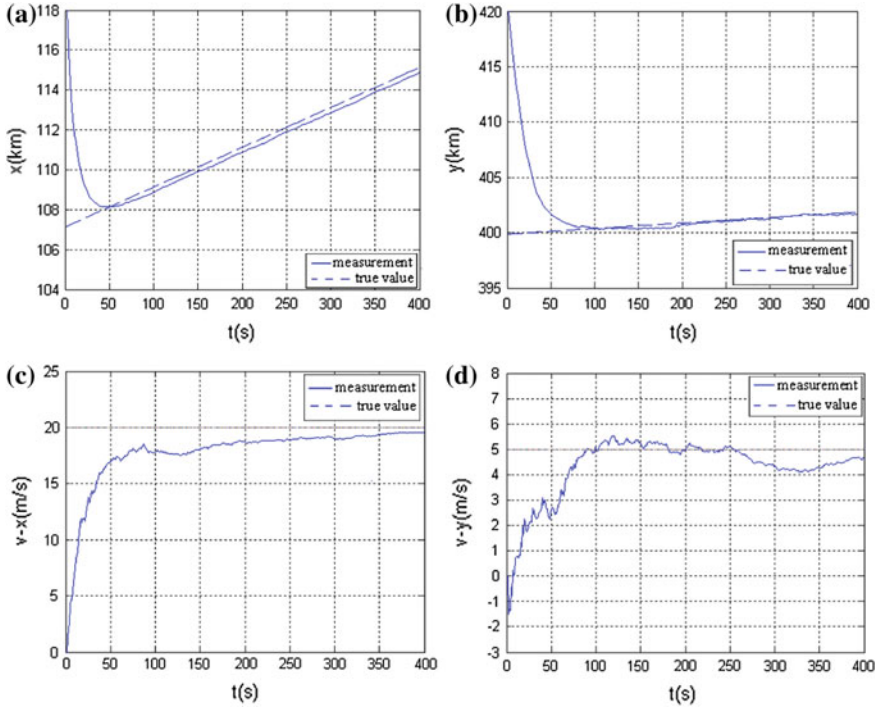


Fig. 2 $\delta_\phi = 0.016$ rad, $\delta_{\dot{\phi}} = 0.012$ rad/s. **a** Trajectory of X direction, **b** trajectory of Y direction, **c** velocity estimation of X direction, **d** velocity estimation of Y direction

so we set the flight path of the observation platform following the reference [14] and accordingly adopt the same initial data. Parameter settings as: baseline lengths of airborne phase interferometer are $d_x = 10$ m and $d_y = 5$ m, frequency of target radiation is $f_T = 3 \times 10^9$ Hz, interval of signal observation is $T = 1$ s, initial position of the moving object is (107.15, 399.88, 0) km, velocity of the target is (20, 5, 0) m/s, initial position of the moving platform is (0, 0, 10) km, and its velocity is (300, 0, 10) m/s, MSE of velocity measurement error is $\delta_v = 0.1$ m/s, MSE of observation platform itself positioning error is $\delta_p = 25$ m, MSE of frequency measurement error is $\delta_f = 10^6$ Hz, measurement accuracy of the phase difference and its rate are, respectively: $\delta_\phi = 0.008$ rad, $\delta_{\dot{\phi}} = 0.006$ rad/s and $\delta_\phi = 0.016$ rad, $\delta_{\dot{\phi}} = 0.012$ rad/s [14]. Simulation results are shown in Figs. 1 and 2.

Simulation results show that estimation error is larger in initial state, but convergence speed is rather faster. In Fig. 1, the maximum positioning error of X direction is about 15 m and Y direction is about 10 m. Velocity error of X direction is about 1 m/s and Y direction is about 0.3 m/s. In Fig. 2, the maximum position error of X direction is about 30 m and Y direction is about 12 m. Velocity error of X direction is about 3 m/s and Y direction is about 0.9 m/s. These illustrate that the

use of MVEKF can effectively realize passive location, and effectively estimate the velocity of the target's movement. But simulation results also show that positioning error and estimation error of velocity will be larger when accuracy of phase difference and its rate decrease. It approves that phase difference and its rate have an important influence on accuracy of positioning.

5 Conclusions

This paper addresses the problem of passive location with single observer. As EKF is affected by initial values and measurement noise, we present an improved MVEKF method in single observer passive location system, using phase difference rate. Simulation results show that the MVEKF is less affected by measurement noise and initial values, achieving a higher positioning accuracy. But the positioning accuracy is affected by phase difference and its rate, the higher the accuracy of phase difference and its rate, the higher the accuracy of positioning.

Acknowledgment This work was financially supported by the Hunan Provincial Natural Science Foundation of China (12JJ2040), the Research Foundation of Education Committee of Hunan Province, China (09A046, 11C0701, 13C435), the Construct Program of the Key Discipline in Hunan Province, China, the Aid program for Science and Technology Innovative Research Team in Higher Educational Institute of Hunan Province, and the Planned Science and Technology Project of Loudi City, Hunan Province, China.

References

1. Sun Z, Zhou Y, He L (1996) Single multi-base active passive positioning technology. National Defense Industry Press, Beijing
2. Zhao G, Li Y, Li T (2007) Algorithm for passive localization based on MVEKF. *J Northwest Polytech Univ* 25:113–116
3. Guo F, Jia X, Huang F (2009) A single observer passive localization method using phase difference changing rate only and its error analysis. *Acta Aeronautica et Astronautica Sinica* 30:1090–1095
4. Liu C, Ding W, Li H (2011) Research on UAV Airborne passive location system based on phase difference measurement. *Comput Meas Control* 19:2105–2108
5. Yang J, Chen S (2001) Latest developments of global airborne fast passive positioning technology. Proceedings of radar tracking technology seminar, Beijing, pp 38–40, March 2001
6. Wu X (2011) An overview of precision moving target celerity passive location development technology of foreign army. *Ship Electron Eng* 31:11–14
7. Zhang X, Zhu H (2001) Lateral positioning technology of airborne radiation on the ground. Proceedings of radar tracking technology seminar, Beijing, pp 46–52, March 2001
8. Chen W, Mao S (2001) New concept of single station high-precision passive tracking. Proceedings of radar tracking technology seminar, Beijing, pp 46–52, March 2001
9. Washin P, Litton develops phased interferometers for passive accurate target fixing. *Aviation Week Space*, pp 73–74, Tech90/10

10. Xi W, Yu BZ, Wang SS (2006) Theoretical analysis of direct-finding targets with rolling-airframe passive radar by phase interference technique. Proceedings of international conference on radar (CIE'06), pp 1–4
11. Xie X (2011) Single observer passive location and tracking algorithm of modified covariance Kalman Filter. *Comput Simul* 28:6–9
12. Song TL, Speyer JL (1985) A stochastic analysis of a Modified Gain Extended Kalman Filter with applications to estimation with bearing-only measurements. *IEEE Trans Autom Control* AC-30:940–949
13. LI B, Ding S, Qiang MA (2011) Study of Extended Kalman Filter applied in passive location. *J CAEIT* 6:622–625
14. Kay SM (2003) Fundamentals of statistical signal processing volume I: estimation theory. Electronic Industry Press, Beijing

Excluded Middle Forest Versus Vantage Point Tree: An Analytical and Empirical Comparison

Qiaozhi Li, He Zhang, Fuli Lei, Gang Liu, Minhua Lu and Rui Mao

Abstract A critical performance issue in searching distance-based indexing trees is that commonly multiple nodes, or data partitions, have to be further examined at each level of the tree. As a result, logarithmic search time is commonly not achievable. To solve this problem, excluded middle forest builds a tree for each data partition to be descended, so that logarithmic search time is achieved for each tree. Promising empirical results are reported from excluded middle forest. However, we observe that what determines whether a data partition has to be further examined is that data composing it, but not its location. Although each tree of the excluded middle forest can be searched in logarithmic time, the overall query performance is encumbered with the existence of multiple trees. We show analytically and empirically that multiple vantage point tree outperforms excluded middle forest.

Keywords Shuffled frog-leaping · Least random number generation · Unequal probability sampling · Multinomial distribution

1 Introduction

In most of them based on VP-tree [1], data are partitioned into two or more parts. Different partition's information is saved in index nodes. Searching process uses partition information to reduce time complexity of search.

Both excluded middle forest [2] and multiple vantage point (MVP) index [3, 4] are for metric-space data. It means that distance-based index can't use data distribution method like kd-tree [5]. Though index based on metric space will have

Q. Li · H. Zhang · F. Lei · G. Liu · M. Lu (✉) · R. Mao (✉)
Guangdong Province Key Laboratory of Popular High Performance Computers,
Shenzhen, China
e-mail: mao@szu.edu.cn

higher generality, it makes the difference of each data object smaller and may cause more search time. So an effective partition method is very important. Same partition method will show different performance in time cost when using different index type and this performance will be shown by distance calculation times in distance-based index.

If partition method could divide data with great difference, may avoid searching lots of useless branch of index. The excluded middle partition method tries to avoid searching useless partition by dividing data set into three subpartitions. The middle of three subpartitions is limited by a max radius and a proportion “m” [6], they will control size of middle subpartition. This method should find a pivot from data object, then find median of distance between each node and pivot. All of data objects which has distance bigger than (median–max radius) and less than (median + max radius) will be excluded as a single partition. If middle partition is bigger than m of data size, decrease its size.

MVP-index and excluded middle forest show different ways to use this partition method. MVP-index uses the middle partition to be a branch of ternary tree and excluded middle forest use it to make a new binary tree. We think the MVP-index will show better performance about calculation times.

Our analysis based on information cost. We think that though excluded middle forest may have better search performance at each tree, it could lose information of the data which excluded. In MVP-index, this information will save in internal node, but excluded middle forest will not save them.

Our test shows in Sect. 3, use three types of data and 8–10 different radius. It shows MVP-index having better performance when searching our analysis.

2 Excluded Middle Forest and MVP-Index Using Excluded Middle Partition Method

We will show the algorithm of this special MVP-index is based on pivot space model [7], and the comparison analysis of performance between MVP-index and excluded middle forest.

2.1 Algorithm of Build MVP-Index

Figure 1 shows the algorithm of building a MVP-index using excluded middle partition method. D denotes the data set to be indexed and “childNode[i].data” denotes to be the subpartition of each node. As excluded partition method requested, the middle partition’s size could be not larger than $m * |D|$. This partition will be set in a single node as a branch of MVP-index. The max and minimum distance between node’s data and pivot will be saved. If $|D| < \text{maxLeafSize}$ (denotes to be a leaf node’s max size), building process will stop and return.

```

Algorithm: building MVP-index by excluded middle partition method

Build(D)
if(|D|>maxLeafSize)
Pivot<-selectPivot(D)
Mid<-sortAndGetMid(D,pivot)
childNode[1]<- dataOf(distance<mid-r)
childNode[2]<- dataOf(distance>mid+r)
childNode[3]<- dataOf(mid-r<=distance<= mid+r)
if(childNode[3]>m*|D|)
childNode[1]<- dataOf(index<mid-m|D|/2)
childNode[2]<- dataOf(index>mid+m|D|/2)
childNode[3]<- dataOf(mid-m|D|/2<=index<=mid+m|D|/2)
end if
childNode[1].build(childNode[1].data)
childNode[2].build(childNode[2].data)
childNode[3].build(childNode[3].data)
end if

```

Fig. 1 Algorithm of building a MVP-index using excluded middle partition method

2.2 Analysis of Performance

As we said, the only difference between excluded middle forest and MVP-index using excluded middle partition method is “MVP-index keep middle partition as a branch, excluded middle forest use them to build another tree.” So we build a model to explain the comparison.

In this case, the MVP-index node which created by excluded data set is called “middle node.” There are two conditions when searching MVP-index’s internal node: 1. the middle node should not be searched, 2. we do not know whether the middle node should be searched or not, so we must search the middle node. Excluded middle forest could always search the middle partition, because its middle partition’s partition information did not save in a node when built. When searching process search each internal node and try to estimate whether middle partition should be searched or not, MVP-index needs to calculate the distance between query and pivot only once, but excluded middle forest cannot know it before searching the next tree. It means if excluded middle forest wants to get same information as MVP tree do, it need more distance calculation.

For a simple example, consider that data just be distributed numbers, in $[0, 7]$, and the width of exclusion is 1. There are seven buckets numbered 1 to 7, each with width 1. The max leaf size also is 1. For tree method, after first pivot and partition, you will get a leaf which is bucket 4. After the second pivot and partition, you will get other 6 leaves. For each search could only compute distance twice. However, for forest method, program should build two trees and get leaves

Table 1 Test suite

| Data type | Index size | Origin radius | Test radius | Number of radius | Last radius |
|----------------|------------|---------------|-------------------------|------------------|-------------|
| Uniform vector | 1000000 | 0 | $0.2i\{i = 0,1\dots9\}$ | 10 | 1.8 |
| String | 50000 | 0 | $i\{i = 0,1\dots8\}$ | 9 | 8 |
| Image | 10000 | 0 | $0.5i\{i = 0,1\dots7\}$ | 8 | 0.35 |

of buckets 1, 3, 5. The first tree should calculate twice, and the second tree should calculate once. It totally takes 3 distance calculation to query the forest.

In fact, we consider that when excluding the middle partition to be a new tree, the pivot which be selected will lose the information of this partition. So the query cannot get partition information of middle partition from calculating with pivot when searching. For getting this information, query must take more calculation, that is, why excluded middle forest always need more distance calculation times.

3 Empirical Results

This section shows our test and result, we are using three types of data: vector, string, and image. The test suite is shown in Table 1. Test suite comes from [8, 9], program based on [10].

We use Euclidean distance for uniform vector; edit distance for string, and L-norms for image. When searching, we use 1,000 query for each test case and using the average results of distance calculation. All of excluded middle forest and partition methods use the $m = 0.5$, max radius = $0.7 * \text{max radius of data set}$ (see Fig. 2).

Those results show the difference. The MVP-index using excluded middle partition method always shows lesser calculation times. The difference is small when search radius is small, and it increases with radius increasing. When the radius is lager enough, the difference will be small, that is, because most of the data objects are being searched.

In fact, excluded middle partition method is a partition method which tries to divide data based on the distance from each data object to pivot. Max radius decides the excluded partition's minimum size, and m decides its max size. This partition method wants to use the middle partition to increase the difference of the other two partitions. So these two parameters should not be too small (because it may make this partition method performs like balance partition method). In big data sets, it may cause excluded middle forest to create thousands of trees. For example, there are 1,000 trees; it means that each query needs to calculate distance at least 1,000 times. Because of those, MVP-index always shows better performance in query.

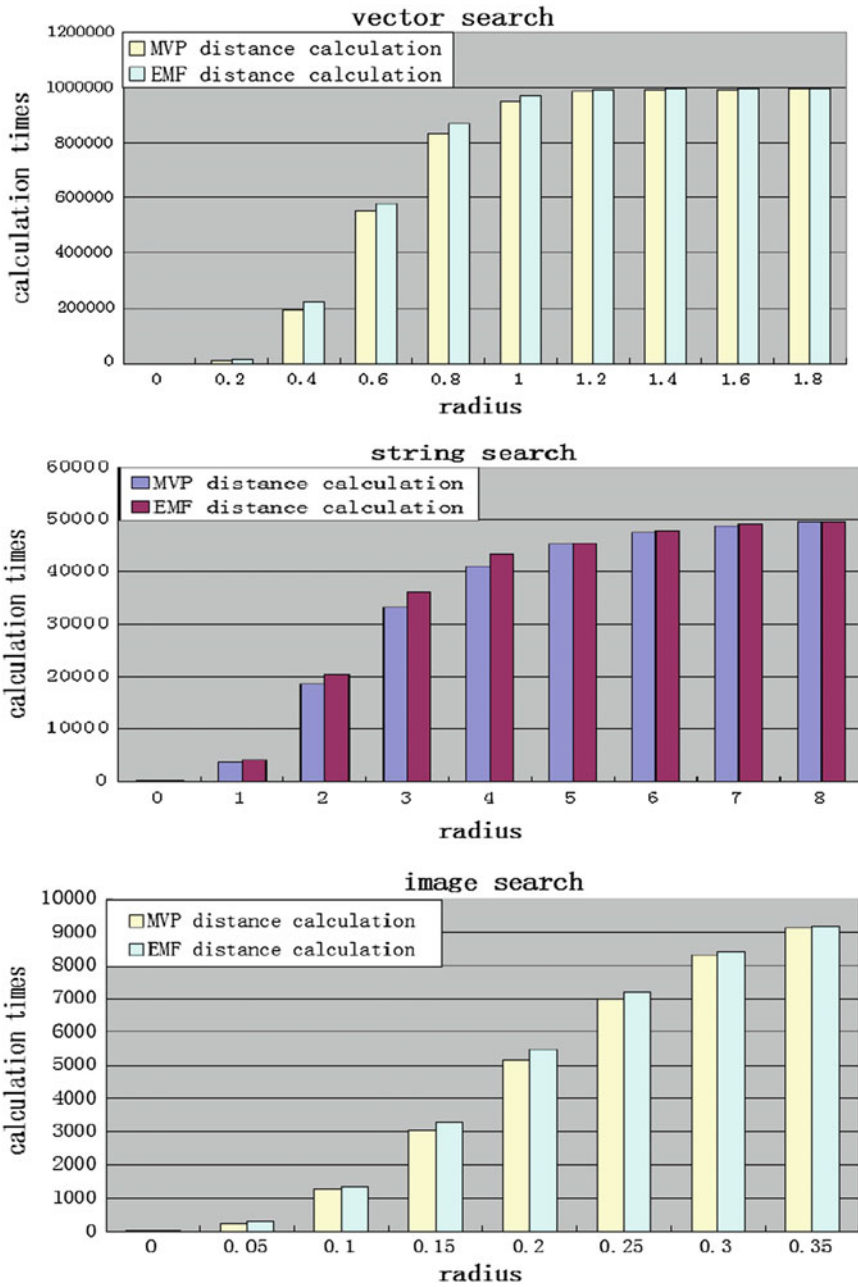


Fig. 2 Test results of vector, string, and image

4 Conclusions and Future Work

We analyze the excluded middle forest and rebuild its partition method in MVP-index, try to find the better data structure when using the same partition method, based on metric space. In our analysis, forest index loses more information than tree index. For gaining this information, forest need more calculation of distance than MVP-index. Actually, because distance-based index lost lots of information when built (but it has higher generality), the partition information is much more important than other index. Little partition information changed may cause great change of distance calculation times.

Condition may be different in parallel indexing. Our next work may try to parallelize the MVP-index using excluded middle partition method and compare it to excluded middle forest. More max radius and m will be tested.

On the other hand, we think the difference of calculation times caused by information loss could not only happen in excluded partition method. It may happen in every forest index. We will test more partition method's performance in MVP-index and forest. We will also try to compare other data structure to MVP-index.

In our test, we are using the excluded partition method, which only has one pivot and three partitions. As described in Sect. 3, this partition method may cause too many trees when used to create a forest. We hope to use more pivots or more partitions of each pivot. It is not only for decreasing number of trees, more pivots and partitions can improve its performance by saving more information into node.

Acknowledgment This research was supported by the following grants: China 863: 2012AA010239; NSF-China: 61170076, U1301252; Shenzhen Foundational Research Project: JCYJ20120613161449764.

References

1. Uhlmann JK (1991) Satisfying general proximity/similarity queries with metric trees. *Inf Process Lett* 40(4):175–179
2. Yianilos P (1999) Excluded middle vantage point forests for nearest neighbor search. In: DIMACS implementation challenge, ALENEX'99, Baltimore, MD
3. Bozkaya T, Ozsoyoglu M (1999) Indexing large metric spaces for similarity search queries. *ACM Trans Database Syst* 24(3):361–404
4. Bozkaya T, Ozsoyoglu M (1997) Distance-based indexing for high-dimensional metric spaces. In: Peckman JM, Ram S, Franklin M (eds) *Proceedings of the ACM SIGMOD international conference on management of data (SIGMOD '97, Tucson, AZ, May 13–15)* ACM Press, New York, NY, pp 357–368
5. Bentley JL (1975) Multidimensional binary search trees used for associative searching. *Commun ACM* 18(9):509–517
6. Xu W, Thompson LP, Miranker DP Empirical evaluation of excluded middle vantage point forest on biological sequences workload. NTSS 2011, Mar 25 2011, Uppsala, Sweden

7. Mao R, Willard LM, Daniel PM (2010) Dimension reduction for distance-based indexing. In: Proceedings of the Third International Conference on Similarity Search and Applications (SISAP2010), pages 25–32, Istanbul, Turkey, September 18–19, 2010
8. SISAP Metric spaces library (2010) http://sisap.org/Metric_Space_Library.html
9. SISAP test suite. http://sisap.org/Metric_Space_Library.html
10. CGeDBIT program. <http://nhpcc.szu.edu.cn/mao/gedbit/index.html>

Research and Simulation of Trajectory Tracking Control Algorithm for Multiwheel Independent Drive Skid Steering Unmanned Ground Vehicle

Yunan Zhang, Yongbao Yan, Nanming Yan and Peng Tian

Abstract In view of performance of multiwheel independent drive skid steering unmanned ground vehicle, this paper describes one kind of improved trajectory tracking control algorithm based on the tracking controller proposed by Kanayama. The ordinate error is introduced to the design of linear velocity, so as to speed up the convergence speed. Moreover, considering the dynamic constraints of vehicle, the constrained control strategy is used to control system to ensure the smooth motion of vehicle. Two PD controllers are used to do closed-loop control for linear velocity and yaw rate so as to ensure the generalized longitudinal driving force and yaw moment. The equivalent distribution method is adopted to distribute longitudinal driving force and yaw moment into the drive torque of six wheels. The simulation results are satisfied.

Keywords Unmanned ground vehicle · Skid steering · Trajectory tracking · PD · Control allocation

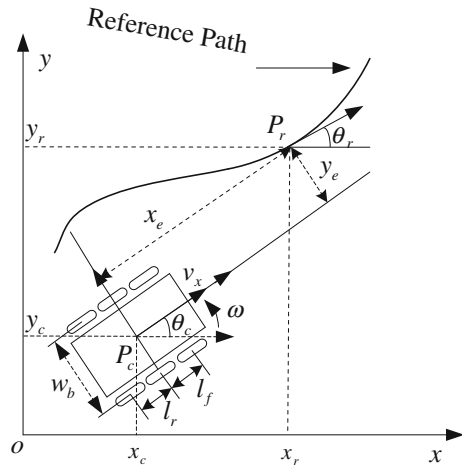
1 Introduction

Recently, diverse unmanned ground vehicles have been developed in order to conduct multitasks such as logistics supports, surveillance, and light combat operation [1].

Skid steering unmanned ground vehicles constitute a genre of nonholonomic vehicles that lack a steering column and are controlled by differential steer mechanism. Absence of a steering column makes them mechanically robust. It is a

Y. Zhang · Y. Yan (✉) · N. Yan · P. Tian
Department of Control Engineering, Academy of Armored Force Engineering,
Beijing, China
e-mail: yyb102@163.com

Fig. 1 Vehicle and coordinate system



kind of multi-input and multioutput nonlinear systems affected by the structured and nonstructured uncertainties, thus increasing the difficulty of its control.

Therefore, trajectory tracking control problem of the nonholonomic vehicle has been valued by scientists around the world.

In recent years, a lot of control methods have been used to solve the vehicle trajectory tracking problems, such as backstepping method [2–4], adaptive method [5], sliding mode method [6], fuzzy control [7, 8].

For the trajectory tracking, smoothing approximation and fast convergence are two important performance indexes. A stable trajectory tracking control law is proposed in [3]. It solves the stability of the trajectory tracking. Literature [4] analyzes the control law in [3]. It illustrates that the control law has some deficiencies in smoothness and convergence speed. There is a certain difficulty in the vehicle’s actual trajectory tracking. In this paper, on the basis of control law of literature [3], the ordinate error is introduced to the design of linear velocity, so as to speed up the convergence speed. Moreover, considering the dynamic constraints of vehicle, constrained control strategy is introduced to control system to ensure smooth motion, Two PD controllers are used to do closed-loop control for linear velocity and yaw rate, so as to ensure the generalized longitudinal driving force and yaw moment. The equivalent distribution method is adopted to distribute longitudinal driving force and yaw moment into the drive torque of six wheels. The simulation results show the effectiveness of the control algorithm (Fig. 1).

2 Vehicle Kinematic Model

There is a skid steering vehicle which is located on a 2D plane in which a global Cartesian coordinate system is defined. The vehicle in the world possesses the three degrees of freedom in its positioning which are represented by a posture

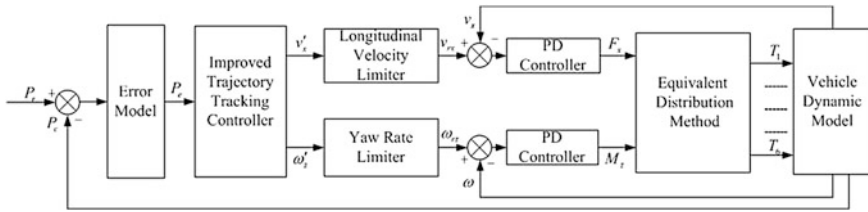


Fig. 2 Control system scheme

$P_c = [x_c \ y_c \ \theta_c]^T$. The heading direction θ_c is taken counterclockwise from x -axis. The vehicle’s motion is controlled by its linear velocity v_x and yaw rate ω , which are also function of time. The vehicle and coordinate system is shown in Fig. 1.

The vehicle’s kinematics equations are defined as:

$$\begin{bmatrix} \dot{x}_c \\ \dot{y}_c \\ \dot{\theta}_c \end{bmatrix} = \begin{bmatrix} \cos \theta_c & 0 \\ \sin \theta_c & 0 \\ 0 & 1 \end{bmatrix} \begin{bmatrix} v_x \\ \omega \end{bmatrix} \tag{1}$$

The reference trajectory is defined by vector $P_r = [x_r \ y_r \ \theta_r]^T$. The heading direction θ_r is taken counterclockwise from x -axis.

$$P_e = \begin{bmatrix} x_e \\ y_e \\ \theta_e \end{bmatrix} = \begin{bmatrix} \cos \theta_c & \sin \theta_c & 0 \\ -\sin \theta_c & \cos \theta_c & 0 \\ 0 & 0 & 1 \end{bmatrix} \begin{bmatrix} x_r - x_c \\ y_r - y_c \\ \theta_r - \theta_c \end{bmatrix} \tag{2}$$

3 Design of Controller and Analysis of Stability

3.1 Design of Controller

Trajectory tracking control problems based on kinematics depend on bounded input v_x and ω . When the vehicle is under any initial error, the reference position $P_r = [x_r \ y_r \ \theta_r]^T$ and the current position $P_c = [x_c \ y_c \ \theta_c]^T$ make the posture error bounded, and $\lim_{t \rightarrow +\infty} \|[x_e \ y_e \ \theta_e]^T\| = 0$. The control system scheme is shown in Fig. 2.

The derivative of the posture tracking errors given in (2) can be written as follows:

$$\dot{P}_e = \begin{bmatrix} \dot{x}_e \\ \dot{y}_e \\ \dot{\theta}_e \end{bmatrix} = \begin{bmatrix} y_e \omega_c - v_c + v_r \cos \theta_e \\ -x_e \omega_c + v_r \sin \theta_e \\ \omega_r - \omega_c \end{bmatrix} \tag{3}$$

The classic kinematic controller is designed as a speed controller based on backstepping method [3].

$$Q = \begin{bmatrix} v'_x \\ \omega'_z \end{bmatrix} = \begin{bmatrix} v_r \cos \theta_e + k_x x_e \\ \omega_r + v_r (k_y y_e + k_\theta \sin \theta_e) \end{bmatrix} \quad (4)$$

where k_x , k_y and k_θ are positive parameters, v_r and ω_r are reference linear velocity and yaw rate.

From the structure of control law (4), we can find something as follows. The adjustment of tracking direction for vehicle mainly depends on the yaw rate, and the elimination of displacement error depends on the linear velocity. The yaw rate is designed based on of the posture errors without considering motion smoothing. The design of the linear velocity only depends on the direction angle error and abscissa error, without considering the ordinate error. If there are ordinate errors, it can be eliminated with combining direction angle and linear velocity. While the control will eventually reach the purpose of eliminating the position errors, but the process is relatively slow, especially abscissa error is smaller, ordinate error is bigger, this characteristic is especially obvious.

We can also find more problems from careful analysis of the control law. The linear velocity will jump suddenly because of a sudden change in the tracking errors in the process of tracking, especially the change of abscissa error.

The jump of velocity is mainly caused by the direct proportion item in the design of linear velocity. Jumping velocity for vehicles or other robots is very bad, and often can cause vehicles or robots judder, even rollover. In addition, jumping velocity puts forward higher requirements on vehicle acceleration performance. If this requirement is beyond the vehicle acceleration ability, the vehicle will not be able to track trajectory well. Moreover, the tracking controller will display the slow convergence speed and exasperate tracking performance. Especially in the early stage of the trajectory tracking, this feature will show quite obvious.

The control law is as follows in this paper:

$$Q = \begin{bmatrix} v'_x \\ \omega'_z \end{bmatrix} = \begin{bmatrix} v_r \cos \theta_e + S \\ \omega_r + v_r (k_y y_e + k_\theta \sin \theta_e) \end{bmatrix} \quad (5)$$

$S = 2k_a \text{sign}(x_e)(1 - 1/\cosh(y_e)) + 2k_x \tanh(x_e)$, where k_x , k_y , k_θ and k_a are positive parameters. $\tanh(x_e)$ is hyperbolic tangent function, $\cosh(y_e)$ is hyperbolic cosine function. Defining sign function as follows:

$$\text{sign}(x_e) = \begin{cases} 1, & x_e \geq 0 \\ -1, & x_e < 0 \end{cases} \quad (6)$$

Considering dynamic characteristic in the process of vehicle movement, if the posture errors are larger, v'_x and ω'_z may be beyond maximum control value. It

will lead to wheel slippage. Therefore, the following control strategy is introduced in control law (5), so as to ensure the smooth movement and avoid wheel slippage.

$$v_{rx} = \int_0^t \text{sat} \left(\frac{dv'_x}{dt} + k_v (v'_x - v_r) \right) dt \tag{7}$$

$$\omega_{rz} = \int_0^t \text{sat} \left(\frac{d\omega'_z}{dt} + k_\omega (\omega'_z - \omega_r) \right) dt \tag{8}$$

k_v and k_ω are positive parameters. v_{rx} and ω_{rz} are limited longitudinal velocity and yaw rate, respectively. v'_x and c are previous longitudinal velocity and yaw rate, respectively.

Two PD controllers are designed for longitudinal velocity and yaw rate. They determine the generalized longitudinal driving force and yaw moment to achieve vehicle motion. Based on multiwheel independent driving and skid steering, the equivalent distribution method can be expressed as follows:

$$T_i = \begin{cases} \frac{0.5w_b F_x + M_z}{w_b} r, & i = 2, 4, 6 \\ \frac{0.5w_b F_x - M_z}{w_b} r, & i = 1, 3, 5 \end{cases} \tag{9}$$

where r is the radius of tire. w_b is the tread, which is the distance between the left and right wheels.

4 Analysis of Stability

Theorem 1 *Assumption:* $v_r > 0$, the control law is (5), then $P_e = 0$ is stable point.

Proof Choose the following Lyapunov function:

$$V = \frac{x_e^2}{2} + \frac{y_e^2}{2} + \frac{1 - \cos \theta_e}{k_y} \tag{10}$$

Apparently, $V \geq 0$. If and only if for $x_e = 0, y_e = 0, \theta_e = 0$, the $V = 0$. The time derivative of V results in

$$\begin{aligned}
\dot{V} &= \dot{x}_e x_e + \dot{y}_e y_e + \frac{\sin \theta_e}{k_y} \dot{\theta}_e = x_e (y_e \omega_c - v_c + v_r \cos \theta_e) \\
&\quad + y_e (-x_e \omega_c + v_r \sin \theta_e) + \frac{\sin \theta_e}{k_y} (\omega_r - \omega) \\
&= -k_x x_e \tanh x_e - \frac{k_\theta}{k_y} v_r \sin^2 \theta_e \\
&\quad - k_a \operatorname{sign}(x_e) x_e \left(1 - \frac{1}{\cosh y_e} \right) \leq 0
\end{aligned} \tag{11}$$

Therefore, V is a Lyapunov function, proof is over.

Theorem 2 *Assumption:* (1) v_r and ω_r are continuous; (2) let \dot{v}_r and $\dot{\omega}_r$ be so small; (3) v_r , ω_r , k_x , k_y , k_θ , and k_a are bounded; (4) if $x_e \omega_r > 0$, the $k_a(1 - 1/\cosh(y_e)) < |\omega_r|$. Then $P_e = 0$ is asymptotically stable for all $t \in (0, +\infty)$.

Proof By substituting (5) into (3), we can linearize (3) nearby $P_e = 0$, it yields

$$\dot{P}_e = AP_e \tag{12}$$

where:

$$A = \begin{bmatrix} -k_x & \omega_r - k_a \operatorname{sign}(x_e) (1 - 1/\cosh y_e) & 0 \\ -\omega_r & 0 & v_r \\ 0 & -v_r k_y & -v_r k_\theta \end{bmatrix}$$

Assumption: the characteristic equation of A is

$$a_3 s^3 + a_2 s^2 + a_1 s + a_0 = 0 \tag{13}$$

where:

$$\begin{aligned}
a_3 &= 1 \\
a_2 &= k_\theta v_r + k_x \\
a_1 &= k_x k_\theta v_r + k_y v_r^2 + \omega_r^2 - k_a \omega_r \operatorname{sign}(x_e) \left(1 - \frac{1}{\cosh y_e} \right) \\
a_0 &= k_x k_y v_r^2 + k_\theta v_r \left[\omega_r^2 - k_a \omega_r \operatorname{sign}(x_e) \left(1 - \frac{1}{\cosh y_e} \right) \right]
\end{aligned}$$

Apparently $a_i > 0$, and then $a_1 a_2 - a_0 a_3 > 0$. According to Hurwitz criterion, all roots of characteristic equation have negative real part, proof is over.

Compared with the control law in [3]: first, the correlation ordinate error item $2k_d \text{sign}(x_e)(1 - 1/\cosh(y_e))$ is introduced to the control law in this paper. The change of ordinate error is limited to $[0, 1)$ based on the characteristic of hyperbolic cosine function. The characteristic of hyperbolic cosine function prevents it from jumping sharp nearby zero and affecting the precision of the tracking under the condition of the abscissa error changed near the zero and ordinate error bigger. Second, in the design of control law, the item $k_x x_e$ is replaced with the item $2k_x \tanh(x_e)$, then the range of the item $k_x x_e$ is changed from the original $(-\infty, +\infty)$ to $(-2k_x, 2k_x)$. This replacement can prevent the output linear velocity of controller exceeding desired speed. By comparing the function features of $k_x \tanh(x_e)$ with $k_x x_e$, we can find that in the initial stage of trajectory tracking, the former is in line with the actual situation of trajectory tracking more than the latter.

5 Simulation and Analysis

In this paper, vehicle dynamic model is developed using “MATLAB SIMULINK” in order to analyze tracking performance of skid steering vehicle and conduct a numerical simulation studies. Tire model in the driving system is designed using a Pacejka tire model. The dynamic model has 12 degrees of freedom (DOF) with the dynamic equations of sprung mass, including translational motions (longitudinal, lateral, vertical), rotational motions (roll, pitch, yaw) and rotational motions of six wheels. Assumption: the center of gravity for vehicle is located at geometrical center. The vehicle is moving on the horizontal plane. The parameters of vehicle are chosen as: the tire-road friction coefficient is $\mu = 0.85$, $m = 1700$ kg, $I_z = 1800$ kg·m², $l_f = 0.85$ m, $l_m = 0$, $l_r = 0.85$ m, $w_b = 1.4$ m, $r = 0.368$ m.

5.1 Simulation of Trajectory Tracking Based on Kinematics

(1) Trajectory tracking of circular arc.

The radius of reference circular arc trajectory is 4 m. The reference linear velocity and yaw rate are $v_r = 2.5$ m/s, $\omega_r = 0.625$ rad/s. The initial position of the reference trajectory is $[4, 0, \pi/2]$, the actual vehicle starts at $[3, -2, \pi/4]$. The parameters of controller are chosen as: $k_x = 5$, $k_y = 13$, $k_\theta = 5$, $k_a = 10$.

(2) Trajectory tracking of line.

The reference linear velocity and yaw rate are $v_r = 2.5$ m/s, $\omega_r = 0$. The initial position of the reference trajectory is $[-5, -5, \pi/4]$, the actual vehicle starts at $[-5, -7, \pi/2]$. The parameters of controller are chosen as: $k_x = 5$, $k_y = 13$, $k_\theta = 5$, $k_a = 10$.

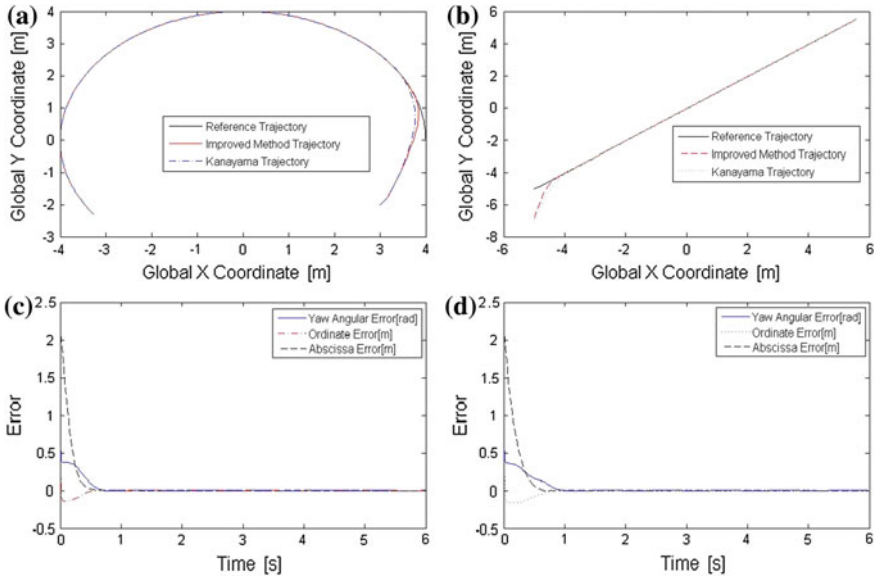


Fig. 3 Simulation of trajectory tracking based on kinematics: **a** trajectory tracking of *circular arc*, **b** trajectory tracking of *line*, **c** posture errors of *circular arc* using the improved method, **d** posture errors of *circular arc* using Kanayama method

The simulation results are shown in Fig. 3. We can see that the improved algorithm in this paper has better tracking capability. The results show that the algorithm accelerates the approximation of the initial tracking stage and makes the tracking more rapid and accurate.

5.2 Simulation of Trajectory Tracking Based on Dynamics

The reference trajectory: (1) $t \in [0\ 20]$ s, the reference trajectory is line, its slope is $\pi/4$. The reference linear velocity and yaw rate are $v_r = 3$ m/s, $\omega_r = 0$; (2) $t \in [20\ 72]$ s, the reference trajectory is circular arc, its radius is 28.57 m. The reference linear velocity and yaw rate are $v_r = 2$ m/s, $\omega_r = 0.07$ rad/s. The initial position of the reference trajectory is $[3, 3, \pi/4]$, the actual vehicle starts at $[0, -2, \pi/3]$. The parameters of controller are chosen as: $k_x = 1, k_y = 0.35, k_\theta = 0.25, k_a = 2$.

The posture errors of trajectory tracking are converged in Fig. 4e. The convergence speed of the abscissa error is lower, but it is converged finally and the asymptotic stability of the closed loop system is guaranteed. The actual velocity and yaw rate can rapidly track linear velocity and yaw rate of controller.

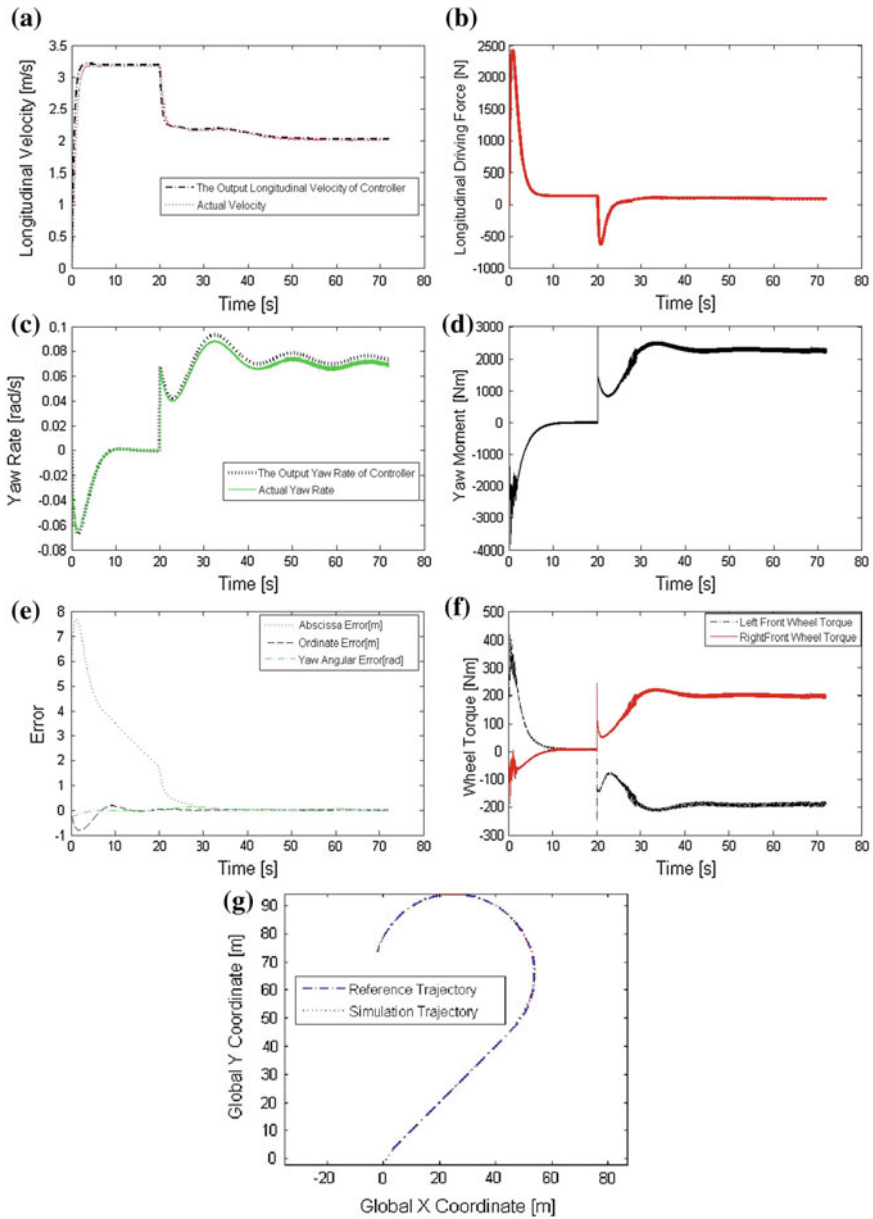


Fig. 4 Simulation of trajectory tracking based on dynamics: **a** longitudinal velocity, **b** longitudinal driving force, **c** yaw rate, **d** yaw moment, **e** tracking posture errors, **f** wheel driving torque, **g** vehicle trajectory

6 Conclusions

Considering the problems of the tracking control algorithm proposed by Kanayama, this paper puts forward an improved control algorithm and analyzes the stability. The impact of ordinate error is introduced to the control law. The improved control algorithm is simulated based on kinematic model. The results show that the algorithm accelerates the approximation of the initial tracking stage and makes the tracking more rapid and accurate. Then, the algorithm is applied to multiwheel independent drive skid steering unmanned ground vehicle. Moreover, considering the dynamic constraints of vehicle, the constrained control strategy is introduced to control system to ensure smooth motion. Two PD controllers are used to do closed-loop control for linear velocity and yaw rate, so as to ensure the required longitudinal driving force and yaw moment. The equivalent distribution method is adopted to distribute longitudinal driving force and yaw moment into the drive torque of six wheels. The simulation results show the tracking control algorithm is available. The vehicle can well track the desired trajectory.

References

1. Kang J, Kim W, Lee J, Yi K (2010) Skid steering-based control of a robotic vehicle with six in-wheel drives. *Proc IMechE Part D: J Autom Eng* 224:1369–1391
2. Fierro R, Lewis F-L (1998) Control of a nonholonomic mobile robot using neural networks. *IEEE Trans Neural Networks* 9(4):589–600
3. Kanayama Y, Kimura Y, Miyazaki F, Noguchi T (1990) A stable tracking control method for an autonomous mobile robot. In: *Proceedings of the 1990 IEEE international conference on robotics and automation*. Cincinnati, OH, USA. IEEE, pp 384–389
4. Li K, Wang S, Guo Z (2008) Adaptive trajectory tracking control method of mobile robot. *J Syst Simul* 20(10):2575–2579
5. Dong W, Kuhnert K-D (2005) Robust adaptive control of nonholonomic mobile robot with parameter and nonparameter uncertainties. *IEEE Robot* 21(2):261–266
6. Park B-S, Yoo S-J, Park J-B, Choi Y-H (2009) Adaptive neural sliding mode control of nonholonomic wheeled mobile robots with model uncertainty. *IEEE Trans Control Syst Technol* 17(1):207–214
7. Das T, Kar I-N (2006) Design and implementation of an adaptive fuzzy logicbased controller for wheeled mobile robots. *IEEE Trans Control Syst Technol* 14(3):501–510
8. Yu S-H, Liu S, Xu H (2008) Adaptive fuzzy trajectory-tracking control of uncertain nonholonomic mobile robots. In: *Proceedings of the IEEE international conference on industrial informatics (INDIN 2008) DCC*, Daejeon, Korea, pp 481–486

A Fast Association Rule Mining Algorithm for Corpus

Shankai Yan and Pingjian Zhang

Abstract In this paper, we propose a new algorithm for mining association rules in corpus efficiently. Compared to classical transactional association rule mining problems, corpus contains large amount of items, and what is more, there are by far more item sets in corpus, and traditional association rule mining algorithm cannot handle corpus efficiently. To address this issue, a new algorithm, which combines the techniques of inverted hashing and the advantage of FP-Growth structure, is designed with enough considerations on the characteristic of corpus. Experimental results demonstrate that the new algorithm has gained a great promotion on performance.

Keywords Text mining · Association rules · Inverted hashing · Apriori algorithm

1 Introduction

Due to the nature of textual data and the broad potential applications, association rule mining in text corpora has attracted the attention of the research scientific community for years. Mining association rules in corpus has been demonstrated to be useful and technically feasible in several application areas like building Statistical Thesaurus, building Latent Semantic Indexing [1], retrieving documents [2], analyzing links among documents [3], and reading recommendations [4].

Qiu et al. [5], have taken into account the weights and semantics and generated enhanced association rules that has richer semantics. Woon et al. [6], discussed

S. Yan (✉) · P. Zhang

School of Software Engineering, South China University of Technology,
Guangzhou, People's Republic of China
e-mail: dawnyesky@gmail.com

P. Zhang

e-mail: pjzhang@scut.edu.cn

how to mining concepts via association rules in corpus. Fuzzy methods are introduced in [7] to improve accuracy. Liu and Hu [8], sentential frequent itemsets are adopted to classify documents.

The focus of this research is the efficiency of association rule mining algorithms. Compared to classical transactional association rule mining problems, corpus contains large amount of items and by far more item sets. The complexity of mining association rules increase greatly as the dimensions of feature grows. Hence, how to quickly find out the association rules in text data set becomes a challenging issue in text mining.

Let $D = \{i_1, i_2, \dots, i_m\}$ be a document consisting of m features, which are obtained through the process of text preprocessing, word splitting, and feature selection. Let T be a set of documents and $W = \{i_1, i_2, \dots, i_n\}$ be a set of items, where each document D is a set of items, such that $D \subseteq W$. An association rule is an instance of the form $X \implies Y$, where $X \subset D$, $Y \subset D$, and $X \cap Y = \phi$. The association rule $X \implies Y$ holds in the text data set T with confidence $c\%$ if $c\%$ of the documents in T contains X and Y simultaneously. The rule $X \implies Y$ has support $s\%$ if $s\%$ of documents in T contains $X \cup Y$. Mining association rules is to find all $X \implies Y$ that with support and confidence greater than or equal to the user-specified minimum value.

To date, there have been several association rules mining algorithms such as Apriori [9], Direct Hashing and Pruning (DHP) [10], FP-Growth [11], etc. And lots of variations on the classical algorithms have been proposed by other researchers, for instance, M-Apriori, M-DHP [1], and so on. Moreover, some of them have been implemented in a parallel form [12] to improve efficiency.

It is commonly recognized in the information retrieval community that words rarely appear in differentiating documents, and furthermore, those words occur in a great amount of documents [13]. Hence, it is reasonable to conclude that the frequent item sets consist of highly frequent words would have a much lower support compared to the transaction data set. Moreover, the number of items in transaction data set is stable, whereas it is substantial and diversified in text data set. This increases the complexity of mining association rules in text data set with the previous classical algorithms.

In this paper, a new algorithm, which combines the techniques of inverted hashing and the advantage of FP-Growth structure, is proposed. Section 2 contains the analysis and design of the new algorithm, and Sect. 3 contains experimental design and results discussions. Further conclusions are contained in Sect. 4.

2 Hash Index Apriori

Due to the difference in characteristics between text and transaction data set, the well-played association rules mining algorithms are not suitable for text data set. Apriori is not appropriate for mining frequent item sets on text data set because of the high memory space requirement for counting the occurrences of a large

number of candidate item sets. DHP needs extra memory space to store the hash table, which has a large number of word entries. That would also cause a large memory usage, which will slow down the machine due to the resource race. But the idea of using hash technology to pruning is bright, which ignores generating the candidate item sets. FP-Growth does a good job on transaction data set, extremely on the dense item set. It means that most of the items have a high support in the data set. Therefore, the data structure of FP-Growth spends less memory space. Meanwhile, it takes less time to traversal the whole data set because the data is compressed into the FP-Tree [14] data structure. On the other hand, when dealing with text data set, FP-Growth will generate a tremendous FP-Tree for the reason that the items have a low support. But the method of data compressing is meritorious, which will improve the whole efficiency.

2.1 Inverted Hash Index

With consulting the good design of DHP and FP-Growth, we propose HI-Apriori based on Apriori. It uses a hash table to store inverted index of document on the words it contains. We can directly delete the entry with support less than the threshold. Following the process framework of Apriori, we can judge an item set whether it is frequent simply by counting the common index of the items inside. Even though we require extra space to store the hash table, we need not keep the candidate item sets in memory. Here is an example; there are five documents with several words (Fig. 1).

document1: {Beijing, London, Seoul}
 document2: {London, Tokyo, Berlin}
 document3: {Beijing, Seoul, Berlin}
 document4: {Beijing, London, Berlin}
 document5: {Beijing, Berlin}

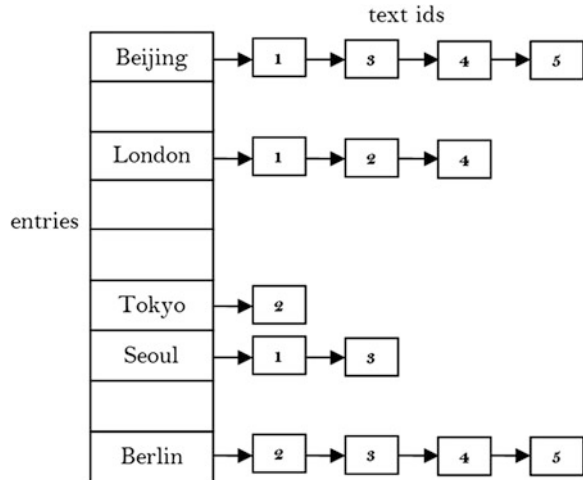
Then we build the inverted hash index for the text data set above.

2.2 Optimize Join Strategy

While joining $F_k \times F_k$ in Apriori for generating candidate item sets to calculate the frequent $(k + 1)$ -item sets, the most frequent operation is prefix matching. If the atomic compare operation is complicated or the amount of comparison is substantial, it will take lots of time at this stage, which will become the bottleneck of the algorithm.

Hence, we come up with a join strategy based on the hash technology. Let $X_{k1} = \{i_{11}, i_{21}, \dots, i_{k1}\}$ be the item set, which need to join later on. Let L_k be a set of item sets, consisting of frequent k -item sets. Let $P_{k1} = \{i_{11}, i_{21}, \dots, i_{(k-1)1}\}$ and

Fig. 1 Example of an inverted hash index



put P_{k1} into a tuple. To insert X_{k1} into the open hash table, we treat P_{k1} as the key and i_{k1} as the value. If the hash conflict cannot be resolved, we union the i'_k and i_k as the value of this entry. After processing all the itemsets in L_k , we can derive new $(k + 1)$ -itemsets from each entry of the hash table by concatenating key and the 2-tuple combinations of the value tuple.

With the assistance of hash technology, we only require a few join on 1-item set, and then concatenate the prefix and the join result. This method can not only reduce the join time, but also improve the whole efficiency of the algorithm.

2.3 HI-Apriori

Given a set of documents, HI-Apriori first splits texts into words with word segmentation tool, and then removes stop words and words with low information. After that it builds the inverted hash index and begins to generate frequent item sets. Finally, it derives the association rules from the frequent item sets just like Apriori does. Here is the main procedure of HI-Apriori.

Main procedure:

Input: texts[]. Output: rules[].

- (1) word_list = ϕ
- (2) index = **build_hash_index**(texts, word_list)
- (3) frequent_itemsets = **hi_apriori**(index, word_list)
- (4) put association rules derived from frequent itemsets into rules[]
- (5) **return** rules[]

The new algorithm we proposed only requires one time database scan. Moreover, it need not generate candidate item sets or count item sets. However, we still need to estimate whether a potential item set is frequent as the algorithm is based on Apriori. We implement this process as a filter pattern, which is the core of HI-Apriori.

The filter firstly uses some general pruning method onto the previous generated frequent item sets [15]. Secondly, it uses the hash technology mentioned earlier to estimate whether the item set is frequent. These two stages are in the same processing flow without any intermediate storage. It only needs the extra memory space to store the hash table.

The details of HI-Apriori algorithm are presented below:

First of all, we call `build_hash_index(texts, word_list)` to put the words into `word_list` and generate inverted hash index.

procedure **build_hash_index**(texts, word_list)

- (1) **for each** text in texts **do begin**
- (2) words = **parse**(text);
- (3) **for each** word in words **do begin**
- (4) **if** word has been recorded **then**
- (5) put text_id into the list behind word and increase the count of the word;
- (6) **else** insert word into hash table and put text_id into the list behind word;
- (7) **return** hash table

Secondly, we can find out all the frequent itemsets by the word list and inverted hash index.

procedure **hi_apriori**(index, word_list)

- (1) **for each** word in word_list **do begin**
- (2) **if** count of word entry is less than min support **then**
- (3) delete the word from the word_list
and the corresponding entry in the hash table;
- (4) $F_1 = \cup$ each word in word_list;
- (5) **for** itemset dimension k from 2 to n **do begin**
- (6) $F_k = \phi$;
- (7) **for each** k-itemset in $F_{k-1} \times F_{k-1}$ **do begin**
- (8) **if filter**(k-itemset) **then**
- (9) $F_k \cup$ k-itemset;
- (10) **return** $\cup F_n$

procedure **filter**(k-itemset)

- (1) **for each** (k-1)-itemset in k-itemset **do begin**
- (2) **if** (k-1)-itemset is not frequent **then**
- (3) **return** false;
- (4) **if** index.get_intersect_count(k-itemset) < min support **then**
- (5) **return** false;
- (6) **else return** true;

The method `get_intersect_count(k-itemset)` use the inverted hash index to calculate the co-occurrence of the items in k -itemset for the purpose that judging the k -itemset is frequent. According to the principle of intersect set calculating, the method is described as:

procedure `get_intersect_count(k-itemset)`

- (1) `cur_min` = the first node in the list of k -itemset index entry with the minimum `text_id`
- (2) **comment:** Due to the inserting point of the list of index entry is at the head of the list, `text_id` is in the decreasing order
- (3) **for each** item in k -itemset **do begin**
- (4) put the first node of the list of item index entry into pointers list `ptrs[]` to present the current position of the list;
- (5) `intersect_count` = 0;
- (6) **while** none of the list reach the end **do begin**
- (7) move along all the pointers of list except `cur_min` to make the `text_id` of all the lists' current place equal;
- (8) `intersect_count++`;
- (9) `cur_min` = the node after current place with the minimum `text_id` among all the lists;
- (10) **return** `intersect_count`;

3 Experiments and Analysis

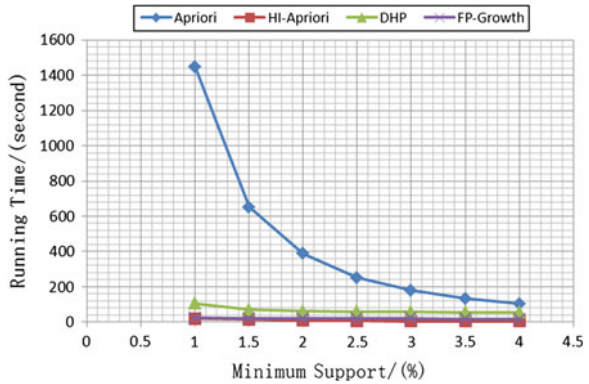
Corpus: the sogou corpus [16]. We choose eight classes of sogou corpus: sports, military, medical care, education, travel, technology, economic, and art. Because of the huge amount of sogou corpus, this experiment just randomly pick up 60+ documents in each class to obtain 500 documents in total as training set, each of which has 1,500 words on average.

Some experiments are carried out on the corpus using several association rules mining algorithms, Apriori, DHP, FP-Growth, and HI-Apriori. All these test runs were made on a machine with 2.0 GHz AMD Athlon(tm) 64 × 2 Dual Core Processor 5,200+ and 2G of DDRII memory.

Experiment I We compared HI-Apriori with Apriori, DHP, and FP-Growth on 200 medium-length documents to find out frequent 2-item sets.

From Fig. 2, it is obvious that Apriori is exploding when the minimum support is less than 2 %. DHP, FP-Growth and HI-Apriori also perform well on mining frequent 2-item sets with a low minimum support. Nevertheless, if we try to mine frequent 3-item sets, DHP and FP-Growth will make the system thresh when the minimum support decrease to 3.5 %. But HI-Apriori can still handle the problem well while the minimum support decrease.

Fig. 2 Use Apriori, DHP, FP-Growth and HI-Apriori to mine frequent 2-itemsets with different minimum support



Experiment II This experiment compared HI-Apriori with Apriori, DHP, and FP-Growth, respectively, to show which aspect HI-Apriori is superior to them.

- (i) We randomly picked up 200 documents to test the performance of HI-Apriori and Apriori on mining frequent 3-item sets with different minimum support.

From Fig. 3, we can see that even though the performance of HI-Apriori is close to Apriori with the high minimum support, HI-Apriori make a great improvement when the minimum support is less than 4 %. To find out frequent k-item sets, Apriori need to scan the data set k times and store the candidate item sets before counting each dimension of frequent item sets. However, HI-Apriori can directly derive the frequent item sets by calculating the intersecting set of the item entries on inverted hash index, which will save more time and memory space.

- (ii) We chose 50 short documents the difference of performance between HI-Apriori and DHP on mining frequent 3-item sets with different minimum support.

From Fig. 4, we can observe that the performance of DHP has a similar trend with HI-Apriori. We choose short documents for the reason that we can treat the data object as if it is a transaction data. We can derive from the result that DHP can be efficient on transaction data set or short documents. However, DHP slows down when the documents become feature-length or mining three or higher frequent item sets. It is because DHP will generate all the subset of the candidate item sets that it takes a long run as generating the candidate item sets does. Nevertheless, HI-Apriori has a better performance both on short and long documents. Meanwhile, HI-Apriori can run efficiently even though on mining high dimension frequent item sets with low minimum support.

- (iii) This experiment compared HI-Apriori with FP-Growth on mining frequent 2-item sets among different document quantity. We made the minimum support to be 5 %.

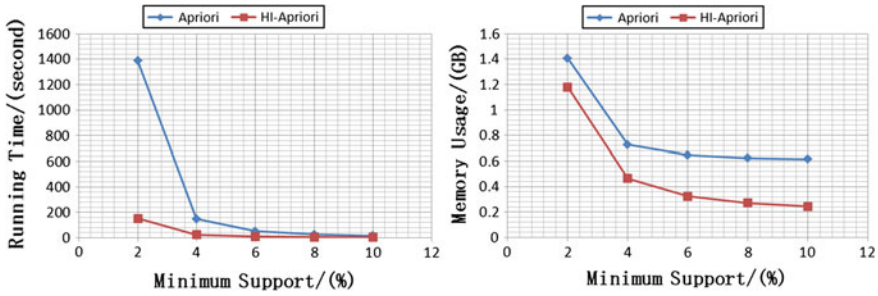


Fig. 3 Use Apriori and HI-Apriori to mine frequent 3-itemsets

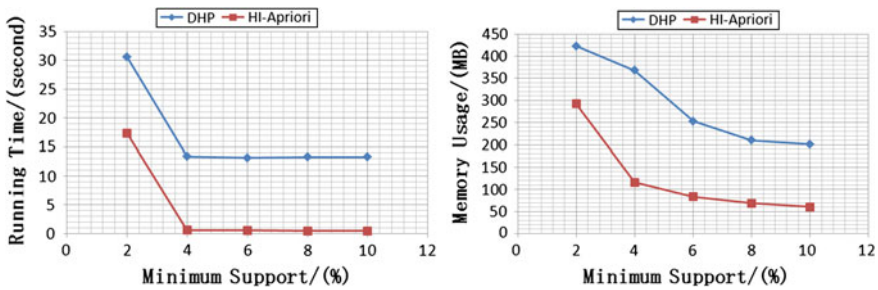


Fig. 4 Use DHP and HI-Apriori to mine frequent 3-itemsets

From Fig. 5, we can see that when mining on less than 40 documents, FP-Growth performs great as well as HI-Apriori even FP-Growth is better. However, when the document quantity increases to 50 FP-Growth, it becomes more time-consuming so that it cannot continue when it rises to 120. In contrast, HI-Apriori keeps the running time short all along even though there is a little bit instability. The reason of this phenomenon is that the characteristic of text data set makes the FP-Tree become higher and holding more branches. Hence, the iterate stack in memory of the FP-Tree becomes giant when the minimum support is less than 5 % or the feature of documents is more than 100.

Experiment III This experiment test HI-Apriori with different parameter and input to observe the scalability of HI-Apriori in diverse situation.

- (i) We let HI-Apriori mine frequent 2-item sets and 3-item sets under a fix minimum support so that we can observe the trend of running time as the document quantity increases.
- (ii) We let HI-Apriori mine frequent 2-item sets and 3-item sets on 500 documents with different minimum support. The object of this experiment is to observe the trend of performance change when the minimum support decreases.

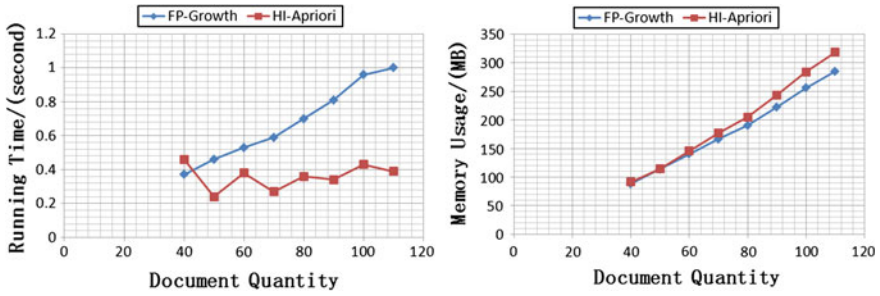


Fig. 5 Use FP-Growth and HI-Apriori to mine frequent 3-itemsets

Fig. 6 Mine frequent itemsets on different document quantity

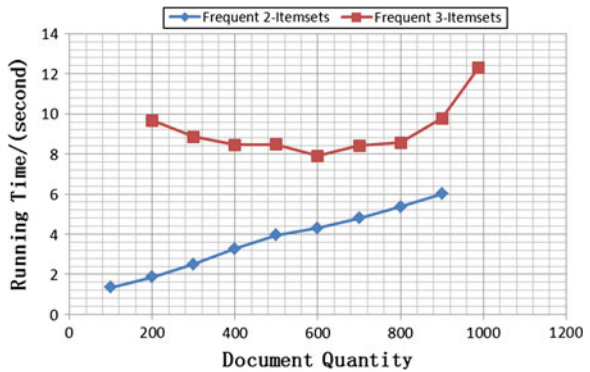
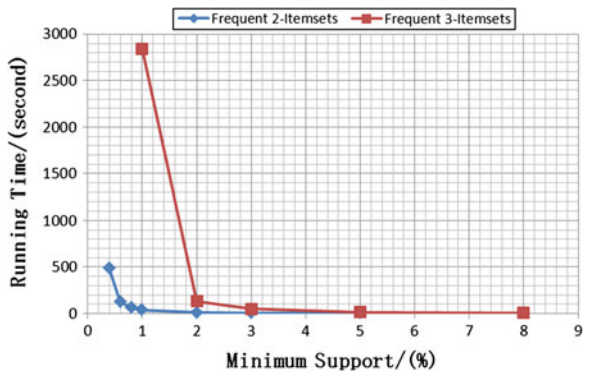


Fig. 7 Mine frequent itemsets with different minimum support



From Fig. 6, it is clear that running time is growing steadily when mining frequent 2-item sets, but it is presented mining frequent 3-item sets has a little bit destabilizing. Because the internal design of the hash table is not appropriate enough to keep it robust, for instance, the hash function and conflict handler.

From Fig. 7, we can see that when minimum support is greater than 2 %, HI-Apriori runs efficiently. However, the running time grows exponentially while the minimum support is less than 2 %. Maybe it is the bottleneck of HI-Apriori on larger data set or distributed database [17] and with lower minimum support.

4 Conclusion

In this paper, a new association rules mining algorithm that takes advantages of inverted hash index and FP-grow tree structure is proposed. Sparse data set like corpus can be handled efficiently by utilizing the advantage of inverted hash index. Moreover, the new algorithm needs to scan the data set only once and does not need to generate large amount of candidate item sets. Experiments show that the new algorithm outperforms existing ones in both efficiency and memory usage.

References

1. H JD, Chung SM (2001) Multipass algorithms for mining association rules in text databases. *Knowl Inf Syst* 3(2):168–183
2. Holt JD, Chung SM, Li Y (2008) Usage of mined word associations for text retrieval. In: 19th IEEE international conference on tools with artificial intelligence, pp 45–49
3. Li G, Zhang X, Yoo I, Zhou X (2009) A text mining method for discovering hidden links. In: IEEE international conference on granular computing, GRC, pp 326–328
4. Zhu Z, Wang J-Y (2007) Book recommendation service by improved association rule mining algorithm. In: Proceedings of 2007 international conference on machine learning and cybernetics, vol 1–7, pp 3864–3869
5. Qiu J, Tang C, Zeng T, Qiao S, Zuo J, Chen P, Zhu J (2007) A novel text classification approach based on enhanced association rule. *Lect Notes Comput Sci* 4632:252–263 (LNAI)
6. Wong MK, Abidi SSR, Jonsen ID (2011) Mining non-taxonomic concept pairs from unstructured text: a concept correlation search framework. In: WEBIST 2011—proceedings of the 7th international conference on web information systems and technologies, pp 707–716
7. Chun-Ling C, Frank T, Tyne L (2009) An integration of fuzzy association rules and WordNet for document clustering. *Lect Notes Comput Sci* 5476, pp 147–159 (LNAI)
8. Liu S-Z, Hu H-P (2007) Text classification using sentential frequent itemsets. *J Comput Sci Technol* 22(2):334–337
9. Agrawal R, Srikant R (1994). Fast algorithms for mining association rules. In: Proceedings of the 20th VLDB Conference, pp 487–499
10. Park S, Chen MS, Yu PS (1997) Using a hash-based method with transaction trimming for mining association rules. *IEEE Trans Knowl Data Eng* 9(5):813–825
11. Kamber M, Han J (2000) *Data mining: concepts and techniques*. Morgan Kaufmann, USA
12. Holt JD, Chung SM (2007) Parallel mining of association rules from text databases. *J Supercomput* 39(3):273–299
13. Holt JD, Chung SM (2002) Mining association rules in text databases using multipass with inverted hashing and pruning. In: 14th IEEE international conference on tools with artificial intelligence, proceedings, pp 49–56
14. Han J, Pei J, Yin Y, Mao R (2004) Mining frequent patterns without candidate generation: a frequent-pattern tree approach. *Data Min Knowl Disc* 8(1):53–87

15. Pasquier N, Bastide Y, Taouil R, Lakhal L (1999) Efficient mining of association rules using closed itemset lattices. *Inf Syst* 24(1):25–46
16. The Sogou corpus, The R&D Center of SOHU. <http://www.sogou.com/labs/dl/t.html>
17. Cheung DW, Ng VT, Ada WF (1996) Efficient mining of association rules in distributed databases. *IEEE Trans Knowl Data Eng* 8(6):911–922

Research and Development of Ultrasonic Power with Frequency Auto-tracing System and Power Auto-controlling System

Xinxing Tang and Dongquan Zhang

Abstract With the rapid development of the electronic technology and the material technology, ultrasonic technology with high power is more widely applied to material processing than ever before. In this paper, an ultrasonic power system was researched and developed according to its components. An optimized and improved solution was raised to realize the stabilities and reliabilities of the whole power system. With the support of the optimized hardware design, a simplified and efficient software framework based on embedded technology was developed to cooperate with the hardware system. Some experiments were taken to research the characteristics of the transformer, which is an important part in the ultrasonic power system. And the experiments prove that proper air gap size to the transformer magnetic core is able to aggrandize the capability of resisting bias.

Keywords Material processing · Ultrasonic power · Frequency auto-tracing · Power auto-controlling · Transformer air gap

1 Introduction

Ultrasonic machining is a new technology that applies the theory that ultrasonic vibration energy can make some physical or chemical characteristics or states of a substance to change instantaneously to material processing. Ultrasonic machining now is applied widely to processing hard and brittle materials like engineering ceramics, glass quartz, diamond and silicon, and so on, which are hard to be

X. Tang (✉) · D. Zhang
Beijing Jiaotong University, Beijing, China
e-mail: 11121551@bjtu.edu.cn

D. Zhang
e-mail: dqzhang@bjtu.edu.cn

processed with classical cutting tools. Ultrasonic machining is also able to processing nonconducting materials. Ultrasonic machining shows its unique advantages of high precision of processing and wide range of usage. Ultrasonic generator or ultrasonic power is an important part in ultrasonic machining device, by which the ultrasonic signal provides energy to an ultrasonic transducer [1]. The working situation of the transducer associates closely with the stability of the ultrasonic power output and the precision of feedback control, which will finally affect the quality of material processing. This paper improves the stability and reliability of ultrasonic power via improving hardware design and therefore simplifying of software algorithm.

An ultrasonic machining system includes an ultrasonic power and a transducer system [1]. The transducer system transforms high-frequency electrical signal to ultrasonic vibration signal on the same frequency, which completes the conversion from electrical energy to ultrasonic mechanical energy. When the frequency of the electric signal of the ultrasonic power equals to the resonant frequency of the transducer, the ultrasonic wave generated from the transducer gets maximum efficiency on the work-piece after being amplified by an ultrasonic horn. While the transducer is working, the resonant frequency of the transducer will drift for the change of some facts such as temperature, load force, and so on. In order to guarantee the transducer's maximum efficiency, the ultrasonic power has to adjust the frequency of its output to trace the resonant frequency of the transducer, which is called frequency auto-tracing [2].

According to the characteristics of the ultrasonic transducer, the ultrasonic power generally consists of a controllable rectifier, a high-frequency inverter, a matching circuit, a control subsystem, a power feedback subsystem, and a phase feedback subsystem, as shown in Fig. 1.

The earliest ultrasonic power used analog circuits, whose dynamic response is slow, and control precision is low, and it is easy to age. As the digital technology develops, digital circuit gradually substitutes analog circuit. Digital circuit is able to eliminate many shortcomings like temperature drift, which are difficult to be overcome for analog circuits; it also can reduce the quantities of the components and simplify the hardware structure so as to increase the reliability of the system [2].

Weixiang et al. from North China Electric Power University [3] used to get frequency-adjustable periodic square wave generated by Pulse Frequency Modulation channel that consists of D/A convert, voltage-controlled square wave signal generator, and dead time generating circuit to control the switching of the transistor in order to adjust the frequency of the power. They also used buck D.C. chopper to adjust the output power of the power device. The researchers from Jiangsu University of Science and Technology [4] applied step size variable policy and PID algorithm to two closed-loop control, which made the power better to drive the ultrasonic vibration load and feature wide frequency tracking range and strong load suiting ability.

Frequency tracking is a very important part in the ultrasonic power system, on which the researches goes on all the time [2]. From 1970 to 1980s, the researchers in Soviet Union made a great progress on frequency auto tracking. In the

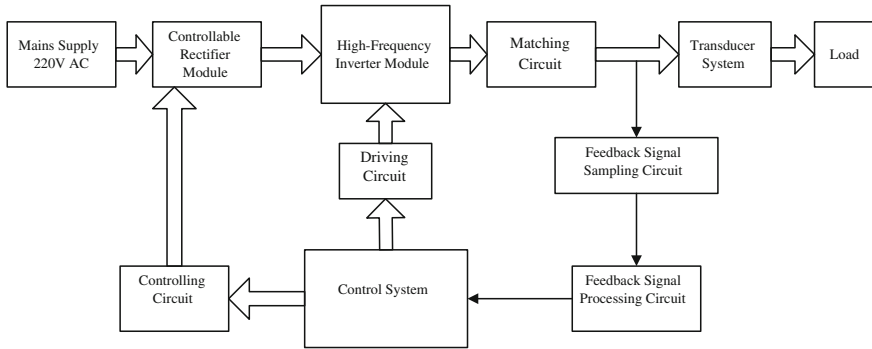


Fig. 1 System diagram of the ultrasonic power

mid-1980s, researchers like Rmaos and others from Spain [5] applied phase-locked and voltage-controlled oscillating system on electro-press ceramic transducer to research the frequency auto-tracing and got satisfied results. Wenjian and Jing'en from School of Mechanical Engineering, Hanzhou Dianzi University [6] applied phase-locked loop technology on the frequency tracking to generate ultrasonic wave with stable and reliable shape, strong tracing capability, frequency resolution of 4 Hz, and a range of 15–25 KHz, in cooperation with PIC16C73 and 8254 programmable counter. While Jie from Meizhouwan Vocational Technology College [7] used current feedback theory to track the frequency automatically by detecting and searching the frequency point of the biggest currency of the main circuit. This method can track the frequency reliably with high precision and low fluctuation, and overcome the shortcomings of general frequency tracking systems such as being uneasy to control the feedback depth and to adjust the circuit parameters. Xiaoyong et al. from Guangdong University of Technology [8] utilized the principle of the phase difference of the currency and the voltage in the circuit of transducer to track the frequency. Through improving the phase detecting circuits, they simplified the frequency tracking program, increased the reliability of the whole power system and gained good processing effect.

But the frequency-tracing precision was still a problem since most of the researches used the controllers directly to generate the PWM signal which is used to adjust the output frequency or the methods they used to detect whether the transducer is on resonant state are complex and not matched well with the PWM generating method, which leads to much complicated software program.

In this paper, an advanced DDS technique was used to generate the PWM signal with much higher frequency precision. And a phase detection method was applied, which made the frequency-tracing process more precise and fast, and also reduced the burden of the controller and the instability of the software program.

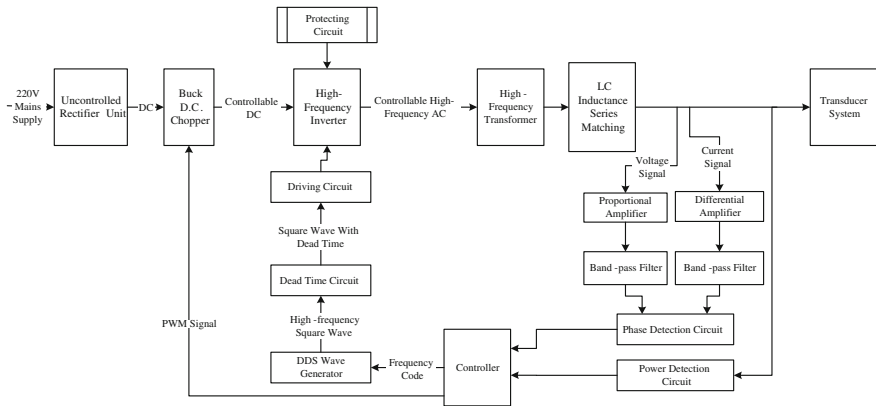


Fig. 2 The system diagram of the ultrasonic power of this paper

2 Hardware Design and Improvement

The ultrasonic power consists of hardware and software, which influence each other collaboratively. Thoughtful hardware design can simplify the software framework dramatically. The system diagram of this paper is shown in Fig. 2. The phase detection circuit is able to response to the state change of the transducer speedily. Then the controller issues an instruction to the DDS wave generator to generate the PWM signal with a corresponding frequency.

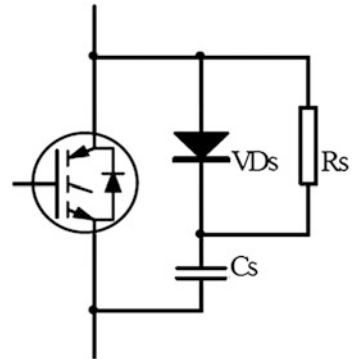
2.1 Controllable Rectifier Module

The function of the rectifier module is to transform the 220 V mains supply to direct current (DC) with controllable voltage. Meanwhile it has to be able to adjust output power automatically. At present, the rectifier circuit mostly uses Diode Uncontrolled Rectifier, Phase Controlled SCR Rectifier or New SPWM Rectifier Circuit. This paper used SCR Uncontrolled Full Bridge Rectifier Circuit to rectify and Buck D.C. Chopper to adjust the output power. The buck D.C. Chopper is able to implement its functionality with just one transistor, by which PWM signal can adjust the output voltage of the rectifier circuit to change the output power of the transducer by controlling switching state of the transistor.

2.2 High-frequency Inverter Module

An inverter that generates high-frequency alternating current (AC) and adjusts its frequency is the main part of the ultrasonic power main circuit. There are multiple

Fig. 3 RCD buffer circuit



switching components in the full bridge inverter circuit, which as a result leads to low voltage for each switching component and high output power. Therefore, ultrasonic power usually uses full bridge inverter circuit as the inverter solution, although it features sophisticated driving circuit.

Most ultrasonic power solutions use the PWM module of a controller to generate square wave with dead time, which is used to control switching of the transistors through a driving module. However, according to analysis, the frequency step width of PWM wave generated directly by the controller can be just about 10 Hz minimally considering the clock speed of the controller, which is so rough that the power will never trace the resonant frequency of the transducer. As a result, the frequency of the power will jump between two points, which may even cause energy storing elements to oscillate and therefore the whole system to crash. In order to solve this problem, this paper used DDS technology into the ultrasonic power to generate square wave with high precision. The frequency register of the DDS chip AD9833 has 28 bits, which makes its output precision up to 0.1 Hz based on 25 MHz clock speed and 0.004 Hz based on 1 MHz clock speed.

There is several milliseconds' delay for transistors between turn-on and turn-off, which probably causes direct short-circuit of two arms of the inverter and the damage of the transistors. This paper chose CD14538 to generate dead time to solve this question. CD14538 can be triggered by both the rising edge and the falling edge of a pulse. The exterior capacity and resistance of the chip decide the duration and precision of the dead time.

Generally, the output voltage of a controller is between 3.3 and 5 V. However, as a high-voltage side switch, the power-switching component requires its grid voltage 10–15 V higher than the drain voltage when driven on. In order to solve this issue, this paper chose IR2110 chip from IR Company to drive the full bridge. Meanwhile, this paper used RCD Buffer Circuit (as shown in Fig. 3) to restrain the surge voltage and the rise rate of turn-off voltage for power-switching components are very liable to be damaged by overvoltage and overheat. RCD Buffer Circuit is

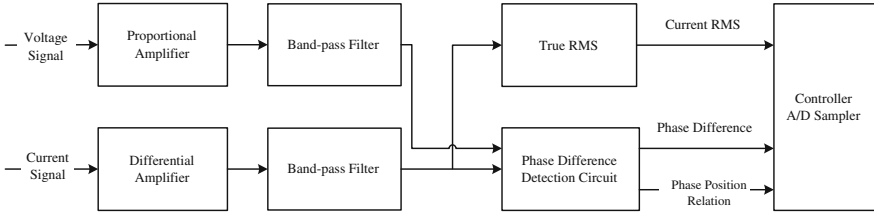


Fig. 4 The signal processing module

able to reduce turn-off loss of the transistors, improve the turn-off track, and can function as a turn-off absorption circuit.

2.3 Matching Circuit

As a load of the ultrasonic power, the transducer shows capacitive impedance. Impedance matching between the transducer and the ultrasonic power is very significant whose quality will directly affect stability of the ultrasonic power. There are two ways, series with inductive load and parallel with inductive load, to match the capacitive load. Inductance series matching, as was chosen as the impedance matching part in this paper, not only can reduce active resistance and improve driving capability, but also has the function of filtering.

2.4 Load Circuit and Sampling Circuit

An important part of the ultrasonic power is the phase detection and power detection of the voltage and current of the transducer circuit. There are many methods to sample the signals. This paper used Resistance Method to take the required samples, whose circuit is simple and signal is without distortion. In order to be input into the controller, the current and voltage signals sampled through the Resistance Method need a series of processes shown in Fig. 4.

3 Software Design and Improvement

Ultrasonic vibration system features multiple peaks whose electrical characteristic is that there are several current maxima for the ultrasonic vibration system, at which the phase of the current synchronizes with the one of the voltage. The biggest maximum is where the resonant frequency of the transducer is. This paper

chose a solution that integrates Full-process Resonant Frequency Search Module and Frequency Auto-Tracing Module.

After starting the power, the control system calls the Full-process Resonant Frequency Search Module to search the resonant frequency point using the current valid value signal from the Signal Processing Module. At this moment, the system stays resonant. When the resonant frequency drifts because of the changes of the work-piece facts such as the temperature and the load force, the system will automatically call the Frequency Auto-Tracing Module repeatedly to adjust the output frequency of the power until the transducer arrives a new resonant state. The flow chart of the program is shown in Fig. 5.

This paper designed a Variable Step Size Tracing solution in the Frequency Auto-Tracing Module, which is able to trace the resonant frequency quickly and precisely. In order to deal with the problem that the value of the phase difference signal probably fluctuates near zero because of the existence of the unwanted signals, this paper set a phase difference threshold. If the phase difference is less than the threshold, the transducer will be considered resonant; otherwise, the system will determine whether the phase difference is bigger than a Big Step Size threshold. The system will adjust the output frequency with the big step size to trace the resonant frequency speedily if the phase difference is bigger. As the process goes on and the phase difference drops to below the Big Step Size threshold, the system will do the output frequency precisely with a small step size. To reduce or increase the output frequency is decided by the relationship between the current phase and the voltage phase, which is either lead or lag. The flow chart of the frequency auto-tracing module is shown in Fig. 6.

4 Experiment

Transformer is used several times as auxiliary device in the whole ultrasonic power, whose quality influences the performance of the power directly. This paper experimented on the air gap of the magnetic core of the transformer and got some conclusions.

A4 papers were used to adjust the air gap size of the magnetic core to get experiment data, which are based on an input frequency of 35 kHz and an EE55 magnetic core with three sets of coils whose turns ratio is 1:2, 1:4, and 1:8, respectively. According to the experiment, there are some data. Only the data based on the coil with turn ratio of 1:2 are shown in Figs. 7, 8 and 9. In addition, all the data got from the experiment are shown in Table 1.

According to the above data, the voltage of secondary side rose up after increasing the air gap size, which was close to each other with one A4 paper and two A4 papers in between though. The ratio of the voltage between the original side and the secondary side was out of balance severely when the air gap size was two A4 paper thick. There was subharmonic in voltage of the original side and the

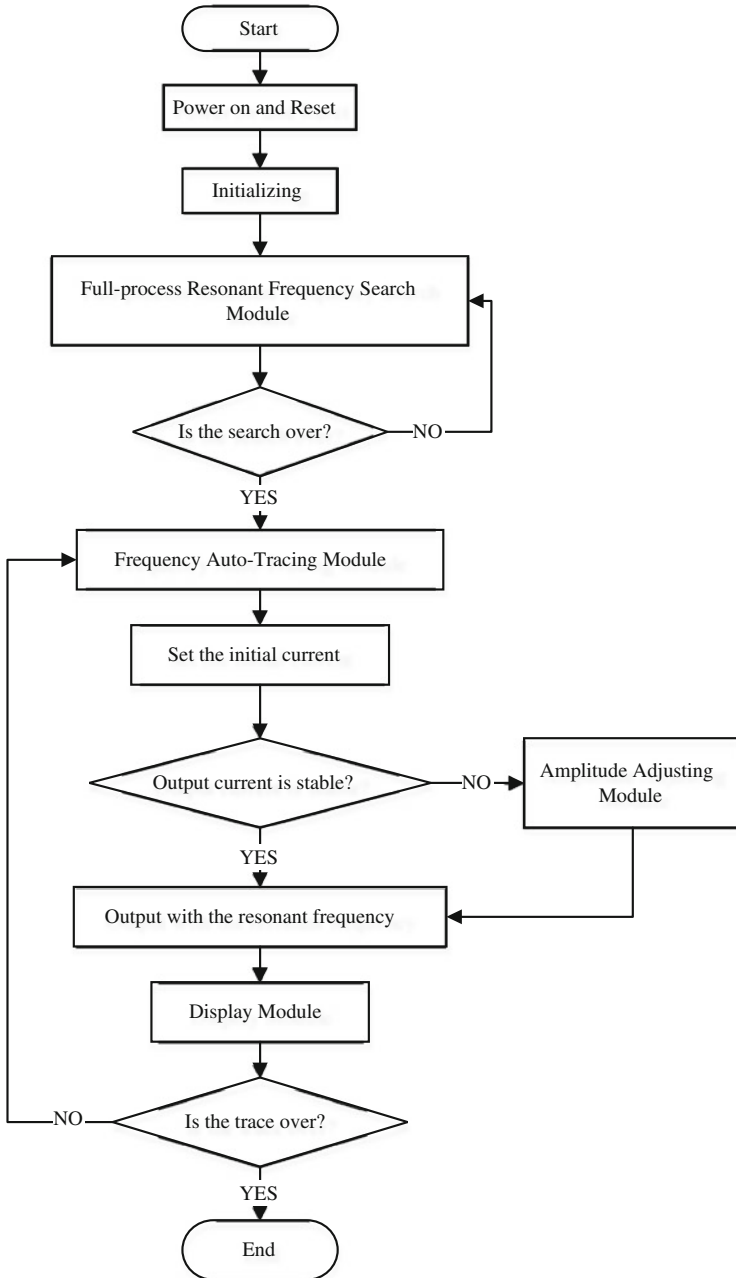


Fig. 5 The flow chart of the Full-process Resonant Frequency Search Module

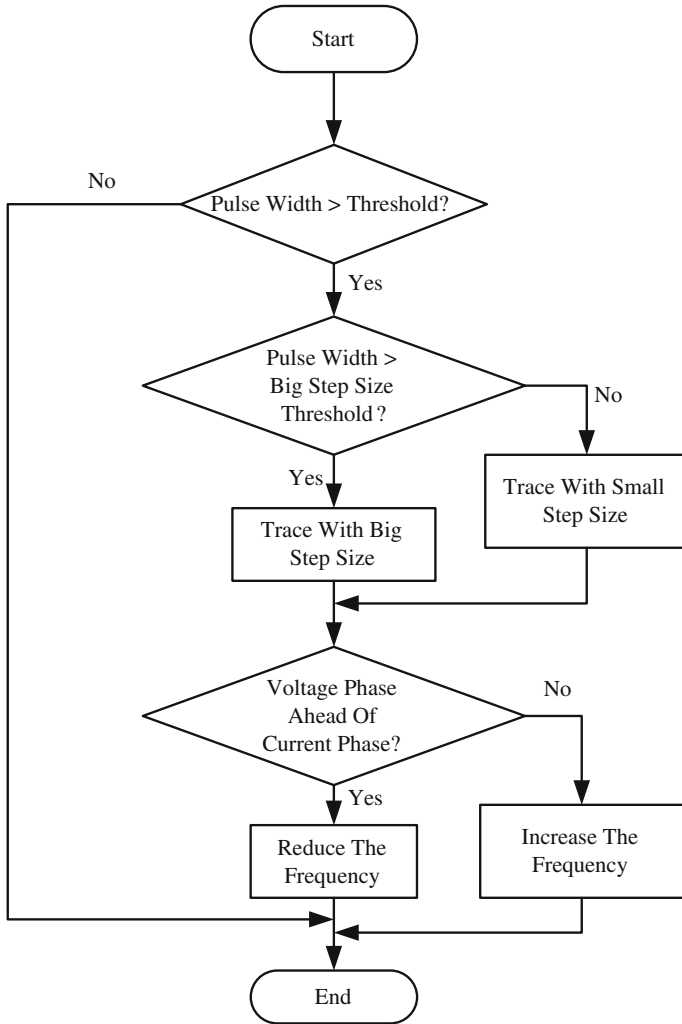


Fig. 6 The flow chart of the frequency auto-tracing module

secondary side when there is just one A4 paper in between; while there is third harmonic when the air gap size is two A4 paper thick.

To increase proper air gap size to the transformer magnetic core is able to aggrandize the capability to resist bias, which improves its linearity of permeability and reduces the magnetic inductivity of the core. The air gap size cannot be too big, or it will cause oversize exciting current and increase the energy loss.

Fig. 7 Voltage of the primary side and secondary side (1:2) when air gap is zero

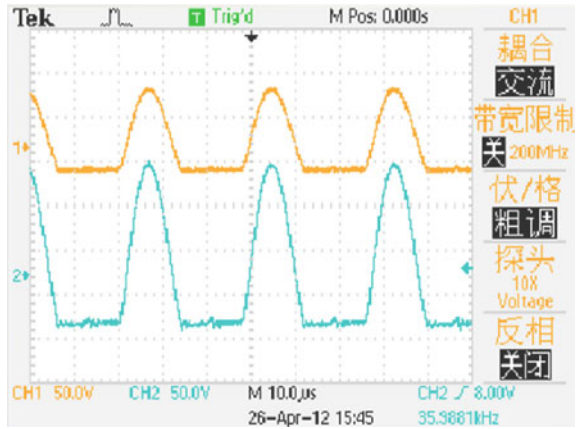


Fig. 8 Voltage of the primary side and secondary side (1:2) when air gap is one A4 paper size

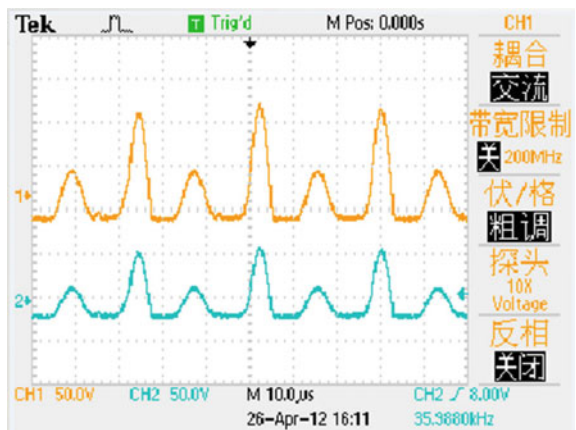


Fig. 9 Voltage of the primary side and secondary side (1:2) when air gap is two A4 papers size

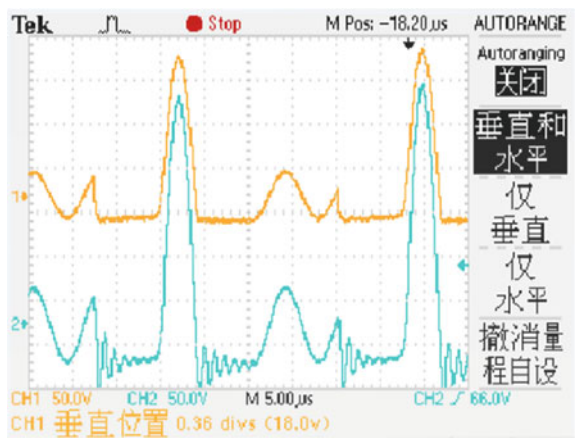


Table 1 The data of the experiment

| Air gap size | Turn ratio | Voltage of original side (V) | Voltage of secondary side (V) |
|---------------|------------|------------------------------|-------------------------------|
| 0 | 1:2 | 90 | 54 |
| | 1:4 | 92 | 184 |
| | 1:8 | 74 | 336 |
| One A4 paper | 1:2 | 122 | 72 |
| | 1:4 | 122 | 200 |
| | 1:8 | 102 | 456 |
| Two A4 papers | 1:2 | 194 | 57 |
| | 1:4 | 184 | 302 |
| | 1:8 | 130 | 456 |

5 Conclusion

This paper has designed an ultrasonic power solution with embedded technology to fulfill frequency auto-tracing function and power auto-controlling function. BUCK D.C. chopper was used to adjust the output power of power device; DDS technique cooperated with phase detection method was applied to get much precise PWM signal for frequency-tracing; and a new dead time circuit was designed to guarantee the safety of the transistors. This paper also has simplified the overall software framework thanks to the improvements of the hardware, and made the detail program easy to write and enhanced efficiency and reliability of the software. In addition, the usage of small-scale power components made the whole size of the ultrasonic power smaller, which realized miniaturization of the high-power supply. Furthermore, the experiments on the transformer in this paper showed that proper air gap size to the transformer magnetic core is able to aggrandize the capability of resisting bias and mend the linearity of permeability. The ultrasonic power based on this paper showed a good quality with perfect stability and high precision.

References

1. Shengfeng R, Minggang X, Yujing H, Xinli W, Jianhua Z (2006) Research on characteristic of workpiece ultrasonically vibrating aided grinding. *Electro Mach Mold* 3:49–51
2. Tao X (2000) The development of power supply used in supersonic generator. *Clean Technol* 12–13
3. Weixiang Z, Yan B, Lingling Z (2006) Development of intelligent power ultrasonic power supply. *Power Electron* 40(6)
4. Lei Z, Jianhua W, Jianyun L (2008) Design of high power ultrasonic power supply based on DSP. *Microcomput Inf* 24:183–184, 314
5. Lopez T, Sauerlaender G, Duerbaum T, Tolle T (2003) A detailed analysis of a resonant gate driver for PWM applications. *APEC 2003 Eighteenth Ann IEEE Appl Power Electron Conf Expo* 3(2):873–878

6. Wenjian H, Jing'en C (2005) The application of PLL for intelligent ultrasonic power. *J Hangzhou Dianzi Univ* 25(4):9–11
7. Jie C (2010) The resonant frequency auto-tracing technology of ultrasonic power. *Mech Electr Technol* 33(2):89–91, 94
8. Xiaoyong L, Yongjun Z, Chunhong L (2009) Improvement of frequency tracking circuit for ultrasonic power. *Electro Mach Mold* 1:38–40, 67

Simulation of STATCOM Effect on the Dynamic Response Performance of HVDC

Wang Weiru and Shi Xincong

Abstract The transient mathematical model for the STATCOM is developed in d-q coordinates in this paper. It constructs a pseudolinear system of STATCOM, using the inverse system method which based on the nonlinear feedback linearization theory. Then, by synthesizing the pseudolinear system, a sliding mode variable structure controller is designed. This article focuses on the effect of dynamic response performance of the HVDC system failure, when using different reactive power compensation devices such as SVC and STATCOM, etc. It also compares STATCOM with conventional PI control with STATCOM with variable structure control. The simulation results indicate that the designed controller can enhance the static and dynamic performance of HVDC system failure better.

Keywords STATCOM · Variable structure control · Reactive power compensation · HVDC · Inverse system method

1 Introduction

In recent years, an increasing number of ultra high-voltage direct current (UHVDC) transmission systems will appear in our AC–DC interconnected power system. The Yunnan-Guangdong ± 800 KV HVDC transmission project, which was put into operation in 2010, is the first UHVDC transmission project in the world [1]. To a certain extent, this has improved the stability of the system.

W. Weiru (✉)

Power Grid Technology Center of Shanxi Electric Power Research Institute, Taiyuan, China
e-mail: hdwangweiru@163.com

S. Xincong (✉)

Dispatch and Control Center of Shanxi Electric Power Company, Taiyuan, China
e-mail: ncepu_shixincong@126.com

However, when a large disturbance occurs, AC–DC interactions often result in the deterioration of the system running state. Therefore, the study on the dynamic characteristics of HVDC system failure has always been the hot. The actual situation indicates that the strength of AC system connected to HVDC, reactive power characteristics, and the performance of converter station controller, etc. have a significant impact on system recovery [2, 3].

Reactive power balance of steady HVDC system is decided by the converter's operating status and the reactive power compensation of the AC-side. Reactive unbalance directly effect the normal commutation of the converter when fault. And the reactive power compensation devices on the commutation bus effect the DC system failure recovery through the AC system. Therefore, reactive power compensation has a significant impact on the dynamic characteristics of HVDC system failure [4–6].

In the reactive power compensation, fixed capacitors have exposed a growing number of drawbacks, while the superior performance of FACTS devices will highlights the enormous advantages in HVDC system. SVC is a capacitor-based device. When reach its operating limits, the reactive current output will drop rapidly as the voltage drop. However, the capacitive current output of STATCOM system may still be maintained even when the voltage in a quite low level; SVC responses too slowly, while STATCOM responses fast, with a good control stability. In order to achieve the same stability limit, the required installed capacity is much smaller than SVC. Therefore, besides using fixed capacitors to provide reactive power in HVDC system, it also can use STATCOM to adjust the reactive power continuously, thereby enhancing the dynamic response performance of the HVDC system under failure. STATCOM controller often used PI control, which is sensitive to parameters and disturbance and its parameters are not easily identifiable. The sliding mode variable structure control is a nonlinear control method. It has many advantages, such as rapid response, insensitive to parameters and disturbance, strong robust, and easier physical realization.

Based on the above background, this paper developed the transient mathematical model for the STATCOM in d-q coordinates. It constructed a pseudolinear system of STATCOM, using the inverse system method which based on the nonlinear feedback linearization theory. Then, by synthesizing the pseudo linear system, a sliding mode variable structure controller is designed. This article focuses on the effect of dynamic response performance of the HVDC system failure, when using different reactive power compensation devices such as SVC and STATCOM, etc. It also compares STATCOM with conventional PI control with STATCOM with variable structure control. The simulation results indicate that STATCOM adopting the developed control strategy can enhance the static and dynamic performance of HVDC system failure better.

2 The Transient Mathematical Model for STATCOM

As shown in Fig. 1, the left side is the structure of STATCOM and the right is the AC bus system of HVDC, ignoring the resistance of converting reactor and converter switching losses. In the figure, phasors U_{sa} , U_{sb} and U_{sc} are, respectively, the three-phase voltage fundamental component of the HVDC AC bus connected to STATCOM; U_{ia} , U_{ib} and U_{ic} are, respectively, the three-phase output voltage fundamental component of converter; i_{La} , i_{Lb} and i_{Lc} are, respectively, three-phase current fundamental component of STATCOM AC bus; U_{dc} is DC voltage of converter; C is the capacitor on converter-side; L is the equivalent inductance of transformer on converter-side.

Considering that the sum of the three-phase currents of the three-phase three-wire system is 0, it may not consider the zero sequence components. Therefore, the mathematical model for STATCOM in synchronously rotating coordinate system can be expressed as formula (1) [7]:

$$\begin{cases} \frac{dI_{dL}}{dt} = \omega I_{qL} - \frac{u_{di}}{L} + \frac{U_{ds}}{L} \\ \frac{dI_{qL}}{dt} = -\omega I_{dL} - \frac{u_{qi}}{L} + \frac{U_{qs}}{L} \\ \frac{dU_{dc}}{dt} = \frac{3(u_{di}I_{dL} + u_{qi}I_{qL})}{2CU_{dc}} \end{cases} \quad (1)$$

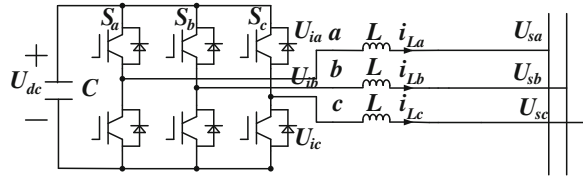
In the formula, u_{di} , u_{qi} , I_{dL} , I_{qL} are, respectively, d -axis and q -axis component of the AC fundamental voltage and current on Converter-side; U_{ds} , U_{qs} are, respectively, the d -axis and q -axis component of fundamental voltage of HVDC AC system bus connected to STATCOM; ω is the angular frequency of system.

The above formula (1) shall be the 3-order model of STATCOM. According to formula (1), for the STATCOM in d-q coordinate, the input is u_{di} , u_{qi} and the output controlled is I_{dL} and I_{qL} . Thus, the PWM rectifier model is a coupled nonlinear system with two-input and two-output, which unable to achieve precise decoupling control by adopting a general linear control technology. This paper will use the inverse system linearization and nonlinear control technology for decoupling to get the control system of STATCOM.

3 Inverse System of STATCOM

In this paper, inverse system method is utilized to complete the precision linear design. The key step is to do variable substitution to the output equation of the inverse system according to a certain rules. That is the forced linearization of nonlinear systems.

Fig. 1 Structure diagram of STATCOM



Taking it into account that the DC voltage U_{dc} is the slow dynamics variable, and more slowly than I_{dL} and I_{qL} . Therefore, U_{dc} can be processed as a constant. Then the state variables of STATCOM are: $X = [x_1, x_2]^T = [I_{dL}, I_{qL}]^T$; Select the output variables: $Y = [y_1, y_2]^T = [I_{dL}, I_{qL}]^T$; the input variables for: $U = [u_1, u_2]^T = [u_{di}, u_{qi}]^T$; Therefore, the model for STATCOM is as follows:

$$\dot{X} = f(X, U) = \begin{cases} \omega x_2 - \frac{u_1}{L} + \frac{U_{ds}}{L} \\ -\omega x_1 - \frac{u_2}{L} + \frac{U_{qs}}{L} \end{cases} \quad (2)$$

It can clearly be seen, STATCOM is a two-input and two-output coupled nonlinear system with two state variables.

Make a derivation to the above output $Y = [y_1, y_2]^T$ according to Inverse system method so that the derivative of output significantly has input control variables $U = [u_1, u_2]^T$. And it has a significant input control variables $U = [u_1, u_2]^T$ in formula (2). Clearly, the system's relative degree is equal to the number of system state variables, so the system is reversible.

Make $v_1 = \dot{y}_1, v_2 = \dot{y}_2$ as a virtual input and $z_1 = y_1, z_2 = y_2$, so the standard form of inverse system for STATCOM model can be written as:

$$\begin{cases} \dot{z}_1 = v_1, \\ \dot{z}_2 = v_2, \\ U = \bar{\phi}(Z, V). \end{cases} \quad (3)$$

In the formula, $Z = [z_1, z_2]^T, V = [v_1, v_2]^T, \bar{\phi}(Z, V)$ is an expression of the inverse system. As formula (3) shown, it can transform this multivariable control coupled system into two subsystems to control.

4 STATCOM Controller Design

After obtaining the inverse system, you can design the switching function according to variable structure control theory [8] to realize variable structure control. Then the virtual control law could be obtained. At the same time, because of using nonlinear

forced linearization method, it is required to make an inverse transformation to the Virtual Control law V in order to obtain the actual control law.

Suppose that the steady-state operating point of STATCOM is: $X_\infty = [I_{dL}^*, I_{qL}^*]^T$. Apply variable structure theory to design the controller on the two linear subsystems in formula (3), sliding surface are, respectively, as follows:

$$\begin{cases} S_1 = z_1 - z_1^*, \\ S_2 = z_2 - z_2^*. \end{cases} \quad (4)$$

In the formula, $z_1^* = I_{dL}^*$, $z_2^* = I_{qL}^*$.

Do derivation to each sliding surface of formula (4), then get:

$$\begin{cases} \dot{S}_1 = (z_1 - z_1^*)' = \dot{z}_1 \\ \dot{S}_2 = (z_2 - z_2^*)' = \dot{z}_2. \end{cases} \quad (5)$$

In the variable structure control, it is hoped that the state variables reach the switching surface according to a certain exponential law, so take exponential convergence rate as follows:

$$\begin{cases} \dot{S}_1 = -k_1 S_1 - \varepsilon_1 \operatorname{sgn}(S_1), \\ \dot{S}_2 = -k_2 S_2 - \varepsilon_2 \operatorname{sgn}(S_2). \end{cases} \quad (6)$$

In the formula, $k_1, \varepsilon_1, k_2, \varepsilon_2$ are all constants greater than zero. Then the Virtual Control V can be obtained:

$$\begin{cases} v_1 = -k_1 S_1 - \varepsilon_1 \operatorname{sgn}(S_1), \\ v_2 = -k_2 S_2 - \varepsilon_2 \operatorname{sgn}(S_2). \end{cases} \quad (7)$$

And then, calculate the actual control input U through inverse transformation, obtain a final result as follows:

$$\begin{cases} u_1 = u_{di} = \omega L I_{qL} + U_{ds} - L[k_1 S_1 \\ \quad + \varepsilon_1 \operatorname{sgn}(S_1)] \\ u_2 = u_{qi} = -\omega L I_{dL} + U_{qs} - L[k_2 S_2 \\ \quad + \varepsilon_2 \operatorname{sgn}(S_2)] \end{cases} \quad (8)$$

5 Simulation

HVDC system model of this article adopts Silvano Casoria (Hydro-Quebec) Simulation Model. The rated voltage of AC-side is 500 KV. At rated operating conditions, the AC filters provide 500 MVA, but SVC or STATCOM provide only 100 MVA. When adopting SVC and STATCOM, respectively, for compensation, the dynamic response characteristics during failure depend largely on their control systems. SVC and STATCOM of this article both apply MATLAB standard control system.

5.1 Inverter Commutation-Side Three-Phase Ground Fault

At $t = 1.0$ s, the inverter commutation-side bus three-phase ground fault occur and the failure continue 0.1 s. The fault grounding resistance is zero.

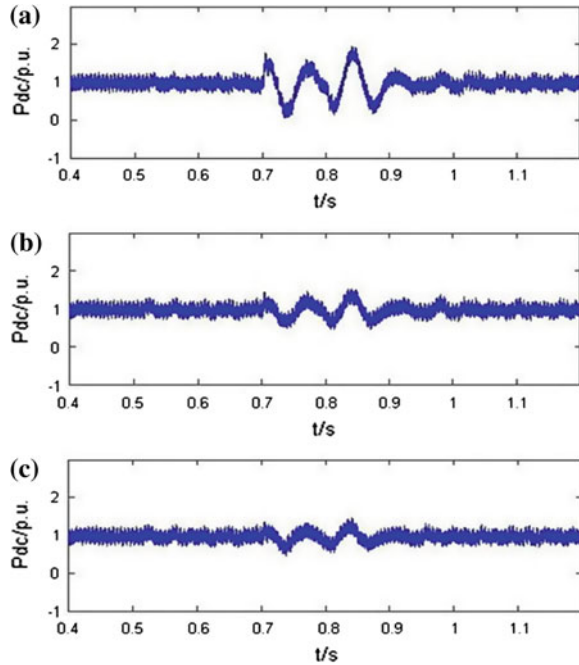
We can see that, when AC system using SVC for compensation, the system recovery slow from Fig. 2. The reason is that during failure and after fault excision TSC is switched repeatedly, which will make the voltage of commutation bus oscillate intensely during recovery and commutation failure. It could prevent this instability to reduce the voltage gain of SVC control loop, but will increase the response time of suppressing the transient over-voltage. Therefore, it is an undesirable ways. When using STATCOM, the system recovers faster and the oscillation amplitude is much smaller, without commutation failure. This is because the STATCOM send and absorb reactive power required by changing the voltage and current waveforms of the voltage source converter, no capacitors and shunt reactors, there is no run-time SVC shortcomings. Its main advantage is almost independent of system voltage and giving out capacitive reactive current. This feature is particularly suitable for the occasion requiring voltage support after failure in HVDC system.

In addition, during failure period, the effect of reactive power compensation by using of variable structure control is superior to that of using conventional control. As the simulation diagram shown, the DC power waveform overshoot of the former clearly much smaller than that of the latter, and the time used to the stable state is shorter than the latter.

5.2 Remote Three-Phase Ground Fault on Converter-Side

To analog a remote three-phase ground fault, make the equivalent impedance of the AC system expressed as two equivalent series impedances, and the short-circuit point is located at the connection of two impedances. Figure 3 describes the recovery characteristics of DC power. From it we can see that the oscillation

Fig. 2 DC power recovery characteristics of Commutation Bus three-phase ground fault

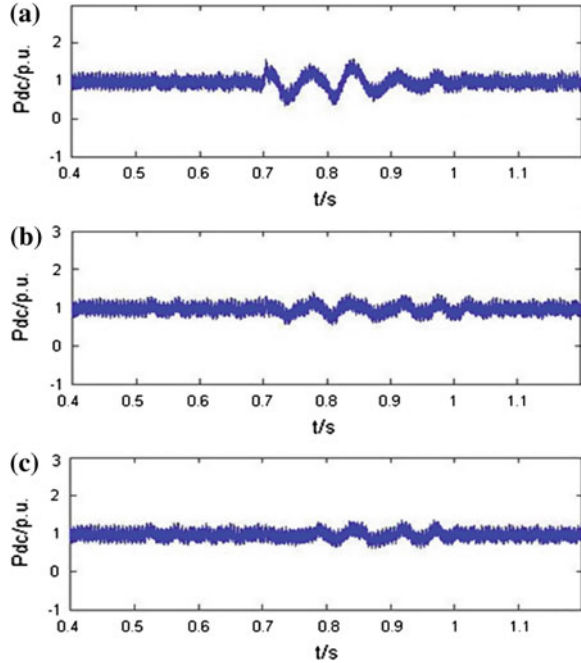


amplitude of DC power is much smaller, and the commutation failure does not appear during recovery process. It indicates that the effect to the recovery of the DC transmission system of the remote ground fault was significantly less than the proximal fault. During failure period, the effect of reactive power compensation by using of variable structure control is superior to that of using conventional control. As the simulation diagram shown, the DC power waveform overshoot of the former clearly much smaller than that of the latter, and the time used to the stable state is shorter than the latter.

6 Conclusion

This paper designed a sliding mode controller for STATCOM according to sliding mode variable structure control theory, using the inverse system method based on nonlinear feedback linearization. It also studied the effect to the dynamic response performance under failure, when using different compensation devices such as SVC, STATCOM, and so on, for reactive power compensation in the AC-DC systems. And then, it compared the designed controller with PI-controlled STATCOM:

Fig. 3 C power recovery characteristics of Commutation Bus three-phase Remote ground fault



1. STATCOM has obvious advantages over SVC for reactive power compensation, whether in the level of transient over-voltage suppression or restoration of the DC power.
2. As the simulation results shown, during failure period, using variable structure control of STATCOM for reactive power compensation has behaved a better effect than those using conventional control of the STATCOM. The DC power waveform overshoot of the former is clearly much smaller than the latter's, and the latter used a longer time to the stable state than the former.
3. When the short-circuit fault emerges on the commutation bus, it has the most negative influence to the HVDC system recovery. The farther the distance from short-circuit point to the commutation bus, the weaker the influence is.

References

1. CIGRE Working Group 03 of Study Committee 14 (1983) Use of static or synchronous compensators in HVDC systems. *Electra* 91:51–82
2. Cheng G-H (2006) Study on strategy of AC-DC power system recovery control (Doctoral thesis). Zhejiang University, Hangzhou
3. Gao W-B (1996) Theory and designed method of variable structure control. Science Press, Beijing, p 2

4. Liu H-C (2004) The nonlinear modal analysis and flexible coordination and control of AC/DC interconnected power system (Doctoral thesis). Sichuan University, Chengdu
5. Xie H-F, Yao Z (2009) The impact of SVC on urgent supporting for UHV DC power. *Electr Power Autom Equip* 29(1):6–10
6. Kunder P (1994) *Power system stability and control*. McGraw-Hill Inc, New York
7. Sato M, Honjo N, Yamaji K (1997) HVDC converter control for fast power recovery after AC system fault. *IEEE Trans Power Deliv* 12(3):1319–1326
8. Wei W-H, Liu W-H, Song Q (2005) Study on strategy of dynamic control for chain-STATCOM of PWM Control with PQ decoupling based on inverse system method. *Chinese J Electr Eng* 25(3):23–28

Research of Interface Composition Design Optimization Based on Visual Balance

Lei Zhou, Cheng-Qi Xue and Kiyoshi Tomimatsu

Abstract In this paper, a metric for visual balance computation is presented, and some optimization models for interface composition design are constructed. The interface composition is exhibited through the minimum bounding rectangle of the elements, four basic parameters of the element— x , y coordinates of the starting point, width and height are used for describing the element positioning. Visual moment is used to represent the product of element size and centrifugal distance, and calculate the balance extent of the opposite sides off the centerline. Three optimization models are constructed towards practical design problems such as layout adjustment, attribute selection and scheme optimization. The case study results show that, the quantitative method is effective in user-interface design process, and provides a theoretical basis for designers' subjective assessment and future computer-aided design.

Keywords Visual balance · Interface composition · Visual moment · Computational aesthetic

1 Introduction

In a sense, how all types of designers, marketers, and developers work is often intuitively based on their own experiences. Although they had been given many kinds of design principles from aesthetic and usability, it's still difficult to apply

L. Zhou · C.-Q. Xue (✉)
School of Mechanical Engineering, Southeast University, Nanjing, China
e-mail: ipd_xcq@seu.edu.cn

L. Zhou
e-mail: 230109043@seu.edu.cn

K. Tomimatsu
School of Design, Kyushu University, Fukuoka, Japan
e-mail: k.tomimatsu2008@gmail.com

these principles into practical work, just like there's no exact framework or system that tells them how to align items or what size to pick according to the principles; they should still just listen to their own feelings to make those decisions.

Balance has been identified as one of the major user-interface factors influence perceived visual aesthetics, as well as some homoionyms equilibrium, symmetry, proportion, contrast and so on [1–5]. Gestalt theory thought that when people were looking at something, they could not stop themselves from exploring a stable and balanced state [6–8]. Normally, the design patterns with higher balance can make the user's visual experience more smooth and comfortable.

In this paper, we first give a brief review of balance metric in computational aesthetic field. Then propose a visual balance metric for interface composition quantitative calculation, and verify its reliability and stability through repeated orthogonal experiments. Finally, propose design optimization methods according to visual balance metric. This study means to realize the transition from aesthetic principle to concrete practices, which can improve the long-term problems of design subjectivity and effectively facilitate designers' mental process.

2 Related Researches

Visual balance is an abstract term that describes people's sense of stability and coordination, which has been pointed out ever since the birth of ancient aesthetic. Fact proved that balanced visual stimuli could evoke special physical and psychological reaction and were valued more positively [9]. As a result, visual balance can be set as an effective indicator for design aesthetic evaluation.

Scholars have created some metrics for visual balance and other similar attributes measurement. Ngo et al. investigated a selection of 57 screens from a variety of multimedia systems, and pointed out 14 aesthetic measures containing balance, equilibrium symmetry [10, 11] and so on. He also used golden section as a dynamic symmetry law for design evaluation [12–14]. Fong-Ling Fu and Chiu-Hung Su proposed six measurements such as screen ratio of navigator to content, font size variety, variety of icon types, color contrast between background and foreground, content density, and number of alignment points for computational metric [15]. Andrew Sears developed a metric for organizing widgets in the user interface [16]. Helen C. Purchase presented metrics for determining the aesthetic quality of a given graph drawing [17]. Yili Liu et al. used binary pixel for symmetry and balance calculation [18]. In his later research, he further improved the computational models which could be used in text-overlaid images [19]. McManus assessed a physicalist interpretation of Arnheim's theory, pointed out a method for image centre of mass (CoM) calculation [20]. YONG used crop and warp operator for image composition enhancement, which also could be integrated into image processing systems [21].

The previous researches verify the feasibility of aesthetic quantitative ideas. However, it can not be ignored that design is a kind of advanced perceptual thinking activity, visual stimuli can change users' feeling delicately, and thus

keeping homology is a very important precondition in scheme compare. In addition, it's easier evaluation than modification. Most research can be just used as an evaluation metric and infer what the effect will be, but hard to show an exact optimization way for the concrete cases. So our objective of this study is to find an effective transforming metric for visual balance and interface composition design, which can straightly guide the modification and optimization in interface design.

3 Visual Balance Metric for Interface Composition

The visual elements susceptible to be perceived should have some or all of the following characteristics: (1) regular structure; (2) distinct and closed contour; (3) in stark contrast with the background; (4) familiar or meaningful to people. Therefore they can be separated from the background, and disposed as an independent information source in the whole space.

3.1 Composition Expression and Positioning

For the element with regular shape, it's easy to position it in the space; but for the irregular shape element, taking people's visual inclusivity into consideration, we adopt minimum bounding rectangle to embody the certain element. Define the lower-left corner of the whole interface as the original point $(0, 0)$, W and H represent the total width and height of interface area respectively. Element location can be expressed by four parameters of its bounding rectangle—the x , y coordinate of the lower-left corner, the width w and height h . Therefore the interface composition can be exactly quantified through these parameter groups.

3.2 Visual Balance Metric

The center area is a special place attracting most attention in the whole interface space [20]. So the objects in the middle of the picture should be more important and attractive than those outside, or the whole graph would be a little unusual for user information reading. According to the reason, designers usually emphasize and highlight the main contents through amplifying their sizes and concentrating them in the center of the interface, while weaken the other insignificant through reducing their sizes and dispersing them into the periphery of the interface, which can create a harmony of visual perception and information delivery. So it's easy to image that there's a latent visual complementary effect between element size and centrifugal distance in people's optic perception.

Seeing from this effect, we propose a visual balance metric evolving from mechanical equilibrium, and define the product of element size and centrifugal distance is defined as the visual moment, by the name of the similar physical law. The metric can be mathematically stated as follows:

$$A = \{ (x_i, y_i, w_i, h_i) \mid V_L = V_R \text{ or } V_T = V_B \} \tag{1}$$

which means the optimal situation of visual balance can be achieved when the visual moment of the opposite parts equates one other, where

$$s_i = w_i * h_i, d_i = |x_i(y_i) + w_i(h_i)/2 - W(H)/2|, V_j = \sum_i^{n_j} s_i * d_i, j = L, R, T, B$$

and s represents element area, d represents element centrifugal distance, n_L, n_R, n_T, n_B represent the elements located in the left, right, top, bottom part of the interface centerline, V_j represents the visual moment of all the elements in corner j .

3.3 Metric Testing

3.3.1 Experiment Design

Considering the diverse layout factors that may influence visual balance perception, here we extract four most critical ones in interface composition—interface aspect ratio, element aspect ratio, element number and visual moment ratio as basic variables to test the visual complementary effect. Experiments are arranged through orthogonal testing method, testing samples are prepared based on four factors and three levels orthogonal table $L_9(3^4)$ (Table 1, Fig. 1). The samples are divided into two groups, with each group nine samples. We intentionally set these two groups a little different in element alignment and interval.

3.3.2 Data Analysis

Twenty-eight students major in design participate in the survey, seven point scale is adopted for the balance evaluation.

Seeing from the range analysis, the best combination of group one and group two are A1(400 * 400) B3(60 * 80) C3(9) D2(1:1) and A1(400 * 400) B2(80 * 60) C3(9) D2(1:1) respectively. The result indicates that visual balance perception performs relatively stable despite there’s a little difference in best element aspect ratio choice of the two groups. When the visual moments on the opposite sides are the same, the samples have higher visual balance score. Additionally, it also proofs that in low element coverage conditions (lower than

Table 1 Experiment factors and levels

| Factor | Level | | |
|-----------------------------------|-----------|-----------|-----------|
| | 1 | 2 | 3 |
| A: interface aspect ratio | 400 * 400 | 600 * 400 | 400 * 600 |
| B: element aspect ratio | 60 * 60 | 80 * 60 | 60 * 80 |
| C: element number | 5 | 7 | 9 |
| D1: y visual moment ratio (x 1:1) | 2:1 | 1:1 | 1:2 |
| D2: x visual moment ratio (y 1:1) | 2:1 | 1:1 | 1:2 |

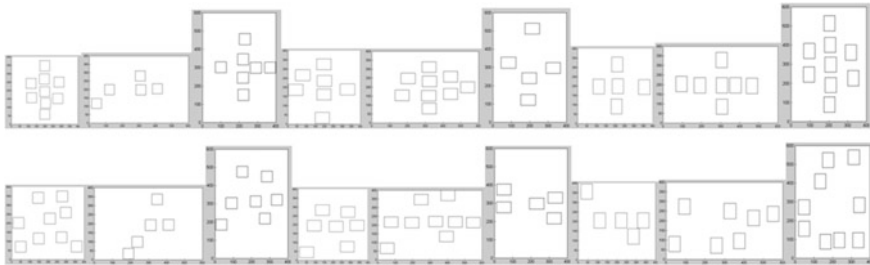


Fig. 1 Two groups of experiment samples. The samples are arranged according to orthogonal table $L_9(3^4)$

50–70 % of the total space), the compact arrangement (A1B2/3C3) is more beneficial to visual balance. However, the element layout features like alignment, symmetry also influence the sense of balance obviously, for the total evaluation of group one (38.2143) is much better than group two (29.1072), so the balance metric will be much accurate as a relative measurement used in similar cases.

In summary, although the visual sense of balance can be influenced by many specific design features, the product of the size and centrifugal distance is a stable relative index for quantifying the interface balance degree.

4 Optimization Model for Composition Design

According to the balance metric proposed in the above paragraph, we can further visualize it into practical design work. Concerning the most common issues we meet in design, propose the following specific calculation and optimization methods.

4.1 Optimization Model for Layout Adjustment

Layout adjustment refers to the element position optimization while keeping element size unchanged. In designers' work, element orientation is always repeated for a better optic feeling.

According to formula 1, set the start point coordinates of the entire elements as the solution set, maintain their w, h value invariant. Establish the optimization model for layout adjustment as follows:

$$\begin{aligned}
 \min_i^{n_j} u(x_i, y_i) &= \sqrt{(V_L - V_R)^2 + (V_T - V_B)^2} \\
 V_j &= \sum_i^{n_j} s_i * d_i, j = L, R, T, B \\
 \text{s.t. } s[(x_i, y_i, w_i, h_i), (x_i^o, y_i^o, w_i^o, h_i^o)] &= 0 \\
 x_i, x_i + w_i \hat{I}[0, W] \\
 y_i, y_i + h_i \hat{I}[0, H] \quad i = 1, 2, \dots, n_{L,R,T,B}
 \end{aligned}
 \tag{2}$$

wherein, s represents overlapping area of different elements (x_i, y_i, w_i, h_i) describes the position of the interface element $i(x_i^o, y_i^o, w_i^o, h_i^o)$ represented the elements except element i .

4.2 Optimization Model for Attribute Selection

Attribute selection refers to the element parameters optimization in a limited space range. When we need to add some element on the basis of the original composition such as new information blocks, engraved lines and decorations, it's important to maintain or even improve the former balance state under certain space constraints.

Define the positioning parameters (x, y, w, h) as the solution set, construct the optimization model for attribute selection as follows:

$$\begin{aligned}
 \min_i^{n_j} u(x_o, y_o, w_o, h_o) &= \sqrt{(V_L - V_R)^2 + (V_T - V_B)^2} \\
 V_j &= \sum_i^{n_j} s_i * d_i, j = L, R, T, B \\
 \text{s.t. } (x_o, y_o, w_o, h_o) \hat{I}(x_c, y_c, w_c, h_c) \\
 \text{i.e } x_o > x_c, y_o > y_c \\
 x_o + w_o < x_c + w_c \\
 y_o + h_o < y_c + h_c \\
 x_o, y_o, w_o, h_o > 0
 \end{aligned}
 \tag{3}$$

wherein (x_o, y_o, w_o, h_o) represents the objective element position attributes, and (x_c, y_c, w_c, h_c) represents the constraint area for the new element.

4.3 Evaluation Model for Scheme Optimization

At the final stage of design process, there should be many similar schemes for choice. Taking visual balance as a benchmark, the best scheme can be selected through following method:

$$\begin{aligned}
 u &= \min_{p_1, p_2, \dots, p_k}^{n_j} \sqrt{(V_{L(T)}/V_{R(B)} - 1)^2} \\
 V_j &= \sum_i^{n_j} s_i * d_i, \quad j = L, R, T, B
 \end{aligned}
 \tag{4}$$

wherein, p_1, p_2, \dots, p_k represent the final schemes. In all the schemes, the one whose visual moments of the opposite sides are close should be chosen.

5 Case Analyses

Take a kind of subrack panel design for example, the function groupware contains: main switch, dial, the coarse and fine adjustment device, indicator lamps of component status and the main switch. According to the function requirements of this user interface, set up three basic interface elements (Fig. 2): the dial display and control elements group (element 1), the indicator lamps and switch group (elements 2) and the main switch (element 3).

5.1 Layout Adjustment

Choose the element starting position as the calculation genes, set the initial layout in (157, 51) (546, 46) (926, 58) as shown in the left of Fig. 3. According to formula (2), after five iterations, the optimization result of the element starting position are (171.91, 65.44) (558.75, 64.50), and (935.38, 65.52), when it reaches the best state of visual balance. Adjust the element to the renewing place as is shown in the right of Fig. 3.



Fig. 2 Interface function elements. The *left* shows the total space for element layout, all the function components are divided into element group 1, 2 and 3 from *left to right*

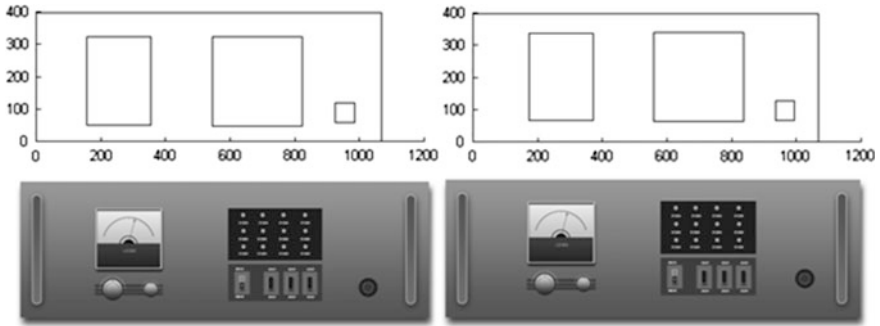


Fig. 3 Layout adjustment. The *left* is the initial interface while the *right* is optimized interface

5.2 Attribute Selection

Take proposal 1 in Fig. 4 (left) as the initial plan, assume that we'd like to add a new element in a restricted area of (850, 130, 1000, 350), apply formula (3) to determine the element parameters.

After 51 times' iteration, the objective element position parameters are (84, 154.72, 37.04, 95.28) in the constraint area, which can get maximum improvement for the interface balance.

5.3 Scheme Optimization

Take Fig. 5 for example, most of the designers think that the upper-right part of the proposal 1 looks a little empty, it seems better if adding a sculptured line or some other decorations just like the proposal 2. Then we can find out the quantitative reason through formula (4).

Calculate the visual moment of inverse sides of the two proposals. The result shows proposal 1 and proposal 2 have better balance proportion in the x direction (1.1383: 1.4336) than that in the y direction (5.3614: 4.2333). Comparably, proposal 2 has higher sense of balance in the y direction, the modification of

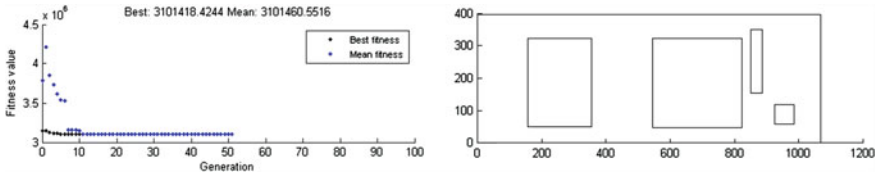


Fig. 4 Optimization process and result



Fig. 5 Proposal 1 and proposal 2

sculptured line improves the unbalanced stage of initial design, so this change is worthy of approval. In the next step, the modification target should be aimed at further adjusting the balance degree in the y direction.

6 Conclusions

Balance refers to a relatively stationary state that the opposing aspects in an object or system are of the same quantity or quality. In different research field, balance shows different meanings and objectives. In design field, balance means a kind of user’s visual perception and feeling, which reflects the coordinate extent of element visual weight in opposite part.

This study analyzes the relationship between visual balance and two important factors of interface composition—element size and centrifugal distance, points out the concept of visual moment as a metric for interface composition evaluation and optimization.

By two rounds of repeated orthogonal experiments, the result shows that visual moment—the product of element size and centrifugal distance performs a stable index for balance measurement. Although the other factors such as interface aspect ratio, element aspect ratio, element number also influence user’s specific perception, visual moment can be a stable relative index for composition quantification.

On the basis of this balance metric, we point out optimization methods towards three kinds of specific design problems—layout adjustment, attribute selection and scheme optimization respectively, which can be a practical ways for overcoming the complete subjective assessment, and realize design quantitative analysis and improvement.

In the future, the study will take other element factors such as color, shape and correlation into consider, and further improve the existing model. On the basis of quantitative methods, construct relevant computer-aided system for real-time interface composition design and analysis, provide a theoretical intellectual support in design process.

Acknowledgements This study is supported by the National Natural Science Foundation, China (No.71071032, 71271053), the Humanities and Social Science Foundation of Ministry of Education, China (No.12YJAZH134), and the Fundamental Research Funds of Southeast University, China (No. CXLX11_0098).

References

1. Arnheim R (1974) Art and visual perception. University of California Press, Berkeley
2. Birkhoff G (1933) Aesthetic measure. Harvard University Press, Cambridge
3. Gombrich E, Gombrich L (1984) Bild und Auge: neue Studien zur Psychologie der bildlichen Darstellung. Klett-Cotta, Stuttgart
4. Tinio P, Leder H (2009) Just how stable are stable aesthetic features? symmetry, complexity, and the jaws of massive familiarization. *Acta Psychol* 130(3):241–250
5. Moshagen M, Thielsch MT (2010) Facets of visual aesthetics. *Int J Hum Comput Interact* 68:689–709
6. UA: Balancing Gestalt Characters. http://www.dandwiki.com/wiki/UA:Balancing_Gestalt_Characters
7. Lehman ML Gestalt principles in architecture: achieving design balance. <http://sensingarchitecture.com/867/gestalt-principles-in-architecture-achieving-design-balance/>
8. Evans C, eHow Contributor. How to identify the values and standards exemplified by Greek art and architecture. http://www.ehow.com/how_6787844_identify-exemplified-greek-art-architecture.html
9. Jacobsen T, Schubotz R, Hofel L, Cramon D (2006) Brain correlates of aesthetic judgment of beauty. *Neuroimage* 29(1):276–285
10. Ngo DCL (2001) Measuring the aesthetic elements of screen designs. *Displays* 22(3):73–78
11. Ngo DCL, Teo LS, Byrne JG (2003) Modelling interface aesthetics. *Inf Sci* 152:25–46
12. Ngo DCL, Ch'ng E (2005) Screen design with dynamic symmetry: a discovery. *Comput Hum Behav* 21(2):307–322
13. Ngo DCL, Ch'ng E (2001) Screen design: composing with dynamic symmetry. *Displays* 22(4):115–124
14. Ch'ng E, Ngo DCL (2003) Screen design: a dynamic symmetry grid based approach. *Displays* 24(3):125–135
15. Fu F-L, Su C-H (2009) Formalizing design guidelines of legibility on web pages. *Hum Interface, LNCS* 5618:17–25
16. Sears A (1993) Layout appropriateness: a metric for evaluating user interface widget layout. *IEEE Trans Softw Eng* 19(7):707–719
17. Purchase HC (2002) Metrics for graph drawing aesthetics. *J Vis Lang Comput* 13:501–516
18. Lai C-Y, Chen P-H, Shih S-W, Liu Y, Hong J-S (2010) Computational models and experimental investigations of effects of balance and symmetry on the aesthetics of text-overlaid image. *Int J Hum Comput Stud* 68(1–2):41–56
19. Bauerly M, Liu Y (2006) Computational modelling and experimental investigation of effects of compositional elements on interface and design aesthetics. *Int J Hum Comput Stud* 64(8):670–682

20. McManus IC, Stover K, Kim D (2011) Arnheim's Gestalt theory of visual balance: examining the compositional structure of art photographs and abstract images. *i-Perception* 2:615–647
21. Jin Y, Wu Q, Liu L (2012) Aesthetic photo composition by optimal crop-and-warp. *Comput Graph* 36(8):955–965

3D Registration Based on the Front and Back Segments of Human Body for Reconstruction

Wan Yan, Long Wenzheng and Tang Hongtai

Abstract Traditional 3D registration methods usually utilize multiple data points segments of the target object. This costs too much time for reconstructing a complete model, and reduces the efficiency. However, at some times, the scanning data are hard to get, and the time is a very important factor. This article proposes a new 3D registration method for human body by just using its front and back point cloud. We use a standard Kinect to obtain the front and back data points of human, extract their contours as the feature points, and adopt the iterative optimization method for registration. Another step of closing the gap, which occurs around the edge, should be used to achieve the complete point cloud model. Experiments demonstrate that it is applicable and convenient to achieve the final accurate result even when the initial positions of the two inputs are far apart.

Keywords 3D registration · 3D reconstruction · Iterative optimization

1 Introduction

Registration is an indispensable process in 3D model reconstruction. It plays an important role in 3D model surface reconstruction, motion detection, object identification et al. It is hard to obtain a complete 3D data of the target object once by using the sensor device, so, registration should be used in order to reconstruct the object's complete 3D model. Given as input two shapes, often called the model and

W. Yan · L. Wenzheng (✉)

College of Computer Science and Technology, Donghua University, Shanghai China
e-mail: sainylong@gmail.com

T. Hongtai

Medical college, Second Military Medical University, Shanghai China

the data, each in its own coordinate system, we purpose to find a transformation that optimally positions that data with respect to the model [1].

Registration problem is wildly concerned by the researchers. It also can be defined as two parts: the global registration and the precise registration. In 1992, a wide-use method called Iterative Closest Point (ICP) [2] algorithm based on iterative optimization technology was proposed by Besl and McKay. Then, a great many algorithms, such as the spin-image representation [3], the representation of the point signature [4], were used as the global registration methods. In the twenty-first century, researchers proposed to use the artificial intelligence algorithms like the genetic algorithm, the simulated annealing algorithm, and the markov model based on statistical optimization [5] to solve the precise registration problem. These methods give us a good result.

In all of the methods mentioned earlier for the recognition, ICP is the most important algorithm because of its registration accuracy and efficiency. Given the two scans, we can achieve a high accurate result by using ICP if the initial position of the two data points is closer enough. The result will be local optimal if the initial position is just not good enough. The original ICP algorithm demands that one data points should contain another, which limits its useful. In 2001, Godin proposed the GICP [6] algorithm, which added the geometric feature into the original ICP. In 2004, Mitra et al. improved the error evaluation function [1] of ICP. All of these improved methods based on ICP aim at speeding up the iterative convergence, improving the accuracy of registration, and reducing the overlapping ratio to make it more useful.

The improved ICP algorithm reduces the demand of the overlapping rate to a certain degree. However, to reconstruct a completed object, it also needs too many segments for registration. Multiple registration process will increase the cumulative error in overlapping area [7].

However, traditional methods cannot meet the users' diversified registration requirements. In some applications such as modeling the burned patients or the severe cases in bad, the efficiency and convenience must be seriously considered.

In this article, we propose a new method, which just uses the front segment and the back segment of human body model without overlapping area for registration. After using their contour feature with iterative optimization method, we can obtain a good result. At the same time, our method is not sensitive to the initial position of the two scans.

2 Registration Theory

Given the two overlapping data points called the model and the data, each data set in its own coordinate system, we need to find the corresponding feature points, which belong to the same part of the target object in the two sets. After that, we can calculate a transformation that superimposes the overlapping area into the

same coordinate system. This spatial transformation is mainly represented as rotation and translation of the rigid object.

We define the data as P , and the model as Q , the transformation are R and T . The optimal spatial transformation can be expressed as that the total distance of the corresponding feature points is zero. The function is as follows:

$$\varepsilon(P, Q) = \min d^2(P, RQ + T) \quad (1)$$

where $d^2(P, RQ + T)$ is the total distance of the corresponding points of P and Q after transformed by matrix R and T . The optimal transformation should minimize the ε .

Ascertaining the corresponding feature points is an important step for registration. Given one point in the data, the original ICP algorithm regards its closest point in the model as its corresponding point. To make sure the precise of the corresponding points, many different feature measurements are proposed in the improved registration algorithm, such as the distance of the point to the plane and the geometric feature. The improved algorithm also adds a new process to delete the mistaken corresponding point. After that, we can get the rotation matrix R and the translation matrix T based on computing the singular value decomposition (SVD), or by using unit quaternion (UQ).

ICP is an optimal matching algorithm based on least square method. It repeats to do the process of confirming the corresponding points set, and computing the optimal rigid transformation, until some convergence criteria, which indicate the correct match, are met.

However, most of the registration algorithms need a high overlapping rate and a good initial position of the two inputs. It restricts the application of 3D reconstruction. When these constraints cannot be reached, the result is poor. Meanwhile, each time we do the registration process, there will be some errors. To finish a completed object model, multiple registrations are needed, which will increase the cumulative error.

With the method we proposed, we can receive an accurate result, even though the inputs have no overlapping area, and their initial position is not good. It overcomes the defect that ICP needs a strict requirement for the input data sets.

3 Registration Algorithm

In the research of reconstructing the 3D model of the burned patients and calculating the total area burned, we propose the method, which just uses a front segment and a back segment of human body model, for registration in the situation that we cannot use the sensor to obtain the data easily because the patients can hardly move. This method can solve the problem of scanning the human body, in different perspective, to get the data. It is efficient to use our algorithm for aligning the two input sets. The flow chart is shown in Fig. 1.

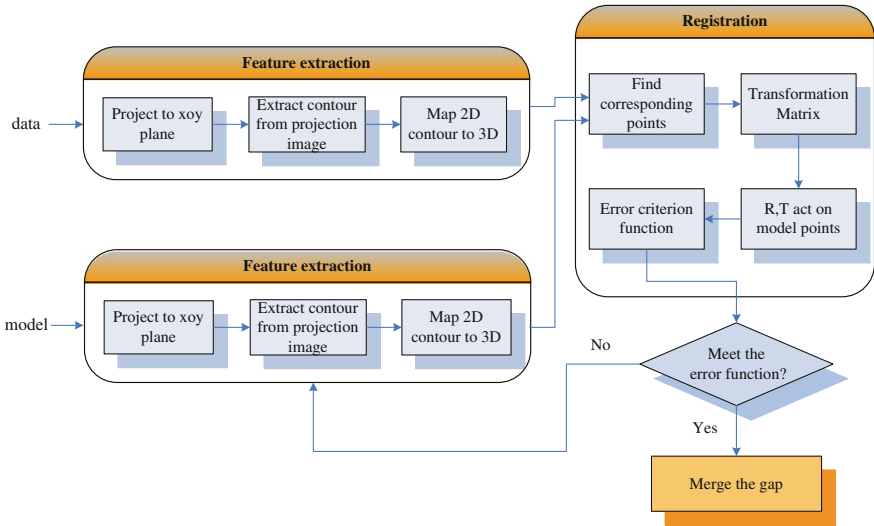


Fig. 1 Registration algorithm flow chart

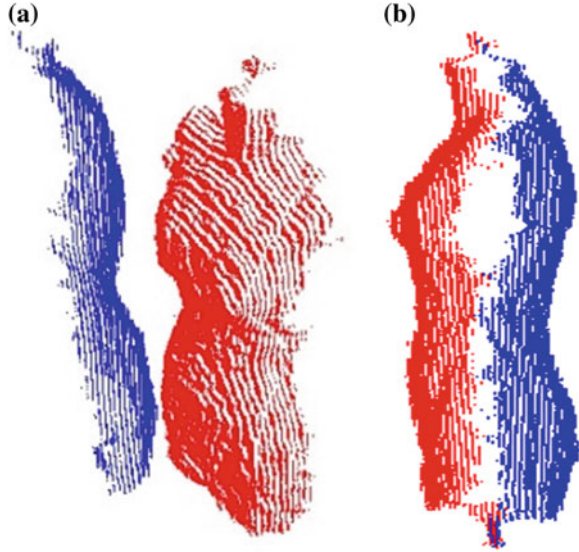
As shown in Fig. 1, the process consists of two parts, the Feature Extraction part and the Registration part. In our method, we use the outline of human body as the feature points and adopt the projection technology to extract the feature by projecting the spatial points onto 2D plane. In Fig. 1, we can see that the contour is extracted from the projected image and then be mapped into 3D coordinate system. The extracted contours of the data and model are regarded as the input of the registration part. Then, we can compute the transformation matrix according to the corresponding points and act the matrix on the model set until the error criterion function is met. With our method, the front segment and the back segment can be aligned to the right position. However, the human body model leaves a narrow gap, in its left and right sides, after registration because of the lost data (the data that we cannot access during the scanning). So, we use interpolation technique to suture the gap and get the completed model.

3.1 Feature Extraction

The original registration algorithms use the overlapping points as the feature points. Their target is to align the two data sets after the corresponding feature points in two coordinates are coincided in one coordinate system. The input sets we use have no overlapping area, so, we cannot use the same feature points and the same rules as the original algorithms .

Considering that our target is not absolutely like the original registration, what we need is to align the front and the back segments to the aligned position. As

Fig. 2 The registration with the mannequin's front and back segments. **a** The initial position of scanning data of mannequin. **b** The final registration result



shown in Fig. 2a is the original data we get, (b) shows the final position we need. This spatial aligned state can be represented as that the position of the contours of these two inputs is aligned. So, we can adopt the contours of the front and back segments as the feature points.

The main step of contour extraction contains:

- (1) Project the 3D data points to the perspective plane.
- (2) Extract the 2D contour from the projected image.
- (3) Map the 2D contour to the original 3D space.

We define the set $P = \{p_i, 1 \leq i \leq n\}$ as the front segment, and $Q = \{q_i, 1 \leq i \leq n\}$ as the back segment. $E_p = \{e_{pi}, 1 \leq i \leq l\}$ is the contour of P , $E_q = \{e_{qi}, 1 \leq i \leq k\}$ is the contour of Q . The feature extraction process is expressed as follow:

$$E_p = h(g(s(P))) \tag{2}$$

where, s is a function, which means the projection operation, g means the contour extraction process, and h is the mapping process.

The 3D data points are projected to the xoy plane, because we fix the scan perspective in the positive front and positive back. So, the contour extracted from the projected image correctly reflects the real outline of the original 3D points.

Define that the set $M = \{m_i, i = 1, 2, 3, \dots, n\}$ is the projected image points in xoy plane, then, the projection function is:

$$M = s(P), \text{ or } m_i(x, y) = s(p_i(x, y, z)).$$

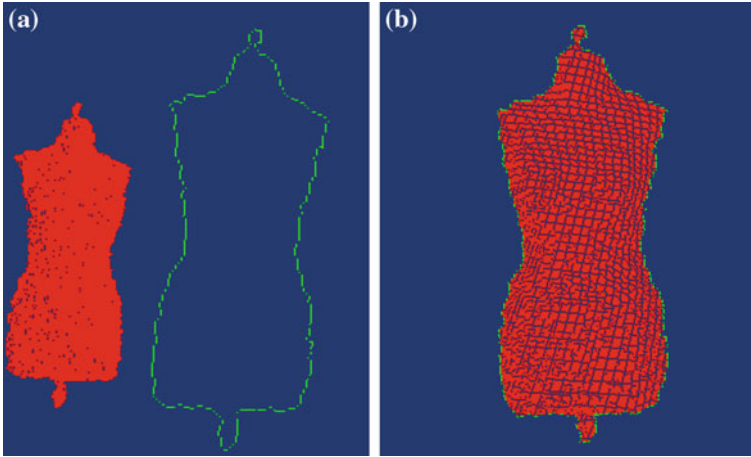


Fig. 3 Feature extraction of the mannequin mode. **a** The contour of the projected image. **b** The real contour of the original points

Define that the set $E'_p = \{e'_i, i = 1, 2, 3, \dots, l\}$ is the contour of set M , the feature extraction function is:

$$E'_p = g(M).$$

Unlike the general image with integral pixels, the pixels in the projected image are scattered. So, we cannot use the traditional image edge detection algorithm to extract its edge directly. Reference [8] proposed to apply the traditional edge detection algorithm after resampling the pixels. However, many edge features will be lost with this method. In this paper, a technique called Move Closest Point is developed in this study by scanning the original projected data to find the contour directly without losing any feature information. The process is:

- (1) Determine the detection area according to the maximum and minimum of the set M both in x and y direction.
- (2) Decide the scanning interval. The scanning interval is not fixed in different situation. We use kinect to achieve the original scanning data, so, we choose an interval, which is slightly higher than the precision. Order that $\Delta x = 4.5 \text{ mm}$, $\Delta y = 2.5 \text{ mm}$.
- (3) Slightly expand the detection area in step (1).
- (4) Scanning the projected data both in x and y direction. Move the scanning point s each time, and calculate the closest point m in M . The point m will be an edge point if the closest point of s is unchanged repeatedly, and add it to the set E' .
- (5) Repeat step (4), until the scan is over. Remove duplicate edge points, and get the final 2D contour set E' .

Then, use the mapping function h to map the 2D contour to the original 3D space, the result is shown in Fig. 3.

Figure 3a shows that our method can extract the 2D outline from the projected image, and (b) shows that the extracted contour of human body model segment is real.

3.2 Registration

Use the method above, we can extract the contour of model segments correctly. However, the position of points in Q will change during transforming the sets P and Q into the same coordinate system. We choose the coordinate system of P as the final system, so, the points in P will not change. It will cause that the contour directly extracted by projecting the model data into xoy plane is not correct.

In this paper, we use an iterative method combined with the feature extraction algorithm above to obtain the contour of Q correctly. Firstly, use the original data to extract their contours and calculate the original transformation matrix; then, act the matrix on the set Q to get the new position of Q ; adopt the feature extraction algorithm to get the contour of Q until the condition, which represents the contour is correct, is met. The function that shows this process is:

$$E_q^k = h(g(s(Q^k)))$$

where, Q^k is Q after being transformed the k th times. E_q^k is the contour of Q^k , and $Q^k = RQ^{k-1} + T$.

The condition, which represents the contour is correct, can be expressed as:

$$f(R, T) = \Delta E_q = \min |E_q^{k+1} - E_q^k|. \quad (3)$$

Equation (3) means that if the number of elements in set E_q does not change between two extraction processes, we consider that we have found the real contour through the iteration.

To calculate the rotation matrix R and the translate matrix T , we need to find out the corresponding feature points in the contour feature sets E_q and E_p . Assume that q_{ei} is an inner point of E_q , we regard the closest point of q_{ei} in E_p as its corresponding point, called p_{ei} . Then, the error functions are:

$$f_1(R, T) = \min \sum_{i=1}^l \|p_{ei} - (Rq_{ei} + T)\|^2 \quad (4)$$

$$f_2(R, T) = \min \sum_{i=1}^l \|p'_{ei} - g(s(Rq_{ei} + T))\|^2 \quad (5)$$

where, $p'_{ei} = g(s(p_{ei}))$, $p_{ei} \in E_p$, $q_{ei} \in E_q$.

Equation (4) represents to minimize the total distance of the corresponding feature points, and (5) means the total distance the projection in xoy plane of the corresponding feature points is minimal.

Reference [9] introduced four methods to compute the final transformation matrix, and compared these four methods in their accuracy, robustness, and efficiency. They are the SVD of a matrix, the orthonormal matrices (OM), the unit quaternion (UQ), and dual quaternion (DQ). These four methods showed a minimal deviation in accuracy and robustness when noise is small. And the efficiency depends on the scale of the point cloud. In practical applications, UQ is widely used for its stability. Reference [10] derived the computing procedure of UQ. We use UQ method in this paper. The registration algorithm in detail is:

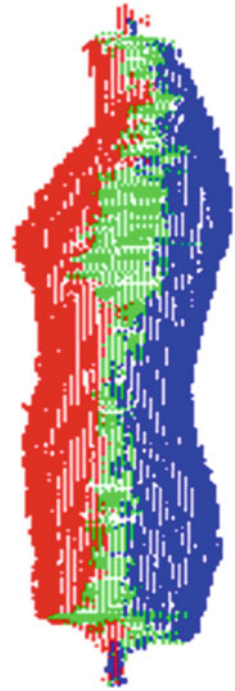
- (1) Extract the contour of P as the set E_p .
- (2) Extract the contour of Q as the initial set E_q .
- (3) For each point in E_p , find out the corresponding point in E_q .
- (4) Delete the inaccurate corresponding points with a distance threshold θ .
- (5) Use UQ method to calculate the rotation matrix R and translation matrix T .
- (6) Act the matrices on set Q^k to get its new position Q^{k+1} .
- (7) Repeat step (2) to (6), until the threshold conditions we set respectively in the equations of (3) (4) (5) are met.

Figure 2 shows the final registration result.

Figure 2a shows that the initial position of the scanning data is bad (b) shows the result after registration and moving the back segment in z direction based on the real thickness of mannequin. We can see that the initial position does not affect us to achieve the right result.

The final issue we need to tackle is to merge the front and back segments to form the completed one. Reference [8] proposed to resample the contour and use linear interpolation to close the gap. Considering the surface of human body is curve, curve interpolation method can be used in this paper to merge the contours. And the bending angle can be controlled. The completed model of mannequin is shown in Fig. 4.

Fig. 4 The completed model after closing the gap



4 Results and Analysis

Standard Kinect is used in our study to obtain the scanning data. The objects we used are the real person and the mannequin. However, during scanning the real people, the posture of this people should not change to make sure that this alteration is rigid transformation. The initial position, model after registration, and the completed one after closing the gap are shown in Fig. 5.

Figure 5a and d show the initial position of the original scanning data. The first one is the worse and the other is bad. The results are good by using the registration method we proposed even though the initial position is terrible (b and e show the result). After merging the gap, the complete point cloud model is reconstructed (Fig. 5c and e).

With our method, we can generate the complete point cloud model of the target object, which is human in this study. This will be hard for ICP when the initial position is bad and no overlapping area is available. We can see that our method is more suitable in this situation and does a good fundamental for the next application.

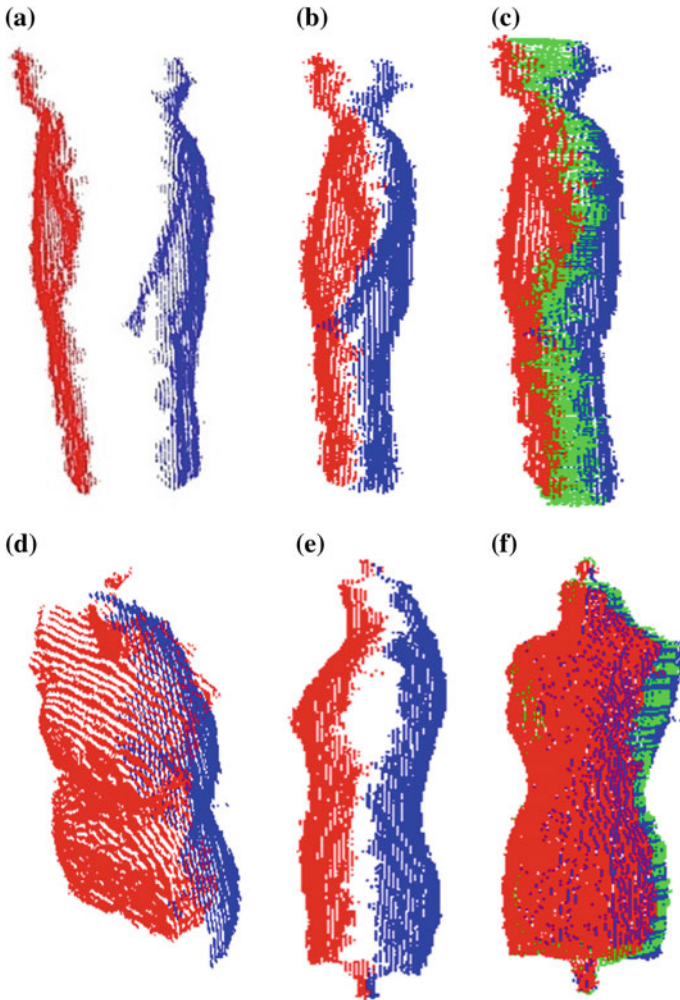


Fig. 5 The registration and gap integration of the front and back segments. **a** The initial position of the real people data. **b** The result after registration **c**. The complete model after merging the gap. **d** The initial position of mannequin data. **e** The result after registration. **f** The complete mannequin point cloud model

5 Conclusion

We have developed a new method for registration by just using the front and the back segments of human body object. In this method, the two input data points for registration have no overlapping area, and their initial position has little effect to the final result. This registration algorithm is more suitable for reconstructing the models of burned patients and the severe cases in bed that could not move. Our

method to reconstruct the whole model is definitely more efficient than the traditional ways, for we only need to do the registration process once.

However, our method requires a high accuracy for the contour of the front and back segments. And the posture of the body should be the same during scanning the front and back data. The gap part of the model may be inaccuracy. Our hope is to improve this method and solve these limits in the future.

Acknowledgments This study is funded by “1255 subject construction Project” of Second Military Medical University (No. CH125510211). This project is supported by the National Natural Science Foundation of China (81372057).

References

1. Mitra NJ, Gelfand N et al (2004) Registration of point cloud data from a geometric optimization perspective. In: Proceedings of eurographics symposium on geometry processing, 2004
2. Besl Paul J, McKay Neil D (1992) A method for registration of 3-D shapes. *IEEE Trans Pattern Anal Mach Intell* 14(2):239–256
3. Johnson AE, Hebert M (1999) Using spin images for efficient object recognition in cluttered 3D scenes. *IEEE Trans Pattern Anal Mach Intell* 21(5):433–449
4. Chua CS, Jarvis R (1997) Point signatures: a new representation for 3d object recognition. *Int J Comput Vision* 25(1):63–85
5. Kim YM, Theobalt C, Diebel J et al (2009) Multi-view image and tof sensor fusion for dense 3d reconstruction. In: Proceedings of IEEE 12th international conference on computer vision workshops (ICCV workshops), 2009, pp 1542–1549
6. Godin G, Laurendeau D, Bergevin R (2001) A method for the registration of attributed range images, third international conference on 3d digital imaging and modeling, Quebec, Canada, 2001, pp 179–186
7. Ezra E, Sharir M, Efrat A (2008) On the performance of the ICP algorithm. *Comput Geom* 41(1–2):77–93
8. Wurong Y (2008) Development of a three-dimensional anthropometry system for human body composition assessment. In: Proceedings of ProQuest 2008
9. Eggert DW, Lorusso A, Fisher RB (1997) Estimating 3-D rigid body transformations: a comparison of four major algorithms. *Mach Vis Appl* 9(5–6):272–290
10. Horn BK, Hilden HM, Negahdaripour S (1988) Closed-form solution of absolute orientation using orthonormal matrices. *J Opt Soc Am* 5(7):1127

Emotional Element Extraction Based on CRFs

Yashen Wang, Quanchao Liu and Heyan Huang

Abstract As the fast development of social network and electronic business, a huge number of comments are generated by users every day. Extraction of emotional elements is an important pre-task of sentiment analysis and opinion mining for comments. In this paper, we extract the emotional elements such as the opinion holder, the comment target, and the evaluation phrase, which previous researches rarely concerned about, especially in Chinese. Based on Conditional Random Fields, we label the evaluation phrase which structure is simple. Then on account of unique characteristics of grammar and syntax of Chinese, we design several rule-based methods to extract evaluation phrase which is in complex structure, as well as comment targets and opinion holders. According to the experimental results, our method improves the performance of emotional element extraction in the domain of sentiment analysis for automobile's Chinese comments. And it also contributes greatly to our subsequent task such as sentiment analysis of social media or comments from other domains.

Keywords Information extraction · Opinion analysis · Evaluation phrase · Comment target · Opinion holder

Y. Wang (✉) · Q. Liu · H. Huang
Department of Computer Science and Technology, Beijing Institute of Technology,
Beijing, China
e-mail: yswang@bit.edu.cn

Q. Liu
e-mail: liuquanchao@bit.edu.cn

H. Huang
e-mail: hhy63@bit.edu.cn

1 Introduction

With the development and maturity of the Internet, more and more users have participated in the construction of the Internet from “reading webpage” to “writing webpage.” Therefore, there are a huge number of comments expressing people’s views and attitudes of certain objects or events in the Internet.

Sentiment analysis aims to determine the attitude of a speaker or a writer with respect to some topic or the overall contextual polarity of a document, and wherein extraction of emotional elements is an important pre-task, which directly determines the efficiency of the post-task [1, 2, 3]. Emotional elements contain many aspects, for example, *opinion holder*, *comment target* (CT), and *evaluation phrase* (EP). The combination of them is similar to the concept of *appraisal expression* proposed in [4].

We define an EP to be an elementary linguistic unit that refers to successive evaluation words and conveys an attitude toward some target. For example, “非常平稳” (*English translation: very smooth*). We also define a *simple evaluation phrase* (SEP) and *complex evaluation phrase* (CEP). Final EPs we extract are composed by both of them. A SEP usually refers to the collocation of degree adverbs and evaluative words, mainly in fixed and simple structure. It usually occurs in the position of attribute, adverbial, and complement. And it can be used as an EP alone and also can be contained in a CEP after expansion. As follows, the underlined parts in every sentence are SEPs.

Example: 凭借领先业界的开发理念以及稳定且极具竞争力的价格。
(*English translation: the industry-leading development concept and very stable and competitive prices.*)

The structure of a SEP is relatively simple, but there are many complicated evaluation phrases in the text, which we call CEP. In many cases, A CEP will contain some SEPs. For example, “在新的大灯造型的配合下显得时尚且动感” (*English translation: Looks stylish and dynamic with the new headlight shape*) contains “新的大灯的” (*English translation: the new headlight*) and “时尚且动感” (*English translation: stylish and dynamic*).

Based on the extraction of EP, We use rule-based method to extract CT and *opinion holder*.

The remainder of this paper is structured as follows. In Sect. 2, we briefly summarize related work. Section 3 gives an overview of data description, including CT *dictionary* and *opinion-bearing verb dictionary*. We design the method of extracting the SEP based on CRFs in Sect. 4. And in Sects. 5 and 6, the methods of extracting the CEP, CT, and *opinion holder* are introduced, respectively. Experimental results are reported in Sects. 7 and 8 concludes our work.

2 Related Work

2.1 Evaluation Phrase

Research about *phrase extraction* mainly focuses on *noun phrase* and *preposition phrase*, and the concern about *EP extraction* is little, especially in Chinese. Whitelaw et al. [5] present a method for sentiment classification based on extracting and analyzing appraisal groups, and [6] present a method to phrase-level sentiment analysis based on subjective expression. Extraction patterns were also used in [7, 8, 9]. Furthermore [10] and [11] present methods for sentiment classification based on compositional semantics analysis.

2.2 Appraisal Expression

The interaction of CT and EP is important for polarity classification. The appraisal expression is first proposed by Bloom et al. [4], and is defined to comprise a *opinion holder*, an EP and a CT. Some scholars have proposed some rule-based methods, and other scholars try to dig the modified relation between EP and CT by using syntactic analysis.

2.3 Opinion Holder

Named entity recognition is often used to extract opinion holder. In addition, [1, 12] use semantic role labeling exploiting the semantic structure of a sentence to identify the opinion holder. And other scholars convert the extraction to classification.

3 Data Description

Our datasets come from expert's evaluation articles and user's comments on Tencent Automobile,¹ Netease Automobile (see Footnote 1), Phoenix Automobile,² and so on. In order to improve the extraction accuracy, we construct dictionaries on CT and opinion-bearing verb.

¹ <http://auto.qq.com/>.

² <http://auto.ifeng.com/>.

Table 1 Part of opinion-bearing verbs

| | | |
|----|----|----|
| 以为 | 主张 | 听说 |
| 认定 | 认为 | 觉着 |
| 感到 | 相信 | 耳闻 |

The dictionary of CT is used to judge whether a potential CT is automobile-correlative. We construct it by using *PMI*. First, we select a group of words (e.g., “发动机” “外观” etc.) concerned with automobiles as the foundation, and then use statistical information to enrich the dictionary. We calculate the PMI between every word in the dictionary and every noun in the corpus. For every dictionary word, we sort the PMIs in descending order, and add the first ten words into dictionary each time. The above process is repeated to enrich the dictionary.

$$PMI(\text{word}_1, \text{word}_2) = \log \left(\frac{P(\text{word}_1 \& \text{word}_2)}{P(\text{word}_1)P(\text{word}_2)} \right) \quad (1)$$

Because opinion holder and *opinion-bearing verb* co-occur generally, our method of extracting opinion holder is based on location of opinion-bearing verb. So we construct such dictionary for *part-of-speech* (POS) *tagging*. We divide opinion-bearing words into two parts: single morpheme verbs (e.g., “说”“道”“称” etc.) and multi-morpheme verbs (e.g., “认为”“透露” etc.). Considering that single morpheme verbs are usually contained in other words, for example “道” is contained in “道路”, we only put multi-morpheme verbs into such dictionary, while single morpheme verbs are processed individually in our algorithm. *HowNet* provides 23 multi-morpheme opinion-bearing verbs as shown in Table 1.

4 The Extraction of SEP Based on CRFs

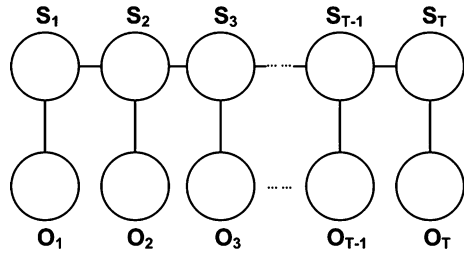
In [13], Conditional random fields (CRFs) are discriminative models and can thus capture many correlated features of the inputs. CRFs have a single exponential model for the joint probability of the entire paths given the input sentence and minimize the influences of the label and length bias. The structure of CRFs used for labeling sequence data is a simple chain figure as Fig. 1.

CRFs are able to detect sequence boundary efficiently. Considering structure of SEP is simple and its position is also fixed, we regard the extraction as a *sequence labeling problem*, and use CRFs model to recognize SEP according to the result labeled.

We choose to use *B/I/O tagging*, where the word labeled B refers to the word at the beginning of a SEP, the word labeled I refers to the word in the middle of a SEP and the word labeled O refers that this word does not belong to any SEP.

The extraction process is divided into two parts of the training and the testing. In the training part, first we choose suitable feature template and obtain training

Fig. 1 The graphical structure of CRFs chain



corpus after manually labeling. Then we use the template to extract features from training corpus and get the corresponding parameters, which are used to construct the final model file. In the testing part, content is labeled by model file used B/I/O tagging and the result labeled is the SEP.

5 The Extraction of CEP Based on Rule

The method described in this section is based on the SEP extracted above. Here, we define a *word combination of a certain POS* to be one or more consecutive words with such POS, and define a *split sentence* to a sentence split by colon, comma, semicolon, period, question mark, and other punctuations.

5.1 The Extraction of CEP Based on Rule

We summarize three complex structure rules: *parenthesis rule*, *preposition phrase rule*, and *adverb phrase rule*.

Parenthesis Rule. The content in parentheses can be extracted as a EP and this EP is responsible for modification of the CT on the left of parentheses. In this rule, we extract all the content in parentheses as EP while parentheses not included and the corresponding CT is the word combination of noun on the left of the parentheses.

Preposition Phrase Rule. Simple preposition phrase often fail to express a certain emotional tendency, but together with complement behind can do it. For each split sentence, we search for preposition from right to left. If we find a preposition, we analyze the content on its right side: after matching rules, if matched, we extract it by merging these words and resetting the POS tagging as EP. Continue this process until reaching the extreme left end. Our preposition phrase rule contains eight basic rules.

Adverb Phrase Rule. Full of sentiment information, Modal adverbs and degree adverbs indicate the speaker’s attitude. Our research mainly focuses on the condition that the adverb phrase is used as predicate or complement, and we search for adverbs in the split sentence and extract words complied with above description as EP. Our adverb phrase rule contains six basic rules.

6 The Extraction of Appraisal Expression Based on Rule

6.1 The Extraction of CT Based on Rule

Using EP as the center, we use CT constructing rules to construct the *word combination of noun* in the context as potential CT. Then we judge whether the potential CT corresponds to this EP by CT extracting rules and whether this CT contains some word in the dictionary of CT.

CT Constructing Rule. After the research on corpus of product comments about automobile and hotel, we have found that for a certain EP, its CT is the nearest word combination of noun on its left or right side in most cases. So we search toward the left and right, respectively, for the nearest word combination of noun in the split.

Example: 无疑/d /wd 飞思/nz 拥有/v 了/lule 出色的/EP 外形/n 设计/vn 。 /wj
(English translation: Undoubtedly, Feisi has excellent shape design.)

Wherein “出色的” (*excellent*) is identified as EP and we set it as the center to construct potential CT by searching toward both left and right. When we search toward the right, we find “外形设计” (*shape design*) and we get “飞思” (*Feisi*) when toward left. These two words are both potential CTs and are sifted by the following rules.

CT Extracting Rule. The CT we get above is only potential and we use the following three rules (decline in priority) to judge whether this CT corresponds to the EP.

Rules 1: EP + CT

Description: the CT is on the right side next to the EP.

In the example of this section, “外形设计” (*shape design*) corresponds to “出色的” (*excellent*). Other extracting rules are shown in the following Table 2:

Negative Judgment Rule. In some cases, the positional relation between a EP and the corresponding CT is a long-distance relationship rather than a adjacent relation. There may be many words between them changing the tone, especially negative verbs.

We set a variable counting the negative words which initial value is zero. Considering negative words are usually preposed in Chinese, when we search from EP toward left to locate the potential CT, and when encountering a negative word, this variable plus one. Finally, if the variable is odd, the EP is negative, otherwise positive.

Table 2 Other CT extracting rules

| ID | Description | Some rules |
|----|--|---|
| 2 | The CT is on the left side next to the EP | CT + EP |
| 3 | The CT is on the right side of the EP but not adjacent | CT + v + EP; CT + * + uls + EP; CT + * + c + EP; CT + * + v + * + ude3 + EP; CT + * + f + EP |

6.2 The Extraction of Opinion Holder Based on Rule

By researching on a large number of comment corpus, we found that the opinion holders are often names of people, community or institution. The positional relation between opinion holder and opinion-bearing verb is close and regular. In addition, the opinion holder contained in the context changes dynamically and so we pay much attention to judging whether the *opinion holder changes* among the split sentences.

First, if there is colon or opinion-bearing verb in split sentence, the opinion holder may change, otherwise it is the same as the one occurs in last split sentence. Then we set the opinion-bearing verb as the center, and search toward left to locate and construct the word combination of noun as potential opinion holder. In the process, we also record the distribution of words and POS tags. At last, corresponding rules are used to judge whether this opinion holder is what we want. For example, if preposition “据” is on the left side next to the opinion holder, this extraction succeeds.

7 Experiments and Results

7.1 Resources and Tool-Kits

Because there is no annotated comment corpus of automobile publicly available for evaluation of extraction, we design topic-focused web crawler, and totally crawl 15,326 sentences as training set after manually annotated and 60 whole articles as testing set from websites mentioned in Sect. 3.

The testing set contains 2,815 SEPs, 3,370 EPs, 3,370 CTs, 3,370 opinion holders, and 3,370 appraisal expressions.

We use ICTCLAS³ to complete Chinese word segmentation and POS tagging. We use CRF++ (version 0.53)⁴ to complete the task of training and testing based on CRFs. The system we developed is shown in Fig. 2 as follows.

³ <http://www.ictclas.com/>.

⁴ <http://crfpp.googlecode.com/svn/trunk/doc/index.html>.



Fig. 2 Emotional element extraction system

7.2 The Evaluation of Emotional Element Extraction

The extraction of emotional elements is evaluated by Precision, Recall, and F-measure.

$$\text{Precision} = \left(\frac{N_3}{N_2} \right) * 100 \% \quad (2)$$

$$\text{Recall} = \left(\frac{N_3}{N_1} \right) * 100 \% \quad (3)$$

$$F - \text{measure} = \frac{(\beta^2 + 1) * p * R}{R + \beta^2 * P}, \text{ where in } \beta = 1 \quad (4)$$

where N_1 is the total number of emotional elements in the testing set, N_2 is the number of what we extract, and N_3 is the number of correct result among the extraction.

8 Results

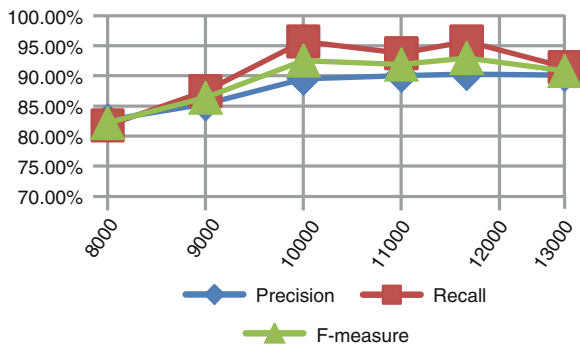
According to the evaluation in Sect. 7.2, we adopt the algorithms in Sects. 4, 5, and 6 to extract emotional elements from the testing corpus. The evaluation is shown in Table 3.

At present, there is no authoritative Chinese corpus for automobile's comments. Only the *opinion mining system for Chinese automobile reviews of Shanghai Jiaotong University* (SJTU) announced its algorithm and evaluation [14]. But the

Table 3 The evaluation of emotional elements

| | N1 | N2 | N3 | Precision (%) | Recall (%) | F-measure (%) |
|---|-------|-------|-------|---------------|------------|---------------|
| SEP | 2,815 | 3,009 | 2,694 | 89.53 | 95.70 | 92.52 |
| EP | 3,370 | 3,052 | 2,328 | 76.03 | 69.08 | 72.38 |
| Comment target | 3,370 | 3,052 | 2,317 | 75.91 | 68.75 | 72.15 |
| Opinion holder | 3,370 | 3,052 | 2,578 | 84.47 | 76.50 | 80.29 |
| Appraisal expression | 3,370 | 3,052 | 2,267 | 74.28 | 67.27 | 70.59 |
| An opinion mining system for Chinese automobile reviews | | | | 61.84 | 78.39 | 69.14 |

Fig. 3 Comparison of extraction results of SEP extraction in training sets with different scales



corpus and the system software haven't been announced. Their extraction of a pair of words in modified relationship is similar to our extraction of the pair of EP and CT. So, we implement their algorithm on our corpus and make a comparison on the result.

As shown in Table 3, both the precision and the recall of SEP extraction is relatively high, because the composition of SEP is regular and its grammatical elements is fixed. In the extraction of both CT and appraisal expression, the F-measures are both high than the result of SJTU reaching a good effect, and especially the precisions are high than that of SJTU about more than 10 %. Through analysis, we find the reason is that we take full use of the positional relationship between the EP and CT, and our rules are more detailed and efficient.

We construct six feature templates to judge what feature collected can perform well. After experiments, we conclude that the features are not the more the better in CRFs model, and the experiment achieves the best result when we consider such features synchronously: the current word, three words before and after it respectively, their POS tags and their binary combined.

We do another experiment aiming at the scale of training set. As shown in Fig. 3, the performance doesn't improve significantly with the increasing scale, and the influence of scale is not obvious when the scale reaches 10,000.

9 Conclusion and Future Work

In this paper, we focused on the characteristics of the different emotional elements and design statistical and rule-based extraction algorithms for EP, CT, and opinion holder. In future the work will focus on the following two aspects:

- (1) Further expansion of the rules and improvement of the algorithm's ability to process the text which does not comply with the syntax specification.
- (2) Combination with syntactic analysis and in-depth study of the relationship between the various emotional elements.
- (3) Although the proposed method focuses on the domain of automobile comment, it can be also adapted to other product domains by constructing corresponding dictionary. We also try to adapt it to the forum discussing issues, or technologies relating to positive and negative aspects of social media.

References

1. Kim SM, Hovy E (2005) Automatic detection of opinion bearing words and sentences[A]. In: Carbonell JG, Siekmann J (eds) *Proceedings of the IJCNLP 2005*. Springer, New York, pp 61–66
2. Popescu AM, Etzioni O (2005) Extracting product features and opinions from reviews[A]. In: Mooney RJ (ed) *Proceedings of the HLT/EMNLP 2005*. Association for Computational Linguistics, Morristown, pp 339–346
3. Pang B, Lee L, Vaithyanathan S (2002) Sentiment classification using machine learning techniques. In: Isabelle P (ed) *Proceedings of the EMNLP 2002*. Now Publishers Inc., Hanover, pp 79–86
4. Bloom K, Garg N, Argamon S (2007) Extracting appraisal expressions. In: Sidner C (ed) *Proceedings of the HLT-NAACL 2007*. Association for Computational Linguistics, Morristown, pp 308–315
5. Whitelaw C, Garg N, Argamon S (2005) Using appraisal groups for sentiment analysis. In: Fuhr N (ed) *Proceedings of the CIKM 2005*. ACM, New York, pp 625–631
6. Wilson T, Wiebe J, Hoffmann P (2005) Recognizing contextual polarity in phrase-level sentiment analysis[A]. In: Brew C, Chien LF, Kirchhoff K (eds) *Proceedings of the HLT/EMNLP 2005*. Association for Computational Linguistics, Morristown, pp 347–354
7. Bloom K, Argamon S (2009) Automated learning of appraisal extraction patterns. *Lang Comput* 71(1):249–260
8. Choi Y, Cardie C, Riloff E (2005) Identifying sources of opinions with conditional random fields and extraction patterns. In: Mooney RJ (ed) *Proceedings of the HLT/EMNLP 2005*. ACL, Morristown, pp 355–362
9. Riloff E, Wiebe J (2003) Learning extraction patterns for subjective expressions. In: Collins M, Steedman M (eds) *Proceedings of the EMNLP 2003*. ACL, Morristown, pp 105–112
10. Moilanen K, Pulman S (2007) Sentiment composition. In: Mitkov R (ed) *Proceedings of the recent advances in natural language processing international conference*, pp 378–382
11. Choi Y, Cardie C (2008) Learning with compositional semantics as structural inference for sub-sentential sentiment analysis. In: Lapata M, Ng HT (eds) *Proceedings of the empirical methods in natural language processing*. ACL, Morristown, pp 793–801

12. Kim SM, Hovy E (2006) Extracting opinions, opinion holders, and topics expressed in online news media text. In: Dale R, Paris C (ed) Proceedings of the ACL workshop on sentiment and subjectivity in text. pp 1–8
13. Lafferty J, McCallum A, Pereira F (2001) Conditional random fields: probabilistic models for segmenting and labeling sequence data. In: 18th International Conference on Machine Learning 2001. ACM Press, Williamstown, MA, USA, pp. 282–289
14. Yao T, Nie Q, Li J (2006) An opinion mining system for chinese auto-mobile reviews. In: Proceedings of the 25th anniversary of the Chinese information processing society of China, Beijing

Study on Multi-class Text Classification Based on Improved SVM

Qiong Li and Li Chen

Abstract Traditional SVM multi-class classification methods such as 1-a-r, 1-a-1, and DAG-SVM are popular learning techniques, but they often have the problems that the input text instances are nonlinear separable or their training/testing process is time consuming. In this chapter, we propose an improved SVM multi-class classification algorithm: first, the nonlinear separable texts in input space are mapped into a high dimensional feature space (Hilbert space) by using Mercer kernel function for obtaining linear separable texts; then in the Hilbert space, we construct SVM multi-class classifiers with binary tree to recognize testing instances. Our experiments demonstrate that for some web text classification problems, the proposed method can effectively solve the nonlinear separable problem existing in input text space, saves training/testing time efficiently, and improves the text classification accuracy.

Keywords Multi-class text classification · Support vector machine (SVM) · Binary tree · Mercer kernel

1 Introduction

Web text automatic classification [1] is widely used in the massive network resource processing. It is a very key and practical technique. The traditional text automatic classification methods such as Bayesian [2], KNN [3], and Neural Networks [4], etc., often have the problems of complex arithmetic, lower efficiency, and poor generalization ability. Recently, Support Vector Machine (SVM) which is based on Statistical Learning Theory and Structural Risk Minimization

Q. Li (✉) · L. Chen

School of Computer Science and Technology, Hankou University, Wuhan, China
e-mail: 81361966@qq.com; lq8081@126.com

Table 1 A comparison among three SVM multi-class classification methods

| Algorithm | #Classifier needing to train speed | Training speed | #Classifier for testing | Testing |
|-----------|------------------------------------|----------------|-------------------------|---------|
| 1-a-r | k | Slow | k | Fast |
| 1-a-1 | $k(k - 1)/2$ | Fast | $k(k - 1)/2$ | Slow |
| DAG-SVM | $k(k - 1)/2$ | Fast | $k - 1$ | Faster |

principle, has been shown to give competitive accuracy and generalization ability for some applications such as text classification. However, Support Vector Machine was originally designed for binary classification, and Web text automatic classification is a multi-class classification problem. Thus, we need to extend it for multi-class classification.

Currently, there are two types of approaches for multi-class SVM [5, 6]. One is by constructing and combining several binary classifiers, while the other is by directly considering all data in one optimization formulation. Because the latter one is time consuming, we usually use the first one. In general, there are three approaches for constructing SVM multi-class classifiers [7, 8]: 1-a-r (1-against-rest), 1-a-1 (1-against-1) and DAG-SVM.

The earliest used implementation for multi-class classification is probably the 1-against-rest method. It constructs k SVM models where k ($k \geq 2$) is the number of classes. Its testing speed is fast, but its training time is long. Furthermore, it has the problem that testing instances may belong to more than one class or not belong to anyone. Another major method is called the 1-against-1 method. This method constructs $k(k - 1)/2$ SVM classifiers where each one is trained on data from two classes. Its training speed is faster than 1-against-rest method, but for the testing time, 1-against-1 method is the worst. The third method is the Directed Acyclic Graph Support Vector Machine (DAG-SVM). Its training phase is the same as the 1-against-1 method by solving $k(k - 1)/2$ binary SVMs. But in the testing phase, it uses a rooted binary directed acyclic graph which has $k(k - 1)/2$ internal nodes and k leaves. An advantage of using a DAG-SVM is that some analysis of generalization can be established. In addition, its testing speed is the best in the three methods. However, its testing result is associated with root node directly; different root node would probably cause different classification results. So it will cause the uncertainty of testing result. A comparison among three SVM multi-class classification methods is given in Table 1.

2 The Improved SVM Algorithm

According to the analysis about the three SVM multi-class classification methods, and on the basis of their successes, this chapter proposes an improved SVM algorithm based on binary tree [9] and Mercer kernel [10]. The proposed method constructs SVM multi-class classifier by using binary tree, efficiently saving training/testing time. Furthermore, the nonlinear separable texts in input space are

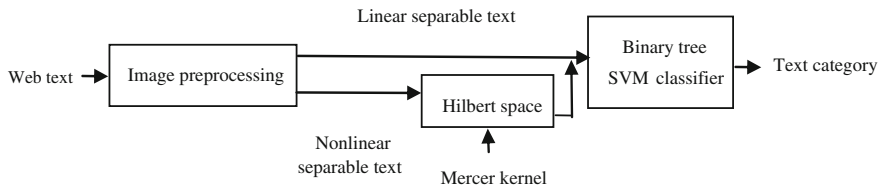


Fig. 1 The improved SVM classification process

mapped into a higher (maybe infinite) dimensional space by Mercer kernel, then they become linear separable texts. Therefore, the improved algorithm effectively solves the nonlinear separable problem in input text space and improves the classification accuracy. The improved SVM classification process is shown in Fig. 1.

2.1 Linear Separable Text

It is well known that binary tree method [11] is a simple and commonly used multi-class approach. It is an extension of the 1-a-r method for multi-class classification. For each class, it trains a classifier by using text associated with this class as positive and all others as negative. Suppose there are k classes, this method only needs to construct k decision functions. In prediction, an instance is associated with a class if the corresponding decision value is positive. Thus, the binary tree method can obtain much faster training/testing speed. In this chapter, we will use the binary tree method to construct SVM classifiers. It will save training and testing times efficiently. The binary tree method belongs to tree-structured classifier; its classification performance is associated with the separability measure of the upper nodes. Usually, in order to achieve the best generalization ability, the binary tree method should get the best value of separability measure between the upper nodes. Therefore, in the process of generating binary tree, the class which has the best separability measure should be recognized first, namely the upper nodes should be divided first.

This paper defines the radius R of the smallest hypersphere containing class C as Separability Measure (SM) of class C . The more larger the value of radius R is, the more larger the value of SM is. Accordingly, the more stronger SM of class C is, the more sooner class C should be divided in the upper node.

Definition 1 Radius R of the smallest hypersphere: Given a set of text instances $\{x_1, x_2, \dots, x_m\}$, where x_i is the feature vector matrices of text instances, $i = 1, 2, \dots, m$, and their class label is C , then the center of class C is $\bar{x} = \frac{1}{m} \sum_{i=1}^m x_i$.

Accordingly, the radius of the smallest hypersphere containing class C is defined as $R = \max_{x_i \in C} \{|x_i - \bar{x}|\}$, $i = 1, 2, \dots, m$. In the equation, $|\bullet|$ is Euclidean distance.

Definition 2 Define SM (SM of class C) as:

$$SM = R = \max_{x_i \in C} \{|x_i - \bar{x}|\}, \quad i = 1, 2, \dots, m. \quad (1)$$

If the input text instances are linear separable, we only use SM in Definition 2 to construct SVM classifiers for recognizing. In contrary, we can use the method in 2.2 to solve the nonlinear separable problem.

2.2 Nonlinear Separable Text

In order to solve the problem of recognizing nonlinear separable text, this chapter uses a map function: Mercer kernel. First, the text instances will be mapped into a higher dimensional Hilbert feature space by using Mercer kernel function, then those text instances belonging to the same category will gather up more tightly, and the different types of text will be farther apart, so that the nonlinear separable texts can be divided linearly. Second, in the higher dimensional Hilbert feature space, this chapter defines R^H (radius of the smallest hypersphere containing some class C in Hilbert space) as the SM^H of class C , and constructs binary tree SVM classifiers with SM^H to realize multi-class text automatic classification.

The recognizing process of nonlinear separable text and its corresponding improved SVM algorithm are as follows:

Given nonlinear separable text instances $x_i \in R^d (i = 1, 2, \dots, n)$, then we use the kernel function φ to map the text vectors x_i into a higher dimensional Hilbert feature space, and then we will get a new set of vectors in Hilbert feature space: $\varphi(x_1), \varphi(x_2), \dots, \varphi(x_n)$. Thus, the dot product of text vectors in Hilbert feature space should be expressed as:

$$K(x_i, x_j) = \varphi(x_i) \cdot \varphi(x_j), \quad i, j = 1, 2, \dots, n \quad (2)$$

Accordingly, Euclidean distance in Hilbert space is:

$$\begin{aligned} d^H(x, y) &= \|\varphi(x) - \varphi(y)\| \\ &= \sqrt{\|\varphi(x) \cdot \varphi(x) - 2\varphi(x) \cdot \varphi(y) + \varphi(y) \cdot \varphi(y)\|} \\ &= \sqrt{K(x, x) - 2K(x, y) + K(y, y)} \end{aligned} \quad (3)$$

The center of class C in Definition 1 is:

$$\varphi(\bar{x}) = \frac{1}{n} \sum_{i=1}^n \varphi(x_i) \quad (4)$$

Radius R^H of the smallest hypersphere containing class C in Hilbert space is defined as:

$$\begin{aligned}
 R^H &= \max_{x_l \in C} \{ \|\varphi(x_l) - \varphi(\bar{x})\| \} \\
 &= \max_{x_l \in C} \{ \|\varphi(x_l) - \frac{1}{n} \sum_{i=1}^n \varphi(x_i)\| \} \\
 &= \max_{x_l \in C} \left\{ \sqrt{K(x_l, x_l) - \frac{2}{n} \sum_{i=1}^n K(x_l, x_i) + \frac{1}{n^2} \sum_{i=1}^n \sum_{j=1}^n K(x_i, x_j)} \right\} \tag{5}
 \end{aligned}$$

Furthermore, SM^H of class C in Hilbert space should be defined as:

$$\begin{aligned}
 SM^H &= R^H \\
 &= \max_{x_l \in C} \left\{ \sqrt{K(x_l, x_l) - \frac{2}{n} \sum_{i=1}^n K(x_l, x_i) + \frac{1}{n^2} \sum_{i=1}^n \sum_{j=1}^n K(x_i, x_j)} \right\} \tag{6}
 \end{aligned}$$

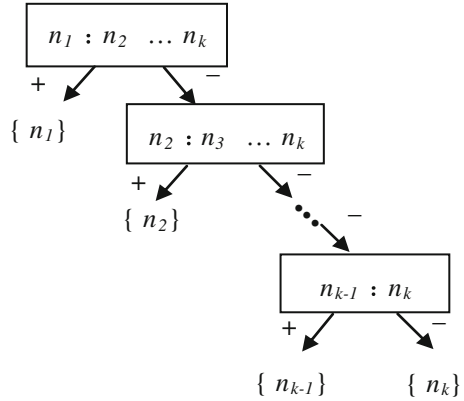
Here, the kernel is radial basis function (RBF):

$$K(x, y) = \exp\left\{-\frac{|x - y|^2}{\sigma^2}\right\} \tag{7}$$

Algorithm The improved SVM method for multi-class text classification (given k ($k \geq 2$) is the number of text categories):

- Step 1: Use the RBF to map the training text instances into a higher dimensional Hilbert feature space
- Step 2: Compute the Separability Measure SM^H of each class
- Step 3: Sort the class labels in order of descending SM^H . If there are two or more than two classes which have the same SM^H , then the class whose class label is smaller will be placed in the front. Finally, we will get an order of the class labels: n_1, n_2, \dots, n_k , here $n_i \in \{1, 2, \dots, k\}$ is class label, $i = 1, 2, \dots, k$
- Step 4: Use SVM training algorithm to obtain optimum hyperplanes between nodes of binary tree. At the root node, select class n_1 as positive and all others as negative, then use SVM training algorithm to get corresponding optimum hyperplane, and then delete the text instances belonging to class n_1 from training samples. Similarly, process the rest nodes in the same way. Finally, we will get the improved binary tree SVM multi-class text categorization model as shown in Fig. 2

Fig. 2 The improved binary tree SVM multi-class text categorization model. The nodes that ‘+’ point to stand for positive sample sets, and the others that ‘-’ points to represent negative sample sets



3 Experiments and Analysis

In our experiment, all text datasets considered are from Internet. We randomly downloaded 583 Chinese page texts, including six categories: Education, Environment, Economy, Military, Livelihoods, and Tourism. The number distribution of text instances is given in Table 2.

We randomly selected 428 text instances as training samples, and the other 155 text instances as testing samples. In the experiment, we use ICTCLAS [12] to realize Chinese word segmentation, use TF-IDF [13] algorithm to solve feature selection problem, and use the algorithm in reference [15] to decrease the dimension of text feature vector [14, 15]. Finally, we compared the performance of the proposed algorithm with the three methods: 1-a-r, 1-a-1, and DAG-SVM. LIBSVM [16, 17] used in the experiment can be available at <http://www.csie.ntu.edu.tw/~cjlin/libsvm/>. The kernel function is RBF. In addition, we use Grid Search and Cross Validation Methods [18, 19] to optimize the kernel parameters. The experimental results are given in Table 3.

The experimental results indicate that compared to 1-a-r, 1-a-1, and DAG-SVM methods, the new method can obtain better performance and classification accuracy, and efficiently saves training/testing time.

4 Conclusions

In this chapter, we discuss and analyze three SVM multi-class classifiers: 1-a-r, 1-a-1, and DAG-SVM method. The three methods are popular techniques for multi-class classification, but they often have the difficulties to effectively recognize nonlinear separable input texts, and their training/testing process is usually time consuming. It is well known that binary tree SVM can achieve better classification accuracy, and Mercer kernel has the function of mapping input text into Hilbert

Table 2 Number distribution of text instances

| Category | Education | Environment | Economy | Military | Livelihoods | Tourism |
|-----------|-----------|-------------|---------|----------|-------------|---------|
| #Instance | 100 | 98 | 94 | 95 | 100 | 96 |

Table 3 Experimental results

| | 1-a-r | 1-a-1 method | DAG-SVM | The improved method |
|-----------------------------------|---------------|-----------------|---------------------|------------------------|
| Kernel parameters (C, γ) | (100, 10 - 4) | (200, 10 - 4) | ($2^9, 2*10 - 5$) | ($2^{-1}, 2^4$) |
| Training time (s) | 67.52 | 56.63 | 56.54 | 47.71 |
| Testing time (s) | 14.23 | 34.32 | 12.35 | 8.93 |
| Classification accuracy (%) | 82.50 % | 81.30 % | 87.60 % | 93.60 % |

space. Therefore, we propose an improved SVM multi-class text classification method based on binary tree and Mercer kernel. Experiments on web texts demonstrate that the improved SVM algorithm can effectively solve the nonlinear separable problem in input text space, enjoys much faster training/testing, and achieves better precision of text classification. For this research work, we had difficulties to obtain the best kernel parameter combination. Thus, a future research direction is to optimize the kernel parameters for better SVM classifiers.

Acknowledgments This study is supported by the Science and Technology Research Planning Foundation of Education Bureau of Hubei Province of China (No. B20128103).

References

1. Liu Y, Wang ZL, Huang YL (2012) Research on classification of large-scale text on GPU platform. *Comput Eng Appl* 48(8):141–143
2. Ji SQ, Shi HB, Wei J (2012) Bagging bayes text classification based on map reduce. *Comput Eng* 38(16):203–206, 211
3. Hu Y, Shi B (2012) Fast KNN text classification algorithm based on area division. *Comput Sci* 39(10):182–186
4. Zhu YX (2012) Text classification algorithm research based on clustering and neural network. *Appl Res Comput* 29(1):155–157
5. Duan Y (2012) Application of SVM in text categorization. *Comput Digital Eng* 40(7):87–88, +149
6. Lee LH, Wan CH, Rajkumar R, Isa D (2012) An enhanced Support Vector Machine classification framework by using Euclidean distance function for text document categorization. *Appl Intell* 37(1):80–99
7. Qian HM, Mao YB, Xiang WB, Wang ZQ (2010) Recognition of human activities using SVM multi-class classifier. *Pattern Recogn Lett* 31(2):100–111
8. Abdelhamid D, Abdelmalik TA (2011) A fast multi-class SVM learning method for huge databases. *Int J Comput Sci Issues* 8(5):544–550

9. Xie L, Fu ZH, Feng W, Luo Y (2011) Pitch-density-based features and an SVM binary tree approach for multi-class audio classification in broadcast news. *Multimedia Syst* 17(2):101–112
10. Sheng BH, Wang JL, Chen ZX (2011) The covering number for some Mercer kernel Hilbert spaces on the unit sphere. *Taiwanese J Math* 15(3):1325–1340
11. Zhao WG, Wang LY (2012) SVM multi-class classification based on binary tree for fault diagnosis of hydropower units. *Inf Int Interdisc J* 15(11A):4615–4620
12. Cai XY, Kou YZ, Shen W, Zhen W (2008) The application and realization of ICTCLAS on Nutch-0.9. *J Ordnance Eng Coll* 20(5):63–66, +70
13. Zhang W, Yoshida T, Tang XJ (2011) A comparative study of TF*IDF, LSI and multi-words for text classification. *Expert Syst Appl* 38(3):2758–2765
14. Zheng W, Lv JX, Zhang JW (2011) Research on feature preextraction method in text classification. *Inf Sci* 1:86–88
15. Wang MC, Wang ZO, Zhang K et al (2005) Rough set text classification rule extraction based on CHI value. *J Comput Appl* 25(5):1026–1028
16. Chang CC, Lin CJ (2012) LIBSVM: a library for Support Vector Machines. <http://www.csie.ntu.edu.tw/~cjlin/papers/libsvm.pdf>
17. Hsu CW, Chang CC, Lin CJ (2010) A practical guide to support vector classification. <http://www.csie.ntu.edu.tw/~cjlin/papers/guide/guide.pdf>
18. Wang JF, Zhang L, Chen GX, He XW (2012) A parameter optimization method for an SVM based on improved grid search algorithm. *Appl Sci Technol* 39(3):28–31
19. Yin JL, Zhu YL (2012) Parameter optimization for Support Vector Machine and its application to fault diagnosis of power transformers. *Electr Meas Instrum* 49(557):11–16

Online Evaluation System of Image Segmentation

Khai Nguyen, Bo Peng, Tianrui Li and Qin Chen

Abstract Over the past few decades, many applications have been developed for quantify the performance of image segmentation algorithms. However, applying standard interactive segmentation software for large image datasets would be an extremely laborious and a time-consuming task. In this chapter, we present an online evaluation framework for analysis and visualization features via Internet communication that serves as a remote system. One of the features of the online evaluation system is the combination of MATLAB and Java to provide benefit platform that create the application with advanced mathematical computation as well as a well-designed graphical interface. This framework provides a web-based tool for validating the efficiency of segmentation algorithms. Experimental results show the possible ways in order to transfer MATLAB algorithm into a MATLAB license-free that make algorithm developed within MATLAB run all cross the platform and available on internet. In addition, the implementation methodology reported can be reused for other similar software engineering tasks.

Keywords Image segmentation · Online system · MATLAB and Java · Evaluation

K. Nguyen · B. Peng (✉) · T. Li
School of Information Science and Technology, Southwest Jiaotong University,
Chengdu 610031, China
e-mail: bpeng@swjtu.edu.cn

Q. Chen
Sichuan Provincial People's Hospital, Chengdu 610072, China

1 Introduction

Over the past two decades, the computer vision community has produced a number of useful algorithms for localizing object boundaries and interactive segmentation techniques in images. For example, snakes [1] have shown to be a useful specification for image contours. Livewire [2] is applied to create the segmentation of 3D boundary surfaces and can be used as a complete control as possible over segmentation during executing process and minimizes the total user's time required for segmentation. Another useful method becoming very popular in recently years is graph cuts [3, 4], it can be employed to efficiently solve a wide variety of low-level computer vision problems, including image smoothing, the stereo correspondence problem, and many others derived from the effort to minimize time consuming.

MATLAB software is one of the most advanced development tools for efficient algorithm development, offering many built-in functions. However, MATLAB-based software requires every user to acquire MATLAB license even if the user simply wants to control the segmentation process or review the result. Some related works have been developed [5–7]. MATLAB Web Server (MWS) is a software tool, designed for front-end MATLAB based Web application development that provide valuable assistance toward research in cervical cancer detection [5]. The annotation MATLAB toolbox is used to label the identity of objects and where they occur in images [6]. MATLAB builder Java toolbox utilizes Java and MATLAB platforms together to create the software for image analysis in pathology via internet communication [7].

Some evaluation algorithms for image segmentation have been developed within MATLAB [8–10]. These evaluation methods can be divided into two categories: supervised evaluation and unsupervised evaluation. In unsupervised evaluation, segmentations are judged by criteria such as the uniformity of colors [11], the shape of object regions [12]. In supervised evaluation, criteria that measure the differences between the segmentation image and the ground truths are used [13–15].

In this paper, we provide an online evaluation system of image segmentation and also utilize various MATLAB's advantages. The main purpose of this work is to investigate possible ways in order to transform MATLAB algorithm into a MATLAB license-free. This online evaluation system features provide the compiler generating code for existing client-side and backend technologies, for example it does not need to download a browser plugin to use a Web application. Furthermore, the system have user-friendly interface, server-side storage, no programming skills, and so forth.

The paper is organized as follows: in Sect. 2, we provide description about three segmentation evaluation methods that condensed the knowledge of discovering techniques for evaluation of image segmentation. In Sect. 3, we apply these three metrics to provide proposed methodology for integrating MATLAB and Java and make it available on internet. Section 4 describes the experiments, lastly the conclusion are outlined in the last section.

2 Image Segmentation Evaluation Methods

2.1 Rand Index

Rand Index (RI) is a natural extension of the idea involving the comparison of two clusterings which have a corresponding extension of the performance measure: instead of counting single elements it counts correctly classified pairs of elements. Thus, the RI [8] as follows:

$$c(Y, Y') = \left[\binom{N}{2} - \frac{1}{2} \left\{ \sum_i (\sum_j n_{ij})^2 + \sum_j (\sum_i n_{ij})^2 \right\} - \sum \sum n_{ij}^2 \right] / \binom{N}{2} \quad (1)$$

Where $c(Y, Y')$ is defined as the total number of any similarities of two clusterings of the same data, Y and Y' . Consider the two clusterings are defined as $Y = \{Y_1, \dots, Y_{K_1}\}$ and $Y' = \{Y_1, \dots, Y_{K_2}\}$. Give a pair of clusterings Y and Y' of the same N points, let n_{ij} be the number of points simultaneously in the i th cluster of Y and the j th cluster of Y' . The value of c depends on both, the number of clusters and the number of elements. The RI takes values in the range $[0, 1]$, where the two clusterings have no similarity and 1 indicates that the clusterings are identical $1-c$ is a measure of distance.

2.2 The Variation of Information Metric

This is an information-theoretic method [9]. This metric defines the distance between two segmentations as the average conditional entropy of one segmentation given the other:

$$VI(S_{\text{test}}, S_k) = H(S_{\text{test}}|S_k) + H(S_k|S_{\text{test}}) \quad (2)$$

The first term in (2) measures the amount of information about S_{test} that we lose, while the second term measures the amount of information about S_k that we have to gain, when going from segmentation S_{test} to ground truth S_k . An equivalent expression of (2) is:

$$VI(S_{\text{test}}, S_k) = H(S_{\text{test}}) + H(S_k) - 2I(S_{\text{test}}, S_k) \quad (3)$$

where H and I represent, respectively, the entropies and the mutual information associated between the segmentation S_{test} and the ground truth S_k . Variation of Information (VI) is a distance metric since it satisfies the properties of non-negativity, symmetry and triangle inequality. If two segmentations are identical, the VI value will be zero. The upper bound of VI is finite and depends on the number of elements in the segments.

2.3 The Global Consistency Error

This measure computes the degree of overlap of regions [10]. It sums up all local inconsistencies for each pixel in the image. It is a region-based measures of segmentation consistency based on the degree of region overlap between clusters. Let $R(S, p_i)$ be the set of pixels in segmentation S that contains pixel p_i . The local refinement error is defined as:

$$E(S_1, S_2, p_i) = \frac{|R(S_1, p_i) \setminus R(S_2, p_i)|}{R(S, p_i)} \quad (4)$$

This error is not symmetric with regard to the compared segmentations, and it takes the value of zero when S_1 is a refinement of S_2 at pixel p_i . The Global Consistency Error (GCE) is then defined as:

$$\text{GCE}(S_1, S_2) = \frac{1}{n} \min \left\{ \sum_i E(S_1, S_2, p_i), \sum_i E(S_2, S_1, p_i) \right\} \quad (5)$$

3 Online Evaluation System Development

3.1 Program Design

The design is developed with the idea based on the understanding of some basic MATLAB functions/commands for translating and using with Java program that display graphics. The Java interface displays computation results read from dataset and the visualizations figures drawn from MATLAB. Figure 1 is a UML model displaying the design of MATLAB-Java integration that provides a visualization of the implementation model. It displays the MATLAB defined functions that the program uses as well as the Java classes. The MATLAB functions are deployed into a component jar file, through MATLAB builder JA. These Java classes can be integrated into Java programs and deployed royalty-free to desktop computers that do not have MATLAB installed using the MATLAB Compiler Runtime (MCR) that is provided with MATLAB Compiler.

Our program has a simple design that uses Graphic User Interface (GUI) components including windows, scroll bar, menus, buttons, and icons for drawing interface components on the screen. Furthermore, we have the special component producing distribution histograms called The Deployment Tool that is a GUI provided by MATLAB Compiler. With The Deployment Tool, we can add MATLAB files to serve as externally visible class methods of Java component such as the distribution histograms component. Thus, the design of our model based on init and figure architecture.

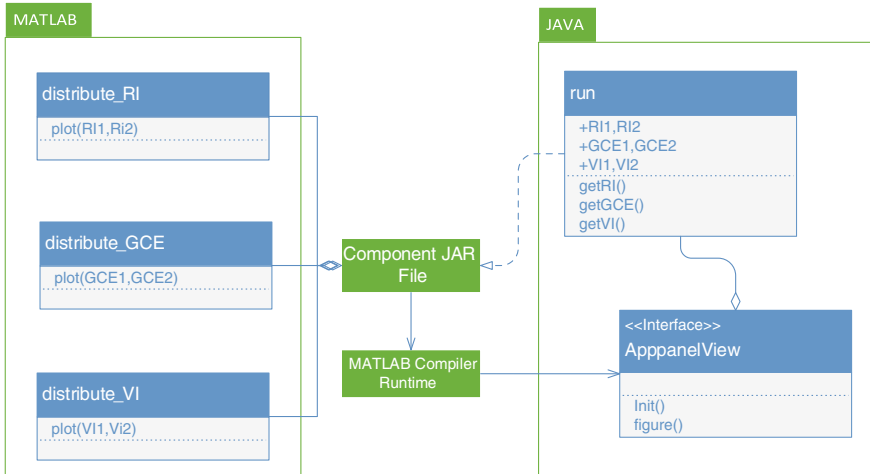


Fig. 1 UML model of MATLAB-Java integration

init() initialize the components in GUI. We will be using Swing components for building interfaces (JFrame, JComponent, JButton, JLabel, JMenu, JPanel, JTextField ...). All Swing components have AWT components as event model and listeners that detect user interaction, mouse click, key press etc.

figure() contains the distribution histograms component and collect data types that converted the input retrieved from the user interaction to pass to MATLAB function for calculating and generating return figure.

3.2 Embedding JAR Package into a Web Page

When displayed with the browser, our Java program would look approximately as shown in Fig. 2. After we create the class that compose our applet and compile them into class files by using Net beans, we create a Webpage on which to place the applet. We place an applet in an HTML document with a command known as an applet tag. The following applet tag will display the applet in Fig. 2.

```
<applet code = "AppPanel.class" archive = "embedded.jar" width = "768" height = "397">
  <param name = "dta0" value = "dataset">
  <param name = "dta1" value = "dataset_10img">
</applet>
```

The applet embedded in our webpage can only load a predetermined set of image dataset by reading parameters that are set up with the HTML tag param, which has name and value attributes. In this case defines two parameters to the AppPanel applet: dta0 with a value of dataset that contains 100 images and dta1

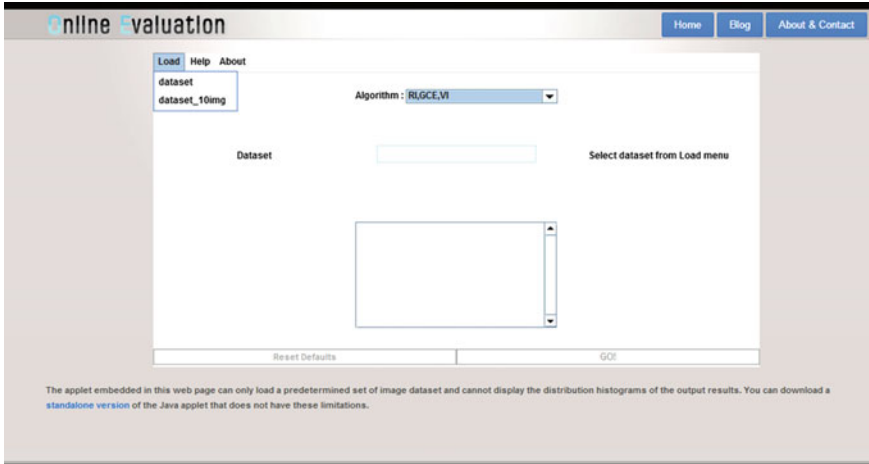


Fig. 2 Browser view

with a value of `dataset_10img` that contains 10 images. Parameters are passed to an applet as following:

```
//Get the applet parameters.
int imgNum = 0;
String at = getParameter("dta" + imgNum);
while(at != null){
  images.add(new JMenuItem(at));
  images.get(imgNum).addActionListener(app);
  imgNum++;
  at = getParameter("dta" + imgNum);}
```

After having an applet's class file and a Webpage that includes the applet, we run the applet by loading the page with a Web browser. The running output results of Java applet are the same with the running output results on Java standalone package but cannot display the distribution histograms of the output results. Thus we allow user download a standalone package link of the Java applet that does not have the limitation.

4 Experiments

Our image dataset consists of 200 images. The images were collected from the hand-labeled segmentations. Half of the segmentations were obtained from presenting the subject with a grayscale image. The images used for calculating were 481×321 and 321×481 .

In our first experiment, we run the input dataset contains 10 images with our ground truth images on our Java program and we obtain the comparison results between the input dataset and ground truth dataset. Then, we repeat these steps

using MATLAB program with the same input and ground truth dataset. We will note and describe that the comparison results running on our application more accurate than running on MATLAB program.

Second, we run the input dataset with 10, 20, 40, 80, 100 images for comparing the running time of our Java application and MATLAB program. We will note that the execution time of our approach could be accepted.

In Table 1, we demonstrate our experiments on the same dataset. We notice the VI results have the same results with MATLAB, in contrast the RI and GCE results are more accurate compared to MATLAB. This is because MATLAB will automatically round to nearest integers if the values obtained from the multiplication of two matrix are larger than 50,000 and vice versa if the values are smaller than 50,000 equal to zero in this case. For example, when perform calculations $n.*n$ in MATLAB, the value of between 12,000 and 15,000 is rounded down to 10,000, and vice versa rounded up to 20,000 if the value is larger than 15,000. In contrast, the results obtained from the multiplication of two matrixes in Java remain the same. Therefore, we can conclude the RI, GCE results in our application more accurate than the MATLAB results.

Good segmentation results are associated with high RI, low GCE, and low VI. We compare the average of RI, GCE, VI results on our first experiment. In this case, according to the results in our Java program, we can conclude “Ground Truth 1” is better than “Ground Truth 2” with high RI and low GCE results. In other hand, the MATLAB program has opposite results that we can conclude “Ground Truth 2” is better than “Ground Truth 1” as shown in Fig. 3.

In the Fig. 4 after the results completed, at the same time, the distribution histograms of the three metrics will be made. The comparison result was drawn in the three different windows that display the comparison results of RI1–RI2, GCE1–GCE2, VI1–VI2. The result images can be saved by the user using MATLAB toolbox that provided by MATLAB Compiler. We run the experiments on our testing dataset with 100 images on each dataset and we find out if the value of RI is higher and GCE, VI is lower, then the image segmented is better.

Runtime comparison. The software testing platform has Intel® Core™ i3 CPU M 350 @2.27 GHz x2, 4.00 GB memory, running a Windows 7 Ultimate SP1 operating system. In order to do a fair runtime comparison between different situations, we take the simulation data sample as testing material. It has 100 sample images on each testing dataset. We arrange the order of the comparison dataset similarity for testing on Java application and MATLAB. The mapping process time between Java double types and MW Array through MATLAB compiler runtime depends on the size of the dataset. Thus, the datasets are large in size, so the mapping process time increased. We can conclude that for small datasets the running time differences for Java application, compare to MATLAB source code, are in an acceptable range. The time gap between those two is due to the variable mapping process, because for Java application, the core algorithm is still running inside MATLAB which running time should equal to the MATLAB source code. Table 2 presents a detail running time comparison between differencing the size of dataset.

Table 1 The comparison of evaluation results

| Image | Java | | | | | | MATLAB | | | | | |
|-------|----------------------|--------|--------|----------------------|--------|--------|----------------------|--------|--------|----------------------|--------|--------|
| | Input-ground truth 1 | | | Input-ground truth 2 | | | Input-ground truth 1 | | | Input-ground truth 2 | | |
| | RI | GCE | VI | RI | GCE | VI | RI | GCE | VI | RI | GCE | VI |
| 1 | 0.8718 | 0.0156 | 0.3201 | 0.8675 | 0.019 | 0.3034 | 0.9298 | 0.0425 | 0.3201 | 0.9340 | 0.0382 | 0.3034 |
| 2 | 0.8938 | 0.0017 | 0.3862 | 0.8583 | 0.0347 | 0.2616 | 0.9078 | 0.0512 | 0.3862 | 0.9433 | 0.0311 | 0.2616 |
| 3 | 0.8476 | 0.0459 | 0.2241 | 0.840 | 0.0535 | 0.1951 | 0.9540 | 0.303 | 0.2241 | 0.9616 | 0.0283 | 0.1951 |
| 4 | 0.8634 | 0.0291 | 0.2911 | 0.8521 | 0.0385 | 0.2426 | 0.9382 | 0.0425 | 0.2911 | 0.9494 | 0.0282 | 0.2426 |
| 5 | 0.8472 | 0.0435 | 0.2269 | 0.8449 | 0.0486 | 0.2153 | 0.9544 | 0.0312 | 0.2269 | 0.9568 | 0.0318 | 0.2153 |
| 6 | 0.823 | 0.0684 | 0.1187 | 0.8093 | 0.0819 | 0.0553 | 0.9785 | 0.0127 | 0.1187 | 0.9923 | 0.0069 | 0.0553 |
| 7 | 0.8716 | 0.0182 | 0.3055 | 0.8419 | 0.049 | 0.2069 | 0.9300 | 0.0326 | 0.3055 | 0.9597 | 0.0288 | 0.2069 |
| 8 | 0.8512 | 0.0402 | 0.2428 | 0.8381 | 0.0521 | 0.1883 | 0.9504 | 0.0354 | 0.2428 | 0.9635 | 0.0233 | 0.1883 |
| 9 | 0.8759 | 0.0149 | 0.3209 | 0.8606 | 0.0305 | 0.2728 | 0.9257 | 0.0347 | 0.3209 | 0.9409 | 0.0333 | 0.2728 |
| 10 | 0.8519 | 0.0411 | 0.2376 | 0.8479 | 0.0425 | 0.2248 | 0.9497 | 0.0287 | 0.2376 | 0.9538 | 0.0268 | 0.2248 |

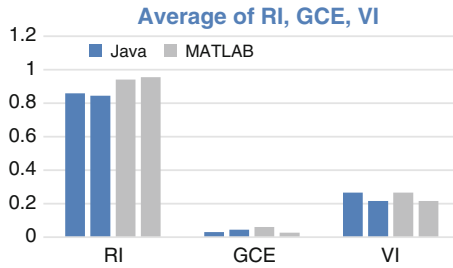


Fig. 3 Average of RI, GCE, VI

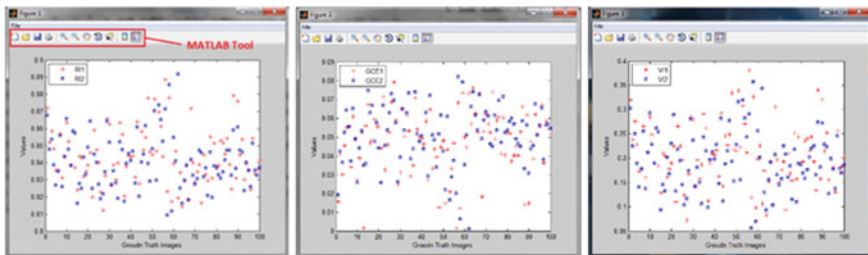


Fig. 4 Distribution histogram of RI, GCE, VI results

Table 2 Runtime comparison between different size of dataset

| Dataset (images) | Running time (s) | | |
|------------------|--------------------|------------------|-----------------|
| | MATLAB source code | Java application | Mapping process |
| 10 | 1'02 | 3'98 | 2'98 |
| 20 | 2'8 | 5'82 | 3'9 |
| 40 | 3'9 | 10'3 | 4'3 |
| 80 | 7'2 | 17'98 | 7'4 |
| 100 | 9'32 | 22'10 | 8'2 |

5 Conclusions

We have presented an online evaluation framework for analysis and visualization features via internet communication. The experiments have confirmed that the successful way to transform MATLAB algorithm to Java-based software that we can easily deploy and do not restricted by MATLAB license any more. By using Java applet technology, our program can run on any workstation with a common web browser. No other applications are required to be installed on the client workstation to use the web-based tool and provide an online supervised tool for validate the efficiency of segmentation algorithms evaluation.

Acknowledgements This work is supported by the National Science Foundation of China under Grants 61202190 and 61175047, the Science and Technology Planning Project of Sichuan Province under Grant 2012RZ0008, and by the Fundamental Research Funds for the Central Universities under Grant 2682013CX055.

References

1. Kass M, Witkin A, Terzopoulos D (1998) Snakes: active contour models. *Int J Comput Vis* 1(4):321–331
2. Falcão A X, Udupa J K, Miyazawa F K (2000) An ultra-fast user-steered image segmentation paradigm: live wire on the fly. *IEEE Trans Med Imaging* 19(1):55–62
3. Boykov YY, Jolly M-P (2001) Interactive graph cuts for optimal boundary and region segmentation. *Int Conf Comput Vis* 1:105–112
4. Boykov YY, Lea GF (2006) Graph cuts and efficient n-d image segmentation. *Int J Comput Vis* 70(2):109–131
5. Xue Z, Antani S, Long RL, Thomas GR (2010) An On-line Segmentation Tool for Cervicographic Image Analysis. In: *IHI '10 Proceedings of the 1st ACM International Health Informatics Symposium*, pp 425–429, ACM press, New York
6. Russell BC, Torralba A, Murphy KP, Freeman WT (2008) LabelMe: a database and web-based tool for image annotation. *Int J Comput Vis* 77(1–3):157–173
7. Markiewicz T (2010) Using MATLAB software with Tomcat server and Java platform for remote image analysis in pathology. In: *10th European congress on telepathology and 4th international congress on virtual microscopy*
8. Rand WM (1971) Objective criteria for the evaluation of clustering methods. *J Am Stat Assoc* 66(336):846–850
9. Meilă M (2007) Comparing clusterings—an information based distance. *J Multivar Anal* 98(5):873–895
10. Martin D, Fowlkes C, Tal D, Malik J (2001) A database of human segmented natural images and its application to evaluating segmentation algorithms and measuring ecological statistics. *Int Conf Comput Vis* 2:416–423
11. Borsotti M, Campadelli P, Schettini R (1998) Quantitative evaluation of color image segmentation results. *Pattern Recogn Lett* 19(8):741–747
12. Ren X, Malik J (2003) Learning a classification model for segmentation. In: *Proceedings of IEEE international conference on computer vision*, pp 10–17
13. Freixenet X, Raba MD, Marti J, Cuff X (2002) Yet another survey on image segmentation: region and boundary information integration. In: *Proceedings of European conference on computer vision*, vol 2352, pp 408–422
14. Pantofaru C, Hebert M (2005) A comparison of image segmentation algorithms. Technical Report, CMU-RI-TR-05-40, Carnegie Mellon University
15. Martin D, Fowlkes C, Tal D, Malik J (2001) A database of human segmented natural images and its application to evaluating segmentation algorithms and measuring ecological statistics. In: *Proceedings of IEEE international conference on computer vision*, vol 2, pp 416–423

Modeling of 3D Personalized Digital Apparel Whole-Human Body Based on Mannequin Components

Xiaping Shi and Senpeng He

Abstract This paper presents a modeling method of three-dimensional (3D) personalized digital apparel whole-human body on the basis of previous researches. This method divides a human body into different components by adding definitions of characteristic parameters, and appending components of head and the four limbs in component template database. Matched component templates are selected and reconstructed according to characteristic data for a specific user. A personalized digital apparel whole-human body will be generated. This is a beneficial exploration for virtual human application. That will provide more perfect technical support for virtual try on (VTO) and Electronic Made To Measure (eMTM).

Keywords Human body modeling · Characteristic parameters · Reconstruct

1 Introduction

With the rapid development of e-commerce, more and more consumers begin to purchase clothes on garment e-commerce platforms, such as Taobao, Vancl, etc. However, at present e-commerce platforms do not solve the problem of virtual try-on effectively when consumers buy clothing online. Whether Most of consumers make a decision to buy only depends on the traditional way such as limited size. The absence of style and overall effect and error resulted by limited size will cause inconsistent with the original idea of consumers. Solving the problem effectively needs a whole set of theory and technology solutions. The Electronic Made To Measure (eMTM) [1] and its implementation will help to solve the dilemma of

X. Shi (✉) · S. He
School of Computer Science and Technology, Donghua University,
Shanghai, People's Republic of China
e-mail: sxp@dhu.edu.cn

customized clothing under Internet environment. Generating 3D personalized digital apparel human body quickly and accurately in eMTM is one of the key technologies to solve the problem.

This paper improves generation of 3D personalized digital apparel human body to imperfect visibility and limited virtual try on (VTO) existed in previous researches. The method supplies human body characteristic parameters and adds components of head and four limbs into the template library. Matched component templates are selected to reconstruct in accordance with characteristic data for a specific user. A personalized digital apparel whole-human body will be generated finally.

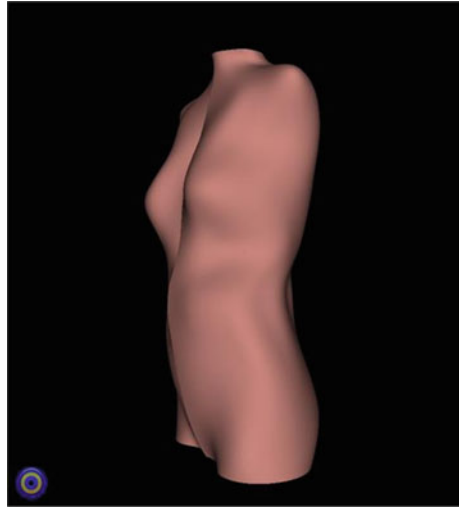
2 Related Works

At present, 3D human body modeling for clothing can be divided into three kinds based on characteristics of modeling: the human body modeling based on 3D body scanner, based on photographs, and based on 3D modeling software [2]. The modeling based on 3D scanner can obtain actual geometry data on surface of human body through a 3D scanner. A human model with the network topology structure of explicit rules can be generated after settling the lack of point cloud data and noise points. Obviously, this method is more accurate but expensive and slow due to essential equipment, so it is difficult to promote in the e-commerce. The modeling based on photographs set up a 3D human model by means of extracting geometric parameters of human body in processed images. Although the cost of the method is low, the accuracy of modeling is not high. The approach based on 3D modeling software applies modeling software such as Maya, 3DMAX, to construct 3D human body. This kind of modeling requires specialized persons for modeling human though it is simple. It also has low accuracy and lacks of personalization [3].

Before we do the research in this paper, we have established a human component template database after classifying human bodies scanned via the human body analysis system. Most similar component templates of human body in the database are chosen according to the template matching algorithm on the basis of gotten characteristic data of a specific user's body. A 3D human model is generated through fine-tuning and fitting the templates to body shape contour of the user, as shown in Fig. 1. This modeling method mainly takes human body's torso into consideration. The torso of human body is the principal part in the clothing project and 3D modeling. It is known as body form in the field of clothing. But this kind of body form is inappropriate for consumers and VTO.

In order to solve the existing deficiencies in constructing 3D apparel human body, the paper proposes the modeling of whole-human body which includes head, torso, and limbs. The component template library is complemented through human characteristic parameters are supplied. Required component templates are found out according to characteristic data for a specific user. A personalized digital complete human body is generated by means of assembling individual components so as to solve that digital apparel human body only has a torso.

Fig. 1 3D digital apparel body form



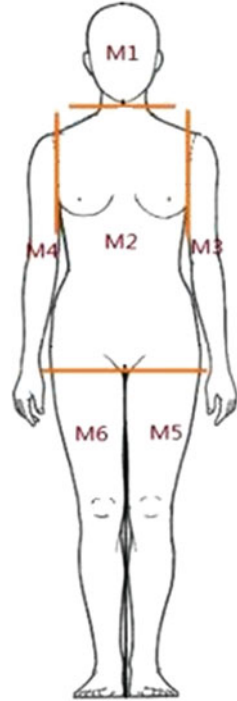
3 Construction of 3D Personalized Digital Whole-Human Body Model

We assume that a whole-human body is defined as Ω , and the i -th component as M_i , where $i = 1, \dots, 6$, respectively correspond to component of head, torso, left-hand, right-hand, left-leg, and right-leg. $M_i \in \Omega$ and $M_1 \cup M_2 \cup M_3 \cup M_4 \cup M_5 \cup M_6 = \Omega$. The j -th cross-section in M_i is represented as S_{ij} , where $S_{ij} \in M_i$, $j = 1, 2, \dots, n$, $S_{i1} \cap S_{i2} \cap \dots \cap S_{in} = \Phi$, $S_{i1} \cup S_{i2} \cup \dots \cup S_{in} = M_i$. $X(S_{ij})$, $Y(S_{ij})$, $X_{\max}(S_{ij})$, $Y_{\max}(S_{ij})$, $X_{\min}(S_{ij})$, $Y_{\min}(S_{ij})$, $X_{\text{cen}}(S_{ij})$, $Y_{\text{cen}}(S_{ij})$ are, respectively, represented as x -coordinate value, y -coordinate value, the maximum and the minimum of x and y , the center of x , y in the S_{ij} cross-section. $X_W(S_{ij})$, $Y_W(S_{ij})$ and $Z(S_{ij})$ are expressed as the width, thickness and height of the cross-section S_{ij} . The coordinate system of this paper is defined as following: the center between two feet bottom is used as the origin, the orientation of the human head as negative Z -axis, the positive orientation of body as positive Y -axis, the direction of the left side of the body as X -axis.

3.1 Definition of Body Components

On the basis of characteristics of human body and clothing structure, we divide a whole-human body Ω into six parts $M_1 \sim M_6$ in accordance with neck cross-section [4], the horizontal of the crotch point and the vertical surface of the armpit point [5], as shown in Fig. 2. This division can not only follows the previous modeling to generate torso of apparel human body but also take into account whole-human body modeling supplying head and limbs.

Fig. 2 Division of body components



3.2 Definition of Head Characteristics

Base on the requirements of modeling 3D digital apparel human quickly and efficiently, the principle of modeling of the head part is that the modeling can reflect the basic features of the head part since the head part is not the main part of the whole-human body modeling for clothing engineering. Therefore, we define three key cross-sections to model the head part.

Definition 1 S_{1Head} is defined as the cross-section of top head with the minimum of z -coordinate in M_1 , that is,

$$S_{1Head} = \{S_{1k} | Z(S_{1k}) < \forall Z(S_{1j}), \quad \{S_{1k}, S_{1j}\} \in M_1, j \neq k\} \quad (1)$$

Definition 2 S_{1HBC} is defined as the cross-section of the maximum head girth which has the largest sum of the width and thickness in M_1 , that is,

$$S_{1HBC} = \left\{ \begin{aligned} &S_{1k} | X_w(S_{1k}) + Y_w(S_{1k}) > \forall X_w(S_{1j}) + Y_w(S_{1j}), \\ &\{S_{1k}, S_{1j}\} \in M_1, j \neq k \end{aligned} \right\} \quad (2)$$

Definition 3 $S_{1\text{Neck}}$ is defined as the neck cross-section that has the maximum of z -coordinate in M_1 , that is,

$$S_{1\text{Neck}} = \{S_{1k} | Z(S_{1k}) > \forall Z(S_{1j}), \{S_{1k}, S_{1j}\} \in M_1, j \neq k\} \quad (3)$$

3.3 Definition of Arm Characteristics

In clothing engineering, the main arm characteristics are arm length and arm circumference. Therefore, we should keep these data features in the definition of arm cross-section.

Definition 4 $S_{4\text{Shoulder}}$ means the acromion cross-section that has the minimum of z -coordinate in M_4 , that is,

$$S_{4\text{Shoulder}} = \{S_{4k} | Z(S_{4k}) < \forall Z(S_{4j}), \{S_{4k}, S_{4j}\} \in M_4, j \neq k\} \quad (4)$$

Definition 5 $S_{4\text{Wrist}}$ means the wrist cross-section that has the smallest sum of the width and thickness in M_4 , that is,

$$S_{4\text{Wrist}} = \left\{ \begin{array}{l} S_{4k} | X_w(S_{4k}) + Y_w(S_{4k}) < \forall |X_w(S_{4j}) + Y_w(S_{4j}), \\ \{S_{4k}, S_{4j}\} \in M_4, j \neq k \end{array} \right\} \quad (5)$$

In order to easily find out the largest cross-sections of the upper arm girth and the lower arm girth, $S_{4\text{Aux}}$ is defined as an auxiliary cross-section whose z -coordinate value is equal to the middle between acromion and wrist, namely

$$S_{4\text{Aux}} = \left\{ S_{4k} \left| Z(S_{4k}) = \frac{Z(S_{4\text{Shoulder}}) + Z(S_{4\text{Wrist}})}{2}, S_{4k} \in M_4 \right. \right\} \quad (6)$$

Definition 6 $S_{4\text{ABC}}$ is the cross-section with the maximum upper arm girth that has the largest sum of the width and thickness between $S_{4\text{Shoulder}}$ and $S_{4\text{Aux}}$, that is,

$$S_{4\text{ABC}} = \left\{ \begin{array}{l} S_{4k} | X_w(S_{4k}) + Y_w(S_{4k}) > \forall X_w(S_{4j}) + Y_w(S_{4j}), \\ \{Z(S_{4k}), Z(S_{4j})\} \in (Z(S_{4\text{Shoulder}}), Z(S_{4\text{Aux}})), j \neq k \end{array} \right\} \quad (7)$$

Definition 7 $S_{4\text{FBC}}$ is the cross-section with the maximum lower arm girth that has the largest sum of the width and thickness between $S_{4\text{Aux}}$ and $S_{4\text{Wrist}}$, that is,

$$S_{4\text{FBC}} = \left\{ \begin{array}{l} S_{4k} | X_w(S_{4k}) + Y_w(S_{4k}) > \forall |X_w(S_{4j}) + Y_w(S_{4j}), \\ \{Z(S_{4k}), Z(S_{4j})\} \in (Z(S_{4\text{Aux}}), Z(S_{4\text{Wrist}})), j \neq k \end{array} \right\} \quad (8)$$

3.4 Definition of Leg Characteristics

Characteristics of leg and arm are similar. This paper takes the right leg as an example to discuss the definition of leg characteristics. The definition of left leg is similar to the right leg one.

Definition 8 $S_{6\text{Crotch}}$ means the crotch cross-section that has the minimum of z -coordinate in M_6 , that is,

$$S_{6\text{Crotch}} = \{S_{6k} | Z(S_{6k}) < \forall Z(S_{6j}), \quad \{S_{6k}, S_{6j}\} \in M_6, j \neq k\} \quad (9)$$

Definition 9 $S_{6\text{Foot}}$ means the sole of foot cross-section that has the maximum of z -coordinate in M_6 , that is,

$$S_{6\text{Foot}} = \{S_{6k} | Z(S_{6k}) > \forall Z(S_{6j}), \quad \{S_{6k}, S_{6j}\} \in M_6, j \neq k\} \quad (10)$$

Definition 10 $S_{6\text{Ankle}}$ means the ankle cross-section that has smallest sum of the width and thickness in M_6 , that is,

$$S_{6\text{Ankle}} = \left\{ \left\{ S_{6k} | X_w(S_{6k}) + Y_w(S_{6k}) < \forall X_w(S_{6j}) + Y_w(S_{6j}), \right\} \right. \\ \left. \left\{ \{S_{6k}, S_{6j}\} \in M_6, j \neq k \right\} \right\} \quad (11)$$

Definition 11 According to the proportion of various parts of human body described in national standard, the knees of women and man are separately located in about 0.28 times and 0.26 times the standing height H , defined as Kn . Therefore $S_{6\text{Knee}}$ is defined as the knee cross-section that has the maximum Y_{\max} and whose Z is equal to $Kn \pm \delta$, we define δ as 5 cm, that is,

$$S_{6\text{Knee}} = \left\{ \left\{ S_{6k} | Y_{\max}(S_{6k}) > \forall Y_{\max}(S_{6j}), \right. \right. \\ \left. \left. \left\{ \{Z(S_{6k}), Z(S_{6j})\} \in [Kn - \delta, Kn + \delta], j \neq k \right\} \right\} \right\} \quad (12)$$

Definition 12 $S_{6\text{TBC}}$ is the cross-section with maximum thigh girth, which has the largest sum of the width and thickness between $S_{6\text{Crotch}}$ and $S_{6\text{Knee}}$, that is,

$$S_{6\text{TBC}} = \left\{ \left\{ S_{6k} | X_w(S_{6k}) + Y_w(S_{6k}) > \forall X_w(S_{6j}) + Y_w(S_{6j}), \right. \right. \\ \left. \left. \left\{ \{Z(S_{6k}), Z(S_{6j})\} \in (Z(S_{6\text{Crotch}}), Z(S_{6\text{Knee}})) j \neq k \right\} \right\} \right\} \quad (13)$$

Definition 13 $S_{6\text{SBC}}$ is the cross-section of maximum calf girth, which has the largest sum of the width and thickness between $S_{6\text{Knee}}$ and $S_{6\text{Ankle}}$, that is,

$$S_{6\text{SBC}} = \left\{ \left\{ S_{6k} | X_w(S_{6k}) + Y_w(S_{6k}) > \forall X_w(S_{6j}) + Y_w(S_{6j}), \right. \right. \\ \left. \left. \left\{ \{Z(S_{6k}), Z(S_{6j})\} \in (Z(S_{6\text{Knee}}), Z(S_{6\text{Ankle}})) j \neq k \right\} \right\} \right\} \quad (14)$$

4 Generation of 3D Personalized Digital Apparel Whole-Human Body

4.1 Structure of Whole-Human Body Components

Characteristic parameters are defined according to human body features. Characteristics of the head and limbs are extracted from human bodies scanned and organized as the storage structure shown in Table 1.

| | |
|------|---|
| Id | Record number. |
| Type | Component type where 5 ~ 9 represents head, left hand, right hand, left leg, and right leg parts, respectively. |
| Kind | Chinese national standard classification value of body shape (GB/T1335) where Y, A, B, C represents four different shapes of human body. |
| Si | Matching index which is the ratio of width and thickness of component cross-section. |
| Sp | The point cloud data of component cross-section. |
| Sk | The key data of component cross-section which contains value of z -coordinate, the minimum, the maximum, center of X -axis, and Y -axis of cross-section. |
| Bi | The basic information of component source which consists of storage path and file name. |

4.2 Matching Process of Component Template

The matching of component templates is processed after obtaining the information of customer body. First the corresponding characteristic parameters of human body are gotten by pretreating customer information. Second the most suitable human body components are selected in the component template database. Then 3D human body component parts are generated by the 3D human body generation module. The matching process is shown in Fig. 3.

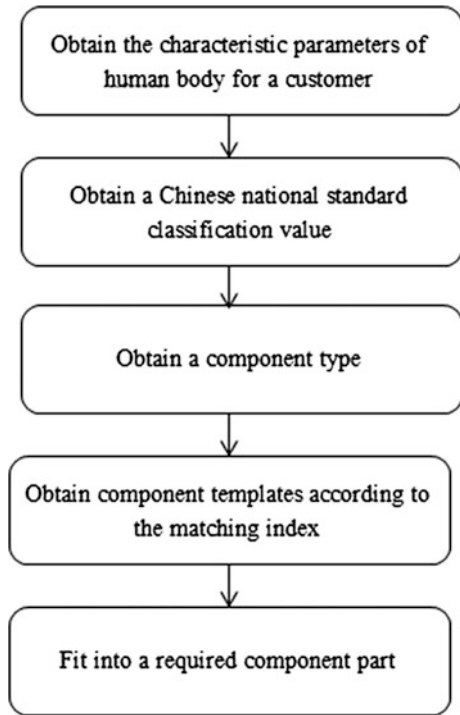
4.3 Combination of Component Parts for a Human Body

After finishing the fitting of all component parts, each component parts need to be combined together each other effectively. The paper adopts the combination method in which each component parts is located in the same coordinate system based on torso component part. The steps of combining parts are as follows:

Table 1 Component structure of whole-human body

| Id | Type | Kind | Si | Sp | Sk | Bi |
|----|------|------|----|----|----|----|
|----|------|------|----|----|----|----|

Fig. 3 Matching process of component templates for a human body



1. Combination of torso and head component parts

The torso component part is combined with the head component part in accordance with the principle in which the center point of the highest cross-section of torso part is coincident with that of the lowest cross-section of head part. The combining process is as follows:

- (1) Find the center point P_{1BC} of the lowest cross-section in head component part M_1 , that is,

$$S_{1B} = \{S_{1k} | Z(S_{1k}) > \forall Z(S_{1j}), \{S_{1k}, S_{1j}\} \in M_1, j \neq k\}. \quad (15)$$

Therefore the coordinates of P_{1BC} is: $(X_{cen}(S_{1B}), Y_{cen}(S_{1B}), Z(S_{1B}))$

- (2) Find the center point P_{2TC} of the highest cross-section in torso component part M_2 , that is,

$$S_{2T} = \{S_{2k} | Z(S_{2k}) < \forall Z(S_{2j}), \quad \{S_{2k}, S_{2j}\} \in M_2, j \neq k\}. \quad (16)$$

Therefore the coordinates of P_{2TC} is: $X_{cen}(S_{2T}), Y_{cen}(S_{2T}), Z(S_{2T})$

- (3) Calculate the displacement from the head to the torso $W_{12} = P_{2TC} - P_{1BC}$.
 (4) All points in the head component part P_{2BR} shift S_{2B} to form the new head M_2 , i.e.,

$$M'_1 = \{P'_i | P'_i = P_i + W_{12}, \quad \forall P_i \in M_1\} \quad (17)$$

2. Combination of torso and leg component parts

The torso component part is combined with the left (right) leg component part according to the principle in which the leftmost (rightmost) point of the lowest cross-section in torso component part is coincident with that of the highest cross-section in left (right) leg component part. Take the right leg as an example and the combining process is as follows:

- (1) Find the rightmost point P_{2BR} of the lowest cross-section S_{2B} in torso component part M_6 , that is,

$$S_{2B} = \{S_{2k} | Z(S_{2k}) > \forall Z(S_{2j}), \quad \{S_{2k}, S_{2j}\} \in M_2, j \neq k\}. \quad (18)$$

Therefore look for P_{2BR} in S_{2B} , which lets the X value of P_{2BR} be equal to $X_{min}(S_{2B})$.

- (2) Find the rightmost point P_{6TR} of the highest cross-section S_{6T} in right leg component part M_6 , that is,

$$S_{6T} = \{S_{6k} | Z(S_{6k}) < \forall Z(S_{6j}), \quad \{S_{6k}, S_{6j}\} \in M_6, j \neq k\}. \quad (19)$$

Therefore look for P_{6TR} in S_{6T} , which lets the X value of P_{6TR} be equal to $X_{min}(S_{6T})$.

- (3) Calculate the displacement from the right leg to the torso $W_{26} = P_{2BL} - P_{6TR}$.
 (4) All points in the right leg component part M_6 shift W_{26} to form the new right leg M'_6 , that is,

$$M'_6 = \{P'_i | P'_i = P_i + W_{26}, \quad \forall P_i \in M_6\} \quad (20)$$

3. Combination of torso and arm component parts

Because the connection surface between arms and torso component parts is not horizontal, the multiple Z values are required when combining these component parts. The torso component part is combined with the left (right) arm according to

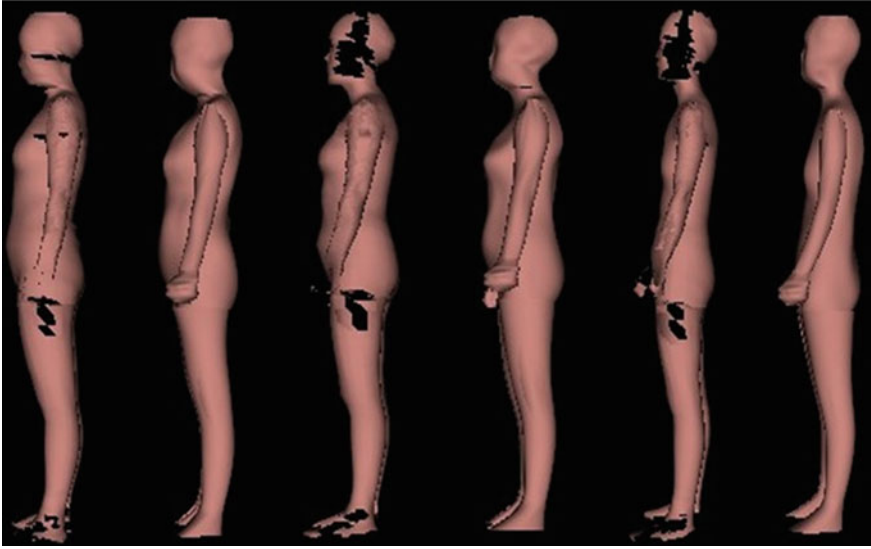


Fig. 4 Experimental results for three individual human bodies (from *left to right*, a pair for one person, odd number is a human body scanned, even number is the human body generated by the method presented)

the principle in which the leftmost (rightmost) point of the shoulder cross-section in torso component part is coincident with the rightmost (leftmost) point of highest cross-section in the left (right) arm component part. Take the right arm as an example and the combination process is as follows:

- (1) Find the rightmost point P_{2SR} of the shoulder cross-section [4] S_{2S} in torso component part. Let the X value of P_{2SR} be $X_{\min}(S_{2S})$.
- (2) Find the leftmost point P_{4TL} of the highest cross-section in right arm M_4 , that is,

$$S_{4T} = \{S_{4k} | Z(S_{4k}) < \forall Z(S_{4j}), \{S_{4k}, S_{4j}\} \in M_4, j \neq k\}. \quad (21)$$

Let the X value of P_{4TL} be $X_{\max}(S_{4T})$.

- (3) Calculate the displacement from the right arm to the torso $W_{24} = P_{2SR} - P_{4TL}$.
- (4) All the points in right arm M_4 shift W_{24} to form the new right arm M'_4 , that is,

$$M'_4 = \{P'_i | P'_i = P_i + W_{24}, \forall P_i \in M_4\} \quad (22)$$

Upon combining component parts for human body, the junctions between component parts need smooth processing in order to improve the visual effect of generated 3D digital apparel human model.

5 Testing and Result

Ten different 3D body samples scanned are selected in each type on the basis of the national standard classification value. A total of 40 body samples are used as templates of human body. Applying the method mentioned above, the key cross-section data is extracted and stored into the template database. We select 60 different 3D body samples scanned as test object to verify the accuracy of generation method for 3D human body. Some experimental results are shown in Fig. 4.

6 Conclusions

This paper presents the modeling of 3D personalized digital apparel whole-human body, which divides the whole body into five components parts and improves the original human component templates. By matching the appropriate component templates and surface-fitting the various components are combined for 3D digital apparel human. Our experimental results have showed that this modeling method is feasible and effective. The virtual human model established by this method is conformed to most people's intuitive understanding of the human body, and lays a solid foundation for research and realization of eMTM.

References

1. Li M, Tang X (2007) The research of electronic made to measure. *Prog Text Sci Technol* 2:97–98
2. Hu X, Cui S, Wang H, Wang J (2008) Digital human body modeling technology for virtual fitting. *China Text Leader* 7:150–156
3. Liu Y-J, Zhang D-L, Yuen MM-F (2010) A survey on CAD methods in 3D garment design. *Comput Ind* 61:576–593
4. Shi X, Chen L. (2013) Clothing Mannequin modeling based on universal human body template database. *Comput Appl Softw* 30(11):153–183
5. Wang CCL (2005) Parameterization and parametric design of mannequins. *Comput Aided Des* 37:83–98

The Fuzzy Controller Design for MEMS Gyro Stable Platform

Jinlong Dong and Bo Mo

Abstract Since a high sensor noise level will limit the gain of a PID controller, an adaptive Kalman filter (KF) has been designed to reduce the noise of MEMS gyro in a stable platform system, which has better performance than a FIR filters, Such as smaller phase lag and lower variance. By using the filtered gyro signal, a T-S fuzzy reasoning module has been constructed to adjust the PID coefficients adaptively. The simulation illustrates that the fuzzy-PID performs better than a classic PID when conquering the disturbance torque acting on platform frame.

Keywords Fuzzy control · Stable platform · MEMS gyroscope · Kalman filter

1 Introduction

Gyroscope stable platform technology, for INS or antenna stabilizing, has been developed since more than 80 years ago. In the basis of classic feedback control theory, sorts of linear controllers, such as phase compensation feedback controller, PID controller etc., have been designed and applied to practical systems. MEMS gyroscope, based on Micro-Electro-Mechanic processing technology, is a kind of low cost and low precision angular rate sensor and is broadly used in various areas, such as automobile, mobile phone, short range weapons etc [1, 2].

Since the low precision, MEMS gyroscope is rarely used in INS system when without other assistance navigation systems. However, for some stable platforms, MEMS gyroscope can easily satisfy the requirements. Since the bad noise

J. Dong (✉) · B. Mo (✉)

School of Aerospace Engineering, Beijing Institute of Technology, Beijing 100081, China
e-mail: hbdjl_001@163.com

B. Mo

e-mail: mobo@bit.edu.cn

performance and large random drift, a filter must be designed to reduce the noise and random drift. Digital filter is the most common solution for noise reduction, but no capability on eliminating random drift. By using optimal estimation theory, many researchers constructed ARMA model, and took it into a KF to estimate the optimal signal to reduce the noise and random drift. In most situations, the result is good for static signals, but not good for dynamic signals [3, 4]. Wavelet transform is another way to process random signals. By using the advantages of multi-resolution, the noise can be reduced to a special level depending on the scale, and the random drift can be also estimated optimally [5]. However, numerous calculation and bad real-time performance limit the application in simple systems.

Fuzzy control theory has developed for nearly 50 years since Zedeh created fuzzy set theory. Fuzzy controller, as a nonlinear system, can be used in sorts of linear or nonlinear systems depending on human's experience. By cooperating with classic PID controller, a fuzzy-PID controller can get a better performance [6].

In the following sections, an adaptive KF will be built to pre-processing the MEMS gyroscope signal in single-axis stable platform. Then, a fuzzy-PID controller has been constructed to stable the platform by contrast with classic PID controller.

2 The Model of Stable Platform with Angular Rate Gyroscope

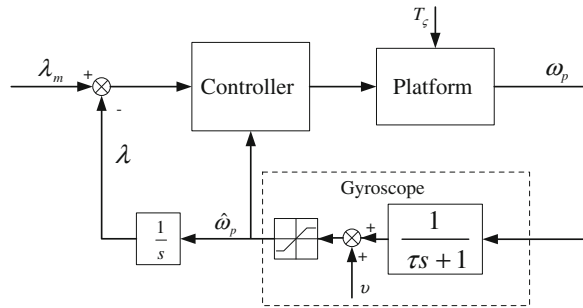
The diagram of a stable platform system is shown in the Fig. 1.

In Fig. 1, T_{ζ} is the disturbance torque acting on the platform, $\hat{\omega}_p$ is the platform angular rate measured by the gyroscope with measurement noise v . The main job of a stable platform system is to conquer T_{ζ} , and to maintain ω_p to zero or keeping λ around the desired angle. However, the control error definitely exists since the friction torque between platform and the frame. Minimizing the error is the destination of controllers design. The system model in open-loop transfer function is shown in (1).

$$G(s) = C(s) \frac{1}{s} \frac{1/K_e}{(\tau_m s + 1)(\tau_e s + 1)} \frac{1}{\tau s + 1} \quad (1)$$

where K_e is the Back-EMF coefficient, τ_m is the mechanical time constant, and τ_e is the electromagnetic time constant.

Fig. 1 The system diagram of gyroscope stable platform



3 Adaptive Kalman Filter Design for MEMS Gyroscope

3.1 The Model of MEMS Gyroscope

Without considering noise, the dynamic equation of a gyroscope can be expressed by (2).

$$a_n \omega^{(n)} + a_{n-1} \omega^{(n-1)} + \dots + a_1 \dot{\omega} + a_0 \omega + b = 0 \tag{2}$$

when the states are $\mathbf{x} = [\omega, \dot{\omega}, \ddot{\omega}]^T$, the state space model of a gyroscope is (3).

$$\begin{cases} \dot{x}_1 = x_2 \\ \dot{x}_2 = x_3 \\ \dot{x}_3 = a_1 x_1 + a_2 x_2 + a_3 x_3 + \xi \end{cases} \tag{3}$$

where ξ is Gauss noise, the differential equation of (3) can be written as (4).

$$\ddot{\omega} - a_3 \ddot{\omega} - a_2 \dot{\omega} - a_1 \omega = \xi \tag{4}$$

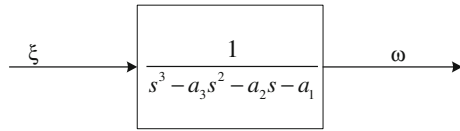
The angular rate measured by MEMS gyroscope is the output of a third-order system with ξ as the input, and the diagram is shown in Fig. 2.

3.2 An Adaptive Kalman Filter Design for MEMS Gyroscope

According to the previous section, the system state space can be constructed as the following.

$$\begin{cases} \dot{\mathbf{x}} = \mathbf{A}\mathbf{x} + \vartheta \\ \mathbf{z} = \mathbf{H}\mathbf{x} + v \end{cases} \tag{5}$$

Fig. 2 Gyro third-order dynamic model driven by a white noise



where $A = \begin{bmatrix} 0 & 1 & 0 \\ 0 & 0 & 1 \\ a_1 & a_2 & a_3 \end{bmatrix}$, $H = [1 \ 0 \ 0]$, v and w are processing and measurement white noise with covariance matrices are Q and R , respectively.

The basis of the adaptive algorithm is that the white noise with large variance can drive a faster dynamic signal. Hence, make the processing noise covariance change along the signal and the signal rate. The adaptive equations for Q are (6).

$$\begin{cases} \eta = (1 - b)/(1 - b^k) & b \in (0, 1) \\ \tilde{Z} = Z(k) - HAX(k - 1) \\ Q(k) = (1 - \eta)Q(k - 1) + \eta[K\tilde{Z}\tilde{Z}^T K^T + P(k) - AP(k)A^T] \end{cases} \quad (6)$$

By filtering the noise in gyro signals, the upper limit of controller gain can be enlarged widely.

4 The Fuzzy-PID Controller Design

The stable platform is a kind of self holding system. A classic PID controller is a linear system, which has a good performance when controlling a linear system. However, when there are nonlinear parts in a system, such as static friction, the performance of a PID will become bad.

Fuzzy systems have a better robustness than a PID regardless the system is linear or nonlinear [7]. According to the experience of experts, a fuzzy model can be designed to adjust the PID parameters, which can increase the control accuracy of a PID controller, and make a linear PID controller performs better in a nonlinear system. A stable platform system with fuzzy-PID controller can be constructed as the Fig. 3.

Let the PID coefficients are k_p , k_i , and k_d . The inputs of fuzzy logic are the absolute of angle error ($|E|$) and the absolute of angular rate ($|\omega|$). The fuzzy sets for $|E|$ and $|\omega|$ are:

$$E = \{\text{Small, Middle, Large}\}, W = \{\text{Zero, Small, Middle, Large}\}$$

The membership functions (MF) of E and W are shown in the Figs. 4 and 5 respectively.

Fig. 3 Fuzzy-PID self-adjusting stable platform system

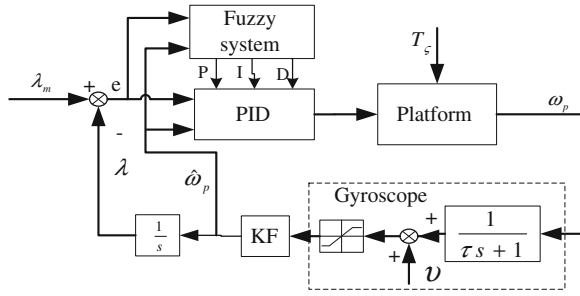


Fig. 4 The error (E)'s membership function plots

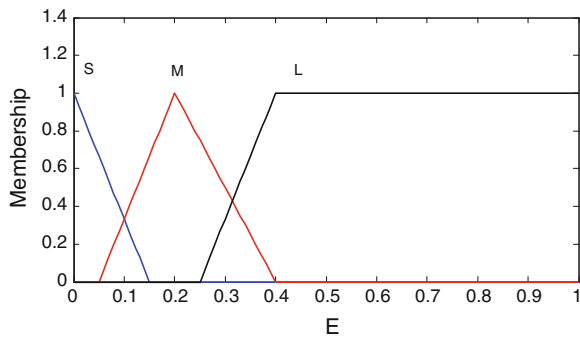
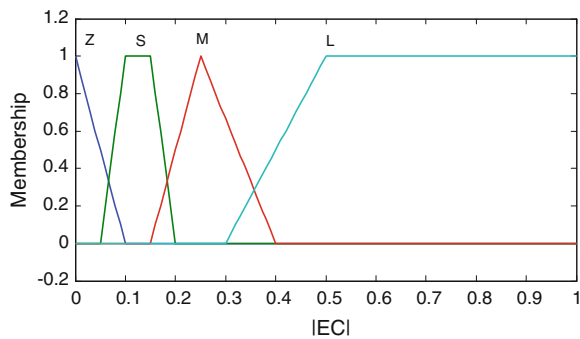


Fig. 5 The angular rate (ω)'s membership function plots



Set the fuzzy model is T-S (Sugeno) style. The outputs of fuzzy system are k_p , k_d , and k_i . The fuzzy reasoning rules are:

1. When $|E|$ is Small and $|\omega|$ is Zero or Small, then $k_p = k_1 |\omega| + k_{p0}$, $k_d = k_{d0}$, $k_i = k_{i0}$;
2. When $|E|$ is Small and $|\omega|$ is Middle or Large, then $k_p = k_1 |\omega| + k_{p0}$, $k_d = k_2 |\omega| + k_{d0}$, $k_i = k_{i0}$;
3. When $|E|$ is Middle and $|\omega|$ Zero, then $k_p = -k_3(1 - |E|) + k_{p0}$, $k_d = k_{d0}$, $k_i = k_{i0}$;

Fig. 6 KF filtered result and FIR filtered result

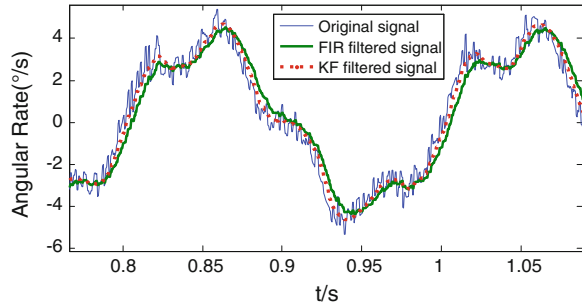


Table 1 Signal variance before and after filtered

| | Original | FIR | KF |
|----------|----------|--------|---------|
| Variance | 0.16 | 0.0136 | 0.00114 |

4. When $|e|$ is Middle and $|\omega|$ is not Zero, then $k_p = -k_3(1 - |e|) + k_{p0}$, $k_d = k_2|\omega| + k_{d0}$, $k_i = 0.5k_{i0}$;
5. When $|e|$ is Large, then $k_p = 1.5k_{p0}$, $k_d = k_2|\omega| + k_{d0}$, $k_i = 1.5k_{i0}$;

where k_{p0} , k_{d0} , and k_{i0} are initial coefficients of PID which make the control system have a proper open loop gain, a proper overshoot and stability; For the ranges of k_1 , k_2 , k_3 obey the limitations that $k_p \in [0.5 k_{p0}, 2 k_{p0}]$, $k_d \in [k_{d0}, 2 k_{d0}]$.

5 Simulations

According to Figs. 1 and 3, create a gyro stable platform system with classic PID controller and Fuzzy controller respectively. The gyro measurement noise is random number with $E\{v\} = 0$, $E\{v^2\} = 0.16$. The disturbance torque, acting on the frame of platform, is a pulse signal alternating positive and negative. The static friction between platform and frame is 8 % of max torque of the motor. The gyro filtered signal from KF and a FIR filter have been plotted in Fig. 6. It can be seen that KF has a smaller phase lag and a lower noise than FIR. The statistics of original signal, KF signal, and FIR filter signal have been list in Table 1.

According to the fuzzy rules, the fuzzy-PID system and the PID system have been created in matlab, the simulation results, shown in Figs. 7 and 8, indicate that the fuzzy-PID controller can get a smaller stabilizing error than PID when conquering disturbance torque, since the PID coefficients adjusted along different angle error and angular rate error. The typical kd curve, adjusted by fuzzy logic, is shown in Fig. 9.

The fuzzy controller is directly determined by experience of designers, hence, different fuzzy logic maybe create completely different results.

Fig. 7 Plat angle controlled by PID and Fuzzy PID

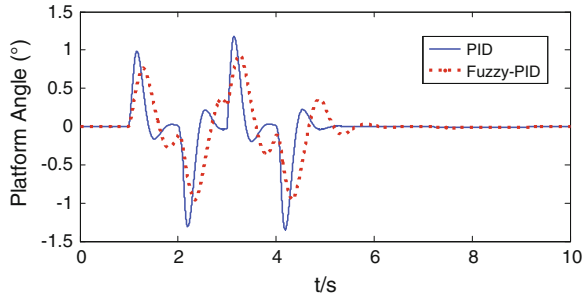


Fig. 8 Plat angular rate controlled by PID and Fuzzy PID

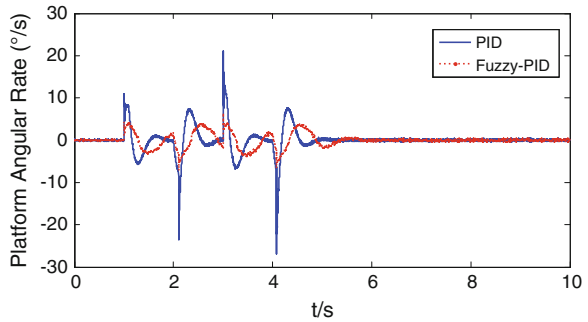
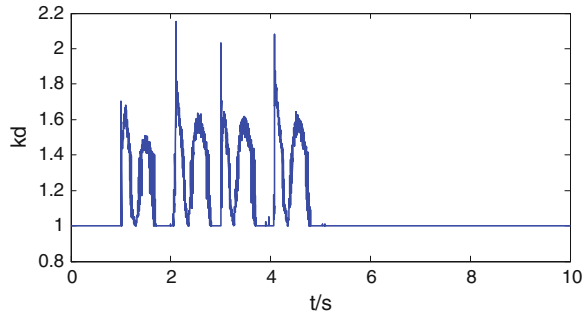


Fig. 9 k_d adjusting curve by fuzzy logic



6 Conclusion

A properly designed fuzzy-PID controller for gyro stable platform can make a better performance than a classic PID, since fuzzy system have a better capability to adapt nonlinear parts in systems. In the simulation, a T-S fuzzy logic, with five fuzzy rules, can adaptively adjust the PID coefficients to suit the system current

state, and make the system error smaller. It is an available approach for application in stable platform control. Meanwhile, an adaptive Kalman filter can efficiently lower the gyro measurement noise, which can enlarge the control gain widely.

References

1. Yongyuan Q (2006). *Inertial Navigation*. Beijing: Science Press
2. David H, Titerton, John L, Weston (2004) *Strapdown Inertial Navigation Technology—2nd Edition*. Beijing: National Defense Industry Press
3. Meng T, Wang H et al. (2009). Error modeling and filtering method for MEMS gyroscope. *Sys Eng Electr* 31(8):1944–1948
4. Zhao W-C, Fu M-Y, et al. (2005). Investigation on Modeling and Filter Methods for MEMS IMU Drift Data. *J Chanese Inertial Tech* 13(6):13–17
5. Su L, Zhou X-M (2009) Application of improved wavelet thresholding method for de-noising gyro signal. *J Chanese Inertial Tech*. 2009; 17(2): 232–235
6. Shi X, Hao Z (2008) *Fuzzy Control and Matlab Simulation*. Beijing: Tsinghua University Press
7. Zeng G, Hu J (2007) *Fuzzy Control Theory and Engineering Application*. Wuhan: Huazhong University of Science & Technology Press

Tree Network Under Space L and Space P Model

Xi Chen, Jianghai Qian and Dingding Han

Abstract Transport network and transport efficiency in building cost under the influence of the interaction will evolve some nontrivial topological features. In particular, when building cost plays an important role, the networks tend to be characteristics of tree structure. Although the cost and efficiency for space under different trade-offs have been the studies in network topology, but the research of the tree structure of network is very rare. In this paper, we analyze two empirical types of tree networks: natural evolution of clonal plant ecology topology and artificial construction of metro network structure. We found that, although the evolution of these two types of networks in optimization strategies, and spatial distribution of resources may be completely different, they are in Space L and Space P models all showing the similar topology. Further, we have compared the two network structures with a random branch tree, it was found that they in the same manner and extent of deviation from the predicted random branching tree. These results show that even a relatively simple shape tree network, also has an abundant structure and organization of universal principles that may be closely related with the function of the system.

Keywords Tree network · Clonal plant · Transport network

X. Chen · D. Han (✉)
East China Normal University, Shanghai, China
e-mail: ddhan@ee.ecnu.edu.cn

X. Chen
e-mail: chenxichacha@sina.com

J. Qian
Shanghai Institute of Applied Physics, Chinese Academy of Sciences, Shanghai, China
e-mail: qianjianghai@sinap.ac.cn

1 Introduction

In the exploring of the spatial network analysis, in recent years, the metro network with the line and site constitutes spatial network that has a very extensive study, abroad Poland 22 urban transport network degree distribution analysis [1, 2], India and Boston metro subway networks have shown small world metric [3, 4], a large subway network evolution model study [5], etc.; Chinese major urban public transport network empirical analysis and reliability studies include Shanghai subway network characteristics and scale-free degree distribution exponent [6], the Chinese railway network scale-free empirical studies [7], the Beijing subway complexity analysis [8], the city transport network, network characteristics analysis [9] as well as Beijing, Shanghai, Guangzhou three major cities in metro networks Empirical comparison [10]. In the process of investigation there have been usually used two kinds of network topology description method: Space L method and the Space P method, the former site the station as the node, if two stations in the routes are adjacent, then they will have an edge between the two nodes; the latter method also regard the station as the node, if the two sites have direct transport route, then they will have an edge. Ecological resources transport network also has space network characteristics, the most typical is clonal plant network and it can be used the same method Space L and Space P constructed network topology model.

When the build-consuming plays an important role in the transport network, the network showing the spatial characteristics of the network tree, this tree structure determines its own internal functions embodied in nontrivial properties. Recently many studies on the metro network for the statistics and calculations reveal subway network topology characteristics, rarely explored from the tree structure of the structural properties of the metro network. In the ecological resources transport networks, due to the geographical environment factors, the growth of clonal plant configuration is often difficult to obtain, making tree network research about cloning plants are rare [11]. The manmade transport networks and natural transport networks are two representative transport networks, to explore these two different types of transport networks, and tap their universal characteristics and predict their functional structure is inevitability.

Tree network is an important component of spatial network, this paper collecting ecological network configuration of natural evolution clonal plants and artificial construction data of metro network, research the characteristics of the two tree structures of the empirical network, while introducing random number theory, compared the actual results with the theoretical analysis, they deviate from random branching tree to explore the manner and predicted extent. Explore the tree structure of the transport network of nonbanal, pervasive characteristics.

2 Data Sources and Access

We collected two types of tree network data: natural evolution of clonal plant *Spartina alterniflora* topology network and artificial construction metro networks.

Spartina through asexual reproduction generates interconnected independent entity, it is a clonal plants of significant spatial distribution, its straw-intensive stout rhizome developed, often extended to a depth of 60 cm in beach soil, growing with complex distribution, making access the *Spartina* distribution of spatial topology become difficult [12–14]. We through grubbed *Spartina* strains plexus in Shanghai Chongming east beach within a certain range, a larger space for the first time under the scope of *Spartina* spatial network configuration, it is a simple tree structure network, as shown in Fig. 1, where the yellow dots represent strains plexus, even edges represent rhizome sections, edge weights represent the number of segments of rhizomes, fractional situations: the denominator represents the number of ramets, the numerator represents the subheading trees. We define the strain cluster as nodes of the network, the rhizome is defined as network undirected edge, rhizome section number indicates the distance between the nodes. This constitutes the spatial tree network with 27 nodes and 26 edges.

We collect the second tree network data of subway network in three Chinese major cities Beijing, Shanghai, and Guangzhou. City subway routes and stations network contains two basic elements, which Beijing has 16 routes, 270 stations; there are 8 routes, 131 stations in Guangzhou; Shanghai has 12 routes, 287 stations. A route composed of several stations, the metro docking stations as nodes, even routes as lines, we can build route and station network. And then the subway network as a simple classic tree network.

3 Structural Analysis

For the natural evolution of *Spartina* topology networks and artificial construction of metro network, according to Space L and Space P method constructed network models, the two models are listed in Table 1 under different network topology.

In Table 1, four network average path length approximately equal to each other, the average degree of networks under Space L model is approximately equal to 2, most of the node clustering coefficients approach is zero, each network average clustering coefficient is approximately zero, obviously these networks in Space L are tree networks. The two types of networks under Space P, the average shortest path length between the two nodes are all between 2.6 and 4.2; clustering coefficient are all above 0.9, which shows the entire transport network has good connectivity, high-level aggregation, with a shorter average path length and a high clustering coefficient of the network. Considering overall the clonal plant network and urban rail transport network has the same characteristics and obvious small world property.

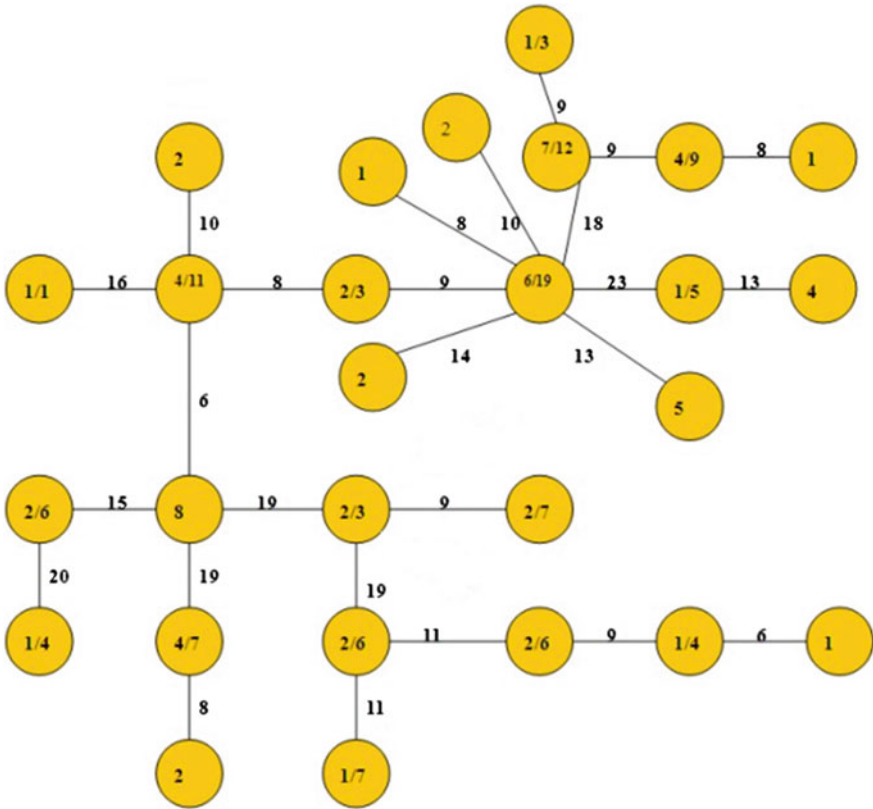


Fig. 1 Spartina genet spatial structure

Table 1 Characteristic values of the Space L and Space P topology

| Network | Average degree | | Average path length | | Average cluster coefficient | |
|-----------|----------------|---------|---------------------|---------|-----------------------------|---------|
| | Space L | Space P | Space L | Space P | Space L | Space P |
| Beijing | 2.15 | 18.44 | 14.4 | 2.9 | 0 | 0.957 |
| Guangzhou | 2.07 | 17.01 | 14.6 | 2.6 | 0 | 0.955 |
| Shanghai | 2.21 | 22.92 | 14.9 | 3.1 | 0.0008 | 0.967 |
| Spartina | 2.04 | 11.58 | 14.5 | 4.2 | 0 | 0.972 |

The two models of network node degree distribution as shown in Fig 2, comparing them we found under Space L in double logarithmic coordinate, it is close to the power law distribution. Exponent of Beijing, Guangzhou, Shanghai metro network and Spartina network is, respectively, 2.237, 2.078, 2.446, and 2.006. This indicates that the network under Space L belonging to scale-free network, with growth and priority connectivity features, the vast majority of nodes degree is

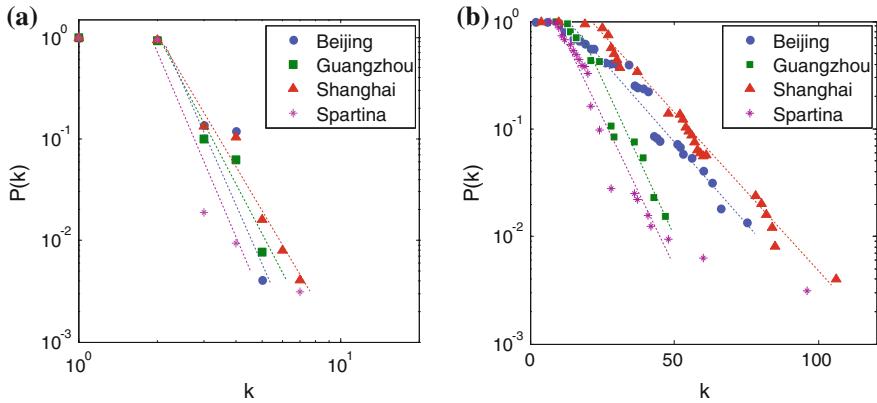


Fig. 2 Degree Distribution under Space L and Space P, **a** under Space L in double logarithmic coordinate, **b** under Space P in semi-logarithmic coordinate

relatively low, but there is a small amount of relatively high degree nodes. In Space P model, the cumulative distribution of the two networks in semi-logarithmic coordinate substantially linear form, shows exponential distribution performance, Spartina growth of new ramets with existing connections to other ramets and three urban rail network stations add new connections are also random.

The node degree value k can be seen as clustering coefficient adjustment factor, double logarithmic coordinates (Fig. 3) degree k of the node with the clustering coefficient $C(k)$ increases as k values presented reduced power law model, when a small value of node degree k , $C(k)$ is almost maintained as a constant, when the value of large value of k , $C(k)$ emerge the power law distribution. In real networks, the physical connection between nodes is often caused to the phenomenon, in the BA scale-free network [15] exists and both network's $C(k)$ are decreasing with k , but the rate of decrease is less than the power law.

Metro network has an important feature of that each side is not even equivalent to the node, as well as passenger traffic exists between the probability of transfer to select the path is not the same. Spartina strains cluster node also exists the flow of energy through different rhizomes in clonal ramets, and the probability is not the same, there has a significant importance difference. Some links in the network than others have more weight, therefore, to promote the operation of the entire network to play a greater role. Weighted connections already available are applied in many real world networks. It is equally necessary to consider the weighted value and its distribution, the intensity of the node weight and the weight value indicates the relationship. In a weighted network, a node i weighted degree value can be defined as the sum of all connected nodes j with i [16], namely

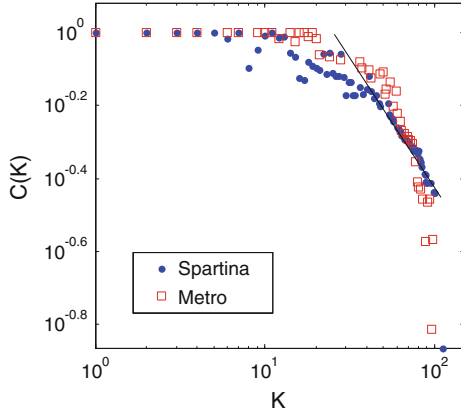


Fig. 3 Evolution between clustering coefficient $C(k)$ and node degree k

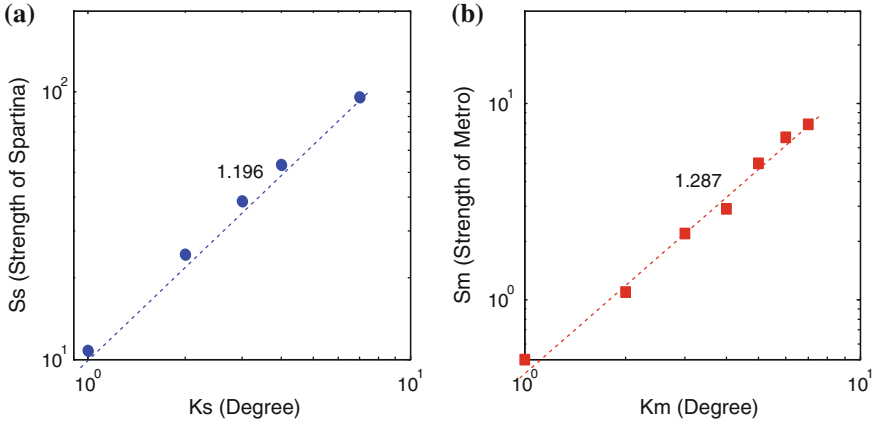


Fig. 4 Node weight and degree distribution. **a** Spartina, **b** Metro

$$s_i = \sum_j w_{ij} \tag{1}$$

The relationship of Spartina node degree and weighed value as shown in Fig. 4, compared with the metro network, the two coefficients are all greater than 1, the node weighted value growth faster than the node degree.

By topological structure analysis can find the direction of the unknown natural breeding derivative Spartina networks and artificial structures are planned generation metro networks, their network causes different structural purposes, and their purposes are not the same. However, the two types of tree structure consuming transport network and transport efficiency in building under the influence of the

interaction will evolve some nontrivial topological features. Although the evolution of these two types of networks, optimization strategies, spatial distribution of resources may be completely different, but they are in Space L and Space P, but all of them showed a similar topology. These topologies and characteristics with the system’s internal transport functions are closely related, Spartina network to obtain rapid and efficient energy transfer nutrients, making strains cluster occupy a good living environment, urban rail transit network to achieve optimal flow for multiply and travel convenient level, both in internal transport network to achieve the purpose is the same, so the performance of unified structure properties. This is closely related with the transport system that functions relatively simple from of a tree network, also has a rich structure and universality.

4 Random Tree

Random tree [17] is generated by the random process which do not have a closed circuit of tree graph, typically used for two different distributions: the tree node is formed by inserting a random arrangement, discrete from a uniform distribution of medium that may improve selection tree; Further, the distribution may be in other forms, such as by repeated splitting, adding, and removing nodes in a random tree directly damage its random structure to maintain a balanced search tree dynamic random order. Size n of random tree generation rules: Initialize a node, then every node and a further increase even edges, vertices denoted $V_n = \{1, 2, \dots, n\}$, every step has been added nodes and nodes connected to the node in any one of the probability distribution of $\{P_{k,i}, i = 1, 2, \dots, k\}$ ($k = 1, 2, \dots, n-1$), the node k is the set $\{1, 2, \dots, k-1\}$ in a node is connected, the connection probabilities $P_{k,i}$ ($i = 1, 2, \dots, k-1$), after n steps the formation of n nodes random tree T_n . Degree of each node is denoted by $d_{n,i}$, assuming that each node also give an initial value, so that the node of degree k has the weighted value, the node which guarantees the value of nonnegative, the integer is similar to the initial node to attract degrees.

As Spartina network and metro transport network in Space L model has a typical random tree structure. To explore the tree structure to explore these two random tree features, we introduce a random expected longest path in the tree and the expected node degree theory to analyze the two types of network tree structure. In random tree theory, the longest path in the tree all paths to estimate the maximum distance, expected maximum node degree estimation tree node degree values. For a node of the tree is n , L is the expected longest path

$$L = \frac{1}{\beta} \log n. \tag{2}$$

where $2\beta e^{1-\beta} = 1$, reduce that $\frac{1}{\beta} \approx 4.311$. D is the expected node degree

Table 2 The longest paths and node degrees under Space L model

| Data | Beijing | Guangzhou | Shanghai | Spartina |
|-----------------------|---------|-----------|----------|----------|
| Expected longest path | 7.4 | 6 | 7.3 | 7 |
| Real longest path | 8 | 7 | 9 | 9 |
| Node expected degree | 17.7 | 8.3 | 16.7 | 9 |
| Node real degree | 14 | 7 | 15 | 6 |

$$D = \frac{n+1}{3}, n \geq 2. \quad (3)$$

according to the formula (2) and (3) calculated the four different sets of two networks of L and D , respectively, and the actual L , D are compared in Table 2.

As can be seen from Table 2, the L and D in real network characteristics in line with the trend estimated expected value, and found them in the same manner and extent of deviation from the expected value of the random branching tree, both reflect the expected small longest path node expected value is too large cases, the actual value of the longest path is too large the actual value is too small, consistent fluctuations. Generally, in the case of the nodes that are densely distributed in complexity network, the communication between any two points or path often cause data overlap, resulting in a waste of limited resources. In the tree structure, the distribution has a single network path, the path of the average high utilization, peripheral expansion is exact and can make the data or resources to spread through the expected direction, reducing the waste of resources, enhance communication efficiency can be expected through the longest path and the expected value estimated efficiency of network communications, the node key, and so on. In the process of laying the metro network, always consider the flow of people and the number of transfers; in Spartina growth process, consider the transmission and use of ecological resources, which need to choose the optimal communication path and high communication efficiency. Therefore, both whether natural selection or artificial structures behave as branches fluctuations and the degree of deviation consistent tree networks.

Characteristic in random tree network is not only with high efficiency in node and route, but also has a general network randomness and effectiveness. In real world phenomena, the construction of a line to transform the line temporarily removed a site, but this does not affect the validity of the entire rail network; similarly, dig a Spartina ramet not derivatives affect the overall rate of genet growth and expansion. Metro transit stations and routes in the process of setting, usually to consider is will be subject to land use planning, road construction costs, environmental protection, economic development planning, and many other factors, so that the same line of new sites and existing sites connection adds a lot of chance and randomness; Spartina growth process equally and shoals humidity, soil salinity, organic content, the natural decline, and coastal resources such as environment-related fungal infection [13, 14], with a root new long stem-like strains

probability is accidental and random. Followed functions and similar effects within these networks, resulting in consistent with the structure of the external, they present the same characteristics of random tree that can be applied to a similar network transport functions, in order to analyze the distribution of resources and ecology of constructed transport network provides the organizing principle of universality.

5 Conclusion

In this article, Spartina and metro transport networks were analyzed from the tree construction, separately construct their Space L and Space P models to study the characteristics and complexity of random trees theory. Through analysis we found that, although the evolution of these two types of networks, optimization strategies, and spatial distribution of resources may be completely different, but they are in space L and Space P all show a similar topology. Furthermore, we bring the two networks random branching tree structure and compare their expected longest path and node degree and the actual parameter values consistent performance, both similar fluctuations, in the same way and extent of deviation from random branching tree prophecy. All networks are reflected Tree structure notable features, reduce resource waste, improve flow efficiency, even relatively simple shape tree network, also has universal features, and has a rich internal structure.

Clonal plant network and metro transport network with tree structure are two typical transport network, the paper through excavation growing Spartina got spatial configuration, and studied from a new perspective of the growth of its transmission and spread of resources, as well as analysis of metro network tree transport and paving way, flow of energy in the network tree structure reflects the efficiency and energy saving, get their characteristics embodied in the tree structure and internal functions are closely related with rich architecture and universal organizing principle. Exploring the tree structure provide a new perspective of the network and optimize the network structure, build quality system has a deeper meaning.

Acknowledgments The research work was supported by National Natural Science Foundation of China under Grant No. 11075057.

References

1. Seaton KA, Hackett LM (2004) Stations, trains and small-world networks. *Physica A* 339(3):635–644
2. Sienkiewicz J, Janusz A (2005) Statistical analysis of 22 public transport networks in Poland. *Phys Rev E* 72(4):46–50

3. Sen P, Dasgupta S, Chatterjee A et al (2003) Small-world properties of the Indian railway network. *Phys Rev E* 67(3):036106
4. Latora V, Marchiori M (2002) Is the Boston subway a small-world network? *Physica A* 314(1):109–113
5. Angeloudis P, Fisk D (2006) Large subway systems as complex networks. *Physica A* 367:553–558
6. Zhang J, Xu X, Hong L et al (2011) Networked analysis of the Shanghai subway network, in China. *Physica A* 390(23):4562–4570
7. Li W, Cai X (2007) Empirical analysis of a scale-free railway network in China. *Physica A* 382(2):693–703
8. Liu S, He W (2012) Network analyses of Beijing subways. In: industrial informatics (INDIN), 2012 10th IEEE international conference on. IEEE, 2012, 1022–1024
9. Zhang J, Zhao M, Liu H, et al (2013) Networked characteristics of the urban rail transit networks. *Physica A Stat Mech Appl* 392(6):1538–1546
10. Wang T, Fang ZG, WU H, et al (2008) An Analysis of complexity of subway network in China. *J Acad Mil Transp* 10(2):24–27
11. Mony C, Garbey M, Smaoui M et al (2011) Large scale parameter study of an individual-based model of clonal plant with volunteer computing. *Ecol Model* 222(4):935–946
12. Wang Q, AN SQ, MA ZJ, et al (2006) Invasive *Spartina alterniflora*: biology, ecology and management one hour payday loan. *Acta Phytotaxonomica Sinica* 44:5
13. Metcalfe WS, Ellison AM, Bertness MD (1986) Survivorship and spatial development of *Spartina alterniflora* Loisel. (Gramineae) seedlings in a New England salt marsh. *Annals Bot* 58(2):249–258
14. Daehler CC, Strong DR (1994) Variable reproductive output among clones of *Spartina alterniflora* (Poaceae) invading San Francisco Bay, California: the influence of herbivory, pollination, and establishment site. *Am J Bot* 81:307–313
15. Ravasz E, Barabási AL (2003) Hierarchical organization in complex networks. *Phys Rev E* 67(2):026112
16. Yook SH, Jeong H, Barabási AL et al (2001) Weighted evolving networks. *Phys Rev Lett* 86(25):5835–5838
17. Moon John W (1968) On the maximum degree in a random tree. *Michigan Math J* 15(4):429–432

Ontology-Based Component Description and Intelligent Retrieval

Li Liu and Youqun Shi

Abstract The key to software reuse based on component is searching for required component from the component library. In this paper, discussion is on the technology of component retrieval based on the combination of ontology and the multi-agent system (MAS). It uses OWL description language to have a component described which is based on the mode of faceted classification. Finally, a component retrieval system based on MAS is designed and implemented, which enables the semantic search under higher recall and precision, but also to improve the search speed. In this way the components searched satisfy more with the need of users.

Keywords Component description · Ontology · Component retrieval · Multi-agent

1 Introduction

The way to retrieve the reusable component fast and efficiently has an effect on the efficiency of software reuse in the software development directly. There are many factors those affect the retrieval efficiency, including the friendliness of the search interface, search strategies, matching mechanism, etc. The method of component retrieval depends on the classification and description of the components, and the classification of the components are ultimately reflected in the description of the component, therefore, a reasonable classification model, a good description language, and excellent retrieval method can improve the efficiency of component retrieval. One of the classification models is the facet-based classification, which is

L. Liu (✉) · Y. Shi
School of Computer Science and Technology, Donghua University, Shanghai,
People's Republic of China
e-mail: llliuli1225@163.com

the method widely used in the practical application, but it is a simple matching based on the syntax level, which is lack of capabilities in representation, understanding, and processing of the knowledge. To solve this problem, the key is to make the component retrieval from syntactic matching based on simple search keywords up to the semantic matching based on knowledge. Ontology based on facet classification description is an effective solution.

The ontology-based component description improves the semantic of component retrieval, but with the expansion of the scale of the component library, the increasing complexity and semantic of component, it is difficult for users to determine the search conditions, and it is difficult to find the desired component quickly from a large number of search results. To deal with these problems, we propose a retrieval solution based on Multi-Agent. First of all, describing the component based on ontology and facet and building the component ontology; Second, establishing a multi-agent system (MAS) which is autonomous and cognitive by creating various of Agent; Finally, achieving a component retrieval system with flexibility, accuracy and intelligence.

2 Ontology-Based Component Description

2.1 Ontology and Web Ontology Language

Ontology is a specification of a conceptualization [1]. Ontology consists of five main elements: Concept, Relation, Function, Instance, and Axiom. Concept is used to indicate a set of entities or things in a particular field; relation is used to describe the interaction of the concept and the properties of concept; Function is a special relation; Instance is the specific thing represented by the concept, the combination of the ontology and related instances are the so-called Knowledge Base; Axiom is used to constrain the range of the properties of class and individual. The goal of the ontology is to capture domain knowledge, to provide a common understanding of the domain knowledge and determine the vocabulary in this domain, and the definition of the relation between these vocabulary and vocabulary. So, ontology-based component description is a solution which is not only to improve the accuracy and integrality of the component description, but also to provide a rich semantic for the facet-based component description.

The Web ontology language (OWL) is a semantic markup language for publishing and sharing ontology on the World Wide Web [2]. OWL is used to publish and exchange ontology, which are formal sets of concepts, relations, and constraints. With the powerful abilities of the semantic presentation and the logical reasoning, the component retrieval and composition will be easy because of the solution of the semantic relations and accurate semantic presentation between resources by the OWL [3].

2.2 Component Ontology Modeling

Component model is an abstract description of the essential characteristics of the component and the relation between components, and it is the basic definition, development, storage, and assembly of the component. And the component classification model based on faceted classification is more common at present. Research community home and abroad have been proposed some component models based on facet description, such as 3C, REBOOT, and Jade Bird Component Model. In this paper, we have defined five facets considering these component models and the actual situation of the component library. These five facets: component basic information facet, component classification facet, component environmental requirement facet, component quality facet, and component functions facet. Component basic information: the basic information of component, including component identification, the size of the component, etc.

Each facet describes component in different sides, each facet has corresponding content, as in Fig. 1

2.3 Describing the Component Based on OWL

The five main elements, which are Concept, Relation, Function, Instance, and Axiom, are abstracted from the component in the process of building component ontology. And relation includes four basic relations which are part-of, kind-of, attribute-of, and instance-of. However, there are not only these four basic relations in practical applications, but we should also increase the types of the relation, which is not only to rich semantic of component for extension and reasoning of semantic, but also to improve the efficiency of component retrieval.

2.4 Creating the Classes of the Component

According to the facet information from Fig. 1, component description ontology mainly related to the five classes, which are the component basic information (ComponentBaseInfo), the component classification (ClassifiedInfo), the component environmental requirement (ComEnvironment), the component quality (ComQualify), and the component function (ComFunction). In this paper, describing the component by using the Protégé 4.2_alpha which is a visual tool developed by Stanford University and OWL.

The following example shows how to describe the component basic information which contains the component identification, the component name, explains how to describe the component with OWL language. We need to abstract these

| Facet | Facet information | | | | | | | | | | | |
|-------------------------------------|------------------------|-----------------------|-----------------------|---------------------------------|-------------------------------|-------------------|------------------------|----------------------------|-----------|-----------------------------|---|------------------------------------|
| Component basic information | identification | name | author | creation time | modification time | size | description | version | type | | | |
| Component classification | application domain | | | component function | | | component sub-function | | | | | |
| Component environmental requirement | computer configuration | database | network | OS | programming language | component format | software dependent | component dependent | | | | |
| Component quality | security | | reuse frequency | | normalization | | reliability | | stability | | | |
| Component function | requested function | | | | | provided function | | | | | | |
| | interface | | | | | | interface address | | | | | |
| | | | | | | | interface parameter | | | | | |
| | inter face ID | inter face name | inter face type | inter face return type | Inter face functi on | direct ion | name | seque nce numb er | type | interfac e class name | interf ace class file addre ss | interfac e functio n name |

Fig. 1 Relation of the component basic information

information into classes, so we can use the `rdfs:subClassOf` to indicate the inheritance between them, as is shown in Fig. 2.

The definition of the class of “the component basic information (ComponentBaseInfo)”:

```
<owl:Class rdf:about="#ComponentBaseInfo">
<rdfs:subClassOf rdf:resource="#Component"/>
</owl:Class>
```

The definition of the subclass of “the component identification (ComBaseInfo)” and “the component author (ComBaseInfoAuthor)”:

```
<owl:Class rdf:about="#ComBaseInfoId">
<rdfs:subClassOf rdf:resource="#ComponentBaseInfo"/>
</owl:Class>
<owl:Class rdf:about="#ComBaseInfoAuthor">
<rdfs:subClassOf rdf:resource="#ComponentBaseInfo"/>
</owl:Class>
```

2.5 Creating the Properties and Individuals of Component

To make the component ontology with richer semantics, we need to define the properties, and to determine the constraints on the properties. OWL property is divided into Object Properties and Data Properties. Object Properties indicates the relation between instances and Data Properties indicates the relation between instance and the data type (e.g., string, integer, etc.).

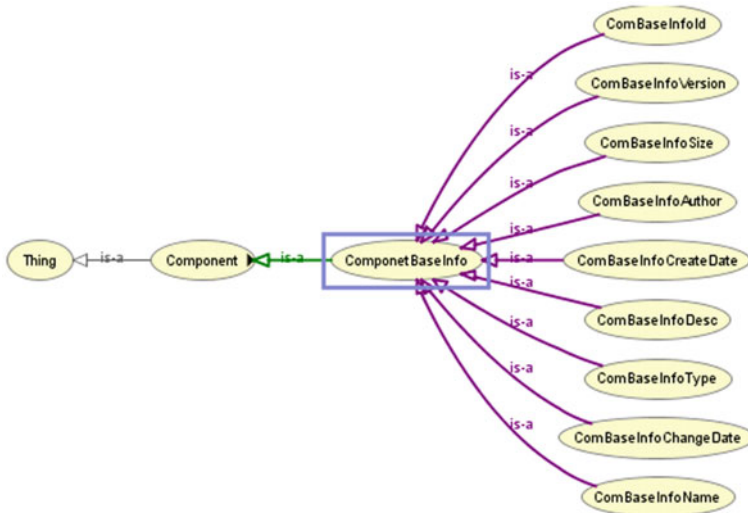


Fig. 2 Relation of the component basic information

In component retrieval process, we define the property of “dependOn”, which means a component depends on some components, and it is the transitive property. This property provides the reasoning basis for the extension of component retrieval. The description of this property based on OWL:

```
<owl:ObjectProperty rdf:about="dependOn">  
<rdf:type rdf:resource="&owl;TransitiveProperty"/>  
<rdfs:domain rdf:resource=" #Component"/>  
<rdfs:range rdf:resource=" #Component"/>  
</owl:ObjectProperty>
```

In order to describe the component basic information integrally, we need to define some properties with constraints on these facets. Such as “has Author” represent “the component basic information” has the property of “component author”, and the type of this property is the string. As is described based on OWL:

```

<owl:DatatypeProperty rdf:about=" hasValue">
  <rdfs:domain rdf:resource="#ComBaseInfoAuthor"/>
  <rdfs:range rdf:resource="&xsd:string"/>
</owl:DatatypeProperty>
<owl:ObjectProperty rdf:about=" hasAuthor">
  <rdfs:domain rdf:resource="#ComBaseInfoAuthor"/>
  <rdfs:subPropertyOf rdf:resource=" #haveBaseInfoFacet"/>
  <rdfs:range>
    <owl:Restriction>
      <owl:onProperty rdf:resource= #hasValue"/>
      <owl:someValuesFrom rdf:resource="&xsd:string"/>
    </owl:Restriction>
  </rdfs:range>
</owl:ObjectProperty>

```

Finally, we create the instances named “FileTransferCom” which has the function of file format conversion, and “FileUploadCom” which has the function of uploading files. And “FileUploadCom” depends on “FileTransferCom”. The identification, author and type of the “FileUploadCom” is “10000002”, “Three”, and “FileProcess”, as shown in Fig. 3.

2.6 Component Storage

The component storage includes the component entities and the component ontology, and we establish the relational database that store the basic information of the components extracted from the component ontology. The component entity stored by the file system includes source code, design, and test documentation, etc. Component ontology and component instances store in the owl file generated by the Protégé. Simultaneously, the corresponding relation between the component ontology and component entities will be established through the component identification and the component storage address, then the retrieval of the component entities will be replaced by the retrieval of the basic information of the components. This storage method possesses reasoning of the ontology, high efficiency of the relational database and high flexibility of the file system. The structure of the component storage is shown in Fig. 4.

In order to better management of the component entities storage, we create some subfolders in accordance with the type of function of the components (e.g., files processing, database-related, network-related, etc.). For example, the source code and related documents of the component named FileConvertCom are stored in the folder name 1000001 together. Users can download the component through the component storage address queried from the database of component basic information by the component identification. The example of the component storage is shown in Fig. 5.

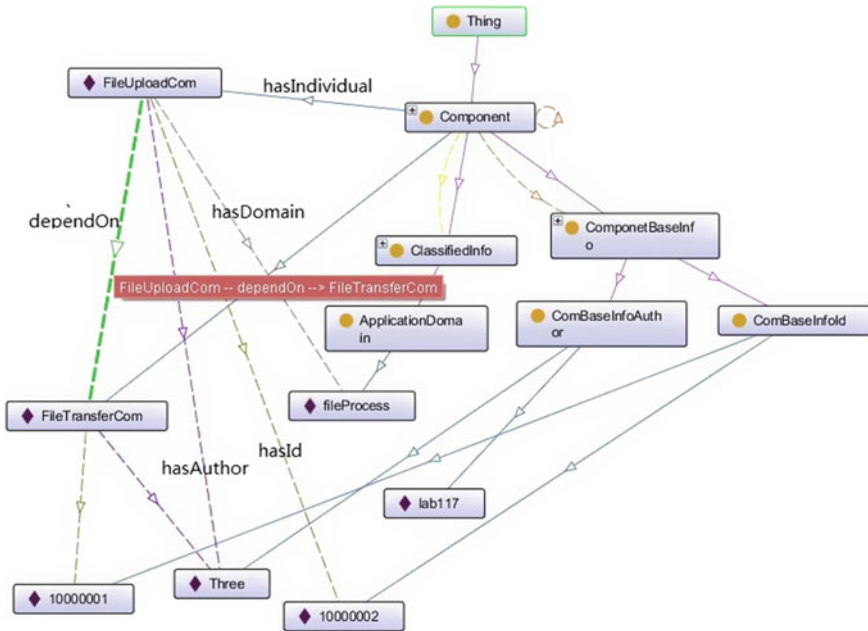
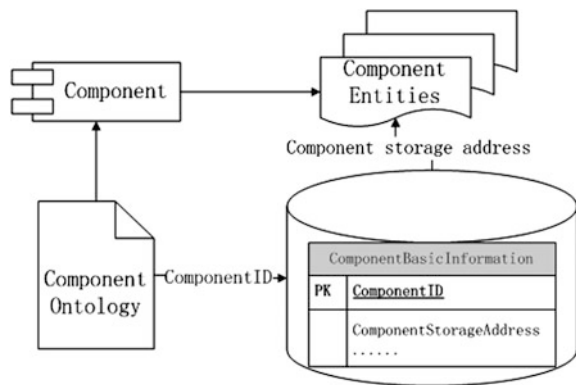


Fig. 3 Part of relations between individuals and properties

Fig. 4 Structure of the component storage



3 Retrieval of Component Based on Multi-agent

3.1 Structure and Process of Component Retrieval

On the basis of characteristics of human body and clothing structure, we divide a whole-human body Ω into six parts M_1-M_6 in accordance with neck cross-section [3], the horizontal of the crotch point, and the vertical surface of the armpit point,

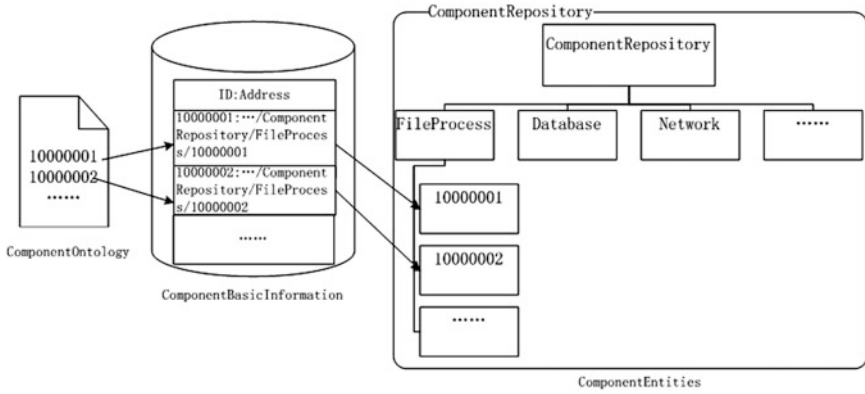


Fig. 5 Example of the component storage

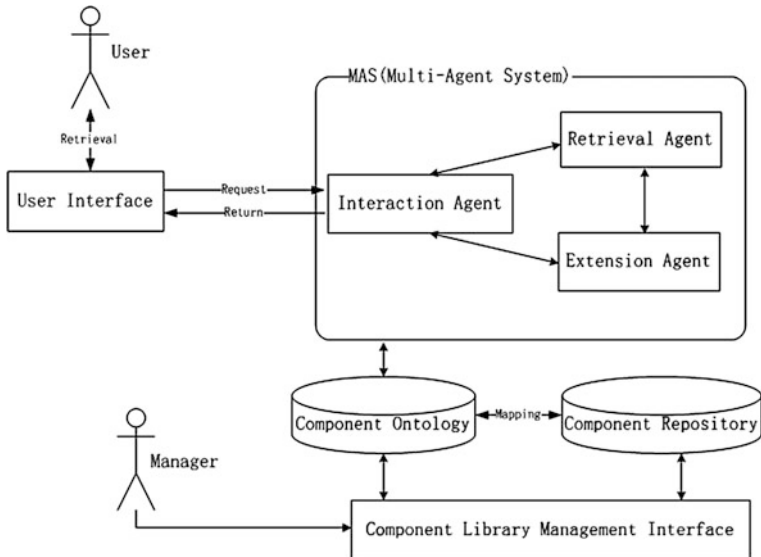


Fig. 6 Structure of the component retrieval

as shown in Fig. 2. This division can not only follow the previous modeling to generate torso of apparel human body but also take into account whole-human body modeling supplying head and limbs.

Based on the research of the facet-based classification of the component model and ontology-based component description, we designed a component retrieval system based on Multi-Agent and the structure of this system is shown in Fig. 6. These agents communicate with each other by using OWL-based content language of the FIFA [4] ACL (Agent Communication Language). The component retrieval

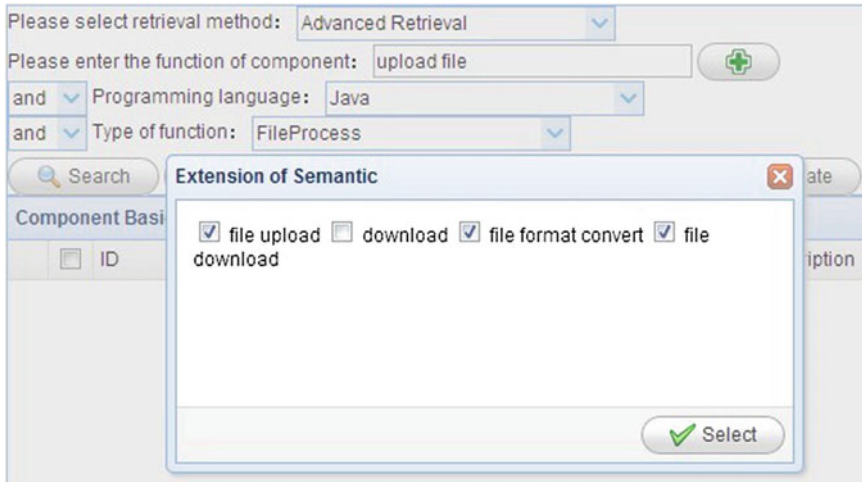


Fig. 7 User interface of the system

system is implemented by using the standard FIPA JADE (Java Agent Development Framework) tool as the development platform.

The system is composed of an user interface (UI), interaction agent (IA), retrieval agent (RA), and extension agent (EA) that search for relevant components.

- UI, where search results are displayed according to the query conditions. It also provides functions of showing the details of the component, downloading component, showing the evaluation of component evaluating component, etc.
- IA that is the bridge of the UI, RA, and EA. The agent encapsulates the query conditions and sends it to RA and EA. The results are returned to UI in a certain order.
- RA that search over the component ontology library, based on search information provided by IA. The results are returned to IA, which passes them to UI be properly presented to the user.
- EA that extends the results by reasoning and passes them to IA.

3.2 Example of Component Retrieval

In this example, the query conditions include function of the component, programming language and type of function which are “upload file”, “Java”, and “FileProcess”. Then we select relevant extension semantic of “upload file” (file upload, file format convert and file download) by click the button of “+”, as is shown in Fig. 7 and the search results are shown in Fig. 8. We can see that the results include the components we retrieved and some related components.

| Component Basic Information | | | | | | | | | |
|-----------------------------|----------|----------------|---------------|------------|-------------|-------------------------|---------------------|----------------------|----------|
| ID | Name | Author | Creation Time | Size | Description | Program | Software Dependence | Component Dependence | |
| 1 | 10000001 | FileConvertCo | Three | 2012-10-10 | 3.3kb | Convert file format to | Java | openoffice & swftor | |
| 2 | 10000002 | FileUploadCo | Three | 2012-10-10 | 4.5kb | Upload some files to | Java | | 10000001 |
| 3 | 10000003 | FileDownloadCo | Three | 2012-10-10 | 4.1kb | Download some files | Java | | |
| 4 | 10000011 | DocToPdf | lab117 | 2013-03-08 | 3.0kb | Convert doc.docx to p | Java | | |
| 5 | 10000020 | PdfToSwf | lab117 | 2013-03-28 | 6.1kb | Convert pdf to swf | Java | | |
| 6 | 10000101 | ToFlv | Three | 2013-01-04 | 8.1kb | Convert rmvb.avi,etc. t | Java | | |

Fig. 8 Retrieval result

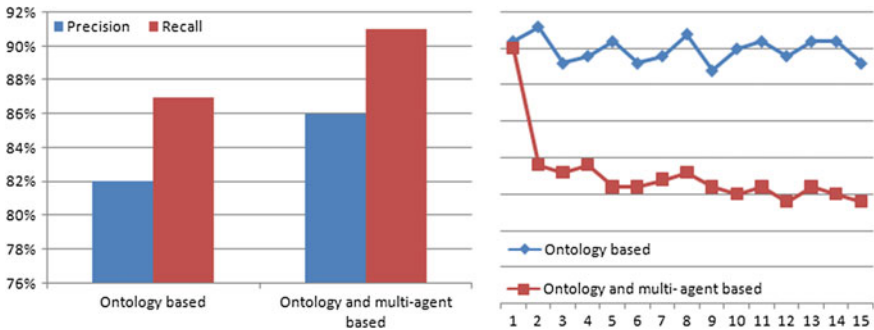


Fig. 9 Experiment results (left precision and recall, right retrieval time)

4 Results Analysis

The precision and the recall is an important index to reflect the effectiveness of retrieval.

Precision: Precision is defined as the number of relevant components retrieved divided by the total number of components retrieved. Precision = Number of relevant components retrieved / Total number of components retrieved.

Recall: Recall is defined as the number of relevant components retrieved divided by the total number of relevant components in the index. Recall = Number of relevant component retrieved / Total number of relevant components in the index.

The results that are retrieved by the method of ontology-based retrieval and the method of multi-agent and ontology-based are shown in Fig. 9.

Acknowledgment In this paper, the component is described formally by using OWL provides a rich semantic support for the facet-based classification. Users can not only retrieve component that is semantic matching, and can retrieve the relevant component through the relation between components. Then, a component retrieval system based on multi-agent which provides more precise and faster retrieval service is implemented by assigning the retrieval tasks to different agents. The system has been implemented, but there are many aspects that need to be improved and perfected, such as how to establish the domain ontology and the component ontology more

precise that can support the extension and reasoning of the semantic better and more precise. For the future work, we should also continue to improve the multi-agent system, such as adding evaluation agent, user model agent, etc., for providing the higher precision and faster service of component retrieval to users. Our goal is to implement a more personalized and intelligent component retrieval system.

References

1. Studer R, Benjamins VR, Fensel D (1998) Knowledge engineering: principles and methods. *Data Knowl Eng* 25(1-2):161–197
2. Bechhofer S et al OWL Web Ontology Language Reference, <http://www.w3.org/TR/2004/REC-owl-ref-20040210/>
3. Korthaus A, Schwind M, Seedorf S (2007) Leveraging Semantic Web technologies for business component specification. *Web Semant Sci Serv Agents WWW* 5:130–141
4. FIPA, FIPA ACL Message Structure Specification (2002) <http://www.fipa.org/specs/fipa00061/SC00061G.pdf>

A New Dynamic Credit Scoring Model Based on the Objective Cluster Analysis

Gao Wei, Cao Yun-Zhong and Cheng Ming-shu

Abstract Importance of early prediction of bad creditors has been increasing extensively. In order to solve the problem that cannot dynamically predict customer credit and population drift, this paper presents a new dynamic credit scoring model. Using the objective cluster analysis (OCA) method, the training set is divided into multiple subareas, and the observation period is divided into several periods. Then, customer credit scoring subclassifiers are established using cost-sensitive support vector machine. The empirical results show that this new dynamic credit scoring model will effectively decrease misclassification rate, and increase accurate rate for bad customers prediction.

Keywords Dynamic credit scoring · Objective cluster analysis · Customer relationship management · Data mining

1 Introduction

With the rapid development of credit industry, customer credit scoring issue is particularly important. Customer credit scoring model is a statistical method used to predict the probability that a loan applicant or existing borrowers will default or become delinquent, which was founded based on the characteristics in number of samples data in history to isolate the effects of various applicant characteristics on delinquencies and defaults [1]. With the credit cards as well as a variety of

G. Wei (✉) · C. Yun-Zhong
Business School of Sichuan Agricultural University, Chengdu, Sichuan, China
e-mail: gaow956@163.com

C. Ming-shu
Urban and Rural Development College of Sichuan Agricultural University,
Chengdu, Sichuan, China

personal consumption credit scale enlarging rapidly, the prevention of credit risk becomes highly concerned issues by financial institutions. In order to provide intellectual support for the decision makers [2], it is very important to establish the credit scoring model matching the customer sample characteristics.

For this purpose, two types of scoring model have been extensively employed in the credit scoring business: application scoring and behavior scoring [3]. Application scoring is used to examine the qualification of applicants for the initial loan service [4]; Credit behavior scoring reflects changing characteristics of borrowers' behavior after the loans are made [5]. At present, most studies establish credit scoring model aimed at new customers' application to decide whether to loan or not. Nevertheless, in fact, about 90 % of revenues are provided by the existed customers [6]. Therefore, it is necessary to establish a credit scoring model based on the existed customers behavior. Thus, we establish a dynamic credit scoring model based on the customers behavior in this paper.

However, the existed credit scoring models need to improve in the following two aspects: on one hand, it rarely considers the population drift problem. Characteristics of the population changes fast in China, such as the increasing loan to buy house, family car. These changes will lead to some changes in potential credit consumption crowds and credit concept of people. It is called population drift, which changes range and quality of sample population with the economic environment, population structure, and way of life [7]. Population drift will lead to the differences between single sample and total samples in the process of building credit scoring model, so that it can't meet the actual case. At present, the main method of dealing with population drift is nearest neighbor algorithm [7] and clustering method [8]. The nearest neighbor algorithm can overcome population drift problem easily, but its computational complexity is too large, and the erroneous judgment is high. Therefore, it has not been widely applied. To solve the population drift problem, Zou et al. [8] used the k -means clustering method to cluster customers in different geographic areas, and obtained the feature similarity customer group. However, it is difficult to accomplish the accurate segmentation on the whole space only by single clustering method. Using clustering ensemble technology, this paper solves the population drift problem. Meanwhile, the existed credit scoring models are mostly static scoring models [9], which need an observation period to evaluate the borrowers' credit. However, the lender always wants to learn all information about the customers' credit, especially those bad customers.

This paper presents a new dynamic credit scoring model based on objective clustering analysis, which can dynamically predict the customer credit and the population drift in credit scoring. This model can predict customer's credit condition dynamically by partitioning the observation period. Using the support vector machine (SVM), this model shows better performance than the traditional classifiers in credit scoring models [10–13]. Meanwhile, SVM algorithm is regarded as a basic classifier in this dynamic credit scoring model.

2 Related Theoretical Knowledge

2.1 Clustering Ensemble

Cluster analysis has been widely applied in customer segmentation. However, there is an ill-posed problem and no single clustering algorithm is able to obtain satisfactory solutions for all types of datasets in customer segmentation. Cluster ensemble emerges as an alternative approach for improving the performance of cluster [14]. Given a set of objects, cluster ensemble is consisting of two principal steps. At the first, it stores the results of some clustering algorithms. Then, it uses a specific consensus function to obtain a final clustering result. Cluster ensemble can go beyond what is typically achieved by a single clustering algorithm in several respects [15]:

Robustness: The combination process must have better average performance than a single clustering algorithm.

Consistency: The result of the combination should be very similar to all combined single clustering algorithm results.

Novelty: Cluster ensemble can find a combined solution unattainable by any single clustering algorithm.

Stability: Result with lower sensitivity can avoid noise and outliers (Fig. 1).

2.2 Objective Cluster Analysis

The objective clustering is conducted in the n -dimensional space of the customer value index evaluated before. Objective clustering of data points is done based on sorting a set of candidate clustering using the consistency criterion to choose the optimized consistent clustering [16]. Here, the concept of dipoles (pairs of points close to each other) is used; one vertex of a dipole goes into one subsample and the other into another. Thus, the greatest possible closeness of points forming the subsamples is achieved. Then the consistency criterion is used to evaluate the consistency of clustering groups on subsamples.

The stage-wise analysis of the algorithm is shown below:

Step 1 Computing the table of inter-point distances. The inter-point distances are calculated as

$$d_{ij} = \sum_{k=1}^m (x_{ik} - x_{jk})^2, \quad i = 1, 2, \dots, n, \quad j = i + 1, i + 2, \dots, n \quad (1)$$

The distance matrix is $D = (d_{ij})_{n \times n}$.

Step 2 Determining the pairs of closest points and partition into subsets. Here the concept of dipoles (pairs of points close to each other) is used. The clusters are to be identified in the two subsets of $A \cap B, C \cap D$. Thus, the

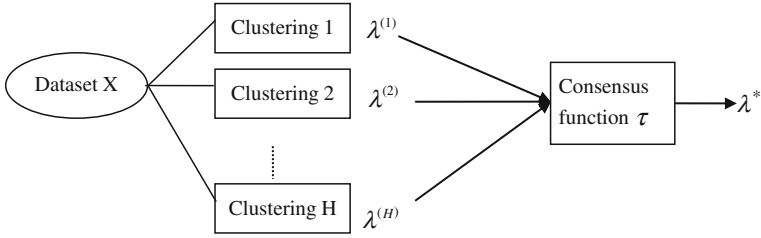


Fig. 1 Diagram of the general process of clustering ensemble

coincidence of clusters is required, representing that they are consistent. This leads to the attainment of a unique choice of consistent clustering.

- Step 3 Clustering. Using the consistency criteria η , where $\eta = (p - \Delta k)/p$, p is considered the total number of vertices, Δk is the corresponding vertices. Grouping the subsets into $k - 1$ clusters. Tables of inter-point distances are to be compiled for the points of each subset A and B. Continuation of the partitioning of the subsets into clusters and evaluation by consistency criterion is followed from $k = n$ to $k = 2$ until the smallest value of criterion is founded. The corresponding clustering scheme is the optimal clustering group.
- Step 4 Repetition of clustering analysis on subsets A and B for all possible sets of variable attributes.
- Step 5 Singling out the unique consistent clustering.

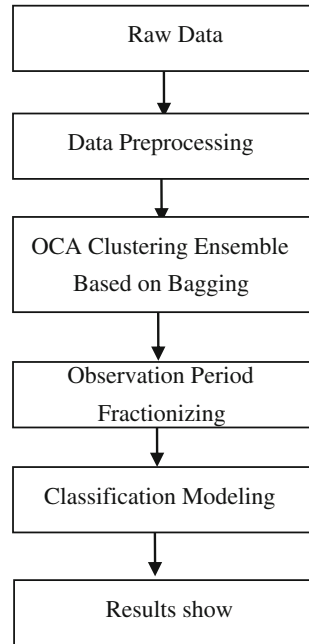
3 Dynamic Credit Scoring Model Based on Clustering Ensemble

In this paper, the whole procedure of the dynamic credit scoring model based on clustering ensemble is shown in Fig. 2.

3.1 OCA Clustering Ensemble Based on Bagging

At Present, most clustering ensemble algorithms use k -means as the basic cluster, which the number of the categories of each basic clustering algorithm is the same and determined subjectively. Banasik et al. [17] pointed out that it could get bad clustering results if the setting method of clustering number is settled not good enough. Therefore, this paper uses objective cluster analysis (OCA) method as the basic clustering. OCA algorithm based on the Group Method of Data Handling

Fig. 2 Flow chart of the proposed model



(GMDH) theory can determine the clustering number automatically, and have strong anti-interference capability.

Clustering ensemble algorithm includes two stages: one is the generation of multiple clustering results; the other is the combination of clustering. This article uses the Bagging sampling technology to produce training set for clustering. Through this technology, generates a number of training sets $\{s_i\}$, $i = 1, 2, \dots, M$ (M represents the number of clustering) from the original dataset X , and cluster each training subsets s_i with OCA algorithm.

OCA can determine the optimal number of clustering objectively, and the number of cluster of each cluster result may be different. So in order to fusion the multiple clustering results, this paper uses similar matrix to fusion multiple clustering results. For the t -th clustering result, the similar matrix M^t is expressed below:

$$M_{ij}^t = \sum_{s=1}^{k_t} I(i \in C_s^t) \cdot I(j \in C_s^t) \tag{2}$$

where, k_t represents the number of clustering in the t -th result clustering; i, j is the customer samples, $1 \leq i, j \leq n$; C_s^t is the s -th class of customer sample set in the t -th clustering result; I is the characteristic function of set C_s^t .

Consequently, the average similarity matrix for L clustering results between sample couples can be expressed as follows:

$$\bar{M} = \frac{1}{L} \sum_{i=1}^L M^i \tag{3}$$

To get the final clustering result, we use similar OCA once again. The difference with OCA is that the original distance matrix D between samples is replaced by the similarity matrix \bar{M} . This method is called OCA_s .

3.2 The Partition of Observation Period

Once the dataset is clustered, the observation horizon is fractionized into several fractional periods and separate classifier is established. This is to make a model which predicts the borrowers' credibility dynamically even though they not satisfy the full observation periods. The whole observation period is T , which is divided into n stages. t is the customer duration, j is the stage that customer belongs to.

$$j = \begin{cases} 0 & 0 < t \leq \frac{T}{n} \\ 1 & \frac{T}{n} < t \leq 2\frac{T}{n} \\ \vdots & \\ n & t \geq T \end{cases} \tag{4}$$

3.3 Classifier Modeling

3.3.1 Cost-Sensitive Support Vector Machine

Generally speaking, the customer type distribution is not balance. To solve the problem, we introduce cost-sensitive learning parameters [18] to the basic model of support vector machine (SVM) classification. For the two classification problem, suppose that the data sample set is (x_i, y_i) , where $x_i \in R^l, y_i \in \{-1, +1\}, i = 1, 2, \dots, n$. Dividing it into two categories by planar $f(x) = w \cdot x_i + b = 0$, then converts solving optimization classification problem into the following optimization problem:

$$\begin{aligned} \min R(w, \xi) &= \frac{1}{2} w^T w + C \left(\sum_{i=1}^n \xi_i \right) \\ \text{s.t. } & y_i(w^T x_i + b) \geq 1 - \xi_i, \xi_i \geq 0, \quad i = 1, 2, \dots, n \end{aligned} \tag{5}$$

where, w represents weight vector; ξ_i represents relaxation factor; C is the penalty function to balance empirical risk and structural risk; b is bias coefficient.

We can get the optimal classification function according to [19, 20].

$$f(x) = \text{sign}\left\{\sum \alpha_i y_i k(x_i \cdot x) + b\right\} \tag{6}$$

where, $k(x_i \cdot x)$ is the kernel function.

According to the characteristics of the customer credit data itself, the retention cost caused by the wrong partition is different. Let the sample dataset is $(x_i, y_i, \cos t_i)$, $x_i \in R^l, y_i \in \{-1, +1\}$, $\cos t_i \geq 0 (i = 1, 2, \dots, n)$, which $\cos t_i$ is the i -th customer retention cost caused by wrong partition, and related to y_i . This problem can be converted into solving the following optimization problem:

$$\begin{aligned} \min R(w, \xi) &= \frac{1}{2} w^T w + C^+ \left(\sum_{\{i/y_i=+1\}}^n \cos t_i \xi_i \right) + C^- \left(\sum_{\{i/y_i=-1\}}^n \cos t_i \xi_i \right) \\ \text{s.t. } & y_i (w^T x_i + b) \geq 1 - \xi_i, \xi_i \geq 0, i = 1, 2, \dots, n \end{aligned} \tag{7}$$

where, C^+, C^- are the penalty functions of the positive and negative samples.

To solve the optimization problem of (7), use its dual Lagrange expression:

$$\begin{aligned} \max Q(\alpha) &= \sum_{i=1}^n \alpha_i - \frac{1}{2} \sum_{i=1}^n \sum_{j=1}^n \alpha_i \alpha_j y_i y_j k(x_i x_j) \\ \text{s.t. } & \sum_{i=1}^n \alpha_i y_i = 0 \\ & 0 \leq \alpha_i \leq C^+ \quad \text{if } y_i = +1 \\ & 0 \leq \alpha_i \leq \cos t_i C^- \quad \text{if } y_i = -1 \end{aligned} \tag{8}$$

Then we can get the optimal classification function:

$$f'(x) = \text{sign}\left\{\sum_{i,j=1}^n \alpha_i y_i k(x_i \cdot x) + b\right\} \tag{9}$$

3.3.2 Dynamic Credit Scoring Model

In Sects. 3.1 and 3.2, we can get k customer categories through OCA cluster ensemble and n sub-observation periods, respectively. We construct $k \times n$ classifiers using cost-sensitive support vector machine algorithm. For a specific customer, he belongs to cluster i for the period j , which is classified applying classifier S_{ij} . As is shown in Fig. 3.

We can predict the customer's credit condition without obtaining customers' information of the whole observation period in the credit scoring model. Based on

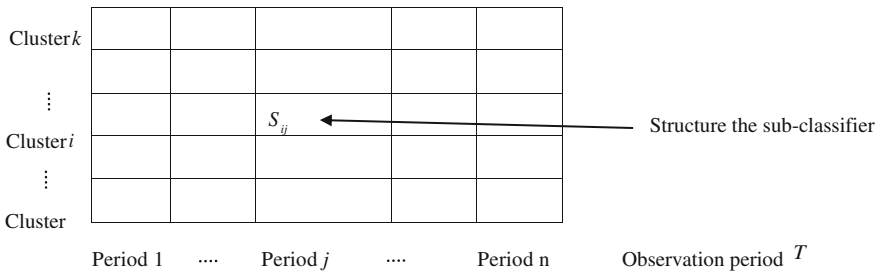


Fig. 3 Construct the subclassifier

the dynamic credit scores results, lenders can determine whether to credit, to mail new products to old customer and how to recoup losses when the customer account condition is bad.

4 Empirical Study

4.1 Data Description

Data is from the credit card customers of some commercial bank in china, and there are 13,200 samples. The index system is divided two parts: the credit scoring index and the behavior scoring index. The credit scoring indexes contain age, sex, education, housing, job; Behavior scoring indexes are customer behavior information such as loan payments, consumption amount, etc. We select a period of a time as the observation period through the historical transaction data sample and take the next period as the performance period. Then, customers are divided into “good customers” and “bad customers” in line with the performance in the performance period. We choose the credit card amounts issued in the Bank from March to May in 2010 and set 12 months from June 2010 to May 2011 as observation period and take 6 months from June to November in 2011 as performance period.

4.2 Experiment Results Analysis

Seventy percent samples are selected randomly from 13,200 samples as training set, and remaining 30 % as the test set. By applying cluster algorithm proposed in Sect. 3.1, 9,240 samples of training set are grouped into three clusters. The number of samples in each cluster is 2,361, 3,960, and 2,919 cluster. The characteristic of each cluster is as follows. Compared with the rest of the two clusters, customers of

Table 1 Misclassification rate in each quarter

| Stage | Single SVM model | Dynamic credit Scoring model based on clustering ensemble | | | |
|-----------|------------------|---|-----------------|-----------------|-----------------|
| | | Cluster 1(2361) | Cluster 2(3960) | Cluster 3(2919) | Average cluster |
| 0 months | 0.298 | 0.305 | 0.314 | 0.264 | 0.293 |
| 3 months | 0.283 | 0.293 | 0.302 | 0.231 | 0.275 |
| 6 months | 0.281 | 0.241 | 0.252 | 0.198 | 0.238 |
| 9 months | 0.278 | 0.259 | 0.233 | 0.193 | 0.229 |
| 12 months | 0.254 | 0.248 | 0.221 | 0.176 | 0.215 |

Table 2 z_1 value of misclassification rate difference

| Observation period | 0 month | 3 months | 6 months | 9 months | 12 months |
|--------------------|---------|----------|----------|----------|-----------|
| 12 months | 1.778 | 1.463 | 1.364 | 0.737 | 0 |

cluster 1 are the members of the wealthy class who has the highest job rank, higher income, own housing, and no loan. Most of the customers of cluster 2 belong to the “middle class” to live in a rent house or purchase house with loan. Customers of cluster 3 appeared to be “working class,” mostly composed of low income level, renting house, or living with their parents.

At the step of observation horizon fractionizing, the entire observational horizon of 12 months was fractionized into 4 quarters: 3, 6, 9, and 12 months. Finally, SVM classifiers are trained for all 3×4 fractions. To assess the proposed model, the effects of clustering and fractionized observation period are investigated. First, the effect of clustering is identified by the comparison of misclassification rate of the validation data between the proposed model and the nonclustered single SVM model with the same dataset. The results are shown in Table 1.

From the computational results in Table 1, the clustering is lower than the misclassification rate of the single SVM model. Not only that, each of the three clusters generally showed a lower misclassification rate, respectively than the single SVM model. The average misclassification rate of the proposed model was derived by the weight proportion of its number of borrows.

Finally, the effect of fractionized observation period can be ascertained through the comparison of misclassification rate between the full observation model and the fractional observation models. The value of fractionized observation period can be verified if the misclassification rate of proposed model does not turn out to be significantly lower than that of full observation model. We test the hypothesis that two proportions of misclassification rate are equal. Table 2 shows the standardized differences between the misclassification rate for fractional observation period of 0, 3, 6, 9, and 12 months. With the significance level 0.10, the value of $z_{0.10}$ is 1.28. The fractional observation model begins to have significantly lower misclassification rate than the entire observation model from the observation period shorter than 9 months. However, we can still say that 9 months of fractional

observation model shows the similar misclassification rate to that of the entire observation model. This illustrates that 9 months of observation period is enough to classify the borrowers credibility overall.

5 Conclusions

This paper proposes a dynamic credit scoring model based on clustering ensemble to evaluate and predict the customer credit condition. First, the training set samples are clustered into multiple subareas using OCA clustering ensemble algorithm to weaken the differences among different subareas samples. Then, the entire observation period is fractionized into several fractional periods. Finally, customer credit scoring subclassifiers are established using cost-sensitive support vector machine. Empirical analysis shows that our model at least has the following advantages:

- (1) Using clustering ensemble first not only makes the prediction model more accurate than the single SVM model, but can get all kinds of customer characteristics.
- (2) The division of observation period makes the model more flexibility in predictive time, and predicts the customer credit dynamically, improves the problem that traditional static model can only attain the credit scoring at a setting time point.

Consequently, the model proposed is significant in management, which helps the decision makers who predict the high default risk of customers in time, provide the commercial bank credit decision-making and customer relationship management with more powerful support.

Acknowledgments This project is supported by the Key Projects of Educational Commission of Sichuan Province of China (Grant No. 13ZA0140) and the Program of Double branch of Sichuan agricultural University (Grant No. 03570421)

References

1. Yu L, Yao X, Lai KK (2011) Credit risk evaluation using a weight least squares SVM classifier with design of experiment for parameter selection. *Expert Syst Appl* 38:15392–15399
2. Xiang H, Yang S (2011) Recent development in key techniques of credit scoring. *Theor Pract Econ* 172(32):20–24
3. Hand D, Sohn SY, Kim Y (2005) Optimal bipartite scorecards. *Expert Syst Appl* 29(3):684–690
4. Hand DJ (2001) Modeling consumer credit risk. *IMA J Math Manage Math* 12:139–155
5. Hsieh N (2004) An integrated data mining and behavioral scoring model for analyzing bank customers. *Expert Syst Appl* 26(4):567–573

6. Zhang J, Wei Q, Zhang B (2012) Special sampling method of rare event in credit score model. *Stat Inf Forum* 11(27):15–19
7. Santi S (2012) Using cluster analysis study to examine the successful performance entrepreneur in Indonesia. *Procedia Econ Finan* 4:286–298
8. Zou P, Yu B, Wang X (2011) Cost-sensitive learning method with data drift in customer segmentation. *J Harbin Inst Technol* 43(1):119–124
9. Thomas LC (2000) A survey of credit and behavioral scoring: forecasting financial risk of lending to consumer. *Int J Forecast* 16:149–172
10. Huang CL, Chen MC, Wang CJ (2007) Credit scoring with a data mining approach based on support vector machines. *Expert Syst Appl* 33(4):847–856
11. Bellotti T, Crook J (2009) Support vector machines for credit scoring and discovery of significant features. *Expert Syst Appl* 36(2):3302–3308
12. Chong Wu, Han Xia (2009) Credit risk assessment in commercial banks on five-class support vector machines ensemble. *Forecasting* 28(4):57–61
13. Gao W, He C, Xiao J (2011) OCA cluster ensemble model for customer segmentation. *J Inf* 30(6):164–168
14. Analoui M (2006) Solving cluster ensemble problems by correlation's matrix. *IFIP Int Fed Inf Proc* 228:227–231
15. Hadjitodorov ST, Kuncheva LI (2007) Selecting diversifying heuristics for cluster ensembles. *Lect Notes Comput Sci* 4472:200–209
16. Ivakhnenko AG, Mueller JA (1992) Parametric and nonparametric selection procedures in experimental systems analysis. *SAMS* 9(5):157–175
17. Banasik JL, Crook JN, Thomas LC (1996) Does scoring a subpopulation make a difference? *Rev Retail Distrib Consum Res* 6:180–195
18. Japkowicz N, Stephen S (2002) The class imbalance problem: a systematic study. *Intell Data Anal* 6(5):429–449
19. Strehl A, Ghosh J (2002) Cluster ensembles: a knowledge reuse framework for combination multiple partition. *J Mach Learn Res* 3(3):583–617
20. T Wei, Zhou Z-H (2005) Bagging-based selective cluster ensemble. *J Softw* 16(4):496–502

Application of the Fully Data-Driven Combination Model for Water Demand Forecasting in the Mountainous Tourist Area

Li Jie, Li Qiang, Huang Yi, Ling Liang, Fang Cheng
and Jiang Zhenzhen

Abstract For water demand forecasting in the mountainous tourist area this paper proposes a novel approach, namely the combination of autoregressive integrated moving average (ARIMA) model and radial basis function (RBF) neural network. And at the same time, the combination model focuses on the characteristics of the mountainous tourist area, which is relatively closed with a smaller scale and the water supply curve is relatively smooth. This model depends on fully data-driven approach, which means that it only relies on the historical data of water demand and ignores external factors to eliminate various unstable factors including the weather, season, tourists, and others, simplifying the model parameters. Combination model can overcome the limitations of the single model in the nonlinear sequence processing, improve the forecasting accuracy. At last, the historical data, which origins from the Mount Huangshan Scenic Area water supply scheduling in 2012, have been tested and achieved significant forecasting effects.

L. Jie · L. Qiang (✉) · H. Yi
School of Computer and Information, Hefei University of Technology, Hefei China
e-mail: 373708284@qq.com

L. Jie
e-mail: Lijie_62@163.com

H. Yi
e-mail: YiHuang63@163.com

L. Liang · F. Cheng
Mount Huangshan Scenic Area Water Supply Ltd. Co., HuangShan China
e-mail: 19459886@qq.com

F. Cheng
e-mail: 1961915275@qq.com

J. Zhenzhen
School of Foreign Languages, Hefei University of Technology, Hefei China
e-mail: 496757789@qq.com

Keywords Fully data-driven approach · ARIMA model · RBF neural network · Combination model

1 Introduction

Water demand forecasting in mountainous tourist area is greatly important to ensure the water for tourism, forest fire prevention, and scenic ecological protection. However, because of the special geomorphic environment in mountainous tourist area, it is quite different between the mountain and city in water supply dispatching mode. Affected by various factors, water demand is quite difficult to predict due to its considerable uncertainty. Owing to a large number of factors and heavy computation [1], traditional methods for forecasting municipal water use, e.g., the gray forecasting [2], wavelet transform [3], and full Bayesian analysis, and other models cannot be directly applied to the mountainous tourist area consumption forecasting. Based on fully data-driven approach, historical data of water supply scheduling are fully used for forecasting, and differential method for process data in order to eliminate seasonal factors influencing on water demand, reduce environmental variables, and influencing factors in models.

On the basis of fully data-driven approach, this paper adopts the combination method of autoregressive integrated moving average (ARIMA) and RBF neural network. The ARIMA model due to its simplicity, flexibility, and feasibility is widely used in the linear prediction, but it shows poor performance in nonlinear data processing. However, RBF neural network model shows good performance in mining nonlinear relationship implied in the data, making up for the deficiency of ARIMA model [4]. Combination model gives full play to the advantages of the two models, that is, ARIMA model is used to specify the linear relationship of data mining sequence, while RBF neural network is illustrated to fit the nonlinear error of the data sequence, further improving the forecasting accuracy.

2 Model Introduction

2.1 ARIMA Model

ARIMA model is currently the mainstream method of time series modeling. The full name of ARIMA model is called autoregressive integrated moving average model, which is proposed by Geogre E. P. Box and Gwilym M. Jenkins in the early 1970s [5]. So it is also known as the Box-Jenkins model. The formula is defined as follows:

$$y_t = \theta_0 + \varphi_1 y_{t-1} + \varphi_2 y_{t-2} + \cdots + \varphi_p y_{t-p} + \varepsilon_t - \theta_1 \varepsilon_{t-1} - \theta_2 \varepsilon_{t-2} - \cdots - \theta_q \varepsilon_{t-q} \quad (1)$$

In the formula, y_t is the sample value. φ_i ($i = 1, 2, \dots, P$) and θ_j ($j = 1, 2, \dots, q$) is the model parameter. ε_i is the white noise sequence obeying normal distribution $N(0, 1)$. p, q is the model order, d is the model differential frequency [6].

2.2 RBF Neural Network

Given the data being trained properly, RBF neural network exploiting the Back Propagation learning algorithm and the recursive algorithm can be close to arbitrary nonlinear function [7]. RBF neural network is also called radial basis function neural network, which is efficient and feedforward. RBF neural network along with its simple structure, fast training speed, possesses the best approximation performance and global optimal characteristics that are prior to other feedforward networks. Meanwhile, it is a kind of neural network as well that can be widely used in platform recognition, nonlinear test function approximation and other fields. First, RBF neural network processes the input sequence, if the optimal order of RBF neural network is m , then an input sequence after treatment is as follows:

$$X = \begin{bmatrix} x_1, & x_2, \dots, x_m \\ x_2, & x_2, \dots, x_{m+1} \\ \dots & \\ x_{n-m}, & x_{n-m+1}, \dots, x_{n-1} \end{bmatrix} \tag{2}$$

RBF neural network hider layer with Gauss kernel function carries on the nonlinear transformation of the input layer. The function is defined as follows:

$$R_i(X') = \exp\left(-\frac{1}{2} \left(\frac{X' - C_i}{\sigma_i}\right)^2\right) \tag{3}$$

Among these parameters, C_i represents the RBF center of the i th hider layer unit, σ_i represents the perception central point width of the i th hidden layer unit, $X' - C_i$ represents the Euclidean distance [8].

3 Data Fitting of Combination Model

3.1 Data Preprocessing

Water demand data are not stationary time series, and range of data fluctuation is larger, which would have an adverse impact on the model of training speed and convergence speed. Therefore, data preprocessing should be conducted before modeling to narrow data range to $[0, 1]$. Assuming the data processed is x' , the maximum value is x_{\max} , the minimum value is x_{\min} , then the preprocessing formula is defined as below:

Table 1 Results of data preprocessing

| Data No. 1–15 | Data No. 16–30 | Data No. 31–45 | Data No. 46–60 | Data No. 61–75 | Data No. 76–90 | Data No. 91–105 | Data No. 106–120 |
|------------------|-------------------|-------------------|-------------------|-------------------|-------------------|--------------------|---------------------|
| 0.464 | 0.116 | 0.267 | 0.291 | 0.443 | 0.329 | 0.405 | 0.845 |
| 0.356 | 0.155 | 0.350 | 0.259 | 0.421 | 0.398 | 0.487 | 0.738 |
| 0.269 | 0.128 | 0.277 | 0.401 | 0.447 | 0.382 | 0.750 | 0.752 |
| 0.398 | 0.170 | 0.296 | 0.436 | 0.335 | 0.332 | 1.000 | 0.698 |
| 0.354 | 0.179 | 0.294 | 0.586 | 0.320 | 0.310 | 0.715 | 0.749 |
| 0.291 | 0.327 | 0.260 | 0.399 | 0.281 | 0.293 | 0.649 | 0.687 |
| 0.200 | 0.360 | 0.209 | 0.370 | 0.405 | 0.389 | 0.754 | 0.810 |
| 0.197 | 0.516 | 0.468 | 0.355 | 0.35 | 0.413 | 0.745 | 0.848 |
| 0.099 | 0.449 | 0.472 | 0.290 | 0.236 | 0.478 | 0.791 | 0.884 |
| 0.151 | 0.628 | 0.510 | 0.297 | 0.537 | 0.564 | 0.699 | 0.749 |
| 0.042 | 0.691 | 0.406 | 0.370 | 0.432 | 0.683 | 0.522 | 0.549 |
| 0.000 | 0.744 | 0.308 | 0.370 | 0.474 | 0.534 | 0.715 | 0.617 |
| 0.023 | 0.565 | 0.394 | 0.661 | 0.428 | 0.494 | 0.343 | 0.808 |
| 0.107 | 0.594 | 0.366 | 0.285 | 0.318 | 0.452 | 0.771 | 0.788 |
| 0.124 | 0.440 | 0.347 | 0.459 | 0.331 | 0.425 | 0.633 | 0.804 |

$$x' = (x - x_{\min}) / (x_{\max} - x_{\min}) \tag{4}$$

Lastly, the predicted results are calculated with the antinormalization, its formula is shown as follows:

$$x = x'(x_{\max} - x_{\min}) + x_{\min} \tag{5}$$

Parts of the data preprocessed are demonstrated in Table 1.

3.2 ARIMA Linear Data Processing

The time series of water demand historical data not only has the linear characteristics but also has the nonlinear characteristics. The linear part in the time series can be fitted by the ARIMA model, and assuming the output sequence is \hat{Y}_t . In the paper, the historical data of the Mount Huangshan Scenic Area water supply scheduling in 2012 is not stationary time series, driven by only historical data of water supply scheduling. After the d steps difference, smooth ARIMA (p, d, q) model formula is defined as follows:

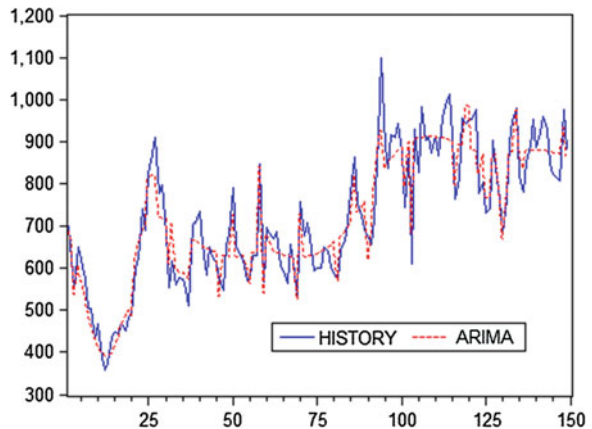
$$\varphi(B)(1 - B)^d y_t = \theta(B)\varepsilon_t \tag{6}$$

In this formula, $\varphi(B) = 1 - \varphi_1 B, \dots, -\varphi_p B^p$ and $\theta(B) = 1 - \omega_1 B, \dots, -\omega_q B^q$, and $\{y_t\}$ stands for time series, B represents the Time-shift operator $(1 - B)^d$

Table 2 ARIMA model parameter selection

| ARIMA (p, d, q) | Smooth R^2 | Significant value |
|---------------------|--------------|-------------------|
| ARIMA (1, 2, 2) | 0.635 | 0.278 |
| ARIMA (1, 2, 4) | 0.781 | 0.929 |
| ARIMA (2, 2, 4) | 0.660 | 0.640 |
| ARIMA (3, 2, 1) | 0.652 | 0.415 |
| ARIMA (3, 2, 3) | 0.648 | 0.457 |
| ARIMA (4, 2, 1) | 0.663 | 0.894 |
| ARIMA (4, 2, 2) | 0.657 | 0.0771 |
| ARIMA (4, 2, 4) | 0.654 | 0.379 |

Fig. 1 ARIMA model data fitting



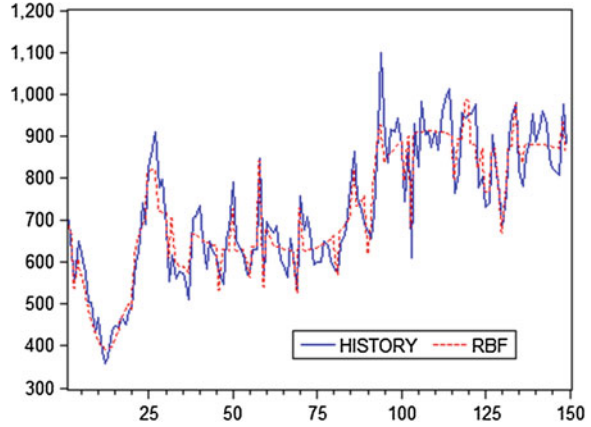
means difference operator, p, d, q refers to model order, $\varphi_1, \varphi_2, \dots, \varphi_p$ and $\omega_1, \omega_2, \dots, \omega_q$ are model parameters, ε_t is that the mean value is zero, but refers to the white noise with some variance.

In this case, the time series is stationary after 2 times difference, and the value of d is 2. The selection of p, q first comes from the qualitative analysis based on autocorrelation and partial autocorrelation graph, and then quantitative analysis is conducted based on the smooth value of R^2 and Significant value. The p, d, q parameter selection table of ARIMA model is demonstrated in Table 2.

As it can be seen from the table, the ARIMA (1, 2, 4) parameter combination smooth R^2 and Significant value is significantly better than that of other combinations, the final model is determined as ARIMA (1, 2, 4), and the fitting effect is as shown in Fig. 1.

In Fig. 1, X-axis refers to time for the unit of day, Y-axis refers to water consumption for the unit of ton. The ARIMA model is used to forecast the Mount Huangshan Scenic Area water demand, and the trend of the data fitted accords with the real data. But as is seen from the figure, there is a large gap between the fitted data and the real data in most of the extreme points, extreme value fitting effect is not satisfying, and there is still more room for improvement.

Fig. 2 Comparison of RBF neural network model and the original data



3.3 RBF Neural Network Residual Fitting

Only using ARIMA model cannot achieve good prediction effect in extreme point. Using RBF neural network to fit nonlinear part of the time sequence, assuming the formula is:

$$e_t = Y_t - \hat{L}_t \tag{7}$$

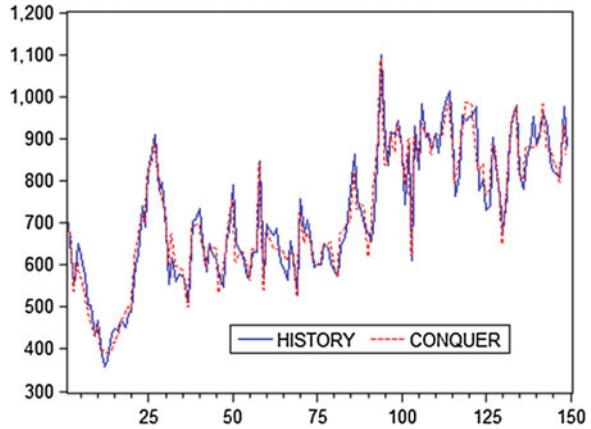
Then the sequence $\{e_t\}$ implies the nonlinear relation of the original sequence. So $\{e_t\}$ is RBF neural network input layer data. Assuming the prediction results of residual sequence $\{e_t\}$ are \hat{N}_t which is obtained by neural network model. In order to compare ARIMA model with combination model, the historical data of the Mount Huangshan Scenic Area water supply scheduling are fitted by RBF neural network shown in Fig. 2:

In Fig. 2, X-axis refers to time for the unit of day, Y-axis refers to water consumption for the unit of ton. As it can be seen from Fig. 2, the historical data of Mount Huangshan Scenic Area predicted only by RBF neural network, the fitting effect is poorer than ARIMA model, and reveals great errors. The implicit correlation of the data series has not been excavated, which fully reflects that only employing the RBF neural network cannot achieve better forecasting results of water demand forecasting in the mountainous tourist area.

3.4 Data Fitting of Combination Model

The final fitting result is the sum of linear part and nonlinear residual part. Assuming forecasting result is \hat{Y}_t , then its formula is described as follows:

Fig. 3 Data fitting of combination model



$$\widehat{Y}_t = \widehat{L}_t + \widehat{N}_t \tag{8}$$

\widehat{L}_t is equal to the linear fitting results of ARIMA model, \widehat{N}_t is defined as the residual fitting results of RBF neural network. Data fitting results are shown in Fig. 3.

In Fig. 3, X-axis refers to time for the unit of day, Y-axis refers to water consumption for the unit of ton. As it can be seen from the figure, combination model achieves better performance than AIRMA model and RBF model. Data fitted is not only in conformity with the trend of real data, but also much closer to the real data in the extreme point than ARIMA model, which shows that combination model overcomes the shortcomings of ARIMA model in the nonlinear model processing, and reduces the model error and improves the accuracy of the model.

4 The Model Forecasting Effect

After the completion of data fitting, water demand can be predicted by the model. This paper takes water demand data in Mount Huangshan Scenic Area in 2012 as samples to predict subsequent 20 days of demand data. The comparison figure of model forecasting effect is described in Sect. 4.1.

4.1 Forecasting Effect of ARIMA Model

In Fig. 4, X-axis refers to time for the unit of day, Y-axis refers to water consumption for the unit of ton. The aforementioned data confirm that forecasting line trend is in accordance with real data, which exist errors, especially in later time, the forecasting data deviate greatly from the real data. Finally, it explains that

Fig. 4 Forecasting of ARIMA model array

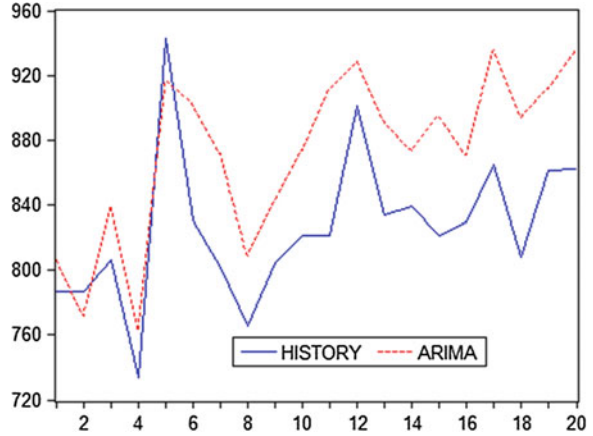
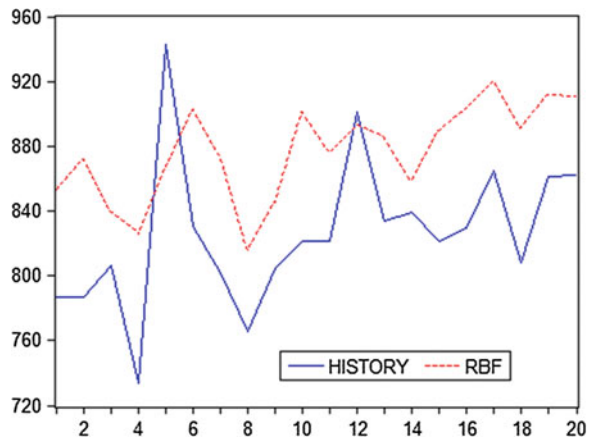


Fig. 5 Forecasting of RBF model data

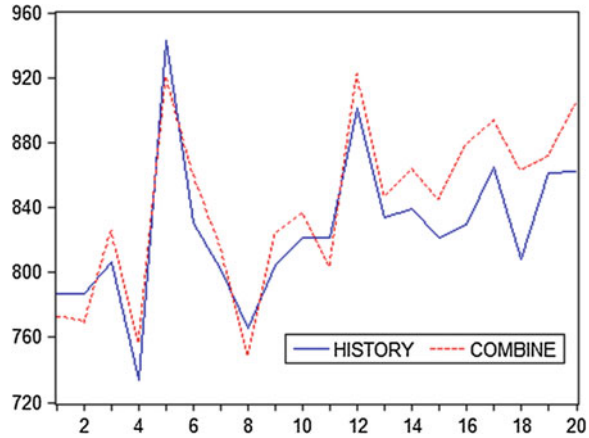


ARIMA model is mostly applied to short-term forecasting, errors will increase as time goes on, and performs poor in the long-term nonlinear forecasting.

4.2 Forecasting Effect of RBF Neural Network Model

In Fig. 5, X-axis refers to time for the unit of day, Y-axis refers to water consumption for the unit of ton. The forecasting effect of RBF neural network model is similar to that of its fitting effect, which presents poor forecasting effect and a huge error between the forecasting value and true value. But as time goes on, the forecasting error is not like the ARIMA model that increases greatly, which states that RBF neural network model can be used to make short-term or medium-term forecasting on the premise of low accuracy of water demand forecasting.

Fig. 6 Data forecasting of combination model



4.3 Forecasting Effect of Combination Model

In Fig. 6, X-axis refers to time for the unit of day, Y-axis refers to water consumption for the unit of ton. According to the forecasting results, it is evident that the combination model achieves better forecasting performance than ARIMA model and neural network, especially in the early forecasting period, which there is a higher degree of agreement between the forecasting value and real value, and improves forecasting accuracy of the model. Although the same error of combination model appears in the later forecasting period just like the ARIMA model, the forecasting accuracy decreases as time goes by. But compared with ARIMA model, forecasting effective time is lengthened, which exhibits that the combination model is more suitable for enhancing forecasting accuracy and effective time.

4.4 Combination Model Test

After the combination model is established, this paper depends on residual analysis to test whether it can be used to conduct data prediction. Having assumed the range of error, then test sample error, if it belongs to the range of error, this declares that the model gets through residual test. Test results are presented in Fig. 7.

In Fig. 7, X-axis refers to residual interval and Y-axis refers to lag phases. Through residual analysis, it is concluded that combination model error which is in the allowed range, can be used for water demand forecasting. In Fig. 7 of residual analysis, the residual is relatively stable in early time, later it begins to fluctuate, which also verifies that the combination model has a high precision for medium and short-term forecasting.

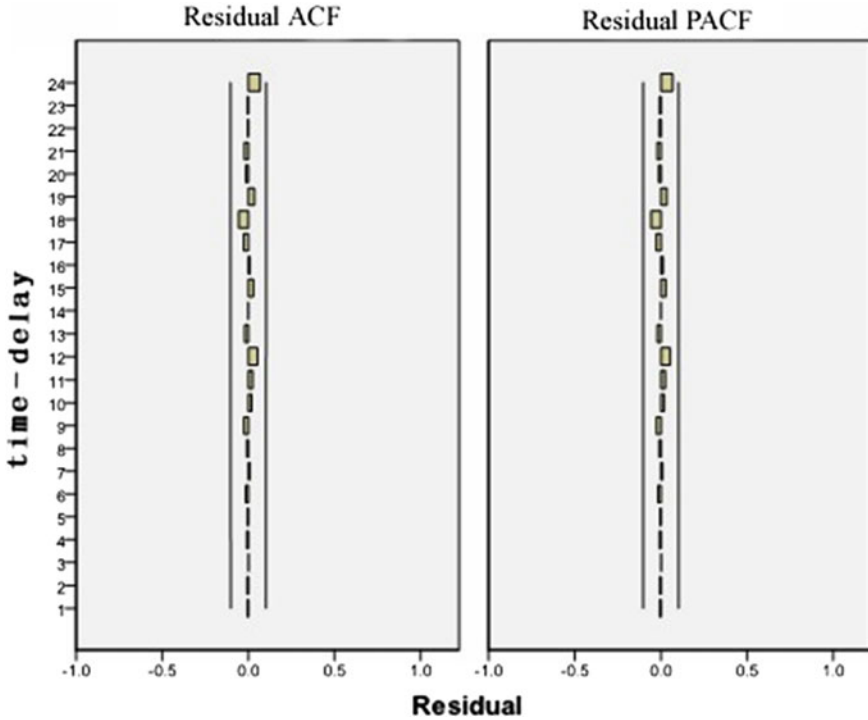


Fig. 7 Residual analysis of combination model

5 Conclusions

This paper proposes a novel approach of water demand forecasting called fully data-driven method on mountain scenic spot, which reduces the data complexity and simplifies the model parameters. At the same time, combining ARIMA with RBF neural network greatly improves the forecasting accuracy. The model modes of combination model are flexible and various that can be reasonably collocated according to the characteristics of historical data and the forecasting accuracy requirements of the model. Judging from the historical data fitting and forecasting results of water supply scheduling in Mount Huangshan scenic spot, it can be clearly demonstrated that combination model performs well in short-term forecasting. In order to obtain a better prediction results, further research may be conducted to combine and improve other predictive models. Furthermore, an appropriate number of water impact factors can be added according to different characteristics of mountain scenic spot to improve the prediction accuracy. Combination model overcomes the limitations of single model of water demand forecasting in the mountainous tourist area, and has significant application prospect.

References

1. An N, Zhao W, Wang J et al (2013) Using multi-output feedforward neural network with empirical mode decomposition based signal filtering for electricity demand forecasting. *Energy* 49(6):279–288
2. Wang C-C, Wang L-P, Cao Y-H (2013) Application of improving the multivariable grey model in the municipal water demand forecasting. *Water Resour Power* 31(2):27–30
3. Lu F, Xu J-H, Wang Z-Y (2013) On the genetic wavelet neural network model of water demand forecasting in the city of Hefei. *Sci Surveying Mapp* 05:28–31
4. Chen C, Chang Y, Chang Y (2009) Seasonal ARIMA forecasting of inbound air travel arrivals to Taiwan. *Transportmetrica* 5(2):125–140
5. Valipour M, Banihabib ME, Behbahani SMR (2013) Comparison of the ARMA, ARIMA, and the autoregressive artificial neural network models in forecasting the monthly inflow of Dez dam reservoir. *J Hydrol* 476(10):433–441
6. Wei CC (2012) RBF neural networks combined with principal component analysis applied to quantitative precipitation forecast for a reservoir watershed during typhoon periods. *J Hydrometeorol* 13(2):722–734
7. Qian G-X, Cui D-W (2012) Application of RBF and GRNN neural network model in the municipal water demand forecasting. *Water Resour Power* 23(5):148–152
8. Xue X, Zhao D-M, Wang J-Y (2012) Wind power forecasting methods based on the combination of ARIMA and double BP neural network. *Electr Power Sci Eng* 28(12):51–52

Cascaded H-Bridge MV Grid and Power Balance Control for PV Systems

Bin Zhang, Zhiyun Bao, Donglai Zhang, Tiecei Li and Zicai Wang

Abstract In this paper, a new centralized cascaded H-bridge medium-voltage (MV) grid topology model based on the three-phase power system is established and presented, including its control strategy. The influence that the power supply imbalance between three phases which caused by PV array partial shading or module mismatch of Cascaded H-Bridge is analyzed as well, based on which the power balance control algorithm is put forward. Simulation and experimental results show that the algorithm is effective and reliable, it improves the conversion efficiency and grid-connected power quality, solves the key problem of cascaded H-bridge topology used in three-phase system, provides a theoretical basis for the development of new high-power photovoltaic grid-connected inverter.

Keywords Photovoltaic grid · Medium-voltage grid · Cascade H-bridge · Three phases imbalance · Power compensation

B. Zhang (✉) · Z. Bao · T. Li · Z. Wang
Harbin Institute of Technology, Harbin, China
e-mail: zhangbin.right@163.com

T. Li
e-mail: litiecei@hit.edu.cn

Z. Wang
e-mail: wangzicai@hit.edu.cn

B. Zhang
Shenzhen Academy of Aerospace Technology, Shenzhen, China

Z. Bao
ShenZhen Polytechnic, Shenzhen, China
e-mail: baozhiyun@yahoo.com.cn

D. Zhang
Harbin Institute of Technology Shenzhen Graduate School, Shenzhen, China
e-mail: zhangdonglai@263.net

1 Introduction

At present, along with the falling cost resulted by technology development, the subsidy for photovoltaic power generation will be less and less. After grid parity, the photovoltaic industry will face greater development as well as more challenges. In 2012, globally, new installed capacity was roughly flat with 2011. The converter market capacity had been up to 5.9 billion dollar on a global scale. From 2012 to 2015, the global market capacity will accumulate up to 26 billion dollar. The inverter manufacturers will benefit more from Chinese market [1–4].

Now, the centralized topology and multistring topology are two main topologies of large-scale PV plants [5, 6]. The centralized topology reaches required voltage and power level via photovoltaic modules connected in series and parallel and a plurality of converters connected in parallel work to meet the power capacity of plant's requirement. This kind of model has the advantage of simple structure and algorithm as well as low cost but it also has the defect that it has only one MPPT controller, which leads to low efficiency [7]. The multistring topology also adopts a centralized inverter grid, but it has a distributed DC-bus connected through a DC–DC converter. If isolation is provided at the AC side, high-frequency transformer is used, and if isolation is required at DC side, low-frequency transformer is used [8]. This topology is very flexible and compatible; it decouples the control between grid and DC-bus, allows independent MPPT control of each string and improves the conversion efficiency of the equipment. The main disadvantage is the higher cost and topology complexity of having additional power converters control systems and sensors [9].

Both configurations above commonly adopt double-level power grid structure, which will not be able to fulfill power rating, power quality, and efficiency requirements of the megawatt PV power station. In recent years, represented by three-level NPC and single-phase cascaded H-bridge inverter topology, the large-scale medium-voltage (MV) grid has been studied in depth [10–13].

Three-level NPC topology greatly improves the power rate of PV system. Yet, as with the traditional centralized topology, this topology requires too many series and parallel battery modules to reach required voltage and rated power [14, 15]. In order to improve its efficiency, DC–DC converters are needed, the number of modules in series needs to be reduced and the independent MPPT needs to be added [16, 17].

Through multistage tandem, the cascaded H-Bridge topology provides voltage rounds MV range, to realize that, several isolated DC modules are needed and each of which has independent MPPT therefore the efficiency of the system transformation is improved [18, 19]. At present, the topology is mainly applied to single-phase system. If it is introduced to three-phase system, the advantages predictable are as follows [20, 21]:

- The switching frequency can decrease manifold (at least three times) so that switching losses will greatly reduced.
- It allows independent MPPT control of PV modules of each H-Bridge, greatly increases the system efficiency.
- This system has unistucture power conversion module (H-bridge), which can eliminate DC–DC converter, reduce the system cost, increase efficiency and enhance system stability.

The output of system can reach the MV range. The grid-connected can be realized without boost transformer, which cuts down the cost further and improves converting efficiency of system.

2 Cascaded H-Bridge MV Grid Topology and Control

The cascaded H-bridge MV grid inverter topology presented in this paper is illustrated in Fig. 1, to reach different voltage range, each phase comprises several H Bridges (3 in Fig. 1) in three-phase power grid. Each H-Bridge is connected to a DC capacitor for storing energy of PV array, and a number of PV components are connected in series and parallel to reach the desired voltage and power.

Modulated using phase-shifted PWM (PS-PWM), each H-bridge itself can produce 2 levels, in Fig. 1, 3 H bridges produce 7 levels totally. Considering isolation, it can be realized by adding low-frequency transformer (no boost, just 1:1). Figure 2 presents the overall control system proposed in this project.

As Fig. 2 shows, the voltage of three-phase power grid gets phase information θ by digital phase-locked loop. The d axis current i_{sd} and q axis current i_{sq} can be obtained from the three-phase current by park transform, error adjusted by the MPPT can output a desired d axis reference i_{sd}^* while the reference current of q axis is set as a fixed value, here i_{sq}^* is 0. The reference voltage of d axis and q axis can be got after three-phase electric current through PI controller. After unbalanced compensation, the 18 H-bridge PWM signal connect grid through PV inverter successfully.

3 PV Array Power Balance Control Algorithm

The circuit in Fig. 2 can be simplified as shown in Fig. 3. Where, v_{ca} , v_{cb} , v_{cc} and i_{ca} , i_{cb} , i_{cc} is the output voltage and current of each phase, respectively, represented by the pulse power. R_s and L_s are line impedance and filter inductance. v_{ca} , v_{cb} , v_{cc} is the grid voltage.

This paper presents a method used to determine whether the clock jitter existed and to extract the characteristics of the noise, based on the contour extraction of two-stage filter signal noise, and the basic process shown in Fig. 3.

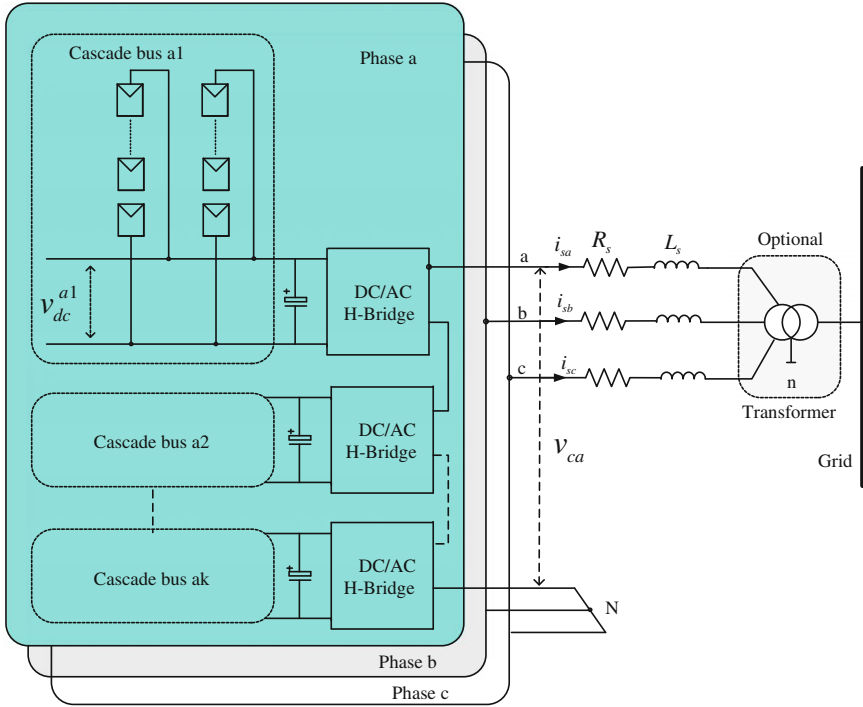


Fig. 1 The cascaded H-bridge MV grid-connected inverter topology

Equations can be listed as follows:

$$\begin{aligned}
 L_s \frac{di_{sa}}{dt} + R_s i_{sa} &= v_{ca} + v_{Nn} - v_{sa} \\
 L_s \frac{di_{sb}}{dt} + R_s i_{sb} &= v_{cb} + v_{Nn} - v_{sb} \\
 L_s \frac{di_{sc}}{dt} + R_s i_{sc} &= v_{cc} + v_{Nn} - v_{sc}
 \end{aligned} \tag{1}$$

where, v_{Nn} is the voltage difference between node N and n . Adding the three equations above can get following equation:

$$\begin{aligned}
 L_s \left(\frac{di_{sa}}{dt} + \frac{di_{sb}}{dt} + \frac{di_{sc}}{dt} \right) + R_s (i_{sa} + i_{sb} + i_{sc}) \\
 = (v_{ca} + v_{cb} + v_{cc}) + 3v_{Nn} - (v_{sa} + v_{sb} + v_{sc}).
 \end{aligned} \tag{2}$$

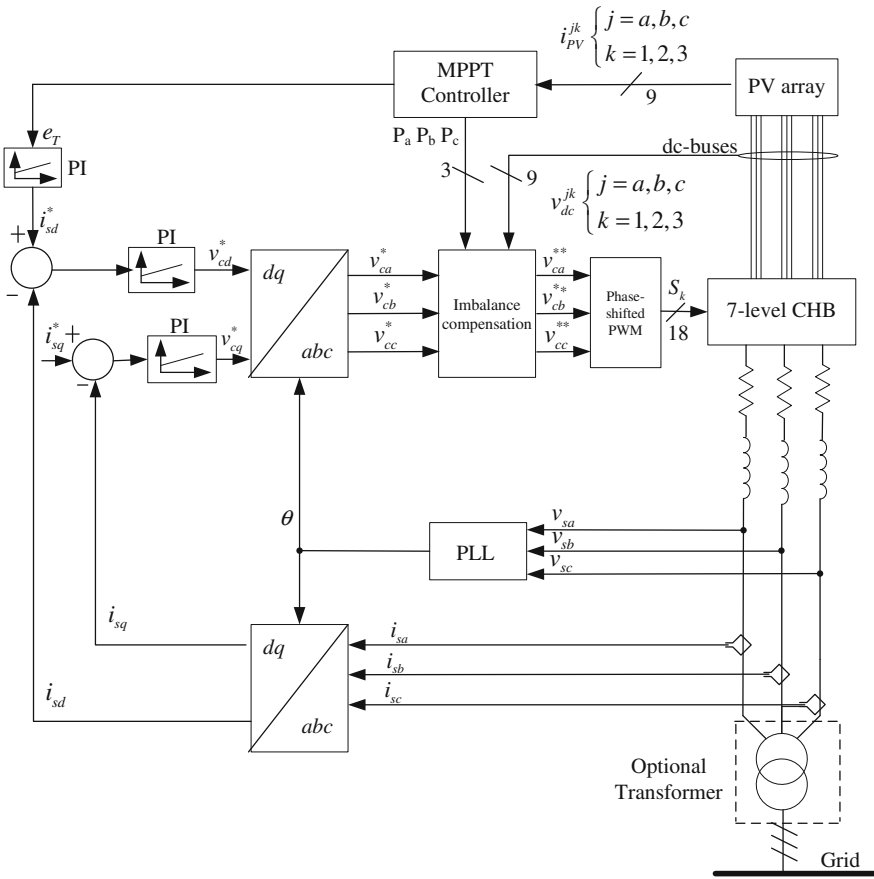
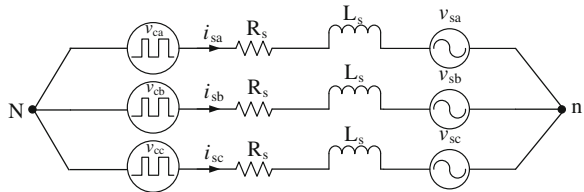


Fig. 2 The cascaded H-bridge MV grid-connected control strategy

Fig. 3 Simplified equivalent circuit of cascaded H-bridge grid topology



The KCL equation at the node N is:

$$i_{sa} + i_{sb} + i_{sc} = 0 \tag{3}$$

$$\frac{di_{sa}}{dt} + \frac{di_{sb}}{dt} + \frac{di_{sc}}{dt} = 0. \tag{4}$$

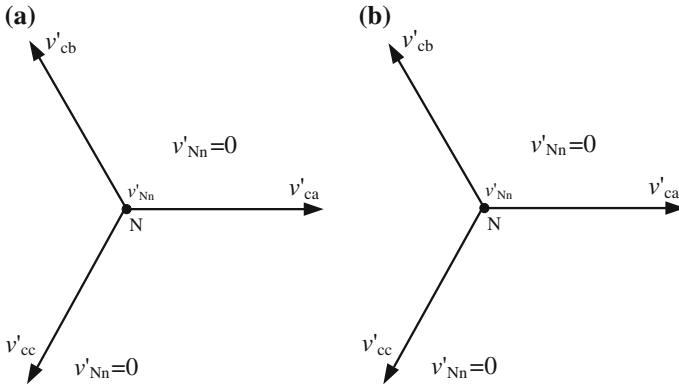


Fig. 4 Three-phase fundamental vector and v'_{Nn} : **a** balanced output, **b** unbalanced output

Supposing the three-phase voltage equilibrium, then:

$$v_{sa} + v_{sb} + v_{sc} = 0 \tag{5}$$

Simultaneous equations including (2–5)

$$v_{Nn} = -\frac{(v_{ca} + v_{cb} + v_{cc})}{3} \tag{6}$$

It can be seen that the voltage difference between node N and n is determined by the output voltage of three phase, no matter whether the output current is balanced or not. This suggests that the neutral point of the converter is adjustable. Meanwhile, the Eq. (1) reveals that v_{Nn} can affect the currents. This suggests that it is possible to redistribute the currents by adjust v_{Nn} .

Because of the existence of filter inductance L_s , only the fundamental component v'_{ca} , v'_{cb} and v'_{cc} of the equivalent pulse power supply v_{ca} , v_{cb} and v_{cc} are concerned. Supposing v'_{Nn} is the fundamental component of v_{Nn} . When three phases are balanced, three-phase output voltage vector can be expressed as shown in Fig. 4a. In Fig. 4b, assuming that the A phase output voltage decreases due to partial shading, at this point adding the same zero-sequence voltage v_o to three-phase output voltage, the fundamental component of new output voltage, v''_{ca} , v''_{cb} and v''_{cc} , can regain balance. It is said that this is a three-phase power redistribution structure in substance. Note that the fundamental component of this zero-sequence voltage v'_o must have the same frequency phase with the A phase.

A zero-sequence voltage algorithm is proposed in this project shown in Fig. 5. This algorithm can compute the weight of each power through monitoring the PV array output power, then weighted max–min sequence can be generated by the traditional max–min sequence adjustment algorithm, and achieve the purpose of adjustment in power of each phase.

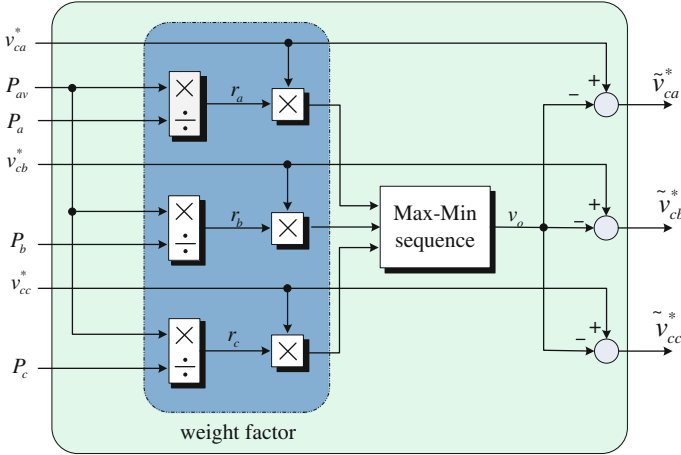


Fig. 5 Three-phase imbalance weighted max–min sequence algorithm

4 Simulation and Experiment

In this section, the simulation model in Fig. 4 is established. The control architecture is shown in Fig. 5. The design of grid voltage and total power is 3.3 kV and 1.5 MVA, respectively. Supposing that light intensity of PV array for A phase drops to 65 % of the origin at $t = 0.15$ s, but there is no imbalance compensation at this point, the inverter output voltage, current, and power are as shown in Fig. 8. The figure shows that output voltage and current of A phase drop as the sunshine intensity drops. And the grid current is imbalanced seriously, in addition, the output power of the other two phases oscillate frequently, which decreases system efficiency (Fig. 6).

Figure 7 shows the zero-sequence voltage v_o given by weighted max–min sequence algorithm. Once the light is imbalanced, fundamental component of v_o has the same frequency and phase with A phase. Output waveform of the inverter is illustrated in Fig. 8 when the weighted max–min sequence algorithm shown in Fig. 5 is adopted. Although the A phase output voltage falls and the three-phase output current overall decline, there is no unbalanced current. And the three-phase output power works more stable at the maximum power point. This method obviously improves the conversion efficiency.

For the cascaded H-bridge grid-connected PV topology proposed in this paper, a small-scale experiment platform has been established. The single-phase PV input voltage is 1000 V DC. Its grid-connected voltage is 380 V AC. Each phase contains 3 H bridges in series. There are 9 H bridges totally, which can produce a 7-level output, as shown in Fig. 9.

Using nine independent DC power supply acting as solar panels, under resistive load, 7-level inverter output voltage and current is illustrated in Fig. 10. It shows

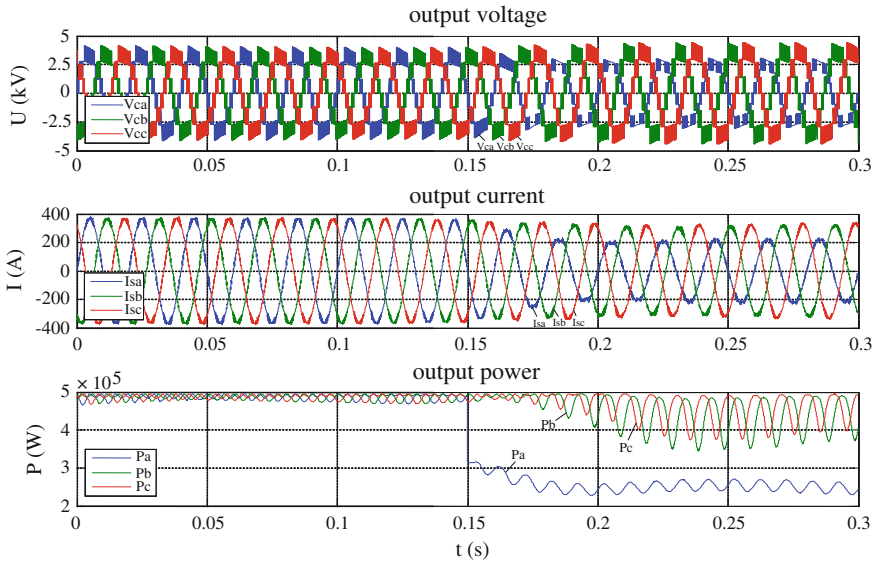


Fig. 6 The inverter output without imbalance compensation

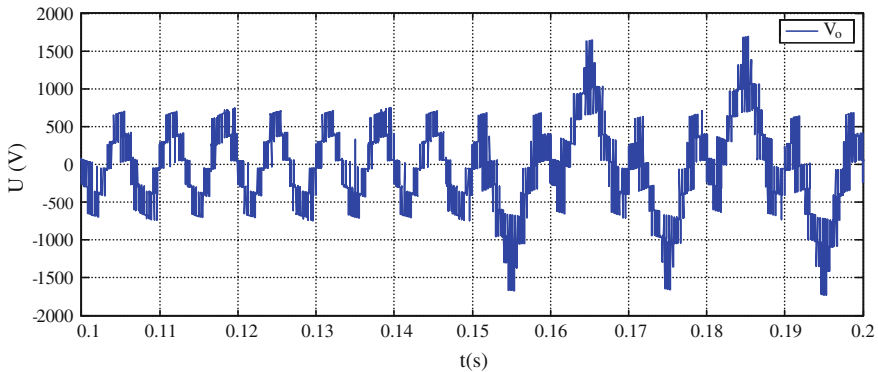


Fig. 7 Zero-sequence voltage given by weighted max–min sequence

that though the 9 H bridges have different inputs, that is there is imbalance between 3 phases, the 3-phase output current is balanced. So power redistribution has been accomplished.

Using nine independent DC power supply acting as solar panels, the experiments was carried out under conditions for different input power, just as Table 1 shows.

Figure 11 shows the 3-phase output current under grid-connected condition. Because that grid itself contains larger harmonic and that grid-connected current is smaller (The rated power is 20 kW, limited to the power of the solar simulator,

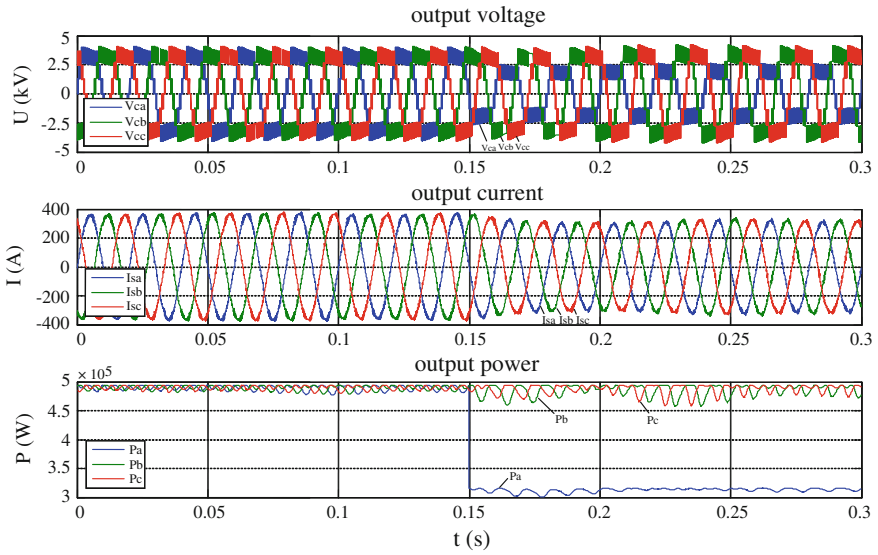
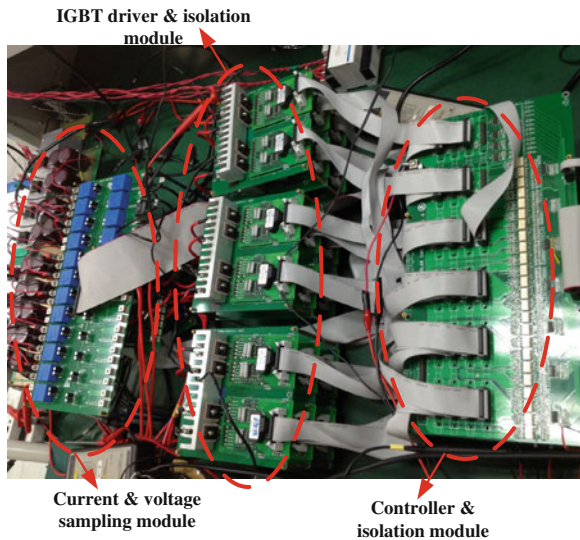


Fig. 8 The inverter output compensated by weighted max–min sequence

Fig. 9 Cascade H-bridge grid-connected PV inverter platform



actual power is 1.45 kW.), the output current harmonic increases steeply compared to the situation of under resistive load. At the same time, it is not difficult to see that the fundamental current of three-phase output still maintains a good balance. These verify the effectiveness of the proposed algorithm.

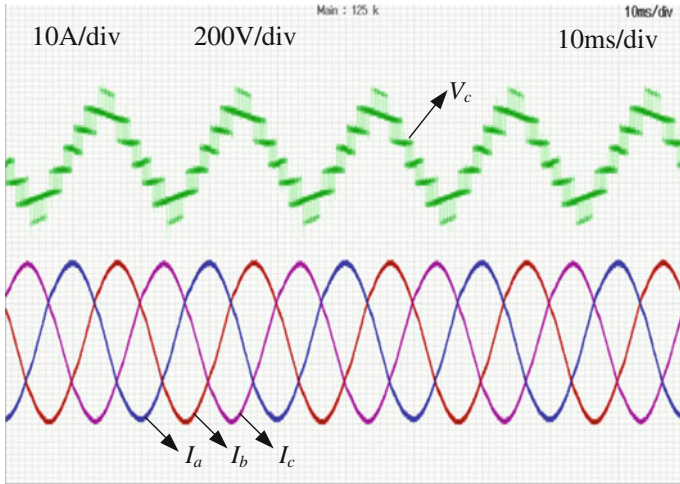


Fig. 10 Output voltage and current waveforms under resistive load

Table 1 Input power of H bridges for 3 phases

| | P_{CH1} (W) | P_{CH2} (W) | P_{CH3} (W) | P_{SUM} (W) |
|-----------|---------------|---------------|---------------|---------------|
| P_A (W) | 124.2833 | 152.37 | 161.8803 | 429.8525 |
| P_B (W) | 145.6822 | 163.7127 | 171.4073 | 492.8607 |
| P_C (W) | 159.887 | 176.778 | 190.9853 | 524.273 |

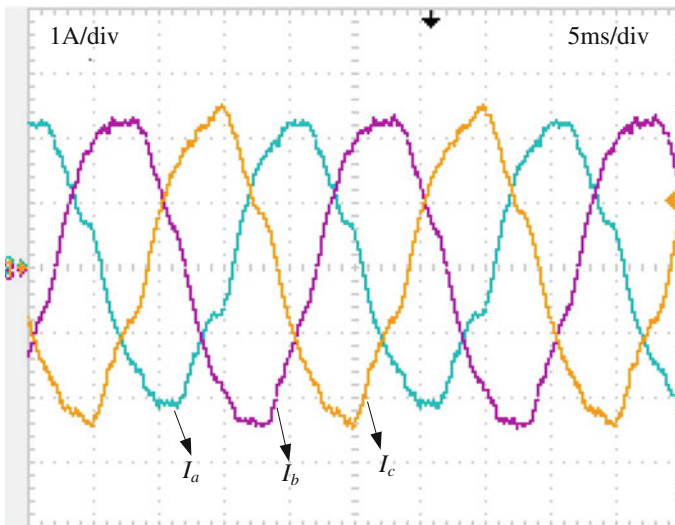


Fig. 11 Output current waveform under grid-connected condition

5 Conclusion

A new large-scale cascaded H-bridge PV MV grid-connected inverter technology is presented. It is based on three-phase power system. And the power balance control algorithm is put forward, which can effectively suppress the unbalanced effect caused by partial shading or module mismatch, improves the conversion efficiency and provides a theoretical basis for the development of new high-power photovoltaic grid-connected inverter.

Acknowledgments This article is supported by International Science and Technology Cooperation Program of China (2010DFB63050).

References

1. EPIA (2010) Global market outlook for photovoltaic until 2014
2. Zhao Z, Lei Y, He F et al (2011) Overview of large-scale grid-connected photovoltaic power plants. *Autom Electr Power Syst* 35(12):101–107
3. Zhang X, Cao R (2011) PV grid-connected power generating and inverter control. China Machine Press, Beijing
4. DG Joint Research Centre (2010) PV status report 2010. European commission
5. Blaabjerg F, Chen Z, Kjaer SB (2004) Power electronics as efficient interface in dispersed power generation systems. *IEEE Trans Power Electron* 19(5):1184–1194
6. Kjar S, Pedersen J, Blaabjerg F (2005) A review of single phase grid connected inverters for photovoltaic modules. *IEEE Trans Ind Appl* 41(5):1292–1306
7. Wasynczuk O, Anwah NA (1989) Modeling and dynamic performance of a self-commutated photovoltaic inverter system. *IEEE Power Eng Rev* 9(9):33–34
8. Meinhardt M, Cramer, G (2001) Multi-string-converter: the next step in evolution of string-converter technology. In: *Proceeding of European power electronics conference*
9. Edrington CS, Balathandayuthapani S, Cao J (2010) Analysis and control of a multi-string photovoltaic (PV) system interfaced with a utility grid. 2010 IEEE power and energy society general meeting, pp 1–6
10. Li M, Li G, Chang-rui LV et al (2011) Neutral point voltage balance control of multi-level grid-connected PV inverters. *East China Electr Power* 39(9):1395–1399
11. Zhao Z, Xu M, Chen Q et al (2012) Derivation, analysis, and implementation of a boost-buck converter-based high-efficiency PV inverter. *IEEE Trans Power Electron* 27(3):1304–1313
12. Liang Z, Guo R, Wang G et al (2010) A new wide input range high efficiency photovoltaic inverter. In: *Energy conversion congress and exposition*, pp 2937–2943
13. Ji B, Hong F, Zhao J (2012) A non-isolated three-level dual buck photovoltaic grid-connected inverter. *Proc CSEE* 32(12):7–13
14. Kouro S, Malinowski M, Gopakumar K et al (2010) Recent advances and industrial applications of multilevel converters. *IEEE Trans Ind Electron* 57(8):2553–2580
15. Zhang Y, Wang C (2012) Synthesis and optimization of SVPWM for three-level NPC PV Inverter. *J Power Supply* 40(2):72–75
16. Kouro S, Asfaw K, Goldman R et al (2010) NPC multilevel multistring topology for large scale grid connected photovoltaic systems. In: *IEEE international symposium on power electronics for distributed generation systems*, pp 400–405

17. Lin M, Kai S, Teodorescu R et al (2011) Comparison of the topologies of high efficiency neutral point clamping photovoltaic inverters. *Trans China Electrotechnical Soc* 26(2):108–114
18. Alonso O, Sanchis P, Gubia E et al (2003) Cascaded H-bridge multilevel converter for grid connected photovoltaic generators with independent maximum power point tracking of each solar array. In: *Power electronics specialist conference*, vol 2, pp 731–735
19. Kerekes T, Teodorescu R, Rodríguez P et al (2011) A new high-efficiency single-phase transformer less PV inverter topology. *IEEE Trans Ind Electron* 58(1):184–191
20. Villanueva E, Correa P, Rodríguez J et al (2009) Control of a single-phase cascaded H-bridge multilevel inverter for grid-connected photovoltaic systems. *IEEE Trans Ind Electron* 56(11):4399–4406
21. Negroni J, Guinjoan F, Meza C et al (2006) Energy-Sampled data modeling of a cascade H-bridge multilevel converter grid-connected PV systems. In: *International power electronics congress*, pp 1–6

Research of Automatic Scoring System of Ship Power Automation System

Wei Nie, Ying Wu and Dabin Hu

Abstract Because the training cost of ship power automation system is high and training security is difficult. Simulation system provides an efficient platform. Combined with the current operating of the simulation system and advanced methods and technology, this paper promotes a way to build the automatic scoring system and realize the scoring arithmetic. The practical needs of training evaluation of ship power automation system were analyzed. Functional requirements and working principle of automatic scoring system was introduced. Finally, the methods of system implementation are discussed.

Keywords Ship power automation system · Automatic scoring system · Simulation system · Scoring arithmetic

1 Introduction

When the real ship training can no longer meet the growing needs of seafarers, people was looking for more efficient, safe, and cost-effective training methods.

The ship power simulation system has realized that the students entering the cabin have the feel of presence, which established a virtual ship power automation system operation environment to make the operator operation with the real boat scene. Many countries [1, 2] have begun to carry out the research and production of the marine simulator. More simulation training system that is better and closer to the real ship is constantly being produced.

Automatic Scoring system is to use programming techniques to automatically assess operation ability of students through a predetermined algorithm, which is

W. Nie (✉) · Y. Wu · D. Hu
College of Naval Architecture and Power, Naval University of Engineering,
Wuhan 430033, China
e-mail: niewei213@163.com

based on expert knowledge and practical experience of technical personnel [3]. The scoring system could manage the training and examination process and analysis assessment identify the weak link of the trainers. It not only has improved the examination efficiency and fairness of the assessment, but also has saved a lot of funding. The scoring system has been applied to practical ship power simulation system and has received a good effect. This paper presents a method to build automatic scoring system for simulator training, which has been applied to simulation system training. The basic principles and main components have been discussed. The key technologies to achieve the system have been described.

2 The Introduction of Simulation System of Ship Power Automation System

Simulation system training is the products of modern science which achieve the purpose of training students.

In the traditional way of training and examination, the ability of students operation relies on the teachers' assessment. After students operate the devices, the teachers judge the level of operation, and finally give grades. Scoring system is to replace the role of coaches, and implements scoring method of coaches by a computer. Automatic scoring system combined with programming techniques and data analysis method to realize scoring.

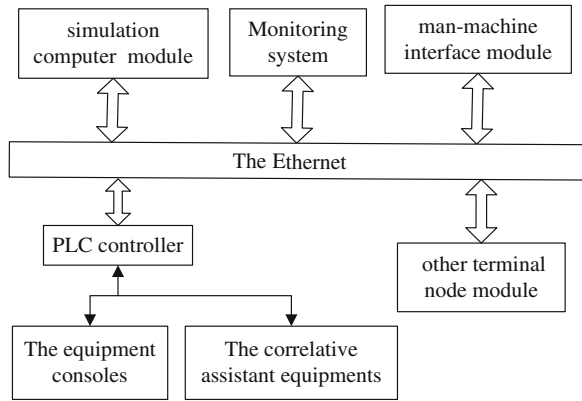
A ship power automation system consists of the simulation computer module, Monitoring system, the man-machine interface module, PLC controller, other terminal node module, and auxiliary support module [4]. All consoles of simulation system are consistent with the real ship, including the arrangement of equipments, the placement of the module, and the sounds of the simulation of real ship. Therefore, the students have a strong sense of reality.

The simulation computer module connected PLC controller with a TCP/IP protocol which form a star topology network structure. It ensure that the data and efficient real-time transfer. The simulation support platform [3–5] software was used for three functions, including the dynamic, steady-state simulation of the main equipment of the ship power system, the operation simulation of normal and fault conditions of the power system, and the data interconnection with other systems.

Monitoring software is similar to a bridge in the system's data flowing. It can exchange the data with other software and obtain the data recording the operation information of students from the consoles. PLC controller which connected to the hardware devices of the consoles communicates with simulation software through the monitoring software. So, PLC controller can timely transfer the state of switch and the button to monitor software.

The man-machine interface module of the simulation system is analog disc input capture and output effect. Although these devices cannot afford a key role, it

Fig. 1 The principle of simulation system of ship power automation system



is the guarantee that the logic of the system is running correctly. It provides a lot of hardware drivers to support external hardware device for read and write operations on the hardware. Figure 1 shows the principle of simulation system of ship power automation system.

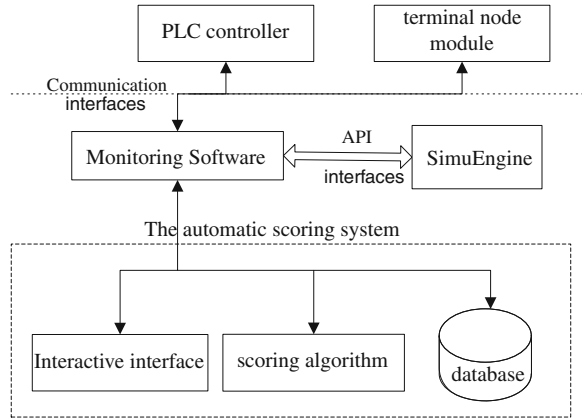
3 The Basic Principle and Function of Automatic Scoring System

Automatic scoring system is to use programming techniques to automatically assess operation ability of students. A good scoring system should be able to genuinely orient to the object of assessment tasks for training. The function of automatic scoring system of engineer training simulator is that evaluates the operation of the students and gives the results of the assessment after the students operated the test subjects. It can not only score the operation, but also can manage the appraisal process, analysis, and save the data in the examination process.

3.1 The Working Principle of Automatic Scoring System

The automatic scoring system mainly consists of interactive interface, scoring algorithm and the database. The main components of the database include the operation information of students, scoring criteria, and basic personal information and examination results. In examination, data information was recorded in the database by a fixed period. Scoring algorithm is to use programming techniques to automatically assess operation ability of students through, which is based on expert knowledge and practical experience of technical personnel that are restored in the database as the assessment standard.

Fig. 2 The main components and principles of the automatic scoring system



Monitoring software stored the data information of students' operation information in the database. Monitoring software realize the data interface between hardware and software. It can exchange the data with other software by API interfaces. It obtains the data recording the student's operation information from the consoles. In the process of general training [5, 6], the teacher makes the judgment to the student's operational level after the end of operation. The teacher's specialized knowledge and practical experience have played the decisive role in this process. It is an invisible criterion in the assessment process. Figure 2 shows the main components and principles of the automatic scoring system.

3.2 The Analysis of Functional Requirements

If engineer training simulator has not the automatic scoring system, the assessment of the operation of the candidates relies on teacher's judgments. Although the methods are very low efficiency and requirements for examiner are very high, it has accomplished three tasks [7].

- (1) Management of the appraisal process.
- (2) Control the operational status of the assessment.
- (3) To play a reasonable score for the operation of the candidates.
- (4) To analyze information and examination results of the appraisal process preserved.

So the automatic scoring system should contain those functions. At the same time, the development of scoring system is based on already mastered operation of the use of the power system simulator operating principle, and already knows the method of scoring algorithms and software implementations.

The software composition of ship power automation system generally can be divided into the testing soft of circuitry module and the simulation training system.

The testing soft of circuitry module is divided into function testing and fault testing, which mainly were used for the inspection and the possible fault detection of circuit module function of control system. The main role of simulation training system is to establish simulation model of control object, realize sound simulation, and examination scores. It consists of simulation software, control software, and sound simulation system and evaluation system.

4 The Scoring Algorithm and Soft Design

The scoring algorithm is an important work in the system design, and a reasonable and efficient scoring algorithm system is very important for the establishment of the automatic scoring system.

After analysis of a variety of methods, this paper used a more efficient algorithm, expert system combined with the analytic hierarchy. Through classifying the possible errors of students' operation, there can be established the math mode of evaluation.

4.1 Scoring Arithmetic

The expert system theory makes use of all aspects of specialist expertise and practical experience as the standard of the automatic scoring. By certain reasoning mechanism, the computer identify the current applicable knowledge from the initial facts, constitute a set of applicable knowledge, and then according to some conflict resolution strategies. By analyzing the recording data, the scoring system obtained operation time steps, instrumentation, and indicator of changes in the situation.

The basis of the automatic scoring system [8] is trainer's expert knowledge and the practical experiences, which are saved in the database by the rule form as the scoring criteria, taking the expert system theory as the instruction. The basic form of rule representation is as follows:

If P then Q

Where P is the premise of the rule, Q is the conclusion.

Simulator operation error can be divided into the following categories [9].

- (1) Significant operational error may endanger the safety of the ship personnel, to damage equipment, and result in significant security incidents.
- (2) Medium operational errors, will not endanger the safety of personnel, but may result in equipment damage and affect the normal operation of the ship.
- (3) General operation errors will not be harm for general equipment and personnel, but do not meet the correct operating procedures.



Fig. 3 The principles of data visit between the software

Analytic hierarchy was applied in training inspection of grading effectively and simple method. Analytic hierarchy made comprehensive evaluation to something using fuzzy mathematical tools. In automatic scoring system, factors set are the projects and subprojects that trainees have chosen, judgments can be set according to actual situation, and evaluation matrix is computed by a predetermined program algorithm. The weight vector of comprehensive evaluation can be carried out during operation of the system by appointed trainers, adjusting the weight value as the new default value which covers the original value.

4.2 The Realization of Automatic Scoring System

The technical problems of the system development process includes achieving students' operating data, data preprocessing, realizing scoring algorithm, a good man-machine interface development, and database issues.

The automatic scoring system has developed aim at the simulation training of ship power automation system. The simulation modeling software of simulation system is SimuEngine. KingView soft is monitoring software. Figure 3 shows the principles of data visit between the software.

The KingView soft can get the operation information of the console through the OPC protocol. SimuEngine gains the data message which needs from the KingView. By SQL function, the KingView visit the data information of automatic scoring system. Automatic scoring system feedbacks the data to the KingView after that the examination has been graded.

The design goal of automated scoring system software includes the following aspects.

- (1) Establishing evaluation mechanism of actual operation ability of Inspection personnel. According to evaluation mechanism, the system could give reasonable results of different aspects, such as proficiency, discharge fault of ability, and knowledge.
- (2) Conducting comprehensive records of the results of the assessment. Through the analysis of recorded data, it could master the evaluation of the learning situation.
- (3) Evaluation system can modify evaluation parameters, including the scoring rules and scoring parameters. The system can modify rules within the jurisdiction and set scoring parameter, such as the weight vector, etc.
- (4) According the projects that trainee chose, the automatic scoring system automatic scoring system gives a reasonable grading by the predetermined

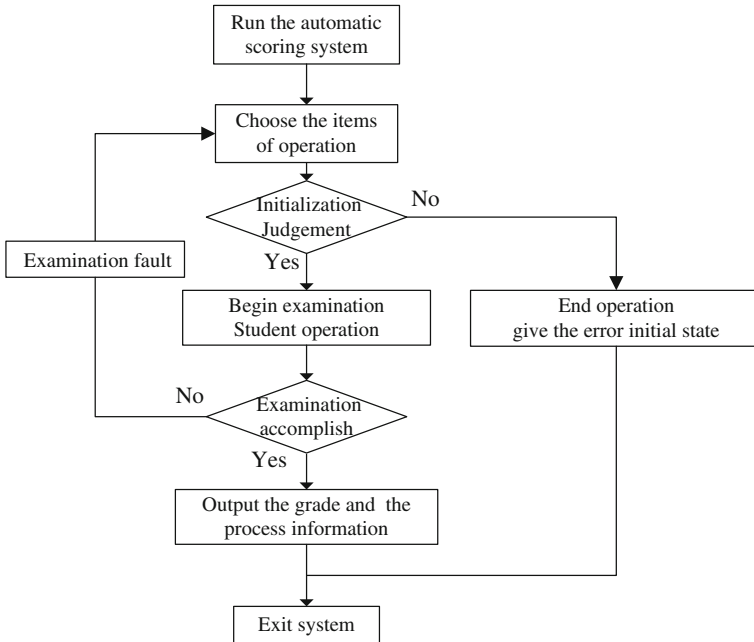


Fig. 4 The operation flow chart of automatic scoring system

algorithm. It can manage trainee’s basic information, to input and save the trainee’s profile, to call and display exam information, such as comprehensive results, operating procedures, error steps, and so on, to print and archive the error information.

Figure 4 shows the operation flow chart of automatic scoring system.

Through the operation of students, it is not only to find errors and defects of the system, but also adjust the distribution of weight coefficient to scoring algorithm, which makes the score of the results more credible. In the process of testing of simulation system, there was constantly revising rating system to make them work together closely.

5 Conclusion

Scoring system of ship power automation system is a great help for training and teaching. A design method of automatic scoring system and the solutions of the key technology were introduced. By Analyzing the recorded data, it can be known that the operator have operated the equipment steps in the evaluation process, which provide the basis for further assessment. After analysis of a variety of methods, this paper used a more efficient algorithm, expert system combined with

the analytic hierarchy, which is the basic of a reasonable and efficient scoring. The implementation method of automatic scoring system also was researched. In practice, it has achieved very good results.

References

1. Han NH, Wang S, Zhang HG, Li S, Li GL, Han X (2000) Maintainers oriented substation automation technique training system. *Autom Electr Power Syst* 02:88–90
2. National Institute of Standards and Technology (2004) Naval education and training PC modeling and simulation guidelines. National Institute of Standards and Technology, Pensacola
3. Bao GJ (2008) Research on the ship maneuvering evaluation system based on ship handling simulator. Dalian Maritime University, Dalian, pp 2–4
4. Nie W, Wu Y (2010) Study of automatic scoring system for simulation training. 2010 3rd international conference on advanced computer theory and engineering (ICATE), Cheng Du, pp 403–406
5. Zhao XT (2008) Improvement of automatic scoring of the power plant simulator training. *Autom Electr Power Syst* 18:74–75
6. Smierzchalski R (2008) Simulation system for marine engine control room. In: International Biennial Baltic Electronics Conference. IEEE, Tallinn Estonia, pp 978–981
7. Fang SY (2005) Application and development of substation training simulation system. *High Voltage Eng* 04:78–81
8. Kong QF, Shong JY, Zhang XD, Wu XX (2010) Technological condition and developmental trend of marine engine simulation training equipment. *Ship Sci Technol* 32:138–140
9. Kumar A, Choi SK, Goksel L (2011) Tolerance allocation of assemblies using fuzzy comprehensive evaluation and decision support process. *Int J Adv Manuf Technol* 55(1–4):379–391

Investigating Individual Driver Performance: Applying DEA on Simulator Data

Seddigheh Babaee, Yongjun Shen, Elke Hermans, Geert Wets and Tom Brijs

Abstract The main purpose of the present study is to investigate individual driver's behavior by using the data from a driving simulator, in order to distinguish the best drivers and identify the problematic behavior of “underperforming” drivers. To this end, 129 participants with different age and gender were enrolled to take part in a particular simulator scenario (i.e., curve taking) and their speed, acceleration, and lateral position, the three most important driving performance indicators based on literature review, were monitored at various points (before, during, and after the curve) while driving a STISIM simulator. As a widely accepted tool for performance monitoring, benchmarking, and policy analysis, the concept of composite indicators (CIs), i.e., combining single indicators into one index score, was employed, and the technique of data envelopment analysis—an optimization model for measuring the relative performance of a set of decision making units, or drivers in this study—was used for the index construction. Based on the results from the model, all drivers were ranked, and valuable insights were gained by comparing the relative performance of each driver. Finally, the sensitivity of the results was examined.

Keywords Data envelopment analysis · Composite indicators · Driver's relative performance · Driving simulator

S. Babaee (✉) · Y. Shen · E. Hermans · G. Wets · T. Brijs
Transportation Research Institute (IMOB), Hasselt University, Wetenschapspark 5 bus 6,
3590 Diepenbeek, Belgium
e-mail: seddigheh.babaee@uhasselt.be

Y. Shen
e-mail: yongjun.shen@uhasselt.be

E. Hermans
e-mail: elke.hermans@uhasselt.be

G. Wets
e-mail: geert.wets@uhasselt.be

T. Brijs
e-mail: tom.brijs@uhasselt.be

1 Introduction

Road safety continues to be one of the world's most serious public health issues. Although road safety actions taken so far have been effective, the number of road fatalities and casualties remain unacceptably high. Every year, the lives of almost 1.24 million people are cut short as a result of road traffic crashes, and around 20–50 million more people suffer non-fatal injuries, with many incurring a disability as a result of their injury [1]. Accordingly, the United Nations has declared the period 2011–2020 as the “Decade of Action for Road Safety”. The aim is to stabilize and then to reduce mortality caused by road crashes worldwide (http://www.who.int/roadsafety/decade_of_action/plan/en/).

To make progress on road safety, it is widely agreed that rather than focusing only on crash data, more policy attention should be paid to the underlying risk factors influencing safety, which can be classified as related to human, vehicle, road, and environment. As mentioned in a large number of in-depth accident investigation studies, inappropriate road user behavior is the major contributory factor in over 90 % and the sole cause in 57 % of all crashes [2, 3, 4]. Moreover, following from the modal split (and the majority of kilometers traveled by drivers), drivers represent a large share in the number of road fatalities (see Table 1) [5]. As a result, better understanding the behavior of different drivers is an essential component for future safety improvements on the roadways of the world.

Over the last decades, although numerous studies have been carried out with the purpose of investigating driver behavior on safety, there is limited research on individual driver risk in the traffic and human factor engineering field. This is an important gap because identifying and analyzing high-risk drivers will greatly benefit the development of proactive driver education programs and safety countermeasures. Therefore, the aim of this study is to evaluate relative performance of (car) drivers at the individual level, using data from a fixed-based driving simulator. The technique of data envelopment analysis (DEA) in general, and the multiple layer DEA-based composite index (CI) model in particular, are employed which to our knowledge is the first time that DEA is used for the evaluation of drivers' performance. The results will lead to distinguish the best drivers and advise some improvements to the underperforming drivers.

2 Methodology

Data Envelopment Analysis (DEA), originally developed by Charnes, Cooper, and Rhodes (CCR) in 1978 [6], is a non-parametric optimization technique that uses linear programming to measure the relative efficiency of a set of decision making units (DMUs), or drivers in this study. It has become an alternative and a complement to traditional central-tendency analyzes and has a number of advantages. As Golany and Roll [7] pointed out, DEA can be applied to: identify sources of

Table 1 Share of road fatalities by road user type and road category [24]

| Road user type | Rural (%) | Motorway (%) | Urban (%) | Total (%) |
|----------------|-----------|--------------|-----------|-----------|
| Driver | 69.10 | 61.07 | 50.47 | 61.31 |
| Pedestrian | 10.68 | 10.65 | 36.70 | 20.78 |
| Passenger | 20.16 | 28.22 | 12.81 | 17.87 |
| Unkown | 0.05 | 0.05 | 0.02 | 0.04 |

inefficiency, rank the DMUs, evaluate the effectiveness of programs or policies, and create a quantitative basis for reallocating.

In recent years, there has been an increasing interest in the application of DEA for composite indicator construction, in which single indicators are aggregated into one index score that provides comparisons of DMUs in complex and sometimes elusive policy issues. Since the first DEA-based CI proposed by Melyn and Moesen [8], various indexes have been developed by using the DEA technique. The environmental performance index [9], the human development index [10], the macro-economic performance index [11], the sustainable energy index [12], the internal market index [13], the technology achievement index [14], and the road safety performance index [15], are examples among others. Furthermore, as a valuable extension of the basic DEA-based CI model, Shen et al. [16, 17] proposed a generalized multiple layer DEA model (MLDEA) and a MLDEA-based CI model, which took the layered hierarchy of indicators into account.

More specifically, suppose that a set of n DMUs is to be evaluated in terms of s indicators (y) with a K layered hierarchy, the MLDEA-based CI model can be formulated as follows [16]:

$$\begin{aligned}
 CI_0 &= \max \sum_{f_1=1}^s \hat{u}_{f_1} y_{f_1 0} \\
 s.t. \quad & \sum_{f_1=1}^s \hat{u}_{f_1} y_{f_1 j} \leq 1, \quad j = 1, \dots, n \\
 & \sum_{f_1 \in A_{f_k}^{(k)}} \hat{u}_{f_1} / \sum_{f_1 \in A_{f_{k+1}}^{(k+1)}} \hat{u}_{f_1} = w_{f_k}^{(k)} \in \Theta, \quad f_k = 1, \dots, s^{(k)}, \quad k = 1, \dots, K - 1 \\
 & \hat{u}_{f_1} \geq 0, \quad f_1 = 1, \dots, s
 \end{aligned} \tag{1}$$

where $s^{(k)}$ is the number of categories in the k th layer ($k = 1, 2, \dots, K$). $s^{(1)} = s$.

$A_{f_k}^{(k)}$ denotes the set of indicators of the f th category in the k th layer.

$w_{f_k}^{(k)}$ denotes the internal weights associated with the indicators of the f th category in the k th layer, which sum up to one within a particular category. Θ denotes the restrictions imposed to the corresponding internal weights.

The main idea of this model is to first aggregate the values of the indicators within a particular category of a particular layer by the weighted sum approach in which the sum of the internal weights equals to one. With respect to the final layer, the weights for all the sub-indexes are determined using the basic DEA-based CI approach. In general, the model (1) reflects the layered hierarchy of the indicators by specifying the weights in each category of each layer. Meanwhile, by restricting the flexibility of these weights, denoted as Θ , consistency with prior knowledge and the obtainment of acceptable layer-specific weights are guaranteed, which cannot be realized in the one layer model. For the detailed deduction process of the model, we refer to Shen et al. [16, 17].

3 Indicators of Driving Behavior and Their Definition

In general, driving behavior is the vehicle control in longitudinal and transverse direction. According to the European “Safety Handbook in Secondary Roads” [18], the speed, acceleration, and lateral position are the three most common parameters to describe and analyze the behavior of a driver. These parameters are physical and geometrical values which can be measured or calculated.

3.1 Speed

The speed is the distance traveled divided by the time of travel. Basically, there are two different speeds: the speed which is only influenced by the traffic facility and the environment and the speed which is additionally influenced by traffic. To investigate the impacts of road geometry and environment, a speed which is not influenced by traffic should be considered. For this purpose, the spot speed can be used which is the speed in a defined spot at a defined time.

3.2 Acceleration

The acceleration is defined as the speed change within a time interval. Regarding the direction of acceleration, there is longitudinal and transverse acceleration. The longitudinal acceleration is a value of speed change and can be used, as well as the centrifugal acceleration, as comfort criterion which gives information about how fast a driver changes the speed or which curve speed is accepted.

3.3 Lateral Position

The lateral position is the position of the vehicle within a lane. It is a geometrical value which is, e.g., the distance between the center of the road and the vehicle's longitudinal axis. This indicator gives the possibility to analyze the driven track. Especially in curves the lateral position of cars is a perfect indicator to investigate corner cutting.

4 Data Collection and Analysis

This study aims to investigate the driving behavior of different drivers in and nearby a curve. Horizontal curves, particularly on two-lane rural roads, have been recognized as a significant safety issue for many years: crash rates are 1.5–4 times higher on horizontal curves than on straight road sections, and 25–30 % of all fatal accidents occur in curves [19].

In doing so, 129 drivers—aged between 18 and 54 years old—were enrolled to drive, using a fixed-based high-fidelity driving simulator (STISIM M400; Systems Technology Incorporated), in an existing stretch of two-lane rural road in Belgium with a left-oriented compound curve, preceded by a long tangent and characterized by complex geometrical alignment. Data on the three aforementioned driving performance indicators, i.e., speed, acceleration, and lateral position, are collected from the simulator.

4.1 Data Processing

Data analysis for these three indicators are based on values obtained at eight different measurement points along the driving scenario, i.e., P1 = 500, P2 = 166 and P3 = 50 m before curve, P4 = curve entry, P5 = middle curve, P6 = curve end, and P7 = 50, P8 = 100 m after curve, for each driver. Before using the raw data in the model, the following process was conducted for each point, separately.

4.1.1 Speed

Apart from the emergency services, nobody should drive faster than the legal speed limit. As a result, based on their driven speed, i.e., below or equal to 70 km/h on the one hand and above 70 km/h on the other. Next, by using hierarchical cluster analysis in SPSS, each group is further divided into several sub-groups. Finally, all the sub-groups were assigned ascending grades starting from 1, illustrating the degree of each driver's performance, so that the lower the grade, the better the

Table 2 The threshold of speed clusters at point 1 (500 m before the curve)

| Drivers driving with a speed ≤ 70 Km/h | | | Drivers driving with a speed >70 Km/h | | |
|---|--------------------|-------|---|--------------------|-------|
| Speed range | Nr. of drivers (%) | Grade | Speed range | Nr. of drivers (%) | Grade |
| (68.54, 70.00) | 35 (27.13%) | Nr. 1 | (70.53,77.47) | 43 (33.33%) | Nr. 4 |
| (64.66, 68.15) | 19 (14.73 %) | Nr. 2 | (77.58, 86.07) | 20 (15.50%) | Nr. 5 |
| (59.03, 61.59) | 8 (6.2 %) | Nr. 3 | (96.25, 106.00) | 4 (4.65%) | Nr. 6 |

Table 3 The threshold of acceleration clusters at point 4 (curve entry)

| Threshold for “Acceleration” in point 4 | | |
|---|--------------------|--------|
| Acceleration range | Nr. of drivers (%) | Grades |
| (0.273, 0.736) | 43 (33.33%) | Nr. 1 |
| (0.751, 0.920) | 36 (27.91%) | Nr. 2 |
| (0.936, 1.126) | 24 (18.60%) | Nr. 3 |
| (1.151, 2.439) | 26 (20.16%) | Nr. 4 |

Table 4 The threshold of lateral position clusters

| Threshold for “Lateral Position” | | Grades |
|--|--|--------|
| $1.3 \leq LP \leq 1.5$ | | Nr. 1 |
| $0.95 < LP < 1.3$ or $1.5 < LP < 1.85$ | | Nr. 2 |
| $LP \leq 0.95$ or $LP \geq 1.85$ | | Nr. 3 |

performance. This process is carried out in each of the eight points, respectively. Table 2 shows the results of clusters at point 1 (500 m before the curve) given the posted speed limit of the road in the simulated and real environment of 70 km/h, all the drivers are first divided into two groups.

4.1.2 Acceleration

Like speed, the hierarchical cluster analysis is applied on the acceleration data at different points. As a result, each group is allocated a grade indicating its performance. Table 3 shows an example of grading at point 4 (curve entry).

4.1.3 Lateral Position

Since the road width in the simulator scenario is 2.8 m, based on the average passenger car dimension, drivers are assigned a grade according to Table 4. A score of 1 indicates best performance because he/she drives in almost the middle of the lane, while a score of 3 is given to the worst performers because they pass either the center-line or edge-line of the road. Finally, drivers not belonging to these two groups are assigned a score of 2.

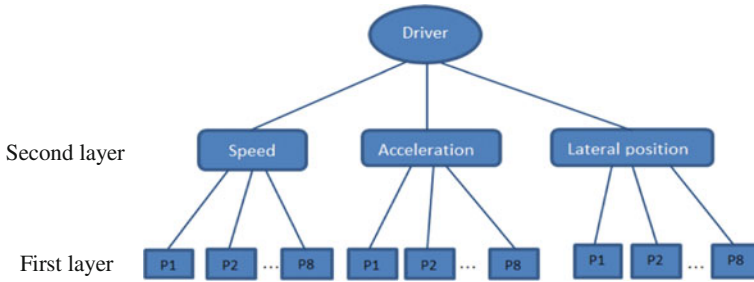


Fig. 1 Hierarchically structured driving behavior indicators

4.2 Model Preparation

In this study, the MLDEA-based CI model is applied to evaluate the driving performance of each of the 129 drivers by taking into account all the 24 hierarchically structured indicators (see Fig. 1). In doing so, the model (1) is restructured by minimizing the resulting index score,¹ subject to the condition that the set of weights obtained in this manner for each driver must also be feasible for all the other drivers included in the calculation.

With respect to the weight restrictions, for the first layer, the driving performance during the curve is considered to be more important than before or after the curve. Therefore, a relative weight restriction is given ensuring that the indicators in and during the curve, i.e., at points P4, P5, and P6, receive a higher weight than the other points. Regarding the second layer, to guarantee that all the three indicators of driver behavior—speed, acceleration, and lateral position—will be used to some extent by the model, the share of each of these three factors in the final index score is restricted to be equal with 30 % variability, which thereby lies between $0.233(= 1/3 \times 0.7)$ and $0.433(= 1/3 \times 1.3)$, respectively, as lower and upper bound, yet is rather broad to allow a high level of flexibility.

5 Results

5.1 Index Scores and Drivers Ranking

By the application of the MLDEA-based CI model, 24 driver performance indicators are now combined into a composite index score for each driver by selecting the best possible indicator weights under the imposed restrictions. As a result, the

¹ Remember that the raw data have been transformed on an ordinal scale with 1 representing the best category.

Table 5 Drivers' ranking

| | | | | | | | | | | | |
|-----------------|----|----|-------|-------|-----|-------|-------|-------|-------|-------|-------|
| Driver's Nr. | 48 | 49 | 47 | 106 | ... | 95 | 21 | 74 | 84 | 28 | 63 |
| Index score | 1 | 1 | 1.003 | 1.019 | ... | 1.984 | 1.991 | 2.006 | 2.015 | 2.039 | 2.088 |

Table 6 Drivers categories

| Performance | Index score | Nr. of drivers each group | Percentage drivers (%) |
|-----------------|-------------|---------------------------|------------------------|
| High | 1 | 2 | 1.55 |
| Relatively high | (1, 1.25] | 45 | 34.88 |
| Medium | (1.25, 1.5] | 45 | 34.88 |
| Relatively low | (1.5, 1.75] | 19 | 14.74 |
| low | >1.75 | 18 | 13.95 |

index score of each driver is calculated in relation to all the other drivers. In case the lowest possible index value is equal to 1, a best performer is identified. Underperforming drivers will obtain an index value larger than 1. Apart from identifying the best performing and underperforming drivers, it is possible to rank them based on their calculated index scores (see Table 5).

Moreover, Table 6 shows the categorization of the drivers into five groups based on their index scores. Drivers with index score larger than 1.25, typically should receive additional training or performance review by supervisors. Furthermore, it is possible to help each driver to improve his/her performance by means of training in the aspect of the most problematic parameter.

5.2 Comparison of Drivers in Terms of Driving Performance Indicators

In order to make comparison between best performing and underperforming drivers, their performance in each aspect is depicted in the following sections.

5.2.1 Speed

Speed is at the core of the road safety problem. Very strong relationships have been established between speed, crash risk, and severity. In fact, speed is involved in all accidents: no speed, no accident. In around 30 % of the fatal accidents, speed is an essential contributory factor [20]. At a higher speed, it is more difficult to react in time and prevent an accident. Figure 2 shows the speed of best performer versus two worst performers. The two underperforming drivers are

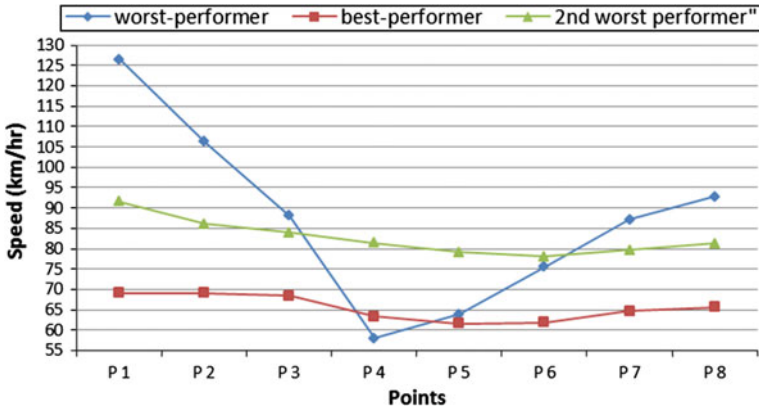


Fig. 2 The speed of the best performer versus two worst performing drivers

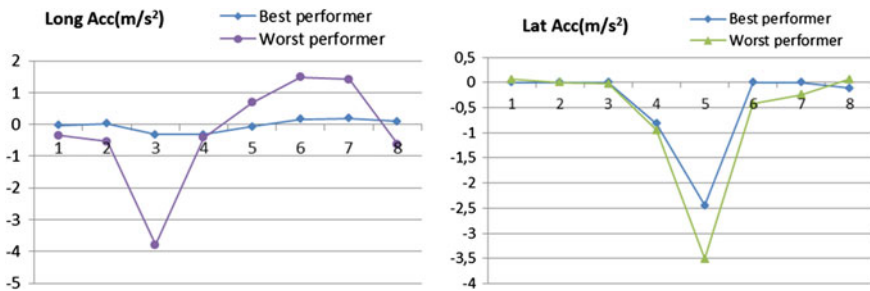


Fig. 3 The acceleration of the best performer versus the worst performer

distinguished as worst performer either because of their high speed or evasive changes during curve. The best performer, on the contrary, drives smoothly below posted speed limit.

5.2.2 Acceleration

The total acceleration can be decomposed into longitudinal acceleration and lateral acceleration. The longitudinal acceleration, indicating how fast a driver changes her/his speed, is shown in the left-hand side of Fig. 3. According to Lamm and Chouriri [21], the observed deceleration rates when approaching horizontal curves should not be significantly different from -0.85 m/s^2 . Even though others [22] proposed higher acceptable values between -1.34 and -1.8 m/s^2 it can be seen that the worst-performer exceeded dramatically the maximum threshold when approaching and leaving the curve. On the other hand, the lateral acceleration—indicative of how fast a driver changes her/his direction, shown in the right-hand side of Fig. 3—confirms inappropriate driving behavior of the worst performer.

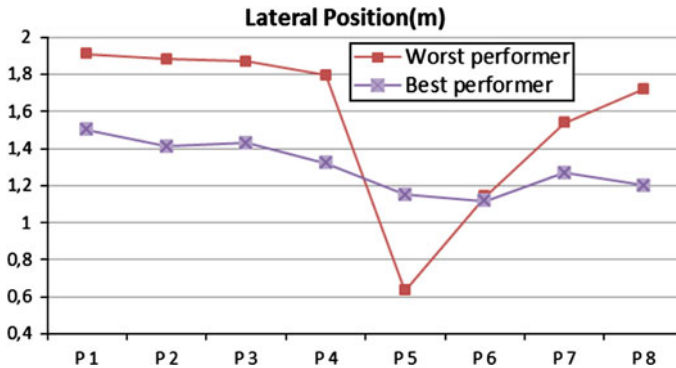


Fig. 4 The lateral position of the best performer versus the worst performer

5.2.3 Lateral Position

When driving, it is commonly accepted that the higher the variability in the lateral position of a vehicle, lesser the safety of driver [23]. By comparing the performance of the best performer and the worst performer with respect to their lateral positions in this experiment shown in Fig. 4, it is easy to see that the worst performer was involved in more dangerous situation. However, according to the threshold of lateral position indicated in Table 4, it should be noted that although the best performer in this experiment was doing obviously better than the worst one, he was still not doing perfect, especially when he was entering and leaving the curve.

6 Sensitivity Analysis

It is important to rigorously investigate the robustness of the indexes or the stability in the output (i.e., drivers' ranking) given small changes in the indicator set. Hence, we considered following 8 scenarios: in scenario 1, the point 1 (500 m before curve) is excluded; in scenario 2, the point 2 (166 m before curve) is excluded, and so on. In each scenario, the index score of each driver was recalculated. The results for the 10-first and 10-last drivers in the ranking are presented in Fig. 5, which provide insight into the sensitivity of each driver's scores with respect to each scenario and indicate driver nr. 48 as a robust, overall best performing driver who obtains an index score of one in all the scenarios.

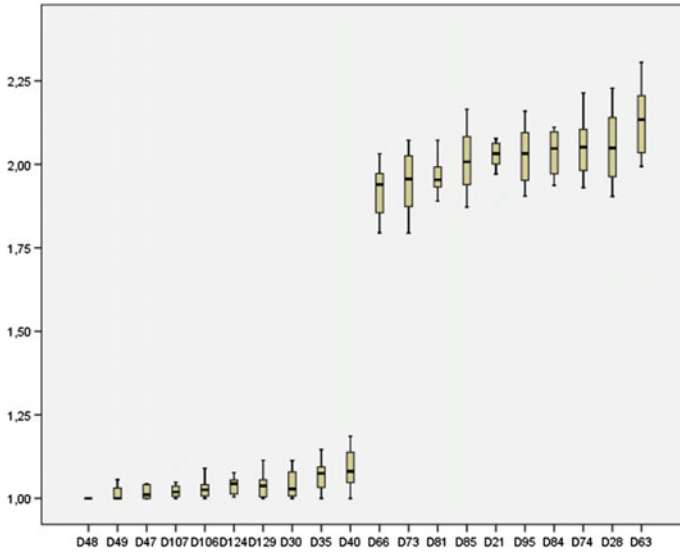


Fig. 5 Boxplot of drivers when eliminating indicators at one point at a time (10-first and 10-last drivers in the ranking)

7 Conclusion and Future Research

In order to measure the multi-dimensional concept of driving performance which cannot be captured by a single indicator at one point in time, we investigated in this study the construction of a composite driving performance index for driver’s evaluation. In doing so, a multiple layer DEA-based composite index model was applied on a hierarchy of driving performance indicators. Based on this model, the most optimal driving performance index score for each of the 129 drivers was determined by combining all the 24 hierarchical indicators. Apart from identifying the best performing and underperforming drivers, all drivers were ranked based on their calculated index scores, and their relative performance with respect to speed, acceleration, and lateral position was compared. In addition, robustness of the results was checked by means of sensitivity analysis. Based on the results, it would be useful to train particular drivers in different tasks in the simulator, according to each driver’s weakness.

Future research on the composite driving performance index can be done concerning the data, i.e., adjusting the model in order to allow the use of raw data instead of assigned grades to different indicator clusters. In addition, other road types or other sections of road (e.g., intersections) as well as roads with different speed limits may be considered.

References

1. Global plan for the decade of action for road safety. 2011–2020 http://www.who.int/roadsafety/decade_of_action/plan/en/. Accessed March. 23, 2013
2. Treat JR, Tumbas NS, McDonald ST, Shinar D, Hume RD, Mayer RE, Stanisfer RL, Castellani NJ (1977) Tri-level study of the causes of traffic accidents, report No. DOT-HS-034-3-535-77 (TAC)
3. Rumar K (1982) The human factor in road safety. Invited paper at 11th Australian Road Research Board Conference, Melbourne
4. Green M, Senders J (2004) Human error in road accidents, Visual Expert, Canada. <http://www.visualexpert.com/Resources/roadaccidents.html>
5. European road safety observatory (2006) <http://www.erso.eu>. Accessed 5 Mar 2007.
6. Charnes A, Cooper WW, Rhodes E (1978) Measuring the efficiency of decision making units. *Eur J Oper Res* 2:429–444
7. Golany B, Roll Y (1989) An application procedure for DEA. *Omega Int J Manage* 17:237–250
8. Melyn W, Moesen W (1991) Towards a synthetic indicator of macroeconomic performance: unequal weighting when limited information is available. In: Public Economics Research, paper 17 CES, KU Leuven
9. Färe R, Grosskopf S, Hernandez-Sancho F (2004) Environmental performance: an index number approach. *Resour Energy Econ* 26:343–352
10. Despotis DK (2005) A reassessment of the human development index via data envelopment analysis. *J Oper Res Soc* 56(8):969–980
11. Ramanathan R (2006) Evaluating the comparative performance of countries of Middle East and North Africa: a DEA application. *Socio-Econ Plan Sci* 40:156–167
12. Zhou P, Ang BW, Poh KL (2007) A mathematical programming approach to constructing composite indicators. *J Ecol Econ* 62:291–297
13. Cherchye L, Moesen W, Rogge N, Van Puyenbroeck T, Saisana M, Saltelli A, Liska R, Tarantola S (2008) Creating composite indicators with DEA and robustness analysis: the case of technology achievement index. *J Oper Res Soc* 59:239–251
14. Cooper WW, Seiford LM, Tone K (2000) Data envelopment analysis: a Comprehensive text with models, applications, references and DEA-solver software. Kluwer Academic Publishers, Dordrecht
15. Hermans E (2009) A methodology for developing a composite road safety performance index for cross-country comparison. PhD thesis, Hasselt university, Hasselt, Belgium
16. Shen Y, Hermans E, Brijs T, Wets G (2013) Data envelopment analysis for composite indicators: A multiple layer model. *Soc Indic Res.* 114(2):739–756
17. Shen Y, Hermans E, Ruan D, Wets G, Brijs T, Vanhoof K (2011) A generalized multiple layer data envelopment analysis model for hierarchical structure assessment: a case study in road safety performance evaluation. *Expert Syst Appl* 38(12):15262–15272
18. Gatti G, Polidori (Poliba) C, Galvez I, Mallschutzke (Ineco) K, Jorna R, Van de Leur (Mobycon) M, Dietze M, Ebersbach D, Lippold C, Schlag B, Weller (Tud) G, Wyczynski (Piap) A, Iman F, Aydin (TGDH) C (2007) Safety Handbook for Secondary Roads, Final Report Contract No. 508164, RIPCORD-ISEREST Deliverable D13
19. SafetyNet (2009a) Roads. Accessed 12 July 2011
20. SafetyNet (2009b) Speeding. Accessed 15 July 2010
21. Lamm R, Choueiri EM (1987) A design procedure to determine critical dissimilarities in horizontal alignment and enhance traffic safety by appropriate low-cost or high-cost projects. Natl Sci Found, Washington
22. Hu W, Donnel ET (2010) Models of acceleration and deceleration rates on a complex two-lane rural highway: Result from a nighttime driving experiment. *Transp Res Part F* 13(6):397–408

23. COST (1999) European co-operation in the field of scientific and technical research, research requirements for horizontal road marking, final report of the action, motorway road marking, EUR 18905, the European Communities, Parlement European Luxembourg, 1991
24. ERF European road statistic (2012). www.erf.be
25. Srinivasan R, Beak J, Carter D, Persaud B, Lyon C, Eccles K, Gross F, Lefler N (2009) Safety evaluation of improved curve delineation. Publication FHWA-HRT-09-045, US Department of Transportation.

Military Information System Access Control Architecture Based on SDO-ARBAC Model

Lin Sun, Yan Jin, Hao Liu and Fangsheng Li

Abstract Having reasonable military information system (MIS) access control architecture, is the important premise and foundation of its safe access. By describing the basic design of its access control architecture, in this paper, access control architecture center, hierarchical structure, and access control workflow of Security Domain Oriented-Administrative Role-Based Access Control (SDO-ARBAC) are discussed, SDLACA access control architecture based on SDO-ARBAC is put forward, which provides theoretical reference for bettering MIS access control architecture.

Keywords Security domain · Architecture centre · Access control · Domain management

1 Introduction

With wide military using of information technology, military information system (MIS) access control has become a key problem, which affects the whole command information system and its resource security, and its performance and application. Studying on the theory and technology of command information system access control, is of great realistic significance of advancing its healthy

L. Sun (✉) · Y. Jin

The Fourth Department, National Defense Information Academy, Wuhan, China
e-mail: lily_bril@163.com

H. Liu

Information Teaching and Research Section, Nanchang Military Academy, Nanchang, China

F. Li

Scientific Research Department, National Defense Information Academy, Wuhan, China

development and application, ensuring generating and strengthening of its supporting capability, and forming systematic operational capability based on information system. And bettering MIS access control architecture is the important part of realizing MIS cross-domain access control.

2 Basic Design of MIS Access Control Architecture

Military information system has distributed architecture and applications, distinctive characteristics of being open, autonomous and heterogeneous, strict security requirements, and a variety of access control requirements, which requires guidance, construction, implementation, and maintenance of MIS access control architecture. And its design should pay attention to meet the demands of autonomy, flexibility, dynamics, security, and scalability. SDIACA is a sound access control architecture.

2.1 Design Goals of SDIACA

SDIACA is a kind of MIS access control architecture based on the Security Domain Oriented-Administrative Role-Based Access Control (SDO-ARBAC) model. Security Domain Oriented-Administrative Role-Based Access Control model provides a comprehensive solution for MIS single-security domain or cross-domain resource access control. SDIACA main design goals are [1]:

- To provide ideas for comprehensive application of SDO-ARBAC Model.
- Taking a single SDO-ARBAC access control domain as a unit, to solve the access control problems of a single SDO-ARBAC access control domain in MIS.
- For comprehensive SDO-ARBAC access control domain, to solve cross-domain resource visit access control problems in MIS.
- By managing SDO-ARBAC access control domain, to solve the access control problems under the circumstance of user changing, authorization changing, dynamic access to or evacuation from security domain.

2.2 Design Thought of SDIACA

For MIS centralized applications, its access control architecture can be divided into three layers from top to bottom, respectively, as the presentation layer, functional layer, and data layer. The presentation layer is the client. The functional layer includes an application gateway composed by an access control conduction

Security Space

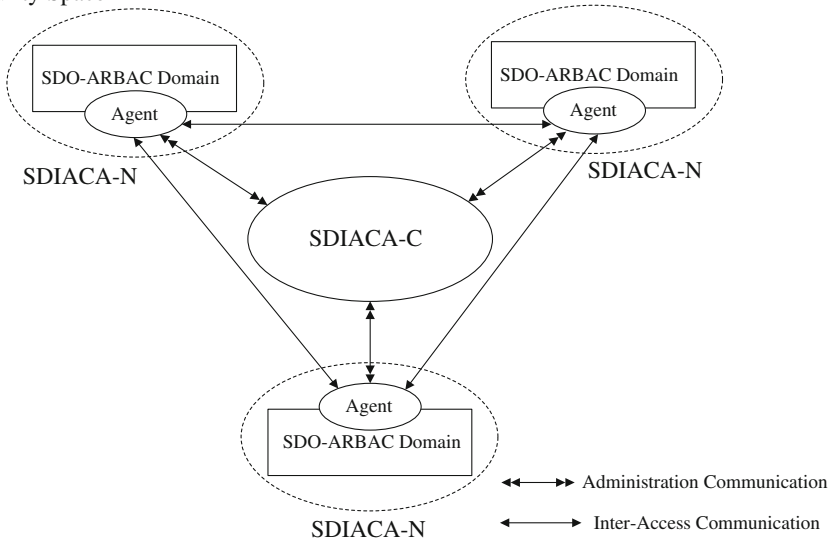


Fig. 1 The structure of SDIACA

function module Access Control Enforcement Function (AEF) and Access Control Decision Function (ADF) module. The data layer includes user/role databases and roles/license database.

SDIACA sets the Architecture Center SDIACA-C (C: Center) in security space SP. (The essence of SP is a kind of security domain whose level is higher than its subsafety domain, thus forming security domain level), and sets each security domain in SP as the architecture node SDIACA-N. Access control in each security domain is conducted by SDIACA-N using SDO-ARBAC model. Cross-domain access control is conducted by SDIACA-N of both visitor using SDO-ARBAC model and I-RMAMD algorithm jointly [1, 2].

2.3 Overall Structure of SDIACA

SDIACA is composed by the Architecture Center SDIACA-C and distributed architecture node SDIACA-N. Architecture Center SDIACA-C is responsible for management and maintenance of SDIACA. Architecture node SDIACA-N is composed by security strategy agent and SDO-ARBAC Domain.

The overall structure of SDIACA is shown in Fig. 1.

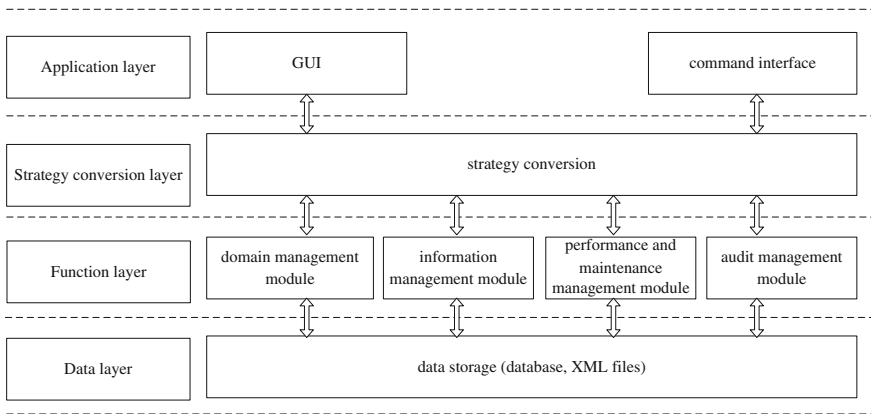


Fig. 2 Hierarchy structure of SDIACA-C

3 MIS Access Control Architecture Center

3.1 SDIACA-C Hierarchy

Architecture Center SDIACA-C is responsible for management and maintenance of SDIACA. And its hierarchy is shown in Fig. 2.

3.2 Application Layer of SDIACA-C

Application layer of SDIACA-C provides access interface to support SDIACA-C administrator's management and maintenance by access interface. Application layer should provide a graphical interface and a command interface. Graphical interface is used to support SDIACA-C administrator's domain management, system maintenance, and information inquiries via an interface (i.e., human-machine interface). Command interface plays a role of support and supplement for graphical interface, which is available for graphical interface's calling or direct input, and should be set aside part of the interface to support extension, system expansion and system interconnects.

3.3 Strategy Conversion Layer of SDIACA-C

Military Information System is an open and a heterogeneous application environment, in which security needs of each part are diverse and variable [3, 4]. It should adhere to the security policy as the core [3]. And by standardization and

verification of security policy, the security strategy of each part and the whole system can be in accordance with the security target. Whether it is a security policy specification based on XML description, semantic-based security policy specification, or the security policy described by proprietary security strategy specification used to support and conduct resource access and exchange visit, for the difference between policy implementation and policy syntax, in resource access communication, strategy conversion should be conducted to maximize the formation of a unified security policy that reduces the extent and likelihood of inconsistencies of data understanding, and reduces the potential resulting security risks. Strategy conversion layer should be set between the application layer and the functional layer to implement the security policy conversion between external communication data and function layer.

3.4 Function Layer of SDIACA-C

SDIACA-C functional layer is mainly composed by domain management module, information management module, operation and maintenance management module, and audit management module.

1. Domain management module: In SDIACA, SDO-ARBAC domain of each SDIACA-N should be registered in domain management module of SDIACA-C. After registration, domain management module provides a global identity or digital certificate issuance, query, change, destruction, and other services for each SDO-ARBAC, to ensure that each SDO-ARBAC domain has a unique legal identity in the safe space to be used for domain authentication, location, and so on.
2. Information management module: On the one hand, information management module can be used for centralized management and storage (actually stored in the data layer) of important information in other functional modules, to ensure the centralization and efficiency of information management, application, and storage. On the other hand, information of key personnel and core resources of all security domains in SP, such as classified staff, global identification of classified resource, and security classification of information, can all be stored and maintained by information management module.
3. Operation and maintenance management module: Operation and maintenance management module monitors SDIACA-C operation, and conduct SDIACA-C maintenance management using mechanism of detection, response, and feedback. Meanwhile, using centralized monitoring, it can cooperate with operation and maintenance management module of SDO-ARBAC in SDIACA-N, and conduct monitoring and maintenance management of each SDIACA-N, which ensures that operation of the overall architecture is safe and reliable.
4. Audit management module: On one hand, audit management module conducts security auditing and recording of operation in the SDIACA-C. On the other

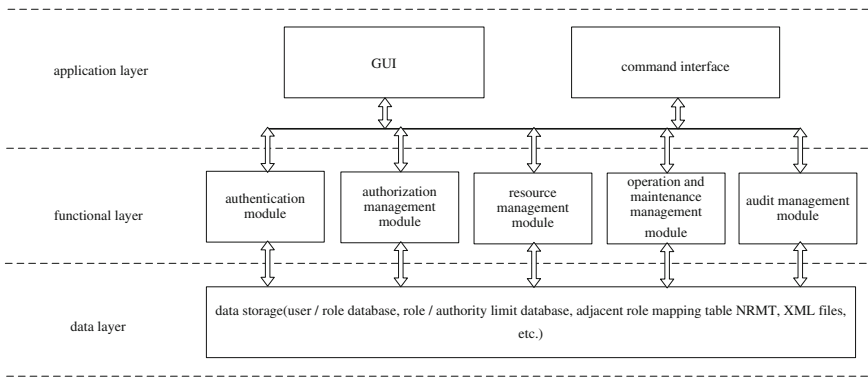


Fig. 3 Hierarchy structure of SDO-ARBAC domain

hand, it carries out save and backup of audit records and message authentication code of SDO-ARBAC domain uploaded by audit management module of SDO-ARBAC domain, and conducts centralized audit.

3.5 SDIACA-C Data Layer

Data layer is in the bottom of the SDIACA-C hierarchy, and plays a supporting role for the above-mentioned layers, especially for the functional layer. Using database or XML files, data layer can store the information and data of the above layers and the information and data relative with resource access, such as SDIACA-N basic information, operation and maintenance information, audit records, key personnel, and core resources, and the like.

4 Hierarchy of SDO-ARBAC Domain

Hierarchy of SDO-ARBAC domain mainly includes application layer, functional layer, and data layer, as shown in Fig. 3.

4.1 Application Layer of SDO-ARBAC Domain

Application layer of SDO-ARBAC domain should likewise provide a graphical interface and a command interface. Using graphical interface, the administrator of SDO-ARBAC domain carries out management and maintenance of the domain,

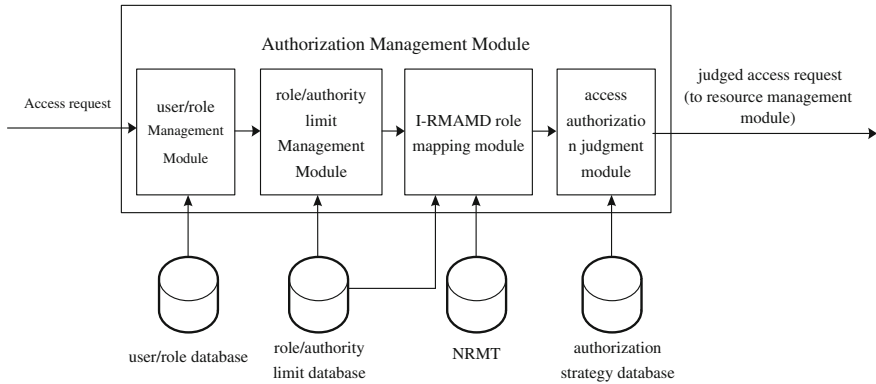


Fig. 4 Authorization management module

and checks system operation status, access to resources situation, and role mapping information. Command interface has the function of auxiliary, supplement, and perfection for graphical interface.

4.2 Functional Layer of SDO-ARBAC Domain

Functional layer of SDO-ARBAC domain is mainly composed by authentication module, authorization management module, resource management module, operation and maintenance management module, and audit management module.

Authentication module is responsible for user authentication, and should achieve the following specific functions: creating, modifying, deleting, and querying of a user, distribution, change, withdrawal and authentication of the user password, account number or digital certificates, strategic management of user password, account number, digital certificates, or bio-characteristics.

Authorization Management module is the core functional module of SDO-ARBAC domain. After authorization management module receives a request for access, it makes judgment of access requests, and sends the judged access request to the resource management module and operates accordingly. Authorization management module is shown in Fig. 4.

Resource management module is resource management agency of SDO-ARBAC domain. Receiving the access request sent by authorization management module, it carries out access operation for managed resource object according to the request, and has a result feedback after the operation. Result of the operation can return to the access control component AEC first, and then return to the user client via the AEC. And it can directly return to the user client, specifically determined by the system design.

Operation and maintenance management module is responsible for centralized maintenance and management of SDO-ARBAC domain, such as setting and

modifying of parameters and rule base, system performance testing, monitoring and maintenance of system operation, and the inspection, analysis, feedback, and exclusion of the system failure, and so on.

Audit Management module is responsible for detailed records of system operation and access to resources, and should have a good capability of record analysis and data mining. According to relative attribute filter events, it can provide it to the administrator in the form of reports to assist the administrator's carrying out query, statistics, and analysis of the system operations and resource access.

4.3 Data Layer of SDO-ARBAC Domain

Data layer of the SDO-ARBAC domain is responsible for information and data storage of the SDO-ARBAC domain. Stored information and data includes: user/role database, role/authority limit database, strategy database, rule base, adjacent role mapping table NRMT (including RNST and RPST), and XML documents.

5 Access control workflow of SDIACA

5.1 Access Control Workflow Within SDO-ARBAC Domain

Access control workflow within SDO-ARBAC domain is conducted by SDO-ARBAC access control system, whose access control workflow is shown in Fig. 5.

1. Access Control Workflow Among SDO-ARBAC Domains. Access control among SDO-ARBAC domains is jointly conducted by access control system of SDO-ARBAC and I-RMAMD algorithm. Its access control workflow is shown in Fig. 6. Both A domain and B domain are SDO-ARBAC access control domains.
2. Access Control Workflow Among Safe Spaces. A security policy set of a safe space is the subset of its internal security domain's security policy set. An entity set of a safe space is the union set of its internal security domain's entity set. When the user needs to carry out cross-safe-space access and the access frequency is reduced [5, 6], it can rely on the management agency of the SDO-ARBAC domain, which has access relationship in the two safe spaces. And access control of DO-ARBAC domain in the two spaces can be directly conducted. When the user needs to carry out cross-safe-space access and the access frequency is increased, safe space of SDIACA can be considered as an architecture node of a safe space with higher level. Relying on the managing agency of SDIACA-C, similar access control and its workflow can be conducted.

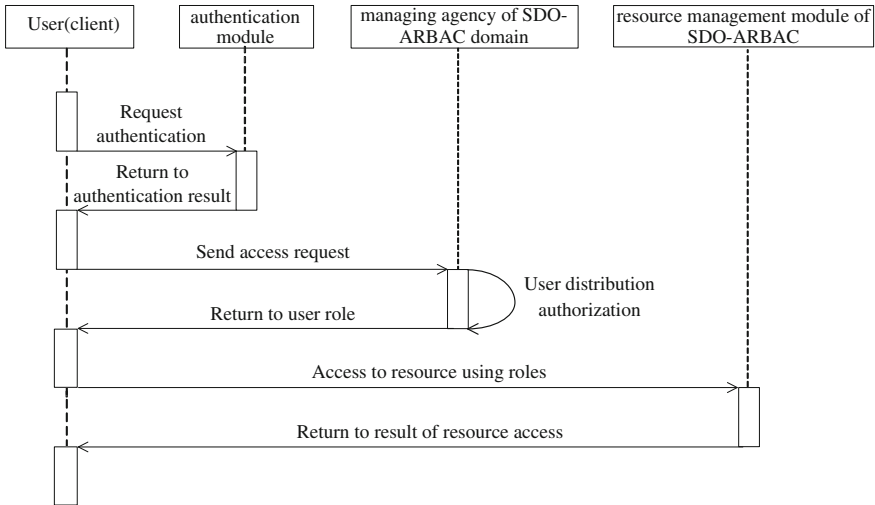


Fig. 5 Access control workflow within a SDO-ARBAC domain

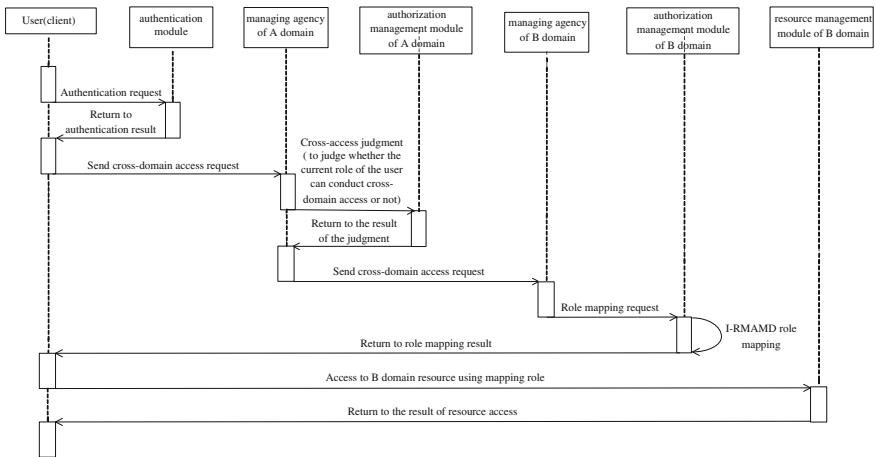


Fig. 6 Access control workflow between two inter-accessing SDO-ARBAC domains

6 Conclusion

SDIACA based on the SDO-ARBAC model is a kind of access control architecture suitable for MISs. By centralized and distributed domain management and operation and maintenance management, cross-domain access control, and safe system audit, it can provide a comprehensive solution for single-domain and cross-domain resource access control, which improves the security access control capabilities of MIS.

References

1. Dai J, Xiao J (2005) Expansion of military security model. *Intell Command Control Syst Simul Technol* 27(4):62–64
2. Pang Z (2008) SA-RBAC with its own authentication mechanism. *Dalian Technology University, Dalian*, vol 12, p 18
3. Wang Y, Hu G, Li J, Ma J, Li J (2008) Group-based access control method. *Mil Commun Technol* 29(3):35
4. Yang H (2011) Access control technology research. *Agric Library Inf Sci* 23(3):92
5. Zou X, Shen HH, Chen B (2009) Study on the method of cross-domain access control based on bidirectional Defense. *Acad exchanges* 10:20
6. Zhang L (2008) Study and application of task-based access control model. *North-China Electric Power University*, vol 12, p 5

Reliability Analysis of Driver Behaviour Under Effect of Head-up Display System: A Probabilistic Risk Assessment in Traffic Operation

Rongjie Lin, Hongfei Mu, Hongwei Guo and Wuhong Wang

Abstract This paper applies the driver behaviour and reliability theory to illustrate the real configuration of HUD-based driving models and the inherent mechanism for the HUD effect. The architecture of HUD-based driving behaviour is proposed and a methodology for HUD-based driving reliability analysis is presented. Then an algorithm for measuring reliability for both HUD-based driving and normal driving has been developed for understanding HUD-based driving error mechanisms. The emphasis of this paper is placed on the modelling of HUD-based driving reliability and the simulating of driving reliability by considering the influence of HUD-related factors.

Keywords Head-up display · Driving reliability · Traffic simulation

1 Introduction

As the number of vehicles grows, traffic accidents have long been a significant problem that has caused increasing concern [1]. The statistical data shows that 80 % of the traffic accidents occurred because of driver factor. According to the causation analysis for traffic accidents, among the accidents caused by drivers, 55–60 % accidents are caused due to the visual errors while 35–40 % accidents occurred because of the decision-making errors [2]. Consequently, it is vital to enhance the visual and decision-making stage to improve the driver safety. Previous relevant studies reveal that drivers mostly use (over 90 %) their vision in

R. Lin · H. Mu · H. Guo · W. Wang (✉)

Department of Transportation Engineering, Beijing Institute of Technology, Beijing, China
e-mail: wangwuhong@bit.edu.cn

obtaining related driving information [3]. Considering that visual errors are important causation among driver accidents, scientists are trying to explore methods to assist drivers to enhance the visual capability. The HUD system which is one aspect of driver assistance technology has gradually become a research focus.

2 Methodology

2.1 HUD-Based Driving Behaviour Analysis

2.1.1 Analysis of Factors Influence the HUD-Based Driving Reliability

When driving on the road environment with the help of HUD system, drivers constantly receive the information of the road environment, vehicle and HUD information presented and make decision and operate the steering wheel and brake to keep driving safe and stable. Because of the effect and limitation of the HUD characteristics, road environment, and some other factors, the driving reliability would decrease which may lead to traffic accidents. Regardless of the factors that are irrelevant to the HUD, the factors that will influence the driving reliability are concluded as follows: (1) Driver's acceptance and adaptation of HUD are needed to consider; (2) The complexity of the information drivers receive also has an influence on the driving reliability; (3) Optical angels, lighting outside the vehicle, brightness of the interface related to the HUD system will influence the driver's visibility about the information projected on the windshield; (4) The design of the interface of HUD will influence the assistance of the HUD.

2.1.2 HUD-Based Driving Behaviour Architecture

Head-up display system provides the advantages of keeping drivers' eyes near the road and of minimised focal reaccommodation time by displaying the information needed on the windshield in front of the driver. During the driving process, driver behaviour consists of information perception, information decision-making, execution in a loop.

The closed loop paradigm can be used to evaluate the internal element of HUD-based driver behaviour in connection with vehicles and environment (Fig. 1): Driver and HUD system can both perceive the information of the road environment and vehicle. The information processing is through driver perception, driver decision-making, and driver execution in the conventional driving. HUD system can identify the information and make decision for the driver besides the

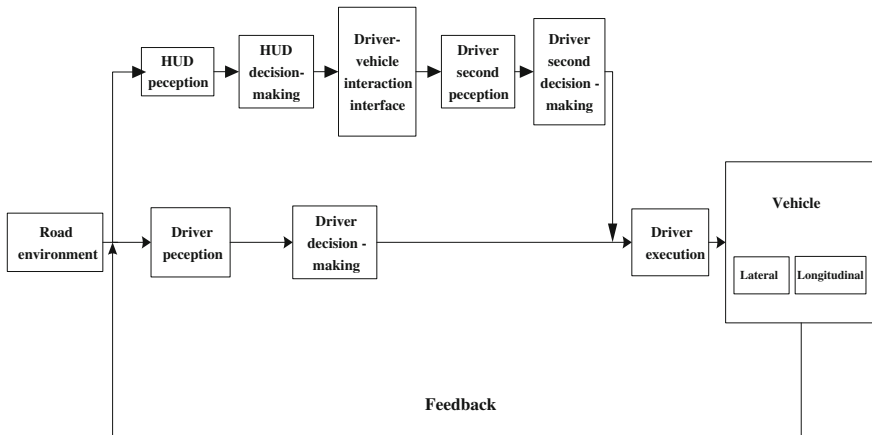


Fig. 1 HUD-based driving behaviour architecture

conventional information process. Then HUD can interact with driver through the driver-vehicle interface. HUD perception and HUD decision-making are assumed to be capable to substitute the driver perception and driver decision-making.

In order to understand the HUD-based driving reliability, we have defined seven terminologies as follows:

1. *HUD-based digital environment* It refers to the digital environment consisting of not only the head-up display, but also the other microelectronic systems equipped in the vehicle.
2. *HUD perception* HUD system can perceive the information of the road environment and the vehicle via the intelligent devices such as the sensors, GPS, and the Internet.
3. *HUD decision-making* HUD system can process the information perceived by the HUD perception stage by the microprocessor and intelligent algorithm and make decision to remind the driver how to do following.
4. *Cognitive capture effect factor* Cognitive capture effect factor refers to the factor involves in the HUD system that will affect the driver by aggravate the driving workload.
5. *HUD acceptance factors* It refers to the acceptance and adaptation of the HUD systems for drivers with different characteristics.
6. *Optical factor* It refers to the optical issues about the HUD system.
7. *Interface design factor* It refers to the quality of the HUD interface design.

2.2 HUD-Based Driving Reliability Analysis

2.2.1 Normal Driving Reliability

The theoretic driving reliability $R(t)$ without HUD can be given by:

$$R(t) = R_S(t) \cdot R_O(t) \cdot R_R(t) = [1 - F_S(t)] \cdot [1 - F_O(t)] \cdot [1 - F_R(t)] \quad (1)$$

where $R_S(t)$, $R_O(t)$, $R_R(t)$ are the theoretic reliability function of perception, decision-making, and execution stage respectively; $F_S(t)$, $F_O(t)$, $F_R(t)$ are corresponding probability functions of error in driving operations for three stages.

As there are many cases when drivers can prevent a traffic incident from becoming a traffic accident by their ability to recover from erroneous action (presented by r), regardless of the factors which are irrelevant to the HUD, normal driving reliability $R_{\text{driver}}(t)$ without HUD can be further written as:

$$R_{\text{driver}}(t) = 1 - (1 - r) \cdot \{1 - [1 - F_S(t)] \cdot [1 - F_O(t)] \cdot [1 - F_R(t)]\} \quad (2)$$

where r is recovery coefficient ranging from 0 to 1.

2.2.2 HUD System Reliability

As to the HUD system, which is independent of driver perception and driver decision-making, if disturbances are neglected, the system structure of HUD system is expressed as a series system with five series connected subsystems: HUD perception system, HUD decision-making system, driver-vehicle interaction interface system, driver second perception system, driver second decision-making system. According to the reliability of series system, the reliability of HUD system, $R_H(t)$, is written as:

$$R_H(t) = R_{HS}(t) \cdot R_{HO}(t) \cdot R_i(t) \cdot R_{S2} \cdot R_{O2} \quad (3)$$

where $R_{HS}(t)$, $R_{HO}(t)$, $R_i(t)$, R_{S2} , R_{O2} are the reliability function of HUD perception system, HUD decision-making system, driver-vehicle interaction interface system, driver second perception system, driver second decision-making system, respectively.

2.2.3 HUD-Based Driver Reliability

Considering that HUD system would cause cognitive capture effect, driver's response time and error will extend as the information increase to a certain extent. Moreover, there is the influence of HUD acceptance factor, optical factor, interface

design factor and driver recovery ability, the actual reliability of driver perception and driver decision-making $R_{SO}(t)$ can be given by:

$$R_{SO}(t) = 1 - g \cdot h \cdot i \cdot j \cdot (1 - r) \{1 - [1 - F_S(t)] \cdot [1 - F_O(t)]\} \tag{4}$$

where g is the measured value of the HUD acceptance factor, h is the measured value of the cognitive capture effect factor, i is the measured value of optical factor, j is the measured value of the interface design factor. According to Wang’s research, the parameter g, h, i, j , are supposed to range from 1 to 2.5.

The actual reliability of driver execution $R'_R(t)$ can be given by:

$$R'_R(t) = 1 - g \cdot h \cdot i \cdot j \cdot (1 - r) F_R(t). \tag{5}$$

Based on the analysis above, incorporated the actual reliability of driver perception and driver decision-making in Eq. (4) into the reliability of HUD system in Eq. (6), the HUD-based driving reliability is given as follows:

$$\begin{aligned} R_{HD}(t) &= R'_R(t) \cdot \{1 - [1 - R_H(t)] \cdot [1 - R_{SO}(t)]\} \\ &= [1 - g \cdot h \cdot i \cdot j \cdot (1 - r)(1 - R_R(t))] \cdot \{1 - g \cdot h \cdot i \cdot j \cdot (1 - r) \\ &\quad [1 - R_S(t) \cdot R_O(t)] \cdot [1 - R_H(t)]\}. \end{aligned}$$

In order to solve the reliability function as shown in Eq. (6), an important concept in reliability engineering is introduced as error rate or failure rate λ . The error rate is the probability that an item (e.g., driver, device) will fail in the time interval. The mathematical expression $R(t)$ of is:

$$R(t) = \exp\left(-\int_0^t \lambda(u)du\right). \tag{7}$$

Considering the effect of driving time on HUD-based driving shaping behaviour, and it is supposed that, let $\lambda_s(t), \lambda_o(t), \lambda_R(t)$ present the basic error rates of perception, decision-making, execution stage; let $\lambda_{Hs}(t), \lambda_{HO}(t), \lambda_I(t), \lambda_{S2}(t), \lambda_{O2}(t)$ be the error rate of HUD decision-making system, driver-vehicle interaction interface system, driver second perception system, driver second decision-making system. So HUD-based driving reliability at driving time t can be expressed as:

$$\begin{aligned} R_{HD}(t) &= R'_R(t) \cdot \{1 - [1 - R_H(t)] \cdot [1 - R_{SO}(t)]\} \\ &= \left[1 - g \cdot h \cdot i \cdot j \cdot (1 - r) \left(1 - \exp\left(-\int_0^t \lambda_R(u)du\right)\right)\right] \\ &\quad \left\{1 - g \cdot h \cdot i \cdot j \cdot (1 - r) \left[1 - \exp\left(-\int_0^t (\lambda_s(u) + \lambda_o(u))du\right)\right]\right\} \\ &\quad \left[1 - \exp\left(-\int_0^t (\lambda_{Hs}(u) + \lambda_{HO}(u) + \lambda_I(u) + \lambda_{S2}(u) + \lambda_{O2}(u))du\right)\right] \Bigg\}. \end{aligned} \tag{8}$$

A variable error rate function which can vary with time elapsed is supposed. A generalisation of the constant-error assumption is a two-parameter error function, which results in a Weibull distribution for the reliability analysis data. The error rate in this case allows for monotonically increasing or decreasing duration dependence and is given by:

$$\lambda(t) = \varphi\alpha(\varphi t)^{\alpha-1}, \quad \alpha > 0, \quad \varphi > 0. \quad (9)$$

3 Simulation and Analysis

3.1 Identification of the Parameters

To analyse the effect of HUD system, simulation of the driving reliability in normal environment and HUD-based digital environment was implemented. It is necessary to identify the parameters in the formula (3) and formula 8 before the simulation.

3.1.1 Value of g, h, i, j, r

The value of g is related to the driver and HUD characteristics. When the drivers' habit, interest can match with the HUD characteristics better, the value of g can be lower.

The value of g, h, i, j are supposed to vary within a range between 1 and 2.5. To measure the parameters more actually, the value of g, h, i, j can be divided as Table 1 according to the fuzzy theory.

The parameter r ranges from 0 to 1. Here it is supposed to be 0.77.

3.1.2 Identification of Variable Error Rate

Drivers could be approximated into three driving levels: skilled driver, average driver, unskilled driver, considering their own individual psychological characteristics. Here, error rates obey the Weibull distribution. Error rates of the three driving stages are obtained by means of statistical analysis, as given in Table 2. With the assistance of HUD perception and HUD decision-making, error rate of driver second perception and decision-making stage would be improved compared to the driver's common status. The error rate $\lambda_{S2}(t)$, $\lambda_{O2}(t)$ were supposed as Table 2.

Primary failure rates for $\lambda_{HS}(t)$, λ_{HO} , $\lambda_J(t)$ can be taken from corresponding reliability experiments and statistical analysis. They are supposed as

Table 1 Value of the parameter g, h, i, j based on fuzzy theory

| Parameter | Very good | Good | Bad | Very bad | Extremely bad |
|-----------|-----------|-------|------|----------|---------------|
| g | 1.0 | 1.375 | 1.75 | 2.125 | 2.5 |
| i | 1.0 | 1.375 | 1.75 | 2.125 | 2.5 |
| h | 1.0 | 1.375 | 1.75 | 2.125 | 2.5 |
| j | 1.0 | 1.375 | 1.75 | 2.125 | 2.5 |

$$\lambda_{H_s}(t) = 0.06 (0.03t)^{1.1}, \lambda_{H_O}(t) = 0.06(0.03t)^{1.1}, \lambda_1(t) = 0.025 (0.01t)^{1.5}.$$

3.2 Simulation Results

3.2.1 Driving Reliability Variation Under Effect of HUD

With the parameters described above, the numerical simulations of driving reliabilities under normal and HUD-based digital environment have been performed. To just illustrate the effect of HUD system, the parameter, g, h, i, j are ignored here. The simulation results via Matrix Laboratory software are presented in Fig. 2.

When the driving time is less than half an hour, the driving reliability is high and stable whether with the assistance of HUD or not. But, after half an hour of driving, the driving reliability without help of HUD decreases rapidly. With the assistance with HUD, the driving reliability varies more slowly and keeps more stable. The reliability values after four hours of driving in normal environment are 0.983, 0.970, 0.955 while the reliability values of HUD-based driving with variable error rate increase obviously to 0.998, 0.996, 0.992 which are all higher than the critical value 0.99.

3.2.2 Influence of g, h, i, j to the Driving Reliability

To analyse the influence of HUD-related factors g, h, i, j to the driving reliability, four situation of the HUD- related factors for the average driver are simulated: (a) all the factors are very good; (b) one of the factors is extremely bad while the others are very good; (c) two of the factors are extremely bad while the others are very good; (d) three of the factors are extremely bad while the other factor is very good. Simulation results are presented as Fig. 3. The values of driving reliability under four situations are respectively 0.996, 0.991, 0.978, 0.945. When more than two of the factors are extremely bad, the value of driving reliability will be lower than 0.99. Especially, the driving reliability decreases obviously if three of the factors are extremely bad.

Table 2 Error rate for different driver levels

| Error rate of different stages | Skilled driver | Average driver | Unskilled driver |
|--------------------------------|-------------------------------|--------------------------------|--------------------------------|
| Driver perception | 0.28 (0.1t) ^{1.8} | 0.3625 (0.125t) ^{1.9} | 0.45 (0.15t) ² |
| Driver decision-making | 0.004 (0.001t) ³ | 0.008 (0.002t) ³ | 0.012 (0.003t) ³ |
| Driver execution | 0.128 (0.04t) ^{2.2} | 0.1485 (0.045t) ^{2.3} | 0.187 (0.055t) ^{2.4} |
| Driver second perception | 0.203 (0.075t) ^{1.7} | 0.28 (0.1t) ^{1.8} | 0.3625 (0.125t) ^{1.9} |
| Driver second decision-making | 0.003 (0.001t) ² | 0.004 (0.002t) ² | 0.006 (0.003t) ² |

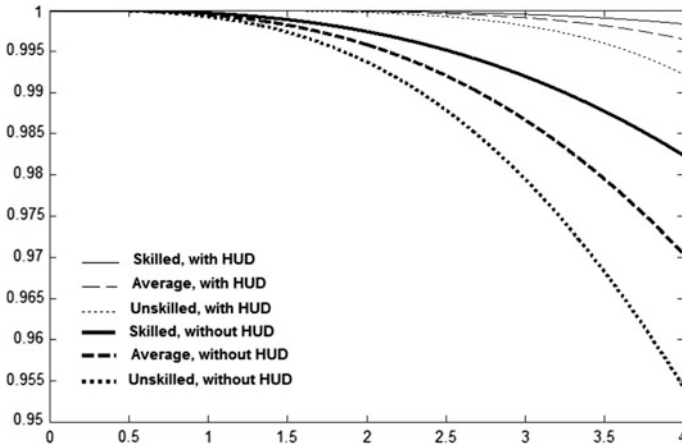


Fig. 2 Driving reliability under normal and HUD-based digital environment

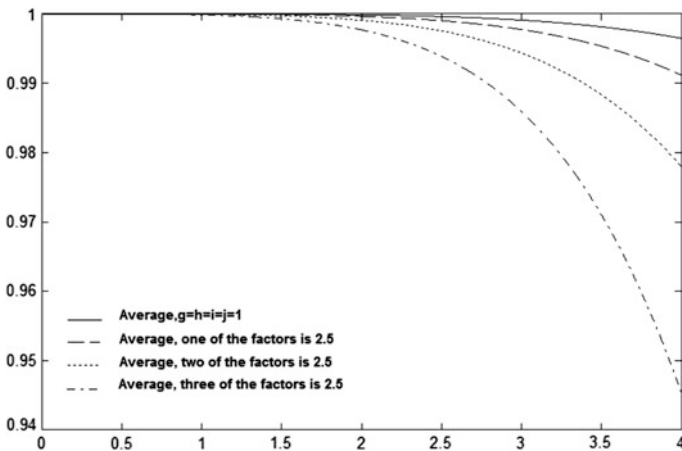


Fig. 3 Driving reliability under influence of g, h, i, j

4 Conclusions

As part of driver assistance system, HUD system can improve the performance and safety of driving, which is presented by the driving reliability analysis and simulation. The information needed by driver can be perceived and processed by the HUD system and projected on the windshield so that the driver perception and decision-making stage can be substituted by the system to certain extent. Accordingly, the higher reliability of such HUD-based digital system will play a more and more important role in driving safety. Meanwhile, it is found that the driver acceptance factor, cognitive capture factor, optical factor, and interface design factor will have influence on the driving safety and may even lead to traffic accidents. Although the results are obtained from assumed parameters, the methodology and theoretical framework in the work are accordance with the characteristic of HUD-based driving and normal driving. However, the approach for identifying and measuring the HUD-related factors is still needed specially to develop by using mathematics or statistics methods from empirical data.

Acknowledgment This research was supported in part by the National Nature Science Foundation of China under grant 51378062, 71301010 and the Introducing Talents of Discipline to Universities under grant B12022.

References

1. Clare K (2003) WHO acts on road safety to reverse accident trends. *The Lancet* 362(4):1125
2. Wang WH, Cao Q, Liu DM (1994) Analysis and assessment of driver's operation reliability. *Vehicle Eng* 16(4):207–213
3. Lansdown TC (1997) Visual allocation and the availability of driver information. In: Gothengater T, Carbonell E (eds) *Traffic and transport psychology: theory and application*. Pergamon, Amsterdam, pp 215–223

Personalized Recommendation Based on Weighted Sequence Similarity

Wei Song and Kai Yang

Abstract The sequential pattern mining-based recommendation has recently become a popular research topic in the field of recommender system. However, this kind of methods usually relies on frequency counts of sequences, which makes low-frequency sequences contribute little for the final recommend results. To solve this problem, in this paper, we propose a weighted sequence similarity-based method, called Personalized Recommendation based on Sequence Similarity (PRSS), for personalized recommendation. First, item-sequence weight model is introduced, which can reflect different importance of different items to different sequences. Then, target users' sequence is compared with historical sequences using similarity function. Finally, the maximal common subsequence is proposed to rank candidate sequences and make recommendation. Experimental results show that PRSS generates more accurate recommendation for the target users.

Keywords Recommender systems · Sequential pattern · Item-sequence weight · Similarity function · Maximal common subsequence

1 Introduction

A recommender system is a Web technology that suggests items of interest to users based on their objective behavior or their explicitly stated preferences [7]. Such systems typically provide the user with a list of recommended items they might prefer, or supply guesses of how much the user might prefer each item. These systems help users to decide on appropriate items, and ease the task of finding interesting items in the collection.

W. Song (✉) · K. Yang
College of Information Engineering, North China University of Technology,
Beijing 100144, China
e-mail: songwei@ncut.edu.cn

Content-based recommender systems try to recommend items similar to those a given user has liked in the past [1, 8]. Indeed, content-based recommender systems analyze item descriptions to identify items that are particular preferred by the user. User preferences can be captured using four types of data: demographic data, rating data, browsing pattern data, and transaction data. Transaction data provides sets of preferred items and can be used to predict future customer preferences. Therefore, some researchers applied the association rule mining technique to extract the accessing sequences to improve recommender system performance [4, 6]. However, such systems incorporate customer transaction data from only a single temporal period, which omits the dynamic nature of a customer's access sequences.

Unlike association rules, sequential patterns [2] may suggest that a user who accesses a new item in the current time period is likely to access another item in the next time period. Thus, sequential pattern mining techniques have been used for recommendation recently [3, 10]. However, there are two main drawbacks of the existing recommendation methods based on sequential pattern. On the one hand, only high-support sequential patterns are used for recommendation, but the simple frequency counts of patterns are not always effective. On the other hand, these methods usually treat all sequences as equally important. However, in real applications, sequential patterns often carry varying significance with respect to each target user.

In this paper, we study the problem of personalized recommendation from the perspective of different effects of different items to different sequences. To realize this target, the item-sequence weight model is introduced at first. Then, by representing sequences as vectors, different similarity functions are discussed. To reflect the alignment similarity of sequences, maximal common subsequence is proposed to rank candidate sequences and make recommendation. Experimental results show that the proposed Personalized Recommendation based on Sequence Similarity (PRSS) method outperforms related approach in terms of accuracy.

2 Related Work

Association rule is a widely used data mining technique that generates recommendations in recommender systems [4, 6]. More specifically, the method tries to discover the relationships between product items based on patterns of co-occurrence across customer transactions. These association rule-based methods are comprised of three steps: (1) Find an association between two sets of products in a transaction database; (2) The active customer's purchase behavior is compared with the discovered association rule base to find the most similar purchasing behaviors; (3) A set of products that the active customer is most likely to purchase is then generated by selecting the top-N most commonly purchased products. However, association rule mining does not take the time stamp into account. Thus, the association rule-based recommender system cannot reflect the dynamic nature of users' behavior.

Unlike association rules, sequential patterns [2] may suggest that a consumer who buys a new product in the current time period is likely to buy another product in the next time period. While association rule discovery covers only intra-transaction patterns (itemsets), sequential pattern mining also discovers inter-transaction patterns (sequences). In essence, frequent sequential pattern discovery can be thought of as association rule discovery over a temporal database. As association rules can be used for recommendation, sequential pattern mining-based recommendation algorithms have been studied for online product recommendation in recent years [10].

The sequential pattern mining-based recommendation is to induce a predictive model from a set of examples (i.e., the sequences in database). The usefulness of sequential pattern mining-based recommendation has, to a certain extent, been demonstrated empirically by past studies on various domains such as Web browsing [10], e-commerce [3], and music [5]. However, a significant shortcoming is that these methods do not perform user-specific sequential pattern mining and, as a result, they cannot give accurate personalized recommendation to users.

Recently, Yap et al. [9] proposed a personalized sequential pattern mining-based recommendation framework. A competence score measure, considering relevance to the target user, and the sequences' recommendation ability, is used for accurate personalized recommendation. Furthermore, additional sequence knowledge is exploited to improve the efficiency and the quality of learning in sequential pattern mining algorithms. However, their framework still depends on support threshold. Thus, if some sequences do not have enough supporting samples, they cannot be used for recommendation.

3 Problem Definition

Let $I = \{i_1, i_2, \dots, i_m\}$ be a finite set of *items*, set $X \subseteq I$ is called an *itemset*. A *sequence* α is denoted by $\langle X_1, X_2, \dots, X_m \rangle$, where X_j ($1 \leq j \leq m$) is an itemset. X_j is also called an *element* of the sequence, and denoted as (x_1, x_2, \dots, x_n) , where x_k ($1 \leq k \leq n$) is an item. Each itemset X_i comprises items with the same timestamp $t(X_i)$, and the different itemsets X_i and X_j in the same sequence cannot have the same timestamp, i.e., $t(X_i) \neq t(X_j)$ ($i \neq j$). The number of instances of items in a sequence is called the length of the sequence.

For example, a sequence $\langle (1, 4) (3) (2, 8) (1, 5) \rangle$ describes a user who accessed the items 1 and 4 at timestamp t_1 , item 3 at timestamp t_2 , items 2 and 8 at timestamp t_3 , and items 1 and 5 at timestamp t_4 .

A sequence database **SDB** is a collection of sequences, i.e., $\mathbf{SDB} = \{S_1, S_2, \dots, S_n\}$ where $|\mathbf{SDB}| = n$ denotes the number of sequences (also the number of users as each user has a corresponding sequence in **SDB**). A sequence $S_i \in \mathbf{SDB}$ ($i = 1, 2, \dots, n$) is a ordered list of itemsets associated with a user U_i .

Given a target user's past sequence S_q and the database of all other users' past sequences, the personalized sequence-based recommendation task is to predict items that the target user is most likely to access in the near future, i.e., those items in the next few item sets that he or she will access.

4 Personalized Sequence-Based Recommendation

4.1 The Item-Sequence Weight Model

In real applications, sequences often carry different significance with respect to each target user. To mine the personalized sequential patterns for a target user, we have to effectively model this varying relevance among the historical sequences for that specific user. Since each sequence in **SDB** belongs to a different user, we can set weights of sequences based on available knowledge on how relevant is each of the sequences compared to the known sequence of the target user. We solve this problem by considering items' appearance in different sequences.

Definition 1 Given sequence database **SDB** and an item b , $SS_b = \{S_i \mid b \in S_i \in \mathbf{SDB}\}$ is the set of sequences containing item b , then the *item-sequence weight* of item b with respect to sequence S_i is defined as:

$$w_{S_i}(b) = \frac{T_{S_i}(b)}{L(S_i)} \times \frac{|\mathbf{SDB}|}{|SS_b|} \quad (1)$$

where $T_{S_i}(b)$ is the number of occurrences of b in S_i ; $L(S_i)$ is the length of sequence S_i , i.e., number of total items in sequence S_i ; $|\mathbf{SDB}|$ and $|SS_b|$ are number of sequences in **SDB** and SS_b , respectively.

The above formula of item-sequence weight consists of two components. The one before sign of multiplication is measured for item b in a sequence S_i . On the contrary, the one after sign of multiplication shows the influence degree of the sequence containing item b within the whole database.

In this paper, the item-sequence weight of each pair of item and sequence is calculated and is used to measure whether an item occurs many times in certain sequences but with less influence to other sequences. The items with high item-sequence weight are considered with high probabilities of recommendation for sequences containing them.

4.2 Weighted Sequence Matching

Given item-sequence weight, we can transform each user's sequence S_i into a *sequence vector* \vec{v}_i , in which each dimension denotes the item-sequence weight of

a unique item. That is, a sequence vector \vec{v}_i is composed of the ordered item-sequence weights of items contained in sequence S_i .

Given a target user's sequence S_q and its sequence vector \vec{v}_q , for each S_i in sequence database **SDB** and its sequence vector \vec{v}_i , we can calculate the similarity between S_q and S_i using the following two functions.

1. Distance-based similarity.

$$\text{sim}(S_q, S_i) = \frac{1}{1 + \sqrt{\sum_{k=1}^m (x_{qk} - x_{ik})^2}} \tag{2}$$

where x_{qk} and x_{ik} are the k th dimension of sequence vectors \vec{v}_q and \vec{v}_i , respectively.

2. Cosine similarity.

$$\text{sim}(S_q, S_i) = \frac{\vec{v}_q \cdot \vec{v}_i}{|\vec{v}_q| |\vec{v}_i|} \tag{3}$$

Given a similarity threshold δ ($0 \leq \delta \leq 1$), only sequences with similarity no lower than δ are used for recommendation.

4.3 Computing Sequences for Recommendation

The two similarity measures discussed in Sect. 4.2 tend to reflect the content similarity rather than the alignment similarity. To compute a personalized score for each sequence S_i in the sequence database to reflect its competency in recommendation for the target user, we propose the following maximal common subsequence to rank the candidate sequences selected by distance-based similarity or cosine similarity.

Definition 2 Given a target user's sequence S_q and sequence S_i in sequence database **SDB**, if there are n common subsequences of S_q and S_i , the *maximal common subsequence* (MCS) of S_q and S_i is defined as:

$$\text{MCS}(S_q, S_i) = \frac{\max(L(\text{CS}_1), \dots, L(\text{CS}_n))}{L(S_q)} \tag{4}$$

where CS_i ($1 \leq i \leq n$) is the i th common subsequences of S_q and S_i , and $L(\text{CS}_i)$ is the length of sequence CS_i .

Compared with the two similarity measures discussed in Sect. 4.2, maximal common subsequence is not only compatible to the user sequence S_q , but also is capable of readily extending beyond S_q to offer more next-items. In this paper, within sequences selected by the similarity function, only the one with highest maximal common subsequence value is used for recommendation.

4.4 Algorithm Description

Based on the above discussion, the proposed PRSS is described in Algorithm 1.

| | |
|--------------------|---|
| Algorithm 1 | PRSS |
| Input | The target user's sequence S_q , SDB (a sequence database), similarity threshold δ |
| Output | The next item recommended to the target user |
| 1) | Compute the sequence vector of the target user's sequence S_q ; |
| 2) | for each sequence S in SDB do |
| 3) | Compute the sequence vector of S_i . |
| 4) | if $sim(S_q, S_i) < \delta$ do |
| 5) | continue ; |
| 6) | else |
| 7) | $S_i \rightarrow CS_q$; |
| 8) | Compute $MCS(S_q, S_i)$ using Eq. (4); |
| 9) | end else |
| 10) | end if |
| 11) | end for |
| 12) | Recommend the next item using the sequence in CS_q with highest MCS value. |

In Algorithm 1, item-sequence weights of items of the target user are calculated using Eq. (1) at first. Then, the target user's sequence is represented by vector composed of item-sequence weights. The similarities between target user sequence and sequences in SDB are computed in the main loop (steps 2–11). Those sequences with similarities higher than threshold are kept in the set CS_q (step 7), and the MCS values of them with the target user's sequence are recorded (step 8). Step 12 recommends to the target user with the sequence with maximal MCS value.

5 Experimental Evaluation

We present a two-part evaluation of our proposed PRSS. In Sect. 5.2, we compare the effectiveness of using different similarity measurements. In Sect. 5.3, we compare the effectiveness in terms of F1-measure of PRSS with the recommendation method (denoted by NRPS in this paper) proposed in [9].

The experiments were performed on a Pentium Dual E2140 1.60 GHz CPU with 2 GB memory, and running on Windows XP. We use the msnbc.com dataset from UCI (<http://www.ics.uci.edu/~mlearn>) for the performance evaluation. It captures the time-ordered sequence of Web pages visited by msnbc users on a day. There are a total of 989,818 sequences, each one corresponding to a different user. To evaluate the recommendation effect on sequences with different lengths, we divide the dataset into seven subsets: I: sequences with lengths in domain of (0, 35]; II: sequences with lengths in domain of (35, 45]; III: sequences with lengths in domain of (45, 55]; IV: sequences with lengths in domain of (55, 65]; V: sequences with lengths in domain of (65, 75]; VI: sequences with lengths in domain of (75, 85]; VII: sequences with lengths in domain of (85, 95].

5.1 Evaluation Measures

The F1-measure performance measure is considered in evaluating the effectiveness of the proposed method. The F1-measure measure is based on two performance measures precision and recall.

Precision is the fraction of recommended product items that are considered interesting, as defined in Eq. (5).

$$\text{precision} = \frac{\text{Number of correctly recommended items}}{\text{Number of recommended items}} \quad (5)$$

In contrast, *recall* is the ratio that the successfully recommended items to all of the accessed items, as defined in Eq. (6).

$$\text{recall} = \frac{\text{Number of correctly recommended items}}{\text{Number of accessed items}} \quad (6)$$

Precision measures how many of the recommended items belong to the actual customer access list, whereas recall measures how many of the items in the actual customer access list consist of recommended items. These measures are simple to compute and intuitively appealing, but they are in conflict, since increasing the size of the recommendation set leads to a decrease in precision but, at the same time, to an increase in recall. Hence, a widely used combination F1-measure Eq. (7), which gives equal weight to both recall and precision, was also employed in the course of our evaluation.

$$\text{F1-measure} = \frac{2 \times \text{precision} \times \text{recall}}{\text{precision} + \text{recall}} \quad (7)$$

5.2 Comparison on Different Similarity Functions

The objective of this experiment is to find a similarity function appropriate to the msnbc.com dataset. To do this, we used the two similarity functions (i.e., distance-based similarity, and cosine similarity) mentioned in Sect. 4.2, and compared the F1-measure. The comparison results are shown in Fig. 1.

For distance-based similarity, the trend of F1-measure is not steady, with the highest value 0.828 and the lowest value 0.381. For cosine similarity, F1-measure increases with the increases of sequences' lengths when sequences' lengths are no higher than 55, while it decreases with the increases of sequences' length when the sequences' lengths are in domain of (55, 75]. The best F1-measure was obtained when sequences' lengths are longer than 75. From the results, we can conclude that cosine similarity is more appropriate for msnbc.com dataset.

5.3 Accuracy Comparison

In this subsection, we compare the performance of the proposed PRSS with NRPS [9] with regard to F1-measure. As NRPS use high-support sequential patterns to recommend, in this set of experiments, minimum support threshold (denoted by min_sup) is also used besides the similarity threshold.

Figure 2 shows the F1-measure comparisons when $\delta = 90\%$ and $\text{min_sup} = 10\%$. Although the F1-measure of PRSS is lower than that of NRPS on dataset with sequences lengths no longer than 35, on average, the F1-measure of PRSS is 43% higher than that of NRPS.

Figure 3 shows the F1-measure comparisons when $\delta = 92\%$ and $\text{min_sup} = 30\%$. The result is almost the same as shown in Fig. 2. On average, the F1-measure of PRSS is 49% higher than that of NRPS.

6 Conclusions

We propose a personalized recommendation method by considering effects of different items for different sequences. Specifically, item-sequence weight model is introduced for representing importance of items and sequences at first. Then, different similarity functions are discussed for selecting appropriate sequences for recommendation. Finally, the maximal common subsequence is proposed for ranking candidate sequences and making recommendation. Compared with related sequence-based recommendation methods, the proposed PRSS method does not rely on support. Thus, some low-frequency important sequences will not be ignored. Experimental results show that PRSS method can achieve more accurate recommendation results.

Fig. 1 Comparison of F1-measure using different similarity function, $\delta = 90 \%$

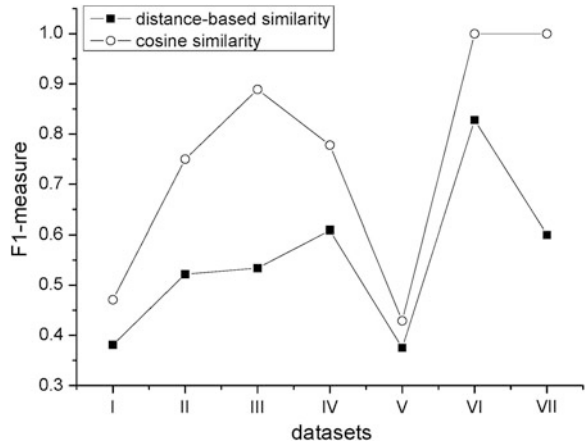


Fig. 2 Comparison of F1-measure between two approaches, $\delta = 90 \%$, $\text{min_sup} = 10 \%$

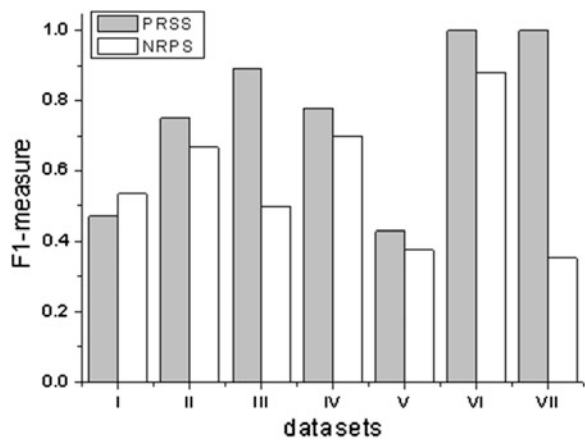
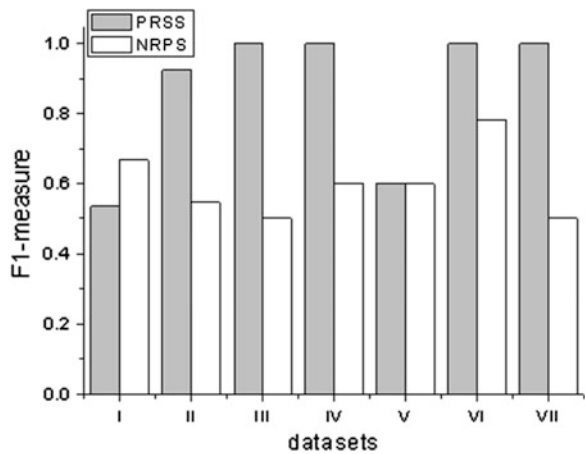


Fig. 3 Comparison of F1 between two approaches, $\delta = 92 \%$, $\text{min_sup} = 30 \%$



Acknowledgments The work is partly supported by the National Natural Science Foundation of China (61105045), Funding Project for Academic Human Resources Development in Institutions of Higher Learning under the Jurisdiction of Beijing Municipality (PHR201108057), Funding Project for Academic Human Resources Development of North China University of Technology (CCXZ201303), and key project of North China University of Technology.

References

1. Agarwal D, Chen B-C, Elango P, Ramakrishnan R (2013) Content recommendation on web portals. *Commun ACM* 56:92–101
2. Febrer-Hernández JK, Palancar JH (2012) Sequential pattern mining algorithms review. *Intell Data Anal* 16:451–466
3. Huang C-L, Huang W-L (2009) Handling sequential pattern decay: developing a two-stage collaborative recommender system. *Electron Commer R A* 8:117–129
4. Kazienko P, Pilarczyk M (2008) Hyperlink recommendation based on positive and negative association rules. *New Generation Comput* 26:227–244
5. Liu N-H (2013) Comparison of content-based music recommendation using different distance estimation methods. *Appl Intell* 38:160–174
6. Paranjape-Voditel P, Deshpande U (2013) A stock market portfolio recommender system based on association rule mining. *Appl Soft Comput* 13:1055–1063
7. Park DH, Kim HK, Choi IY, Kim JK (2012) A literature review and classification of recommender systems research. *Expert Syst Appl* 39:10059–10072
8. Pera MS, Ng Y-K (2013) A group recommender for movies based on content similarity and popularity. *Inf Process Manage* 49:673–687
9. Yap G-E, Li X-L, Yu PS (2012) Effective next-items recommendation via personalized sequential pattern mining. In: *Proceedings of 17th international conference on database systems for advanced applications*, pp 48–64
10. Zhou B, Hui SC, Fong ACM (2006) Efficient sequential access pattern mining for Web recommendations. *KES J* 10:155–168

Design and Analysis of DVMCK Transmission System

Liu Yang, Yanli Shang, Xiaoyu Yin and Guoxin Zheng

Abstract Differential very minimum chirp keying (DVMCK) as a novel high bandwidth efficiency modulation scheme is proposed. The DVMCK transmission system model is elaborated based on Simulink within MATLAB. The absolute code is converted to differential code for carrying out very minimum chirp keying (VMCK) modulation. The demodulation result is obtained by comparing with a pre-defined threshold. The final demodulation data stream of the VMCK transmission system shows the excellent performance in the simulation. The DVMCK transmission model is easy to implement and has strong properties to resist synchronization error.

Keywords VMCK · DVMCK · Modulation · Synchronization error · SER

1 Introduction

With the quick development of 4G technologies, the apparent contradiction between the information data rates and radio spectrum resources becomes increasingly outstanding. The improvement of the bandwidth efficiency is necessary and imperative [1, 2]. A series of higher bandwidth efficiency modulation schemes have been investigated in recent years. In 1997, the very minimum shift keying (VMSK) modulation with extremely high bandwidth efficiency was proposed by Walker [3]. In 2001, Sayhood and Wu proposed the very minimum

L. Yang (✉) · X. Yin · G. Zheng
Key Laboratory of Specialty Fiber Optics and Optical Access Networks, Shanghai
University, SHU, Shanghai China
e-mail: yangliu0806@126.com

Y. Shang
Information Management and Engineering Department, Hebei Finance University, HBCF,
Baoding Hebei China

waveform difference keying (VWVK) modulation in which the minimum different sinusoidal waves were used to modulate the binary information [4]. In 2007, Zheng came up with the very minimum chirp keying (VMCK) modulation in which the binary data was formed by raising or reducing the frequency in one-bit period [5]. Realization of UNB system based on FIR filter was proposed in [6]. The performance of UNB modulation based on VMCK in AWGN channel was analyzed in [7]. Feng et al. [8] presented BER analysis and verification of EBPSK system in AWGN channel. Zhang [9] assessed different ultra-narrow band formats. The digital impacting filters were described in [10]. In this paper, the differential very minimum chirp keying (DVMCK) modulation is proposed. The DVMCK transmission system model is elaborated based on Simulink within MATLAB, and the final demodulation data stream at the output of the DVMCK transmission system reveals the excellent performance.

The rest of the paper is organized as follows. Section 2 describes the expressions of VMCK modulated signals and the structure of the DVMCK transmission system. Section 3 presents the model of the DVMCK transmission system on Simulink platform within MATLAB, and discusses experimental configuration, data and simulation results for the DVMCK system. Finally, Sect. 4 summarizes the characteristics of the DVMCK signals and provides some interesting fields for further research.

2 Transmission Scheme

2.1 VMCK Modulation Signals

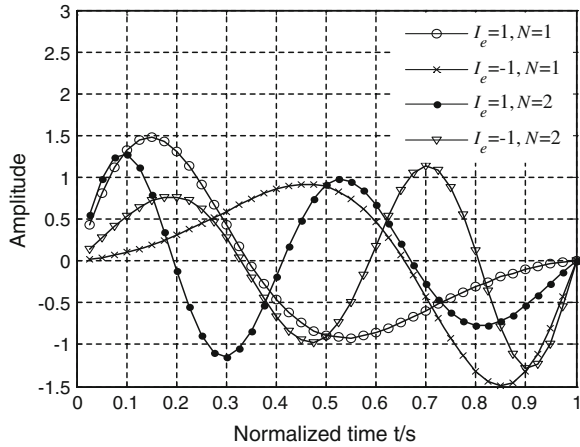
As a novel communication, the VMCK scheme is an extended application of the chirp signal characteristics. The general expression of the VMCK signals can be defined as [11]:

$$s_N(t) = \sum_{k=-\infty}^n [1 + I_e \alpha_N - 2I_e \alpha_N f_s (t - kT)] \cdot \sin\{2\pi N f_s [1 + I_e \alpha_N - I_e \alpha_N f_s (t - kT)](t - kT)\} \quad (1)$$

where N is the numbers of signal period, f_s is the frequency of the signal at the middle of the bit and equals to the bit transmission rate. α_N is the chirp modulation factor of different period, and T is the signal period.

When $I_e = -1$ or $I_e = 1$, $s_N(t)$ represents data 0 and data 1, respectively. So the multiperiods VMCK signals also can be represented as:

Fig. 1 VMCK waveforms of single and two periods



$$s_0(t) = (1 - \alpha_N + 2\alpha_N f_s t) \sin[2\pi N f_s (1 - \alpha_N + \alpha_N f_s t)t] \quad (2)$$

$$0 < \alpha_N \leq 1, 0 \leq t \leq T$$

$$s_1(t) = (1 + \alpha_N - 2\alpha_N f_s t) \sin[2\pi N f_s (1 + \alpha_N - \alpha_N f_s t)t] \quad (3)$$

$$0 < \alpha_N \leq 1, 0 \leq t \leq T$$

The integrations of $s_0(t)$ and $s_1(t)$ are equal to zero within one symbol period. The VMCK signals are easy to be demodulated at the receiver due to eliminating direct current offset. Figure 1 shows VMCK waveforms of single and two periods with $N = 1$, $\alpha_1 = 0.696$, and $N = 2$, $\alpha_2 = 0.36$, respectively.

2.2 DVMCK Transmission System Structure

The DVMCK modulation is comprised of four modules: Binary absolute code module, XOR module, Unit Delay1 module, and VMCK modulation module. For the binary sequence, the absolute code is converted to differential code to modulate by using exclusive OR (XOR) operation. The DVMCK demodulation is composed of five modules: Multiplier module, Unit Delay2 module, Integrator module, Comparator module, and NOT operation module. The binary absolute code will be obtained by comparing with a pre-defined threshold.

The structure of the DVMCK signal transmission system model is shown in Fig. 2. The binary absolute code is converted to differential code to modulate by XOR module and Unit Delay1 module.

The VMCK modulated signal $s(t)$ of differential code passes through Unit Delay2 module, and then the delay signal $s'(t)$ can be written as:

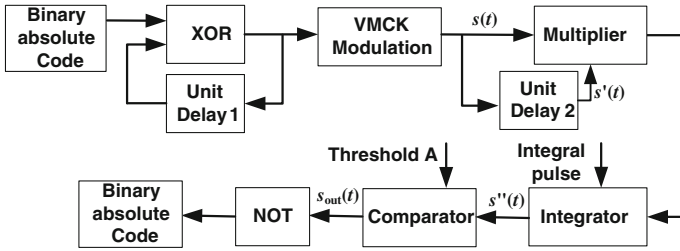


Fig. 2 DVMCK transmission system model

$$s'(t) = s(t - \tau) \tag{4}$$

The VMCK modulated signal $s(t)$ and the delay signal $s'(t)$ are both fed into Multiplier module. The interval of the integral pulse is equal to one symbol period T , and the result of the Integrator module is computed as

$$s''(t) = \int_0^T s(t)s'(t)dt \tag{5}$$

Then, the demodulated data stream is obtained at the output of the comparator, where the integration result is compared with a pre-defined threshold value A .

$$s''(t) \geq A \Rightarrow s_{out}(t) = 1 \tag{6}$$

$$s''(t) < A \Rightarrow s_{out}(t) = 0 \tag{7}$$

Finally, the binary sequence from the Comparator module is carried out NOT operation for being consistent with the input absolute code.

3 Simulation Results and Discussion

3.1 DVMCK Transmission System Model

The simulation of the DVMCK transmission system will be designed in Simulink within MATLAB and the system block is shown in Fig. 3. First, the DVMCK modulation signals are transmitted from workspace of MATLAB. The DVMCK modulated signal is generated based on binary differential sequence. Then the signal is demodulated by the receiver. The DVMCK modulated signal and the DVMCK modulated signal with one unit delay are both fed into the Product module. The result of the Product module is carried out by integration operation

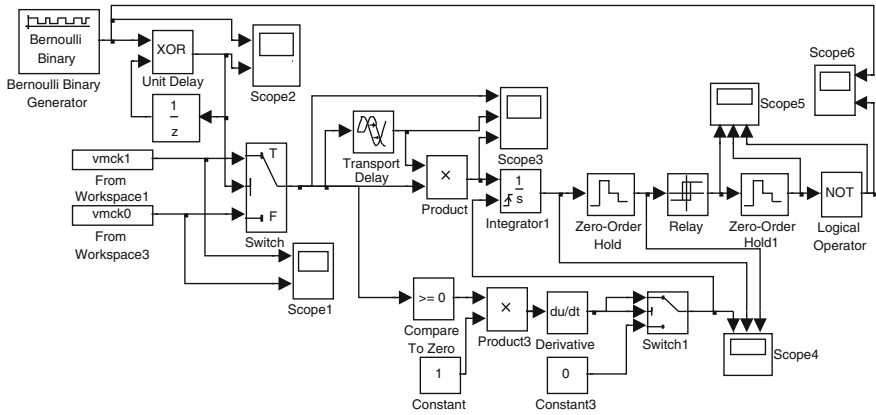


Fig. 3 The module connection graph of DVMCK system in Simulink

based on the integral pulse. The Zero-order hold and the Relay modules can accomplish the sampling and output the binary data. Finally, the binary absolute code sequence will be obtained by the NOT logical operation module.

The scope 1 displays “1” and “0” signal of VMCK which are set as the modulation signals, as shown in Fig. 4. The scope 2 displays the binary absolute code generated by Bernoulli binary generator, and meanwhile, it displays the differential code converted by XOR operation, as shown in Fig. 5.

The DVMCK-modulated signal is generated based on binary differential sequence, as shown in the first subplot of Fig. 6. The middle subplot of Fig. 6 is the DVMCK modulated signal with one unit delay. The DVMCK modulated signal and the DVMCK modulated signal with one unit delay are both fed into the Product module. The product result is shown in the last subplot of Fig. 6.

The integral pulse is generated based on zero-crossing detection of the DVMCK modulated signal, as shown in the first subplot of Fig. 7. The Integrator result is shown in the middle subplot of Fig. 7. After that, the Zero-order hold module carries out the sampling, where the sampling time is half-period. The result of the Zero-order hold module is shown in the last subplot of Fig. 7.

The Relay module which is compared with a pre-defined threshold value can obtain the binary data, and its result as shown in the first subplot of Fig. 8. The function of the other Zero-order hold module is to convert the unipolar Return-to-Zero (RZ) codes to unipolar codes as shown in the middle subplot of Fig. 8. Finally, the binary absolute code sequence will be achieved through the NOT logical operation module in the last subplot of Fig. 8.

Figure 9 shows the binary absolute code of the transmitting and the demodulation result of the receiving. The demodulation result is very exactly except for one-period delay arisen from two Zero-order hold modules. The process of the DVMCK signal demodulation is effective obviously.

Fig. 4 VMCK modulation signals

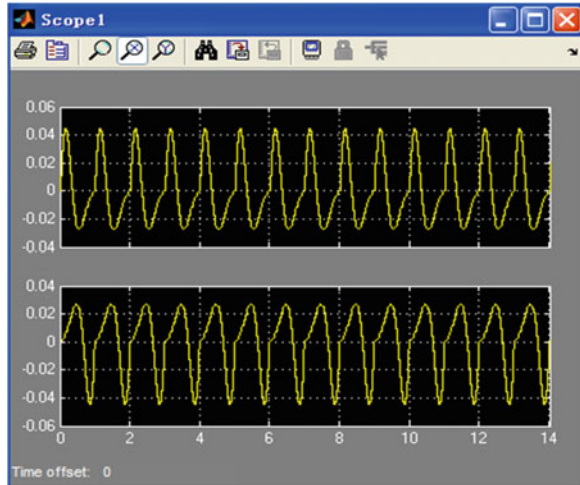
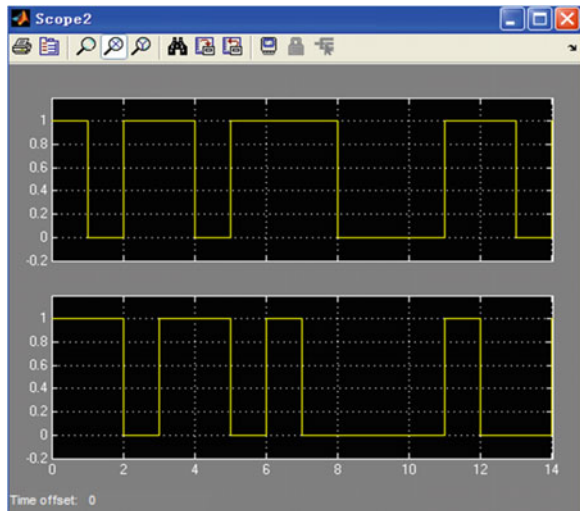


Fig. 5 Binary absolute code and differential code



3.2 Performance Analysis

In the simulation, the DVMCK signal with $N = 1$, $\alpha_1 = 0.696$ is transmitted in the AWGN channel. The input sequence is 100,000 symbols in length. The fundamental wave frequency is set to 1 kHz and each signal sample point is set to 100.

The SER for differential and correlation demodulation is shown in Fig. 10, and both of that have an excellent communication performance. The two SER curves

Fig. 6 Input and output of Product module

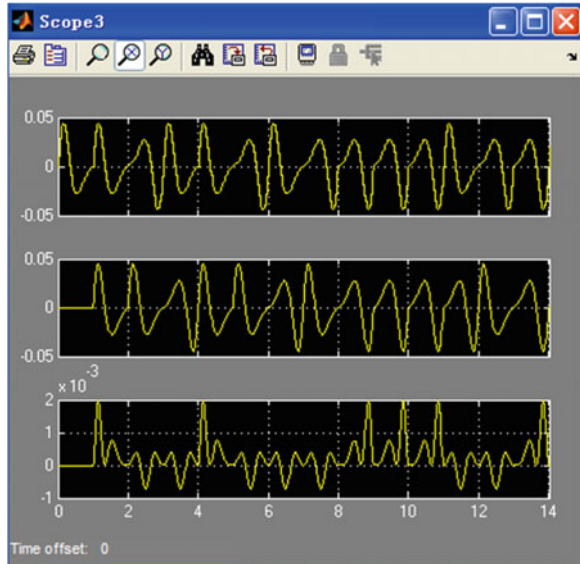
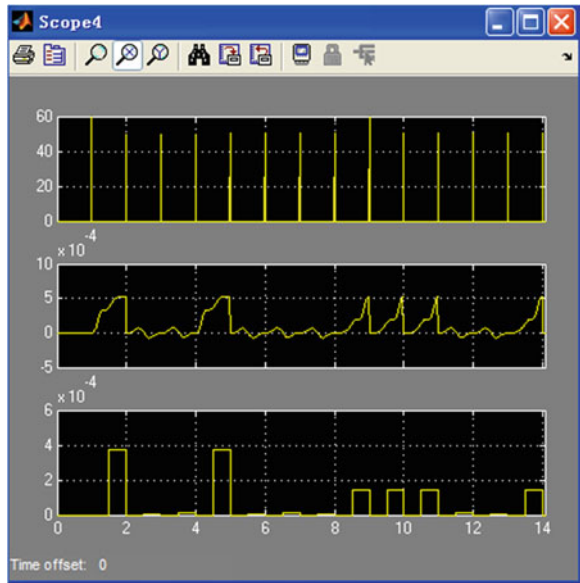


Fig. 7 Integral impulse, Integration, and sampling



are lower than 10^{-3} when SNR is higher than 0 dB. Although the SER performance of correlation demodulation is superior to differential demodulation, the DVMCK transmission model is easy to implement.

Fig. 8 The process of code conversion

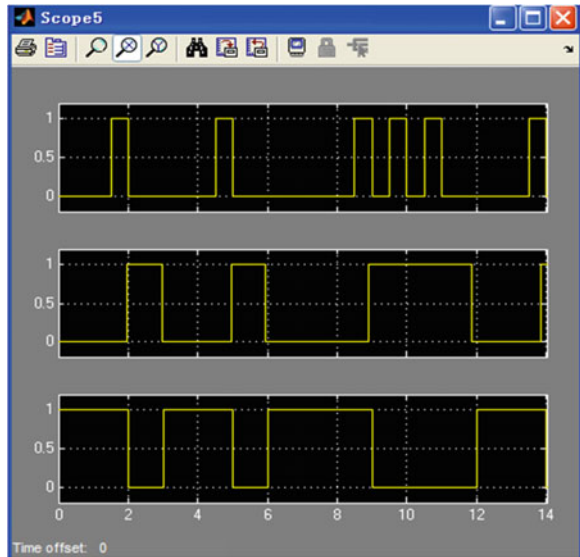
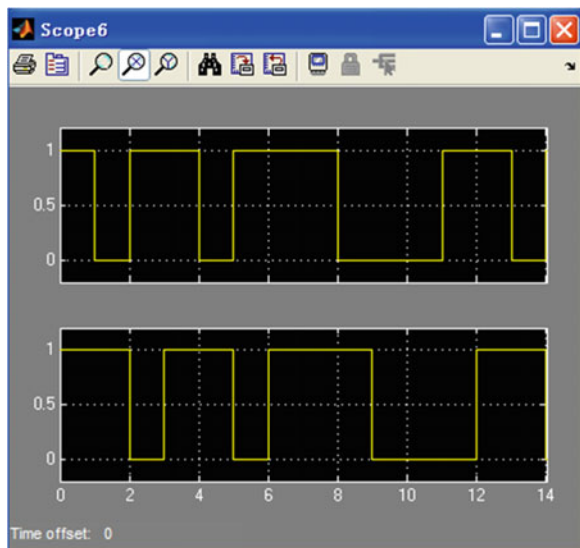


Fig. 9 The code of transmitting and receiving



These synchronization error percentage curves of DVMCK are shown in Fig. 11 with SNR = 10, 5, 0, and -5 dB. The DVMCK system's capability of anti-synchronization error is getting better with the increasing SNR. As long as SNR is greater than 0 dB, the system has strong properties to resist synchronization error.

Fig. 10 SER for differential and correlation demodulation

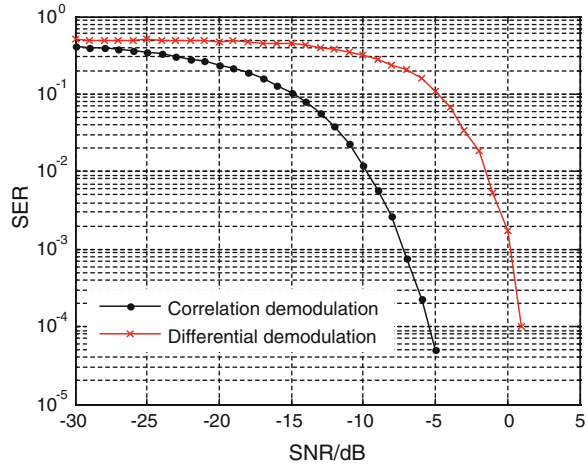
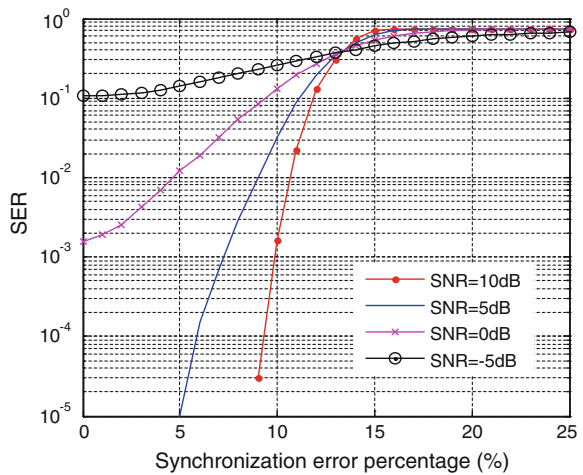


Fig. 11 Synchronization error percentage of DVMCK



4 Conclusion

The DVMCK transmission system and performance have been discussed in this article. The transmission system is simulated under the Simulink within MATLAB. The process of modulation and demodulation of the DVMCK transmission system have been analyzed in detail. The Simulink module obtains the final demodulation data stream with the excellent performance and has strong properties of resistance to synchronization error in the research. DVMCK as a novel high bandwidth efficiency modulation scheme will be combined with 4G technologies.

Acknowledgment This work was supported by Shanghai Leading Academic Discipline Project S30108, NSFC 61132003, NSFC 61171086, and Youth Science Foundation of Jiangxi Educational Committee GJJ13322.

References

1. Rowell C, Lam EY (2012) Multiple frequency band and high isolation mobile device antennas using a capacitive slot. *IEEE Trans Antennas Propag* 60:3576–3582. doi:[10.1109/TAP.2012.2201077](https://doi.org/10.1109/TAP.2012.2201077)
2. Lee W, Lee I, Kwak JS et al (2012) Multi-BS MIMO cooperation: challenges and practical solutions in 4G systems. *IEEE Wirel Commun* 19:89–96. doi:[10.1109/MWC.2012.6155881](https://doi.org/10.1109/MWC.2012.6155881)
3. Walker HR (1997) VPSK and VMSK modulation transmit digital audio and video at 15 bits/sec/Hz. *IEEE Trans Broadcast* 3:96–103. doi:[10.1109/11.566830](https://doi.org/10.1109/11.566830)
4. Saywood KH, Wu LN (2001) Raise bandwidth efficiency with sine-wave modulation VMSK. *Microwaves and RF* 40:79–84. http://apps.webofknowledge.com/full_record.do?product=WOS&search_mode=GeneralSearch&qid=12&SID=3Dln@H2olDm2JK1Hahc&page=1&doc=1
5. Zheng GX, Feng JZ, Jia MH (2007) Very minimum chirp keying as a novel ultra narrow band communication scheme. In: *Proceedings of the information, communications and signal processing (ICICS 07)*, IEEE press, Dec 2007, pp 1–3. doi: [10.1109/ICICS.2007.4449888](https://doi.org/10.1109/ICICS.2007.4449888)
6. Li B, Zhou WX, Zhou Z et al (2008) Realization of UNB system based on FIR filter. In: *Proceedings of the IEEE international symposium on communication and information technologies (ISCIT 2008)*, IEEE press, Aug 2008, pp 190–195. doi: [10.1109/ISCIT.2008.4700180](https://doi.org/10.1109/ISCIT.2008.4700180)
7. Yang L, Zheng GX, Li YB, Sun X (2011) Performance analysis of UNB modulation based on VMCK in AWGN channel. In: *Proceedings of the IET international communication conference on wireless mobile and computing (CCWMC 2011)*, IET press, Nov 2011, pp 207–210. doi: [10.1049/cp.2011.0876](https://doi.org/10.1049/cp.2011.0876)
8. Feng M, Wu LN, Ding JJ (2011) BER analysis and verification of EBPSK system in AWGN channel. *IEICE Trans Commun* E94B:806–809. doi:[10.1587/transcom.E94.B.806](https://doi.org/10.1587/transcom.E94.B.806)
9. Zhang SK (2012) Assessing different ultranarrowband formats. *Microwaves and RF* 51:76–79. <http://mwrf.com/systems/assessing-different-ultranarrowband-formats>
10. Feng M, Wu LN, Gao P (2012) From special analogous crystal filters to digital impacting filters. *Digit Signal Proc* 22:690–696. doi:[10.1016/j.dsp.2012.02.011](https://doi.org/10.1016/j.dsp.2012.02.011)
11. Yang L, Zheng GX, Ding QF, Sun X (2013) Optimal design of VMCK high-order BPF. *JCIT* 8:512–520. <http://www.aicit.org/JCIT/ppl/JCIT2531PPL.pdf>

Research of Turbofan Engine Performance Assessment Method Based on Analytic Network Process Theory

Shuming Li, Niansu Yang and Yanxiao Huang

Abstract Turbofan engine performance directly related to the safety of the operation of the aircraft, so improve the reliability of the turbofan engine performance evaluation is crucial. Based on assessment method of the turbofan engine performance at home and abroad and the perspective of the engine working principle and the performance degradation mechanism, this paper adopts a new assessment theory—Analytic Network Process Theory (ANP) to analyze the interactions and dependencies between the performance parameters in order to build a turbofan engine performance evaluation network hierarchy, and then use Superdecisions software to calculate various performance parameters weight vector. At the same time, the two PW series engine operating parameters data for instance, dimensionless processing the parameters and weighted, finally get two engine performance index to assess the performance of the turbofan engine. The results show that the ANP theory increases the accuracy and reliability of the engine performance assessment, which has a high practical value for timely assessing the performance of engine state.

Keywords Turbofan engine · Analytic network process theory · Limit supermatrix · Performance index

S. Li · N. Yang (✉)

Aeronautical Engineering Institute, Civil Aviation University of China, Tianjin China
e-mail: nsyang@sina.cn

Y. Huang

Vocational and Technical College, Civil Aviation University of China, Tianjin China

1 Introduction

As the power plant of the airliner, turbofan engine performance directly determines the aircraft flight safety; so it is necessary to study deeply the method for assessment of engine performance reliable, and provides a set of effective methods for timely identify the performance state of the engine and renewal.

At present, the performance assessment of turbofan engine used to take advantage of limited key parameters, or make use of analytic hierarchy process, grey theory, and information entropy method through the use of multiple performance parameters of the information fusion to assess the performance of the engine. The disadvantage of the former is the only key parameter to characterize the performance of engine, and this will cause the omission of important parameters of engine eventually lead to lower assessment of the accuracy; the latter problem is ignored the relation between important parameters on engine performance. Therefore, to improve the accuracy of the turbofan engine performance assessment, this paper was first introduced the Analytic Network Process theory (ANP) in the engine evaluation field, using a combination of qualitative and quantitative analysis method to assess the turbofan engine performance and puts forward the concept of the turbofan engine performance index.

2 Analytic Network Process Theory

Based on the theory of system engineering of AHP method, Prof. Saaty presents a new approach for decision making to adapt to nonindependent incremental structure, namely the analytic network hierarchy theory. The theory is an information processing method combining qualitative analysis with quantitative analysis, and the performance parameters correlation can clearly be described. The theory of ANP structure is divided into two parts: the first part is control layer, including the target and principles for decision making, and all decision criteria are considered independent of each other and dominated only by the target; the second part is the network layer, it is composed of parameter group which is all dominated by control layer, and the internal structure of the network is the mutual influence. About ANP for decision-making and evaluation of the general steps and weights detailed calculations, see [1], below only focuses on unweighted super matrix, weighted super matrix, and limit super matrix construction arithmetic.

2.1 Unweighted Super Matrix and Weighted Super Matrix Arithmetic

Unweighted super matrix reflected on the left of the various parameters on the degree of influence on the top of each parameter in the matrix form. It is built firstly through interdependence of the parameters, then build parameter-level judgment matrix, and obtain normalization of the weight vector, but all those must be via the judgment matrix hypothesis testing.

Assuming the control layer of ANP have parameters $A_1, A_2 \dots A_n$, the network layer has group parameters $B_1, B_2 \dots, B_n$, among the B_i it has parameters $C_{i1}, C_{i2}, \dots, C_{in}$ ($i = 1, 2, \dots, N$), the parameter A_s within the control layer as the criterion, the parameter C_{j1} ($l = 1, 2, \dots, N_j$) within B_j as a subcriteria, the parameters compared with each other among parameter set B_i in accordance with the impact of the size about C_{j1} , according to this, construct judgment matrix is shown in Table 1:

By using engine value method obtain rank vector: $W_{i1}^{(j1)}, W_{i2}^{(j1)}, \dots, W_{in}^{(j1)}$, Denoted W_{ij} as:

$$W_{ij} = \begin{bmatrix} W_{i1}^{(j1)} & W_{i1}^{(j2)} & W_{i1}^{(j3)} & \dots & W_{i1}^{(jn_i)} \\ W_{i2}^{(j1)} & W_{i2}^{(j2)} & W_{i2}^{(j3)} & \dots & W_{i2}^{(jn_i)} \\ \vdots & \vdots & \vdots & \ddots & \vdots \\ W_{in_i}^{(j1)} & W_{in_i}^{(j2)} & W_{in_i}^{(j3)} & \dots & W_{in_i}^{(jn_i)} \end{bmatrix} \tag{1}$$

The column vector among W_{ij} is rank vectors in which the parameters $C_{i1}, C_{i2}, \dots, C_{in_i}$ among B_i compared with the parameters $C_{j1}, C_{j2}, \dots, C_{jn_i}$ among the B_j in accordance with the impact of the size. If a parameter is limited only by the impact of a parameter in a parameter group or completely unaffected, then directly give W_{ij} 1 or 0, ultimately obtain unweighted supermatrix:

$$W_{ij} = \begin{bmatrix} W_{11} & W_{12} & W_{13} & \dots & W_{1N} \\ W_{21} & W_{22} & W_{23} & \dots & W_{2N} \\ \vdots & \vdots & \vdots & \ddots & \vdots \\ W_{N1} & W_{N2} & W_{N3} & \dots & W_{NN} \end{bmatrix} \tag{2}$$

The sub-block of unweighted supermatrix W_{ij} is listed normalized, but W are not. So taking A_s as the criterion, each group of parameters under the A_s compared the importance of the criteria B_i , is given in Table 2:

Obtaining weighting matrix:

Table 1 Comparison between parameters of judgment matrix

| C_{jl} | $C_{i1}, C_{i2}, \dots, C_{in_i}$ | Normalized eigenvectors |
|------------|-----------------------------------|-------------------------|
| C_{i1} | $e_{11}, e_{12}, \dots, e_{1n_i}$ | $W_{i1}^{(j)}$ |
| C_{i2} | $e_{21}, e_{22}, \dots, e_{2n_i}$ | $W_{i2}^{(j)}$ |
| \vdots | \vdots | \vdots |
| C_{in_i} | $e_{i1}, e_{i2}, \dots, e_{in_i}$ | $W_{in_i}^{(j)}$ |

Table 2 Comparison between group parameters of judgment matrix

| B_j | B_1, B_2, \dots, B_N | Normalized eigenvectors |
|----------|---------------------------------|-------------------------|
| B_1 | $d_{11}, d_{12}, \dots, d_{1n}$ | C_{1j} |
| B_2 | $d_{21}, d_{22}, \dots, d_{2n}$ | C_{2j} |
| \vdots | \vdots | \vdots |
| B_N | $d_{n1}, d_{n2}, \dots, d_{nn}$ | C_{Nj} |

$$C_{ij} = \begin{bmatrix} C_{11} & C_{12} & C_{13} & \cdots & C_{1N} \\ C_{21} & C_{22} & C_{23} & \cdots & C_{2N} \\ \vdots & \vdots & \vdots & \ddots & \vdots \\ C_{N1} & C_{N2} & C_{N3} & \cdots & C_{NN} \end{bmatrix} \tag{3}$$

Weighted the unweighted super matrix can get W_{ij}^* , its columns sum equal to 1:

$$W_{ij}^* = C_{ij} W_{ij} \quad i = 1, 2, \dots, N, j = 1, 2, \dots, N. \tag{4}$$

2.2 Limit Super Matrix Arithmetic

Because of the interdependent relationship exists between performance parameters or feedback effect, leading to the degree of influence between parameters is complicated. Here, ANP theory based on the weighted Super matrix limit processing, get the limit Super matrix, eventually through normalized weight vector to get each stable parameter, solve the problem as follows:

$$\overline{W}_{ij}^\infty = \lim_{t \rightarrow \infty} \left(\overline{W}_{ij}^* \right)^t \tag{5}$$

3 Build a Turbofan Engine Performance Evaluation System

Based on the previous studies, this paper almost uses QAR information turbofan engine running parameters combined with turbofan engine AD/SB information to construct the system of the turbofan engine performance parameters so as to assess the engine performance.

Based on the nature and source of all parameters, the performance parameters of the engine are basically divided into four categories: gas path parameters, structure parameters, vibration parameters, and environmental parameters, and the correlation of various parameters on the other parameters and related degrees, build a network hierarchical relationship of the turbofan engine performance parameters.

3.1 Correlation Analysis of the Turbofan Engine Performance Parameters

3.1.1 Gas Path Parameters

As engine operating, because of gas path component performance degrades that will result in the gradual degradation of engine performance. So engine performance can be assessed by the engine gas path parameters [2].

Exhaust Gas Temperature (EGT): the size of EGT reflect the key parameters of the engine performance—the level of the total temperature before the gas turbine. Largely determines the performance of the engine, turbine guider work safety and life. EGT is extremely sensitive to a decline in efficiency of compressor and turbine bleed air system failure [3], so EGT is affected by the fuel flow, air temperature, fuel temperature, etc.

Fuel Flow (FF): the size of the fuel flow determines the speed of the high and low pressure rotor speed, thus affecting the engine air flow, affect the compressor pressure ratio and thrust. Therefore, in the state where the nozzle area unchanged, FF affect computed airspeed, EPR and the size of the EGT.

Fuel Temperature (FT): fuel is maintained at an appropriate temperature and better fuel atomization, accelerate the formation of a mixed gas, and ensure the stability of combustion and improve the combustion efficiency. Therefore, FT directly impact on FF, EPR, and EGT.

Engine Pressure Ratio (EPR): the inlet of the low pressure compressor total pressure is affected by total air pressure, total air pressure and total air temperature is the corresponding, so EPR is affected by N1, N2.

The percentage of Low-pressure rotor speed (N1): it is affected by FF and Low-pressure rotor vibration.

The percentage of High-pressure rotor speed (N2): it is affected by FF and High-pressure rotor vibration.

Computed Airspeed (CAS): it is only affected by FF.

3.1.2 Basic Structure Parameters

In turbofan engine, some structure related to gas path parameters, through sensor passing structural parameters to the electronic engine controller (EEC), which managing and coordinating engine-related functions.

Fuel Cutoff Switch (FCS): the size of the fuel flow through the sensor sends a signal to the EEC to control the FCS [4].

Fuel Shutoff Valve (FSV): it is dominated by FCS, and affects FF.

Throttle Resolver Angle (TRA): the size of it will affect FF, and the size of FF through the sensor sends a signal to the EEC to adjust the TRA.

PW 2.5 Bleed Act (PW2.5 BA): exhaust gas from the high pressure compressor, the greater of the trap door opened, and the more gas exhausted, the total air flow is reduced, and it will affect the EPR and EGT.

Bleed High-Press Sov (BHPS): it is mainly through the air entraining limit the temperature and pressure of the downstream [5], so it will the EPR and EGT.

3.1.3 Vibration Parameters

According to the rate which is the value of engine high-pressure and low-pressure rotor vibration change or change trend, the same structure can be analyzed turbofan engine working condition to assess the performance of the engine.

Low-pressure rotor vibration coefficient (N1 VIB): N1 VIB will affect the size of the low-pressure rotor speed.

High-pressure rotor vibration coefficient (N2 VIB): N2 VIB will affect the size of the high-pressure rotor speed, and it will be affected by PW2.5 BA.

3.1.4 Environmental Parameters

Total Air Temperature (TAT): TAT and CA is highly interdependent relationship.

Corrected Altitude (CA): it will affect the open degree of PW2.5 BA.

3.2 Engine Performance Evaluation System

Build a turbofan engine performance parameters hierarchy system and network system. Through the above analysis of correlation on the performance of PW series turbofan engine model and based on four main parameters and 16

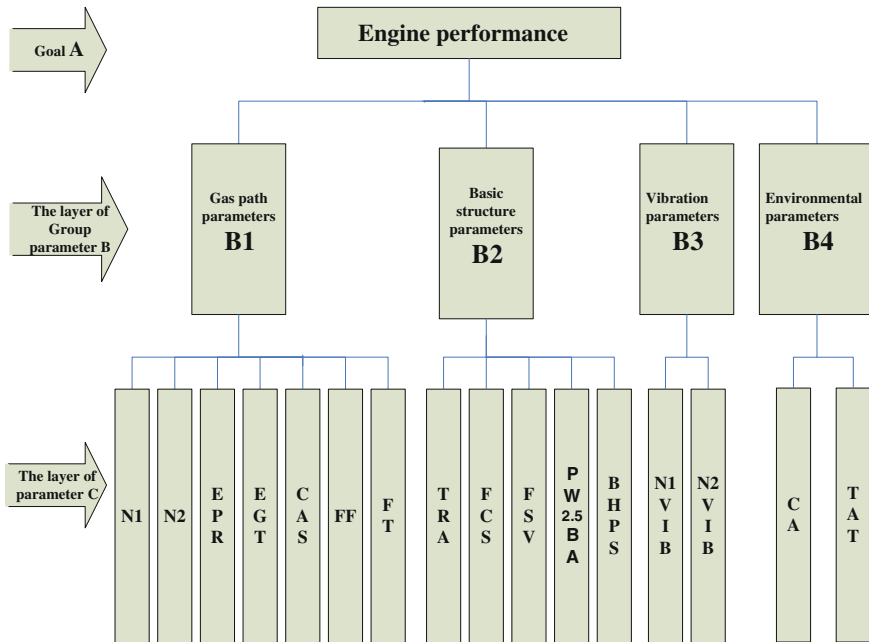


Fig. 1 Turbofan engine performance parameters hierarchy system

subparameters, build a turbofan engine performance parameters hierarchy system, is shown in Fig. 1.

The network system in the layer of group parameter *B* and parameter *C* is shown in Figs. 2 and 3.

4 The PW Series Turbofan Engine Performance Evaluation on the Basis of ANP

Calculate each of the performance parameters the weight vector. Because of the ANP weight vector calculation is very complex, the actual need Superdecisions software calculated [6]. First, make the engine performance evaluation ANP model based on the logical parameters relationship between Figs. 2 and 3, which is shown in Fig. 4; after that, take engine performance evaluation as the goal and the gas path parameters as the criterion, given an example of the parameters in gas path parameter according to their priority effect on EGT construct the judgment matrix. The normalized weight vectors and the consistency of judgement matrix are shown in Fig. 5.

Fig. 2 The network system in B

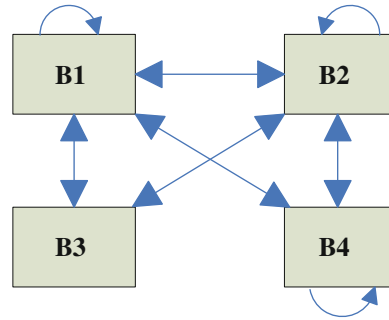
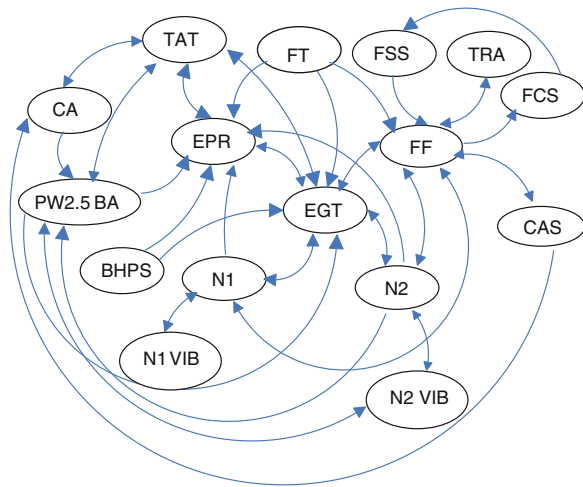


Fig. 3 The network system in C



The other parameters as described in steps input, eventually the stable weight vector of the parameters are derived based on the unweighted matrix, the limit matrix, cluster matrix algorithm, is shown in Fig. 6.

Turbofan engine performance parameters dimensionless Processing. Dimensionless algorithm. Engine performance parameters are mainly three types: the bigger the better efficiency type, the smaller the better cost type (1 minus the dimensionless value in order to better calculate the engine performance appraisal papers, so that it becomes the bigger the better) and parameter values as close as possible from the optimal value of fixed type. Different types of indicators need to adopt different conversion methods, the method is relatively mature, are not discussed here.

As the plane took off, the engine is at full power take-off and engine performance parameters of the most dramatic performance, so this collection of aircraft in the take-off the climbing stage engine performance parameters: climb to fly from the ground (0 ft) to the required height (4,500 ft) information per second

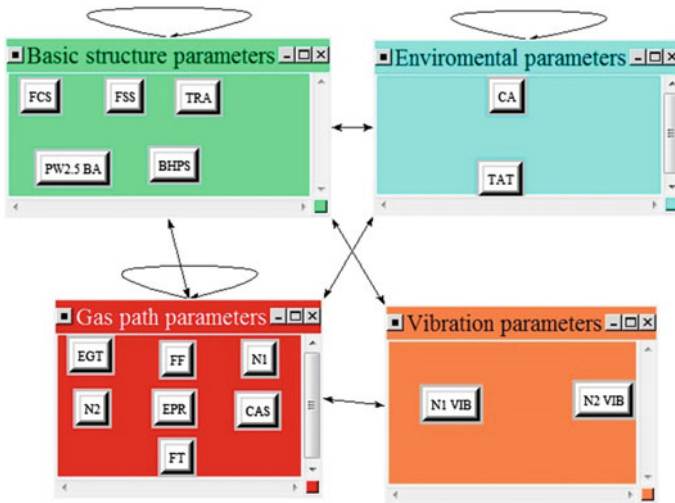
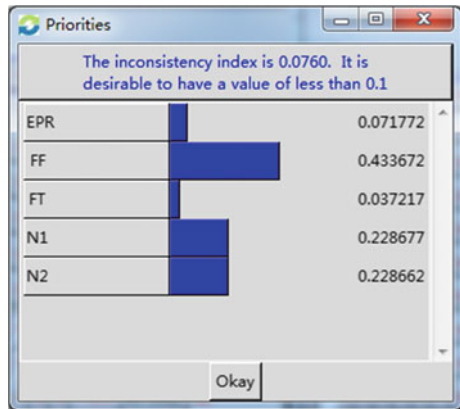


Fig. 4 ANP model

Fig. 5 Inconsistency index



between a big difference, so use the average value of the parameter to characterize the performance of turbofan engine.

Performance parameters classification. Based on the function and properties of parameters, this paper classified those is shown in Table 3.

Performance parameters dimensionless results. After processing the raw data in the two PW series engine, the dimensionless value of δ_1 and δ_2 is shown in Table 4 (for FSS, FSS, as well as BHPS only RUN or SHUT, and the original data are all RUN, so this paper defined it as 1 or 0).

Comprehensive assessment of engine performance. Summarize the results of previous studies and combined with the reality of the turbofan engine performance management, this paper presents the concept of the performance index that is each

Fig. 6 Stable weight vector (R_x)

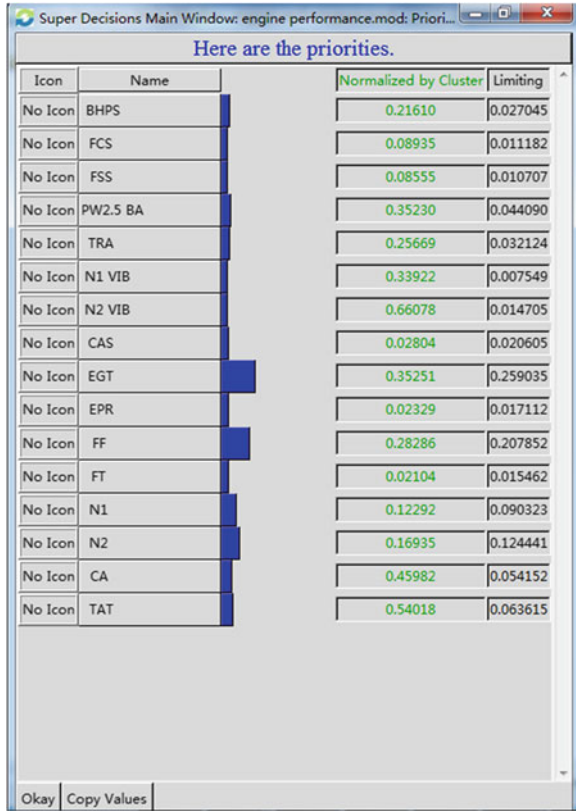


Table 3 Parameter PROPERTIES

| Classification | Engine performance parameters |
|-----------------|--|
| Efficiency type | EPR, N1, N2, CAS, CA |
| Cost type | EGT, FF, N1 VIB, N2 VIB |
| Fixed type | FT, PW2.5 BA, TAT, TRA, FCS, FSS, BHPS |

Table 4 Value of performance parameters dimensionless

| Value | CA | TAT | TRA | N1 | N2 | EPR | EGT |
|------------|----------|----------|----------|----------|----------|----------|----------|
| δ_1 | 0.446465 | 0.414141 | 0.474747 | 0.439394 | 0.363636 | 0.498485 | 0.782828 |
| δ_2 | 0.497101 | 0.459259 | 1 | 0.492593 | 0.266667 | 0.543434 | 0.594444 |
| | FT | N1VIB | N2VIB | PW2.5BA | CAS | FF | |
| δ_1 | 0.939394 | 0.25477 | 0.448485 | 1 | 0.569697 | 0.560852 | |
| δ_2 | 0.666667 | 0.494118 | 0.322222 | 1 | 0.541667 | 0.554491 | |

performance parameters dimensionless processing values multiply the corresponding parameters of each the weight vector.

$$\text{Performance index: } Z = \delta_i \times R_x (i = 1, 2; x = 1, 2, \dots, 16) \quad (6)$$

According to the weight vector Fig. 6 and Table 2 stable weight vectors, two engine performance comprehensive assessment values can be gotten:

$$Z_1 = 0.606524 > Z_2 = 0.567552 \quad (7)$$

Obviously, the first engine performance is better than the performance of the second engine. The two engines in the actual work with the circumstances of no accident; the first engine safety running time is indeed worked 600 h longer than the second engine. Therefore, the use of ANP theory launched to evaluate the performance of sufficient accuracy, the results are reliable.

Of course, if the engine receives the AD/SB information, regardless of the state of the engine, must be timely repair accordingly.

5 Conclusions

This paper is the first time introduced the ANP theory into engine performance assessment; it is also considered the interactions and dependencies between parameters and establishes a nonlinear relationship of the turbofan engine multiattribute comprehensive assessment model.

According to this model, the weight vector contains the logic of the performance parameters and the performance index can be calculated, meanwhile, using two PW Series engine's performance parameters to assess the performance of the engine; the results show that ANP theory is sufficient accuracy for Engine performance assessment, for timely renewal and maintenance support of the engine is of great help. Of course, in the calculation, also found that the calculation process of this method is more complex or difficult, for future algorithm also needs further improvement, in order to improve the computing speed.

Acknowledgments This work is supported by Fundamental Research Funds for the Central Universities in 2012 (Research on Aero-engine Performance Evaluation Model Faced on Cloud theory (ZXH2012p003)). The authors would like to thank them very much.

References

1. Jaw LJ (2005) Recent advancements in aircraft engine health management (EHM) technologies and recommendations for the next step. In: Proceeding of Turbo Expo 2005, 50th ASME international gas turbine and aero engine technical congress, Reno-Tahoe, Nevada. ASME paper no. GT-2005-68625

2. Song H, Li C, Li X, Song W (2010) Aero-engine health assessment research. *Aviat Univ Air Force* 11:28–33 (in Chinese)
3. Luan SG (2008) The aviation engine condition monitoring method and system based on the sample gas path parameters. *Harbin Inst Technol* 12:62–77 (in Chinese)
4. Boeing 747-400 Aircraft Maintenance Manual (Boeing 747-400 AMM):28-22-00-7-23, 36-11-00-1-6, 75-32-00-1-5
5. Peng R (2006) B737 electrical systems training manual, vol 2. Weapon Industry Press, Beijing, pp 72–105 (in Chinese)
6. Cheng K, Yu X (2012) ANP method of reverse logistics service providers and superdecisions software realization. *Fuzhou Univ School Manag* 2:32–37 (in Chinese)

A Cellular Automata Model on Bus Signal Priority Strategies Considering Resource Constraints

Liying Wei, Lili Zhang and Zhilong Wang

Abstract This article studied bus signal priority (BSP) strategies at road intersections containing bus lane through simulation. Based on cellular automata (CA) theory, the coordination of single-phase buses and cars under different BSP control strategies is studied and the “speed-distance” condition is introduced in transit signal priority, with which two indicators for evaluation considered resource constraints are proposed, namely, fuel consumption and exhaust emissions. The effect on the consumption of general vehicles from bus signal priority is shown by CA simulation, and the judgment of the bus priority level is determined by the calculation of fuel consumption and exhaust emissions.

Keywords Bus priority · Cellular automata · Fuel consumption · Exhaust emissions

1 Introduction

In order to relieve the congestion of urban traffic, bus signal priority control has been launched. However, the unconditional use of bus priority during the peak time is bound to increase the impact on the large number of social vehicles, which may cause a decline of comprehensive benefits. In this paper, the collaboration of

L. Wei (✉) · L. Zhang · Z. Wang
Department of Traffic Engineering, School of Traffic and Transportation,
Beijing Jiaotong University Beijing, No.3 Shang Yuan Cun,
Hai Dian District Beijing, People's Republic of China
e-mail: lywei@bjtu.edu.cn

L. Zhang
e-mail: 10121083@bjtu.edu.cn

Z. Wang
e-mail: 11120900@bjtu.edu.cn

buses and social vehicles at the intersection with bus lanes and bus signal priority strategies are studied as to improve the overall traffic efficiency and resource utilization of the intersections.

The study of bus signal priority has been developed since Wilbur and others applied bus signal priority on two signalized intersections through manual control [1]. Later Ludwick filed unconditional priority in early simulation models [2]. Furth and Muller implemented the conditional bus priority in the Eindhoven of Finland [3]. In 1991, Casey raised that the bus priority would interrupt general traffic volume [4]. This means signal coordination runs more effective than bus priority on the urban trunk roads, especially at peak times. In 2000, Jeason and Ferrira studied on the best bus ratio and bus volume for the bus-only signal under different saturations by comparing vehicle delays within and without bus-only signal [5]. In 2004, Ngan studied vehicle delay of buses at intersections in different traffic conditions and different signal control, and concluded the most applicable bus signal priority under high bus volume, low turn-left flows, and low flow rate conditions [6]. Based on cellular automata model, this article studies traffic flow at intersections by simulation, and resource constraints is proposed in the transit priority strategies, through which results the relevant indicators for evaluation.

2 Index of Resource Constraints

The indexes of intersection resource constraints include fuel consumption and exhaust emissions, of which a set of formulas are derived. Each interval in the simulation takes 1 s, and the simulation process duration τ takes T_2 steps. If the timing starts from the step T_1 ($T_1 < T_2$), then $\tau = T_2 - T_1$.

2.1 Fuel Consumption Index

Fuel consumption of traffic flow at signalized intersections depends not only on the consumption of a single vehicle driving through the intersection, but also on the traffic volume, signal timing, and the decelerating or accelerating delay. When considering the fuel consumption of intersections, the accelerating and deceleration delays arising from fuel consumption should be considered. Since the acceleration is the rate of velocity change, and it is proportional to the engine power, which is direct proportion to the fuel consumption, vehicle speed also has correlation with the fuel consumption.

According to data [7], the average fuel consumption of an idling buses is about 4.5 l h^{-1} , and the fuel consumption of an idling car 1.5 l h^{-1} . The consumption for a driving bus is 30 l/100 km , and a driving car for 12 l/100 km .

Fuel consumption of buses and cars in different conditions is calculated as follows:

$$l_{i_idling} = t_{j,i} \cdot L_i \tag{1}$$

$$l_{i_move} = \frac{x_{j,i} \cdot L'_i}{100} \tag{2}$$

where l_{i_idling} as the total fuel consumption of the i th vehicle in idle condition, l_{i_move} as the total fuel consumption of the i th vehicle in driving condition, $t_{j,i}$ as the idling time of the i th vehicle on the j th lane, $x_{j,i}$ as the actual driving distance of the i th vehicle on the j th lane, L_i as the fuel consumption of an idling vehicle, L'_i as the fuel consumption of a driving vehicle.

2.2 Exhaust Emissions Index

The calculation of traffic emissions can be divided into the emissions of the vehicles driving on the road sections and the emissions of the idling entrance vehicles. The formula of emissions [8] will be modified in this article, therefore the emissions E has the expression as follows:

$$E = \sum_j (EF^{PCU} \times q_j \times t_j) + \sum_j (EFI^{PCU} \times q_j \times d_j) \tag{3}$$

where E as the intersection emissions, units g ; j as the j th road section at the intersection; q_j as the traffic volume of the j th section, units pcu/h ; t_j as the travel time on the j th section, units s ; d_j as the vehicle idling time at the signalized intersection, namely the duration for vehicles from arriving at the stop line to starting again; EF^{PCU} as the emission factor of a PCU, units $g/pcu \cdot h$; EFI^{PCU} as the idling emission factor of a PCU, units $g/pcu \cdot h$. In this paper, the exhaust emissions mainly refers to CO emission factor, which is given by $EF^{PCU} = 45 \text{ g/pcu} \cdot h$ and $EFI^{PCU} = 5 \text{ g/pcu} \cdot h$.

3 Model Parameters

3.1 Size of Cells

Regard the roads as one-dimensional discrete lattice chain of length L , and each lattice can either be empty or occupied by exactly one vehicle in each interval. The buses and social vehicles have different maximum speeds and vehicle lengths. The size of a typical car is $5 \times 3 \text{ m}$. Through the data collection, the gap between

vehicles driving on the section can be determined by general 5 ~ 10 m, and the queue gap behind the stop line can be determined by general 2 m. Therefore, the length of a cell is set as 3.75 m, then each car takes up 2 cells, and bus takes up 4 cells. The speed of each vehicle at time t are described by $V_i(t)$, $V_i(t) \in [0, V_{\max}]$.

The location of the i th vehicle at time t is given by $X_i(t)$, which leads to the distance of the i th vehicle and the $(i + 1)$ th vehicle at time t recorded as $D_i(t)$ can be expressed as:

$$D_i(t) = X_{i+1}(t) - X_i(t) - l_{i+1} \quad (4)$$

where l_{i+1} as the length of the $(i + 1)$ th vehicle.

3.2 Parameters

(1) The number of lanes

Assuming both of the two roads at the cross intersection are four lanes in each direction, of which each approach contains a right turn lane, a bus lane, a left turn lane for general vehicles, and a through lane for general vehicles. The bus lane is located at the left side of the right turn lane in order for buses access to the linear bus station.

(2) The detector location

Taking the northern approach with maximum traffic volume as examples, assuming that the length of the road section vehicles behind the stop line is 45 cells. The distance between detector and stop line is 120 m, namely 32 cells, as the length of the 16 cars or 8 buses.

(3) The vehicle arrival

Assuming the vehicles follows negative binomial distribution. The arrival probability of buses and cars within a certain steps can be determined through investigation. In this paper, the arrival probability of buses is given by $\rho_{\text{bus}} = 0.05$ veh/s, the arrival probability of social vehicles in straight lanes is given by $\rho_{\text{car}} = 0.167$ veh/s, and that for left-turn cars is given by $\rho_{\text{car_left}} = 0.07$ veh/s.

(4) The maximum speed

The maximum for bus speed recorded as $V_{\max,\text{bus}}$ is 3, which equals to the actual speed of 40.5 km/h; and maximum speed for car recorded as $V_{\max,\text{car}}$ is 4, which equals to the actual speed of 54 km/h.

(5) The maximum green extension and the maximum red truncation

The maximum green extension and the maximum red truncation are similar in actuated control, which refer to the maximum for the bus signal priority in order to maintain optimal split. And the current light should be changed immediately when reaching the maximum.

In this paper, the east-to-west and north-to-south straight phases involve bus priority strategy, so the probability of left-turn arrivals and the left-turn queue length need to be considered in the derivation of the maximum green extension and red truncation, and the vehicles between the detector and the stop line should be emptied before the end of the left-turn green time.

The green time for left-turn phase can be divided into three parts, of which the first part, Δg_1 , is used for meet the loss of previous green extension, the second part, Δg_2 , is used for empty the vehicles queuing on the lanes before the left-turn phase begins, and the third part, Δg_3 , is used for meet the loss of next red truncation.

Assuming that $g_1 = 20$, $g_2 = 40$, $g_3 = 20$, $g_4 = 40$ s, as the probability of left-turn vehicles arrival $\rho_{\text{car_left}} = 0.07$ veh/s is certain, when the third phase starts, there is about four vehicles per lane arrives at the corresponding entry, of which the signal state has been red for 60 s. According to observation, a total green time of at least 10 s, which includes start losing time is necessary for vehicles queuing in left-turn lanes. Therefore, the left 10 s of left-turn phase g_3 is used to supply bus priority with extended time or cut down time for the adjacent straight phases. To guarantee the benefits for buses and social vehicles, assume in this article that the maximum extension or truncation time of two priority strategies are both 5 s.

4 The CA Model for Single-Phase Coordination

4.1 The CA Model

(a) Bus signal priority control strategies

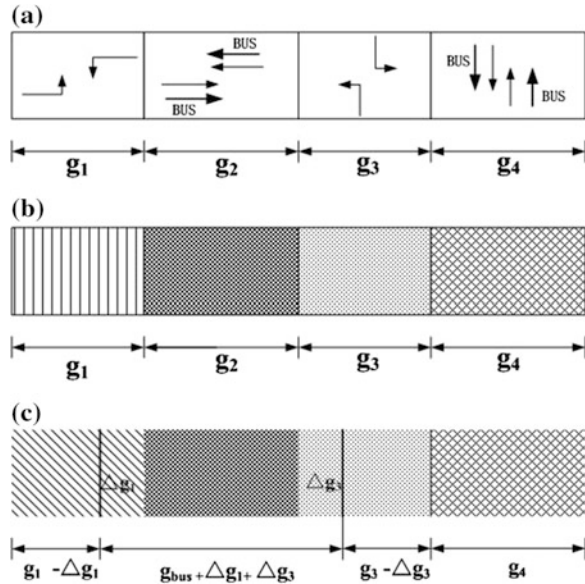
In this paper, conditional bus priority strategies are divided to green extension and red truncation. The bus speed at the vehicle detectors is given as V_{bus} , thus the time buses for stop line $t = L/V_{\text{bus}}$. When a bus reaches the detector, if the remaining green time for buses $g'_{\text{bus}} < t$, the g'_{bus} need to be extended, and if the remaining red time for buses $r'_{\text{bus}} \geq t$, the r'_{bus} need to be shorten.

In the simulation, $g_i (i = 1, 2, 3, 4)$ and g_{bus} respectively means the i th phase green time and the bus lane green time. Assuming that when a bus driving in the straight lane and east-to-west straight general vehicles both meet the second phase, then the bus green extension $\Delta g_{\text{bus}} = \Delta g_3$. The bus red truncation $\Delta r_{\text{bus}} = \Delta g_1$. In view of the little impact to right turn from signal control, the conflicts of vehicles, nonmotorized vehicles, and pedestrians are not considered. Thus, the extend green time for buses is given as $\Delta g_{\text{bus}} + \Delta r_{\text{bus}}$ (Fig. 1).

(b) VDR model

VDR model [9] is applied as follow rules:

Fig. 1 BSP timing of simulated intersection



(1) Determine stochastic noise

$$p = \begin{cases} p_0, & V_{j,i}(t) = 0 \\ p_1, & V_{j,i}(t) > 0 \end{cases} \quad (5)$$

where p as the stochastic randomization, p_0 as the probability of slow-to-start rule, given as 75 % [10], p_1 as the ratio of vehicles that do not follow the rule, and $p_0 > p_1$.

(2) Acceleration:

$$V_{j,i}(t + 1) = \min\{V_{j,i}(t) + 1, V_{j,max}\} \quad (6)$$

(3) Braking:

$$V_{j,i}(t + 1) = \min\{V_{j,i}(t) + 1, \text{gap}_{j,i}(t)\} \quad (7)$$

$$\text{gap}_{j,i}(t) = X_{j,i+1}(t) - X_{j,i}(t) - l_i \quad (8)$$

(4) Randomization:

$$V_{j,i}(t + 1) = \max\{V_{j,i}(t) - 1, 0\} \quad (9)$$

(5) Driving:

$$X_{j,i}(t + 1) = X_{j,i}(t) + V_{j,i}(t + 1) \tag{10}$$

where $X_{j,i}(t)$ and $V_{j,i}(t)$ are the position and speed of the i th vehicle on the j th lane at time t , $V_{j,\max}$ as maximum speed of vehicles on the j th lane, $gap_{j,i}(t)$ as gap between the i th and the $(i + 1)$ th vehicle on the j th lane, and l_i for the length of the i th vehicle.

If the signal state is red when a vehicle arrives at the intersection, it should stop to wait. And if $S_j(t + 1) = r$, $X_{j,i}(t + 1) \geq X_{j,i}$ and $X_{j,i}(t) < X_{j,i}$, then $X_{j,i}(t) = X_{j,i} - 1$ and $V_{j,i}(t + 1) = 0$, otherwise enter the next step. Where $X_{j,i}$ as the stop line's location of the lanes for general vehicles, and $S_j(t)$ as the signal state the j th lane at time t . If the signal state is green, then $S_j(t) = g$, or $S_j(t) = r$, in which g and r refers to green light and red light, respectively.

4.2 Bus Priority Strategies

(a) Green extension

If the east-west straight signal state is green when i th bus arrives at the detector (a, b, c, d) at time t , namely $S_{\text{bus}}(t) = g$, then the remaining green time in this approach can be calculated by $g'_{\text{bus},i}$, and the maximum green extension allowed for buses is recorded as $\Delta g_{\text{bus}}^{\max}$.

If $g'_{\text{bus},i} < L/V'_{\text{bus},i}(t)$ and $L/V'_{\text{bus},i}(t) - g'_{\text{bus},i} \leq \Delta g_{\text{bus}}^{\max}$, then update the current green time for buses, which is given by $G'_{\text{bus}} = G'_{\text{bus}} + L/V_{\text{bus},i}(t) - g'_{\text{bus},i}$, otherwise the current signal for buses does not extend the green time.

(b) Red truncation

If the signal state is red when the i th bus arrives at the detectors (a, b, c, d) at time t , namely $S_{\text{bus}}(t) = r$, then the remaining red time in this approach can be calculated by $r'_{\text{bus},i}$, and the maximum red truncation allowed for buses is recorded as $\Delta r_{\text{bus}}^{\max}$.

If $r'_{\text{bus},i} > L/V'_{\text{bus},i}(t)$ and $r'_{\text{bus},i} - L/V_{\text{bus},i}(t) \leq \Delta r_{\text{bus}}^{\max}$, then to update the current red time for buses, which is given by $R'_{\text{bus}} = R_{\text{bus}} - [r'_{\text{bus},i} - L/V_{\text{bus},i}(t)]$, otherwise the current signal for buses does not truncate the red light.

In this article, the bus priority strategy based on bus speed, distance from the stop line and the remaining time is called "speed-distance" condition.

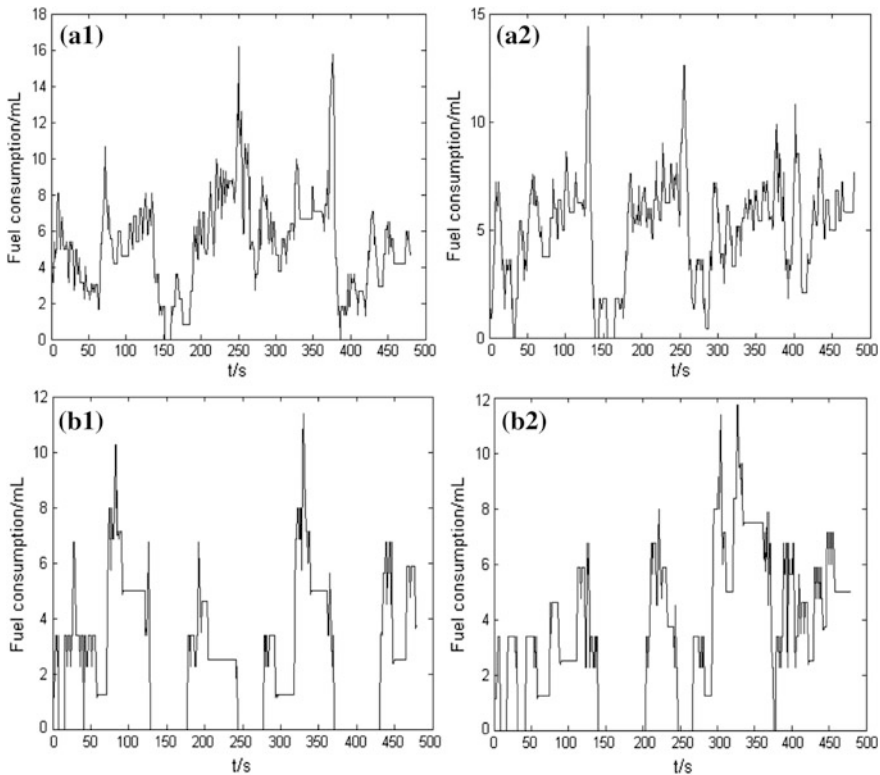


Fig. 2 Fuel consumption under different control strategies

4.3 Efficiency Indicators

In order to meet the actual congestion, the average index values of four cycles is used when calculating the ultimate indicators so as to observe the optimal rule of the various indicators. The simulation phase-sequence is set as follows: (1) east-to-west straight; (2) east-to-west left turn; (3) north-to-south straight; and (4) north-to-south left turn.

(a) Fuel consumption

The simulation results of fuel consumption are shown in Fig. 2. Among them Fig. 2a1 and a2 separately show the straight lane consumption with BSP strategy and no BSP strategy, and Fig. 2b1 and b2 separately show the bus lane consumption with the corresponding strategies. Through comparing figures, fuel consumption of the intersection also have cyclical characteristics. Fuel consumption indicator stays higher in green phase duration, while it stabilizes in a small range during the red time, and this is due to vehicles in the driving makes more consumption than idling vehicles.

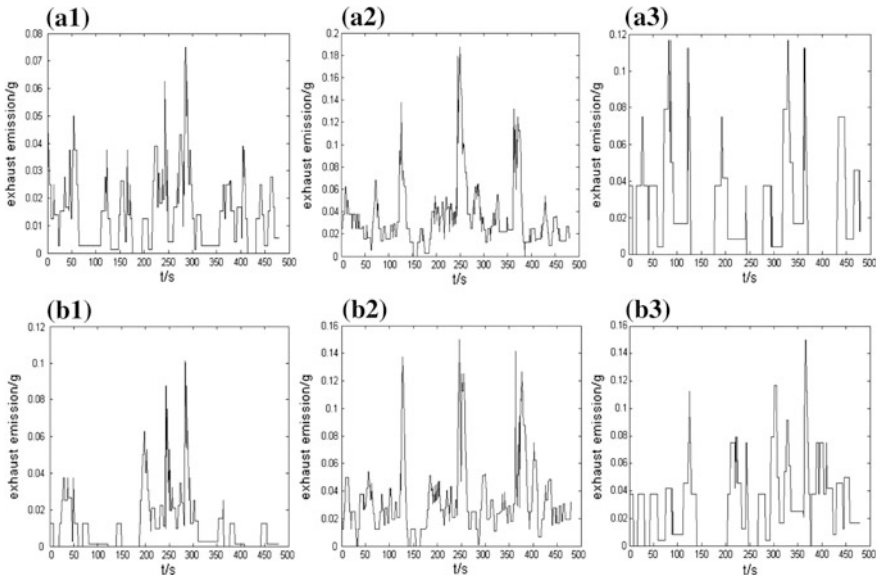


Fig. 3 Exhaust emissions under different control strategies

From Fig. 2, with the bus priority strategies, the lines paralleling to the horizontal axis obviously decreased, which means that buses and straight-line vehicles wait less time and go through the intersection more smoothly, resulting in higher fuel consumption.

(b) Exhaust emission

Exhaust emission is associated with vehicle type, traffic volume, delay time, travel time and whether vehicle driving or no, and it is calculated in two parts, in which one part is the exhaust emission from driving vehicles in motion and the other part is the exhaust emission from idling vehicles. From the simulation curves below, we can see vehicles exhaust more emissions during driving time. Figure 3a1–a3 separately show the left-turn lane, straight lane, and bus lane consumption with BSP strategy, and Fig. 3b1–b3 show the corresponding lanes consumption with no BSP strategy.

Through comparison of the indicators above, due to the calculation formula itself of fuel consumption and exhaust emissions, more idling vehicles waiting at the intersection, the less fuel consumption, and exhaust emissions they produced. However, this makes no expression that idling is an environment friendly way of driving, as the loss of time resources resulting from idling cannot be covered by the reduction of consumption and emissions. Thus, the determination of time using bus priority signal control under constrained conditions is necessary.

5 Conclusion

In this paper, the process of bus and general vehicles collaboration at signalized intersections with bus priority is studied by simulation. Balanced targets of consumption and emissions between different control strategies, the resource effects of bus priority strategies at intersections is analyzed, which is designed to provide theoretical supports and technical tools to bus priority strategies with higher comprehensive benefits.

Acknowledgments This study is supported by the Young Scientists Fund of the National Natural Science Foundation of China (71101008), the Key Project of Chinese National Programs for Fundamental Research and Development (973 program) (2012CB725403) and the Fundamental Research Funds for the Central Universities (2012JBM057) and the China Scholarship Fund.

References

1. Elias, Wilbur J (1976) The Greenback experiment-signal pre-emption for express buses: a demonstration project. California Department of Transportation, Sacramento, Report DMT-014
2. Ludwick JS (1976) Bus priority system: simulation and analysis. Final Report, the Mitre Corporation. Prepared for the U.S Department of Transportation, Report No.UTAVA-06-0026-1
3. Kui-hong G (2010) Research on bus priority signal coordination control and simulation in urban road intersections. Beijing Jiaotong University, Beijing (in Chinese)
4. Casey et al (1991) Advanced public transportation system: the state of the art, U. S. Department of Transportation Urban Mass Transportation Administration, Component of Department IVHS Initiative, Apr 1991
5. Jepson D, Ferrira L (2000) Assessing travel time impacts of measures to enhance bus operation. Part 2: study methodology and main findings. Road Transp Res 9(1):4-19
6. Ngan N, Sayed T, Abdelfatah A (2004) Impacts of various traffic parameters on transit signal priority effectiveness. J Public Transp (S1077-291X) 7(3):71-93
7. Shen-pei Z (2009) Research on traffic signal control strategies in urban intersections based on emission factors. Wuhan University of Technology, Wuhan (in Chinese)
8. Qiao-jun X (2000) Research on vehicle fuel consumption in the urban transportation system. Southeast University, Nanjing (in Chinese)
9. Bin J, Zi-you G, Ke-ping L et al (2007) Models and simulations of traffic system based on the theory of cellular automaton. Science Press, Beijing (in Chinese)
10. Lei Z (2010) Research of microscopic traffic simulation based on cellular automata and fuzzy control. Southwest Jiaotong University, Chengdu (in Chinese)

A Fast Gradual Shot Boundary Detection Method Based on SURF

Zhonglan Wu and Pin Xu

Abstract Video shot boundary detection is a key technology of content-based video retrieval, and has been extensively studied in these years. But researchers tend to sacrifice speed for a higher accuracy. To improve the performance of the algorithm and reduce the computational cost, Hue, Saturation, Value (HSV) histogram is introduced into the pre-processing of the video to output the candidate gradual shot segments. Then we use speeded up robust features (SURF) to detect the gradual shot boundaries. The experiment results show that the method can improve the speed with a high degree of accuracy.

Keywords Video retrieval · Gradual shot change · Shot boundary detection · HSV histogram · SURF

1 Introduction

With the rapid development of computer network and multimedia technology, digital videos have being gotten more and more extensive applications, people are increasingly concerned about how to retrieve the information they need from a bilious stream of videos. Therefore, It has become important that how to organize and retrieve the video information, especially in the field of database and information retrieval. The information retrieval which is based on textual data originally cannot meet the demand of the people. Because of the variety of the video data, the subjectivity of human when describing video content and the consuming time of generating text indexing manually, the content-based video retrieval technology emerges, and becomes more and more popular in the field of multimedia.

Z. Wu (✉) · P. Xu
Communication University of China, Beijing 100024, China
e-mail: m_orchid@126.com

The so-called video shot boundary detection is segmenting the video into many shots automatically and can determine the types of shot change. It is the first and most important step in content-based video retrieval. Because of the complexity of the scenes in the video, there are many approaches to implement the shot boundary detection. Such as the algorithm based on pixel comparison [1], the algorithm based on histogram [2], the algorithm based on edge features [3] and the algorithm based on compressed domain, such as the algorithm based on DCT coefficients [4] and the algorithm based on motion vectors [5].

Generally speaking, there are two kinds of shot change types, one is of shot abrupt change and the other is shot abrupt change. Yet many researchers tend to sacrifice the speed for a higher accuracy. For example, the paper [6] combines the correlation coefficient, YUV histogram difference and running average difference to detect the shot boundary, although it can achieve a good result, the overhead is huge. Speeded up robust features (SURF) is an improvement on Scale-invariant feature transform (SIFT). It has several good characteristics, such as high speed and stable algorithm. It also can detect more feature points. SURF can remain the same despite of rotations, scaling, illumination changes, and also can remain stable regardless of the changes of perspective, affine transform and noise. Therefore, we can use it to implement the video shot boundary detection. Yet it costs a lot of time if we use SURF for all the video frames. In order to improve the performance of the algorithm and reduce the computational cost, videos are firstly pretreated. Then we output the candidate gradual shot segments according to HSV (Hue, Saturation, Value) histogram blocks difference, and then extract the SURF of the candidate gradual shot segments and finally use the support vector machine (SVM) classification separator to implement the gradual shot boundary detection.

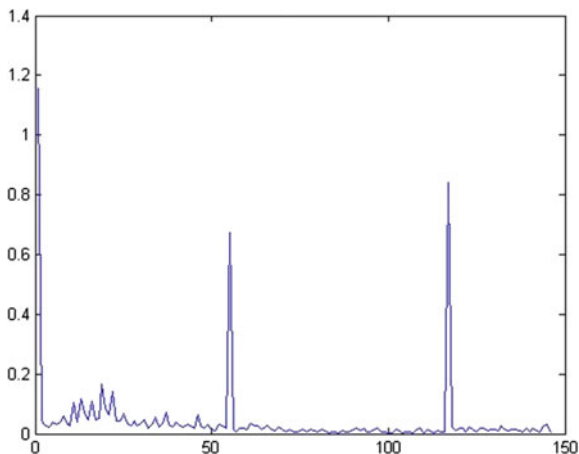
This paper is arranged as follows: [Sect. 2](#) is the pre-treatment, we use HSV histogram method to output the candidate gradual shot segments. [Section 3](#) introduces the gradual shot detection method. And [Sect. 4](#) is experience results, then comes the conclusion in [Sect. 5](#).

2 Pre-treatment

2.1 Frame Difference Measurement

The number of gradual shot frames is far less than the total number of frames in a video, and the difference of adjacent frames is very small in a shot. Therefore, if the difference between the first and the last frame in a short sequence of frames is very small, then we can consider that the shot may not contain any shot boundary and can be filtered. Based on this principle, we divide the video into many 11-frame sequences. Sequence N starts from frame $10 * N$ and ends with frame $10 * (n + 1)$, then we calculate the difference between the first and last frame in each 11-frame sequence.

Fig. 1 Lena quantization histogram



We use HSV spatial model to implement color features statistics. According to human visual resolving power, we divide the hue (H) into eight parts, the saturation (S) into three parts and value into three parts, and structure one-dimensional feature vector [7] (Fig. 1):

$$G = 9H + 3V + S; \tag{1}$$

Finally, we calculate the frame difference using chi-square distance of histogram G . The computational formula is as follows:

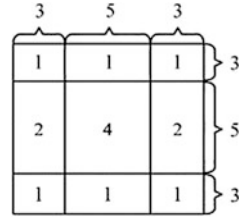
$$d^{10}(n) = \sum \frac{\{f(10(n+1)) - f(10n)\}^2}{f(10(n+1)) + f(10n)} \tag{2}$$

$d^{10}(n)$ is the difference between the first and last frame of each 11-frame sequence, $f(10n)$ is the histogram vector of G . Because using histogram to express the feature of a picture frame will lost spatial information of the pixels, so we firstly divide the image into many blocks. Considering that subtitles and advertisements always appear in the surrounding of the video frame while the important information is always concentrated in the middle part of the video frame, we use golden section strategy proposed in paper [8], it divides the image frame into nine parts non uniformity, as show in Fig. 2.

After that, we use the weighted sum of $d_i\{f(10(n+1)), f(10n)\}$ ($i = 1, 2, \dots, 8$) to express the frame difference between frame $f(10(n+1))$ and frame $f(10n)$, while $d_i\{f(10(n+1)), f(10n)\}$ is difference of block i between frame $f(10(n+1))$ and frame $f(10n)$. It is defined as follows:

$$D = \frac{\sum_{i=0}^8 d_i\{f(10(n+1)), f(10n)\} * w_i}{\sum_{i=0}^8 w_i} \tag{3}$$

Fig. 2 Blocks



2.2 Adaptive Local Threshold

For 11-frame segments, we use adaptive local threshold to determine whether it contains shot boundary or not. We firstly set a sliding window whose size is 10. Then we calculate the threshold T_L in a sliding window and use the threshold to determine whether there is a shot boundary. After that we move the sliding window to the next ten 11-frame segments to calculate next threshold and determine whether there is a segment which may contain a shot boundary. We do this repeatedly until the end of the video. The formula of threshold T_L is as follows:

$$T_L = 1.1U_L + 0.6\left(\frac{U_G}{U_L}\right)\sigma_L \tag{4}$$

U_L is the mean of the frame difference in a sliding window while σ_L is the standard deviation. U_G is the mean of the frame difference between the first and last frame of all the 11-frame segments. The sliding window is shown in Fig. 3.

In the practice application, we find that there may be some video segments which contain the shot boundaries but cannot be found by the algorithm below, because the frame difference between the first and last frame is less than the local threshold. Therefore, we introduce another formula to determine whether it is the segment which may contain a shot boundary:

$$(d^{10}(n) > 3d^{10}(n - 1) \cup d^{10}(n) > 3d^{10}(n + 1)) \cap d^{10}(n) > 0.8U_G \tag{5}$$

It is because that in this case, the frame difference is far less or more than the adjacent frames difference.

The 11-frame segments which meet the above conditions may contain shot boundaries and should be sent to further detect. Considering that abrupt shot change often happens between two frames while gradual shot change happens among many frames and this change can be identified by naked eyes. The 11-frame segment consists of 10 frames and it is less than 0.5 s, so we can consider that it always will have a shot boundary only in a 11-frame segment. Therefore, we consider that if the segment is independent and doesn't connect to other frame segments, it may be the candidate abrupt shot segment. And the 11-frame segments which are linked together may be the candidate gradual shot segments. We

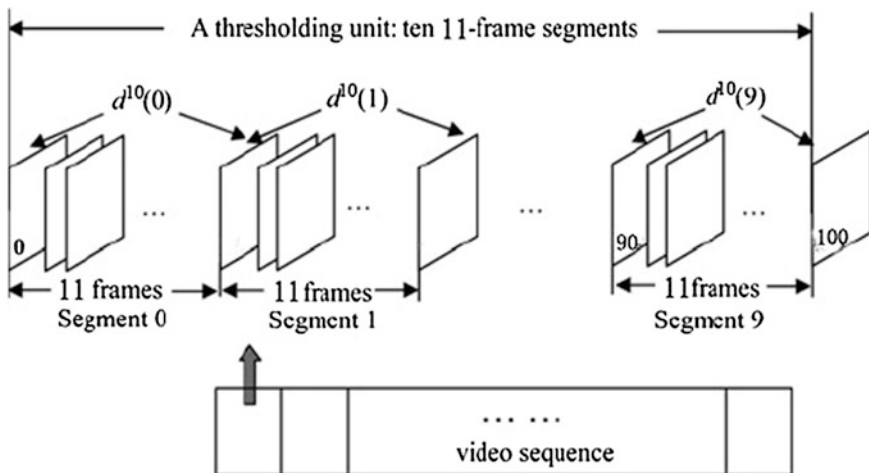
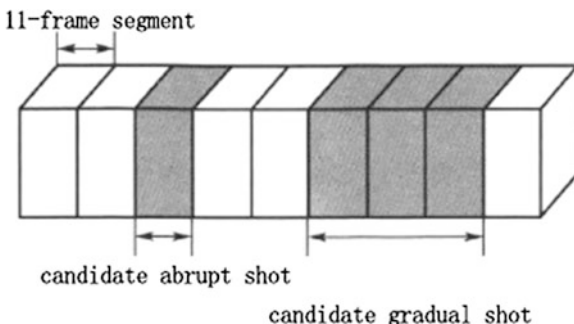


Fig. 3 Ten 11-frame segments

Fig. 4 Candidate abrupt and gradual shot



sent these segments for further detection to determine whether there is a shot boundary. As shown in Fig. 4.

3 The Detection of Gradual Shots

SURF is an improvement on SIFT. It has several good characteristics, such as high speed and stable algorithm. It also can detect more feature points. SURF can remain the same performance despite of rotations, scaling or illumination changes, and also can remain stable regardless of changes of perspective, affine transform, noise. And one important reason for shot false retrieval is the influence of illumination, object motion and camera motion. So we can use the algorithm

based on SURF to detect gradual shot. We compare the SURF between adjacent frames and use SVM to classify.

Statistical learning theory is a theory which studies machine learning pattern from small samples. SVM is based on VC dimension theory and the principle of minimize risk in machine learning theory. Sample space is mapped to a higher dimensional feature space and even an infinite dimensional feature space (Hilbert Space) by non linear mapping. Therefore, the nonlinear separable problem in original sample space can transfer into linear separable problem. SVM solves the problem of the dimensions cleverly and is specifically for the limited samples. Considering that, we use the SVM classification separator to implement the gradual shot boundary detection.

We firstly extract the SURF from candidate gradual shot segments and then implement the feature points matching between adjacent frames and calculate the number of matching feature points $S(f(n), f(n + 1))$, then we can get a vector $D_S(t)$. Finally, we use $D_S(t)$ as the input layer of SVM, and the output layer of SVM will be the type of shot change. $D_S(t)$ is defined as follows:

$$D_S(t) = \{S(f(0), f(1)), S(f(1), f(2)), \dots, S(f(n), f(n + 1))\} \quad (6)$$

We choose radial basis function (RBF) as the kernel function of SVM, that is

$$K(X_i, X_j) = \exp\left(-r\|X_i - X_j\|^2\right), \quad r > 0 \quad (7)$$

while X_i, X_j is the vector for training, r is the parameter of the kernel function.

4 Experiment Results

There is no good standard to evaluate the performance of shot boundary detection. Recall and precision are commonly used today. The recall and precision are defined as following:

$$\text{Recall} = \frac{N_c}{N_c + N_m} \quad (8)$$

$$\text{Precision} = \frac{N_c}{N_c + N_f} \quad (9)$$

N_c is the number of correct detections, N_m is the number of missed detection, N_f is the number of false detection. We test five videos to achieve the results. The results are shown in Table 1.

While R is the number of shots in a video and D is the number of shots we detect.

Table 1 Experience result

| Video | Frame num | Gradual shots (R/D) | Recall (%) | Precision (%) |
|---------|-----------|---------------------|------------|---------------|
| Video 1 | 899 | 4/4 | 100 | 100 |
| Video 2 | 643 | 3/3 | 100 | 100 |
| Video 3 | 809 | 3/3 | 100 | 100 |
| Video 4 | 688 | 0/1 | 100 | 88.9 |
| Video 5 | 779 | 3/4 | 100 | 90.9 |

Table 2 Drop rate

| Video | Video 1 | Video 2 | Video 3 | Video 4 | Video 5 |
|---------------|---------|---------|---------|---------|---------|
| Drop rate (%) | 87.6 | 90.6 | 87.5 | 93.0 | 89.6 |

To prove that the algorithm will reduce the computational cost, Table 2 is the ratio of the segments which don't contain the shot boundary and be filtered during the pretreatment.

We can conclude from the two tables below that the method can improve the speed with a high degree of accuracy.

5 Conclusion

In this paper, HSV histogram is introduced into the pre-processing of the video to output the candidate gradual shot segments. Then we use SURF to detect the gradual shot boundaries. The experiment results show that the method can improve the speed with a high degree of accuracy. But the precision is still not very satisfactory, we can try to use multi-feature algorithm to compensate for the surf feature in the future.

References

1. Zheng J, Zou F (2004) An efficient algorithm for video shot boundary detection. In: Proceedings of 2004 international symposium on intelligent, vol 2004, pp 266–269
2. Li S, Li J, Wang L, Wang J (2010) A shot boundary detection algorithm based on improving the twin-threshold method. *Microcomput Appl* 31(7):11–16 (in Chinese)
3. Zabih R, Miller J (1993) Automatic partitioning of full motion video. *Multimedia Syst* 1(1):10–28
4. Chen X, Sun T, Jiang X, Fang Z (2010) Threshold setting algorithm for video shot boundary detection based on dynamic training. *Comput Appl Softw* 27(1) (in Chinese)
5. Ma C, Huang B, Lu Z (2011) Shot boundary detection based on information of macroblocks movement. *Comput Eng Appl* 47(23) (in Chinese)

6. Hameed A (2009) A novel framework of shot boundary detection for uncompressed videos. *IEEE Emerg Technol* 274–279
7. Lin Q, Jiang W (2010) Approach of shot-boundary detection based on multi-feature fusion. *Comput Eng Appl* 46(13):171–174 (in Chinese)
8. Sun S, Zhuo L (2009) An adaptive double threshold shot boundary detection method based on cause an effect. *Meas Tech* 28(5) (in Chinese)

The Optimal Inventory Model of Two Warehouses: Time-Varying Demand Considering Credit Period

Yuntao Hu

Abstract It is assumed that the demand rate of goods is a time-varying function; meanwhile, suppose that OW and RW have different rate of deterioration and the limitation of continuous transportation is relaxed. Based on the assumptions, inventory models of two warehouses whose time-varying demand considering credit period are constructed, thus may have a widely application. Besides, the existence of the optimal replenishment strategy is proved by providing examples on calculating the optimal replenishment cycles and sensitivity analysis is also done on relevant parameters.

Keywords Inventory model • Credit period • Inventory model

1 Introduction

With the development of in-depth research on logistics and subdivision studies on the functions of logistics, inventory management, as a key subsystem of logistics system, is also making great progress in its research. In the narrow sense, inventory refers to the material stock in a temporary stagnation in a warehouse; in the broad sense, it also includes the product which are being manufactured, processed, and transported. In their models, Bose et al. [1] did research on linear demand and constructed inventory models allowing shortage and considering inflation and time discount. Hariga [2] discussed the optimization problems of inventory quantity of deteriorating items in the general time-varying demand situation. Hariga's model supposed that demand is a logarithmic concave function of time. Sark et al. [3] studied the optimization problems of inventory strategy of deteriorating items in

Y. Hu (✉)

Logistics Faculty, Chengdu University of Information Technology, Chengdu 610025, China
e-mail: huyuntao76@cuit.edu.cn

the time-varying demand and inflation situations. Chung and Tsai [4] considered the time value of money in the inventory model of deteriorating items in linear trend demand, therefore got the total cost of discount related with replenishment cycle numbers and time of shortage; meanwhile, the algorithm of the optimal replenishment cycle numbers and time of shortage had also been provided. Goyal and Giri [5] summed up the previous researches on deteriorating items.

Bhunia and Maiti [6] constructed two inventory models in which demand is a linear function of time and shortage was taken into consideration. In the case of allowing shortage, Zhou [7] put forward inventory models of two warehouses in which demand rate is a general time-varying function [8]. Lee and Ma [9] studied inventory models of two warehouses in the condition of a finite period of time-varying demand; besides the algorithm was given. Kar et al. [10] studied the models of two warehouses in the condition of linear demand. In the article, they supposed that economic size lot depends on replenishment cost. Recently, Lee and Hsu [11] studied the optimal inventory model in the situation of time-varying demand and limited productivity.

Almost all the articles above assumed that purchasers must pay immediately after the order; however, in actual life, if purchasers has a long-term cooperation with suppliers or purchasers would order a large amount of product for one indent, then suppliers would provide purchasers a credit period. Within the credit period, the purchasers need not pay for the goods; while beyond the credit period, the purchasers need to finish the payment. The interest revenue of the commodity sales during the credit period is shared by purchasers. Goyal [12] was the first to study the EOQ model of signal goods allowing deferred payment. Aggarwal and Jaggi [13], who extended Goyal's model, considered the inventory strategies of deteriorating items in the condition of deferred payment supposing both demand rate and rate of deterioration were constants. Jamal, Sarker and Wang [14] put forward a deferred payment model in the case of allowing shortage of goods. Hwang and Shinn [15], who considered pricing of retailers and order quantity under the premise of credit period, constructed a model in which interest, price of product, and credit period were interrelated; meanwhile, they proved the existence of the optimal order cycle which could maximize profit.

In this paper, the author supposes that two warehouses have different rates of deterioration and RW is given priority to use; besides, the author considers two conditions that suppliers offer a credit period to purchasers as well as purchasers to customers. [Section 2](#) introduces basic assumptions and symbolic representation, which provides the foundation to construct the inventory model. [Section 2.3](#) proposes the solving algorithm of the model. In [Sect. 3](#), the author provides numerical examples in order to verify the effectiveness of the model and the algorithm. Based on [Sect. 3](#), the [Sect. 4](#) provides sensitivity analysis. Finally [Sect. 5](#) concludes the whole paper.

2 Mathematical Modeling

2.1 Symbols

The symbols in this section are as follows:

W : The volume for OW;
 Q : Order Quantity;
 Q^* : optimal order quantity;
 $D(t)$: function of demand rate;
 a : deterioration rate of OW;
 b : deterioration rate of RW;
 T : length of order cycle;
 T^* : optimal replenishment cycle;
 A : ordering cost for one time;
 c : purchasing price for a unit of product;
 s : selling price for a unit of product;
 C_q : purchasing cost in a cycle;
 M : credit period of purchasers;
 N : credit period of customers;
 I_e : interest rate gained by purchasers by depositing money in a bank;
 IE : interest earned by purchasers in a cycle;
 I_p : interest rate of carrying inventory beyond credit period paid by purchasers;
 IP : interest paid by purchasers in a cycle;
 H_O : carrying charge in OW in every cycle;
 H_R : carrying charge in RW in every cycle;
 $TC_i(T)$: total cost of T in a specific interval in a unit of time ($i = 1, 2, \dots, 7$);
 $TC(T)$: total cost in a unit of time within a cycle;
 $TC(T^*)$: optimal cost in a unit of time within a cycle;
 t_w : time spent when inventory of RW decreases to 0;
 $I_o(t)$: stock level of OW in $[0, T]$;
 $I_{o,1}(t)$: stock level of OW in $[0, t_w]$ when using two warehouses;
 $I_{o,2}(t)$: stock level of OW in $[t_w, T]$ when using two warehouses;
 $I_r(t)$: stock level of RW in $[0, t_w]$ when using two warehouses;
 K : carrying charge for a unit of product in RW in a unit of time;
 H : carrying charge for a unit of product in OW in a unit of time;
 T_a : time spent when inventory of OW decreases from W to 0.

2.2 Basic Hypothesis

- (1) The time from orders to delivery is fixed;
- (2) Shortage is disallowed;
- (3) Deteriorating goods are totally lost and cleaned out from stock;

- (4) Suppliers offer a credit period M to purchasers; purchasers offers a credit period N to customers, $M > N$;
- (5) $I_p > I_e$;
- (6) When $T > M$, purchasers pay interest of inventory goods to suppliers after $T = M$; when $T \leq M$, purchasers need not pay interest to suppliers;
- (7) When $T > M$, purchasers can gain interest of the sold goods within $[0, M]$; When $T \leq M$, purchasers can gain interest of the sold goods within $[0, T]$;
- (8) Only when OW is full that RW is to be used and RW is given priority to use. OW and RW has different rate of deterioration, when deterioration occurs in OW , there isn't replenishment by transporting product in RW ;
- (9) The volume for OW is W and RW has limitless volume;
- (10) The stock is at the end of every cycle.

2.3 Modeling

Situation One: Only OW is used as shown in Fig. 1.

In this situation, the inventory curve satisfies the following differential equation:

$$\begin{cases} \frac{dI_o(t)}{dt} = -aI_o(t) - D(t), & 0 \leq t \leq T \\ I_o(T) = 0 \end{cases}$$

By solving the equation, we can get the inventory volume of OW within $[0, T]$:

$$I(t) = e^{-at} \int_t^T D(u)e^{au} du, \quad 0 \leq t \leq T,$$

Situation Two: Both OW and RW are used as shown in Fig. 2.

As the goods in RW are given priority to use, within $[0, t_w]$, the inventory in RW satisfies the following differential equation:

$$\begin{cases} \frac{dI_r(t)}{dt} = -bI_r(t) - D(t), & 0 \leq t \leq t_w \\ I_r(t_w) = 0 \end{cases}$$

By solving the above equation, we can get the inventory volume of RW within $[0, t_w]$:

$$I_r(t) = e^{-bt} \int_t^{t_w} D(u)e^{bu} du, \quad 0 \leq t \leq t_w,$$

Fig. 1 Inventory curve when only OW is used

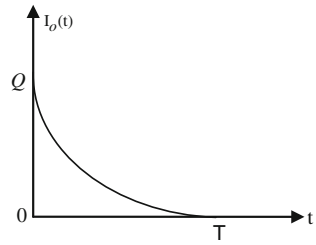
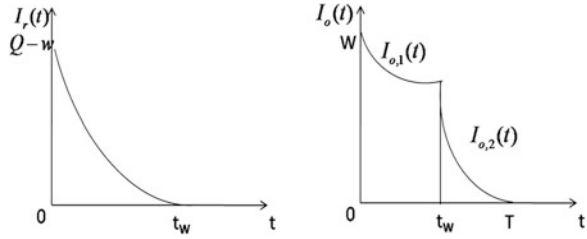


Fig. 2 Inventory Curve of OW and RW



Within $[0, t_w]$, the inventory volume of OW is lost by deterioration, which satisfies the following differential equation:

$$\begin{cases} \frac{dI_{o,1}(t)}{dt} = -aI_{o,1}(t), & 0 \leq t \leq t_w \\ I_{o,1}(0) = w \end{cases}$$

By solving the above equation, we can get the inventory volume of OW within $[0, t_w]$:

$$I_{o,1}(t) = we^{-at}, \quad 0 \leq t \leq t_w$$

Within $[t_w, T]$, inventory in OW are deteriorated and consumed, which satisfies the following differential equation:

$$\begin{cases} \frac{dI_{o,2}(t)}{dt} = -aI_{o,2}(t) - D(t), & t_w \leq t \leq T \\ I_{o,2}(T) = 0 \end{cases}$$

By solving them, we can get the inventory volume of OW within $[t_w, T]$:

$$I_{o,2}(t) = e^{-at} \int_t^T D(u)e^{au} du, \quad t_w \leq t \leq T$$

It is easy to know that $I_{o,1}(t_w) = I_{o,2}(t_w)$ and $w e^{-at_w} = e^{-at_w} \int_{t_w}^T D(u) e^{au} du$.

Calculation of Order Quantity:

Let $\int_0^{T_a} D(t) e^{at} dt = W$, then we know that: if and only if $T > T_a, Q > W$, then $Q = I_{o,1}(0) + I_r(0) = w + I_r(0) = w + \int_0^{t_w} D(u) e^{bu} du$; when $T \leq T_a, Q \leq W$, $Q = \int_0^T D(u) e^{au} du$, purchasing cost $Cq = A + cQ$.

Calculation of Carrying Charge of OW:

(1) When $T \leq T_a (Q \leq W)$, carrying charge will satisfy,

$$\begin{aligned} H_0 &= h \int_0^T I_o(t) dt = h \int_0^T e^{-at} \int_t^T D(u) e^{au} du dt \\ &= h \left[-\frac{1}{a} e^{-at} \int_t^T D(u) e^{au} du \right]_0^T - \int_0^T \frac{1}{a} e^{-at} D(t) e^{at} dt \\ &= \frac{h}{a} \left[\int_0^T D(u) e^{au} du - \int_0^T D(u) du \right] \\ &= \frac{h}{a} \int_0^T D(u) (e^{au} - 1) du \end{aligned}$$

(2) When $T > T_a (Q > W)$, carrying charge will satisfy,

$$\begin{aligned} H_0 &= h \left[\int_0^{t_w} I_{o,1}(t) dt + \int_{t_w}^T I_{o,2}(t) dt \right] \\ &= h \left[\int_0^{t_w} w e^{-at} dt + \int_{t_w}^T e^{-at} \int_t^T D(u) e^{au} du dt \right] \\ &= \frac{hw}{a} (1 - e^{-at_w}) + \frac{h}{a} \int_{t_w}^T D(t) [e^{a(t-t_w)} - 1] dt \end{aligned}$$

Calculation of Interest Paid by Purchasers:

(1) When $T \leq M$:

Interest Paid $IP = 0$

(2) When $t_w \leq M < T$, the interest paid will satisfy,

$$\begin{aligned}
 IP &= cI_p \int_M^T I_{o,2}(t) dt = cI_p \int_M^T e^{-at} \int_t^T D(u) e^{au} du dt \\
 &= \frac{cI_p}{a} \int_M^T D(t) [e^{a(t-M)} - 1] dt
 \end{aligned}$$

(3) When $M < t_w \leq T$, the interest paid will satisfy,

$$\begin{aligned}
 IP &= cI_p \left[\int_M^{t_w} I_r(t) dt + \int_M^{t_w} I_{o,1}(t) dt + \int_{t_w}^T I_{o,2}(t) dt \right] \\
 &= cI_p \left[\int_M^{t_w} e^{-bt} \int_t^{t_w} D(u) e^{bu} du dt + \int_M^{t_w} w e^{-at} dt + \int_{t_w}^T e^{-at} \int_t^T D(u) e^{au} du dt \right] \\
 &= cI_p \left[\frac{1}{b} \int_M^{t_w} D(t) (e^{b(t-M)} - 1) dt + \frac{w}{a} (e^{-aM} - e^{-at_w}) + \frac{1}{a} \int_{t_w}^T D(t) (e^{a(t-t_w)} - 1) dt \right]
 \end{aligned}$$

Calculation of Interest Earned by Purchasers:

(1) When $T \leq N$:

$$IE = sI_e(M - N) \int_0^T D(t) dt$$

(2) When $N < T \leq M$:

$$IE = sI_e(M - N) \int_0^N D(t) dt + sI_e \int_N^T D(t)(M - t) dt$$

(3) When $T > M$:

$$IE = sI_e(M - N) \int_0^N D(t) dt + sI_e \int_N^M D(t)(M - t) dt$$

Calculation of Total cost in a Unit of Time:

Total cost $TC(T)$ in a unit of time within $[0, T] = [\text{Purchasing cost} + \text{Carrying charge of OW} + \text{Carrying charge of RW} + IP - IE]/T$.

Case 1 For $T_a < N$, there are five situations as follow:

- (1) When $0 < T \leq T_a$, there is no need to use RW and to pay interest; at this moment, the total cost in a unit of time is marked as $TC_1(T)$.

$$TC_1(T) = \frac{1}{T} \left[A + c \int_0^T D(u)e^{au} du + \frac{h}{a} \int_0^T D(t)(e^{at} - 1)dt - sI_e(M - N) \int_0^T D(t)dt \right]$$

- (2) When $T_a < T \leq N$, RW needs using while there is no need to pay interest, at this moment the total cost in a unit of time is marked as $TC_2(T)$.

$$TC_2(T) = \frac{1}{T} \left\{ A + c \left(w + \int_0^{t_w} D(u)e^{bu} du \right) + \frac{hw}{a}(1 - e^{-at_w}) + \frac{h}{a} \int_{t_w}^T D(t) \left[e^{a(t-t_w)} - 1 \right] dt + \frac{k}{b} \left[\int_0^{t_w} D(t)e^{bt} dt - \int_0^{t_w} D(t)dt \right] - sI_e(M - N) \int_0^T D(t)dt \right\}$$

- (3) When $N < T \leq M$, RW needs using while there is no need to pay interest, at this moment the total cost in a unit of time is marked as $TC_3(T)$.

$$TC_3(T) = \frac{1}{T} \left\{ A + c \left(w + \int_0^{t_w} D(u)e^{bu} du \right) + \frac{hw}{a}(1 - e^{-at_w}) + \frac{h}{a} \int_{t_w}^T D(t) \left[e^{a(t-t_w)} - 1 \right] dt + \frac{k}{b} \left[\int_0^{t_w} D(t)e^{bt} dt - \int_0^{t_w} D(t)dt \right] - sI_e(M - N) \int_0^N D(t)dt - sI_e \int_N^T D(t)(M - t)dt \right\}$$

- (4) When $t_w \leq M < T$, RW needs using and interest needs paying, at this moment the total cost in a unit of time is marked as $TC_4(T)$.

$$TC_4(T) = \frac{1}{T} \left\{ A + c \left(w + \int_0^{t_w} D(u)e^{bu} du \right) + \frac{hw}{a}(1 - e^{-at_w}) + \frac{h}{a} \int_{t_w}^T D(t) \left[e^{a(t-t_w)} - 1 \right] dt + \frac{k}{b} \left[\int_0^{t_w} D(t)e^{bt} dt - \int_0^{t_w} D(t)dt \right] + \frac{cI_p}{a} \int_M^T D(t) \left[e^{a(t-M)} - 1 \right] dt - sI_e(M - N) \int_0^N D(t)dt - sI_e \int_N^M D(t)(M - t)dt \right\}$$

- (5) When $M < t_w \leq T$, RW needs using and interest needs paying, at this moment the total cost in a unit of time is marked as $TC_5(T)$.

$$\begin{aligned}
 TC_5(T) = & \frac{1}{T} \left\{ A + c \left(w + \int_0^{t_w} D(u)e^{bu} du \right) + \frac{hW}{a} (1 - e^{-at_w}) + \frac{h}{a} \int_{t_w}^T D(t) [e^{a(t-t_w)} - 1] dt \right. \\
 & + \frac{k}{b} \left[\int_0^{t_w} D(t)e^{bt} dt - \int_0^{t_w} D(t) dt \right] \\
 & + cI_p \left[\frac{1}{b} \int_M^{t_w} D(t) (e^{b(t-M)} - 1) dt + \frac{W}{a} (e^{-aM} - e^{-at_w}) + \frac{1}{a} \int_{t_w}^T D(t) (e^{a(t-t_w)} - 1) dt \right] \\
 & \left. - sI_e(M - N) \int_0^N D(t) dt - sI_e \int_N^M D(t)(M - t) dt \right\}
 \end{aligned}$$

When $T_a < N$, from the above discussion, we can get:

$$TC(T) = \begin{cases} TC_1(T) & 0 < T \leq T_a \\ TC_2(T) & T_a < T \leq N \\ TC_3(T) & N < T \leq M \\ TC_4(T) & t_w \leq M < T \\ TC_5(T) & M < t_w \leq T \end{cases}$$

Case 2 For $N \leq T_a < M$, there are five situations as follow:

- (1) When $0 < T \leq N$, the total cost in a unit of time is $TC_1(T)$.
- (2) When $N < T \leq T_a$, only OW is used and there is no need to pay interest, at this moment the total cost in a unit of time is marked as $TC_6(T)$.

$$\begin{aligned}
 TC_6(T) = & \frac{1}{T} \left\{ A + c \int_0^T D(u)e^{au} du + \frac{h}{a} \int_0^T D(u)(e^{au} - 1) du \right. \\
 & \left. - sI_e(M - N) \int_0^N D(t) dt - sI_e \int_N^T D(t)(M - t) dt \right\}
 \end{aligned}$$

- (3) When $T_a < T \leq M$, RW needs using and there is no need to pay interest, at this moment the total cost in a unit of time is marked as $TC_3(T)$.
- (4) When $t_w \leq M < T$ ($M < T \leq T1$), RW needs using and interest needs paying, at this moment the total cost in a unit of time is marked as $TC_4(T)$.

- (5) When $M < t_w \leq T (T > T1)$, RW needs using and interest needs paying, at this moment the total cost in a unit of time is marked as $TC_5(T)$. To sum up, when $N \leq T_a < M$:

$$TC(T) = \begin{cases} TC_1(T) & 0 < T \leq N \\ TC_6(T) & N < T \leq T_a \\ TC_3(T) & T_a < T \leq M \\ TC_4(T) & M < T \leq T1 \\ TC_5(T) & T > T1 \end{cases}$$

Case 3 For $T_a \geq M$, there are five situations as follow:

- (1) When $0 < T \leq N$, there is no need to use RW and to pay interest, at this moment the total cost in a unit of time is marked as $TC_1(T)$.
- (2) When $N < T \leq M$, there is no need to use RW and to pay interest, at this moment the total cost in a unit of time is marked as $TC_6(T)$.
- (3) When $M < T \leq T_a$, there is no need to use RW while interest needs paying, at this moment the total cost in a unit of time is marked as $TC_7(T)$

$$TC_7(T) = \frac{1}{T} \left\{ A + c \int_0^T D(u)e^{bu} du + \frac{h}{a} \int_0^T D(u)(e^{au} - 1) du + \frac{cI_p}{a} \int_M^T D(t) [e^{a(t-M)} - 1] dt - sI_e(M - N) \int_0^N D(t) dt - sI_e \int_N^M D(t)(M - t) dt \right\}$$

- (4) When $T > T_a, t_w \leq M (T_a < T \leq T1)$, RW needs using and interest also needs paying, at this moment the total cost in a unit of time is marked as $TC_4(T)$.
- (5) When $T > T_a, t_w > M (T > T1)$, RW needs using and interest also needs paying, at this moment the total cost in a unit of time is marked as $TC_5(T)$. Therefore, when $T_a \geq M$:

$$TC(T) = \begin{cases} TC_1(T) & 0 < T \leq N \\ TC_6(T) & N < T \leq M \\ TC_7(T) & M < T \leq T_a \\ TC_4(T) & T_a < T \leq T1 \\ TC_5(T) & T > T1 \end{cases}$$

Finally, according to the above three cases, it follows that

$$TC(T^*) = \begin{cases} \min \left\{ \min_{0 < T \leq T_a} TC_1(T), \min_{T_a \leq T \leq N} TC_2(T), \min_{N \leq T \leq M} TC_3(T), \min_{M \leq T \leq T_1} TC_4(T), \min_{T \geq T_1} TC_5(T) \right\}, T_a < N \\ \min \left\{ \min_{0 < T \leq N} TC_1(T), \min_{N \leq T \leq T_a} TC_6(T), \min_{T_a \leq T \leq M} TC_3(T), \min_{M \leq T \leq T_1} TC_4(T), \min_{T \geq T_1} TC_5(T) \right\}, N \leq T_a < M \\ \min \left\{ \min_{0 < T \leq N} TC_1(T), \min_{N \leq T \leq M} TC_6(T), \min_{M \leq T \leq T_a} TC_7(T), \min_{T_a \leq T \leq T_1} TC_4(T), \min_{T \geq T_1} TC_5(T) \right\}, T_a \geq M \end{cases}$$

3 Numerical Example

Let $w = 100$, $h = 1$, $k = 3$, $I_p = 0.08$, $I_e = 0.05$, $a = 0.05$, $b = 0.03$, $c = 100$, $s = 150$, $M = 0.25$, $N = 0.1$, $A = 400$, $D(t) = 1000e^{0.95t}$, according to the above cases, we can get $T_a = 0.0953$, so it follows that $T_a < N$. Then it can be known

$$TC(T^*) = \min \left\{ \min_{0 < T \leq T_a} TC_1(T), \min_{T_a \leq T \leq N} TC_2(T), \min_{N \leq T \leq M} TC_3(T), \min_{M \leq T \leq T_1} TC_4(T), \min_{T \geq T_1} TC_5(T) \right\}$$

There exists the optimal ordering cycle T^* , $T_1 = 0.325$; by use of Matlab, the results are shown in the Table 1.

From the Table 1, it can be found that the optimal replenishment cycle $T^* = 0.0869$, the optimal total cost $TC(T^*) = 107950$, the optimal ordering amount $Q^* = 90.78$. There is no need to use RW.

4 Sensitivity Analysis

To better understand the effects of changes of all parameters on the total cost in a unit of time, sensitivity analysis is done in this chapter. The analyzed parameters are as follows: rate of deterioration a and b , ordering cost A , purchasing price c , selling price s , carrying cost of OW h , carrying cost of RW k , interest paid I_e , interest earned I_p , credit period of purchasers M , credit period of customers N , demand rate $D(t)$. When sensitivity analysis is being done, only one parameter is changed for one time while others remain the same. The fluctuation ratio of the total cost of the model $PCI = \frac{TC^0 - TC^*}{TC^*}$ in which TC^0 represents the optimal total cost after changes of parameters TC^* represents the optimal total cost before changes of parameters. The analysis results can be seen in Tables 2, 3, 4, 5. When the value of A changes, the calculation result as follows:

From the above chart, when rate of deterioration of OW increases, the total cost also increases. When the value of b changes, the calculation result as follows:

From the above chart, when rate of deterioration of RW increases, the total cost remains the same because at this moment, the optimal inventory strategy refers

Table 1 Computing results

| Model | $\min_{0 < T \leq T_0} TC_1(T)$ | $\min_{T_1 \leq T \leq N} TC_2(T)$ | $\min_{N \leq T \leq M} TC_3(T)$ | $\min_{M \leq T \leq T1} TC_4(T)$ | $\min_{T \geq T1} TC_5(T)$ | $\min_{T > 0} TC(T)$ |
|-----------------------|---------------------------------|------------------------------------|----------------------------------|-----------------------------------|----------------------------|----------------------|
| Optis ^a | $T_1^* = 0.0869$ | $T_2^* = 0.0953$ | $T_3^* = 0.1$ | $T_4^* = 0.25$ | $T_5^* = 0.325$ | $T^* = 0.0869$ |
| Opt OA ^a | $Q_1^* = 90.78$ | $Q_2^* = 100$ | $Q_3^* = 105.17$ | $Q_4^* = 283.70$ | $Q_5^* = 383.29$ | $Q^* = 90.78$ |
| Min Cost ^a | $TC_1^*(T_1^*) = 107950$ | $TC_2^*(T_2^*) = 108000$ | $TC_3^*(T_3^*) = 108040$ | $TC_4^*(T_4^*) = 114760$ | $TC_5^*(T_5^*) = 119200$ | $TC^*(T^*) = 107950$ |

^a *Optis* = optimal solution, *Opt OA* = optimal ordering amount, *Min Cost* = the minimum cost

Table 2 Results under different a

| a (%) | T* | Q* | TC* | PCI (%) |
|-------|--------|-------|------------|---------|
| -20 | 0.0873 | 91.21 | 1.0790E+05 | -0.0463 |
| -10 | 0.0871 | 90.99 | 1.0793E+05 | -0.0185 |
| 10 | 0.0867 | 90.54 | 1.0797E+05 | 0.0185 |
| 20 | 0.0864 | 90.32 | 1.0800E+05 | 0.0463 |

Table 3 Results under different b

| b (%) | T* | Q* | TC* | PCI (%) |
|-------|--------|-------|------------|---------|
| -20 | 0.0869 | 90.77 | 1.0795E+05 | 0.0000 |
| -10 | 0.0869 | 90.77 | 1.0795E+05 | 0.0000 |
| 10 | 0.0869 | 90.77 | 1.0795E+05 | 0.0000 |
| 20 | 0.0869 | 90.77 | 1.0795E+05 | 0.0000 |

Table 4 Results under different N

| N (%) | T* | Q* | TC* | PCI |
|-------|--------|-------|------------|---------|
| -20 | 0.08 | 83.29 | 1.0783E+05 | -0.1112 |
| -10 | 0.0869 | 90.81 | 1.0787E+05 | -0.0741 |
| 10 | 0.0868 | 90.73 | 1.0803E+05 | 0.0741 |
| 20 | 0.0868 | 90.70 | 1.0811E+05 | 0.1482 |

Table 5 Results under different N

| D(t) | T* | Q* | TC* | PCI (%) |
|-----------------|--------|-------|------------|---------|
| $1000e^{0.85t}$ | 0.0917 | 95.63 | 1.0733E+05 | -0.5743 |
| $1000e^{0.75t}$ | 0.0962 | 100 | 1.0684E+05 | -1.0283 |
| $1000e^{0.65t}$ | 0.0967 | 100 | 1.0633E+05 | -1.5007 |
| $1000e^{0.55t}$ | 0.0976 | 100 | 1.0583E+05 | -1.9639 |

that there is no need to use RW. When the value of N changes, the calculation result as follows:

As the credit period given to customers by purchasers increases, the total cost in a unit of time also increases. When the value of $D(t)$ changes, the calculation result as follows:

From the above chart, as the demand rate increases, the total cost in a unit of time also increases and the ordering cycle shortens.

5 Conclusion

In this paper, based on different time-varying demand rate and different rate of deterioration, the author discusses the inventory strategy of two warehouses in the condition of allowing deferred payment, disallowance of shortage, and offering a credit period to customers. By means of the discussion, there exists an optimal replenishment cycle. Meanwhile, the author gives the numerical examples about solving the optimal replenishment cycle and the minimum cost. Finally, sensitivity analysis is done about the total cost in a unit of time concerning the changes of all parameters.

References

1. Bose S, Goswami A, Chaudhuri KS (1995) An EOQ model for deteriorating items with linear time—dependent demand rate and shortages under inflation and time discounting. *J Oper Res Soc* 46:771–782
2. Hariga MA (1996) Optimal EOQ model for deteriorating items with time-varying demand. *J Oper Res Soc* 47:1228–1246
3. Sarker BR, Jamal AMM, Wang SJ (2000) Supply chain models for perishable products under inflation and permissible delay in payment. *Comput Oper Res* 27(2):59–75
4. Chung KJ, Tsai SF (2001) Inventory systems for deteriorating items with shortages and linear trend in demand-taking account of time value. *J Oper Res Soc* 28(1):915–934
5. Goyal SK, Giri BC (2001) Recent trends in modeling of deteriorating inventory. *Eur J Oper Res* 134:1–16
6. Bhunia AK, Maiti M (1998) A two-warehouse inventory model for deteriorating items with a linear trend in demand and shortages. *J Oper Res Soc* 49:287–292
7. Zhou YW (1994) Comment on an economic order quantity model for items with two levels of storage for a linear trend in demand. *J Oper Res Soc* 43(7):721–724
8. Zhou YW (1997) An optimal EOQ model for deteriorating items with two warehouses and time-varying demand. *Mathematica Applicata* 10(2):19–23
9. Lee CC, Ma CY (2000) Optimal inventory policy for deteriorating items with two-warehouse and time-dependent demands. *Prod Plan Control* 11:689–696
10. Kar S, Bhunia AK, Maiti M (2001) Deterministic inventory model with two levels of storage, a linear trend in demand and a fixed time horizon. *Comput Oper Res* 28:1315–1331
11. Lee CC, Hsu S-L (2009) A two-warehouse production model for deteriorating inventory items with time-dependent demands. *Eur J Oper Res* 194:700–710
12. Goyal SK (1985) Economic order quantity under conditions of permissible delay in payments. *J Oper Res Soc* 36:335–338
13. Aggarwal SP, Jaggi CK (1995) Ordering policies of deteriorating items under permissible delay in payments. *European J Oper Res* 46:658–662
14. Jamal AMM, Sarker BR, Wang S (1997) An ordering policy for deteriorating items with allow- able shortage and permissibel delay in payment. *Eur J Oper Res* 48:826–833
15. Hwang H, Shinn SW (1996) Retailer's pricing and lot sizing policy for exponentially deteriorating products under the condition of permissible delay in payments. *Comput Oper Res* (6):539–547

Sampled-Data Synchronization for Chaotic Neural Networks with Mixed Delays

Rui-Xing Nie, Zhi-Yi Sun, Jian-An Wang and Yao Lu

Abstract This paper focuses on designing an appropriate sampled-data controller to deal with the problem of master–slave synchronization for chaotic neural networks with discrete and distributed time varying delays in the presence of a constant input delay. The striking feature of this article is that we utilize the decomposition approach of delay interval when constructing a new Lyapunov functional. Besides, combining with the input delay approach and the linear matrix inequalities (LMIs) method, the desired sampled-data controller gain can be obtained by using the Matlab software to solve a series of LMIs. Finally, a numerical example is provided to verify the effectiveness of the given results.

Keywords Master–slave synchronization · Chaotic neural networks · Sampled data controller · Lyapunov functional

1 Introduction

Since the master–slave (drive response) concept which was proposed by Pecora and Carroll in their pioneering work [1], researchers have spent considerable time and efforts to achieve the master–slave synchronization of chaotic neural networks with time delays. We must notice that it cannot be avoided generating time delays when the neuron transmitting signals during real application. Moreover, the advent of time delays will cause the neural networks' presented complicated and instable

R.-X. Nie · Z.-Y. Sun (✉) · J.-A. Wang · Y. Lu
School of Electronics Information Engineering, Taiyuan University of Science
and Technology, Taiyuan 030024, Shanxi, China
e-mail: sunzhiyi@263.net

R.-X. Nie
e-mail: xingxing135168@163.com

Table 1 Maximum sampling interval h for different η

| | | | | | |
|--------|------|------|------|------|------|
| η | 0.01 | 0.02 | 0.03 | 0.04 | 0.05 |
| h | 0.21 | 0.18 | 0.15 | 0.13 | 0.10 |

performance. In order to make the results more universal, many articles [2, 3] take the time delays into account while analyzing the chaotic neural networks. Compare with [2], the authors of [3] considered the time varying delays instead of constant time delays, and obtained less conservative results.

So far, various control schemes are applied to achieve the synchronization of chaotic neural networks, which include impulsive control [4], adaptive control [5], state feedback control [6], sampled data control [7], pinning control [8].

Among these control schemes, the sampled data control technology has enjoyed widespread adoption due to its own outstanding advantages. The sampled data controller takes up low communication channel capacity and has high resistance to anti-interference, which can accomplish the control task more efficiently. Thanks to the input delay approach [9], we can deal with the discrete term more easily. In [10], For the sake of getting sufficient exponential synchronization conditions, the authors made use of Lyapunov stability theory, input delay approach as well as linear matrix inequalities (LMI) technology. But this article did not take the signal transmission delay into account. To the best of the authors' knowledge, Little literature has been investigated the master–slave synchronization schemes for neural networks with discrete and distributed time varying delays using sampled-data control in the presence of a constant input delay, and still remains challenging.

From the foregoing discussions, the major thrust of the paper is to discuss the problem of master–slave synchronization for neural networks with mixed time varying delays (discrete and distributed delays) by utilizing sampled data control in the presence of a constant input delay. The desired sampled data controller can be obtained through computing some LMIs which depend on the Lyapunov functionals. The usefulness of input delay approach is also considered. Besides, the introduction of decomposition approach of delay interval will make our results less conservative. The proposed synchronization control scheme is verified through simulation results.

Notation: The notations which are used in this article are defined as: R^n and $=$ denote the n —dimensional Euclidean space and the set of all $m \times n$ real matrices, respectively. The notation $X > Y (X \geq Y)$, where X and Y are symmetric matrices, means that $X - Y$ is positive definite (positive semidefinite). I and 0 represent the identity matrix and a zero matrix, respectively. The superscript “ T ” denotes matrix transposition, and $\text{diag}\{\dots\}$ stands for a block diagonal matrix. $\|\cdot\|$ denotes the Euclidean norm of a vector or the spectral norm of matrices. For an arbitrary matrix B and two symmetric matrices A and C , $\begin{bmatrix} A & B \\ * & C \end{bmatrix}$ denotes a symmetric matrix, the “*” are symmetric elements that stand for the symmetric matrix. If the

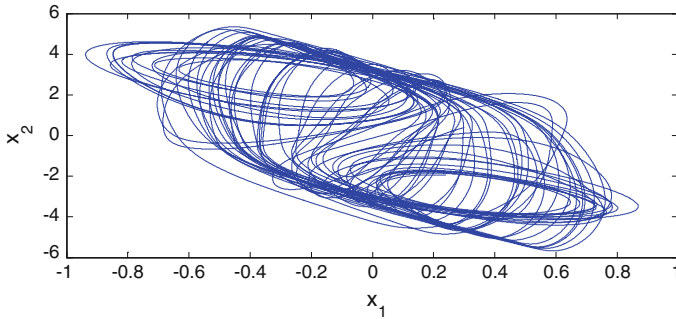


Fig. 1 Chaotic behavior of the master system (1)

dimensions of matrices are not particularly pointed out, we will deem the matrices have appropriate dimension for mathematical operations.

2 Model and Preliminaries

Consider a neural network with mixed delay as follow:

$$\dot{x}(t) = -Cx(t) + Af(x(t)) + Bf(x(t - \tau(t))) + D \int_{t-\sigma(t)}^t f(x(\theta))d\theta + J \quad (1)$$

where $x(t) = [x_1(t)x_2(t)x_3(t) \cdots x_n(t)]^T \in R^n$ and $f(x(k)) = [f_1(x_1(t))f_2(x_2(t))f_3(x_3(t)) \cdots f_n(x_n(t))]^T$ are, respectively, the state variable and the neuron activation function; $C = \text{diag}\{c_1, c_2, c_3, \dots, c_n\}$ is a diagonal matrix with positive entries; $A = (a_{ij})_{n \times n}$, $B = (b_{ij})_{n \times n}$, and $D = (d_{ij})_{n \times n}$, are, respectively, the connection weight matrix, the discretely delayed connection weight matrix and the distributedly delayed connection weight matrix; $\tau(t)$ denotes the time varying delay, and satisfies $0 \leq \tau(t) \leq \tau, \dot{\tau}(t) \leq u$; $\sigma(t)$ is expression of the distributed delay which is supposed to satisfied $0 \leq \sigma(t) \leq \sigma$. The mentioned definitions of τ, u and σ are constants.

With regard to the neuron activation function, the following hypotheses will come into play.

Assumption 1 There exists some constants $L_i^-, L_i^+, i = 1, 2, 3 \dots n$, such that the activation function $f(\cdot)$ is satisfied with $L_i^- \leq \frac{f_i(\vartheta_1) - f_i(\vartheta_2)}{\vartheta_1 - \vartheta_2} \leq L_i^+$ for ϑ_1, ϑ_2 , and $\vartheta_1 \neq \vartheta_2$.

In this paper, neural networks system (1) is deemed as the master system and a slave system for (1) will be designed as

$$\dot{y}(t) = -Cy(t) + Af(y(t)) + Bf(y(t - \tau(t))) + D \int_{t-\sigma(t)}^t f(y(\theta))d\theta + J + u(t) \quad (2)$$

where D, A, B and C are matrices as in (1), and $u(t) \in R^n$ is the control input to be designed.

The synchronization error signal is described as $e(t) = y(t) - x(t)$, then the error signal system can be exhibited as

$$\dot{e}(t) = -Ce(t) + Ag(e(t)) + Bg(x(t - \tau(t))) + D \int_{t-\sigma(t)}^t g(e(\theta))d\theta + u(t) \quad (3)$$

where $g(e(t)) = f(y(t)) - f(x(t))$.

In this paper, we define the updating signal time of Zero-Order-Hold (ZOH) by t_k , and assume that the updating signal (successfully transmitted signal from the sampler to the controller and to the ZOH) at the instant t_k has experienced a constant signal transmission delay η . Here, the sampling intervals are supposed to be less than a given bound and satisfy $t_{k+1} - t_k = h_k \leq h$.

The h represents the largest sampling interval. Thus, we can obtain that $t_{k+1} - t_k + \eta \leq h + \eta \leq d$.

The main aim of this paper is to achieve the synchronization of the master system (1) and slave system (2) together with the following sampled-data controller

$$u(t) = Ke(t_k - \eta), \quad t_k \leq t < t_{k+1}, \quad k = 0, 1, 2, \dots \quad (4)$$

where K is the sampled data feedback controller gain matrix to be determined.

Applying control law (4) into the error signal system (3)

$$\dot{e}(t) = -Ce(t) + Ag(e(t)) + Bg(x(t - \tau(t))) + D \int_{t-\sigma(t)}^t g(e(\theta))d\theta + Ke(t_k - \eta) \quad (5)$$

Defining $d(t) = t - t_k + \eta$, $t_k \leq t < t_{k+1}$, besides, $0 \leq d(t) \leq d$. Then error signal system can be described as the following condition

$$\dot{e}(t) = -Ce(t) + Ag(e(t)) + Bg(x(t - \tau(t))) + D \int_{t-\sigma(t)}^t g(e(\theta))d\theta + Ke(t - d(t)) \quad (6)$$

Next, we shall briefly introduce the lemmas which will be used in this paper.

Lemma 1 (Jensen inequality) [11] For any matrix $\omega > 0$, there existing scalars α and $\beta (\beta > \alpha)$, a vector function $\phi : [\alpha, \beta] \rightarrow R^n$ such that the integrations concerned are well defined, then

$$(\beta - \alpha) \int_{\alpha}^{\beta} \phi(\gamma)^T \omega \phi(\gamma) d\gamma \geq \left[\int_{\alpha}^{\beta} \phi(\gamma) d\gamma \right]^T \omega \left[\int_{\alpha}^{\beta} \phi(\gamma) d\gamma \right] \tag{7}$$

Lemma 2 (Extended Wirtinger inequality) [12] For any matrix $Z > 0$, if $\varphi(t) \in \omega[a, b]$ and $\varphi(a) = 0$, then following inequality holds:

$$\int_a^b \varphi(\zeta)^T Z \varphi(\zeta) d\zeta \leq \frac{4(b-a)^2}{\pi^2} \int_a^b \dot{\varphi}(\zeta)^T Z \dot{\varphi}(\zeta) d\zeta \tag{8}$$

Lemma 3 The constant matrix $Y \in R^{n \times n}$ is a positive definite symmetric matrix, if the positive scalar d is satisfied with $0 \leq d(t) \leq d$, and the vector-valued function $\dot{y} : [-d, 0] \rightarrow R^n$ is existent, then the integral term $-d \int_{t-d}^t \dot{y}^T(\zeta) Y \dot{y}(\zeta) d\zeta$ can be defined as

$$-d \int_{t-d}^t \dot{y}^T(\zeta) Y \dot{y}(\zeta) d\zeta \leq \begin{bmatrix} y(t) \\ y(t-d(t)) \\ y(t-d) \end{bmatrix}^T \begin{bmatrix} -Y & Y & 0 \\ * & -2Y & Y \\ * & * & -Y \end{bmatrix} \begin{bmatrix} y(t) \\ y(t-d(t)) \\ y(t-d) \end{bmatrix} \tag{9}$$

3 Main Results

In this section, a synchronization criterion will be presented which can make sure that the slave system (2) is synchronized with master system (1). Above all, we are going to divide the sampling interval into three parts, respectively, $[-\eta, 0]$, $[-\eta, -(\eta + \frac{h}{2})]$, $[-(\eta + h), -(\eta + \frac{h}{2})]$

$$\begin{aligned} \Sigma_{11} &= R_1 + R_2 - R_3 + Z_1 + Z_2 - F_1 V_1 - 2GC, \Sigma_{12} = P - \gamma GC - G - L_3 M \\ \Sigma_{15} &= F - GC, \Sigma_{19} = V_1 F_2 + GA, \Sigma_{22} = \tau^2 R_3 + \eta^2 Z_2 + \frac{h^2}{4} Z_4 + \frac{h^2}{4} Z_6 + h^2 W_1 - 2\gamma G \\ \Sigma_{25} &= G - \gamma F, \Sigma_{33} = (u - 1)R_1 - 2R_3 - F_1 V_2, \Sigma_{44} = -R_2 - R_3 \\ \Sigma_{55} &= -2Z_4 - \frac{\pi^2}{4} W + 2F, \hat{\Sigma}_{55} = -2Z_6 - \frac{\pi^2}{4} W + 2F \\ \Sigma_{56} &= Z_6 + \frac{\pi^2}{4} W, \Sigma_{66} = -Z_1 - Z_2 + Z_5 - Z_6 - \frac{\pi^2}{4} W \\ \Sigma_{77} &= Z_3 - Z_4 - Z_5 - Z_6, \Sigma_{88} = -Z_3 - Z_4, \Sigma_{99} = \sigma^2 Q - V_1 \end{aligned}$$

then the slave system (1) is synchronized with master system (2). Furthermore, the sampled data controller gain can be obtained by $K = G^{-1}F$.

Proof Construct a discontinuous Lyapunov functional for the error system (7)

$$V(t) = \sum_{j=1}^7 V_j(t), \quad t \in [t_k, t_{k+1}) \tag{12}$$

$$V_1(t) = e(t)^T P e(t) + 2 \sum_{i=1}^n m_i \int_0^{e_i} (g_i(\theta) - L_i \theta) d\theta$$

$$V_2(t) = \int_{t-\tau(t)}^t e(\theta)^T R_1 e(\theta) d\theta + \int_{t-\tau}^t e(\theta)^T R_2 e(\theta) d\theta + \tau \int_{-\tau}^0 \int_{t+\theta}^t \dot{e}(\theta)^T R_3 \dot{e}(\theta) d\theta d\xi$$

$$V_3(t) = \int_{t-\eta}^t e(\theta)^T Z_1 e(\theta) d\theta + h \int_{-\eta}^0 \int_{t+\theta}^t \dot{e}(\theta)^T Z_2 \dot{e}(\theta) d\theta d\xi$$

$$V_4(t) = \int_{t-(h+\eta)}^{t-(\eta+\frac{h}{2})} e(\theta)^T Z_3 e(\theta) d\theta + \frac{h}{2} \int_{-(h+\eta)}^{-(\eta+\frac{h}{2})} \int_{t+\theta}^t \dot{e}(\theta)^T Z_4 \dot{e}(\theta) d\theta d\xi$$

$$V_5(t) = \int_{t-(\eta+\frac{h}{2})}^{t-\eta} e(\theta)^T Z_5 e(\theta) d\theta + \frac{h}{2} \int_{-(\eta+\frac{h}{2})}^{-\eta} \int_{t+\theta}^t \dot{e}(\theta)^T Z_6 \dot{e}(\theta) d\theta d\xi$$

$$V_6(t) = \sigma \int_{-\sigma}^0 \int_{t+\theta}^t g(e(\theta))^T Q g(e(\theta)) d\theta d\xi$$

$$V_7(t) = (d - \eta)^2 \int_{t_k - \eta}^t \dot{e}(\theta)^T W \dot{e}(\theta) d\theta - \frac{\pi^2}{4} \int_{t_k - \eta}^{t - \eta} (e(\theta) - e(t_k - \eta))^T W (e(\theta) - e(t_k - \eta)) d\theta$$

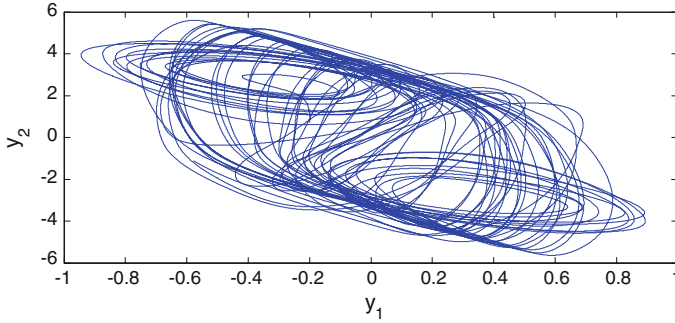


Fig. 2 Chaotic behavior of the slave system with $u(t) = 0$

$V_7(t)$ can be rewritten as

$$V_7(t) = (d - \eta)^2 \int_{t-\eta}^t \dot{e}(\theta)^T W \dot{e}(\theta) d\theta + (d - \eta)^2 \int_{t_k-\eta}^{t-\eta} \dot{e}(\theta)^T W \dot{e}(\theta) d\theta - \frac{\pi^2}{4} \int_{t_k-\eta}^{t-\eta} (e(\theta) - e(t_k - \eta))^T W (e(\theta) - e(t_k - \eta)) d\theta$$

$$M = \text{diag}\{m_1, m_2, \dots, m_n\} \geq 0$$

From the **Lemma 2**, we can infer $V_7(t) \geq 0$. Furthermore, $V_7(t)$ will vanish at $t = t_k$. Therefore, we can conclude that $\lim_{t \rightarrow t_k^-} V(t) \geq V(t_k)$.

Next, we will compute the derivative of $V(t)$ with the corresponding trajectory of system (6)

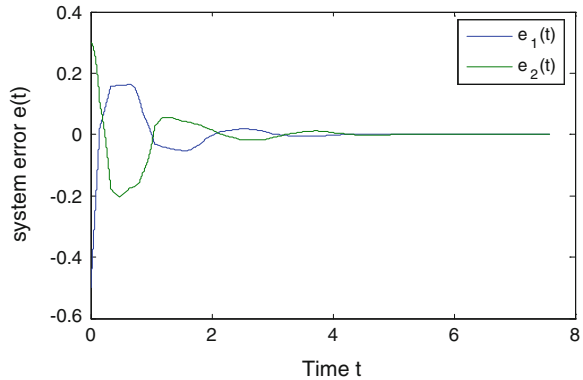
$$\begin{aligned} \dot{V}_1(t) &= 2e(t)^T P \dot{e}(t) + 2(g(e(t))^T - L_3 e(t)^T) M \dot{e}(t) \\ \dot{V}_2(t) &\leq e(t)^T R_1 e(t) + (u - 1)e(t - \tau(t))^T R_1 e(t - \tau(t)) + e(t)^T R_2 e(t) - e(t - \tau)^T R_2 e(t - \tau) \\ &\quad + \tau^2 \dot{e}(t)^T R_3 \dot{e}(t) - \tau \int_{t-\tau(t)}^t \dot{e}(\theta)^T R_3 \dot{e}(\theta) d\theta - \tau \int_{t-\tau}^{t-\tau(t)} \dot{e}(\theta)^T R_3 \dot{e}(\theta) d\theta \end{aligned}$$

According to **Lemma 1**

$$-\tau \int_{t-\tau}^t \dot{e}(\theta)^T R_3 \dot{e}(\theta) d\theta \leq \begin{bmatrix} e(t) \\ e(t - \tau) \end{bmatrix}^T \begin{bmatrix} -R_3 & R_3 \\ * & -R_3 \end{bmatrix} \begin{bmatrix} e(t) \\ e(t - \tau) \end{bmatrix} \tag{13}$$

Consequently, the following inequality holds

Fig. 3 State responses of error system



$$\begin{aligned} \dot{V}_2(t) &\leq e(t)^T R_1 e(t) + (u-1)e(t-\tau(t))^T R_1 e(t-\tau(t)) + e(t)^T R_2 e(t) - e(t-\tau)^T R_2 e(t-\tau) + \tau^2 \dot{e}(t)^T R_3 \dot{e}(t) \\ &\quad + \begin{bmatrix} e(t) \\ e(t-\tau(t)) \end{bmatrix}^T \begin{bmatrix} -R_3 & R_3 \\ * & -R_3 \end{bmatrix} \begin{bmatrix} e(t) \\ e(t-\tau(t)) \end{bmatrix} + \begin{bmatrix} e(t-\tau(t)) \\ e(t-\tau) \end{bmatrix}^T \begin{bmatrix} -R_3 & R_3 \\ * & -R_3 \end{bmatrix} \begin{bmatrix} e(t-\tau(t)) \\ e(t-\tau) \end{bmatrix} \\ \dot{V}_3(t) &\leq e(t)^T Z_1 e(t) - e(t-\eta)^T Z_1 e(t-\eta) + \eta^2 \dot{e}(t)^T Z_2 \dot{e}(t) + \begin{bmatrix} e(t) \\ e(t-\eta) \end{bmatrix}^T \begin{bmatrix} -R_3 & R_3 \\ * & -R_3 \end{bmatrix} \begin{bmatrix} e(t) \\ e(t-\eta) \end{bmatrix} \\ \dot{V}_4(t) &= e\left(t - \left(\eta + \frac{h}{2}\right)\right)^T Z_3 e\left(t - \left(\eta + \frac{h}{2}\right)\right) - e(t-(h+\eta))^T Z_3 e(t-(h+\eta)) + \left(\frac{h}{2}\right)^2 \dot{e}(t)^T Z_4 \dot{e}(t) \\ &\quad - \int_{t-(h+\eta)}^{t-(\eta+\frac{h}{2})} \dot{e}(\theta)^T Z_4 \dot{e}(\theta) d\theta + \left(\frac{h}{2}\right)^2 \dot{e}(t)^T Z_4 \dot{e}(t) - \int_{t-(h+\eta)}^{t-(\eta+\frac{h}{2})} \dot{e}(\theta)^T Z_4 \dot{e}(\theta) d\theta \\ \dot{V}_5(t) &= e(t-\eta)^T Z_5 e(t-\eta) - e\left(t - \left(\eta + \frac{h}{2}\right)\right)^T Z_5 e\left(t - \left(\eta + \frac{h}{2}\right)\right) + \left(\frac{h}{2}\right)^2 \dot{e}(t)^T Z_6 \dot{e}(t) \end{aligned}$$

According to **Lemma1** and **Lemma 3**, if $d(t) \in [-(h + \eta), -(\eta + \frac{h}{2})]$, then the following inequalities hold

$$- \int_{t-(h+\eta)}^{t-(\eta+\frac{h}{2})} \dot{e}(\theta)^T Z_4 \dot{e}(\theta) d\theta \leq \begin{bmatrix} e(t - (\eta + \frac{h}{2})) \\ e(t - d(t)) \\ e(t - (h + \eta)) \end{bmatrix}^T \begin{bmatrix} -Z_4 & Z_4 & 0 \\ 0 & -2Z_4 & Z_4 \\ 0 & 0 & -Z_4 \end{bmatrix} \begin{bmatrix} e(t - (\eta + \frac{h}{2})) \\ e(t - d(t)) \\ e(t - (h + \eta)) \end{bmatrix} \tag{14}$$

$$- \int_{t-(\eta+\frac{h}{2})}^{t-\eta} \dot{e}(\theta)^T Z_6 \dot{e}(\theta) d\theta \leq \begin{bmatrix} e(t - \eta) \\ e(t - (\eta + \frac{h}{2})) \end{bmatrix}^T \begin{bmatrix} -Z_6 & Z_6 \\ * & -Z_6 \end{bmatrix} \begin{bmatrix} e(t - \eta) \\ e(t - (\eta + \frac{h}{2})) \end{bmatrix} \tag{15}$$

If $d(t) \in [-(\eta + \frac{h}{2}), -\eta]$, we have similar inequalities.

$$\begin{aligned} \dot{V}_6(t) &= \sigma^2 g(e(t))^T Q g(e(t)) - \sigma \int_{t-\sigma}^t g(e(\theta))^T Q g(e(\theta)) d\theta \\ &\leq \sigma^2 g(e(t))^T Q g(e(t)) - \int_{t-\sigma}^t g(e(\theta))^T d\theta Q \int_{t-\sigma}^t g(e(\theta)) d\theta \\ \dot{V}_7(t) &\leq (d - \eta)^2 \dot{e}(t)^T W \dot{e}(t) - \frac{\pi^2}{4} \begin{bmatrix} e(t - \eta) \\ e(t_k - \eta) \end{bmatrix}^T \begin{bmatrix} -W & W \\ * & -W \end{bmatrix} \begin{bmatrix} e(t - \eta) \\ e(t_k - \eta) \end{bmatrix} \end{aligned}$$

Based on the error system (6), for any appropriately dimensioned matrices G_1 and G_2 , the following equations are true

$$\begin{aligned} 0 &= 2[e(t)^T G_1 + e(t_k - \eta)^T G_1 + \dot{e}(t)^T G_2] \left[-\dot{e}(t) - Ce(t) + Ag(e(t)) \right. \\ &\quad \left. + Bg(e(t - \tau(t))) + D \int_{t-\sigma(t)}^t g(e(\theta)) d\theta + Ke(t - d(t)) \right] \end{aligned} \tag{16}$$

where G_1 and G_2 are defined as $G_1 = G$, $G_2 = \gamma G$.

Besides, we can obtain from **Assumption 1** that for $j = 1, 2, 3, \dots, n$:

$$0 \leq \begin{bmatrix} e(t) \\ g(e(t)) \end{bmatrix}^T \begin{bmatrix} -L_j^- L_j^+ e_j e_j^T & -\frac{L_j^- + L_j^+}{2} e_i e_i^T \\ * & e_j e_j^T \end{bmatrix} \begin{bmatrix} e(t) \\ g(e(t)) \end{bmatrix} \tag{17}$$

where e_j stands for the unit column vector with 1 element on its j th row and zeros elsewhere. Therefore, the following inequality can be derived, for any appropriately dimensioned matrices $V_1 > 0$ and $V_2 > 0$.

$$0 \leq \left\{ \begin{bmatrix} e(t) \\ g(e(t)) \end{bmatrix}^T \begin{bmatrix} -L_1 V_1 & L_2 V_1 \\ * & -V_1 \end{bmatrix} \begin{bmatrix} e(t) \\ g(e(t)) \end{bmatrix} + \begin{bmatrix} e(t - \tau(t)) \\ g(e(t - \tau(t))) \end{bmatrix}^T \begin{bmatrix} -L_1 V_2 & L_2 V_2 \\ * & -V_2 \end{bmatrix} \begin{bmatrix} e(t - \tau(t)) \\ g(e(t - \tau(t))) \end{bmatrix} \right\} \tag{18}$$

Now substituting (16) and (18) to $\dot{V}(t)$, and letting $K = G^{-1}F$, then the following inequality will be achieved

$$\dot{V}(t) \leq \chi(t)^T (\Xi_k) \chi(t), \quad k = 1, 2 \tag{19}$$

where

$$z(t) = \left[e(t)^T \quad \dot{e}(t)^T \quad e(t - \tau(t))^T \quad e(t - v)^T \quad e(t - d(t))^T \quad e(t - \eta)^T \quad e(t - (\eta + \frac{h}{2}))^T \quad e(t - (\eta + h))^T \quad g(e(t))^T \quad g(e(t - \tau(t)))^T \quad \int_{t-\sigma(t)}^t g(e(\theta))^T d\theta \right]^T$$

Thus, based on (10) and (11), we can conclude that $\dot{V}(t) \leq -\zeta \|e(t)\|^2$ for a small scalar $\zeta > 0$.

According to the Lyapunov stability theory, it can be inferred that the slave system (2) is synchronized with the master system (1). This completes the proof.

Remark 1 A new synchronization criterion for the master system (1) and slave system (2) are introduced in Theorem 1 through constructing a novel Lyapunov functional. Numerous LMIs which are applied to derive sufficient conditions which can be calculated effectively by the Matlab LMI control toolbox.

Remark 2 Thanks to the term $V_7(t)$ as well as the decomposition method of delay interval, the sawtooth structure characteristic of sampling input delay is used properly, and the existing results will be improved significantly.

4 Numerical Example

In this simulation, we choose the activation functions as $f_1(s) = f_2(s) = \tanh(s)$. The parameters of master system (1) and slave system (2) are assumed as

$$C = \begin{bmatrix} 1 & 0 \\ 0 & 1 \end{bmatrix}, A = \begin{bmatrix} 1.8 & -0.15 \\ -5.2 & 3.5 \end{bmatrix}, B = \begin{bmatrix} -1.7 & -0.12 \\ -0.26 & -2.5 \end{bmatrix},$$

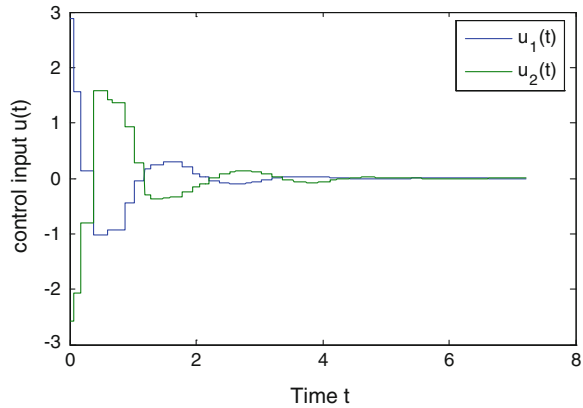
$$D = \begin{bmatrix} 0.6 & 0.15 \\ -2 & -0.12 \end{bmatrix}$$

It is clear that $L_1 = 0, L_2 = 0.5I$.

We suppose that $J = 0$, discrete delay $\tau(t) = \frac{e^t}{e^t + 1}$, distributed delay $\sigma(t) = 0.5 \sin^2(t)$. The other parameters are defined as $\tau = 1, u = 0.25$ and $\sigma = 0.5$. The initial values of master system and slave system are presented as $x(0) = [0.3 \quad 0.4]^T, y(0) = [-0.2 \quad 0.7]^T$, respectively. The chaotic behavior of the master system and the slave system without controller are given in Figs. 1 and 2, respectively.

While employing Theorem 1, we create Table 1 to show the relationship between the transmission delay η and the maximum values of sampling interval h . From Table 1, we can get the largest sampling interval $h = 0.21$ when the corresponding constant delay $\eta = 0.01$. Calculating the LMIs (10) and (11), the controller gain is presented as

$$K = \begin{bmatrix} -5.7352 & 0.0702 \\ 1.1632 & -6.6532 \end{bmatrix}$$

Fig. 4 Control input $u(t)$ 

Based on the mentioned controller gain, the response curves of control input (4) and system error (6) are exhibited in Figs. 3 and 4, respectively. Clearly, numerical simulations demonstrate that the designed controller can achieve master–slave synchronization.

5 Conclusions

In this paper, the problem of master–slave synchronization has been studied for chaotic neural networks with discrete and distributed time varying delays in the presence of a constant input delay. Based on the Lyapunov stability theory, input delay method as well as the decomposition approach of delay interval, we construct a new Lyapunov functional and derive the less conservative results. Ultimately, numerical simulations demonstrate the advantage and effectiveness of the obtained results.

References

1. Pecora LM, Carroll T (1990) Synchronization in chaotic systems. *Phys Rev Lett* 64:821–824
2. Yang XS, Zhu QX, Huang CX (2011) Lag stochastic synchronization of chaotic mixed time-delayed neural networks with uncertain parameters or perturbations. *Neurocomputing* 74:1617–1625
3. Wu ZG, Park JH, Su HY, Chu J (2012) Discontinuous Lyapunov functional approach to synchronization of time-delay neural networks using sampled-data. *Nonlinear Dyn* 69:2021–2030
4. Li XD, Rakkiyappan R (2013) Impulsive controller design for exponential synchronization of chaotic neural networks with mixed delays. *Commun Nonlinear Sci Numer Simulat* 18:1515–1523

5. Sun YH, Cao JD (2007) Adaptive lag synchronization of unknown chaotic delayed neural networks with noise perturbation. *Phys Lett A* 364:277–285
6. He GG, Shrimali MD, Aihara K (2007) Partial state feedback control of chaotic neural network and its application. *Phys Lett A* 371:228–233
7. Wu ZG, Park JH, Su HY, Chu J (2012) Discontinuous Lyapunov functional approach to synchronization of time-delay neural networks using sampled-data. *Nonlinear Dyn* 69:2021–2030
8. Li LL, Cao JD (2011) Cluster synchronization in an array of coupled stochastic delayed neural networks via pinning control. *Neurocomputing* 74:846–856
9. Fridmana E, Seuretb A, Richardb JP (2004) Robust sampled-data stabilization of linear systems: an input delay approach. *Automatica* 40:1441–1446
10. Zhang CK, He Y, Wu M (2010) Exponential synchronization of neural networks with time-varying mixed delays and sampled-data. *Neurocomputing* 74:265–273
11. Gu K, Kharitonov VK, Chen J (2003) *Stability of time-delay systems*. Birkhauser, Boston
12. Liu K, Suplin V, Fridman E (2011) Stability of linear systems with general sawtooth delay. *IMA J Math Control Inf* 27:419–436

The Design and Optimization of Inherent Frequency of Combined Triaxial High-g Accelerometer

Xu He, Zhenhai Zhang, Kejie Li, Ran Lin, Zhiqing Li,
Liang Zhang and Shuai Hou

Abstract The triaxial high-g accelerometer provides an effective solution to the accurate explosion positioning of the penetration weapon. The combined design type is the mainstream of the triaxial high-g accelerometer. Based on MEMS technology, the accelerometer has advantages of small volume and light quality. The combined structure determines that the overall stability of the accelerometer is influenced by every single chip. In order to improve the natural frequency of the chip and avoid the occurrence of resonance, an optimization method of the membrane-island structure, combined with mechanics of elasticity, is proposed in this paper. The optimization method is validated by finite element analysis and high shock calibration experiment. The rationality of the combined structure of the accelerometer is validated at the same time.

X. He (✉) · Z. Zhang (✉) · K. Li (✉) · R. Lin (✉) · Z. Li (✉) · L. Zhang (✉)
S. Hou (✉)
Beijing Institute of Technology, Beijing, China
e-mail: onimushahx@163.com

Z. Zhang
e-mail: zhzhang@bit.edu.cn

K. Li
e-mail: likj@bit.edu.cn

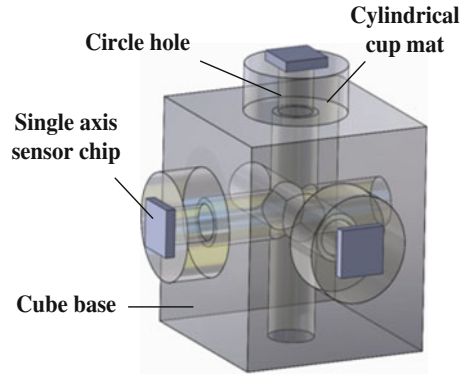
R. Lin
e-mail: 87355531@qq.com

Z. Li
e-mail: lizhiqingnanjing@126.com

L. Zhang
e-mail: 451612754@qq.com

S. Hou
e-mail: houshuaikd@qq.com

Fig. 1 The combined triaxial accelerometer



Keywords Triaxial accelerometer · High-g · Optimization · Natural frequency · MEMS{#,10}

1 Introduction

The triaxial high-g accelerometer has very important significance in the areas of explosion, high-impact experiment, and penetration weapon fuze research. Two kinds of structure styles are used in the development. One is single-chip integration, another is multi-chip combination. The technical difficulty of single-chip integration is how to solve the cross coupling between the coordinate data. The multi-chips combinations avoid the cross coupling between data because chips are high-g and independent of each other. It is shown in Fig. 1. Combining with the MEMS technology, it will greatly reduce the volume and quality [1]. The core component of combined triaxial high-g accelerometer is made up of three orthogonal assembly of the high-g accelerometer chip, so the natural frequencies of each chip directly affect the overall stability of the accelerometer. When the frequency of outside load system is in close proximity to chips' natural frequency, it produces chips resonance phenomenon, resulting in measurement data errors, even causes damage to the chip and the accelerometer. In order to avoid this situation, it is necessary to research the method of increasing the natural frequency of the chip. This optimization method improves the working frequency, broadens the bandwidth, and eliminates resonance phenomenon. Finally, the accelerometer is validated by high-impact calibration experiment [2] and can meet the use of requirements in high-impact experiment and penetration weapon fuze areas.

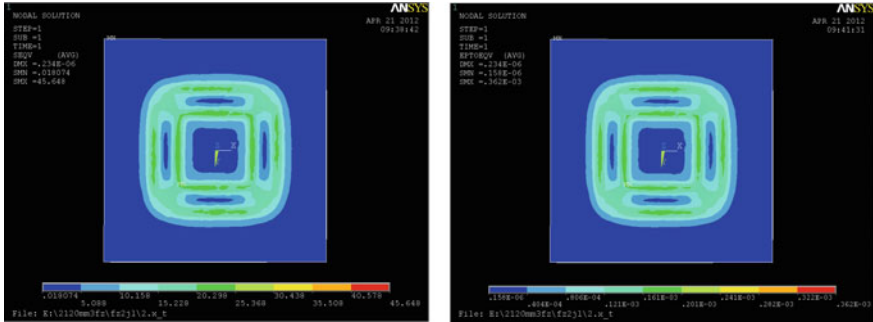


Fig. 2 The results of the simulation before optimization

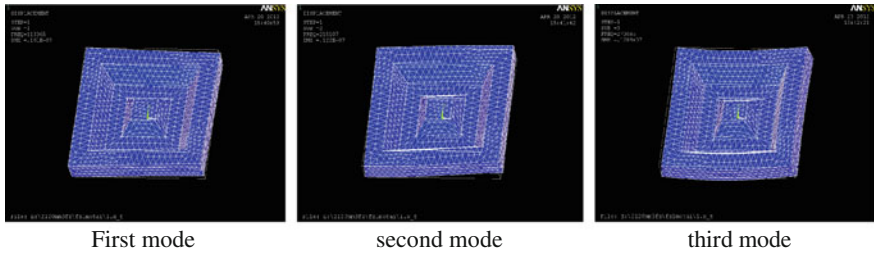
2 Analysis the Structure of the Accelerometer Before Optimization

2.1 Static Finite Element Analysis

The single-axis high-g accelerometer’s range is larger than 0.15×10^6 g and it is silicon. It uses a membrane-island structure with clamped boundary while the thickness of the island is slightly thinner than the silicon frame. The pressure-sensitive resistances are set on chip positive special location—this location is on the junctions of membrane and island and of membrane and framework, and these structures are processed by MEMS technology. This resistances form a Wheatstone bridge circuit.

The chip is chosen as the simulation object. The purpose of the simulation is to test whether the chip can be able to bear high-g impact. Parameters are set as follows. The density of silicon is 2.33×10^3 Kg/m³, young modulus of silicon is 130×10^3 MPa, Poisson ration of silicon is 0.18, and model element type is set to solid 45, 8 nodes, and 3D unit. The framework of chip’s back is set to fix and the z-axis direction of the chip is loaded 0.15×10^6 g gravity acceleration. The simulation results are shown in Fig. 2.

Figure 2 shows that the maximum of Vonmises stress is 45.648 MPa and the maximum of Vonmises strain is 362 $\mu\epsilon$. All these values are within a reasonable range, and less than the ultimate tension strength of silicon material. So the structure of the chip has good elastic properties and can work well in high shock environment.



| SET | TIME/PREQ | LOAD STEP | SUBSTEP | CUMULATIVE |
|-----|-------------|-----------|---------|------------|
| 1 | 0.11337E+06 | 1 | 1 | 1 |
| 2 | 0.21511E+06 | 1 | 2 | 2 |
| 3 | 0.27369E+06 | 1 | 3 | 3 |
| 4 | 0.44099E+06 | 1 | 4 | 4 |
| 5 | 0.49090E+06 | 1 | 5 | 5 |
| 6 | 0.54070E+06 | 1 | 6 | 6 |
| 7 | 0.72969E+06 | 1 | 7 | 7 |
| 8 | 0.79158E+06 | 1 | 8 | 8 |
| 9 | 0.82347E+06 | 1 | 9 | 9 |
| 10 | 0.84956E+06 | 1 | 10 | 10 |

Frequency of each mode

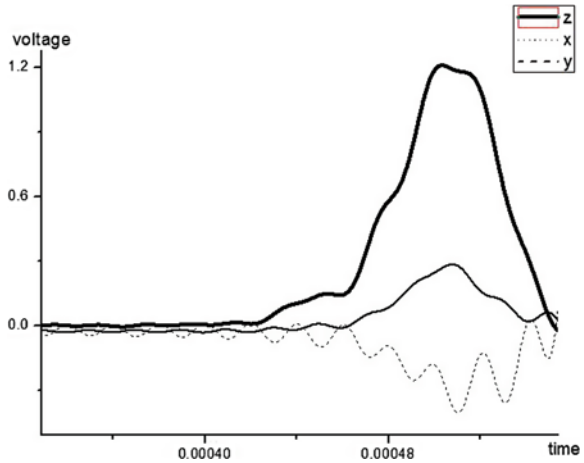
Fig. 3 The results of model simulation

2.2 Vibration Modal Analysis

Vibration is an ordinary phenomenon in mechanical system, but most of the systems are not expected to have resonant phenomenon. Because the resonance may destroy part of the structure, structural modal analysis is required to determine whether the design of the structure is reasonable [3]. Each order natural frequency and vibration mode of the model is got by the vibration analysis. The frequency bandwidth of the chip and structural stability is determined through the natural frequency value. The modal analysis results of the chip are shown in Fig. 3.

Figure 3 shows that first-order model is mainly the displacement of chip elastic unit along the z-axis and its frequency is 113.37 KHz; second-order model is mainly the rotation of chip elastic unit on the y-axis; and third-order model is mainly the torsion of chip elastic unit on the x-axis. In practice, the natural frequency determines the working frequency bandwidth. The higher natural frequency is, the wider working frequency is.

Fig. 4 The results of the experiment before optimization



3 High Shock Calibration Experiments Before Optimization

The combined triaxial high-g accelerometer is calibrated by using air cannon [4]. The results of high shock calibration experiment are shown in Fig. 4.

Figure 4 shows that the bold curve is the output voltage of z-axis data; black dash curve is the output voltage of x-axis data; dot curve is the output voltage of y-axis data. The nonlinear signal of z-axis data is shown in the figure, the main reason for this phenomenon is that chip is in resonance under high-impact environments. In order to avoid the occurrence of resonance, it is necessary to optimize the chip structure for improving its natural frequency.

4 The Theoretical Basis of Chip Structure Optimization

Accelerometer is a linear system and is independent of the time variable. Its output signal can be a good response to the input signal, and this requires accelerometer itself has a very good stability and wide working frequency band. The work frequency range is determined by natural frequency and damping ratio. The improvement of natural frequency may lead to increase the working frequency and improve the stability of the accelerometer [5]. According to the resonance phenomenon shown in Fig. 4, an optimizing method to the structure of the chip, combined with mechanics of elasticity, has been proposed.

The elastic movement of the high-g accelerometer chip is similar to mass-spring-damper mechanical system, so the natural frequency formula of mass-spring system can be used to analyze the movement of the simplified elastic unit of

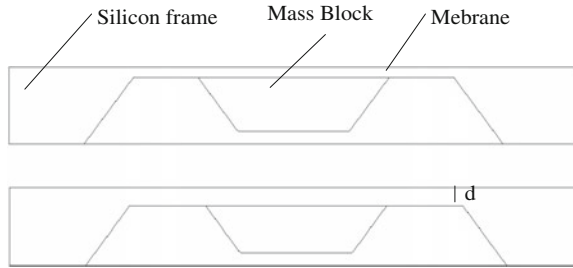


Fig. 5 Before optimization and after optimization

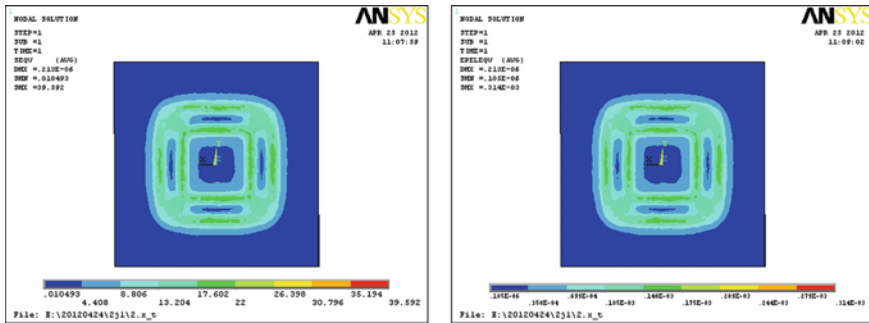


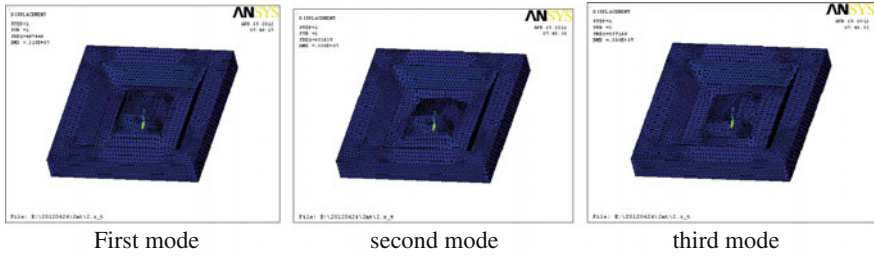
Fig. 6 The results of the simulation after optimization

chip. The formula is $f = 1/2\pi\sqrt{m/k}$, f is the vibration frequency, m is the mass, k is elastic coefficients and $k = WD/L^3$, D is bending stiffness; L is the length of the membrane, W is the width of the membrane. The elastic part of membrane-island structure is simplified to membrane structure, so the bending stiffness formula is $D = Eh^3/12(1 - \nu)$, E is the elastic modulus of silicon; h is the thickness of the membrane. It can be concluded that reduce mass quality and increase the thickness of the membrane can be improving the natural frequency of accelerometer. Optimization of the structure is shown in Fig. 5.

5 Analysis the Structure of the Accelerometer After Optimization

5.1 Static Finite Element Analysis

The optimized structure is analyzed by finite element analysis. All parameters are set as before. The results of the simulation are shown in Fig. 6.



***** INDEX OF DATA SETS ON RESULTS FILE *****

| SET | TIME/FREQ | LOAD STEP | SUBSTEP | CUMULATIVE |
|-----|-------------|-----------|---------|------------|
| 1 | 0.49745E+06 | 1 | 1 | 1 |
| 2 | 0.85364E+06 | 1 | 2 | 1 |
| 3 | 0.85717E+06 | 1 | 3 | 1 |
| 4 | 0.16926E+07 | 1 | 4 | 1 |
| 5 | 0.16943E+07 | 1 | 5 | 1 |
| 6 | 0.23371E+07 | 1 | 6 | 1 |
| 7 | 0.25754E+07 | 1 | 7 | 1 |
| 8 | 0.26408E+07 | 1 | 8 | 1 |
| 9 | 0.27623E+07 | 1 | 9 | 1 |
| 10 | 0.29035E+07 | 1 | 10 | 1 |

Frequency of each mode

Fig. 7 Model simulation results

Figure 6 shows that the maximum of Vonmisse stress is 39.592 MPa and the maximum of Vonmisse strain is 314 $\mu\epsilon$. All these values are within a reasonable range, and less than the ultimate tension strength of silicon material. So the structure of the chip has good elastic properties and can work well in high shock environment.

5.2 Vibration Modal Analysis

The modal analysis results of the chip are shown in Fig. 7.

Figure 7 shows that first-order model is mainly the deformation of chip elastic unit along the z-axis and its frequency is 497.45 KHz. The natural frequency of the optimized structure is greatly increased after optimization.

6 High Shock Calibration Experiments After Optimization

The stability of the accelerometer is validated by high-impact calibration experiment [6]. The results of high shock calibration experiment are shown in Fig. 8.

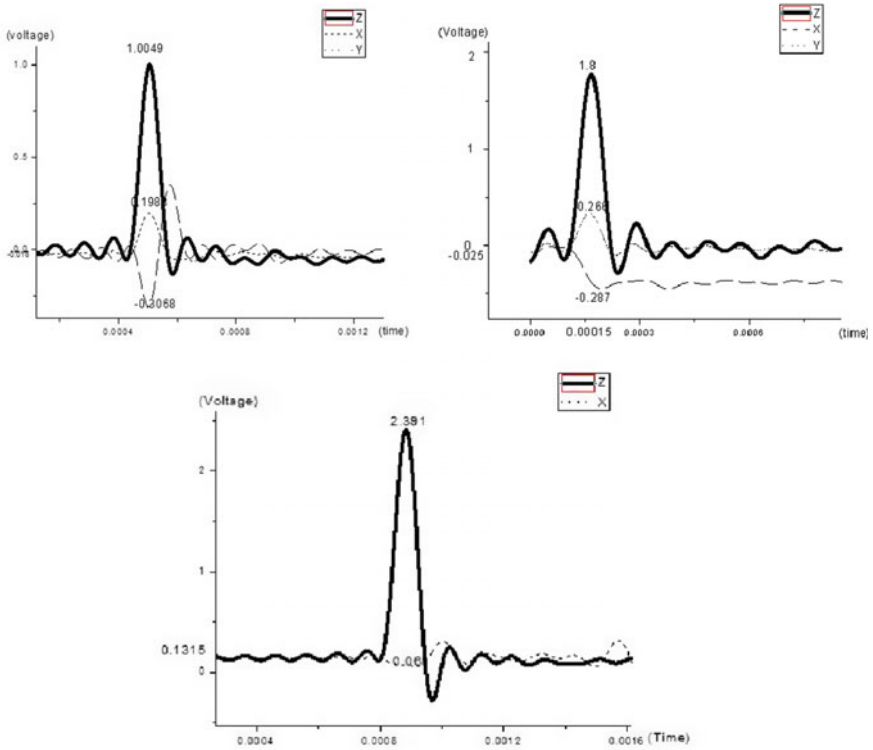


Fig. 8 The results of the experiment after optimization

Figure 8 shows that the output of the accelerometer is a complete linear signal and has no resonance phenomenon. Curves are very smooth, so this optimization method is effective, at the same time, the structure of the accelerometer is reasonable by the experiment.

7 Conclusions

The combined triaxial high-g accelerometer is mainly used in high-impact, penetration weapons field, and so on. The natural frequency of the chip directly affects the stability of the accelerometer. Therefore, research on the method to improve natural frequency of the accelerometer chip has important significance. The optimization methods have been proposed by analyzing accelerometer's structure and combined with mechanics of elasticity. The natural frequency of the accelerometer is increased by increasing the thickness of the membrane and reducing the mass block. Finally, the rationality of the optimized structure of the chip is verified by the finite element simulation and high shock calibration experiment. At

the same time, the optimization method is validated; by the way, the resonance phenomenon was eliminated. The accelerometer can work very well in the condition of high impact and penetration weapon fuze.

Acknowledgments This work was supported by the National Natural Science Foundation of China (Grant No. 61273346), the Specialized Research Fund for the Doctoral Program of Higher Education (Grant No. 20121101120009), the National Defense Major Fundamental Research Program of China (Grant No. C × × × 2011 × × 03), the National Defense Key Fundamental Research Program of China (Grant Nos. A × × × 2011 × × 05 and A × × × 20132010), the Excellent Young Scholars Research Fund of Beijing Institute of Technology (Grant No. 2012YG0203), the Program for the Fundamental Research of Beijing Institute of Technology (Grant Nos. 2013CX04031, 2011CX02023, and 20110242019), and the Program of Introducing Talents of Discipline to University, China (Grant No. B08043).

References

1. Zhang ZH, Li KJ, Ren XR, Liu J (2008) Design, simulation and optimization of sensing chip of high-g three-axis MEMS accelerometer. *Acta Armamentarii* 6:690–696
2. Zhu ZQ, Shi YB, Liu XP, Zhang Q (2009) Penetration test of high-g micro accelerometer. *Electron Des Eng* 17:53–54
3. Shi YB, Zhu ZQ, Liu XP, Du K, Liu J (2010) Design and impact analysis of a high-g accelerometer. *Explo Shock Waves* 30:329–332
4. Fan JB, Zu J, Lin ZS, Xu P, Zhao XD (2012) Shock calibration for a high-g accelerometer using a laser interferometer. *J Vib Shock* 31:149–153
5. Li P, Shi YB, Zhu ZQ, Du K, Liu J (2013) An optimization method for natural frequency of MEMS high-g accelerometer. *Chin J Sens Actuators*. 23:388–392
6. Wang WJ, Hu SP (2006) Calibration of high shock accelerometers. *Explo Shock Waves* 26:568–571

Design and Simulation of Variable Pitch Control System Based on Fuzzy Model Reference Adaptive

Hongche Guo, Manjia Hu, Tao Li and Gangqiang Li

Abstract This paper focuses on large wind turbine hydraulic variable pitch system, in allusion to the limitations of traditional PID controller, and controls characteristics and performance requirements of variable pitch system, variable pitch system is controlled with the fuzzy model reference adaptive control strategies, its adaptive mechanism is a flexible structured fuzzy logic controller (flexible structured fuzzy logic controller-FS-FLC). This system has both simple structure of a general feedback control system and good ability of adaption. Besides, using FS-FLC as an adaptive mechanism improves the robustness and tracking accuracy of the control system. Simulation results show that the design improves the stability of the system output power, and has good control quality and robustness.

Keywords Wind turbine · Variable pitch · Reference model · Fuzzy adaptive · Flexible structure

1 Introduction

With the increasing unit capacity of wind turbines, variable speed pitch fan is widely used [1, 2]. The wind turbine output power is instable because of the randomness of the wind speed, time variability of the unit's parameters, and the nonlinear property of system and strong coupling property of the system [3]. Therefore, it is very important to control the stability of the output power of the

H. Guo (✉) · M. Hu
Hunan Institute of Science and Technology, Yueyang 414006, China
e-mail: hongchegu@163.com

T. Li · G. Li
Jinan Railway Vehicles Equipment CO., LTD, Jinan 250022, China

wind turbine. By adjusting the blade pitch and changing the angle of attack of the airflow to the blades, the starting torque is provided by the pitch control system during the start-up process of the wind generator, and the aerodynamic torque is obtained by changing the wind power generator when the wind velocity is too high, thereby the pitch control system can maintain unit power output constant.

The pitching system has two forms including motor drive and hydraulic drive, the hydraulic variable pitch technology is slightly simpler than electric variable pitch in terms of the overall composition. The function of hydraulic brake can be integrated into the same hydraulic system to achieve this branch function when using the hydraulic variable pitch technology. The electric variable pitch technology needs configure additional hydraulic braking system to achieve this branch function. Compared with the electric variable pitch system, for hydraulic variable pitch system, the hydraulic drive's unit volume is smaller, has lighter weight, better dynamic response, larger torque, and without the transmission mechanism. When the power loss, full feathering propeller can be done on the blade taking the accumulator as an alternate power source without designing a backup power supply.

Traditional PID control method is widely used with its simple algorithm, high reliability in the control of wind power, but its adaptive ability is poor and it is difficult to achieve the desired controlling effect [4]. Fuzzy controller does not rely on an accurate model of the controlled object, can have both static and dynamic performance of the system, and show good control quality and robustness [5]. According to the own characteristics and operational characteristics of the wind turbine, a fuzzy model reference adaptive control strategy, which is applied to hydraulic pitch system is proposed in this paper, can improve the stability of the wind turbine output power.

2 The Design of Fuzzy Adaptive Variable Pitch Control System

2.1 Characteristics of Wind Turbine

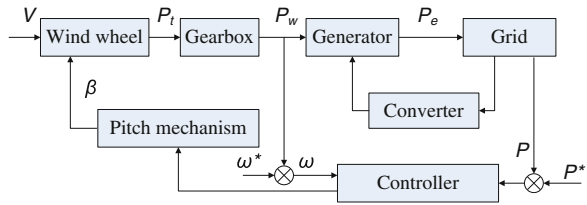
Structure of variable speed-variable pitch wind turbine is shown in Fig. 1. It is constituted mainly by the wind wheel, gear box, generator, variable pitch adjusting mechanism, grid, controller, and inverter.

The relationship between output power of the wind turbine and wind speed is:

$$P_r = \frac{1}{2} \rho \pi R^2 C_p(\lambda, \beta) v^3. \quad (1)$$

The relationship between wind energy, wind turbine output torque, and wind speed is:

Fig. 1 Structure of variable speed-variable pitch wind turbine



$$T_r = \frac{1}{2} \rho \pi R^2 C_q(\lambda, \beta) v^2. \tag{2}$$

where C_p is wind energy coefficient, C_q is torque coefficient, and the relationship between the both is:

$$C_p(\lambda, \beta) = \lambda C_q(\lambda, \beta) \tag{3}$$

where λ —tip speed ratio of the wind turbine, v —wind velocity, ρ —air density, R —the radius of rotation of the wind wheel, β —the paddle angle.

2.2 Fuzzy Model Reference Adaptive Control

In order to solve the problem of the control system caused by parameter variations and external disturbance, which make the system performance unstable, adaptive control is often used. Fuzzy control is a simple and practical control method, it does not need mathematical model and parameters of the controlled object, and have uncertainty on object parameter and adaptability on nonlinear, so using a fuzzy adaptive mechanism that can replace the complex conventional adaptive institutions is considered to implement adaptive control.

In Fig. 2, the FMRAS [6] is a dynamic control strategy for variable pitch hydraulic servo system. The system consists of the controlled object, reference model, fuzzy adaptive mechanism, and general proportional adjustment. Hydraulic servo system is the controlled object; reference model is used to produce the desired output response of the hydraulic servo system; fuzzy adaptive mechanism is a fuzzy controller with flexible structure [7, 8], which produce a fuzzy adaptive signal on the basis of the difference between the output of the reference model and the output of the controlled object and the change rate, applying on the controlled object, and making its output tends to be the output of the reference model; proportional adjustment is used to improve the response speed of the system, the values of which are selected according to the performance system requirement.

Figure 3 shows the variable pitch system’s configuration diagram of the entire control system, the pitch angle of the blades need to be planned offline in advance. As design structures of three hydraulic servo systems in the variable pitch system are exactly the same, the tracking reference model can be selected the same, and

Fig. 2 Block diagram of fuzzy model reference adaptive system

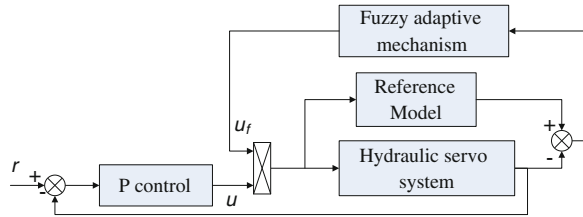
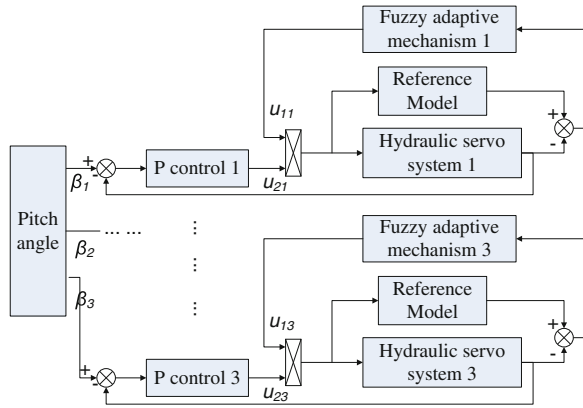


Fig. 3 Variable pitch system's configuration diagram of control system



the selection of reference model can be based on the variable pitch hydraulic servo system dynamics model and ideal parameters. When the parameters of variable pitch system change or uncertain due to movement or external disturbances, three dynamic characteristics of the servo systems tend to be the same with the effect of fuzzy adaptive mechanism. As a result, the fan blade will move harmonically, run smoothly, and have good tracking accuracy. The control system has characteristics such as simple structure, convenient design, and easy to realize real-time and online. It not only maintains the structural characteristics of the general feedback control system, but also has a certain degree of adaptation function.

2.3 Fuzzy Adaptive Mechanism of Soft Structure

Fuzzy controller (FLC), which is widely used in the field of, is proposed by Mamdani and his aides, so it is also called the FLC of Mamdani type. Its regulation relies mainly on the adjusted front member and the membership function of rear member. Some researchers adjust by modifying scale factor, quantizing factor. Fuzzy control rules is a summary of the controlled object fuzzy information and operating experience, when there are factors on controlled object, such as non-linear, uncertainties, and coupling, it is difficult to obtain perfect control rules,

which will affect the control performance. Parameterized set operator is used in Mamdani-type FLC by the flexible structure of the fuzzy controller, which can refine and improve the fuzzy control rules flexibly. In general, it is a promotion and integration of Mamdani-type FLC.

(1) *Mamdani-type FLC(M-FLC)*

Assuming a FLC with multiple-input single-output, its fuzzy control rules can be described as:

$$\text{IF } U_1 = B_{i1} \text{ AND } \dots \text{ AND } U_r = B_{ir} \text{ THEN } V = D_i, \quad i = (1, 2, \dots, m).$$

The B_{ij} is the former fuzzy subset of r inputs, D_i is the latter fuzzy subset of the output variable V . For the convenience, $B_{ij}(x)$, $D_i(y)$ denote the membership function of the fuzzy subset separately, the domain of B_{ij} is $X_j, j = (1, 2, \dots, r)$, the domain of V is the finite set Y , assumed, the dimension of X_j and Y respectively is $\text{Card}(X_j) = PJ$ $\text{Card}(Y) = q$, Mamdani's inference method can be integrated as four laws:

(A1) Synthesis logical AND of the former's fuzzy rules is expressed by set operator MIN (\wedge), the trigger level of the i th fuzzy rules is:

$$\tau_i = B_{i1}(u_1) \wedge \dots \wedge B_{ir}(u_r).$$

(A2) The composite operator of former and latter is determined by the set operator MIN (\wedge), the effective output of the i th fuzzy rule is:

$$F_i(y) = \tau_i \wedge D_i(y).$$

(A3) The logical OR is expressed by the set operator MAX (\vee), the output F of controller is:

$$F(y) = \bigvee_{i=1}^m F_i(y) = \bigvee_{i=1}^m \tau_i \wedge D_i(y).$$

(A4) Defuzzification with the center of area (COA) method or the maximum average method (MOM):

$$y^{\text{COA}} = \frac{\sum_{j=1}^q F(y_j)y_j}{\sum_{j=1}^q F(y_j)}$$

$$y^{\text{MOM}} = \sum_{y_j \in G} y_j / l$$

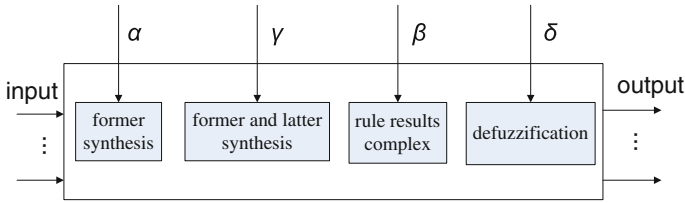


Fig. 4 Flexible structure fuzzy controller

where Y_j is the great basis points value which membership function reached, l is the number of basis points.

(2) *FS-FLC theory*

Set operators AND and OR in Mamdani method are replaced with set operators S-OWA-AND, S-OWA-OR, S-OWA-PRODUCT, and defuzzification is applied in step A4 with BADD method.

Parameters of flexible fuzzy controller can be fully adjusted and may also be partially adjusted, and its structure is shown in Fig. 4. Taking this FS-FLC as institutions of variable pitch system fuzzy model reference adaptive control strategy, and it will enhance its ability regulation and obtain better dynamic control performance.

3 Research of Simulation

Taking the variable pitch system single-channel hydraulic servo system as controlled object, then simulate and analyze. The input and output variables of fuzzy adaptive institutions are:

$$E_i = yd_i - yk_i, E_i \in X$$

$$\Delta E_i = E_i - E_{i-1}, \Delta E_i \in Y$$

$$u_i = u_i, u_i \in Z$$

where i is the sampling time of FLC, X, Y, Z are the domain of discourse of input and output variable,

$$X = \{-6, -5, -4, -3, -2, -1, -0, +0, \dots + 5, +6\}$$

$$Y = \{-6, -5, -4, -3, -2, -1, 0, \dots + 5, +6\}$$

$$Z = \{-7, -6, -5, -4, -3, -2, -1, 0, \dots + 6, +7\}.$$

Analyzing control process with the basic feedback deviation control principle, the fuzzy control rules should be determined based on the system output and the

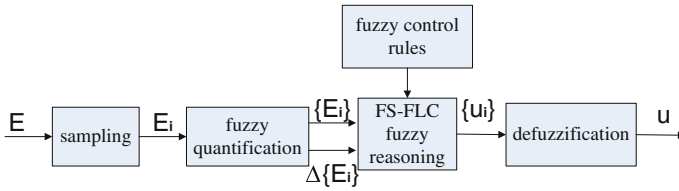


Fig. 5 Fuzzy adaptive mechanism design block diagram

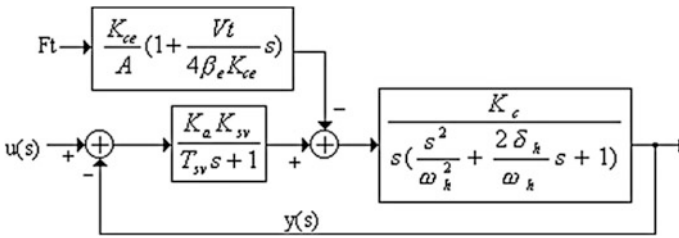


Fig. 6 Single hydraulic cylinder control model block diagram

trend of the error and the error of the reference model, this rule can be described with the following 19 fuzzy conditional statements.

The principle of the entire fuzzy adaptive control mechanism is shown in Fig. 5.

The mathematical model of the variable pitch system single-channel electro-hydraulic servo system is shown in Fig. 6.

Where F_t —effective force act on active hydraulic joint, $U(s)$ —the servo valve input, $Y(s)$ —displacement output, K_{ce} —total leakage coefficient, V_t —total compression volume, β_e —total elastic coefficient, K_a —magnification times of amplifier, K_{sv} —the servo valve coefficient, T_{sv} —time constant of the servo valve, A —area of the hydraulic cylinder piston, K_c —gain of the hydraulic cylinder, ω_h —the natural frequency of the hydraulic cylinder, δ_h —the power element damping ratio, B_n —total damping coefficient, M_t —total mass, ε —duty ratio of hydraulic cylinder ratio. The design parameter values as shown in Table 1.

Figure 7 shows the simulation block diagram of the variable pitch system single-channel hydraulic servo system. The uncertainty of the variable pitch system appears in many ways, especially leakage coefficient of the hydraulic system, changes of load and external disturbances. In the simulation, the performance of the system can be controlled by observing the changes in these parameters, and compare conventional PD control with the simulation results of fuzzy model reference adaptive control strategy of the FS-FLC adaptive mechanism. Besides, PD control parameters derived from the Walsh function identification, and its value is:

$$k_p = 12.4, k_d = 1.68.$$

Table 1 System parameters

| Symbol | Value | Unit |
|---------------|----------------|----------|
| Mt | 35 | kg |
| Vt | $1.393e^{-4}$ | m^3 |
| β_e | $7e^{+8}$ | N/m^2 |
| $A1$ | $4.91e^{-4}$ | m^2 |
| K_{ce} | $6.14e^{-12}$ | m^5/NS |
| Bn | 128.13 | NS/m |
| ε | 0.686 | |
| Ka | 0.001 | A/V |
| K_{sv} | $2.5198e^{-2}$ | m^3/SA |
| T_{sv} | 0.002 | S |
| ω_h | 313.674 | rad/S |
| δ_h | 0.2 | |

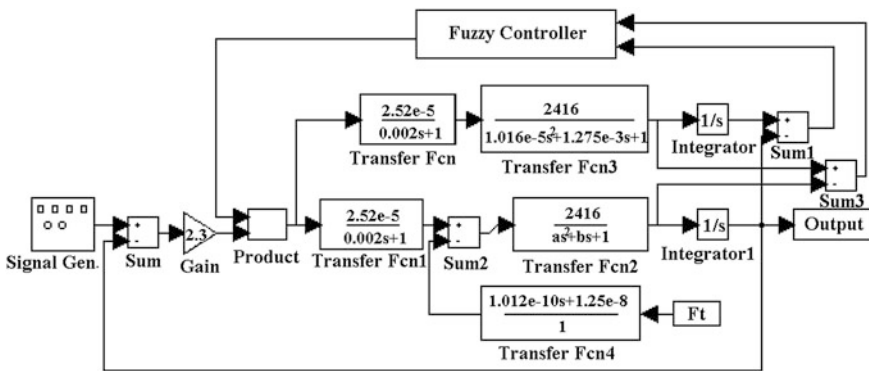


Fig. 7 Simulation block diagram

Adjustable parameters of the fuzzy controller of the flexible structure are taken as:

$$\alpha = 1, \beta = 0.8, \gamma = 0.5, \delta = 10.$$

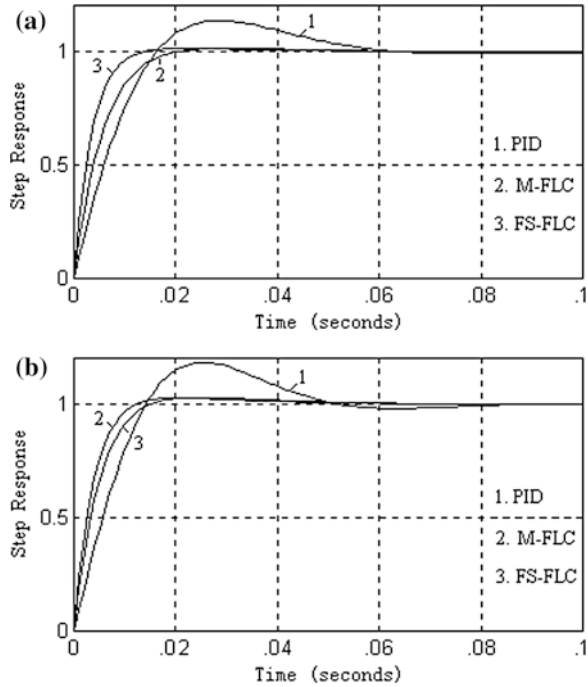
The parameter of proportional regulator is taken as:

$$k = 2.3.$$

The system simulation curves are shown in Fig. 8.

As shown from each curve of the figure, as the load, the leakage coefficient and the changes of disturbing force, the relative stability of general feedback control is deteriorated. Under the action of strong time-varying coupling interference generated during the rapid movement of the variable pitch system and variable inertia, track curve can deviate from the input signal path easily, which will result in

Fig. 8 Simulation curve.
a $Mt = 35 K_{ce} = 6.14e^{-12}$
b $Mt = 50 K_{ce} = 6.14e^{-12}$



serious waveform distortion with low tracking accuracy and large deviation. But the tracking curve of corresponding fuzzy model reference adaptive control strategy is not influenced primarily by the variations of parameter and disturbances, under the control of which, the paddle will always be able to track the desired moving signal quickly.

4 Conclusion

Note that the wind turbine is nonlinear and the system is uncertain, fuzzy model reference adaptive control strategy replaces the traditional adaptive institutions with fuzzy adaptive mechanism, which have simple structure of general feedback control system and good ability to adapt. Besides, as an adaptive mechanism, FS-FLC improves the robustness of the control system and the tracking accuracy of pitch angle. Simulation analysis shows that three variable pitch hydraulic servo mechanisms can maintain good characteristics by tracking the same ideal reference model, at the same time, the parameters changes in a wide range and external interference exists. The algorithm of this control way is simple and easy to be implied using the computer control system, it has a high practical value.

References

1. Hua G, Geng Y (2008) Output power level control of variable-speed variable-pitch wind generators. In: Proceeding of the CSEE, Beijing, vol 28, issue 25, pp 130–137
2. Sahin DA (2004) Progress and recent trends in wind energy. *Prog Energy Combust Sci* 30(5):501–543
3. Petru T, Thirineger T (2002) Modeling of wind turbines for power system studies. *IEEE Trans Poere Syst* 17(4):1132–1139
4. Hua F, Aiwei F, Yaosong X (2006) The vector control of induction motor drive based on single neuron. In: Proceeding of the CSEE, Beijing, vol 26, issue 1, pp 127–131
5. Xingjia Y, Yanan Z, Qingding G (2009) Design and analysis of three-dimensional fuzzy controller for large wind turbine. In: Proceeding of the CSEE, Beijing, vol 29, issue 26, pp 112–117
6. Guvenc L (1995) Adaptive closed loop material testing using fuzzy logic control. In: Proceedings of international conference on systems, man and cybernetics, vol 5, issue 3, pp 2478–2482
7. Yager RR (1988) On ordered weighted averaging aggregation operators in multi-criteria decision making. *IEEE Trans Syst Man Cybern* 18:183–190
8. Yager RR (1994) Analysis of flexible structured fuzzy logic controllers. *Dmitar P Filev Tom Sadeghi* 24:1035–1043

Modeling Prices in Electricity Spanish Markets Under Uncertainty

G. Miñana, H. Marrao, R. Caro, J. Gil, V. Lopez and B. González

Abstract The price of electricity in the Mibel is very changeable. This creates a lot of uncertainty and risk in market actors. Due to continuous changes in demand and marginal price adjustment, buyers and sellers cannot know in advance the evolution of prices. The study of this uncertainty motivates this work. Unlike other published work, this paper analyzes the perspective of the buyer and not the seller's perspective, as is usual in the literature. The aim of this work is to develop predictive models of electric price to build tools to manage and reduce the risk associated with the volatility of the wholesale electricity market, and therefore provide better opportunities for small traders to participate in that market. On the other hand, these models are useful to large industrial consumers by enabling them to design strategies to optimize its production capacity in function to signals of electricity market price and can get better on their production costs. Therefore, this article is based on the prediction of energy prices instead of demand. This paper analyzes the model of energy prices to determine the key variables that define its final value. The proposed model has been applied to Mibel 2012. The results suggest the use of several models based on calendar and taking into account different combinations.

Keywords Energy cost · Electricity Spanish market · Linear regression · Uncertainty · Decision making

G. Miñana (✉) · H. Marrao · R. Caro · J. Gil · V. Lopez · B. González
Department of Arquitectura de Computadores, Universidad Complutense de madrid,
Prof. José García Santesmases s/n, 28040 Madrid Spain
e-mail: guamiro@fdi.ucm.es

1 Introduction

Electricity is the main energy source from today's society. Every sector depends on it, from industry to people. The lack of this good would collapse most of the world's activities and with it the society as we know it. One can say that the today and tomorrow's world has defined the availability of this good.

Every market depends on the kind of good that it trades. Electricity could not be stored (it can be stored in small amounts, but not in a way that could replace a power plant) and the electrical market depends on the distribution grid and it requires that generation equals the consumption at every instant. These characteristics define the need of an electrical system that can coordinate demand and generation. In general, the full electrical system divided into four activities that required a higher coordination: Generation, transport, distribution, and consumption.

Traditionally, the electrical market prices were regulated by the government. With the evolution and growing of such good in Europe, the electrical market deregulation led countries to create electrical markets in order to fulfil their needs. In Spain, the "Mercado Ibérico de Electricidad," known as Mibel and created in 2009, is the result of the effort made by Spain and Portugal as response to the deregulation. Other countries in Europe have created similar markets (as for example Nord Pool or EEX).

In Spain, Mibel covers around 65 % of the traded energy. Power Derivatives and Bilateral Contracts cover the other 35 %. Figure 1 shows the actual Mibel operation in the time frame [1–3]. The Mibel is actually a sequence of markets: Derivatives Markets set prices for electricity for future. The Day-Ahead Market manages the most important amount of electricity and defines the hourly prices using a marginal price setting. Agents trade energy and a generation program is set for the day ahead. The other markets are less important, economical, but very important to guarantee stability and efficiency, mainly, due to the "generation equals consumption" principle.

The Day-Ahead Market has a very high volatile price. This is due to the constant changes in the demand and the marginal price setting. Two consecutive hours, may give very different prices (a small increase of the demand may result in a much higher energy price). This feature led some grand consumers to prefer Derivatives Market or Bilateral contracts to minimize risks and guarantee a stable price even with higher value to the average Daily Market Price.

Risk management in electrical prices, search for the best contract in order to guarantee consumers' profit and producers' profit. The Market prices are used as reference to set Derivatives and Bilateral Contracts. So, generators, grand consumers, and electrical traders, always try to find the best solution. Average consumers must get their electricity by electrical traders.

The scope of this work is to provide tools in order to evaluate, safely, different scenarios and strategies (mid and long term). In the Mibel framework, consumers and traders may negotiate their electricity. This reflects the need to find good

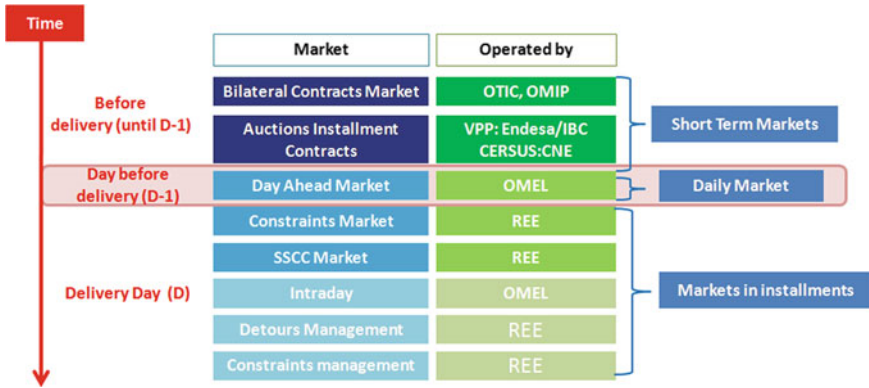


Fig. 1 The actual Mibel operation in the time frame

models and forecast methods, so consumers, traders, and generators may use them in their decision-making procedures. The availability of such tools may extend traders’ activities and increasing the number of agents that participate in such markets.

There are a great amount of studies regarding the Electrical Demand, but the mid- and long-term price studies are mainly reserved for the generators and reflect their production cost models [4–9]. Market price modeling may help general industry to take into account market prices in their production cost models. For average, consumers may use such Modeling and Prediction techniques to extend their negotiation capabilities.

The rest of the paper is organized as follows. In Sect. 2, we present a modeling electricity prices. The Sect. 3 shows the results of applying the multivariate linear regression method to find the variables that affect the final value of the price. In Sect. 4, we present conclusions and future work.

2 Modeling Electricity Price

2.1 Day-Ahead Market

The day-ahead market is determined by matching offers from generators to bids from consumers to develop a classic supply and demand price, on an hourly interval, and is calculated for Spain and Portugal, in which the system operator’s load flow model indicates that constraints that will bind transmission imports [10, 11].

This market closes a day before the physical delivery of the product (Electricity), and the price is set by the marginal generator (the last generator used to fulfill demand needs). Due to the marginal characteristics the price paid to all generators is the one set by the marginal generator.

This market is called day-ahead because it closes a day before the product is physically traded and sets the generation program that is managed by the system operator.

In the Mibel framework, there are some special features: Generators are grouped by the technology they use to produce Power and Electricity. This is a convention because different generators have different cost and this grouping and order of entering the market is set to ensure safe competition between generators.

It also takes into account the inflexible demand and the flexible demand (some consumers have the capability to wait for the right price to perform their activities, as for example hydro-pumping power generators). Figure 2 is a schematic representation of the Hour price setting evaluation in the Mibel's day-ahead market.

As said before, the day-ahead market sets the price and with it the power generation program for an hour for the 24 h of the following day. Although, the electrical power system operator may add or remove generators in order to ensure efficiency and stability in the physical power grid.

2.2 *Mathematical Modeling*

In this section, first, we describe how the day-ahead market variables that influence on the electricity price are represented. Then, the mathematical method applied is shown. The method analyzes and identifies the variables that most influence on the price.

2.2.1 **Definition of Variables**

The variables involved in the problem under study are the following: On one side, the day-ahead market starts with the information of forecasting the demand and the wind energy generation, per hour. We have represented these variables by this way:

$$D_i = \text{demand in } h_i$$

$$WG_i = \text{wind power generation in } h_i$$

$$h_i = \text{hour of day } \{i = 1, \dots, 24\}$$

These two variables induce some uncertainty to the day-ahead market result. In this first work, these variables will not be considered as predictions.

Also, it must be taken into account that electricity demand is very variable over the months, days, and even hours. In order to analyze the calendar effect on electricity demand, and therefore on the price, we have defined the following variable.

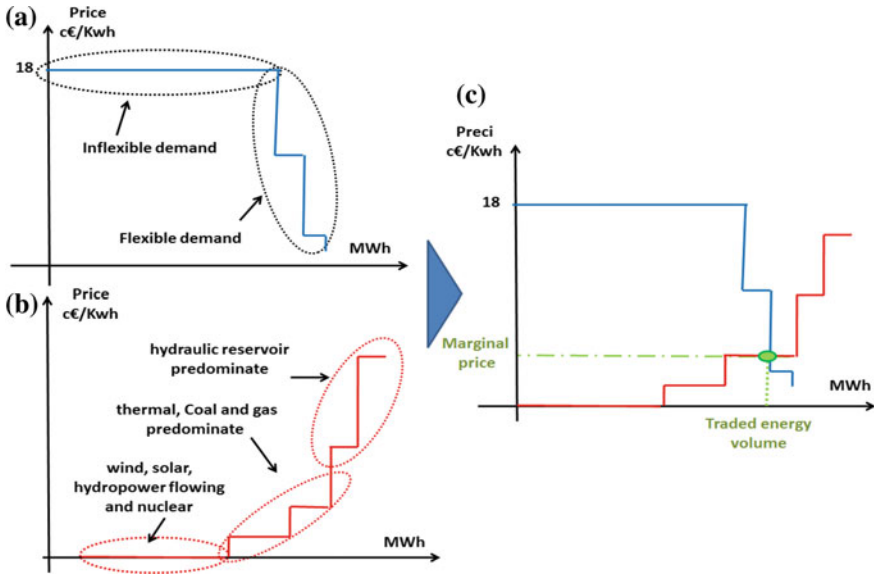


Fig. 2 Schematic representation of the hour price setting evaluation in the Mibel's day-ahead market

$$D_i = \text{day of the week } \{i = 1, \dots, 7\}$$

$$D_l = \begin{cases} 1 & \text{if working day} \\ 0 & \text{if nonworking day} \end{cases}$$

$$S = \begin{cases} 0 & \text{if winter} \\ 1 & \text{if spring} \\ 2 & \text{if summer} \\ 3 & \text{if autumn} \end{cases}$$

On the other side, we have the outputs of the day-ahead market. These are the marginal price of electricity and the volume of electricity traded by technology (we have not considered all available technologies, only the most important), per hour. We have represented these variables by this way:

$$HV_i = \text{traded Hidropower Volume in } h_i$$

$$NV_i = \text{traded Nuclear Volume in } h_i$$

$$FGV_i = \text{traded Fuel—Gas Volume in } h_i$$

ICV_{*i*} = traded Imported Coal Volume in *h_i*

CCV_{*i*} = traded Combined Cycle Volume in *h_i*

SRV_{*i*} = traded Special Regimen Volume in *h_i*

EMP_{*i*} = Electrical Marginal Price in *h_i*

2.2.2 The Model

The electric market can be analyzed from multiple ways. For this first phase of this work, we have decided to apply Multiple Linear Regression (MLR) to analyze the linear correlations between two or more independent variables. The target is to select the optimal set of independent variables to explain the behavior of electric price. Then, we can formulate a general model of multiple linear regressions in the following way:

$$Y_i = \beta_0 + \beta_1 X_{i,1} + \beta_2 X_{i,2} + \beta_3 X_{i,3} + \dots + \beta_{p-1} X_{i,p-1} + \varepsilon_i$$

where the dependent variable is $Y_i = \text{EMP}_i$ and the independent variables are $X_i, j \in \{\text{RE}_i, \text{WG}_i, \text{NV}_i, \text{SRV}_i, \text{HV}_i, \text{ICV}_i, \text{CCV}_i, \text{FGV}_i\}$. Previously, we have tested the knowledge requirements needed by MLR.

3 Results

In this section, we present the analysis of the results obtained by applying the MLR technique. SPSS tool is the software used.

We created a database with the inputs and outputs of day-ahead market of the years 2012. This information has been obtained from the market operator [1]. It must take into account that there is one day with 23 h and other day with 26 h. This is due to the time change that takes place twice a year. For that these days to have 24 h we have replicated or removed the hour 2.

In order to study the calendar effect on price market, we have split the dataset generating 18 samples. These samples depend on the variables, *S* (season), *D₁* (nonworking day or working day) and *TS* (time slot) and they have been represented by this way: $\text{Sample}_i = f(S, D_1, TS) i = 1, \dots, 18$. The *S* and *D₁* variables have been defined previously. The *TS* variable represents the different time slots in which the day can split. These time slots are based on the hours of high, normal, and low electric demand taking into account also the seasonality. This is the recommended partition by the electrical grid operator and it tries to reflect the Iberian Peninsula reality [12].

$$TS = \begin{cases} T_1 & \text{if } S = 0, 3 \\ T_2 & \text{if } S = 1, 2 \end{cases}$$

$$T_1 = \begin{cases} 0 & \text{if } 0 < h_i \leq 8 \\ 1 & \text{if } (8 < h_i \leq 18) \text{ or } (22 < h_i \leq 24) \\ 2 & \text{if } 18 < h_i \leq 22 \end{cases}$$

$$T_2 = \begin{cases} 0 & \text{if } 0 < h_i \leq 8 \\ 1 & \text{if } (8 < h_i \leq 11) \text{ or } (15 < h_i \leq 24) \\ 2 & \text{if } 11 < h_i \leq 15 \end{cases}$$

The Table 1 shows summary of descriptive statistics for some of the samples. We can note the variations of the mean price and the standard deviation by our calendar criterion. For instance, the mean price in the whole dataset is 48,02 units and the standard deviation is 12,22 units. However, for the sample f(0,0,2) the mean price is 65,38 units and the standard deviation is 7,21 units. These results confirm the importance of the calendar effect on the market price.

In the Table 2, we can see the Pearson correlation coefficients for some of the samples. The first thing to note is that the variables WG (wind power generation) and SRV (traded special regimen volume) reduce marginal price and the other variables increase it. In the case of nuclear energy, the values in Table 2 show that there are samples in which this variable reduces the price and others in which this variable increases the price. This is because this method does not reflect the character constant of the traded volume of this technology.

The second observation we can make is that, in most of the samples, the variables that most influence on the price are the traded volume of imported coal, combined cycle, and conventional hydraulics. Also, there are some samples in which the demand, the wind generated and the traded special regimen volume become important. All of these variables have different weights depending on the sample. These results also confirm the importance of the calendar effect on the marginal price.

The following equations show the models obtained for some samples.

$$Y_{f(0,0,2)} = 22,448 + 0,14I * CIV + 0,02 * HV - 0,01 * SRV$$

$$Y_{f(0,1,2)} = 4,836 + 0,04 * HV + 0,13 * ICV + 0,01 * CCV$$

$$Y_{f(2,0,2)} = -26,359 - 0,02 * WG + 0,03 * D + 0,04 * HV + 0,02 * ICV$$

$$Y_{f(2,1,2)} = 36,745 + 0,06 * HV + 0,01 * CCV + 0,01 * NV$$

In the statistics summary of the each model, we can see that the figures of *R* squared corrected are greater than 0.06, and the figures of *P*-value are less than 0.04, for all samples. This mean the proposed models are suitable.

Table 1 Summary of descriptive statistics for some of the samples

| Dataset | Sample = f(0,0,2) | | Sample = f(0,1,2) | | Sample = f(2,0,2) | | Sample = f(2,1,2) | | | |
|---------|-------------------|----------|-------------------|----------|-------------------|----------|-------------------|----------|----------|---------|
| | Average | σ | Average | σ | Average | σ | Average | σ | | |
| EMP | 48.08 | 12.22 | 61.09 | 9.51 | 65.38 | 7.21 | 46.98 | 5.34 | 55.35 | 5.02 |
| D | 28771.16 | 5018.88 | 32289.00 | 2650.47 | 36848.73 | 3094.47 | 26428.54 | 735.61 | 33560.41 | 2435.03 |

Table 2 Pearson correlation coefficients

| Sample | Demand | | Traded electric power volume | | | | | |
|----------|--------|--------|------------------------------|--------|-------|-------|-------|--------|
| | D | WG | NV | SRV | HV | ICV | CCV | FGV |
| f(0,0,0) | 0.564 | -0.435 | -0.29 | -0.413 | 0.15 | 0.676 | 0.602 | 0.347 |
| f(0,0,1) | 0.635 | -0.274 | 0.012 | -0.425 | 0.442 | 0.766 | 0.741 | 0.337 |
| f(0,0,2) | 0.671 | -0.104 | 0.446 | -0.277 | 0.533 | 0.302 | 0.676 | 0.249 |
| f(0,1,0) | 0.669 | -0.505 | -0.427 | -0.436 | 0.201 | 0.714 | 0.73 | 0.243 |
| f(0,1,1) | 0.445 | -0.462 | 0.206 | -0.333 | 0.643 | 0.374 | 0.653 | 0.232 |
| f(0,1,2) | 0.492 | -0.27 | 0.124 | -0.215 | 0.63 | 0.533 | 0.53 | 0.201 |
| f(2,0,0) | 0.284 | -0.718 | -0.332 | -0.711 | 0.396 | 0.792 | 0.46 | 0.162 |
| f(2,0,2) | 0.476 | -0.306 | 0.013 | -0.774 | 0.473 | 0.247 | 0.423 | -0.177 |
| f(2,1,0) | 0.578 | -0.533 | -0.039 | -0.432 | 0.541 | 0.562 | 0.615 | 0.146 |
| f(2,1,2) | 0.568 | -0.475 | 0.034 | -0.322 | 0.637 | 0.139 | 0.452 | -0.453 |
| f(3,1,0) | 0.507 | -0.615 | -0.333 | -0.613 | 0.433 | 0.635 | 0.762 | 0.136 |
| f(1,1,0) | 0.475 | 0.531 | -0.495 | -0.474 | 0.626 | 0.666 | 0.721 | 0.177 |
| f(1,1,2) | 0.326 | -0.633 | -0.473 | 0.614 | 0.651 | 0.521 | 0.723 | 0.025 |

Furthermore, we can observe that some important variables have been eliminated of the models. For example, the traded nuclear volume has been eliminated in almost every sample, and the traded special regimen volume has been removed in some samples. This is because this technique does not take into account neither the special character of nuclear energy and the energies of special regime (both types of technologies are offered at price 0), nor the marginal character of the electricity market.

4 Conclusion and Future Work

In this paper, we have presented a Linear Dependency Analysis among Electric Market Prices and the amount of energy produced by each technology, the electric demand and the wind power generated. The object of this work has been to analyze and identify the variables that most influence on the price. To achieve this goal, we applied Multiple Linear Regression (MLR) using SPSS tool.

On one hand, this method has confirmed that is correct and necessary to analyze the dataset in function of the season, if the day is working day or nonworking day, and the time slot. Therefore, this technique offers different models depending on these variables.

Furthermore, this method reveals deficiencies in interpreting the marginal character of the price of electricity. Therefore, they are to look for other modeling and forecasting techniques that take into account the special characteristics of nuclear energy and the energies of special regime, the marginal character of the electricity market and the uncertainty introduced by demand and wind power.

In conclusion, we can say that this analysis shows us that it is good to have a range of prediction models and a decision-making algorithm to choose the best model for each situation.

In order to find the best method to model and predict the electric energy price for each sample, the next step is to apply different prediction techniques (Exponential smoothing and, moving average, the near-neighbors, neuronal networks) and make a comparison among them. After the modeling and forecasting, we are going to develop a decision-making model using fuzzy logics. This will allow us to choose the best prediction model for each situation. The codification that we have presented in this work will be used in order to obtain the logical fuzzy system that uses the defined Models.

References

1. www.omel.es
2. <http://www.mibel.com/>
3. <http://www.omip.pt/>
4. Nuno D, de Jorge S, Pedro FC (2004) Electricity markets simulation: an application to the Iberian electricity market—MIBEL
5. González CM (2012) Predicción de la demanda eléctrica horaria mediante redes neuronales artificiales. Technical Report Departamento de Economía Cuantitativa, Universidad de Oviedo
6. Shahidehpour M, e Zuyi Li HY (2001) Market operations in electrical power systems forecasting, scheduling and risk management. Wiley, New York
7. Taylora JW, Buizzab R (2003) Using weather ensemble predictions in electricity demand forecasting. *Int J Forecast* 19(1):57–70
8. Taylo JW (2003) Short-term electricity demand forecasting using double seasonal exponential smoothing. *J Oper Res Soc* 54:799–805. doi:10.1057/palgrave.jors.2601589
9. Taylor JW, de Menezes LM, McSharry PE (2006) A comparison of univariate methods for forecasting electricit demand up to a day ahead. *Int J Forecast* 22(1):1–16
10. <http://www.omel.es/>
11. <http://www.esios.ree.es/>
12. BOE: ORDEN ITC/2794/2007. de 27 Sept

Research on Key Technologies for Jail Incident Prevention and Response System

Guofeng Su, Jianguo Chen, Fengzhi Liu and Quanyi Huang

Abstract For the purpose of the administrators' capability enhancement of prison security prevention and response, and the implementation of emergency collaborative management, the paper points out the importance of building Jail Incident Prevention and Response System (JIPRS), and specifically describes the architecture and functions of the JIPRS, as well as puts forward interoperability emergency response system consisting of national, regional, prison three-level command centers. JIPRS includes emergency duty, resource management, forecasting and early-warning, event disposal, simulation exercise, and other functions. The critical technologies required in the JIPRS are expounded, including criminal risk recognizing and quantification, emergency analysis and decision, three-dimensional simulation and exercise, etc. These studies provide strong support for the JIPRS building at home and abroad.

Keyword Prison emergency · Prevention and response system · Criminal risk recognizing · Three-dimensional simulation and exercise

G. Su (✉) · J. Chen · F. Liu · Q. Huang
Department of Engineering Physics, Tsinghua University, Beijing China
e-mail: sugf@tsinghua.edu.cn

J. Chen
e-mail: chenjianguo@tsinghua.edu.cn

F. Liu
e-mail: fengzhiliu@tsinghua.edu.cn

Q. Huang
e-mail: quhuang@tsinghua.edu.cn

1 Introduction

Prison, as Law Enforcement Agency of national Criminal Law, is focused by all level of prison administration institutions maintaining prison safety and stability of the prison. In recent years, worldwide endangering public safety activities occurs frequently such as violent activities and terrorist activities. In the wake of changed constitution of criminal in prison and the increased proportion of violent crime, gangs commit, heavy committed, intelligent crime, and drug-related crimes, it becomes fierce between prison renovation and reformation and rebelling [1]. October 15, 2011, in Mexico Tamaulipas Matamoros State prison criminal's massive brawl happened resulting in 20 deaths and 12 injured. August 19, 2012, riots happened in Venezuelan capital Lagasse Neiya Er first prison resulting in 25 deaths and 43 people injured. Through concluding all categories of prison incident cases, several problems were found which exist in work of prison incident prevention and response including difficult early-risk identification and quantization, poor operability of planning, defective linkage institution among multidepartment, etc. [1].

To realize intelligent prison management, scientific emergency response, and incident processing planning, it is necessary that construct prison incident prevention and response system. All levels of government and research staff construct a series of prison prevention and emergency management research, which improves construction of prison prevention and emergency response system. American prison prevention system gives full play to technical advantages and adopts fingerprint image matching, intelligent video surveillance, personnel positioning technology based on Internet of the thing to support prison safety operation. British prison administration makes corresponding prison incident emergency response system under the efficient framework of golden, silver, and copper [2].

This paper researches and analyzes overall architecture and key technologies of prison incident prevention and response system, with purpose that provide scientific direction for constructing prison emergency system and support timing scientific reasonable and effective decision-making with comprehensive intelligent information support and visualization combat platform.

2 Incident Prevention and Response System Architecture Design

2.1 Overall System Architecture

Prison emergency prevention and response system architecture needs to be constructed variously based on different type, size, sensitivity degree, and national political systems. Through an extensive research, the paper proposes a more typical three-level network architecture model, as shown as in Fig 1.

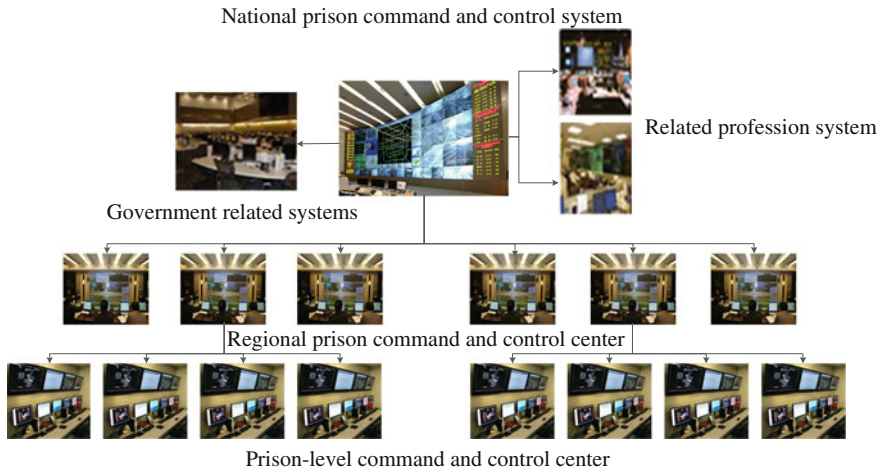


Fig. 1 The architecture of prison incident prevention and response system

All levels of emergency command center are key nodes in prison incident emergency command network, as well as specific carriers for implementing prison emergency system functions. The prison emergency incident prevention and response system is deployed in emergency command and control center, accessing to internal system like prison administration, video surveillance, visiting management, and prison safety prevention system, besides, accessing to external system like military, police, firefighting, traffic, medical care, atmosphere, and other departments. Then conduct interconnected and intercommunicated prison emergency command and response system. The structure of JIPRS deployed in the prison command and control center is shown in Fig 2.

2.2 System Function

Prison command and control center could realize unified prisons operation supervision and issues processing in administrative area. While incident happened, low-level center report incident information and on-site collected information to superior center. The superior center supplies low-level center the functions including prediction and early-warning, assistant decision-making, distance control, command, and control.

The system contains foundational modules like emergency duty, resources management, risk surveillance analysis, emergency incident processing, prison visualization and three-dimensional simulation and exercise, and emergency GIS, etc.

1. Emergency duty is the foundation of emergency management and guarantee of incident processing, which includes information receive and report, duty and shifting, address book management, and incident management, as well as emergency resources management, etc. Emergency resources management

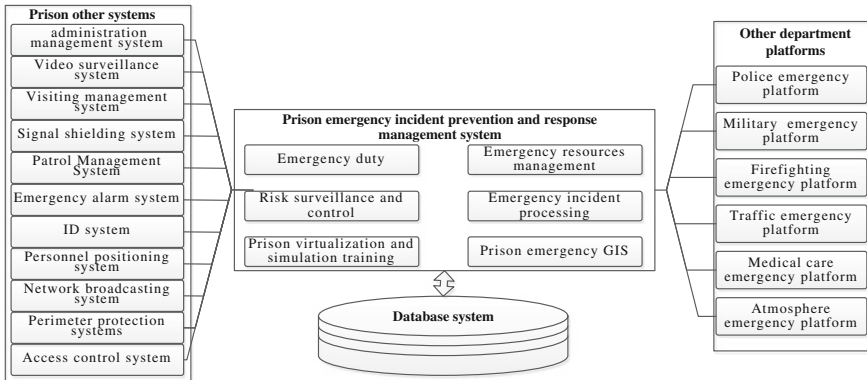


Fig. 2 The structure of prison incident prevention and response system

could realize resources preparedness and spatial distribution in real-time via emergency resources query, statistics, analysis, and other operations.

2. Risk surveillance analysis realizes information collection and mining of prison situation and prevention system situation, and implements prediction analysis and risk analysis with prediction analysis model, and provides basis for incident processing.
3. Emergency incident disposal is a key leading decision analysis and dispatching work, which automatically associating with corresponding SOPs [3]. Decision analysis capabilities via various consultations conduct preliminary proposal supplement and complete to form the final disposal program.
4. Three-dimensional simulation refers to simulate prison incident development with virtual reality method supporting dispatch forces drill and practice and supplying reference for planning check and modification.
5. GIS system supports various prison administration and emergency business operations. With capability of GIS powerful spatial analysis, the system could implement network analysis, buffer analysis, overlay analysis, digital elevation model, and spatial measurement, and other spatial analysis functions, for the purpose of audio-visual display, and assistant analysis.

3 Prison Emergency Incident Prevention and Response System Key Technologies

3.1 Criminal Risk Identification and Quantification Technology

By means of various intelligent surveillance methods, monitoring inmate dynamic safety situation in real-time, mastering post implement and safety management information, and supervising safety device and facilities operation. Integrating

with deep inside early-warning information which may be influence prison stability, prison dynamic safety situation is mastered firmly.

3.1.1 Intelligent Risk Identification

Various risk factors lead to prison unexpected incidents, including abnormal behavior of the inmate, super-charge in prison cells, significant hazard source in area, regional epidemic, alert infrastructure security risks, monitoring programs, and so on. Internet of the thing based positioning technology for criminal's abnormal behavior identification provides a wealth of foundational information data. ZigBee is a new short-range, low-rate wireless transmission technology with low power consumption, low cost, low rate, short time delay, large network capacity, high reliability, and high security features, which is often adopted in variety personnel positioning systems [4]. ZigBee-based prison personnel positioning intelligent behavior analysis and abnormal event analysis, on the one hand could avoid the occurrence of unexpected events and support preventive measures, on the other after emergency occurred supply rapid location and personnel rescue.

Intelligent video surveillance technology applied within the prison security system become mature increasingly. Face recognition-based video surveillance, detection of abnormal aggregation, and cross-border technology have been widely adopted by modern prison security system [5]. Perimeter detection technology is applied to detect moving intrusive target and its behavior in the warning area, conducts face recognition for intrusive target and image comparison with criminal's image information stored in database, once the match is successful, immediately issue warning, and at the same time identify their trajectories [6].

3.1.2 Inmate Risk Degree Quantification

Prison emergency incident prediction needs to confirm predication indicator, implement quantification of prediction indicator perimeter, and define prediction threshold. To ensure surveillance indicator, grasp main aspect of the conflict and lock main point, and select core indicator which directly impacts on prison and causes great harm. Monitor risk indicator quantification assignment refers to transfer ordinary related incident to corresponding description for indicator quantification. Table 1 shows the indicators for monitoring early-warning and dangerous coefficient mapping relation, the highest index coefficient is 10, the lowest value is 0, the higher the coefficient, the greater the **risk**.

To strengthen the analysis and judgment of these early-warning indicators can find out the regularity, universality, and tendentious issues. It helps to promote data value-added and improve the data utilization. When the emergency happens, the collection, processing, integration, analysis and researching of indicators data should be strengthened, which is a work that shift from the risk subjective identification to the scientific analysis, from lag information to advanced information

Table 1 Early-warning and monitoring indicators and risk coefficient

| Category | Indicators | Status | Danger coefficient | |
|---|--|---|--------------------|-----|
| 1 Criminal under the tight watch | Life imprisonment, postponed death, more than 20 years | Thought and emotional stability | 1 | |
| | | Thought and emotional instability | 5 | |
| | | Violent | 7 | |
| | | First instance death penalty | 10 | |
| 2 Self-injury self-mutilation hunger strike | Suicide | Suicidal remarks | 7 | |
| | | Suicidal behavior | 10 | |
| | Hunger strike | Hunger strike ≤ 4 days | 2-4 | |
| | | Hunger strike ≥ 4 days | 5-10 | |
| | Self-injury self-mutilation | No sharp foreign body ingestion | 3 | |
| | | Sharp foreign body ingestion | 5-10 | |
| 3 Break prison jailbreak | Break prison, escape, red prison, jailbreak | Head hit a hard object | 3 | |
| | | There escape, prison, Jailbreak attempt | 10 | |
| 4 Disease | A variety of device quality; heart disease | Arrhythmia | 5-10 | |
| | | Hypertension | Low-risk | 1-4 |
| | | | Intermediate risk | 7 |
| | | | Danger | 10 |
| | Cerebrovascular disease | Risk | 10 | |
| | | | 10 | |
| | Diabetes | Diabetes | 5-8 | |
| | Heart, brain and kidney disease | Heart, brain and kidney disease, and diabetes | 10 | |
| | Drug | Moderate or severe drug withdrawal reactions | 5-10 | |
| | 5 Serious violation | Single assault physically abuse | | 1-4 |
| Multiple beatings physically abuse | | | 5-10 | |

Coefficient of monitoring indicators takes the date as a reference. Quantifiable monitoring indicators were set to white, yellow, orange, and red four warning logo to represent different risk degrees. In the Table 1, the score of dangerous degree is marked as $X_i, i \in \{1, 2, 3, 4, 5\}$, Table 2 is the security warning signal identification table When prison cells have several risk factors occurred in the prison cell, take greatest risk factor monitoring indicator without accumulation

early-warning-related information and inside information, from working feedback model to decision-making one. All of above provide a powerful information support for safety management to effective emergency response service and decision-making Table 2.

Table 2 The signal identification of early-warning

| Warning signal | Red | Orange | Yellow | White |
|----------------|------------------|-----------------|-----------------|-----------------|
| Risk degree | $X_i \in [9-10]$ | $X_i \in [5-8]$ | $X_i \in [2-4]$ | $X_i \in [0-1]$ |

3.2 Prison Emergency Incident Analysis and Decision-Making Technology

Analysis and research to incident emergency in prison is comprehensively considering incident cause, development trend and impaction, etc. The analysis technology based on GIS thematic map is an effective consultation and assessment method. After the analysis and research, emergency decision for prison incident can be made to select more suitable disposal measures, which is based on digital emergency plans.

3.2.1 Thematic-Based Analysis and Judgment Technology

Thematic maps, based on Geographic Information System (GIS), apply graphical elements and various styles to express intentions of publisher. It is a powerful way that analyzes and deploys sea data. Through distributing thematic maps to a different units or personnel can make the viewer to understand the current situation, to grasp the enemy force distribution and clear emergency disposal tasks. For the typical emergencies in prison, Table 3 lists some basic thematic maps servicing commanders from the different level departments to provide analytical judgments.

3.2.2 Decision-Making Technology Based on Digital Planning

Intelligent decision-making support based on digital planning is a key technology, which can offer automatically some solving measures [7]. Content of emergency planning is composed of six elements that can be expressed as: $DPLAN = \langle \text{Type, Organs, Events, Actions, Rules, Restrictions, Resource} \rangle$.

where, Type refers to plan classification collection, and prison emergency plan is generally classified into comprehensive plans, specific plans and on-site disposal plan. Organ is a collection of various emergency organizations; Events defines a various incident collection in emergency planning. Actions is plan-related disposal measures set; Rules is rule set of planning, which represents the code of conduct for principals; Restrictions is the set of constraints; Resources is a resource collection [8].

After emergency plan in prison is digitized, the mathematical model of assistant decision rule can be defined as follows: let T be a rule set of n transactions, each transaction is marked with a classification y. Let I T contained in the affairs of all

Table 3 Thematic maps for jail incident analysis and judgment

| No. | Thematic map | Elements |
|-----|---|--|
| 1 | Current situation thematic map | Incident-occurred area, dispose strength, circumstances of the incident, warning area |
| 2 | Surroundings thematic map | Hazards, protection objectives, site of the incident, the event affected area |
| 3 | Power distribution thematic map | Site of the incident, the police, armed police, department of transportation, fire stations, hospitals, the red cross, the military and all other disposal units |
| 4 | Power scheduling thematic map | Site of the incident, the required number of resources, embarked on the path to achieve the time |
| 5 | Forces dispatched thematic map | Site of the incident, blocking bayonet, sniper, alert staff |
| 6 | Fled comprehensive analysis of thematic map | Escape trajectory prediction fled, fled regional prediction |
| 7 | Fugitive character context map | People associated with fugitive |
| 8 | Abscond destination network diagram | Criminals birthplace, workplace and living places |
| 9 | Events impact statistical thematic map | Casualties, economic loss, depletion of human and material resources |
| 10 | Distribution of contraband hiding places | Guns, bullets, props, drugs, etc. |
| 11 | Patients spatial distribution of thematic map | Outbreaks of infection or poisoning patients dormitory where the distribution |
| 12 | Distribution of fire equipment and facilities | Site of the incident, fire hydrants, fire extinguishers, etc. |

the combinations, Y for all categories identified, and there is $I \cap Y = \phi$. Emergency assistant decision rule refers to obtain implication relation from the emergency plans:

$$E \cup C \rightarrow A \cup M$$

E is a set in emergency plans, C is a constraint set, A is a collection of processing measurement, and M is a collection of resource requirements. Emergency assistant decision-making rules refer to ultimately generate a complete the user-specified minimum support and minimum confidence limit of frequent item sets, i.e., decision support strategy. The support degree refers to include an inference rule transaction account the percentage of overall transaction, confidence is the inference rule already exists, also includes E, C, A, M percentage.

Emergency assistant decision-making method firstly generates all frequent item sets, and then generates confidence rules greater than the minimum confidence level from the frequent concentration. Frequent item sets must contain implication relations antecedent and pieces that derive results to set R must be satisfied: $R \cap (E \cup C) \neq \phi$ and $R \cap (A \cup M) \neq \phi$ the most frequent item sets the number of items, the higher priority its deduced decision result.

3.3 Three-Dimensional Simulation Technology

As the particularity of the prison functions involving prison emergencies military exercise with high degree of risk and difficulty, three-dimensional simulation training of the prison incident disposal drills have special significance [9]. Through virtual reality technology builds the prison and its surrounding environment; the virtual scene provides visual support for incident processing. The key technologies refer to emergency drill workflow engine technology and rule inference based script technology.

3.3.1 Emergency Drills Process Engine Technology

Emergency drill workflow configuration management could automatically determine the process flow according to custom business rules. Its functions include: explaining process definition; creation process instance, and control its execution; scheduling activities; worksheet for users to add work items; Workflow execution subsystem may include multiple workflow engines, different workflow engine jointly conduct collaboration workflow.

3.3.2 Rule-Based Script Deduction Technology

Script deduction is the core part of three-dimensional simulation drill, inference rule is a method of problem description, the formula can be given in the form of implication composed of several statements, and be able to produce as a rule to use. Rule-based script inference works as follows:

1. The workflows of disposal and decision-making put into the database.
2. According to certain policy rules, selecting the rules from the rule base, then the selected results will match the known facts. If the existing facts in the repository consistent with the premise of the selected rules, then the match are successful, otherwise the match fails.
3. When more than one rule is matched successfully, the reasoning mechanism should be able to choose one piece according to some policy rules to perform.
4. The rules to be executed, if the rule is not a problem after the target member, when it is one or more conclusions, these conclusions could be added into the comprehensive database; when it is one or more operations, perform these operations.
5. The rules to be executed, if the latter part of the rules meets the conditions of the problem ending, and stop reasoning.
6. In the problem-solving process, remember the sequence of rules applied so that eventually is able to give the solution path of the problem.

4 Conclusions

Prison incident prevention and response system help better prison management unit to prepare and response kinds of incident, which including criminal escape, hostage-taking, assaulting a police officer, commit suicide, the impact of prison violence, natural disasters, and other emergencies. This paper describes the prison emergency prevention and response system architecture and functional components, a detailed analysis of the key technologies on building prison emergency preparedness and response system. Prison incident prevention and response system construction will support emergency management and command dispatch more intelligently, visualization, and transparency, improving prison emergency response capability, and enhancing the overall prison administration ability to minimize the social harm and property damage.

Acknowledgments The authors would like to thank the support of the National Science and Technology Support Program (Study On Emergency Surveillance Strategies and Emergency Consultation Technologies for Grave Accidents, Grant No. 2012Z10135) and the National Natural Science Foundation of China (Problems and Integrated Research Platform for Scenario Response Based National Emergency Platform System, Grant No. 91024032).

References

1. Zhou J (2009) Causes of emergency events in prison and its characters. *J Hubei Univ Police* 5:116–119
2. Li F (2010) Research on the prison emergency management of China. Shan Dong University, ShanDong
3. Jianguo GAO, Yan JIA (2004) Chinese prison seismic disaster and emergency. *Measure J Disaster Prevent ion Mitig Eng* 24(4):447–450
4. Yan-you Q, Guang-wen L (2010) A infrastructure management information system with GIS and IOT. *Things Geogr Inf Syst* 5(10):17–21
5. Zhang F (2011) Design and implement of intelligent video surveillance system for jail. University of Electronic Science and Technology of China, Chengdu
6. Usmani AS, Rotter JM, Lamont S (2001) Fundamental principles of structural behavior under thermal effects. *Fire Saf J* 36(1):721–744
7. Jiang H, Huang J (2009) The study on the issues of scenario evolution in real-time decision making of infrequent fatal emergencies. *J Huazhong Univ Sci Technol: Soc Sci* 23(1):104–108
8. Hanratty T, Hammeil II, Robert J, Yen J, McNeese M, Oh S, Kim H-W, Minotra D, Strater L, Cuevas H, Colombo D (2009) Knowledge visualization to enhance human-agent situation awareness within a computational recognition-primed decision system. In: *IEEE workshop on situation management*
9. Han JH, Zhang YQ, Wei ZC (2008) Research of rule-based model of discrete event system and rule matching. *J Syst Simul* 6(1394–1396):1419

Design of Improved Fuzzy PID Controller Based on the Temperature Control System of Large Inertia and Time Delay

Longkui Wang, HongXin Li and Yaru Wang

Abstract It is very common to control the temperature in all areas of industrial production, the temperature control system always has large inertia and time delay and it is complicated and uncertain. The article combines S7-300PLC and software of Matlab, analyzes the temperature control effects of conventional PID controller and self-tuning Fuzzy PID controller. On this basis, an improved self-tuning fuzzy PID control algorithm is given in this paper. The experimental results show that this control system achieves real-time precise control of temperature, improves the control efficiency, has a profound practical significance.

Keywords Temperature control · S7-300PLC · Fuzzy PID controller

1 Introduction

It is very common to control the temperature in all areas of industrial production, but the control objects are different at the different industrial applications. Due to the different internal mechanism of the industrial control, the process of temperature control system is complicated and changeable, having a large inertia and time delay [1]. For the conventional PID controller, a system model of the controlled object must be created at the first, but for the temperature control system with large inertia and time delay, it is very difficult. Other hand, due to the presence of airflow in the actual environment, the proliferation, and so on, self-tuning fuzzy PID controller controlled very well in the case of simulation could not effectively control the controlled object in the practical application.

L. Wang (✉) · H. Li · Y. Wang
School of Information Science and Engineering, Lanzhou University,
Lanzhou 730000, China
e-mail: lkwang11@lzu.edu.cn

The paper analyzes the conventional PID controller and self-tuning fuzzy PID controller for temperature control, on the basis of self-tuning fuzzy PID controller, an improved fuzzy PID controller for temperature control system with large inertia and time delay is designed through adding a function of automatic identification and cleared. In the article, the hardware connection to the electric furnace is achieved by using the S7-300PLC, using the software of Matlab achieves the algorithm call. The actual operation results show that: the modified fuzzy PID controller eliminates the large overshoot in the original temperature control, and adjusts the temperature to the desired temperature value in a short time.

2 System Hardware and Software Components

The hardwares of control system contain S7-300 PLC, temperature sensor, temperature transmitter, SCR power unit, and electric heating control objects. The hardware structure of the connection is shown in Fig. 1.

Since the control objects are generally at the industrial production site in the actual industrial control, which has a certain distance from the control terminal, we use the PLC master-slave design. In the experiment, Siemens S7-300 series PLC is used, the model is CPU315-2DP, the PLC master control the program, the PLC slave engages in the real-time temperature data acquisition, controlling the signal output.

We select PT100 platinum resistance sensor, which has the characteristics of relatively good linearity, strong oxidation resistance, small error, and a wide range of temperature; use RWB temperature transmitter, which is two-wire integrated transmitter, has the characteristics of easy to install, high stability, anti-interference ability, high conversion accuracy, power supply is 24 V, output signal is 4–20 mA current. In order to adjust the power of the electric furnace, we select TZ100 series thyristor resistive load power adjustment unit, which can adjust the duty cycle of the circuit breaking according to the control signal.

In the system, running softwares include Siemens programming software STEP7, Siemens configuration software WinCC, and Matlab. In the control process, the functional modules in STEP7 realize the conversion between actual measured quantities data and digital data. We use WinCC to achieve the real-time monitoring of control process [2], WinCC monitor main screen is shown in Fig. 2.

The control algorithm is implemented rely on the powerful computing capacity of Matlab, the data exchange between STEP7 and Matlab via OPC communication protocol.

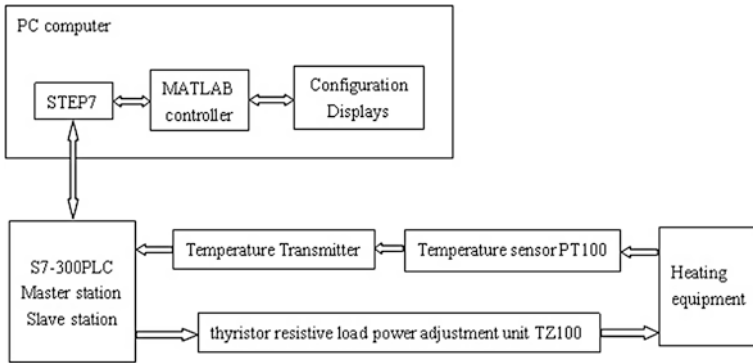


Fig. 1 Block diagram of the hardware system

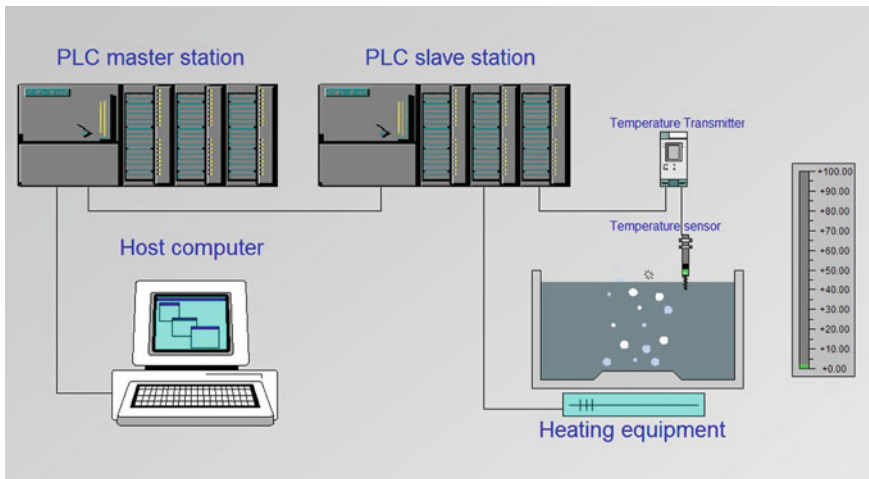


Fig. 2 WinCC monitor main screen

3 Dynamic Performance Analysis and Mathematical Model of the Controller Object

3.1 Dynamic Performance Analysis of the Controlled Object

The “heating-temperature rise” characteristics of controlled object are very complex in temperature control system. Temperature of an object is not a lumped parameter, but a distributed parameter, with the input and output of the energy, the temperature change has relationship not only with time, and also with the different position of object. Precise mathematical model cannot use ordinary differential

equations (time) to describe, but describe using partial differential equations (time and space).

In control process, it mainly contains three heat transfer method: conduction, convection, and radiation. The thermal conductivity is that the heat generated by the electric furnace rise the water temperature through the furnace wall; the convection mainly refers that due to uneven heating, the temperature of water at different positions of the furnace is different and flows for the heat exchange; thermal radiation is that the water in the furnace radiates heat to the external environment. It is very difficult to establish a precise mathematical model of the controlled object, because the input heat is the heat energy transformed from electrical energy, which transfer to the controlled object by conduction, but there are three kinds of heat transfer in heat dissipation.

In the temperature control system, only one “point” value in the temperature field of controlled object can be measured by a temperature sensor, when we use multiple sensors, we can only have a general understanding of temperature distribution, cannot accurately obtain the dynamic distribution of temperature in the entire temperature field. Based on these factors, when we treat one point value or more point values measured by the sensor as a lumped parameter, treat the controlled object as a lumped parameter object, linearize that at the equilibrium point of dynamic characteristics and use linear control system to control the controlled object, it is difficult to achieve a precise control.

3.2 *The Mathematical Model of the Controlled Object*

In the article, the controlled object is an electric furnace, which is a time-varying nonlinear systems with great inertia and time delay, its running processes is heating-heat-heating. Once the temperature is too high, it can only rely on natural cooling in the absence of refrigeration equipment. For the electric furnace, the input signal is a voltage U , the output signal is the furnace temperature T . When there is some heat flowing in, the temperature of water will rise, the process can be described as the following differential equation:

$$C \frac{dT}{dt} = q \quad (1)$$

where C is the heat capacity of water-kJ/(kg · °C), T is the water temperature-°C, q is the heat poured into water in the unit time-J.

Taking into account the electric furnace distribute heat to the ambient air and heat conduction, Eq. (1) can be re-described as follows:

$$C \frac{dT}{dt} = q - \frac{T - T_0}{R} \quad (2)$$

where T_0 is the ambient temperature, R is the thermal resistance of the electric furnace wall. Q can be considered the heating power of the electric furnace, Eq. (2) can be expressed as follows:

$$C \frac{dT}{dt} + \frac{T - T_0}{R} = \frac{u^2}{r} \tag{3}$$

where u is the supply voltage, r is the internal resistance of the electric furnace.

As can be seen, the differential equations of the electric furnace are nonlinear differential equations. Although the electric furnace system can be equivalent to a linear system by linearization method, the heating process itself is a complex multi-variable input process and many factors should be considered in this process. In addition, the heat transfer of the temperature sensing element, thermal resistance also need be considered. According to the principle of thermal equilibrium, the heat balance equation of the thermal resistance is shown as follows:

$$\Delta q = C_1 \frac{dT_2}{dt} = \alpha S(T_1 - T_2) \tag{4}$$

where C_1 is the heat capacity of the thermal resistance, T_1 is the water temperature, T_2 is the temperature of the thermal resistance, Δq is the heat which pass to the thermal resistance from water per hour, α is the convective heat transfer coefficient between the water and the surface of thermal resistance, S is the surface area of the thermal resistance.

In Eq. (4), α , S are not easy to determine, the heat taken away through heat radiation in unit time cannot be accurately measured. Convective heat transfer is a complex process affected by many factors and its intensity fluctuates widely. α reflects the strength of the convective heat transfer, which relates to many factors that affect the heat transfer process, for example: the physical properties of the fluid, the causes of the convection, the size, shape, and relative position of the heat transfer surfaces. In view of the above factors, it is difficult to establish an accurate mathematical model of the controlled objects.

4 The Design and Testing of the Controller

Because of simple principle, easy to implement, independent control parameters and strong robustness, traditional PID controller has become a most widely used automatic controller. In the digital computer, the mathematical model of the PID controller can be expressed as follows:

$$u(k) = K_p \left[e(k) + \frac{T_s}{T_i} \sum_{i=0}^k e(i) + T_d \frac{e(k) + e(k-1)}{T_s} \right] \tag{5}$$

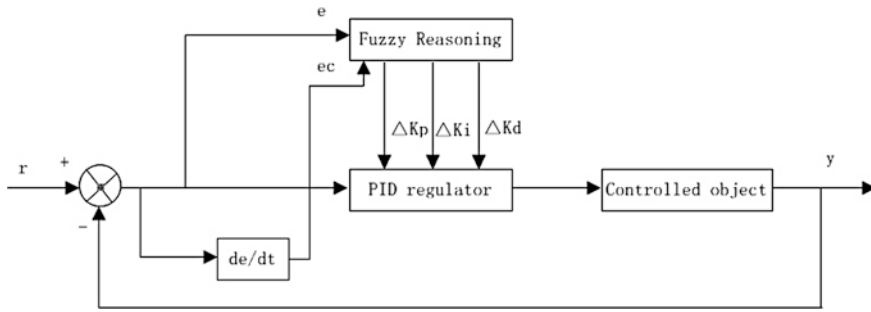


Fig. 3 Structure diagram of fuzzy PID controller

Table 1 The rules of fuzzy control

| e/ec | NB | NM | NS | ZO | PS | PM | PB |
|------|----------|----------|----------|----------|----------|----------|----------|
| NB | PB/NB/PS | PB/NB/NS | PM/NM/NB | PM/NM/NB | PS/NS/NB | ZO/ZO/NM | ZO/ZO/PS |
| NM | PB/NB/PS | PB/NB/NS | PM/NM/NB | PS/NS/NM | PS/NS/NM | ZO/ZO/NS | NS/ZO/ZO |
| NS | PN/NB/ZO | PM/NM/NS | PS/NS/NM | PS/NS/NM | ZO/ZO/NS | NS/PS/NS | NS/PS/ZO |
| ZO | PN/NM/ZO | PM/NM/NS | PS/NS/NS | ZO/ZO/NS | NS/PS/NS | NM/PM/NS | NM/PM/ZO |
| PS | PS/NM/ZO | PS/NS/ZO | ZO/ZO/ZO | NS/PS/ZO | NS/PS/ZO | NM/PM/ZO | NB/PB/ZO |
| PM | PS/ZO/PB | ZO/ZO/NS | NS/PS/PS | NM/PS/PS | NM/PM/PS | NB/PB/PS | NB/PB/PB |
| PB | ZO/ZO/PB | ZO/ZO/PM | NM/PS/PM | NM/PM/PM | NM/PM/PS | NB/PB/PS | NB/PB/PB |

Although most of the temperature control system using this control algorithm, the control effect of PID controller depends largely on the tuning of the controller parameters, and the parameter tuning process is complicated depending on the type of the object model. In addition, PID control is better to control the linear systems, but is not ideal for the control of nonlinear systems. The temperature control system is a typical nonlinear time-varying system, and the impact factors are complicated and changeable as previously described [3]. If using PID controller, the parameters must be adjusted at any time according to the changes of the controlled object, which will affect the normal operation of the system.

Self-tuning fuzzy PID controller is composed of a standard PID controller and fuzzy self-tuning institutions, the diagram shown in Fig. 3.

Where y is the measured value, e is the error, ec is the changing rate of the error [4]. In the process of system operation, based on the fuzzy relationship between the three parameters of PID K_p , K_i , K_d and e , ec , the changes of e and ec are continuously detected, which calculated through r and y , and the three parameters of the PID controller are online modified using the fuzzy reasoning in order to achieve the parameters' self-tuning.

The fuzzy subset of input variables e and ec is $\{NB, NS, NM, ZO, PM, PB\}$, the fuzzy subset of output variable K_p, K_i, K_d is $\{ZO, PS, PM, PB\}$, the input membership function is the gaussian function, the output using triangular membership functions, based on the output characteristics of the system, the fuzzy control rules as shown in Table 1:

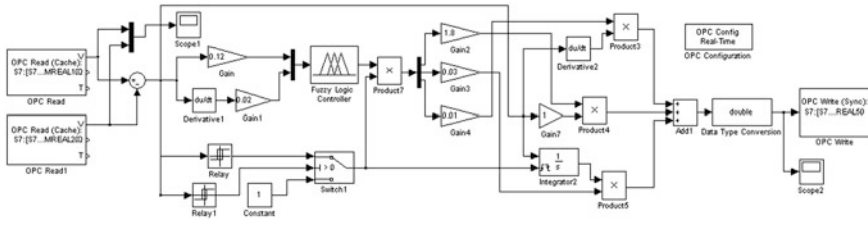


Fig. 4 The system structure of improved self-tuning fuzzy PID controller

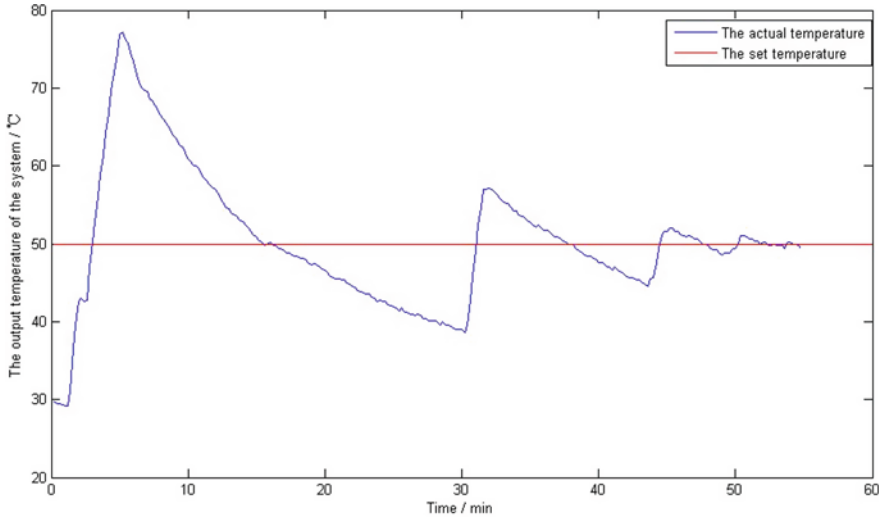


Fig. 5 The temperature control curve of conventional PID

The fuzzy factor $K_e=0.12$, $K_{ec}=0.02$, the defuzzification factor $up = 1.8$, $ui = 0.03$, $ud = 0.01$. e , and ec are quantified as fuzzy quantity on $(-3, 3)$ by K_e and K_{ec} , which are dynamic processed into the amounts of fuzzy control using the rules of the fuzzy control, the fuzzy range is $(0, 3)$. The results are defuzzificated by up , ui and ud , the three parameters of PID controller is obtained at last.

Since there is a large overshoot in the actual control process, it needs a long time to reach steady. We add a function of automatic identification and clear on the basis of self-tuning fuzzy PID controller. When the actual temperature is closed to the set temperature (temperature difference about $2\text{ }^\circ\text{C}$), the output of controller is to be cleared by the block of Relay and Switch. Once the heating device receives this signal, they will stop heating and the self-tuning fuzzy PID controller restarts when the temperature difference is about $0.5\text{ }^\circ\text{C}$, then continue to use the controller implementing the fine-tuning of temperature, ultimately achieve the purpose of the precise adjustment of temperature. The system structure of improved self-tuning fuzzy PID controller is shown in Fig. 4:

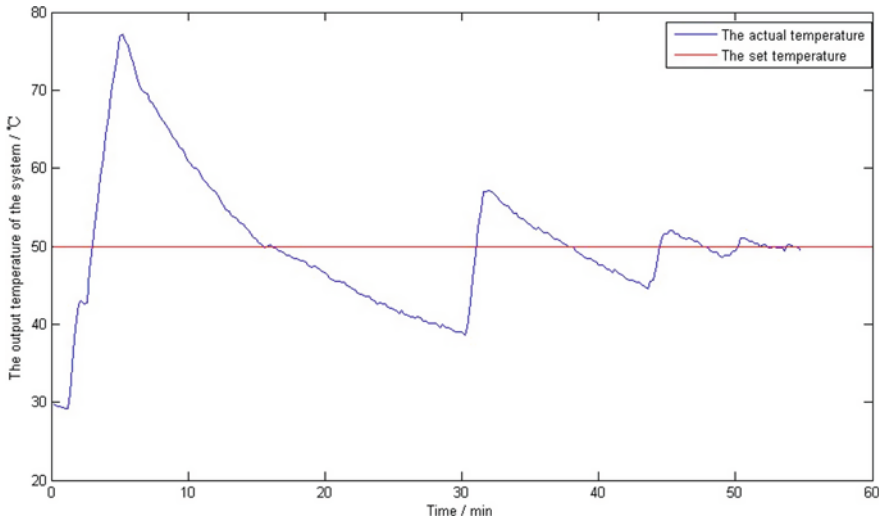


Fig. 6 The temperature control curve of fuzzy self-tuning PID controller

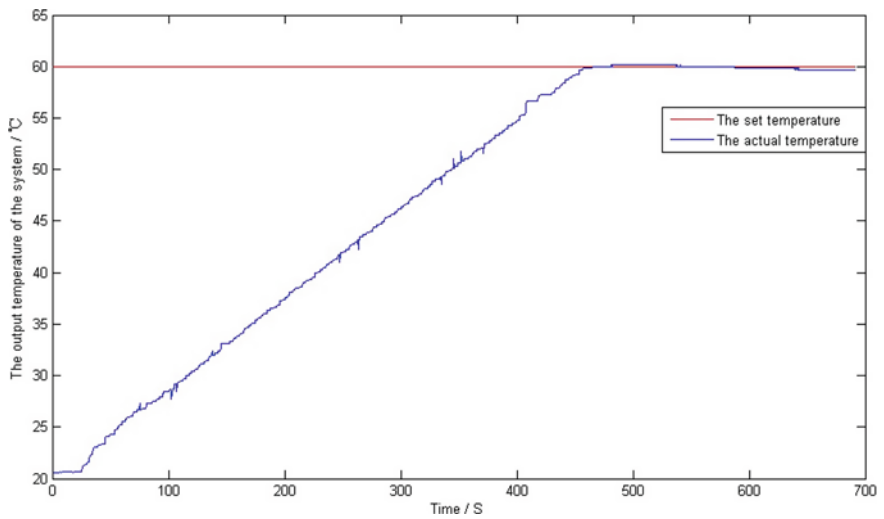


Fig. 7 The temperature control curve of improved fuzzy self-tuning PID controller

In the experiments, we separately use the conventional PID controller, fuzzy self-tuning PID controller and the improved fuzzy self-tuning PID controller to control the electric heating furnace, the control results shown in Figs. 5, 6 and 7:

From the control effects, we could see that the improved controller can achieve the desired temperature in a shorter time, and have good stability, superior control performance and no overshoot.

5 Conclusions

Based on the analysis of conventional PID and fuzzy self-tuning PID controller, an improved fuzzy self-tuning PID controller has been designed in this paper and used in the actual temperature control system of electric furnace. The experimental results show that the improved fuzzy self-tuning PID controller has good control effect, strong stability, no overshoot, and high control efficiency.

References

1. Fan J, Zheng B (2008) Development of temperature control theory. *Ind Furn* 30:12–14
2. Yu H, Zhang W, Shi X (2009) Temperature control system based on PLC and WinCC. *Process Control Comput* 22:6–8
3. Lin X, Yan J, Jianhui W, Tong G, Xiangyi D (2008) Design of fuzzy-PID controller based on prediction model and its realization in PLC. In: *Control and decision conference, 2008. CCDC 2008*. Chinese, pp 3808–3811
4. Zhang G (2002) *Fuzzy control and matlab applications*. Xi'an Jiaotong University Press

Research on Predictive Control of Evaporator Superheat System with Time-Delay Based on DMC Intelligent Optimization

Jun Xie, Songli Wang, Yuwei Wang and Jianzhong He

Abstract As for the evaporator superheat with the characteristics of large time delay, this paper puts forward predictive control method with intelligent rolling optimization. Based on the input data of the object to identify the object dynamic model of the evaporator superheat, it predicts the next time output of the system using the prediction model based on Dynamic Matrix Control (DMC), to control the superheat requirements in the target range. The experimental results show than using the control method of DMC, the system runs stable, and has strong anti-interference. Compared with conventional PID control, the DMC control runs more accurately, and can get better control effect.

Keywords Evaporator superheat · Intelligent rolling optimization · Predictive control · Dynamic matrix control (DMC)

1 Introduction

In the cold storage system, the flow rate of refrigerant into evaporator plays a significant role in change of cold storage temperature. The current method is that evaporator superheat selected as control variable constitutes control loop with electronic expansion valve (EEV) and the valve controls the superheat temperature to keep storage temperature stable around the setting value. However, because of the complex process, there is large inertia and delay characteristics within evaporator

J. Xie (✉) · S. Wang · Y. Wang · J. He (✉)

School of Optical-Electrical and Computer Engineering, University of Shanghai for Science and Technology, Shanghai, China
e-mail: 547699825@qq.com

J. He

e-mail: hjzhyf@163.com

superheat plant. For such a complicated controlled plant, the traditional PID is difficult to obtain good control effect; this paper introduces the predictive control method, with intelligent rolling optimization, for controlling the complex process. Because predictive control can predict the system output changes in the future, online and repeated optimization calculation according to the prediction model can timely eliminate the time-delay, model mismatch, the error generated by the interference and other factors, to achieve the best control of evaporator superheat.

2 Intelligent Optimizing: Dynamic Matrix Control

The dynamic matrix control (DMC) is a predictive control algorithm with intelligent rolling optimization, using the unit step response, which is easy to get, as a system model and adaptive to the plant with pure delay object and open-loop asymptotic stability. DMC algorithm includes three parts, predictive model, rolling optimization, and feedback correction. DMC system block diagram shown as Fig. 1.

In Fig. 1, w is for set value of evaporator superheat, $u(k)$ for the evaporator input meaning the EEV opening degree, $y(k)$ for the evaporator output, $y_r(k+i)$ for the reference track; $y_m(k)$ for prediction model of evaporator, $e(k)$ for the model error, and $y_p(k+i)$ for the error corrected prediction model.

2.1 The Prediction Model

The prediction model of evaporator plant consists of two parts, the output $Y_0(k+1)$ generated by past control and the output response $A\Delta U(k)$ generated by current input.

$$Y_m(k+1) = Y_0(k+1) + A\Delta U(k)$$

where $Y_m(k+1)$, the predicting model output vector, usually denoted as

$$Y_m(k+1) = [y_m(k+1|k) \dots y_m(k+p|k)]^T.$$

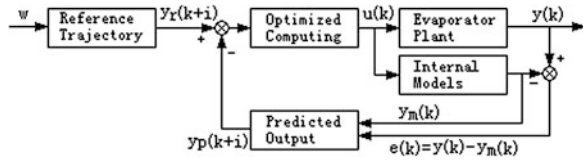
The $Y_0(k+1)$, the initial prediction model, usually denoted as

$$Y_0(k+1) = [y_0(k+1|k) \dots y_0(k+p|k)]^T$$

and the M items of continuous control increment vector to solve is

$$\Delta U(k) = [\Delta u(k) \dots \Delta u(k+M-1)]^T$$

Fig. 1 DMC system block diagram



$$A = \begin{bmatrix} a_1 & & & 0 \\ \vdots & \ddots & & \\ a_M & \dots & \dots & a_1 \\ \vdots & & & \vdots \\ a_P & \dots & \dots & a_{P+M-1} \end{bmatrix}$$

where A is matrix composed of step response coefficient, called dynamic matrix. P is the prediction step length, M the control step length. Generally $M < P < N$, N is prediction model step length.

2.2 Intelligent Rolling Optimization

In the evaporator superheat control of refrigeration system, the control objective is to make the evaporator superheat along the reference trajectory $y_r(k+i)$ gradually reach the set value W . Therefore, we select the intelligent rolling optimal performance index function as

$$\min J(k) = \sum_{i=1}^P q_i (y_r(k+i) - y_m(k+i|k))^2 + \sum_{i=1}^M r_i \Delta u(k+i-j)^2$$

where the reference trajectory usually takes a first-order exponential form, as follows

$$y_r(k+i) = y(k) + [w - y(k)] \left(1 - e^{-iT_s/t} \right).$$

Through the way to limit, it can get the optimal control increment solution

$$\Delta U(k) = (A^T Q A + R)^{-1} A^T Q (y_r(k) - A_0 U(k-1) - h e(k)).$$

In the actual control, it takes the first term as real-time control incremental only, that is

$$u(k) = [10 \dots 0] (A^T Q A + R)^{-1} A^T Q Y(k+1) - A_0 U(k-1)$$

Using the above-obtained control increment, we can calculate at step k moment control action $u(k)$ to put on the plant, that is the opening degree of EEV within evaporator flow control actuator as below

$$u(k) = u(k-1) + \Delta u(k)$$

2.3 Feedback Compensation

Considering the time-varying, nonlinear, and various random disturbances in the refrigerating system, there are some error between the prediction model and actual model. Therefore, it is necessary to correct with predictive error by real-time calculation as below

$$e(k+1) = y(k+1) - \tilde{y}m(k+1|k).$$

Correct output predictive value with the above-predictive error

$$\tilde{y}_{cor}(k+1) = \tilde{y}Nm(k) + h e(k+1).$$

After taking correct output predictive value into shift operation, we define an initial predictive value at the new step moment as below

$$\tilde{y} No(k+1) = S \tilde{y}_{cor}(k+1).$$

And redefine the new step moment as step k moment, so $\tilde{y}NO(k+1)$ will be regarded as a new initial predictive value $\tilde{y}NO(k)$ at the step k moment, and then takes part in calculation of controlling increment at the new time with the former P components and the expected outputs together.

3 The Dynamic Model of the Evaporator Superheat

3.1 Experimental Facility

In this paper, we choose the evaporator superheat as the controlled process value and its experimental facility as shown in Fig. 2.

In the Fig. 2, E is for evaporator, Comp for compressor, Cds for condenser, $V1$ for solenoid valve, $V2$ for EEV, P for pressure sensor, $P1$ for inlet pressure measured by press transducer P , $T2$ for the evaporation temperature measured by the temperature sensor, y for superheat, w for the set point of superheat and u for controller output.

3.2 The Measurement of Evaporator Superheat

The instantaneous evaporator superheat y can be measured by the following approach: First, the evaporation temperature $T2$ is measured by the temperature sensor at the entrance of the evaporator. And the inlet pressure $P1$ of the evaporator is measured by pressure sensor at the exit, then transforms $P1$ into corresponding inlet pressure temperature $T1$. Finally, the static value of the superheat can be obtained by the difference between $T1$ and $T2$ ($T1-T2$). As for the dynamic value, it is need to add the pure delayed time to the basis date.

The function expression of instantaneous evaporator superheat y is:

$$y = f\left((T1(P1) - T2), \frac{d}{dt}\right).$$

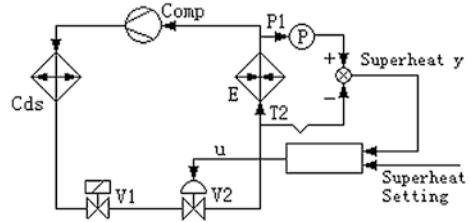
3.3 The Establishment of Evaporator Superheat

According to the features of evaporator, we can use one-order transfer function plus time delay to represent approximately the response of evaporator superheat to the opening of EEV as below

$$G(s) = \frac{Y(s)}{U(s)} = \frac{Ke^{-T_d s}}{1 + T_s s}$$

where, the gain K , time constant T and pure delayed time T_d can be calculated by the response rising curve of the superheat along with the opening changing of EEV.

Fig. 2 Refrigeration evaporator superheat control system diagram



To determine the above three parameter values, we apply a short-time pulse signal to EEV under the condition of the normal operation of the system, and then we can get a corresponding response curve of superheat. According to the input/output data of EEV-superheat loop, we can make use of generalized least squares identification method to determine the above transfer function parameters as below

$$T = 100 \text{ s}, T_d = 30 \text{ s}, K = 0.28 [1].$$

In general, the ratio between the pure delayed time T_d of the superheat object and the time constant T is greater than 0.3. Therefore, the controlled process is a typical large pure delayed plant.

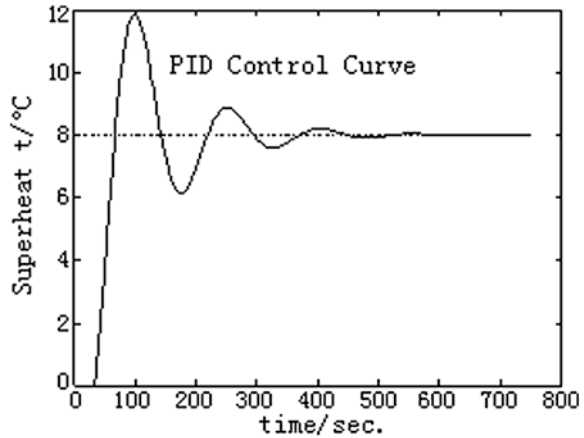
4 System Simulation

4.1 DMC Control Parameter Selection

There are some parameters to be determined in the DMC control, such as, the sampling period T_s , the sequence model length N , the intelligent rolling optimization steps P , and the control steps M . We now discuss those parameters below.

- (1) The sampling period T_s and the length of the sequence model N
The selection of the sampling period should meet Shannon sampling theorem. Considering controlled process with a large time delay, it is suitable for $T_s \leq 0.25T_d$, in which T_d is a large delay time. To make the model parameters a_i ($i = 1, 2, \dots, N$) contain the dynamic information of plant as complete as possible, it usually requires step response after NT steps to be close to the steady-state value.
- (2) The intelligent rolling optimization steps P and the error weighting matrix Q
In order to make dynamic optimization meaningful, firstly, the optimization steps P must exceed the delay section of the plant step response and cover the main parts of dynamic response. Here Q is set to the unit matrix.
- (3) The control steps M and the control weighting matrix R
 M is the number of optimal control values in the future. Since the control action applied to the plant is rolling optimization during on-line and real-time in the DNC algorithm, $M = 1$ is suitable. The control weighting matrix R can be adjusted according to the control effect.

Fig. 3 Traditional PID control effect



4.2 The Comparison of Control Methods

In order to highlight the advantages of Dynamic Matrix Control, in this paper, we have a comparison of effects between the PID control and DMC control.

- (1) PID control algorithm. According to Ziegler–Nichols parameter tuning formula, PID parameters can be determined as below
 $K_p = 10.71, T_i = 100$ s.
 The Superheat process is a plant with large time delay and subjective to various noises, traditional PID control will have a greater overshoot and tend to oscillation, therefore, the control effect with PI is better than with PID, we give the PI simulation results as shown in Fig. 3.
- (2) For DMC, we mainly study the selection of prediction steps P and control steps M with intelligent rolling optimization. According to the step response of the evaporator plant, we can define the sampling period $T_s = 5$ s, model length $N = 150$. Firstly, let $M = 1$, that is control steps. We change $P = 30, 50$ and 80 respectively, and compare three simulation results with above different P . the simulation results are shown in Figs. 4 and 5.

4.3 The Intelligent Predictive Control Effect Analysis

- (1) Comparing superheat response in Fig. 4 with Fig. 5, we can see that PID control has bigger overshoot and waving, and dynamic matrix control is smooth and its response curve can smoothly reach the target degree of superheat, although PID control superheat output rise time is faster than the dynamic matrix control.

Fig. 4 When $M = 1$, the different predictions of the control effect of length P

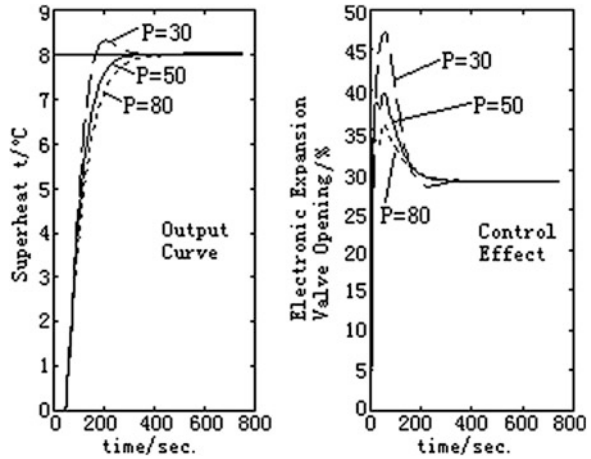
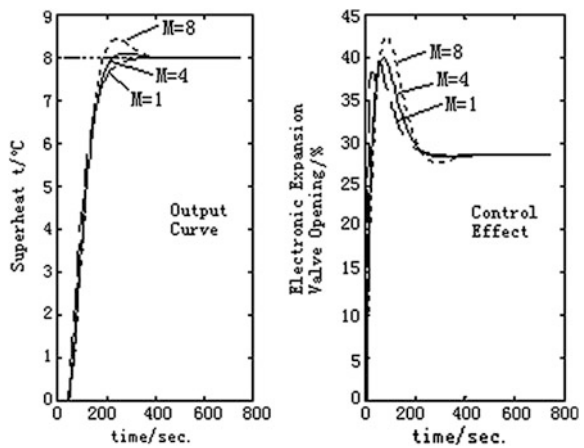


Fig. 5 When $P = 50$, the length M of the different control effect



Considering that the opening change of EEV should be as smooth as possible in actual codling control, to avoid frequent opening and stop and assure its life. So the regulation time and overshoot of the superheat are the important indexes during the transition process to reaches the set value.

- (2) As illustrated in the Figs. 4 and 5, we can make the superheat change smoothly to be an ideal control result, by adjusting the parameters in the dynamic matrix control with $P = 50$ and $M = 1$.
- (3) Comparing it with the PID, we know that for the plant with large time delay, overshoot is large when it uses PID control, while the control action of dynamic matrix control changes rather smoothly, and enable to reach process stable quickly.

Additionally, in the real cold store, evaporator model parameters change along with refrigerant flow changing, for example, gain and delay time would increase. When the models change, the PID parameters set originally cannot obtain a good control effect. Dynamic matrix control with intelligent rolling optimization has a low requirement about model precision and a good adaptability.

5 Conclusions

We can use DMC approach with intelligent rolling optimization to target the large time delay characteristics of evaporator superheat plant; DMC is predicting the entire delay system changes in advance and improving predictive control effect in the way of identifying the dynamic model of controlled plant. DMC simulation and experimental results show in our paper that the method is simple, with high reliability and good control effects.

References

1. Shu D (1996) Predictive control system and its application. Machinery Industry Press, Beijing

Fault Diagnosis Based on Principal Component Analysis and Support Vector Machine for Rolling Element Bearings

Zhicai Zhou, Dongfeng Liu and Xinfu Shi

Abstract An intelligent fault diagnosis method of rolling element bearings based on statistics analysis, principal component analysis (PCA), and support vector machine (SVM) is presented. The method consists of three stages. First, due to the fact that it is hard to obtain sufficient fault samples in practice, different features are extracted as many as possible to acquire more fault characteristic information. Second, the original feature set is compressed with PCA from 43 to 4 dimensions. Finally, the compressed feature set is fed into SVM classifier to identify the fault patterns of the rolling element bearings. For comparison, the back propagation neural network (BPNN) is also utilized to solve the same problem. The results show that the proposed method can achieve higher accuracy and adaptability than BPNN when facing high-dimensional, nonlinear, and a smaller number of samples.

Keywords Support vector machine · Principal component analysis · Fault diagnosis · Rolling element bearings

1 Introduction

Rolling element bearings in rotating machinery have been widely used in the modern manufacturing industry whose operational statuses have a direct impact on the performance of the machine. According to statistics, 30 % of the rotating machinery failures were caused by bearing faults. Therefore, the research on bearing fault diagnosis method [1] has a very important practical significance.

Some intelligent fault diagnosis methods, such as artificial neural network, have been successfully applied to automated detection and diagnosis of machine

Z. Zhou (✉) · D. Liu · X. Shi
Qingdao Oil Detection and Analysis Center, Naval University of Engineering, No. 33,
Baotou Road, Shibei District, Qingdao, Shandong, People's Republic of China
e-mail: oncehappy@gmail.com

conditions [2–4]. It is a heuristic technique that relies on the experience and its learning process is based on empirical risk minimization (ERM) principle, thus it is prone to over-fitting and low generalization ability in the case of the small sample size. In addition, it is hard to determine the number of hidden layers and nodes of the neural network without experience, and the network structure and algorithm will also be in complicated condition as high-dimensional complex samples. Therefore, simpler and more accurate approaches are needed which allow relatively unskilled operators to make reliable decisions with high-dimensional and smaller number of samples.

Support Vector Machines, proposed by Vapnik, is a new machine learning method based on statistical learning theory (SLT) by utilizing structural risk minimization (SRM) principle, and it has a good performance to solve the problems such as a smaller sample number, nonlinearity, high dimension, and local optimal solution. Recently, SVM has been found to be remarkably effective in many real-world applications [5–8].

2 Feature Extraction

The fault characteristic information extracted from the collected data directly affects the accuracy and reliability of fault diagnosis. In order to acquire more fault characteristic information, different features, including time-domain statistical characteristics, frequency-domain statistical characteristics, and empirical mode decomposition (EMD) energy entropies, are extracted.

2.1 *Statistical Characteristics in Time-Domain*

Statistical methods which have been widely used in fault diagnosis and pattern recognition can provide the physical characteristics of time domain data. In this paper, we divide the original data into some signals of 4,096 data points. Fairly 11 feature parameters [4] are extracted from each of these signals for the study.

2.2 *Statistical Characteristics in Frequency-Domain*

Frequency-domain feature is another description of a signal. It reveals some information which cannot be indicated in time-domain. In this paper, 13 frequency-domain feature parameters [4] are extracted from the vibration signals.

When mechanical equipments fault occur or operate anomaly, the corresponding vibration or noise signals usually show nonstationary characteristics. The traditional feature extraction method plays an important role in stationary signals,

but for nonstationary signal, it does not reflect the signal amplitude changes with the frequency variation accurately. Here, we demodulate the vibration signals with Hilbert transform [9] and the demodulation spectrums are further processed to extract another 13 frequency-domain feature parameters.

$$a + b = c \tag{2.1}$$

2.3 EMD Energy Entropy

The EMD, in contrast to almost all the previous methods, works in temporal space directly rather than in the corresponding frequency space. It is intuitive, direct, and adaptive, with a posteriori defined basis derived from the data [10]. The decomposition has implicitly a simple assumption that, at any given time, the data may have many coexisting simple oscillatory modes of significantly different frequencies, one superimposed on the other. Each component is defined as an intrinsic mode function (IMF). In our experiment, the first six IMFs containing almost all valid information are selected. The EMD energy entropies are calculated from the IMFs of each signal and six energy features are obtained.

Now, we got a feature set containing 43 features, which simultaneously covers the characteristic information in time-domain and frequency-domain.

3 Review of PCA

When a big number of feature characteristics are used for pattern recognition, it is equivalent to identify the fault patterns in high-dimensional space. Then, in order to avoid the curse of dimensionality and discard irrelevant or redundant features, the feature characteristics need to be compressed.

Suppose there is a given training sample set

$$x_k = (x_{1k}, x_{2k}, \dots, x_{Nk})^T \quad (k = 1, 2, \dots, M) \tag{3.1}$$

where N is the number of the demission of feature set, and M is the data sets of each condition. Then the Principal Component Analysis method can be depicted as follows:

Step 1: Calculating the normalized data sets of original sample sets

$$\tilde{x}_{ik} = \frac{(x_{ik} - \bar{x}_i)}{\sigma_i} \quad (k = 1, 2, \dots, M) \tag{3.2}$$

where $\bar{x}_i = \frac{1}{M} \sum_{k=1}^M x_{ik}$, $\sigma_i^2 = \frac{1}{M} \sum_{k=1}^M (x_{ik} - \bar{x}_i)^2$ ($i = 1, 2, \dots, N$);

then getting the new feature set

$$\tilde{x}_k = (\tilde{x}_{1k}, \tilde{x}_{2k}, \dots, \tilde{x}_{Nk})^T \quad (3.3)$$

Step 2: Calculating the covariance matrix

$$C = \frac{1}{M} \sum_{k=1}^M \tilde{x}_k \tilde{x}_k^T \quad (3.4)$$

Step 3: Computing the characteristic equation about covariance matrix C :

$$Cv = \lambda v \quad (3.5)$$

where λ is the eigenvalue of C , and v is the eigenvector corresponding eigenvalue λ .

Then arranging the eigenvalues in descending order $\lambda_1 \geq \lambda_2 \geq \dots \geq \lambda_N$, and the corresponding eigenvectors are v_1, v_2, \dots, v_N ;

Step 4: According to preset compression dimension number p or the cumulative contribution η_0 , the minimum p satisfied $\eta \geq \eta_0$ is calculated and standardizing the first p eigenvectors

$$\tilde{v}_i = \frac{v_i}{\|v_i\|} \quad (i = 1, 2, \dots, p) \quad (3.6)$$

Step 5: Projecting \tilde{x}_k onto various standardized eigenvectors and the compressed eigenvectors are calculated as follows:

$$y_{ik} = \langle \tilde{v}_i, \tilde{x}_k \rangle \quad (i = 1, 2, \dots, p; k = 1, 2, \dots, M) \quad (3.7)$$

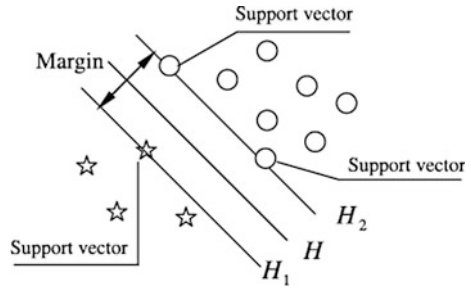
Through the principal component analysis, it is possible to eliminate the components of the correlation between the original feature eigenvectors [11] and remove less fault information to reduce the number of dimensions of the feature space. With PCA it does not generate a lot of loss of information to achieve the compression of feature dimension.

4 Review of SVM

SVM is developed from SLT which is presented by Vapnik. Its basic principle can be illustrated in two-dimensional way [12] which is shown in Fig. 1. It shows the classification of a series of points for two different classes of data, class A (circles) and class B (pentacles). SVM tries to place a linear boundary H between the two classes and orients them in such way that the margin is maximized, namely, the distance between the boundaries is maximal. The nearest data points in each class used to define the margin are known as support vectors.

Suppose that a given training sample set $(x_1, y_1), (x_2, y_2), \dots, (x_N, y_N)$, where $x_i \in R^N$ is a N dimensional vector, and $y_i \in \{-1, +1\}$. The boundary H_1 and H_2 can be expressed as $(w \cdot x) + b = \pm 1$, where w is a weight vector and b is a bias.

Fig. 1 Classification of data by SVM



Consider making all the training samples are correctly classified, it should satisfy the following conditions:

- When $y_i = 1, (w \cdot x) + b \geq 1$;
- When $y_i = -1, (w \cdot x) + b \leq -1$

The optimal hyperplane separating the data can be obtained as a solution to the following constrained optimization problem:

$$\begin{cases} \min \frac{1}{2} \|w\|^2 + C \sum_i \xi_i \\ st : y_i((w \cdot x_i) + b) \geq 1 - \xi_i \end{cases} \quad (4.1)$$

Here training vectors x_i are mapped into a higher (maybe infinite) dimensional space by the function ϕ . SVM finds a linear separating hyperplane with the maximal margin in this higher dimensional space. $C > 0$ is the penalty parameter of the error term. Furthermore, $K(x_i, x_j) = \phi(x_i)^T \cdot \phi(x_j)$ is called the kernel function. There are four basic kernels as following:

- linear: $K(x_i, x_j) = x_i^T x_j$
- polynomial: $K(x_i, x_j) = (\gamma x_i^T x_j + r)^d, \gamma > 0$
- radial basis function (RBF): $K(x_i, x_j) = \exp(-\gamma \|x_i - x_j\|^2), \gamma > 0$
- sigmoid: $K(x_i, x_j) = \tanh(\gamma x_i^T x_j + r)$

Here, $\gamma, r,$ and d are kernel parameters.

Then, applying Lagrange Multiplier and considering the conditions of Karush-Kuhn-Tucker:

$$\alpha_i(y_i((x \cdot x_i) + b) - 1) = 0 \quad (4.2)$$

The optimal hyperplane could be depicted as follows:

$$M(x) = Sgn\left(\sum_{S.V.} \alpha_i^* y_i (\phi(x) \cdot \phi(x_i)) + b^*\right) = Sgn\left(\sum_{S.V.} \alpha_i^* y_i K(x, x_i) + b^*\right) \quad (4.3)$$

5 Fault Diagnoses

The bearings vibration data sets used in the paper come from Case Western Reserve University of USA [13]. Single-point faults were introduced to the test SKF bearings using electro-discharge machining with fault diameters of 0.007 or 0.021 inches. The test bearings were tested under the four different loads (0, 1, 2, 3 hp) and conditions: (i) normal, (ii) inner race fault, (iii) outer race fault, and (iv) rolling element fault, respectively.

In order to verify the effectiveness of the proposed method, we select a different type of fault vibration signals which are collected under various loads and different fault categories and severities. The detailed description of the data set is shown in Table 1.

Failure label is divided into seven categories, and a total of 16 samples are collected as one data sample set for each fault type in four different loads (0, 1, 2, 3 hp). The 112 data samples are divided into 56 training samples and 56 testing samples. In order to identify the different grades of faults, we solve the seven-class classification problem.

According to the feature extraction methods mentioned in Sect. 2, 43 fault features are extracted from the samples and then presented to normalization processing. In particular need to be emphasized, here we take the training and testing samples together to normalization processing in order to make the training model with greater adaptability and accuracy. The normalized feature data is compressed from 43 to 4 dimensional with PCA (here we set the cumulative contribution $\eta_0 = 90$), as shown in Fig. 2.

Here, we choose the RBF kernel which has fewer numerical difficulties for model training and recommend a grid search on C and γ using cross-validation which can prevent the overfitting problem. The best (C, γ) for the training model is (9.1896, 0.18946).

For comparison, the back propagation neural network (BPNN) is also utilized to solve the same seven-class classification problem. The BP neural network consists of four layers in which the node number of input layer, hidden layer, and output layer is 43, 25, 12, and 7, respectively.

As results are shown in Table 2, SVM shows better classification performance and higher accuracy than BPNN for the same training and testing samples in bearings fault classification. This is due to that BPNN requires training sample set should cover all possible inputting area. In other words, BPNN requires a complete set of training samples. So it is difficult to establish an accurate model for a smaller sample number. In addition, BPNN searches the minimum value through the local optimal solution, which does not guarantee the results exactly the same as the global optimal solution.

To test the effect of the PCA technique in this work, we carried out another experiment on the original data set with SVM and BPNN respectively. Here, the BPNN also consists of four layers in which the node of input layer, hidden layer, and output layer is 4, 4, 8, and 7, respectively.

Table 1 Description of bearing data set

| Label of classification | Operating condition | Defect size(inches) | The number of training samples | The number of testing samples |
|-------------------------|---------------------|---------------------|--------------------------------|-------------------------------|
| 1 | Normal | – | 8 | 8 |
| 2 | Inner race | 0.007 | 8 | 8 |
| 3 | Outer race | 0.007 | 8 | 8 |
| 4 | Rolling element | 0.007 | 8 | 8 |
| 5 | Inner race | 0.021 | 8 | 8 |
| 6 | Outer race | 0.021 | 8 | 8 |
| 7 | Rolling element | 0.021 | 8 | 8 |

Fig. 2 Principal component of the original data set with PCA

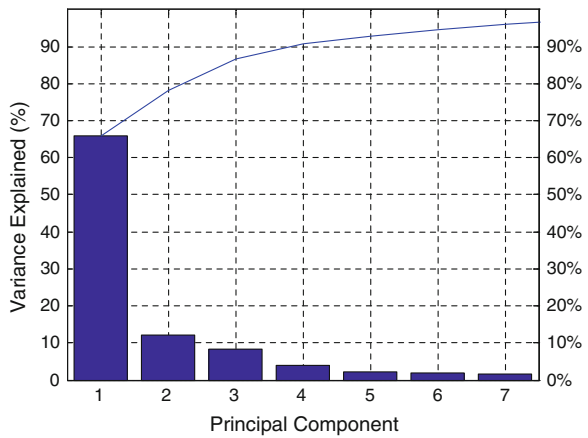


Table 2 The results of data set with SVM and BPNN

| Feature compression | Training model | Total time (s) | Accuracy (%) |
|---------------------|----------------|----------------|---------------|
| PCA | SVM | 6.29 | 100 (56/56) |
| PCA | BPNN | 7.34 | 96.43 (54/56) |
| None | SVM | 8.67 | 100 (56/56) |
| None | BPNN | 9.16 | 92.86 (52/56) |

By comparing the original data set to the compressed data set with PCA, we can see that SVM is still able to maintain good accuracy in the face of high-dimensional data. The model training time increases as more data dimensions. But for BPNN, the accuracy with original data set is worse than the compressed data set. This is due to BPNN learning slows down in face of high-dimensional data set and the redundant or irrelevant information also has an impact on the correctness of the training model.

6 Conclusions

A new automatic recognition method to intelligent fault diagnosis of rolling element bearings based statistics analysis, PCA, and SVM, is proposed in this paper. It provides the possibility to fulfill the automatic recognition to machinery faults with high accuracy even with high-dimensional and a smaller number of samples. In order to derive more faulty information, time-domain statistical characteristics, frequency-domain statistical characteristics, and EMD energy entropies are extracted, respectively. Then, the feature sets are compressed by applying PCA technique to remove irrelevant or redundant information. Finally, cross-validation and grid search are used for optimal parameters of SVM model, and the effectiveness of the model is demonstrated by the testing results. For comparison, BPNN is also utilized to solve the same problem. The results show that the proposed method can achieve high accuracy and adaptability when facing high-dimensional, nonlinear and a smaller number of samples.

Acknowledgments This work is supported by Defense Advance Research Fund of China (No. ZJ201181).

References

1. Nikolaou NG, Antoniadis IA (2002) Rolling element bearing fault diagnosis using wavelet packets. *NDT&E International* 35:197–205
2. Shen C, Wang D, Kong F, Tse PW (2013) Fault diagnosis of rotating machinery based on the statistical parameters of wavelet paving and a generic support vector regressive classifier. *Measurement* 46:1551–1564. doi:[10.1016/j.measurement.2012.12.011](https://doi.org/10.1016/j.measurement.2012.12.011)
3. Saimurugan M, Ramachandran KI, Liang S, Sugumaran V et al (2011) Multi-component fault diagnosis of rotational mechanical system based on decision tree and support vector machine. *Expert Syst Appl* 38:3819–3826. doi:[10.1016/j.eswa.2010.09.042](https://doi.org/10.1016/j.eswa.2010.09.042)
4. Lei Y, He Z, Zi Y (2008) A new approach to intelligent fault diagnosis of rotating machinery. *Expert Syst Appl* 35:1593–1600. doi:[10.1016/j.eswa.2007.08.072](https://doi.org/10.1016/j.eswa.2007.08.072)
5. Kim H-C, Pang S, Je H-M, Kim D, Bang SY (2003) Constructing support vector machine ensemble. *Pattern Recogn* 36:2757–2767. doi:[10.1016/S0031-3203\(03\)00175-4](https://doi.org/10.1016/S0031-3203(03)00175-4)
6. Guo G, Li SZ, Chan KL (2001) Support vector machines for face recognition. *Image Vis Comput* 19:631–638
7. Fei S, Zhang X (2009) Fault diagnosis of power transformer based on support vector machine with genetic algorithm. *Expert Syst Appl* 36:11352–11357. doi:[10.1016/j.eswa.2009.03.022](https://doi.org/10.1016/j.eswa.2009.03.022)
8. Thissen U, Van Brakel R, De Weijer AP, de Weijer AP, Melsse WJ, Buydens LMC (2003) Using support vector machines for time series prediction. *Chemometr Intell Lab Syst* 69:35–49. doi:[10.1016/S0169-7439\(03\)00111-4](https://doi.org/10.1016/S0169-7439(03)00111-4)
9. Huang NE, Wu Z (2008) A review on Hilbert-Huang transform: method and its applications to geophysical studies. *Rev Geophys* 46. doi:[10.1029/2007RG000228](https://doi.org/10.1029/2007RG000228)
10. Rajakarunakaran S, Venkumar P, Devaraj D, Surya Prakasa Rao K (2008) Artificial neural network approach for fault detection in rotary system. *Appl Soft Comput* 740–778. doi:[10.1016/j.asoc.2007.06.002](https://doi.org/10.1016/j.asoc.2007.06.002)

11. Li Z, Yan X, Yuan C, Peng Z, Li L (2011) Virtual prototype and experimental research on gear multi-fault diagnosis using wavelet-autoregressive model and principal component analysis method. *Mech Syst Signal Process* 25:2589–2607. doi:[10.1016/j.ymssp.2011.02.017](https://doi.org/10.1016/j.ymssp.2011.02.017)
12. Yang Y, Yu D, Cheng J (2007) A fault diagnosis approach for roller bearing based on IMF envelope spectrum and SVM. *Measurement* 40:943–950. doi:[10.1016/j.measurement.2006.10.010](https://doi.org/10.1016/j.measurement.2006.10.010)
13. Case Western Reserve University (2005). Bearings vibration data centre. <http://www.eecs.cwru.edu/laboratory/bearing>. Accessed 20 July 2005

The Study on Risk Rating Model of Commercial Bank Credit Based on SVM

Menggang Li, Zuoquan Zhang and Rongquan Bai

Abstract According to the basic theories of Logit regression analysis and support vector machine (SVM), this article involves improved binary classification combination algorithm to increase the accuracy. In addition, using financial data of listed companies to test this improved model, it shows a better way of classification. When applying this model, there are some innovations: 1. Choose optimized composite indicator as a variable through principal component analysis and get more information; 2. Introduce Logit parameter model to the quadratic to increase prediction accuracy; 3. Put forward a combination of improved Logit model with SVM to increase prediction accuracy. This paper is supported by the Industrial Safety Engineering (239010522).

1 Basic Model Analysis

1.1 Logit Model

Define probability of default as:

$$P_i = \frac{e^{\alpha + \beta^T x_i}}{1 + e^{\alpha + \beta^T x_i}} \quad (1)$$

Logit Model [1] is a linear function about the natural logarithm of the ratio of default:

M. Li

Center for Industrial Security Research, Beijing Jiaotong University, Beijing, China

Z. Zhang (✉) · R. Bai

School of Science, Beijing Jiaotong University, Beijing, China

e-mail: zqzhang@bjtu.edu.cn

$$\ln \frac{p_i}{1-p_i} = \alpha + \beta^T x_i \quad (2)$$

1.2 Support Vector Machine

Support Vector Machine (SVM) was put forward by a Russian scholar called Vapnik, that a new way on machine learning is based on the statistics theories, which has already been widely applied on classification [2, 3].

Algorithm on SVM Classifier:

1. Suppose the known training set called T as follows:

$$T = \{(x_1, y_1), \dots, (x_l, y_l)\}, \quad x_i \in \mathbb{R}^n, \quad y_i \in \{+1, -1\}, \quad i = 1, 2, \dots, l \quad (3)$$

2. Choose kernel function $K(x, x')$ and appropriate penalty parameter C to set up the optimization problem to find the best solution $\alpha^* = (\alpha_1^*, \dots, \alpha_l^*)^T$

$$\begin{aligned} \min_{\alpha} \quad & \frac{1}{2} \sum_{i=1}^l \sum_{j=1}^l y_i y_j \alpha_i \alpha_j K(x_i, x_j) - \sum_{j=1}^l \alpha_j \\ \text{s.t.} \quad & \sum_{i=1}^l y_i \alpha_i = 0 \\ & 0 \leq \alpha_i \leq C, \quad i = 1, \dots, l \end{aligned} \quad (4)$$

3. Choose one component α_j^* of α^* , which is between zero and C , and calculate the equation below.

$$b^* = y_j - \sum_{i=1}^l y_i \alpha_i^* K(x_i, x_j) \quad (5)$$

4. Attain a decision function recorded as:

$$f(x) = \text{sgn} \left[\sum_{i=1}^l y_i \alpha_i^* K(x_i, x) + b^* \right] \quad (6)$$

1.3 Comparison and Analysis Between Logit Model and SVM

According to the form above, these two algorithms can be complementary. Based on this point, the combined model between Logit and SVM is put forward (Table 1).

Table 1 Comparison and analysis between logit model and SVM

| | Advantage | Disadvantage |
|-------------|---|--|
| Logit model | (1) No requirement of whether data shows a normal distribution; (2) decide degree of influence of different factors; (3) evaluate quickly; (4) be good at large amount of samples | If there is something wrong with data, the result can be influenced greatly because this model completely relies on data |
| SVM | (1) Apply kernel function to avoid curse of dimensionality;(2) no requirement of whether data shows a normal distribution; (3) depend on support vector rather than sample | It can only be applied on a few samples and not solve the classification problem |

1.4 Model Improvement

1.4.1 QFL Model

In this article, Logit model is improved and Quadratic Form Logit (QFL) [4] has been introduced. The quadratic is used to change interaction among variables. The QFL model is showed below:

$$F(y) = \frac{1}{1 + \exp\left(\alpha + \sum_{i=1}^n \beta_i x_i + \sum_{i=1}^n \sum_{j=i+1}^n \gamma_{ij} x_i x_j\right)} \tag{7}$$

1.4.2 PCA-QFL Model

Suppose that there is financial data of n companies and each has p variables to be tested.

Use principal component analysis to reduce the dimensionality of variables and then attain the integrated ones recorded as $F_1, F_2, \dots, F_m (m \leq p)$.

Use them as independent variables and introduce them to the QFL Model so as to get the PCA-QFL Model.

1.4.3 PCA-QFL and SVM Integrated Model

A combination of classification algorithm is put forward based on PCA-QFL model and SVM to reduce empirical risks when learning support vector machine, increasing classification accuracy.

PCA-QFL and SVM Integrated Classification Algorithm:

1. Suppose the known training set called T as follows:

$$T = \{(x_1, y_1), \dots, (x_l, y_l)\}, \quad x_i \in R^n, \quad y_i \in \{+1, -1\}, \quad i = 1, 2, \dots, l.$$

Use the Maximum Likelihood Estimates to get parameters of PCA-QFL model recorded as α, β, γ , and get results p_i corresponding to samples.

2. Calculate the mean of probability of negative and positive points according to the equation below:

$$\begin{aligned} p &= \frac{1}{n_1} \sum p_i & \text{if } p_i < 0.5 \\ \dot{p} &= \frac{1}{n_2} \sum p_i & \text{if } p_i > 0.5 \end{aligned} \quad (8)$$

3. The results p_i are divided into four internals:

$$A = [0, p), B = [p, 0.5), C = [0.5, \dot{p}], D = (\dot{p}, 1] \quad (9)$$

Calculate classification accuracy of the samples corresponding to each internal. The sample inputs of internals A and D can quote the classification outcomes of PCA-QFL model.

4. Because p corresponds to the separation point between positive and negative ones, which is equal to 0.5, larger errors may turn up on the edge of classification. And then the sample inputs of internals B and C are not fit in the outcomes of PCA-QFL. Thus, it is advisable to use SVM classification as mentioned in 2.4.4 and Gaussian radial basis kernel function. After classifying the sample inputs of internals B and C again, classification accuracy can be calculated.
5. For sample space of internals B and C , comparing PCA-QFL model and the rate of accuracy of SVM algorithm, choose the better one as the final result.

In the PCA-QFL and SVM integrated algorithm, the traditional logit regression model regarding 0.5 as separation point, has been improved. The classification results of fuzzy internals B and C from QFL model are revised by SVM classification algorithm. Thus, the risk of false judgment on sample near the classification boundary, ever showing in PCA-QFL model, is reduced.

2 Empirical Analysis

2.1 Data Collection and Pretreatment

To test whether the improved model is effective, financial data of 192 listed companies in 2011 was used in empirical analysis. Select solvency, per share index, profitability, operating ability, and capital structure as five classifications.

They include 21 indexes. Use SPSS to make pretreatment [5] including data standardization, calculation of correlated coefficient matrix, characteristic roots, and unit eigenvectors of R and principal component representation.

2.2 Model Improvement Experiment

2.2.1 PCA-Logit Model Experiment

Regarding $F_1, F_2, F_3, F_4, F_5, F_6, F_7$ and F_8 as variables and making experiment by SPSS, we get the results as follows (Table 2):

2.2.2 PCA-QFL Model Experiment

We introduce quadratic and use QFL to make experiment because of correlation among variables. After eight iterations, get the results as follows:

$$p = \frac{1}{1 + e^{-(-0.923 - 1.067F_1 - 3.146F_2 - 1.846F_4 + 1.574F_7 + 2.01F_8 - 1.732F_1 \cdot F_7 - 1.469F_2 \cdot F_4 + 1.758F_2 \cdot F_8)}} \tag{10}$$

At the same time the classification results are below and there are some improvements (Table 3):

2.2.3 PCA-QFL and SVM Integrated Model Experiment

According to the results to calculate, we get the results:

$$p = 0.1045, \dot{p} = 0.9084$$

According to probability, we get four internals:

$$[0, 0.1045), [0.1045, 0.5), [0.5, 0.9084], (0.9084, 1]$$

There is a misclassification in $[0.1045, 0.5)$ and no misclassification in $(0.9084, 1]$. Because the rate of misclassification in $[0.1045, 0.9084]$ is 28 %, use LIBSVM [6, 7] to make classification experiment on financial data of this internal (Fig. 1).

We reverse the parameter (C, γ) of C-SVC and choose a better one, and then we get the results:

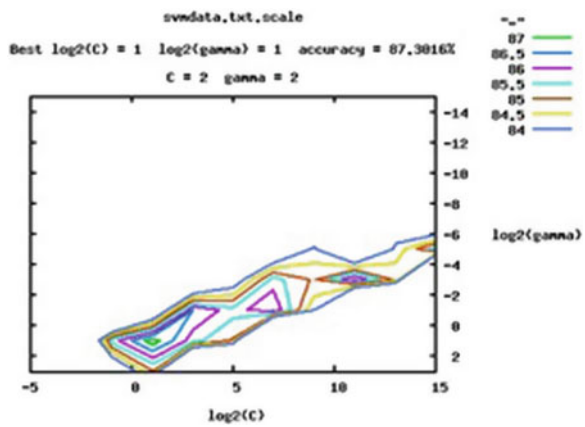
Table 2 PCA-logit model experiment results

| | | Compliance | Default | Accuracy (%) |
|-----------------|------------|------------|---------|--------------|
| Risk of default | Compliance | 54 | 9 | 85.7 |
| | Default | 5 | 58 | 92.1 |

Table 3 PCA-QFL model experiment results

| | | Compliance | Default | Accuracy (%) |
|-----------------|------------|------------|---------|--------------|
| Risk of default | Compliance | 58 | 5 | 92.1 |
| | Default | 6 | 57 | 90.5 |

Fig. 1 SVM classification results



$$C = 2.0, \gamma = 0.125$$

Cross-validation accuracy is equal to 87.3016 %. The accuracy of data on testing set after applying model is equal to 85.1852 %.

Through the experiment, we can get in the interval [0.1045, 0.9083], the accuracy in SVM that is equal to 85.1852 %, is higher than that in PCA-QFL, which is equal to 82 %.

2.3 Result Analysis

We compare the results of PCA-Logit model, PCA-QFL model, and PCA-QFL and SVM integrated model when making experiment on financial data having been collected (Table 4).

Table 4 Comparison of the three models' results

| | SVM | PCA-logit | PCA-QFL | PCA-QFL and SVM integrated |
|--------------|------|-----------|---------|----------------------------|
| Accuracy (%) | 85.2 | 88.9 | 91.3 | 95.2 |

3 Conclusion and Outlook

This article talks about the binary classification combination algorithm based on Logit regression and support vector machine and verifies the feasibility of this combined algorithm by empirical analysis on financial data of 192 listed companies in 2011.

However, there are some problems that remain unsolved. First, due to limited resource, a large-scale experiment is absent and thus how large a scale of sample is waiting to be tested. Second, choosing cross-sectional data in 2011 make it still veiled whether it can use to solve such problem as time series.

References

1. Wang JC (2006) Logistic regression model-method and application. Higher Education Press, Beijing
2. Burges CJC (1998) A tutorial on support vector machines for pattern recognition. *Data Min Knowl Disc* 2(2):121–167
3. Deng NY, Tian YJ (2004) The new method on researching data: support vector machine. Science Press, Beijing
4. Abe S (2010) Support vector machines for pattern classification. Springer, New York
5. Luo YT (2010) SPSS statistical analysis from basic to practice. Publishing House of Electronics Industry, Beijing
6. Pang SL (2005) Credit rating and stock market predict model and apply. Science Press, Beijing
7. <http://www.csie.ntu.edu.tw/~cjlin/LinChih-Jen>. A practical guide to support vector classification

Development of a BCI Simulated Application System Based on DirectX

Banghua Yang, Qian Wang, Zhijun Han, Hong Wang
and Liangfei He

Abstract This paper proposes a novel Brain Computer Interface (BCI) simulated application system based on DirectX. In the application system, a virtual car built by 3D Studio Max is imported into the DirectX, first. Then the transformation matrix is designed for the car to achieve the control of movement. Some objects are developed in virtual scenes for enhancing realistic immersion, such as the sky and obstacles. The virtual car can receive the control commands from Electroencephalography (EEG) signal processing system by the TCP/IP protocol. Finally, the virtual car can perform turning left, turning right, moving straight, and so on. The simulated results show that it is available to implement the real-time control by EEG signal. The designed system can not only be used as a simulated application but also be used as feedback for subjects. What is more, as no need for robotics and other hardware, the system is cost-effective, interesting, and ease of use. Potentially, the system can promote the research of BCI application and feedback.

Keywords Brain computer interface (BCI) · DirectX · Application system · TCP/IP

1 Introduction

A Brain Computer Interface (BCI) is a kind of interface to implement the communication and control between our brain and computers or other equipments. Of various BCI methods, Electroencephalography (EEG) is the most studied potential

B. Yang (✉) · Q. Wang · Z. Han · H. Wang · L. He
School of Mechatronic Engineering and Automation, Shanghai University, Shanghai, China
e-mail: yangbanghua@shu.edu.cn

Q. Wang
e-mail: lvmaogui.123@163.com

noninvasive interface, mainly due to its fine temporal resolution, ease of use, portability, and low set up cost, bearing great potentials for rehabilitation, assistive application, such as augmenting or repairing human cognitive or sensory motor functions [1]. The EEG signal generated by thinking activities of our brain can be transformed to control the computer or other electronic equipments, by analyzing and processing with proper analytical algorithms. So the nature of a BCI is that it extracts people's ideas from EEG and applies the corresponding orders to control other equipments.

For past few years, with the improvement of Brain Science, Cognitive Science, Electronic Measurement Technology, and Information Technology, the research of a BCI developed rapidly and is being paid more and more attention, especially in fields of Cognitive Neuroscience, Pattern Recognition, Rehabilitation Engineering, Control Science and Engineering. The BCI system can be applied to rehabilitation of the disabled with normal mind, assistive control, entertainment, or brain cognition of able-bodied persons. The application system base on BCIs is promoted constantly. However, due to the EEG's susceptibility to noise, extensive training is required before users can work the technology. At the same time, a real BCI system needs robotics or other hardware and the cost is high. So before the real application system establishment, a simulated application or feedback training system is necessary, which can verify the feasibility of a BCI system and lay a solid foundation for its practical application [2].

With the booming Virtual Reality (VR), infusion of 3D game with BCI technology can be a choice for a BCI application. The VR technology is exactly a kind of development tools to achieve the high-quality simulated system. It can receive commands and furnish them to control a simulation system in real time. In a secular view, it will be cost-effective solution. Because of the virtuality of the generated simulated environment upon the reality, the VR technology can configure the ideal operating environment, which is widely employed for simulation of the real hardware system in BCIs. DirectX, known as DirectX Software Develop Kit, is one of the Virtual Reality Technology. It is a set of Application Programming Interface (API) using for developing the high-performance multimedia programs, which is mainly based on Visual C++ and Visual Basic. Owing to the enhanced features and functionality of C++, the joint development of interactive graphics application programs combined C++ with DirectX has become mainstream in the game and media applications [3, 4].

Realizing that 3D game in conjunction with BCI may provide a promising alternative approach for BCI simulated application, a 3D virtual car for BCI application systems based on DirectX is designed in this paper. The car model built by 3D Studio Max is imported into the DirectX and transformed to the world space for moving control. Considering the reality for the subject, the sky and other real things are imitated in the scene, as well as the collision detection. Besides, the data communication mode is designed, which applies TCP/IP protocol to receive commands from the analyzed and processed EEG and then controls the virtual car real time according to the translated commands. It is available to implement the

movement without any special intelligent control strategy. As there is no need for robotics and other hardware, the system is cost-effective. The system parameters are easy to be modified, so it is also flexible. All we need to do is constructing the virtual scene and configuring the system function. Moreover, the system can also be used to test the validity of the control directly and indicate the accuracy of EEG classification. With establishing a sense of achievement, so that subjects are interested in using it continuously.

Generally, this paper is organized as follows: In [Sect. 2](#) we overview the whole BCI system proposed in the paper and the function of every part. Then the [Sect. 3](#) shows the detailed design of this BCI simulated application system. [Section 4](#) describes the TCP/IP communication between signal acquisition and processing system and the proposed application system. An initial experimental result is also given in this section. At last, the conclusion is drawn in [Sect. 5](#).

2 System Overview

The proposed BCI system diagram is shown in [Fig. 1](#). It consists of following two parts: one is the BCI signal acquisition and processing system, the other is the DirectX application system. The EEG signals are generated when subjects imagine the right or left-hand movement. These signals are collected and processed by the signal acquisition and processing system. And then EEG signal is transformed to the real number ranging from -1 to 1 to control the movement of the virtual car. To easily control, the real number is transformed to the defined control command format further. After that, the final command is generated and sent to the DirectX application system to control the movement of the virtual car through the TCP/IP protocol.

The command signal from the BCI signal acquisition and processing system is received by our proposed application system to implement the corresponding movement of the car, through the TCP/IP. In the meantime, subjects also obtain the feedback information from the computer displayer about the effect of the car controlling and then adjust their imaginary movement. During the experiments, subjects can practice themselves over and over again to adjust the way of motor imagery in time, in order to generate the optimal EEG signal.

[Figure 2](#) is the diagram of signal acquisition and processing system of BCI. First, the EEG signals collected by a 16-channel electrodes cap are amplified by a high-precision biological amplifier that is developed by Tsinghua University. Next amplified signals are collected by the collection software and sent to the Matlab signal processing part. Then the Matlab software platform processes signals including feature extraction and classification. Here, we apply the CSP (Common Spatial Patterns) to extract the EEG features and classify them by Linear Classification Algorithm. The CSP algorithm is very frequently used for this purpose and excellent classification results have been reported using it for preprocessing in

Fig. 1 Diagram of the BCI system

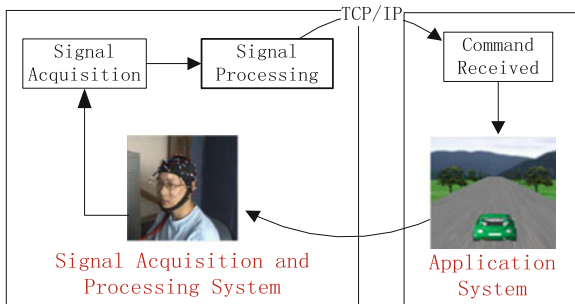
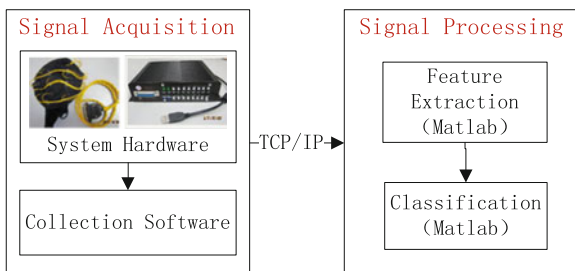


Fig. 2 Diagram of signal acquisition and processing system



BCIs based on motor imagery [5]. A 6-dimensional feature vector is obtained by the CSP and then is classified. At last, the recognition results are sent to the application system to control the movement of the virtual car through the TCP/IP.

3 Application System Design

In this section, some steps are described to implement a BCI experimental application system. In the paper, we build the BCI application system based on DirectX, with the virtual scene constructed and functions configured, which can be used to control the virtual car by EEG in real time. And further collision detection between the virtual car and obstacles can be achieved in the system to make users the feeling of reality.

3.1 Loading 3D Model

As it consists of a set of API, DirectX can support most of multimedia application development, especially in 3D graphics. In DirectX, Direct3D is responsible for 3D graphics [6]. Although DirectX provides a powerful interface function it is not only a waste of time but also very prone to error to try model vertexes data one by one in order to build a complicated model with Direct3X. Therefore, it is necessary

to employ a professional 3D modeling application instead of reducing modeling work of DirectX, such as 3D Studio Max [7].

3D Studio Max (3ds Max) is a kind of 3D graphics modeling and animation software developed by Autodesk. The software has excellent modeling performance but poor controlling performance. In this case, it may be feasible that we can build the complicated model with 3ds Max and then control the model in DirectX. The detailed steps are as follows:

- Using 3ds Max to model the car and export the .X file (providing the special 3D mesh file to DirectX including textures, material, etc., of vertex). This paper applies the Panda Plugin to complete the task.
- Calling the function `D3DXLoadMeshFromX()` to load X file to read model data and create the mesh object. Implemented code is as follows:

```
LPD3DXBUFFER cAdjBuffer = NULL;
LPD3DXBUFFER cMtrlBuffer = NULL;
D3DXLoadMeshFromX(L"BCIcar3.X",D3DXMESH_MANAGED,cd3dDevice, &cAdjBuffer, &cMtrlBuffer, NULL, &NumMtrls, &cMesh);
```
- Rendering the model. When all above loading is completed, the information of .X file can be rendered in drawing. As so many parts need to be drawn and every part should be set up its textures and materials before drawing, so generally, a for-loop is applied here to read in the information and draw.

3.2 Matrix Transformation

After loading in the former step, the model is in its own local coordinate system, in which is not easy to determine and control the model. So it is necessary to transform the model from the local space to the world space, called world transformation. It is comprised of translation, rotation and scaling.

Aiming to translate the model in world space, translation matrix is created. The matrix is as following equation:

$$T(p) = \begin{pmatrix} 1 & 0 & 0 & 0 \\ 0 & 1 & 0 & 0 \\ 0 & 0 & 1 & 0 \\ p_x & p_y & p_z & 1 \end{pmatrix}. \quad (1)$$

In this paper, the translation matrix is created by calling the function `D3DXMatrixTranslation()` to implement the translation movement of the virtual car in world space. The factor p in the above matrix is represented by the moving distance of the car in every axis.

In DirectX, the rotation matrix is mainly used for adjusting the direction angle of model and view of camera. The paper applies the rotation matrix to change the traveling direction of the virtual car. It is known that DirectX uses the left-hand

rectangular coordinate system, in which the positive x-axis goes right, the positive y-axis goes up and the positive z-axis goes into the page [7, 8]. So, the car model is located in x-z plane. In fact, the turning left or right command of the virtual car is implemented as rotating about the y-axis. Then the rotation matrix would be created like that:

$$Y(\theta) = \begin{pmatrix} \cos \theta & 0 & -\sin \theta & 0 \\ 0 & 1 & 0 & 0 \\ \sin \theta & 0 & \cos \theta & 0 \\ 0 & 0 & 0 & 1 \end{pmatrix}. \quad (2)$$

The `D3DXMatrixRotationY()` can be called for this rotation matrix. Note that either translation or rotation transform should be executed by right multiplying a $4 * 4$ matrix.

$$\begin{pmatrix} X_1 \\ Y_1 \\ Z_1 \\ 1 \end{pmatrix} = \begin{pmatrix} \cos \theta & 0 & -\sin \theta & 0 \\ 0 & 1 & 0 & 0 \\ \sin \theta & 0 & \cos \theta & 0 \\ 0 & 0 & 0 & 1 \end{pmatrix} \begin{pmatrix} X \\ Y \\ Z \\ 1 \end{pmatrix}. \quad (3)$$

So if the original vector of the car is assumed as (X, Y, Z) , to multiply with the $4 * 4$ matrix, it can be extended to four-dimensional, that is $(X, Y, Z, 1)$ [7]. The rotation transform result can be described as Eq. (3). The new value is $(X_1, Y_1, Z_1, 1)$, in which X_1, Z_1 can be expressed in the following Eq. (4):

$$\begin{aligned} X_1 &= X \cos \theta - Z \sin \theta \\ Z_1 &= X \sin \theta + Z \cos \theta. \end{aligned} \quad (4)$$

And the value of Y remains the same, which make it possible that the car only rotates about y-axis in the x-z plane without moving on y-axis. The executed code is as follows:

```
//Define the rotation angle
const float TO_RADIANS = (1 /180.0f) * 3.1415926f;
float rad = carRotationY * TO_RADIANS;
//Create the rotation matrix to turn
D3DXMATRIX rotateMatrix;
D3DXMatrixRotationY(&rotateMatrix, rad);
//Create translation matrix to move
positionX += newX;
positionZ += newZ;
D3DXMATRIX translateMatrix;
D3DXMatrixTranslation(&translateMatrix, positionX,0.0f,positionZ)
```

Fig. 3 The whole outdoor design for virtual scene



Remember that the virtual car not move as ordered only with the transformation listed above. The transformed matrix should be applied in world space to accomplish the final transformation. The function `SetTransform()` is called for this task.

3.3 Scene Set

The sky is important for outdoor scene, which can help to foil other objects in the scene. Therefore, the system employs the skybox technique to render the sky in order to improve sense of immersion [9].

We use 5 rectangle planes and 24 vertexes with texture coordinates to form a cube as the virtual sky and render it with texture maps of the real sky, which is shown in Fig. 3. Besides, in view of the better visual effect to subjects, some other objects are added into the scene, such as trees. In our system, the Billboard technique is applied to render trees, that is: map the tree picture on a rectangle to simulate the 2D picture in the 3D space and rotate the rectangle along with the camera, which makes 2D trees a great 3D sense.

3.4 Collision Detection

It is necessary to detect the collision in 3D application system. If not, objects can pass into others, which go against rules of our real world without any feeling of the reality [10]. In the 3D space, objects have the properties just like real ones. So collision detection cannot depend on the axis detection. The bounding sphere is employed in our paper which wraps around the outside object. When detecting, the center distance between spheres is compared with the sum of radius. It is available to judge whether collision happened [10, 11].

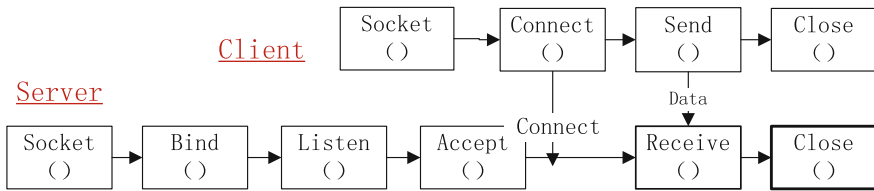


Fig. 4 The flow of TCP/IP communication

4 TCP/IP Communication and Results

In this paper, the DirectX application system communicates with signal acquisition and processing system through TCP/IP, to receive commands in real time. For the real time and synchronism between data collection and moving control, signals collected by the signal acquisition system are transformed to the real number ranging from -1 to 1 to control the movement of the virtual car. For easy control, the real number is transformed to the defined control command format further. After that, the final command is generated and sent to the DirectX application system to control the movement of the virtual car through the TCP/IP, such as turning identify “D,” moving identify “S.” If the command is received as “D+L10,” the car would turn left 10° . Similarly, “D+R10” represents the car would turn right 10° .

Figure 4 shows the flow of communication through the TCP/IP. The proposed system defines a port number, as the TCP server. When monitoring the connecting request from Client, it would communicate with Client and receive data. In this procedure, the connection is kept until the whole experiment time is out. The detailed steps of the Server communication are as follows:

- Create a listening socket and associate a local address (IP and Port) with it.
- Listen to Client and call `Accept()` to wait for the connection request from Client.
- Once connected, receive data from Client.
- When time out, close the listening socket.

Communicating with EEG Signals processing system, the application system receives the command and implements corresponding movement. The left picture in the Fig. 5 shows that the car moves along its original direction before the collision. When knocking against the obstacles, the car could not move at once until the subject adjusts the command to turn left or right and then move on, as shown in the right picture of Fig. 5 .

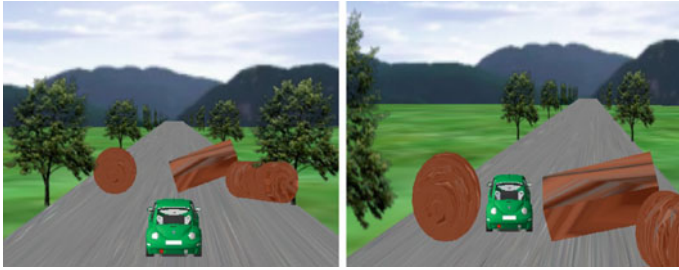


Fig. 5 The experimental results of the application system before and after the collision

5 Conclusion

The application system based on DirectX proposed in this paper applies the motor imagery to control a 3D car. The system is easy to operate and reflects the subject's thinking state. It is shown in the experiment that this system is not only a simulated application system but also provide the real-time feedback intuitively for subjects. The scene built in the system is easy to arouse the EEG with the strong immersion and interactivity, which could reduce the training time. Furthermore, this system can also reflect the effects of EEG preprocessing and classification, that is to say that the less time subject spends for crossing all obstacles, the better classification is performed. In a word, with sense of reality and immersion, this novel simulated application system lays a good foundation for the BCI application and feedback system.

Acknowledgments This work was supported by Grants from the National Natural Science Foundation of China (Grant No.60975079, 31100709), Innovation Program of Shanghai Municipal Education Commission (11YZ19, 12ZZ099).

References

1. Jiang LJ, Guan CT, Zhang HH, Wang CC, Jiang B (2011) Brain computer interface based 3D game for attention training and rehabilitation. In: Proceedings of the 6th IEEE conference on industrial electronics and applications, Beijing. doi:[10.1109/ICIEA.2011.5975562](https://doi.org/10.1109/ICIEA.2011.5975562)
2. Chin ZY, Ang KK, Wang CC, Guan CT (2010) Online performance evaluation of motor imagery BCI with augmented-reality virtual hand feedback. In: Proceedings of the 32nd annual international conference of the IEEE, EMBS, Buenos Aires. doi:[10.1109/IEMBS.2010.5627911](https://doi.org/10.1109/IEMBS.2010.5627911)
3. Wang ZL, Shi L, Li ZG (2008) Prototype of a virtual environment develop platform based on DirectX. In: Proceedings of the 3rd IEEE conference on industrial electronics and applications, Singapore. doi:[10.1109/ICIEA.2008.4582524](https://doi.org/10.1109/ICIEA.2008.4582524)
4. Scherer R, Proll M, Allison B, Muller-Putz GR (2012) New input modalities for modern game design and virtual embodiment. In: Proceedings of the IEEE conference on virtual reality short papers and posters, CA. doi:[10.1109/VR.2012.6180932](https://doi.org/10.1109/VR.2012.6180932)

5. Wentrup MG, Buss M (2008) Multiclass common spatial patterns and information theoretic feature extraction. *IEEE Trans Biomed Eng* 55(8):1991–2000. doi:[10.1109/TBME.2008.921154](https://doi.org/10.1109/TBME.2008.921154)
6. Zhang Q, Qu NS (2006) Construction of three-dimensional landscape model by using VC, Opengl and Directx. *Mod Surv Mapp* 29(1):18–20. doi:[10.3969/j.issn.1672-4097.2006.01.005](https://doi.org/10.3969/j.issn.1672-4097.2006.01.005)
7. Xiahou JB, Mu Y (2012) Loading and rendering XFile in DirectX. In: Proceedings of 2012 international conference on computer science and electronics engineering, Hangzhou
8. Luna FD (2007) Introduction to 3D game programming with DirectX 9.0. Duan F. (ed) vol 5, 1st edn, Tsinghua University Press, Beijing, pp 64–75
9. Ping S, Tao Y (2010) Research and realization of modeling method for virtual geographic scenes. In: Proceedings of the 2nd international conference on information science and engineering ICISE, Hangzhou
10. Guan JH, He HW, Liang YF (2008) Research on real-time collision detection for vehicle driving in the virtual environment. In: Proceedings of the international conference on information and automation, ICIA, Changsha
11. Salim FD, Loke SW, Rakotonirainy A, Srinivasan B, Krishnaswamy S (2007) Collision pattern modeling and real-time collision detection at road intersections. In: Proceedings of IEEE conference on intelligent transportation systems, ITSC, WA. doi:[10.1109/ITSC.2007.4357693](https://doi.org/10.1109/ITSC.2007.4357693)

A Research on Hybrid Simulated Annealing Algorithm for Cargo Loading Problem

Shaoyong Yu, Junrong Yan and Shunzhi Zhu

Abstract Cargo loading problem is an NP-complete problem. An approximate algorithm based on heuristic and annealing algorithm was proposed and used to implement a system to solve this problem. Experiments show that, loading factor was improved by about 3 % and efficiency was speed to nearly two times.

Keywords Three-dimensional packing · CLP · Heuristic algorithm · Annealing algorithm

1 Introduction

The definition of cargo loading problem is to achieve the highest loading rate when putting the cargo into boxes, given a certain number but different sizes of cargo boxes and cargo. The increase of cargo loading rate is conducive to the logistics enterprises to reduce transportation costs while improving the efficiency of cargo arriving, so it has a very strong practical value. However, the loading problem is a NP-complete problem in theory, and the usual solving method is approximate calculation. Currently, researches on this issue are mainly based on genetic algorithm [1–8], heuristic algorithms [9–11], simulated annealing algorithm [2, 12, 13], and so on.

S. Yu (✉) · S. Zhu

Department of Computer Science and Technology, Xiamen University of Technology,
Xiamen, Fujianuse, China
e-mail: syyu@xmut.edu.cn

S. Zhu

e-mail: szzhu@xmut.edu.cn

J. Yan

College of Computer and Information Science, Northeastern University, Boston, MA, USA
e-mail: junrongyan@gmail.com

As an adaptive probabilistic optimization algorithm, the genetic algorithm has many characteristics, such as simple operation, high efficiency, and implicit parallelism. It can be used for optimization of complex systems, but it is very difficult to find the method of coding and fitness function for the actual problem. The heuristic algorithm often considers many factors about cargo loading. For instance, the directional constraints, the load capacity constraints, the stability constraints, the placement of cargo, the loading sequence of cargo, and so on. But it is not satisfied to use heuristic methods simply. As a kind of common and effective approximation algorithms, simulated annealing algorithm is proposed in recent years, which is suitable for solving large-scale combinatorial optimization problems. Simulated annealing algorithm has many advantages, such as simple description, flexible, and less constrained by the initial conditions, etc. But it is slow convergence, performing a long time and easy to fall into local optimum.

Based on the specific application of logistics terminal distribution, this paper combined heuristic algorithm with simulated annealing algorithm to achieve the efficient cargo loading system.

2 Hybrid Simulated Annealing Algorithm

2.1 Mathematic Description of Loading Problem

There are many classification methods of CLP. The most important method was proposed by Dyckhoff from Germany. Category one: Designating certain containers and cargo, requiring loading total cargo using containers as few as possible. Category two: using a single container to load largest total volume of cargo as the goal.

Based on the application of logistics terminal distribution, this paper focuses on the single container loading problem. Such problems can be defined as: given a cuboid container C , and its length, width, and height can be marked as L, W, H ; given a set of rectangular cargo $G = \{g_1, g_2, \dots, g_n\}$, and the length, width, and height can be marked as l_i, w_i, h_i , volume $V_i = l_i \times w_i \times h_i$. Suppose S is a subset of G , the collection for all cargo loaded into container C . Defining V_s as the sum of all cargo volume from $S, V_s = \sum_{g_i \in S} V_i$, and the loading rate is: $LE = \frac{V_s}{L \times W \times H}$, and the single container loading problem is to seek a solution to maximize the LE.

2.2 Simulated Annealing Algorithm

Simulated annealing algorithm was proposed by Metropolis to solve the sample problems during the process of physics annealing. The core idea is to select large contribution during sampling, avoiding a lot of meaningless sampling, shortening

the sampling search space, and can get better results. Kirkpatrick applied this algorithm to solve combinatorial optimization problems, a good solution to the TSP. Its main ideas and the steps are [14]:

- (1) Initialization: Randomly generate an initial solution S (the starting point of iterative algorithm), given a higher initial temperature T , the number of iterations for each value of T is L .
- (2) For $K = 1 \dots L$ do the first (3) to (6) step.
- (3) Generate a new solution S' .
- (4) Calculate the increment $\Delta t = C(S') - C(S)$, which $C(S)$ is the evaluation function.
- (5) If $\Delta t < 0$, accept S' as the new current solution, otherwise using the probability $\exp(-\Delta t/T)$, accept S' as the new current solution.
- (6) If the termination condition is satisfied, the output current solution is the optimal solution, the program ends.
- (7) T gradually decreases and tends to 0, and then turn to (2) step.

2.3 Heuristic Algorithm

The two basic goals of computer science is to find an algorithm that can be proved efficiently in execution and an algorithm that can get the optimal solution or suboptimal solution [15]. The heuristic algorithms attempt to provide one or all the targets at a time. For example, it can usually find a very good solution, but there is no way to prove that it cannot get the worse solution. It usually solves the problem in a reasonable time, but there is no way to prove that it can always solve the problem in such a speed.

Heuristic algorithm is proposed compared with the optimization algorithm, it can be defined as follows: It is an intuitive or empirical algorithm constructed in an acceptable cost (refer to computation time and space). It can provide a feasible solution for the optimization problem. The deviation between the feasible solution and the optimal solution cannot be necessarily estimated in advance.

2.4 Implementation of Hybrid Simulated Annealing Algorithm

Using simulated annealing algorithm to get the optimal solution of combinatorial problems needs to search a large solution space, and could not get the best results in a limited time. But for the practical application, we often do not need the optimal solution in theory, thus we just quickly get the suboptimal solution. This

paper uses a hybrid heuristic and simulated annealing algorithm to solve the optimization loading problem in logistic dispatching goods.

The basic idea of this algorithm is: First, using the composite block generation algorithm to calculate the cargo loading sequence to get candidate blocks. Composite block is a module which is made up of multiple cargos. In this module, the quantity and display direction of cargo are arbitrary. The composite block makes the loading block is not only one kind of cargo at each time, to accelerate the speed of loading.

Second, the heuristic algorithm is used to guide the choice of blocks in the loading process. This algorithm will calculate the viable block list based on the box volume in descending order at each stage according to the remaining space, and then select the loading block. Next, it will recut the remaining space for next loading. Through this way, we can establish the mapping between the loading sequence and the placement program to optimize the next loading program.

Finally, using the simulated annealing algorithm to optimize the placement program. The completed hybrid simulated annealing algorithm is shown in Fig. 1.

During the initial searching, the algorithm uses a zero vector, MaxSeq in length, as the initial loading sequence, and then it uses basic heuristic algorithm to calculate to get an initial loading program as the optimization program. Next, the simulated annealing algorithm is used for solving the optimization problem. The variables t_s , t_f , dt , and $length$ are used to control the annealing process, the t_s represents the initial temperature, the t_f represents the terminal temperature, the dt represents the annealing coefficient, and the $length$ represents Markov chain length.

3 Experiment Result

In order to display the effect and loading process, this paper uses Java3D technology to realize it. The Java3D technology provides the creation, manipulation, and rendering of 3D entities in high level, so that the development work has become extremely simple. At the same time, the lower API of Java 3D depends on the existing three-dimensional graphics system, such as Direct 3D, OpenGL QuickDraw, 3D, and XGL. It can help to generate all kinds of forms, color, and mapping, and it also can make the shape change, move, and generate 3D animation. The loading process and effect are shown in Fig. 2.

3.1 Theoretical Experiment Result

Testing data referred in reference [13], which has seven files in all, each file has 100 examples, 700 examples in all, has been used to verify the algorithm. Table 1 is the result compared with that referred in reference [10].

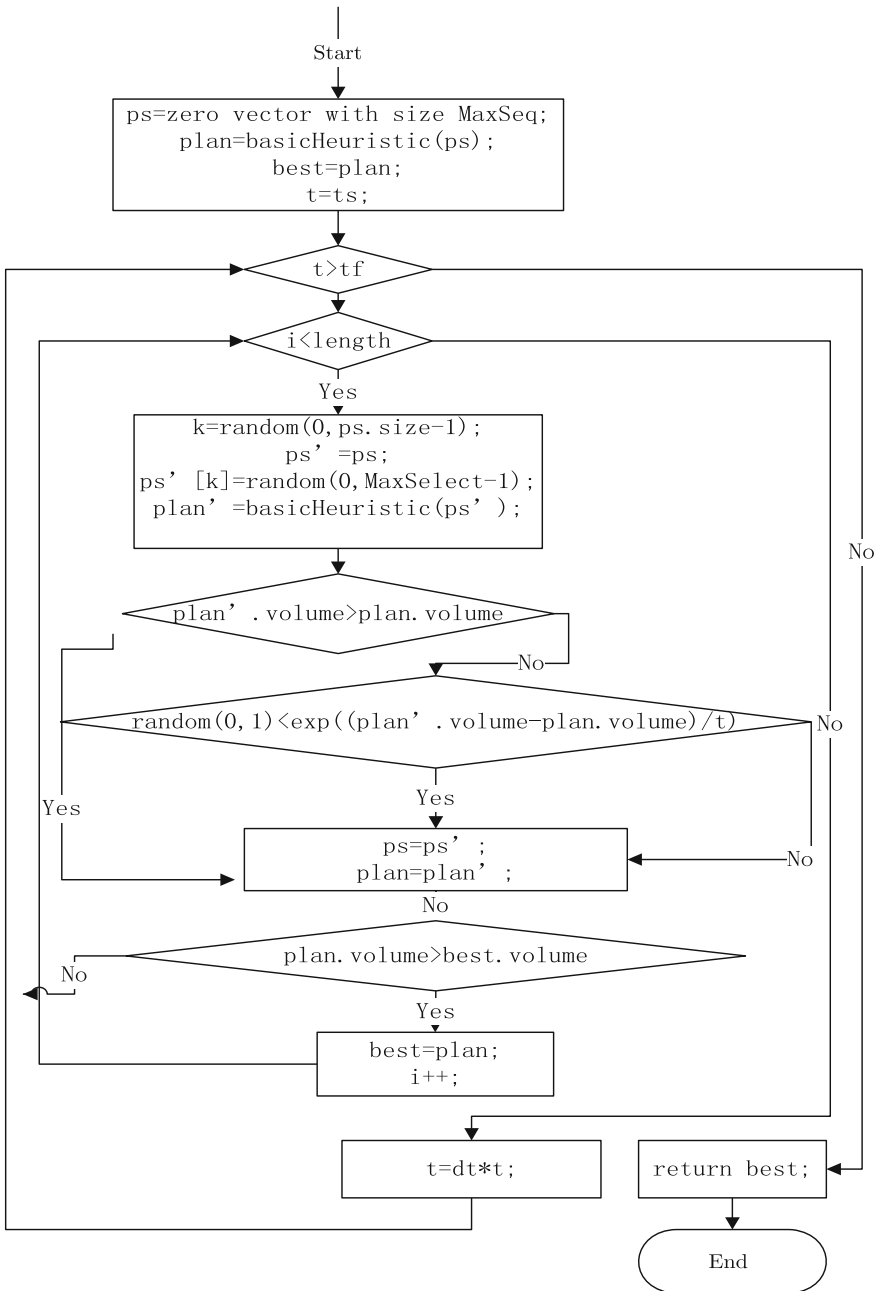


Fig. 1 Process diagram of combinational simulated annealing algorithm

Fig. 2 Demo of loading

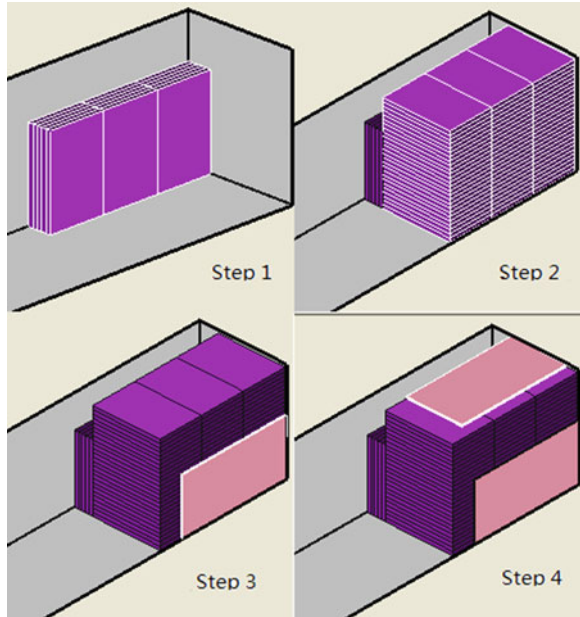


Table 1 Result of four different algorithms

| Testing file | Box type | Loading rate (%) | | | |
|--------------|----------|------------------|-------|-------|-----------------------------------|
| | | Bischoff | A.LIM | ZDF | Combinational simulated annealing |
| Thepack1.txt | 3 | 85.4 | 87.4 | 89.94 | 89.78 |
| Thepack2.txt | 5 | 86.25 | 88.7 | 91.13 | 91.46 |
| Thepack3.txt | 8 | 85.86 | 89.3 | 92.09 | 92.45 |
| Thepack4.txt | 10 | 85.08 | 89.7 | 91.94 | 91.37 |
| Thepack5.txt | 12 | 85.21 | 89.7 | 91.72 | 91.55 |
| Thepack6.txt | 15 | 83.874 | 89.7 | 91.45 | 91.34 |
| Thepack7.txt | 20 | 82.92 | 89.4 | 90.94 | 90.48 |
| Average | 10 | 84.942 | 89.1 | 91.32 | 91.21 |

We can conclude from the result that the loading rate of this algorithm is lower than that of the state-of-art algorithm, but is very close. Because our algorithm pay more attention to practice use and the execution speed that ignores the precision.

3.2 Effect of Practical Use

This system has been operated in Xiamen Yulong Logistics Co Ltd. In order to verify the effectiveness of this loading system, we did experiments in applying field, respectively, loading six cars of rigid objects and six cars of soft objects

Table 2 Comparison of manual guidance and software guidance

| Cargo type | Loading rate (%) | | Loading time (cars/min) | |
|--------------|------------------|----------|-------------------------|----------|
| | Manual | Software | Manual | Software |
| Rigid object | 95 | 97.8 | 63 | 35 |
| Soft object | 98 | 98.3 | 57 | 33 |

Table 3 Comparison of TED, hires, salary, and customer satisfaction

| Cargo type | TED (t/h) | | Hires (person) | | Salary (Yuan/person) | | Satisfaction (100 %) | |
|--------------|-----------|----------|----------------|----------|----------------------|----------|----------------------|----------|
| | Manual | Software | Manual | Software | Manual | Software | Manual | Software |
| | | | | | | | (%) | (%) |
| Rigid object | 1.86 | 2.36 | 7 | 4 | 3000 | 3400 | 92 | 96 |
| Soft object | 1.46 | 2.04 | 7 | 4 | 3000 | 3400 | 92 | 96 |

under the guidance of human and software. The experimental results are shown as Table 2. From the experimental results, we can see that either for the loading of rigid objects or soft object, both the loading time, and loading rate have been improved to some extent after using this loading system. Wherein, rigid object’s loading rate improves about 3 %, soft object’s loading rate does not change significantly, increases only 0.3 %, but the loading time is shortened 42–44 %. In summary, the cargo loading efficiency can be improved greatly by using the hybrid approximation algorithm based on the combination of heuristic algorithm and simulated annealing algorithm to realize three-dimensional loading.

While, through the comparison we can found that, for rigid objects, the loading rate by software’s guiding increases more significantly than soft objects. The main reason is that the soft object can be extruded, it will be accumulated at manual loading while software guidance without considering the circumstances.

After the operation in last two years, the Xiamen Yulong Logistics Co Ltd has counted the cargo throughput of one day, the number of employees, the wages and the customer satisfaction surveys the same time of year. It can be seen from Table 3 that, the throughput has been improved significantly and the time of shipment also has been reduced greatly. Meanwhile, the number of employees has been declined and the average wage has increased, while the company’s expenses have been reduced significantly. The conclusion can be proposed that the cargo loading system can help improve the work efficiency, save money and win the satisfactory of customers.

4 Conclusion

The hybrid simulated annealing algorithm can effectively improve the cargo loading rate and loading efficiency, and combine with Java3D technology to making the loading process more visual. This paper mainly focuses on the loading

of regular rectangular cargo. However, in many cases, the shape of the cargos are not regular rectangular. In addition, for some logistics enterprises, it also needs to take the sequence of cargo loading into consideration. These are the areas in this paper, which need to be improved in the future.

Acknowledgments This study was supported by National Science Foundation Project (61070151), University Innovation Project (3502Z20123037) and Introduction Project (3502Z20099011) of Technology Plan of Xiamen.

References

1. He D, Cha J, Jiang Y (2001) Research on solution to complex container loading problem based on genetic algorithm. *J Softw* 12(9):1380–1385
2. Bu L, Yin C (2002) A genetic and simulated annealing algorithm for optimal sequential casing of less-than-carload freights. *J Southwest JiaoTong Univ* 37(005):531–535
3. Bu L, Yei X, Pu Y, Chang J (2004) Optimization based on genetic algorithm for three-dimensional packing in a single container. *China Railway Sci* 25(4):108–111
4. Jiang B, Xiong W (2007) Hybrid genetic algorithm solving for three-dimensional container loading problem. *Comput Eng Appl* 43(26)
5. Xu G, Yu J (2008) DNA genetic algorithm for solving container loading problem. *Comput Eng Appl* 44(022):237–240
6. He G, Liu K (2003) Genetic algorithm for optimizing distribution project of logistic center. *Syst Eng Theory Pract* 23(4):76–81
7. Chen D, Chen Z (2010) A mixed integer programming model of three-dimensional bin-packing problem and improved genetic algorithms. *Math Pract Theory* 40(2):142–147
8. Chen Y, Wu X, Song Y (2002) Hybrid genetic algorithm for bin-packing problem with constraints. *Operat Res Manag Sci* 11(4):21–25
9. Liu J, Ma G, Huang Y (2005) Research on heuristic algorithm based on for combination three-dimensional packing. *J Eng Gr* 26(1):22–25
10. Zhang D (2007) A combinational Heuristic algorithm for the three-dimensional packing problem. *J Softw* 18(9):2083–2089
11. Yan W, Shao H, Tian Y (2002) A Heuristic algorithm for three dimension packing problem. *Inf Control* 31(4):353–356
12. Defu Z, Yu P, Zhu W, Chen H (2009) A hybrid simulated annealing algorithm for the three-dimensional packing problem. *Chinese J Comput* 32(11)
13. OR-Library. <http://mscmga.ms.ic.ac.uk/info.html> [EB/OL]
14. Steinbrunn M, Moerkotte G, Kemper A (1997) Heuristic and Ran2 domized optimization for the join ordering problem. *VLDB J* 6(3):8–17
15. BAIDU WIKI. <http://baike.baidu.com/view/752809.htm> [EB/OL]
16. Dereli T, Das GS et al (2010) A hybrid simulated annealing algorithm for solving multi-objective container loading problems. *Appl Manual Intell* 24:463–486
17. Li Z (2011) Research on the model of three-dimensional container loading. *Silicon Valley* 1

A Hub-Network Layout Problem Balancing the Budget and Passenger Transport Cost

Chunping Hu, Tiantian Gan, Zheng Zhang and Kun Qian

Abstract In a given network in rural areas with weak infrastructures, passengers need to transfer in a hub to the destination, while hub and network layout will both affect travel time and costs. In order to improve infrastructure service level and to reduce the passenger transport cost, two measures are proposed: increase hub facilities or increase route facilities. The problem is how to balance the increase of infrastructure investment and the decrease of passenger transport cost under the assumption of a given demand. Based on this problem, an integrated optimization model is established and applied to a small network. In addition, if the network should be rebuilt, a budget constraint could be added to the above model. We analyzed the sensitivity of two measures on the budget, which will help allocate the limited budget reasonably and provide decision reference on balancing hub and route construction.

Keywords Hub-network · Infrastructures · Passenger transport cost · Integrated optimization model · Budget constraint

1 Introduction

With the speeding up of urbanization process, weak transport infrastructure problem in the urban–rural intersection zone is increasingly prominent. The role of passenger transport hubs in city is just like the role of intersections in the road network, and the hub is the bottleneck of passenger transport system (see [1]).

In the existing road network with weak infrastructure, the number and layout of hubs and lines could both affect travel costs and time in passenger transport system. Increasing lines or hubs in the network can improve the passenger travel

C. Hu · T. Gan (✉) · Z. Zhang · K. Qian
MOE Key Laboratory for Urban Transportation Complex Systems Theory and Technology,
Beijing Jiaotong University, Beijing, China
e-mail: 11114232@bjtu.edu.cn

service, and reduce the costs of passenger transportation system. Some related papers [2, 3] illustrated how to lay the hubs reasonably in a given network in order to improve travel efficiency, ignoring the adjustment of the network, or at the network level, many scholars [4–7] studied the network design problem (NDP) with the same purpose. However, most studies above do not take the infrastructure construction budget into account, and assume the unlimited budget, which is not realistic in a real planning decision-making. In addition, some scholars [7, 8] studied the network line adjustment based on the hub layout, while other scholars [9–12] consider the construction cost of hub layout problem, without considering network line adjustment.

Therefore, from the perspective of the supply of transportation infrastructure, this chapter intended to establish an integrated optimization model with limited budget so as to improve transfer travel network services, and to provide government planning and decision-making departments a scientific basis for distributing hub-network construction cost reasonably under the condition of limited budgets.

2 The Model

2.1 Basic Assumptions and Symbol Definition

Before establishing the model, the assumptions are given as following:

1. Passengers should transfer in a hub to another bus to arrive
2. Each node in the network represents a passenger flow demand, or a station;
3. Service capability of the hubs here is not restricted.

In order to describe the integrated optimization model considering hub layout and network design, the symbols are defined as follows:

- N represents a collection of network nodes,
- P represents a collection of alternative links between nodes,
- d_i represents passenger flow demand derived by node i ,
- M represents the total passenger flow demand $\sum_{i \in N} d_i$ derived by all nodes in the network,
- t_{ij} represents passenger transport rate of per unit length and flow on line (i, j) ,
- f_i represents the costs of constructing a hub on the node i ,
- l_{ij} represents the length of line (i, j) ,
- c represents the line construction cost rate of per unit distance.

The decision variables are:

$$Z_i = \begin{cases} 1 & \text{if a hub is located at node } i, \\ 0 & \text{if not.} \end{cases}$$

$$X_{ij} = \begin{cases} 1 & \text{if line } (i,j) \text{ is constructed, Where } i < j \\ 0 & \text{if not} \end{cases}$$

Y_{ij} and Y_{ji} , respectively, stand for the passenger flow from i to j and j to i on line (i, j) . W_i represents the demand that can be meted by a hub located at node i .

2.2 Objective Function and Constraint

Assuming that all the parameters are negative, the objective function of the integrated optimization model is:

$$\min U = \sum_{(i,j) \in P} t_{ij} (Y_{ij} + Y_{ji}) + \sum_{i \in N} f_i Z_i + \sum_{(i,j) \in P} c.l_{ij} X_{ij} \tag{1}$$

On the basis of the objective function (1), establish the constraints as follows:

$$\sum_{j \in N} Y_{ji} + d_i = \sum_{j \in N} Y_{ij} + W_i, \quad \forall i \in N, \tag{2}$$

$$W_i \leq MZ_i, \quad \forall i \in N, \tag{3}$$

$$Y_{ij} \leq MX_{ij}, \quad \forall (i, j) \in P, \tag{4}$$

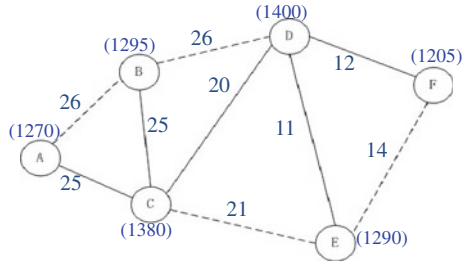
$$Y_{ji} \leq MX_{ij}, \quad \forall (i, j) \in P, \tag{5}$$

$$Y_{ij}, Y_{ji} \geq 0, \quad X_{ij} \in \{0, 1\}, \quad \forall (i, j) \in P, \tag{6}$$

$$W_i \geq 0, \quad Z_i \in \{0, 1\}, \quad \forall i \in N. \tag{7}$$

The objective function is to minimize the sum of travel costs, hub construction costs, and line construction costs. Equation (2) is a flow conservation equation, which represents the inbound flow to a node must equal to the outbound flow from a node. And the inbound flow include the transfer passenger demand from all other nodes to the node and the passenger flow demand produced by the node itself, accordingly, the outbound flow includes the transfer passenger flow demand from the node to all the other nodes and the passenger flow demand flow out from the node itself. Equation (3) shows that only a hub is located at the node, the node itself can digest the transfer service to positive. Similarly (4) and (5) show that only a line is constructed between nodes, the line will have flow in both directions. Equation (6) are standard non-negativity and integer constraints.

Fig. 1 The original small transportation network



3 Example Application

3.1 A Small Network

We construct a small network with six nodes (Fig. 1), and our goal is to layout several transfer hubs in the existed network. The train of thought is that regard all these six nodes as common station first, then improve some as transfer hubs. So, the problem can be summarized as following:

1. Which station should be promoted to transfer hubs?
2. Is considering the adjustment of the line simultaneously beneficial?

We set per unit length construction costs of virtual lines as u , so the layout costs for each line is $c_{ij} = ut_{ij}l$.

Assumes that the passenger demand of each node in the network as shown in Table 1.

Figure 2 is the results of pure hub location layout optimization, regardless of the road network line improvement. Total network cost is 5127.

3.2 Integrated Optimization Considering Hub Location and Network Design

Apply the integrated optimization model to the small network. When the range of per distance construction cost of the line is $8.0 \leq c \leq 12.0$, the result is shown in Fig. 3, with the total cost of 4560. When the range of per distance construction cost of the line is $0 \leq c \leq 8.0$, the result is shown in Fig. 4, with the total cost of 4320. The results show that different rates of line construction cost could make different optimization results.

Table 1 Demand of each point in the sample network

| Node | A | B | C | D | E | F |
|--------|----|----|----|----|----|----|
| Demand | 33 | 32 | 15 | 17 | 31 | 35 |

Fig. 2 Pure hub layout location optimization result

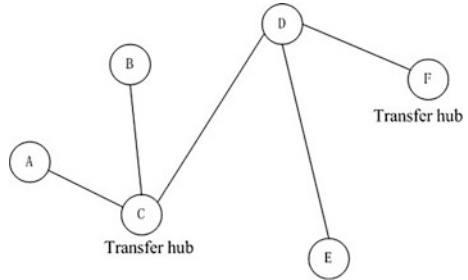
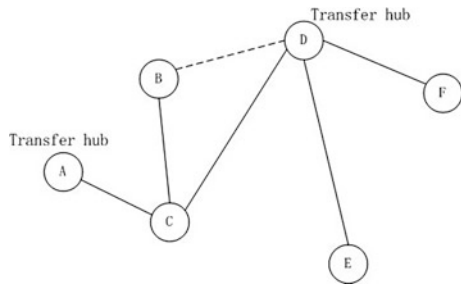


Fig. 3 Optimization result when $8.0 \leq c \leq 12.0$



According to the example, we can see two potential benefits of increasing a route:

1. The decrease of passenger transport costs,
2. Reduce the transfer hub construction investment.

So if the construction cost of the line is less than benefits brought by the line, it suggests that our model helps to make the decision between hub construction and line construction on the basis of balancing the budget and passenger transport cost.

3.3 Budget Constraint and Sensitivity Analysis

In the above example network, such problem will often appear in the real world: The government needs to build a new infrastructure network, but the budget of the investment is given. For a given budget, we still hope to keep efficient passenger transport network, and to minimize the network passenger transport costs. Therefore, the optimization goal is simplified as:

Fig. 4 Optimization result when $0 \leq c \leq 8.0$

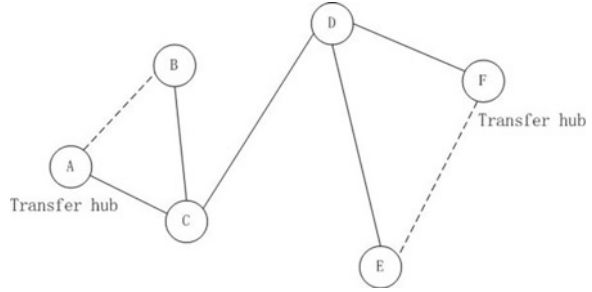
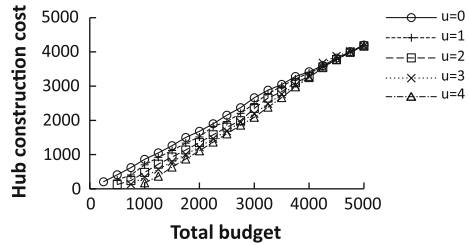


Fig. 5 The relationship between hub layout cost and the total budget



$$\text{Minimize } \sum_{(i,j) \in P} t_{ij} Y_{ij}$$

Adding an investment budget constraint:

$$\sum_{i \in N} f_i Z_i + \sum_{(i,j) \in P} c_{ij} X_{ij} \leq B$$

The purpose is to study what kind of decisions should government to do under the condition of limited budgets, more hubs or more lines.

Due to hub construction cost is fixed, we can make sensitivity analysis on the model through changing the budget B and unit rate u of the line construction cost.

Figure 5 shows that hub construction investment and the total budget is almost linear growth, and with the increase of total budget, government should care more about hub construction investment. At the same time, line construction cost decline gradually (Fig. 6).

As shown in Fig. 7, total travel cost decreases with the increase of total budget, which suggests the effectiveness of the increasing budget in improving network services. Obviously, with the increase of total budget, the infrastructure construction costs make a linear upward trend, and accordingly, passenger transport cost declines gradually.

Fig. 6 The relationship between line construction cost and the total budget

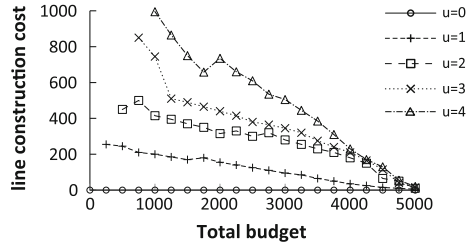
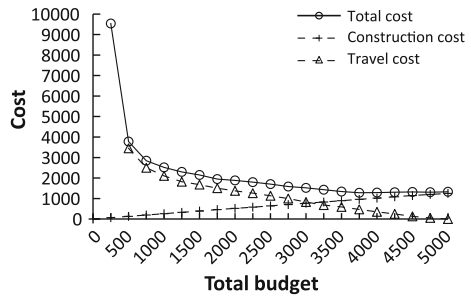


Fig. 7 The relationship, the related costs, and the total budget



4 Conclusion

This chapter studied weak infrastructure areas, in order to improve the travel efficiency of the existing network, an integrated optimization model is established so as to balance the budget and passenger transport cost, and to minimize the total cost with the limited budget.

The example demonstrated the effectiveness of the increasing budget in improving network services. With the increase of total budget, more hub facilities should be built, while with the decrease of total budget, more line facilities should be built. This chapter assumes that the demand of each node is given, so it remains to be further research in the case of demand variable.

Acknowledgments This study is supported by the National Natural Science Foundation of China (71131001), the National Basic Research Program of China (2012CB725406), and the Fundamental Research Funds for the Central Universities (2012YJS062).

References

1. Li X, Xiao W, Chen D et al (2010) Layout optimizing model of external passenger transport hub in metropolis. *J Traffic Transp Eng* 10(2):75–76
2. Gelareh S, Nickel S (2011) Hub location problems in transportation networks. *Transp Res Part E*

3. Chen H (2001). Research on the highway bus terminals layout and location methods. *J Highw Transp Res* 18(3)
4. Gelareh S (2008). Hub location models in public transport planning. Thesis. Universitätsbibliothek
5. Wu S, Shi Q, Lu H (2005) Traffic efficiency-based urban public traffic network distribution model. *Eng J, China Civil*, p 1
6. Lan GUI (2006) An optimal model and algorithm for the transportation network design problem. *Syst Eng* 24(12):26–32
7. Zhang G, Lu J, Xian Q (1992) Network design problem based on equity and priority. *J Transp Syst Eng Inf Technol* (5)
8. Berman O, Ingco DI, Odoni AR (1992) Improving the location of minisum facilities through network modification. *Ann Operat Res*
9. Bhadury J, Gewali LP, Chandrasekaran R, Badr M (1998) Network design subject to facility location. In: *INFORMS national meeting*, Montreal
10. Campbell J (2005) Strategic network design for motor carriers. *Logistics systems: design and optimization*. Springer, New York
11. Daskin MS (1995) Network and discrete location: models, algorithms, and applications. Wiley, New York
12. Chowdhury NMMK (2009) Virtual network embedding with coordinated node and link mapping. *INFOCOM, IEEE*

Synchronization Control in Vertical Ship Lift Based on Relative Coupling Strategy

Yang Gang and Zhang Jiabing

Abstract As the main hoist system of the vertical ship lift has poor synchronicity when load disturbance, a relative coupling compensation of multi-motor synchronous control strategy was proposed to the control system, and a fuzzy PID speed compensator was adopted. Finally, the results of the simulation in MATLAB 7.11/SIMULINK showed that the system had a good synchronicity and stability behavior.

Keywords Vertical ship lift · Multi-motor · Relative coupling · Fuzzy PID

1 Introduction

Ship lift is a kind of navigation structure, which can help the ship to overcome the water level difference. At present, navigation structure mainly includes ship lock and ship lift. Compared with the ship lock, ship lift has the advantage of water conservation and short time of sailing. Ship lift is an integrated system, which includes electrical, mechanical, and other objects. Ship lift mainly consists of ship chamber, lift motor, bearing, guide device, drive, brake, protective devices, and other components. The main lift system of ship lift was designed to many dispersed sets of winding motor. It usually consists of four symmetrical distribution of motors. The main lift synchronous system consists of mechanical and electrical synchronous system. The mechanical synchronous system means four winding motor shafts were connected through mechanical rigidity when lift ship was designed. The electrical synchronous system strategically uses the drive control of the four winding motors to keep pace when the ship lift working. For the main lift

Y. Gang (✉) · Z. Jiabing

College of Information Science and Engineering, Huaqiao University, Quanzhou, China
e-mail: 15980901046@163.com

system of ship lift, the most important thing is the control system should ensure that the ship is horizontal during the ship lift working, which means that the speed of the four motors of ship lift should keep consistent. The main lift control system of ship lift was studied in many papers, such as Refs. [1, 2]. Most of the research object was Yantan ship lift, Gaozhouba ship lift, Geheyang ship lift, and other famous ship lift in China. For the control method of a motor, these papers mostly used torque and speed double-loop control method. For the control of four motors, there are mainly three ways: the first scheme, four motors have separate speed and torque loop. They are work independently, without any association. This control method is obviously not able to achieve the synchronous control system when one of the motors is disturbed, and the speed or torque is not synchronized. The second scheme, the load balancing through the torque loop control. Choose one of the motor as the master motor and other three motors as slave motor. Four motors have separate torque loop, but share the same motor speed loop. This control method only has one speed loop and can hardly guarantee the slave motor speed accuracy control. The third scheme, the load balancing through speed loop control method. Four motors have its own speed loop and torque loop. Select one motor as master motor. Each of the remaining motors add a load balance regulator. The regulator input is the difference between the given torque of master motor and the slave motor, the output is appended to the slave motor reference speed. This control method also uses master–slave control mode. So this kind of control scheme of synchronous performance is not good. In this paper, a relative coupling compensation is introduced to control the lift motor.

Ship lift is difference in the mechanical design and on-site environmental conditions of the ship lift is also different. So the main lift control of ship lift requirements are not the same. Ship lift in this chapter is that motor shaft is not mechanically connected. The above described three main ship lift control systems are mainly suitable for four lift motor rigidly connected through mechanical axis, because the motor shaft rigidly connected by mechanical systems needs to synchronize torque balance. If the torque is not balanced, may cause mechanical axis jitter, then causing the lift motor not synchronized. For the motor shaft without mechanically connected systems, in order to ensure the ship lift system is kept horizontal, the only need is that the speed of motors is consistent with each other. The respective lift motor torque can be of some difference.

2 Ship Lift Synchronous Control System

The main lift system of vertical ship lift is a multi-motor synchronous control system. Multi-motor synchronous control system has two kinds of control methods, mechanical synchronous and electric synchronous [3, 4]. We only need to research the electric synchronous in this chapter.

Electric synchronous in a controlled manner by controlling the rotational speed of each motor and using a control strategy to achieve multiple motors

synchronous. Compared with the mechanical synchronous control mode, the electric synchronous control method is very flexible. There are many electric synchronous control strategies. Consist of noncoupled parallel control, noncoupled master–slave control, virtual electronic shaft control, cross-coupling control, and relative coupling control.

Noncoupled parallel control is a system that each motor separately control. This control method cannot achieve multi-motor coordination and synchronous control. Noncoupled master–slave control method is that one of the motor is selected as the master motor and the others are slave motor. Master motor control signal given by the system, and the slave motor control signal is from the master motor. Compared with parallel control, this control method can only improve the control accuracy of master motor. Because only the change of master motor can be reflected from the slave motor, but the change of slave motor cannot be followed. This control method is clearly not a good method to achieve coordination of motor control requirements.

Virtual electronic shaft synchronous control is a virtual simulation of the mechanical axis of the physical characteristics. The disadvantage of this control method is the reference input of each motor is not the actual system input, there is a certain bias, and the multi-motor system will not be synchronous when the system starting, stopping, and load disturbance.

In the early eighties of last century, Cross-coupled control is proposed by KOREN [5]. Then a variety of control strategies based on its method are proposed by many scholars at home and abroad. Cross-coupled control mainly through the deviation between two motors actual speed. If the deviation exists, cross-coupled control system will distribute compensation to the motor speed control loop according to certain proportion. This control method can effectively improve synchronous of the multi-motor control system, but only for two motors. When the system is more than two, cross-coupled control strategy would not fit.

Relative coupling control is based on the cross-coupled control. The main idea of relative coupling control is that the feedback speed of each motor subtract the feedback speed of other remaining motor, the sum of difference of speed as the compensation signal to the speed loop of motor. This method can be applied to two or more motors control system. This control strategy can make the control system to achieve good synchronous control effect. The following figure is relative coupling compensation control block diagram based on four motors (Fig. 1).

Speed compensation module consists of two parts: speed feedback module and PID controller module. The speed feedback module is based on the relative coupling strategy. In the speed compensation module 1, the speed feedback module structure is shown in Fig. 2.

In the Fig. 2, $k_i = J_1/J_i$ ($i = 2, 3, 4$). And J_i ($i = 1, 2, 3, 4$) stands for the rotational inertia of the four motors. Other speed feedback modules have a similar structure. Finally, the composite error is input into the PID controller.

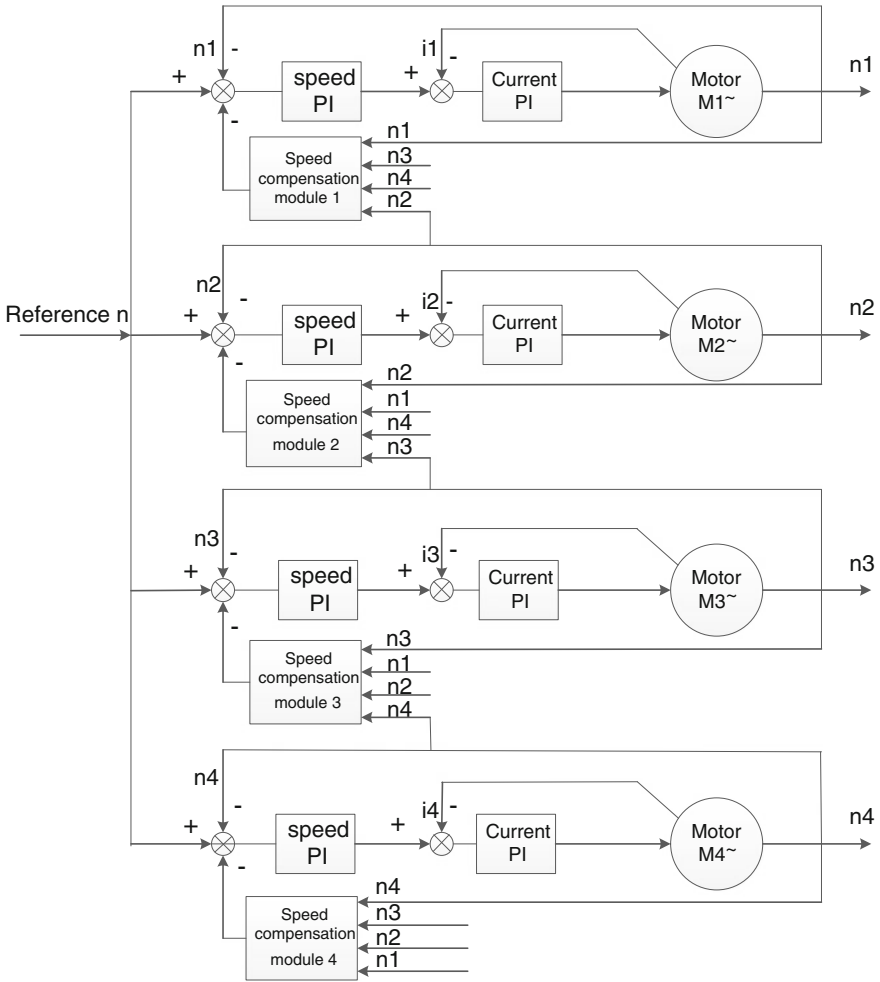


Fig. 1 Control block diagram based on the relative coupling

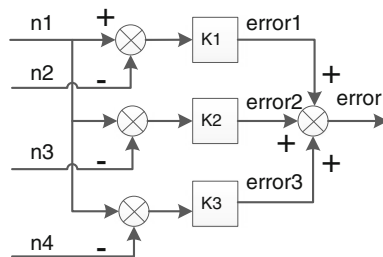


Fig. 2 Speed feedback module

3 Fuzzy PID Control Algorithm

PID controller is a control method, which is widely used in industry. Advantages of PID control algorithm are simple and easy to use. PID controller has some disadvantages. Such as Control accuracy is not ideal when control system is time-variant and nonlinear. Because you could not modify the control parameters online. With the emergence of artificial intelligence (AI), AI combined with PID can be a good strategy to overcome some shortcomings of traditional PID. Neural networks and fuzzy control method are often used by us. Moreover, practical experience showed that these control methods can obtain a good effect. As the ship lift control system is generally nonlinear and time variability when running, we adopt the method of PID controller combined with fuzzy controller. So that the system can have a strong adaptive capacity.

Fuzzy controller consists of four parts: fuzzification, fuzzy control rule base, fuzzy reasoning, and fuzzy solution. Fuzzy PID controller is a control algorithm combined fuzzy control with PID control. Based on the PID control, fuzzy PID control algorithm using the theory of fuzzy control to modify the three parameters of PID controller. The three parameters are proportional coefficient K_p , integral coefficient K_i , differential coefficient K_d . The target of fuzzy PID controller is to optimize the three parameters, so that the controller can make the system always optimum when the parameters of system are changed. The structure of the fuzzy PID is shown in Fig. 3.

The three parameters of PID are not adjusted alone, but three parameters need to be considered together. According to experience, we should follow certain principles on the adjustment of parameters. Such as when deviation $|e|$ gets bigger, in order to improve the response speed of system, the value of ΔK_p should be of larger. At the same time, in order to avoid deviation e instant gets large, the value of ΔK_d should be of smaller. In order to prevent the system response appear larger, usually take $K_i = 0$. Deviation variation $|ec|$ showed that the size of the deviation change rate. When the value of $|ec|$ is larger, the value ΔK_p should be of smaller and the value of K_i should be of larger [6, 7]. According to the experience, we can obtain the three parameters of adjustment rule table (Tables 1, 2 and 3).

In the above three tables, NB stands for negative big, NM stands for negative middle, NS stands for negative small, ZO stands for zero, PS stands for positive small, PM stands for positive middle, PB stands for positive big. These are the language variable of e and ec . And the scope of universe of discourse is $\{-3, -2, -1, 0, 1, 2, 3\}$. The membership function of e and ec are trigonometric function.

Finally, according to the following formula, we can get three values of PID parameters.

$$K_p = K_{p0} + (e, ec)p = K_{p0} + \Delta K_p \tag{1}$$

$$K_i = K_{i0} + (e, ec)i = K_{i0} + \Delta K_i \tag{2}$$

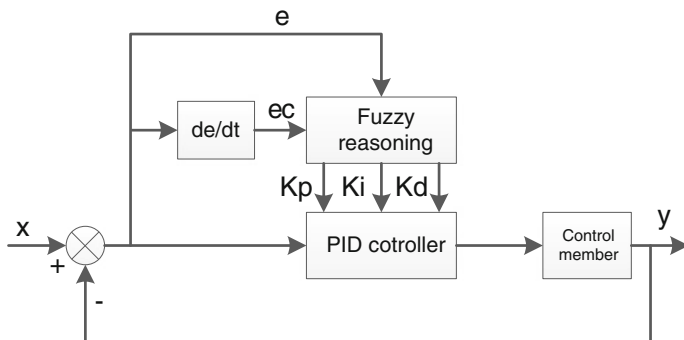


Fig. 3 Fuzzy PID controller

Table 1 ΔK_p rule

| e | ec | | | | | | |
|----|----|----|----|----|----|----|----|
| | NB | NM | NS | ZO | PS | PM | PB |
| NB | PB | PB | PB | PB | PB | ZO | NS |
| NM | PB | PB | PM | PM | PM | NS | NM |
| NS | PB | PM | PM | PS | PS | NM | NB |
| ZO | ZO | ZO | ZO | ZO | ZO | ZO | ZO |
| PS | NB | NM | NS | PS | PS | PM | PB |
| PM | NM | NS | ZO | PM | PM | PB | PB |
| PB | NS | ZO | PS | PB | PB | PB | PB |

Table 2 ΔK_i rule

| e | ec | | | | | | |
|----|----|----|----|----|----|----|----|
| | NB | NM | NS | ZO | PS | PM | PB |
| NB | PB | PB | PB | PB | PM | PS | ZO |
| NM | PB | PB | PB | PM | PS | ZO | ZO |
| NS | PB | PM | PS | PS | ZO | NS | NM |
| ZO | NM | NS | ZO | ZO | ZO | NS | NM |
| PS | NM | NS | ZO | PS | PS | PM | PB |
| PM | ZO | ZO | PS | PM | PM | PB | PB |
| PB | ZO | PS | PB | PB | PB | PB | PB |

$$K_d = K_{d0} + (e, ec)d = K_{d0} + \Delta K_d \tag{3}$$

From above formula, we can see that the values of fuzzy PID controller parameters are obtained by the predetermined values of traditional PID parameters.

Table 3 ΔKd rule

| e | ec | | | | | | |
|----|----|----|----|----|----|----|----|
| | NB | NM | NS | ZO | PS | PM | PB |
| NB | PB | PB | PB | NB | NB | NM | NS |
| NM | PB | PB | PM | PM | ZO | PS | PM |
| NS | PB | PM | PM | NS | PM | PB | PB |
| ZO | ZO | ZO | ZO | ZO | ZO | ZO | ZO |
| PS | PB | PB | PM | NS | PM | PM | PB |
| PM | PM | PS | ZO | NM | PM | PB | PB |
| PB | NS | NM | NB | NB | PB | PB | PB |

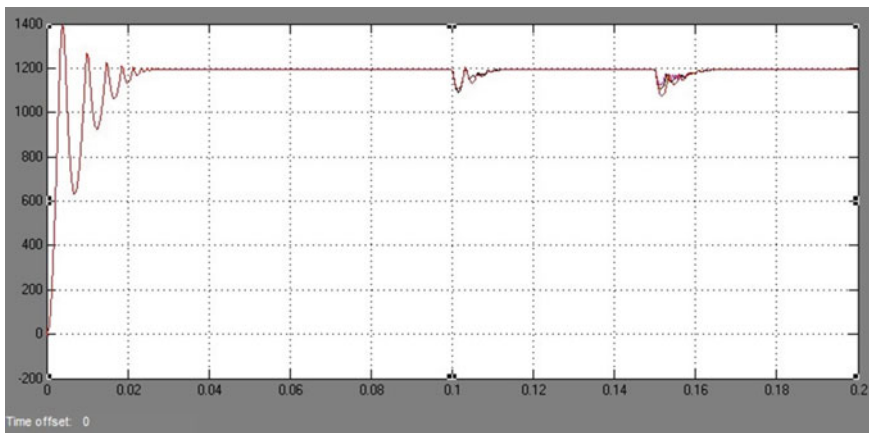


Fig. 4 PID for the synchronous control of four motors

4 Simulation and Analysis

According to the control block diagram shown in Fig. 1, we have performed the simulation by MATLAB 7.11/SIMULINK. The results are shown in the Figs. 4 and 5.

All of the reference speeds of the four motors are 1,200 r/min. Then we do the following action: at 0.1 s, we given the motor 1 a step torque sign of 1 N * M to 2 N * M and the motor 2 a step torque sign of 1 N * M to 3 N * M. And at 0.15 s, we given the motor 3 a step torque sign of 1 N * M to 2 N * M and the motor 4 a step torque sign of 1 N * M to 2.5 N * M. Further, the two cases of ordinary PID controller and fuzzy PID controller were both simulated.

From the above two simulation results, we can see that the four motors have good synchronous both in the ordinary PID control and fuzzy PID control. This

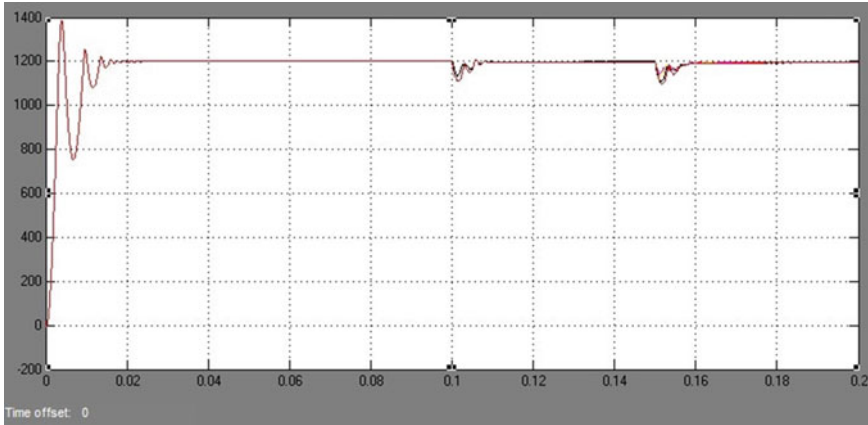


Fig. 5 Fuzzy PID for the synchronous control of four motors

indicated relative coupling compensation control strategy can make the system have good synchronous performance.

From the compared Fig. 4 with Fig. 5, we found that the fuzzy PID controller is much better than ordinary PID controller in dynamic following and synchronous effect of four motors when the torque of motor is changed.

5 Conclusions

The relative coupling control strategy was used in this chapter. And on this basis, combined fuzzy PID controller, we got speed compensator of four motors. Verified by simulation of fuzzy PID compensator shown four synchronous motors had good control effect. And compared ordinary PID compensator with fuzzy PID compensator through the simulation, we could see that the fuzzy PID compensator had better dynamic characteristics and high anti-interference capability.

References

1. Shi XJ, Liao PL, Yi CH (2006) Design and realization of the upper computer monitoring and control system of the Caobazhou ship lift. *Hydropower Autom Dam Monit* 3:007
2. Yi CH, Shi XJ, Liu J (2012) Design and realization of electrical control system for hydraulic shiplift. *Water Power* 10
3. Nunez C, Alvarez R, Cervantes I (2004) Comparison of multi-motor synchronous techniques. In: *IECON 2004. 30th Annual conference of IEEE industrial electronics society, 2004*, vol 2, pp 1670–1675

4. Liu F, Zhang X, Liu L (2002) Synchronous control theory and practical study of multi-motor synchronous driving system. *Basic Autom* 4:027
5. Koren Y (1980) Cross-coupled biaxial computer control for manufacturing systems. *ASME. J Dyn Syst Meas Control* 102(4):265–272
6. Wang N, Meng X, Xu Q (2008) Fuzzy control system design and stability analysis for ship lift feedback fin Stabilizer. In: 7th World congress on intelligent control and automation. WCICA 2008, pp 1223–1228
7. Tang KS, Man KF, Chen G et al (2001) An optimal fuzzy PID controller. *IEEE Trans Ind Electron* 48(4):757–765

Study on Security Domain-Oriented Military Information Systems Access Control Model

Yan Jin, Hao Liu, Lin Sun and Jing Song

Abstract The access control of military information systems (MIS) is an important issue that imposes significant influence on the MIS security. First of all, we did in-depth analysis of the main factors of access control model, such as the basic principle and constraints of models, the formal definition of model components, and the permissions and inheritance of models. Furthermore, the idea of security domain management and control is introduced in this chapter and based on existing access control model, SDO-ARBAC (Security Domain-Oriented-Administrative Role-Based Control Model) is built which is more suitable for MIS access control.

Keywords Security domain · Access control · Model components · Basic constraints

1 Introduction

With the rapid development of MIS, the current MIS are facing increasingly prominent problems of access control. The existing access control models are difficult to meet the more and more diverse and urgent demand of MIS access control. In order to adapt the characteristics and the way of distributed

Y. Jin (✉) · L. Sun

The Fourth Department, National Defense Information Academy, Wuhan China
e-mail: lily_bril@163.com

H. Liu

Information Teaching and Research Section, Nanchang Military Academy,
Nanchang China

J. Song

The Third Department, National Defense Information Academy, Wuhan China

management of MIS, the security domains of MIS should be the objects to be access controlled. The needs of MIS access control can be well met by using distributed association with centralized access control.

2 The Division of MIS Security Domain

Within the context information security, security domain refers to a group of computers which constitute a network and share a common directory database and information security policy. Security domains of MISs are some logical subnetworks or networks divided from the MIS according to the difference of the nature, users, safety objectives and safety strategies of the information. Every logical subnetwork or networking the same security domain has the same security protection needs, security access control, and border control strategies.

The business subsystems are the basis for security domain division. Some key factors, such as the features of services, the conditions of network and management, information flow and business relationships should be considered particularly when security domains of MIS are divided.

Each business subsystems of the MIS are divided into security domains in accordance with the following procedures. A. To examine the access relations; B. To divide the computing security domain; C. To divide the user security domain; and D. To divide the network security domain. The security domain divisions of a business subsystem are shown in Fig. 1 [1].

3 The Extension of the Access Control Model to the MIS Security Domain

In-depth analysis and understanding of the requirement of access control model is the premise and foundation to guarantee the correctness of model extension and applicability of model itself. The following factors should be paid attention when access control models are extended to the MIS security domain [2, 3]:

1. The security policy of MIS security domain. From the perspective of MIS security domain, the extension of the access control model should comply with the security policy of security domain to ensure the consistency of security policy of access control model and security domain.
2. Different permissions and permissions inheritance of MIS. Since different roles correspond to different assignments and responsibilities, the permissions of these roles should be broken down from the perspective of permissions protection and application requirements to differentiate the permissions and permissions inheritance. It is beneficial to reduce the risk of permissions leakage by carrying out fine-grained access control.

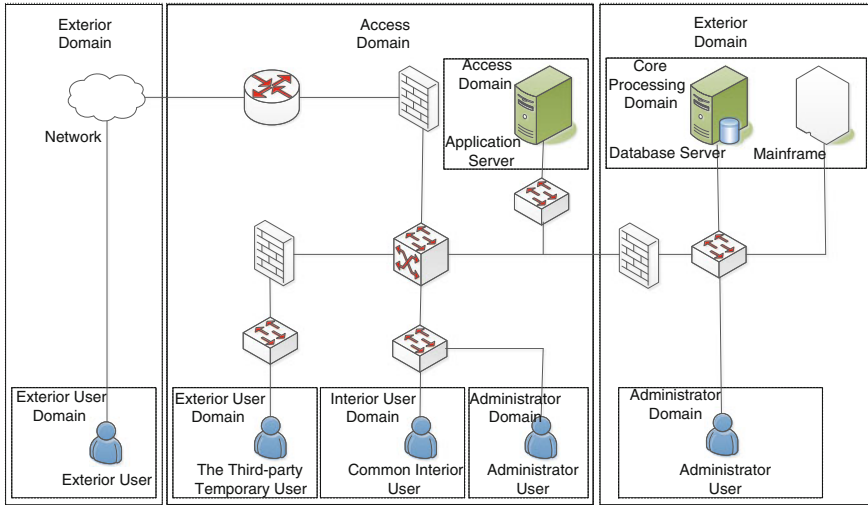


Fig. 1 The sketch map of security domain division of a business subsystem

3. Diversity of access control constraints of MIS. The extension of access control models to MIS security domain should be based on the refinement and enrichment of existing models. Other key issues should also be considered such as Role Cardinality Constraints, Duty Separation Constraints, Pre-condition Constraints, Security Domain Constraints, Delegation Constraints, Time Constraints, and Minimum Permissions Constraints, etc.

4 SDO-ARBAC Model for Information Security Domain

According to the requirements of access control model extension to MIS security domain, we can extend the role-based access control model to MIS security domain. The SDO-ARBAC (Security Domain-Oriented-Administrative Role-Based Access Control) model is regarded as the fittest one for the MIS.

4.1 The Basic Principle of the SDO-ARBAC Model

The basic structure of SDO-ARBAC model is depicted in Fig. 2.

The basic principles of the SDO-ARBAC model [4] are:

1. It is based on the idea of security subdomain access control and management to divide the MIS security domain. Security subdomain access control and management will improve the capacity and efficiency of distributed access control and management of the model and the overall system.

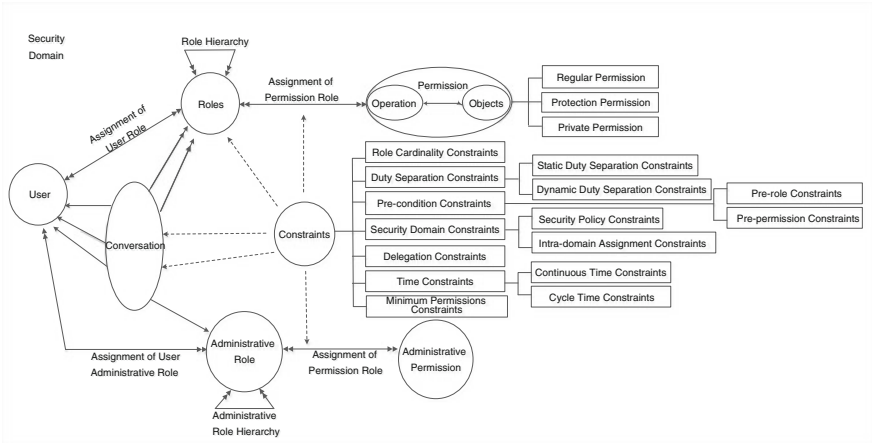


Fig. 2 The basic structure of SDO-ARBAC model

2. The refinement of access control granularity, the better protection of role’s permissions and the reduction of the risk of permissions leakage can be achieved by the role’s permissions classification and refinement and by using different ways of permissions inheritance for different roles.
3. The basic constraints of RBAC model are kept and some new constraints, such as security domain constraints, delegation constraints, time constraints, and minimum permissions constraints, are added to the SDO-ARBAC model in order to further regulate the access control mechanism.
4. SDO-ARBAC model use security domains as basic units to implement the access control. The authorization of across security domains and resource access can be achieved by the mapping mechanism.

4.2 The Formal Definition of SDO-ARBAC Model Components

SDO-ARBAC Model can be divided into several different components which include sets, relations set-valued functions, permissions, inheritance, and basic constraints, and they all can be defined in a formal way.

4.2.1 Sets

Let N be the set of natural numbers; the sets in the SDO-ARBAC model are:

- SDs: Security Domains Set, $SDs = \{sd_{i1} \in N\}$;
- Users(sd): Users (User or Autonomous Agent)Set, $Users(sd) = \{u_{i1} \in N\}$;
- Roles(sd): Roles Set, $Roles(sd) = \{r_{i1} \in N\}$;

- Ops(sd): Operations Set, $\text{Ops}(sd) = \{\text{opili} \in N\}$;
- Obs(sd): Objects Set, $\text{Obs}(sd) = \{\text{obili} \in N\}$;
- Perms(sd): Permissions Set, $\text{Perms}(sd) = \{\text{pili} \in N\}$, $\text{Perms} = 2(\text{Ops}(sd) \times \text{Obs}(sd))$;
- ARoles(sd): Administrative roles Set, $\text{ARoles}(sd) = \{\text{arili} \in N\}$;
- APerms(sd): Administrative Permissions Set, $\text{APerms}(sd) = \{\text{apili} \in N\}$;
- Sessions(sd): Sessions Set, $\text{Sessions}(sd) = \{\text{sili} \in N\}$;
- Consts(sd): Constraints Set, $\text{Consts}(sd) = \{\text{cili} \in N\}$.

4.2.2 Relations

The relations of SDO-ARBAC Model include:

1. Users-Role assignment relation $\text{UA}(sd)$. $\text{UA}(sd) \subseteq \text{Users}(sd) \times \text{Roles}(sd)$. $\text{UA}(sd)$ is many-many mapping from $\text{Users}(sd)$ to $\text{Roles}(sd)$. One user can have several roles and one role can be assigned to several users. $(u, r) \in \text{UA}(sd)$ means user u has the role r and the permissions of role r .
2. Role-Permissions assignment relation $\text{PA}(sd)$. $\text{PA}(sd) \subseteq \text{Perms}(sd) \times \text{Roles}(sd) \times \text{Ptypes}$. $\text{PA}(sd)$ is many-many mapping from $\text{Perms}(sd)$ to $\text{Roles}(sd)$. Ptypes is the type of permission and defines the way of permission inheritance. $(p, r, \text{ptypem}) \in \text{PA}(sd)$ means role r has the Ptypes permission p .
3. Role Hierarchy partial ordering relation $\text{RH}(sd)$. $\text{RH}(sd) \subseteq \text{Roles}(sd) \times \text{Roles}(sd)$. $\text{RH}(sd)$ is the Partial ordering relation of $\text{Roles}(sd)$. $(ri, rj) \in \text{RH}(sd)$ means ri is the parent role of rj and rj is the child role of ri . Parent role inherits all or part of the permissions of child role. If $(ri, rj) \in \text{RH}(sd)$, let $ri \geq rj$, if $ri \neq rj$, let $ri > rj$. There is no need to specify the way of permission inheritance in $\text{RH}(sd)$ because it has been defined in $\text{PA}(sd)$ by Ptypes .

4.2.3 Set-Valued Function

Set-Valued Functions of SDO-ARBAC model are:

- $\text{regular_roles}(u: \text{Users}(sd), sd) \rightarrow 2\text{Roles}(sd)$. This function returns the roles set belongs to user u , $\text{regular_roles}(u, sd) = \{r \in \text{Roles}(sd) | (u, r) \in \text{UA}(sd)\}$;
- $\text{regular_perms}(r: \text{Roles}(sd), sd) \rightarrow 2\text{Perms}(sd)$. This function returns the permissions set belongs to user u , $\text{regular_perms}(r, sd) = \{p \in \text{Perms}(sd) | r \geq rj (rj, p, \text{ptypem}) \in \text{PA}(sd)\}$;
- $\text{admini_aroles}(u: \text{Users}(sd), sd) \rightarrow 2\text{ARoles}(sd)$. This function returns the administrative roles set belongs to user u , $\text{admini_aroles}(u, sd) = \{ar \in \text{ARoles}(sd) | (u, ar) \in \text{AUA}(sd)\}$;
- $\text{Op}(p: \text{Perms}(sd), sd) \rightarrow \{\text{op} \subseteq \text{Ops}(sd)\}$. This function returns the operations set corresponding to permissions p ;

- $\text{Ob}(p: \text{Perms}(\text{sd}), \text{sd}) \rightarrow \{\text{ob} \subseteq \text{Obs}(\text{sd})\}$. This function returns the objects set corresponding to permissions p ;
- $\text{arole_sd}(\text{ar}: \text{ARoles}(\text{sd})) \rightarrow \text{SDs}$. This function returns security domain corresponding to administrative roles ar , $\text{arole_sd}(\text{ar}) = \{\text{sdl_sd} \in \text{SDs}\}$;
- $\text{perm_sd}(p: \text{Perms}(\text{sd})) \rightarrow \text{SDs}$. This function returns security domain corresponding to permissions perm , $\text{perm_sd}(p) = \{\text{sdl_sd} \in \text{SDs}\}$;
- $\text{aperm_sd}(\text{ap}: \text{APerms}(\text{sd})) \rightarrow \text{SDs}$. This function returns security domain corresponding to administrative permissions aperm , $\text{aperm_sd}(\text{ap}) = \{\text{sdl_sd} \in \text{SDs}\}$;
- $\text{session_sd}(s: \text{Sessions}(\text{sd})) \rightarrow \text{SDs}$. This function returns security domain corresponding to sessions s , $\text{session_sd}(s) = \{\text{sdl_sd} \in \text{SDs}\}$.

4.3 Permissions and Inheritance of SDO-ARBAC Model

There are three kinds of permissions in the SDO-ARBAC model. They are Normal Perms, Protected Perms, and Private Perms.

The inheritance of Normal perms is on the basis of role hierarchy. The Protected Perms can be inherited by parent roles as Private Perms of parent roles. The Private Perms cannot be inherited by any roles in order to avoid the spread of sensitive permissions and reduce the workload of permissions management. Accordingly, there are three kinds of inheritance relations: Normal Perms inherited with Normal Inheritance (NI), protected perms inherited with Direct Inheritance (DI), and Forbidden Inheritance (FI) for Private Perms. NI is partial ordering dominant inheritance relation. Normal Perms inherited with NI are still Normal Perms. Protected perms inherited with DI by parent roles become Private Perms of parent roles which cannot be inherited by any roles. Private Perms are forbidden to inheritance of any roles [5, 6].

4.4 Basic Constraints of SDO-ARBAC Model

Basic constraints of SDO-ARBAC model include Role Cardinality Constraints, Duty Separation Constraints, and Pre-condition Constraints.

4.4.1 Role Cardinality Constraints

Role Cardinality Constraint is used to specify the number of a role that can be authorized or activated. It can be described by the following two kinds of formal description:

- For $\forall sd \in SDs, \forall r \in Roles(sd)$, let M be the role cardinality of r . Function $UN(r, sd)$ returns the number of users which are distributed by role r in role hierarchy of security domain sd . Function $MaxUN(r, sd)$ returns the maximum number of users. Then $UN(r, sd) \leq MaxUN(r, sd) \leq M$ [110].
- For $\forall sd \in SDs, \forall r \in Roles(sd)$, let M be the role cardinality of r and $\#$ be the number. Then $\#assigned_users(r, sd) \leq M \wedge \#authorized_users(r, sd) \leq M$ [99].

4.4.2 Duty Separation Constraints

Duty Separation Constraints can be divided into static and dynamic duty separation constraints according to their timing of application and operation. Static Duty Separation Constraints: $SSD(sd) \in (2Roles(sd) \times N)$. N is a set of natural numbers. $SSD(sd)$, implemented by the role static mutexes, is defined at the stage of user assignment and independent of session and role activation. If the relation of two roles is static mutexes, any user cannot have these two roles at the same time.

Dynamic Duty Separation Constraints $DSD(sd) \in (2Roles(sd) \times N)$. N is a set of natural numbers. $DSD(sd)$, implemented by the role dynamic mutexes and is defined at the stage of role activation and applied in a session. If the relation of two roles is dynamic mutexes, any user can have these two roles, but cannot activate them in the same session at the same time.

4.4.3 Pre-condition Constraints

Pre-condition Constraints include Pre-role Constraints and Pre-permission Constraints.

Pre-role Constraints: $PreR(sd) \in 2Roles(sd) \times N$. When the role r_j is assigned to the user u , u should have the specific pre-role set or the pre-role r_i . Pre-condition Constraints are opposite to the Duty Separation Constraints. It can be used to restrict the user's qualification of assigning the roles. The formal description is $(\forall sd \in SDs)(\forall u \in Users(sd))(\forall r_i, r_j \in Roles(sd))((r_i, r_j) \in PreR(sd)) \wedge (u \in assigned_users(r_j, sd)) \Rightarrow u \in assigned_users(r_i, sd)$.

Pre-permission Constraints: $PreP(sd) \in 2Perms(sd) \times N$. When the permission p_j is assigned to the role r , r should have the specific pre-permission set or the pre-permission p_i . Pre-permission Constraints can be used to restrict the conditions of the role authorization. The formal description is $(\forall sd \in SDs)(\forall r \in Roles(sd)) (\forall p_i, p_j \in Perms(sd))((p_i, p_j) \in PreP(sd)) \wedge (p_j \in assigned_perms(r, sd)) \Rightarrow p_i \in assigned_perms(r, sd)$.

5 Conclusion

The idea of security domain management and control is introduced to address the problem of the existing access control models applying in the MIS. SDO-ARBAC is built by the improvement of the formal definition of model components, the proper definition of the roles, the refinement of the permission, differentiating the permission inheritance, keeping and changing the basic constraints, and adding the Security Domain Constraints, Delegation Constraints, Time Constraints, and Minimum Permissions Constraints. Consequently, the better management capacity can be entitled to the model and security domains can be better used as the basic units to implement the access control, so that the requirements of access control of MIS are met.

References

1. Chen B, Wang Z, Ai P, Xu F (2006) The research overview of constraints on the RBAC model. *Comput Eng* 200632(9)
2. Shao S (2009) Research and implementation of access control. Beijing University of Posts and Telecommunications, Beijing, vol 2, p 2
3. Wang J, Jia L, Yao H (2011) Research on RBAC-based distributed file-level security access control system. *Comput Res Dev (Suppl 2)*:24
4. Wang X, Gu T, Guo Y, Zheng Y, Zong J, Gong B (2009) An algorithm for role mapping across multi-domains employing RBAC. *Chinese J Electron* 18(1):37–41
5. Wang X, Liu Q (2009) Study on the trust and permission leakage in ARBAC model. *Res Dev* 7:16
6. Zhu Y (2006) Study on the practical application of ARBAC model and its application in Intranet monitoring University of Electronic Science and Technology, Chengdu, vol 12, pp 24–26

Optimizing Control of Multiobjective Based on Improved PSO Algorithm for Excavator

Bo Bi and Lei Li

Abstract Different controller is radically different in control effect. For the same controlled process, aimed at the puzzle of being difficult to select the controller for the incompatibility among control performance index, this paper proposes a sort of improved PSO algorithm. Based on the construction of objective function in multi-performance index parameter, the algorithm could quickly search and converge to optimizing control parameter in global optimal extremum, and single out the controller through performance comparison excellently. In the paper, it took the controller selection of excavator system as an example, designed the algorithm of multi-modal HSIC controller for excavator, and the simulation demonstrated that the HSIC-based controller could be stronger in robustness and better in dynamical and steady control quality compared with improved PID controller. The research result shows that it is reasonable and applicable to optimizing selection of controller.

Keywords Excavator · Control parameter · Improved PSO algorithm · Optimizing selection of controller

1 Introduction

Green manufacturing as a new-type sustainable development manufacturing pattern is oriented to the future of modern manufacturing. The control problem in green manufacturing implies multiobjective optimizing control, has to make

B. Bi (✉)

International School, Chongqing Jiaotong University, Chongqing, China
e-mail: 804805129@qq.com

L. Li

College of Automation, Chongqing University, Chongqing, China

overall plans taking all factors into consideration in the whole control process, and hence how to select the controller and its control parameter has become a key technique puzzle. The following explores the optimizing selection of multiobjective controller parameter based on improved Particle Swarm Optimization (PSO) algorithm [1].

2 Fusion Control Algorithm Based on PSO and GA

PSO and Genetic Algorithm (GA) is the evolutionary algorithm based on the theory of biology evolutionism and genetics, etc., for solving optimization problem. PSO algorithm has a lot of superiorities such as being faster in convergence rate, less in parameter tuning, simpler and easier in implementation, and has always been used in controller parameter tuning [2]. GA is a sort of search method based on principles of biology evolution, and it has better ability for global optimization, and also is widely used for parameter optimization strategy of randomization [3, 4]. Up to now, GA algorithm has been a mature analysis method and is widely used in many fields such as combination optimization and so on. Comparing PSO with GA algorithm, there are some differences [5]. Both PSO and GA represent the simulation and research of biological world laws, and are a sort of stochastic search technique having global optimization characteristic and implicit parallelism. However, in the face of multiobjective optimizing control, there appear disadvantages of premature convergence and low convergence. So we can fuse both the superiority of PSO and GA algorithm to improve the control algorithm in the actual control engineering.

3 Improvement of PSO Algorithm Based on Genetic Thought

The crossover-mutation characteristic in biology can efficiently search the global optimal solution and improve the PSO algorithm. In the iteration process, first the 1/3 particle individual of the best fitness makes the selection operation directly go into the next generation, and then makes crossover between any two form 1/3 particle in next generation. Finally the 1/3 particle is formed through mutation operation. By means of genetic crossover operator operating, particle diversity is increased, taking full superiority of particle characteristic in best fitness so as to make better characteristics carry through the heredity, quicken the convergence speed of particle, enlarge the search area through mutation operation of partial particle, and therefore avoid the premature phenomenon of local optimization.

3.1 Selection of Nonlinear Descending Inertia Weight

In the search algorithm, the inertia weight coefficient w determines the global and local search ability. Expression (1) shows a sort of descending function of nonlinear inertia weight and has better convergence speed than linear inertia weight coefficient; therefore it could obtain better solving quality.

$$w_i = (w_{\text{start}} - w_{\text{end}}) \cdot \left(\frac{t_i}{t_{\text{max}}}\right)^2 + (w_{\text{start}} - w_{\text{end}}) \cdot \left(\frac{2 \cdot t_i}{t_{\text{max}}}\right) + w_{\text{start}} \quad (1)$$

in which, t_{max} , w_{start} , w_{end} is, respectively, the most iteration number of generation, maximum and minimum of initial inertia weight, and t_i is the current iteration number of generation.

3.2 Operating Implementation for Genetic Operator

- ① Selection operation adopts proportion selection operating. It first computes the summation of all individual fitness in the population and then computes the proportion of individual fitness in the whole fitness summation. To select 1/3 particle of best performance makes selection operating directly go into the next generation so as to keep the heredity of best evolution ability in particle population.
- ② Crossover operating first selects 1/3 particle to put into a set, and pays a random crossover probability of each particle in the set, and then makes crossover operating between any two. Here, it must pay attention to that to ensure to produce next generation particle of the same number so as to maintain the number and not change the population particle, and the update formula of position and speed for new particle is shown as, respectively, formulas (2) and (3). Secondly it makes the fitness evaluation again for sub-particle of new generation produced, and makes comparison with parent particle fitness. If the fitness of sub-particle is better than parent particle fitness then it would be replaced, otherwise it keeps parent particle to go into the next generation.

$$\begin{cases} X_1(t') = \text{rand}() \cdot X_1(t) + (1 - \text{rand}()) \cdot X_2(t) \\ X_2(t') = \text{rand}() \cdot X_2(t) + (1 - \text{rand}()) \cdot X_1(t) \end{cases} \quad (2)$$

$$\begin{cases} V_1(t') = \frac{V_1(t)+V_2(t)}{|V_1(t)|+|V_2(t)|} \cdot |V_1(t)| \\ V_2(t') = \frac{V_1(t)+V_2(t)}{|V_1(t)|+|V_2(t)|} \cdot |V_2(t)| \end{cases} \quad (3)$$

in which, X represents the position vector in D dimension space, $X(t)$ and $V(t)$ is, respectively, the position vector and speed vector of the space used for selecting crossover operating particle, and $X'(t)$ and $V'(t)$ is,

respectively, the space position and speed vector of new generation particle after crossover. $Rand()$ is a random vector of search space over interval $[0, 1]$.

- ③ Mutation operating first selects anew initializing method so as to avoid getting into the premature convergence. Secondly, it makes comparison between fitness of new generation and parent particle, and its process is similar to crossover operating.

3.3 Flowchart of Algorithm

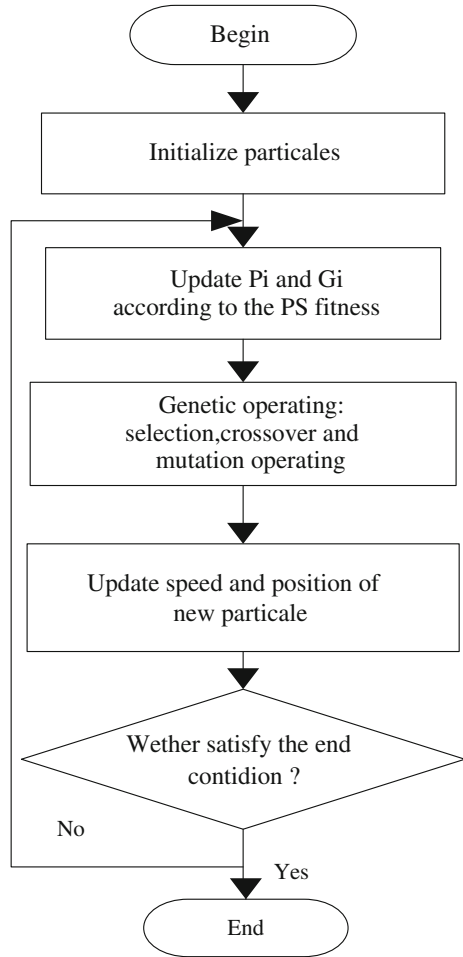
The operation step of improved PSO algorithm is as the following, and Fig. 1 shows the flowchart of improved PSO algorithm of inertia factor nonlinear descending with fused genetic algorithm.

- ① Initialize the particle swarm.
- ② Update the inertia weight coefficient according to formula (1), to make evaluation of population and compute fitness $F(X_i)$ of each particle according to the objective function.
- ③ Execute the genetic operator operating.
- ④ Update the individual extremum of each particle in the population, and make comparison between current $F(X_i)$ and itself individual extremum P_i . If $F(X_i)$ excels P_i then it would update the individual extremum P_i by $F(X_i)$.
- ⑤ Update the global extremum of population, and make the comparison among all P_i produced newly by each particle in the whole population with global P_g in history. If there exists that P_i fitness value of particle excels P_g then the global extremum P_g would be updated by P_i .
- ⑥ Update the speed and position of particle by (2) and (3), and produce the new population $X(t + 1)$.
- ⑦ Judge whether it satisfies the end condition (usually it is set as the error precision or most iteration generation of times). If it is not satisfied then it would be returned to Step ②, and otherwise it stops the search, and outputs the result.

4 Simulation Experiment

Here it takes controller selection of excavator control system as an example, aiming at being difficult to select the controller it designs the algorithm, makes the experiment of system simulation based on comparative analysis, and finally finds the expected controller.

Fig. 1 Flowchart of improved PSO algorithm



4.1 Controller and Its Algorithm Design

For convenience of comparison in control performance, here it designs two sorts of control algorithm.

- ① Improved PID algorithm

$$\begin{cases} u = \text{sgn}(e) \cdot U & (|e| > E) \\ u = K_p \cdot e + K_i \cdot \int_0^t e \cdot dt + K_d \cdot \dot{e} & (|e| \leq E) \end{cases} \quad (4)$$

In which, E is the error feature threshold level. U, K_p, K_i and K_d is respectively the control parameter, U can be gotten from experience. K_p, K_i and K_d can be gotten by method proposed in this paper.

② HSIC-based algorithm

$$\begin{cases} u = \text{sgn}(e) \cdot U & (|e| \geq E_1) \\ u = K_{P1} \cdot e + K_{D1} \cdot \dot{e} & |e| < E_1 \cap |e| \geq E_2 \\ u = K_{P2} \cdot e + K_{D2} \cdot \dot{e} & |e| < E_2 \cap |\dot{e}| \geq \dot{E}_1 \\ u = K_{P3} \cdot e + K_{D3} \cdot \dot{e} & |e| < E_2 \cap |\dot{e}| < \dot{E}_1 \cap |e| > E_3 \cap |\dot{e}| > \dot{E}_2 \\ u = u_{n-1} & |e| \leq E_3 \cap |\dot{e}| \leq \dot{E}_2 \end{cases} \quad (5)$$

in which, E, \dot{E} is, respectively, the threshold level of error and its change rate, $U, K_{P1}, K_{D1}, K_{P2}, K_{D2}, K_{P3}$ and K_{D3} is, respectively, the control parameter. Where U can be gotten through the experience, the other can be gotten by method proposed in this paper.

In order to coordinate the contradiction in energy saving and control quality, and to get better steady and dynamic characteristic, the objective function is selected as below.

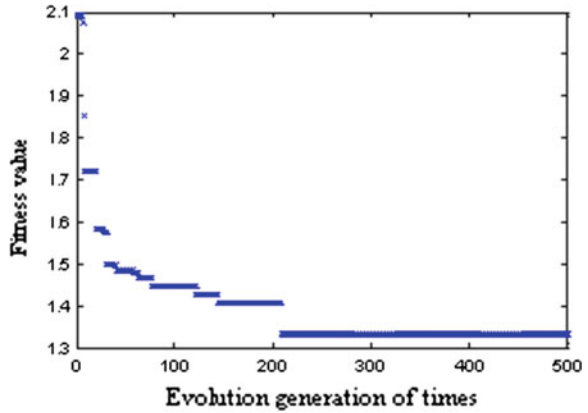
$$J = w_1 \cdot \int_0^t (|e(t)| + u^2(t)) dt + w_2 \cdot \sigma \quad (6)$$

where σ is the overshoot of system, and w_1, w_2 is respectively the weight value.

4.2 Optimization of Controller Parameter

Both PID and HSIC-based algorithm adopt improved PSO algorithm to tune the control parameter, and make input setting be the number of the most particle swarm as 50, number of the most iteration times as 500, learning factor $c_1 = c_2 = 1.2$, inertia weight coefficient $w_{\text{start}} = 1.2$ and $w_{\text{end}} = 0.4$, genetic crossover factor is 0.7, and mutation operating adopts initializing pattern. Under the environment of Matlab, by means of order of Simset and Sim in M file, it can optimize the parameter of the said control algorithms, and Fig. 2 demonstrates the process of simulation iteration by control Algorithm 2. The optimizing result of tuned control parameter is respectively $K_p = 0.3984, K_i = 0.0017, K_d = 3.2402$ for control Algorithm 1, and $K_{P1} = 6.3395, K_{D1} = 8.854, K_{P2} = -6.7065, K_{D2} = 0.14814, K_{P3} = 26.468, K_{D3} = 3.0530$ for control Algorithm 2.

Fig. 2 Iteration curve of control Algorithm 2



4.3 Simulation and Its Analysis

The assumed process model of excavator control is shown as below.

$$G(s) = \frac{7.8125}{74s + 1} \cdot e^{-20s} \tag{7}$$

Under the environment of Matlab, the simulation experiment adopts the above optimized control parameter of improved PSO algorithm, under the condition of step input being 2, the response curve of system is shown as in Fig. 3. It can be seen from the response curve that the curve of control Algorithm 1 has faster response time and larger oscillation, and it appears the overshooting phenomena, but for the curve of control Algorithm 2 it owns the smooth and steady response curve, and there is not any overshooting. The comparative result of simulation demonstrates that the control Algorithm 2 has better control quality than the control Algorithm 1.

In order to analyze the anti-jamming performance, it imposes a pulse disturbance signal with pulse width being 10 s and pulse amplitude being 0.5 at the time $t = 100$ s, and the response curve is shown as in Fig. 4. From the curve comparison it can be seen that it is very small in system overshoot for control Algorithm 2, and it is very large in system overshoot and also large in oscillation frequency and amplitude, and therefore the control algorithm owns better anti-jamming performance.

In order to inspect the robustness of control algorithm, a first-order inertial system is added into the original process model $G(S) = 1/(5S + 1)$, under the condition of the same input, the system response is shown as in Fig. 5. From the response curve it can be seen that the control algorithm has better robustness.

Fig. 3 Response curve respectively by PID and HSIC

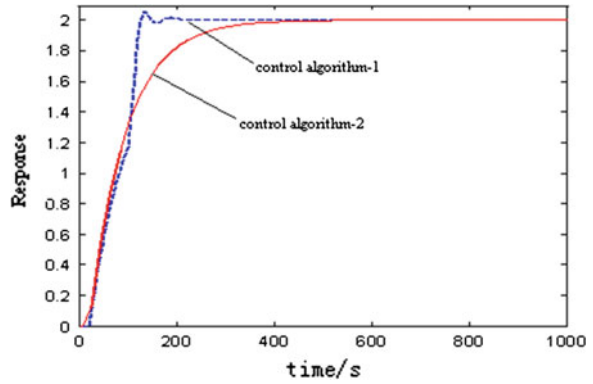


Fig. 4 Response curve with a disturbance

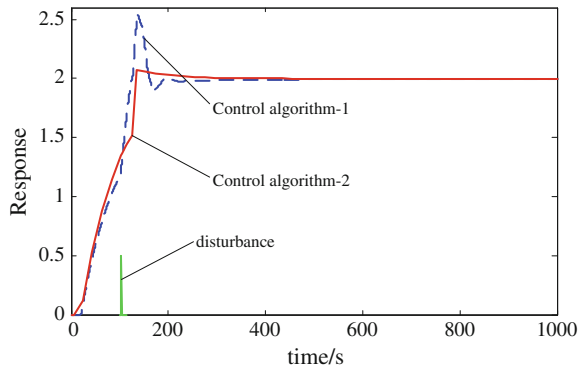
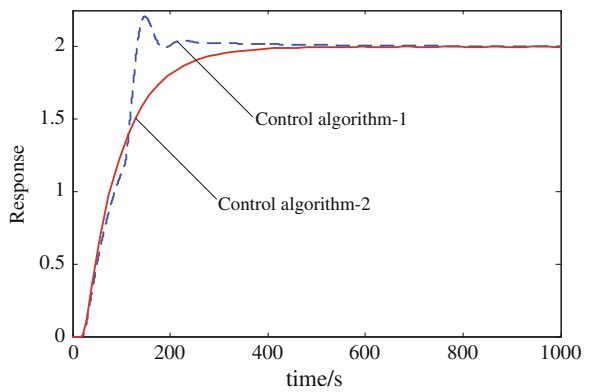


Fig. 5 Response curve adding a first-order system



5 Conclusions

Aimed at the same process model of excavator control system, it designed two sorts of control algorithm, namely the improved PID control algorithm and the multi-modal control algorithm based on HSIC. By means of improved PSO algorithm, it tuned the optimizing control parameter for two sorts of control algorithm. Under the environment of Matlab, the comparison of simulation result shows that the proposed parameter tuning method based on improved PSO algorithm can obtain better control effect for optimizing control of multi-objective for excavator.

References

1. Peer ES, Van den Bergh F, Engelbrecht AP (2003) Using neighborhood with the guaranteed convergence PSO. In: 2003 IEEE swarm intelligence symposium. doi: [10.1007/978-3-540-74377-4_1](https://doi.org/10.1007/978-3-540-74377-4_1)
2. Kaiyou L (2006) Particle swarm optimization and its application research. Southwest University, Chongqing, pp 23–72
3. Wang H (2008) Comparative study on four sorts of intelligent algorithm. Fire Control Command Control 33:71–75
4. Wang Y, Li W (2005) A simulated annealing algorithm for training empirical potential functions of protein folding. Chen Res Chinese U doi: 1005-9040(2005)-01-073-05
5. Hai-bin D, Dao-bo W, Xiu-fen Y (2007) Research on some novel bionic optimization algorithms. Comput Simul doi: 1006-9348(2007)03-0169-04

Parallel Genetic Algorithm Applied to Spacecraft Reentry Trajectory

Wenya Zhou, Hongtu Ma, Zhigang Wu and Kuilong Yin

Abstract The Parallel Genetic Algorithm (PGA) is applied in this paper to solve the reentry trajectory problem of spacecraft. First, the time variable t in motion equations of spacecraft is replaced with velocity v , which can increase the robust of the solution and reduce the computation cost. Second, the control inputs are constructed with the inspiration of proven methods. Finally, PGA is applied to find one global optimization solution. The optimal trajectory is obtained with this method and the result is pretty good comparing with other methods.

Keywords Parallel Genetic Algorithm (PGA) · Reentry trajectory optimization · Variable replacement

1 Introduction

Most of the optimal control problems are nonlinear, therefore generally it is difficult to obtain analytical solution. Numerical solution techniques for trajectory optimization problems are usually classified as indirect and direct methods [1]. Indirect method is preferable from the accuracy point of view, where two-point boundary value problem (TPBVP) has to be solved according to Pontryagin extreme principle in order to satisfy terminal constraints and target conditions. As for nonlinear system, it is very difficult to solve TPBVP mainly due to two reasons: (1) it is a tough work to get the analytical expressions of the transversal conditions;

W. Zhou · H. Ma (✉) · K. Yin
School of Aeronautics and Astronautics, Dalian University of Technology,
No.2 Linggong Road Dalian 116023, Liaoning, China
e-mail: laomax@mail.dlut.edu.cn

Z. Wu
State Key Laboratory of Structural Analysis for Industrial Equipment, No.2 Linggong Road
Dalian 116023, Liaoning, China

(2) it is hard to evaluate the initial values of co-states because the co-state variables are without physical meaning. Direct method is preferred to solve complex problems, as the analytical expressions for necessary conditions and initial guess for the co-state variables are not required [2].

Global optimization methods or so-called evolutionary algorithms are attracting more attention in recent years among all direct methods [3, 4]. The well-known direct method is Genetic Algorithms (GA), which models the evolution of species based on Darwin's principle of survival of the fittest. GA was first introduced by Holland in 1975 [5] and then followed and modified by other researchers [6]. Parallel Genetic Algorithm (PGA) takes the full advantages of computing resources and greatly improves the computational efficiency [7, 8]. With the popularity of multi-core CPU and GPU, PGA certainly becomes the most promising method.

This paper presents one new method to solve the optimal problems based on experienced results and making the best of computing resource. The structure of this paper is organized as follows: Sect. 2—Motion equations for reentry spacecraft are given; Sect. 3—PGA optimization method and mapping procedure are described; Sect. 4—Results are presented.

2 Problem Formulation

The classical motion equations of spacecraft as given in [9] are as follows:

$$\dot{h} = v \sin \gamma \quad (1)$$

$$\dot{v} = -\frac{D}{m} - g \sin \gamma \quad (2)$$

$$\dot{\gamma} = \frac{L \cos \beta}{mv} + \cos \gamma \left(\frac{v}{R_e + h} - \frac{g}{v} \right) \quad (3)$$

$$\dot{\theta} = \frac{v}{R_e + h} \cos \gamma \cos \psi \quad (4)$$

$$\dot{\psi} = \frac{L \sin \beta}{mv \cos \gamma} + \frac{v}{R_e + h} \cos \gamma \sin \psi \sin \theta \quad (5)$$

$$\dot{\phi} = \frac{v}{R_e + h} \cos \gamma \sin \psi / \cos \theta \quad (6)$$

where, altitude h , velocity v , flight-path angle γ , latitude θ , azimuth ψ and longitude ϕ are system state variables. Angle of attack α and bank angle β are system control variables.

Table 1 Constant parameters and basic data of spacecraft

| Sym. | Value | Sym. | Value | Sym. | Value |
|-------|--|----------|--------------------------|-------|--------------------------|
| μ | 398603.2 km ³ /s ² | ρ_0 | 0.0381 kg/m ³ | R_e | 6371.2 km |
| h_r | 7.25 km | S | 249.91 m ² | m | 2861.96 kg |
| a_0 | -0.20704 | a_1 | 0.029244 | b_0 | 0.07854 |
| b_1 | -6.1592×10^{-3} | b_2 | 6.21408×10^{-4} | c_0 | 1.06723181 |
| c_1 | 1.92138×10^{-2} | c_2 | 2.12863×10^{-4} | c_3 | 1.01172×10^{-6} |

Gravity acceleration g and atmospheric density ρ are expressed by

$$g = \mu / (R_e + h)^2, \quad \rho = \rho_0 \exp(-h/h_r) \tag{7}$$

and are used to determine the lift and drag,

$$L = \frac{1}{2} C_L S \rho v^2, \quad C_L = a_0 + a_1 \hat{\alpha} \tag{8}$$

$$D = \frac{1}{2} C_D S \rho v^2, \quad C_D = b_0 + b_1 \hat{\alpha} + b_2 \hat{\alpha}^2$$

where $\hat{\alpha} = 180\alpha/\pi$. The reentry initial conditions for spacecraft are given as follows:

$$h(0) = 79.248 \text{ km}, \quad \phi(0) = 0^\circ, \quad \theta(0) = 0^\circ$$

$$v(0) = 28090.368 \text{ km/h}, \quad \gamma(0) = -1^\circ, \quad \psi(0) = 90^\circ \tag{9}$$

The time T of spacecraft reaching interface of terminal area energy management is unknown [9]. The terminal conditions of reentry trajectory are

$$h(T) = 24.384 \text{ km}, \quad v(T) = 2743.2 \text{ km/h}, \quad \gamma(T) = -5^\circ \tag{10}$$

The objective of optimization problem is to maximize the cross range, which is equivalent to maximizing the latitude $\theta(T)$.

The heat transfer rate applied to the spacecraft is defined as $q = q_a \cdot q_r$, where

$$q_a = c_0 + c_1 \hat{\alpha} + c_2 \hat{\alpha}^2 + c_3 \hat{\alpha}^3 \tag{11}$$

$$q_r = 1927451509.31354 \sqrt{\rho} \cdot (v/10000)^{3.07} \tag{12}$$

The constant parameters in above formulas and basic data of spacecraft are listed in Table 1.

Since the end time T is unknown and not included in terminal constraints, using time t as the independent variable of equations will cause troubles. During real reentry phase, velocity always decreases monotonically and determines the kinetic energy of spacecraft. In addition, velocity is one of the terminal conditions.

Velocity v is used in this paper instead of time t . It shall be noted that there is no relationship between longitude and other states, then equations of motion with velocity v as independent variable will become

$$\dot{h} = v \sin \gamma / \left(-\frac{D}{m} - g \sin \gamma \right) \quad (13)$$

$$\dot{\gamma} = \left[\frac{L \cos \beta}{mv} + \cos \gamma \left(\frac{v}{R_e + h} - \frac{g}{v} \right) \right] / \left(-\frac{D}{m} - g \sin \gamma \right) \quad (14)$$

$$\dot{\theta} = \frac{v}{R_e + h} \cos \gamma \cos \psi / \left(-\frac{D}{m} - g \sin \gamma \right) \quad (15)$$

$$\dot{\psi} = \left(\frac{L \sin \beta}{mv \cos \gamma} + \frac{v}{R_e + h} \cos \gamma \sin \psi \sin \theta \right) / \left(-\frac{D}{m} - g \sin \gamma \right) \quad (16)$$

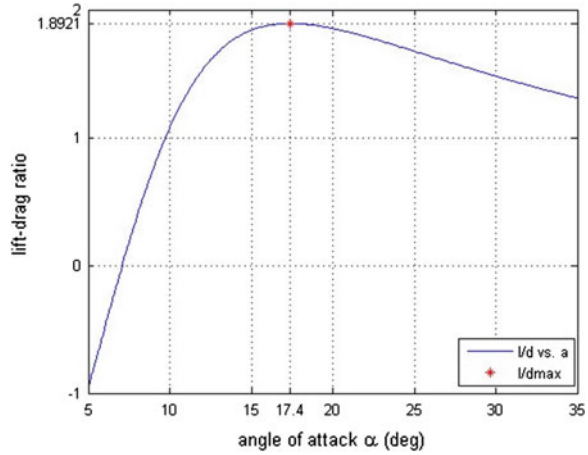
3 Parallel Genetic Algorithm

Genetic Algorithm (GA) is one population-based optimization method. It mimics survival of the fittest rule in nature and this concept is used to perform optimization-like tasks. In general, the following steps will be employed in GA:

1. Initialization: Randomly create population.
2. Evaluation: Evaluate the fitness of each individual in population. If the terminal condition is satisfied, GA will stop, otherwise, it will step in.
3. Selection: Select high fitness individuals.
4. Crossover: Pick up pairs of selected individuals to generate new population by crossover method.
5. Mutation: Select some individuals and change their genes. And then turn to Step 2.

Multi-core CPU is very popular nowadays. Multi-core CPU can be given full play in parallel computation. GA is very proper for parallel computation at different levels. Basic parallelization operation, like parallel fitness evaluation, can accelerate the optimization program. Parallelization calculation of multipopulation can increase the probability of best solution for each process of computing. For one population in one process, if the probability of obtaining the unsatisfied solution is p and $p < 1$, then repeat the process n times independently, the probability of obtaining the satisfied solution will be $1 - p^n$. Parallelization calculation of multipopulation is used in this paper. Randomly generate 2 initial populations and repeat the process 8 times independently for each population.

Fig. 1 Lift to drag ratio versus angle of attack



3.1 Control Inputs

The control inputs $\alpha(v)$ and $\beta(v)$ might have two forms in order that PGA method is used to solve the problem addressed in Sect. 2. One is so-called collocation method, in which control inputs are discrete on velocity nodes. It might lead to the control inputs unsmooth. Inputs even can reach the bottom edge at one node but top edge at next node. This is not applicable for the practical control. The other is function-based assumption method, in which control inputs are the function of velocity. The latter one will be used in this paper and it is necessary to find the relationship between control inputs and velocity.

Function (8) can be rewritten as

$$\frac{L}{D} = \frac{a_0 + a_1 \hat{\alpha}}{b_0 + b_1 \hat{\alpha} + b_2 \hat{\alpha}^2} \tag{17}$$

It is shown that lift to drag ratio is the function of angle of attack. The spacecraft under the flight condition with maximum lift to drag ratio can reach the approximate maximum cross range based on previous experience. In Fig. 1, it is shown that the maximum lift to drag ratio is 1.8921 with the angle of attack at 17.4°. So it is assumed that the angle of attack $\alpha(v)$ is constant and around 17.4° during reentry.

$$\alpha(v) = x_1 \tag{18}$$

Then one sine function is added to meet the upwards and downwards fluctuation.

$$\alpha(v) = x_1 + x_2 \sin(x_3 v + x_4) \tag{19}$$

From [10], the bank angle $\beta(v)$ is about 75° at the initial point of reentry and becomes to about 0° at terminal point. And the velocity v is 28090.368 and

2743.2 km/h at initial point and the terminal point, respectively. Let us assume $\beta(v)$ is a linear function

$$\beta(v) = y_1v + y_2 \quad (20)$$

Similarly, add one sine function to meet the fluctuation.

$$\beta(v) = y_1v + y_2 + y_3 \sin(y_4v + y_5) \quad (21)$$

3.2 Fitness Function

The objective of optimization problem formed is to maximize the latitude $\theta(T)$. One penalty function is applied to meet the terminal constraints $h(T)$ and $\gamma(T)$, so the object function is written as

$$O = -\theta(T) + r_1|h(T) - 24.384| + r_2|\gamma(T) - (-5)| \quad (22)$$

Then the fitness function is

$$F = 500 - O \quad (23)$$

Obviously, the optimization result will be influenced by regulating parameter r_1 and r_2 . If $r_1 = r_2 = 0$, the terminal constraints are ignored. If $r_1 = r_2 \rightarrow \infty$, the terminal constraints must be satisfied. Base on current experience, terminal latitude $\theta(T)$ is around 30° . In this paper, the selecting principle of parameter r_1 and r_2 is that if the deviation of terminal altitude or terminal flight-path angle increases 10 %, the terminal latitude should increase more than 10 %. Herein select $r_1 = 3/2.4384$ and $r_2 = 3/0.5$.

4 Results

The optimization process has been performed on the PC with Intel Core i5-2400 (4 cores) @ 3.1 GHz, and 4.0 GB memory (3.17 GB available). The population size is 40 and number of generations is 200. The results are presented in Fig. 2 and listed in Table 2 for comparison.

From Fig. 2a, we can find that the angle of attack is within the range of around 16.95 to 17.50° and close to 17.4° at which the lift-drag ratio is maximum as stated in Sect. 3. The bank angle in Fig. 2b is very close to that in Ref. [10]. And in Fig. 2d, velocity is decreasing monotonically, which shows that the assumption of velocity in Sect. 2 is reasonable. The flight-path angle in Fig. 2e is around 0° at the

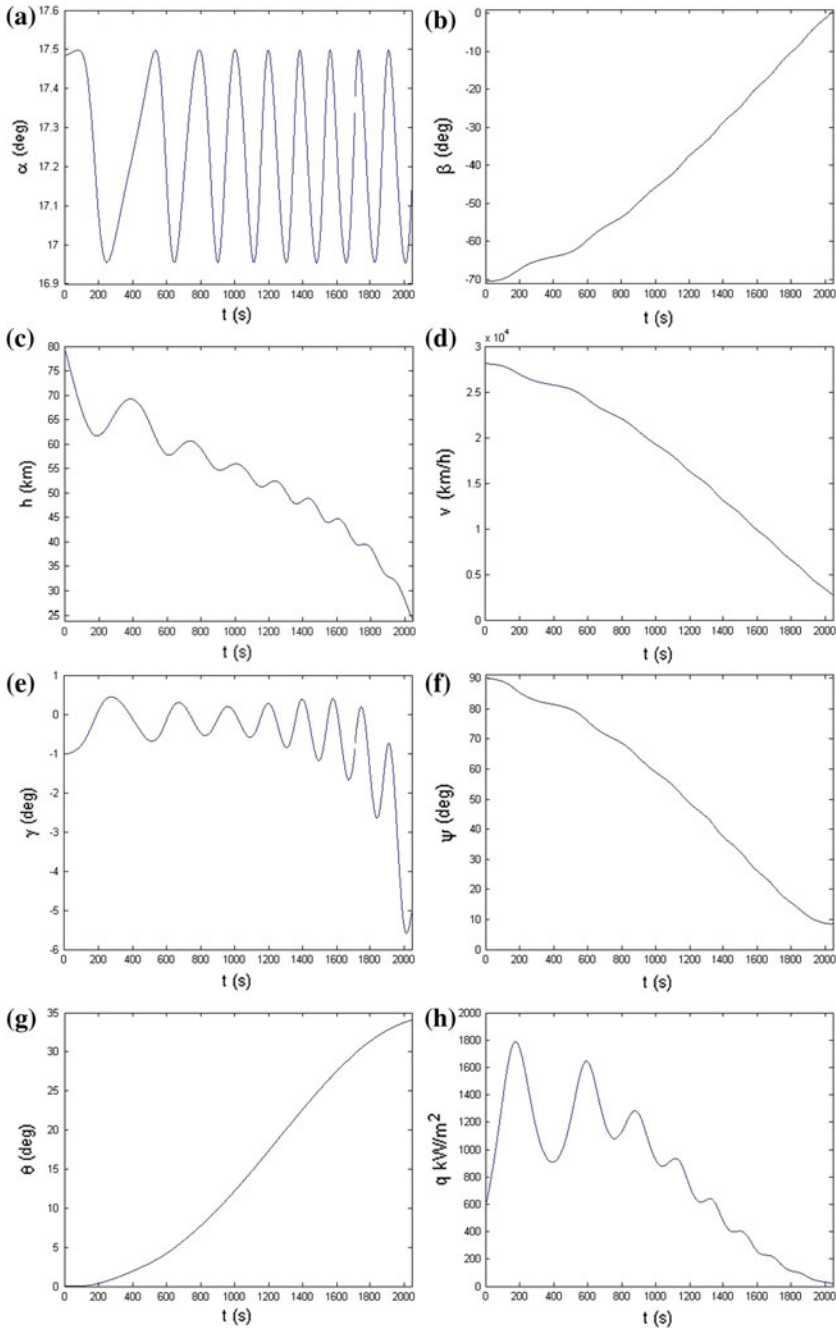


Fig. 2 Results of PGA for reentry trajectory optimization. **a** Angle of attack versus time. **b** Bank angle versus time. **c** Altitude versus time. **d** Velocity versus time. **e** Flight-path versus time. **f** Azimuth versus time. **g** Latitude versus time. **h** Heating versus time

Table 2 Comparison of optimization result

| Parameter | PGA | Ref. [12] PSO | Ref. [10] Indirect Method |
|--------------------------------|--------|---------------|---------------------------|
| Run times, s | 500 | 186 | 46.2 |
| θ , deg | 34.07 | 34.1 | 34.14 |
| h , km | 24.365 | 24.487 | 24.384 |
| v , km/h | 2743.2 | 2739.0 | 2743.2 |
| γ , deg | -5.067 | -5.5 | -5.0 |
| q_{\max} , kW/m ² | 1786.3 | 1974.12 | 1910.2 |

beginning, which means the spacecraft is under the so-called Quasi-equilibrium glide stage [11]. We can also find that the flight-path angle returns to -5° , which means the penalty function is effective and the terminal constraint is satisfied.

Table 2 shows that all terminal conditions are satisfied with an error of less than 1.5 % for all parameters. The flight-path angle is much closer to -5° while comparing with [12]. The maximum heating is lower than that in [10, 12], which is a beneficial factor for spacecraft. Although the computation is slower, less repeating times can be considered. GPU can be used for parallel computation to get more advantage than that by CPU. So if the program is executing by GPU, the cost will be further reduced.

5 Conclusions

This paper demonstrates that PGA is an efficient and accurate method to optimize the reentry trajectory. Substituting variable time with velocity is a better way to solve the constraints problem with free terminal time. Near-optimal results can be obtained by this proposed approach in this paper without solving two-point boundary value problem derived from Hamiltonian function.

References

1. Harpold JD, Graves CA (1979) Shuttle entry guidance. *J Astronaut Sci* 27(3):239–268
2. Zhou WY, Wang YS, Sun XM et al (2010) Optimal reentry trajectory for CAV using Gauss pseudospectral method. In: *The 2nd international conference on engineering computation*, Beijing
3. Pontani M, Conway BA (2010) Particle swarm optimization applied to space trajectories. *J Guid Control Dyn* 33(5):1429–1441
4. Premalatha K, Natarajan AM (2009) Hybrid PSO and GA for Global Maximization. *Int J Open Probl Comput Sci Math* 2(4):597–608
5. Holland JH (1992) *Adaptation in natural and artificial systems: an introductory analysis with applications to biology, control, and artificial intelligence*, 2nd edn. MIT Press, Cambridge
6. Ma YJ, Yun WX (2012) Advances in research on genetic algorithm. *Appl Res Comput* 29(4):1201–1206

7. Jin P, Song BF, Zhong XP (2011) Structure optimization of large composite Wing Box with parallel genetic algorithm. *J Aircr* 48(6):2145–2148
8. Jones B, Crossley W, Lyrantzis A (1998) Aerodynamic and aeroacoustic optimization of airfoils via a parallel genetic algorithm. In: 7th AIAA/USAF/NASA/ISSMO symposium on multidisciplinary analysis and optimization
9. Betts JT (2001) Practical methods for optimal control using nonlinear programming. Society for Industrial and Applied Mathematics, Philadelphia
10. Graichen K, Petit N (2008) Constructive methods for initialization and handling mixed state-input constraints in optimal control. *J Guid Control Dyn* 31(5):1334–1343
11. Shen ZJ, Lu P (2003) Onboard generation of three-dimensional constrained entry trajectories. *J Guid Control Dyn* 26(1):111–121
12. Rahimi A, Kumar KD, Alighanbari H (2012) Particle swarm optimization applied to spacecraft reentry trajectory. *J Guid Control Dyn* 36(1):307–310

Predicting the Heating Value of Rice Husk with Neural Network

Wan Yu and Congping Chen

Abstract Higher heating value (HHV) is an important property defining the energy content and thereby efficiency of fuels. In this paper, the correlation between the proximate analysis/ultimate analysis of some rice husk and HHV was discussed. It was found that the correlation between HHV and proximate, ultimate analysis was nonlinear. Therefore, two models were developed with artificial neural networks to predict HHV of rice husk by its proximate and ultimate analysis. A total of 25 samples of rice husk selected from the literature and experiments were used as the training data to build and train the two nets. Then, several samples selected randomly were used as predicting samples to check the accuracy of the two nets, respectively. A higher precision of 1.8 % relative error in the prediction results was obtained through this method, while the relative error of linear empirical equations given in the literature was more than 12.7 %. By this method, HHV can be estimated directly from the proximate analysis and ultimate analysis of rice husk when the HHV measurement equipment was not available.

Keywords Neural network · Higher heating value · Proximate analysis · Ultimate analysis

1 Introduction

Rice husk is an important biomass fuel. The higher heating value (HHV) is an important standard to evaluate the quality of fuel, and is the basis to calculate the heat balance, heat efficiency, and coal consumption rate [1]. There are complex relationships between HHV and its chemical components. The chemical

W. Yu (✉) · C. Chen
College of Mechanical and Material Engineering, China Three Gorges University,
Yichang 443002, Hubei, China
e-mail: yuwan110@126.com

compositions of rice husk are characterized as coal in terms of proximate and ultimate analysis. The proximate analysis typically involved determination of volatile matter (V), moisture (M), ash (A), and fixed carbon (FC) contents, whereas the ultimate analysis included an assessment of the levels of carbon (C), hydrogen (H), oxygen (O), nitrogen (N), and sulfur (S) contents.

The HHV of rice husk was measured experimentally using a bomb calorimeter. However, this method required exact instruments and relevant experimental technique, and had the disadvantages of easily influenced by environmental conditions, complicated measure method, and high measure cost [2]. So it was not suitable for power plants. There also existed another method to estimate the heating value by linear empirical equations based on proximate and ultimate analysis. But the estimation results were usually far away from the actual data.

Artificial neural network (ANN), as a new mathematic method, has been widely used in research areas of industry process. In this paper, back-propagation neural network (BPNN), a method of neural network in mathematic software package MATLAB, was used to predict HHV of rice husk based on the proximate and ultimate analysis.

2 Experimental Data

The proximate and ultimate analysis data and HHV of 25 rice husk samples were used for this research. Seven rice husk samples from different areas in China were collected and tested by the researcher, and 18 other rice husk samples were chosen from the literature. All proximate and ultimate analysis data were converted to the “air dried” basis (ad) using the following expression:

$$Q_{ad,gr} = (100 - M_{ad})(100 - M_{ar})Q_{ar,gr} \quad (1)$$

$$X_{ad} = (100 - M_{ad})(100 - M_{ar})X_{ar} \quad (2)$$

$$V_{ad} = V_{daf}(100 - M_{ar} - A_{ar})(100 - M_{ad})/(100 - M_{ar})/100 \quad (3)$$

where Q_{gr} is the HHV, and X can denote the moisture, ash, fixed carbon, carbon, hydrogen, oxygen, nitrogen, and sulfur content. The final data of rice husk are shown in Table 1.

The correlations between the HHV of rice husk and its proximate/ultimate analysis data were investigated using plots shown in Fig. 1. For proximate analysis, the HHV showed a poor linear correlation to the moisture content and fixed carbon content. For ultimate analysis, the five contents all showed poor linear correlations to the HHV. It can be concluded that correlation between HHV and proximate/ultimate analysis was not linear. The linear empirical equations based on proximate and ultimate analysis and linear regression method were not suitable to predict the HHV of rice husk. Therefore, a BPNN method was discussed in this paper.

Table 1 Characteristics of rice husk

| No | Proximate analysis (%) | | | | Ultimate analysis (%) | | | | LHV (kJ/kg) | References | | | |
|----|------------------------|-----------------|-----------------|------------------|-----------------------|-----------------|-----------------|-----------------|-------------|------------|-----------------|-----------------|-----------------|
| | A _{ad} | | V _{ad} | | C _{ad} | | H _{ad} | | | | O _{ad} | N _{ad} | S _{ad} |
| | M _{ad} | A _{ad} | V _{ad} | FC _{ad} | C _{ad} | H _{ad} | O _{ad} | N _{ad} | | | | | |
| 1 | 10.47 | 12.69 | 60.11 | 16.73 | 36.99 | 5.46 | 33.97 | 0.32 | 0.10 | 14,210 | | | |
| 2 | 8.77 | 12.29 | 62.39 | 16.55 | 36.53 | 5.35 | 36.35 | 0.60 | 0.11 | 13,560 | | | |
| 3 | 9.66 | 14.29 | 60.03 | 16.02 | 41.35 | 5.67 | 28.09 | 0.85 | 0.09 | 12,920 | | | |
| 4 | 9.50 | 11.24 | 65.21 | 14.05 | 44.21 | 5.17 | 29.04 | 0.74 | 0.10 | 15,431 | | | |
| 5 | 9.88 | 15.17 | 61.76 | 13.19 | 40.12 | 4.35 | 29.74 | 0.67 | 0.07 | 14,720 | | | |
| 6 | 10.05 | 16.04 | 60.82 | 13.09 | 36.68 | 5.38 | 31.03 | 0.73 | 0.09 | 11,250 | | | |
| 7 | 12.45 | 8.68 | 62.56 | 16.31 | 37.16 | 5.08 | 35.92 | 0.63 | 0.08 | 16,349 | | | |
| 8 | 12.30 | 12.26 | 60.98 | 14.46 | 40.00 | 5.03 | 29.75 | 0.53 | 0.13 | 14,544 | [3] | | |
| 9 | 2.69 | 7.25 | 72.46 | 17.89 | 43.76 | 7.45 | 36.45 | 2.40 | 0.00 | 16,747 | [4] | | |
| 10 | 10.00 | 13.35 | 61.43 | 15.23 | 30.26 | 4.38 | 41.48 | 0.51 | 0.02 | 15,606 | [5] | | |
| 11 | 7.46 | 16.31 | 61.69 | 14.54 | 35.10 | 3.87 | 36.77 | 0.48 | 0.00 | 18,120 | [6] | | |
| 12 | 7.30 | 15.70 | 57.40 | 19.60 | 42.80 | 4.48 | 29.33 | 0.37 | 0.02 | 16,791 | [7] | | |
| 13 | 4.64 | 17.48 | 63.64 | 14.21 | 37.99 | 4.64 | 34.66 | 0.49 | 0.07 | 14,843 | [8] | | |
| 14 | 10.58 | 13.23 | 59.95 | 16.24 | 34.29 | 4.44 | 36.63 | 0.71 | 0.11 | 14,273 | [9] | | |
| 15 | 10.30 | 14.00 | 55.60 | 20.10 | 38.00 | 4.55 | 32.40 | 0.69 | 0.06 | 14,980 | [10] | | |
| 16 | 10.00 | 16.38 | 60.84 | 12.78 | 38.34 | 4.59 | 30.10 | 0.46 | 0.02 | 13,654 | [11] | | |
| 17 | 6.00 | 16.92 | 51.98 | 25.10 | 37.60 | 4.89 | 32.61 | 1.89 | 0.09 | 13,400 | [12] | | |
| 18 | 10.30 | 14.00 | 55.60 | 20.10 | 38.00 | 4.55 | 32.40 | 0.69 | 0.06 | 14,980 | [13] | | |
| 19 | 10.10 | 14.70 | 64.10 | 11.10 | 33.98 | 4.50 | 36.23 | 0.54 | 0.00 | 13,300 | [14] | | |
| 20 | 10.00 | 18.00 | 59.76 | 12.24 | 33.84 | 4.88 | 32.90 | 0.34 | 0.03 | 13,803 | [11] | | |
| 21 | 10.00 | 16.92 | 60.57 | 12.51 | 37.89 | 4.48 | 30.29 | 0.36 | 0.02 | 12,839 | [11] | | |
| 22 | 10.00 | 22.14 | 56.70 | 11.16 | 34.83 | 4.23 | 28.23 | 0.45 | 0.01 | 12,931 | [11] | | |
| 23 | 11.00 | 12.99 | 58.00 | 18.01 | 34.20 | 4.86 | 36.60 | 0.32 | 0.04 | 13,594 | [15] | | |
| 24 | 10.00 | 18.00 | 59.76 | 12.24 | 33.84 | 4.88 | 32.90 | 0.34 | 0.03 | 13,803 | [16] | | |
| 25 | 10.00 | 11.52 | 66.60 | 11.88 | 38.07 | 5.49 | 33.75 | 0.99 | 0.04 | 14,670 | [17] | | |

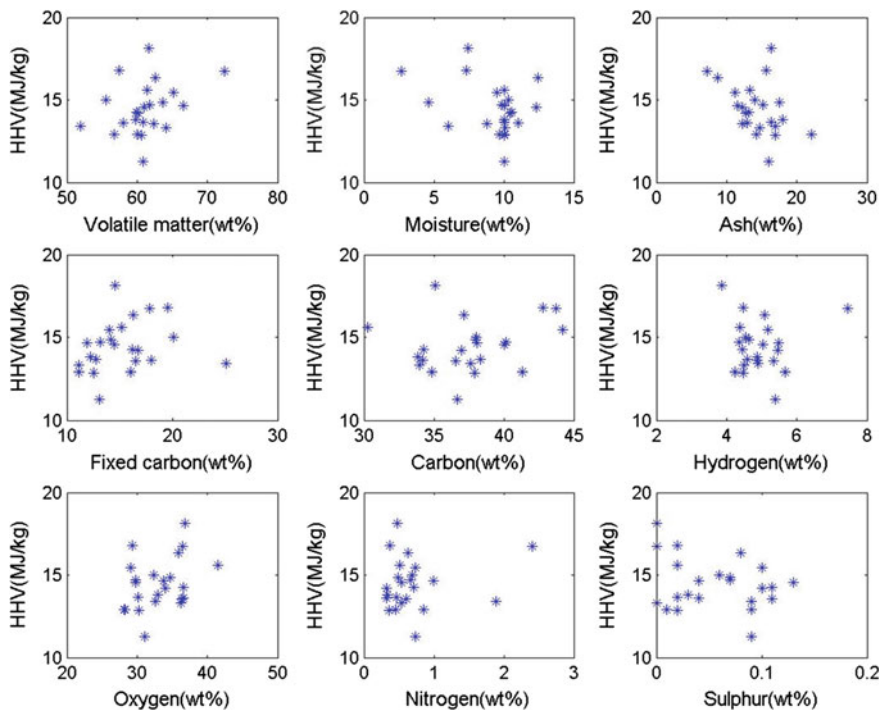


Fig. 1 Correlations between HHV of rice husk and its proximate and ultimate analysis

3 Prediction of HHV with BPNN

ANN is an empirical modeling tool analogous to the behavior of biological neural structures. ANN is a powerful tool with the ability to identify underlying highly complex relationships from input–output data only. One of the major advantages of neural network is efficient handling of highly nonlinear relationships in data, even when the exact nature of such relationship is unknown. It is considered as a nonlinear statistical identification technique.

In this paper, BPNN, a method of neural network in mathematic software package MATLAB, is used to predict the HHV of rice husk based on proximate and ultimate analysis. The architecture of BPNN is shown in Fig. 2.

This network usually consists of three layers described as input, hidden, and output layers, and I, J, K, L determines the node numbers of the input, first hidden, second hidden, and output layers, respectively. The number of nodes in the hidden layer measures the nonlinear degree between the input and output, but there was no uniform criterion of selection in theory. The number of hidden layers and the optimal number of nodes can be obtained through comparing training results of every BPNN model. Each interconnection had a scalar weight (W_{ij}) associated

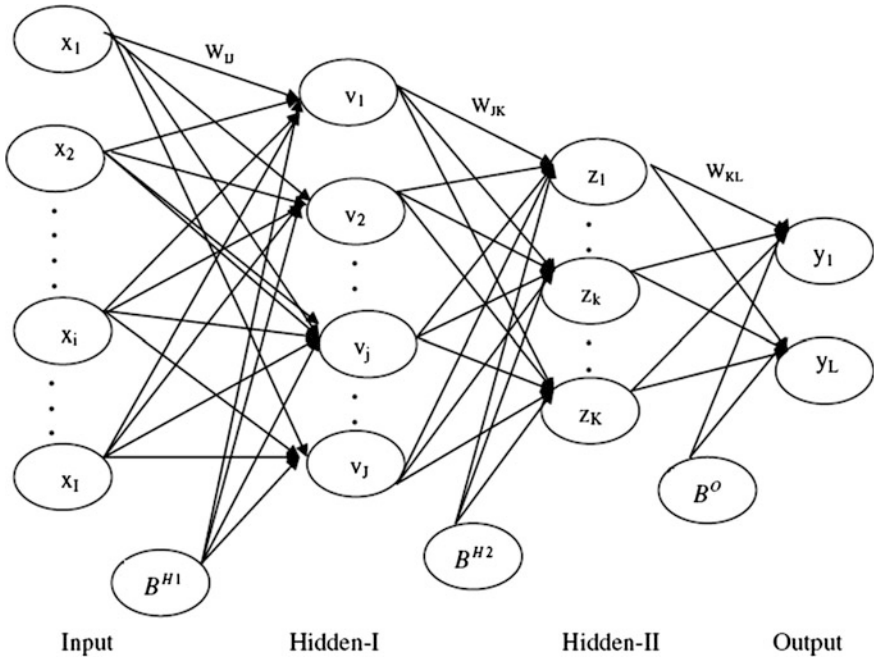


Fig. 2 BPNN architecture with two hidden layers

with it, which modified the strength of the signal. In addition, a bias can also be used, which was another neural parameter that was summed with the neuron’s weighted inputs.

In this paper, two models were built based on proximate and ultimate analysis, respectively. Model 1 was based on proximate analysis (*V, M, A, and FC* contents), which was made of four nodes in the input layer. Model 2 was based on the ultimate analysis (*C, H, O, N, and S* contents), which was made of five nodes in the input layer. The HHV was the only required output and so one node was used in the output layer both in models 1 and 2. The proximate and ultimate analysis of the 6th–25th samples listed in Table 1 was used to build and train the net models, respectively. Then the first to fifth samples listed in Table 1 were used to check the predicting precision of the two models.

The performance of the two BPNN models was valued by error analysis. The widely utilized error function was known as “root mean squared error” (RMSE), which was calculated as:

$$RMSE = \sqrt{\sum_{i=1}^N (HHV_p^i - HHV^i)^2 / N}$$

where N denotes the number of patterns in the data set; i denotes the pattern index; HHV and HHV_p respectively represent the experimental and BPNN-predicted outputs. Otherwise, the relative error is defined as:

$$\text{relative error} = |(\text{LHV}_c - \text{LHV})/\text{LHV}| \times 100\%$$

4 Results and Discussion

The tan-sigmoid transfer function (tansig) was used in the hidden layers, and the linear transfer function (purelin) was used in the output layer. Through a series tests using different initial number of layers and nodes, a 4-6-3-1 BPNN based on proximate analysis and a 5-7-4-1 BPNN based on ultimate analysis gave the best results for models 1 and 2, respectively. Figures 3 and 4 illustrate the training results of HHV by two models, respectively.

It was found that there was small difference between the training results of models 1 and 2. Because proximate analysis and ultimate analysis can both describe the fuel characteristics of rice husk, it had the same effect on HHV.

Then the two models were used to predict HHV of the other five samples with their proximate analysis and ultimate analysis data. Some linear empirical equations for calculating the HHV of biomass fuel were collected as follows [18]:

$$\text{HHV} = -1.3675 + 0.3137C + 0.7009H + 0.0318O \quad (4)$$

$$\text{HHV} = 0.312FC + 0.1534V \quad (5)$$

The HHV were calculated by these equations with the data in Table 1. The comparison of calculated HHV by equations and predicted HHV by BPNN models are shown in Fig. 5.

The performance of the BPNN models and linear empirical equations were evaluated by RMSE, relative error. It was found that, compared with linear empirical equations, the BPNN method showed high precision in predicting HHV of rice husk. The maximum relative error of linear empirical equations can be up to 28.6 %, but only 2.8 % of BPNN. The average relative error of linear empirical equations can be up to 12.7 %, but only 1.8 % of BPNN. BPNN model 2, which used ultimate analysis of carbon, hydrogen, oxygen, nitrogen, and sulfur contents as model inputs, had a higher precision in predicting HHV of rice husk than BPNN model 1, which used proximate analysis of volatile matter, moisture, ash, and fixed carbon contents as model inputs. The reason may be that, fuel consisted of organic and inorganic matters and the proximate analysis was a chemical index of fuel assuming a uniform material, while ultimate analysis gave specific chemical compositions.

Fig. 3 Training results of model 1

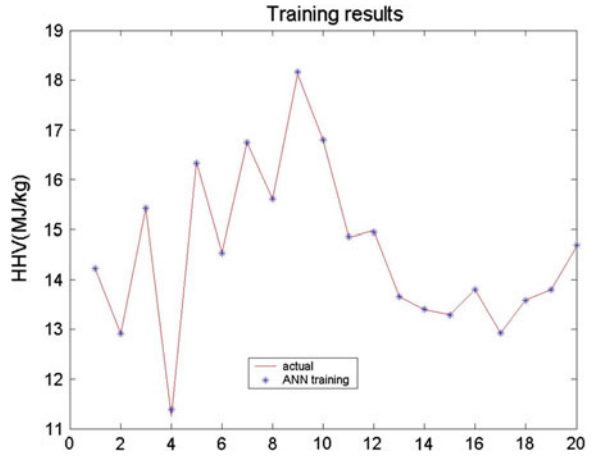


Fig. 4 Training results of model 2

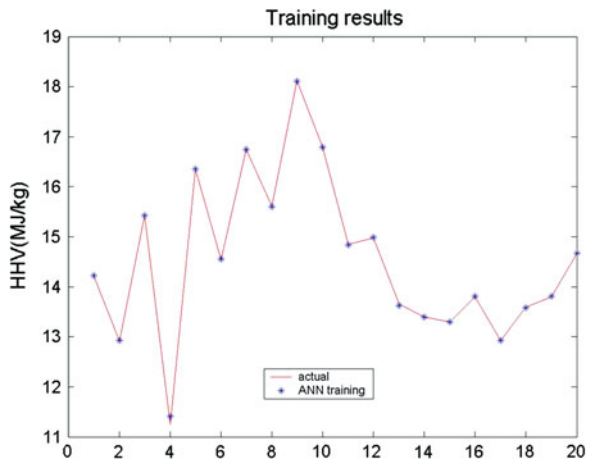
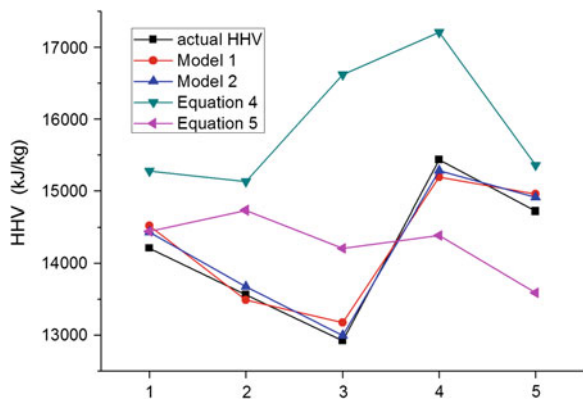


Fig. 5 Prediction results of HHV



So, using the BPNN method to predict the HHV based on proximate and ultimate analysis was a good way with reasonable accuracy, which was better than calculating HHV with linear empirical equations. If there were more samples used as training samples of BPNN model, a more predicting precision could be obtained.

5 Conclusions

HHV showed poor linear correlation to proximate/ultimate analysis of rice husk. It can be concluded that there were strong nonlinear correlations between HHV and proximate/ultimate analysis. Compared with linear empirical equations, the BPNN method showed high precision in predicting HHV of rice husk. A higher precision of 1.8 % relative error was obtained through BPNN method, while the relative error of linear empirical equations was more than 12.7 %. So the BPNN method is a reasonable way to predict HHV based on proximate and ultimate analysis of rice husk.

Acknowledgments This project was supported by Science Foundation of China Three Gorges University: NO 0620120013, Research on drying and combustion mechanism of municipal sewage sludge.

References

1. Shuangyin T, Deli Y, Zhigen Z (2000) Implications and their relation of different coal's calorific values. Report Stand 21(4):15–16
2. Jun H, Baoshan Z, Daishe W, He B (2006) Identifying and appraising of coal calorific experimental formula. Coal Convers 29(1):1–5
3. Guo X, Wang S, Wang Q, Guo Z, Luo Z (2011) Properties of bio-oil from fast pyrolysis of rice husk. Chin J Chem Eng 19(1):116–121
4. Zhou L, Yang H, Wu H, Wang M, Cheng D (2013) Catalytic pyrolysis of rice husk by mixing with zinc oxide: characterization of bio-oil and its rheological behavior. Fuel Process Technol 106:385–391
5. Abu Bakar MS, Titiloye JO (2013) Catalytic pyrolysis of rice husk for bio-oil production. J Anal Appl Pyrol 103:362–368
6. Li R, Zhong ZP, Jin BS, Zheng AJ (2012) Application of mineral bed materials during fast pyrolysis of rice husk to improve water-soluble organics production. Bioresour Technol 119:324–330
7. Janvijitsakul K, Kuprianov VI (2008) Major gaseous and PAH emissions from a fluidized-bed combustor firing rice husk with high combustion efficiency. Fuel Process Technol 89(8):777–787
8. Sun S, Zhao Y, Ling F, Su F (2009) Experimental research on air staged cyclone gasification of rice husk. Fuel Process Technol 90(4):465–471
9. Duan F, Chyang C, Chin Y, Tso J (2013) Pollutant emission characteristics of rice husk combustion in a vortexing fluidized bed incinerator. J Environ Sci 25(2):335–339
10. Madhiyanon T, Sathitruangsak P, Soponronnarit S (2009) Co-combustion of rice husk with coal in a cyclonic fluidized-bed combustor (ψ -FBC). Fuel 88(1):132–138

11. Mansaray KG, Ghaly AE (1999) Determination of kinetic parameters of rice husks in oxygen using thermogravimetric analysis. *Biomass Bioenergy* 17(1):19–31
12. Fang M, Yang L, Chen G, Shi Z, Luo Z, Cen K (2004) Experimental study on rice husk combustion in a circulating fluidized bed. *Fuel Process Technol* 85(11):1273–1282
13. Madhiyanon T, Sathitruangsak P, Soponronnarit S (2011) Influences of coal size and coal-feeding location in co-firing with rice husks on performance of a short-combustion-chamber fluidized-bed combustor (SFBC). *Fuel Process Technol* 92(3):462–470
14. Rozainee M, Ngo SP, Salema AA, Tan KG (2010) Computational fluid dynamics modeling of rice husk combustion in a fluidised bed combustor. *Powder Technol* 203(2):331–347
15. Kuprianov VI, Janvijitsakul K, Permchart W (2006) Co-firing of sugar cane bagasse with rice husk in a conical fluidized-bed combustor. *Fuel* 85(4):434–442
16. Mansaray KG, Ghaly AE, Al-Taweel AM, Hamdullahpur F, Ugursal VI (1999) Air gasification of rice husk in a dual distributor type fluidized bed gasifier. *Biomass Bioenergy* 17(4):315–332
17. Armesto L, Bahillo A, Veijonen K, Cabanillas A, Otero J (2002) Combustion behaviour of rice husk in a bubbling fluidised bed. *Biomass Bioenergy* 23(3):171–179
18. Sheng C, Azevedo JLT (2005) Estimating the higher heating value of biomass fuels from basic analysis data *Biomass and Bioenergy* 28(5):499–507

Research on UAV Collision Avoidance Strategy Considering Threat Levels

Bin Fang and Tefang Chen

Abstract This paper classifies the threat levels and studies the methods of UAV collision avoidance considering the threat levels, establishes the collision avoidance control strategy using UAV heading angle control, speed control, and the combinations of the two above strategies, and establishes a multi-objective cost function model and a multi-objective optimal decision method. Carrying out simulation experiments, we analyze the effect of UAV collision avoidance strategy through heading angle and speed changing.

Keywords Collision avoidance · Threat levels · Cost function · Heading angle control · Speed control

1 Introduction

With a large number of Unmanned Air Vehicles (UAVs) put into use in military and civilian areas, UAV safety problems such as obstacle avoidance [1, 2], collision avoidance, etc. [3, 4], are getting more and more attention. UAV collision and other accidents not only cause economic loss but may even seriously affect the overall task, so having a valid collision avoidance strategy is the key to improve the success rate of the mission.

Many researchers have made a thorough study of UAV collision avoidance and propose many methods. McLain [5] uses collaborative planning approach to solve

B. Fang (✉) · T. Chen

School of Traffic and Transportation Engineering, Central South University,
Changsha, China
e-mail: aifudi@163.com

T. Chen

School of Information Science and Engineering, Central South University, Changsha, China

the multi-UAV crash problem, Bilimoria et al. [6] use geometric optimal method, amend the UAV's speed and position with the dynamic obstacles used as the origin of coordinate. Collision conflict happens when the velocity vectors of the threat intersect with the protection circles of UAV; they propose a method to change the direction of the angular velocity and tangent to the safety circle of the UAV to achieve collision avoidance. Zu et al. [7], Zhang and Tan [8] establish the relative coordinate system, using the relative velocity for collision avoidance planning in the acceleration space. Li et al. [9, 10] propose a UAV dynamic collision avoidance algorithms in a three-dimensional space based on optimization theory.

In this paper, we classify the levels of dynamic threat referencing the analysis and summary of the above methods and propose the strategies of multi-object optimization collision avoidance with consideration of the constraints, conditions such as time cost, collision matrix, etc. The combinations of the angle change and speed change are used to achieve effective and fast collision avoidance of UAVs.

2 Modeling of UAV Collision Problem

2.1 Safety Circle and Relative Coordinates

Let UAV has a safety circle with safe radius R , the collision conflict happens when the relative trajectory between dynamic obstacle and UAV intersects with the safety circle of UAV. Airborne radars with detection radius R_r scan the surrounding environment periodically, can get the position coordinate of dynamic obstacle relative to the UAV, and carry on the conflict detection, as shown in Fig. 1.

Set 'xoy' as the absolute coordinate system, 'x'o'y' is the relative coordinate system in which the origin point is the position of UAV. The coordinates of obstacle detected by the UAV radar are (x_p, y_p) and (x_{rp}, y_{rp}) relatively in coordinates system 'xoy' and 'x'o'y' [11].

2.2 Levels of Collision Threat

The distance between dynamic obstacle and UAV has great influence on strategies adoption for collision avoidance. For example, when adopting the method of changing the heading angle to handle the UAV collision avoidance problem, the variable in the heading angle $\Delta\varphi$ relies not only on the distance d between UAV and the obstacles, but also on the shortest distance d_τ from the UAV to the obstacle trajectories. The minor value of $\Delta\varphi$ is adopted when the value of d or d_τ is relatively larger, to ensure collision avoidance and to reduce the possibility of deviation from the original route of flight simultaneously.

Fig. 1 Safety circle, detection radius, and coordinate

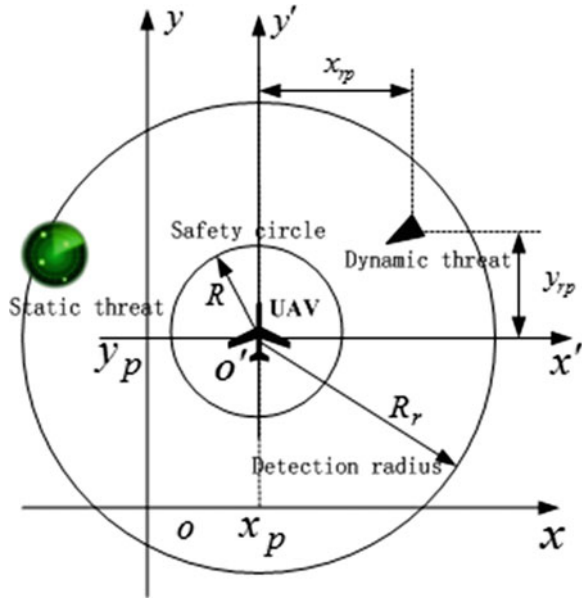


Table 1 Levels of collision threat

| d_τ | d | Levels of collision threat |
|-------------------------------|------------------|----------------------------|
| $d_\tau > R$ | | 0 |
| $\frac{R}{2} < d_\tau \leq R$ | $d > 3R$ | 1 |
| | $2R < d \leq 3R$ | 2 |
| | $d < 2R$ | 3 |
| $d_\tau \leq \frac{R}{2}$ | $d > 3R$ | 2 |
| | $2R < d \leq 3R$ | 3 |
| | $d < 2R$ | 4 |

This paper proposes the levels of collision threat according to the key factors d_τ and d which affect the decisions of collision avoidance and then determine the appropriate amount of control. The levels of collision threat are shown as in Table 1:

3 Autonomous Collision Avoidance Control Strategy

3.1 The Strategy of Heading Angle Control

When there is an intersection between the predicted trajectory of obstacle and UAV security circles, we can handle UAV collision avoidance problems by way of changing the heading angle. The variable of heading angle change $\Delta\varphi$ is

Table 2 Different course angle control strategy under different levels of collision threat

| Levels | $\Delta\varphi$ |
|--------|--|
| 0 | $\Delta\varphi = 0^\circ$ following original route |
| 1 | $\Delta\varphi = 15^\circ$ |
| 2 | $\Delta\varphi = 30^\circ$ |
| 3 | $\Delta\varphi = 45^\circ$ |
| 4 | $\Delta\varphi = 60^\circ$ |

associated with the distance d when the obstacle is detected for the first time and the distance d_τ of the closest distance between the UAV and the obstacle, and may also be viewed as a function $\Delta\varphi = f(d, d_\tau)$ containing two independent variables, $\Delta\varphi$ which must also meet certain constraints taking into account the dynamic constraints of UAV simultaneously:

$$\begin{cases} \Delta\varphi = f(d, d_\tau) \\ \Delta\varphi_{\min} \leq \Delta\varphi \leq \Delta\varphi_{\max} \end{cases} \quad (1)$$

We can adopt different course angle control strategy according to the levels of collision threat; select the minor $\Delta\varphi$ of course angle change when the d is relatively larger, or the d_τ is relatively larger. The specific heading angle control strategy is shown in Table 2.

Set the azimuth of the obstacle located in the relative coordinate system denoted as α , the azimuth of intersection point between the obstacles predicted trajectory and the UAV security circle are denoted as β , the range of β alters from 0° to 360° , the relationship between α and β exists two possibilities:

- (1) If $\beta < \alpha$ (Fig. 2), indicating that the origin of the relative coordinate system is in the right front of the relative trajectory of the obstacle, the result of collision avoidance decision should make the relative trajectory of obstacle turn to the left side.
- (2) If $\beta > \alpha$ (Fig. 3), indicating that the origin of the relative coordinate system is in the left front of the relative trajectory of the obstacle, the result of collision avoidance decision should make the relative trajectory of obstacle turn to the right side.

3.2 The Strategy of Speed Control

When a collision threat is detected, another way of collision avoidance is changing speed. The amount of speed change variable Δv is associated with the distance d when the obstacle is detected for the first time and the distance d_τ of the closest distance between the UAV and the obstacle.

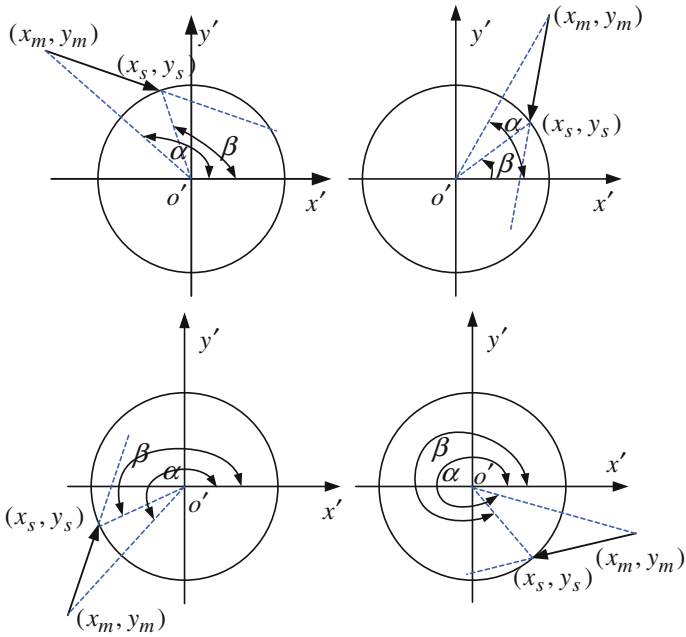


Fig. 2 $\beta < \alpha$ (Four quadrants)

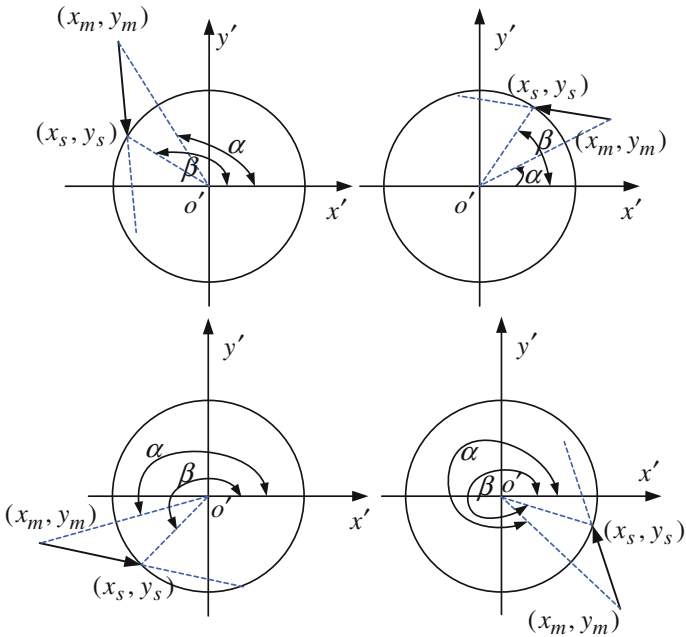


Fig. 3 $\beta > \alpha$ (Four quadrants)

Fig. 4 Time advance map of UAV and obstacles to the intersection point

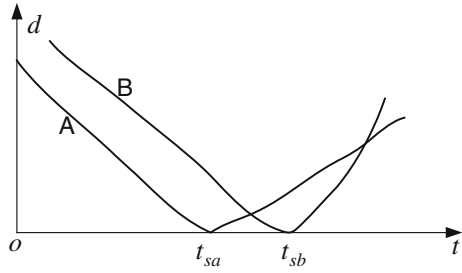


Table 3 Different speed control strategy under different levels of collision threat

| Levels | When UAV falls behind: Δv | When UAV leads ahead: Δv |
|--------|---------------------------------------|---------------------------------------|
| 0 | $\Delta v = v_0$ Follow initial route | $\Delta v = v_0$ Follow initial route |
| 1 | $\Delta v = 0.9v_0$ | $\Delta v = 1.1v_0$ |
| 2 | $\Delta v = 0.7v_0$ | $\Delta v = 1.3v_0$ |
| 3 | $\Delta v = 0.7v_0$ | $\Delta v = 1.3v_0$ |
| 4 | $\Delta v = 0.5v_0$ | $\Delta v = 1.5v_0$ |

$$\begin{cases} \Delta v = g(d, d_\tau) \\ v_{\min} \leq v \leq v_{\max} \end{cases} \quad (2)$$

The most important issue that needs to be considered during the process of speed control is to detect the time at which the UAV and the dynamic obstacle arrive in the intersection point between the UAV and the predicted trajectory of the dynamic obstacle, respectively, and then adjust UAV speed accordingly. Figure 4 shows the time line from the UAV and dynamic obstacles to the intersection point. And, t_{sa} denotes the time consumption from UAV to the intersection point, t_{sb} denotes the time consumption from the dynamic obstacle to the intersection point, $t_{sba} = t_{sb} - t_{sa}$ denotes the time interval of the UAV and dynamic obstacle arrival at the intersection point, respectively. Obviously, the smaller the t_{sba} is, the higher the likelihood of collision will happen, UAV needs to change speed greater; the bigger the t_{sba} is, the smaller the likelihood of collision will happen, UAV needs to change speed less.

The strategy of speed control is presented according to the levels of collision threat, as shown in Table 3, in which v_0 denotes the initial speed of UAV.

3.3 The Combination of Collision Avoidance Strategy

Because of the speed change range limitation, simple change in speed cannot achieve collision avoidance purposes completely; at the same time, a simple change in course angle will cause the collision avoidance time to be too long, so

Table 4 Collection of collision avoidance strategy

| | |
|------------|---|
| ω_i | $\omega_1 =$ Change the heading angle φ to left or right $\omega_2 =$ Slowdown or accelerate speed v $\omega_3 =$ Change the heading angle φ to left and slowdown speed v $\omega_4 =$ Change the heading angle φ to right and slowdown speed v $\omega_5 =$ Change the heading angle φ to left and accelerate speed v $\omega_6 =$ Change the heading angle φ to right and accelerate speed v |
|------------|---|

adopt the combination of the two strategies, namely the strategy of combination of course angle control and speed control.

A collection of collision avoidance strategy is defined, as shown in Table 4.

4 Collision Avoidance Control Strategy Based on Multiobjective Optimization

Collision control strategies not only consider the effect of collision avoidance, but also consider the time required, the complexity of the control strategy, and other factors. Therefore, analyze various factors that affect collision avoidance control strategy, and then construct the objective cost function and get the optimization strategies of collision avoidance.

4.1 Time Cost

In the process of establishing objective cost function, considering the time cost, let UAV_{*i*} denote the *i*th UAV, t_{i0} denote the start time of the collision avoidance, and t_{i1} denote the end time of collision avoidance and return to the initial route, so the time used for total process is:

$$\Delta t_i = t_{i1} - t_{i0} \tag{3}$$

4.2 Conflict Matrix

Assuming there are *n* UAVs, define a collision matrix $A = \{a_{ij}\}$ between UAV_{*i*} and other UAVs as:

$$a_{ij} = \begin{cases} 1, & \text{if UAV}_i \text{ interact with UAV}_j \\ 0, & \text{if UAV}_i \text{ not interact with UAV}_j \end{cases} \tag{4}$$

At the initial stage, all elements of the conflict matrix R are zero during the flight if the UAV_{*i*} detects potential threats such as UAV_{*j*} may be entering its safety circle, then the corresponding element in the conflict matrix is updated to 1, and needs to take appropriate collision avoidance strategy. There exists a possibility of a collision between UAV_{*i*} and other UAVs after collision avoidance strategy is taken, if a potential collision exists the corresponding element in the matrix is updated to 1. The sum of total UAVs which may have potential conflict with UAV_{*i*} as below:

$$J_A = \sum_{i=1}^n a_{ij} \quad (5)$$

4.3 Effect of Collision Avoidance

If UAV_{*i*} detects a threat source j , and its predicted trajectory has an intersection with the safety circle, the effect of collision avoidance is represented by the distance d_{ij} between UAV_{*i*} and threat source j , R is the radius of the safety circle:

$$\begin{cases} d_{ij} \geq R, \text{ UAV}_i \text{ don't have intersection with } j \\ d_{ij} < R, \text{ UAV}_i \text{ may have intersection with } j \end{cases} \quad (6)$$

4.4 The Complexity of Collision Avoidance Strategy

Assuming the complexity of changing course is the same as changing the speed, the combination control strategy of changing course and changing speed is two times that of a single strategy:

$$\begin{cases} c_{l_simple} = C \\ c_{l_complex} = 2C \end{cases} \quad (7)$$

C is a constant of operational complexity.

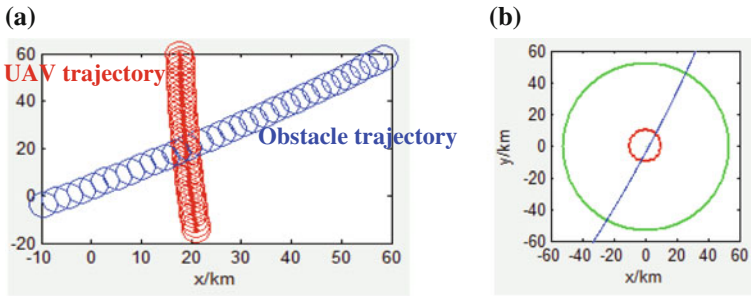


Fig. 5 a Absolute trajectory of UAV and obstacle. b Trajectory of obstacle in relative coordinate system

4.5 The Combinatorial Optimization Strategy

Considering the above factors, combinatorial optimization functions are given for collision avoidance:

$$T(\omega_i) = w_1 \Delta t_i + w_2 \sum_{i=1}^n a_{ij} + w_3 (d_{ij} - R) + w_4 c_l \tag{8}$$

w_i is weight, ω_i is collision avoidance strategy (as shown in Table 4). By optimizing the cost function, the optimal control strategy is:

$$\omega_{opt} = \arg \min_{\omega_i \in \Omega} T(\omega_i) \tag{9}$$

5 Simulation

Assume $R = 10$ km is the radius of UAV safety circle, $R_r = 50$ km is the detection radius of airborne sensor, the range $\Delta\varphi$ of course angle is $-\pi/3 \sim \pi/3$, the speed range $v = 50 \sim 100$ m/s. UAV1 found obstacles, predicted the motion track, and detected potential collision threat. Figure 5a shows an absolute trajectory, Fig. 5b are trajectories in the relative coordinate, it is apparent that the predicted obstacle trajectory intersected with the UAV safety circle.

Figures 6 and 7 are the collision results only to change the heading angle or speed; Fig. 8 is the collision avoidance result of changing the speed of UAV firstly and then changing the heading angle, we can see that the effect of mixed strategies is better than a single strategy.

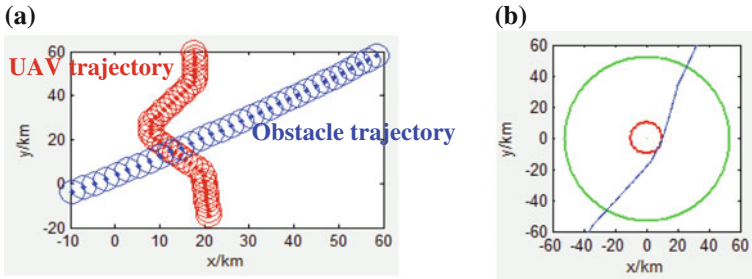


Fig. 6 a Trajectory of UAV and obstacle with changing heading angle. b Trajectory of obstacle with changing heading angle in relative coordinate system

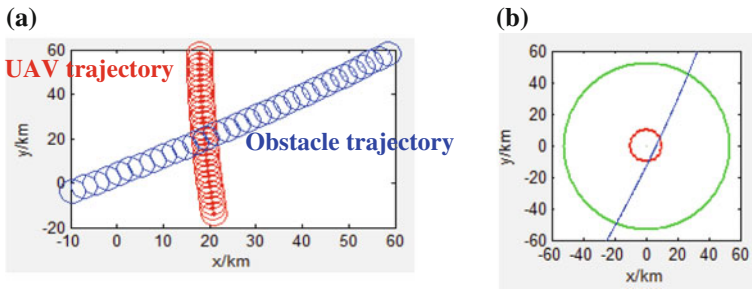


Fig. 7 a Trajectory of UAV and obstacle with changing speed. b Trajectory of obstacle with changing speed in relative coordinate system

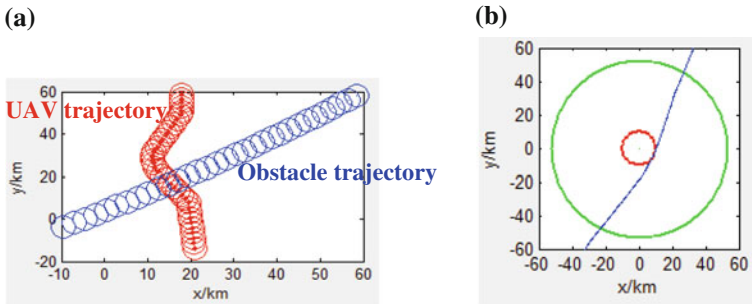


Fig. 8 a Trajectory of UAV and obstacle with changing heading angle and speed. b Trajectory of obstacle with changing heading angle and speed in relative coordinate system

6 Conclusion

In this work, according to the distance between UAV and dynamic threats, model the threat levels, adopt heading angle control, speed control, and a combination of the two strategies. Establishing multiobjective collision avoidance control methods based on a variety of factors to achieve the optimal decision under different tasks and collision avoidance constraints. Finally, carrying out simulation experiments, analyze and compare effectiveness of various collision avoidance strategies.

References

1. Chakravarthy A, Ghose D (1998) Obstacle avoidance in a dynamic environment: a collision cone approach. *IEEE Trans Syst Man Cybern Part A Syst Hum* 28:562–574
2. Shin H-S, Tsourdos A, White BA (2008) UAV conflict detection and resolution for static and dynamic obstacles. In: AIAA guidance, navigation and control conference and exhibition, Hawaii, pp 1–21. doi: [10.2514/6.2008-6521](https://doi.org/10.2514/6.2008-6521)
3. Wang X, Yadav V, Balakrishnan SN (2007) Cooperative UAV formation flying with obstacle/collision avoidance. *IEEE Trans Control Syst Technol* 15(4):672–679
4. Hwang I, Tomlin C (2002) Multiple aircraft conflict resolution under finite information horizon. In: Proceedings of the AACC American control conference, Anchor-age
5. McLain T (2001) Cooperative rendezvous of multiple unmanned air vehicles. In: American control conference, pp 2309–2314. doi: [10.1109/ACC.2001.946096](https://doi.org/10.1109/ACC.2001.946096)
6. Bilimoria K, Sridhar B, Chatterji G (2000) FACET: future ATM concepts evaluation tool. In: The 3rd USA/Europe air traffic management R&D seminar, Naples, pp 1–10
7. Zu D, Han J, Tan D (2007) LP-based path planning method in acceleration space for mobile robot. *Acta Automatica Sinica* 33:1036–1042
8. Zhang F, Tan D (2003) A new real-time and dynamic collision avoidance method of mobile robots based on relative coordinates. *Robot* 25:31–34
9. Li X, Wei R, Zhou J (2010) UAV three-dimensional path planning based on improved genetic algorithm. *J Northwest Polytech Univ* 28:343–348
10. Li X, Zhang J, Xie W (2011) Research on autonomic collision avoidance method for UAV. *Flight Dyn* 29:50–53
11. YAO Y, ZHOU X, ZHANG K (2007) Dynamic trajectory planning for unmanned aerial vehicle based on sparse A* search and improved artificial potential field. *Control Theory Appl* 27:953–959

The Identification of Convex Function on Riemannian Manifold

Xiaosong Cui, Xin Wen, Yunxia Zhang, Li Zou and Yang Xu

Abstract The necessary and sufficient condition of convex function is significant in nonlinear convex programming. This paper presents the identification of convex function on Riemannian manifold by use of Penot generalized directional derivative and the Clarke generalized gradient. Our objective here is to extend the content and proof the necessary and sufficient condition of convex function to Riemannian manifolds.

Keywords Riemannian manifold · Convex function · Optimality condition · Generalized gradient

1 Introduction

Manifold is the space with the local property of Euclidean space. We often judge the warp of the space by measuring its space. The standard of the measurement is called metric. Metric is an intrinsic property and the space with metric is called Riemannian space. Riemann manifold is a differential manifold which has Riemannian metric. Expanding the optimization based on linear space to the nonlinear space (such as Riemannian manifold) is a hot topic in this research field [1].

X. Cui · X. Wen · Y. Zhang · L. Zou (✉)

School of Computer and Information Technology, Liaoning Normal University,
Dalian 116081, China
e-mail: zoulicn@163.com

L. Zou

State Key Laboratory for Novel Software Technology, Nanjing University,
Nanjing 210093, China

Y. Xu

Department of Mathematics, Southwest Jiaotong University, Chengdu 610031,
Sichuan, China

In order to have more in-depth study of nonsmooth and its related problems, several important tools for analyzing nonsmooth problem have been extended from European space to Riemannian Manifold [2–5].

In 2004, Ledyac and others established the concept and algorithm of subdifferential of nonsmooth function in Riemannian Manifold and proved that the solution of Hamilton–Jacobi equation defined on Riemannian Manifold is unique. They also have discussed the concept and variational principle of approximate subdifferential in Riemannian Manifold [6, 7]. In 2005, Azagra and others discussed the Ferrera subdifferential which defined on finite dimensional Riemannian manifold and relevant limit subdifferential and analyzed the issues of differential inclusion which defined on differential manifold by using the concept of generalized derivative [8, 9]. Sanyang Liu and others expanded (MP) problem from linear space to differential manifold and Fritz John necessary optimality conditions on Riemann manifold was given [10]. In 2008, Gang Xiao and others solved the nondifferentiable multiobjective optimization problems with equality and inequality constraints from Euclidean space to Riemannian manifolds and derived the Fritz John necessary conditions with generalized gradient formula for weak Pareto optimal solutions from Ekeland variational principle [11]. Wang et al. established the semi-local convergence of sequences which is generated by the Gauss–Newton method (with quasiregular initial points) for the convex composite function $h \circ F$ on Riemannian manifold [12] by using the majorizing function technique. Bento et al. presented a steepest descent method with Armijo’s rule for multicriteria optimization in the Riemannian context. Assuming quasiconvexity of the multicriteria function and non-negative curvature of the Riemannian manifold, they proved full convergence of the sequence to a critical Pareto point [13].

Convex programming is of great significance in the study of nonlinear programming theory. Based on the above research results, we will in parallel extend the identification of convex function and the optimality conditions of constraint problems from linear space to Riemannian Manifold in order to solve the convex programming problem in Riemannian Manifold. This paper is set out as follows. In Sect. 2, we briefly review some preliminary concepts. In Sect. 3, we introduce the identification of convex function on Riemannian manifold. We make some concluding remarks and suggest future research in this area in Sect. 4.

2 Preliminaries

Let R^n be an n -dimensional Euclidean space, the i th coordinate of point $p \in R^n$ is denoted by $(p)^i$, i.e., $(\)^i$ is the i th coordinate function of R^n .

Definition 2.1 [14] Let M be a Hausdorff topological space. If every point p of M has an open neighborhood $U \subset M$, such that an open subset of U and n -dimensional Euclidean space is homeomorphous, then M is called an n -dimensional topological manifold.

Definition 2.2 [10] Let $f(x)$ be a real-valued function defined on Riemannian manifold, $x_0 \in U \subset M$ and (U, φ) be a coordinate plot which contains x_0 . If $\forall x, y \in U$, there exists a constant L such that

$$|f(y) - f(x)| \leq L|\varphi(y) - \varphi(x)|.$$

Then $f(x)$ is a function which meets the local Lipschitz condition in the neighborhood of x_0 .

Definition 2.3 [10] Let function $f : M \rightarrow R$ be a meet local Lipschitz condition in the neighborhood of the point $x \in M$ and (U, φ) be a coordinate plot which contains x . The *Clarke* generalized directional derivative of f at x along the direction of $v \in T_xM$ is denoted by

$$\begin{aligned} f^\circ(x; v) &= \limsup_{\substack{y \rightarrow \varphi(x) \\ t \downarrow 0}} \frac{f \circ \varphi^{-1}(y + t\varphi_{*x}(v)) - f \circ \varphi^{-1}(y)}{t} \\ &= (f \circ \varphi^{-1})^\circ(\varphi(x); \varphi_{*x}(v)), \end{aligned} \tag{1}$$

where $t \rightarrow 0$.

Definition 2.4 [10] Let $f(x)$ be a function denoted in Riemannian manifold (M, g) and meet local Lipschitz condition in the neighborhood of the x . Then the elements of the subset of cotangent space T_x^*M of x

$$\hat{\partial}f(x) = \{ \zeta \in T_x^*M | f^\circ(x; v) \geq \langle \zeta, v \rangle, \forall v \in T_xM \} \tag{2}$$

is said to be Clarke generalized gradient where f is at x .

The norm of generalized gradient is denoted with

$$\|\zeta\|_\varphi := \sup\{ \langle \zeta, v \rangle, v \in T_xM, \|v\| \leq 1 \} \tag{3}$$

Definition 2.5 [15] Let $f: M \rightarrow R$ meet local Lipschitz condition in the neighborhood of $x \in M$ and (U, ϕ) be a coordinate plot which contains x . We define Penot generalized directional derivative of f at x along the direction of $v \in T_xM$ as follows,

$$\underline{d}f(x; v) = \liminf_{\substack{u \rightarrow v \\ t \downarrow 0}} \frac{f \circ \varphi^{-1}(y + t\varphi_{*x}(u)) - f \circ \varphi^{-1}(y)}{t} = \underline{d}(f \circ \varphi^{-1})(\varphi(x); \varphi_{*x}(v)) \tag{4}$$

$$\bar{d}f(x; v) = \lim_{u \rightarrow v} \sup_{t \downarrow 0} \frac{f \circ \varphi^{-1}(y + t\varphi_{*x}(u)) - f \circ \varphi^{-1}(y)}{t} = \bar{d}(f \circ \varphi^{-1})(\varphi(x); \varphi_{*x}(v)) \tag{5}$$

$$\underline{d}^2f(x; v; w) = \lim_{u \rightarrow \omega} \inf_{t \downarrow 0} \frac{f \circ \varphi^{-1}(y + t\varphi_{*x}(v) + t^2\varphi_{*x}(u)) - f \circ \varphi^{-1}(y) - t\underline{d}f(x; v)}{t^2} \tag{6}$$

$$\bar{d}^2f(x; v; w) = \lim_{u \rightarrow \omega} \sup_{t \downarrow 0} \frac{f \circ \varphi^{-1}(y + t\varphi_{*x}(v) + t^2\varphi_{*x}(u)) - f \circ \varphi^{-1}(y) - t\bar{d}f(x; v)}{t^2}. \tag{7}$$

If $\underline{d}f(x; v) = \bar{d}f(x; v)$, we define $df(x; v)$ as Penot generalized directional derivative of f at x along the direction of $v \in T_xM$;

If $\underline{d}^2f(x; v; \omega) = \bar{d}^2f(x; v; \omega)$, we define $d^2f(x; v; \omega)$ to represent second-order Penot generalized directional derivative of f at x along the direction of $v \in T_xM$;

If both $df(x; v)$ and $d^2f(x; v; \omega)$ exist, then

$$d^2f(x; v; \omega) = \lim_{y \rightarrow \varphi(x), t \downarrow 0} \frac{f \circ \varphi^{-1}(y + t\varphi_{*x}(v) + t^2\varphi_{*x}(\omega)) - f \circ \varphi^{-1}(y) - tdf(x; v)}{t^2}. \tag{8}$$

3 The Identification of Convex Function on Riemannian Manifold

Theorem 3.1 (First-order necessary and sufficient condition of convex function)

Let M be an m -dimensional Riemannian manifold and U be a geodesic convex set where $U \subset M$. If $f : U \rightarrow \mathbb{R}$ meets local Lipschitz condition in U , then the necessary and sufficient condition that f is geodesic convex function in U is as follows.

For $\forall x, y \in U$, there exists

$$f \circ \varphi^{-1}(y + \varphi_{*x}(v)) \geq f \circ \varphi^{-1}(y) + \nabla(f \circ \varphi^{-1})(y)^T(y - x).$$

Proof (Necessary condition) For $\forall t \in [0, 1]$, there exists

$$\varphi^{-1}(y) + t[\varphi^{-1}(y + \varphi_{*x}(v)) - \varphi^{-1}(y)] = t\varphi^{-1}(y + \varphi_{*x}(v)) + (1 - t)\varphi^{-1}(y) \in U.$$

Then according to the first-order Taylor expansion,

$$\begin{aligned} f \circ (\varphi^{-1}(y) + t[\varphi^{-1}(y + \varphi_{*x}(v)) - \varphi^{-1}(y)]) \\ = f \circ \varphi^{-1}(y) + t\nabla(f \circ \varphi^{-1})(y)^T(y - x) + o(t). \end{aligned} \quad (9)$$

Since f is geodesic convex function in U , then

$$\begin{aligned} f \circ (\varphi^{-1}(y) + t[\varphi^{-1}(y + \varphi_{*x}(v)) - \varphi^{-1}(y)]) &= f \circ (t\varphi^{-1}(y + \varphi_{*x}(v)) + (1-t)\varphi^{-1}(y)) \\ &\leq tf \circ \varphi^{-1}(y + \varphi_{*x}(v)) + (1-t)f \circ \varphi^{-1}(y). \end{aligned} \quad (10)$$

Then from two simultaneous equations of (9) and (10), we get

$$f \circ \varphi^{-1}(y + \varphi_{*x}(v)) + (1-t)f \circ \varphi^{-1}(y) \geq f \circ \varphi^{-1}(y) + t\nabla(f \circ \varphi^{-1})(y)^T(y - x) + o(t)$$

that is,

$$f \circ \varphi^{-1}(y + \varphi_{*x}(v)) \geq f \circ \varphi^{-1}(y) + \nabla(f \circ \varphi^{-1})(y)^T(y - x) + \frac{o(t)}{t}. \quad (11)$$

It follows from $t \rightarrow 0^+$ that $\frac{o(t)}{t} \rightarrow 0$, hence

$$f \circ \varphi^{-1}(y + \varphi_{*x}(v)) \geq f \circ \varphi^{-1}(y) + \nabla(f \circ \varphi^{-1})(y)^T(y - x).$$

(Sufficient condition) For $\forall t \in [0, 1]$, let $z = tx + (1-t)y$.

From the known conditions it follows that

$$f \circ \varphi^{-1}(y) \geq f \circ \varphi^{-1}(y + (1-t)\varphi_{*x}(v)) + \nabla(f \circ \varphi^{-1})(y + (1-t)\varphi_{*x}(v))^T(x - z) \quad (12)$$

$$\begin{aligned} f \circ \varphi^{-1}(y + \varphi_{*x}(v)) &\geq f \circ \varphi^{-1}(y + (1-t)\varphi_{*x}(v)) \\ &\quad + \nabla(f \circ \varphi^{-1})(y + (1-t)\varphi_{*x}(v))^T(y - z). \end{aligned} \quad (13)$$

Hence

$$tf \circ \varphi^{-1}(y) \geq tf \circ \varphi^{-1}(y + (1-t)\varphi_{*x}(v)) + t\nabla(f \circ \varphi^{-1})(y + (1-t)\varphi_{*x}(v))^T(x - z) \quad (14)$$

$$\begin{aligned} (1-t)f \circ \varphi^{-1}(y + \varphi_{*x}(v)) &\geq (1-t)f \circ \varphi^{-1}(y + (1-t)\varphi_{*x}(v)) \\ &\quad + (1-t)\nabla(f \circ \varphi^{-1})(y + (1-t)\varphi_{*x}(v))^T(y - z) \end{aligned} \quad (15)$$

Then from (14) and (15), it follows that

$$\begin{aligned}
 &tf \circ \varphi^{-1}(y) + (1 - t)f \circ \varphi^{-1}(y + \varphi_{*x}(v)) \\
 &\geq f \circ \varphi^{-1}(y + (1 - t)\varphi_{*x}(v)) + \nabla(f \circ \varphi^{-1})(y + (1 - t)\varphi_{*x}(v))^T(tx + (1 - t)y - z).
 \end{aligned}
 \tag{16}$$

Since $z = tx + (1 - t)y$ that

$$\begin{aligned}
 &tf \circ \varphi^{-1}(y) + (1 - t)f \circ \varphi^{-1}(y + \varphi_{*x}(v)) \geq f \circ \varphi^{-1}(y + (1 - t)\varphi_{*x}(v)) \\
 &= f \circ (t\varphi^{-1}(y) + (1 - t)\varphi^{-1}(y + \varphi_{*x}(v)))
 \end{aligned}$$

Thus, f is geodesic convex function in U .

Theorem 3.2 (First-order necessary and sufficient condition of strictly convex function) *Let M be an m -dimensional Riemannian manifold and U be a geodesic convex set. Let $U \subset M$, $f : U \rightarrow \mathbb{R}$ meet local Lipschitz condition in U , and then the necessary and sufficient condition that f is geodesic strictly convex function in U is as follows.*

For $\forall x, y \in U$, there exists

$$f \circ \varphi^{-1}(y + \varphi_{*x}(v)) > f \circ \varphi^{-1}(y) + \nabla(f \circ \varphi^{-1})(y)^T(y - x).$$

Proof (Necessary condition) In a similar way with proof of Theorem 3.1, we get

$$f \circ \varphi^{-1}(y + \varphi_{*x}(v)) > f \circ \varphi^{-1}(y) + \nabla(f \circ \varphi^{-1})(y)^T(y - x).$$

(Sufficient condition)

Since f is a strictly convex function that f is a convex function. For any two different points x, y where $x, y \in U$, there exists $z = \frac{1}{2}x + \frac{1}{2}y$, and then $z \in U$.

From Theorem 3.1, it follows that

$$\begin{aligned}
 f \circ \varphi^{-1}(y + \frac{1}{2}\varphi_{*x}(v)) &\geq f \circ \varphi^{-1}(y) + \nabla(f \circ \varphi^{-1})(y)^T(z - x) \\
 &= f \circ \varphi^{-1}(y) + \nabla(f \circ \varphi^{-1})(y)^T(\frac{1}{2}x + \frac{1}{2}y - x) \\
 &= f \circ \varphi^{-1}(y) + \frac{1}{2}\nabla(f \circ \varphi^{-1})(y)^T(y - x).
 \end{aligned}
 \tag{17}$$

Since f is a strictly convex function that

$$\begin{aligned}
 f \circ \varphi^{-1}(y + \frac{1}{2} \varphi_{*x}(v)) &= f \circ (\frac{1}{2} \varphi^{-1}(y) + \frac{1}{2} \varphi^{-1}(y + \varphi_{*x}(v))) \\
 &< \frac{1}{2} f \circ \varphi^{-1}(y) + \frac{1}{2} f \circ \varphi^{-1}(y + \varphi_{*x}(v)).
 \end{aligned}
 \tag{18}$$

Then it follows from (17) and (18) that

$$\frac{1}{2} f \circ \varphi^{-1}(y) + \frac{1}{2} f \circ \varphi^{-1}(y + \varphi_{*x}(v)) > f \circ \varphi^{-1}(y) + \frac{1}{2} \nabla(f \circ \varphi^{-1})(y)^T (y - x).$$

That is,

$$f \circ \varphi^{-1}(y + \varphi_{*x}(v)) > f \circ \varphi^{-1}(y) + \nabla(f \circ \varphi^{-1})(y)^T (y - x)$$

Theorem 3.3 (Second-order necessary and sufficient condition of convex function) *Let M be an m -dimensional Riemannian manifold and U be a geodesic convex set. Let $U \subset M, f : U \rightarrow R$ meet local Lipschitz condition in U and (U, ϕ) be a coordinate plot which contains x , and second-order Penot generalized directional derivative of f at x along the direction of $v \in T_x M$ exists. Then the necessary and sufficient condition that f is geodesic convex function in U is as follows.*

For any $x \in U$, there exists $d^2f(x; v, w) \geq 0$.

Proof (Necessary condition) Assume that for any $x \in U$, there exists $d^2f(x; v, w) \geq 0$. For any two different points x, y , from Taylor expansion it follows that

$$\begin{aligned}
 f \circ \varphi^{-1}(y + \varphi_{*x}(v)) &= f \circ \varphi^{-1}(y) + \nabla(f \circ \varphi^{-1})(y)^T (y - x) \\
 &\quad + \frac{1}{2} (y - x)^T \nabla^2(f \circ \varphi^{-1})(z) (y - x)
 \end{aligned}
 \tag{19}$$

Note that $z = tx + (1 - t)y, 0 \leq t \leq 1$.

Since U is a geodesic convex set that $z \in U$. From the known conditions, it follows that

$$d^2f(x; v, w) \geq 0.$$

Hence

$$(y - x)^T \nabla^2(f \circ \varphi^{-1})(z) (y - x) \geq 0,
 \tag{20}$$

so that

$$f \circ \varphi^{-1}(y + \varphi_{*x}(v)) \geq f \circ \varphi^{-1}(y) + \nabla(f \circ \varphi^{-1})(y)^T(y - x)$$

Therefore, f is geodesic convex function in U according to Theorem 3.2. (Sufficient condition)

Since U is a geodesic convex set, thus for any $x \in U$ and any given nonzero vector l , there exists a sufficiently small positive number t , and thus $x + tl \in U$, it follows from Taylor expansion that

$$f \circ \varphi^{-1}(x + tl) = f \circ \varphi^{-1}(x) + t\nabla(f \circ \varphi^{-1})(x)^T l + \frac{t^2}{2} l^T \nabla^2(f \circ \varphi^{-1})(\bar{x})l + o(t^2) \tag{21}$$

Since f is geodesic convex function in U , using Theorem 3.2, we have

$$f \circ \varphi^{-1}(x + tl) \geq f \circ \varphi^{-1}(x) + t\nabla(f \circ \varphi^{-1})(x)^T l. \tag{22}$$

Hence

$$\frac{t^2}{2} l^T \nabla^2(f \circ \varphi^{-1})(\bar{x})l + o(t^2) \geq 0. \tag{23}$$

Let $t \rightarrow 0^+$, then

$$\frac{o(t^2)}{t^2} \rightarrow 0.$$

Thus,

$$l^T \nabla^2(f \circ \varphi^{-1})(\bar{x})l \geq 0.$$

That is, for any $x \in U$, there exists $d^2f(x; v, w) \geq 0$.

Theorem 3.4 (Second-order necessary and sufficient condition of strictly convex function) *Let M be an m -dimensional Riemannian manifold and U be a geodesic convex set. Let $U \subset M, f : U \rightarrow \mathbb{R}$ meet local Lipschitz condition in U and (U, ϕ) be a coordinate plot which contains x and second-order Penot generalized directional derivative of f at x along the direction of $v \in T_x M$ exist. Then the necessary and sufficient condition that f is geodesic strictly convex function in U is as follows.*

For any $x \in U$, there exists $d^2f(x; v, w) > 0$.
 Proof is similar to the proof of Theorem 3.3.

4 Conclusions

In this paper, we introduce the classical Clarke generalized directional derivative and generalized gradient. Then we extend the identification of convex function and proof of the theorem of the first-order necessary and sufficient condition of convex function and strictly convex function to Riemannian manifolds by the use of Penot generalized directional derivative. We have also given the second-order necessary and sufficient condition of convex function and strictly convex function. In this way, we can do more research about optimization method on differential manifold. In the future, the theorem and the application of the equality constrained optimization problems and the inequality constrained optimization problems will be explored.

Acknowledgments This work is partly supported by the National Natural Science Foundation of China (Grant No. 61105059, 61175055, 61173100), International Cooperation and Exchange of the National Natural Science Foundation of China (Grant No. 61210306079), China Postdoctoral Science Foundation (Grant No. 2012M510815), Liaoning Excellent Talents in University (Grant No. LJQ2011116), Sichuan Key Technology Research and Development Program (Grant No. 2011FZ0051), Radio Administration Bureau of MIIT of China (Grant No.[2011]146), China Institution of Communications (Grant No.[2011]051), Sichuan Key Laboratory of Intelligent Network Information Processing (Grant No.SGXZD1002-10).

References

1. Udriste C (1994) Convex functions and optimization methods on Riemannian manifolds. Kluwer Academic Publishers, Dordrecht
2. Daniel A, Juan F, Lopez-Mesas F (2005) Nonsmooth analysis and Hamilton-Jacobi equations on Riemannian manifolds. *J Funct Anal* 220(2):304–361
3. Ledyaev YS, Zhu QJ (2004) Techniques for nonsmooth analysis on smooth manifolds: local problems. *Lect Notes Control Inf Sci* 301:283–297
4. Ledyaev YS, Zhu QJ (2004) Techniques for nonsmooth analysis on smooth manifolds δ : deformations and flows. *Lect Notes Control Inf Sci* 301:299–311
5. Daniel A, Juan F (2005) Proximal calculus on Riemannian manifolds. *Mediterr J Math* 2(4):437–450
6. Ledyacv YS, Zhu QJ (2004) Techniques for nonsmooth analysis on smooth manifolds i: local problems. *Lect Notes Control and Inf Sci* 301:283–297
7. Ledyacv YS, Zhu QJ (2004) Techniques for nonsmooth analysis on smooth manifolds ii: deformations and folws. *Lect Notes Control Inf Sci* 301:299–311
8. Azagra D, Ferrera J, Lopez-Mesas F (2005) Nonsmooth analysis and Hamilton-Jacobi equations on smooth manifolds. *J Funct Anal* 220:304–361
9. Azagra D, Ferrera J (2005) Proximal calculus on Riemannian manifolds. *Mediterr J Math* 2:437–450
10. Liu S, Zhu S, Xiao G (2007) Fritz John necessary optimality condition on Riemannian manifolds. *J Liaoning Norm Univ* 30:268–272
11. Gang X, Sanyang L (2008) Necessary optimality conditions of nondifferentiable multiobjective programming on Riemannian manifolds. *J Jilin Univ Sci* 46(2):209–213
12. Wang J, Yao J, Li C (2012) Gauss-Newton method for convex composite optimizations on Riemannian manifolds. *Eng Village* 53:5–28

13. Bento G, Ferreira O, Oliveira P (2012) Unconstrained steepest descent method for multicriteria optimization on Riemannian manifolds. *Sci Citation Index* 154:88–107
14. Lang S (1969) *Analysis II*. Addison-Wesley, Reading
15. Weiwei F (2009) *Optimality conditions on Riemannian manifold of nonsmooth optimization*. Liaoning Technical University, Liaoning

A Method for Dehazed Image Quality Assessment

Zhongyi Hu and Qiu Liu

Abstract The development of general purpose no-reference approaches to dehazed image quality evaluation still lags in recent advances in image dehazing methods. While a number of image dehazing methods have been established and have shown to perform well, these are correlating highly with subjective evaluation of image quality. Toward ameliorating this we introduce the DIAS (Dehazed Image Assessment using Statistics) which is a no-reference approach to dehazed image quality assessment (DIQA) that does not assume a specific type of distortion of the image. It is based on detecting dehazed image quality based on Circularly Symmetric Gaussian Normalization Procedure Visible Edges Feature and it requires no training. The method is shown to correlate highly with human perception of quality. Our contribution in this direction is the development of dehazed image quality assessment method based on Circularly Symmetric Gaussian Normalization Procedure Visible Edges Feature which does not require exposure to distorted images priori and training.

Keywords Dehazed image quality assessment · Circularly symmetric Gaussian · Visible edges feature

Z. Hu · Q. Liu (✉)

Intelligent Transport Systems Research Center, Wuhan University of Technology,
Wuhan 430063, Hubei, People's Republic of China
e-mail: qliu2000@163.com

Z. Hu

e-mail: hujunyi@163.com

Q. Liu

School of Automation, Wuhan University of Technology, Wuhan 430070, Hubei,
People's Republic of China

1 Introduction

Due to the influence of atmosphere particles such scattering effect in haze weather, it causes different degrees of reduction of the scene visibility. Quality of outdoor images is usually degraded which loose the contrast and color fidelity. Thus it greatly affects the processing of the video image effects and postanalysis. Therefore, many scholars have further studied in image dehazing [1–3]. However, there exist only few methods specifically for dehazed image quality assessment. At present, there exist approaches to DIQA research are varied and commonly follow one of two trends. One is quality assessment by image contrast, and the other is quality assessment by consolidated image contrast and color. The former is the most widely used method of Tarel and Hautière which based on the visible edge for no-reference image quality evaluation [4, 5]. The latter, such as in [6–8], this approach extracts features of global or local contrast from images to measure the grade of image enhancement and combine the three indexes of hue, RGB element and histogram similarity in order to evaluate the quality of image color. We seek to observe that the emphasis of DIQA is the detailed and clarity of the image. So, in this paper, we present the DIQA method based on visible edges feature of the images.

2 Feature Extraction

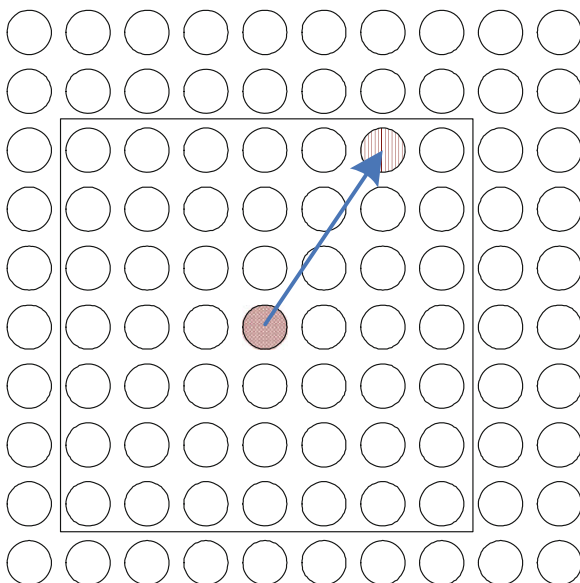
2.1 Normalization Procedure

Nowadays, many researchers in the natural image multiscale transform modeling statistical study are gratifying achievements. Ruderman has observed that applying a local nonlinear operation to log-contrast luminances to remove local mean displacements from Circularly Symmetric Gaussian and to normalize the local variance of the log contrast has a decorrelating effect [9]. In this paper, we applied this idea to evaluate the dehazed image quality, such an operation may be applied to a given intensity image $I(x, y)$ to produce:

$$\hat{I}(x, y) = \frac{I(x, y) - \alpha(x, y)}{\beta(x, y) + \gamma} \quad (1)$$

Where $\hat{I}(x, y)$ is the image after normalization procedure, $I(x, y)$ is original image, $x \in (1, 2, \dots, H)$ and $y \in (1, 2, \dots, W)$ are spatial indices, H and W are the image height and width, respectively. γ is a very small number that prevents instabilities from occurring when the denominator tends to zero, in order to calculate Facilitatively, we set $\gamma = 1$. α and β are nonlinear normalization factor, respectively, such as: Eqs. (2) and (3).

Fig. 1 I_{kl} schematic diagram



$$\alpha(x, y) = \sum_{k=-K}^K \sum_{l=-L}^L g_{kl} I_{kl}(x, y) \tag{2}$$

$g = \{g_{k,l} | k = [-K, \dots, K], l = [-L, \dots, L]\}$ is a 2D weight kernel of circularly symmetric Gaussian function. In our implementation, we set $K = 3$ and $L = 3$. Such as Fig. 1, where \odot is $I(x, y)$, and \ominus is I_{kl} . k and l are distance of $I(x, y)$ from I_{kl} . We found performance varies with changes in the k and L in the performance evaluation result.

$$\beta = \sqrt{\sum_{k=-K}^K \sum_{l=-L}^L g_{kl} (I_{kl}(x, y) - \alpha(i, j))^2} \tag{3}$$

2.2 Visible Edges Feature

It is clearer than the original image when the hazing image is dehazed, and its visible edges feature intensity will be improved. The dehazed image's noise will interfere with the accuracy of the visible edge strength estimation, so we will remove edge noise by the Gaussian Low-Pass Filtering.



Fig. 2 Dehazing result of different algorithms

Table 1 Result of dehazed image quality assessment

| Image | Original | Histogram | Fattal | He |
|-------|----------|-----------|--------|--------|
| Value | 0.2158 | 0.2275 | 0.2237 | 0.2208 |

$$\bar{I}(x, y) = I(x, y) * G_{fl}(x, y) \tag{4}$$

In Eq. (4), $\bar{I}(x, y)$ is the filtered image, $I(x, y)$ is the dehazed image, and Zero-Mean Gaussian kernel G_{fl} will be defined as,

$$G_{fl}(x, y) = ke^{\frac{\|\sqrt{x^2+y^2}\|_2^2}{c^2}} - \delta \tag{5}$$

Where k and c are Gaussian constant, respectively, in this paper, we set $k = 3$ and $c = 0.5$. δ is zero-mean parameters.

An ideal dehazing method for image restoration results should not be lost visual information visible, at the same time the edge intensity will be improved. We detect the normalized image's edges of $\hat{I}(x, y)$ by Canny operator, and get the average value of the detected edges $I_e(x, y)$. L_s is the visible edge strength of the original image, such as Eq. (6)

$$L_s = \frac{1}{HW} \sum_{x=1}^H \sum_{y=1}^W I_e(x, y) \tag{6}$$

3 Experiment

In this paper, it will be verified the performance of the algorithm using experiments. We select the current-advanced dehazing algorithm to compare the results, from left to right in Fig. 2 are the results of original image, Histogram Equalization Dehazing Method, Fatal's, and He's, respectively [10]. We can find from Fig. 2, the subjective visual effect of Histogram Equalization Dehazing Method, Fatal's and He's are strengthened successively. And the experimental results in Table 1 were also verified the subjective view.

4 Conclusion and Discussion

We detailed the algorithm Visible Edges Feature extracted, and demonstrated how features correlate with human perception. The denoising algorithms of Zero-Mean Gaussian Filter is effective in reducing the impact of noise characteristics in the visible edges, and the contrast and brightness impact on the experimental results are reducing to minimize by Circularly Symmetric Gaussian Normalization Procedure. In this paper, the experimental results show that we have developed DIQA a new approach to dehazed image quality assessment algorithm can be applied to the current dehazing method's assessment and compare. The halo artifacts which often appear during dehazing process, color shifts, and oversaturated by excessive image enhanced or mistake of atmosphere optical transmission. Using all these three factors of color tone reproduction degree, image structure information, and visible edges feature, the effect of dehazing methods can be evaluated objectively.

Acknowledgments The authors acknowledge the financial support from the Fundamental Research Funds for the Central Universities, Natural Science Foundation of China (project No.: 51279152) and Zhejiang Provincial Natural Science Foundation of China (project No.: LY12F02015). The author is grateful to the anonymous referee for a careful checking of the details and for helpful comments that improved this paper.

References

1. Zhu P, Zhu H, Qian X et al (2004) An image clearness method for fog. *J Image Graph* 9(1):124–128 (in Chinese)
2. Fattal R (2008) Single image dehazing. *ACM Trans Graph* 27(3):1–9
3. He K, Sun J, Tang X (2011) Single image haze removal using dark channel prior. *IEEE Trans Pattern Anal Mach Intell* 33(12):2341–2353
4. Tarel JP, Hautière N (2009) Fast visibility restoration from a single color or gray level image. In: *Proceedings of the 12th IEEE international conference on computer vision*. Kyoto, Japan: IEEE, pp 2201–2208
5. Hautière N, Tarel JP, Aubert D, Dumont E (2008) Blind contrast enhancement assessment by gradient ratioing at visible edges. *Image Anal Stereol J* 27(2):87–95
6. Li D-P, Yu J, Xiao C-B (2011) No-reference quality assessment method for defogged images. *J Image Graph* 16(9):1753–1757 (in Chinese)
7. Guo F, Cai Z-X (2012) Objective assessment method for the clearness effect of image defogging algorithm. *Acta Automatica Sinica* 38(9):1410–1419 (in Chinese)
8. Yao B, Huang L, Liu C-P (2009) Research on an objective method to compare the quality of defogged images. In: *Proceedings of Chinese conference on pattern recognition*. Nanjing, China: IEEE, pp 1–5 (in Chinese)
9. Ruderman DL (1994) The statistics of natural images. *Netw Comput Neural Syst* 5(4):517–548
10. Information on <http://research.microsoft.com/en-us/um/people/kahe/cvpr09/>

Tactics Decision-Making Based on Granular Computing in Cooperative Team Air Combat

Dongqi Meng, Yufei Wang, Ying Chen and Lin Zhong

Abstract For the purposes of real time and accuracy characteristics in air combat, the granular computing theory is introduced to the tactics decision analysis in cooperative team air combat, and a new approach to intelligent decision based on tolerance granularity space model is presented. A complex problem can be divided into several smaller ones, which are easily understood and solved according to the ideal of granular computing. The tolerance granularity space model is constructed by means of the inner-class distance defined in the attributes space. A variety of tactical information is effectively mapped into different granular layers in order to achieve the correct classification for tactics. In order to enhance the decision accuracy, a reduction method of tactics features based on granular computing is proposed, which directly gets the best and minimal reduction set to construct the tolerance granularity space model for the best decision accuracy. The simulation results show the model is endowed with better decision performance than the integration model of rough sets and neural networks.

Keywords Cooperative team air combat · Tactics decision-making · Granular computing · Tolerance granularity space model · Attribute reduction

1 Introduction

Combat situation of the team is the basis of tactics decision in cooperative team air combat. There are various factors that affect combat situation, for example, the number of the fighters, team location, altitude, the performance of aircrafts, and

D. Meng · Y. Wang · Y. Chen (✉)
Department of Aviation Life-Saving, Aviation University of Air Force,
Changchun, China
e-mail: Mdq3377@sina.com

L. Zhong (✉)
95927 Unit, Air Force, Cangzhou, China
e-mail: zhonglin2686@sina.com

the performance of missiles. However, there is no exact mathematical model to present the relation between these factors and tactics decision in cooperative team air combat. This is a semi-structured or unstructured decision problem of how combat situation information merges getting the final program of the tactical decision-making. The research achievements on tactics in cooperative team air combat at present are seldom seen. The optimization method for large-scale air combat formation tactics based on genetic algorithm is developed in the literature [1]. The fuzzy neural network is used to discuss air combat formation tactics beyond the visual range in the literature [2]. The literature [3] presents the method of tactical decision based on integration of rough sets and neural networks in cooperative team air combat.

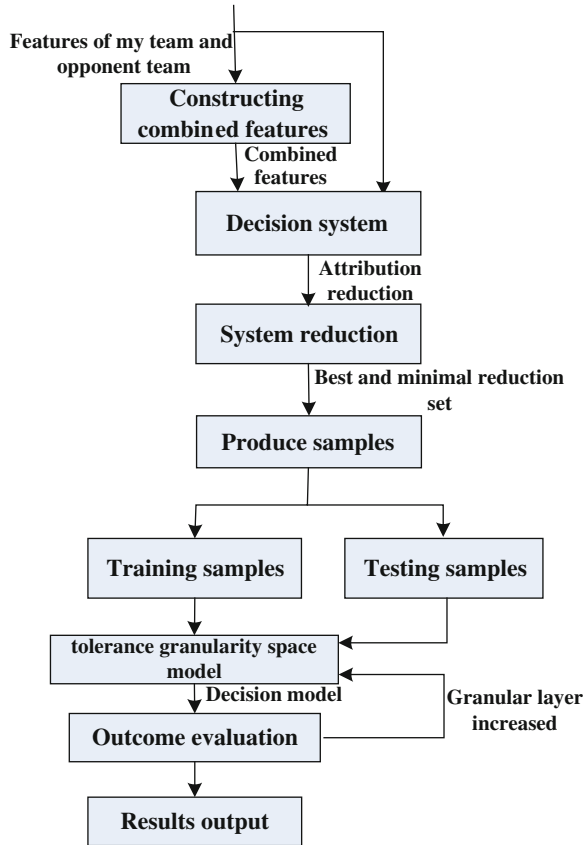
Granular computing is a new emerging research in artificial intelligence at present, and simulates the intelligence of mankind when they deal with a lot of problems with complex information. Because of the limited capacity of mankind, a lot of complex information is divided into several simpler information blocks according to their characteristics and performance in order to conveniently deal with the information, namely the original “coarse” set of objects divided into a large number of “fine particles” in the collection of small objects.

For purposes of the real time and accuracy characteristics in air combat, a new approach to intelligent decision based on tolerance granularity space model is presented, and it is applied for tactical decision in cooperative team air combat.

2 Basic Idea

The tactics beyond visual range in cooperative team air combat includes single tactics and a combination of tactics. This is the key of tactics decision where the tactics are selected quickly and accurately under conditions of complexity. The basic idea is shown in Fig. 1. First, combined features are constructed from my team and opponent team features and all features are normalized. The features include single features and combined features. The single features merely depict my team or the opponent team. The combined features are used to present a situation between my team and the opponent team. The first step is the basis of the decision. Then all tactical features are reduced according to an algorithm of attribute reduction. The purpose of the step is to reduce redundant attributes for real time. The single features and combined features are inputted into the decision system, and the reduced attributes are obtained. The best and minimal attribute set is obtained from reduced attributes by system reduction. Lastly, the best and minimal reduction set is used to construct the tolerance granularity space model, and the model is applied to tactical decision in cooperative team air combat. The last step is the key of real time and accuracy decision-making. First, the production samples are produced based on the best and minimal reduction set. The samples

Fig. 1 Tactical decision system in cooperative team air combat based on tolerance granularity space model



include training samples and testing samples. Secondly, the training samples are used to train tolerance granularity space model, and the testing sample is used to test the model. Thirdly, the number of granular layer is increased or not according to outcome evaluation.

3 Constructing Combined Features

In order to make the decisions quickly and accurately, we need to get more sensitive features. From comparative analysis of all tactical features that influence the tactics, some combined features are more sensitive than single features [3]. As the basis of the research, the basic principle in cooperative team air combat beyond visual range is: my team is always in a good attacking original position and

prepares for the launch before the enemy. Based on this principle, the paper selects 13 strategies in cooperative team air combat beyond visual range, which include 10 attacking strategies (seven single strategies and three combined strategies) and three defense strategies, for example, head direct attack strategy, pincer attack strategy, and combined thinning strategy. The following combined features are constructed under the requirement of 13 strategies:

- Advantage function of angle S_T [3]:

$$S_T = (\phi_A - \phi_T) / \pi \quad S_T \in [-1, 1] \quad (1)$$

which ϕ_A, ϕ_T is the enter angle and azimuth of opposite team, respectively.

- Relative advantage function of radar S_Q :

$$S_Q = (S_{AQ} - S_{TQ}) / 150 \quad S_Q \in (-1, 1) \quad (2)$$

which S_{AQ} is the maximum detecting distance of my radars, S_{TQ} is the maximum detecting range of opposite radars.

- Relative advantage range function between my missiles and opposite missiles S_M :

$$S_M = (S_{MA} - S_{MT}) / 10 \quad S_M \in [-5, 5] \quad (3)$$

where S_{MA} is the maximum range of fire of my mediate distance missiles, S_{MT} is the maximum range of fire of opposite mediate distance missiles (Km).

- Relative advantage function between my radars' upward-looking capability and opposite radars' downward-looking capability S_R

$$S_R = (D_{SS} - D_{XS}) / 50 \quad S_R \in (-1, 1) \quad (4)$$

where D_{SS} is the upward-looking detecting range of my radars and D_{XS} is the downward-looking detecting range of opposite radars. Similarly, relative advantage function between my radars' downward-looking capability and opposite radars' upward-looking capability S_R' is obtained.

- Advantage function of velocity S_V :

$$S_V = (V_A^2 - V_T^2) / V_A^2 \quad (5)$$

which V_A is the velocity of my team, V_T is the velocity of opposite team.

- Advantage function of potential S_H :

$$S_H = (H_A - H_T)/H_A \tag{6}$$

which H_A is the height of my team, H_T is the height of opposite team.

4 An Attribute Reduction Method Based on Granular Computing

According to the theory of granular computing, the granular entropy is introduced as the heuristic information that is used to distinguish the attribute importance, and presents quantitatively the classification ability of attribute knowledge. The attributes are reduced efficiently and the best and minimal reduction set is obtained.

4.1 Basic Definition

Definition 1 Assume $U/R = \{X_1, X_2, \dots, X_n\}$ is the knowledge of a finite set of objects U , the granular entropy of knowledge is

$$I(U/R) = - \sum_{i=1}^n G(X_i) \log G(X_i) \tag{7}$$

where $G(X_i) = |X_i|/|U|$, $|\bullet|$ denotes a base of set.

Definition 2 An information system is a quadruple $S = (U, A, V, f)$, $A = C \cup D$ is a finite attribute set of objects and A is divided into two sets, conditional attributes C and decision set D . Every attribute $a \in R$, V_a denotes its value domain. Every attribute has a decision function $f : U \times R \rightarrow V$. Assume $B \subseteq C$, then the rule F that S and B produce is presented as:

$$F = \wedge \{(a, v) : a \in B \quad \text{and} \quad v \in (V_a \cup \{*\})\} \rightarrow d = v_d$$

where $v_d \in V$, the symbol “*” denotes that attribute value is independent of this rule. Assume $P \subset C$, importance of any attribute $a \in C - P$ relative to decision attribute D is:

$$\text{Sig}(a, P, D) = I(D/P) - I(D/P \cup \{a\}) \tag{8}$$

This shows the importance of any attribute $a \in C - P$ about attribute set P is the measure that attribute a added to P causes changes in the amount of

information. The value $\text{Sig}(a, P, D)$ is greater, attribute $a \in C - P$ is more important for attribute set P .

4.2 Reduction Algorithm

According to the concept of relative importance, the most important attribute is added to reduction set until relative granular entropy on decision attribute is equal to relative granular entropy between condition attribute set and decision attribute. The specific steps are as follows:

- (1) Compute relative granular entropy between conditional attribute set and decision attribute, namely $I(D/C)$;
- (2) Compute granular entropy of every conditional attribute in the conditional attribute set, and conditional attribute with biggest granular entropy is thought as a parameter of reduction set, namely $I(U/\{c\}), c \in C, P = \max I(U/\{c\})$;
- (3) Determine if the information of reduction set is equal to that of nonreduction set ($I(D/P) = I(D/C)$). If it is certain, switch step (6), else switch step (4);
- (4) Compute importance of the other conditional attributes and get the conditional attribute with biggest granular entropy, namely $\text{Sig}_P(c), \{ci \in C - P | \max(\text{Sig}(ci))\} (c \in C - P)$;
- (5) Add the conditional attribute of last step to reduction set, namely Switch step (3);
- (6) Output best and minimal reduction set $\text{RED}(C)$, namely $\text{RED}(C) = P$.

If we get several features with maximum value in the process of reduction, the feature parameter that focuses on the front has priority.

5 Intelligent Decision Method Based on Tolerance Granularity Space Model

5.1 Basic Definition

Definition 3 [4] Tolerance relation is reflexive and symmetric binary relation. The distance function is used to present the tolerance relation:

$$\text{dis}(\alpha, \beta | \omega, d) \Leftrightarrow \sum_{i=1}^n \omega_i (\alpha_i \oplus \beta_i) \leq d, \text{ where } \alpha = (\alpha_1, \dots, \alpha_n), \beta = (\beta_1, \dots, \beta_n),$$

$$\alpha_i \oplus \beta_i = \begin{cases} 1, & \text{if } |\alpha_i - \beta_i| > r \\ 0, & \text{if } |\alpha_i - \beta_i| \leq r \end{cases} i = 1, \dots, n \cdot \alpha, \beta. \text{ is a } n\text{-dimension vector, } \alpha_i, \beta_i$$

is tactical feature value, respectively, r is called tolerance granule, ω is a n -dimension weight vector, d is a parameter of tolerance relation.

Definition 4 Zheng et al. [4] Tolerate granule consists of intension and extension. The intension is assigned a vector and the extension is a set of objects or granules.

In this paper, the intension is tactical rule and the extension is a set of objects that are compatible with intension. If objects of extension in a granule conflict with tactical rule, this granule called conflict tolerates granule, else it is called compatible tolerate granule. Intension of compatible tolerate granules can only be used as tactical rule. However, cooperative team tactical features may overlap to different degrees in the same attribute because of different types of tactical states. It influences the credibility of tolerate granule’s intension, therefore the concept of confidence level of tolerate granule is introduced into conflict tolerate granule. Intension of conflict tolerate granules can also be used as tactical rule.

Assume N_{cd} is the number of samples that satisfy the condition $c = v$ and $d = d_i$, N_c is the number of samples that satisfy the condition $c = v$. Then, the confidence level of tolerate granule is defined as $CL(a_i) = N_{cd}/N_c$. According to Definition 2, the tactical rule in tolerate granularity space model is defined as:

$$F = \begin{cases} (a_1 = ev_1) \wedge (a_2 = ev_2) \dots \wedge (a_{n-1} = ev_{n-1}) \\ \rightarrow d = v_d & \max(CL(a_i)) \geq CL_v \\ 0 & \text{else} \end{cases} \quad (9)$$

where $ev_i (i = 1, 2, \dots, n - 1)$ is the mean of samples in i th feature and CL_v is valve value of confidence level.

The confidence level of compatible tolerate granule is 1. If confidence level of conflict tolerate granule is greater than valve value, its intension is credible. In order to compute the classifying capability of decision rule, the concept of support degree for tolerate granule is introduced.

If the number of samples that extension of tolerate granules covers is N' and the number of all samples is N , the support degree for tolerate granule is defined as $S = N_1/N$.

5.2 Construct Tolerate Granularity Space

Tactical feature values are discrete in tactics decision model for cooperative team air combat. The same feature values of different tactics have these ranges themselves that are not fixed. These change with equipment of my and opposite team and combat environment. According to the characteristic of data itself and Definition 3, the feature values of tactical samples are centered and all samples that center the

center and that the difference between feature values and center is less than or equal to r are searched by tolerate granularity r . The samples are attributed to a compatible tolerate granule. By changing the weight vector ω to adjust the sample center, all compatible granules are obtained. The tolerate granularity space is

$$r = \mathbf{D}_s * \omega \quad (10)$$

where $\mathbf{D}_s = (d_{s1}, d_{s2}, \dots, d_{sn})$ is distance vector that is made up of minimal intra-class distances for every feature. In the process of constructing tolerate granularity space model, feature attributes are selected with the change of vector ω . The elements of ω belong to interval (0,1) and r is adjusted with the change of vector ω . Because constructing tolerate granules produces tactical rule, when $d = 0$, distance function is the equivalence relation.

5.3 Tactical Decision Algorithm

Based on tolerate granularity space model, from the first layer all samples for decision making are computed according to tactical rules. The following concrete steps are followed:

- (1) Select initial granular set GS;
- (2) Cycle the following steps for each of the testing samples for decision-making;
- (3) If there is only one matching compatible tolerate granule, or there are several matching compatible tolerate granules whose intension present the same decision of tactical rule, then switch step (7);
- (4) If there are several matching compatible tolerate granules that have sub-granules, then switch step (6);
- (5) If there are several matching compatible tolerate granules that have no sub-granules, then compute the support degrees of several granules and determine samples to be decision making based on tactical rule with the maximal support degree. If there are several tolerate granules with the maximal support degree, compute the distances between the objects for decision making and the tactical rule and select the object with minimal distance as the decision result. Switch step (2) and make a decision for the next testing sample;
- (6) Assume the number of maximal layers of these matching compatible tolerate granules is i , select all matching compatible tolerate granules' $i + 1$ th offspring granules for constructing decision granular set GS' and make decisions based on tactical rules denoted by the intension of tolerate granules in set GS' . Switch step 3);

Fig. 2 Granular entropy of features

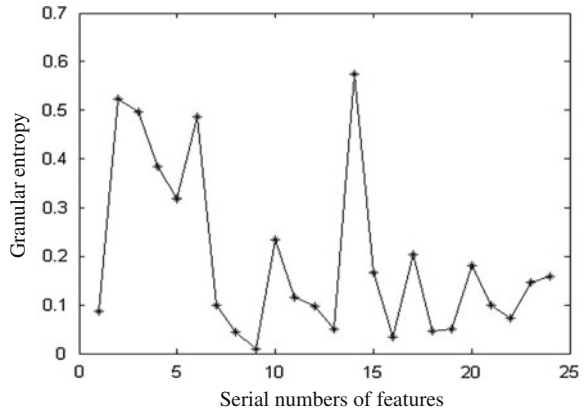


Table 1 Tactics decision results in cooperative air combat

| The number of features | 5 | 6 | 7 | 8 | 9 |
|------------------------|------|------|------|------|------|
| Decision accuracy (%) | 88.6 | 90.0 | 92.3 | 92.4 | 91.1 |

- (7) If the decision result of the object to be decision making is tactical rule presented by matching tolerate granule’s intension, switch step (2) and make a decision for the next sample.

6 Performance Study

400 samples are selected. 300 samples are used to train the model, and 100 samples are used to test the model. According to training samples, combined features are constructed. Then all features (17 single features and 7 combined features) are normalized. Granular entropy of each feature is computed (Fig. 2). The reduction algorithm is used to get 7 dimension reduction attribute set that consists of 4 combined features and 3 single features. They are advantage function of angle, relative advantage function of radar, relative advantage range function of missile, relative advantage function between my radars’ upward-looking capability and opposite radars’ downward-looking capability, distance, height of opposite team and shooting states of opposite missiles. In order to compare with each other, 5–7 attributes in reduction set with maximal granular entropy are selected an used to construct tolerate granularity space model, respectively (CL = 0.9). 1–2 features that are removed with maximal granular entropy is added into the reduction set, and 8–9 features are used to construct tolerate granularity space model,

respectively ($CL = 0.9$). The results are shown in Table 1. The results show that the reduction algorithm is effective.

The model presented by this paper is compared with the decision method based on fuzzy neural network presented by Ref. [2] and the decision method based on integration of rough sets and neural networks is presented by Ref. [3]. The decision accuracy of the method presented by Ref [2] is 56.9 % and that of the method presented by Ref. [3] is 79.6 %, and is lower than the accuracy of this method (92.3 %). The method presented by Ref. [2] does not reduce redundant features. Although the method presented by Ref. [3] reduces redundant features, the two methods deal with information at only one level or on a particular set from the perspective of granular computing and does not take advantage of the relation and interaction between granules. The simulation shows the method takes more advantages of tactical information provided by feature values in the same features than other methods.

7 Conclusion

Based on the attribute reduction algorithm and tolerate granularity space model, intelligent decision method with the basic idea of granular computing is presented in this paper. Attribute reduction algorithm can reduce tactical features effectively and remove all unnecessary features. A variety of tactical information is mapped into different granular layers using tolerate granularity space model in order to achieve the classification for tactics. The tactics decision problem for cooperative team air combat is solved by dealing with not only the classification of attacking tactics, but also defending tactics, especially combined tactics. Therefore, it increases the difficulty of decision problem. The decision accuracy of the model for variety tactics in this paper is 92.3 %. It states that the tolerate granularity space model has good decision-making capacity for cooperative team air combat. Compared with other models, the simulation results show the superiority of the proposed method.

Acknowledgments This study is supported by “863 National High-Tech Program of China” (No. 2010AA8090514C).

References

1. Mulgund S, Harper K, Krishnakumar K, Zacharias G (2001) Large-scale air combat tactics optimization using genetic algorithms. *AIAA J Guid Control Dyn* 24(1):140–142
2. Li F, Sun L, Tong M (2001) A tactical decision support system for BVR air combat based on neural network. *J Northwestern Polytech Univ* 19(2):317–322

3. Zhong L (2008) Study on intelligent decision-making for cooperative team air combat under condition of complexity. Xi'an
4. Zheng Z, Hu H, Shi ZZ (2005) Tolerance granular space and its applications. In: IEEE International conference on granular computing, Piscataway, NJ USA. IEEE, pp 367–372

Graph Cuts-Based Feature Extraction of Plant Leaf

Feng-hua Lv and Hang-jun Wang

Abstract As leaf is one of the most important organs in a plant, contour features of plant leaves are important for the identification of plant species. So researchers have proposed many methods to improve the progress of the plant identification. In this paper, we present a graph cuts-based method using Min-Cut/Max Flow algorithm to obtain the leaf blade section. Then, five basic features are computed to further obtain six digital morphological features. These experimental results show that the graph cuts algorithm and the presented leaf features are important for leaf recognition.

Keywords Plant leaf · Graph cuts · Statistical features · Feature extraction

1 Introduction

There are about 250,000 species of flowering plants that have been named and classified on earth [1]. It is impossible for a man to know more than a tiny fraction of the total number of plants, which makes the further research difficult. So providing a computer plant identification system for the central management of plant data becomes very significant.

Although flower and fruit characters have proved very useful in both botany and paleobotany, these organs are not available for study. So, in spite of the success of Linnaeus's sexual system and its descendants, there is a great need to be able to

F. Lv
Jinhua Polytechnic, Jinhua 321007, China
e-mail: 213837053@qq.com; whj@zafue.edu.cn

H. Wang (✉)
Tianmu College, Zhejiang A&F University, Lin'an 311300, China
e-mail: whj@zafue.edu.cn

identify and classify dispersed leaves [2]. Leaf is one of the most important organs in a plant, also venation and contour features of plant leaves are important for the identification of plant species, the exploration of genetic relationship among plants, and the reconstruction of accurate surface models.

Classification of leaves can occur through many different designative schema, and the type of leaf is usually characteristic of a species, although some species produce more than one type of leaf. External leaf characteristics (such as shape, margin, hairs, etc.) are important for identifying plant species, and botanists have developed a rich terminology for describing leaf characteristics. These structures are a part of what makes leaves determinant; they grow and achieve a specific pattern and shape, then stop. Other plant parts like stems or roots are nondeterminant, and will usually continue to grow as long as they have the resources to do so [3, 4].

In the past decade, various approaches have been proposed for characterising plant leaves. For example, Baker used Digital image processing to estimate leaf area of Douglas-fir trees (*Pseudotsuga menziesii*) as a nondestructive technique in 1996 [5]. Chien developed an image processing algorithm using the elliptical Hough transform to determine position, orientation, and leaf area of seedling leaves from top-view images [6]. Four varieties of vegetable seedlings at various growth stages were used to test the efficacy of the measurement algorithm. Iwata investigated the inheritance of citrus leaf shape by analyzing a diallel set of crosses of five citrus varieties/selections by leaf contours extracted by image processing and described with elliptic Fourier descriptors [7]. The results indicate that elliptic Fourier descriptors can be successfully applied to the quantitative genetic analysis of citrus leaf shape.

These methods mostly concentrated on the contour representation for the recognition of the leaf, and typically this division is based on low level cues such as intensity, homogeneity, or contours. Four popular approaches based on such cues are threshold techniques, edge-based methods, region-based techniques, and connectivity preserving relaxation methods [8]. But these approaches' difficulty lies in formulating and including prior knowledge into the segmentation process. Segmentation by computing a minimal cut in a graph is a new and quite general approach for segmenting images in recent years. This approach guarantees global solutions, which always finds best solutions, and in addition these solutions are not depending on a good initialization.

As applied in computer vision, graph cuts can be employed to efficiently solve a wide variety of low-level computer vision problems, such as image smoothing, the stereo correspondence problem, and many other computer vision problems that can be formulated in terms of energy minimization. For example, Zhou [9] presents four technical components, i.e., color, texture information, structure tensors, and active contours, to improve graph cut-based algorithms, which are developed to tackle the problem of segmenting a foreground object out from its complex background. The integration of these components overcomes the difficulties in handling images containing textures or low contrast boundaries and producing a smooth and accurate segmentation boundary. Zheng [10] proposed a modified

localized graph cuts-based active contour models with a narrow band energy function to solve local segmentation in the presence of surrounding nearby clutter and intensity inhomogeneity. Yang [11] proposed a color-texture descriptor to enhance the effects of segmentation by integrating the compact multi-scale structure tensor (MSST), total variation (TV) flow, and the color information. Kim [12] presented an object segmentation method using a histogram-based graph cut algorithm with automatically generated label maps, which consists of three steps including, preprocessing, label map generation and update, and object segmentation.

In this paper, we present a new Min-Cut/Max Flow algorithm to improve the performance of standard augmenting path techniques on graphs in plant leaf statistical features extraction. Standard augmenting paths-based algorithms, such as the Dinic algorithm [13], work by pushing flow along nonsaturated paths from the source to the sink until the maximum flow in the graph G is reached. The new min-cut/max-flow algorithm belongs to the group of algorithms based on augmenting paths, which builds search trees for detecting augmenting paths [14]. Experimental results show that the graph cuts algorithm present a well segmentation performance in plant leaf. Moreover, segmentation results are the guarantee for further extracting statistical features of plant leaf accurately.

2 Image Segmentation with Graph Cuts

2.1 Background on Graph Cuts

A graph cut is the process of partitioning a directed or undirected graph into disjoint sets. Here, we define some terminologies that will be used in this paper for explaining the graph cuts-based image segmentation method.

A directed-weighted (capacitated) graph $G = (V, E)$ consists of a set of nodes V and a set of directed edges E that connect them, where $V = \{v_1, \dots, v_n\}$ corresponds to the image elements, which might represent pixels or regions in the Euclidean space. Each edge $(v_i, v_j) \in E$ has a corresponding weight $w(v_i, v_j)$ which measures a certain quantity based on the property between the two vertices connected by the edge. A graph usually contains some additional special nodes that are called terminals, which correspond to the set of labels that can be assigned to pixels in computer vision fields. If we concentrate on the case of graphs with two terminals, the terminals are usually called the *source*, s , and the *sink*, t . In Fig. 1a, we show a simple example of a two terminal graph on a 3×3 image with two labels.

Normally, there are two types of edges in the graph: n -links and t -links. n -links connect pairs of neighboring pixels. Thus, they represent a neighborhood system in the image. The cost of n -links corresponds to a penalty for discontinuity between the pixels. t -links connect pixels with terminals (labels). The cost of a t -link connecting a pixel and a terminal corresponds to a penalty for assigning the corresponding label to the pixel.

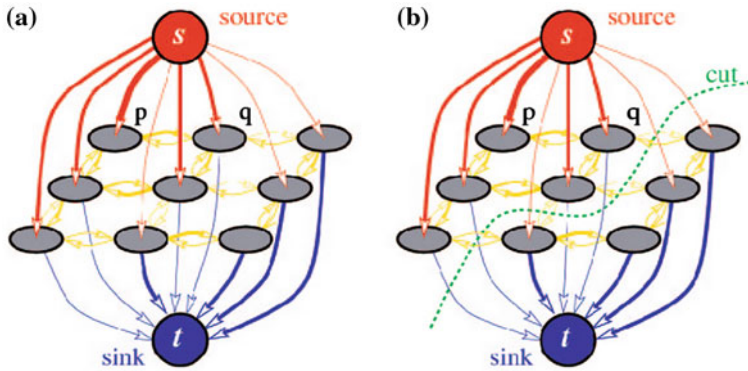


Fig. 1 Example of a directed capacitated graph. Edge costs are reflected by their thickness [14]. **a** A graph G . **b** A cut on G

2.2 Energy Function and Minimized Method

Image segmentation partitions an image into some mutually exclusive components, such that each component A is a connected graph $G' = (V', E')$, where $V' \subseteq V, E' \subseteq E$, and E' contains only edges built from the nodes of V' . This process can be performed with cuts associating energy to each cut. So these techniques finding energy minimizing cuts in graphs have received a lot of attention in the computer vision field.

Strategies for optimizing the energy functional can be various. For those defined on discrete set of variables, the combinatorial min-cut/max-flow graph cut algorithm [15] is a prominent one. Greig is the first to find out that powerful min-cut/max-flow algorithms can be used to minimize certain energy functions [16]. The energy function is defined by:

$$E(f) = \sum_{p \in P} D_p(f_p) + \sum_{(p,q) \in N} V_{p,q}(f_p, f_q) \tag{1}$$

where N is a set of all pairs of neighboring pixels. f_p is the label of the image pixel p . D_p measures how well label f_p fits pixel p given the observed data. $V_{p,q}$ is the boundary term for measuring the interaction potential.

The goal of this energy function is T find a labeling f that assigns each pixel $p \in P$ a label $f_p \in L$, i.e., fulfill the task of image task.

In this paper, we use the graph cut energy functional encodes both the constrains from user interaction and the regularization of the image smoothness under the MAP-MRF method of Greig et al. by incorporating additional contextual constraints into minimization of the Potts energy:

$$E(f) = \sum_{p \in P} D_p(f_p) + \sum_{(p,q) \in N} K_{(p,q)} \cdot T(f_p \neq f_q) \quad (2)$$

where, function T is 1 if the condition inside the parentheses is true and 0 otherwise. Suppose I is the observed image and I_p is the intensity observed at pixel $p \in P$. Then,

$$D_p(f_p) = \min\left(|f_p - I_p|^2, \text{const}\right) \quad (3)$$

Here, let the label f_p should be close to the observed intensity I_p . The parameter const is used to make the data penalty more robust against outliers, i.e., pixels which do not obey the assumed noise model. The algorithm is very stable with respect to const which simply helps to smooth out the few outlying pixels.

The intensities of pixels in the first image contain information that can significantly influence our assessment of disparities without even considering the second image. We can easily incorporate contextual information into the framework by allowing $K_{(p,q)}$ to vary depending on the intensities I_p and I_q . Let,

$$K_{(p,q)} = U(|I_p - I_q|) \quad (4)$$

Each $K_{(p,q)}$ represents a penalty for assigning different disparities to neighboring pixels p and q . In practice, Boykov [17] found the following simple function to work well:

$$U(|I_p - I_q|) = \begin{cases} 2u & \text{if } |I_p - I_q| \leq 5 \\ u & \text{if } |I_p - I_q| > 5 \end{cases} \quad (5)$$

where, u is the Potts model parameter in Eq. (1).

2.3 Features Extraction of Plant Leaf

For the study of plant leaf classification, we are concerned with the morphological characteristics, such as leaf shapes, leaf apex, leaf base, leaf margin, leaf lobes, leaf venation, etc. So it needs to define many leaf features to obtain these characteristics. In this paper, we first use five basic geometric features, physiological length, physiological width, area, perimeter, and diameter. Then, based on such five basic features, we can define six digital morphological features used for further leaf processing.

The five basic features are defined as follow:

- (1) Physiological length: The distance between the two terminals of the main vein of the leaf is defined as the physiological length, which is denoted as L_p .

- (2) Physiological width: The line passing through the two terminals of the main vein, one can plot infinite lines orthogonal to that line. The longest distance between points of those intersection pairs between those lines and the leaf margin is defined as the physiological width, which is denoted as W_p .
- (3) Area: The value of leaf area is easy to evaluate, just counting the number of pixels of foreground value on smoothed leaf image. It is denoted as A .
- (4) Perimeter: Leaf perimeter is calculated by counting the number of pixels consisting leaf margin, denoted as P .
- (5) Diameter: The diameter is defined as the longest distance between any two points on the margin of the leaf. It is denoted as D .

Based on the five-basic features introduced above, we can define six digital morphological features used for further processing.

- (1) Aspect ratio:

$$L_p/W_p \quad (6)$$

- (2) Form factor:

$$4\pi A/P^2 \quad (7)$$

- (3) Rectangularity:

$$L_p W_p/A \quad (8)$$

- (4) Narrow factor:

$$D/L_p \quad (9)$$

- (5) Perimeter ratio of diameter:

$$P/D \quad (10)$$

- (6) Perimeter ratio of physiological length and physiological width:

$$P/(L_p + W_p) \quad (11)$$

3 Experiments

A database containing many color leaf images with different leaf characteristics from 32 plant species in Hainault Forest Website, <http://www.hainaultforest.co.uk/> was used to conduct the experiments.

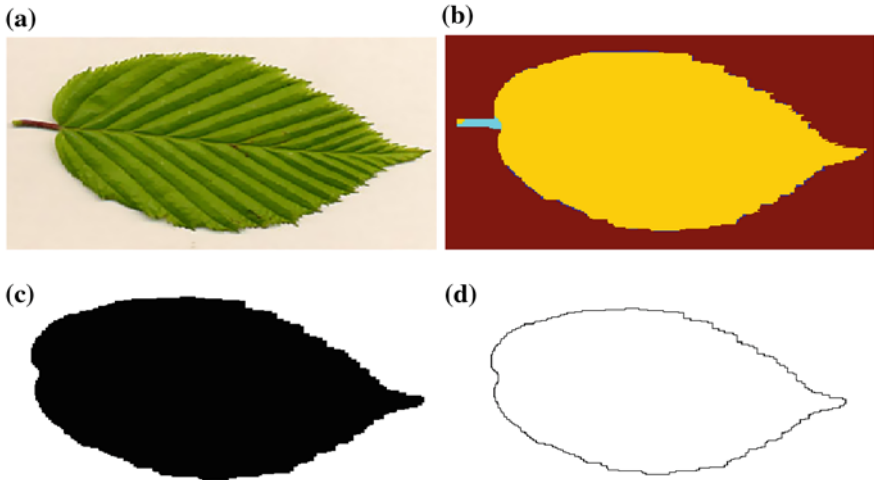


Fig. 2 Experiment results for plant species *Carpinus betulus*. **a** presents leaf image; **b** segmentation result with graph cuts; **c** blade section of the leaf; **d** edge of the blade (**c**)

Table 1 Five basic features

| Features | | Value |
|----------------------|-------|--------|
| Physiological length | L_p | 359 |
| Physiological width | W_p | 214 |
| Area | A | 55,214 |
| Perimeter | P | 1,180 |
| Diameter | D | 371 |

Table 2 Six morphological features

| Features | | Value |
|---|-------------------|--------|
| Aspect ratio | L_p / W_p | 1.6776 |
| Form factor | $4\pi A / P^2$ | 0.4983 |
| Rectangularity | $L_p W_p / A$ | 1.3914 |
| Narrow factor | D / L_p | 1.0334 |
| Perimeter ratio of diameter | P / D | 3.1806 |
| Perimeter ratio of physiological length and physiological width | $P / (L_p + W_p)$ | 2.0593 |

Here, we use the plant species *Carpinus betulus* as an example to illustrate our method's performance and the features extracted from this sample. The image segmentation is finished by graph cuts introduced in Sect. 2. The parameters used in energy function which is minimized via graph cuts are referred to the Kolmogorov's paper shown in [18]. The experiment results for *C. betulus* are demonstrated in Fig. 2. In this figure (a) presents leaf image; (b) segmentation result with graph cuts; (c) blade section of the leaf; (d) edge of the blade (c).

From Fig. 1, we can find that graph cuts have the capability to complete the segmentation task of plant leaf. In Fig. 1b shows that different color region represents different object, which are background, with reddish brown; blade with yellow; petiole with cyan. So, with graph cuts method, we can get all the components from leaf image. Thus, leaf features can be calculated from these components, such as physiological length, which is based on two terminals of the main vein of leaf.

After obtaining the segmented image, five basic features are computed, which are listed in Table 1. Based on five basic features, we can also easily compute the six digital morphological features defined in Sect. 2.3. These leaf features in Tables 1 and 2 can be used to form leaf characteristics, which are important for leaf recognition applications.

4 Conclusions

This paper introduces a graph cuts-based method using Min-Cut/Max Flow algorithm to obtain the leaf blade section. A good segmentation result is important for further extracting statistical features of plant leaf accurately, which is the premise of the identification of plant species.

As we know, providing a computer plant identification system for the management of plant data becomes very significant. However, automatic plant species recognition based on leaf is just a wish up to now. How to segment leaf components from various difficult backgrounds and what leaf features can represent plant species? There is still a lot of work waiting for us to accomplish.

Acknowledgment The work reported in this paper was supported by Jinhua Polytechnic under the research grant 2011S002, and the Talent Start-up Foundation of Zhejiang A&F University under grant No. 2013FR059.

References

1. Fu H, Chi Z (2006) Combined thresholding and neural network approach for vein pattern extraction from leaf images. *IEE Proc Vis Image Signal Process* 153:881–892
2. Daly DC, Hickey LJ, Johnson KR, Mitchell JD, Wilf P, Wing SL (2009) *Manual of leaf architecture*. CABI, Anderson

3. Du JX, Wang XF, Zhang GJ (2007) Leaf shape based plant species recognition. *Appl Math Comput* 185(2):883–893
4. Ye Y, Chen C, Li CT, Fu H, Chi Z (2004) A computerized plant species recognition system. In: *IEEE proceedings of 2004 international symposium on intelligent multimedia, video and speech processing*, 2004 pp 723–726
5. Baker B, Olszyk DM, Tingey D (1996) Digital image analysis to estimate leaf area. *J Plant Physiol* 148:530–535
6. Chien CF, Lin TT (2002) Leaf area measurement of selected vegetable seedlings using elliptical Hough transform. *Trans ASAE* 45(5):1669–1677
7. Hiroyoshi I, Hirohisa N, Seishi N (2002) Diallel analysis of leaf shape variations of citrus varieties based on elliptic Fourier descriptors. *Breed Sci* 52:89–94
8. Eriksson AP, Barr O, Astrom K (2006) Image segmentation using minimal graph cuts. Published at: Swedish symposium on image. <http://www.maths.lth.se/vision/publdb/reports/pdf/eriksson-barretal-ssia-06.pdf>
9. Zhou H, Zheng J, Wei L (2013) Texture aware image segmentation using graph cuts and active contours. *Pattern Recogn* 46(6):1719–1733
10. Zheng Q, Dong E, Cao Z, Sun W, Li Z (2013) Modified localized graph cuts based active contour model for local segmentation with surrounding nearby clutter and intensity inhomogeneity. *Signal Process* 93(4):961–966
11. Yang Y, Han S, Wang T, Tao W, Tai X (2013) Multilayer graph cuts based unsupervised color-texture image segmentation using multivariate mixed student's t-distribution and regional credibility merging. *Pattern Recogn* 46(4):1101–1124
12. Kim D, Paik J (2012) Automatic moving object segmentation using histogram-based graph cut and label maps. *Electron Lett* 48(19):1198–1199
13. Dinic EA (1970) Algorithm for solution of a problem of maximum flow in networks with power estimation. *Soviet Math Dokl* 11:1277–1280
14. Yuri B, Vladimir K (2004) An experimental comparison of min-cut/max-flow Algorithms for energy minimization in vision. *IEEE Trans Pattern Anal Mach Intell* 26(9):1124–1137
15. Boykov Y, Gareth FL (2006) Graph cuts and efficient N-D image segmentation. *Int J Comput Vision* 70(2):109–131
16. Peng B, Zhang L, Zhang D (2013) A survey of graph theoretical approaches to image segmentation. *Pattern Recogn* 46(3):1020–1038
17. Yuri B, Olga V, Ramin Z (2001) Efficient approximate energy minimization via graph Cuts. *IEEE Trans PAMI* 20(12):1222–1239
18. Vladimir K, Ramin Z (2004) What energy functions can be minimized via graph cuts? *IEEE Trans Pattern Anal Mach Intell* 26(2):147–159

Research on Integration of 3D Digital Definition for Marine Diesel Engine Parts

Hui Zhang, Ge Yang and Sheng-wen Zhang

Abstract Integration method of expressing and exchanging information based on 3D digital definition is proposed for design and manufacturing of marine diesel parts in order to address the inconvenience of information presentation and obstruction of message delivery in currently 3D modeling and 2D drawing combination way. To express the design intent such as geometrical dimension and tolerance in integrated model, annotations are attached which will be employed to plan the routine, and to set the technical parameters during process planning. Process models with saved attributes and values are adopted for presentation and visualization of process planning courses. To handle complication of notes and overlapping of figures because of complex of marine diesel parts, view set classification is processed to manage the intricate information so that details can be presented completely exactly and reasonably. On the NX software platform, internal storage data format and symbolic demonstration mappings are analyzed for extraction of information, and secondary development are implemented to offer ways of information application usage. At last, the integrated 3D digital definition and application of marine diesel engine parts are realized.

Keywords Digital definition · Integration · Marine diesel parts

1 Introduction

Nowadays, in the processing of marine diesel engine parts, the product definition information is expressed by 2D drawing and 3D models together. The parts are designed in 3D model, but the conventional 2D engineering drawings are still the

H. Zhang (✉) · G. Yang · S. Zhang
School of Mechanical Engineering, Jiangsu University of Science and Technology,
Zhenjiang, China
e-mail: zimmerman532@yahoo.com

main manufacturing basis. This 3D modeling combined with 2D drawing mode is a great obstruction for efficiency improvement of factory production [1], which causes the inconvenience of information presentation and delay of message delivery and thus strongly affects the benefits of the company.

The marine diesel parts are fairly shape complex and has great impact on the engine's function performance, so high manufacturing standards are required [2]. Engineering drawings are inefficient for conveying such complex shapes and many redundant drawings are needed to express one single part. In such condition, the design information is pro to error. Considering, 3D modeling with 2D drawing are not quite fit for the design and manufacturing of marine diesel engine parts because that parts' information transmission are involuntarily broken and thus are not passing fluently through the entire manufacture workflow.

A new design and manufacturing pattern focusing on the integration and complexity of the marine diesel engine parts are proposed, which utilizes one single software platform for integrated 3D design with modeling and process planning. CAD and CAPP are merged together, and model modification demands can be delivered seamlessly, thus integration degree is quite high. Product information such as design intent, process planning, detailed parameters, are all based on 3D digital modeling with annotations attached.

To handle complication of notes and overlapping of figures because of complex of these parts, view set classification is processed to manage the intricate information so that details can be presented completely, exactly, and reasonably. Digital data and normal GB figures correspondence are also analyzed to study the 3D digital information extraction. At last, NX secondary development are done to demonstrate the capability to join the scattered information and to simple the complicated operation and thus decrease the high requirement of operators [3].

2 3D Digital Definition of Marine Diesel Parts

3D Digital Definition is basically Model-Based Definition (MBD) which uses the integrated 3D models to completely express the product definition information. The expression method and labeling rule of all Product Manufacturing Information (PMI) such as dimension, tolerance, and manufacturing requirement has been provided in detail [4–6]. In MBD, 3D models became the sole manufacturing basis, and changed the traditional method that takes the engineering drawing as main manufacture basis but 3D models as auxiliary only. Full 3D geometric information and nongeometric information expression method are studied with respect to MBD standards, i.e., ASME Y14.41 and GB/T 24734, and view set classification are proposed to organize and manage the related information.

2.1 Detailed 3D Representation of Marine Diesel Parts

For this research, cylinder cover, one of the most typical parts of the marine diesel engine is utilized for analyzing the validation and efficacy of our approach. Cylinder cover is complicated for its working condition of multi liquid fluid medium, structural intricacy of complex geometry boundary and combustion space surrounded by base plane, piston top, and cylinder inwall, so it is quite mistakable on engineering drawings.

2.2 “Feature”-Based Modularization of Definition

Because of the complication of cylinder cover, group technology discipline is used for modularization and unitization of the same or similar areas on the design model to simplify the definition, and these areas are defined as various sorts of features. These features' definition includes geometric shape and nongeometric information, and are packaged and expressed as a whole. They can be displayed as columns of features with tags and attributes in the 3D modelling software platform. While being used for CAD stages, definitions are only needed once by operators, and then features can be used anywhere for the same type without being sectioned or annotated. So the trivial and time-consuming detailed definition work only needed to be done onetime. This method is quite effective for complicated parts with many duplicate features on it.

2.3 Information Management

Cylinder cover has many geometric and nongeometric information for its complexity, and if they are all annotated and shown together, tremendous symbolic and lines are displayed on the computer's limited desktop, and causes inconvenience and visual confusion. So Information organization and management are required. In this research, View set classification is proposed for managing different kinds of information. Model viewing is provided by most CAD modeling software. In our view classification, views are categorized according one specific rules, i.e., different PMI types such as dimension and tolerance, or usage such as milling and lathing et al. During CAD phase, necessary views are appended. The application not only can be adopted in CAD's attribute classification, but also be used in CAPP's stages. During process planning, different working steps and areas can be described. The classification is illustrated in Fig. 1.

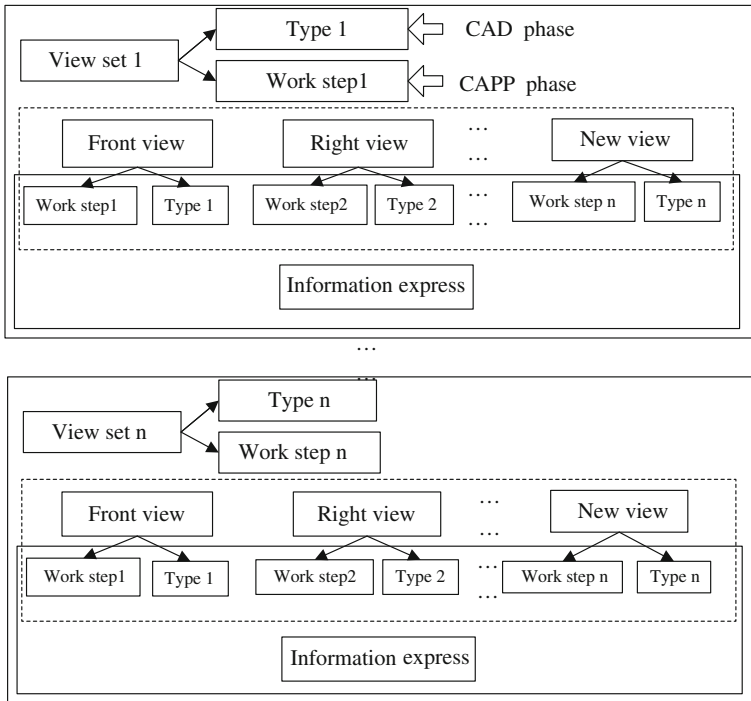


Fig. 1 Different stages and different types of full 3D information management by view set

3 3D Process Modeling and Application

In the traditional 2D process planning, products' information coordination within is rather low level, the parts' process models' dimension, tolerance, and roughness, etc., are not effectively associated with CAD models and sometimes even not connected with them. While process planning, the CAD 3D models are first transmitted and exported to another data formation, e.g., lightweight model, and then handled in another specific process planning software. This work line costs many efforts. In our full 3D product definition, 3D modeling are used as the sole carrier of product information including process modeling. So the features and parameters can all be utilized for engineering procedure establishment. And the integration is enhanced and efficacy is improved. The details are illustrated in Fig. 2.

The cylinder cover digital modeling is on NX software platform, and so does the 3D process planning. There is no need to consider the compatibility of engineering procedure determination and process planning with main design platform according with the integration discipline of design and fabrication [7]. Association technology is used, and associated copy of geometry is carried out to build in process models and to simulate the real working procedure. So the overall information association can be ensured to unify the one data source.

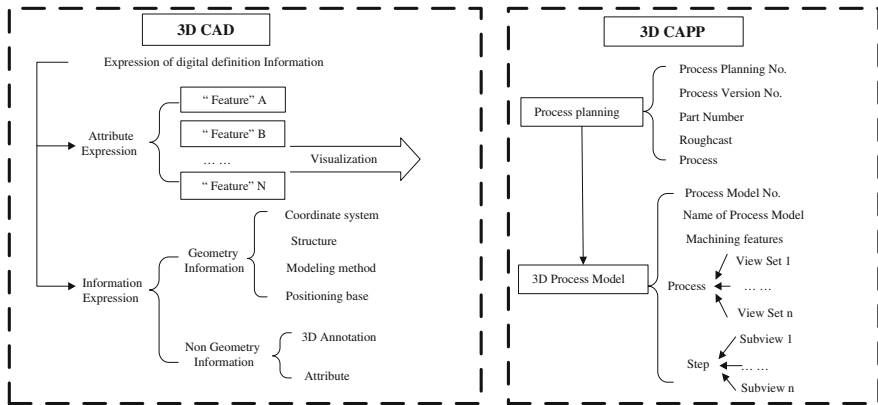


Fig. 2 Design and process integration block diagram

4 Implementation and Application

All our implementations are based on NX software.

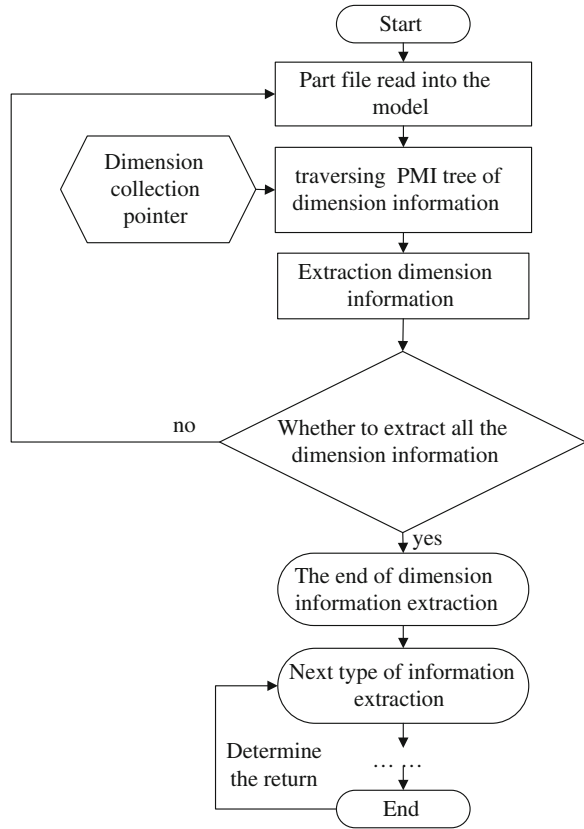
4.1 Information Extraction

So the overall information association can be ensured to unify the one data source. The PMI information extraction is based on NX/Open secondary development with C++ language. The detailed procedure is described as follows: read the cylinder cover parts, initialization the PMI collection, define and set the iterate, traverse through the PMI structure, main dimension, tolerance, and attached notes can all be collected. The extraction flow path of dimension is illustrated in Fig. 3. Other kinds of PMI are the same.

4.2 Implementation of PMI Feature

Definition of 3D digital model can be realized by information representation method called attribute expression way, different kind of PMI information can be annotated by different kind of attributes. The associated feature or geometry is connected, detailed parameters can be stored by attribute values for further manufacturing. By secondary development, annotation class related functions are fully exploited, the legacy UG/Open tag can also be used. The one typical extraction result of cylinder cover is demonstrated in Fig. 4. The diameter dimension together with form and position tolerance are extracted with respect to structural trees and 3D models.

Fig. 3 Process of information extraction



4.3 The Mapping Relationship of Internally Store Information and Graphical Information on NX Software

Because of information extraction based on three-dimensional modeling software platform, three-dimensional marked symbols have their special storage format, The NX platform identify such format and then turning into engineering drawing logo which displayed on the full three-dimensional model. The mapping relationship of internal storage symbol information and display symbol information that exists. For example: insert the diameter symbol φ and $S\varphi$, the, respective, contents of the internal stored are: $\langle O \rangle$ and $S \langle O \rangle$. This leads to the result of extract information content is stored internally, so establish a mapping mechanism is needed. The other symbols Mapping situation are as shown in Table 1.

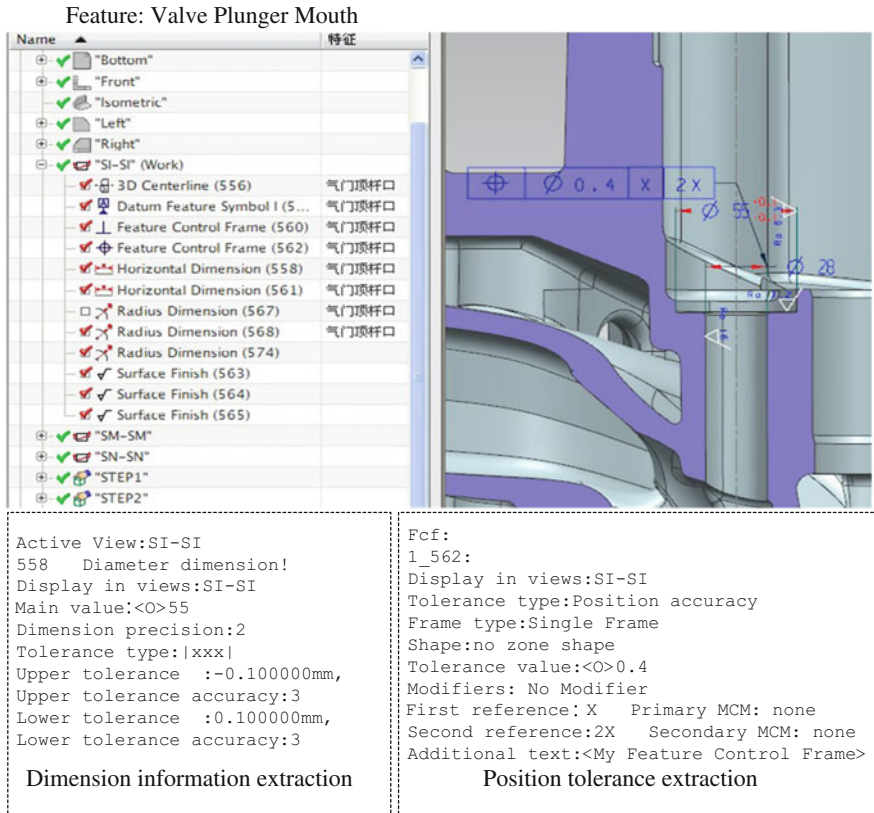


Fig. 4 Feature-based information extraction

Table 1 The mapping relationship between storage symbol and graphical

| Symbolic name | Countersink | Countersunk hole | Depth | Slope | Square | Between insert | Insert ohm |
|---------------------|-------------|------------------|-------|-------|--------|----------------|------------|
| NX symbol | ∇ | ⌋ | ↪ | ∠ | □ | ↔ | Ω |
| Mapping information | <#C> | <#B> | <#D> | <#G> | <#F> | <#h> | <\$2> |

4.4 Application

Based on the previous research, application on full 3D digital definition for cylinder cover is developed. The work flow and interface is illustrated in Fig. 5. First, digital definition is carried out by NX software modeling and PMI annotation for geometric and nongeometric information. The notes and attributes are attached,

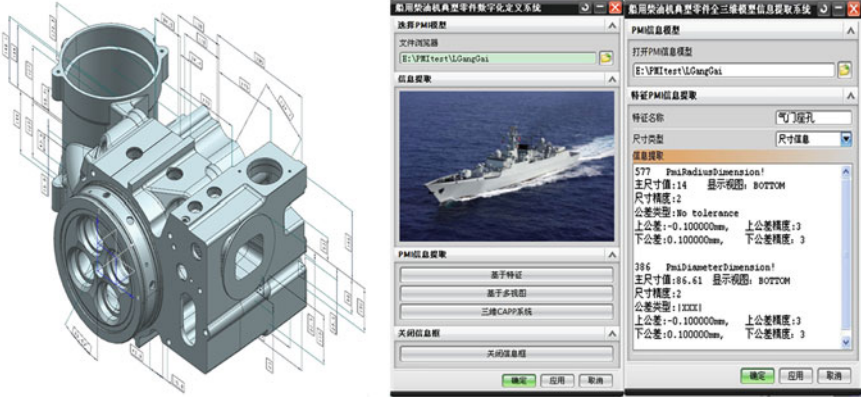


Fig. 5 Interface of the system operation

with notes classified by different annotation planes and different view sets, attributes by wrapped features. Then information are extracted and design intents are identified for process planning, and the necessary detail information can be obtained by operator’s selection. Then they can be output to be further used in following CAPP and CAM phases.

5 Conclusion

Full 3D product definition is a research focus, in which the one data source information and obtainment is the bottleneck. For the complexity of marine diesel engine parts, attributes, and notes are attached to the 3D model during CAD phase, to build the full definition without engineering drawings. And this 3D model serves as the only one information carrier through the entire design and manufacture workflow. All CAD and CAPP work can be done in one software platform and high integration can be achieved. Feature definition and view set classification are proposed to organize and manage the complicated product information. The information extraction is also fully exploited. The automation can be improved by our approach. And as a exploration of MBD application in shipping industry [8], it has great application prospect, and can be spread out. The 3D digital definition application for CAM will be our following research emphasis and direction.

References

1. Shao-fei J, Shuang-xia P, Pei-en F, You-Zhong X (2002) Description of feature combinations of part and its application for CAD/CAPP integration. *J Comput Aid Des Comput Graph* 14:795–800
2. Sheng-wen Z, Yu-ling D, Gui-cheng W, Chang-qi Y, Wei J (2011) CAD/CAPP/CAM integration system for frame parts of marine diesel. *Comput Integr Manuf Syst* 17:760–766
3. Ling X, Sheng-wen Z, Cheng-shun Z, Xi-feng F (2012) Research on processing technology and NC programming technology of marine propeller. *Ship Eng* 34:47–49/66
4. Ersan A, Ulvi S, Nedim A (1999) Data extraction from CAD model for rotational parts to be machined at turning centres. *Turk J Eng Environ Sci* 23:339–347
5. Hu L, Shuang H, Yu-qing F (2008) Model based digital definition technology. *Aeronaut Manuf Technol* 3:78–81
6. Virgilio Q, Louis R, Robert P, Frederick V, Fawzi K (2010) Will model-based definition replace engineering drawings throughout the product lifecycle? A global perspective from aerospace industry. *Comput Ind* 61:497–508
7. Bley H, Franke C (2004) Integration of product design and assembly planning in the digital factory. *CIRP Ann Manuf Technol* 53:25–30
8. Sheng-wen Z, Liang Z, Xi-feng F, Wei J (2008) Research on NC programming technology for complex components of marine diesel. *Ship Build China* 49:66–72

The Temperature Control of Laser Thermal Desorption System Based on Parameters Self-Tuning Fuzzy PID Algorithm

Buyun Wang, Linna Ma, Xiaoyan Liu and Jianguang Zhou

Abstract In view of the high-power laser could make the temperature rise on the samples, this paper proposes a controller based on parameters self-tuning fuzzy PID algorithm. The controller can be not only applied to the single control object based on Fuzzy empirical formula according to the PID parameters online correcting, but also can effectively deal with the temperature control model of LTDS uncertainly, nonlinear, time-varying, hysteresis, and so on. And in this paper, we make a simulation comparative experiment between the traditional PID control and the fuzzy adaptive PID control by using Matlab Simulink toolbox. The experiment result shows that fuzzy adaptive PID is better than the traditional control algorithm on overshoot, settling time and other performance indicators, and it can effectively improve control accuracy of the temperature control system.

Keywords Laser thermal desorption system · Temperature control · Fuzzy adaptive PID controller · MATLAB simulation

1 Introduction

Laser beam in the laser thermal desorption system (LTDS) is highly concentrated relying on electric energy, and in the process it can generate prodigious amounts of heat rapidly. Due to the nonlinearity, time-varying, and hysteresis quality of the temperature control system, it is impossible to establish a precise mathematical model, and then the control effect of the conventional PID control algorithm is difficult to achieve the ideal effect. However, compared with the traditional PID,

B. Wang · L. Ma · X. Liu · J. Zhou (✉)
Institute of Cyber-Systems and Control, Zhejiang University, Hangzhou, China
e-mail: jgzhou@zju.edu.cn

B. Wang
e-mail: dylan0120@vip.qq.com

fuzzy adaptive PID algorithm has the advantages of fast response speed, small overshoot, strong anti-interference ability, and good control performance. Fuzzy adaptive control does not need to establish accurate mathematical model because it could make use of fuzzy logic reasoning to complete the control decision process by utilizing the fuzzy rule base, which is set up based on expert knowledge and the experience of the operator [1]. Allow for temperature is the main monitoring parameter for LTDS, the fuzzy adaptive PID controller that is designed in this paper can respond and adapt to all kinds of complicated situations in the most effective way (Fig. 1).

Aiming at the high requirements of stability and reliability to the LTDS, this article puts to use infrared temperature sensor and signal conditioning circuit with high sensitivity, stc12c5a60s2 to complete the A/D conversion function and the improved parameters self-tuning fuzzy PID algorithm to guaranteed the performance index of the system.

2 Design of Fuzzy Adaptive PID Controller

The nature of the fuzzy adaptive PID controller is online adjustment of the PID controller parameters according to the fuzzy control rule. We can see from Fig. 2, the error (E) and the rate of change of error (EC) are input variables, ΔK_p , ΔK_i and ΔK_d are output variables [2, 3]. Fuzzy subsets of variables in this article are all {negative big, negative middle, negative small, zero, positive small, positive middle, positive big} ({NB, NM, NS, ZO, PS, PM, PB} for short) and are taken $[-6, 6]$ as basic range. We choose Gaussian functions to define membership functions of input variables, while triangle functions are selected to the output variables.

The tuning principle of PID control parameters [4–6]:

- (1) The effect of coefficient of proportionality K_p is to accelerate the response speed and improve system regulation accuracy. With the increasing of K_p , the system will show a faster response speed, higher regulation accuracy, however it is easy to arouse overshoot even lead to instability. While it will reduce the regulation accuracy and slower the response speed so that the deterioration of the system performance if K_p is too little.
- (2) The integral coefficient K_i is used for eliminating steady-state error. The greater K_i is, the faster steady-state error elimination rate is. Yet the response process will produce integral saturation phenomenon and then turn up a large overshoot when K_i is too large.
- (3) The differential coefficient K_d plays an important role in improving the dynamic characteristics of the system. However, the oversize of given quantity could lead to extending regulation time and the decline of system anti-interference ability.

According to the above rules and expert's knowledge, we can draw the control rules of fuzzy controller as given in Tables 1, 2, and 3.

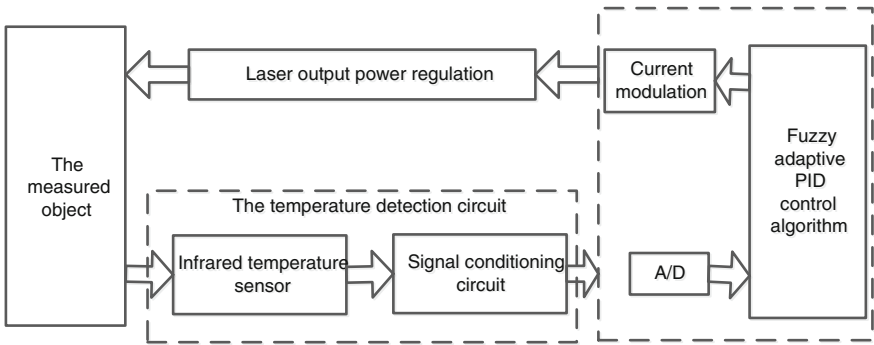


Fig. 1 Block diagram of laser thermal desorption system (LTDS)

Fig. 2 Principle diagram of fuzzy adaptive PID

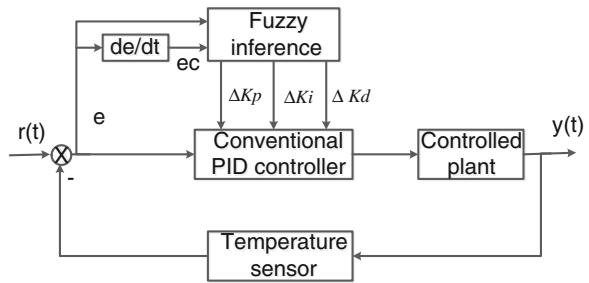


Table 1 Fuzzy control rules for ΔKp

| ΔKp | EC | | | | | | |
|-------------|----|----|----|----|----|----|----|
| | NB | NM | NS | ZO | PS | PM | PB |
| E | NB | NM | NS | ZO | PS | PM | PB |
| NB | PB | PB | PM | PM | PS | ZO | ZO |
| NM | PB | PB | PM | PS | PS | ZO | NS |
| NS | PM | PM | PM | PS | ZO | NS | NS |
| ZO | PM | PM | PS | ZO | NS | NM | NM |
| PS | PS | PS | ZO | NS | NS | NM | NM |
| PM | PS | ZO | NS | NM | NM | NM | NB |
| PB | ZO | ZO | NM | NM | NM | NB | NB |

Through the fuzzy inference and centroid method for defuzzification operation, three parameters of the controller are obtained as below:

$$Kp = Kp0 + \Delta Kp \tag{1}$$

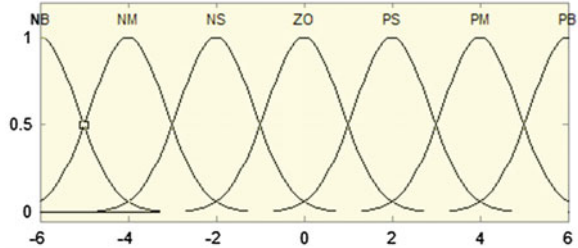
Table 2 Fuzzy control rules for ΔKi

| ΔKi | EC | | | | | | |
|-------------|----|----|----|----|----|----|----|
| E | NB | NM | NS | ZO | PS | PM | PB |
| NB | NB | NB | NM | NM | NS | ZO | ZO |
| NM | NB | NB | NM | NS | NS | ZO | ZO |
| NS | NB | NM | NS | NS | ZO | PS | PS |
| ZO | NM | NM | NS | ZO | PS | PM | PM |
| PS | NM | NS | ZO | PS | PS | PM | PB |
| PM | ZO | ZO | PS | PS | PM | PB | PB |
| PB | ZO | ZO | PS | PM | PM | PB | PB |

Table 3 Fuzzy control rules for ΔKd

| ΔKd | EC | | | | | | |
|-------------|----|----|----|----|----|----|----|
| E | NB | NM | NS | ZO | PS | PM | PB |
| NB | PS | NS | NB | NB | NB | NM | PS |
| NM | PS | NS | NB | NM | NM | NS | ZO |
| NS | ZO | NS | NM | NM | NS | NS | ZO |
| ZO | ZO | NS | NS | NS | NS | NS | ZO |
| PS | ZO | ZO | ZO | ZO | ZO | ZO | ZO |
| PM | PB | NS | PS | PS | PS | PS | PB |
| PB | PB | PM | PM | PM | PS | PS | PB |

Fig. 3 Membership function diagram of input variables (E , EC)



$$Ki = Ki0 + \Delta Ki \tag{2}$$

$$Kd = Kd0 + \Delta Kd \tag{3}$$

In the formula (1)–(3), $Kp0$, $Ki0$, and $Kd0$ are all initial value set in advance (Figs. 3, 4).

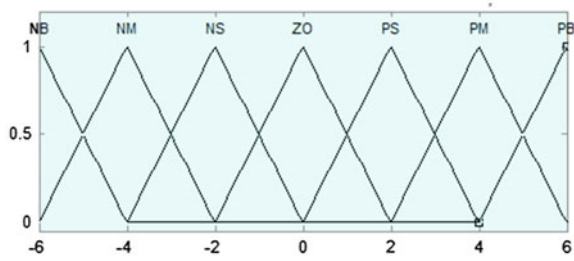


Fig. 4 Membership function diagram of output variable (ΔK_p , ΔK_i , ΔK_d)

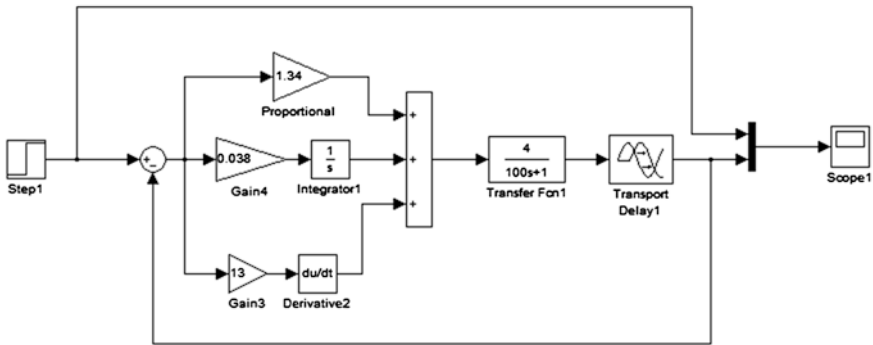


Fig. 5 Simulation structure diagram of conventional PID

3 Simulation

Considering that it is difficult to obtain data in real system experiments due to the special nature of LTDS, using MATLAB on the fuzzy adaptive control system simulation is helpful to real-time testing and debugging. Simulations of the control system including the traditional PID controller have been carried out in MATLAB environment [7, 8]. The simulation structure diagrams are shown in Figs. 5 and 6.

The simulation results are shown in Figs. 7 and 8. Figure 7 shows response curve of conventional PID control system, while Fig. 8 shows response curve of parameters self-tuning fuzzy PID control system.

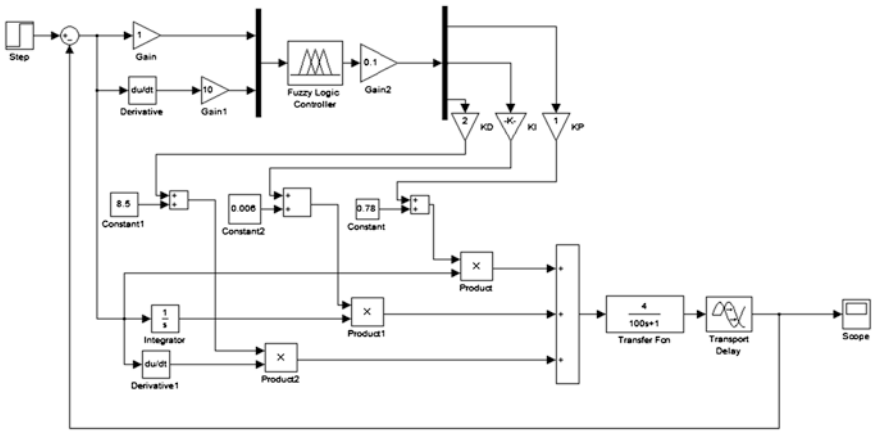


Fig. 6 Simulation structure diagram of fuzzy adaptive PID

Fig. 7 Response curve of conventional PID system

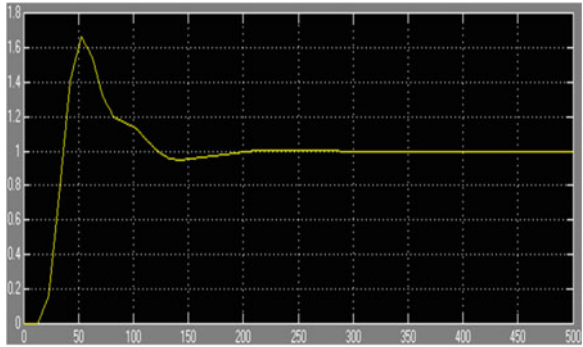
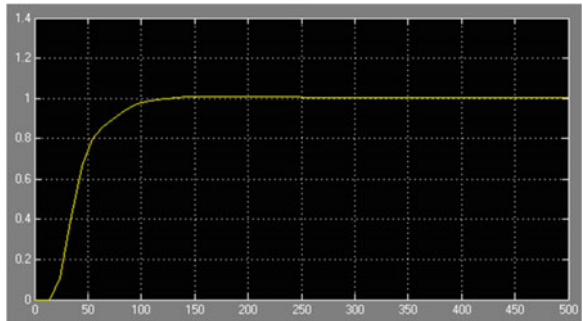


Fig. 8 Response curve of fuzzy adaptive PID control system



4 Conclusions

This preliminary study indicates that the dynamic quality and stability of the control system is improved largely when the fuzzy adaptive controller is introduced. The application of fuzzy adaptive controller in LTDS makes the shortening of the settling time and disappearance of system overshoot. Therefore, parameters self-tuning fuzzy PID controller proposed in this paper would meet the requirements more efficiently.

References

1. Xianqiang Z, Lianwu G, Tingjun W (2012) Application of fuzzy PID control in a stable circuit on a platform. *Appl Sci Technol* 39(6):14–17
2. Feng H, Yuefeng Y, Jun G, Bing Z (2004) Design and simulation study of fuzzy parameter self-tuning PID controller. *Opt Precis Eng* 12(2):235–239
3. Huijun W, Youde L (2011) Designed fuzzy PID controller of EPS assistance system. *Manuf Autom* 33(2):34–36
4. Xiaolong D, Jianlin Z, Jinjun L, Jing C, Lulin Y (2011) Research and application of air conditioning system in textile industry based on fuzzy PID. *Chin J Sci Instrum* 32(4):763–768
5. Jianwei W, Lixin T (2012) Design and simulation of temperature control system based on Fuzzy Adaptive PID control. *J Hefei Norm Univ* 30(6):35–37
6. Guomin S, Maoyang H, Xiaohua J, Zhaozhen L (2005) Feed-forward pressure control of common rail system based on parameters self-tuning fuzzy PID algorithm. *J Southeast Univ (National Science Edition)* 35(3):465–468
7. Lin M, Jianhua W (2013) Research on fuzzy PID controller based on Matlab. *Mod Electr Tech* 36(3):165–167
8. Zaihua W, Lijun M (2007) Intelligent house fuzzy temperature control system designation and simulation based on matlab. *Journal of Dezhou University* 23(4):81–84

Stock Market Forecast Based on RBF Neural Network

Teng Ji, Wengang Che and Nana Zong

Abstract The stock market is an investment market that is full of risk and return, to obtain higher benefits while reducing the risk of investors is the pursuit of the goal, the radial basis function network with its simple structure, excellent global approximation properties to arouse the wide attention of scholars. This paper is based on RBF neural network, through the examples of the empirical analysis; the results show that, the network has good learning and generalization ability, and achieved good results in the stock market trend prediction.

Keywords Outlier · Financial data · Artificial neural network · RBF algorithm · Stock prediction

1 Introduction

With the ceaseless development of the stock market in our country, stock investment has become an important part in people's daily life. Research on stock price trend of listing corporation and prediction of a company's stock price, not only has a very attractive application value, but also has the theoretical significance, and it is concerned by investors and academic community. The financial data are usually highly noisy and contain outliers. And efficient markets hypothesis demonstrates that the market prices fully reflect all available information. After the birth of the stock market, some people continue to use various way to study the laws of the stock market, and predict the stock market's future trend. The research of the stock market price fluctuation helps to reveal the financial market operation rules for portfolio selection, asset pricing, financial futures and options, and other

T. Ji (✉) · W. Che · N. Zong

Key Laboratory of Computer Technology Application of Yunnan Province, Kunming University of Science and Technology, Kunming, People's Republic of China
e-mail: jiteng1028@163.com

financial derivatives pricing, and risk management provides theoretical basis. Stock forecasting theory and methods emerge in an endless stream, and these prediction methods reveal the stock market operation rules to a certain extent, but the complexity of internal structure and the changing of external factors decided the variability of the stock market; the methods of analysis and prediction of the effect is not ideal [5]. The neural network has good nonlinear characteristic; it is especially suitable for nonlinear processing, so the neural network is an effective method of nonlinear prediction of stock market [3]. Artificial neural network for forecasting stock is getting more and more attention, especially the ability of robust nonlinear mapping and self-learning of the artificial neural network, not as time series prediction based on subjective setting model; therefore, it is very practical in financial time series forecasting.

This paper is based on composite index closing point each trading day of the last year, with the daily closing price as samples, the help of the computer language MATLAB tools, and the establishment of a radial basis function neural network, and then forecast.

2 The Basic Theory of Artificial Neural Network

2.1 Introduction of Artificial Neural Network

Artificial neural network. Nerve network that is widely interconnected by a large number of processing units is the human abstract, simplification, and simulation, reflect the human basic properties [2]. Artificial neural network is obtained from studies of human physiological structure to study human intelligent behavior, simulation of brain information processing function. Artificial neural network is composed of simple processing units that comprised a large number of parallel distributed processors; the processors have characteristics of memory and experience knowledge of the natural. The similarities of it and human are summarized as two respects: one is through the learning of process that the information of the knowledge to access knowledge from external environment; two is the internal neurons (synaptic weights) is used to store the access to knowledge and information.

From the basic model of the neural network, the main types are: feed-forward, feedback, self-organization, and random network. In recent years, due to the combination of fuzzy analysis, wavelet theory and neural network, so the formation of a fuzzy neural network and wavelet neural network [10].

2.2 BP Neural Network

Because of the good approximation, the error back propagation (Error Back Propagation) network is used most widely. BP neural network is a kind of having three layers or more than three layers structure without feedback, and connection to the network. Each layer contains one or more neurons, with total interconnection modes, that the unit of each lower connected the unit of each upper, and the neurons that exist in the same layer do not connect with each other, the adjacent layers of neurons connect each neuron with adjustable weights, and there is no feedback of each neurons [7]. The information from the input layer transfers to the hidden layer, until the output layer. Each neuron weighted and integrated all or part of its input, and according to the form of the activation function of the form to generate a corresponding output. Training is from a starting point along the error function of the inclined plane, and gradually achieves the least error, while the network error surface is high dimensional rough error curve, and therefore, in the process of learning might fall into a local minima. So BP neural network has some limitations.

2.3 Radial Basis Function

Radial Basis Function neural network is composed of a kind of input layer and output layer. RBF neural network approximates a linear combination of arbitrary function that is composed of a group of orthogonal and normalized radial basis function. Nonlinear transform from input layer to the hidden layer by radial basis function as nonlinear transform, whereas the hidden unit to the output space is a linear map, therefore the output layer weights adjustment can be directly calculated by linear programming equation, greatly accelerate the learning speed, avoid the local minima problem. The fitting plane of a basis function, which is composed of each of the network hidden layer neuron transfer function, the network named after that. RBF network is not only fast convergence, but also has small fitting error. The hidden layer activation function of the BP network is the overall situation; if we want to further improve the fitting precision, there is need to increase the number of hidden layer units or select more than one hidden layer structure of the network, but that is very easily lead to fit the local oscillation. It can approximate any continuous function with arbitrary precision, especially for solving classification problems [12]. This paper use RBF neural network to the prediction of market index.

3 Theory of Radial Basis Function Neural Network

Radial basis function network is presented on the basis of biological local regulation and overlapping receptive field knowledge, and it is in reference of a localized receptive fields to perform the function mapping artificial neural network. The RBF has the best approximation and global approximation properties. It has been confirmed that the RBF radial basis network could approximate any continuous function with any precision, RBF neural network structure diagram as shown in figure. RBF neural network is a kind of feed-forward neural network, which is composed of input layer, layer, and output layer [9]. The weight of the RBF network train from a layer to a layer. It use unsupervised training on radial base weight training, and design the algorithm of the error correction of the output layer weights. In RBF network, the function of the input layer to the hidden layer is a kind of nonlinear mapping, and the output is linear [14]. So RBF networks can be considered as the original nonlinear separable feature space, which is transformed into a linear separable space, through the reasonable selection of the transformation in the new central issue linearly separable space, then use a linear unit to solve the problem, thus easily reach from the nonlinear input output space to space mapping purposes. It is worth pointing out, since the RBF network weights algorithm is a single layer, the working principle of it is the using of clustering function. The RBF network is a network of local approximation, which makes it faster than BP network from 2 to 3 orders of magnitude faster.

The inputs of the network is (x_1, x_2, \dots, x_m) . The outputs of the network is (y_1, y_2, \dots, y_p) . The I neurons inputs of the hidden layer is: $K_i = \sqrt{\sum_j (w_{1ji} - x_j)^2} \times b_i, j = 1, 2, \dots, m, i = 1, 2, \dots, n$, w_{1ji} is the weights of the j input neurons into the I hidden layer neuron. x_j is the vector of the j , b_i is the threshold of the i hidden layer neuron.

The I neurons output of hidden layer :

$$R_{il} = \exp\left(\frac{-0.8326^2 \times \sum_j (w_{1ji} - x_j)^2}{c_i^2}\right).$$

The parameter c (called the extended constant) to regulate the sensitivity of the function, the relationship of b and c is: 6 in $c = 0.832/b$, the size of c reflects the response width. The value of c is increasingly big, neurons asked smoothness is better. The output layer activation function for the pure linear function. So the output layer neurons output:

$$y_l = \sum_i R_{il} w_{2il}, (i = 1, 2, \dots, n; l = 1, 2, \dots, p)$$

According to the known input and the corresponding target and the known extended constant c , repeated training network until satisfying error request, obtains two finally, weights, in theory. The nonlinear mapping relationship can approximate any continuous nonlinear function.

4 The Prediction of Stock Price Using RBF Neural Network

4.1 Stock Price Prediction with MATLAB

In the stock market, a lot of factors influence the stock price, and also the index of the changes of stock market. In order to forecast stock price directly, using the stock's closing price as learning data samples and predicting object.

Assuming that a time series $x = \{x_i | x_i \in R, i = 1, 2, \dots, L\}$, now through the sequence of the first m values predict P time value. A division of data (see Table 1) for each sample of the former m values as input of RBF neural network, P value as the target output. Through learning from the R^m to the R^p output space mapping so as to achieve the purpose of time series prediction.

4.2 Build a Network Model

Chose the sample data. From November 5, 2010 to November 5, 2011 index of SSE Composite Index as the sample data.

Data preprocessing. In order to improve the accuracy of RBF network, the data are normalized, all data linearly mapped to $(-1, 1)$.

Establish RBF network and training. The 10 trading days of data as the input of the network, after 10 trading days as output data, received a total of 24 sets of training data (Fig. 1).

Validation of the prediction data. The test data will be input into the trained network. Get the forecasting results, and compare with the real data. According to the degree of fitting and the computation time to adjust the spread value of the network parameters [4]. To obtain better effect and performance. Fitting degree chooses the average prediction error measure:

$$\text{MEE} = \frac{1}{n} \sum_n \frac{|p_n - r_n|}{r_n} \times 100 \%$$

4.3 Training Results

After repeated training and prediction test, the RBF neural network Spread parameters select different values, network training results as shown in Fig. 2.

At this time, the RBF neural network training is not the optimal fitting effect. In general, in order to achieve better fitting effect, Spread parameters should be small. But too small Spread parameters may lead to severe overtraining problems, and

Table 1 Method of data division

| Input | Output |
|----------------------------------|--|
| x_1, x_2, \dots, x_m | $x_{m+1}, x_{m+2}, \dots, x_{m+p}$ |
| x_2, \dots, x_m, x_{m+1} | $x_{m+2}, x_{m+3}, \dots, x_{m+p+1}$ |
| | |
| $x_k, x_{k+1}, \dots, x_{m+k+1}$ | $x_{m+k}, x_{m+k+1}, \dots, x_{m+k+1}$ |

Fig. 1 The structure of RBF neural network

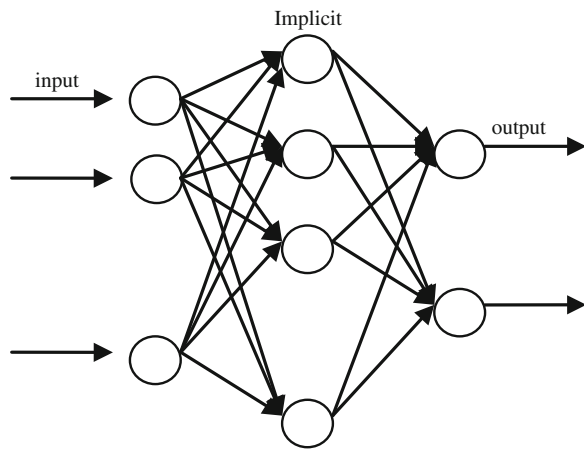
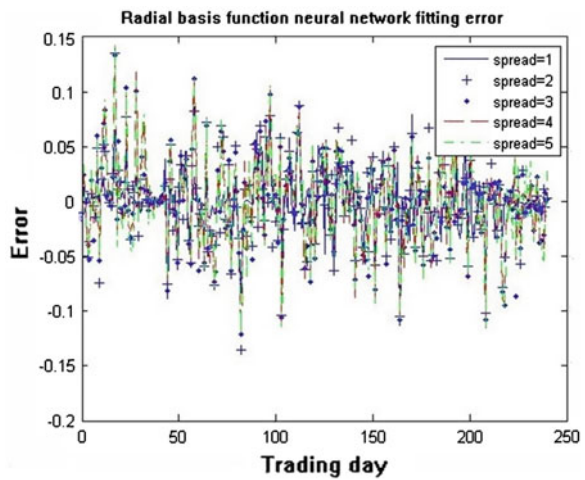


Fig. 2 RBF fitting error under different spread parameters



therefore, to be integrated into the training error of forecasting in order to ensure the generalization ability of neural network [13]. This paper is based on the spread = 1 calculation, as shown in Fig. 3.

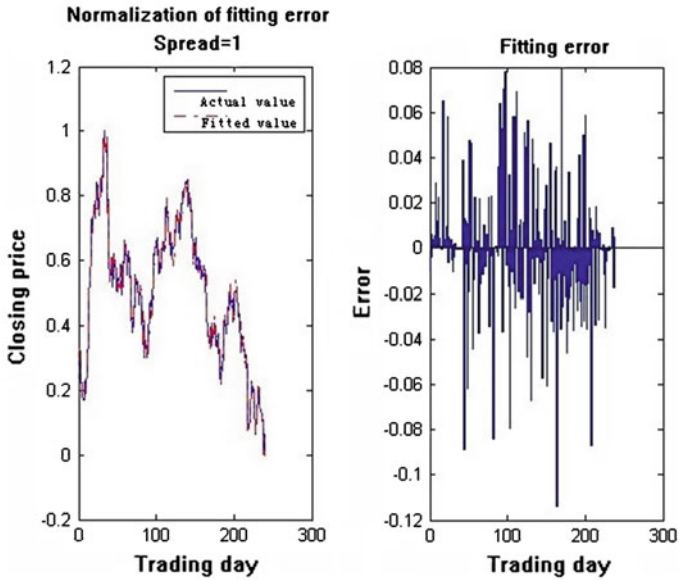
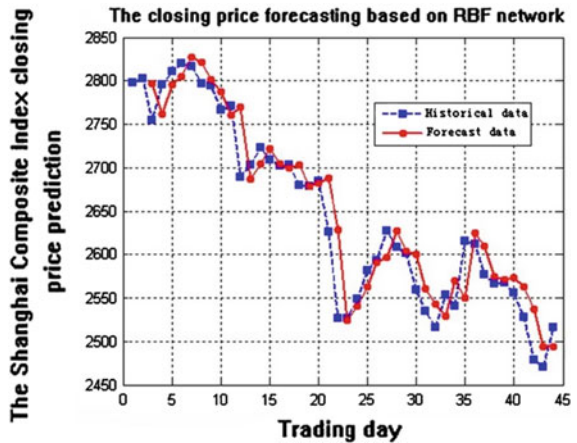


Fig. 3 RBF fitting error under spread = 1

Fig. 4 The RBF neural network prediction results



4.4 Predictors of Outcome

Network design is completed. Use the training set and test data for testing. Use the trained RBF neural network on November 8, 2011 to December 20th SSE Composite Index prediction. A total of 30 trading days, the results shown in Fig. 3. The average prediction error of 1.4387 %, the neural network has good prediction effect (Fig. 4).

5 Conclusion and Prospect

Using the nonlinear mapping of neural network could achieve arbitrary data function approximation, without the need for explicit details of the model. This paper use RBF neural network to achieve the SSE Composite Index prediction. The model has good generalization ability, and has a certain reference value to the stock market prediction.

For this data, RBF neural network has faster speed and better prediction results of fitting than BP neural network. Because of the particularity of the stock market, although the training of BP neural network fitting effect is much better than RBF neural network, the forecast result is not ideal, and the prediction data cannot reflect the real condition of data.

In recent years, domestic and foreign scholars are trying to study more effective economic forecasting methods, to improve the prediction quality and efficiency. Neural networks with excellent properties, which are increasingly attracting people's attention, will be in more extensive areas of application.

References

1. Brown B, Aaron M (2001) The politics of nature. In: Smith J (ed) The rise of modern genomics, 3rd edn. Wiley, New York
2. Dod J (1999) Effective substances. In: The dictionary of substances and their effects. Royal Society of Chemistry. <http://www.rsc.org/dose/title> of subordinate document. (Cited 15 Jan 1999)
3. Slifka MK, Whitton JL (2000) Clinical implications of dysregulated cytokine production. *J Mol Med*. doi:10.1007/s001090000086
4. Smith J, Jones M Jr, Houghton L et al (1999) Future of health insurance. *N Engl J Med* 341:325–329
5. South J, Blass B (2001) The future of modern genomics. Blackwell, London
6. Yu J, Sun Z, Valeri K (2003) Based on BP neural network modeling and decision making system of stock market. *Process Theory Pract* 37(5):17–21
7. Kim K (2006) Artificial neural networks with evolutionary instance selection for financial forecasting. *Expert Syst Appl* 30:519–526
8. Youshou W, Zhao M (2001) A tunable activation function of the neuron model and its application with supervised learning. *Sci China E* 3L(3):263
9. Wang Y, Zhang W (2007) MATLAB based RBF neural network modeling and application. *J Teach Coll* 2007(2):118–120
10. Sun Q, Zhu J (2002) Stock price based on genetic neural network forecasting. *Comput Eng Appl* 5:237–298
11. Zheng P, Ma Y (2000) Based on RBF neural network for stock market modeling and forecasting. *J Tianjin Univ* 23(4):183–186
12. Guo L, Gao J, Yang J et al (2009) Criticality evaluation of petrochemical equipment based on fuzzy comprehensive evaluation and a BP neural (J) ELSEVIER network. *J Loss Prev Process Ind* 22:469–476
13. Jixiong D, Li Z, Liang H (2006) RBF neural network are determined parameters of the new method of. *Microprocessor* 4:48–50
14. Qiangen X, Luo S, Jianyu L (2003) Radial basis function neural network is an online learning algorithm. *J North Jiaotong Univ* 27(2):90–92

Research on the Fluid Capacitance Detector Using the Technology of Capacitance Detecting

Zheng Fang, Jianguang Zhou, Xiaoyan Liu and Sijia Liang

Abstract Fluid detection is of great importance in the industrial processes and chemical analysis-reported methods must have the contact with the sample and require a long time to finish the detection. This paper raised a novel method and made a fluid detector to detect fluid by using the capacitance detecting chip AD7745, which can make the detection in a short time. By testing gas, water, and different concentrations of ethanol, we got the results that the detector can effectively distinguish different substances and make the primary quantitative analysis.

Keywords Fluid detector · Capacitance detecting · AD7745

1 Introduction

Fluid is widely used in chemical analysis and industrial processes. The characteristic parameters of fluid are usually the important symbols in the process of industrial production [1]. Therefore, the accurate detection of the fluid makes a sense. The reported fluid detection methods include gas chromatography, HPLC method, Evaporative light-scattering method, and so on. Methods raised above usually have contact with the sample when detecting, which may affect and change the properties of the sample, meanwhile, it's not convenient to detect the fluid by using these methods. Also, these methods may cost a long time. Aimed at solving these problems, we designed and implemented a kind of noncontact fluid capacitance detector with high-precision in this paper.

Z. Fang · J. Zhou (✉) · X. Liu · S. Liang
Department of Control Science and Engineering, Zhejiang University, Hangzhou, China
e-mail: jgzhou@zju.edu.cn

Table 1 Relative dielectric constant

| Substance | Temperature (°C) | Relative dielectric constant |
|----------------------------------|------------------|------------------------------|
| O ₂ | 0 | 1.00051 |
| N ₂ | 0 | 1.00058 |
| Vacuum | 0 | 1 |
| Et ₂ O | 0 | 4.335 |
| C ₂ H ₅ OH | 20 | 25.7 |
| H ₂ O | 20 | 81.5 |
| Glycerine | – | 45.8 |

In this paper, we first give the theory of the capacitance detector. Then, a detailed introduction of the hardware design and the software process is given. Finally, we made some tests to the capacitance detector, the results show that the capacitance detector can effectively make qualitative and quantitative analysis to the fluid.

2 Principle of the Capacitor

Different substance has different dielectric constants, which can be seen in the Table 1. When different substance through the capacitor, it may leads to the change of the dielectric constants between the two plates in the capacitor, as shown in Fig. 1. So the capacitance values of the capacitor will vary as the change of dielectric constants between the capacitor plates, the capacitance values will have a direct relationship with the substances [2].

As the capacitance values have a direct relationship with the materials, we use a capacitance detecting chip to detect the values, a micro controller is used to convert the values to digital data, then transform the data to the computer, we can record the data and process it on the computer.

When two different media mixed by medium1 and medium2, the effective dielectric constant can be expressed as below.

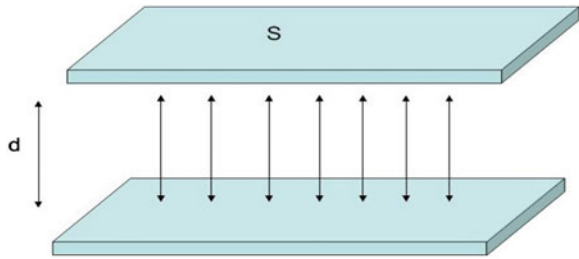
$$\sqrt{\epsilon_1} = D\sqrt{\epsilon_2} + (1 - D)\sqrt{\epsilon_3} \tag{1}$$

In the (1), the ϵ_1 is the dielectric constant of the mixed media, ϵ_2 is the dielectric constant of medium1, ϵ_3 is the dielectric constant of medium2, D represents the volume fraction of the medium1 in the mixed media [3].

The relationship between the capacitance of the two plates and the dielectric constant of the plates is given in (2).

$$C = \epsilon * \epsilon_0 * S/d \tag{2}$$

Fig. 1 Principle of capacitor



In the (2), ϵ_0 is the dielectric constant of the vacuum, $\epsilon_0 = 8.86 \times 10^{-12}$ F/m, S is the area of the plate, d is distance of the two plates, when structure of the capacitor is fixed, the capacitance is given in (3).

$$C = K * \epsilon \tag{3}$$

K is a constant, and is decided by the structure and the size of the capacitor. Therefore, the capacitance of the capacitor is only decided by the medium. Thus, we make use of this relationship to design the capacitance detector.

3 Design of the Capacitance Detector

3.1 Structure of the System

The capacitance detector system consists of fluid capacitor, capacitance detector, micro controller and the computer. When the computer sends the command of collecting data, the capacitance detector chip AD7745 obtains the capacitance value from the fluid capacitor and converts it to digital data. The MSP430 micro controller communicates with the AD7745 by using I₂C protocol to get the data timely [4]. Finally, the micro controller transmits the data to the principal computer through RS232 communication protocol. The structure of the system is shown in Fig. 2.

The structure of the fluid capacitor is given in Fig. 3. Arrow in the figure represents the direction of fluid flow, two flexible printed circuit boards make up two plates, the capillary tube fabricated between the two boards is used as channel. Two wires named A and B welded on the two boards connect to the capacitance detector chip, so the chip can easily get the capacitance values.

Fig. 2 Structure of the system

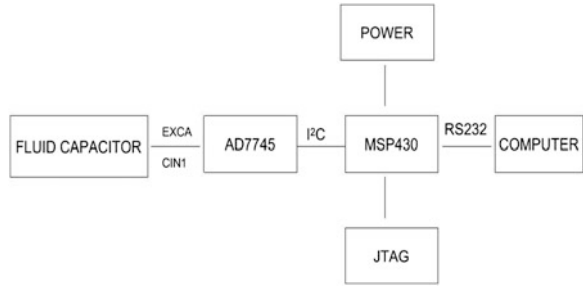
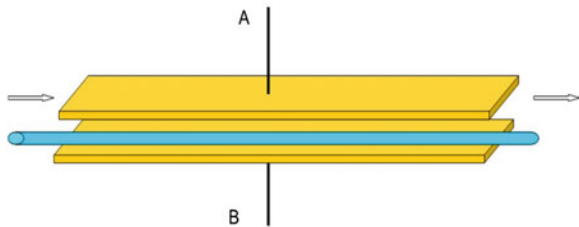


Fig. 3 Structure of the fluid capacitor



3.2 Choose of the Capacitor Detector Chip

From the given material in Table 1, we choose O₂ and N₂ because their dielectric constant is so close. We take the structure of the fluid capacitor in Fig. 3, and calculate the two capacitance values as below:

$$C_{O_2} = \epsilon * \epsilon_0 * S/d = 1.00051 * 8.86 * 10^{-12} * \pi/2 * 3 * 10^{-6} * / (3 * 10^{-4}) = 139243.53aF \quad (4)$$

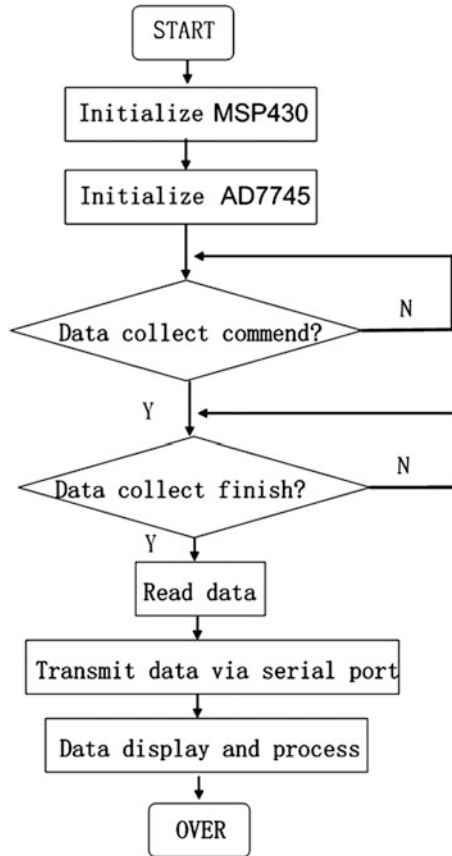
$$C_{N_2} = \epsilon * \epsilon_0 * S/d = 1.00058 * 8.86 * 10^{-12} * \pi/2 * 3 * 10^{-6} * / (3 * 10^{-4}) = 139253.27aF \quad (5)$$

$$C_{N_2} - C_{O_2} = 9.7 \text{ aF} \quad (6)$$

From (6) we can see, the difference of the two values is 9.7aF, we should choose a detector that its resolution is lower than 9.7aF.

The AD7745 digital capacitance converter is fabricated by AD company with the advantage of high resolution and low-power. It has a high resolution of ± 4aF, which is far less than the requirements of above theoretical calculation. The error of the chip can be up to 4fF, meanwhile, the linearity is as high as 0.01 %, its largest input common-mode offset capacitance can reach 17pF [5]. So we choose AD7745 as the capacitor detector chip.

Fig. 4 Block diagram of the micro controller system



4 Design of the System’s Software

4.1 Design of the Micro Controller System

The system software includes control, data collect, and data transmit three parts. When the system is powered on, the microcontroller MSP430 will be initialized, then the MSP430 send commend to initialize the AD7745 and to test the serial port. After initializing, system waits for the commend to collect data [6]. When the commend of collecting data was sent from the principal computer, MSP430 controls the AD7745 to obtain the capacitance values, then converts them to digital data. Finally, the microcontroller transmits the digital data to the principal computer through the serial port [7]. Then we can make some process to the data. The software block diagram of the microcontroller system is given in Fig. 4.

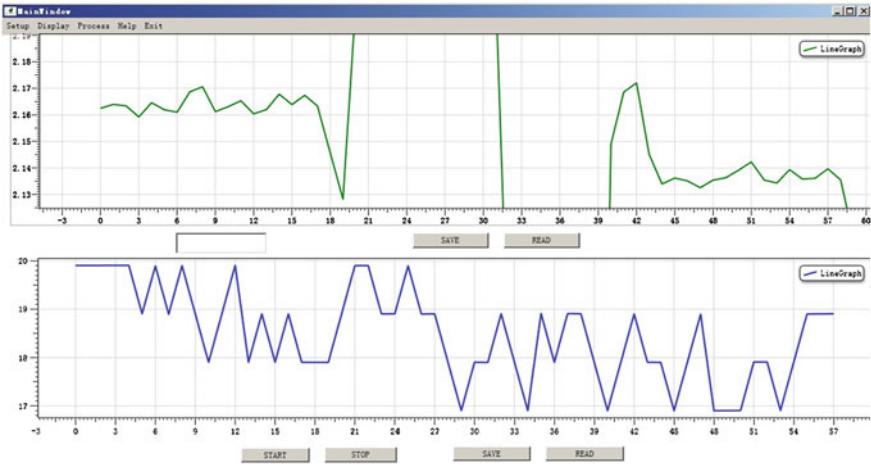


Fig. 5 Interface of the software

4.2 Design of the PC Software

For the aim to monitor the capacitance data timely, we use the c # to develop PC software based on the VS2010 platform [8]. The software consists of serial port setup, data collect and process, data save and query three parts. When the digital data is transmitted from the micro controller, the software creates an array to store the capacitance data dynamically then the software uses the timer “Dispatcher” to draw the data on the data display ActiveX [9]. The interface of the software is shown in Fig. 5.

5 Test of the Capacitance Detector

In order to test the system, we choose gas, water, and different concentrations of ethanol (volume percent is 20, 40, 60, 80 %) as the samples. By using the peristaltic pump, we push the samples into the fluid capacitor one by one. The horizontal axis presents time, vertical axis means capacitance.

5.1 Qualitative Analysis

Before the samples were injected in the fluid capacitor, the capillary is filled with air, so the base value of the figure is the capacitance value of gas. Results of different samples are shown in Table 2.

Table 2 Result of qualitative analysis

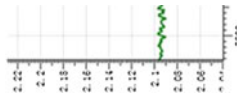
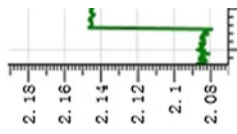
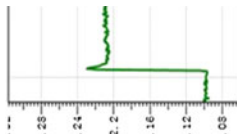
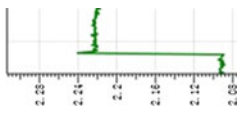
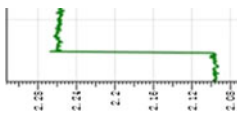
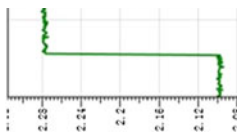
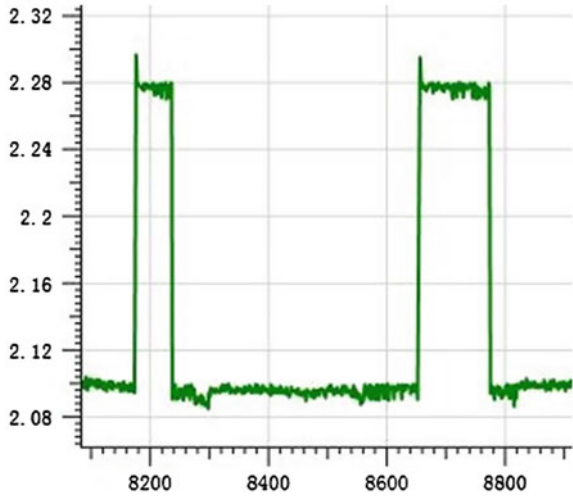
| | Gas | Water | 20 %C ₂ H ₅ OH | 40 %C ₂ H ₅ OH | 60 %C ₂ H ₅ OH | 80 %C ₂ H ₅ OH |
|-----------|---|---|---|---|---|---|
| Results |  |  |  |  |  |  |
| Value(pf) | 2.090 | 2.145 | 2.210 | 2.222 | 2.259 | 2.278 |

Fig. 6 Results of the quantitative analysis



The results show that within a certain error range, this fluid capacitor can easily distinguish different substance and make basic qualitative analysis.

5.2 Quantitative Analysis

In the quantitative test, we use the peristaltic pump cooperated with the injector to help finishing the experiment. Select 1 ml quantity and 2 ml quantity ethanol solution with 80 % volume percent as the samples. We set the speed of the peristaltic pump at 1 ml/min, and the samples are sent into the fluid capacitor one by one, the capacitance values variation are shown in Fig. 6.

Figure 6 shows that the duration time of the capacitance change has a positive relationship with the quantity of the sample. When the 1 ml quantity ethanol solution was injected in by the peristaltic pump at a speed of 1 ml/min, the duration time of the capacitance change is almost 57 s. When the 2 ml quantity ethanol solution was injected in by the peristaltic pump at a speed of 1 ml/min, the duration time of the capacitance change is almost 115 s. So we can calculate the quantity of the samples in the formula as below.

$$V_1 = 1 \text{ ml/min} * 57 \text{ s} = 0.95 \text{ ml} \tag{7}$$

$$V_2 = 1 \text{ ml/min} * 115 \text{ s} = 1.91 \text{ ml} \tag{8}$$

From (7) and (8), we can get the conclusion that, the fluid capacitor system can detect the quantity is 0.95 ml when the sample amount is 1 ml, the error is 5 %. And the fluid capacitor system can detect the quantity is 1.91 ml when the sample

amount is 2 ml, the error is 4.5 %. The error of the detection is relatively small. What's more, the analysis time is decided by the amount of the sample so that we can control the analysis time on demand. Therefore, this detector can effectively make the basic qualitative and quantitative analysis to the fluid.

6 Conclusion

This paper provides a novel device to detect fluid quickly and accurately with the advantage of no contact so that will not damage the sample. Results from the experiment show that this system can effectively make qualitative and quantitative analysis to the fluid. This device can be used in food detecting field to judge some wine or to detect some substance that is harmful to people's health. While in the actual test, we come across a problem that the capacitor can be easily influenced by the outside environment. So this increases the requirements of the working environment. Therefore, we hope to strengthen the ability to resist electromagnetic interference in the coming work.

References

1. Shao N, Gavrilidis A, Angeli P (2009) Flow regimes for adiabatic gas-liquid flow in microchannels. *Chem Eng Sci* 64(11):2749–2761
2. He WW, Zhao X, Li YT, Lu GZ (2008) Design and implementation of AD7745 based micromachined capacitive accelerometer interface circuit. *Chin J Sens Actuators* 21(3):529–532
3. Liu HC, Teng ZS, Luo B (2011) Design of digital sensor for oil quality detection based on AD7745. *Transducer Microsyst Technol* 30(9):95–97
4. Chen B, Hu XB, Sun H (2011) Design of capacitive differential pressure sensor based on AD7745. *Transducer Microsyst Technol* 30(6):740–741
5. Guo YR, Huang YS, Chen X (2009) The application of AD7745 in water content measuring circuit in oil well. *Instrum Technol* 14(2):14–15
6. Guo Q, Xie K, Jiang HM, Wang H (2008) Principle and application of capacitance to digital converter AD7745. *Mod Electron Tech* 31(14):170–172
7. Chen L, Chen RW (2006) The application of AD7745 in micro mechanical capacitive sensors measuring circuit. *Instrum Cust* 13(4):75–76
8. Yin J (2012) The analysis and design of pair programming based on C#. *Comput Knowl Technol* 8(10):2270–2271
9. Zhang DW, Lu ZW (2007) Object oriented analysis, design and programming. *Optics Precis Eng* 8(6):568–571

Research on the Safety of Yangtze River LNG Transport and Storage System

Shouhui He, Hanhua Zhu, Haofei Huang, Xiaowei Xu
and Suping Zhao

Abstract This article defines LNG transport and storage system, builds the physical model and elaborates the source and storage, various kinds of filling models and technological processes according to the construction of LNG transport and storage system in the middle and upper reaches of Yangtze River; It discusses the safety of it in-depth and puts forward a set of monitoring systems and prevention systems. This may provide scientific and reasonable basis for the development of LNG industry and safety manufacturing management.

Keywords LNG · Transport and storage · Risk · Monitoring and prevention system

1 Introduction

Our country is in the stage of adjusting energy structure and clean energy is recommended. LNG, an efficient, clean, and environment-friendly energy, is widely used in various kinds of industries. However, it has the risk of fire, explosion, RPT (Rapid Phase Transition), low temperature, suffocation, etc. Severe damages will occur once it releases and diffuses. Researches on LNG transport and storage system and safety precautions have a vital significance, which can promote the development of LNG industry, reduce accidents occurrence, and decrease the losses.

S. He (✉) · H. Zhu · H. Huang · X. Xu · S. Zhao
School of Energy and Power Engineering, Wuhan University of Technology, Wuhan, China
e-mail: supremehe@163.com

2 LNG Transport and Storage System

2.1 Definition of LNG Transport and Storage System

Generally speaking, LNG is transported to dock by LNG ship or lorry. It is conveyed to pipe (C) and finally stored in tank. The transport and storage system in this article includes LNG pipe line, LNG tank. It is shown in Fig. 1.

LNG tank should be equipped with two injection pipelines, one at the top and the other the bottom. LNG can be filled into tank using injection pipelines. Injection pattern depends on the specification of LNG to be stored. It can be stored either from the top (B) if the density of LNG to be stored is bigger than that in tank, or else, from the bottom (A).

2.2 Form of Yangtze River LNG Transport and Storage System

In general, Yangtze River LNG transport and storage system includes two parts: one is the supply of LNG and the other is the storage part [1].

The first part (the supply) is divided into two parts: supply on land and on water. The front one includes LNG tank supply, lorry and satellite station. LNG ship is the main way of supply on water.

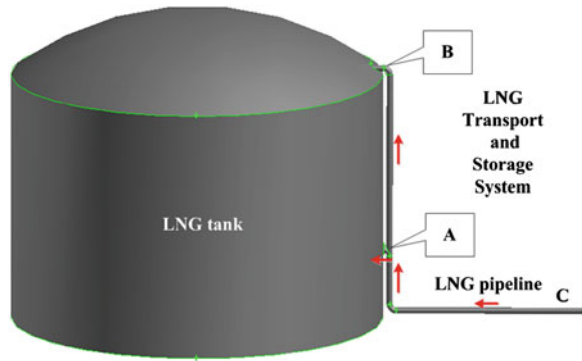
The second part is the storage of LNG. Generally, the most important instrument for storing is the tank which can be placed on land or wharf boat. The two parts are shown in Fig. 2.

The following aspects need to be taken into account when selecting the mode

- (1) Mode of LNG tank supply: the ship is small, some technical questions like fixed position of LNG tank need to be considered, and the safety performance is relatively low.
- (2) Mode of LNG lorry: the cost is relatively low, but the supply is limited.
- (3) Mode of LNG ship supply: flexible and convenient, but the cost is too high.
- (4) Mode of LNG satellite station: range of application is extensive, but more factors of safety need to be considered for this mode and the cost is too high.

On the basis of safety, economy, conditions of Yangtze River middle and upper reaches and the development of LNG industry, this project takes the following plan: The source is from LNG lorry; LNG tank can be built on wharf boat; LNG lorry can travel to wharf boat or on the shore; Mode of LNG ship supply may be a common way in the long-term. Mode selection is shown in Fig. 3.

Fig. 1 LNG transport and storage system



2.3 Technological Process

Technological process of Yangtze River LNG transport and storage system includes: unloading process, pressure regulation process and refuel process [2].

(1) Unloading process

LNG carried by the lorry is transferred to the tank by liquid pump.
That is: LNG lorry → liquid pump → tank.

(2) Pressure regulation process

LNG lorry can be supercharged by supercharger when unloading.
That is: supercharger → LNG lorry.

Pump some LNG from tank using liquid pump and regulate pressure by means of vaporizer after the unloading process. Stop gasification when the saturation pressure of LNG tank reaches the setting pressure.

That is: LNG tank → liquid pump → vaporizer → LNG tank.

(3) Refuel process

Pump LNG from the tank by liquid pump, fill LNG power driven vessel with LNG through LNG dispenser.

Pump LNG from lorry using liquid pump, fill LNG power driven vessel with LNG through LNG dispenser.

That is:

LNG tank → liquid pump → dispenser → LNG power driven vessel;

LNG lorry → liquid pump → dispenser → LNG power driven vessel;

Process flow diagram of this project is shown in Fig. 4.

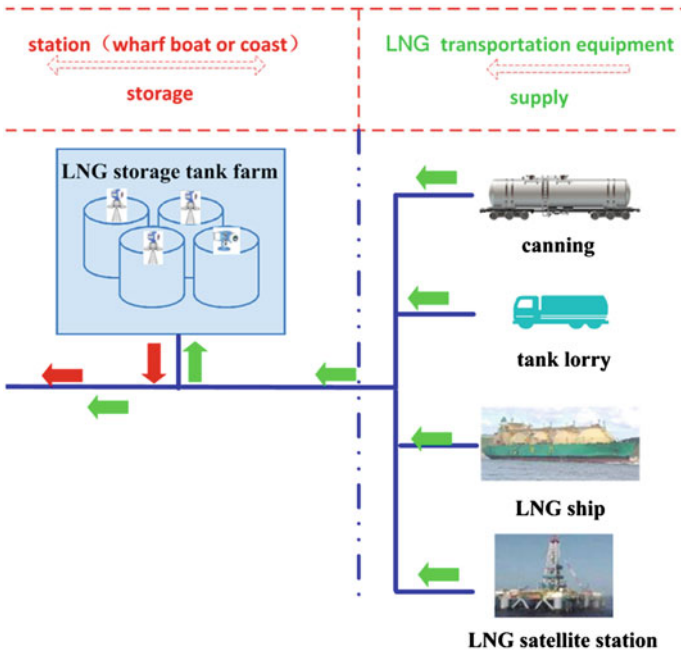


Fig. 2 Form of Yangtze River LNG transport and storage system

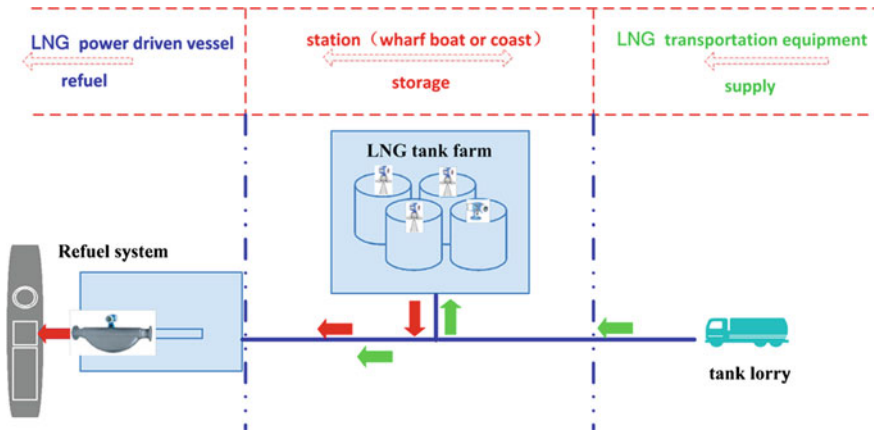


Fig. 3 Mode selection

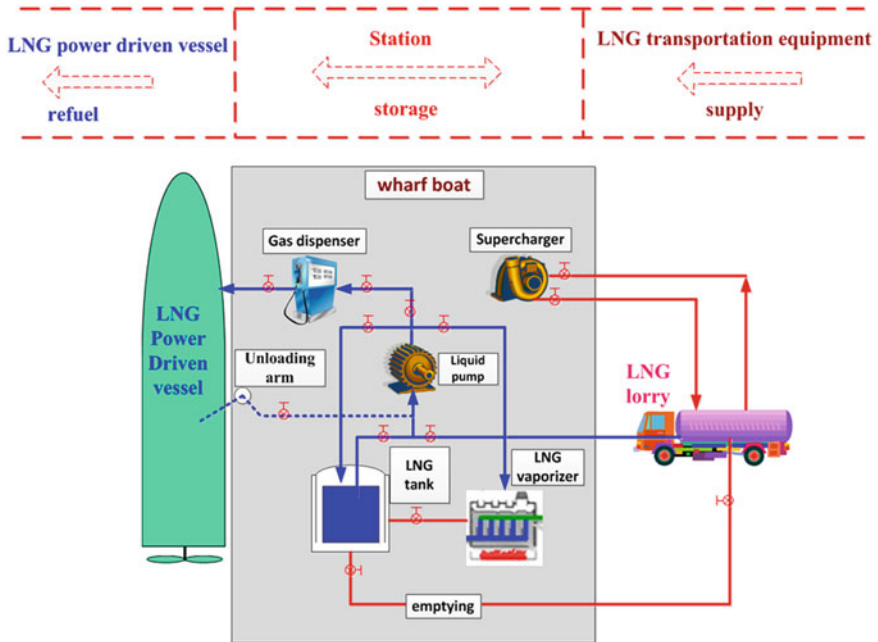


Fig. 4 Technological process

3 Safety of LNG Transport and Storage System

Enterprises related should take effective actions to prevent and control the release and diffusion of LNG in consideration of the hazardous characteristics of it.

- (1) Prevention and control measures should be started from design stage during which LNG transport and storage system (pipeline, tank), cofferdam area and fire extinguishing system are the most important parts.
- (2) Minimize the danger which may be caused by handling process and dispose risk once it happens.
- (3) Set up a set of monitoring system and accident prevention system.

3.1 Process Design

3.1.1 Design of Transport and Storage System: Pipeline

Materials should meet the requirements of LNG cryogenic properties and flame retardant property. Large difference in temperature and temperature variation should be considered when designing pipeline and structural support. So,

corresponding measures such as waterproof, heat insulation, and inflaming retarding should be taken to prevent freeze and embrittlement [3].

Usually, the easiest leakage is at flange connection, welded pipe line and valve should be used as far as possible when designing. In addition, quality of welding line and welding rod should be paid attention to.

3.1.2 Design of Transport and Storage System: LNG Tank

Tanks can be above ground, but also “buried” or partly below ground. The whole design of the LNG tank is focused on “keeping the LNG cool and liquid”.

Materials used in manufacturing LNG tanks must meet the requirements of LNG cryogenic properties. For LNG tanks with bilayer structure, they must not only meet the requirements of LNG cryogenic properties, but also bear work stress of medium. So, Materials used in manufacturing LNG tanks must be good mechanical behavior and can endure low temperature [4].

Pressure inside LNG tank must be controlled within a permissible range, there are some potential danger when LNG tanks have high pressure or negative pressure. So, pressure control system must be installed, providing pop-off valve and antvoid valve as well. Pop-off valve can prevent LNG tank from overpressure and antvoid valve can feel local atmosphere pressure.

Purification treatment must be conducted before the first time filling LNG tank or after stopping the internal repair. Inert gases, nitrogen commonly used, can cement out the air or natural gas inside the tank, this action can avoid risk caused by mixture of air and LNG inside tank. In addition, there should be reasonable safe distance on the basis of volume among LNG tanks.

3.1.3 Design of Cofferdam Area

In order to alleviate damages caused by LNG leakage, cofferdam area should be set up around LNG tank. Its role is to restrict the diffusion if leakage occurs. It consists of fire dike, protecting wall or drainage system [5].

3.1.4 Fire Extinguishing System

Generally, fire extinguishing system includes fire fighting water system, dry powder system, foam extinguishing system, and mobile fire extinguisher. Fire fighting water is used to cool device but not to control flame.

Dry powder system—Powder extinguishing agent is the most effective action to put out fire with heavy pressure; Dry powder, carbon dioxide, and alkyl halide fire extinguishing agent are used to put out fires with lower leakage rate. Gas sources should be immediately cut off, or, it may rekindle.

Foam extinguishing system can erupt a mass of foam, decrease quantity of heat, reduce the steam rate effectively and diminish scope blanketed by combustible gas [6].

3.2 Monitoring System and Prevention System of LNG Transport and Storage System

3.2.1 Monitoring System

The monitoring system may include the following parts:

- (1) Tank farm monitoring and management system;

The main function of this system is to monitor the safety of production and transportation. It is convenient to data reading and easy to master the situation of the monitoring area. It also can realize information sharing, link up each monitoring site, inspect safety situation of each key site, and dispose emergency in time.

- (2) Metering system;

The main function of this system is to meter the inventory level and handling capacity.

- (3) Voltage regulating system;

The main function of this system is to adjust the pressure of LNG tank and ensure the pressure inside it within a permissible range.

- (4) Security system;

The main function of this system is to monitor the safety of LNG transport and storage system and to prevent the accidents from happening and dispose emergency in time.

- (5) Handling system;

Ensure the safety of loading and unloading operation when LNG lorry arrives to transport and storage area.

- (6) Business system;

Transact all the business of LNG transport and storage system.

All constituent parts and each function of monitoring system are shown in Fig. 5

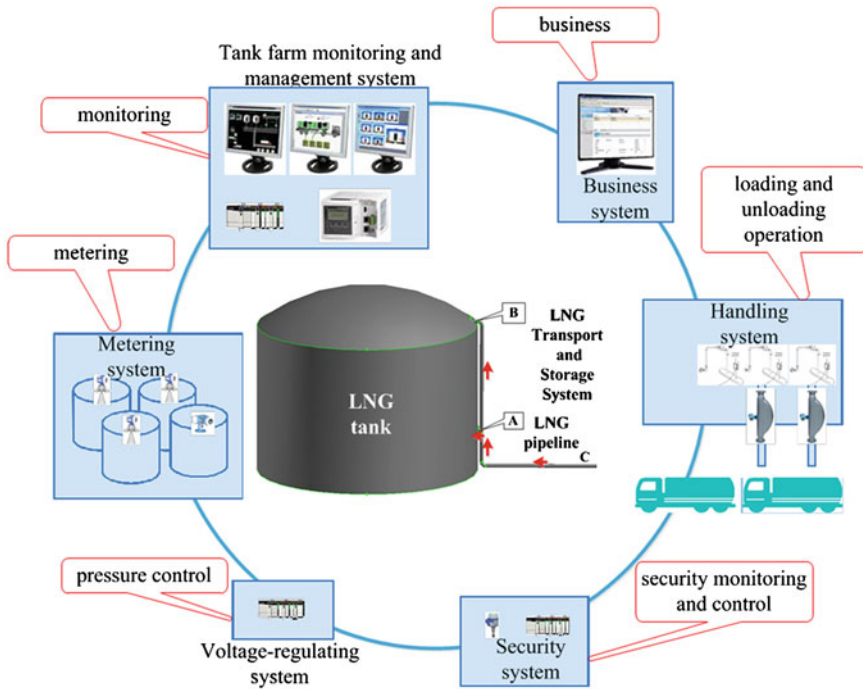


Fig. 5 Monitoring system of LNG transport and storage system

3.2.2 Prevention System

LNG will produce a strong gasification phenomenon when release and diffusion takes place. There would be liquid bath on the ground or water when the leakage is larger. Fire would occur if combustion source exists.

(1) Control steam

LNG will produce a strong gasification phenomenon when release and diffusion takes place. This may cause fire or explosion if steam concentration is too high. People should try to lower it and accelerate the diffusion rate in order to decrease the risk.

The effective way to accelerate vapor diffusion is to use high-expansion foam system. Using high foaming, people could reduce the possibility of fire or explosions, evaporation of LNG and concentration of combustible gas on the ground.

Another effective way to reduce vaporization rate is to use thermal insulation material on fire dike or on the surface of collecting liquid bath [7]. Materials, such as foam glass, have the effective role of fire prevention.

(2) Control or guide liquid bath

There would be liquid bath of the ground or water when the leakage is larger. Cofferdam area should be installed in order to reduce the damage caused by liquid

bath. Generally, the volume of cofferdam area is larger than that of LNG tank in view of the storage ability would decline due to snows or something else.

In addition, an impounding area could be made via digging guide groove around tank [8]. To valves that may leak, baffle should be installed at the layup and catch tray in the below, then, LNG could be led to collecting liquid bath by means of guide groove.

(3) Fire control

Combustion source should be strictly controlled after the fire. Cut off the gas source to control leakage. In order not to cause secondary damage, stable combustion of leaked gas is allowed if the leakage could not be effectively controlled.

In addition, cooling protection measures should be conducted on the storage tank on fire and equipments nearby.

4 Conclusions

This article discusses from the definition of LNG transport and storage system, physical model of it, source and storage, various kinds of filling models to technological processes according to the construction of LNG transport and storage system in the middle and upper reaches of Yangtze River; It discusses the safety of LNG transport and storage system in-depth. The following conclusions could be easily drawn:

- (1) Definition of LNG transport and storage system is given, and physical model of this system is structured.
- (2) Various kinds of filling models are evaluated according to the construction of LNG transport and storage system in the middle and upper reaches of Yangtze River, each of which is evaluated from economy to security and the most suitable one is selected and corresponding technological processes are given.
- (3) A set of monitoring and prevention system which would effectively control and protect the LNG transport and storage system is put forward.

References

1. Danish Maritime Authority (2012) North European LNG infrastructure project: a feasibility study for an LNG filling station infrastructure and test of recommendations. Danish Maritime Authority, Copenhagen
2. Chen J (2007) Safety evaluation of special terminal for LNG. Dalian Maritime University, Dalian
3. Phil C, Mike J, Ben H (2007) A summary of some experimental data on LNG safety. *J Hazard Mater* 140(3):429–438

4. Ronald PK, Donald LE (2007) Lessons learned from LNG safety research. *J Hazard Mater* 140(3):412–428
5. Kovalets IV, Maderich VS (2006) Numerical simulation of interaction of the heavy gas cloud with the atmospheric surface layer. *Environ Fluid Mech* 4(6):313–340
6. Tauseef SM (2011) CFD-based simulation of dense gas dispersion in presence of obstacles. *J Loss Prev Process Ind* 24(4):371–376
7. Lvings MJ, Jagger SF, Lee CJ (2007) Evaluating vapor dispersion models for safety analysis of LNG facilities research project. The Fire Protection Research Foundation, Massachusetts
8. Yu G, Zhang B, Wu W (2008) Numerical analysis of the dispersion for LNG vessel release on water. *J Dalian Marit Univ* 34(2):170–172

Research on Reversal Lane Application Method of Urban Road Network Based on the Bi-level Programming

Qihong Yu and Rui Tian

Abstract When the direction of traffic flow is asymmetric and the road capacity is insufficient, the two-way traffic capacity of the road can adapt to traffic demand dynamically through changing the direction of the lane, which can ease traffic congestion. This paper proposes the implement conditions of variable lanes for road section and verifies that the intersections connected with variable lanes can deal with the increased traffic successfully. Meanwhile, a bi-level programming model was established. The upper-level is the integrated optimization of lane allocating and the lower-level represents a network equilibrium mode, which predicts the drivers' reaction to any given lane allocation. Then, a heuristic solution algorithm is proposed to solve the bi-level programming model. The numerical test results show that the algorithm increases the capacity of the road network significantly and the two-way traffic is more balanced.

Keywords Congestion · Reversible lane · Heuristic solution algorithm · Bi-level programming model

1 Introduction

With the accelerated process of urbanization in China, the large and medium-sized cities are facing more and more transport problems. In order to alleviate traffic congestion, some domestic and abroad cities attempted to use the reversible lane technology to improve the operational status of the transportation system.

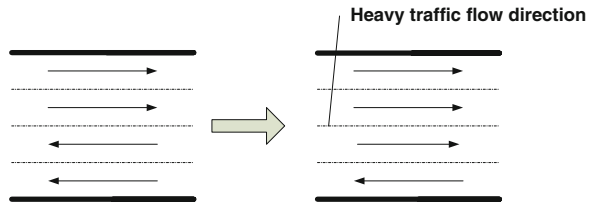
Q. Yu (✉)

Department of Electric Information Engineering,
The City College of Jilin, JianZhu University, Changchun, China
e-mail: 1217552735@qq.com

R. Tian

Jilin Communications Polytechnic, Changchun, China

Fig. 1 The total capacity of the road is increased by reversing the directionality of a middle lane



Reversible lane is a method to increase traffic flow without adding additional roads or lanes. That is, when the two-way traffic flow distribution is not balanced in a road network, a lane direction will be changed temporarily to relieve the congestion problem as shown in Fig. 1.

Brian Laurence introduced reversible lane application in the United States and pointed out that the United States also lacks available operating reversible lane design standards and implementation basis (see [1, 2]). In most cases, a fixed time period reversible lane control was taken based on road sections of the history of the survey data. Zhang introduced to use the bi-level programming model chaos optimization approach to seek the optimization method of the reversible lane in the road network [3]. Sheu studied the reversible lane in alleviating temporary road congestion caused by traffic accidents and other aspects of the application. A certain time-varying variable lane embodiment and forecasting vehicle traffic behavior, stochastic systems modeling method was proposed and the results can provide decision support for traffic incident management [4]. Hausknecht introduced dynamic real-time control lane in accordance with the changes in the traffic. A linear programming model and bi-level programming model were proposed. The results showed that the road network efficiency improved by 72 % after the adjustment of the lane [5].

The following are the specific research on the sections, intersections, and road network.

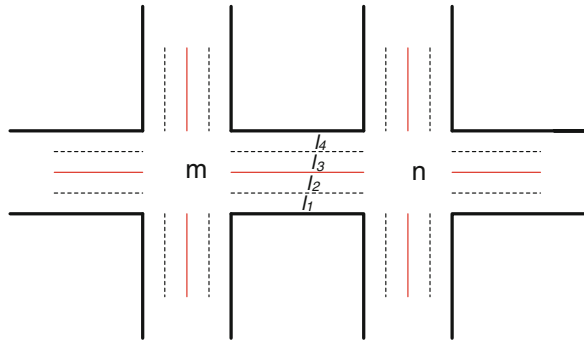
2 Lane Reversal for a Road Section

First, we should consider the impact of lane reversal on a single road. Assuming that there is a two-way road section with four-lane between intersections m and n . m_n for the lanes from m to n ; n_m for the lanes from n to m . As shown in Fig. 2, $m_n = \{l_1, l_2\}$, $n_m = \{l_3, l_4\}$.

$$c(L) = \sum_{l \in L} c(l) \tag{1}$$

where, $c(l)$: the capacity of lane l is the maximum vehicles entering the lane per hour; $c(L)$: the capacity of a set L of lanes. For convenience of study, the potential lane reversal impact on the capacity is ignored.

Fig. 2 Lane reversal in a road



Assuming that m and n are generated vehicles at the target traffic rates $\beta(m_n)$ and $\beta(n_m)$. As the capacity of lanes is limited, the vehicles into the lane are limited. So we use the effective traffic rates $\lambda(m)$ and $\lambda(n)$ to represent. Namely, $\lambda(m_n) = \min\{\beta(m), c(m_n)\}$, $\lambda(n_m) = \min\{\beta(n), c(n_m)\}$. m_n is saturated when $\lambda(m_n) = c(m_n)$, m_n is oversaturated when $\beta(m) > c(m_n)$. The number of vehicles beyond the capacity is denoted by $\beta(m) - c(m_n)$. Obviously, when m_n is oversaturated, it must be saturated. m_n is undersaturated when $c(m_n) > \beta(m)$ and the remaining capacity is $c(m_n) - \beta(m)$. Similarly, when m_n is undersaturated, m_n is not saturated. The saturation of n_m is defined in the same manner.

The throughput of the road R is the sum of the effective traffic rates of the lanes ($\lambda(m) + \lambda(n)$). Now we assume that the direction of the lane $l \in m_n$ is reversed. By the above definition, the throughput of the road increases only if

$$\lambda(m_n) + \lambda(n_m) < \lambda'(m_n) + \lambda'(n_m) \tag{2}$$

where, $\lambda'(m_n) = \min\{\beta(m), c(m_n) - c(l)\}$ and $\lambda'(n_m) = \min\{\beta(n), c(n_m) + c(l)\}$.

So we can draw the following conclusions: As shown in Fig. 1, lane reversal is beneficial only when one of the directions is oversaturated while the other is undersaturated.

3 Lane Reversal for an Intersection

First, since the intersection is often the bottleneck in a traffic stream, it is necessary to analyze intersection of reversing the direction of the lanes. Preventing traffic congestion which is caused by more than the capacity of the unsaturated direction lanes after reversing, we use the example to verify whether the new increase in the incoming traffic to the direction of the reversing land can be handled when the vehicle from different road into the intersection at the same time.

As shown in Fig. 3, it has six lanes on the intersection. Initially, both incoming lanes and outgoing lanes have three lanes. We suppose the target traffic rate of the

Fig. 3 The lanes reversal on the westbound road of an intersection

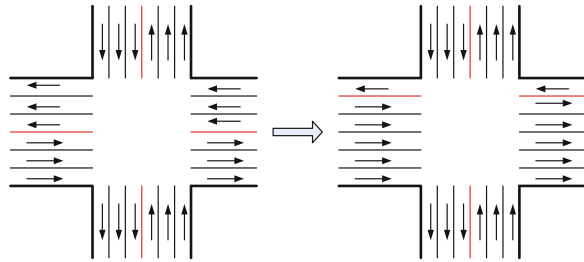


Table 1 The importing road directivity

| Import road | Import-road traffic pch/h | Directivity |
|-------------|---------------------------|-------------|
| East | 5,200 | 0.76 |
| South | 1,550 | 0.48 |
| West | 1,250 | 0.24 |
| North | 1,470 | 0.52 |

eastbound road to be 5,600 vehicles per hour, the target traffic rate of westbound road to be 1,300 vehicles per hour, and the target traffic rates of both northbound and southbound roads to be 1,800 vehicles per hour. Directivity coefficient is determined by a number of vehicles in one direction and the opposite direction with this contrast ratio of total number of vehicles. According to our survey data, we can draw Table 1.

In accordance with the lane reversal set condition, the directivity coefficient is greater than 3/4 which meets the requirements. The north–south direction of traffic flow remained equilibrium. The east–west direction traffic is unbalanced. We try to improve the capacity of the intersection by changing the direction of the east–west lanes. The new lane configuration is shown in Fig. 3.

For simulation, the software VISSIM is used. We repeated the experiment 20 times and took the mean value as reference. In each run, two aspects are measured:

- (1) The total number of vehicles entering the intersection during the 1-h period.
- (2) The number of vehicles entering the intersection from each road during a 1-h period.

According to the simulation results, we get the average of the number of vehicles and the 95 % confidence intervals, as shown in Table 2.

4 Lane Reversal for a Road Network

From the above, we can draw that the lane reversal can improve throughput on individual roads and individual intersections. But the real problem is whether (and how much) lane reversal can help in a complete road network. To solve this problem, we model a road network.

Table 2 The average vehicle and 95 % confidence interval

| | Before reversal | After reversal | Change (%) |
|-----------------|-----------------|----------------|------------|
| Eastbound road | 4915.3 ± 7.2 | 5428.5 ± 10.6 | 10.4 |
| Southbound road | 1482.6 ± 12.8 | 1420.3 ± 11.9 | -4.2 |
| Westbound road | 1306.2 ± 12.5 | 1279.5 ± 8.7 | -2 |
| Northbound road | 1490.7 ± 13.5 | 1497.1 ± 14.2 | -0.4 |
| Intersection | 9197.5 ± 36.2 | 9720.4 ± 29.6 | 5.7 |

4.1 Bi-level Programming Model

In this paper, we use a bi-level programming method to establish lanes adjustment optimization model under the bidirectional flow imbalance condition. The lower layer problem is the user equilibrium assignment mode. The upper layer problem is the model considering the user route choice behavior lane direction adjustment and signal timing parameters optimization and the goal is the maximum spare capacity of the road network.

In the urban road network, due to the difference in land layout, population, and commercial distribution, leading to OD pair on traffic demand is different. We set μ as the growth multiplier of the OD matrix; assume that the total number of two-way lanes of a road is invariable, that is:

$$n_{ij} + n_{ji} = n_a, \quad ij \in A, \quad ji \in A. \tag{1}$$

where n_{ij} is the number of road lanes which is from intersection i to the adjacent intersection j . n_a is a sum of the number of lanes in a road, it is a constant. A is the set of road sections. We supposed the traffic signal control on the sections, so that the traffic flow does not exceed the capacity:

$$f_{ij-1}(\mu, \varphi, \lambda, n) \leq x_{\max} S \lambda_{ij} \quad j \in R, \quad ij \in A \tag{2}$$

where, f_{ij-1} : lane traffic flow in road sections ij , it is a function of μ, φ, λ, n ; φ : vector of the intersection cycle countdown for the road network; λ : vector of green ratio; n : vector of the number of lanes; x_{\max} : maximum flow of saturation; S : a lane saturated flow; λ_{ij} : green ratio intersection i to the intersection j ; R : the set of signalized intersections.

Because of the existence of the lost time in the intersection, to a signalized intersection j :

$$\sum_{n=1}^{N_j} \lambda_{jn} + L_j \varphi_j = 1, \quad j \in R \tag{3}$$

where, N_j : the number of phases j ; λ_{jn} : the green ratio of the n phase; L_j : lost time of signal timing; φ_j is the countdown of the cycle T_j .

Signal control parameters should also satisfy the boundary constraints:

$$\frac{1}{T_{\max}} \leq \varphi_j \leq \frac{1}{T_{\min}}, \quad j \in R \tag{4}$$

$$\lambda_{\min} \leq \lambda_{ij} \leq \lambda_{\max}, \quad j \in R \tag{5}$$

where, T_{\min} , T_{\max} : the lower and upper limits of the cycle. K_{\min} , K_{\max} : the lower and upper limits of the green ratio. In summary, the upper programming model is:

$$\max z = \sum_{r \in O, s \in D} \mu_{rs} q_{rs} \tag{6}$$

$$s.t \quad n_{ji} + n_{ji} = n_{ij}, \quad ij \in A, \quad ji \in A, \quad f_{i,j-1}(\mu, \varphi, \lambda, n) \leq x_{\max} S \lambda_{ij} \quad j \in R, \quad ij \in A.$$

$$\sum_{n=1}^{N_j} \lambda_{jn} + L_j \varphi_j = 1, \quad j \in R, \quad \frac{1}{T_{\max}} \leq \varphi_j \leq \frac{1}{T_{\min}}, \quad j \in R, \quad \lambda_{\min} \leq \lambda_{ij} \leq \lambda_{\max}, \quad j \in R$$

where, O is the set of origin points; D is the set of the destination points; r is a starting node, $r \in O$; s is a termination node, $s \in D$; q_{rs} is the current traffic demand. μ_{rs} is the traffic demand growth multiplier. $f_{i,j-1}(\mu, \varphi, \lambda, n)$ is calculated by the underlying user equilibrium model [6]:

$$\min \sum_{ij \in A} \int_{f_{i,j-1}(\mu, \varphi, \lambda, n)} t_{ij}(w) dw, \tag{7}$$

$$s.t \quad \sum_{k \in K} h_{k,rs} = \mu_{rs} q_{rs}, \quad \forall r \in O, \quad s \in D, \quad f_{ij} = \sum_{r \in D} \sum_{s \in D} \sum_{k \in K_{rs}} h_{k,rs} \delta_{ij,k,rs}, \quad \forall ij \in A,$$

$$f_{ij-1} = \frac{f_{ij}}{n_{ij}}, \quad \forall ij \in A, \quad \lambda_{\min} \leq \lambda_{ij} \leq \lambda_{\max}, \quad j \in R,$$

$$h_{k,rs} \geq 0, \quad \forall r \in O, \quad s \in D, \quad k \in K_{rs}.$$

where, K_{rs} is the set of paths which form r to s . $h_{k,rs}$ is the flow starting point r to end point s in the path $k(k \in k_{rs})$. t_{ij} is travel time functions of the sections ij . The total travel time t_{ij} is composed of two parts, that is, road sections travel time, and intersection delay time. Road travel time functions generally use the *BPR* function represent:

$$t_{1,ij} = t_{0,ij} \left[1 + \alpha \left[\frac{f_{ij}}{S n_{ij}} \right]^\beta \right] \tag{8}$$

where, $t_{o,ij}$ is free travel time of road section. α, β are regression coefficients, $\alpha = 0.15, \beta = 4$.

Independent signal intersection delay can take recommended type in HCM (2000) [7] (without regard to the initial queuing delay):

$$t_{2,ij} = \frac{0.5T_j(1 - \lambda_{ij})}{1 - [\min(1, x_{ij})\lambda_{ij}]} + 900u \left[(x_{ij} - 1) + \sqrt{(x_{ij} - 1)^2 + \frac{8vwx_{ij}}{c_{ij}u}} \right] \tag{9}$$

where, T_j is cycle time of $j, T_j = 1/\varphi_j; c_{ij}$ is the capacity of $ij, c_{ij} = n_{ij}S\lambda_{ij}; x_{ij}$ is the saturation of $ij, x_{ij} = f_{ij}/c_{ij}; u = 0.25, v = 0.5, w = 1$.

4.2 Heuristic Solution

To solve the problem, under the constraint condition, we should consider the varieties of OD demand multiplier, the number of lanes, and balanced road sections single-lane traffic due to signal parameter changes. Balanced road sections single-lane traffic is nonlinear in function and the functional form is unknown. Therefore, it does not directly predict the changes. Thus, we use a linear function approach to the nonlinear function $f_{i,j-1}(\mu, \varphi, \lambda, n)$. To do this, we must calculate their derivatives. Due to the number of lanes n being an integer variable, in this paper we use difference quotient as approximation of the derivative [8].

Setup $\mu_0, \varphi_0, \lambda_0, n_0$ are initial values. $f_{i,j-1}(\mu, \varphi, \lambda, n)$ is balanced road sections single-lane traffic, so:

$$\begin{aligned} f_{ij-1}(\mu, \varphi, \lambda, n) \approx & f_{ij-1}(\mu_0, \varphi_0, \lambda_0, n_0) + \sum_{r \in O, s \in D} \left[\frac{\partial f_{ij-1}(\mu_0, \varphi_0, \lambda_0, n_0)}{\partial \mu_{rs}} \right] (\mu_{rs} - \mu_{0,rs}) \\ & + \sum_{j \in R} \left[\frac{\partial f_{ij-1}(\mu_0, \varphi_0, \lambda_0, n_0)}{\partial \varphi_j} \right] (\varphi_j - \varphi_{0,j}) \\ & + \sum_{ij \in A, j \in R} \left[\frac{\partial f_{ij-1}(\mu_0, \varphi_0, \lambda_0, n_0)}{\partial \lambda_{ij}} \right] (\lambda_{ij} - \lambda_{0,ij}) \\ & + \sum_{ij \in A} \left[\frac{\Delta f_{ij-1}(\mu_0, \varphi_0, \lambda_0, n_0)}{ij} \right]. \end{aligned} \tag{10}$$

Substituting the formula into the upper level model, the upper problem becomes an integer linear programming problem of OD demand multiplier, the number of lanes and signal parameters, which can be solved using branch and bound method . Using the optimal solution obtained from the upper layer problem to solve the lower layer problem once again, we can get a new equilibrium link flow. Repeating the basic ideas, it can get a new set of optimal parameter values. Double counting, and finally it converges to the optimal solution of the original level programming model.

4.3 Numerical Example

In Fig. 4, O represents an OD node and □ represents a signalized intersection node; line segments with an arrow represent road section with direction and the digital before brackets is the initial number of lanes, the digital in brackets is the free flow travel time (unit: s). The road network has 4 OD pairs (5 → 2, 6 → 9, 1 → 10, and 10 → 1), 18 road sections, and 10 nodes (the nodes of 3, 4, 7, and 8 are four separate signalized intersections, which are two-phase controlling). The single lane saturated flow is 1,800 pcu/h and road sections time and a signal control delay time are calculated by the formula (8)–(10). The current OD demand is shown in Table 3.

In this paper, we adopt two methods to study comparatively.

- (1) the traditional traffic forecast method;
- (2) the proposed lane and timing joint optimization bi-level programming model.

In the calculation, the total losses time of the intersection is 10 s.

$$T_{\min} = 30 \text{ s}, T_{\max} = 180 \text{ s}, \delta = 0.05, \lambda_{\min} = 0.05, \lambda_{\max} = 0.95, x_{\max} = 0.9.$$

Set initial solution $\mu_{52} = 1$, each intersection signal cycle length is 90 s.

Figure 5 is a lane path and flow distribution map by traditional method establishing (outside the brackets is the number of lanes and inside the brackets is the distribution of traffic flow).

Figure 6 is the optimization result after seven iterations calculated by the proposed model.

In the method I showed, the results show that the lane direction between the OD does not change. The traffic flow of OD pairs 5 → 2 is 1,485 pcu/h, the traffic flow of OD pairs 6 → 9 is 1,562 pcu/h, the traffic flow of OD pairs 1 → 10 is 4,823 pcu/h, and the traffic flow of OD pairs 10 → 1 is 3,674 pcu/h. The total traffic flow of road network is 11,508 pcu/h.

The results of the optimized method II showed that the traffic flow of OD pairs 5 → 2 are all assigned in the shortest path 5 → 4 → 3 → 2 and the traffic flow is 1,637 pcu/h. The traffic flow of OD pairs 6 → 9 are all assigned in the shortest path 6 → 7 → 8 → 9 and the traffic flow is 1,852 pcu/h. The traffic flow of OD pairs 1 → 10 are all assigned in the shortest path 1 → 4 → 8 → 10 and 1 → 3 → 7 → 10 and the traffic flow are 5,234 and 5,423 pcu/h. The traffic flow of OD pairs 10 → 1 is 3,156 pcu/h. The total traffic flow of road network is 17,302 pcu/h. The path 1 → 3 → 7 → 10 number of lanes is 5 (the reverse path 10-7-3-1 number of lanes is 3). The path 1-4-8-10 number of lanes is 7 (the reverse the path 10-8-4-1 number of lanes is 1). So we can see, traffic distribution is more uniform after optimized and the road resources can be more fully utilized. The total capacity of the road network gets an increase of 50.3 % than before the optimization.

Fig. 4 Road network structure

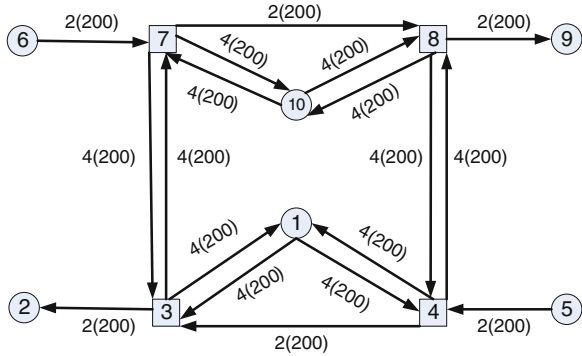


Table 3 OD demand

| OD pairs | The current OD demand | The OD demand growth factor |
|-----------|-----------------------|-----------------------------|
| q_{52} | 1,000 | 1.0 |
| q_{69} | 1,000 | 0.9 |
| q_{110} | 1,000 | 3.2 |
| q_{101} | 1,000 | 2.4 |

Fig. 5 The lane path and flow distribution before optimization

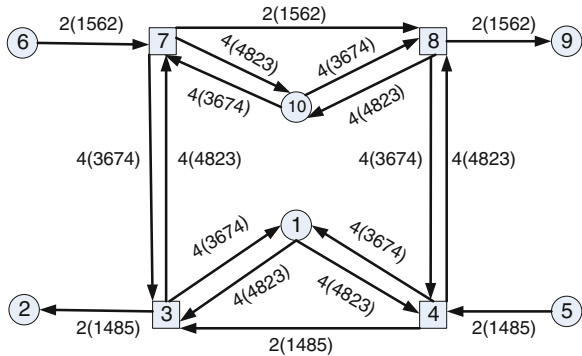
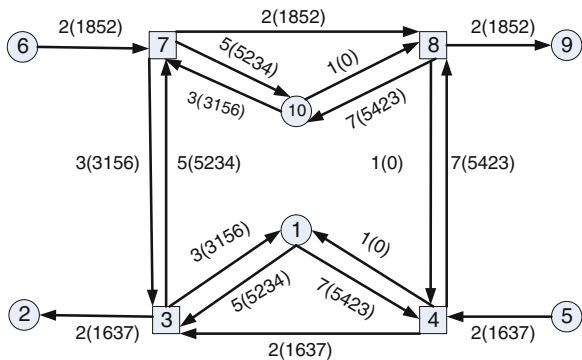


Fig. 6 The lane path and flow distribution after optimization



5 Conclusion

In this paper, we proposed a research framework on reversible lane, and made a feasibility study for lane shift according to the road sections, intersections, and real-time traffic flow changes of the road network. Through the research, we found that under ideal conditions, reversing the direction of the lane can improve the utilization of the road.

For the intersection, we obtained that the traffic imbalance crossroads of implementation of variable lane can process the additional traffic due to lane change. In road networks, we have established a bi-level programming model and adopted heuristic algorithm to solve it. The results show that through the rational allocation of the number of lanes of the road in both directions and making a more balanced distribution of traffic between each path, the proposed model can reduce urban traffic congestion while increasing the road network capacity. In this paper, we used traffic signal control, but we did not specify in the text for the simple calculation. In the future, we should focus on the complete road network and real-time adjust the lane and evacuate traffic according to the timely traffic to improve the operational efficiency of the road.

References

1. Brian W, Laurence L (2006) Reversible lane synthesis of practice. *J Transp Eng* 132: 933–944
2. Brian W, Laurence L (2006) Planning and operational practice for reversible roadways. *ITE J* 38–43
3. Zhang H-Z, Gao Z-Y (2007) Optimization approach for traffic road network design problem. *Chin J Manag Sci* 15(2):86–91
4. Sheu JB, Ritchie SG (2001) Stochastic modeling and real-time prediction of vehicular lane-changing behavior. *Transp Res Part B* 35:695–7161
5. Hausknecht M, Au T-C (2011) Peter stone dynamic lane reversal in traffic management. In: 14th IEEE ITS Conference ITSC, pp 1929–1934
6. Zhang P, Li W, Chang Y (2010) Reserve capacity model for urban road network with variable lanes. *J Southwest Jiaotong Univ* 45(2):255–260
7. Transportation Research Board (2000) Highway capacity manual, Chapter 16. National Research Council, Washington, pp 19–22
8. Song Y, Gao Z (1998) A heuristic solution algorithm for the continuous equilibrium network design problem. *J Northern Jiaotong Univ* 22(6):19–24

Multi-robot Formation Discrete Kinematics Model and Formation Control

Jin Wu, Guoliang Zhang, Jing Zeng and Jun Xu

Abstract The kinematics model of distributed multirobots formation was modeled in time-discrete condition with revolving round the formation center. Then make use of it to keep the desired front-end turn toward velocity orientation. At the same time, to converge to the desired geometry formation and the desired motion regular, a kind of communication topology graphs were defined, and a distributed discrete coordination control algorithm was proposed based on those graphs. A sufficient and necessary condition of asymptotic stability of the formation system is proved, and the convergence region of feedback control parameter is obtained. Lastly proved that the formation can converge to the desired geometry formation and to the desired motion regular under this sufficient and necessary condition. Simulation shows that the control algorithm can make the multirobots form the desired geometry formation and converge to the desired motion regular. It suggests that the control algorithm is effective and correct.

Keywords Formation control · Kinematics model · Stability analyses · Distributed control · Algebraic graph theoretic

1 Introduction

Formation control is a hot point of multirobot cooperative control. The aim of formation control is that multirobot system active adjusts every robot's behavior to make them from certain geometry shape. In fact, formation control is a kind of firm geometry agglomeration control. It is applied to many spheres such as multirobot cooperative control [1], multivehicle formation control [2], multiple unmanned

J. Wu (✉) · G. Zhang · J. Zeng · J. Xu
High-Tech Institute, Xi'an 710025, Shaanxi, People's Republic of China
e-mail: wujinrtj@163.com

aerial vehicles cooperative control [3], multiple underwater vehicles orientation control [4], multispacecraft formation control [5, 6], and so on.

The stability of multirobot system is the guarantee which multirobot formation complete different kinds of task based on. For stability of formation control with continuous model, Fax [7] had done much work by graph theory. Zheng [8] had done similar work with discrete-time based on output feedback. Yang [9] had analyzed stability of formation control in which multirobot formation moves with desired velocity under limited communication. Wang [10] had proposed a new definition of Input-to-State String Stability and analyze the string stability from the input-to-state view and singular perturbation theory. Jang [11] had proposed a distributed formation control algorithm based on communication delay by consensus theory, and obtained delay-independent and delay-dependent stable conditions, respectively, in the form of linear matrix inequality (LMI) based on Lyapunov stability theorem. However, there are few researches for discrete-time distributed multirobots formation with revolving round the formation center.

In this paper, the aim of multirobot formation control is to control a group of robots to form desired shape and move with desired velocity and track, and then to complete the task. This paper includes two part work: (1) set up the kinematics model of distributed multirobots formation in time-discrete condition with revolving round the formation center and resolve the question that keeping the desired front-end turn toward velocity orientation; (2) a distributed discrete coordination control algorithm was proposed, and a sufficient and necessary condition of asymptotic stability of the formation system is proved. The convergence region of feedback control parameter is obtained. Lastly prove that formation can converge to the desired geometry formation and the desired motion regular under this sufficient and necessary condition.

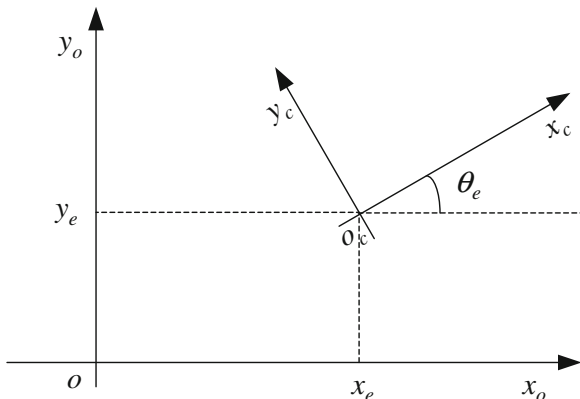
2 Discrete Kinematics Model of Multirobots system

Consider a multirobot formation consist of N universal wheel robots, R_i , $i = 1, 2, \dots, N$. Let $X_{oi} = [x_{oi}, y_{oi}, \theta_{oi}]^T$ and $V_{oi} = [v_{xoi}, v_{yoi}, \omega_{oi}]^T$ be the status in world coordinates $x_o o_o y_o$. Abstract formation center a virtual robot R_e , and its status is $X_e = [x_e, y_e, \theta_e]^T$, $V_e = [v_{xe}, v_{ye}, \omega_e]^T$. Generally speaking in world coordinates $x_o o_o y_o$, every robot is satisfied follow kinematics model:

$$\begin{cases} X_{oi}(k+1) = X_{oi}(k) + V_{oi}(k)T \\ V_{oi}(k+1) = V_{oi}(k) + U_{oi}(k)T \end{cases} \quad (1)$$

Here $T > 0$ is sampling time. However, when multirobot formation move with revolving round the formation center, that is to say ω_e is a function about k , transport motion of robot R_i includes revolving part relative to R_e . Due to this

Fig. 1 World coordinates and center coordinates



revolving part, kinematics model of robot in multirobot formation is different form formula (1). The work in this paper is discussed just under this situation.

2.1 Coordinate Transforming Relation

Based on right-hand corkscrew rule, set up center coordinates whose original point o_c is (x_e, y_e) and whose x_c orientation is the orientation of virtual robot R_e . Then rotate angle of center coordinates relative to world coordinates is θ_e .

From Fig. 1, we can know the coordinate transforming relation between world coordinates and center coordinates is following that:

$$\begin{cases} x_c = (x_o - x_e) \cos \theta_e + (y_o - y_e) \sin \theta_e \\ y_c = -(x_o - x_e) \sin \theta_e + (y_o - y_e) \cos \theta_e \\ \theta_c = \theta_o - \theta_e \end{cases}$$

$$\Rightarrow \begin{cases} v_{xc} = (v_{xo} - v_{xe}) \cos \theta_e + (v_{yo} - v_{ye}) \sin \theta_e \\ \quad - (x_o - x_e) \omega_e \sin \theta_e + (y_o - y_e) \omega_e \cos \theta_e \\ v_{yc} = -(v_{xo} - v_{xe}) \sin \theta_e + (v_{yo} - v_{ye}) \cos \theta_e \\ \quad - (x_o - x_e) \omega_e \cos \theta_e - (y_o - y_e) \omega_e \sin \theta_e \\ \omega_c = \omega_o - \omega_e \end{cases}$$

Matrix formulation is following that:

$$\mathbf{q}_c = \begin{bmatrix} A & O \\ B & A \end{bmatrix} (\mathbf{q}_o - \mathbf{q}_e) \quad (2)$$

$$\begin{aligned}
 \mathbf{q}_o &= [x_o, y_o, \theta_o, v_{xo}, v_{yo}, \omega_o]^T & \mathbf{q}_e &= [x_e, y_e, \theta_e, v_{xe}, v_{ye}, \omega_e]^T \\
 \mathbf{q}_c &= [x_c, y_c, \theta_c, v_{xc}, v_{yc}, \omega_c]^T \\
 A &= \begin{bmatrix} \cos \theta_e & \sin \theta_e & 0 \\ -\sin \theta_e & \cos \theta_e & 0 \\ 0 & 0 & 1 \end{bmatrix} & B &= \begin{bmatrix} -\omega_e \sin \theta_e & \omega_e \cos \theta_e & 0 \\ -\omega_e \cos \theta_e & -\omega_e \sin \theta_e & 0 \\ 0 & 0 & 0 \end{bmatrix}
 \end{aligned}$$

Assume that in world coordinates, multirobot system model is $\Gamma_o(X_o, V_o, U_o)$ in which status vectors are $X_o = [X_{o1}^T, X_{o2}^T, \dots, X_{oN}^T]^T$ and $V_o = [V_{o1}^T, V_{o2}^T, \dots, V_{oN}^T]^T$. At the same time, assume that in center coordinates, multirobot system model is $\Gamma_c(X_c, V_c, U_c)$ in which status vectors are $X_c = [X_{c1}^T, X_{c2}^T, \dots, X_{cN}^T]^T$ and $V_c = [V_{c1}^T, V_{c2}^T, \dots, V_{cN}^T]^T$. Then every robot abides by following formula: $X_{ci} = A(X_{oi} - X_e)$, $V_{ci} = A(V_{oi} - V_e) + B(X_{oi} - X_e)$.

Therefore we can get following relationship for multirobot system which includes N robots $X_c = I_N \otimes A(X_o - X_e^*)$, $V_c = I_N \otimes A(V_o - V_e^*) + I_N \otimes B(X_o - X_e^*)$. Here I_N is a unit matrix whose dimensionality is N ; $X_e^* = \mathbf{1}_N \otimes X_e$, $V_e^* = \mathbf{1}_N \otimes V_e$, $\mathbf{1}_N$ is a column vector whose dimensionality is N .

2.2 Discrete Model in Each System

In center coordinates, multirobot discrete model in system Γ_c is as to formula (3).

$$\begin{cases} X_c(k+1) = X_c(k) + V_c(k)T \\ V_c(k+1) = V_c(k) + U_c(k)T \end{cases} \tag{3}$$

Here $U_c(k) = U_c(X_c(k), V_c(k))$, is control input of system Γ_c in center coordinates. And in world coordinates, formation center virtual robot abides by following discrete model.

$$\begin{cases} X_e^*(k+1) = X_e^*(k) + V_e^*(k)T \\ V_e^*(k+1) = V_e^*(k) + U_e^*(k)T \end{cases} \tag{4}$$

Here $U_e^*(k) = \mathbf{1}_N \otimes U_e(k)$, and $U_e(k)$ is control input of formation center virtual robot in world coordinates, which also is control input to make formation center move with desired regular. That is to say, formation center motion regular can be summarized as formula (4). In order to describe the question conveniently, we set up an equation as follows: $A_N(k) = I_N \otimes A(k)$, $A_a = [I_N \otimes A(k+1)]^{-1}[I_N \otimes A(k)]$, $A_{b1} = [I_N \otimes A(k+1)]^{-1}[I_N \otimes B(k)]$, $A_{b2} = [I_N \otimes A(k+1)]^{-1}[I_N \otimes B(k+1)]$.

We can get discrete model of system Γ_o in world coordinates as follows:

$$\begin{bmatrix} X_o(k+1) \\ V_o(k+1) \end{bmatrix} = \Psi(k) \begin{bmatrix} X_o(k) \\ V_o(k) \end{bmatrix} + \mathbf{H}(k) \begin{bmatrix} X_e^*(k) \\ V_e^*(k) \end{bmatrix} + \begin{bmatrix} O_{Nd} \\ U_o(k)T \end{bmatrix} \quad (5)$$

$$\Psi(k) = \begin{bmatrix} A_a + A_{b1}T & A_aT \\ -A_{b2}A_a + A_{b1} & A_a \end{bmatrix} \quad \mathbf{H}(k) = \begin{bmatrix} I_{Nd} & TI_{Nd} \\ O_{Nd} & I_{Nd} \end{bmatrix} - \Psi(k)$$

$$U_o(k) = -A_{b2}A_{b1}[X_o(k) - X_e^*(k)] - A_{b2}A_a[V_o(k) - V_e^*(k)] + A_N^{-1}(k+1)U_c(k) + U_e^*(k) \quad (6)$$

Here $U_o(k) = U_o(X_o(k), V_o(k))$, is control input of system Γ_o in world coordinates.

Definition 1 If desired relative position vector of each robot relative to formation center is $X_{p1}, X_{p2}, \dots, X_{pN}$, we call $P = [X_{p1}^T, X_{p2}^T, \dots, X_{pN}^T]^T$ as formation vector, in which $X_{pi} \in R^3$.

From Definition 1, we can easily know that N robots form certain formation and move with desired regular if we have $X_{ci} - X_{pi} = \mathbf{0}$, $V_{ci} = \mathbf{0}$, $i = 1, 2, \dots, N$ in center coordinates. Let $X_c^* = X_c - P, V_c^* = V_c$, and then from formula (5) we can get discrete model of system Γ_c^* in which status vector are X_c^* and V_c^* as follows:

$$\begin{cases} X_c^*(k+1) = X_c^*(k) + V_c^*(k)T \\ V_c^*(k+1) = V_c^*(k) + U_c^*(k)T \end{cases} \quad (7)$$

Here $U_c^*(k) = U_c^*(X_c^*(k), V_c^*(k)) = U_c(X_c(k) - P, V_c(k))$, is control input of system Γ_c^* .

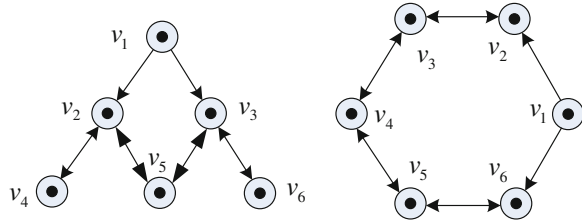
3 Communication Graph and Control Protocol

3.1 Communication Graph

In multirobot system, each individual communicate with others through radio communication network. This network includes two parts, one is based on data packet, and the other is based on measuring information. In this paper, we use a communication topological graph stand for communication relationship of the network. Algebraic graph theoretic is an important tool to research cooperative control and analysis multirobot formation control stability.

Let $G = (V(G), E(G))$ be a directed graph of order N , where, $V(G) = \{v_1, v_2, \dots, v_N\}$ is the set of nodes, $E(G) \subseteq V \times V$ is the set of edges, and its

Fig. 2 A few Ω graphs



adjacency matrix is A . The node indexes belong to a finite index set $\{1, 2, \dots, N\}$. An edge of G is denoted by $e_{ij} = (v_j, v_i)$. The adjacency matrix is defined as $a_{ii} = 0$ and $a_{ij} \geq 0$. $a_{ij} > 0$ if and only if $e_{ij} \in E(G)$. The set of neighbors of node v_i is denoted by $N_i = \{v_j | v_j \in V(G), (v_j, v_i) \in E(G)\}$. The in-degree and out-degree of node v_i are defined, respectively, as $d_{in}(v_i) = \sum_{j=1}^N a_{ij}$, $d_{out}(v_i) = \sum_{j=1}^N a_{ji}$. Then, the graph Laplacian with the directed graph is defined as $L = [l_{ij}]$, where $l_{ii} = d_{in}(v_i)$ and $l_{ij} = -a_{ij}$, $i \neq j$. An important fact of L is that all the row sums of L are zero and thus $\mathbf{1}_N = [1, 1, \dots, 1]^T$ is an eigenvector of L associated with the eigenvalue $\lambda = 0$. A directed path is a sequence of ordered edges of the form $(v_{i_1}, v_{i_2}), (v_{i_2}, v_{i_3}), \dots$, where $v_{i_j} \in V(G)$. If a directed graph has the property that (v_i, v_j) belongs to $E(G)$ for any $(v_j, v_i) \in E(G)$, the directed graph is called undirected. If there is a directed path from every node to every other node, the graph is said to be strongly connected.

Here we let robot R_i stand for v_i in communication topological graph $G = (V(G), E(G))$. If a communication path from R_i to R_j existed, we have $(v_i, v_j) \in E(G)$, that is to say, R_j is a neighbor of R_i . In order to make multirobot formation form desired shape and keep formation center move with desired motion regular, we let R_1 enact the pilot of multirobot formation. And then the pilot creates a virtual robot R_e in formation center, and controls R_e moving based on the intention of the task. Robot R_1 just can transport its status information to its neighbors, and broadcast control protocol u_e of center virtual robot R_e to environment. But robot R_1 cannot receive information from other robot, which is to say that R_1 will not be any robot's neighbor. In communication network, each robot just communicates with its neighbors. We define a kind of graph as follows:

Definition 2 Graph $G = (V(G), E(G))$ is a directed graph with generation tree, in which $(v_1, v_i) \notin E(G)$, $i = 2, 3, \dots, N$. $G^* = (V^*(G^*), E^*(G^*))$ is a subgraph which we get by eliminating node v_1 in graph G , and $E^*(G^*) = \{(v_i, v_j) \in E(G) | v_i, v_j \in V^*(G^*)\}$, $V^*(G^*) = \{v_2, v_3, \dots, v_N\}$. If G^* is a bidigraph and strongly connected, we call graph G as Ω graph. Figure 2 shows two graph which belong to Ω graph. In this paper, the communication topological graph which we adopt belongs to Ω graph. Here we have a theorem about Ω graph.

Theorem 1 *If $G \in \Omega$, then zero is one eigenvalue of L , and the rest $N - 1$ eigenvalues are all positive and real.*

Proof Due to $G \in \Omega$, we can assume that adjacency matrix, in-degree matrix and Laplacian matrix of graph G as follows:

$$A = \begin{bmatrix} 0 & 0 & 0 & \cdots & 0 \\ a_{21} & 0 & a_{23} & \cdots & a_{2N} \\ a_{31} & a_{32} & 0 & \cdots & a_{3N} \\ \vdots & \vdots & \vdots & \ddots & \vdots \\ a_{N1} & a_{N2} & a_{N3} & \cdots & 0 \end{bmatrix} \quad D = \begin{bmatrix} 0 & 0 & 0 & \cdots & 0 \\ 0 & d_2 & 0 & \cdots & 0 \\ 0 & 0 & d_3 & \cdots & 0 \\ \vdots & \vdots & \vdots & \ddots & 0 \\ 0 & 0 & 0 & \cdots & d_N \end{bmatrix}$$

$$L = D - A = \begin{bmatrix} 0 & 0 & 0 & \cdots & 0 \\ -a_{21} & d_2 & -a_{23} & \cdots & -a_{2N} \\ -a_{31} & -a_{32} & d_3 & \cdots & -a_{3N} \\ \vdots & \vdots & \vdots & \ddots & \vdots \\ -a_{N1} & -a_{N2} & -a_{N3} & \cdots & d_N \end{bmatrix}$$

Because $G^* = (V^*(G^*), E^*(G^*))$ is a bidiagraph and strongly connected, we know $a_{rs} = a_{sr}$ ($2 \leq r \leq N, 2 \leq s \leq N, r \neq s$). And we can assume that real symmetric matrix L_2 is as follows

$$L_2 = \begin{bmatrix} d_2 & -a_{23} & \cdots & -a_{2N} \\ -a_{32} & d_3 & \cdots & -a_{3N} \\ \vdots & \vdots & \ddots & \vdots \\ -a_{N2} & -a_{N3} & \cdots & d_N \end{bmatrix} \Rightarrow |\lambda I - L|$$

$$= \begin{vmatrix} \lambda & 0 & 0 & \cdots & 0 \\ a_{21} & \lambda - d_2 & a_{23} & \cdots & a_{2N} \\ a_{31} & a_{32} & \lambda - d_3 & \cdots & a_{3N} \\ \vdots & \vdots & \vdots & \ddots & \vdots \\ a_{N1} & a_{N2} & a_{N3} & \cdots & \lambda - d_N \end{vmatrix} = |\lambda| |\lambda I - L_2|$$

Let $\lambda(L)$ be eigenvalue aggregate of matrix L , and let $\lambda(L_2)$ be eigenvalue aggregate of matrix L_2 , then we have $\lambda(L) = \lambda(L_2) + \{0\}$. According to related knowledge in matrix theory, we have following theorem:

Theorem 2 *Eigenvalues of real symmetric matrix are all real.*

According to Theorem 2, we know that eigenvalues of L_2 are all real, and $\lambda(L_2)$ is a set of real numbers. Therefore, $\lambda(L)$ also is a set of real numbers which is to say that eigenvalues of L are all real.

Lemma 1 *If $L \in \mathbb{R}^{N \times N}$ is Laplacian matrix of directed graph $G = (V(G), E(G))$, and $\mathbf{1}_N = [1, 1, \dots, 1]^T \in \mathbb{R}^N$, we have few conclusions as follows:*

- (1) *L has one 0 eigenvalue at least, and $\mathbf{1}_N = [1, 1, \dots, 1]^T$ is an eigenvector of L associated with the eigenvalue $\lambda = 0$, $L\mathbf{1}_N = \mathbf{0}$.*
- (2) *If graph G includes generation tree, then 0 is single eigenvalue of L , and the rest $N - 1$ eigenvalues all have positive real-part.*

From Lemma 1, we know that there is only one 0 eigenvalue in $\lambda(L)$ and the rest $N - 1$ eigenvalues are all positive real.

3.2 Control Protocol

In communication network, each robot just communicates with its neighbors, and gets them status information. Therefore in system Γ_c^* , we adopt control protocol as follows: $u_{ci}^* = \sum_{j \in N_i} \omega_1(X_{cj}^* - X_{ci}^*) + \sum_{j \in N_i} \omega_2(V_{cj}^* - V_{ci}^*)$. In this control protocol, N_i is the neighbor collection of robot R_i . Consequently, in multirobot system Γ_c^* , we have $U_c^*(k) = -\omega_1(L \otimes I_d)X_c^*(k) - \omega_2(L \otimes I_d)V_c^*(k)$. Here d is the dimensionality of X_{ci}^* , and $d = 3$ in this paper. I_d is unit vector whose dimensionality is d . We can get kinematics model of closed-loop system Γ_c^* as follows from formula (7)

$$\begin{cases} X_c^*(k+1) = X_c^*(k) + V_c^*(k)T \\ V_c^*(k+1) = V_c^*(k) - \omega_1(L \otimes I_d)TX_c^*(k) - \omega_2(L \otimes I_d)TV_c^*(k) \end{cases} \quad (8)$$

Let us put $X_c^* = X_c - P$, $V_c^* = V_c$ into $U_c^*(k)$. And we thus have the following control protocol of closed-loop system $\Gamma_c: U_c(k) = -\omega_1(L \otimes I_d)[X_c(k) - P] - \omega_2(L \otimes I_d)V_c(k)$. Consequently, the kinematics model of closed-loop system Γ_c is

$$\begin{cases} X_c(k+1) = X_c(k) + V_c(k)T \\ V_c(k+1) = V_c(k) - \omega_1(L \otimes I_d)[X_c(k) - P]T - \omega_2(L \otimes I_d)V_c(k)T \end{cases} \quad (9)$$

From formula (6), we can get following equation:

$$U_o(k) = -[A_{b2}A_{b1} + \omega_1(L \otimes I_d)A_a + \omega_2(L \otimes I_d)A_{b1}](X_o - X_e^*) - [A_{b2}A_a + \omega_2(L \otimes I_d)A_a](V_o - V_e^*) + \omega_1[L \otimes A^{-1}(k+1)]P + U_e^*(k)$$

Let $a_1 = A_{b2}A_{b1} + \omega_1(L \otimes I_d)A_a + \omega_2(L \otimes I_d)A_{b1}$, $a_2 = A_{b2}A_a + \omega_2(L \otimes I_d)A_a$, $a_3 = \omega_1[L \otimes A^{-1}(k+1)]$. And we thus have the following control protocol of closed-loop system Γ_o :

$$U_o(k) = -a_1[X_o(k) - X_e^*(k)] - a_2[V_o(k) - V_e^*(k)] + a_3P + U_e^*(k) \quad (10)$$

Let $U_f(k) = -a_1[X_o(k) - X_e^*(k)] - a_2[V_o(k) - V_e^*(k)] + a_3P$. And then we have $U_o(k) = U_f(k) + U_e^*(k)$. That is to say, $U_o(k)$ includes two parts. First part is $U_f(k)$ which is formation control input. And second part is $U_e^*(k)$ which make formation center move following desired motion regular. $U_e^*(k)$ is created by task planning module, and broadcasted by pilot robot. In fact, $U_e^*(k)$ is external input in system Γ_o .

We know that system Γ_c^* comes from system Γ_c by linear transformation, and system Γ_c comes from system Γ_o by translation and rotation transformation. Consequently, system Γ_c^* is stabile equal that system Γ_c is stabile, and then system Γ_o is stabile if system Γ_c is stabile.

4 Formation Control Algorithm Stability Analysis

4.1 Related Theorem and Corollary

Let $L^* = L \otimes I_d$. State equation of system Γ_c^* is following matrix formulation:

$$\begin{bmatrix} X_c^*(k+1) \\ V_c^*(k+1) \end{bmatrix} = \Phi \begin{bmatrix} X_c^*(k) \\ V_c^*(k) \end{bmatrix} \quad \Phi = \begin{bmatrix} I_{Nd} & TI_{Nd} \\ -\omega_1 L^* T & I_{Nd} - \omega_2 L^* T \end{bmatrix} \quad (11)$$

Here I_{Nd} is unit vector whose dimensionality is Nd . Stability of closed-loop system Γ_c^* depends on distribution of eigenvalues of matrix Φ . First we have two theorems about eigenvalues of matrix L^* .

Theorem 3 [11] *If $\lambda_1, \lambda_2, \dots, \lambda_N$ are all eigenvalues of matrix L , eigenvalue collection of matrix L^* is $\{(\lambda_1)_d, (\lambda_2)_d, \dots, (\lambda_N)_d\}$, in which $(\lambda_i)_d$ is a subcollection whose elements all are λ_i , and number of elements is d , namely $(\lambda_i)_d = \{\lambda_i, \lambda_i, \dots, \lambda_i\}$.*

Theorem 4 [11] *1 is an eigenvalue of matrix Φ .*

According to theory of Lyapunov stability, closed-loop system Γ_c^* is stabile iff all eigenvalues of matrix Φ locate interior of unit circle in complex plane. Thus we can get following corollary:

Corollary 1 *Necessary and sufficient condition of closed-loop system Γ_c^* stability is that spectral radius of matrix Φ is 1.*

4.2 Stability Analysis

According to Corollary 1, we know that the key question about designing controller is how to choose feedback control parameter (ω_1, ω_2) to make eigenvalues of matrix Φ locate interior of unit circle in complex plane. First, we give following theorem:

Theorem 5 *Necessary and sufficient condition of closed-loop system Γ_c^* stability is that feedback control parameter (ω_1, ω_2) locates interior of \mathfrak{R} in $\omega_1 - \omega_2$ plane. Here \mathfrak{R} is $\mathfrak{R} = \{(\omega_1, \omega_2) | \omega_2 > 0, \omega_1 < \omega_2/T, \omega_1 > 2\omega_2/T - 4/\lambda_{\max}T^2\}$, and λ_{\max} is the maximize eigenvalue of matrix L .*

Proof Necessity: Let in-degree of nets in communicate topological graph $G \in \Omega$ are d_1, d_2, \dots, d_N , thus we know that track of matrix Φ is $T_r(\Phi) = Nd + T_r[I_{Nd} - \omega_2L^*] = 2Nd - \omega_2Td \sum_{i=1}^N d_i$. Because all eigenvalues of matrix Φ locate interior of unit circle in complex plane, we have $\sum \lambda(\Phi) < 2Nd$. Due to $T_r(\Phi) = \sum \lambda(\Phi)$, we can get $\omega_2 > 0$. Let γ is anyone of matrix Φ 's eigenvalues. Thus we have

$$|\gamma I_{2Nd} - \Phi| = 0 \Rightarrow \begin{vmatrix} (\gamma - 1)I_{Nd} & -TI_{Nd} \\ \omega_1 TL^* & (\gamma - 1)I_{Nd} + \omega_2 TL^* \end{vmatrix} = 0$$

If $\gamma = 1$, the above formula is right, and $(\omega_1, \omega_2) \in \mathbb{R}^2$. And if $\gamma \neq 1$, we have

$$\begin{vmatrix} (\gamma - 1)I_{Nd} & -TI_{Nd} \\ O_{Nd} & (\gamma - 1)I_{Nd} + \omega_2 TL^* + \omega_1 T^2 L^*/(\gamma - 1) \end{vmatrix} = 0 \\ \Rightarrow -(\gamma - 1)^2 / [\omega_2 T(\gamma - 1) + \omega_1 T^2] \in \lambda(L^*)$$

Consequently, we know $-(\gamma - 1)^2 / [\omega_2 T(\gamma - 1) + \omega_1 T^2]$ is an eigenvalue of matrix L^* . According to property (3) in corollary 1, we know that the number of L^* 's 0 eigenvalues is d , and the rest $(N - 1)d$ eigenvalues all are positive real. Generally speaking, we let $-(\gamma - 1)^2 / [\omega_2 T(\gamma - 1) + \omega_1 T^2] = \lambda_i$. Obviously, when $\lambda_i = 0$, we have $\gamma = 1$. Let $\gamma = a_i + jb_i$, $a_i, b_i \in (-1, 1)$. We thus have $(a_i + jb_i - 1)^2 / [\omega_2 T(a_i + jb_i - 1) + \omega_1 T^2] = -\lambda_i$. Because imaginary parts in the above formula two sides are equal, we can get

$$2(a_i - 1)[\omega_2 T(a_i - 1) + \omega_1 T^2] = [(a_i - 1)^2 - b_i^2]\omega_2 T \Rightarrow \omega_1/\omega_2 \\ = (a_i - 1)^2 + b_i^2 / 2(1 - a_i)T$$

Due to $a_i < 1, \omega_2 > 0, T > 0$, we thus get $\omega_1 > 0$. When $\lambda_i > 0$, we have

$$\begin{aligned} [\omega_2 T(\gamma - 1) + \omega_1 T^2] \lambda_i + (\gamma - 1)^2 &= 0 \Rightarrow \gamma \\ &= 1 + [-\omega_2 T \lambda_i \pm \sqrt{(\omega_2 T \lambda_i)^2 - 4\omega_1 T^2 \lambda_i}] / 2 \end{aligned} \quad (12)$$

Due to $\|\gamma\| < 1$, we discuss two following situations.

- (1) If $\omega_2^2 \lambda_i^2 - 4\omega_1 \lambda_i \geq 0 \Rightarrow \omega_1 \leq \omega_2^2 \lambda_i / 4$, γ is real number, and $-1 < \gamma < 1$. Namely, we have

$$\begin{aligned} \|\gamma\| &= \left\| 1 + [-\omega_2 T \lambda_i \pm \sqrt{(\omega_2 T \lambda_i)^2 - 4\omega_1 T^2 \lambda_i}] / 2 \right\| < 1 \\ &\Rightarrow \begin{cases} \omega_1 > 2\omega_2 / T - 4 / \lambda_i T^2 \\ \omega_2 < 4 / \lambda_i T \end{cases} \end{aligned}$$

Consequently, we get $(\omega_1, \omega_2) \in \mathfrak{R}_{i1} = \{(\omega_1, \omega_2) | \omega_1 > 0, 0 < \omega_2 < 4 / \lambda_i T, \omega_1 > 2\omega_2 / T - 4 / \lambda_i T^2, \omega_1 \leq \omega_2^2 \lambda_i / 4\}$. That is to say (ω_1, ω_2) locates interior of \mathfrak{R}_{i1} .

- (2) If $\omega_2^2 \lambda_i^2 - 4\omega_1 \lambda_i < 0 \Rightarrow \omega_1 > \omega_2^2 \lambda_i / 4$, γ is complex number. Due to $\|\gamma\| < 1$, we have

$$\|\gamma\| = \left\| 2 - \omega_2 T \lambda_i \pm \sqrt{(\omega_2 T \lambda_i)^2 - 4\omega_1 T^2 \lambda_i} \right\| / 2 < 1 \Rightarrow \omega_1 < \omega_2 / T$$

Consequently, we can get $(\omega_1, \omega_2) \in \mathfrak{R}_{i2} = \{(\omega_1, \omega_2) | \omega_1 > 0, \omega_2 > 0, \omega_1 < \omega_2 / T, \omega_1 > \omega_2^2 \lambda_i / 4\}$. Namely (ω_1, ω_2) locates interior of \mathfrak{R}_{i2} .

According to consequence of situation (1) and (2), we know that $(\omega_1, \omega_2) \in \mathfrak{R}_{i1} \cup \mathfrak{R}_{i2}$ for every eigenvalue which is not zero. Moreover, we have $\mathfrak{R}_{i1} \cup \mathfrak{R}_{i2} = \{(\omega_1, \omega_2) | \omega_2 > 0, \omega_1 < \omega_2 / T, \omega_1 > 2\omega_2 / T - 4 / \lambda_i T^2\}$. Consequently, we can get $(\omega_1, \omega_2) \in \cap_{i=1}^{N-1} (\mathfrak{R}_{i1} \cup \mathfrak{R}_{i2}) = \mathfrak{R}$. Namely, $(\omega_1, \omega_2) \in \mathfrak{R}$. Necessary is proved.

Sufficient: From formula (12), we know $\gamma = 1$ when $\lambda_i = 0$. And when $\lambda_i > 0$, we have $\gamma = 1 + [-\omega_2 T \lambda_i \pm \sqrt{(\omega_2 T \lambda_i)^2 - 4\omega_1 T^2 \lambda_i}] / 2$. Due to $(\omega_1, \omega_2) \in \mathfrak{R}$, we can get $\|\gamma\| < 1$ easily. Namely, when $(\omega_1, \omega_2) \in \mathfrak{R}$, closed-loop system Γ_c^* is stabile. Sufficiency is proved.

4.3 Convergence Analysis

We know that closed-loop system Γ_c^* stability is not equal to that multirobot system converges to desired formation shape and motion regular. In fact that, we have the following convergence theorem about closed-loop system Γ_c^* .

Theorem 6 *Stability of closed-loop system Γ_c^* is sufficient condition of closed-loop system Γ_c^* convergence.*

Proof Let $\{(\gamma_1)_d, (\gamma_2)_d, \dots, (\gamma_{2N})_d\}$ is eigenvalue collection of matrix Φ , in which $(\gamma_i)_d$ is a subcollection whose element are all γ_i and number of elements is d , namely $(\gamma_i)_d = \{\gamma_i, \gamma_i, \dots, \gamma_i\}$. According to Corollary 3 and Theorem 4, we know that when $(\omega_1, \omega_2) \in \mathfrak{R}$, $\gamma_{2N-1} = \gamma_{2N} = 1$, $\|\gamma_i\| < 1$, $i = 1, 2, \dots, 2N - 2$. Let

$$\Phi_2 = \begin{bmatrix} I_N & TI_N \\ -\omega_1 TL & I_N - \omega_2 TL \end{bmatrix} \in \mathbf{R}^{2N \times 2N}$$

Thus we have $\Phi = \Phi_2 \otimes I_d$. From corollary 3, we know eigenvalue collection of matrix Φ_2 is $\{\gamma_1, \gamma_2, \dots, \gamma_{2N}\}$. According to matrix theory, we can find a matrix H to make matrix Φ_2 become following Jordan form

$$\Phi_2 = H \sum H^{-1} = H \begin{bmatrix} \gamma_1 & 0 & 0 & 0 & 0 \\ 0 & \gamma_2 & 0 & 0 & 0 \\ \vdots & \vdots & \ddots & \vdots & \vdots \\ 0 & 0 & 0 & 1 & 1 \\ 0 & 0 & 0 & 0 & 1 \end{bmatrix} H^{-1} \tag{13}$$

Here $H = [h_1, h_2, \dots, h_{2N-1}, h_{2N}]$, and h_{2N-1} is a eigenvector of matrix Φ_2 associated with the eigenvalue $\gamma = 1$. We thus have $\Phi_2 h_{2N-1} = h_{2N-1}$. Let $H_{(2N-1)1} = [h_{(2N-1)1}, h_{(2N-1)2}, \dots, h_{(2N-1)N}]^\tau$, $H_{(2N-1)2} = [h_{(2N-1)N+1}, h_{(2N-1)(N+2)}, \dots, h_{(2N-1)2N}]^\tau$. We have

$$\begin{bmatrix} I_N & I_N \\ -\omega_1 L & I_N - \omega_2 L \end{bmatrix} \begin{bmatrix} H_{(2N-1)1} \\ H_{(2N-1)2} \end{bmatrix} = \begin{bmatrix} H_{(2N-1)1} \\ H_{(2N-1)2} \end{bmatrix} \Rightarrow \begin{cases} H_{(2N-1)2} = O_{N \times 1} \\ -\omega_1 LH_{(2N-1)1} = O_{N \times 1} \end{cases}$$

Due to properties of matrix L , we have $LH_{(2N-1)1} = O_{N \times 1}$ when $H_{(2N-1)1} = k_1 \mathbf{1}_N$ ($k_1 \in \mathbf{R}$). Consequently, we can get $H_{(2N-1)1} = k_1 \mathbf{1}_N$, $H_{(2N-1)2} = O_{N \times 1}$. According to formula (21), we have $\Phi_2 H = H \sum \Rightarrow \Phi_2 h_{2N} = h_{2N-1} + h_{2N}$. Let $H_{(2N)1} = [h_{(2N)1}, h_{(2N)2}, \dots, h_{(2N)N}]^\tau$, $H_{(2N)2} = [h_{(2N)N+1}, h_{(2N)(N+2)}, \dots, h_{(2N)2N}]^\tau$.

We thus have

$$\begin{bmatrix} I_N & I_N \\ -\omega_1 L & I_N - \omega_2 L \end{bmatrix} \begin{bmatrix} H_{(2N)1} \\ H_{(2N)2} \end{bmatrix} = \begin{bmatrix} H_{(2N-1)1} \\ H_{(2N-1)2} \end{bmatrix} + \begin{bmatrix} H_{(2N)1} \\ H_{(2N)2} \end{bmatrix} \Rightarrow \begin{cases} H_{(2N)1} = k_2 \mathbf{1}_N \\ H_{(2N)2} = k_1 \mathbf{1}_N \end{cases} \quad (k_2 \in \mathbf{R})$$

According to properties of Jordan matrix, we can get

$$\Phi_2^k = H \sum_{i=0}^{k-1} H^{-1} = H \begin{bmatrix} \gamma_1^k & 0 & 0 & 0 & 0 \\ 0 & \gamma_2^k & 0 & 0 & 0 \\ \vdots & \vdots & \ddots & \vdots & \vdots \\ 0 & 0 & 0 & 1 & k \\ 0 & 0 & 0 & 0 & 1 \end{bmatrix} H^{-1}$$

Due to $\|\gamma_i\| < 1, i = 1, 2, \dots, 2N - 2$, we thus have $\gamma_i^k = 0 (k \rightarrow +\infty), i = 1, 2, \dots, 2N - 2$. Consequently, we have

$$\Phi_2^k = [h_1, h_2, \dots, h_{2N-1}, h_{2N}] \sum_{i=0}^{k-1} H^{-1} (k \rightarrow +\infty) \Rightarrow \Phi_2^k = \mathbf{e} \otimes \mathbf{1}_N \quad (k \rightarrow +\infty),$$

$$\mathbf{e} = \begin{bmatrix} e_1 & e_2 & \cdots & e_{2N} \\ m_1 & m_2 & \cdots & m_{2N} \end{bmatrix}$$

Due to $\Phi = \Phi_2 \otimes I_d$, when $k \rightarrow +\infty$, we have $\Phi^k = (\Phi_2 \otimes I_d)^k = \Phi_2^k \otimes I_d = \mathbf{e} \otimes [I_d \ I_d \ \dots \ I_d]^T$. Combining formula (14), when $k \rightarrow +\infty$, we have

$$\begin{bmatrix} X_c^*(k+1) \\ V_c^*(k+1) \end{bmatrix} = \Phi \begin{bmatrix} X_c^*(k) \\ V_c^*(k) \end{bmatrix} = \Phi^k \begin{bmatrix} X_c^*(0) \\ V_c^*(0) \end{bmatrix} \Rightarrow \begin{bmatrix} X_c^*(k+1) \\ V_c^*(k+1) \end{bmatrix} = \begin{bmatrix} \mathbf{1}_N \otimes \mathbf{e}_0 \\ \mathbf{1}_N \otimes \mathbf{m}_0 \end{bmatrix}$$

Here $\mathbf{e}_0 = \sum_{i=1}^N e_i X_{ci}^*(0) + \sum_{i=1}^N e_{N+i} V_{ci}^*(0), \mathbf{m}_0 = \sum_{i=1}^N m_i X_{ci}^*(0) + \sum_{i=1}^N m_{N+i} V_{ci}^*(0)$. In system Γ_c^* , due to $V_{c1}^*(0) = \mathbf{0}, X_{c1}^*(0) = \mathbf{0}, u_{c1}^* = \mathbf{0}$, we have $V_{c1}^*(k+1) = V_{c1}^*(0) = \mathbf{0}, X_{c1}^*(k+1) = X_{c1}^*(0) = \mathbf{0}$. Consequently, we can get $\sum_{i=1}^N e_i X_{ci}^*(k+1) + \sum_{i=1}^N e_{N+i} V_{ci}^*(k+1) = \mathbf{0}, \sum_{i=1}^N m_i X_{ci}^*(k+1) + \sum_{i=1}^N m_{N+i} V_{ci}^*(k+1) = \mathbf{0}$. And then we have following formula when $k \rightarrow +\infty, X_c^*(k+1) = \mathbf{0}, V_c^*(k+1) = \mathbf{0}$.

Consequently, in system Γ_c , we have $X_c(k+1) = P, V_c(k+1) = \mathbf{0}, (k \rightarrow +\infty)$. Namely, multirobot system converges to desired formation shape. Due to coordinate transformation relationship (4), we can get $X_o = (I_N \otimes A)^{-1} X_c + X_e^*, V_o = -(I_N \otimes A^{-1} B A^{-1}) X_c + (I_N \otimes A)^{-1} V_c + V_e^*$. Consequently, when $k \rightarrow +\infty$ in system Γ_o , we have

Fig. 3 Formation shape and communication topological graph

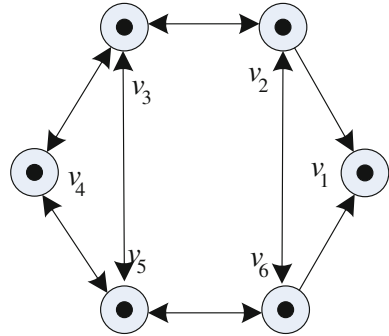
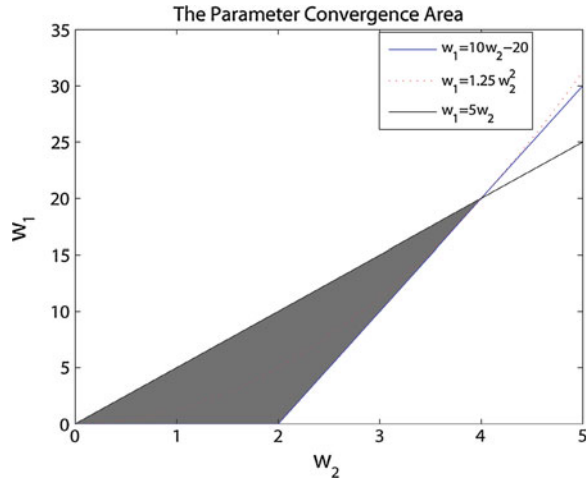


Fig. 4 $\omega_1 - \omega_2$ convergence domain



$$\begin{bmatrix} X_o(k) \\ V_o(k) \end{bmatrix} = \begin{bmatrix} [I_N \otimes A(k)]^{-1} P \\ -[I_N \otimes A^{-1}(k)B(k)A^{-1}(k)]P \end{bmatrix} + \begin{bmatrix} X_e^*(k) \\ V_e^*(k) \end{bmatrix}$$

Namely, multirobot system converges to desired motion regular.

5 Simulation Results

In simulation, multirobots system includes six robots. Formation shape and communicate topological graph is as Fig. 3. Then Laplace matrix L is as follows. Maximum eigenvalue of matrix L is $\lambda_{\max} = 5$. In experiment, $T = 0.2$ s, and convergence domain of parameter is as Fig. 4. In this paper, we bracket off avoid collision between robots.

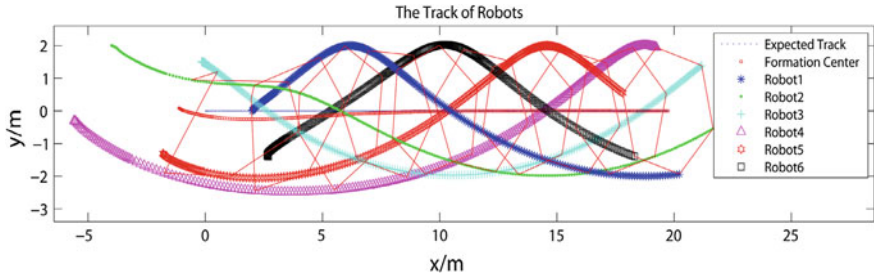


Fig. 5 The trajectory of six robots with revolving round the formation center

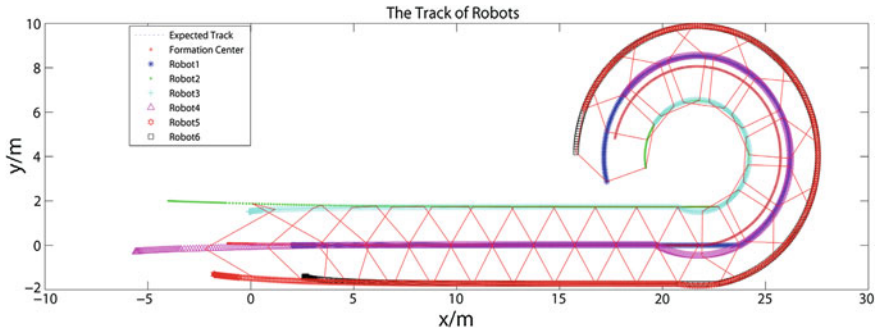


Fig. 6 The trajectory of six robots with formation center moving along desired trajectory

$$L = \begin{bmatrix} 0 & 0 & 0 & 0 & 0 & 0 \\ -1 & 3 & -1 & 0 & 0 & -1 \\ 0 & -1 & 3 & -1 & -1 & 0 \\ 0 & 0 & -1 & 2 & -1 & 0 \\ 0 & 0 & -1 & -1 & 3 & 1 \\ -1 & -1 & 0 & 0 & -1 & 3 \end{bmatrix}$$

Experiment 1: In convergence domain \mathfrak{R} , we choose a group parameter (ω_1, ω_2) , in which $\omega_1 = 0.1, \omega_2 = 1.5$. Initial position of robots are $(3.4, 0.2, 0)$ $(4, 2, 0)$ $(-3, 1.5, 0)$ $(-5.6, -0.3, 0)$ $(-1.8, -1.3, 0)$ $(2.7, -1.4, 0)$, and initial velocity all are $(0,0,0)$. Initial position of center virtual robot is $(0, 0, 0)$, and velocity V_e becomes from $(0, 0, 0)$ to $(0.2, 0, 0.1)$ by uniformly accelerated. The trajectory of six robots is as Fig. 5. From Fig. 5, we can know easily that six robots form desired formation shape and move with revolving round the formation center.

Experiment 2: Parameter (ω_1, ω_2) and initial status of every robot are same as Experiment 1. During multirobot formation motion, we design that center virtual robot moves along a desired trajectory. The trajectory of six robots is as Fig. 6. We can find that six robots form desired formation shape and keep the desired front-end turn toward velocity orientation when formation moves along a desired curve.

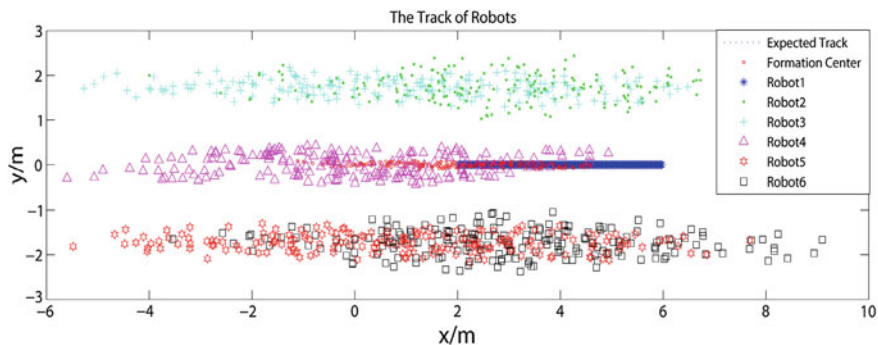


Fig. 7 The trajectory of six robots with $\omega_1 = 5$, $\omega_1 = 1$

Experiment 3: As a reference, we have Experiment 3. We choose $\omega_1 = 5$, $\omega_1 = 1$, which are out of convergence domain. The trajectory of six robots is as Fig. 7. We can observe easily that the trajectory of six robots is emanative.

6 Conclusion

In this paper, we mainly study the question of multirobot cooperative formation control with revolving round the formation center. First, based on robot kinematics model in center coordinates, we get multirobot discrete kinematics model (5) and control input (6) in world coordinates by coordinate transformation. Second, we define a kind of communicate topological graphs. And then based on these graph, we make use of control input (10) to coordination control multirobot formation. At the same time, we analyze control stability and get convergence domain of parameter. Lastly, we use six robots to simulate experiment which suggests that the control algorithm is effective and correct.

References

1. Ding XC, Kloetzer M, Chen Y, Belta C (2011) Automatic deployment of robotic teams. *IEEE Robot Autom Mag* 18(3):75–86
2. Zhiying Yu, Ge Guo, Fang Qian (2012) Vehicle formation control based on input-output feedback linearization. *J Dali Marit Univ* 38(1):111–117
3. Deng W, Wang X, Wang X et al (2011) Controller design of UAVs formation keep and change. *Comput Simul* 28(10):73–78
4. Yu J, Zhang A, Wang X et al (2007) Direct adaptive control of underwater vehicles based on fuzzy neural networks. *Acta Automatica Sinica* 33(8):840–848
5. Chung SJ, Ahsun U, Slotine JJ (2009) Application of synchronization to formation flying spacecraft: Lagrangian approach. *J Guid Control Dyn* 32(2):512–526
6. Zhang S, Duan G (2011) Cooperative control for distributed satellite formation keeping. *J Astronaut* 32(10):2140–2145

7. Alexander Fax J, Murray RM (2004) Information flow and cooperative control of vehicle formations. *IEEE Trans Autom Control* 49(9):1465–1477
8. Zheng J, Yan W (2008) A distributed formation control algorithm and stability analysis. *Acta Automatica Sinica* 34(9):1107–1112
9. Yang B, Fang H (2009) Distribution underwater vehicles formation control with limited communication. *J Huazhong Univ Sci Technol* 37(2):57–60
10. Jia Wang (2008) Mutli-agent system control and stability analysis. Nanjing University of Science and Technology, Nanjing
11. Jiang L, Zhang R (2012) Multi-robot formation control and stability analysis for limited communication. *J Jiangsu Univ* 33(1):65–71

New Scheduling Algorithm in Hadoop Based on Resource Aware

Peng Xu, Hong Wang and Ming Tian

Abstract Hadoop MapReduce is a popular distributed computing model that has been deployed on large clusters like those owned by Yahoo and Facebook. In a practical data center of that scale, it is a common scenario that I/O bound jobs and CPU bound jobs, that demand complementary resources, run simultaneously on the same cluster. In current Hadoop scheduling algorithm, parallelization of these two kinds of job has not been concerned. In this paper, we propose a new resource aware scheduling algorithm. With this algorithm we can classify the type of work and node workload reasonably, and the algorithm mainly solve the problems that affect the processing rate which arise during resource contention. Finally, the experiments and performance analysis of the algorithm proved that the algorithm could significantly improve the system's throughput.

Keywords Hadoop · MapReduce · Resource aware · Schedule

1 Introduction

As the Internet scale keeps growing up, enormous data needs to be processed in many Internet Service Providers. MapReduce [1] framework is now becoming a leading example solution for this. Hadoop [2, 3] is an open source project of the Apache Foundation, it is Google's MapReduce programming model and the GFS [4] file system open source implementation. Hadoop [2, 3] MapReduce is a programming model and software framework for writing applications that rapidly process vast amounts of data in parallel on large clusters of compute nodes. Under such models of distributed computing, many users can share the same cluster for

P. Xu · H. Wang (✉) · M. Tian
Shandong Provincial Key Laboratory for Novel Distributed Computer Software Technology,
Shandong Normal University, Jinan 250014, China
e-mail: wanghong106@163.com

different purpose. Situations like these can lead to scenarios where different kinds of workloads need to run on the same data center. For example, these clusters could be used for mining data from logs which mostly depends on CPU capability. At the same time, they also could be used for processing web text which mainly depends on I/O bandwidth.

The performance of MapReduce system closely ties to its task scheduler. Lot of work has been done in the scheduling problem. Current scheduler in Hadoop uses a single queue for scheduling jobs with a FIFO [5] method. Yahoo's capacity scheduler [6] as well as Facebook's fair scheduler [7] uses multiple queues for allocating different resources in the cluster. Using these scheduler, people could assign jobs to queues which could manually guarantee their specific resource share.

In practical scenarios, many kinds of jobs often simultaneously run in the data center. These jobs compete for different resources available on the machine, jobs that require computation compete for CPU time while jobs like feed processing compete for IO bandwidth. The Hadoop scheduler is not aware of the nature of workloads and prefers to simultaneously run map tasks from the job on the top of the job queue. This affects the throughput of the whole system which, in turn, influences the productivity of the whole data center. I/O bound and CPU bound processing is actually complementary [8]. This suggests that a CPU bound task can be scheduled on a machine on which tasks are blocked on the IO resources. In this paper we propose a new resource aware scheduling algorithm, the main idea of the algorithm is as follows: First, We classify job workloads into two types (I/O type and CPU type), and put the job into two different queues (I/O queue and CPU queue). Jobs in the CPU queue or I/O queue are assigned separately to parallel different type of workloads. Second, we will classify node workload into I/O type and CPU type. We select the appropriate tasks to run according to the workload of the node. In this way, we will not only improve the response time of the system, but also improve the utilization of the resources.

The rest of the paper is organized as follows. [Section 2](#) describes the related work of this article. [Section 3](#) introduces our new scheduler. [Section 4](#) validates the performance increase of our new scheduler through a suit of experiments. Finally we conclude in [Sect. 5](#).

2 Scheduling in Hadoop

As of v0.20.1, the default scheduling algorithm in Hadoop operates off a first-in first-out (FIFO) basis. Beginning in v0.19.1, the community began to turn its attention to improving Hadoop's scheduling algorithm, leading to the implementation of a plug-in scheduler framework to facilitate the development of more effective and possibly environment-specific schedulers.

Since then, two of the major production Hadoop clusters—Facebook and Yahoo—developed schedulers targeted at addressing their specific cluster needs, which were subsequently released to the Hadoop community.

2.1 Default FIFO Scheduler

The default Hadoop scheduler operates using a FIFO queue. After a job is partitioned into individual tasks, they are loaded into the queue and assigned to free slots as they become available on TaskTracker nodes. Although there is support for assignment of priorities to jobs, this is not turned on by default.

2.2 Fair Scheduler

The Fair Scheduler [6] was developed at Facebook to manage access to their Hadoop cluster, which runs several large jobs computing user metrics, etc., on several TBs of data daily. Users may assign jobs to pools, with each pool allocated a guaranteed minimum number of Map and Reduce slots. Free slots in idle pools may be allocated to other pools, while excess capacity within a pool is shared among jobs. In addition, administrators may enforce priority settings on certain pools. Tasks are therefore scheduled in an interleaved manner, based on their priority within their pool, and the cluster capacity and usage of their pool.

As jobs have their tasks allocated to TaskTracker slots for computation, the scheduler tracks the deficit between the amount of time actually used and the ideal fair allocation for that job. As slots become available for scheduling, the next task from the job with the highest time deficit is assigned to the next free slot. Over time, this has the effect of ensuring that jobs receive roughly equal amounts of resources. Shorter jobs are allocated sufficient resources to finish quickly. At the same time, longer jobs are guaranteed to not be starved of resources.

2.3 Capacity Scheduler

Yahoo's Capacity Scheduler [7] addresses a usage scenario where the number of users is large, and there is a need to ensure a fair allocation of computation resources among users. The Capacity Scheduler allocates jobs based on the submitting user to queues with configurable numbers of Map and Reduce slots.

When a TaskTracker slot becomes free, the queue with the lowest load is chosen, from which the oldest remaining job is chosen. A task is then scheduled from that job. Overall, this has the effect of enforcing cluster capacity sharing among users, rather than among jobs, as was the case in the Fair Scheduler.

2.4 Late Scheduler

The default implementation of speculative execution relies implicitly on certain assumptions, the two most important of which are listed below:

1. Tasks progress in a uniform manner on nodes
2. Nodes compute in a uniform manner.

In the heterogeneous clusters that are found in real-world production scenarios, these assumptions break down very easily. Zaharia et al. [9] propose a modified version of speculative execution that uses a different metric to schedule tasks for speculative execution. Instead of considering the progress made by a task so far, they compute the estimated time remaining, which provides a far more intuitive assessment of a straggling tasks' impact on the overall job response time. They demonstrate significant improvements by LATE over the default speculative execution implementation.

3 Resource Aware Scheduling

While the two improved schedulers described above attempt to allocate capacity fairly among users and jobs, they make no attempt to consider resource availability on a more fine-grained basis. Given the pace at which CPU and disk channel capacity has been increasing in recent years, a Hadoop cluster with heterogeneous nodes could exhibit significant diversity in processing power and disk access speed among nodes. Performance could be affected if multiple processor-intensive or data-intensive tasks are allocated onto nodes with slow processors or disk channels respectively. This possibility arises as the JobTracker simply treats each TaskTracker node as having a number of available task "slots." Even the improved LATE speculative execution could end up increasing the degree of congestion within a busy cluster, if speculative copies are simply assigned to machines that are already close to maximum resource utilization.

HADOOP-3759 [10] and HADOOP-657 [11] address this partially: 3759 allows users to specify an estimate for the maximum memory their task requires, and these tasks are scheduled only on nodes where the memory per node limit exceeds this estimate; 657 does the same for the available disk space resource. However, both the scheduler does not consider the type of workload of the nodes and tasks.

In this paper, we propose a resource aware scheduling algorithm. Jobs and nodes to be classified according to the resource workload. We select the appropriate tasks to run according to the workload of the node.

3.1 Workloads Classification

3.1.1 MapReduce Procedure Analysis

MapReduce contains a Map phase grouping data in specified key and a Reduce phase aggregating data shuffled from map nodes. Map tasks are a bag of independent tasks which use different input. They are assigned to different nodes in cluster. In the other hand, reduce tasks depend on the output of map tasks. All reducer nodes are not able to begin computing because just one map node slows down; and in Reduce phase, tasks could directly begin to run the application logic because the input data is already shuffled in memory or local disk. So the Map phase is critical to the whole procedure. In this phase, every node performs their map task logic which is similar in one job, and shuffles result data to all reducer nodes. Therefore, we predict job workload by analyzing job's Map phase history. In the Map phase, every node does three actions: (1) init input data; (2) compute map task; (3) store output result to local disk.

3.1.2 Classification of Job Workloads

According to the utilization of I/O and CPU, we give a classification of workloads on the Map phase of MapReduce. As we say, every node in the Map-Shuffle phase does three actions. The ratio of the amount of map data input (MDI) and map data output (MDO) in a single map task depends on the type of workload. We define a variable β as the application logic of particular workload where:

$$MDO = \beta * MDI \quad (1)$$

We assume that tasks in the same job have the same β value. We define a variable n as the number of concurrent running tasks on one node. We define MTCT which means the Map Task Completed Time and DIOR which means Disk I/O Rate.

As for a map task, the operations of the I/O in disk include input and output. In the process of program running, every node has n map tasks which are synchronously running. Multiple tasks share the disk I/O bandwidth when the system stably runs. In our opinion, if the summation of MDI + MDO of n map tasks divided by MTCT is still greater than the bandwidth of disk I/O, then this kind of task is I/O type. We use formula (2) to define the type of I/O workload.

$$n * (MDI + MDO)/MTCT = n * (1 + \beta)MDI/MTCT > DIOR \quad (2)$$

The second class of workload is different with the former one. Its map tasks are CPU type. In this class, the ratio of the I/O data of map tasks to the runtime is less than DIOR. We use formula (3) to define the type of cpu workload.

$$n * (MDI + MDO)/MTCT = n * (1 + \beta)MDI/MTCT < DIOR \quad (3)$$

3.1.3 Classification of Node Workloads

Workload type of the node will be affected by many factors, such as disk I/O rate, CPU usage, and memory utilization. In this paper, we use CPU usage and disk I/O rate to classify the workload type of node.

We define L_{cpu} and $L_{I/O}$ which means the current CPU usage and current disk I/O rate. And define $BASE_{cpu}$ and $BASE_{I/O}$ which means CPU usage threshold and disk I/O rate threshold. When the node CPU usage or disk I/O rate exceeds the threshold value, it may be caused by competition for resources, and reduce the overall system throughput. Therefore, when the node CPU usage or disk I/O rate exceeds the threshold value, the node will no longer schedule the corresponding types of tasks. The threshold value set by the system administrator according to the hardware configuration of the node and the actual operating conditions. Each node's use heartbeat to send their L_{cpu} , $L_{I/O}$, $BASE_{cpu}$ and $BASE_{I/O}$ to the Jobtracker. Jobtracker use this information to divide the workload type of the node. We use formula (4) to define the I/O workload node.

$$L_{cpu}/BASE_{cpu} > L_{I/O}/BASE_{I/O} \quad (4)$$

Cpu workload node is different with I/O workload node. The node current I/O usage is larger than the CPU usage. We use formula (5) to define the I/O workload node.

$$L_{I/O}/BASE_{I/O} > L_{cpu}/BASE_{cpu} \quad (5)$$

3.2 Scheduling Algorithm

The Resource Aware scheduler contains a CPU Job Queue where jobs of CPU Class stand in, an I/O Job Queue where jobs of I/O Class stand in, a CPU Task Queue where task of CPU Class stand in, an I/O Task Queue where task of I/O Class stand in, and a Wait Queue where all jobs stand in before their type is determined. Each queue works independently, and serves a FCFS with priority strategy just like Hadoop's current job queue.

The algorithm basic steps are as follows:

1. Users submit jobs to the Wait Queue and wait to determine the job's type.
2. If both CPU Job Queue and I/O Job Queue are empty. Then the scheduler get a job from the top of Wait Queue and assigns one map tasks of this job to a TaskTracker, we use Formulas (2), (3) for predicting the job type. Then Insert the job to CPU Job Queue or I/O Job Queue.
3. The scheduler select job from CPU Job Queue or I/O Job Queue to run, these two types of jobs on the cluster running at the same time. Scheduler insert all the tasks of the job into Task Queue which with the same type of the job workload.
4. When TaskTracker has idle slots, it use heartbeat to send their L_{cpu} , $L_{I/O}$, $BASE_{cpu}$ and $BASE_{I/O}$ to the Jobtracker. With the formulas (4), (5) JobTracker determine the workload type of the node.
5. If the node is CPU type, then determine the I/O Task Queue is empty or not
6. If the I/O Task Queue is not empty, then determine whether the node's $L_{I/O}$ is greater than $BASE_{I/O}$. If the node's $L_{I/O}$ is greater than $BASE_{I/O}$, then the node no longer accept new tasks. If the node's $L_{I/O}$ is less than $BASE_{I/O}$, Scheduler will get a task from the top of the I/O Task Queue and assign the task to the node.
7. If the I/O Task Queue is empty, then determine whether the node's L_{cpu} is greater than $BASE_{cpu}$. If the node's L_{cpu} is greater than $BASE_{cpu}$, then the node no longer accept new tasks. If the node's L_{cpu} is less than $BASE_{cpu}$, Scheduler will get a task from the top of the CPU Task Queue and assign the task to the node.
8. If the node is the I/O type, the operation flow is similar to the CPU type.

The algorithm pseudo-code is as follows:

```

Users to submit jobs to the Wait Queue
/*determine the job type base on the formulas (2), (3)*/
if (n*(1 + β)MDI/MTCT > DIOR) then
  Put this job into the I/O Job Queue;
end if
if (n*(1 + β)MDI/MTCT < DIOR) then
  Put this job into the CPU Job Queue;
end if
/*Put All the tasks of the job into task queue*/
The schedule get a job from I/O Job Queue or CPU Task Queue
if the job come from CPU Job Queue then
  Put All the tasks of the job into CPU Task Queue
end if
if the job come from I/O Job Queue then
  Put All the tasks of the job into I/O Task Queue
/*JobTracker assign task to TaskTracker*/
determine the node type base on the formulas (4), (5)
if ( $L_{cpu}/BASE_{cpu} > L_{I/O}/BASE_{I/O}$ ) then
  determine the I/O Task Queue is empty or not
  if (I/O Task Queue is not empty) then

```

```

determine whether the node's  $L_{I/O}$  is greater than  $BASE_{I/O}$ 
if ( $L_{I/O} > BASE_{I/O}$ ) then
Return;
else then
get a task from the top of the I/O Task Queue and assign the task to the node
end if
if (I/O Task Queue is empty) then
determine whether the node's  $L_{cpu}$  is greater than  $BASE_{cpu}$ 
if ( $L_{cpu} > BASE_{cpu}$ ) then
Return;
else then
get a task from the top of the CPU Task Queue and assign the task to the node
end if
end if
if ( $L_{cpu}/BASE_{cpu} < L_{I/O}/BASE_{I/O}$ ) then the operation flow is similar to the cpu
type

```

4 Evaluation

Our experiment is that we compare the resource aware scheduling algorithm with Hadoop original scheduling algorithm. We build a cluster with four hosts, one of which is a master node and the other three is Slave node. Operating system is Linux Ubuntu 12.10, Hadoop version is 0.20.2, and java environment is jdk-7u17-linux. Cluster configuration is shown in Table 1.

Literature [12] has proven that TeraSort job belongs to I/O class and Grep Count job belongs to CPU class. Therefore, in our experiments we select TeraSort job and Grep Count job as the test job. In order to ensure the accuracy and validity of the experimental data, every job runs five times and we will get the average value of the job completion time. According to the complete time of the job, we could analyze the improvement of performance.

Experiment 1: We use Hadoop original scheduling algorithm and the Resource Aware scheduling algorithm run the Grep Count job, and input 2G, 4G, and 6G data for testing. The experimental results shown in Fig. 1.

As we can see from Fig. 1, when the input data is relatively small, two algorithms are basically the same on the job completion time. But with the amount of data increases, Resource Aware scheduling algorithms becomes increasingly evident in the improvement of job's completion time. When we input 6G data, Resource Aware scheduling algorithms improves the throughput by 30 %. This is because when the input data is small, the load pressure of the node is relatively small, the execution time of the two algorithms is substantially the same. But with the amount of data increases, the load pressure of the node also increases, and tasks of the node will generate competition for resources, thereby increasing the completion time of the job. Our scheduling algorithm fully consider the node's

Table 1 Cluster configuration

| Machine type | CPU configuration | Disk I/O rates (M/s) |
|--------------|-------------------|----------------------|
| Master | 4-core Intel Xeon | 150 |
| Slave1 | 2-core Intel Xeon | 120 |
| Slave2 | 1-core Intel Xeon | 100 |
| Slave3 | 1-core Intel Xeon | 100 |

Fig. 1 Use FIFO and the resource aware scheduling algorithm run the Grep Count job

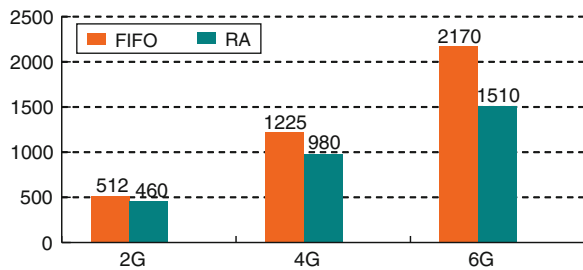
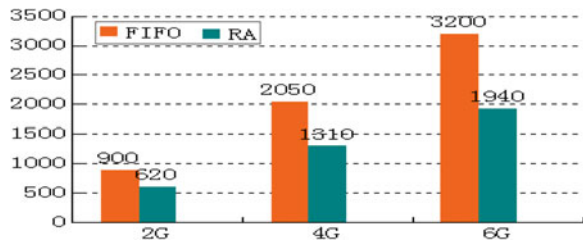


Fig. 2 Use FIFO and the resource aware scheduling algorithm run the Grep Count and TeraSort



workload condition, when the node’s workload exceeds the base value, it will no longer run other tasks. The algorithm effectively reduce the competition for resources, and improve the completion time of job.

Experiment 2: We use Hadoop original scheduling algorithm and the Resource Aware scheduling algorithm run the Grep Count job and TeraSort job simultaneously, and input 2G, 4G, and 6G data for testing. The experimental results shown in Fig. 2.

As we can see from Fig. 2, when we input 2G data, Resource Aware scheduling algorithms can significantly improve the completion time of the job. And with the input data increases, the improvement is increasingly evident. When we input 6G data, Resource Aware scheduling algorithms improves the throughput by 40 %. This is because the resource aware scheduling algorithm divide the job’s workload type, it makes the CPU type job, and I/O type job run simultaneously on the cluster. It is unlike the FIFO algorithm in which the job executed by the submit sequence. And the resource aware scheduling algorithm also divide the node’s workload type. It assign tasks in accordance with the node’s type and workload

conditions. Therefore, when the amount of data increases, the algorithm is more apparent on improve the completion time.

5 Conclusion

In this paper we analyze the typical MapReduce workloads on the MapReduce system, and classify them into two type. We also divide the node's workload type. We propose the Resource Aware scheduling algorithms based on the classification, it assign tasks in accordance with the node's type and workload conditions. And it can effectively avoid the competition for resources and workload imbalance. Our experiments have shown that the Resource Aware Scheduler could significantly increase the system's throughput.

References

1. Dean J, Ghemawat S (2008) MapReduce: simplified data processing on large clusters. *Commun ACM* 51(1):107–113
2. Apache Hadoop. Hadoop [EB/OL] (2009-03-06). http://hadoop.apache.org/common/docs/r.0.18.2/hdfs_design.pdf
3. Yahoo. Yahoo! Hadoop Tutorial [EB/OL]. http://public.yahoo.com/gogate/hadoop_tutorial/start-tutorial.html
4. Ghemawat S, Gogioff H, Leung PT (2003) The Google file system. In: *Proceedings of the 19th ACM symposium on operating systems principles*, pp 29–43
5. HADOOP-3759: Provide ability to run memory intensive jobs without affecting other running tasks on the nodes [EB/OL]. <http://issues.apache.org/jira/browse/HADOOP-3759>
6. Hadoop Capacity Scheduler. http://hadoop.apache.org/common/docs/current/capacity_scheduler.html
7. Hadoop Fair Scheduler. <http://hadoop.apache.org>
8. Wiseman Y, Feitelson DG (2003) Paired gang scheduling. *IEEE Trans Parallel Distrib Syst* 14(6):581–592
9. Zahafia M, Konwinski A, Joseph A (2008) Improving MapReduce performance in heterogeneous environments. In: *Proceedings of the 8th Usenix symposium on operating systems design and implementation*, pp 29–42
10. <https://issues.apache.org/jira/browse/HADOOP-3759>
11. <https://issues.apache.org/jira/browse/HADOOP-657>
12. Chao T, Zhou H, He Y et al (2009) A dynamic MapReduce scheduler for heterogeneous workloads. In: *Proceedings of the 8th international conference on grid and cooperative computing, China*, pp 218–224

Developing a New Counting Approach for the Corrugated Boards and Its Industrial Application by Using Image Processing Algorithm

Ufuk Cebeci, Fatih Aslan, Metin Çelik and Halil Aydın

Abstract Packaging plays a very important role in marketing. Thanks to packaging, the goods while in transit and the products located onto retail shelves are protected. In order to gain competitive advantages in the market, the way of packaging should be assessed and managed effectively. Having many advantages such as versatility, recyclability, and cheapness; corrugated boards packaging is widely used and increasing popularity in the world. Due to the high rate usage of corrugated board, the production of corrugated board becomes more of an issue. In the current situation, corrugated boards placed onto each other on pallets before delivery are counted manually. The situation leads to waste and extra cost for the factory. The approach mentioned in this paper aims to automate this process by using image processing algorithms and to eliminate all wastes related to manual counting process. There is no scientific research studied related to this problem. An algorithmic approach is applied by using sample images provided by a company corresponding to corrugated boards. Therefore, the automated counting system for corrugated board is proposed by this study.

Keywords Corrugated board • Counting objects • Image processing algorithm • Image processing techniques • Image classification

U. Cebeci (✉) • F. Aslan
Department of Industrial Engineering, Istanbul Technical University,
34367 Macka, Istanbul, Turkey
e-mail: cebeci@itu.edu.tr

F. Aslan
e-mail: aslanfat@itu.edu.tr

M. Çelik
Azim Packaging, Istanbul, Turkey
e-mail: metincelik@azimambalaj.com.tr

H. Aydın
Turkey BSS Software, Istanbul, Turkey
e-mail: halilaydin@bssyazilim.com.tr

1 Introduction

Image is defined as the visual description of the objects in nature. According to Qidwai and Chen [1], digital image is the state of digitized and extracted version of images from three dimensions into two dimensions. Digital image is a function such an $\alpha(x, y)$ that has two variables. These variables are the position of coordinates and the value of this function represents the intensity or brightness. The scientific definition of digital image is that the image is extracted by using the analog image of $\alpha(x, y)$ from two-dimensional continuous space into two-dimensional discrete space as a result of sampling process defined as digitization [1].

In digital images, most widely used term in order to denote the element of an image is pixel. Beside this definition, pixel is identified as the intersection point of row and columns. All techniques related to image processing is applied to pixels. Furthermore, the operations in image processing are performed based on operators such as arithmetic operator, convolution operator, and gradient operator used by many methods in image processing.

Image processing is an operation which alters the nature of images in the manner to improve visual interpretation and to transform images into a suitable state that could be perceived by autonomous machine by using computers [2]. Gonzalez and Woods examined processes performed in image processing into three different categories [3]:

Low-level Process. This process includes primitive operations (noise reduction, contrast enhancement, etc.). Input and output are identified as images.

Mid-level Process. Input is characterized by an image, however; output is attributes of the image such as edges. Image segmentation could be given as an example for this type of processes.

High-level Process. This level contains higher operations and beside the mid-level it gives meaning to the images. Text recognition and detection of counterfeit money are among the application of high-level process.

2 Corrugated Boards in Industrial Packaging

The raw material of the corrugated board is the recycled paper. There are many different types, sizes, and shapes of corrugated boards. The corrugated board provides high-level environment-friendly packaging. Products which are fragile, hard, soft, solid, and liquid could easily be packed and protected thanks to the board. Corrugated board is produced from two sheet combination and glued to a corrugated inner medium. The shape of corrugated board is shown in Fig. 1.

There are many benefits of the corrugated board packaging [4]:

- *Sustainable.* Completely recyclable and 100 % natural.
- *Cheapness.* It could be produced by recycled paper.

Fig. 1 Corrugated board [4]



- *Safe and Hygienic.* Due to having disposable characteristics and certified by Good Manufacturing Practice.
- *Superior Protection.* Resistant to impact, vibration, dropping, and shock.
- *High-technology and Innovation.* Adaptable to technological developments (RFID) and innovations (Cooler corrugating).
- *Informative and Promotional.* Strong marketing tool for companies in order to increase the value in the market.
- *Ideal Logistic Partner.* Packaging is fundamental component and guarantee maximum stocking and space use.

3 The Methods Used for Counting of Corrugated Board Algorithm

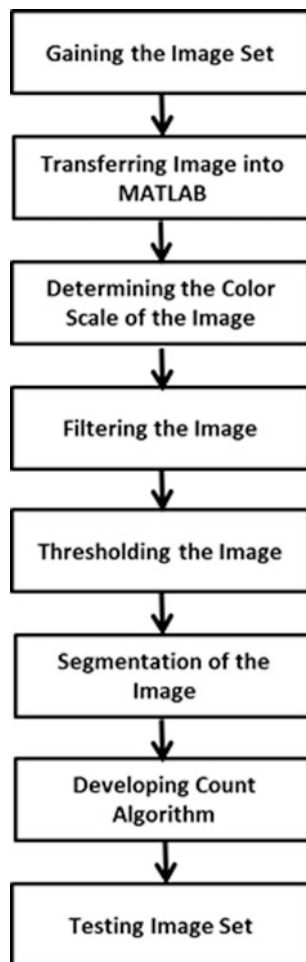
In corrugated boards counting algorithm, different methods related to image processing are utilized. The algorithm is developed in MATLAB software. The general and detailed flow of the original algorithm are shown in Figs. 2 and 3, respectively.

The methods will be explained one by one in order to show the advantages of usage in this algorithm.

Adaptive Histogram Equation. All histogram equation methods are based on color value distribution and aim to adjust contrast. Distinctively, adaptive histogram performs this type of adjustment locally which means to remove the low contrasts, brightness, and saturations in the local part of the image. Philip states that this method produces effective results to homogenize color density [5]. As a result, image defects caused by perspective could be eliminated.

Sobel Filter. This filter is basically used in order to find the edges in the image and based on derivative approach. MATLAB offers a function called *fspecial* for the Sobel filter by utilizing from h matrix. The matrix used to find the horizontal edges is shown in Fig. 4. Moreover, Sanduja and Patial [6] stated that this filter removes spurious noises and makes the edge smoother. Besides, Shrivakshan and Chandrasekar [7] explained that Sobel filter provides more simplicity than the other filters using the approach of the Gaussian. Therefore, the method is faster and gives effective results.

Fig. 2 General flow of the algorithm



Erosion. This method performs the morphological process based on a structural element for gray-colored images. In addition to many different shaped and sized of structural elements (line, square, disk, etc.) offered by MATLAB, it could be formed by an operator. Therefore, operators could use structural elements arbitrarily and do not obliged to use available ones.

The working principal of this method is based on the rule of the mask of the pixels which are defined by structural element matrix. The method assigns the value of the minimum element inside the mask window as a value of centered pixel in the mask area. Example is shown in the Fig. 5. Structural element of this process is defined as 3-3 square matrix.

Dilation. Dilation is the one of the process that is executed basic morphological process for grayscale images. Dilation process is materialized based on the

Fig. 3 Detailed flow of the original algorithm

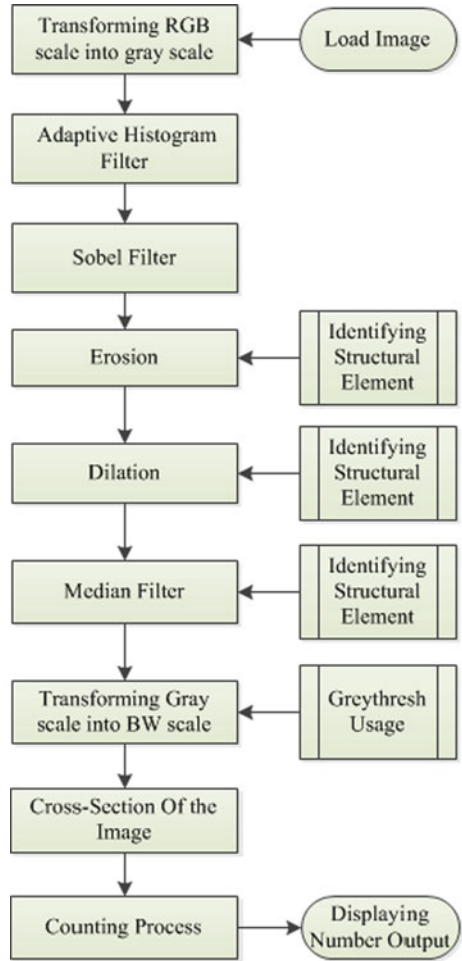


Fig. 4 Sobel horizontal edge (h) matrix [10]

$$\begin{bmatrix} +1 & +2 & +1 \\ 0 & 0 & 0 \\ -1 & -2 & -1 \end{bmatrix}$$

Fig. 5 Erosion (Martin et al. [11])

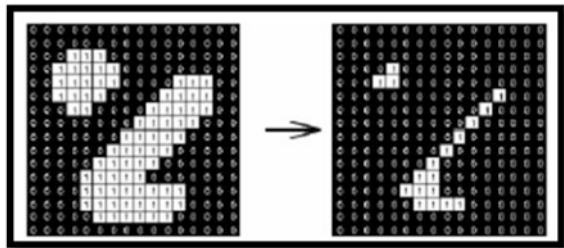


Fig. 6 Dilation (Martin et al. [11])

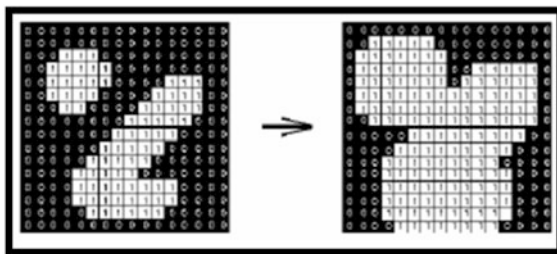


Fig. 7 Median filter application

| | | |
|----|----|----|
| 6 | 2 | 0 |
| 3 | 97 | 4 |
| 19 | 3 | 10 |

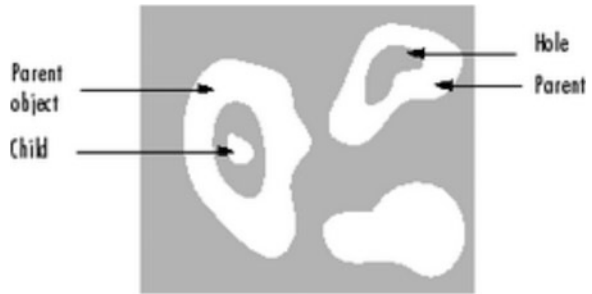
identified one structural element like erosion. The working logic is the reverse of the erosion. Therefore, determined structural element matrix is carried to the whole image by taking every pixel as a center. In contrast to erosion, the maximum value of the element is assigned as pixel value. The example is shown in the Fig. 6 regarding dilation process which is performed by using 3-3 square matrix.

Chitra and Balakrishnan [8] stated that dilation and erosion methods are used to smooth the boundary of the objects and do not change the area of them. In addition, these methods are consecutive and firstly applied erosion followed by dilation in the opening operation. The erosion method is firstly applied for our algorithm due to the opening operation structure.

Median Filter. Median filter is used in order to remove the image noise. This filter could be used to preprocess for other subsequent process. The filter is applied by means of mask matrix. The image is scanned by this identified matrix. In each window, the values of pixel are ordered from the minimum to maximum value. As a result of alignment, the value in the middle is assigned as the value of the centered pixel. It is widely used method in image processing in order to remove noise without causing damage to the edges. The example is shown in Fig. 7 regarding to this filter. In this example, the central element is altered from 97 to 4 which will be in the middle when the numbers are ordered.

Graythresh. This threshold is used to obtain black-white images from gray images. According to this method, pixel values which is above the examined threshold level is colored white, conversely it is colored black when the pixel value is below the level. By means of this method, the image is transformed from grayscale into BW images.

Fig. 8 Classification of BW color [12]



Threshold level is determined by two methods:

- *Operator observation*: In this method, the operator observes the different results by trying different threshold values that is defined arbitrarily. According to the observations, the optimal threshold level is determined.
- *MATLAB Function (Graythresh)*: To find the best threshold level of the gray images, a MATLAB function called *graythresh* is used. This function utilizes from *Otsu method* in order to find the optimal threshold level. Briefly, the method assumes that image consists of two color categories as back and front hand. The variance value is calculated for both two classes. The value which minimizes the variance value is given as an optimal threshold level (Wang [9]).

Classification of the Black-White Color. To classify black-white colors, MATLAB offers a function called *bwboundaries*. The function is used in order to determine objects, hollowed structure substances (called *parent*) and spongy structure substances (called *child*). These types of objects are shown in Fig. 8. The important point is that the function is only available for BW-scaled images.

4 The Original Algorithm Developed for Corrugated Board

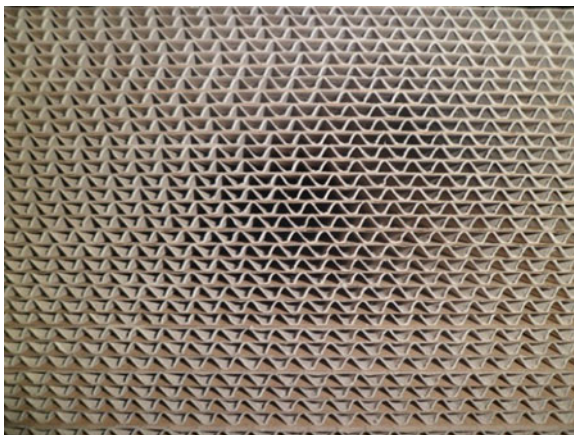
The methods used in this algorithm are explained in Sect. 3. In Sect. 4, it will be pointed out specific issues which make the algorithm original.

This algorithm is developed by using 15 different images of finished corrugated boards produced by *Azim Packaging*. The reason why these images are selected is to demonstrate the verification and the robustness of the algorithm. The images have different characteristics including quality (abnormal sinus curves, etc.) and size (such as bigger or smaller sinus curves). All images of 15 selected products are shown in Appendix-1. The results of our algorithm related to these images are shown in Table 1.

In this section, the algorithm is performed step by step on only one image which is selected from 15 images and the results of each step is given at the end of relevant step.

Table 1 Results

| Photo no. | Actual number | Found number | Average processing time [sec] |
|-----------|---------------|--------------|-------------------------------|
| 1 | 32 | 32 | 1.52 |
| 2 | 38 | 38 | 1.57 |
| 3 | 40 | 40 | 1.55 |
| 4 | 45 | 45 | 1.53 |
| 5 | 47 | 47 | 1.52 |
| 6 | 48 | 48 | 1.56 |
| 7 | 48 | 48 | 1.59 |
| 8 | 52 | 52 | 1.53 |
| 9 | 56 | 56 | 1.52 |
| 10 | 65 | 66 | 1.57 |
| 11 | 42 | 41 | 1.58 |
| 12 | 45 | 44 | 1.55 |
| 13 | 45 | 46 | 1.55 |
| 14 | 55 | 56 | 1.62 |
| 15 | 39 | 41 | 1.57 |

Fig. 9 Original image

The original image and its magnified part of the image are shown in Figs. 9 and 10, respectively.

Step (1) Adaptive Histogram Equation: After RGB-colored original image is loaded into MATLAB, it is firstly converted into grayscale. Then adaptive histogram method is applied in order to remove background noise caused by the perspective. The former and the latter images are shown in Figs. 11 and 12, respectively.

Compared with Figs. 11 and 12, it is noticed the perspective noise placed in the middle is removed in the latter image. In addition, the color of the image becomes more homogeneous than the former one.

Fig. 10 Magnified part of the original image



Fig. 11 Before adaptive histogram

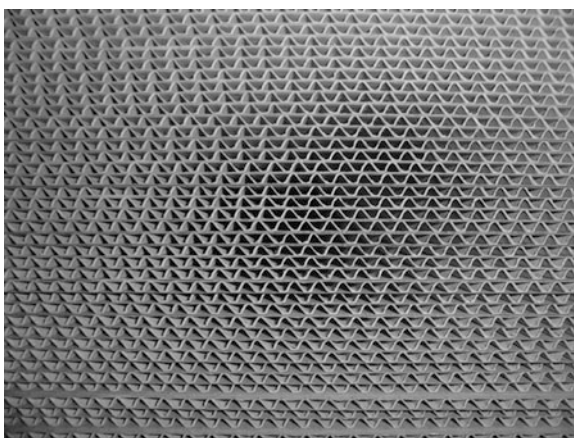


Fig. 12 After adaptive histogram

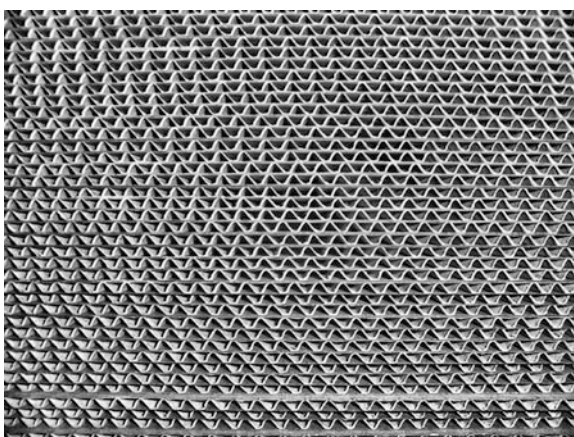
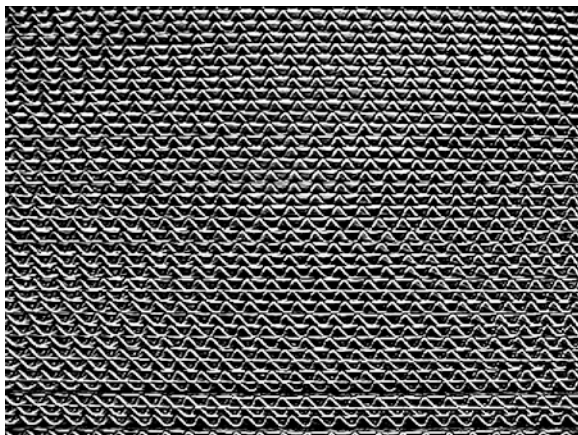
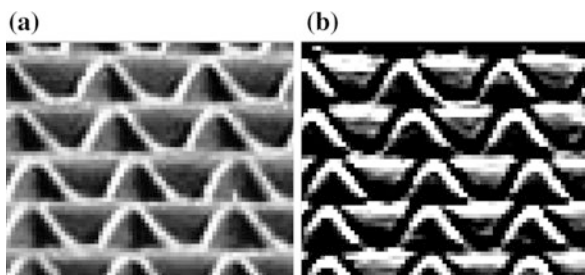


Fig. 13 After sobel filter**Fig. 14** **a** Before sobel and **b** after sobel

Step (2) Sobel Filter: This filter is applied in order to emphasize horizontal lines. Filtering image is shown in Fig. 13. In addition, the difference between the former and the latter images is shown in Fig. 14a, b, respectively. This step also supports the next step by making the horizontal edges more visible.

Step (3) Erosion: This step is the most important step for the success of the algorithm. The point is to remove the sinusoidal curves between the lines by using structural element.

Definition of Structural Element: As stated in Sect. 3, the structural element is generally defined as either available MATLAB elements or completely by user. In our algorithm, after analyzing the image in detail we define our structural element instead of using available MATLAB elements.

According to analyses of the images, the width of the sinus curves located between two lines changes mostly in the range of 2–5 white pixels. Therefore, structural element is formed as matrix in 1×6 sized. To clarify the idea, as mentioned in Sect. 3, the smallest value inside the frame is assigned to the center element. Hence, this matrix makes the erosion of the white pixels in the sinus curves substantially guaranteed. Furthermore, the values of the matrix elements do

Fig. 15 **a** Before erosion and **b** after erosion

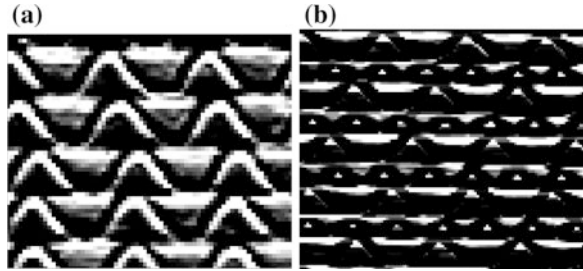
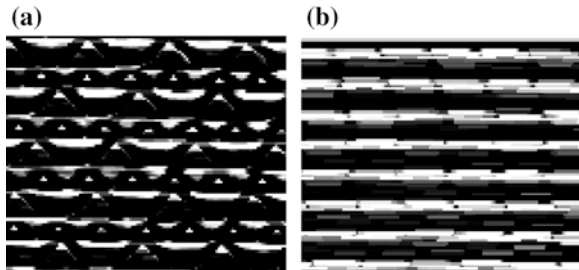


Fig. 16 **a** Before dilation and **b** after dilation



not affect this process. For this reason, the value of 1 (one) is given arbitrarily to all elements of the matrix.

Key Point of This Step. Thanks to removing sinus curves, the next steps could be performed easily. The latter and the former images are shown in Fig. 15a, b, respectively.

Step (4) Dilation: This step is complementary of the erosion method. In the previous step, when removing the sinus curves, horizontal lines are affected negatively. Therefore, it brings out discontinuity in some points. In order to recover, dilation method is applied. The latter and the former images are shown in Fig. 16a, b.

Compared with Fig. 16a, b, it is remarked that the lines are more continuous in the latter one.

Step (5) Median Filter: As stated in Sect. 3, this filter is used as preprocessor to the subsequent process to remove the image noises. Specifically, for this image the noises around the horizontal lines make the lines wider and less distinctive. This filter is also applied after analyzing the characteristics of the image. The analysis shows that the thickness of the horizontal edge is almost 4 pixels. The related figure is shown in Fig. 17. In this figure, the difference between two y positions gives value 4. Therefore, the mask matrix of the median filter is selected as [4 4] sized.

The before and after median filter is applied, the images are shown in the Fig. 18a, b, respectively.

After median filter is applied, the horizontal lines become more clear as shown in Fig. 17b.

Fig. 17 Magnified former image

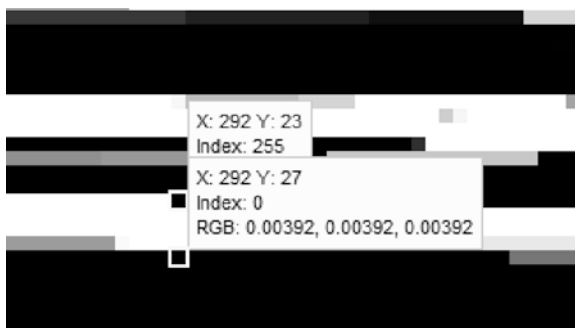
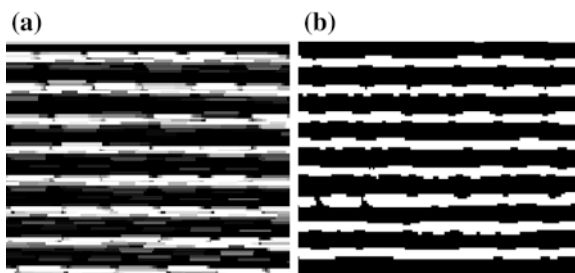


Fig. 18 **a** Before median and **b** after median



Step (6) Transforming into BW Scale: After median filter, the image is converted into binary image in order to carry out the counting process. The working principle of this method is mentioned in Sect. 3. Then, the vertical cross section is taken from the middle area of the image due to the quality issues (smoothness, continuity of lines, etc.) compared to the other areas of the image.

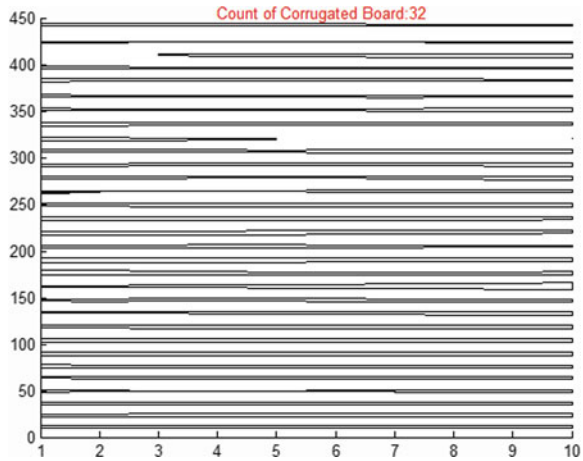
Note Determination of cross section width is a critical issue. The reason why this width is important will be explained in the next step.

Step (7) Counting Process: After segmentation, the last step of the algorithm is to find the number of corrugated boards. In order to count, *bwboundries* function defined in MATLAB is utilized. The working principle is mentioned in Sect. 3. Briefly, this function traces the interior and exterior boundaries of the objects and detects them. The essential point is that the image must be binary where nonzero pixels show the objects while zero pixels show the background. In our algorithm, *bwboundries* function takes the binary image as an argument and finds the number of the objects. The output of this function is assigned to a variable. The length of the variable gives the count of the corrugated board. The related figure is shown in Fig. 19.

5 Results

In this algorithm, seven steps are carried out in order to find the number of corrugated boards. These steps are applied to 15 images selected from real production area of *Azim Packaging Company*. The results are shown in Table 1. In

Fig. 19 Counting of corrugated board



this table, actual number of corrugated boards, the found number by our algorithm, and average processing time for each figure are given.

As shown in Table 1, the algorithm could find the true count for the images between photo nos. 1–9 accurately. The algorithm converges into the true number with 1 difference for the images between photo nos. 10–14. The algorithm converges into the true number with 2 differences for the photo no. 15.

The algorithm could accurately find the true number at the rate of 60 % and the remaining images have some defects caused by alignment and the quality of the photographs. Therefore, with 1 difference could be accepted in the range of success. As a result, the success rate is 94 %.

In this section, the important key performance indicators (KPI) are:

- *The independency to the initial data.* In this algorithm, despite selected images show different characteristics, the results are satisfactory and show the flexibility of the algorithm developed. As a result, our algorithm is not dependent on initial data.
- *The processing time.* Processing time is measured by using MATLAB commands. Table 1 shows the average processing time. The average value is found in a way that each figure is run 10 times so each value includes the average of 10 running time value. In addition, the values change between the range of 13 and 17 s. As a result, average processing time could be accepted as nearly 15 s.
- *The accuracy of results.* The success rate is given in this section as 94 %.

Finally, our image processing algorithm is successful in counting of corrugated boards.

6 Conclusions

In this study, the application of corrugated board counting is performed by using a new image processing algorithm. After applying the algorithm with real products, the results are satisfactory and reasonable.

Our paper is the first study about this subject because no other scientific study analyzed this problem.

The algorithm offers fast and efficient solution to counting problem of corrugated boards and not dependent on initial data.

As a further research of this study, video processing can be tried to compare the results for industrial applications. QFD—Quality Function Deployment—technique can be used to match the technical specifications and customer needs for a counting machine. In addition, this counting algorithm should be integrated with production machines and ERP systems. The total counting time of algorithm may be improved if the time of production line is faster than counting time of the algorithm.

The method can be applied to other industrial problems such as sheet and paper counting.

A.1 7 Appendix

Corrugated Board Images in Different Numbered and Shaped

Photo 1 Unprocessed
Corrugated Boards Image-1

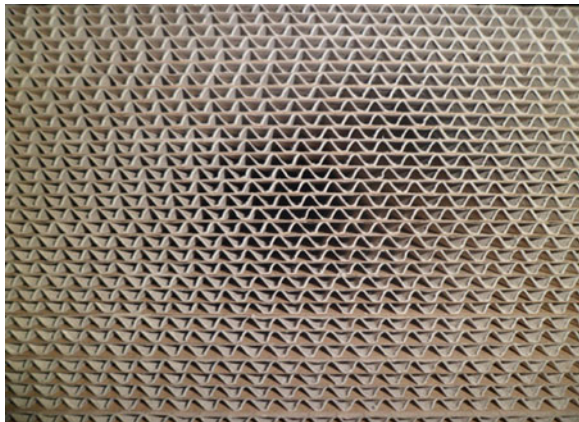


Photo 2 Unprocessed
Corrugated Boards Image-2

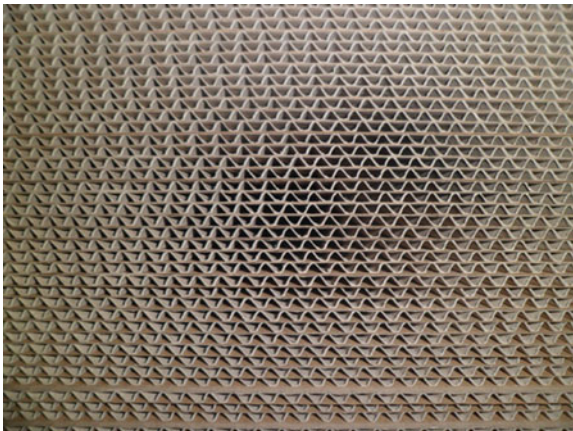


Photo 3 Unprocessed
Corrugated Boards Image-3

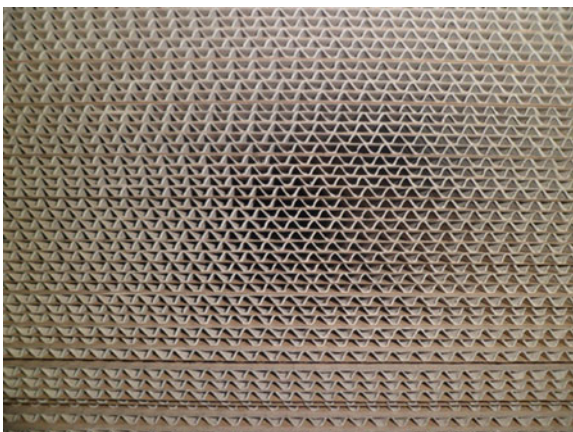


Photo 4 Unprocessed
Corrugated Boards Image-4

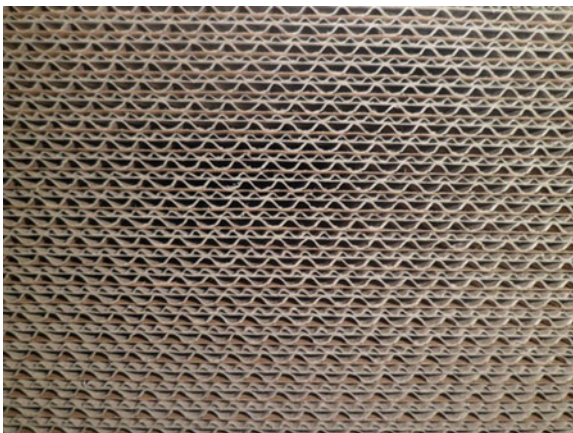


Photo 5 Unprocessed
Corrugated Boards Image-5

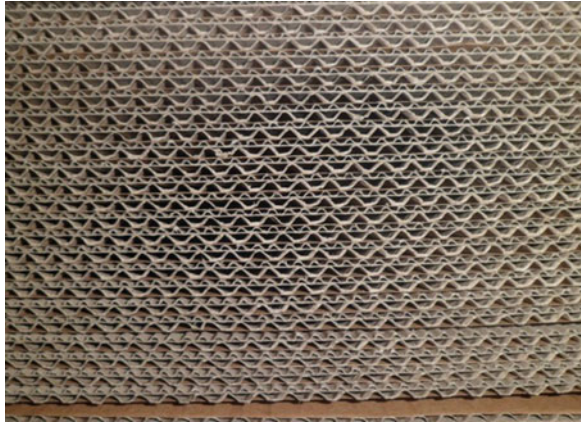


Photo 6 Unprocessed
Corrugated Boards Image-6



Photo 7 Unprocessed
Corrugated Boards Image-7



Photo 8 Unprocessed
Corrugated Boards Image-8

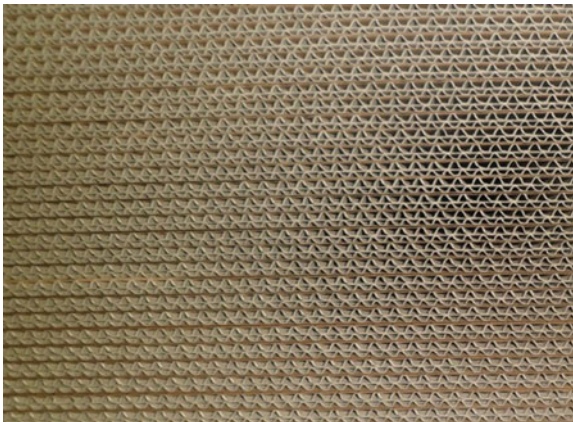


Photo 9 Unprocessed
Corrugated Boards Image-9



Photo 10 Unprocessed
Corrugated Boards Image-10

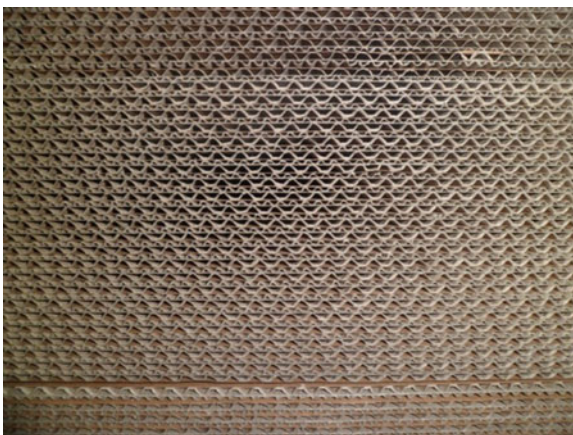


Photo 11 Unprocessed
Corrugated Boards Image-11

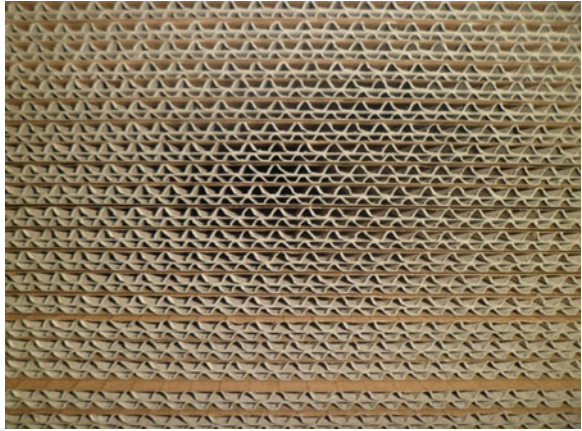


Photo 12 Unprocessed
Corrugated Boards Image-12

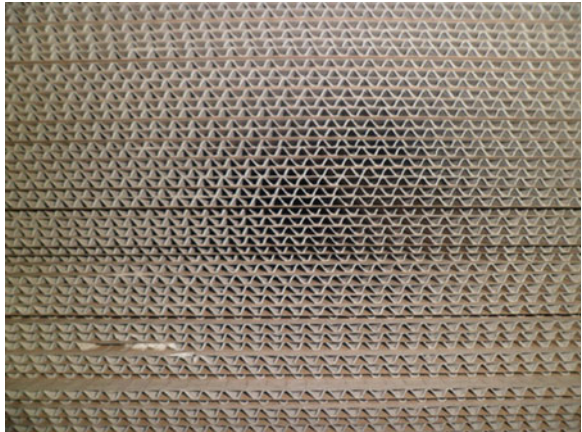


Photo 13 Unprocessed
Corrugated Boards Image-13



Photo 14 Unprocessed
Corrugated Boards Image-14

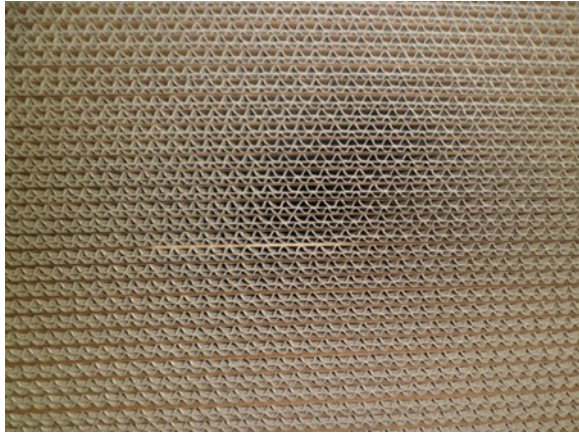
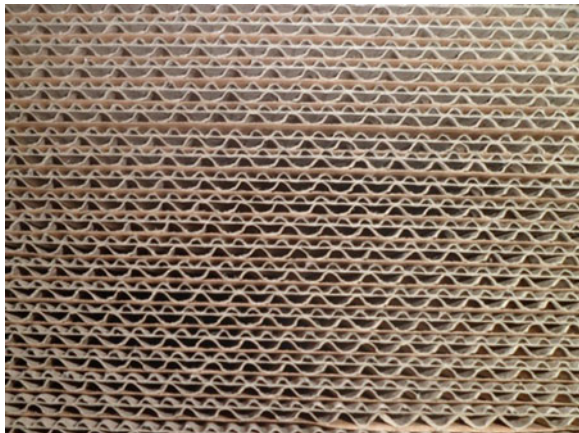


Photo 15 Unprocessed
Corrugated Boards Image-15



References

1. Qidwai U, Chen CH (2010) Digital image processing an algorithmic approach with Matlab. C.R.C Press, New York
2. McAndrew A (2004) An introduction to digital image processing with Matlab notes for SCM2511 image processing 1. Wellington, Canada
3. Gonzalez C, Woods R (2007) Digital image processing. Prentice Hall Press, New Jersey
4. URL-1 <http://www.fefco.org/>. Accessed 2013
5. Philip S (2009) Adaptive histogram equalization. University of Utah, USA
6. Sanduja V, Patial R (2012) Sobel edge detection using parallel architecture based on FPGA. Int J Appl Inf Syst 3(4):20–24, New York, USA
7. Shrivakshan GT, Chandrasekar C (2012) A comparison of various edge detection techniques used in image processing. Int J Comput Sci 9(1):270–276
8. Chitra S, Balakrishnan G (2012) Comparative study for two color spaces HSCbCr and YCbCr in skin color detection. Appl Math Sci 6(85):4229–4238

9. Wang L (2003) Threshold selection by clustering gray levels of boundary. Department of Biomedical Engineering, Institute of Biomedical Engineering, Tsingua University, Beijing, pp 1983–1996
10. URL-2 <http://www.mathworks.com/help/images/ref/fspecial.html>. Accessed 2013
11. Martin F et al (2000) New advances in automatic reading of VLP's. In: Proceedings of SPC Marbella, Spain, pp 126–131
12. URL-3 <http://www.mathworks.com/help/images/ref/bwboundaries.html>. Accessed 2013

Complex Systems Modelling for Virtual Agriculture

Lei Zhang and Liqi Han

Abstract Agriculture is a key development for survival of all the human beings. When the population is increased while the arable land surface is reduced, emerging technologies are greatly required to improve agricultural productions. One of the emerging research domain that could contribute to this improvement is computational plant modelling, which treats plants as complex systems and uses simulations to carry out virtual experiments as an alternative to the time- and resource- consuming real-world investigations. Plant models could focus on different levels progressing from atoms to the whole atmosphere. Architectural models and functional-structural models, mainly addressing the organ-level development and function, have been widely developed against problems in agricultural practice. However, almost all the current plant models and supporting software tools are not user-friendly enough, leaving an interval for us to fill before virtual agriculture becomes more “real” and “realistic”.

Keywords Complex systems · Computational modelling · Virtual plants · Digital agriculture · Virtual experiments

1 Introduction

Plants are widely called the Green Factory. They make up 99.9 % of the Earth’s biomass, capture photons, air, water, and minerals, and then synthesise all the necessary products we need to survive. The food we eat, the oxygen we breathe, the medicine we use, and even the biodiesel that is expected to replace petroleum, all rely on plants. Thus, plants play a vital role in sustaining other forms of life,

L. Zhang · L. Han (✉)

School of Computer Engineering, Weifang University, Weifang 261061, Shandong, China
e-mail: liqi.han@wfu.edu.cn

including us—the humans. As the foundation and a powering source of human civilization, agriculture has been remarkably developed. However, behind this rapid development there is also overuse of chemical fertilisers and pesticides, high requirement of fuel and electricity, as well as immoderate demand for land from the wild. How to feed the increasing population with safely and effectively improved agriculture becomes an urgent issue for the whole world.

Undoubtedly, genetic studies, which focus on the modification of plant itself, are leading the improvement of agricultural productivity. Mutant crops, usually with an altered phenotype in terms of organ size or number, are created every day. Nevertheless, the intermediate mechanisms between genotypes and phenotypes, such as the long- and short- signalling processes related to mutation, are still largely unclear. Since these processes might have the capability of triggering synthesis of unknown substances, it is always reasonable to suspect the safety of such products before the detailed mechanisms are clear. Even if the size of a type of organs can be augmented and meanwhile the safety can be guaranteed, would this change decrease the whole plant's performance in carbon allocation, light interception and other functions? If this occurred, the entire productivity of a plant could be lowered rather than be increased. Moreover, assuming a single plant had been optimised, would this result in the optimization of the whole field? Perhaps not, since the optimized individuals with higher capabilities might have to compete for limited resources (such as light and nutrients) and thereby reduce overall productivity of the group. All this is to say, the mutated species should be sufficiently investigated and tested before they are applied in agriculture.

It is always possible to base these investigations and tests on lab or field experiments. The problem is, however, how much time, how many resources and how many labours would it cost for such experiments? To test a new mutant, the breeding, the cultivation, the measurement, the data analysis and then the conclusion might take decades to be completed, without mentioning how many people and resources are involved. For the signalling-related studies, it could be more challenging, since many signals cannot be observed or detected at all with current biological technologies.

When real-world experiments could not solve the problem effectively, virtual experiments might have a chance. No matter how complex the biological systems are, the similarity between them and engineered system [1–3] leads to a systematic view of their internal and external processes [4, 5]. Behind the complexity, represented by nonlinearity, dynamics, self-organisation and unpredictability, there are simple rules constituting interactions between different components at different scales. Computational modelling, capable of supporting massive datasets as well as handling enormous number of constituents, is an ideal option to simulate the lower level activities and the consequent emerging system-level behaviours.

In this paper, we will first review the major principles about plant modelling and then discuss how these models could be used to server virtual experiments for agriculture.

2 Basis of Plant Models

Conventionally, the biological models are classified into four forms [6]: verbal, diagrammatic, physical, and formal. If a model describes a system using human languages, it is called a verbal model. If a diagram is used to abstract the inter-related objects and their relations as a graphical representation, it is a diagrammatic model. A physical model is a mock-up of the real system. If a model uses mathematical languages, usually in form of a group of mathematical equations, to express a system, it is characterised as a formal model. The computational models evolve from mathematical models, because they use algorithms to organise their structures and require computer programmes to handle their implementations. A computational model could be defined as ‘a set of computational codes, executable in some software/hardware environment, that transform a set of input data into a set of output data, with the input, output, and transformation typically having some interpretation in terms of real-world phenomena’ [7].

Biological systems are highly organised with multiple hierarchical levels (sometimes referred to as scales): atom, molecule, organelle, cell, tissue, organ, organ system, organism, population, community, ecosystem and biosphere [8]. An entity at a given level is a system composed by some of its lower level objects, and in turn functions as an object for a higher level system. Thus, this hierarchy is also used to classify plant models [9]. A ‘bottom-up’ model uses lower level processes to investigate higher level phenomena; a ‘top-down’ model views the system behaviour as a result of “phenomenological relation” with external factors [6].

According to how it is built and how it is used to study a system, a model can also be characterised as “empirical” or “mechanistic” [6]. An empirical or descriptive model simply describes the observed data or phenomena, while a mechanistic model is process-oriented and represents the mechanisms (either known or hypothesised) that cause the observed system behaviours.

3 Plant Architectural Models

The topology of a plant includes different interconnected components or modules [10–12], such as internodes, leaves and flowers that are produced by apical meristems (for shoot growth) or root tips (for root growth). Each component has its own geometric information, such as “shape, size, orientation and spatial location” [13]. The topological and geometrical organisation of plant components together is called plant architecture [13]. The efforts to study plant architecture using computational modelling are therefore called plant architectural modelling, which have been widely made since the 1980s [14–17].

In the past three decades, plant architectural models have been built with different techniques or tools, such as L-systems [18], AMAP [19] and LIGNUM [20]. Despite the differences, these techniques share the same underlying philosophy [21]:

they all describe ‘a growing branching structure in terms of the activities of individual plant modules’. For example, the plant shoot architecture can be simulated with different components that are produced iteratively in hierarchical orders. Compared with the shoot, the root architecture looks much more irregular, but it can also be decomposed into axes with different orders and each axis can be decomposed into different segments [22].

In architectural models, the plant modules are coded with different types of data structures, such as a string of symbols [9], a list of elementary length units [23] or a multiscale tree graph [13]. Each type of data structure has its own advantages. The use of symbols allows categorisation of architectural modules, thereby all modules under the same category are processed in the same way, reducing the number of growth rules and makes model specifications concise [21]. Rather than treating internodes as single components, the use of elementary length units divides an inter-branch section into lower scale elements, which is more suitable to the irregular and flexible architecture of a root. In the multiscale tree graph paradigm, a branch is usually broken down into a group of growth units at first and then a number of successive internodes at lower scales, addressing the growing patterns observed in tree architectures.

4 Functional-Structural Plant Models

Underlying the complex behaviours of plant development are far more than just topological and geometric rules. Plant architecture is also shaped by external factors and internal physiological processes [24–26], such as light environment (influenced by neighbouring plants), resource allocation and signalling regulation. The work to integrate representation of plant function and structure in computational models is called functional-structural plant modelling [21, 24, 27–31], also known as virtual plant modelling [32, 33].

In functional-structural plant models considering environmental factors, plant architecture is an interface between internal and external systems [24]: on one hand, the architectural modules sense environmental changes that have further impacts on internal physiological processes; on the other hand, the spatial distribution and dimension of these modules also influence the local environment. For instance, a leaf not only captures radiant energy for photosynthesis and thereby serves as a source of carbon, but also makes shade that could affect the local light environment of its neighbouring leaves. There is also a feedback characteristic in functional-structural modelling on endogenous processes, where the interconnected architectural components form a network for the function of physiological fluxes. A network like this includes where the fluxes start (the sources), where they pass through (the channels) and where they stop to work (the sinks). The networks are changed by plant development (adding or dropping sources and sinks, extending channels, etc.), and the changed networks regulate plant growth in return. These complex interactions occurring over space and time lead to an

“emergent” appearance of a plant represented by its final architecture. Hence, plant architecture also directly reports the underlying processes. This reporter can either be compared with data from real-plant experiments to test the reasonability of hypothesised physiological mechanisms, or be used for prediction of the consequences of changes to self- or environmental- parameters.

A variety of software tools have been developed for building functional-structural plant models. One of the most widely used platform is *L-studio* [34], providing a plant modelling environment with two *L*-system-based simulators [18, 35]: *cpfg* and *lpfg*. It not only enables users to formulate biological rules in form of computer programmes, but also supports 3D visualisation with step-by-step implementation of those rules. The context-sensitive functionality of *L-studio* allows plant modules to exchange information (through parameter values) with their neighbouring modules, thus facilitating simulations of internal flows. *L-studio* is built for Windows operating systems, its Linux version is called Virtual Laboratory (VLab) [34]. VLab was developed by the same team with *L-studio* and possesses most of its functionality. GroIMP [36] is another L-system-based modelling package, using XL as the programming language. XL is an extension of Java and could be run at different operating system environments. Thus, the simulation programmes developed with GroIMP can be executed on both Windows and Linux without changes. GREENLAB [37–39] is a functional-structural modelling tool evolving from the AMAP approach [19]. Similar with L-systems, GREENLAB models a plant as modular composition and supports 3D visualisation, but integrates statistical functionality that could be straightforwardly used for parameter optimisation. OpenAlea is an open-source software platform with ease of use, reusability and extendibility as well as collaborative development as its typical features [40]. An advantage of OpenAlea is that it could bring all different models developed with different tools or programmed with different languages together and enable them to communicate with one another. The development team of OpenAlea aim at providing a visual programming scheme (simply by drawing and connecting diagrams as well as setting parameters with a graphical interface) for the users to accomplish this integration, making it much easier to develop more comprehensive functional-structural models addressing different aspects and factors of a plant.

5 Using Plant Models in Virtual Agriculture

Computational plant models, focusing on mechanisms and factors at different levels, have been broadly developed in the past few decades. This has set a solid ground to apply these models into agricultural practices. Here, we briefly introduce two published examples that could be used for such applications.

5.1 Modelling Root Development and Signal Regulation of Legumes

Legumes occupy only 12–15 % of Earth's arable surface, but provide 27 % of the world's primary crop production and more than 35 % of the world's processed vegetable oil [41]. They also have great potential as a sustainable source of biodiesel production [41, 42]. Legumes are also a major “nitrogen-fixer”, fixing 200 million tonnes of nitrogen each year [43], which could be used as alternative to the pollutive synthesised fertilisers. Underlying these important values there is a key developmental process called nodulation. The nodulation not only influences the productivity of legume plants, but also determines the quality and quantity of natural nitrogen fixation. Such a process is controlled by a signalling system called autoregulation of nodulation (AON) [44–48]. However, due to the subtleness and complexity of plant signals, detailed mechanisms of AON still remain largely unknown.

In order to have a better understanding of how AON works and even what the signals are, a functional-structural model has been built for simulation of legume root development as well as signalling control [49–51]. This model overcomes two difficulties: simulation of the 3D architecture of root development with nodulation and synchronisation of the signalling-developmental processes with various rates. Since nodulation and autoregulation regulation are twisted dynamically and intricately, it is hard to validate the hypothesised signalling mechanisms. To address this, a virtual-experiment strategy called “Computational Complementation” [52] was addressed too, providing a feasible and effective approach not only for studying AON but also for investigation of other signalling mechanisms.

5.2 Sensitivity Analysis of Apple Tree Architecture to Light Interception Efficiency

Apple is one of the most popular and important fruits in the world. The 3D foliage distribution of an apple tree greatly influences its light interception efficiency and therefore has a strong impact on its productivity. Although architectural variations have been found among apple tree cultivars [53], there is still a difficulty to integrate those traits in breeding programmes [54]. And the fieldworks of growing and measuring apple trees are extremely time-costing and exhausting.

To allow virtual experiments as an alternative, MAppleT [55], a functional-structural model for simulation of apple tree development, has been developed. A most recent effort using MAppleT [56–58] is to integrate it with a light environmental simulator called Fractalysis [59] to test how the different combinations of architectural traits influence light interception efficiency at different scales: every metamer, every growth unit, every branch and the whole tree. This study not

only demonstrates how the time- and resource-saving virtual experiments are feasible and reasonable, but also provides a methodology for ideotype definition and genetic improvement of apple trees.

6 Discussion and Conclusion

In many cases, the validity of the published plant models has been accepted by the scientific community, but the applications of such models into agricultural practice are far from enough. The interval between science and practice, however, is not that big. In fact, most of the most difficult problems, either methodological or technical, have been well addressed. Look at the published modelling works: many of them are based on sufficient database, reasonable rules, appropriate approaches and strategies; even some modellers open their source code to help others repeat the simulations. Nonetheless, assuming the ‘others’ are ordinary agronomists or farmers, how much could they handle the code? This could be where the bottleneck really is. Thus, a user-friendly interface to operate the simulations as well as the efficiency of computing to support PC-based implementations should also draw more attentions. Once this interval is filled, virtual agriculture will have more ‘real’ productions.

References

1. Weng G et al (1999) Complexity in biological signaling systems. *Science* 284:92–96
2. van Riel NAW (2006) Dynamic modelling and analysis of biochemical networks: mechanism based models and model-based experiments. *Brief Bioinform* 7:364–374
3. Stelling J (2007) Understandable complexity. *Sci STKE* :pe9
4. Minorsky PV (2003) Achieving the in silico plant. *Systems biology and the future of plant biological research. Plant Physiol* 132:404–409
5. Hammer GL et al (2004) On systems thinking, systems biology, and the in silico plant. *Plant Physiol* 134:909–911
6. Haefner JW (2005) *Modeling biological systems: principles and applications*. Springer, New York
7. Hill LL et al (2001) A content standard for computational models. *The Magazine of Digital Library Research* 7
8. Krogh D (2009) *Biology: a guide to the natural World*. Pearson/Benjamin Cummings, San Francisco
9. Prusinkiewicz P (1998) Modeling of spatial structure and development of plants. *Sci Hortic* 74:113–149
10. Hanan JS, Room PM (1996) Practical aspects of virtual plant research. In: Michalewicz MT (ed) *Advances in computational life sciences*. Kevin Jeans, Collingwood
11. Halle F et al (1978) *Tropical trees and forests: an architectural analysis*. Springer, Heidelberg
12. Room PM et al (1994) Module and metamer dynamics and virtual plants. In: Begon M, Fitter AH (ed) *Advances in ecological research*. Academic Press, London

13. Godin C et al (1999) A method for describing plant architecture which integrates topology and geometry. *Ann Bot* 84:343–357
14. Honda H et al (1981) Computer simulation of branch interaction and regulation by unequal flow rates in botanical trees. *Am J Bot* 68:569–585
15. Honda H et al (1982) Two geometrical models of branching of botanical trees. *Ann Bot* 49:1–12
16. de Reffye P et al (1988) Plant models faithful to botanical structure and development. *Comput Graph* 22:151–158
17. Prusinkiewicz P et al (1988) Development models of herbaceous plants for computer imagery purposes. *Comput Graph* 22:141–150
18. Prusinkiewicz P, Lindenmayer A (1990) *The algorithmic beauty of plants*. Springer, New York
19. Jaeger M, de Reffye P (1992) Basic concepts of computer simulation of plant growth. *J Biosci* 17:275–291
20. Perttunen J et al (1996) LIGNUM: a tree model based on simple structural units. *Ann Bot* 77:87–98
21. Prusinkiewicz P (2004) Modeling plant growth and development. *Curr Opin Plant Biol* 7:79–83
22. Danjon F, Reubens B (2008) Assessing and analyzing 3D architecture of woody root systems, a review of methods and applications in tree and soil stability, resource acquisition and allocation. *Plant Soil* 303:1–34
23. Jourdan C, Rey H (1997) Modelling and simulation of the architecture and development of the oil-palm (*Elaeis guineensis* Jacq.) root system. *Plant Soil* 190:217–233
24. Godin C, Sinoquet H (2005) Functional-structural plant modelling. *New Phytol* 166:705–708
25. Barthélémy D, Caraglio Y (2007) Plant architecture: a dynamic, multilevel and comprehensive approach to plant form, structure and ontogeny. *Ann Bot* 99:375–407
26. Vos J et al (2010) Functional-structural plant modelling: a new versatile tool in crop science. *J Exp Bot* 61:2101–2115
27. Hu B, Jaeger M (2003) Plant growth modeling and applications. In: *Proceedings PMA03: 2003 International symposium on plant growth modeling, simulation, visualization and their applications*. Springer
28. Fourcaud T et al (2008) Plant growth modelling and applications: the increasing importance of plant architecture in growth models. *Ann Bot* 101:1053–1063
29. DeJong TM et al (2011) Using functional-structural plant models to study, understand and integrate plant development and ecophysiology. *Ann Bot* 108:987–989
30. Guo Y et al (2011) Plant growth and architectural modelling and its applications. *Ann Bot* 107:723–727
31. Hanan J (2012) Functional structural plant modelling: applications beyond the plant. In: Kang M, Dumont Y (ed) *Plant growth modeling and applications, proceedings of PMA12*. IEEE Computer Society
32. Room P et al (1996) Virtual plants: new perspectives for ecologists, pathologists and agricultural scientists. *Trends Plant Sci* 1:33–38
33. Hanan J (1997) Virtual plants—integrating architectural and physiological models. *Environ Model Softw* 12:35–42
34. Prusinkiewicz P (2004) Art and science for life: designing and growing virtual plants with L-systems. *Acta Hort* 630:5–28
35. Lindenmayer A (1968) Mathematical models for cellular interaction in development, Parts I and II. *J Theor Biol* 18:280–315
36. Hemmerling R et al (2008) The rule-based language XL and the modelling environment GroIMP illustrated with simulated tree competition. *Funct Plant Biol* 35:739–750
37. Hu BG et al (2003) GreenLab: a new methodology towards plant functional-structural model—structural part. In: Hu B, Jaeger M (ed) *Plant growth modeling and applications. Proceedings PMA03: 2003 international symposium on plant growth modeling, simulation, visualization and their applications*. Springer

38. Yan HP et al (2004) A dynamic, architectural plant model simulating resource-dependent growth. *Ann Bot* 93:591–602
39. Guo Y et al (2005) Parameter optimization and field validation of the functional–structural model GREENLAB for maize. *Ann Bot* 97:217–230
40. Pradal C et al (2008) OpenAlea: a visual programming and component-based software platform for plant modelling. *Funct Plant Biol* 35:751–760
41. Graham PH, Vance CP (2003) Legumes: importance and constraints to greater use. *Plant Physiol* 131:872–877
42. Scott PT et al (2008) *Pongamia pinnata*: an untapped resource for the biofuels industry of the future. *BioEnergy Res* 1:2–11
43. Kinkema M et al (2006) Legume nodulation: successful symbiosis through short- and long-distance signalling. *Funct Plant Biol* 33:707–721
44. Carroll BJ et al (1985) A supernodulation and nitrate-tolerant symbiotic (*nts*) soybean mutant. *Plant Physiol* 78:34–40
45. Carroll BJ et al (1985) Isolation and properties of soybean [*Glycine max* (L.) Merr.] mutants that nodulate in the presence of high nitrate concentrations. *Proc Natl Acad Sci USA* 82:4162–4166
46. Delves AC et al (1986) Regulation of the soybean-rhizobium nodule symbiosis by shoot and root factors. *Plant Physiol* 82:588–590
47. Gresshoff PM (2003) Post-genomic insights into plant nodulation symbioses. *Genome Biol* 4:201
48. Oka-Kira E, Kawaguchi M (2006) Long-distance signaling to control root nodule number. *Curr Opin Plant Biol* 9:496–502
49. Han L et al (2007) Virtual soybean—a computational model for studying autoregulation of nodulation. In: The 5th international workshop on functional structural plant models, Napier, New Zealand
50. Han L et al (2009) Modelling root development with signalling control: a case study based on legume autoregulation of nodulation. In: Li B et al (eds) *Plant growth modeling and applications*, proceedings of PMA09. IEEE Computer Society, Los Alamitos
51. Han L et al (2011) A functional-structural modelling approach to autoregulation of nodulation. *Ann Bot* 107:855–863
52. Han L et al (2010) Computational complementation: a modelling approach to study signalling mechanisms during legume autoregulation of nodulation. *PLoS Comput Biol* 6:e1000685
53. Lespinasse Y (1992) Breeding apple tree: aims and methods. In: The joint conference of the EAPR breeding and varietal assessment section and the EUCARPIA potato section, Landerneau, France
54. Laurens F et al (2000) Integration of architectural types in French programmes of ligneous fruit species genetic improvement. *Fruits* 55:141–152
55. Costes E et al (2008) MAppleT: simulation of apple tree development using mixed stochastic and biomechanical models. *Funct Plant Biol* 35:936–950
56. Da Silva D et al (2012) Light interception efficiency of apple trees: a multi-scale computational study based on MAppleT model. In: Luo W et al (ed) *Proceedings of the fourth international symposium on models for plant growth, environmental control and farm management in protected cultivation*. Acta Hort
57. Han L et al (2012) Investigating influence of geometrical traits on light interception efficiency of apple trees: a modelling study with MAppleT. In: Kang M, Dumont Y (ed) *Plant growth modeling and applications*, proceedings of PMA12. IEEE Computer Society
58. Han L et al (2013) Sensitivity analysis of light interception to geometrical traits of apple trees: an in silico study based on MAppleT model. In: Bourgeois G (ed) *Proceedings of the Ninth international symposium on modelling in fruit research and Orchard management*. Acta Hort
59. Da Silva D et al (2008) Multiscale framework for modeling and analyzing light interception by trees. *Multiscale Model Simul* 7:910–933

Analysis on the Concepts of Knowledge and Knowledge Engineering: Based on the Perspective of “Information Complex Holographic Person”

Tianbo Zhang

Abstract To carry out scientific research on natural and social phenomena, humanity hypothesis is the foundation and the logic origin. To conduct theoretical and mathematical analysis, modeling is the starting point and the key link. On the basis of building “Whole Effect Human Body Model”, this paper gives a preliminary analysis on system and knowledge and other related concepts by virtue of “Information Complex Holographic Person” hypothesis. Newton’s first law is approximate. Knowledge and knowledge engineering can be divided into “three types and five levels”. The “three types” are: hard knowledge, soft knowledge, clever knowledge, “hard knowledge engineering”, “soft knowledge engineering” and “clever knowledge engineering”; the “five levels” are: littoscopic-knowledge, littoscopic-knowledge engineering, microscopic-knowledge, microscopic-knowledge engineering, macroscopic-knowledge, macroscopic-knowledge engineering, cosmoscopic knowledge, cosmoscopic knowledge engineering, bulgoscopic-knowledge and bulgoscopic-knowledge engineering.

Keywords Information complex holographic person · Knowledge engineering · Whole effect · Modeling · “External elements” of the system (environment)

T. Zhang (✉)
Guangdong Industry Technical College, No. 152, Xingang West Road,
Guangzhou City 510300, Guangdong, China
e-mail: 1985101083@gditc.edu.cn

1 Introduction

Humanity hypothesis and theoretical modeling are foundations and starting points of the scientific research on human nature and social phenomena. Different Humanity hypotheses will come to different scientific theories. There is no exception to this in modern or ancient times, in China or elsewhere. With the development of technology, human society enters a new century of knowledge explosion, the information age, the network society, the virtual world, Smart Planet, ecological civilization and globalization. Humanity hypothesis in which “tools man”, “biological man” and “rational economic man”, “social man”, “moral person” and “self-realization person”, etc. take human as an abstract and holistic individual has been substituted by the so-called “Complex Holographic Information Person”. Therefore, we must rethink and re-examine previous theories in the building of science. This paper argues that Newton’s first law does not exist at all or is only an approximate law; basic ideas of mathematical or computer modeling should also be adjusted accordingly; concepts such as knowledge and knowledge engineering, etc. should also have a different meaning or classification.

2 “Whole Effect Human Body Model” Hypothesis (Klein-Menger-Koch-Gravitation Human Body Model)

“Sphinx” mystery in Ancient Greece is still a mystery. Why can the brain which is composed of ordinary matter produce mystical awareness? Is there a model which can give an abstract design of complex human body? Based on complex system theory, quantum theory, information theory, holographic theory, genetic engineering, noetic science and common sense theory, etc., this paper incorporates the following four aspects and proposes “Whole Effect Human Body Model” or “Klein-Menger-Koch-Gravitation Human Body Model”.

First, considering contact surface through which human body and the external world exchange material, energy and information. Human can interact with the environment by using his own external senses, and he can also communicate with the outside world by using internal organs to eat food and inhale air. By this token, the contact surface is similar to the Mobius surface. On the whole, human body is like a “Klein bottle” with breaks.

Second, analyze from the internal configuration of human body. The structure of the major systems which constitute human body such as the blood system, endocrine system and epidemic prevention system, etc. is similar to “Sierpinski Carpet” in the plane or “Menger Sponge” in three-dimensions. The surface area is large but the volume is very small, such as the distribution of artery and vein in the body.

Third, analyze from littoscopic field and quantum characters. In the limited brain there is infinite consciousness, which is similar to the Koch Curve (snowflake curve)

in the plane. That is to say, within a limited area there are disjoint curves with infinite length. For nerve cells, neurons, axons or dendrites, etc. in the brain, there should be “Koch highlight” or “Coch Deformation” which is formed by “Koch Operation”. Analyzed from quantum theory in littoscopic or microscopic aspect, the so-called “Wave-particle Duality” will become the “Fluctuation-Particle-Information-Awareness Four Images” (short for WPIAFI) [1].

Fourth, consider the way in which the human body and the environment interact. For the given system which is taken as the research object, the constituent elements may be classified by the orientation specified in the system. These elements can be divided into elements inside the system (short for internal elements) and elements outside the system (short for external elements). The external elements are the environment of the given system. Characteristics of the system are mainly decided by elements inside the system. In addition to direct contact in a general sense, the effect of gravity on human body is all-around. The effect of gravity has three characteristics: firstly, the effect of external environment on internal elements is all-around. In terms of morphological rules, point of action of universal gravitation can be attributed to the effect on the centroid of the entire object; secondly, elements within the system also interact with each other; thirdly, acting carrier and media have not been detected by so far. In addition to gravity, universal gravitation from elements outside the system on human body is negligible.

Synthesizing the above four points, the paper holds that human body is a complex giant system embedded with antinomy which is composed of approximately 30 kinds of elements, i.e. “Klein-Menger-Koch-Gravitation” Human Body Model (short for KMKG Human Body Model), or referred to as “Whole Effect Human Body Model”. Here the so-called “whole effect” means: first, all the system elements involve in functioning; second, all the system elements fully function; third, the interaction between the system and the outside world is holographic, and the result is real-time holographic to the system or a hologram holographic point; fourth, the feedback is full-dimensional. Reaction can be considered as direct feedback, and the feedback is the inverse effect; in addition, there is indirect feedback.

3 “Information Complex Holographic Person” Hypothesis

The author proposed that human should be regarded as a open, complex and giant system [2]—with the features of a hierarchical structure, complexity, holography and self-awareness, which is composed of tens of trillions of sub-systems, small systems (human tissues such as muscle, blood vessels, etc.) and big systems (functional organs such as hands, feet, skin and brain, etc.). The system can be called “Giant Complex Adaptive Intelligent System”(short for GCAIS—“Information Complex Holographic Person” (short for ICHP) [3]. A slight move in one part may affect the situation as a whole. Every movement of a person, though seen

simple, is GCAIS's response and processing activity to external information in the reality [4]. Any system with the participation of human is "Giant Complexity Adaptive Intelligent System" (GCAIS). Therefore, knowledge and knowledge engineering are all GCAIS.

Consciousness is explicit expression of the quantum behavior of thinking cells in the brain, and memory is the thinking cells in the brain "Koch protruding"'s "Koch prominent fractal". Brain with limited capacity can accommodate infinite "Koch protruding" [5]. So the brain has infinite memory. A thinking process is a group of brain cells' "Koch Operation", and continuous thinking process is a series of thinking Koch operation [5]. Therefore, consciousness or thinking is spirit, and they are not independent of substance (human brain cells). Instead, they are the basic properties of neurons in the brain. That is to say, spirit is not separate entity, and human's spirit and neurons in the brain cannot be split.

4 Newton's First Law is Approximate

Newton's first law is also called The Law of Inertia, which shows that all the objects will remain at rest or keep moving in a straight line at constant speed unless it is acted upon by a force. The object of which the mass is M is taken as the research object. In general, the force acting upon the object can be divided into 6 parts, namely, contact force F_J acted upon by other objects at the adjacent boundary; electromagnetic force F_D acted upon by other objects; gravity F_G acted upon by the earth; the ground support force F_C ; gravitation F_W acted upon by the environment or elements outside the system; complementary force F_H acted upon by the impact from the observer; thus the resultant force F_Z that the object is acted upon is:

$$F_Z = F_B + F_D + F_G + F_W + F_C + F_H = Ma$$

This formula is the expression of Newton's second law, where a represents accelerated speed the object obtained.

If an object is not acted upon by a net force, there can be nothing but that all the 6 forces are zero. That is to say, gravity F_G may keep balance with ground support force F_C . But as to the uneven distribution of cosmic material, it is impossible that gravitation F_W becomes zero. In other words, in the universe there is no object which is not acted upon by external force. Newton's first law is just a hypothetical law. Actually it does not exist.

Only when contact force F_J is negligible relative to gravitation F_W , electromagnetic force F_D and complementary force from the observer F_H , and while gravitational force F_G keeps balanced with support force F_C , Newton's first law and Newton's second law are approximately established, namely:

$$F_Z = F_J + F_D + F_G + F_W + F_C + F_H \approx F_J = Ma$$

5 Thinking Approach of Theoretical Modeling

Like humanity hypothesis, modeling is the key link and the important step to conduct mathematical analysis by virtue of mathematical tools. Mass point, point charge, the electric field lines of force, the ideal voltage source, rigid, light line and ideal gas, etc. are commonly used physical model. The most basic models in control theory are: input and output, respectively, focus on a specific port or channel plus control or interference channels and feedback channels. Professor Miao Dongsheng said: “Human body is a complex system. Its boundary is a fractal structure. In this structure everywhere is continuous and dense to protect human body against external damages; and there are pores leading to the outside world almost everywhere to accept outside information and transmit information to the outside world [6].” This “Whole Effect Human Body Model” shows that: in a variety of modeling processes, the following four factors should be considered, namely: firstly, whether the channel between the system and the environment formed by the research object is clear or complex, such as an unbounded channel with a border. Secondly, what the carrier or medium between elements inside the system and elements outside the system (environment) is, such as electromagnetic force, gravity, mass or energy, etc. Thirdly, the interaction among elements in the system and the way in which these elements interact should be considered. Fourthly, the feedback is a kind of reaction.

6 Concepts and Classification of Knowledge Thinking

Knowledge is a concept produced in the ancient times. But so far, there is no one accepted definition as to what knowledge is. Xiong Deyong and He Jinsheng defined knowledge as conceptualized and symbolized orderly combination of information that can be reproduced or can be produced in the way which subject of knowledge combines and assimilates object of knowledge by using its inherent schema of cognition. To be concise, this paper defines knowledge as follows: knowledge is the crystallization of human social practice, which includes the physical activities, events (shi) activities, and information activities (including consciousness) human performs.

According to the three categories of human needs, knowledge can be divided into “hard knowledge” and “soft knowledge” and “clever knowledge”. “Hard knowledge” refers to all sorts of things and all forms of food, clothing, shelter and transportation characterized by substance or directly felt by human senses, such as daily necessities, cars, buildings and other objects. Another example is something that is expressed by human morphology (dance), and so on. “Soft knowledge” refers to non-material forms, books or symbols, as well as friendship and love in social groups, and other related things. “Clever knowledge” refers to something that is expressed by information, virtual entity or data. The knowledge contained

in knowledge is also “clever knowledge”, such as pun and double meanings and so on. Hard knowledge is the foundation; soft knowledge is the main body; clever knowledge is the soul. Clever knowledge can play a big role in commanding, controlling, regulating and facilitating hard knowledge and soft knowledge.

As early as 1970s, Qian Xuesen believed that science and technology explore the objective world from five levels of spatial and temporal scales, namely, the littoscopic concept (superstring, 10^{-34} cm), microscopic (quantum mechanics, 10^{-15} cm), macroscopic (10^2 m), cosmoscopic (the theory of relativity, 10^{21} m) and the bulgoscopic concept (10^{40} m) [7]. Similarly, divided by spatial and temporal scales, knowledge can be divided into five levels: “littoscopic-knowledge”, “microscopic-knowledge”, “macroscopic-knowledge”, “cosmoscopic-knowledge” and “bulgoscopic-knowledge”.

“Littoscopic-knowledge”, also called “meta-knowledge”, is the result obtained by performing related research on the causes, conditions and elements of “self-knowledge”, which is similar to the concept of “knowledge gene” or “Knowledge DNA”, etc. first proposed by Mr. Li [8]. It is also equivalent to psychological “wave-particle duality” of “quantum psychology” and “quantum management [9]”. “Littoscopic-knowledge” is the foundation or source of knowledge creation, which generates innovative ideas through the material fields and thought field of field material [10].

“Microscopic-knowledge” is aggregations of “littoscopic-knowledge”. It is equivalent to Li Bowen’s “knowledge cell”. Namely, “Knowledge DNA” is known as fundamental principle formed by integrating one or several “Knowledge DNA” and its application scope and conditions, etc. This is similar to the micro-scope of “ideological meme” or “memetics” proposed by British evolutionary biologist Richard Dawkins in 1978 [11].

“Macroscopic-knowledge” refers to branches of knowledge in general, which is often referred to as narrowly defined knowledge, such as the knowledge theoretical systems of physics, chemistry, mathematics and other disciplines.

“Cosmoscopic-knowledge” involves complex objects, and covers great spatial and temporal span, and consists of huge amount of heterogeneous elements. It refers to widely defined knowledge in general, which can be cross-interdisciplinary and cross-systematical comprehensive knowledge.

“Bulgoscopic-knowledge” refers to the knowledge systems which have a greater impact on all human activities and the entire human race, i.e. the whole community. For the modern society, it refers to the transfer, exchange, integration and innovation of knowledge and other issues in the United Nations or among countries.

For knowledge is about accumulation of the experience of human practice, the complexity of human leads to the complexity of knowledge. In addition to the characters of following common sense, such as truthfulness, relativity, dynamic nature, subjectivity, incompleteness, ambiguity and inexactness, expressiveness, storability (memorability), cumulateness, constitutive property, transitivity, original nature, scalability, doubling, situation and vitality etc., knowledge also has quantum character, holographic character, fractal character, emergent property and distributed character and so on.

7 Definition of Knowledge Engineering

The term “Knowledge Engineering” was first proposed by U.S. intelligence expert EA Feigenbaum. It is also known as knowledge processing study. The research contents include three major elements: knowledge acquisition, knowledge representation and the use and the application of knowledge. But the connotations of Chinese phrase “工程” (Gongcheng) are much richer than the English word “Engineering” or “project”. In the research area of social sciences, “工程” (Gongcheng) is widely used, such as “211 Projects”, “Vegetable Basket Project” and “deal fails, project delays” and other expressions.

In terms of a wide range of social activities, engineering can be given a simple and broad definition: “engineering” is purposeful and systematic practice conducted by human society. Engineering involves human resource, finance, material, events, information and other factors. And different disciplines give their own connotations and extensions of engineering respectively. Engineering is a part of human activities. All kinds of Engineering are human activities.

Therefore, knowledge engineering can be defined as purposeful and beneficial practice conducted by human to obtain knowledge. In this regard, knowledge engineering can be divided into three categories: “hard knowledge engineering”, “soft knowledge engineering” and “clever knowledge engineering”. And it can be classified into five layers: “littoscopic-knowledge engineering”, “microscopic-knowledge engineering”, “macroscopic-knowledge engineering”, “cosmoscopic-knowledge engineering”, and “bulgoscopic-knowledge engineering”.

8 Conclusion

In summary, humanity hypothesis is enriched with the progress of times, and the related theory also changes accordingly. “Information Complex Holographic Person” is the inevitable product of the knowledge explosion, the information age, social network, virtual world and ecological civilization in the new century. It will certainly have a profound impact on concepts of system, knowledge, engineering, management, education and culture, etc. This paper focuses on the construction of modeling and preliminary definition and classification of knowledge and knowledge engineering in order to explore new theories for inspiration.

Acknowledgment This paper is funded by the following three educational scientific research fund projects: Guangdong Province Education Science “12th Five-Year Plan” Project in 2012 (name: Research on School and Enterprise Cooperating to Construct an Integrated and Super-market-style Training Base, Grant No.: 2012JK091); Association of Higher Education of Guangdong Province Higher Education Scientific Research Programs in 2012 (Name: Research on School-enterprise Cooperation and People-oriented Modern Vocational Education System Embodying the Concept of Lifelong Education, Grant No.: GJB125095), and Guangzhou Philosophy Social Science Issues in 2013 (13G33), Guangdong Provincial Higher Rectors’ Conference 2013 annual key subject of the project (GDXLHZD014) and 2013 Guangdong Industry Technical College teaching reform project (JG201365) funding.

References

1. Tianbo Z (2012) Analysis of quality of higher education connotation. In: Fifth educational reforms and management engineering annual conference. Education and Research Press, Chongqing, Zhou Bing, pp 9–13
2. Tianbo Z, Xu H, Hu S, Lin Z (2011) Based on the training base of the action system construction and exploring. *Res Explor Lab* 30(08):437–441
3. Tianbo Z (2012) Integration mechanism of school training resources and practice - to build the arts center as an example. *Lab Res Explor* 31(07):445–448
4. Tianbo Z, Luo Y (2012) Faculty building in higher vocational college based on evolution of humanity hypothesis: Guangdong Industry Technical College teachers in the cases. *Education Teaching Forum* 37:224–227
5. Tianbo Z (2012) Vocational education hierarchy of sight the construction of modern vocational education system in China. In: The third teaching management and curriculum construction academic annual meeting, Education Research Press, vol 3001, pp 28–33
6. Miao D (2001) Fractal and complexity. *Sys Dialect Univ* 11(2):7–13
7. Qian X (2005) Organization and management of technology: systems engineering, the “wisdom of the key”: Qian of systems science, Shanghai Jiaotong University Code. Shanghai Jiaotong University Press, Shanghai, p 2
8. Li B (1985) On science of heredity and variation. *Sci Sci Manage* (10):21–25
9. Rongshuang Z (2008) Quantum consciousness- a new sense of quantum psychology interpretation. *Xuzhou Norm Univ (Philos Soc Sci)* 34(02):125–128
10. Wang Y, He J (2010) Based on brain science and neural network knowledge creation. *Branch Technol Manage Res* 3:6–8
11. Jinsheng H, Wenjuan L (2011) Knowledge genes of the origin, content and development. *Sci Res* 29(10):1454–1459

High Precision Brushless DC Motor Position Feedback Technology for Three-Axis Turntable

Guanda Liu, Bo Mo, Haiwen Zhu and Jin Lin

Abstract The flight simulating three-axis turntable used to simulate the spatial angular movement of the aircraft, its ground-based simulation experiment depends directly on the credibility of the angle measuring. Aiming at high-precision position feedback requirements, designed a circuit board of motor drive based on a combination of DSP and CPLD, the hardware design, graphics programming. Analysis of simulation experiments is described here in detail. The fourfold frequency encoder value is used in combination with the rotary transformer, through the comparison of the data analysis to verify the position feedback techniques have good feasibility and versatility.

Keywords Turntable · BLDCM · Fourfold frequency · Double position feedback

1 Introduction

Three-axis Flight Simulating Turntable consists of driving system, servo system, machinery, feedback system, experimental component, etc. Since the world's first simulator in 1945 from the Massachusetts Institute of Technology developed to date, its development tendency from single-axis to multi-axis form, apply to the professional, related to standardization, control to real-time, software to intelligent, rotation rate to wide range, and position to high precision.

Turntable Simulates aircraft angular movement of the whole navigation, it is the core of vehicle semi-physical simulation experiment on the ground. When simulation, DSP receives and tracks tri-axial framework for RT position signals from controller, convert it to a physical movement can be recognized by the sensor

G. Liu (✉) · B. Mo · H. Zhu · J. Lin

School of Aerospace Engineering, Beijing Institute of Technology, Beijing, China
e-mail: 1983@bit.edu.cn; guandalu@126.com

and can provide experimental conditions for 100–150 mm diameters based on inertial compound guidance mode, lasers, satellites, and variety of smart seeker. Turntable adopted tri-axis vertical U–O–O structure and driving by servo device, motor, gear-box, shaft-driven system; Technology combined motor side encoder with frame-side resolver enforce double closed-loop, high precision position feedback. The signals shift, fourfold frequency resolution, risk avoid, and 32-bit counter are included Self-developed Turntable Drive Board, design focuses. Framework-end hollow rotating transformer mainly used as comparison between absolute angular position measurement and design effects.

2 Principle

2.1 Servo Control System of Simulation Turntable Brushless DC Motor

Simulating Turntable's inner, middle, and outer three-axis framework, characterization of aircraft navigation movement of roll, pitching, yaw. With single-axis framework as an example, BLDCM servo control system is shown in Fig. 1. Among them, single-axis position directives and photoelectric encoder, resolver after compensation algorithm for feed forward, forming in real time speed instruction; speed instruction with differential speed feedback received after the compensation filter algorithm, forming real time current instruction; current instruction after the compensation optimization algorithm and three-phase feedback current through the motor, Resolver combination, the torque output to the turntable single-shaft frame.

Electronic circuit, servo system adopts relying on DSP+CPLD into the main framework of the circuit board, DSP's frequency is 160 M, address is 24-bit, data is 8-bit, parallel working mode, combined with microsecond-level single-axis encoder position high-speed to extract signal, for simulation of IPC to fully level three-axis position directive have milliseconds real-time responsiveness.

2.2 Double Closed-loop Position Feedback Technology of Simulating Turntable

In BLDCM servo drive system, the feedback sensors of the measurement for angular position and angular velocity include DC tachometer, photoelectric encoder, and resolver. From the perspective of control tasks, due to DC Tachometer cannot have the exactly detection for ultra-low speed bi-directional stability are not suitable for Simulator applications, thus adopting Incremental Photoelectric Encoder with sine and cosine Resolver combinations position

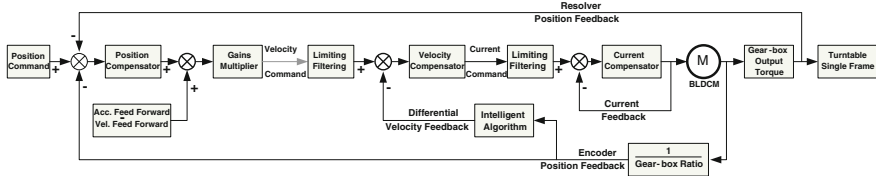


Fig. 1 Servo control system diagram of single-axis framework simulation turntable with brushless DC motor

feedback program. Encoder output from fourfold frequency multiplication signal through the Reducer to the axle frame has had relatively high precision. After power-on, reset to find a return to absolute zero, and contrast with High-accuracy Encoder for position feedback reference, requires Resolver with ability to measure absolute position to complete.

Resolver is an AC controlling motor can output and rotor corner into Function electrical signals, structure hollow, and brushless injection setting absolute angular position measurement components, installed in Reducer ending output, the advantages are no machinery wear, and no sensitive electronic devices out-put signal with strongly anti-mutations interference capacity, and resistance temperature humidity changes, and resistance impact vibration, by selected model are hollow rotating transformer, accuracy between 0.5 and 3', equipped with angular bit decoding transmitter, according to requirement to provides absolute angular position for industrial PC of lap 16-bit resolution, optional digital signal (RS422 serial port) or analog (0–10 V) output interface, applies typical for the ultra-low speed requiring a high degree of stability of the Simulator turntable's middle box, outer box.

$$\Delta\varphi_{out} = \frac{\Delta\varphi_{in}}{i_{Gear}} = \frac{2\pi / (f_{Enc-fre} * n_{Enc-line})}{i_{Gear}} \text{ rad} = \frac{360^\circ}{i_{Gear} * f_{Enc-fre} * n_{Enc-line}} \quad (1)$$

Motor Encoder resolution is 500 lines/Res, 2,000 counts/Res after fourfold frequency, angular accuracy is about $0.18^\circ = 10.8' = 648''$. Refer to Eq. (1), with a reduction ratio range 100–250 Cycloid reducer, angular accuracy up to 2.6–6.5'', basically satisfy accuracy measurement requirements of three-axle low-speed smooth angular movement. With a reduction ratio range 5–10 planetary reducer, angle accuracy is about 1.1–2.2'', fully meet accuracy requirements of the box high-speed rolling-angle movement. Assumes that the limit exists, high-speed gearbox output speed maximum for 20 rps, reduction ratio *i* value 10, conversion to motor Ending, Encoder $\omega_{Max} = 200 \text{ rps} = 40,000 \text{ counts/s}$, equivalent to 0.1 M clock. Fourfold frequency for Incremental Photoelectric Encoder, CPLD clock should be at least 8 times faster than the fastest Encoder clock, which is higher than 0.8 M. Encoder in the text adopted fourfold frequency 20 M clock, can fully qualified Simulator's application requirements.

Table 1 High-speed tri-axis flight simulation turntable performance expectations indicators

| Reference/frame | Inner | | Middle | Outer |
|-------------------------------|---------------------|----------------------|---------------------|---------------------|
| | Low speed | High speed | | |
| Minimum stable angle speed | 0.001°/s | 0.25°/s | 0.001°/s | 0.001°/s |
| Maximum angle speed | 300°/s | 20r/s | 150°/s | 100°/s |
| Maximum angle acceleration | 500°/s ² | 1000°/s ² | 500°/s ² | 300°/s ² |
| Angle range | ±360° | ±360° | ±360° | ±120° |
| Angular measurement precision | ±3'' | ±3' | ±3'' | ±3'' |
| Angular control precision | ±5'' | ±5' | ±5'' | ±5'' |
| Frequency | 3 Hz | 5 Hz | 2 Hz | 2 Hz |

For smart ammunitions testing requirements, tri-axis flight simulation turntable performance expectations indicators have been shown in Table 1. Replacement drives for inner framework with low speed and high speed different roll movement, applied to each flight type, roll type semi-physical simulation experiment of smart ammunitions seeker. Middle framework representation in pitching motion is similar to inner framework, O-type structure, equipped with slip ring, is free to swing 360°. Characterization Yaw movement in outer framework, driving shaft without slip ring, the requirement taking other two frameworks into account, set to ±120° angle range, include Software intelligent limit, additional trips switches for hardware limit to achieve double security, and to prevent wound damage the device [1].

3 Design

3.1 Overview of the Encoder Signal Processing

CPLD includes two programming methods: VHDL language, logic graphics, and the latter is easier to understand and transplant. Quartus software can program clock frequency and fourfold frequency resolution avoiding competition risk phenomenon in CPLD, and used in reversible counting circuits 74193, high frequency decoding 74138, synchronous acquisition 74273, points read technology 74541, acquired by DSP through CPLD direct 32-bit signed integer value data for speed and position feedback Intelligent algorithm.

In the signal conversion, encoders with line driver DS26LS31, the receiver can adopt chips DS26LS32, SN75175, MC3486 to convert differential signal to single signal, core part of the circuit as shown in Fig. 2. Though HCPL-063L isolation circuit to convert single signal from 5 V side to a 3.3 V level signal that compatible with the CPLD, complete signal Schmidt by MAX924 or MAX944, can effectively increase the single signal frontier of steep, reduce transport noise, supply to logic circuits.

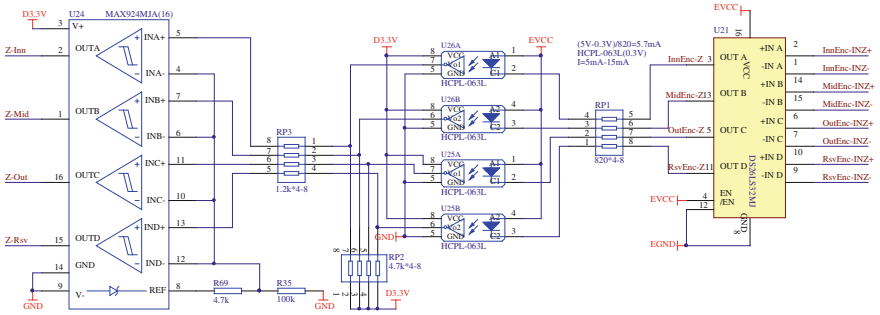


Fig. 2 DS26LS32 differential convert to single-ending module

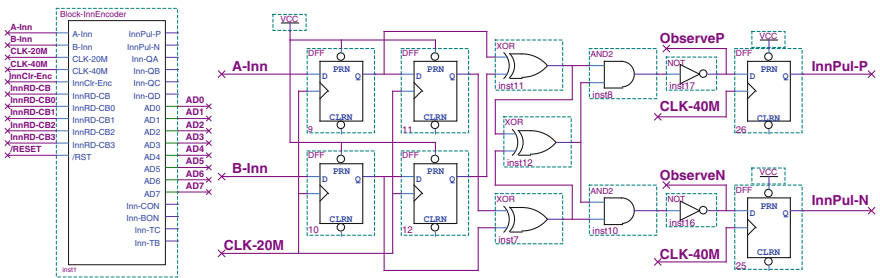


Fig. 3 Inner encoder counter module and fourfold frequency logic circuit

3.2 Fourfold Frequency Resolution in CPLD

As for software, take inter box Encoder module as example, its inter fourfold frequency resolution logic core as shown in Fig. 3. A-Inn, B-Inn of which are transmitted to the CPLD single signals a, b, which is a phase difference of 90° quadrature square wave pulse trains, phase relationships reflect BLDCM turning direction. Software for fourfold frequency practical logic circuits contains VHDL language description, logical image build and Quartus language, the key is to identify a, b signal rising edge and falling edge, when the input signal with delayed signals can have a frequency multiplier circuit after XOR [2, 3]. Analysis and testing, determine design of with a logical structure to build two-channel simultaneous output of positive and reverse pulse.

3.3 CPLD Reversible Counter Logic

It is noteworthy that after two channel pulse signal ObserveP and ObserveN via the clock is 40 M D trigger, trans InnPul-P, InnPul-N signal to the inner 74193 counter

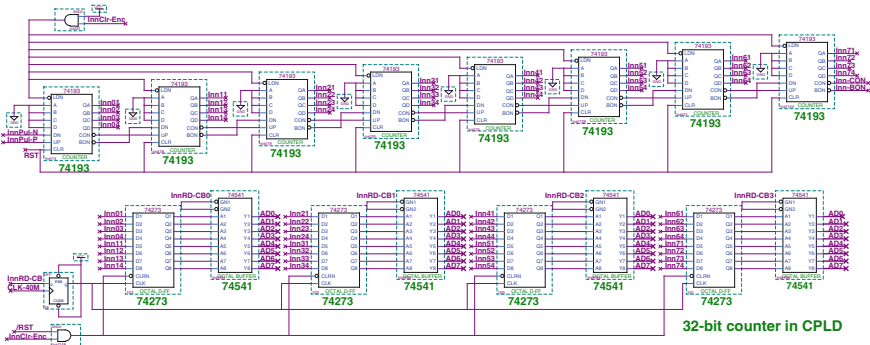


Fig. 4 Encoder 32-bit reversible counter logic

tip UP Terminal and the DN Terminal, here adopts D trigger not sensitive to Burr features [4]. In the phase of ObserveP, ObserveN pulse signal output maintain, D trigger read the above logic signal, synchronized with the clock generated signal trans to 74193 positive and negative counting pulse input, similar convert the asynchronous circuit to synchronous circuit, effectively solving the phenomenon of adventure in a cascade circuit in the counting process [5].

Based on CPLD graphic modules to build 32-bit reversible counter of encoder core logic as shown in Fig. 4, that part of the logic include three main graphics modules: 74193 four-bit binary adding/subtracting counters to clear asynchronously; 74273 register contains eight D-trigger with asynchronous clear Terminal; 74541 octal a three-State bumpers. Counter module is made up of eight 74193 counters, latch module consist of four 74273 registers, read module include four 74541 bumpers. During initialization, /RST, RST means reset function. Wait for the axis found zero completely, then InnClr-Enc set encoder value to zero. During work, connect 40 M clock synchronization positive and reverse pulse sequence ObserveP and ObserveN each access inner 74193 UP, DN-side implementation reversible counting function, particularly to ensure that the data signal input during update with the 40 M clock synchronization, to avoid adventure phenomenon occurs, when carrying, borrowing, loading process result in a counting error. 74138 chip select signals available to low address lines. To low InnRD-CB address lines, leveraging 74273 for 32-bit synchronous data latches; lower /RD to low InnRD-CB0, InnRD-CB1, InnRD-CB2, InnRD-CB3 respectively address lines, man can use 74541 to read 32-bit latched data in real-time. Counting module requires synchronous one 32-bit latches, four asynchronous 8-bit timesharing to read five times to complete latches reading function in single axial code value. 160 M DSP, to finish a three-axis value of latches takes only about 0.1 us. This position feedback scheme compatible with all 8-bit microcontroller, with slightly modified can be used for 16-bit parallel bus.

Table 2 10 variables in the simulation waveform

| Node no. | Name | Instructions |
|----------|-------------|--|
| 0 | A-Inn | Inner incremental photo-electric encoder: A single signal |
| 1 | B-Inn | Inner incremental photo-electric encoder: B single signal |
| 2 | CLK-40 M | CPLD clock from outer: 40 M |
| 3 | CLK-1 M | CPLD frequency reference clock: 1 M |
| 4 | ObserveP | Inner with fourfold frequency, normal turning pulse no. pulse |
| 5 | ObserveN | Inner with fourfold frequency, reversion pulse no. pulse |
| 6 | Inn-CON | CPLD inner Encoder module, outer 74193 counter carry terminal |
| 7 | Inn-BON | CPLD inner Encoder module, outer 74193 counter borrow terminal |
| 8 | Counter-i32 | 32-bit signed int counter value, $-2147483648 \sim 2147483647$ |
| 9(41) | Counter-u32 | 32-bit unsigned int counter value, $0 \sim 4294967295$ |

4 Simulation and Experimental Simulation

4.1 Analysis of Waveform Simulation

By Quartus software, waveform simulation and analysis of 10 representatives is extracted in the process variable, defined as shown in Table 2.

With 32-bit reversible counter module simulation waveform as shown in Fig. 5, Simulation waveform intercepts 106–136 us of simulation process, 30 us typical waveform can be divided into three stages: the first stage is after motor reverse pass zero point, time for 106–118 us, yards value by +3 decreasing to -4; the second stage is motor by anti-conversion to normal turning moments, time for 118–122 us, yards value maintained -4; the third stage is motor normal turning pass zero point, time for 122–136 us, yards value by -4 increasing to +3.

By observing simulation data Counter-i32 and Counter-u32 was informed, based on synchronous collection, time-sharing reading access to get fourfold frequency code value change as expected uniformity continuous. Zero position, signed 32-bit integer, -1 corresponds to an unsigned 32-bit integer 4,294,967,295. The principle Quartus for waveform simulation proved through software programming can be effectively solving CPLD counter build in adventure, verify the feasibility of fourfold frequency counts, latch, extraction from encoder with graphical programming.

4.2 Analysis of Double Closed-loop Position Feedback Experiments

BLDCM position feedback testing includes four steps: **First**, when power up, The program command resolver intelligence return to zero position, and clear corresponding axis motor encoder code value. **Second**, to control specify angular

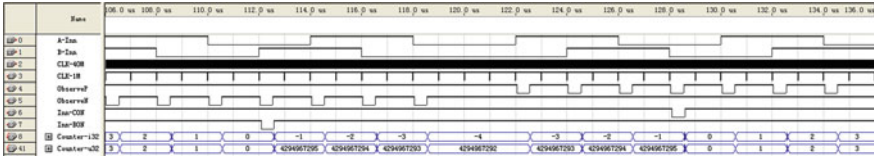


Fig. 5 Encoder 32-bit reversible counter module simulation waveform

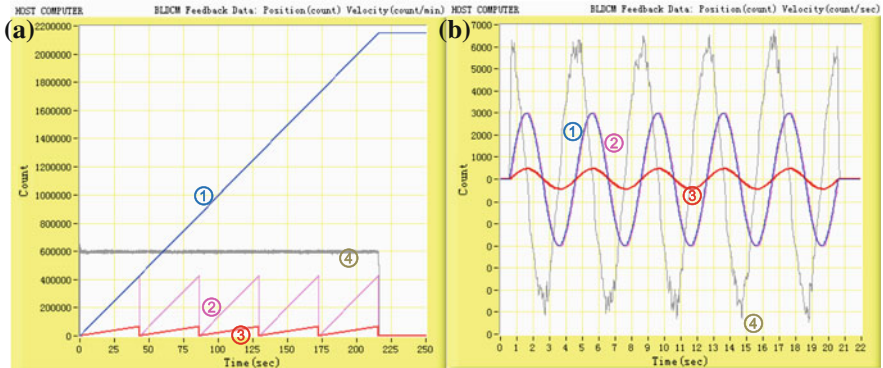


Fig. 6 Motor (a constant speed b sine trajectory) movement code value curve

displacement motor to rotate in steady rate, to observe changing between motor code value and resolver code. **Third**, to set the step 1 ms, to upload encoders, Rotary value transmit to PC in FIFO communication protocol by RS422 serial port and stored. **Fourth**, to have experiment data analysis.

To verify the fourfold frequency reliability of technology of encoder in the article, select middle-framework as testing, experimental parameters are as follows: motor encoder 500 line/r, ratio $i_{Gear} = 215.2$, Resolver 16-bits (A displays U32, B displays I32). A for frame ending in constant five circles in 600,000/2,000/215.2 = 1.394 rpm, B for the frame ending sine curves with the frequency 0.25 Hz and amplitude 2.5°, runs for five cycles. A, B movement's value curve as shown in Fig. 6a, b, due to length limited, only using the typical linear and rotary movement to take five cycle separately for testing screenshots: curve ① is motor target location, curve ② is motor actual location, curve ③ is resolver actual location, curve ④ represent motor speed by Encoder code value. Observation on Fig. 6a, b, comparing fourfold frequency code value with Resolver code value known that there is no accumulation error when constant speed, sine oscillating rotation error-free.

5 Summary

BLDCM with high precision position feedback design, that enable the Flight Simulator to take crawling lower speed stability and the basis for short-time overloading to guarantee control provides precision for brushless motor drive position-loop and speed-loop. To take incremental Photoelectric Encoder and Resolver double location feedback design can effective play both of respective measurement advantage, both solve to get absolute position and requires high relative precision, and mutual for supplementary, through a variety of intelligent processing method, such as return zero, position monitoring, speed solutions filtering, current loop, etc. Design improved system running of reliability, and reference value on multiply-axis position feedback design.

In self-developed turntable motor driver board, encoder position feedback parts design is stable and reliable. Circuit design completes encoder's line driver signal conversion. Software programming develops counter circuit without adventure phenomenon, and use of high frequency decoding, synchronization acquisition, time-sharing reading technology. With Quartus graphics, coding for encoder fourfold frequency, 32-bit counter, equipped with additional absolute angle measuring device can form a double high precision position feedback loop. The design not only suitable for turntable, but also be used in "intelligent gait control of Biped Robot," and suitable for other similar applications of high precision electrical position feedback, have well versatility.

References

1. Huan Y (2010) The design and research of three-axis flight simulating turntable. Beijing Institute of Technology, D. BeiJing, pp 12–20
2. Han Z, Li W, Wang T, Wang S (2000) Analysis of encoder fourfold frequency. *J ChongQing Autom Instrum* 26(12):38–40
3. Chao J, Wang X (2007) Fourfold frequency multiplication circuit design of incremental optoelectric encoder based on FPGA. *J Shang Hai Instrum Technol* 07(6):17–21
4. Chu Z, Weng M (2002) Design and application of FPGA. Xidian University Press, M. Xian, pp 210–213
5. Xuan L (2005) The competition risk in FPGA and the methods of avoiding. *J. Mod Electr Technol* 28(10):119–120

Punctuation Prediction for Chinese Spoken Sentence Based on Model Combination

Xiao Chen, Dengfeng Ke and Bo Xu

Abstract Punctuation prediction is very important for automatic speech recognition (ASR). It greatly improves the readability of transcripts and user experience, and facilitates following natural language processing tasks. In this study, we develop a model combination based approach for the recovery of punctuation for Chinese spoken sentence. Our approach models the relationships between punctuation and sentence by the different ways of sentence representation. And the relationships modeled are combined by multi-layer perception to predict punctuation (period, question mark, and exclamation mark). Different from previous studies, our proposed approach is designed to use global lexical information, not only local information. Results indicate that, compared with the baseline, our proposed method results in an absolute improvement of 10.0 % unweighted accuracy and 4.9 % weighted accuracy, respectively. Our approach finally achieves an unweighted accuracy of 86.9 % and a weighted accuracy of 92.4 %.

Keywords Punctuation prediction · Model combine · Global lexical information

1 Introduction

Current automatic speech recognition (ASR) systems mostly output a stream of words with no structure information such as sentence boundary and punctuation. Therefore, the words are hard for human to read and understand them, and they are difficult for following natural language processing tasks. But, the words inserted structure information can help following application systems (for example, information retrieval [1] and machine translation [2]). So, it is crucial to enrich

X. Chen (✉) · D. Ke · B. Xu

Interactive Digital Media Technology Research Center (IDMTech), Institute of Automation,
Chinese Academy of Sciences, Beijing 100190, People's Republic of China
e-mail: xiao.chen@ia.ac.cn

speech recognition transcription. It can also be used, in automatic essay scoring task, for punctuation correction.

In recent years, several approaches [3–11] to punctuating the output of a speech recognizer have been investigated. Early researchers adapted the ASR system for dealing with restoring punctuation [5, 6]. They considered punctuations as words, and included the punctuations in the recognizer dictionary. The language model (LM) is trained with punctuated text. And the acoustic model is trained with silence, breathing, and some other nonspeech intervals in the speech utterance. The punctuations are inserted directly or with a rescoring process that further employs more information. Later, researchers also predicted punctuation by post-processing the recognizer's output. Some of them provided the LM-based method. In [3, 9], they took raw word sequences from speech recognition as their input, and generated punctuation with language information by directly using N-gram LM. In [10], the author predicted punctuation with language information and acoustic information. The final LM consists of a combination of a number of sub-LMs including a multi-layer perception for trigger words, a forward trigram, and a backward trigram. Some researchers introduced hidden event language model (HELM) based method [4]. They viewed boundary detection and punctuation insertion task as a hidden event detection task, and detected hidden events between words by a 4-g hidden event LM. There are some researchers using conditional random fields (CRF) based [11] or maximum entropy (ME) based [7, 8] method. They considered punctuation prediction as labeling task, and restored punctuation with CRF and ME.

Previous studies view punctuation prediction as a sequence labeling tasks. Punctuation is predicted by using sequence labeling model (HELM, CRF, ME) and local information around the position considered. For example, in reference [7], information used for prediction punctuation around position i refers to local lexical information $W_{i-2}W_{i-1}W_iW_{i+1}W_{i+2}$ and local historical tag information $Tag_{i-2}Tag_{i-1}$. Reference [11] provides a compensation for the lack of long distance dependence in the model. But, limited by the model, it is not the real global information of sentence and its computational complexity is high. Based on the above consideration, the idea of this paper is to view punctuation prediction as a classification task, and restore punctuation by using global lexical information modeled on various sentence representation and model combination.

This paper focuses on the task of punctuation prediction for Chinese spoken sentence (reference sentence). We first described an HELM based baseline, then proposed a new model combination based method. To evaluate the performance, we, first, prepared testing data from real system and corpus for training spoken translation system; second, built three testing sets and selected assessment criteria; finally, tested approaches on the testing sets. Experimental results show that, compared with baseline, the proposed method achieves to 86.9 and 92.4 % in unweighted accuracy and weighted accuracy. Correspondingly, it has an absolute improvement of 10.0 and 4.9 %, respectively.

The rest of the paper is organized as follows: [Sect. 2](#) outlines the baseline and our proposed method; [Sect. 3](#) contains our experimental set, results and analysis; [Sect. 4](#) presents some conclusions and possible directions of future work.

2 Model Combination-Based Punctuation Prediction Method

The idea of this paper is to restore punctuation by combining different models which model the relationship between punctuation and global lexical information by different sentence representations. We first adopt bag-of-words model (BoW), which is a simplifying representation used in natural language processing and information retrieve. In this model, a sentence is represented as an unordered collection of words, disregarding grammar and even word order. But people always use the whole information of sentence to understand it in daily life. So we also use whole sentence directly to represent sentence. In this representation, sentence is represented as a sequence of words. Besides these two representations, we take a compromise of the representations above. A sentence is divided into front part and back part (we call them half-sentences). The sentence is an unordered collection of two half-sentences, but the half-sentence itself is an ordered sequence of words. In the following, we simply name them BoW model, half-sentence model and whole-sentence model, respectively. Having the representation of sentence, the relationships of sentence and punctuation can be modeled using different representations (detailed description is in the following part.). Because the three models describe sentence from different representations, each model has its own characters. The performance may be improved by model combination, according to ensemble learning. [Figure 1](#) shows the framework of algorithm.

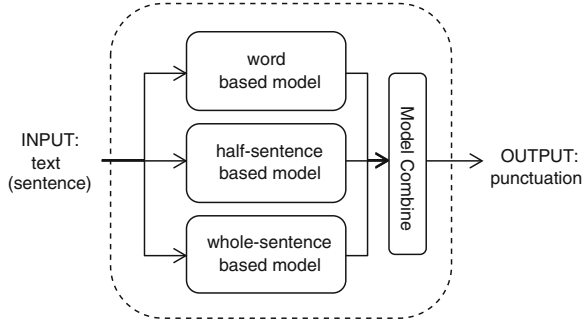
2.1 Models

Three models are introduced for modeling the relationships between sentence and punctuation. They are explained in the following paragraphs (formula in question mark, for example).

2.1.1 Model Based on Word Level

Sentence is represented by BoW model. Probability between punctuation and sentence is computed by probability between punctuation and all words in the bag. For example, given a sentence $S = "W_1 W_2 \dots W_N X"$, here W_i is a word and X is a punctuation. The sentence S is decomposed into a set of words. And a new set

Fig. 1 The framework of the proposed algorithm. It consists of three models which model the relationships between sentence and punctuation by different sentence representations



WGSET is built, whose elements are the triples consisting of words in bag-of-words. The relationship between X and S is just the relationship between X and *WGSET*, and is just the relationship between X and all triples $(w_i w_j w_k)$ in set *WGSET*.

In the training phase, the co-occurrence of punctuation X and all possible triples $(w_i w_j w_k)$ is computed. The conditional probability $p(X|w_i w_j w_k)$ can be obtained by the co-occurrence. During testing, the probabilities can be obtained by querying the conditional probability of X given the triples, and by the following formula (1).

$$P_1 = \frac{p(? | w_1 w_2 \dots w_n)}{\sum_{x=?!} p(x | w_1 w_2 \dots w_n)} \approx \frac{\prod_{\text{all}} p(? | w_i w_j w_k)}{\sum_{x=?!} \prod_{\text{all}} p(x | w_i w_j w_k)} \tag{1}$$

For a dictionary with 50,000 items, the total number of conditional probability for three punctuations is about 375,000 billion $(50,000 * 50,000 * 50,000 * 3)$. There is a serious data sparse problem for the limited training data. So this paper gives a back off algorithm computing conditional probability $p(? | w_i w_j w_k)$, which is not available directly. The formula is

$$p(? | w_i w_j w_k) \approx p(? | w_i w_j) p(? | w_i w_k) p(? | w_j w_k) \tag{2}$$

$$p(? | w_i w_j) \approx p(? | w_i) p(? | w_j) \tag{3}$$

All conditional probability can be computed by the two back off formulas (2) and (3). The final probabilities of punctuations given sentence can be computed by formula (1).

2.1.2 Model Based on Half-Sentence Level

The sentence is divided into two half-sentences by the word in the middle of sentence. They are named the head part and tail part of sentence. Probability between punctuation and sentence is computed by probability between punctuation and each part of sentence. The probability of whole sentence is computed by

$$P_2 = \frac{p(? | w_1 w_2 \dots w_n)}{\sum_{x=.,?!} p(x | w_1 w_2 \dots w_n)} \approx \frac{p(? | W_{\text{head}}) \times p(? | W_{\text{tail}})}{\sum_{x=.,?!} p(x | W_{\text{head}}) \times p(x | W_{\text{tail}})}. \quad (4)$$

Here, $p(? | W_{\text{head}})$ is the probability of question mark given head part of sentence, and $p(? | W_{\text{tail}})$ is the probability of question mark given tail part of sentence.

Training phase involves modeling the influence of each part of sentence to punctuations by training a backward LM and a forward LM using all training data. During testing, the test sentence is divided into two parts, and the probability of punctuation given sentence is computed by formula (4).

2.1.3 Model Based on Whole-Sentence Level

We do not decompose the sentence at all. We view sentence as a whole object, and compute the probability of punctuation given sentence directly. The formula is

$$P_3 = p(? | W) = \frac{p(W | ?) \times p(?)}{p(W)} = \frac{p(W | ?) \times p(?)}{\sum_{x=.,?!} p(W | x) \times p(x)}. \quad (5)$$

In training phase, the training data is divided into three parts by class. For each part, a LM is trained by removing all punctuations. Then we get three LMs. Given the testing sentence, the likelihood probabilities $p(W | x)$ can be computed by the previous LMs. Then the final probability P_3 can be obtained by proportion of punctuations $p(x)$ and formula (5).

2.2 Model Combination

Given a testing sentence, the probability between sentence and punctuation under each model above can be computed. Then MLP is used to combine all probabilities and do the final classification.

3 Experiments and Analysis

3.1 Data

We performed experiments on two corpuses. Corpus A is collected from the real system “ZTSpeech,” which is a spoken speech translation system. The speech is segmented and transcribed by speech recognizer, and annotated by professional

Table 1 The size of each data set (number of sentence)

| TEST1 | TEST2 | TEST3 | TRAIN |
|-------|-------|--------|---------|
| 3.734 | 2.519 | 55.161 | 557.737 |

Table 2 The proportion of samples of each class in each data set (%)

| Class\dataset | TEST1 | TEST2 | TEST3 | TRAIN |
|------------------|-------|-------|-------|-------|
| Period | 54.5 | 41 | 68.7 | 65.1 |
| Question mark | 37.6 | 38.3 | 28.9 | 29.7 |
| Exclamation mark | 7.9 | 20.8 | 2.4 | 5.2 |

annotators. Corpus A has total 3,734 sentences and they are all spoken style. We used it as the main testing set named TEST1. Corpus B is from the spoken machine translation data. Corpus B has 615 million Chinese sentences. It has two parts: testing sets (TEST2, TEST3) and training set (TRAIN). The proportion of each class in TEST2 is roughly equal. The proportion of each class in TEST3 is roughly the same as TRAIN's. The information about training set and testing sets is given in Tables 1 and 2.

3.2 Assessment

To access the total performance of the punctuation task, we use two classification accuracies. One is weighted accuracy (WA) which is defined as:

$$WA = \frac{\text{correct number of samples}}{\# \text{ number of samples}} \times 100 \%. \quad (6)$$

And the other is unweighted accuracy (UA), which is defined as:

$$UA = \frac{\text{sum of accuracy of each class}}{\# \text{ number of class}}. \quad (7)$$

Unweighted accuracy is the arithmetic mean of accuracy of each class. Weighted accuracy is the weighted mean of accuracy of each class. The weights are the proportion of each class in the test set. Because the weighted accuracy concerned to the proportion of each class in the test set, it is not appropriate to compare performance on the testing sets which have a different proportion distribution.

In addition, we use precision, recall and F-measure to measure the performance of the algorithm. They are defined by the following equations:

$$\text{Precision} = \frac{\# \text{ correctly predicted punctuation symbols}}{\# \text{ predicted punctuation symbols}} \quad (8)$$

$$\text{Recall} = \frac{\# \text{ correctly predicted punctuation symbols}}{\# \text{ expected punctuation symbols}} \quad (9)$$

$$\text{F - measure} = \frac{2 \times \text{Precision} \times \text{Recall}}{\text{Precision} + \text{Recall}}. \quad (10)$$

3.3 Experiments Result and Analysis

3.3.1 Whole Performance of Two Approaches

Figure 2 shows that the method proposed outperforms baseline with a great improvement. The average performance of UA on three testing sets achieve to 86.8 % with an absolute improvement of 10.0 %. The average performance of WA on three testing sets achieve to 92.4 % with an absolute improvement of 4.9 %. The method proposed has a better result because the proposed method models global information of sentence by three different models, not only the local information around punctuation position.

In addition, compared with TEST2 and TEST3, the performance of TEST1 is worse. This is because the data of TEST2, TEST3 and TRAIN all come from corpus B. Their performance is higher because their style is similar. But the data of TEST1 come from the collection of real spoken translation system on mobile phone, which has a larger difference with corpus B. This means that the selection of training data should consider the real scene of application to reduce the degree of mismatch.

3.3.2 Detailed Performance of the Approaches to Punctuation Prediction

Table 3 shows the detailed performance of baseline and proposed punctuation prediction algorithm on testing sets. On the testing sets, the improvements of F-measure of period, question mark and exclamation mark obtained by the method proposed are 0.036, 0.056, and 0.156, respectively. The method proposed has better results because the proposed method models global information of sentence by three different models, not only the local information around punctuation position.

It can be seen that the performance of exclamation mark is much worse than the performance of period and question mark. There are two reasons. One reason is that the proportion of exclamation sentence in training set is too small (only

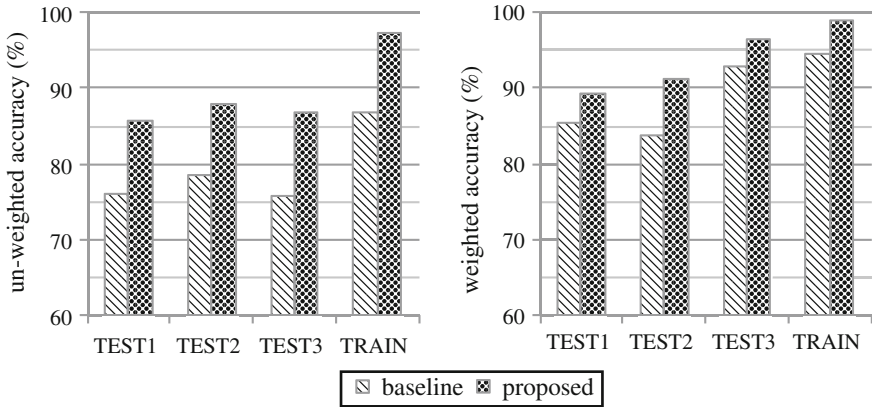


Fig. 2 Performance of baseline and our proposed method on training set and testing sets. Our method outperforms baseline (HELM). (Left) unweighted accuracy (UA); (Right) weighted accuracy (WA)

Table 3 The detailed performance of punctuation prediction algorithm on testing sets and training set

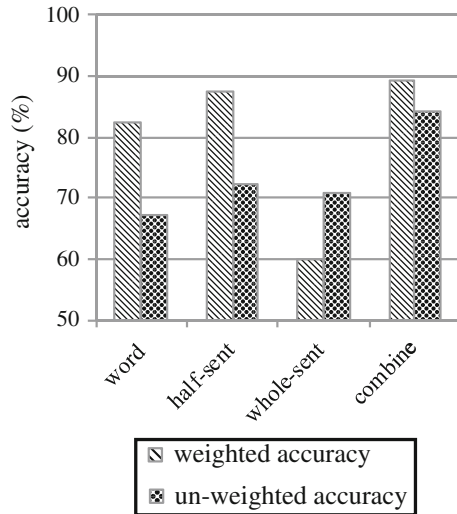
| Dataset | Method | Period | | | Question mark | | | Exclamation mark | | |
|---------|----------|--------|-------|-------|---------------|-------|-------|------------------|-------|-------|
| | | Pre. | Rec. | F | Pre. | Rec. | F | Pre. | Rec. | F |
| TEST1 | HELM | 0.842 | 0.951 | 0.893 | 0.929 | 0.782 | 0.849 | 0.646 | 0.556 | 0.597 |
| | Proposed | 0.902 | 0.916 | 0.909 | 0.931 | 0.889 | 0.910 | 0.695 | 0.773 | 0.732 |
| TEST2 | HELM | 0.735 | 0.972 | 0.837 | 0.965 | 0.874 | 0.917 | 0.957 | 0.514 | 0.669 |
| | Proposed | 0.845 | 0.976 | 0.906 | 0.977 | 0.962 | 0.969 | 0.976 | 0.706 | 0.819 |
| TEST3 | HELM | 0.931 | 0.971 | 0.951 | 0.942 | 0.870 | 0.905 | 0.629 | 0.435 | 0.515 |
| | Proposed | 0.971 | 0.979 | 0.975 | 0.967 | 0.954 | 0.961 | 0.730 | 0.671 | 0.699 |
| TRAIN | HELM | 0.940 | 0.982 | 0.961 | 0.966 | 0.909 | 0.937 | 0.920 | 0.711 | 0.802 |
| | Proposed | 0.991 | 0.995 | 0.993 | 0.993 | 0.990 | 0.991 | 0.976 | 0.940 | 0.958 |

5.2 %). This makes the training relatively insufficient. The other reason is that, besides some sentences with obvious exclamation words, the majority of exclamation sentences is similar with statements and interrogative sentences (may be distinguished by speech). The performance of question mark is the best among three punctuation marks. The main reason is that the training data of question mark is sufficient and its proportion is 29.7 %. The second reason is that the majority of question sentence have obvious clue words which benefit classification.

3.3.3 Performance Improved by Model Combination

Figure 3 shows the performance of each model alone and model combination on testing set TEST01. The performance of model combination is much better than

Fig. 3 The performance of each model alone and model combination. Performance improves by combination



the performance of each model alone. The reason is that the models based on different sentence representation of BoW, half-sentence and whole-sentence have different characteristics.

4 Conclusions and Future Work

We have demonstrated a combined approach for the recovery of punctuation (period, question mark and exclamation mark) for Chinese spoken sentence (reference sentence). Our proposed approach is built on top of various sentence representations. By them, different model of punctuation can be obtained, respectively. The final prediction is done by model combination. Unlike previous work, our proposed approach is designed to use global lexical information, not only local information. Experimental results show that, our proposed approach outperforms the widely used approach based on the hidden event LM. Our proposed approach obtains an absolute improvement of 10.0 and 4.9 % on unweighted accuracy and weighted accuracy, respectively.

Directions for future improvement include improving global lexical features based model by integration of other textual features (part of speech, syntactic and semantic information) and prosodic features (pause, intonation).

Acknowledgments This work is supported by National Program on Key Basic Research Project (973 Program) under Grant 2013CB329302 and National Natural Science Foundation of China under Grant 61103152.

References

1. Favre B, Grishman R, Hillard D, Heng J, Hakkani-Tur, D, Ostendorf M (2008) Punctuating speech for information extraction. In: Proceedings of IEEE international conference on acoustics, speech and signal processing, ICASSP 2008, pp 5013–5016
2. Paulik M, Rao S, Lane I, Vogel S, Schultz T (2008) Sentence segmentation and punctuation recovery for spoken language translation. In: Proceedings of IEEE international conference on acoustics, speech and signal processing, ICASSP 2008, pp 5105–5108
3. Beeferman, D., Berger, A., & Lafferty, J. (1998). Cyberpunc: a lightweight punctuation annotation system for speech. In: Proceedings of IEEE international conference on acoustics, speech and signal processing, ICASSP 1998, pp 689–692
4. Stolcke A, Shriberg E, Bates R, Ostendorf M, Hakkani, D, Plauche M, Tür G, Lu Y (1998) Automatic detection of sentence boundaries and disfluencies based on recognized words. In: Proceedings of ICSLP, pp 2247–2250
5. Chen J (1999) Speech recognition with automatic punctuation. In : Proceedings of Eurospeech, pp 447–450
6. Kim J-H, Woodland P (2001) The use of prosody in a combined system for punctuation generation and speech recognition. In: Proceedings of Eurospeech
7. Huang JGZ (2002) Maximum entropy model for punctuation annotation from speech, ICSLP-2002, pp 917–920
8. Batista F, Moniz H, Trancoso I, Mamede N (2012) Bilingual experiments on automatic recovery of capitalization and punctuation of automatic speech transcripts. *IEEE Trans Audio Speech Lang Proc* 20(2):474–485
9. Gravano A, Jansche M, Bacchiani M (2009) Restoring punctuation and capitalization in transcribed speech. In: Proceedings of IEEE international conference on acoustics, speech and signal Processing, ICASSP 2009, pp 4741–4744
10. Wenzhu S, Yu RP, Seide F, Ji W (2009) Automatic punctuation generation for speech. In: Proceedings of IEEE workshop on automatic speech recognition and understanding, ASRU 2009, pp 586–589
11. Lu W, Ng HT (2010) Better punctuation prediction with dynamic conditional random fields. In: Proceedings of the 2010 conference on empirical methods in natural language processing, pp 177–186

Research on Book Purchases Evaluation System Based on EFGA Neural Networks

Hongxia Liu and Yuhua Liu

Abstract On the basis of comparison and analysis of domestic and foreign book purchases technology, this article focuses on the weak point of current method along with proposing a new way to deal with book purchases question. And we construct a book purchases model on the basis of improved genetic algorithm of neural networks. This method designs a genetic algorithm which is combined with effect factors. Thus, we could optimize the weighs and thresholds, together with making dynamic adjustment for neural networks structure, in order to reach the best situation of neural networks. Then, we develop computer-aided book purchases evaluation system based on this model. The trial results show the feasibility and effectiveness of using neural networks which built by EFGA practice, in solving book purchases question.

Keywords Book purchases · Neural network · Genetic algorithm · Effect factor

1 Introduction

Book purchase is the first key link of library business by providing material base for library service. It plays a primary role in building library books storage system and guaranteeing book quality to adopt good or bad book purchase method. Moreover, the method that we adopt also influences the effectiveness of using books by readers together with accomplishing library task. Thus, book purchase method is the base of guaranteeing the whole library work efficiently and the quality of library service. Book purchase work is responsible for raising book

H. Liu (✉)

Hunan Institute of Science and Technology, Yueyang 414006, China
e-mail: liuhongxia@yeah.net

Y. Liu

Hunan international Economics University, Changsha 410205, China

quality, satisfying readers' appetite, adjusting storage reasonably, optimizing document resource structure, and realizing the value of library.

"Offer the most appropriate books to reader at the most suitable time" is the objective of all libraries. It is librarians' responsibility to realize this goal. Nowadays, there are several methods [1-4] of book purchasing in domestic and foreign countries: formal subscription, textbook outline, all in orders, simple purchase according to the circulation statistics of some kind book. However, the book purchase procedures of these methods all obtain weak point. Since 1950s, genetic algorithm and neural networks of artificial intelligence have been in prosperity. This phenomenon provides new developing opportunity for optimization, prediction, classification, pattern recognition questions, and so on [5]. It also provides scientific solution for the key link in building a library-book purchase. This article is about how to apply computer technology to book purchase in library according to the weak points in process of purchasing books currently. Also, we improve the key technology in book purchase along with proposing a book purchase model based on improved genetic neural networks. We design a relative scientific and high efficiency computer-aided book purchase evaluation system.

2 Genetic Neural Networks and Improved Genetic Algorithm

2.1 Genetic Neural Networks

According to initial topological structure of given book purchase neural network, this article first accomplishes network training through genetic algorithm with effect factor (EFGA) instead of conditional BP algorithm. In the process of training, EFGA can not only adjust the weight threshold of neural networks dynamically but also adjust number of neurons and number of connection weights. Then, we do classifying determination for book purchase by trained neural networks.

2.2 Improvement of Genetic Algorithm

To make neural network astringe effectively and quickly is the key point in neural network for book purchase application. In standard genetic algorithm, each individual is presented by one chromosome. Chromosome is composed by gene sequences. If we assume C' presents chromosome, g' presents gene, chromosome can be presented as $C' = g'_1, g'_2, \dots, g'_n$, among this formula n is the number of genes in chromosome. If the function φ is the reflection from genotype to phenotype, fitness function is f , individual adaptive value is $f(\varphi(C'))$. However, the above express mode cannot express the influence degree of each gene g'_i to the

whole chromosome. Thus, this article forwards the concept of gene affects factor. First, we give the definition and explanation for relative concept terminology.

Definition 1 Normal gene value (Abbreviation: Normal value), present normal value of gene in standard genetic algorithm. We use g to present, $g \in R$.

Definition 2 Gene Effect Factor (Abbreviation: Effect Factor), presenting the influence degree of gene normal value to the whole chromosome, in other words some gene whether promote, inhibit or has nothing to do with the whole chromosome, we use e present, $e \in [-1, 1]$.

Definition 3 Gene effective value (Abbreviation: Effective Value), presenting the actual influence value to chromosome from gene normal value, we use v present, thus $v = g * e$.

Base on the definition of above effect factor, each gene includes two parts of information: one part is normal value g , the other part is effect factor e . If we use C presents chromosome which is with effect factor, thus $C = (g_1, e_1) (g_2, e_2) \dots (g_n, e_n)$. And for convenience of description, we assume $G' = g_1, g_2, \dots, g_n, E' = e_1, e_2, \dots, e_n$, among these formula n is the number of genes which compose chromosome C . If the reflection from genotype to phenotype is function ϕ , and fitness function is f , individual adaptive value can be presented as $f(\phi(G', E'))$.

When effect factor is bigger than zero, this gene improves chromosome, the bigger of positive value the more improvement influence; When effect factor is little than zero, this gene inhibits chromosome, the little of negative value the more inhibition influence.

2.2.1 Genetic Algorithm with Effect Factor

On the basis of standard genetic algorithm and effect factor, this article names this method as EFGA, main description for algorithm is presented below:

- (1) Initiation
- (2) Selection
- (3) Intersection.

The process could be described as below:

Assume the two k th individuals that participate in intersection are:

$$C_1^k = (g_{11}^k, e_{11}^k)(g_{12}^k, e_{12}^k) \cdots (g_{1i}^k, e_{1i}^k) \cdots (g_{1n}^k, e_{1n}^k) \tag{1}$$

$$C_2^k = (g_{21}^k, e_{21}^k)(g_{22}^k, e_{22}^k) \cdots (g_{2i}^k, e_{2i}^k) \cdots (g_{2n}^k, e_{2n}^k). \tag{2}$$

If C_1^k and C_2^k only do intersection operation in i th position, the $k + 1$ th individuals are:

$$C_1^{k+1} = (g_{11}^{k+1}, e_{11}^{k+1})(g_{12}^{k+1}, e_{12}^{k+1}) \cdots (g_{1i}^{k+1}, e_{1i}^{k+1}) \cdots (g_{1n}^{k+1}, e_{1n}^{k+1}) \tag{3}$$

$$C_2^{k+1} = (g_{21}^{k+1}, e_{21}^{k+1})(g_{22}^{k+1}, e_{22}^{k+1}) \cdots (g_{2i}^{k+1}, e_{2i}^{k+1}) \cdots (g_{2n}^{k+1}, e_{2n}^{k+1}). \tag{4}$$

Thus, except (g_{1i}^k, e_{1i}^k) and (g_{2i}^k, e_{2i}^k) change after intersection, the others

$$g_{1q}^k = g_{1q}^{k+1}, e_{1q}^k = e_{1q}^{k+1}, g_{2q}^k = g_{2q}^{k+1}, e_{2q}^k = e_{2q}^{k+1}, q = 1, 2, \dots, i - 1, i + 1, \dots, n. \tag{5}$$

We can use common method in standard GA algorithm for gene normal value g_{1i}^k, g_{2i}^k . This article adopts self-adapting linear intersection, its process is:

$$g_{1i}^{k+1} = \alpha_k g_{2i}^k + (1 - \alpha^k) g_{1i}^k \tag{6}$$

$$g_{2i}^{k+1} = \alpha_k g_{1i}^k + (1 - \alpha^k) g_{2i}^k. \tag{7}$$

Among these formulas, α is a decreasing value along with the increasing value of evolution generation, initiated value of α is 0.4. To its following generation, we assume $\alpha^{k+1} = 0.99\alpha^k$ until $\alpha^{k+1} < 0.05$ or reaching the maximum step of iteration. This kind of intersection's advantage is that we can generate new individuals in relative wider range during the beginning of evolution, and do little damage to good individuals during the late stage of evolution.

Regarding the processing of effect factor e_i , we define the following three methods:

$$\textcircled{1} e_{1i}^{k+1} = e_{1i}^k, e_{2i}^{k+1} = e_{2i}^k \tag{8}$$

$$\textcircled{2} e_{2i}^{k+1} = e_{2i}^{k+1} = (e_{1i}^k + e_{2i}^k) / 2 \tag{9}$$

$$\textcircled{3} e_{2i}^{k+1} = e_{2i}^{k+1} = (\gamma_1^k e_{1i}^k + \gamma_2^k e_{2i}^k) / (\gamma_1^k + \gamma_2^k) \tag{10}$$

In specific application of this article, when chromosome certain gene in chromosome do intersection operation, the processing method for effect factor is $\textcircled{3}$, experiment result also shows method $\textcircled{3}$ is more effective.

(4) Mutation

Assume the k th individual, which participates in mutation operation, is:

$$C_j^k = (g_{j1}^k, e_{j1}^k)(g_{j2}^k, e_{j2}^k) \cdots (g_{ji}^k, e_{ji}^k) \cdots (g_{jn}^k, e_{jn}^k). \tag{11}$$

Among this formula, $j \in \{1, 2, \dots, m\}$, C_j^k presents certain chromosome in the k th individual of species group.

If only do mutation operation in i th position, the $k + 1$ individual is:

$$C_j^{k+1} = (g_{j1}^{k+1}, e_{j1}^{k+1})(g_{j2}^{k+1}, e_{j2}^{k+1}) \cdots (g_{ji}^{k+1}, e_{ji}^{k+1}) \cdots (g_{jn}^{k+1}, e_{jn}^{k+1}). \tag{12}$$

Except (g_{ji}^k, e_{ji}^k) change after mutation,

$$g_{1q}^k = g_{1q}^{k+1}, e_{1q}^k = e_{1q}^{k+1}, q = 1, 2, \dots, i - 1, i + 1, \dots, n. \tag{13}$$

We can use common method in standard GA algorithm for gene normal value, this article adopts the method that adds or minus one disturbance, the process is:

$$g_{ji}^{k+1} = \begin{cases} g_{ji}^k + \beta^k * \text{random}(-\delta, \delta) & \text{random}(0, 1) \geq 0.5 \\ g_{ji}^k - \beta^k * \text{random}(-\delta, \delta) & \text{random}(0, 1) < 0.5 \end{cases} \tag{14}$$

Regarding effect factor, we assume that when it starts to mutate, it is in a state of regression. Thus, we define a regression factor Δt . When certain gene in chromosome starts to mutate, the processing to its effect factor is to multiply effect factor and regression factor $\Delta t \in (0.8, 0.95)$, just as (15):

$$e_{ji}^{k+1} = \Delta t * e_{ji}^k. \tag{15}$$

Among this, $\text{random}(0.8, 0.95)$ generate random value that is in accordance with homogeneous distribution between 0.8 and 0.95. Experiment result also says that the mutation processing for effect factor is effective.

(5) Species group update

When the best individual does not satisfy the requirement and the process does not reach the maximum iteration step, the evolution turns to procedure Step(2) and do next round of evolution.

2.2.2 EFGA-Optimized Neural Network

Genetic algorithm includes 5 basic elements: code scheme, selection of fitness function, design of genetic operation, initiation method for group, setting of genetic parameters. These 5 basic elements compose the core of genetic algorithm,

also the key of using EFGA optimize neural network. In this article, these 5 elements are defined as below:

Design of Code Scheme

In the process of using EFGA optimize neural network, we adopt real-coded method style. The basic principle is: connection weights, hidden units threshold, and neural threshold of output layer in layers' neural of network compose the code chain. Corresponding to the weight or threshold in an assured link of neural network, we array it to form a code chain. And every code chain presents a distribution state of one kind of weight and threshold in neural network. A series code chain presents a series of different weight and threshold of neural network.

Among this, w_{uv}^r is the connection weight between u th node in layer r th and v th node in layer $r + 1$ th, h_{uv}^r is the exist factor between u th node in layer r th and v th node in layer $r + 1$ th. b_u^r is the threshold of u th node in layer r th. h_u^r is the exist factor of threshold of u th node in layer r th. h_{uv}^r, h_u^r is corresponding with the effect factor e in EFGA, also functions of effect factor e , their value is 0 or 1. 0 presents this connection weight or threshold is noneffective, 1 presents this weight or threshold is effective. The definition is below:

$$h = g(e) = \begin{cases} 0 & -\theta \leq e \leq \theta \\ 0 & e < -\theta, e > \theta \end{cases} \tag{16}$$

Among the above formula, θ is a set threshold, its range of value is (0, 0.1). We can see that, this code method could provide all information of the question which needs to be settled. And we can use different kinds of genetic operations conveniently.

Selection of Fitness Function

The objective of genetic algorithm optimization is to find certain weight matrix W_0 and threshold matrix B_0 to maximize fitness function. So, we can define the objective function of genetic neural network as:

$$E(C) = \min((E(C_j))_k), \quad k = 1, 2, \dots, \text{generations}, j = 1, 2, \dots, m. \tag{17}$$

Due to the fact that genetic algorithm can just evolve toward the direction which increases fitness function value, we can use fitness function to compose the reciprocal form of objective function. In order to guarantee that the value of fitness function is not too little, we adopt a relative big coefficient M , thus the fitness function can be illustrated as below:

$$\text{fitness}(C_j) = M/E(C_j) \quad j = 1, 2, \dots, m. \tag{18}$$

In the process of this article, $M = 1,000$.

Design of Genetic Operation

- (1) Selecting Operator
- (2) Intersection Operator
- (3) Mutation Operator.

Initiation Method for Species

According to the detailed requirement of question, we generate initial species group Pop randomly, and any chromosome in Pop can be decoded to an entire neural network according to above code strategy.

Set of Genetic Parameters

According to practical application experience, we select appropriate species group size, selecting probability, intersection probability, mutation probability, and other relative parameters ultimately.

The method and procedure of using EFGA to optimize neural network, we can use flow chart to describe.

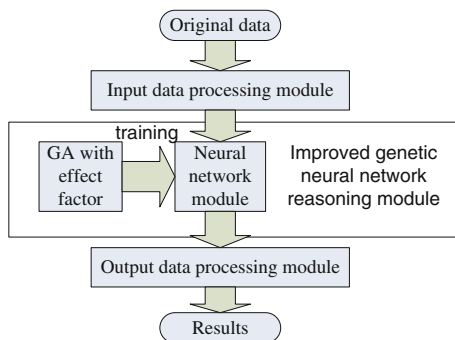
Among this, the process of evaluating individual is composed by three procedures: ①Each chromosome C_j is decoded to neural network; ②Use training sample to do forward calculation for neural network, and calculate $E(C_j)$; ③Use (18) calculate the fitness $fitness(C_j)$ of each chromosome.

3 Book Purchase Model on The Basis of EFGA Neural Network

In the intelligent book purchase system constructed by this article, both the knowledge storage in learning process and reasoning in the process of getting the result operate in neural network module. Thus, we realize the combination of knowledge storage and reasoning. In other words, one neural network realize all of this, neural network module is the core of system. Moreover, the training of neural network module is accomplished by EFGA, thus, EFGA is the key in system.

According to the above principle, the book purchase system on the basis of improved genetic neural network mainly contains the following modules: Initiation setting module, improved genetic neural network reasoning module (including design of neural network, training to neural network by EFGA and reasoning of trained neural network), output module. Figure 1 is the whole structure of system model. Among this, data input module accepts outside data and does prior

Fig. 1 Structure of Book Purchase based on EFGA Neural Network



processing, and provide processed data to improved genetic neural network reasoning module. The result shows parts, mainly rely on human computer interface to output the final result according to requirement.

4 Simulation Experiment

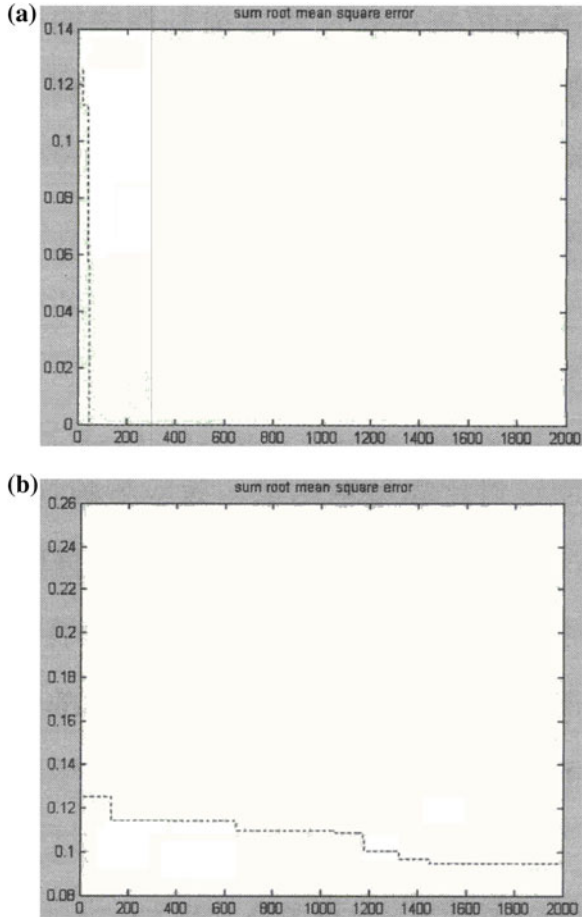
In order to verify the feasibility and effectiveness of book purchase model based on improved genetic neural network, under the same experimental condition, we use EFGA and BP algorithm separately to train the neural network module of book purchase mode, then analyze the results.

EFGA and BP algorithm obtain the same input sample when training neural network module: the input sample all come from the 3,000 book purchase data in Hunan institute of science and technology during 2005–2010, among this, the training group is 24,000, testing group is 6,000.

According to the above method and parameters, we train neural network module separately by EFGA and BP algorithm. The process of training of neural network by EFGA is shown by (a) Fig. 2. Regarding training neural network by BP algorithm, after verification by testing method, when the number of neurons in hidden layer reaches 13, the training result is relative best. (b) in Fig. 2 presents the training process.

In Fig 2, constringency speed when training neural network of EFGA is faster than that of BP algorithm. Under the same training step, the exactness of neural network of EFGA is higher than that of BP algorithm.

Fig. 2 Experiment result of training by EFGA and BP algorithm to neural network module. **a** Error curve figure of training neural network by EFGA. **b** Error curve figure of training neural network by BP algorithm



5 Conclusion

In the process of building book purchase system, we adopt book purchase model based on improved genetic algorithm neural network. In the process of realizing this system in detail, we analyze the featuring data of book; get certain number of sample from book purchase history, doing prior processing. Neural network can get useful knowledge and store them in network after learning through the sample that has been learned by prior learning. Finally, user can use trained neural network to make judge that whether a book should be purchased. Thus, we solve the core question in book purchase. Application of system does favor of decision for librarians, and increases the efficiency of purchasers along with decreasing the prime cost of purchasing books.

References

1. Feisheng Y (2005) Document interview study. Anhui University Press, Hefei
2. Xia L (2005) A review of college libraries' gathering and purchasing books. *J Acad Library Inf Sci (Hefei)* 23(1):46–49
3. Williams MR (2001) Building a world-class book collection: the Tomash library. *IEEE Ann Hist Comput* 23(4):39–43
4. Cunlu Z, Peiqing H, Ziping W (2004) Application of data mining to book purchase. *Inf Sci (Changchun)* 22(5):581–583
5. Youshen X, Jun W, Loming F (2004) Grasping-force optimization for multi-fingered robotic hands using a recurrent neural network. *IEEE Trans Robot Autom* 20(3):549–554

Study on Scene-Driven Emergency Drill Method

Xin Li, Guofeng Su, Shaobo Zhong, Fushen Zhang, Chao Huang, Hongyong Yuan, Quanyi Huang and Jianguo Chen

Abstract Based on the analysis of traditional emergency drills and simulated emergency drill characteristics, the construction and express method of structured scene model was proposed, including the emergency scene classification, the setting of evolution and development conditions and the structured expression of emergency scene. The scene-driven key technology and model was described, such as the evolutionary relationship of scenes, the reasoning model of scene chain and transition model of scene. On the basis, the emergency drill model of scene-driven was proposed. The model is dynamic and has high similarity with the real emergencies, which plays an important role to improve the effect of emergency drills.

Keywords Emergency drill · Simulation drill · Scene · Scene-driven

1 Introduction

Emergencies generally happen with many characteristic, such as sudden, uncertain, dangerous and difficult to resolve. The emergencies will lead to heavy casualties and property losses, and also affect the economic political, military and cultural as well as social stability. Many of them have late effects and long-term effects [1]. For many emergencies, it is difficult to reconstruct in the same scale, such as earthquake, floods, landslides, mudslides, forest fires, mining accidents, pandemics, etc. In order to cope with various emergencies, we should make the

X. Li · G. Su · S. Zhong (✉) · F. Zhang · C. Huang · H. Yuan · Q. Huang · J. Chen
Department of Engineering Physics, Tsinghua University, Beijing China
e-mail: zhongshaobo@tsinghua.edu.cn

X. Li · G. Su · S. Zhong · F. Zhang · C. Huang · H. Yuan · Q. Huang · J. Chen
Institute for Public Safety Research, Tsinghua University, Beijing China

emergency plan and according to the emergency plan, carry out emergency drills under different scenarios [2].

In traditional emergency drill, the departments, units, and people of emergency command system often perform their respective responsibilities and tasks according to the emergency plan under the preconceived condition [3]. So that, people can resolve the emergencies more orderly, fast and efficient, which will reduce the losses caused by emergencies [4]. Practice has proved that the emergency drill could reduce casualties and property losses and quickly recover the society to normal state from disaster [5, 6]. But the traditional emergency drill has several limitations [7]. For example, the traditional emergency drill costs, the number of participating people is limited, the simulation environment is simple and it's easily to become a mere formality [8], which make the effect of emergency drill limited.

2 Scene-Driven Emergency Drill

Because of the constraints of traditional emergency drill, in recent years, the simulation drill based on the computer technology is becoming an important way to enhance emergency response capacity [9, 10]. Scene-driven emergency drill is one kind of simulation drill. Its core idea is to divide the drill process into several different scene stages and study the constituent element and construction method of each scene. The complete simulation drill process is constructed by the combination of different scenes.

Because of the separation of simulation drill process, the drill process could be controlled freely through the scene matching, scene control and other operations, which could ensure the logic and smoothness of the drill. By using the scene-driven emergency drill, the initial environment could be set to any time, any place, any participating people and any scene of emergency, which achieves the "double-blind" drill effect. In order to accomplish the drill task, the participating people have to know the disposal method of emergency and must be familiar with the emergency scene. So that, they could skillfully master the emergency response of their work fields which will improve their capability of responding to all types of emergency.

Scene-driven emergency drill has many characteristics, like flexibility and relatively low cost. It is easy to control, ease to use, authenticity, could be used as training system and could be monitored and played back, which has widely application range and application security.

The execution of scene-driven emergency drill mainly includes three steps as shown in Fig. 1: scene construction, evolution process control and finally the scene-driven emergency drill. Through the classification of emergency scene, evolution setting and the structured expression of scene, the emergency will be constructed. After that, the evolution process control could be realized by scene relations research, scene matching method and transition model. Then the

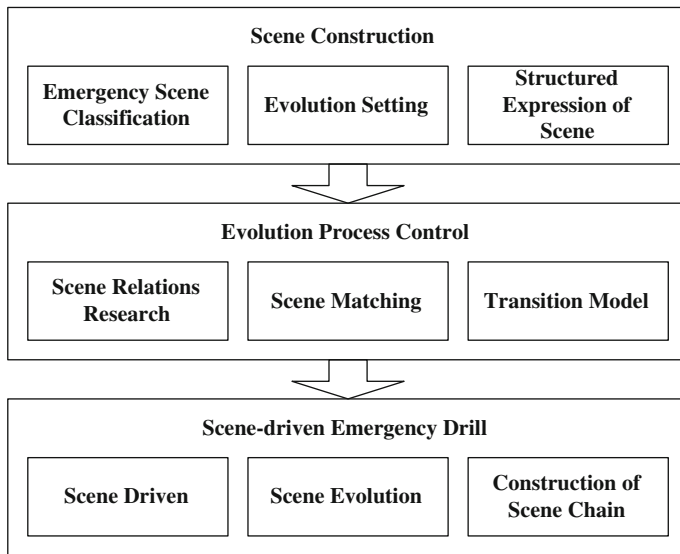


Fig. 1 Steps of scene-driven emergency drill

scene-driven emergency drill could be realized through the construction of scene chain by the scene driven model and scene evolution model.

3 Construction and Expression of Structured Scene Model

The occurrence and development of emergency is related to many factors which are very complicated. The evolution of emergency has many manners, such as transformation, spread, and coupling. In order to realize the scene-driven emergency drill, the structured expression of emergency scene should be realized firstly. The reconstruction of emergency scene needs to design the parameters of environment data, like natural environment, social environment, and information environment and so on, according to the emergency scene and the characteristics of its evolution. The scene parameters include time, space, facilities, environment, people, society and driving conditions, and some other information.

The constructed and expression of emergency scene is the basis of realizing the scene-driven emergency drill. In the emergency drill, the scene could be connected and operated which will from a high similar emergency scene and help to improve emergency drill effect. The construction and expression method of emergency scene includes:

3.1 Classification of Emergency Scene

In the expression process of emergency scene, we need to classify the type of emergency scene. The classification of emergency scene is different from general emergency classification. The characteristic of the scene and the emergency measures need to be considered. The development and evolution of emergency will be divided into different stage of scene. The emergency drill is the combination of different scenes according to the characteristic of the emergency and the emergency measures.

3.2 Evolution and Development Settings of Emergency Scene

Without the emergency measures, the emergency scene will develop as its own characteristics. With the effect of emergency measures, the development and evolution of emergency will be changed. For example, after the heavy rainstorm meteorological disaster, without the emergency measures, large residential area could be flooded as the development of torrent. But through the opening water gate, the dewatering and strengthen prevention and other emergency measures, the flood could be controlled within the acceptable range of urban safety. So the evolution condition, the development direction, and the relationship of different scene need to be set. The drill scene could develop to different direction with different scene condition and different emergency measures. In this way, the scene-driven emergency drill will be realized.

3.3 Structured Expression and Characteristics Extraction of Emergency Scenes

The first step of scene construction is characteristics extraction and structure expression of scene, which is the basis of the emergency scene model framework construction. Through the scene extraction and analysis of different type of emergencies, the structured emergency scene model could be established. The environment of emergency scene structured expression mainly includes natural environment, social environment and information environment. The structure of scene parameters needs to be designed according to the emergency scene and its development characteristics. The structured scene model can be described using a multigroup:

$$S = \{T, SI, F, E, P, A, R, ED, DC, \dots\}. \quad (1)$$

Here, S is the structured scene model, T is time information, SI is space information, F is facilities information, E is environment information, P is organization personnel, A is action, R is results of disposal, ED is evolution direction, and DC is development direction. Based on this model, the drill model could be constructed:

$$D = \{S_1, S_2, S_3, \dots, S_e\}. \quad (2)$$

Here, D is scene-driven emergency drill, S_n is the N scene, S_e is the end scene.

Through the expression of structured emergency scene model and the construction of simulation drill model, the standardized management of scenes and smooth transitions between scenes of emergency drill could be realized, including the generation of scene, the elimination of scene and the change of scene parameters and so on, which will make the emergency scene has a higher freedom of control and has a high similarity with the real environment.

4 Analysis of Scene Evolution

The scene-driven emergency drill is made up of a series of scenes. The connection of multiscene and their relationship form the scene chain. The construction of scene chain is according to the disaster chain and event chain. Through the characteristic of emergency and the emergency measures, the development of emergency will be designed. Based on this, the scene chain will be logic and smooth.

4.1 Construction of Evolution Relationship of Scene

According to the theory of disaster chain and event chain, the evolution relationship has a variety of forms, including tandem scenes, one-to-many scenes, many-to-one scenes, parallel scenes and circular scenes and so on. Tandem scenes are that one scene one scene develops into the next scene without triggering other scenes. One-to-many scenes mean one scene might develop into many other two or more scenes. Many-to-one scenes mean many scenes develop into one scene finally. The parallel scenes mean two or more scenes proceed at the same time. In this condition, the scenes develop and affect each other, which make it possible to form new scene. The circular scenes mean the scene is circulatory. The construction of scene chain needs the construction of those scene evolution relationships first.

The development procession of emergency and its derivative events involved in the development is always changing. Generally the development of scene has several situations as shown in Fig. 2. One scene might develop into next one or more scenes under certain conditions like the condition 1, 2, 3, 6. Two or more scenes might develop into one scene under several certain conditions like the

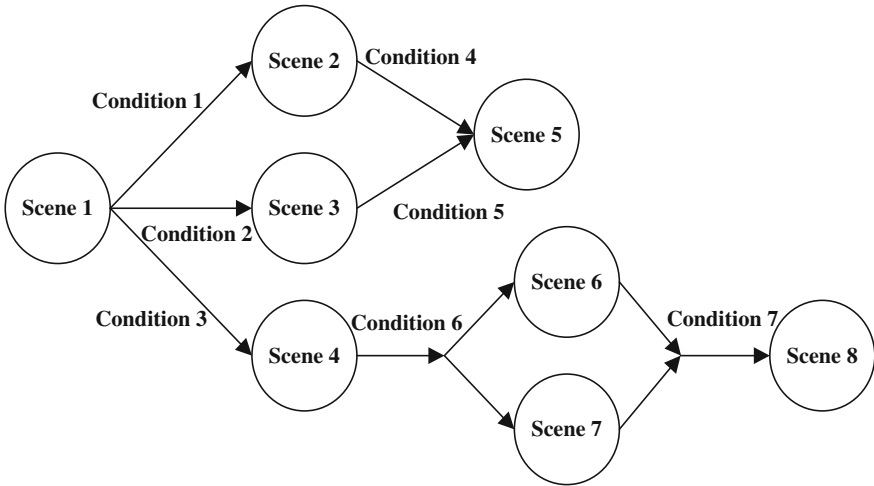


Fig. 2 Diagram of scene evolutionary relationships

condition 4, 5. Two or more scenes might develop into one scene under one certain condition like the condition 7.

Through the study of development direction of scene and the evolution condition, the scene chain will be established according to the natural evolution law, the external influences and the emergency measures by the integrating of development direction and driving condition. So that, in the emergency drill, as the intervention of emergency measures and the development of scene, the scene will development toward different direction under different conditions. Then, the scene chain will be formed and the scene-driven emergency drill will be realized.

4.2 Scene Matching and Scene Chain Reasoning Model

During the disposal process of emergency, different scenes have certain relationship, such as mutually exclusive relationship, inclusion relationship, undertake relationship, parallel relationship, and so on. The matching relationships need to be considered in the scene development. The development of scene could be logic and has a high degree of similarity by the scene matching model. Then the fuzzy matching rules will be studied according to the characteristics of emergency, the external conditions, and the current trend. By the combination of matching relationship and matching rules, the simulation scene which is closest to the current emergency drill will be found from the scene library, which makes the connection of different scenes more logic.

In the scene-driven emergency drill, because one scene might develop into more scenes and many scenes might develop into one scene, the development

model needs to be studied using the scene chain reasoning model. The development trend of scene will be determined through the analysis of emergency development situation and the emergency measures. So that, the evolution condition from one scene to the next scene will be analyzed. To achieve this function, the scene model and its evolution rules need to be analyzed. For example, the rainstorm meteorological disaster may lead to the generation of other scenes, such as evacuation scene, medical rescue scene, flood plugging scene and so on. The development needs to be reasoned by the scene parameters of rainstorm meteorological disaster. Such as, in what circumstances, people need evacuation and in what circumstances, people need medical relief.

4.3 Scene Transition Model

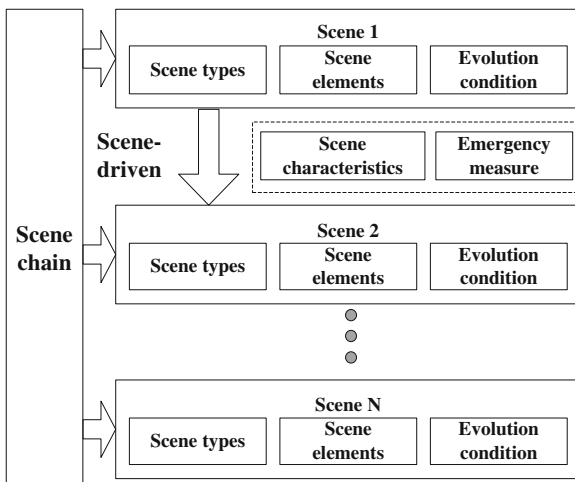
Scene transition model is the key to realize the smooth transition of the emergency drill. Based on the structured emergency scene, the scene transition model defined the method and rules of scene structure and parameters between the transitions of scenes. The parameters of previous scene may be used as the parameters of the next scene, but there is likely to change. For example, the evacuation scene might lead to the personnel placement scene and life and material support scene. Then the staff number of evacuation scene could be used in the personnel placement scene and life and material support scene. The scene transition model will define the change and the relationship between different scenes when transforming. Through the scene transition model, the smooth transition and seamless connection of different scenes in the emergency drill will be ensured.

5 Scene-Driven Emergency Drill Framework

The gestation, occurrence, and development of emergency are typical temporal and spatial evolution process. Its evolution process and development is affected by the emergency scene features and emergency measures. The scene-driven emergency drill method mainly studies the evolution mechanism and development direction considering the effect of emergency measures. Through the study of emergency scene construction method, the initial scene of emergency will be established. Under the driven of scene characteristics and emergency measures, the emergency scene will develop as shown in Fig. 3.

The generation, elimination, and change of different scenes form the dynamic scene chain. The scene-driven emergency drill is guided by the dynamic scene chain. Through the establishment of structured scene model, every scene contains scene type, scene elements, evolution conditions, and some other parameters. The parameters need to be defined before the drill. The drill process will develop according to the scene features and the emergency measures. In a fixed scene, the

Fig. 3 Scene-driven emergency drill model



different intervention method and different levels could lead the scene to different direction. Through the scene reasoning model, the development of scene will be in line with the actual emergency disposal process. Through the scene transition model, the development of scenes could be control, such as the increase, elimination of the scene, and change of scene parameters. Those models make the drill process closer to the real situation and have a high degree of freedom of control.

6 Conclusion

The article first contrast and analyze the limitations of traditional emergency drill and the characteristics of simulation drill. The concept of scene-driven emergency drill was put forward. The construction and expression method of structured scene model was discussed including the classification of emergency scene, the evolution conditions setting of emergency scene, and the structured expression of scene. Through the analysis of scene evolution relationship, the scene evolution relationship, scene chain reasoning model and scene transition model were proposed. Based on this, the scene-driven emergency drill method was put forward which has many characteristics like multi-dimension and dynamic. The model improves the similarity with real emergency and increases the tension of the simulation drill, which will improve the drill effect.

Acknowledgment The authors would like to thank the support of the National Natural Science Foundation of China (Study on Pre-qualification Theory and Method for Influences of Disastrous Meteorological Events, Grant No. 91224004), the National Natural Science Foundation of China (Study on Systematical Integration Theory and Method of Emergency Technologies for Unconventional Incidents, Grant No. 91024024), the National Natural Science Foundation of China (Key Scientific Problems and Integrated Research Platform for Scenario Response Based

National Emergency Platform System, Grant No. 91024032), the National Science and Technology Support Program (Internet of Things IntelliSense based Integrated Monitoring System of Typical Urban Risk Sources Research, Grant No. 2011BAK07B00) and the National Natural Science Foundation of China (Study on Emergency Decision-making Based on Generalized Knowledge Coupling, Grant No. 70901047).

References

1. Liu CF (2011) Method of simulation emergency drill. Jilin University, Jilin
2. Jia QL, Zhou BJ (2010) Earthquake disaster scenario simulation technology. *J Comput Res Dev* 47:1038–1043
3. Liao N, Ma MH (2010) Review of simulation drill system. *China Sci Technol* 20:273, 258
4. Shang JW, Wu QH (2009) Case analysis of emergency exercise abroad and its revelation to China. *China Health Serv Manage* 24:63–65
5. Jiao TX (2009) Discussion on emergency drill of petrochemical enterprise. *J Saf Sci Technol* 5:181–184
6. Song HH, Zhang LJ, Xing PY, Cheng Q (2009) Discussion on implementation of simulation system of chemical accident emergency rescue. *J Saf Sci Technol* 5:99–102
7. Zhou Y (2011) Design and implementation of emergency plan 3D automatic exercise system based on the Quest3D. Xidian University, Xi'an
8. Mei YL (2012) Study on the computer three-dimension simulation system of emergency exercise. *J Saf Sci Technol* 8:92–97
9. Chen JG, Xu SX, Huang GW (2012) Design and implementation of a virtual emergency drilling system. *J Shenzhen Inst Inf Technol* 10:33–37
10. Sun CJ, Liu L (2010) Design and realization of the emergency rescue simulation training system. *Comput Appl Pet* 67:3–6

The Research of Component-Based Software Development Application on Data Management in Smart Education

Lijuan Liu, Youqun Shi and Ran Tao

Abstract By taking into account the requirement of smart education platform, it gives the implementation of data management with component-based software development (CBSD). First, the concept components were extracted as reuse goal, and then a facet-based model was established to describe components: later on components were developed in Model View Controller (MVC) pattern which makes components have relatively independent interfaces to support software reuse. And an example was used to show the development process, which successfully realized the effective data management. The result shows that this method used in smart education has achieved good performance in practice, and components are reused in systems successfully, in this way, it improves the development efficiency which contributes to data management.

Keywords Component · Smart education · Model view controller · Software reuse · Data management

1 Introduction

As the development of information industry, smart education [1] is a new form of education. Data management is most complicated and important for education, which is the foundation in smart education platform. For example, users' data and exam's data are indispensable in smart education. So data management has good effect on smart education's quality. To promote smart education, a platform needs to be developed. Traditional development contains requirement analysis, design, implement and so on, these stages cannot execute concurrently, and software

L. Liu (✉) · Y. Shi · R. Tao

School of Computer Science and Technology, Donghua University, Shanghai, China
e-mail: liulijuan123job@126.com

function is difficult to keep up with the change of demand, so maintenance workload is so big to achieve flexible function.

To solve these problems, it uses component-based software development (CBSD) method [2] for data management implement, which concentrates on the reliability and extensibility of components. CBSD eliminates the repetitive work by absorbing the past project experience, in this way, it provides reused components for smart education and improves efficiency in data management.

2 Smart Education and Platform Architecture

In this study, we build a comprehensive smart platform to support smart education [3], besides the architecture and data management solution are given.

2.1 Concept of Smart Education

Smart education refers to gathering smart and realize smart through various channels and mechanisms, providing strong support for school and even the social development. Compared with traditional education, it needs higher requirement for data amount in smart education. Since teaching forms have changed, simple data storage method cannot meet the practical requirements. For example, when a school recruits students for the public students' examination, enrollment data cannot simply go through the paper records by manpower, because for the data of exam and review students, etc., all these need to be collected and operated rapidly.

2.2 Architecture

The architecture of smart education platform contains independent three-layers: the UI layer, development, and application platform layer, data center layer. As is shown in Fig. 1, UI layer refers to the unified portal shown to the user. Development and application platform layer refers to the school management, student management, etc. Specific tasks are assigned to each module such as role, permission, log [4]. Data center layer refers a set of tools and utilities, first it processes RAW DB (raw data processing) and then it puts Processed DB (data that have been processed) into data center.

Layered architecture has convenient, unified data input and output, which gives independent interfaces in smart education development.

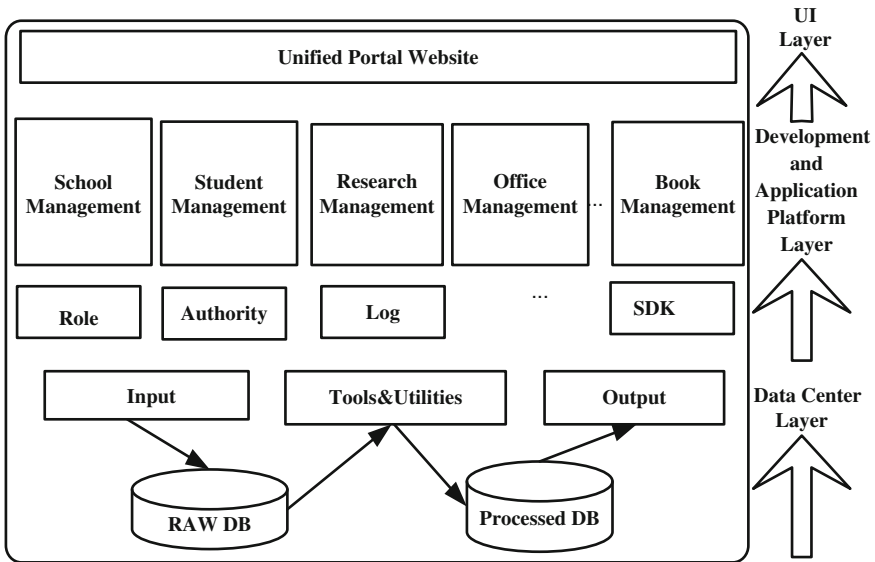


Fig. 1 Platform software structure diagram

2.3 Data Management Solution

Data management solution integrates all aspects of data, including teaching, learning, and management. Good management of mass data helps to build education metropolitan area network and smart digital campus group. The solution implements the teaching digitization, learning digitization, management digitization. As an efficient way for teachers and learning skill for students, it supports for education management and decision making.

Figure 2 shows diagram of data management solution in smart education, the education ministry establishes distributed databases, while affiliated schools stores their local data and upload to the local education bureau. When education ministry needs all data, global data will be distributed to the basic database by each module database; when ministry does not need to manage all data, it just gets data from Education Bureau from local data, which reduces physical workload. In this way, data will be shared and remote controlled. This kind of data management solution improves the data reading efficiency and reduces the response time.

3 Component-Based Software Development Method

CBSD focuses on the reuse of existing components rather than code writing, making it faster to develop a system. On the one hand, it reduces the cost of software development and maintenance; on the other hand, it supports upgrading

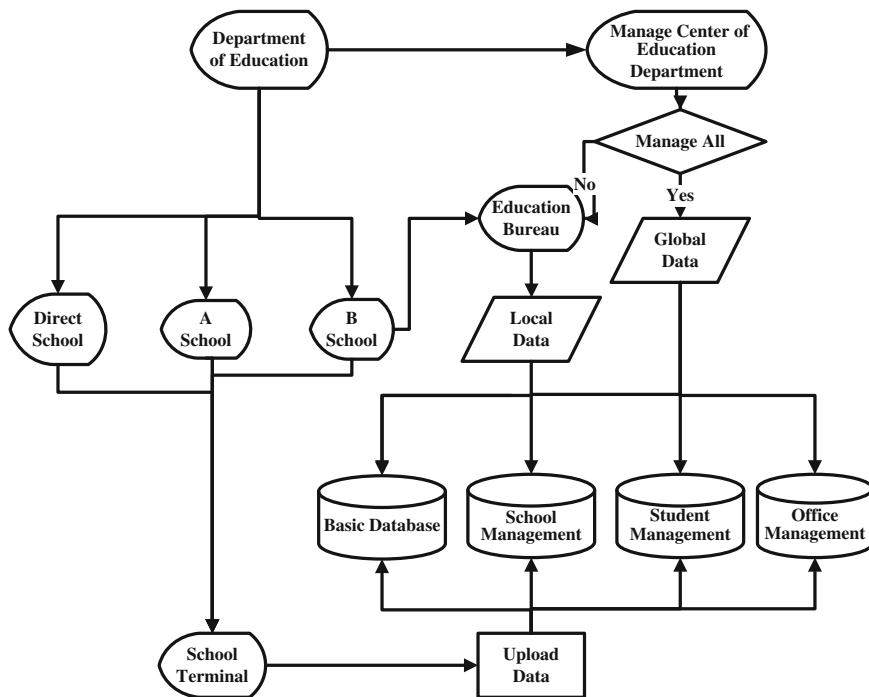


Fig. 2 Data management in smart education

large system. During the process, components can be reused to multiple modules, at the same time they are closely related to each other, as shown in Fig. 3.

For CBSD, the key problem is to know what kind of reuse components. To get the clear component reuse goal, a faceted-based model is given to describe components, and then components are developed in MVC pattern.

3.1 Component

Components are software entities which have a relatively independent function and can be clearly identified in the software system. Besides, their interface can be assembling designated. Concept components refer to components which meet the business requirement, and they are goals of extracting reuse components. Based on the classification principles of concept components [5]: (1) the way class interacts with other classes; (2) service class separate division; (3) dependency rules with other classes, reusable components can be accurately divided [6].

After we get concept components, it is necessary to specify them. We establish a faceted classifies-based component model [7]. As shown in Fig. 4, a component is

Fig. 3 Relationship between components in smart education

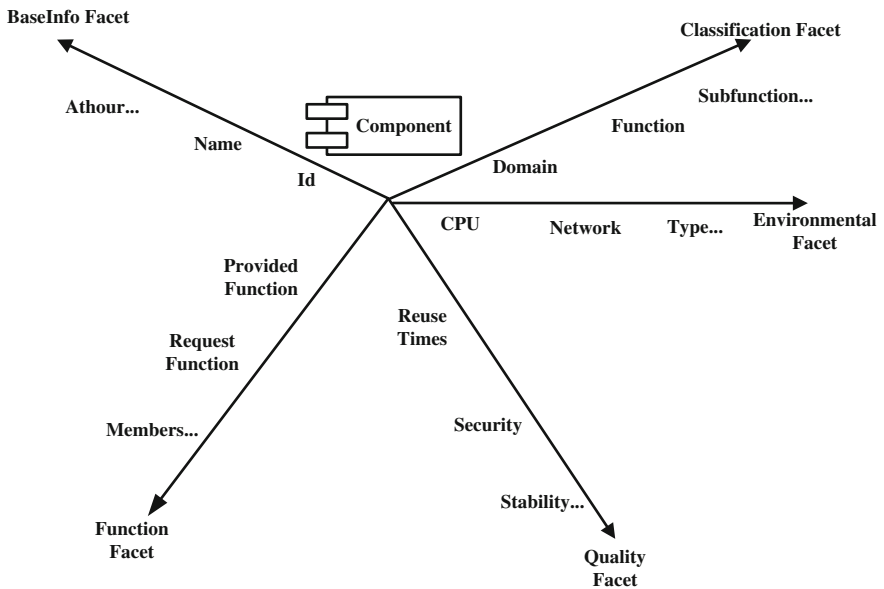
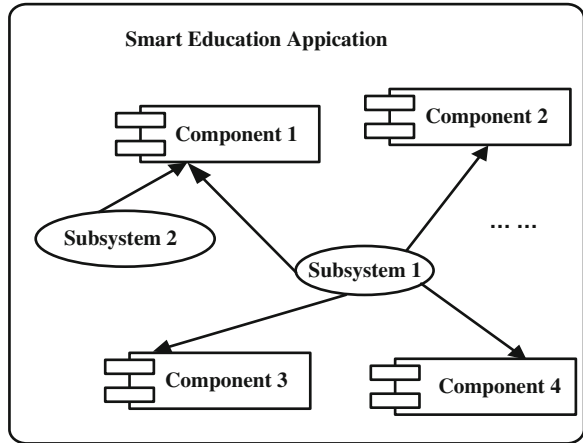


Fig. 4 A component description model based on faceted classifies

described from five facets: component basic information facet, component classification facet, component environmental requirement facet, component quality facet, and component function facet [8].

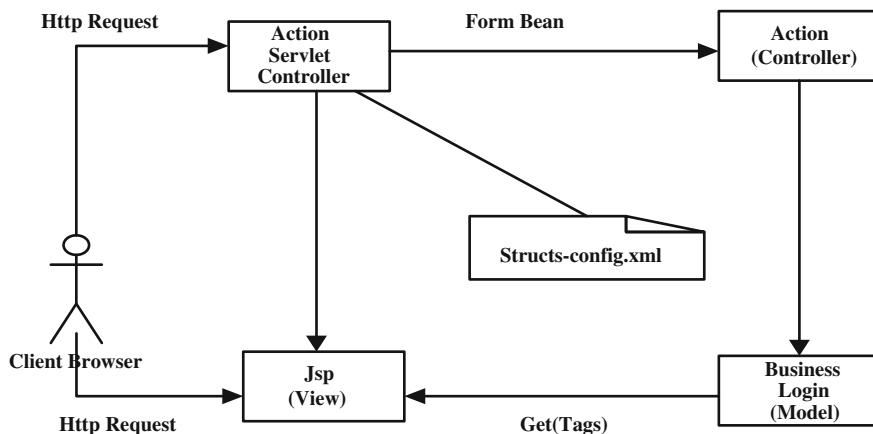


Fig. 5 Working principle of MVC pattern

3.2 Model View Controller Pattern

Components are developed in MVC pattern with independent interfaces. The MVC [9] is one of the commonly used designing patterns. M represents the Model layer, which contains all behaviors and data needed, V represents the view layer, which contains data provided by the real model, and C represents the controller, which maps model layer to the view layer, handling the respond to the request. From reuse aspect, MVC pattern lets the page contain only a small amount of code, which makes reuse more quickly. However, for JSP and Servlet pattern, it contains all codes in a JSP page, so the maintenance is difficult. Based on this, we adopt MVC pattern.

The working principle of MVC pattern is shown in Fig. 5, the client browser first sends a request to a page, this request will be passed to Controller through Form Bean, and Controller will pass it to the business logic model for processing, and then related method is called, later on it returns to the Action Controller, passing the result to JSP page [10]. The jumping and processing have already been deployed in the struts-config.xml configuration file. As we can see, MVC has a better encapsulation of component interface, making it easier for developing.

4 Application Instance

In smart education platform, we give the process of reuse by a component development instance in two subsystems: select course system and drop-in system. Select course system ensures normal study arrangement, drop-in system enables school recruit drop-in students, and both of them need to manage large amounts of data.

4.1 Component Extraction

Due to different requirement of two systems for data management, we analyze function of each component as follows;

(1) Database operation component in drop-in subsystem

Drop-in subsystem provides exam registration, scores release, students' admission, etc. Data need to be frequently updated between the Excel file and backend database. So Excel data should be imported to backend database, and the data in the database should be exported to Excel file too.

(2) Printing component in select course system

Select course system provides student course selection and courses arrangement, etc. Among them, admission paper printing needs to manage large amounts of data. Printing components can show the table data by a clear user interface.

Based on above analysis, data dump concept component is extracted with classification principle. Described by facet classifies-based model, For data dump concept component, the id is 100025, it has import and export data function and it does not depend on other components, as is shown in Table 1.

4.2 Development

We develop components with MVC pattern, which contains Entity, Dao, Controller, Service and View packages, and the role of each package is shown in Table 2. In this way, the function is developed independently and clearly.

4.2.1 View Layer

View layer mainly shows the page which presents to user. User will input some data such as score, reflected as "ExamId", "Math". Following is the part code:

```
form name = 'form1' method = 'post' action = 'addinfo.jsp'>
  <tr ><td height = '27' colspan = '4' > &nbsp;   (*) </td ></tr>
  <td height = '25' > ExamId: </td>
  <td width = '177' > <input type = 'text' name = 'ExamId'>
  <td height = '25' > Math: </td>
  <td width = '177' > <input type = 'text' name = 'math'>
```

Table 1 Data dump component description (part)

| BaseInfo facet | | Component function facet | | Environment requirement facet | |
|------------------|---------------------|--------------------------|------------------------|-------------------------------|----------------|
| Component id | 100025 | Provide function | Import and export data | Component type | Business logic |
| Component name | Data dump component | | | Dependent component | No |
| Component author | Sam | | | | |

Table 2 Role of each package

| | |
|------------|--|
| Entity | Model layer, data entities, map the field in table |
| Dao | Model layer, data access object |
| Service | Model layer, implement services |
| View | View layer, such as form pages |
| Controller | Control layer, control data |

4.2.2 Model Layer

Model layer contains the Dao, Service, and Entity package, which encapsulates producing instances (e.g., business logic). Data dump components operates Excel. Basic objects of Excel are HSSFWorkBook (workbook), HSSFSheet (work tables), HSSFRow (rows), HSSFCell (cells). Each row and each cell has its own related property. Among them, cell is the smallest unit to be edited and stored.

To realize import and export data function, we use POI API in JAVA, which can read, write, modify, and control data in Excel file. In addition, POI does not call the Windows API, so it's not limited in Windows system environment. With the cross-platform feature, this component can be widely used.

Take data import function in development for example, model layer has access to data, which is reflected in code of setCellValue. Part of Code in instance is described as follows:

```

Admission adm = new Admission();
Student stu = new Student();
ArrayList < Student > stuList = new
ArrayList < Student > ();
row2.createCell((short)
5).setCellValue(stu.getAdmission().getPreOrNot());
for (int i = 1; i < nRow; i++) {
String ExamId = sheet.getRow(i).getCell(0).
getStringCellValue();

```

4.2.3 Control Layer

Control layer contains operation such as controlling page jumping, which handles the relative response for the request from View layer. Control layer get user object from the page, then it storages data object such as ExamId. Part code is followed:

```
Map model = new HashMap();
String username=
session.getAttribute(‘‘username’’).toString();
User user = (User)userService.getUserByName(username);
String userId = user.getUserId();
String ExamId = request.getParameter(‘‘ExamId’’);
String Math = request.getParameter(‘‘Math’’);
return new ModelAndView(‘‘ImportExcel’’, model);
```

4.3 Component Reuse

Due to the normative interface and good generality, to use data dump component, it only needs to call component according to BaseInfo parameters (e.g., id and author). In the end course, selection subsystem and drop-in subsystem reuse the data dump components successfully, in this way it eliminates the repetition code and test work. At the same time, because of independent interfaces, it improves the quality and the development efficiency as a whole.

5 Related Work Comparison

For smart education implementation, research mainly focuses on the micro technology or detail management, lacking of generality. Paper [11] introduces UML modeling to understand the application requirement, but it only stays on the concept of management model and it is difficult to apply to other projects. Paper [12] discusses the ETL (Extract Transfer Load and Cleaning, data storage, transformation, and loading) to handle Excel document data, which mainly concentrates on the technology process: however, it does not take into account the efficiency. Compared to the above work, the main contributions of this paper are:

- (1) Used concept components for reuse target as innovation.
- (2) Had given a smart education platform architecture, satisfying data reading efficiency and response time.
- (3) Established a facet-based description model to describe components.
- (4) Used MVC pattern for components development, which improves the efficiency and make components reusable.

6 Conclusions

In this paper, the method based on component software development is used for data management in smart education. By an instance, this paper explains component reuse process. The result shows this method have good portability, which meets data management requirement in smart education.

Future work will concentrate on the expansion of functional requirement, combined with component execution efficiency, it will support the application of smart education better and make reuse process more simple.

References

1. Ann J (2005) Learning technologies: affective and social issues in computer-supported collaborative learning. *Comput Educ* 44(4):395–408
2. Yunfeng Z (2008) Introducing smart structures technology into civil engineering curriculum: education development at Lehigh University. *J Prof Issues Eng Educ Pract* 134(1):257–291
3. Liuqin C (2007) Smart city: new hot spot of global urban development. *J Qingdao Univ Sci Technol (Soc Sci)* 27(1):57–68
4. Finco S (2007) A smart power integrated circuit educational tool. *IEEE Trans Power Electron* 22(4):109–125
5. Yushen J (2009) A component model based on MVC pattern. *Ordinance Ind Autom* 03 28(3):28–32(in Chinese)
6. Jinbao Z (2012) Smart education cloud service: a new model for information service in education. *Open Edu Res* 06 18(3):61–64(in Chinese)
7. Chi Z (2007) Research on software component interfaces. *Extending Microelectron Comput* 24(3):521–525
8. Shoichi TC, Kkassufication Q (2013) Aggregate and component entities in RDA:model and description. *Taylor & Francis* 17(5):351–357
9. Yi-jun B, Gang C, Jin-xiang D et al (2008) Bottom-up mining of XML query patterns to improve XML querying. *J Zhejiang Univ Sci A* 9(6):744–756
10. Ke F, Xiaoping L, Qian W (2008) Components selection method for multi-domain models. *J Southeast Univ* 138(11):35–39(in Chinese)
11. Xiangzong W, Ying C, Zengliang L (2008) Component-Base software developing method for group companies management information system. *J Nat Sci* 13(1):037–044
12. Mohamme M, Mohd SA, Abdul BM (2011) Extending ETL framework using service oriented architecture. *Procedia Comput Sci* 3:110–114. doi:[10.1016/j.porcs.2010.12.019](https://doi.org/10.1016/j.porcs.2010.12.019)

Driving Intention Inference Based on Dynamic Bayesian Networks

Fang Li, Wuhong Wang, Guangdong Feng and Weiwei Guo

Abstract Driving intention inference can anticipate the driving risk in advance, drivers have enough time to respond and avoid accident. There are several models for identifying driving intention in recent years. However, these methods infer driving intention without considering the impact of past driver behavior on current station, and only take a few basic factors into account, such as speed, accelerate, etc., which reduce the inference accuracy to some extent. To attack this, a four-step framework for driving intention inference is proposed. The main contribution includes driving behavior factors selecting analysis which can choose the main impacting factors, and improving the existing inferring model based on pattern recognition method. The improved method can consider the impact of past driver behavior on current station with add Auto-regression (AR). Experiments show that our framework can provide a good result for driving intention, including lane changing and braking intention inference. Moreover, compared to the tradition model, the improved model improves the correct recognition rate.

Keywords Driving intention · AR-HMM · Pattern recognition

1 Introduction

Intelligent Transport Systems (ITS), driving support systems that reduce driving burden and increase safety, are being developed in recent years. But advanced driver assistance systems cannot replace driver for accomplishing driving task. And, driver is the only one judger during driving. Prediction of driver's intention can provide enough time for drivers to respond before moving into the dangerous

F. Li (✉) · W. Wang (✉) · G. Feng · W. Guo
Department of Transportation Engineering, Beijing Institute of Technology, Beijing, China
e-mail: 025@bit.edu.cn

W. Wang
e-mail: wangwuhong@bit.edu.cn

zone. Hence, it is important to construct a driver model that considers driver intentions and psychological function when inferring driver behavior.

In 1999, driving intention was firstly proposed by Pentland. In this area, the driving states are treated as patterns, hence the driving intention inference are changed to pattern recognition. After nearly 10 years of development, there are existing two popular kinds of models based on pattern recognition methods for driving intention inference, Hidden Markov Model (HMMs) and based on fuzzy reasoning respectively. Such research show that fuzzy reasoning methods are an advantage in dealing with experience models, hence the driving intention inference models based on fuzzy reasoning can well merge vehicle dynamics and driver's experience and get a quantified driving intention [1–3]. However, the compatibility of different membership functions and fuzzy rules will affect inference results, which severely delay their development and adoption.

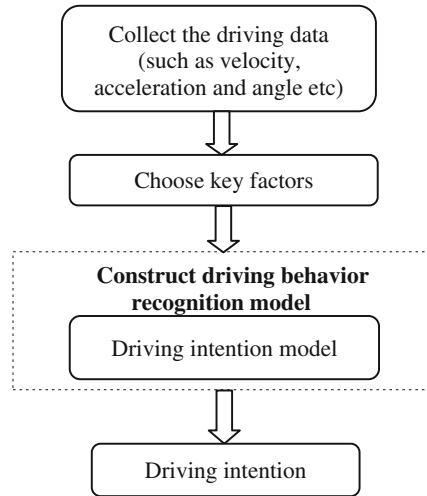
Driving intention inference models based on HMM are well-developed. Andrew Liu et al. [4] proposed to build driving intention inference model by using HMM, and focused on using visual scanning behavior to infer driver's intention. Toru Kumagai et al. [5] analyzed braking intention at intersection by using HMM with dynamic linear weight function analysis for the first time. According to Keskinen' four layer theory for driving behavior, Shigeki et al. [6] built driving behavior prediction model to implement the first layer, and traditional gauss bayesian network model with steering angle as single input was put forward to predict the probability of lane changing. Holger et al. [7] identified each driving operation by using the most typical signal. Houhaijing et al. [8] predicted lane change intention by using continuous HMM, and driving behavior data was collected by driving simulator. In addition to the above models, a large number of research literatures [9–12] are also focusing driving intention in the dynamic bayesian network (DBN).

However, the existing driving intention models only choose one factor as input. But driving behaviours are affected by human, vehicle, and road environment factors. Hence, one driving factor cannot capture the real driving condition. Also, as the most popular driving intention inference model, HMM cannot consider the impact of past driving behavior on current driving behavior.

In order to attack above shortages, a four-step framework has been proposed to predict driving intention, as is shown in Fig. 1. The framework includes data collect, main factors selecting, driving intention building, and calculate driving intention probability. The first step can be achieved by vehicle devices, vehicle sensors, and video, etc., and this context will be not described in this paper. We focus on analysis of the second step and the third step.

The rest of this paper is organized as follows: Sect. 2 presents analysis on driving behavior factors and main factors selecting of driving behavior. In Sect. 3, auto regression (AR) is introduced into HMM model for inferring driving intention. Experiment results on both comparison of driving intention inference models and comparison of are given in Sect. 4. Conclusions and future work are presented in Sect. 5.

Fig. 1 Flowchart of predicting lane-changing probability



2 Driving Behavior Analysis

Driving behavior shaping factors are characterized by the driver driving behavior characteristic, vehicle performance, and of road environment, namely, the driver state, vehicle state, and road environment factors constitute the connotation of driving behavior shaping factor. But which driving behavior shaping factors should be contained, different research purposes should choose different factors. There are two kinds of statements: the first statement takes the impact factors of vehicle function and road environment on driving behavior as the driving behavior shaping factor, and the other one takes the influence factors of vehicle function and driver characteristics on driving behavior as driving behavior shaping factor. In fact, driving behavior is a result of the combined actions of all driving behavior shaping factor regardless of driver characteristics, vehicle performance, or road environment, that belongs to the category of the driving environment, and should be seen as a part of the driving behavior shaping factor. Thus, driving intention should consider all the influence factors on driving behavior.

Using lane change intention as an example, intuitively, the influence factors for lane change include steering angle and acceleration of following vehicle, relative speed between lead vehicle and following vehicle, etc. But, in the previous literature studies, steering angle is the only one factor that is set as input. The only one factor that cannot capture all driving state information, leading to reduced inference accuracy.

In order to testify the above statement, SPSS software is used to analyze the influence factors of lane change. Test data is collected by driving simulator, described in Sect. 4.1. Vehicle function parameters are collected by vehicle devices. Road environment factors are collected by UC-win/Road software. Driver

Table 1 Lane change shaping factors

| Factor | Weight | Percent (%) | Cumulative percent (%) |
|--------|-----------|-------------|------------------------|
| 1 | 4.144 | 25.899 | 25.899 |
| 2 | 3.692 | 23.077 | 48.976 |
| 3 | 2.366 | 14.787 | 63.763 |
| 4 | 1.666 | 10.409 | 74.173 |
| 5 | 1.203 | 7.519 | 81.692 |
| 6 | 1.170 | 7.312 | 89.003 |
| 7 | 0.793 | 4.958 | 93.961 |
| 8 | 0.731 | 4.569 | 98.531 |
| 9 | 0.231 | 1.441 | 99.972 |
| 10 | 0.004 | 0.025 | 99.997 |
| 11 | 0.000 | 0.003 | 100.000 |
| ... | ... | ... | ... |
| 41 | 1.296E-26 | 8.098E-27 | 100.000 |

Table 2 Main shaping factors of lane change

| Variable | Means |
|----------|-----------------------------|
| x_1 | Steering |
| x_2 | Distance to lane center |
| x_3 | Distance to object in front |
| x_4 | Distance to object behind |
| x_5 | Relative speed |
| x_6 | Following acceleration |

state parameters are collected by sensors. We take above three data into SPSS software and conclude the results in Table 1.

According to Table 1, contribution of top six factors is close to 90 %, namely, these six factors can embody most of lane change context. The detail information of six factors is shown in Table 2.

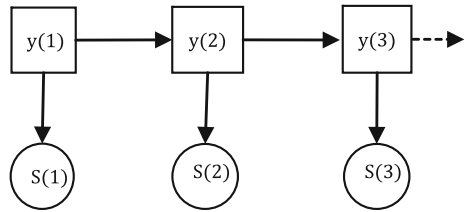
3 Driver Behavior Intention Inference

3.1 Probability Model

BNs can be roughly divided into static and dynamic types, and the dynamic type DBN is used for this study considering that it is possible to extract measurement dynamic driving station.

Now, HMM is the most popular model for driving intention inference, as shown in Fig. 2. Driving condition and station components of driver behavior hierarchy Level 2 are assigned to discrete nodes. The rectangle nodes denote driving condition (such as vehicle speed, acceleration, and so on), which are set as hidden nodes. And the ellipse nodes denote driving station (such as braking, lane

Fig. 2 HMM structure



changing, and so on), which can be directly observed. Then, in order to represent context-dependency of driver behavior, these nodes were connected with each other, condition and station have context. Also, manoeuvring of hierarchy Level 1 is assigned to Gaussian nodes. In the HMM model, learning is performed as the combination of time-series driving state and driving behavior data at that time.

Formulas of HMM are denoted as follows:

$$\delta_j(t + 1) = \sum_i \alpha_{i,j} \delta_i(t)$$

$$y(t) = N\left(\mu_i, \sum_i\right) \tag{1}$$

where t is discrete time, $\delta_i(t)$ is the probability of state i at time t . $\alpha_{i,j}$ is the state transition probability from state i to j . $y(t)$ is the driving data vector at time t . $N(\mu, \Sigma)$ is normal distribution, whose mean is μ and co-variance matrix is Σ .

As shown in the model of Fig. 2, there is no direct relationship between driving state $t-1$ and driving state t , which means that the model do not consider the impact of the past driving behavior on current driving behavior. In order to consider this impact, AR has been introduced into HMM model, namely called AR-HMM model, as is shown in Fig. 3.

Figure 3 shows the other sort of DBNs constructed with AR-HMM in which observable values depend on the previous ones. Formulas of AR-HMM are denoted as follows:

$$\delta_j(t + 1) = \sum_i \alpha_{i,j} \delta_i(t)$$

$$y(t) = N(\mu_i + \omega_i y(t - 1), \sum_i) \tag{2}$$

where ω_i is weight matrix, which enables the previous value vector $y(t-1)$ to effect on the current value vector $y(t)$. This structure is greatly appropriate to make behavioral models since the current behavior is strongly associated with past actions. For this reason, AR-HMM is applied to a behavioral model in the other research [9, 10]. We also decided to use this structure to create a new driving behavior model concerning past driving actions.

Fig. 3 AR-HMM structure

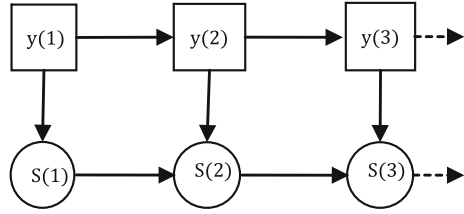
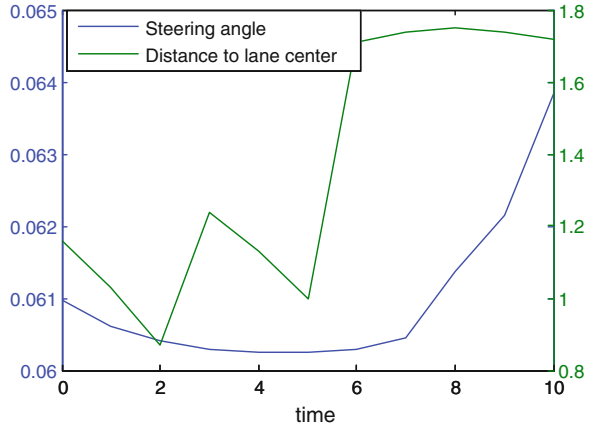


Fig. 4 An example of current driving trigger



3.2 Inference Method Considering Transitions of CDT

To consider the past actions of drivers, we defined Current Driving Trigger (CDT) which indicates past driving data of both velocity and pedal stroke. Figure 4 is an example of CDT regarding 10 s past driving behavior beginning with time t1 and ending with time t2. CDT was used as an input of DBNs to construct a driving behavior model.

To make a driving behavior model considering a chain in dynamic flow of the past actions, AR-HMM was adopted to express continuous transitions of CDT. A formula (2) was expanded to include transitions of CDT as follows. Where the variables are denoted in Table 3).

$$\begin{aligned}
 \begin{bmatrix} y_{CDTA}(t) \\ y_{CDTD}(t) \end{bmatrix} &= N \left(\begin{bmatrix} \mu_A \\ \mu_D \end{bmatrix} + \begin{bmatrix} \tilde{w} O_n \\ O_n \tilde{w} \end{bmatrix} \begin{bmatrix} y_{CDTA}(t-1) \\ y_{CDTD}(t-1) \end{bmatrix}, \Sigma \right) \\
 \mu_A &= [0 \quad 0 \quad \dots \quad \mu_{A_n}]^E \\
 \mu_D &= [0 \quad 0 \quad \dots \quad \mu_{D_n}]^T \\
 \tilde{w} &= \begin{bmatrix} O_{n-1} & E_{n-1} \\ 0 & O_{1,n-1} \end{bmatrix} \tag{3}
 \end{aligned}$$

Table 3 Symbols for AR-HMM

| Symbol | Explanation |
|---------------|--|
| $y_{CDTA}(t)$ | CDT of steering angle at time t |
| $y_{CDTD}(t)$ | CDT of distance to center lane at time t |
| n | Length of CDT ($n = 1$ is 0.1 s) |
| μ_A | Mean value of CDT of steering angle |
| μ_D | Mean value of CDT of distance to center |
| \tilde{w} | Weight matrix |
| $E_{m,n}$ | $m \times n$ unit matrix |
| $O_{m,n}$ | $m \times n$ zero matrix |

Note that when $n = 1$, the above formulas are the same as conventional methods because CDT reflects just-past action. In this study, the CDT length is up to 50 that consider 5 s past actions

4 Experiments

The experiment was conducted within a driving simulator loading a real car composed with pedals (gas and brake) and a steering wheel as input devices, and was controlled by driving simulating software named UC-win/Road. Vehicle devices recorded driver’s control input including gas pedal position, brake pedal position, and steering wheel angle, and vehicle sensors recorded driver’s physiological, and psychological state parameters.

Driving behavior data were collected at a sampling rate of 10 Hz and stored without compression on a disk drive for further computer off-line analysis. The simulator faces 80-inch screen showing programmed traffic environment with some vehicles and circuit road.

4.1 Comparison of HMM and AR-HMM

In order to fairly compare HMM model and AR-HMM model for inference driving intention, the test data is chosen from [13], two sets of lane changing data, as shown in Figs. 5 and 6 respectively. These two sets of data were collected from three drivers under normal lane change (LCN) and emergency lane change (LCE) conditions, respectively.

Three types of driver behavior at time of lane change were considered: normal lane keeping (LKN), normal right lane change (LCN), and emergency right lane change (LCE).

The test data of Figs. 5 and 6 was set as the input value, the toolbox Bayes Net Toolbox (BNT) [14], developed at U.C. Berkeley, which includes HMM model and AR-HMM model, was applied to learn lane change intention. Results of two models were shown in Figs. 7, 8, 9 and 10, respectively.

Figures 7 and 8 are the results of HMM and AR-HMM under norm lane change condition. As a whole, the inference performance of AR-HMM shows

Fig. 5 Steering angle of LCN

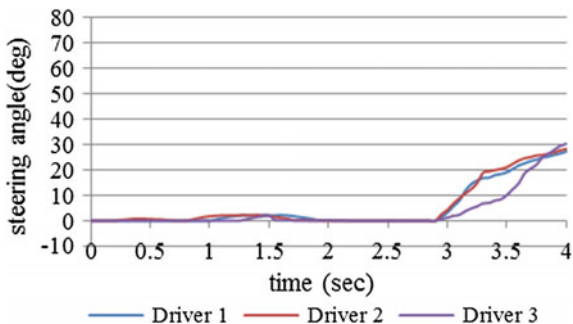


Fig. 6 Steering angle of LCE

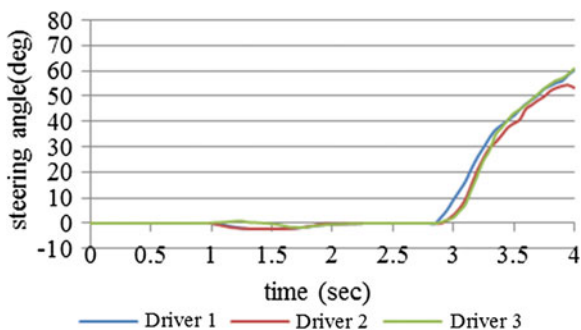
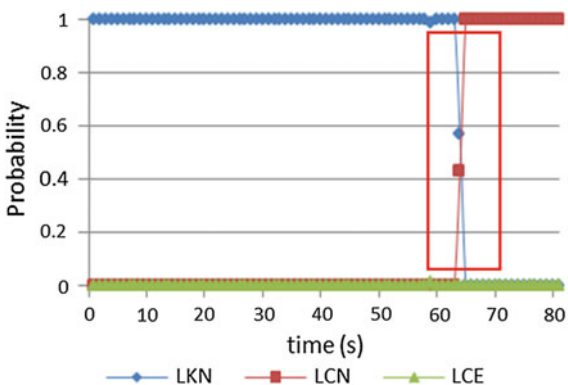


Fig. 7 Results of HMM under LCN



better than HMM model, especially in the red box part. Figures 9 and 10 are the results of HMM and AR-HMM under LCE condition. The curve of AR-HMM model is smoother than the curve of HMM, which demonstrates that AR-HMM is more accurate than HMM for LCE intention inference.

Figures 9 and 10 are the results of HMM and AR-HMM under LCE condition. The curve of AR-HMM model is smoother than the curve of HMM, which demonstrates that AR-HMM is more accurate than HMM for LCE intention inference.

Fig. 8 Results of AR-HMM under LCN

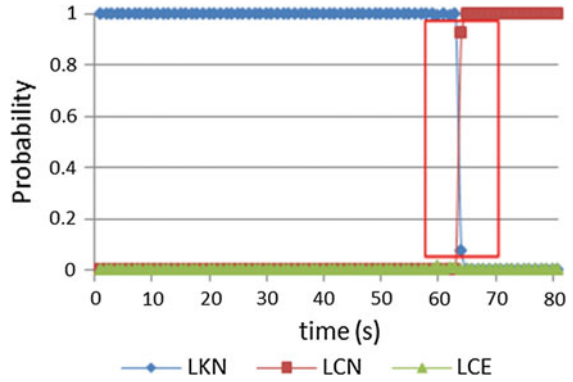


Fig. 9 Results of HMM under LCE

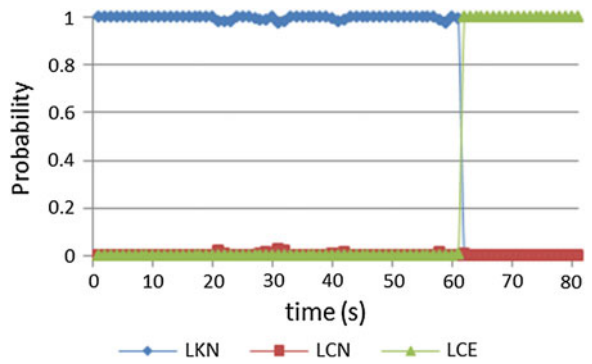
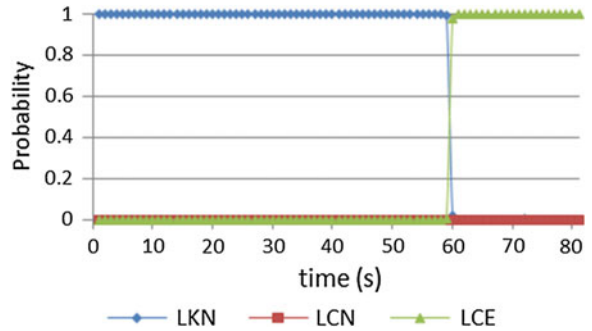


Fig. 10 Results of AR-HMM under LCE



4.2 Impact of Driving Behavior Factors

In the previous literature studies, a single driving behavior factor was used to infer driving intention. However, driving intention is affected by multifactors, including driver, vehicle, and road environment, as is analyzed in Sect. 2.

Fig. 11 Results of lane change (*single factor*)

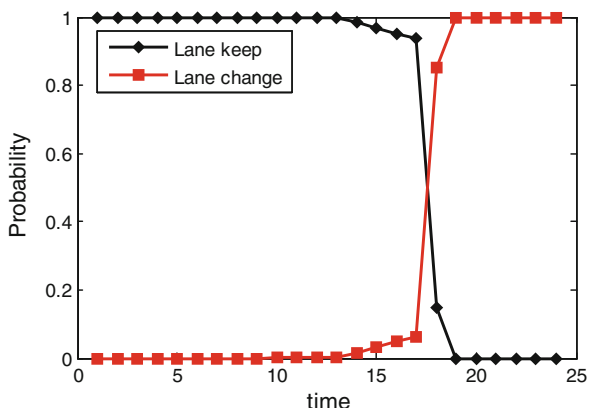
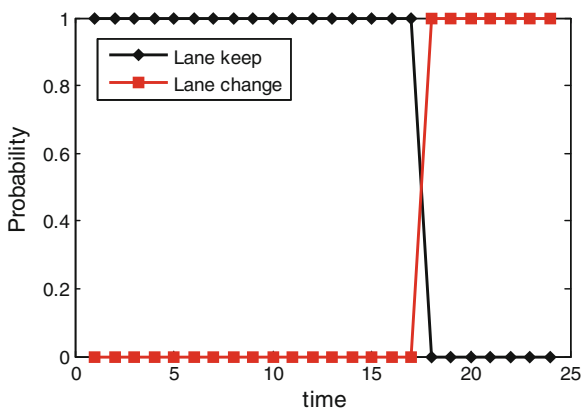


Fig. 12 Results of lane change (*multifactors*)



Similarly, we also choose lane change as the test sample. The previous research focused on steering angle when they predict lane change probability. Here, steering angle and the main other factors selected in Sect. 2 are used to infer lane change. The results are shown in Figs. 11 and 12.

Figure 11 shows the inference results of AR-HMM when only set steering angle as input. Figure 12 gives the inference results of AR-HMM when select the main factors for lane change as input. Obviously, the results of Fig. 11 are worse than Fig. 12. Hence, it is very important to add selecting main factors step in driving intention inference.

To sum up, our proposed framework for driving intention inference can provide a good performance, and analysis on driving factor is a critical part when infer driving intention. In addition, AR-HMM model can provide a better inference performance than HMM model since considering the impact of past driving behavior on current driving behavior.

5 Conclusion

In this research, we proposed a new framework of predicting driving behavior included four steps. The driving data, velocity, and pedal stroke, etc., are collected by driving simulator. After analyzing driving behavior impacting factors, the main factors are selected as input for driving intention inference. To consider the impact of past driving behavior on current driving behavior, AR-HMM model has been applied to construct driving behavior model for inference of driver behavior. Using results of this study we have revealed that considering main factors of driving behavior and past movements is a great influence for modeling driving behavior and predicting driving intention probability accurately.

References

1. Oliver N, Pentland A (2000) Graphical models for driver behavior inference in a smart car. In: IEEE intelligent vehicles symposium, pp 7–12
2. Wang Y, Song J et al (2006) Integrated inference of driver's intentions and driving environment and real-time algorithm. *Chin J Mech Eng* 42(4):206–212
3. Changfu Z, Xiao Y et al (2009) Driving intentions identification and behaviors prediction in car lane change. *J Jilin Univ* 39(1):27–32
4. Liu A, Salvucci D (2001) Modeling and prediction of human driver behavior. In: IEEE international conference on human-computer interaction
5. Kumagai T, Sakaguchi Y et al (2003) Prediction of driving behavior through probabilistic inference[C]. In: international conference on engineering applications of neural networks, pp 117–123
6. Tezuka S, Soma H et al (2006) A study of driver behavior inference model at time of lane change using Bayesian networks [C]. In: IEEE international conference on industrial technology, pp 2308–2313
7. Berndt H, Emmert J et al (2008) Continuous driver intention inference with hidden Markov models. In: Conference on intelligent transportation systems, Beijing 12–15 Oct 2008
8. Hou H, Jin L, Niu Q, Sun Y (2011) Driver intention inference method using continuous hidden Markov model [J]. *Int J Comput Intell Syst* 4(3):386–393
9. Abe K, Miyatake H, Oguri K (2007) A study on switching AR-HMM driving behavior model depending on driver's states[C]. In: IEEE intelligent transportation systems conference, Seattle, WA, pp 806–811
10. Amata H et al (2009) Prediction model of driving behavior based on traffic conditions and driver types. In: IEEE conference on intelligent transportation systems, pp 747–752
11. Ito T, Naito T et al (2004) Prediction of driver's turning intention for car navigation system. In: Proceedings of the 11th world congress on ITS, Nagoya, pp 95–99
12. Cacciabue PC, Carsten O (2010) A simple model of driver behaviour to sustain design and safety assessment of automated systems in automotive environments. *Appl Ergonomics* 41:187–197
13. Tezuka S, Soma H et al (2006) A study of driver behavior inference model at time of lane change using Bayesian networks. In: IEEE international conference on industrial technology, pp 2308–2313
14. Kevin Murphy's Bayes Net Toolbox for Matlab <https://code.google.com/p/bnt/>

A Review on Hybrid Vehicle Powertrain Matching and Integrated Control Based on ECVT

Guogeng Zhang

Abstract Powertrain Matching has a greater impact on dynamics, fuel economy, and emissions performance. In order to improve the Hybrid Vehicle efficiency and drive quality, and reduce the pollutions, taking electronic continuously variable transmission (ECVT) as the research object, we comprehensively analyzed the Vehicle Matching Theory, Integrated Control and Intelligent Calibration, and developed a road map for the current and future ECVT technologies: taking the engine power loss rate, fuel utilization, and purification rate of pollutants as the optimization objectives; matching the ECVT, Engine, Motor and Battery with Vehicle's best working status; and establishing the ECVT Matching and Intelligent Calibration and Control Strategy.

Keywords Powertrain matching · Integrated control · Intelligent control · ECVT

1 Powertrain Matching

The traditional vehicle matching is focusing on the best economy matching or the best dynamic matching [1]. Only few researchers could take all factors into consideration [2].

1.1 CVT Matching

In order to get a good matching between transmission and engine, proposed an optimal economy control method with consideration of both engine and CVT efficiency to calculate the combinations between the engine torque and CVT ratio

G. Zhang (✉)

Department of Mechanical Engineering, Zhejiang University, Hangzhou 310027, China
e-mail: zhangguo168.com@163.com

[3]. Used the coefficient of the torque capacity factor as affecting the matching between a power source and a CVT [4], or chose acceleration and travel smoothness as the evaluation indexes, and took the gear ratio control system as an ideal system, approximating the target ratio level to control the transmission ratio [5].

Designed a speed ratio control method which could limit variation of CVT speed ratio under the condition of ensuring economy and power performance [6] and used the optimal matching line control strategy to solve the problem that the existing control strategy of CVT vehicles cannot guarantee the lowest fuel consumption when driving at slope road and nonsteady working conditions [7, 8].

In order to seamlessly match the vehicle road load to the engine optimal operating region, Jian and Chau [9] proposes a new ECVT system for power-split hybrid electric vehicles, this integrated machine can achieve both power splitting and mixing.

1.2 Hybrid Power System Matching

ECVT is used on the Hybrid vehicle. Being different from CVT, it has two mechanical points and two electrical points [10]. However, the CVT matching strategy could give us a good guide in ECVT Matching. In order to have a deep understand on ECVT Matching, we also need to pay more attention on the Hybrid Power System Matching.

Internal combustion engines waste a majority of the energy they consume, with only 20 % actually going into moving the vehicle, an optimized EV can achieve a 63 and 60 % over hybrids [11]. Some researchers take the fuel economy and motor efficiency [12, 13] or the minimization of the life cycle cost [14] as the optimization objective or proposes parameters matching scheme for HEV based on the concurrent consideration of driving conditions, power flow control strategy, and power performance [15].

Based on fuzzy logic control for energy flow management between internal combustion engines, Majdi et al. [16] developed an online strategy and based on the efficiency model and the longitudinal dynamic equations of the mild hybrid power system, Qin et al. [17] built the experimental numerical model for the efficiency of key components of a mild hybrid electric vehicle with CVT, and used the sequential quadratic programming algorithm to calculate the optimization of system efficiency of the mild hybrid electric vehicle under different driving conditions.

1.3 Hybrid Power System Intelligent Matching Model

From Fig. 1, the customers set the vehicle performance goals during the fuel consumption, emission, dynamics, and driving quality by themselves. When customer confirms the vehicle performance goal, the integrated system set a

comprehensive optimization, and based on the road cycle information databases, the system could intelligent recognition the optimization regional, it controls the transmission ratio engine, battery, and motor's working model and help them to work in an economy state, in which we also should consider the product's life.

This model help us to understand the demand of each function block and it also help the engineers set an economic and matching goals of engine, battery, motor, and transmission.

2 Integrated Control

We could get different control codes with different control strategies for the Powertrain matching theory. Hybrid electric vehicle and ECVT is a very complicated nonlinear system, whose performance is affected by lots of control parameters. The routine optimization approach is inefficient and the reliability of optima depends on the precision of model.

2.1 Classical Control Stagey

In view of the problem of conventional dynamic matrix controller: Using too much resources of transmission control unit due to too heavy computation in the process of speed ratio tracking for continuously variable transmission, some researchers designed an improved dynamic matrix controller; it takes chaos optimization algorithm as its rolling optimization strategy to solve the problem of real time calculation of optimal control amount [18], implanted a fuzzy logic controller for parallel hybrid electric vehicles [19], or proposed a control strategy combining fuzzy control and particle swarm optimization for a hybrid electric bus [20], used a control strategy based on Fuzzy PID aimed at the nonlinear and time lag problems of CVT ratio control system [21], used the conventional and nonlinear PID theory in tracking control of the goals for velocity and engine speed [22].

For achieving minimum fuel consumption and emissions, Zhang et al. [23] applied a multiobjective genetic algorithm optimization method to getting the optima of work modes and energy distribution in different city bus cycles. Liu et al. [24] proposed a dual-mode engine torque balancing control strategy.

2.2 Chaotic Strategy

In Motor Drives, UHK has much research in Chaotic. In order to employ time-delay feedback to anticontrol, a permanent magnet DC motor system for vibratory compactors, Wang and Chau [25] implemented a new electrically chaotic compactor, a series of simulations are conducted to verify that the proposed electrically

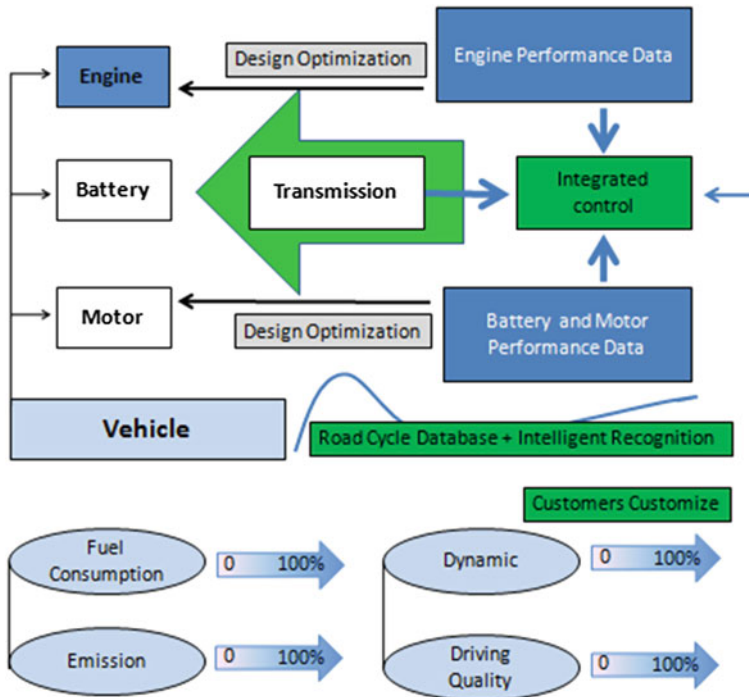


Fig. 1 Intelligent matching model

chaotic compactor not only offers better compaction effects than the conventional one, but also provides higher flexibility than the mechanically chaotic compact or Wang [26] proposed a chaotic pulse width modulation closed-loop induction motor drive, which are implemented to improve the electromagnetic compatibility for electric propulsion, he also designed a new chaotic permanent magnet synchronous motor drive [27] and identified chaotic vibration in the automotive wiper system [28].

Zhang et al. [29] proposed and implemented a new hybrid chaotic pulse width modulation scheme for the reduction of electromagnetic interference in alternating current motor drives, which possesses a hybrid characteristic; the peaky EMI is suppressed while the occurrence of low-order noises is reduced. Chaotic also could be used in establishing the limiting conditions of operation of magnetorheological fluid dampers in vehicle suspension systems [30].

3 Intelligent Control

Intelligent is widely used in electric locomotive and high-speed train, but there will be a long way to develop on vehicle.

3.1 Intelligent Control

In order to improve the steady state efficiency of permanent magnet synchronous motor system for rail vehicles, Sheng et al. [31] presented the online intelligent integrated optimal control strategy for PMSM efficiency optimization. Xie et al. [32] applied the intelligent coordinated and predictive control in the hybrid power coordinated control system of fuel cell middle size bus.

Based on the IHEV, Li et al. [33] developed an adaptive cruise control system with hybrid propulsion system. The hierarchical control structure, which is integrated with double mode switch adaptive cruise control, multiple energy management, driving/braking system coordinate control is proposed and applied to the vehicle control system and Manzie et al. [34] used a simple algorithm for shaping the velocity profile of an intelligent vehicle subjected to different degrees of traffic information. Driving cycle self-learning system [35], a machine learning approach to train an intelligent power controller for a series hybrid electric vehicle [36], and an intelligent intervehicle device to a convoy of in-contact vehicles [37] are also presented.

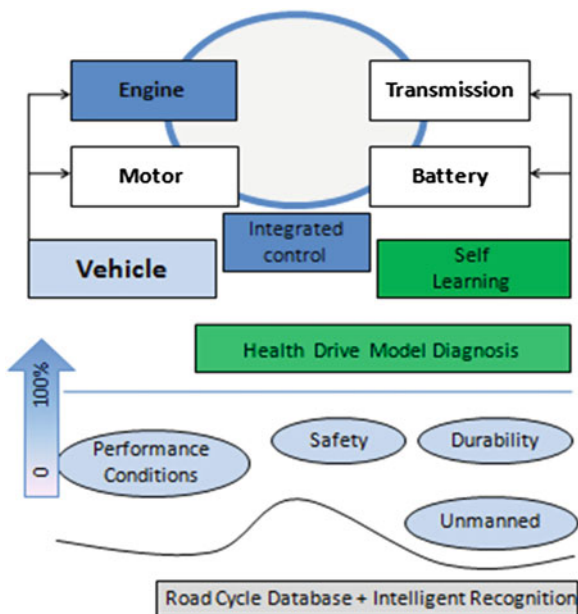
The Intelligent in other areas also could broad our view in Intelligent Calibration of ECVT such as:

Sooraska and Klomkarn [38] introduced that Chaotic signals have been adopted to generate gaits for robots via simple and effective chaotic circuits within or without CPUs, and the signals are used to guide a robot to navigate chaotically, and Grizzle [39] used Markov process in the synthesis of hybrid systems, and Bowen et al. [40] presented a distributed algorithm for mobile sensor networks to monitor the environment. The mobile sensor nodes are able to self-organize.

3.2 Self-learning Powertrain Matching Model

From Fig. 2, the system automatics identification the customers' driving model, and the system set the influence of each performance goal based on the customers' habits. Some of the drivers do not have a health driving habits, so we implanted a control system diagnostic module, which could correct the performance goals based on the drivers' habits, which help the powertrain matching system achieve the self-learning function. And it controls the transmission ratio engine, battery and motor's working model, and helps them to work in an economy state.

Fig. 2 Self-learning powertrain matching model



In this system, we also consider the safety, powertrain durability and unmanned model, which could help driver to enjoy the driving.

4 Conclusions

With environment protection and energy problems being taken into account, New Energy Vehicles will have an accelerated development. In addition, E-vehicle and Hybrid may be the main developing trends.

First, from the published literatures, we find that most researchers pay more attention on the control strategy of Hybrid, but not the matching of the engine, motor, battery, and transmission. Powertrain matching is very important and it is a fundamental research for every company.

Second, different control objects have its appropriate strategies. With the different driving behaviors and road characteristics, an exact estimation of parameters usually cannot be made. How to use the Chaos Theory in Vehicle Integrated Control and Intelligent Calibration is worth to study.

Lastly, different drivers have different driving habits, the calibration of transmission and engine depends on the cars but not the drivers. We could build a calibration system based on the individual driving habits, which has self-learning ability and could make intelligent judgments.

In the future research, we will take ECVT as the study objects and mainly undertake the following tasks:

- (a) Taking engine power loss rate, fuel utilization and purification rate of pollutants as the optimization objectives; considering the matching of ECVT, Engine, Motor and Battery with Vehicle working status, and establishing the ECVT Matching Theory to improve the vehicle efficiency.
- (b) Based on the Matching Theory and Chaos Theory, we will develop the ECVT control strategy and based on the different driving habits, we establish the Intelligent Calibration Theory and Self-study Control Strategy.

References

1. Zhang BS, Fu TJ, Zhou YS et al (2004) Matching of V-belt type continuously variable transmission with engine and its control strategy. *J Jilin Univ: Eng Technol Ed* 34(1):65–70 (in Chinese)
2. Kai JB, Zhang GG, Zhang M (2014) Analysis of impact of powertrain matching to engine exhaust temperature. *Shanghai Auto* 3:59–62
3. Luo Y, Sun DY, Qin DT, Hen R, Hu FB (2010) Fuel optimal control of CVT equipped vehicles with consideration of CVT efficiency. *Chin J Mech Eng* 46(4):80–84
4. Zheng CH, Lim WS, Cha SW (2011) Performance optimization of CVT for two-wheeled vehicles. *Int J Autom Technol* 12(3):461–468
5. Zhang YL (2005) Research of metal belt type continuously variable transmission speed electronic control systems and strategy. Hunan University, Changsha, p 3
6. Wang JX, Wang QN, Zhou YS, Wang XY (2009) Research on CVT speed ratio control based on external characteristic of engine. *Autom Technol* 10:1–4
7. Zhang SP, Zhang YK, Wang QN, Zhang L (2010) Ratio control strategy of continuously variable transmission for ramp-driving working condition. *J Jiangsu Univ: Nat Sci Ed* 31(3):273–277
8. Zhang SP, Zhang YK, Wang QN, Zhang L (2010) CVT ratio control strategy optimization under non-steady working conditions. *J Jilin Univ (Eng Technol Ed)* 40(4):895–900
9. Jian L, Chau KT (2010) Design and analysis of a magnetic-gear electronic-continuously variable transmission system using finite element method. *Prog Electromagn Res* 107:47–61
10. Chau KT, Cheng M (2010) The new drive technology of electric vehicles, vol 4. China Machine Press, Beijing, p 195
11. Sweeting WJ, Hutchinson AR, Savage SD (2011) Factors affecting electric vehicle energy consumption. *Int J Sustain Eng* 4(3):192–201
12. Sun DY, Zhuang JB, Qin DT, Liu ZJ (2010) Simulation on the control strategy of a new super-mild hybrid transmission system. *J Mech Eng* 46(1):37–42
13. Xiao Q, Wang QF (2008) parameter matching method for hybrid power system of hydraulic excavator. *China J Highw Transp* 21(1):121–126
14. Yu YB, Wang QN, Wang JX, Zhao XX (2008) Parameter matching and optimization of on-board synergic electric power supply system of hybrid electric vehicle. *J Jilin Univ (Engine Technol Ed)* 38(4):764–768
15. Ji XJ, Li SJ, Fang ZD (2011) A research on the parameters matching for the powertrain of single-axle parallel HEV. *Autom Eng* 3(188–193):202
16. Majdi L, Ghaffari A, Fatehi N (2009) IEEE international conference on robotics and biomimetics, ROBIO 2009, p 842–847
17. Qin DT, Hu MH, Yang YL, Shu H (2008) Optimization of system efficiency for the mild hybrid electric vehicle with continuously variable transmission under the motor and engine combined working conditions. *J Mech Eng* 44(11):171–177

18. Xue DL, Li Q, Zhou YS (2010) Application of improved dynamic matrix control to speed ratio tracking of continuously variable transmission. *Autom Eng* 8:699–702
19. Nashed MNF, Wahsh S, Galal H (2010) Parallel hybrid electric vehicle performance under different road cycles. *International conference on electric power systems, high voltages, electric machines*, 2010, pp 44–49
20. Yin AD, Zhao H, Zhang H (2011) A study on the control strategy for hybrid electric bus based on fuzzy control and particle swarm optimization. *Autom Eng* 33(7):553–557
21. He R, Ma CG, Zhang Y, Xia JJ, Wu HX (2009) Study of fuzzy PID control for V-belt CVT based on genetic algorithm. *Mach Des Manuf* 5:202–204
22. Zuo YH, Xiang CL, Yan QD, Liu H, Li HC (2010) E-CVT control research based on nonlinear PID. *J Mech Transm* 34(4):10–12, 16
23. Zhang X, Song JF, Tian Y, Zhang X (2009) Multi-objective optimization of hybrid electric vehicle control strategy with genetic algorithm. *J Mech Eng* 45(2):36–40
24. Liu G, Song DC, Chen HM, Chen M (2010) Modeling and control strategy of parallel hybrid system in hydraulic excavator. *J Tongji Univ(Nat Sci)* 38(7):1079–1084
25. Wang Z, Chau KT (2008) Anti-control of chaos of a permanent magnet DC motor system for vibratory compactors. *Chaos, Solitons Fractals* 36(3):694–708
26. Wang Z, Chau KT, Cheng M (2008) A chaotic PWM motor drive for electric propulsion. *IEEE Vehicle Power and Propulsion Conference*, 2008
27. Wang Z, Chau KT, Jian LN (2008) Chaotization of permanent magnet synchronous motors using stator flux regulation. *IEEE Trans Magn* 44(11) (Part 2):4151–4154
28. Wang Z, Chau KT (2009) Control of chaotic vibration in automotive wiper systems. *Chaos, Solitons Fractals* 39(1):168–181
29. Zhang Z, Chau KT, Wang Z, Li WL (2011) Improvement of electromagnetic compatibility of motor drives using hybrid chaotic pulse width modulation. *IEEE Trans Magn* 47(10):4018–4021
30. Naik RD, Singru PM (2009) Establishing the limiting conditions of operation of magneto-rheological fluid dampers in vehicle suspension systems. *Mech Res Commun* 36(8):957–962
31. Sheng YF, Yu SY, Gui WH, Hong ZN (2010) Efficiency optimization of permanent magnet synchronous motor for rail vehicles based on intelligent integrated control. *J Cent South Univ Sci Technol* 41(6):2252–2257
32. Xie CJ, Du CJ, Quan SH (2009) Hybrid power control system of fuel cell middle size bus. *J Mech Eng* 45(6):188–192
33. Luo YG, Chen T, Zhou L, Zhou GQ, Li KQ (2010) Adaptive cruise control system of Besturn intelligent hybrid electric vehicle. *Chin J Mech Eng* 46(6):2–7
34. Manzie C, Watson HC, Halgamuge S, Lim K (2006) A comparison of fuel consumption between hybrid and intelligent vehicles during urban driving. *J Autom Eng* 220(1):67–76
35. Zhu DW, Xie H, Yan Y, Song ZL (2010) Control strategy dynamic optimization of the hybrid electric bus based on driving cycle self-learning. *Chin J Mech Eng* 46(6):33–38
36. Chen ZH, Kiliaris L, Murphey YL, Masrur MA (2009) Intelligent power management in SHEV based on roadway type and traffic congestion levels. *5th IEEE vehicle power and propulsion conference*, 2009, pp 915–920
37. Gonzalez VA, Renfrew A, Brunn P (2009) Application of the “contact convoy” concept to hybrid electric vehicles. *IEEE Trans Veh Technol* 58(1):39–47
38. Sooraska P, Klomkam K (2010) “No-CPU” chaotic robots: from classroom to commerce. *IEEE Circuits Syst Mag* 10(1):46–53
39. Grizzle J (2009) Advances in discrete event, nonlinear, and stochastic systems modeling and control: a symposium in honor of Steven I. Marcus (conference reports). *IEEE Control Syst Mag* 29(5):120–122
40. Bowen L, Gu, D, Hu, H (2010) Environmental field estimation of mobile sensor networks using support vector regression. *2010 International Conference on Intelligent Robots and Systems, IROS 2010—conference proceedings*, pp 2926–2931, 2010

The Time Series Pattern of Traffic Flow on an Accident Section

Feng Peng, Jifu Guo and Qi Xu

Abstract The time series pattern of traffic flow on the accident section is investigated in this paper. The mean value, standard deviation, Hurst exponent, and cycle length of traffic flow on the accident section make clear that the traffic flow shows long-term correlation and regular pattern as well as obvious fluctuation in a short stage, and the cycling period is about 40 min. The time series of traffic flow on the accident section is converted into a complex network by using the visibility algorithm. It can be inferred from the topological features of the constructed complex network that the complex network is scale-free, small-world, and hierarchically constructed, verifying that the time series displays fractal characteristics and a tight connection exists among the time series of driver behaviors. Otherwise, there are some extreme relative velocities in the original traffic flow, and these faster relative velocities appearance in the form of group.

Keywords Traffic flow · Accident section · Time series · Complex network

1 Introduction

In this paper, we study the traffic flow on road section in working time which is influenced by a traffic accident. The result of the analysis may guide making specific induced information on variable message sign. It can reduce the time of driver wasted on the way, and enhance the efficiency of urban road transit. To find the time series pattern of traffic flow on the accident section, we investigate the time series of relative velocities through statistics, rescaled range, and complex network analyses.

F. Peng (✉) · J. Guo · Q. Xu
MOE Key Laboratory for Urban Transportation Complex Systems Theory and Technology,
Beijing Jiaotong University, Beijing China
e-mail: pengfeng2020@126.com

Statistical and rescaled range analyses are comparatively mature techniques, which have been broadly used in time series analysis. In recent years, complex network theory has flourished in time series analysis. And it is interesting that some study results have made a bridge between time series and graphs or networks [1–6].

Complex networks from corresponding time series can be produced with different methods. The researches of the first type deal with many time series to constitute a complex network with each vertex delegating a time series and the weight of a link between two vertices characterized by the correlation coefficient of the two time series [7] or by the space between the two time series [8]. Lacasa et al. [5, 6, 9] proposed a new method for time series which is called the visibility algorithm and attracted much attention due to its simplicity and high efficiency. Lacasa et al. have shown that time series structure is inherited in the associated complex network.

Therefore, the constructed complex network allows us to use tools of complex network theory for characterizing time series simply. However, most discussions at present mainly focus on stationary time series produced with theoretical models. The applications to analyze real-life data are rare, especially in the area of traffic and transportation. So far the visibility algorithm to analyze real-time series is mainly proposed in fields of occurrence of hurricanes in the United States, stock market indices, foreign exchange rates, and energy dissipation rates in three-dimensional fully developed turbulence [10–14].

The rest of this paper is organized as follows. The data collection and pretreatment are given in Sect. 2. There is also an overview of the time series of relative velocities. In Sect. 3, the general laws of the time series are presented to find the stability and fluctuation feature of traffic flow on the accident section. In Sect. 4, the time series are converted into a complex network by using the complex network algorithm, and some topological features are studied to find the correlation among data points of traffic flow on the accident section. Finally, some conclusions and research prospect are given in Sect. 5.

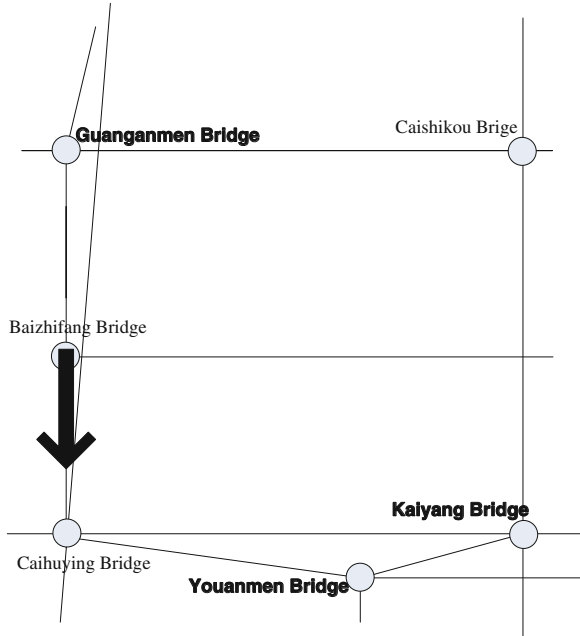
2 Data Collection and Pretreatment

In this paper, the traffic accident which we studied was happened on a road section in Beijing. Figure 1 shows the sketch of region where the accident section located.

In Fig. 1, the road section where the black arrow situated is the accident section. All statistical rules are derived from empirical traffic data which collected from a detector installed on the west side of the accident section. The data are collected from 12:30 to 16:46 on November 18, 2012 at an interval of five minutes. Each data stands for the average velocity of traffic flow on the accident section at a certain time point. Therefore, the 52 original data constitute a time series.

In this study, there is normalized processing of original data. Denote V_r as the relative velocity, V_r is a scalar, which is calculated by:

Fig. 1 The area of Baizhifang bridge's traffic accident



$$V_r = \begin{cases} V_a/V_d & (0 \leq V_a \leq V_d) \\ 100 & (V_a > V_d) \end{cases}$$

where V_a is average velocity, and the original data are representative V_a . V_d is the design velocity of the road and it is a constant value. In our case, the value of V_d is 80 km/h. So the range of V_r is [0, 100]. When V_r is belong to [0, 20], that stand for the accident section is crowding. While V_r is located (20, 50), which mean the accident section is amble. And it is the best situation while V_r is pertain to [50, 100]. In this condition, the accident section is unimpeded. Therefore, we can get 52 V_r , they also compose a time series. Figure 2 exhibits the general fluctuation pattern of the time series of relative velocities.

3 General Law of the Time Series of Traffic Flow on the Accident Section

In this section, the time series of traffic flow on the accident section is discussed from two visual angles: statistical and time series analyses.

In this study, we divide the whole period into five stages. The first stage is the epoch before the traffic accident happened. The second stage starts from the moment when the traffic accident happens to the moment when there is prompt

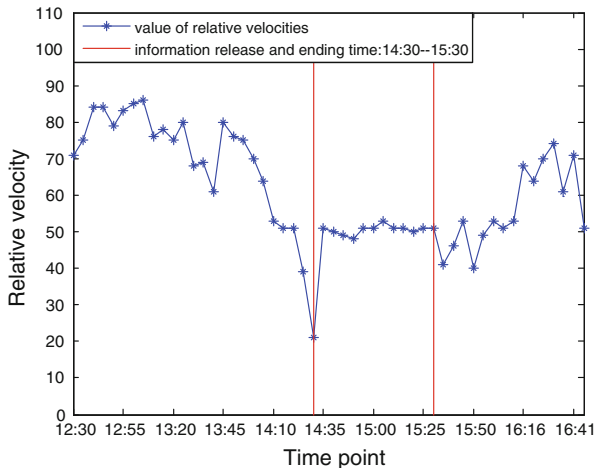


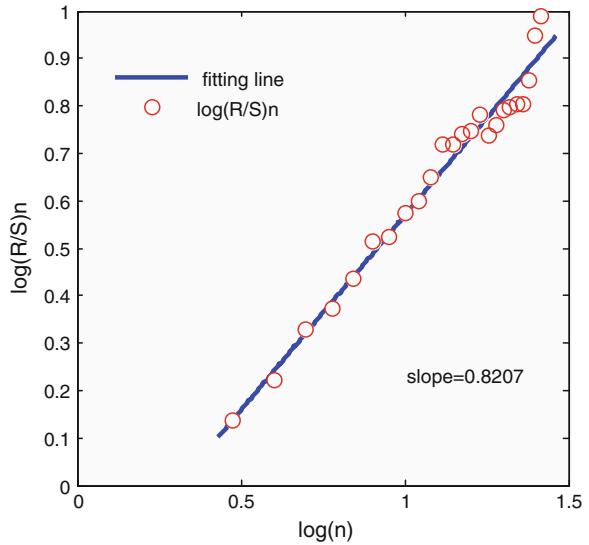
Fig. 2 The time series of traffic flow on the accident section

Table 1 Mean values and standard deviations of traffic flow on the accident section

| Stage | First | Second | Third | Fourth | Fifth | Total |
|--------------------|-------|--------|-------|--------|-------|-------|
| Mean value | 76.9 | 62.1 | 48.1 | 54.8 | 59.0 | 61.3 |
| Standard deviation | 7.3 | 14.2 | 8.6 | 10.9 | 7.5 | 14.7 |

information on the variable message sign. The third stage is the epoch of prompting information release and ending time on variable message sign. The fourth stage is from the moment of variable message sign cancel the information issue to the moment of traffic order returned to normal. The last stage is the epoch of after the accident affected. We calculate the mean value and the standard deviation of relative velocities of five stages and the whole period, which are displayed in Table 1. From the results, we see the general fluctuation pattern of every stage. The first stage has the largest mean value and the smallest standard deviation. This suggests that before the traffic accident happened the traffic on the road is in the best shape and the traffic flow is steady. The second stage’s standard deviation is the largest one. This indicates that the road condition declines rapidly. The third stage has the smallest mean value meanwhile has a relatively low standard deviation. This makes clear that some drivers change the path when they saw prompt information on the variable message sign. The fourth stage has a relative high standard deviation. It can be explained that road conditions is slowly getting better. The last stage has a low standard deviation and the road condition is stable. The whole period has a medium mean value and large standard deviation. It can include that the whole period time series pattern of traffic flow on the accident section shows fluctuation features.

Fig. 3 Plots of $\log(R/S)_n$ of traffic flow on the accident section versus $\log(n)$



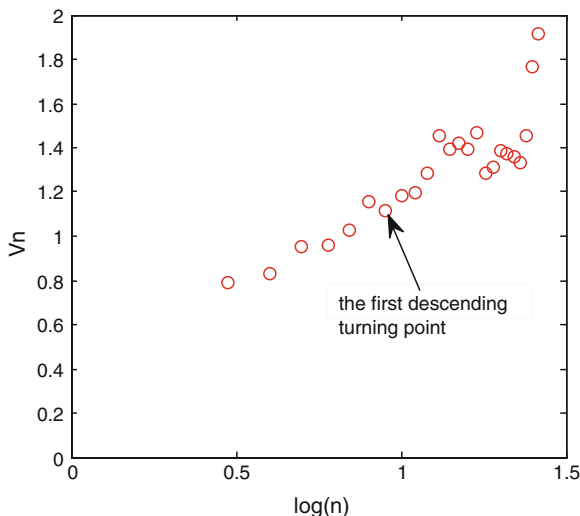
From the other visual angle, we study the time series pattern of traffic flow on the accident section by Hurst exponent (H for short). The more H diverges from 0.5 and approaches to 1, the more regular and persistent there will be in the time series. When H is closer to 0.5, the time series will be more noise and fluctuation. And the time series are deemed to be anti-persistent when H descends to 0.

In our case, we use the process of rescaled range analysis [15, 16] to acquire the H and the V -statistic of the time series. V -statistic is used to identify the length of non-periodical cycle. As displayed in Fig. 3, the consequence is that the H of the whole period of traffic flow on the accident section is 0.8207 with $R^2 = 0.98$. Therefore, traffic flow on the accident section does not obey the random walk but reveals long-term correlation and regular pattern.

Otherwise, from Fig. 4 we can get that the V -statistic increases with time point $\log(n)$ in an accelerative trend, which indicates that the length of non-periodical cycle is far beyond the whole period of 260 min. However, we may estimate from Fig. 2 that there exists a short-term cycling period in the traffic flow, since the curve displays some kinds of periodic variation. A closer inspection exposes that the curve of V_n versus $\log(n)$ begins to shake after n has arrived at 8 in Fig. 4. And $n = 8$ is the first descending turning point, indicating that the cycling period is about 40 min.

In brief, the general law of the time series of traffic flow on the accident section shows both stability and fluctuation features, and there is an obvious fluctuation in some short stages. From long-term perspective, the traffic flow is fluctuant and correlated, and the cycling period is about 40 min.

Fig. 4 Plots of V-statistic of traffic flow on the accident section versus $\log(n)$



4 Complex Network Analysis on the Time Series of Traffic Flow on the Accident Section

Consider a traffic flow series y_t with a length of N . We can convert the time series into complex network according to the visibility algorithm [5]. If there is a straight line that connects the data points in the vertical bar chart of the time series, provided that this “visibility line” does not transect any intermediate data height. More formally, a complex network is acquired from a time series according to the following visibility criterion [5]: two arbitrary data (t_a, y_a) and (t_b, y_b) where $y_a, y_b > 0$ in the time series have visibility, and consequently become two vertices in the associated graph, if any other data (t_c, y_c) such that $t_a < t_c < t_b$ fulfills

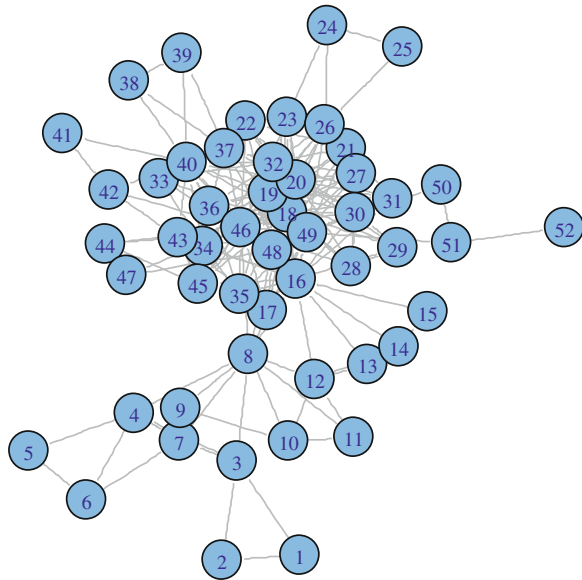
$$y_c < y_a + (y_b - y_a) \frac{t_c - t_a}{t_b - t_a}$$

As shown in Fig. 5, the time series of traffic flow on the accident section is converted into a complex network using the algorithm introduced above. We can get the statistic features of the original time series by exploring some topologic characteristics of the complex network with 52 vertices and 209 edges.

In this research, we used eight statistical indicators to study the complex network, which are the average degree, accumulative degree distribution, the average clustering coefficient, average path length, diameter, the average values of clustering coefficients of vertices with degree k , the Pearson’s correlation coefficient, and nearest neighbors average connectivity.

The degree is a significant characteristic of a vertex [17]. Based on the degree of the vertices, it is possible to obtain many measurements for the network [18].

Fig. 5 Network mapped from the time series of traffic flow on the accident section



We can research the structure of the constructed network by using the average degree of network $\langle k \rangle$ and degree distribution [19]. For reducing the noise, we research the accumulative degree distribution. In our case, the $\langle k \rangle$ of the constructed complex network is 8.04. Figure 6 shown that the accumulative degree distribution for the constructed network obeys a power law $P(k) = 1.25 k^{-0.65}$ with $R^2 = 0.83$. Therefore, the constructed complex network is a scale-free network.

So the time series of traffic flow on the accident section shows fractal characteristics. The consequence verifies the fact that the power-law degree distribution is related to fractal, which has been mightily discussed recently [5, 6, 9–11, 20–23].

The average clustering coefficient $\langle C \rangle$ and average path length L are the important conceptions to depict the statistical characters of the associated network transferred from time series. In our research, the $\langle C \rangle$ of constructed network is 0.72, the L of constructed network is 2.9. Figure 7 displays the law of the average path length grows with total number of vertices in the complex network.

The fact that the constructed complex network has a large clustering coefficient and a small average path length L increases with N in the logarithmical pattern, which confirms the small-world phenomenon, namely the complex network is a small-world network.

From that we can see there is a tight connection between the vertices even they are located far away from each other, since there are visibility lines between the corresponding original data points in the time series. Therefore, it can be deduced that there is a certain relation between different periods of time range affected by the traffic accident. In other words, it is not random or no connection between the past and the future in the time series of driver behaviors.

Fig. 6 The accumulative degree distribution of the constructed complex network

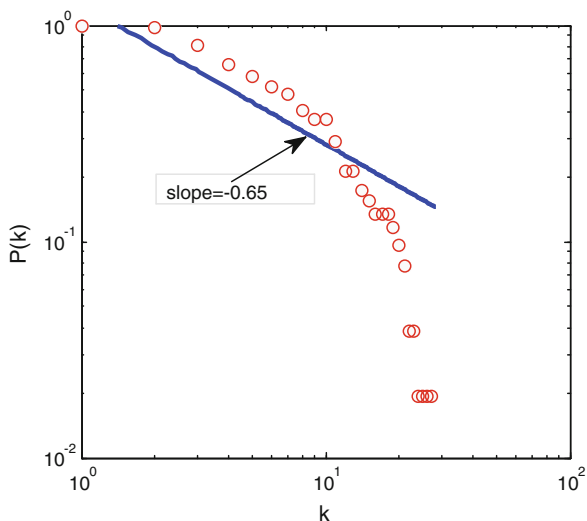
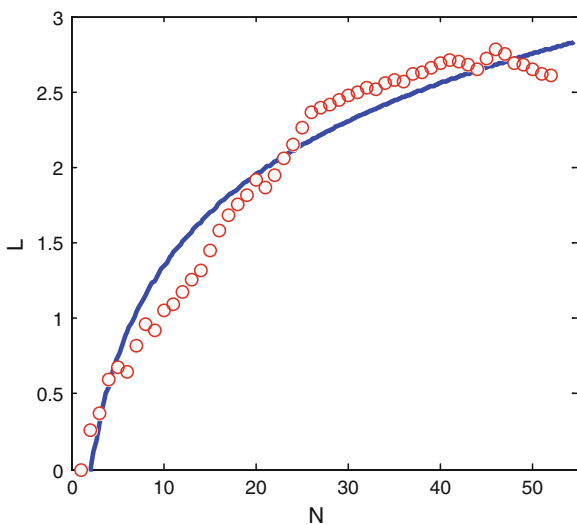


Fig. 7 The average path length grows with the total number of vertices in the network in the logarithmical pattern



Diameter of network is basic conception to depict the statistical features of the network. $\bar{C}(k)$ is the average values of clustering coefficients of vertices with degree k . It can be calculated as follows:

$$\bar{C}(k) = \langle c/k \rangle = \sum_{i=1}^n C_i/n$$

The complex network is considered to be hierarchically constructed if $\overline{C}(k) \propto k^{-\alpha}$.

The diameter for the constructed complex network is 8. Figure 8 shows the pattern of the $\overline{C}(k)$ decreases with k , we can derived that it obeys $\overline{C}(k) = 0.70k^{-0.24}$ with $R^2 = 0.99$.

So the complex network which converted from the time series of relative velocities has a hierarchical structure. The result means that if a vertex in the complex network has a larger degree, its neighbors do not tend to connect with each other. These vertices are the hub vertices in the scale-free network.

The hub vertices are corresponding to the extreme data points that have relatively greater observations in the time series than their directly connected and even unconnected neighbors. For instance, vertex 16 has a comparatively high degree $k = 21$ and a low clustering coefficient $C = 0.30$, and the relative velocity of the corresponding time point is 80 much larger than the value of relative velocities of its neighbor vertices. The relative velocities are 68, 69, 61 on the time point before 13:45 and 76, 75, 70 after 13:45 respectively. Correspondingly, vertex 16 has many neighbors in the network which are separated into two parts and connected with each other with a small probability. Therefore, it can be concluded that some extreme relative velocities will be shown in the homogeneous flow on such a pattern.

Recently, it is often interesting to check for correlations between the degrees of different vertices, which have been discovered to play an important role in many structural and dynamical network properties [24]. The most natural approach is to consider the correlations between two hub vertices in a scale-free network. A way to determine the degree correlation is by calculating the Pearson’s correlation coefficient of the degrees at both ends of the edges [25]:

$$r = \frac{M^{-1} \sum_{j > i} k_i k_j A_{ij} - [M^{-1} \sum_{j > i} \frac{1}{2} (k_i + k_j) A_{ij}]^2}{M^{-1} \sum_{j > i} \frac{1}{2} (k_i^2 + k_j^2) A_{ij} - [M^{-1} \sum_{j > i} \frac{1}{2} (k_i + k_j) A_{ij}]^2}$$

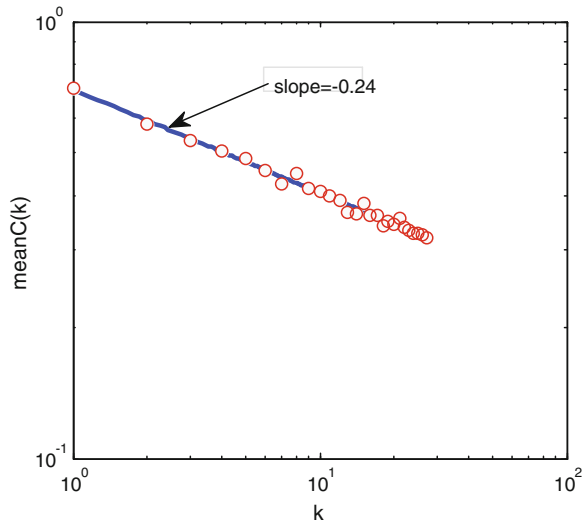
where M is the total number of edges in the network and A_{ij} is the element of the adjacency matrix of the network. The k_i and k_j are the degrees of the hub vertices at the ends of the edge. If $r > 0$, one can argue that the network is assortative; if $r < 0$, the network is disassortative; for $r = 0$, there are no correlation between hub vertices degrees.

The correlation of degree between one vertex and its nearest neighbors can be measured by the quantity of nearest neighbors average connectivity [26]:

$$\langle k_{nn} \rangle = \sum_{k'} k' p(k'/k)$$

where $p(k'/k)$ stand for the probability of a vertex with degree k connecting to a vertex with degree k' . $\langle k_{nn} \rangle$ can be used to research the relation between the degree of a certain vertex and the average of its nearest neighbors.

Fig. 8 The average value of the clustering coefficients decreases with the degree



The r of the complex network is 0.112. Figure 9 shows that the relation between $\langle k_{nn} \rangle$ and $\langle k \rangle$ in the constructed network. Figure 10 displays the relation between the vertex degree in the network and the average relative velocity in the time series. Obviously, they are all positively correlated.

The value of r means the network is assortative mixing with the hub vertices being attractive to each other, namely the vertices with high degree tend to link with the vertices also having high degree. The fact that $\langle k_{nn} \rangle$ and k are positively correlated implies that the larger degree a certain has, the larger average degree of its neighbors is. The relation between k and the average relative velocity verifies that the vertices with larger degree correspond to the original data points with larger value.

The clustering phenomenon of the hub vertices in the complex network means that the extreme data points in the time series appear in the form of group, in other words, a faster relative velocity is always accompanied with other faster velocities. Consequently, there are some unimpeded periods in the time range affected by the traffic accident. For an example, from 13:10 to 14:00 with an average relative velocity of 73.45.

To summarize, the complex network converted from the relative velocities time series are scale-free, have the small-world effect, and are hierarchically constructed. The original data time series are verified to have a fractal feature, and there is a tight relationship among the extreme data points. Furthermore, the faster relative velocities are appearance in the form of group.

Fig. 9 Plots of nearest neighbors average connectivity versus degree

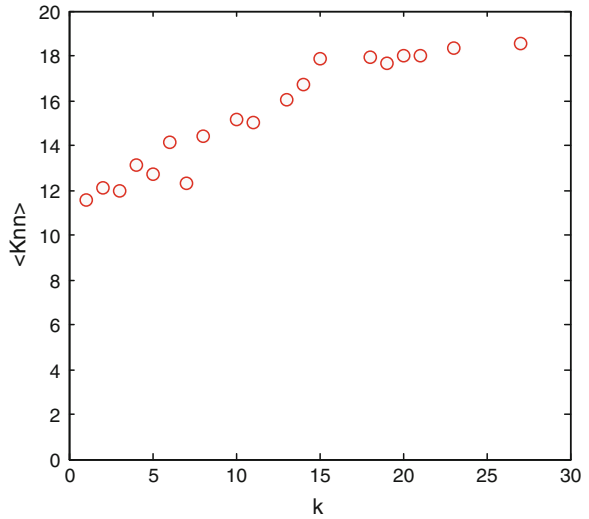
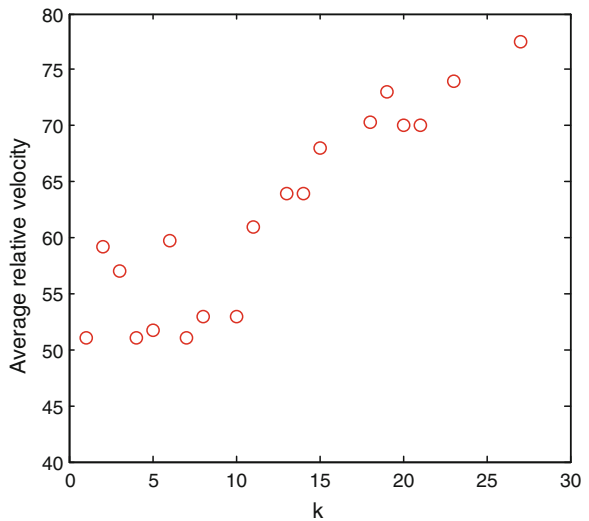


Fig. 10 Plots of the vertex degree versus the average relative velocity



5 Conclusions and Prospect

Traffic flow on road sections changes quickly. Because it affected by many unexpected factors. In our study, there was a traffic accident happened on the road section, traffic flow on the accident section is investigated from two different perspective.

First, the general law of the time series of traffic flow on the accident section is researched by the method of statistical and rescaled range analysis. The

consequence is that the mean value, standard deviation, Hurst exponent, and cycle length of traffic flow on the accident section confirm that the time series pattern shows both stability and fluctuation features, and the cycling period is about 40 min.

Second, the complex network converted from the time series using the visibility algorithm is studied by complex network theory. The result indicates the constructed complex network is a scale-free network. It can conclude that the time series displays fractal characteristics. The complex network is a small-world network, and there is a tight connection between data points. The complex network has a hierarchical structure. Furthermore, the relation between the degree of one vertex and degree of its neighbors, the relation between the vertex degree and the average relative velocity prove that the high relative velocities are inevitably appeared in the form of group.

The method and the conclusions of this paper may be helpful for analysis the road section traffic flow which is influenced by other special circumstances such as traffic control, large-scale activities, heavy weather, and so on. And the consequence of the analysis may guide making specific induced information on variable message sign. In addition, our study may enrich the research of the relation between the time series of traffic flow and complex networks. When the accumulative degree distribution of the constructed complex network obeys a power law, the time series is proved to have fractal feature. And how to use the constructed complex network to distinguish different types of fractal series is worth further explore.

References

1. Zhang J, Small M (2006) *Phys Rev Lett* 96:238701
2. Zhang J, Luo X, Nakamura T, Sun J, Small M (2007) *Phys Rev* 75:016218
3. Xu X, Zhang J, Small M (2008) *Proc Natl Acad Sci USA* 105:19601–19605
4. Zhang J, Sun J, Luo X, Zhang K, Nakamura T, Small M (2008) *Phys D* 237:2856–2865
5. Lacasa L, Luque B, Ballesteros F, Luque J, Nuno JC (2008) *Proc Natl Acad Sci USA* 105:4972–4975
6. Lacasa L, Luque B, Luque J, Nuno JC (2009) *Europhys Lett* 86:30001–30004
7. Plerou V, Gopikrishnan P, Rosenow B, Amaral LAN, Stanley HE (1999) *Phys Rev Lett* 83:1471–1474
8. Onnela JP, Chakraborti A, Kaska K, Kertesz J (2002) *Eur Phys J B* 30:285–288
9. Luque B, Lacasa L, Ballesteros F, Luque J (2009) *Phys Rev* 80:046103
10. Liu C, Zhou W, Yuan W (2010) *Phys A* 389:2675–2681
11. Elsner BJ, Jagger TH, Fogarty EA (2009) *Res Lett* 36:L16702
12. Yang Y, Wang J, Yang H, Mang J (2009) *Phys A* 388:4431–4437
13. Ni XH, Jiang ZQ, Zhou WX (2009) *Phys Lett A* 373:3822–3826
14. Lasaca L, Lueque B, Lueque J, Nuno JC (2009) *Europhys Lett* 86:30001
15. Hurst HE (1951) *Trans Am Soc Civ Eng* 116:770
16. Yoon SM, Kang SH (2008) *J Korean Econ* 9:403
17. Dorogovtsev SN, Mendes JFF (2004) *arXiv:cond-mat/0404593v4*
18. Da Costa LF, Rodrigues FA, Travieso G, Villas Boasa PR (2007) *Adv Phys* 56:167–242

19. Albert R, Barabasi AL (2002) *Rev Mod Phys* 74:47–97
20. Song CM, Havlin S, Makse HA (2005) *Nature* 433:392
21. Goh KI, Salvi G, Kahng B, Kim D (2006) *Phys Rev Lett* 96:018701
22. Kim JS, Goh KI, Kahng B, Kim D (2007) *New J Phys* 9:177
23. Gallos LK, Song CM, Makse HA (2007) *Phys A* 386:686
24. Maslov S, Sneppen K (2002) *Science* 296:910–913
25. Newman MEJ (2002) *Phys Rev Lett* 89:208701
26. Pastor-Sarorras R, Vazquez A, Vespignani A (2001) *Phys Rev Lett* 87:258701

The Hinterland Spatial Structure Evolution of Competitive Port Based on ArcGIS

Jiafang Zhuang and Siqin Yu

Abstract Contention for hinterland is the main component of port competition. To competitive ports in the same port cluster, study of hinterland is more important. By using breakpoint model and Huff model with ArcGIS tools, the article is carried on research of hinterland areas changing between ports of Shanghai and Ningbo. The research has shown that hinterland areas of Ningbo port was gradually expanding, while less hinterland cities were selecting Shanghai port from 1990. Soft power of a port is becoming an essence attracting hinterland cities. The improvement of traffic accessibility and the decline of distance impedance coefficient between ports and hinterland cities will bring positive effects to dominant ports. In order to adopt targeted strategy and seize competitive advantage, ports are positive to define competitive front- hinterland cities in spatial structure evolution.

Keywords Competitive port · Hinterland · Spatial structure · ArcGIS

1 Introduction

Contention for hinterland is the main component of port competition. There are competitions among port clusters, among ports in a cluster and among port enterprises in a port as well. Study on port hinterland and its spatial structure evolution helps contribute to the reasonable programming and distribution of the urban areas and promote the overall level of regional economy. It's also an important basis for determining the port sizes and stages of development. In the perspective of port development, study on port hinterland and its spatial structure

J. Zhuang · S. Yu (✉)

Economics and Management School, Shanghai Maritime University, Shanghai, China
e-mail: jinhaichen2005@163.com

evolution also helps contribute to understand the strengths and weaknesses in port operating. So that the enterprise can be clear in position and promote its competition ability. To competitive ports in the same port cluster, such study is more important. ArcGIS as a comprehensive, scalable GIS platform, which provides Spatial query and analysis, spatial information extraction, Spatial Comprehensive analysis, data-mining and knowledge discovery, modeling, and other functions, provides strong and powerful support for the science to efficiently analyze and explain the relationship between geographical characteristics and spatial pattern [1]. This paper intends to study the hinterland spatial structure evolution based on ArcGIS.

2 Method

The word “hinterland” derives from German, meaning the land lying beyond. It refers to the collection and distribution area around the port. Hinterland is the zone around the port for cargo gathering and distribution and passenger coming from and going to. It’s the basis of existence and development for ports. In 1934, the German scholar E. A. Kautz published “Das Standortproblem der Seehäfen,” which was a prelude to study on the relationship between port and hinterland. After that all kinds of qualitative and quantitative research and study were constantly emerging, and they were gradually deepening along with the development and changes in the world economic technology and shipping.

In order to find the demarcation boundary of a particular port hinterland area, domestic and foreign scholars research from the regional economy [2], spatial structure, economic geography, and other multidisciplinary perspective. Among which the administrative divisions according to the administrative district is the most traditional method. The methods on the basis of geographical range are diagram method (including bisecting angle and vertical line method), layers method and pivot and ligament method. The methods on the basis of freight volume are traffic of goods hinterland method and location quotients technique. There are also breakpoint method and Newtonian rheological model on the basis of the gravitational law, etc. [3]. Among them, the quantitative analysis method developed on the basis of W. J. Reilly’s “The law of retail gravitation” by applying the idea of gravitational law is more applicable to the study on hinterland of competitive port [4].

2.1 Breakpoint Method

Breakpoint method is the way P. D. Converse developed on the basis of W. J. Reilly’s “The law of retail gravitation”, which is used to divide the attracting scope between two cities. It shows that city hinterland areas are decided by the

city’s size and the distance between the adjacent two cities. To divide the attracting scope between two cities is actually to form a center city attracting scope by finding the balance point of the two cities, namely, the so-called breaking point or the market boundary position, and connecting the breaking point between the center of the city and the surrounding areas with a smooth curve.

Extend the city attraction to the surrounding areas to the port attraction to the hinterland in the analysis of port hinterland problems. The area of the port hinterland can be determined by finding the breaking point and the made of the breaking point area.

Set X as the breakpoint location, $R_{ij} = r_{ix} + r_{jx}$, available formula is:

$$r_{ix} = \frac{R_{ij}}{1 + \sqrt{P_j/P_i}} \tag{1}$$

In the formula: Where r_{ix} is the distance between the breaking point and the port; R_{ij} is the distance between the two ports; P_i and P_j is the size of the port i and j . It can be seen, there are two aspects of factors affecting port attraction: one is the port size, the larger size, the larger attraction to the surrounding hinterland; second is the distance, as the distance increases, the port attraction weakened accordingly.

2.2 Huff’s Model

The law of probability gravitation proposed by the American scholar D. L. Huff on the basis of W. J. Reilly’s The law of retail gravitation also applied the idea of gravitational law as the basic guiding ideology. But it’s more general, has more extensive applicability of solving the problems. Huff’s model [5] described as:

$$P_{ij} = U_j / \sum_{k=1}^n U_k. \tag{2}$$

Here P_{ij} is the choice probability of consumer i in store j ; U_j and U_k , respectively is the utility of choosing store j and k ; k is all possible choices ($k = 1, 2, \dots, n$). Obviously, larger utility and greater attraction a store own, the probability of consumers shopping in the commercial space is greater. On the contrary, less attraction a store own, the probability of consumers shopping in the commercial space is less.

When the choice of hinterland to port is thinking by analogy with the consumer’s choice to the store, space gravity of consumption behavior can be extended to space gravity of ports which is applied to the analysis of port hinterland area [6]. Hinterland area can be served based on the port or the choice the hinterland will make to the port conforms to the same principle: be inversely

proportional to the distance between port and hinterland, whereas be proportional to the port attraction to the hinterland. Therefore, use the Huff's Mode and further decomposed it into:

$$P_{ij} = \frac{U_j}{\sum_{k=1}^n U_k} = \frac{S_j d_{ij}^{-\beta}}{\sum_{k=1}^n (S_k d_k^{-\beta})}. \quad (3)$$

In this formula, P_{ij} is the choice probability of the hinterland city i in port j ; U_j and U_k , respectively is the utility of choosing port j and k ; k is all possible choices ($k = 1, 2, \dots, n$). Utility U_j is thought to be associated with port j 's influence S_j and the transportation distance d_{ij} between port and hinterland, β is the distance friction coefficient. In hinterland city, the denominator in the formula is the same for all the ports j , thus the bigger numerator, the larger probability. This means that, the port hinterland area can be determined as long as the largest collection of numerator $S_j d_{ij}^{-\beta}$ was found. Namely the port hinterland area is made up of the maximum choice probability of a port hinterland, and the area is a continuous distribution surface of probability.

3 Empirical Analysis

3.1 The Research Object and Data

The article chooses ports of Shanghai and Ningbo as the object. Shanghai and Ningbo is located in eastern coastal of China. The geographical space distance of them is 180 km on the road. Two harbors are both among the world's port ranks at present. Most of the lands to the hinterland are cross or jointly owned. With the rapid development of the two ports, the battle of hinterland is becoming increasingly fierce. Quantitative analyzing of the hinterland areas changing between the two ports and identifying different hinterland cities' attractiveness to these two ports in common hinterland area helps contribute to making rational decision to the ports.

Port data used in this paper collected from China Ports Year Book [7]. Considering the existed difference between these two ports' Commodity structure, as well as the core of competition of the hinterland is more correlated with the container goods, so here chooses the container throughput rather than the port throughput as the indicator reflecting the port attraction S_j [8]. Data of the selected year, from 1990 to 2005 selected every five years interval data, from 2006 to 2012 per year as interval of selected data. Use the road maps of Jiang Su, ZheJiang, Shanghai, An Hui provinces in respective year for port and hinterland city distance, use ArcGIS for vectorization processing, and use the Network Dataset function to obtain the shortest transport distance between the port and hinterland

cities [9]. According to van truck road condition set the speed to 80 km/h. The choice of hinterland cities for the research object is: taking Shanghai and Ningbo as the center, choosing the cities within the 400 km circle of the two cities together. For convenience, the distance friction coefficient β is set to 2.

3.2 *The Hinterland Spatial Structure Evolution of Port*

When the attractiveness to a hinterland city's choice of Shanghai port or Ningbo port is equal, namely the probability was 0.5; there appears the so-called breaking point. The probability fracture surface formed by the connection of breaking points is the boundary of the two port hinterland areas. The following figure shows the hinterland areas changing of the two ports in 1990, 2000, and 2012. The blue base area is the hinterland area taking Shanghai port as the center; above the harbor as the center of the hinterland, the yellow base area is the hinterland area taking Ningbo port as the center, the red curve is the boundary line dividing the hinterland areas of these two ports in the probability of 0.5. There are color differences from deep to shallow layered color in various base color, color gradient with 10 % probability for each division, the deeper the color refers to the areas in higher probability. Based on this, the hinterland cities in the dark blue area have the highest probability to choose Shanghai port. Accordingly, with the blue color becomes shallow, the probability of the hinterland cities in the shallow blue areas choosing Shanghai port will gradually decline. Figures 1, 2 and 3, respectively show the hinterland area of Shanghai and Ningbo two ports in 1990, 2000, and 2012.

It can be seen from the figure, the changing of hinterland areas within 400 km range of the two ports presents the following characteristics in more than 20 years: (1) Shanghai port's attractiveness to the hinterland cities dropped significantly. In 1990, the hinterland cities (in the dark blue area) had 90 % possibility of selecting Shanghai port account for nearly 90 % of the object cities of the study. That is to say, Shanghai is the only option of the hinterland city for provinces—Jiang Su, ZheJinag, and An Hui. In 2000, the hinterland cities had 90 % possibility of selecting Shanghai port that has been narrowed down to 50 % of the object cities of the study. By 2012, the number of hinterland cities selecting Shanghai port as their inevitable choice further reduced. More hinterland cities demonstrated hesitation against the selecting of Shanghai port. It can be seen from the figure, the hinterland cities have 50, 60, or 70 % probability of selecting Shanghai port gradually increased. (2) Hinterland areas of Ningbo port was gradually expanding. The hinterland of Ningbo port in 1990 generally failed to cross out Ningbo, namely the Ningbo port container cargo carrier is basically limited to Ningbo's own case. By 2000, the scope of the hinterland cities to select Ningbo port was larger, but the area was still limited. By 2012, while Ningbo port had the advantage of attraction in the southern hinterland cities in ZheJiang, the scope of its hinterland area has obviously expanded to western ZheJiang, and the hinterland cities considered trying to select Ningbo port continues to increase.

Fig. 1 Hinterland areas of ports of Shanghai and Ningbo in 1990

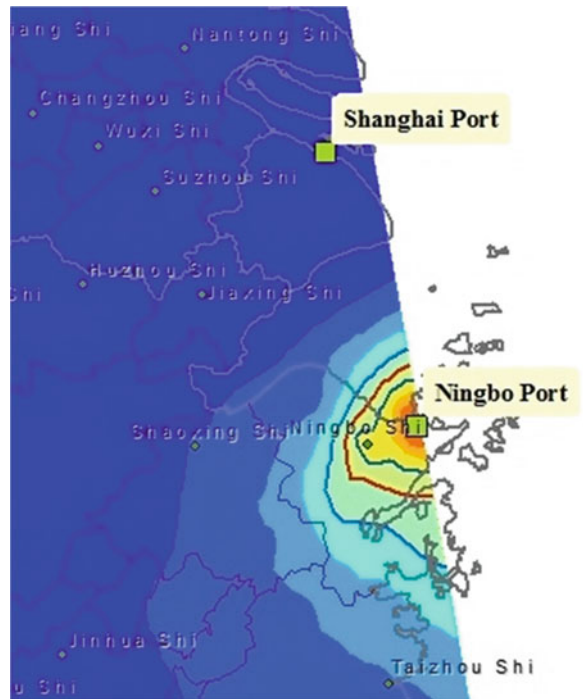


Fig. 2 Hinterland areas of ports of Shanghai and Ningbo in 2000

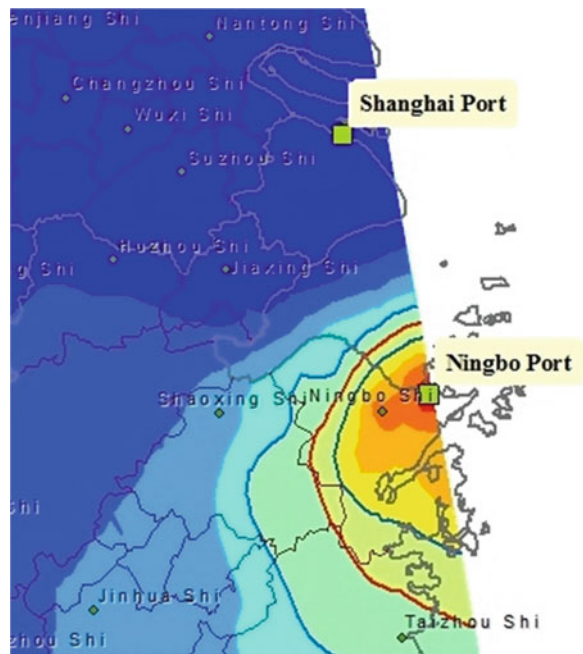
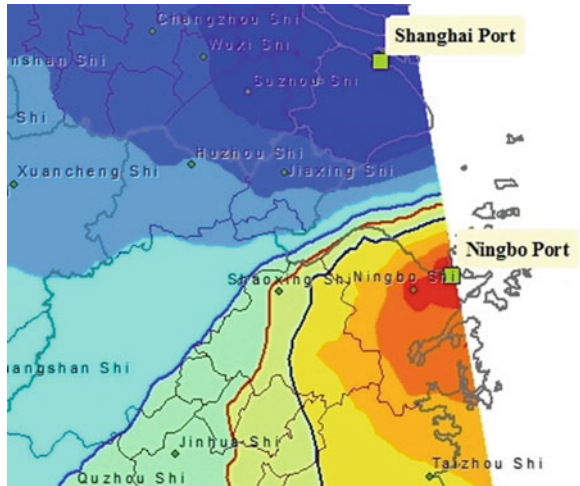


Fig. 3 Hinterland areas of ports of Shanghai and Ningbo in 2012



Superimpose the mapping results of calculation of the selected year data onto a picture, the gradually changing process of the hinterland areas between ports of Shanghai and Ningbo from 1990 to 2012 can be seen. Curve in Fig. 4 below indicates the year, shows as the year two ports’ hinterland boundary, namely the probability for the 0.5 lines.

As a competitive port owns the common land to the hinterland, competition between ports is the most direct and intuitive in the hinterland competition. For competitive ports, the selecting of the hinterland cities is a process of either/or choice, is the choice which the probability of a port hinterland city is higher means that the possibility of the supply of goods to rivals is lower. Therefore, firmly grasp the hinterland cities means the competition victory.

The promotion of the competitiveness of the port and the port city’s influence is the important driving force for the port to win the competitive advantage. When the hinterland face multiple choice of port, the final choice is related to the comprehensive evaluation results of alternative port directly. This comprehensive evaluation is no doubt related to the geographical location, natural conditions such as ports, and hardware facilities, etc. But with the improvement of the condition of transportation by land and the propulsion of sea-rail combined transport and Door to Door service, etc., there is a corresponding increase in attention on the factors of port scale, management level, the quality of service, etc. [10]. As an important indicator to reflect the scale of port, throughput changes show the important trend of port development. In this study, what behind the hinterland expanding of Ningbo port is the average rate of increase of the container throughput of Ningbo port. It’s about 36 % between 1990 and 2012. Accordingly, the average rate of increase of the container throughput of Shanghai port is about 22 %. Compared with the large container supply of goods brought by the average increase of about 25.4 % of the imports and exports in Jiang Su and ZheJiang provinces at the same

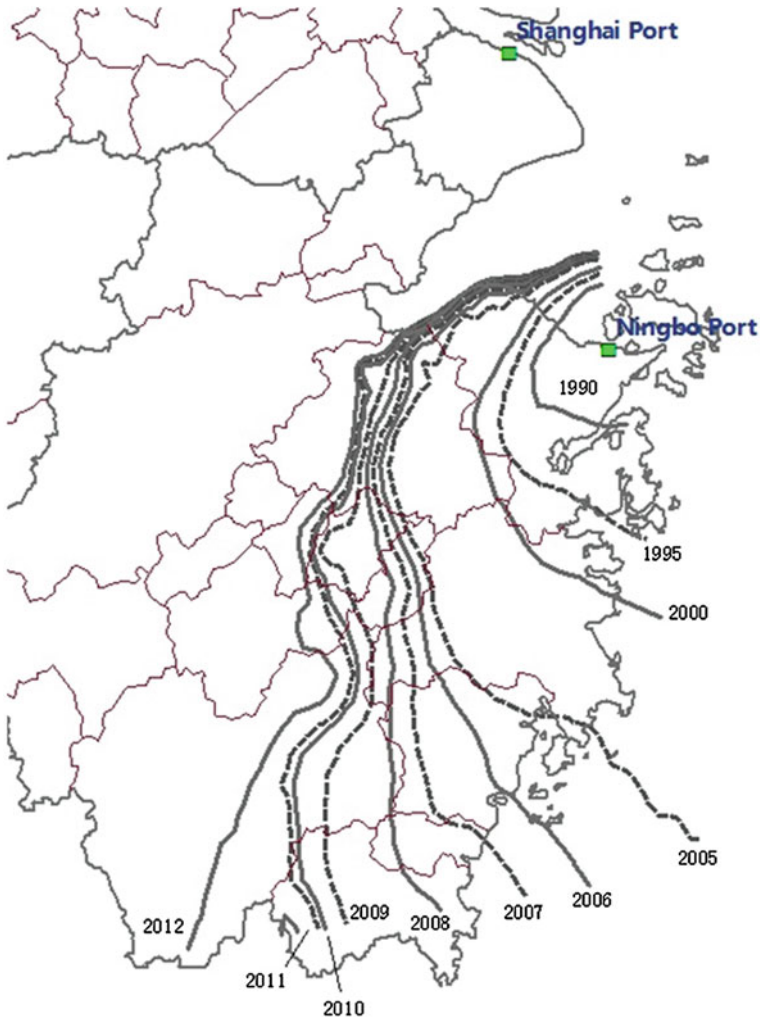


Fig. 4 Hinterland areas changing between ports of Shanghai and Ningbo from 1990 to 2012

period, Ningbo port obviously gained a larger share in the “big cake.” For the competition among ports in a cluster, one must face problem as: the switching costs of hinterland city transforming port selection is relatively low, which leads to more hinterland cities choosing to give up the original port turned to higher probability of its rival. So how to enhance port soft strength in the areas of management and service level, and increase Flexible adhesive force between port and hinterland cities is particularly important to enhance the comprehensive competitiveness of the port.

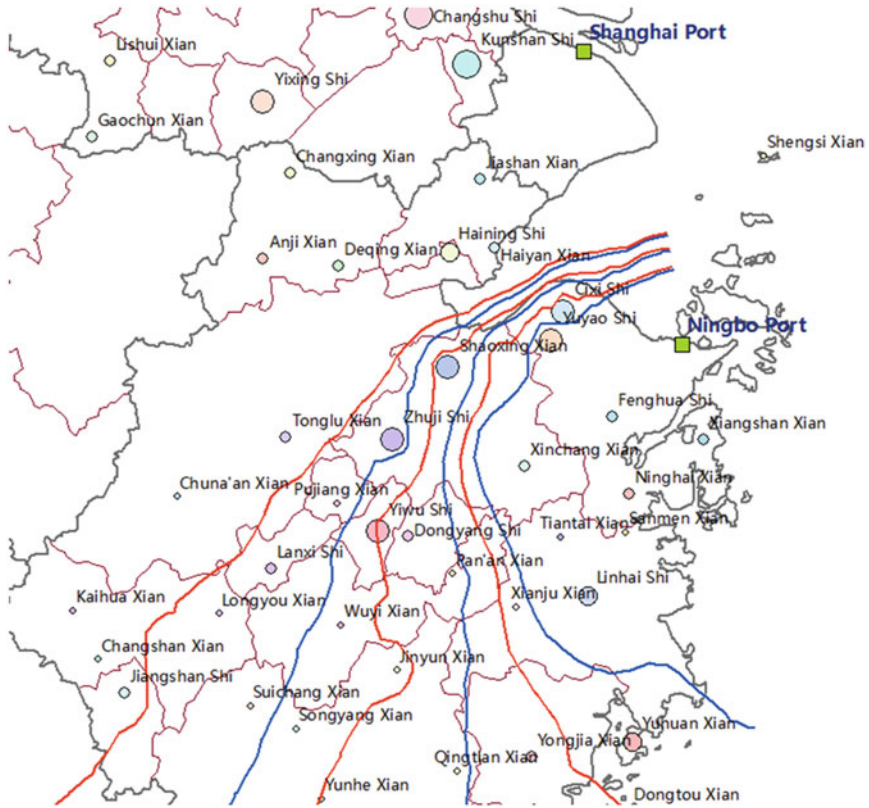


Fig. 5 The probability surface of 0.4 and 0.6 about ports of Shanghai and Ningbo from 2008 to 2012

The construction of transport infrastructure and the network optimization still have an important impact on port selection, and the ports own competitive advantage benefit more from it. As the most basic factors affecting port selection, time factors, and cost factors can never be ignored. The hinterland cities will avoid making detour port choice behavior itself is a very good description. In this study, the hinterland cities closer to Shanghai has the highest probability of selecting Shanghai port. And the suppliers closer to Ningbo in spatial distance gradually developed in Ningbo port after abandoned in Shanghai port is also based on this reason. In addition, it should be pointed out, in order to simplify, the distance friction coefficient β is set to 2 in this study model. but in fact, for any β model itself can be deduced a result: to reduce friction coefficient is to larger the hinterland scope of the ports with big port city's influence, namely the ports own competitive advantages will show more obvious advantages by the improvement of traffic accessibility and the decline of distance impedance coefficient between ports and hinterland cities. In this sense, the winner between the ports of Shanghai and Ningbo will gain more benefits from the Hangzhou Bay Bridge opened to traffic.

The hinterland spatial structure evolution of competitive port is a gradual process, having a clear grasp of the hinterland cities in competitive edge is conducive to the port to formulate effective competition strategy. Normally, the common hinterland is a relatively abstract space range, difficult to refer to a certain or some specific hinterland city. The probability surface reflecting hinterland city area in this study provides intuitive basis for finding frontier competition hinterland city. View the probability of curved surface of the selection of the Shanghai port and Ningbo port from 2008 to 2012 between 40 and 60 %, the hinterland city area in the period in two ports' competitive edge can be obtained. Then consider the economic development of the hinterland city in that period, especially the development of foreign trade and other conditions, the hinterland cities such as Shaoxing, Zhuji, Yiwu, Dongyang, and Lanxi shown in Fig. 5 that are both attractive to Shanghai port and Ningbo port can be selected. The ports can make targeted strategic choice on the basis of this. Ningbo port, for example, got the possession of the hinterland cities Jinhua, Yiwu, and Quzhou after 2010 through the establishment of dry port strategy.

4 Conclusion

By using ArcGIS tools, the article is carried on research of the hinterland areas changing among ports in a cluster by empirical analysis, used the competitive ports of Shanghai and Ningbo as example. The research has shown that ArcGIS can be well applied to the hinterland spatial structure evolution of the port. While the adoption of the ArcGIS provides an accurate network basic information for the research, its various mapping provides intuitive display effect for the conditions in the scope of port hinterland and its evolution process. The adoption of Breakpoint Method and Huff's model that applied the idea of gravitational law as the basic guiding ideology, on one hand, conforms to the common sense of the choosing probability of a port "be inversely proportional to the distance between port and hinterland, whereas be proportional to the port attraction to the hinterland." On the other hand, it also avoids the data requirements such as the volume between port and hinterland city that are not easy to complete for.

Hinterland is the most basic resource for the survival and development of the port, as a common land to the competitive ports, contention for hinterland is lifeblood. Therefore, grasping the hinterland spatial structure evolution has the vital significance to the competitive ports. In the situation that the time and cost factors is relatively weak, soft power of a port such as port scale, management level, service quality, port image is becoming an essence attracting hinterland cities. The improvement of traffic accessibility and the decline of distance impedance coefficient between ports and hinterland cities will bring positive effects to dominant ports. In order to adopt targeted strategy and seize competitive advantage, ports are positive to define competitive front- hinterland-cities in spatial structure evolution.

After the text edit has been completed, the paper is ready for the template. Duplicate the template file by using the Save As command, and use the naming convention prescribed by your conference for the name of your paper. In this newly created file, highlight all of the contents and import your prepared text file. You are now ready to style your paper; use the scroll down window on the left of the MS Word Formatting toolbar.

References

1. Wang F (2009) Quantitative methods and applications based on GIS. The Commercial Press, Beijing, pp 23–25
2. Yang W, Liang J (2000) Advanced economic geography. Peking University Press, Beijing, pp 78–79
3. Dong X, Wang R, Han Z (2010) Analysis on the evolution of spatial structure of Port Hinterland. *Econ Geogr* 30(11):1761–1766
4. Weng Q, Chen P (2009) Domestic and foreign research review on Port Hinterland Economic. *Shipping Manage* 31(2):21–25
5. Jiang X, Zhang P (2013) Analysis of the evolution of Huff Model based on the Liaoning Coastal Port Hinterland. *Geogr Sci* 33(3)
6. Wang J, Yang Z, Lu C (2005) Discussion on two kinds of new methods of Port Hinterland Division. *Navig China* 64(3):57–61
7. Chinese Ports Yearbook Editorial Office (1990–2011) China ports year book. China's Ports, Beijing
8. Liu W, Dong J, Xia X (2005) Study on the quantitative model and empirical analysis of Port Hinterland. *Mar Traffic Eng* (11):25–28
9. Gan G, Wang J (2005) Economic hinterland space application in the port service potential evaluation model. *J Grad Sch Chin Acad Sci* (22)6:364–370
10. Liu B, Zhu C, Che Q (2007) Spatial economic hinterland of port and its empirical research. *Econ Geogr* (6):904–909

Research and Implementation of a General Model for Agent Electronic Commerce Website

Xiaoling Xia and Niu Zhang

Abstract The electronic commerce has matured, including various forms. Nowadays, people not only participate in the native electronic commerce, but also join in the commerce from other countries. Owing to many causes, the electronic commerce among countries is difficult. Hence, the agent e-commerce websites appear. These agent websites can make people join in other countries' electronic commerce actions synchronously. The synchronous technology is the core that these websites have realized. This paper proposes a general agent model to achieve this kind of website, using data API or HttpClient to get the data in the foreign e-commerce websites assures the instantaneity of information and reduces the overheads of database. By modifying and optimizing the Web automatic testing tool—Selenium, the Web server can automatically complete shopping in the real electronic commerce websites in order to achieve the synchronous technology. The model has greater compatibility, generality, and stability.

Keywords E-commerce agent model · HttpClient · Selenium · RC synchronous technology

1 Introduction

As the e-commerce technology matures, the mode of e-commerce becomes more various. Various innovative concepts and creative products based on Internet technology are constantly being launched and a wide range of shopping mode

X. Xia (✉) · N. Zhang (✉)

School of Computer Science and Technology, Donghua University, Shanghai 201620, China
e-mail: sherlysha@dhu.edu.cn

N. Zhang

e-mail: zhangniu88@163.com

emerged on the Internet [4]. The form and number of the e-commerce site has been greatly enriched and the number of people involved in shopping online is also growing rapidly. In this case, people continue to try different new forms of e-commerce. In countries all over the world, they all have their own well-known and unique e-commerce sites, such as Alibaba, eBay, yahoo, etc. The domestic e-commerce website has been unable to meet the demand of the people to participate in e-commerce activities. Thus, people gradually began to try shopping online on aboard e-commerce site. And the group of user grows larger and larger. However, due to language barriers, it is difficult for a foreign bank account to pay and the mailing process is complex, so business is unwilling to bear the risk that the products are sent abroad, and many other objective factors can also result that people cannot shopping online fast and smooth cross-country.

In order to optimize the form of e-commerce, an agent for nonnational e-commerce website industry came into emerging. In this stage, there are following two agent ways applied widely: one is to commission through the line agency solely to make a purchase; the other one is to use a professional agent e-commerce website. The former one is less interactive and more complicated. We must communicate with the agency all the time, demanding real-time shopping online, having a tremendous impact on our shopping. The latter one gradually becomes the mainstream way because of the friendly interaction and convenient operation. People shopping on the foreign e-commerce site are as convenient as shopping on the domestic e-commerce site through the agency. The traditional way to agent an e-commerce website is by a Web-Crawler crawling target e-commerce website, which is synchronized to the agent e-commerce website. Through a proxy e-commerce sites, product information on the foreign e-commerce site can be visited by us. After selecting a product we want to purchase, the agent e-commerce website logs in the target of foreign e-commerce website page to bid for the product by analogizing the way of logging the browser. Finally, the information of success or failure for the purchase returns to us.

With enhanced Internet security, such approach gradually started to show a variety of drawbacks:

1. Some of the e-commerce websites will send user name and password by the front-end script encrypted to the server when users login. Analog browser login need to customize the corresponding encryption algorithm, which is often difficult to achieve;
2. The way of login by analog browser will be defined as hacking by some of the e-commerce website, resulting in failure to login the target site, and it can even cause that IP addresses get blocked and thus purchasers cannot bid for later operations;
3. In different e-commerce sites, the hidden field contained in the form is not the same in the submission of the form to purchase products. Detailed analyses are needed for different websites, so that the corresponding code written is versatile and not good, and error-prone.

To solve the above problem, this paper presents a model of a more versatile and stable agent e-commerce website. The model uses two alternative accesses to foreign e-commerce website information, translated automatically by the program, and then synchronized to the agent e-commerce website; only part information is stored in the agent e-commerce website database. People browse the latest information of the products, select, and make a purchase through agent e-commerce website. After receiving purchase products information, the agent e-commerce website automatically run real browser (such as Chrome, IE, etc.) through Selenium, jumping to the foreign e-commerce website, automatically performing all the processes of shopping online, and finally returning success or failure of the information. The site developed by the model is suitable for various types of agent e-commerce websites. It has solved the drawbacks of traditional methods previously mentioned. In addition, by modifying the Selenium tools and browser settings, it is possible to further reduce the information transmission delay.

2 JSON

Nowadays, lots of large websites are willing to share their data on the Internet and they provide open data API in order to make others acquire the data easily. One main format of the data is JSON. JSON (JavaScript Object Notation) is a lightweight data-interchange format. It is easy for humans to read and write. It is easy for machines to parse and generate. It is based on a subset of the JavaScript Programming Language, Standard ECMA-262 3rd Edition—December 1999. JSON is a text format that is completely language independent but uses conventions that are familiar to programmers of the C-family of languages, including C, C++, C#, Java, JavaScript, Perl, Python, etc. These properties make JSON an ideal data-interchange language [1].

JSON is built on two structures: object and array. The first structure is more widely used. It is an unordered set of name/value pairs. An object begins with { (left brace) and ends with } (right brace). Each name is followed by : (colon) and the name/value pairs are separated by (comma), i.e., {key1:value1, key2:value2}. In the process of data transmission, JSON is passed in the form of text. When we use JSON, we should consider parsing JSON object in each case. JSON has some good features: Self-Description, hierarchical structure, and it can be easily parsed. JSON is already a part of the JavaScript standard. Now most browsers support JSON perfectly.

3 HttpClient

The Hyper-Text Transfer Protocol (HTTP) is perhaps the most significant protocol used on the Internet today. Web services, network-enabled appliances, and the

growth of network computing continue to expand the role of the HTTP protocol beyond user-driven Web browsers, while increasing the number of applications that require HTTP support. Designed for extension while providing robust support for the base HTTP protocol, the Http Components are of interest to anyone building HTTP-aware client and server applications such as Web browsers, Web spiders, HTTP proxies, Web service transport libraries or systems, which leverage or extend the HTTP protocol for distributed communication [2].

Increasing number of Java applications need to access the network resource directly through the HTTP protocol. Although the `java.net` package in the JDK provides the basic functions to access to the HTTP protocol, but for most applications, the functions provided by the JDK library itself is not rich or flexible enough. `HttpClient` is a subproject under the Apache Jakarta Common to provide efficient, latest, feature-rich client programming toolkit supporting for the HTTP protocol, and it supports the latest version of the HTTP protocol and recommendations.

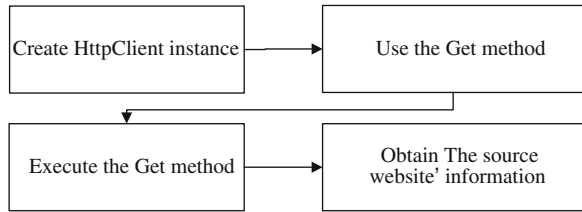
The `HttpClient` provides many functional components, very flexibly designed, easy to use and widely used. It implements all the methods of the HTTP, and it is used to achieve the GET method in proxy auction site. Using this method, we can get all the information of the corresponding page of foreign e-commerce website. First create an instance of `HttpClient`, and then choose to use the GET method to pass in the linking address. Then perform the GET method, and all the data will be available in the target page and releasing the link. The specific implementation steps are shown in Fig. 1.

The fundamental premise of agent auction site is that when people browse the product information, the latest information of the goods in the source e-commerce site can be displayed. It requires that the agent e-commerce website grab the latest data each time in response to the browser request. At this point, we can use the `HttpClient` GET method to grab the real-time data of the e-commerce site of the goods, display in the agent e-commerce website page and ensure as much information in real-time as possible.

4 Selenium

Selenium is an open source tool for Web application testing developed by Thoughtworks company [5]. Web application testing tool is the module used to control the tested Web application, simulate the manual test steps, and finish the test. Selenium runs the browser for testing directly and supports many browsers, like Chrome, Firefox, IE, etc. Selenium also supports automatic recording and automatic generation, so it is able to perform the system function tests excellently [6]. All the tests are run in the browser, just like one real user did it. From the perspective of end users testing the application, it makes the browser automatic compatibility testing possible. Selenium is easy to be applied and suitable for case scripts written by various programming languages.

Fig. 1 Procedures of HttpClient to obtain web data



Selenium Remote Control (RC) is a main project of Selenium; it can use a definite programming language to write the testing scripts, including Java, Javascript, PHP, Perl, C#, Ruby, and Python. In this paper, we write the scripts using Java. Otherwise, Selenium RC supports almost every browser. Selenium RC components two parts: Selenium Server and Client Libraries. Selenium Server launches and kills browsers, interprets, and runs Selenium commands passed form test program, and reports the results back to program. Selenium Server bundles Selenium-core and automatically injects into the browser. This occurs when scripts open the browser (using a client library API function). So Selenium-core (with its JavaScript commands) must be placed in the same origin as the auto scripts. We use Proxy Injection mode so that the Selenium Server acts as a client-configured HTTP proxy that sits between the browser and the auto scripts. It acts as a Web server that delivers the auto acts to the browser.

Client Libraries provide the supports that allow you to run Selenium commands from a program of your own design. A Selenium client library provides a programming interface (a set of functions) which run Selenium commands from your own program. The Client Library takes a Selenium command and passes it to the Selenium Server for processing a specific action; it also receives the result of that command and passes it back to your program. So in order to create an auto program you can simply write a program that runs a set of Selenium commands using a Client Library API.

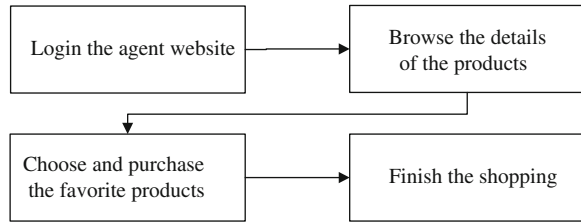
Selenium RC is great for testing complex AJAX-based Web user interfaces under a Continuous Integration system. It is also an ideal solution for users of Selenium IDE who want to write tests in a more expressive programming language rather than the Selenese HTML table format [3].

5 Implementation of Agent e-Commerce Site

The main function of the agent e-commerce website is to make people involve in the shopping online on aboard e-commerce sites. The procedure to participate in these activities through the agent sites is shown as Fig. 2.

First, register and login a personal account at an agent e-commerce website. Click on the links of the homepage to pages of different products, to get access to the newest and detailed product information. Then choose products you want to

Fig. 2 Procedure to achieve shopping online through the agent site



buy and confirm the purchase. When the website shows whether it's a successful purchase or not, it is the end of a transnational shopping online via agent e-commerce website.

In order to achieve the above process, we further research the technology on data API, HttpClient and Selenium. By integrating them, this paper proposes a kind of more versatile realization model of agent e-commerce website. In the process of the shopping online above, all the product information in the agent e-commerce website homepage, product categories page, and product details page, are acquired from the source e-commerce site. To the foreign e-commerce sites which supply data API, we can get their data in JSON format through the API. Then we parse and make them shown in the agent e-commerce website. To the other foreign e-commerce sites, we can use HttpClient crawl the data in the target e-commerce websites in real-time, synchronously update the data to the agent e-commerce website. These two methods effectively assure the instantaneity of the information. Meanwhile, the agent e-commerce website's database doesn't need to store a large number of product information or synchronously update the database. It greatly reduces the overheads of the database. When we get the data, the model use the translator API supplied by Microsoft Company to translate the data to specified language automatically. On the premise of guaranteeing data readability, we don't need expense extra manpower costs.

After viewing the product details, we will choose our favorite products and confirm to pay. At the moment, the user name (registered in the agent e-commerce website), the URL (products in original page of the source e-commerce site), the price, and the quantity are encapsulated and transferred to the agent e-commerce website's Web server. The Web server follows the predefined mapping rule to obtain the corresponding user name and password in the foreign e-commerce site. Then the server passes the previous URL and quantity, new user name and password to Selenium RC.

In the process of the agent e-commerce website to realize, there are some redundant functions in Selenium RC. In order to reduce the overhead of the deputy shopping's implementation and improve the performance of Web automatic test in the server, we simplify and optimize the Selenium RC tools:

1. The agent e-commerce website only need to use a kind of browser. The browser used in our system is Chrome, which involves less overhead. We have removed the codes support the other browsers in Selenium RC. Meanwhile, we

invoke the ChromeDriverServer driver in the server and prohibit Chrome loading the multimedia files. Finally, we disable Chrome auto saving password function and close all the plug-ins. With these above ways, Selenium RC is able to open Chrome and load every page more quickly. Otherwise, the agent e-commerce website only needs low-bandwidth. It is effective to ensure low latency of information transmission.

2. Selenium RC only supports the scripts written by Java program language. In this paper, all the system test scripts are written by Java, so we don't need to think over other program languages. Then we can further simplify Selenium RC. In the meanwhile, we encapsulate the functional code written by Java and simplified Selenium RC together. We only provide the agent e-commerce website with data API.

After simplifying and integrating Selenium RC as above, the agent e-commerce website transfers parameters to Selenium RC. When receiving the parameters, Selenium RC automatic starts up Chrome. Then Chrome goes to the foreign e-commerce website's logon page and input the user name and password automatically.

If login verification is successful, the page will automatically redirect to the product's source page according to the incoming URL. Selenium automatically inputs the quantity into the corresponding form and confirms the purchase of product. Because of some e-commerce websites need secondary confirmation, the page will redirect to secondary confirmation page and Selenium confirms the purchase of product once again. Then Selenium waits for the result of purchase information. It has been set the maximum waiting time. No matter the purchase succeeds or fails, Selenium always modifies the identification field of the specified table in the agent e-commerce website database. Finally, Selenium automatically closes the browser and all the process is end. During Selenium running, the agent e-commerce website server keeps thread waiting and timing query the identification field of the specified table. Depending on different results, it returns different pages to the agent e-commerce website. In order to avoid deadlock caused by network failure or other reasons, we set the maximum threads waiting time in advance. In that case, the agent e-commerce website would display a specific page. At this point the shopping online function through the agent e-commerce website has been completed and achieved. The key process to realize the proxy shopping online function is shown in Fig. 3.

6 Experiments

What we have done in this paper is based on an agent e-commerce website using SSH framework (Struts, Spring and Hibernate) +Eclipse +MySQL to develop. It is agent for a Japanese e-commerce site to achieve agent shopping online. During the test, we ensure that the bandwidth is as large as possible. Meanwhile, we keep

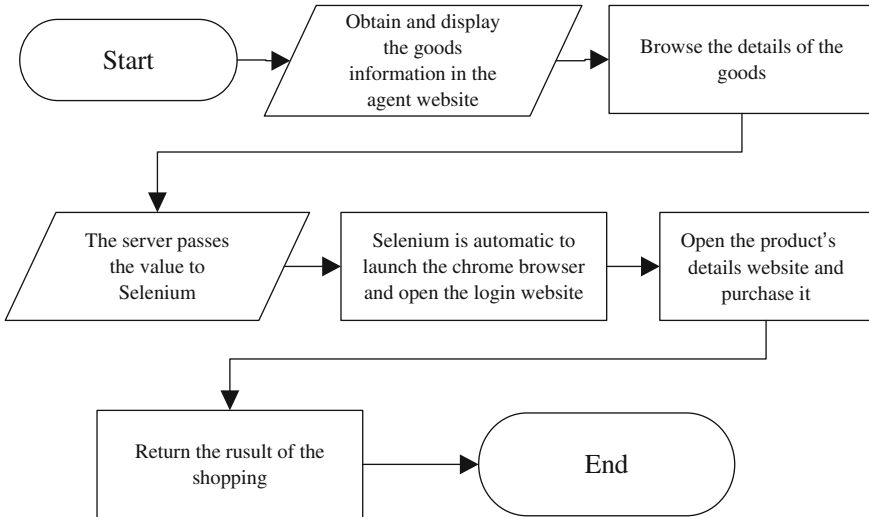


Fig. 3 Agent e-commerce website flow chart

Chrome from loading all multimedia data and unnecessary plug-ins so that Chrome can reduce page load time and improve the agency’s synchronous speed.

Here is the design of framework of agent e-commerce website, as shown in Fig. 4.

First, login the agent e-commerce website and browse some product details. The detail information shown in the page is acquired by data API. It is the same as the source e-commerce website as shown in Fig. 5.

All the information in the above page is English, which has been translated to language designated by auto translating function. Click the purchase button and confirm to submit. The data are transferred to the server. After getting the data, the server queries the database and passes the useful parameters to Selenium. Then selenium opens Chrome. Chrome initialization interface is shown in Fig. 6.

The page redirects to the login page. Selenium inputs the user name and password in the form and submits automatically. The page is shown in Fig. 7.

After a successful login, the page redirects to the source page of product details in e-commerce site. Selenium automatically inputs quantity and confirms the purchase. As shown in Fig. 8.

When Selenium finishes the shopping online, it returns the result to agent e-commerce website server. And the server shows the final result in the browser. At the moment, Chrome has been closed automatically. The agent shopping online is finished.

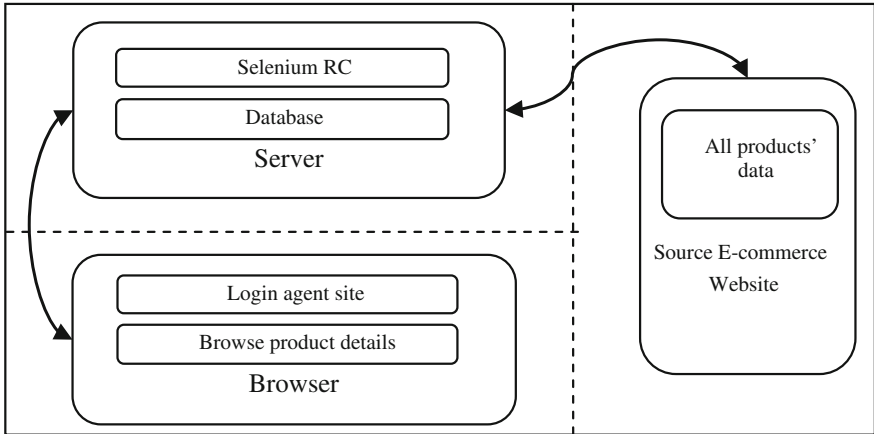


Fig. 4 Framework of agent e-commerce website

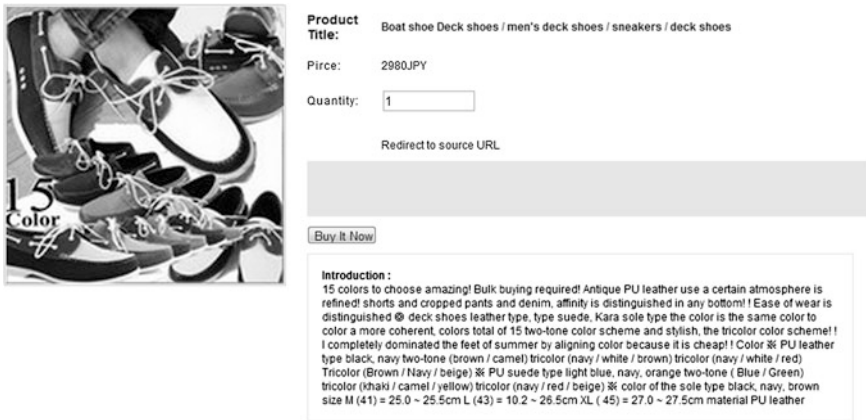


Fig. 5 Product details page in agent website

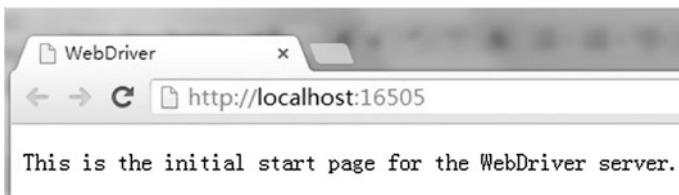
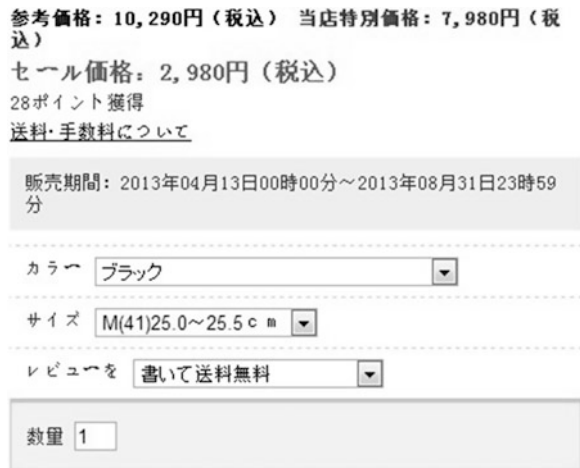


Fig. 6 Selenium starts up chrome

Fig. 7 Login source e-commerce website



Fig. 8 Product details page



7 Conclusion

Based on network agent e-commerce, this paper discusses and integrates the functions of data API, HttpClient, and Selenium and applies them to agent e-commerce website system developed based on SSH framework. As a result, we establish a universal and practical implementation model of agent e-commerce website. This model offers an excellent human-computer interaction experience: the whole process of agency is realized at the server end and front-end interface only shows product information and results of the purchase. In this paper, we give

a glance at Selenium and extend a new use of auto testing tools. The next step of our research will further perfect the model and will also seek new application areas.

References

1. Introducing JSON [EB/OL] (2013). <http://www.json.org>
2. Apache HttpComponents [EB/OL] (2013). <http://hc.apache.org/>
3. Selenium-Web Browser Automation [EB/OL] (2013). <http://docs.seleniumhq.org>
4. Yang Lijing (2011) The design and implementation of web automation test for e-commerce sites. Ocean University of China, Qingdao
5. Ying Wu (2011) Web automation test framework based on selenium. Public Commun Sci Technol 18:187–188
6. Automated acceptance tests using Selenium [EB/OL] (2006) <http://www.ibm.com/developerworks/cn/java/wa-selenium-ajax/>

Singular Optimal Control for Uncertain Systems

Shuhu Sun and Yuanguo Zhu

Abstract If a dynamic system is influenced by uncertain factors, it can be described by an uncertain differential equation. Uncertain optimal control problem is an optimization problem based on uncertain differential equations. For an uncertain optimal control model, if the switching function that determines the values of the control function is consistently zero within a time interval, then the model belongs to a singular case. Inspired by Johnson and Gibson's work, this paper establishes an approach for the solutions of a singular uncertain optimal control model. For a class of uncertain optimal control model where the drift term of the uncertain system and objective function are both linear in control variables, the singular optimal control function may be solved by making use of the fact that the optimal value of the Hamiltonian function is zero in a singular control interval. An example is used to show that the proposed method is efficient.

Keywords Optimal control · Singular · Uncertainty · Differential equation

1 Introduction

Optimal control problem and stochastic optimal control problem have been of great interest for engineers and mathematicians since 1950. Achieving a given task in a shortest possible time or a minimum consummation of fuel has been a major performance criterion for many systems such as rocket vehicles, industrial robots

S. Sun · Y. Zhu (✉)

Department of Applied Mathematics, Nanjing University of Science and Technology,
Nanjing 210094, Jiangsu, China

e-mail: ygzhu@njust.edu.cn

and so on. The optimal controlling of the problem may be a bang-bang or singular control. Many work concentrated on bang-bang or singular control problems, for example [1–7].

In 2007, Liu [8] established uncertainty theory which now is a branch of mathematics for modelling human uncertainty [9]. A fundamental concept in uncertain theory is uncertain measure having normality, self-duality, and countable subadditivity. Based on uncertain variable, uncertain process and canonical process were introduced by Liu [10]. Moreover Liu [11] presented uncertain differential equation. Based on uncertain differential equation, Zhu [12] modelled an uncertain optimal control problem and presented an equation of optimality for solving the problem. In addition, Xu and Zhu [13] dealt with a bang-bang control model for uncertain systems. Now we will introduce an uncertain singular control model in this paper.

2 Preliminary

Some concepts in uncertain theory may be seen in [8]. Let Γ be a nonempty set, and \mathcal{L} be a σ -algebra over Γ . Each element $A \in \mathcal{L}$ is called an event. For any event A , $\mathcal{M}\{A\}$ is a number in $[0, 1]$. The set function \mathcal{M} is called an uncertain measure if it satisfies three axioms: normality, self-duality, and countable subadditivity. An uncertain variable is a measurable function from an uncertainty space $(\Gamma, \mathcal{L}, \mathcal{M})$ to the set R of real numbers. The uncertainty distribution $\Phi: R \rightarrow [0, 1]$ of an uncertain variable ξ is defined by $\Phi(x) = \mathcal{M}\{\xi \leq x\}$ for $x \in R$. The expected value of an uncertain variable ξ is defined by $E[\xi] = \int_0^{+\infty} \mathcal{M}\{\xi \geq r\} dr - \int_{-\infty}^0 \mathcal{M}\{\xi \leq r\} dr$ provided that at least one of the two integrals in finite. The variance of ξ is $V[\xi] = E[(\xi - e)^2]$ if ξ has a finite expected value e . The uncertain variables $\xi_1, \xi_2, \dots, \xi_m$ are said to be independent if $\mathcal{M}\{\bigcap_{i=1}^m (\xi_i \in B_i)\} = \min_{1 \leq i \leq m} \mathcal{M}\{\xi_i \in B_i\}$ for any Borel sets B_1, B_2, \dots, B_m of real numbers. For numbers a and b , $E[a\xi + b\eta] = aE[\xi] + bE[\eta]$ if ξ and η are independent uncertain variables.

Liu [10] introduced the concept of uncertain process. Let K be an index set and $(\Gamma, \mathcal{L}, \mathcal{M})$ an uncertainty space. An uncertain process is a measurable function from $K \times (\Gamma, \mathcal{L}, \mathcal{M})$ to the set of real numbers. An uncertain process X_t is called to have independent increments if $X_{t_0}, X_{t_1} - X_{t_0}, X_{t_2} - X_{t_1}, \dots, X_{t_k} - X_{t_{k-1}}$ are independent uncertain variables for any time t_0, t_1, \dots, t_k with $t_0 < t_1 < \dots < t_k$. An uncertain process X_t is said to have stationary increments if, for any $t > 0$, the increments $X_{s+t} - X_s$ are identically distributed uncertain variables for all $s > 0$. In addition, Liu [11] defined a canonical process C_t which satisfies: (i) $C_0 = 0$ and almost all sample paths are Lipschitz continuous; (ii) C_t has stationary and

independent increments; (iii) every increment $C_{s+t} - C_s$ is a normal uncertain variable with expected value 0 and variance t^2 , denoted by $C_{s+t} - C_s \sim N(0, t)$, whose distribution is

$$\Phi(x) = \left(1 + \exp\left(\frac{-\pi x}{\sqrt{3}t}\right) \right)^{-1}, \quad x \in R.$$

For any partition of closed interval $[a, b]$ with $a = t_1 < t_2 < \dots < t_{k+1} = b$, the mesh is written as $\Delta = \max_{1 \leq i \leq k} |t_{i+1} - t_i|$. Then the uncertain integral of X_t with respect to C_r is

$$\int_a^b X_t dC_t = \lim_{\Delta \rightarrow 0} \sum_{i=1}^k X_{t_i} \cdot (C_{t_{i+1}} - C_{t_i})$$

provided that the limit exists almost surely and is finite. If there exist two uncertain processes μ_t and σ_t such that $Z_t = Z_0 + \int_0^t \mu_s ds + \int_0^t \sigma_s dC_s$ for any $t \geq 0$, then we say Z_t has an uncertain differential $dZ_t = \mu_t dt + \sigma_t dC_t$.

Definition 1 (Liu [11]) Suppose C_r is a canonical process, and f_1 and f_2 are some given functions. Then

$$dX_t = f_1(t, X_t)dt + f_2(t, X_t)dC_t \tag{1}$$

is called an uncertain differential equation.

Chen and Liu [14] proved an existence and uniqueness theorem of solution of uncertain differential equation. If f_1 is a vector-value function, f_2 is a matrix-value function, X_t is an uncertain vector, and C_t is a multi-dimensional uncertain canonical process, then (1) is a system of uncertain differential equations.

Definition 2 (Yao and Chen [15]) Let $\alpha \in (0, 1)$ Uncertain differential equation (1) is said to have an α -path X_t^α if it solves the corresponding ordinary differential equation $dX_t^\alpha = f_1(t, X_t^\alpha)dt + |f_2(t, X_t^\alpha)|\Phi^{-1}(\alpha)dt$ where $\Phi^{-1}(\alpha)$ is the inverse uncertainty distribution of standard normal uncertain variable, i.e., $\Phi^{-1}(\alpha) = \frac{\sqrt{3}}{\pi} \ln \frac{\alpha}{1-\alpha}$.

Theorem 1 (Yao and Chen [15]) Let X_t^z be the solution and α -path of the uncertain differential equation (1), respectively. Then for any $t \geq 0$, we have $M\{X_t \leq X_t^z\} = \alpha$.

3 Model

Consider the following model:

$$\left\{ \begin{array}{l} J(0, x_0) \equiv \max_{\mathbf{u}_s \in [-1, 1]^r} E \left[\int_0^T (\mathbf{X}_s, \mathbf{u}_s, s) ds + h(\mathbf{X}_T, T) \right] \\ \text{subject to} \\ \quad d\mathbf{X}_s = b(\mathbf{X}_s, \mathbf{u}_s, s) ds + L(\mathbf{X}_s, \mathbf{u}_s, s) dC_s \\ \quad \mathbf{X}_0 = \mathbf{x}_0, \end{array} \right. \tag{2}$$

where \mathbf{X}_s is a state vector of dimension n with the initial state $\mathbf{X}_0 = \mathbf{x}_0$ at time 0, \mathbf{u}_s is a decision (control) vector of dimension r taking values in $[-1, 1]^r$, $f: \mathbb{R}^n \times \mathbb{R}^r \times [0, +\infty) \rightarrow \mathbb{R}$ is an objective function, and $h: \mathbb{R}^n \times [0, +\infty) \rightarrow \mathbb{R}$ is a function of terminal reward. In addition, $b: \mathbb{R}^n \times \mathbb{R}^r \times [0, +\infty) \rightarrow \mathbb{R}^n$ is a column-vector function, $L: \mathbb{R}^n \times \mathbb{R}^r \times [0, +\infty) \rightarrow \mathbb{R}^{n \times k}$ a matrix function, and $C_s = (C_{s_1}, C_{s_2}, \dots, C_{s_k})^\tau$, where $C_{s_1}, C_{s_2}, \dots, C_{s_k}$ are independent canonical process. Note that \mathbf{v}^τ is used to denote the transpose of the vector or matrix \mathbf{v} . The final time $T > 0$ is fixed or free.

Definition 3 If there exist $g_i(t, x) (i = 1, 2, \dots, r)$ such that the optimal control of the model (2) is

$$u_i^* = \text{sgn}\{g_i(t, x)\} \text{ or } u_i^* = -\text{sgn}\{g_i(t, x)\}, \quad i = 1, 2, \dots, r,$$

then $g_i(t, x)$ is said to be a switching function for $i = 1, 2, \dots, r$, and the model (2) is a bang-bang control problem.

Definition 4 If there is an interval $[t_1, t_2] (t_1 < t_2)$ such that $g_i(t, x) \equiv 0$ on it, then the control component $u_i(t)$ is singular on $[t_1, t_2]$.

The Hamiltonian function is written by Ge and Zhu [16] for the mode (2) as

$$H(\mathbf{X}_t, \mathbf{u}_t, \psi_t, t) = f(\mathbf{X}_t, \mathbf{u}_t, t) + \psi_t^\tau b(\mathbf{X}_t, \mathbf{u}_t, t) \tag{3}$$

where ψ_t is a vector-valued Lagrange multiplier function.

Theorem 2 (Ge and Zhu [16]) *Let \mathbf{u}_t^* be an optimal control of the model (2) and \mathbf{X}_t^* the corresponding state. If $\nabla_{\mathbf{u}} f(\mathbf{x}, \mathbf{u}, t), \nabla_{\mathbf{x}} b(\mathbf{x}, \mathbf{u}, t)$ and $\nabla_{\mathbf{x}} \sigma(\mathbf{x})$ are bounded, then*

$$\nabla_{\mathbf{u}} H(x_t, \mathbf{u}_t^*, \psi_t, t) = 0 \text{ almost surely,} \tag{4}$$

where at time $t, \mathbf{X}_t^* = \mathbf{x}_t$.

4 Linear Systems in Control Variable

We now consider a special case of the model

$$\left\{ \begin{array}{l} J(0, x_0) \equiv \max_{\mathbf{u}_s \in [-1, 1]^r} E \left[\int_0^T (f(X_s, s) + w(X_s, s)^\tau \mathbf{u}_s) ds + h(X_T, T) \right] \\ \text{subject to} \\ d\mathbf{X}_s = (v(X_s, s) + \beta(X_s, s)\mathbf{u}_s) ds + L(X_s, \mathbf{u}_s, s) dC_s \\ \mathbf{X}_0 = \mathbf{x}_0. \end{array} \right. \quad (5)$$

If the system has the state $\mathbf{X}_t = \mathbf{x}$ at t , the optimal value of the model (5) is denoted by $J(t, \mathbf{x})$.

For the model (5), we have

$$H(\mathbf{X}_s, \mathbf{u}_s, \psi_s, s) = f(\mathbf{X}_s, s) + \psi_s^\tau v(\mathbf{X}_s, s) + (w(\mathbf{X}_s, s)^\tau + \psi_s^\tau \beta(\mathbf{X}_s, s)) \mathbf{u}_s = I + F \mathbf{u}_s \quad (6)$$

where $I = f(\mathbf{X}_s, s) + \psi_s^\tau v(\mathbf{X}_s, s)$ and $F = w(\mathbf{X}_s, s)^\tau + \psi_s^\tau \beta(\mathbf{X}_s, s)$.

Let $J(t, \mathbf{x})$ be twice differentiable on $[0, T] \times R^n$. It follows from the equation of optimality in Xu and Zhu [13] that

$$-J_t(t, \mathbf{x}) = \max_{\mathbf{u}_t \in [-1, 1]^r} \{f(\mathbf{x}, t) + w(\mathbf{x}, t)^\tau \mathbf{u}_t + (v(\mathbf{x}, t) + \beta(\mathbf{x}, t)\mathbf{u}_t)^\tau \nabla_x J(t, \mathbf{x})\}, \quad (7)$$

where $J_t(t, \mathbf{x})$ is the partial derivative of $J(t, \mathbf{x})$ in t , $\nabla_x J(t, \mathbf{x})$ is the gradient of $J(t, \mathbf{x})$ in \mathbf{x} . By the equation (7) we can obtain a sufficient condition such that the model (5) is singular.

Theorem 3 Let $J(t, \mathbf{x})$ be twice differentiable of $[0, T] \times R^n$, and

$$w(\mathbf{x}, t)^\tau + \nabla_x J(t, \mathbf{x})^\tau \beta(\mathbf{x}, t) = 0, \quad \forall t \in (t_1, t_2)$$

where $0 \leq t_1 < t_2 \leq T$. Then the model (5) is singular in (t_1, t_2) .

Proof It follows from (7) that

$$-J_t(t, \mathbf{x}) = \max_{\mathbf{u}_t \in [-1, 1]^r} \{f(\mathbf{x}, t) + w(\mathbf{x}, t)^\tau \mathbf{u}_t + (v(\mathbf{x}, t) + \beta(\mathbf{x}, t)\mathbf{u}_t)^\tau \nabla_x J(t, \mathbf{x})\}. \quad (8)$$

Letting \mathbf{u}_t^* take the optimum in the right side of (8) yields

$$\begin{aligned} & \max_{\mathbf{u}_t \in [-1, 1]^r} \{f(\mathbf{x}, t) + w(\mathbf{x}, t)^\tau \mathbf{u}_t + (v(\mathbf{x}, t) + \beta(\mathbf{x}, t)\mathbf{u}_t)^\tau \nabla_x J(t, \mathbf{x})\} \\ & = f(\mathbf{x}, t) + w(\mathbf{x}, t)^\tau \mathbf{u}_t^* + (v(\mathbf{x}, t) + \beta(\mathbf{x}, t)\mathbf{u}_t^*)^\tau \nabla_x J(t, \mathbf{x}). \end{aligned}$$

We have

$$\max_{\mathbf{u}_t \in [-1, 1]^r} \{w(\mathbf{x}, t)^\tau \mathbf{u}_t + \nabla_{\mathbf{x}} J(t, \mathbf{x})^\tau \beta(\mathbf{x}, t) \mathbf{u}_t\} = w(\mathbf{x}, t)^\tau \mathbf{u}_t^* + \nabla_{\mathbf{x}} J(t, \mathbf{x})^\tau \beta(\mathbf{x}, t) \mathbf{u}_t^*. \tag{9}$$

Denote $\mathbf{u}_t^* = (u_1^*(t), u_2^*(t), \dots, u_r^*(t))^\tau$ and

$$w(\mathbf{x}, t)^\tau + \nabla_{\mathbf{x}} J(t, \mathbf{x})^\tau \beta(\mathbf{x}, t) = (g_1(t, \mathbf{x}), g_2(t, \mathbf{x}), \dots, g_r(t, \mathbf{x})). \tag{10}$$

We have

$$u_i^*(t) = \begin{cases} 1, & \text{if } g_i(t, \mathbf{x}) > 0 \\ -1, & \text{if } g_i(t, \mathbf{x}) < 0 \\ \text{singular,} & \text{if } g_i(t, \mathbf{x}) = 0, t \in (t_1, t_2), \end{cases} \tag{11}$$

for $i = 1, 2, \dots, r$. Thus the model (5) is singular in (t_1, t_2) . □

If the system and objective of the model (5) are explicitly independent of time, the Hamiltonian function may be written as $H(\mathbf{X}_t, \mathbf{u}_t, \psi_t)$, and the model may be rewritten as

$$\left\{ \begin{array}{l} J(0, \mathbf{x}_0) \equiv \max_{\mathbf{u}_s \in [-1, 1]^r} E \left[\int_0^T (f(\mathbf{X}_s) + w(\mathbf{X}_s)^\tau \mathbf{u}_s) ds + h(\mathbf{X}_T) \right] \\ \text{subject to} \\ \quad d\mathbf{X}_s = (v(\mathbf{X}_s) + \beta(\mathbf{X}_s) \mathbf{u}_s) ds + A(\mathbf{X}_s) d\mathbf{C}_s \\ \quad \mathbf{X}_0 = \mathbf{x}_0, \end{array} \right. \tag{12}$$

where $f: \mathbb{R}^n \rightarrow \mathbb{R}$, $w: \mathbb{R}^n \rightarrow \mathbb{R}^r$, $h: \mathbb{R}^n \rightarrow \mathbb{R}$, $v: \mathbb{R}^n \rightarrow \mathbb{R}^n$, $\beta: \mathbb{R}^n \rightarrow \mathbb{R}^{n \times r}$ and $A: \mathbb{R}^n \rightarrow \mathbb{R}^{n \times k}$ are twice differential. In addition, $\mathbf{C}_s = (C_{s_1}, C_{s_2}, \dots, C_{s_k})^\tau$, where $C_{s_1}, C_{s_2}, \dots, C_{s_k}$ are independent canonical process.

Based on the analysis for such type of Hamiltonian function by Johnson and Gibson [3] and Wonham [17], we have $H^*(\mathbf{X}_t, \mathbf{u}_t^*, \psi_t) = 0$, where H^* is the Hamiltonian function with \mathbf{u}_t replaced by the optimal control \mathbf{u}_t^* . Inspired by the Johnson and Gibson’s work [3], in the sequel, we will establish a method to find the optimal control when the model (5) is singular.

We consider the case of $r = 1$ in the model (12). That is, the control variable is of one dimension: $\mathbf{u}_s = u_s$. The Hamiltonian function

$$\begin{aligned} H(X_s, u_s, \psi_s) &= f(X_s) + w(X_s) u_s + \psi_s^\tau (v(X_s) + \beta(X_s) u_s) \\ &= f(X_s) + \psi_s^\tau v(X_s) + [w(X_s) + \psi_s^\tau \beta(X_s)] u_s \end{aligned} \tag{13}$$

where ψ_s satisfies

$$-d\psi_s = \nabla_x H(\mathbf{X}_s, u_s, \psi_s) ds + \psi_s^\tau \nabla_x A(\mathbf{X}_s) dC_s \quad (14)$$

by Ge and Zhu [16]. Thus

$$I = f(\mathbf{X}_s) + \psi_s^\tau v(\mathbf{X}_s), \quad F = w(\mathbf{X}_s) + \psi_s^\tau \beta(\mathbf{X}_s). \quad (15)$$

Theorem 4 For the model (12) (where $r = 1$), we have

$$I(t) = \dot{I}(t) = \ddot{I}(t) = \dots = 0, \quad (16)$$

and

$$F(t) = \dot{F}(t) = \ddot{F}(t) = \dots = 0 \quad (17)$$

in a singular optimal control time interval.

Proof It follows from Theorem 2 that $F(t) = 0$. Thus (17) holds in a singular optimal control time interval. Since the function H is explicitly independent of time, we have $H^*(X_t, u_t^*, \psi_t) = I + Fu^* \equiv 0$ by [17] in a singular optimal control time interval. Hence $I(t) = 0$, and then (16) holds. \square

Remark 1 If there exists a state such that (16) and (17) hold in a time interval, then the model (12) is singular in the interval, and then the optimal control may be derived.

5 Example

Let us consider the following example

$$\left\{ \begin{array}{l} J = \max_u \left[\int_0^T \frac{1}{2} X_2^2(s) ds \right] \\ \text{subject to} \\ \begin{array}{l} dX_1(s) = (2X_1(s) + u(s)) ds \\ dX_2(s) = -(X_2^2(s) + X_1(s) + u(s)) ds + \sigma dC_s \\ |u(s)| \leq 3, 0 \leq s \leq T \end{array} \end{array} \right. \quad (18)$$

where $\sigma > 0$. The Hamiltonian function

$$H = \frac{1}{2}X_2^2 + z_1(2X_1 + u) - z_2(X_2^2 + X_1 + u)$$

where (z_1, z_2) satisfies

$$-d(z_1, z_2) = \nabla_x H^T ds = (2z_1 - z_2, X_2 - 2z_2X_2)ds.$$

Thus

$$I = \frac{1}{2}X_2^2 + 2z_1X_1 - z_2(X_2^2 + X_1), \quad F = z_1 - z_2.$$

We have to test whether the model is singular by the dynamic of the states. The uncertain states of the system may be formed by their α -path (X_1^α, X_2^α) which satisfies

$$\begin{cases} dX_1^\alpha(s) = (2X_1^\alpha(s) + u(s))ds \\ dX_2^\alpha(s) = -\left((X_2^\alpha(s))^2 + X_1^\alpha(s) + u(s)\right)ds + \sigma \Phi^{-1}(\alpha)ds \end{cases} \tag{19}$$

where $\Phi^{-1}(\alpha) = \frac{\sqrt{3}}{\pi} \ln \frac{\alpha}{1-\alpha}, 0 < \alpha < 1$. Corresponding function I is

$$I = \frac{1}{2}(X_2^\alpha)^2 + 2z_1X_1^\alpha - z_2\left((X_2^\alpha)^2 + X_1^\alpha\right).$$

It follows from $I = 0$ that

$$2z_1X_1^\alpha - z_2\left((X_2^\alpha)^2 + X_1^\alpha\right) = -\frac{1}{2}(X_2^\alpha)^2. \tag{20}$$

It follows from $F = 0$ that

$$z_1 = z_2. \tag{21}$$

It follows from $\dot{F} = 0$ that $\dot{z}_1 = \dot{z}_2$. Since $-\dot{z}_1 = 2z_1 - z_2, -\dot{z}_2 = X_2^\alpha - 2z_2X_2^\alpha$, we have

$$2z_1 - z_2 = X_2^\alpha - 2z_2X_2^\alpha. \tag{22}$$

By (20), (21) and (22), we have

$$X_2^\alpha(X_2^\alpha + 2X_1^\alpha) = 0. \tag{23}$$

Therefore, the model (18) is a singular optimal control problem on the trajectory of the state:

$$X_2^\alpha = 0 \quad \text{or} \quad X_2^\alpha + 2X_1^\alpha = 0.$$

On the trajectory $X_2^\alpha = 0$, we obtain the optimal control $u^* = -X_1^\alpha + \sigma\Phi^{-1}(\alpha)$ by (19). On the trajectory $X_2^\alpha + 2X_1^\alpha = 0$, we have $\dot{X}_2^\alpha + 2\dot{X}_1^\alpha = 0$. That is

$$-\left((X_2^\alpha)^2 + X_1^\alpha + u\right) + \sigma\Phi^{-1}(\alpha) + 2(2X_1^\alpha + u) = 0.$$

Thus the optimal control is

$$u^* = -3X_1^\alpha + (X_2^\alpha)^2 - \sigma\Phi^{-1}(\alpha) = 4(X_1^\alpha)^2 - 3X_1^\alpha - \sigma\Phi^{-1}(\alpha).$$

6 Conclusions

In this paper, a singular optimal control model for uncertain systems is established. Specially, a method is introduced to find the control for the model where the system is linear in control variable. An example is considered to show the efficiency of the proposed method.

Acknowledgment This work is supported by the National Natural Science Foundation of China (No. 61273009).

References

1. Balakrishnan AV (1980) On stochastic bang bang control. *Applied Mathematics and Optimization*. 6:91–96
2. Christopheit N, Helmes K (1982) On Benes bang-bang control problem. *Appl Math Optim* 9:163–176
3. Johnson CD, Gibson JE (1963) Singular solutions in problems of optimal control. *IEEE Trans Autom Control* 8:4–15
4. Simaan M (2002) Optimal bang-bang controls for a two-compartment model in cancer chemotherapy. *J Optim Theory Appl* 114:609–637
5. Vakhrameev SA (1997) A bang-bang theorem with a finite number of switchings for nonlinear smooth control system. *J Math Sci* 85:2002–2016
6. Vossen G (2010) Switching time optimization for bang-bang and singular controls. *J Optim Theory Appl* 144:409–429
7. Walsh GR (1972) A numerical example of optimal bang-bang controls. *J Eng Math* 6:165–174
8. Liu B (2007) *Uncertainty theory*, 2nd edn. Springer-Verlag, Berlin

9. Liu B (2010) *Uncertainty theory: a branch of mathematics for modelling human uncertainty*. Springer-Verlag, Berlin
10. Liu B (2008) Fuzzy process, hybrid process and uncertain process. *J Uncertain Syst* 2:3–16
11. Liu B (2009) Some research problems in uncertainty theory. *J Uncertain Syst* 3:3–10
12. Zhu Y (2010) Uncertain optimal control with application to a portfolio selection model. *Cybern Syst Int J* 41:535–547
13. Xu X, Zhu Y (2012) Uncertain bang-bang control for continuous times model. *Cybern Syst Int J* 43:515–527
14. Chen X, Liu B (2010) Existence and uniqueness theorem for uncertain differential equations. *Fuzzy Optim Decis Making* 9:69–81
15. Yao K, Chen X (2013) A numerical method for solving uncertain differential equations. *J Intell Fuzzy Syst* 25:825–832
16. Ge X, Zhu Y (2013) A necessary condition of optimality for uncertain optimal control problem. *Fuzzy Optim Decis Making* 12:41–51
17. Wonham WM (1962) Variational formulation of control problem (Lecture notes). Control and Information System Lab, School of Electrical Engineering, Purdue University, Lafayette, Indiana, p11